Evaluation of Alternative In-Flight Fire Suppressants for Full-Scale Testing in Simulated Aircraft Engine Nacelles and Dry Bays

William L. Grosshandler,
Richard G. Gann and
William M. Pitts, Editors

NIST

United States Department of Commerce

Technology Administration

National Institute of Standards and Technology

April 1994
NIST SP 861

Evaluation of Alternative In-Flight Fire Suppressants for Full-Scale Testing in Simulated Aircraft Engine Nacelles and Dry Bays

William L. Grosshandler,
Richard G. Gann and
William M. Pitts, Editors

NIST

Certain commercial products are identified in this report in order to specify adequately the equipment used. Such identification does not imply recommendation by the National Institute of Standards and Technology, nor does it imply that this equipment is the best available for the purpose.

Building and Fire Research Laboratory
National Institute of Standards
and Technology
Gaithersburg, MD 20899

U.S. Department of Commerce
Ronald H. Brown, Secretary
Technology Administration
Mary L. Good,
Under Secretary for Technology

National Institute of Standards
and Technology
Arati Prabhakar, Director

April 1994

NIST SP 861

National Institute of Standards
and Technology
Special Publication 861
Natl. Inst. Stand. Technol.
Spec. Publ. 861
852 pages (May 1994)
CODEN: NSPUE2

U.S. Government Printing Office
Washington: 1994

For sale by the Superintendent
of Documents
U.S. Government Printing Office
Washington, DC 20402

EXECUTIVE SUMMARY

William L. Grosshandler, Richard G. Gann and William M. Pitts
Building and Fire Research Laboratory

Bromotrifluoromethane (halon 1301 or CF_3Br) has been the fire-fighting agent of choice for decades to protect inaccessible spaces aboard aircraft in flight because of its inherent ability to inhibit combustion while possessing a high liquid density and stability, and low boiling point, electrical conductivity, corrosiveness, toxicity and cost. The bromine atom, which is credited with giving halon 1301 its strong inhibition character, reacts readily in a catalytic cycle to destroy ozone molecules. By international agreement, commercial production of CF_3Br has ceased in order to protect the stratospheric ozone layer. No alternative agents are available which have all the positive characteristics of halon 1301. Hence, there is an urgency to finding a replacement chemical in order to maintain aircraft safety. The affected government agencies and industries have a large stake in minimizing the impact of making a transition because of the potentially huge costs involved and military readiness implications.

The US Air Force, Navy, Army and the Federal Aviation Administration pooled their resources to support a comprehensive 17 month study at NIST to help them select the best chemicals to include in a full-scale fire suppression test program at Wright-Patterson Air Force Base. The sponsors were concerned with two specific applications: protection of commercial and military aircraft engine nacelles, and protection of military aircraft dry bay areas. The engine nacelle is the portion of the airframe which surrounds the main jet engines. In the event of a component failure, fuel and other flammable materials can accumulate, ignite from a hot surface, and threaten the integrity of the nacelle. The fire extinguishers are activated remotely following an alarm signal to the crew. Dry bays are located in the wings and fuselage of the aircraft and vary considerably in geometry. They contain a variety of electronic and mechanical components, and are either adjacent to fuel tanks or have fuel, hydraulic or lubricating fluid lines passing through them. The threat is from an anti-aircraft projectile which ruptures a fuel tank or flammable fluid line, necessitating rapid and automatic detection, agent release and suppression to avoid possible loss of the aircraft.

The specific objectives of the research program are listed below. New metrics have been developed along the way which can be used to rate other fire fighting compounds for a variety of applications.

1. Determine the best two candidates for each application from the following list of gaseous agents provided by the sponsors:

   C_2F_6 (FC-116), C_3F_8 (FC-218), C_4F_{10} (FC-31-10), and cyclo-C_4F_8 (FC-318);

   CH_2F_2 (HFC-32), C_2HF_5 (HFC-125), CH_2F_2 (60%)/C_2HF_5 (40%) (HFC-32/HFC-125), $C_2H_2F_4$ (HFC-134a), C_3HF_7 (HFC-227ea), and $C_3H_2F_6$ (HFC-236fa); and

   CHF_2Cl (HCFC-22), and C_2HF_4Cl (HCFC-124).

2. Identify the best practical alternative from among chemicals not on the list of twelve.

3. Ascertain whether or not sodium bicarbonate powder is a viable option.

The resources of three NIST organizations [the Building and Fire Research Laboratory (BFRL), the Chemical Science and Technology Laboratory (CSTL) and the Materials Science and Engineering Laboratory (MSEL)] were enlisted to conduct the research, involving close to forty NIST staff members. Subcontracts were made to Lawrence Livermore Laboratory, the University of California at San Diego and Yale University in support of the coordinated effort. Tasks were organized around the following topics: thermodynamic properties of alternative agents; fluid dynamics of agent discharge; flame suppression effectiveness; flame inhibition chemistry and the search for additional fire fighting chemicals; agent stability under storage and discharge residue; metals corrosion; elastomer seal compatibility; and human exposure and environmental impact.

New experimental methods were developed to screen the multitude of chemicals in a manner which would allow extrapolation to the full-scale test. The agents were rated according to their following innate physical properties which are independent of the release mechanism or performance in the fire, with the desired magnitude given in parentheses: saturation liquid density {high}, normal boiling point {low}, thermal expansion {low}, thermal stability {high}, solubility of nitrogen in agent {low}, atmospheric lifetime {short}, agent residue {low}, corrosion of metals {low}, swelling of polymers {low} and durability of elastomers and greases {high}. The performance criteria for evaluating fire suppression effectiveness were the concentrations {low} necessary to extinguish a laminar opposed-flow diffusion flame (OFDF), a small pool fire (cup burner), a turbulent spray flame, a high speed premixed deflagration, and the amount of acid gases (HF and HCl) formed during the suppression process. Discharge performance was evaluated from the time required {short} for the agent to be discharged, dispersed, mixed and evaporated upon sudden release at high pressure. Agent toxicity and potential exposure to humans was also rated on a relative basis. The likely availability of an alternative (and indirectly, its cost) were important considerations as well because the Air Force testing schedule dictated that enough be available for them to perform a full-scale test matrix in 1994, and to begin installing the agent in the fleet beginning in 1996.

The research uncovered deficiencies in a number of compounds which were of enough concern to recommend against testing them in the full-scale test program. FC-116 required the largest storage volume of the twelve agents on the original list. This is because its critical temperature is only 20 °C, leading to uncertainty in the design of the storage vessel and the rate at which material could be discharged. The mixture of HFC-32 and HFC-125 required the second highest storage volume; and in addition, high over-pressures in the detonation/deflagration tube were experienced. HFC-236fa could not be recommended for the present aircraft applications because it has the highest boiling point and is the most difficult to vaporize at the low temperatures which are likely to be encountered. FC-318 and FC-31-10 also suffer from high boiling points and poor evaporation. In addition they are compatible with fewer materials and have very long atmospheric lifetimes. The HCFC-22 was compatible with the fewest materials, and has the highest ODP of the core agents evaluated.

The positive attributes of an agent needed to suppress one kind of fire are not necessarily the same needed to suppress a different kind of fire. As a result, a different set of recommendations is made for the simulated full-scale engine nacelle and dry bay testing. HCFC-124 required the least amount of material to extinguish the nonpremixed flames and HFC-125 vaporizes well at low temperatures; both are recommended for testing in the engine nacelle. FC-218 is recommended as the first alternate. The most efficient agent of all is the sodium bicarbonate powder. A partial full-scale test matrix is recommended to determine if possible operational difficulties can be overcome. One additional gaseous candidate was identified that was more effective than halon 1301 in suppressing the

nonpremixed flames, iodotrifluoromethane (CF_3I). It is recommended that it also be included in the engine nacelle test program, but limited availability may prevent the test matrix from being completed. Atmospheric chemistry, stability, compatibility and toxicity testing is still underway, so that the recommendation for full-scale testing of CF_3I comes with a caution.

The primary candidate for simulated full-scale dry bay testing is FC-218. It vaporizes relatively easily, which is critical for quickly dispersing the agent through the dry bay in cold weather, and is relatively effective in attenuating shock wave pressure and speed in the premixed closed tube experiments. HFC-125 should also perform well in cold weather, and is the second recommended candidate for dry bay testing. However, high over-pressures were noticed in the premixed closed tube experiments. Should these occur during full-scale tests, HFC-227ea is recommended as a back-up. Sodium bicarbonate is not recommended for this application because, as a powder, rapid dispersion is hindered by clutter within the dry bay. The CF_3I suppressed the premixed flame at lower concentrations than the other agents, but was not as effective as halon 1301. A partial test matrix is recommended for CF_3I, with the previously mentioned precautions holding.

Details of all aspects of the research program are provided in different sections of this special publication. The rationale for arriving at critical conclusions and the scientific basis supporting the above recommendations are discussed. A significant amount of resources went into selecting the best candidates for full-scale evaluation, and work is continuing at NIST to determine long term compatibility of the recommended agents with metals and polymers. A method for predicting the acid gases produced when alternative agents pass through the fire is under development, parameters which can increase the effectiveness of the agents by optimizing their release are being investigated, and techniques are being developed for measuring the concentration of the agent once it is discharged.

TABLE OF CONTENTS

Page

Page

Page

Page

Page

Page

Page

ACKNOWLEDGMENTS

The contributors to this Special Publication were many. Specific authorship is indicated at the beginning of each major section, and is acknowledged here in alphabetical order: Mr. Carlos Beauchamp, Mr. Emil Braun, Mr. Brett Breuel, Dr. Donald Burgess, Mr. Thomas Cleary, Mr. William Cleveland, Dr. Leonard Cooper, Mr. James Dante, Mr. James Fink, Dr. Glenn Forney, Dr. Richard Gann, Prof. Grzegorz Gmurczyk, Dr. William Grosshandler, Dr. Anthony Hamins, Mr. Richard H. Harris, Jr., Dr. Ferenc Horkay, Dr. Barbara Levin, Dr. Gregory Linteris, Dr. Gregory McKenna, Dr. Thomas Moffat, Dr. George Mulholland, Dr. Marc Nyden, Mr. Richard Peacock, Dr. Cary Presser, Dr. William Pitts, Mr. R. Gregory Rehwoldt, Dr. Richard Ricker, Prof. Kalyanasundaram Seshadri, Mr. Mark Stoudt, Dr. Wing Tsang, Ms. Isaura Vazquez, Dr. William Waldron, Jr., Prof. Phillip Westmoreland, Dr. Jiann Yang, and Dr. Michael Zachariah.

A number of additional NIST staff played critical roles in support of the large number of research activities. These include Mr. James Allen, Mr. Michael Glover, Dr. Robert Huie, Mr. Darren Lowe, Mr. William Rinkinen and Dr. Kermit Smyth. The assistance of Ms. Paula Garrett in organizing and editing the final report is gratefully acknowledged.

The research described in this publication was supported by the following agencies of the federal government:

Wright Laboratory
Flight Dynamics Directorate
Vehicle Subsystems Division
Survivability Enhancement Branch
Mr. Michael Bennett

Naval Air Systems Command
Subsystems Branch
Fuel and Fluid Power Systems Section
Mr. James Homan

Army Aviation and Troop Command
Mr. Daniel McEneany

Department of Transportation
Federal Aviation Administration
Technical Center
Mr. Larry Curran

In addition to the program managers listed above, the authors wish to acknowledge the active role played by the staff of each of the sponsors: Lt. Kurt Lee, Lt. Gretchen Brockfeld, Capt. Rene Little and Maj. Samuel Carbaugh of the U.S. Air Force; Mr. David Thurston, of the U.S. Navy ; Mr. C.P. Sarkos and Ms. Louise C. Speitel of the Federal Aviation Administration. All helped ensure that the research remained appropriately focused and timely.

Special mention is in order of the tireless effort maintained by Mr. Bennett of Wright Laboratory, who coordinated this cross-services effort from concept to completion. His skills as a manager, engineer and visionary were all tapped, and each was equally essential to the success of the project. The assistance provided by Lt. Gregg Caggianelli and Lt. Brett Poole on the details of the operation of the Aircraft Engine Nacelle Test Facility and the Aircraft Survivability Research Facility are gratefully acknowledged.

To make a significant contribution to a problem as complex as aircraft fire suppression in so short a period of time required the cooperation of the airframe makers, equipment manufacturers and chemical suppliers. The information and assistance provided by the following companies was appreciated and is hereby acknowledged: Pacific Scientific, Systron-Donner and Walter Kidde

Aerospace; McDonnell Douglas, Lockheed, and Boeing; Allied Signal, E.I. DuPont, Great Lakes Chemical, PCR and 3M.

Interactions with researchers in other laboratories were essential to obtain additional insight and to avoid wasteful duplications of effort. Dr. Don Wuebbles of Lawrence Livermore Laboratories provided key calculations on stratospheric ozone depletion; Dr. Andrezej Miziolek of the Army Research Laboratory, Dr. Ronald Sheinson of the Naval Research Laboratory and Dr. Thomas Jackson of Wright Laboratory were involved in numerous technical discussions; Dr. Carl Melius of Sandia Laboratory and Prof. Mitch Smooke of Yale University provided critical data and numerical calculations for the kinetics study. The contributions of all these scientists and engineers are acknowledged.

1. INTRODUCTION

William L. Grosshandler, Richard G. Gann, William M. Pitts
Building and Fire Research Laboratory

1.1 Background

1.1.1 Halons and the Ozone Layer. The Montreal Protocol of 1987 identified halon 1301 (CF_3Br) as one of a number of halogenated chemicals that were sufficiently deleterious to stratospheric ozone that their continued production and use required limitation. An amendment to the Protocol caused commercial halon production to cease at the beginning of 1994 (Harrington, 1993). The focus of concern is that the halon molecule is sufficiently stable in the lower atmosphere that it will eventually be transported to the stratosphere unaltered. There the carbon-bromine bond is vulnerable to photodissociation by solar ultraviolet radiation. The liberated bromine atom then enters into a catalytic cycle which has the net effect of consuming the shielding ozone.

Much has been written in the scientific and popular literature on how bromine and chlorine atoms lead to depletion of the ozone layer. Conferences are held annually (*e.g., The 1993 International CFC and Halon Alternatives Conference*, 1993; *Halon Alternatives Technical Working Conference*, 1993) to discuss progress in finding replacements for technologically important ozone depleting chemicals. An exhaustive study of the atmospheric chemistry of fluorinated compounds being considered as alternatives to halons and chlorofluorocarbons (CFCs) was commissioned by the World Meteorological Organization (1989). Background on the halon/ozone issue is also provided by Andersen (1987) and Grant (1989). Additional articles are cited in the report by Pitts *et al.* (1990).

Ford (1975) has traced the development of CF_3Br for firefighting purposes since its original formulation in the 1940s. Halon 1301 has been the agent of choice for fire suppression on board aircraft for decades because of its inherent ability to inhibit flames at low concentrations while exhibiting a number of additional strongly positive attributes, including a high level of stability, high liquid density, low boiling point, low electrical conductivity, low corrosiveness, low toxicity, and low cost. These properties are desirable for many applications, but the penalty placed upon excessive weight or volume on board commercial and military aircraft tightly constrains the choices of suitable alternatives.

The elimination of new production of halon 1301 has forced the manufacturers, owners, and users of aircraft to search for an alternative. Since it may take years to retrofit the large fleet of current aircraft, there is an urgency to identify one or more chemicals soon. The retrofit process will likely be expensive. The bromine atom in halon 1301 which is responsible for the ozone destruction is also largely responsible for the molecule's high fire suppression effectiveness. If the alternative chemicals do not contain a moiety like bromine and are less efficient suppressants, then new, larger agent storage and delivery components will need to be designed. To avoid costly design mistakes, extensive performance data regarding the amount of agent required for flame extinction and the compatibility of the alternatives with the delivery system and aircraft construction materials is essential.

1.1.2 Aircraft Engine Nacelles and Dry Bays. There are a number of distinct areas in need of protection against an in-flight fire in an airplane, including the cockpit, passenger compartment, baggage areas, auxiliary power units, fuel tank ullages, engine nacelles, and dry bays. The research

program described in this publication focussed on the latter two. The requirements and constraints of the engine nacelle and dry bay areas are quite different, and the methods used to arrive at the best choice for an alternative to halon 1301 for each application differ accordingly.

The engine nacelle is the portion of the airframe which surrounds the main jet engines. It varies in shape and size but is typically annular with a length and diameter of the same order as the engine it encases. Fuel and hydraulic lines, pumps and lubrication systems are located within the nacelle volume. Ventilation is provided to prevent the build-up of combustible vapors, and drain holes on the underside are used to reduce the amount of fluid that could pool following a leak. The engine's combustion chamber liner is isolated from the nacelle wall, but surface temperatures up to 700 °C can exist during operational extremes. The firefighting agent can be located directly adjacent to the nacelle or removed by tens of meters and piped to the fire zone, depending upon the availability of space. An example of a nacelle and fire suppression system is shown schematically in Figure 1.

The operational requirements for commercial and military engine nacelle protection are similar. Thermal sensors are used to determine when an abnormal, overheated condition exists in the nacelle region. In such a case, the flight of the airplane is leveled and the designated crew member arms the appropriate halon 1301 bottle and fires the release mechanism. The halon is stored at pressures in the range of 2 to 4 MPa, and the certification process requires that enough agent be available to maintain a minimum concentration (about 6% by volume) throughout the nacelle for a minimum time interval (about 0.5 s) to ensure that the fire will be extinguished and not relight. Many systems have a duplicate bottle to be used as a back-up should the first shot be unsuccessful.

Dry bays refer to normally closed spaces, often adjacent to flammable liquid storage areas and in which a combustible mixture and an ignition source could co-exist following penetration by an anti-aircraft projectile. The fire threat is unique to military aircraft. Dry bays vary considerably in volume, typically being in the range of 0.2 to 3.0 m^3. They are located in the wings and fuselage, and their shape is most often irregular, as can be seen in Figure 2. Aspect ratios up to 10:1 are not uncommon. The bays may or may not be ventilated, and are usually cluttered with electronic, hydraulic and mechanical components. Compared to the events leading to engine nacelle fire suppression, the required timing is two orders-of-magnitude faster for dry bay protection. High speed infrared detectors sense the initial penetration of the projectile and automatically arm and fire the halon bottle. The storage bottles are located directly in or adjacent to the protected space to minimize the time needed to flood the volume totally. The entire suppression sequence occurs in less than 100 ms and requires no crew intervention.

1.1.3 Full-scale Simulations. Fire suppression is affected by a combination of the agent's physical properties, chemistry and transport phenomena, making it a highly nonlinear process and difficult to scale. Full-scale tests are needed to extend bench-scale experiments and validate theoretical models before aircraft safety systems can be reliably designed. The Survivability Enhancement Branch of Wright Laboratory, located at Wright-Patterson Air Force Base, Ohio, operates unique full-scale aircraft engine nacelle and dry bay fire test facilities. How these facilities are to be used to identify the best near-term alternative to halon 1301 is outlined by Bennett (1992). The Design of Experiments (DOX) methodology which has been adopted allows the minimum number of full-scale tests to have the maximum impact on identifying the critical parameters which influence an engine nacelle or dry bay fire. The range of parameters chosen was determined by the Air Force after surveying existing military aircraft manufacturers and users (Mascarella, 1993).

The Aircraft Survivability Research Facility (ASRF) at Wright-Patterson AFB consists of a gun range in which an anti-aircraft round can be directed at a precise location in a full-size test article in a repeatable, controlled manner while maintaining the safety of the operating personnel. Rectangular boxes with internal volumes between 0.28 and 2.8 m^3 have been used to simulate actual aircraft dry

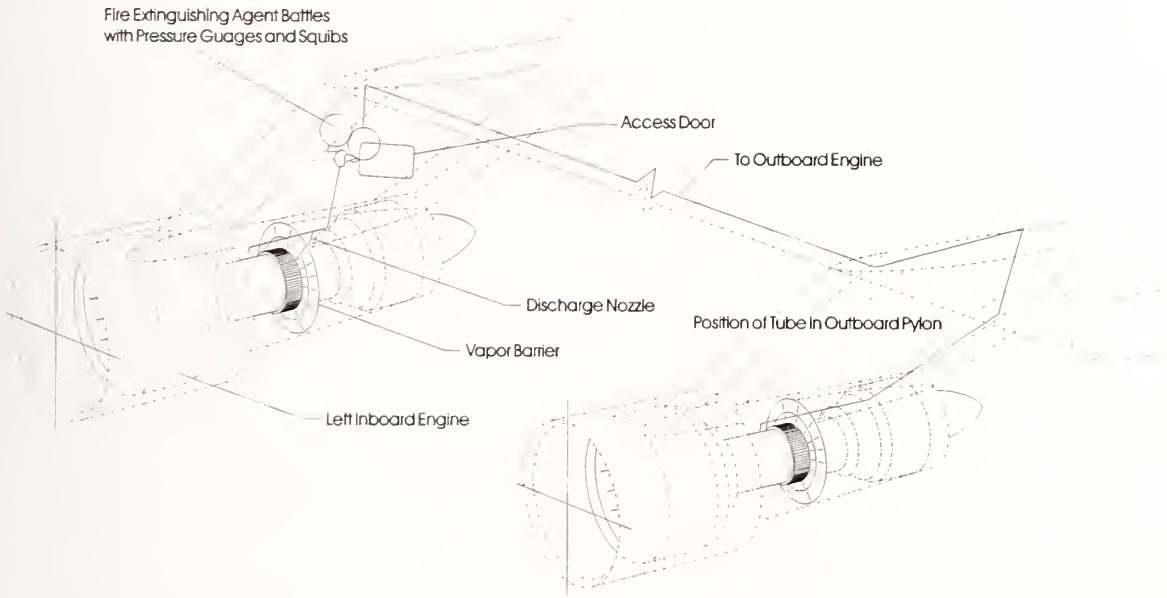

Figure 1. Schematic diagram of wing-mounted engine nacelle and fire extinguishing system (based upon C5-A and provided by M.L. Kolleck, Booz-Allen & Hamilton, Inc.).

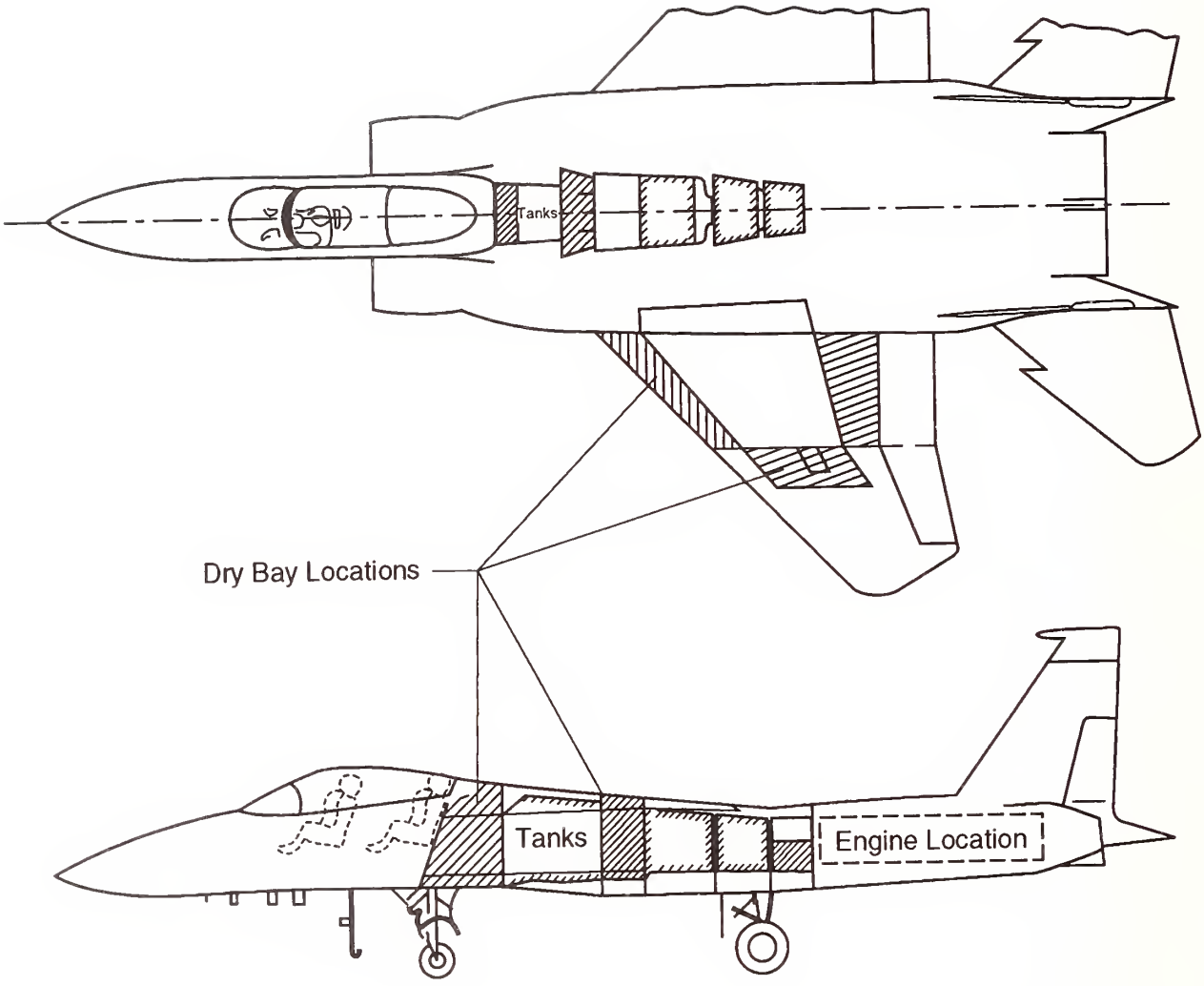

Figure 2. Schematic diagram of typical dry bays in an aircraft (taken from Figure 1 of Heinonen *et al.*, 1990).

bays. A fuel tank is located behind the dry bay so that it will rupture following the impact of a fired projectile. Dry bay geometry (aspect ratio), internal obstructions, location and timing of the release of the firefighting agent, the type and amount of fuel released, and the characteristics of the projectile are some of the parameters which can be varied. Jet engine exhaust streams can be directed past the test article to simulate the high speed flows experienced in flight. A typical test article is shown in Figure 3.

The Aircraft Engine Nacelle (AEN) facility (Figure 4) was designed to simulate a 120° arc segment of a full size engine nacelle. The air flow, air temperature, and air pressure can be varied to cover the range experienced by an actual aircraft in flight. A fire from a fuel spray or ruptured hydraulic fluid line can be simulated, and the amount of clutter, location and timing of agent injection, and hot-surface temperature are some of the parameters which can be precisely controlled. The AEN is used to determine the amount of agent necessary to extinguish a realistic engine nacelle fire, and can compare the relative effectiveness of two different agents in suppressing a nearly identical fire. A full 360° simulated engine nacelle with adjustable diameter core is a new addition to the facility.

1.1.4 Agents Selected for Screening. In a study by Pitts *et al.* (1990), an exploratory list of over 100 possible halon alternatives was constructed. These included both high boiling point and low boiling point compounds for replacements of halon 1211 and halon 1301, respectively. The chemicals embodied a range of chemical and physical principles thought to affect flame suppression capability. Examination of these chemicals, then, provides a basis for the search for alternatives to the current commercial halons. This list included the following classes of compounds:

- saturated and unsaturated halocarbons,
- halogenated hydrocarbons containing single and double-bonded oxygen,
- sulfur halides,
- phosphorous compounds,
- silicon and germanium compounds,
- metallic compounds, and
- inert gases.

Zallen (1992) reviewed past investigations of firefighting agents, starting with the seminal work by Purdue University (1950). In that early investigation, the concentrations necessary to inhibit a mixture of heptane and air from igniting were tabulated for over 50 chemicals. An objective was to identify general purpose agents which were effective, clean, stable and less toxic than CCl_4. A large number of halocarbons were scrutinized, along with a few compounds containing sulfur, phosphorous and silicon. Zallen (1992) summarized the extensive work done by the U.S. Navy (*e.g.*, Sheinson *et al.*, 1989) and the New Mexico Engineering Research Institute (*e.g.*, Tapscott *et al.*, 1990) for ship-board and ground-based aircraft fire suppression, respectively, before arriving at his recommendations to the U.S. Air Force for their in-flight applications. An important consideration was the likely availability of the chemical in large quantities for full-scale testing in 1994, and fleet installation by 1996.

Zallen recommended four perfluorocarbons (FCs), six hydrofluorocarbons (HFCs), and two hydrochlorofluorocarbons (HCFCs). The core candidate compounds actually selected by the Air Force for screening are shown in Table 1. Several compounds in the table were not on Zallen's list: a 60%/40% mixture by mass of HFC-32 and HFC-125, sodium bicarbonate powder, and HFC-236fa. The HFC-32/125 mixture and sodium bicarbonate were added by the Air Force; HFC-236fa was added following a press release soliciting additional chemicals that met the criteria discussed above

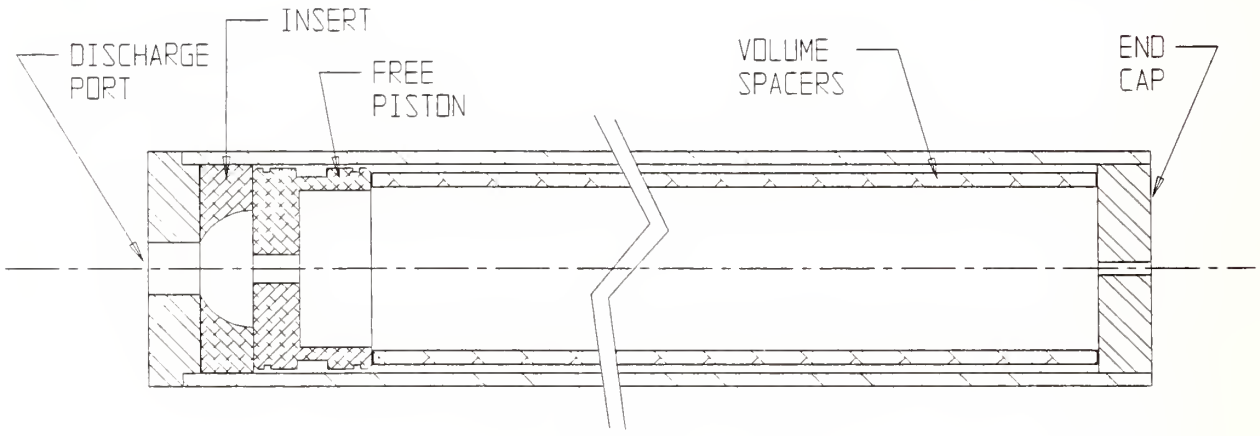

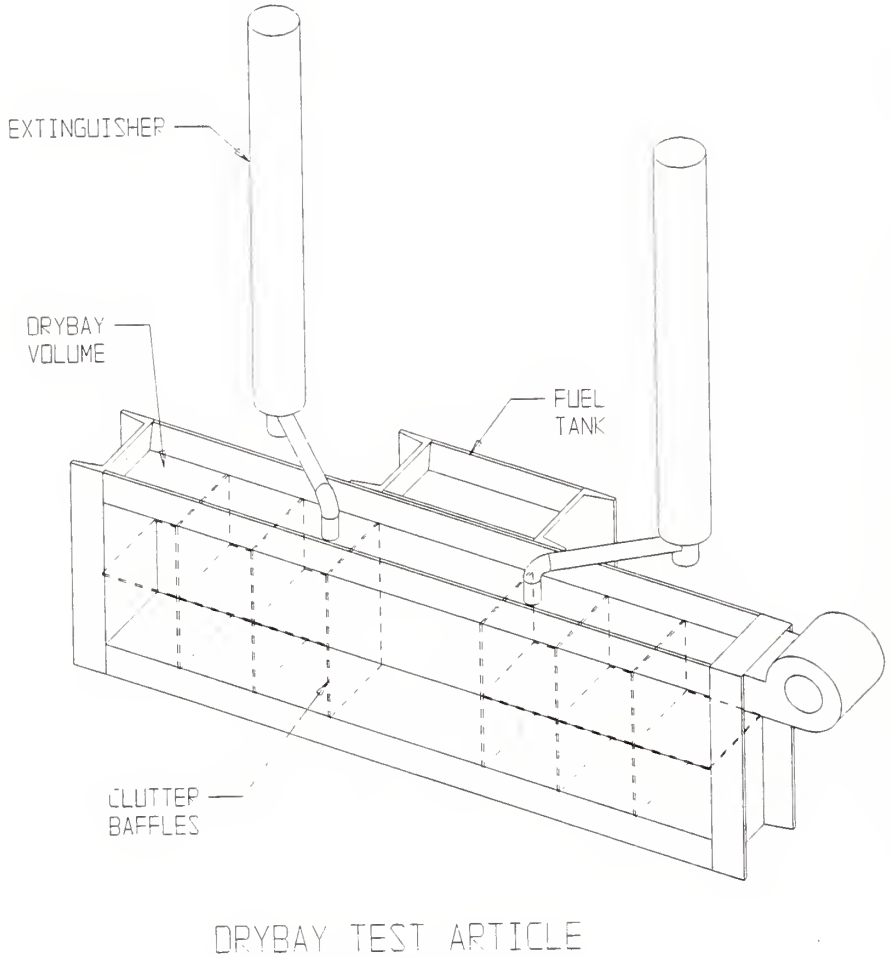

Figure 3. Example of test article used in live-fire dry bay simulator at WPAFB Aircraft Survivability Research Facility (provided by B. Poole, WPAFB).

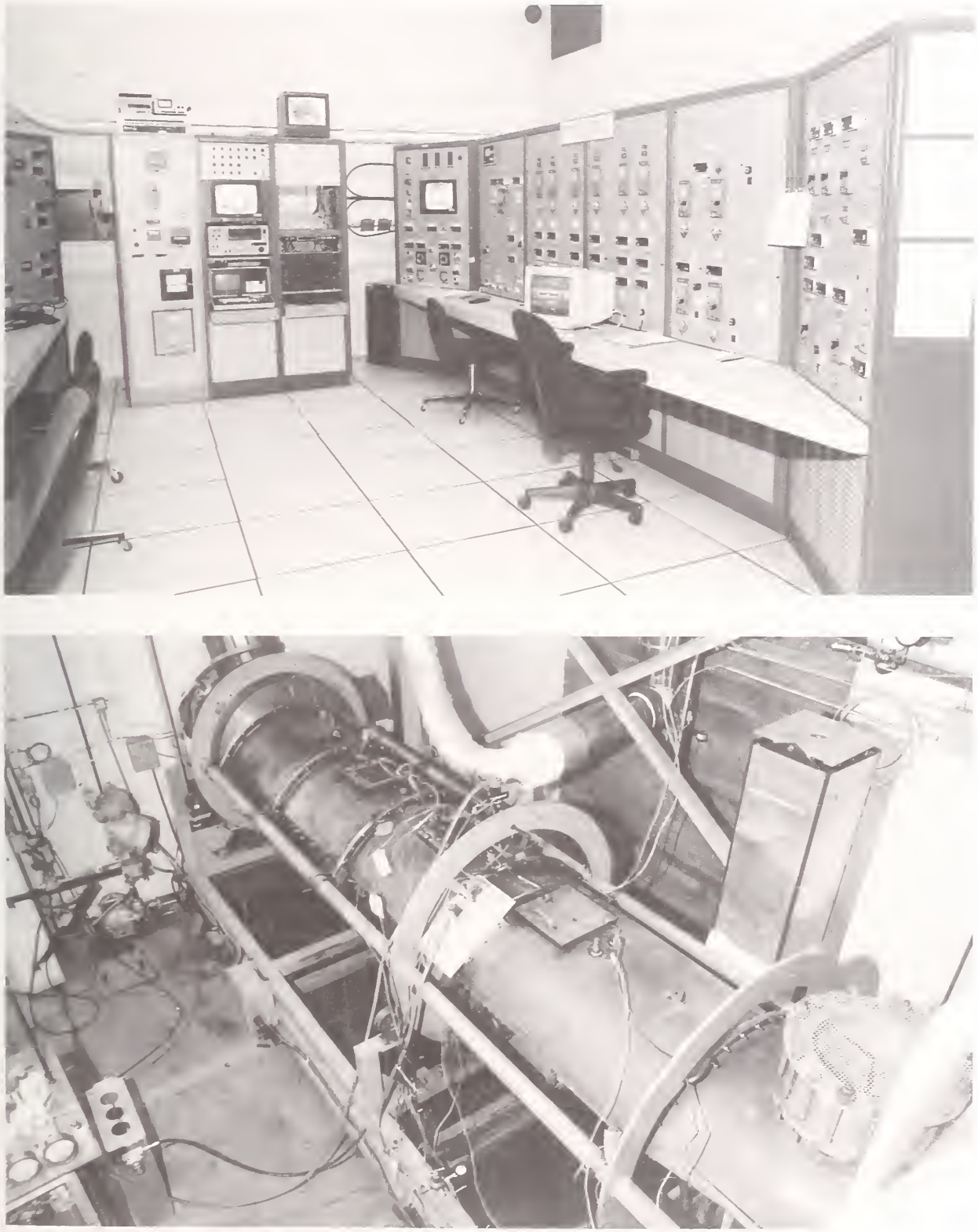

Figure 4. Aircraft Engine Nacelle test facility at WPAFB (provided by G. Caggianelli, WPAFB).

Table 1. Core chemicals examined

Chemical Formula	Designation	IUPAC Name
C_2F_6	FC-116	hexafluoroethane
C_3F_8	FC-218	octafluoropropane
C_4F_{10}	FC-31-10	decafluorobutane
cyclo-C_4F_8	FC-318	octafluorocyclobutane
CH_2F_2	HFC-32	difluoromethane
C_2HF_5	HFC-125	pentafluoroethane
CH_2F_2 (60%)/C_2HF_5 (40%)	HFC-32/125 (60/40)	-
$C_2H_2F_4$	HFC-134a	1,1,1,2-tetrafluoroethane
C_3HF_7	HFC-227ea	1,1,1,2,3,3,3-heptafluoropropane
$C_3H_2F_6$	HFC-236fa	1,1,1,3,3,3-hexafluoropropane
CHF_2Cl	HCFC-22	chlorodifluoromethane
C_2HF_4Cl	HCFC-124	2-chloro-1,1,1,2-tetrafluoroethane
$NaHCO_3/SiO_2$ (1%)	-	sodium bicarbonate/silicon dioxide

(Kosko, 1993). On Zallen's list but not included among the core candidates were HFC-23 and HFC-143a. HFC-32 was dropped early in the NIST research program because testing confirmed that it was flammable at concentrations likely to be encountered. A full test program was therefore carried out for eleven gaseous potential alternatives and sodium bicarbonate.

1.2 Objectives and Task Summary

This research program began in 1992, funded jointly by the Air Force, Army, Navy and the Federal Aviation Administration because of their mutual interest in aircraft safety. The program entailed:

- establishing a comprehensive experimental program to screen the performance of the agents listed in Table 1, plus other promising chemicals, as a means to identify the best candidates for subsequent full-scale aircraft fire extinguishment evaluation at Wright Laboratory; and

- addressing the compatibility of these agents with flight systems, people, and the environment.

Based on these data, three candidates for each of the two applications (dry bay and engine nacelle) were to be recommended for full-scale evaluation at Wright-Patterson AFB. These did not need to be the same sets. Ideally, each set would include the top two candidates from Table 1.

If the search for additional chemicals uncovered other promising candidates, then the best of these was to be recommended for full-scale testing as well. Otherwise, a third chemical from Table 1 would be identified. These recommendations were to be presented to the sponsors in September, 1993. Following the sponsors' selection of chemicals for full-scale testing, longer-term compatibility experiments to increase confidence in the preliminary results were to continue, with a report on that phase of the research to be delivered by September 30, 1995.

Sections 2-9 of the current report document the research activities related to the fire fighting effectiveness of possible alternatives, and research activities dealing with various aspects of the agents' compatibility with aircraft construction materials and associated systems. Establishing a scientific basis upon which to choose the best alternatives has been an overriding objective of the program. The facilities developed and knowledge gained in meeting this objective go well beyond the specific applications to aircraft, and advance fire suppression technology in general. A summary of the major conclusions are given and significant recommendations are highlighted in Section 10.

In the course of searching for alternative agents and in developing these facilities, certain products were used and are identified by trade name in this report to adequately document the research performed. Such identification does not imply recommendation by the National Institute of Standards and Technology, nor does it imply that this commercial equipment is the best available for the purpose intended.

1.2.1 Fire Suppression Effectiveness Screening. Because of storage weight and volume constraints, the new suppressant should demonstrate optimal efficiency for quenching flames. The thermodynamic state, transport properties, and combustion chemistry of an agent are critical to this ability. An experimental design was chosen that allowed these three aspects of the different agents to be examined under conditions which isolated the influence of the many independent parameters. Considerable thought was given to the most appropriate means to relate the results of the individual tests to overall performance criteria. The uncertainty in each experiment was estimated by replication when appropriate. In other cases, analogy to similar experimental procedures, experience with related test methods, and theoretical calculations were used to establish error limits.

The thermodynamic state of a pure substance is defined by its density over a range of pressures and temperatures. In mixtures, the solubility of one material into another influences the state as well. Quantitative thermodynamic state relations are incomplete for many of the pure alternative agents, and very little data on the solubility of pressurizing gases into the liquid agent existed at the start of this investigation. An objective of this task was to measure the pressure of the agent at -60 °C, 25 °C and 150 °C in a constant volume vessel, with the agent pure and in mixtures with CHF_3 and N_2. The temperatures chosen span the maximum anticipated range of exposure of a storage bottle in the field. The solubility of the pressurizing gas was measured at room temperature and 4 MPa, a typical halon 1301 bottle pressure. Section 2 presents the results of the thermodynamic study.

The release and delivery of the agent is particularly critical for dry bay protection, where events leading to a threatening over-pressure occur in less than 50 ms. The behavior of the agent during conditions of vessel blow-down and the characterization of the dispersion, mixing and evaporation of the resulting two-phase turbulent jet are the objects of investigation in Section 3.

Four different flame suppression experimental facilities were designed with the objective of examining the flame extinction properties of the agents over the whole range of conditions likely to be encountered by aircraft in flight. The facilities, briefly mentioned in the following paragraphs, are described and the suppression concentrations are tabulated in Section 4.

The first suppression facility, an opposed-flow diffusion flame (OFDF) burner, is an excellent test-bench for evaluating an agent's extinguishing efficiency over a broad range of flame conditions. The reasons for this are five-fold:

1. the geometry of the flow is eliminated as variables in the system;

2. the flow field strain rate is an independent variable;

3. the system is steady, one-dimensional, and accessible to probing;

4. the reactant flow rates are relatively small, enabling extensive testing with limited quantities of chemicals; and

5. the concentrations and temperatures of the agent, fuel, and oxidizer are easily controlled and repeatable.

Cup burner measurements, which have been relied upon almost exclusively in the past to determine suppression concentrations, were made in the second facility and compared to the OFDF results. The cup burner is also flexible, and was used to assess the impact of multiple fuels on the ability of all the agents, including the sodium bicarbonate powder, to suppress the flames.

In the third facility, a turbulent spray burner was built to simulate a fire created by a ruptured fuel or hydraulic fluid line in an engine nacelle, or the splash of fuel into a dry bay. This is because threatening fires are invariably turbulent, and the turbulence influences the mixing of the fuel and air, the heat released, and the products of combustion. The amount of agent (gaseous or powder) and the rate of injection were independent parameters which could be controlled with this facility.

The speed of an accelerating turbulent flame near the detonation limit can reach magnitudes two orders higher than that of the spray flame. The interaction of the agent with a detonation could not be predicted from the other flame results. Thus, a detonation tube (the fourth facility) was used to simulate the threat posed by an impending explosion. The reduction in velocity and pressure build-up of the high speed, turbulent flame was used as a quantitative measure of the agent's effectiveness in suppressing the detonation.

Significant improvements to suppression performance are likely to occur only if the agent is able to inhibit key chain-branching reactions in the combustion process. It would be beneficial to understand the mechanisms by which alternative agents extinguish a flame. If such chemical intervention were possible with materials that were tailored to degrade before threatening the atmosphere, then additional environmental constraints might be overcome, and opportunities for enhancing the performance of advanced aircraft through the reduction in bulk of the onboard fire suppression system might exist. To assist in gaining the objective of superior chemical inhibition, the elementary reactions of different classes of chemicals were examined, and a partial understanding of how the molecular structure influences the suppression process and the atmospheric reactivity of the neat agent was obtained. Section 5 outlines the progress made to date on the kinetics of fluorine inhibited flames and possible routes to acid gas formation. Alternative chemicals beyond the core list from Table 1 are discussed, with the rationale for choosing them and our current assessment of their potential. The development of an understanding of the acid gas formation process is ongoing, and a method of estimating the amount formed during suppression of a given fire threat will be provided in the September, 1995 report.

1.2.2 Compatibility with Systems and People. A desirable suppressant also needs to have minimal harmful interactions with aircraft materials, people, and the environment. A set of tasks were designed to provide essential data on the stability of the chemicals, compatibility of the chemicals and their by-products with both metallic and polymeric materials, and definition of possible limitations for exposure of people and the environment. The approach followed from an earlier study (Gann *et al.*, 1990), in which preliminary screening procedures and criteria were developed for the **general** evaluation of alternatives to both halons 1211 and 1301. The advanced procedures developed here are more directly applicable to the conditions in engine nacelles and dry bays.

The compatibility studies covered a range of storage conditions. Based on information supplied by the Air Force, it was presumed that the agent storage would be initially at 25 °C and 4.1 MPa. In flight, these could rise to 150 °C and 5.8 MPa. Thus, the stability of a chemical and its potential damage to the storage vessel were examined under these conditions. Lower temperatures and pressures are also possible in service. However, lesser damage would occur under these conditions, and we deemed reduced temperature measurements unnecessary.

At present, the storage times on board aircraft are of the order of five years. In order to enable a selection of the most promising chemicals by the September 30, 1993 deadline, only much shorter exposures were possible. Phenomenological modeling, based on exposures at various time intervals, has been pursued to increase confidence in the extrapolation to longer times. Were severe non-linear effects observed for some chemicals, NIST would recommend against their use or would suggest that shorter storage times be implemented. For those chemicals selected for further testing, longer exposures (*e.g.*, one year) will be performed to improve confidence in the extrapolations. The procedures and data are presented in Section 6. The results of the long-term experiments will be summarized in the September, 1995, report.

During storage under elevated pressure and perhaps temperature, it is desirable that the agent not harm the storage container. This could result in leakage of the chemical over time or even in-flight rupture of the bottle. With the assistance of the sponsors, a list of current and potential materials for storage bottles was compiled. This included eight metal alloys, six elastomer o-rings, and three lubricants. Approximately one-month exposures at *ca.* 150 °C and 5.8 MPa provided data on the potential for affecting the storage materials. The metals corrosion research is discussed in Section 7. Section 8 details the study of the compatibility of polymeric materials which could be in contact with the agent under the above range of conditions.

Following dispensing, the suppressant chemical spends time in and near the flames, leading to some decomposition and the production of potentially harmful by-products. It is known that the fluids in Table 1 produce HF and, in two cases, HCl. To a first order, it was presumed that the yields of HF from the various chemicals would pose the same threat to aircraft materials, thus providing little differentiation among the chemicals. Testing of this will be reported in the September, 1995 report. Pilot examination of the potential for $NaHCO_3$ and its by-products was performed, since there was reason to expect a serious interaction with the aluminum used in aircraft bodies. This is presented in Section 7.

There are two other key components affecting the selection of alternative suppressants. First, one must be able to predict the potential exposure of people during an accidental discharge. The simplest assumption is that the distribution of the chemical in a confined space is uniform. Experiments were conducted to verify the validity of this hypothesis. Second, with the rapidly-changing regulations for protecting the earth's environment, it is necessary to know the pertinent requirements for testing of these families of chemicals. Both of these topics are discussed in Section 9.

1.3 References

Andersen, S.O., "Halons and the Stratospheric Ozone Issue," *Fire Journal 81*, 56-62 and 116-125, May/June (1987).

Bennett, M., "Halon Replacement for Aviation Systems," *The 1992 International CFC and Halon Alternatives Conference Proceedings*, pp. 667-670, The Alliance for Responsible CFC Policy, Frederick, MD, September 29-October 1, 1992.

Ford, C.L., "An Overview of Halon 1301 Systems," in *Halogenated Fire Suppressants*, (Gann, R.G., editor), pp. 1-63, American Chemical Society, Washington, DC, 1975.

Gann, R.G., Barnes, J.D., Davis, S., Harris, J.S., Harris, R.H., Herron, J.T., Levin, B.C., Mopsik, F.I., Notarianni, K.A., Nyden, M.R., Paabo, M., and Ricker, R.E., *Preliminary Screening Procedures and Criteria for Replacements for Halon 1211 and 1301*, NIST Technical Note 1278, August 1990.

Grant, C.C., "Halons and the Ozone Layer: An Overview," *Fire Journal 83*, 58-62 and 78-81, September (1989).

Halon Alternatives Technical Working Conference Proceedings, New Mexico Engineering Research Institute, Albuquerque, May 11-13, 1993.

Harrington, J.L., "The Halon Phaseout Speeds Up," *NFPA Journal*, pp. 38-42, March/April, 1993.

Heinonen, E.W., Moore, T.A., Nimitz, J.S., Skaggs, S.R., Beeson, H.D., and Moussa, N.A., *Fire/Explosion Protection Characterization and Optimization: Phase II - Alternative Dry Bay Fire Suppression Agent Screening*, NMERI OC 90/20, Report JTCG/AS-90-T003.

Kosko, J.E., press release, Public Affairs, NIST, February 22, 1993.

Mascarella, S., Booz-Allen & Hamilton Inc., Survivability/Vulnerability Information Analysis Center, personal communication, October 6, 1993.

Pitts, W.M., Nyden, M.R., Gann, R.G., Mallard, W.G., and Tsang, W., *Construction of an Exploratory List of Chemicals to Initiate the Search for Halon Alternatives*, NIST Technical Note 1279, National Institute of Standards and Technology, Gaithersburg, MD, August 1990.

Purdue Research Foundation and Department of Chemistry, *Final Report on Fire Extinguishing Agents*, AD 654322, Purdue University, West Lafayette, IN, July 1950.

Sheinson. R.S., Penner-Hahn, J.E., and Indritz, D., "The Physical and Chemical Action of Fire Suppressants," *Fire Safety Journal 15*, 437-450 (1989).

Tapscott, R.E., Moore, J.P., Lee, M.E., Watson, J.D., and Morehouse, E.T., *Next Generation Fire Extinguishing Agent Phase III*, ESL-TR-87-03, Air Force Engineering and Services Center, Tyndall AFB, FL, April 1990.

The 1993 International CFC and Halon Alternatives Conference Proceedings, The Alliance for Responsible CFC Policy, Frederick, MD, October 20-22, 1993.

World Meteorological Organization, *Scientific Assessment of Stratospheric Ozone: 1989*, Report No. 20, Alternative Fluorocarbon Environmental Acceptability Study (AFEAS), 1989.

Zallen, D.M., *Halon Replacement Study*, SBIR Report No. ZIA-92-001 to Aeronautical Systems Division, Wright-Patterson AFB, Zallen International Associates, Albuquerque, February 28, 1992.

2. THERMODYNAMIC PROPERTIES OF ALTERNATIVE AGENTS

Jiann C. Yang and Brett D. Breuel
Building and Fire Research Laboratory

2.1 Introduction

Depending upon their applications, current halon 1301 (CF_3Br) bottles are normally filled to about half of the bottle volume, and the bottle is then pressurized with nitrogen to 4.1 MPa (600 psig) at room temperature. The purpose of using the pressurization gas is to expedite the discharge of the agent and to increase the penetration distance of the agent during discharge. However, this driving force, *i.e.*, the total pressure in the bottle, will vary depending on the ambient temperature because the vapor pressure of the agent and the solubility of the pressurization gas in the liquid agent vary with temperature. The current military specification (MIL-C-22284A) for halon 1301 containers stipulates that the container should have a proof pressure of 9.62 MPa (1400 psig), a burst pressure of 12.37 MPa (1800 psig), and a frangible disc that will rupture at a pressure between 8.59 MPa (1250 psig) and 9.62 MPa (1400 psig) at 70 °C. In order to explore the possibility of using existing halon 1301 bottles for "drop-in" replacement agents or to provide safety guidelines on bottle design for the alternative agents, two important tasks are to determine (1) the solubility of the pressurization gas in the liquid agent and (2) the final pressure of the vessel when exposed to different ambient temperatures.

In the first task, some thermodynamic properties of the core agents listed in Section 1 were measured. Halon 1301 was also included in this study for the purposes of reference and comparison with the alternative agents. In particular, the objective was to determine the final equilibrium pressure in the bottle when the bottle, filled with either a pre-determined amount of pure agent or with agent and pressurization gas, was exposed to different temperatures. Experiments on pure agents were performed in order to obtain the vapor pressure data when documented data were not available. Two pressurization gases, nitrogen and CHF_3 (HFC-23), were used in the study. Trifluoromethane (CHF_3) was explored as a pressurization gas because it itself could be used as a fire suppressing agent. Another property that makes CHF_3 a potential candidate as a pressurization gas is its vapor pressure of 4.16 MPa (606 psia) at 20 °C, which is high enough to pressurize the vessel to the appropriate level.

The second task of this study was to determine the solubility of the pressurization gas in the agent at room temperature. Specifically, the objective was to measure the amount of the gas initially used to pressurize the bottle to 4.1 MPa. This part of the study, in essence, determined the initial condition of the vessel.

For the purpose of reference, selected thermo-physical properties of pure agents are tabulated in Table 1 where MW is the molecular weight, T_b is the normal boiling point (at 0.101 MPa), T_c is the critical temperature, P_c is the critical pressure, p_{sat} is the saturation vapor pressure at 25 °C, ρ_c is the critical density, ρ_l is the saturated liquid density at 25 °C, C_{pl} is the isobaric liquid heat capacity at T_b, C_{p2} is the isobaric liquid heat capacity at 25 °C, and h_{fg} is the latent heat of vaporization at T_b. The properties of CHF_3 are also included in the table. One mixture is included which is 60% (by mass) HFC-32 and 40% HFC-125. Table 2 lists the characteristic constants used to estimate the

Table 1. Tabulated values of selected thermo-physical properties of agents

Agent	MW (kg/mol)	T_b	T_c	P_c	p_{sat}	ρ_c	ρ_l	C_{pl}	C_{p2}	h_{fg} (kJ/kg)
		(°C)		(MPa)		(kg/m^3)		(kJ/kg K)		
HFC-236fa	0.152	-1.5[a]	130.6[a]	3.17[a]	0.27[a]	430[a]	1356[b]	1.114[c]	1.179[c]	150[d]
FC-31-10	0.238	-2.0[e]	113.2[e]	2.32[e]	0.27[f]	600[e]	1497[g]	0.951[c]	1.017[c]	96[f]
FC-318	0.200	-7.0[h]	115.2[h]	2.77[h]	0.31[h]	619[f]	1499[h]	1.009[h]	1.098[h]	112[h]
HCFC-124	0.137	-13.2[h]	122.5[h]	3.65[h]	0.38[h]	565[i]	1357[h]	1.080[h]	1.111[h]	162[h]
HFC-227ea	0.170	-16.4[j]	101.7[j]	2.90[j]	0.47[k]	621[j]	1395[k]	1.074[h]	1.177[h]	131[k]
CF_3I	0.196	-22.0[l]	122.0[m]	4.04[m]	0.49[n]	871[m]	2106[b]	0.542[c]	0.592[c]	106[d]
HFC-134a	0.102	-26.2[h]	101.2[h]	4.05[h]	0.67[h]	508[o]	1209[h]	1.269[h]	1.395[h]	217[h]
FC-218	0.188	-36.8[h]	72.0[h]	2.67[h]	0.88[h]	629[f]	1321[h]	0.977[h]	1.151[h]	101[h]
HCFC-22	0.087	-40.9[h]	96.2[h]	5.04[h]	1.05[h]	525[f]	1192[h]	1.116[h]	1.239[h]	229[h]
HFC-125	0.120	-48.6[h]	66.3[h]	3.62[h]	1.38[h]	571[p]	1190[h]	1.107[h]	1.358[h]	160[h]
HFC-32/125	0.067	-52.5[q]	73.2[q]	5.04[q]	1.67[q]	479[q]	1040[q]	1.449[c]	1.763[c]	287[q]
CF_3Br	0.149	-57.8[h]	67.0[h]	3.95[h]	1.61[h]	745[r]	1551[h]	0.670[h]	0.881[h]	111[h]
FC-116	0.138	-78.2[f]	19.7[f]	2.98[f]	-	608[f]	-	0.956[c]	-	117[f]
CHF_3	0.070	-82.1[r]	25.6[r]	4.82[r]	4.69[s]	516[r]	0.685[s]	1.269[h]	-	240[h]

[a]From Du Pont Chemicals Data Sheet, personal communication (1993)
[b]Estimated by the modified Rackett method (Reid *et al.*, 1987)
[c]Estimated by the method of Rowlinson (Reid *et al.*, 1987)
[d]Estimated by Pitzer acentric factor correlation (Reid *et al.*, 1987)
[e]From Daubert and Danner (1993)
[f]From Braker and Mossman (1980)
[g]From Brown and Mears (1958)
[h]From Gallagher *et al.* (1993)
[i]From Shankland *et al.* (1990)
[j]From Great Lakes Chemical Corporation (1993)
[k]From Hoechst AG, personal communication (1992)
[l]From Kudchadker *et al.* (1979)
[m]From Sladkov and Bogacheva (1992)
[n]Estimated by the method of Lee and Kesler (Reid *et al.*, 1987)
[o]From Piao *et al.* (1991)
[p]From Allied Signal Inc. (1990)
[q]From Allied Signal Inc. (1991)
[r]From ASHRAE Inc. (1969)
[s]From Platzer *et al.* (1990)

isobaric ideal-gas heat capacities ($C_p{}^o$) of all the agents used in this study. The sources of these data are also documented in Tables 1 and 2.

Table 2. Characteristic constants used to calculate C_p^o (kJ/kg K) as a function of temperature T (K); $C_p^o = A + BT + CT^2 + DT^3 + (E/T)$

Agent	A	B	C	D	E
HFC-236fa[a]	-8.05×10^{-2}	4.01×10^{-3}	-3.82×10^{-6}	1.33×10^{-9}	0
FC-31-10[a]	-1.59×10^{-1}	4.24×10^{-3}	-4.41×10^{-6}	1.60×10^{-9}	0
FC-318[b]	4.51×10^{-2}	3.33×10^{-3}	-3.22×10^{-6}	1.14×10^{-9}	0
HCFC-124[c]	1.76×10^{-1}	2.12×10^{-3}	-1.00×10^{-6}	0	0
HFC-227ea[a]	-4.61×10^{-2}	3.70×10^{-3}	-3.54×10^{-6}	1.22×10^{-9}	0
CF_3I[a]	3.81×10^{-2}	1.53×10^{-3}	-1.70×10^{-6}	6.60×10^{-10}	0
HFC-134a[c]	-5.26×10^{-3}	3.30×10^{-3}	-2.02×10^{-6}	0	15.82
FC-218[d]	6.88×10^{-2}	3.31×10^{-3}	-3.41×10^{-6}	1.28×10^{-9}	0
HCFC-22[b]	1.61×10^{-1}	2.08×10^{-3}	-1.70×10^{-6}	5.28×10^{-10}	0
HFC-125[c]	1.90×10^{-1}	2.47×10^{-3}	-1.44×10^{-6}	0	0
HFC-32/125[e]	3.82×10^{-1}	1.62×10^{-3}	-3.85×10^{-7}	0	0
CF_3Br[f]	1.47×10^{-1}	1.45×10^{-3}	-1.42×10^{-6}	5.01×10^{-10}	0
FC-116[b]	1.03×10^{-1}	3.04×10^{-3}	-2.98×10^{-6}	1.05×10^{-9}	0
CHF_3[b]	5.49×10^{-2}	2.97×10^{-3}	-2.62×10^{-6}	8.97×10^{-10}	0

[a]Estimated by the method of Joback (Reid *et al.*, 1987)
[b]From Yaws *et al.* (1988)
[c]From Allied Signal Inc. (1990)
[d]From Fang and Joffe (1966)
[e]From Allied Signal Inc. (1991)
[f]From Property Data Bank (Reid *et al.* 1987)

2.2 Experimental Apparatus and Procedures

The pressure-temperature relationship for pure agents and agent/pressurization gas mixtures at one fill condition (*i.e.*, the volume of the liquid agent in the vessel was fixed in all the experiments) was measured. Except for the experimental procedure, the same apparatus was used in both studies. For pure agents and agent/nitrogen mixtures, pressure measurements were determined at three temperatures, −60 °C, 22 °C, and 150 °C. For agent/CHF_3 mixtures, pressure measurements were obtained at −60 °C, 22 °C , and at the maximum temperature which did not cause the pressure to exceed the safe operating limit of the vessel (for reasons to be discussed).

A fill condition of 1/3 of the vessel volume was selected because the so-called liquid-full condition could be avoided when the vessel was heated to high temperatures. To illustrate the significance of the liquid-full condition, let us consider a *PT* (pressure-temperature) phase diagram for a pure substance for the purpose of simplicity and clarity. Figure 1 shows the general behavior of a pure substance. The saturation curve (or the vapor pressure curve), which represents the existence of

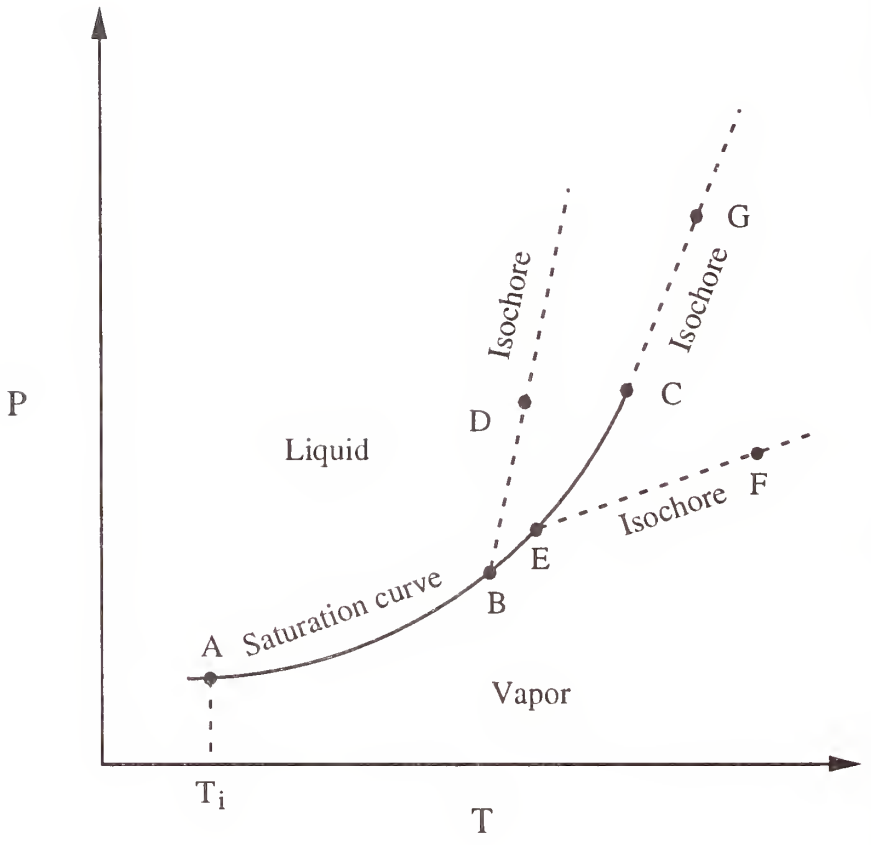

Figure 1. *PT* diagram showing the saturation curve for a pure substance and isochores.

two phases (vapor and liquid) in equilibrium, separates the vapor and liquid regions. The curve terminates at the critical point *C*. If one puts a fixed amount (*M*) of a liquid-vapor mixture of a pure substance in a closed vessel with a volume *V* at T_i (represented by point *A* in Figure 1) and raises the temperature of the vessel, two things will happen: the liquid vaporizes and at the same time expands. The heating process at first follows the saturation curve until a single phase state is reached. This state depends on the ratio of *M* to *V*, or the fill density (ρ_{fill}) of the vessel. If ρ_{fill} is greater than the critical density (ρ_c), continuous heating initially from point *A* causes the liquid-vapor interface (the meniscus) to rise because the rate of thermal expansion of the liquid is faster than its vaporization rate. Eventually, a state (point *B*) on the saturation curve will be reached where the liquid completely fills the vessel. This condition is termed *liquid-full*. The location of point *B* can be determined by identifying the temperature at which the saturation liquid density is equal to ρ_{fill}. Further heating of the vessel beyond point *B* can only occur in the liquid region along the liquid constant density line (or isochore), *BD*, corresponding to the constant ρ_{fill}. If ρ_{fill} is less than ρ_c, heating initially from point *A* causes the meniscus to recede due to the slower rate of thermal expansion of the liquid than its vaporization rate. The liquid eventually will completely vaporize, and the vessel is filled with vapor. The state at which this happens is represented by point *E*, which can be located by finding the temperature at which the saturated vapor density is equal to the fill density. Further heating beyond point *E* will only occur along the vapor isochore, *EF*, corresponding to the fixed ρ_{fill}. If ρ_{fill} is equal to ρ_c, heating will cause little change in the level of the meniscus because the rate of thermal expansion of the liquid is more or less balanced by its vaporization rate. The heating process will follow the saturation curve until the critical point *C* is reached where the meniscus disappears. Further heating then follows the critical isochore, *CG*. Note that the critical isochore has the same slope as the saturation curve at the critical point. Figure 1 clearly illustrates the undesirable feature of heating the vessel beyond the liquid-full condition because a small increase in temperature can create a dangerous over-pressure large enough to rupture the vessel.

2.2.1 Pure Agents. The experimental set-up is shown in Figure 2. A stainless steel (SS 304) vessel was used to measure the pressure-temperature relationship of the eleven agents. The vessel was tested hydrostatically to 20.6 MPa (3000 psia).

A K-type thermocouple (Omega TJ36-CASS-116U-12) was inserted into the vessel to monitor the internal temperature of the vessel in order to ensure that thermal equilibrium was reached between the vessel interior and the ambience. For high temperature (150 °C) measurements, the vessel was immersed in a silicone oil bath heated with an immersion heater (Cole-Parmer Model L-01266-02). For low temperature measurements, the vessel was submerged in a heat transfer fluid (Dow Corning Syltherm XLT) which was cooled by two immersion coolers (NESLAB). One cooler (Model IBC-4A) had a cooling capacity between 20 °C and −30 °C whereas the other (Model CC100-II) had a capacity between −25 °C and −100 °C. The rationale for using two coolers was that the cooling time of the heat transfer fluid to the required temperature (−60 °C) was greatly reduced and that together with the immersion heater the entire temperature range, from −60 °C to 150 °C, was covered.

A pressure relief valve (Nupro Model 177-R3A-K1-E) with a relieve pressure of 15.5 MPa (2250 psig) was used in the experimental set-up to prevent any accidental pressure overshoot when the vessel was exposed to high ambient temperature. A pressure transducer (DRUCK Model PDCR 330) was used to measure the internal pressure of the vessel. The transducer had an accuracy of 6.9 kPa (1 psi) and an operating range from 0.101 MPa (14.7 psia) to 13.8 MPa (2015 psia).

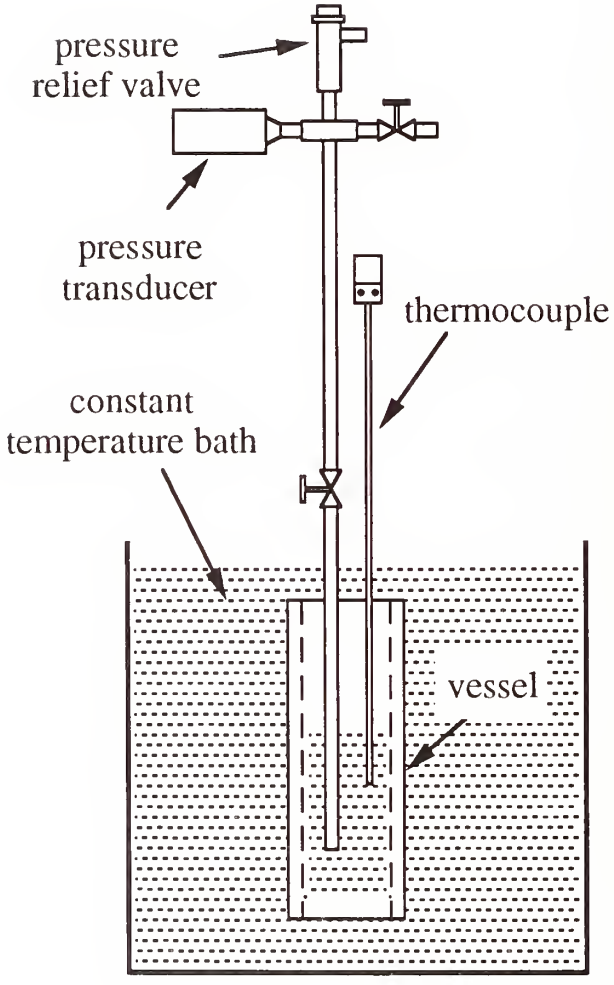

Figure 2. Schematic of temperature-pressure measurement experimental set-up.

There were two needle valves (Whitey SS-ORS2) in the apparatus. The one that was attached to the pressure vessel was used for filling and the other was used for isolating the apparatus from the vacuum pump line or the pressurization gas supply line.

The total internal volume of the experimental apparatus was determined as follows. For the vessel together with the attached needle valve, the internal volume was measured by filling them with de-ionized water and weighing them on an electronic scale with an accuracy of 0.1 g. After this volume was determined, the entire system (Figure 2) was evacuated for at least 5 minutes and pressurized with nitrogen to a fixed pressure at room temperature. The lower needle valve was then closed, confining nitrogen to the vessel. The nitrogen remaining in the rest of the system was bled out. With the lower needle valve closed, the apparatus was evacuated for at least 5 minutes by connecting a vacuum line to the upper needle valve. The upper needle valve was then closed before removal of the vacuum line from the apparatus. The lower needle valve was then fully opened, allowing the nitrogen in the vessel to expand throughout the apparatus. The final pressure of the set-up was recorded after thermal equilibrium with room temperature had been reached. Knowing the initial pressure (before expansion), the initial volume (lower needle valve together with the vessel), and the final pressure (after expansion), the total internal volume of the system was calculated by using the ideal gas law and was found to be 53.2 ± 0.5 cm^3.

The experimental procedure was as follows. The vessel together with its needle valve was initially disconnected from the experimental set-up and evacuated for at least 5 minutes. The vessel was then connected to the agent supply bottle (not shown in Figure 2). By immersing the vessel in dry ice, liquid agent was dispensed through the needle valve into the vessel by condensing gaseous agent from the supply bottle. No attempt was made to remove noncondensible gases, if there were any, in the liquid agents. The amount of agent used in each of the experiments was approximately equal to the amount required to fill one-third of the vessel volume with liquid agent. The vessel was then weighed on an electronic balance with an accuracy of 0.1 g to determine the actual mass of the agent. The vessel was re-connected to the experimental set-up, which was then evacuated for at least 5 minutes before the needle valve attached to the vessel was opened fully. The apparatus was then immersed in the controlled temperature bath. The pressure of the vessel was recorded from the pressure transducer read-out when the internal temperature had reached thermal equilibrium with the bath temperature. Note that since FC-116 is a gas at room temperature, the 1/3 fill condition was not applicable to this agent. Although liquid FC-116 could stilled be dispensed by condensing gaseous FC-116 in the dry-ice-cooled vessel, this approach was not taken because the amount of liquid mass in the vessel could cause a huge pressure rise when the vessel was warmed back to room temperature. An average fill density of about 370 kg/m^3 was used for FC-116. This fill density was governed by the pressure of the agent supply bottle, *i.e.*, gaseous FC-116 was dispensed into the vessel directly from the supply bottle until an equilibrium pressure was reached in both the vessel and the supply bottle.

2.2.2 N_2/Agent and CHF_3/Agent Mixtures. As mentioned in the beginning of this section, the same experimental set-up for evaluating pure agents was used for the mixtures. The experimental procedure is described in the following paragraph.

After a pure liquid agent was dispensed in the vessel as described above and the vessel was re-connected to the experimental set-up, the pressurization gas supply line was then connected to the upper needle valve. The supply line together with the experimental set-up was evacuated for at least 5 minutes before initiating a slow flow of the pressurization gas. The lower needle valve was then fully opened to allow the gas to bubble slowly through the liquid agent until an equilibrium pressure of approximately 4.1 MPa (600 psia) was reached. Repetitive bubbling of the pressurization gas was required before the final equilibrium pressure could be obtained. This value of pressure was selected

in order to simulate a charging pressure commensurate with existing halon 1301 vessel. The vessel was then immersed in the controlled temperature bath. Once the vessel was in thermal equilibrium with the bath, the pressure of the vessel was recorded.

2.2.3 Solubility of N_2 and CHF_3 in Agents. Figure 3 shows a schematic of the apparatus used for solubility measurements. The experimental apparatus included the same stainless steel vessel used in the pressure-temperature measurements, a needle valve for dispensing the liquid agent and pressurization gas, a thermocouple, and a pressure transducer (DRUCK Model PDRR 330). The actual volume of the system was determined by pressurizing it with nitrogen to 4.02 MPa and then weighing it on an electronic scale with an accuracy of 0.1 g. Knowing the temperature, the pressure, and the mass of nitrogen, the volume was then calculated by using a generalized correlation for the compressibility factor (Smith and Van Ness, 1975). The total volume of the apparatus was found to be 53.9 $\pm$ 0.6 cm^3.

The experimental procedure was as follows. The apparatus was evacuated for at least 5 minutes before the agent was dispensed to the vessel. The same filling and pressurization procedure were used as in the pressure-temperature measurements for mixtures. After pressurization with nitrogen or CHF_3, the amount of pressurization gas required to pressurize the vessel to the specified final pressure was then obtained by weighing the apparatus. This amount corresponded to the sum of the mass of nitrogen or CHF_3 in the vapor phase and that of the dissolved nitrogen or CHF_3 in the liquid agent.

2.3 Results and Discussion

2.3.1 Pure Agents. Table 3 summarizes the results (averages of at least two runs $\pm$ half the range) of temperature-pressure measurements for pure agents at 150 $\pm$ 1 °C. Fill density is defined as the ratio of the mass of the agent to the volume of the apparatus (53.2 cm^3). The third column shows the measured final pressures at 150 $\pm$ 1 °C. For all the agents evaluated, the final pressures at 150 °C were less than 11 MPa (1600 psia). At −60 °C, the final pressures for all the agents, except HFC-27ea and FC-116, were below 0.101 MPa (14.7 psia) which is below the measuring range of the pressure transducer. For FC-116, an average final pressure of 0.25 MPa was found at −61 °C. For HFC-227ea, an average final pressure of 0.18 MPa was measured at −60 °C. Subsequent measurements of HFC-227ea from a different agent bottle showed an average value below 0.101 MPa. The results of HFC-227ea reported herein were obtained by using the agent supply bottle that gave a final pressure of 0.25 MPa at −60 °C, which represented the worst case.

Since the amount of agent and the volume of the apparatus (53.2 cm^3) were constant, an existing equation of state was used to predict the final pressure at the final temperature along an isochore or constant density line. The Peng-Robinson equation of state (Peng and Robinson, 1976) has recently been used to correlate thermodynamic properties of refrigerants and their mixtures (Abu-Eishah, 1991). It is given by

$$P = \frac{RT}{v - b} - \frac{a(T)}{v(v + b) + b(v - b)} \tag{1}$$

where v is the molar volume, R is the universal gas constant, and T is the absolute temperature (in K). The parameters a and b are given in terms of the reduced temperature ($T_R \equiv T/T_c$), and the acentric factor, ω:

Table 3. Comparison of measured pressures at 150 ± 1 °C with calculated values from REFPROP and the Peng-Robinson equation of state

Agent	Fill density (kg/m^3)	P_f (MPa) measured	P_f (MPa) REFPROP	error[a] (%)	P_f (MPa) P-R EOS	error[b] (%)
HFC-236fa	467 ± 2.0	4.50 ± 0.03	-	-	4.24	5.8
FC-31-10	523 ± 0	3.45 ± 0.01	-	-	3.76	9.0
FC-318	526 ± 1.1	4.05 ± 0.01	4.31	6.7	4.40	8.6
HCFC-124	471 ± 2.4	4.93 ± 0	5.22	5.9	5.27	6.9
HFC-227ea	495 ± 1.3	5.13 ± 0.04	5.27	2.7	5.41	5.5
CF_3I	733 ± 0.1	5.19 ± 0.01	-	-	6.06	16.8
HFC-134a	430 ± 0.8	6.80 ± 0.02	7.53	10.7	7.73	13.7
FC-218	500 ± 3.5	5.41 ± 0.02	5.89	8.9	6.11	12.9
HCFC-22	436 ± 2.7	8.48 ± 0.13	9.25	9.1	9.48	11.8
HFC-125	456 ± 1.2	7.73 ± 0.07	8.60	11.3	8.90	15.1
HFC-32/125	390 ± 0.5	10.78 ± 0.07	-	-	12.67	17.5
CF_3Br	605 ± 0.3	8.11 ± 0	-	-	9.07	11.8
FC-116	368 ± 5.9	6.77 ± 0.10	-	-	7.70	13.7

[a]error (%) = $|P_f$ (measured) - P_f (REFPROP)| x $100/P_f$ (measured)

[b]error (%) = $|P_f$ (measured) - P_f (P-R EOS)| x $100/P_f$ (measured)

$$a(T) = a(T_c)\,\alpha(T_R,\omega) \tag{2}$$

$$a(T_c) = 0.45724\frac{R^2 T_c^2}{P_c} \tag{3}$$

$$\alpha = [1 + \beta(1 - T_R^{1/2})]^2 \tag{4}$$

$$\beta = 0.37464 + 1.54226\,\omega - 0.26992\,\omega^2 \tag{5}$$

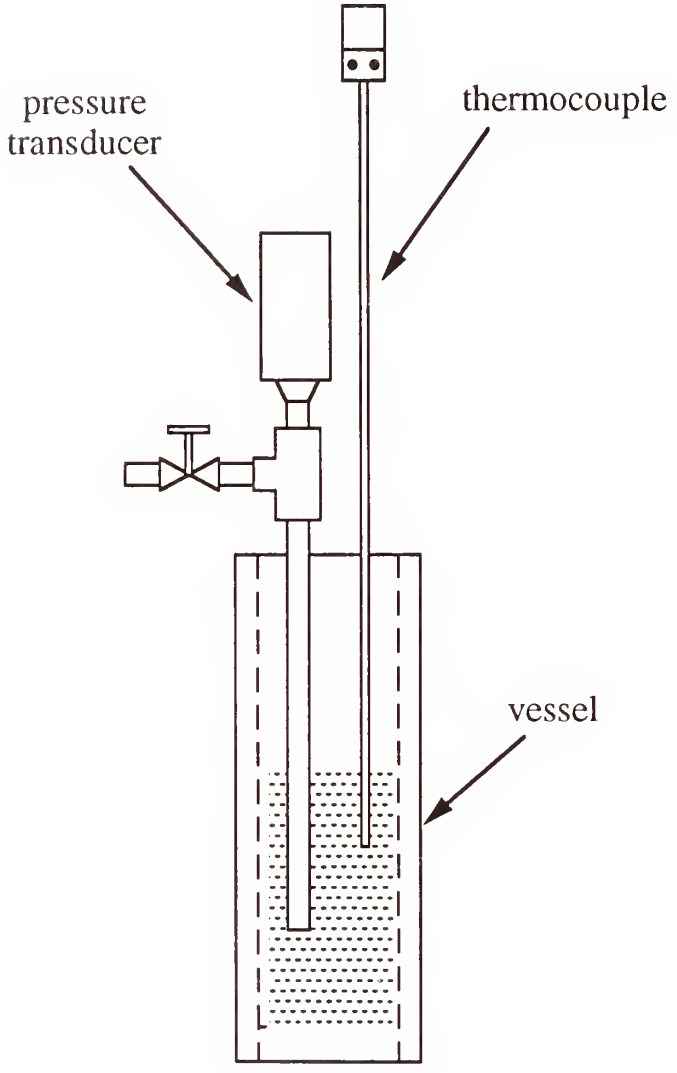

Figure 3. Experimental set-up for solubility measurement.

$$\omega = -\log\left(\frac{P_{sat}}{P_c}\right)_{T/T_c = 0.7} - 1.000 \tag{6}$$

$$b = 0.07780\frac{RT_c}{P_c} \tag{7}$$

In addition, the computer program, REFPROP (Gallagher *et al.*, 1993) was used to compare with the calculated results obtained by using the Peng-Robinson equation of state. REFPROP was developed by using the Carnahan-Starling-DeSantis equation of state (Morrison and McLinden, 1986):

$$\frac{Pv}{RT} = \frac{1 + y + y^2 - y^3}{(1 - y)^3} - \frac{a^*}{RT(v + b^*)} \tag{8}$$

$$y = \frac{b^*}{4v} \tag{9}$$

$$a^* = a_0 \exp(a_1 T + a_2 T^2) \tag{10}$$

$$b^* = b_0 + b_1 T + b_2 T^2 \tag{11}$$

where a_0, a_1, a_2, b_0, b_1, and b_2 are parameters obtained from fitting of limited experimental data. Table 3 also summarizes the results obtained from REFPROP and the Peng-Robinson equation of state (P-R EOS). The calculations were based on the conditions (average values) given in the second and third columns in Table 3. The blank entries in Table 3 imply that those agents are not currently included in REFPROP.

From Table 3, it appears that REFPROP predicts the final pressures much closer to the experimental values than the Peng-Robinson equation of state. In all cases, except for HFC-236fa, both equations of state tend to overestimate the final pressures.

2.3.2 N_2/Agent and CHF_3/Agent Mixtures. Table 4 tabulates the results (averages of at least two runs ± half the range) of N_2/agent mixtures. The third column shows the initial pressures of the vessel at 23 ± 1 °C, the fourth column lists the final pressures of the vessel when the temperature is at −60 ± 1 °C, and the fifth column tabulates the final pressures of the vessel at 150 ± 1 °C.

At −60 °C, there was still significant residual pressure in the vessel. This residual pressure was mainly due to the nitrogen in the vapor phase because the contribution to the pressure from the agent vapor was insignificant due to very low vapor pressure (< 0.101 MPa) of the agent at −60 °C. Therefore, the initial pressurization of the vessel with nitrogen ensures that enough residual driving force to propel the agent out of the vessel is still present when the vessel is discharged at a cold ambience. Without the pressurization gas, the vapor pressure of the agent was so low that the out-

driving force was the static head of the liquid agent when the vessel was placed in the vertically downward position.

At 150 °C, the final pressures of all the agents, with the exception of the HFC-125/HFC-32 mixture, were below 13.7 MPa (2000 psia). For the mixture, the experiment was terminated at 140 °C because the pressure was close to exceeding the operating range of the pressure transducer.

The results of CHF_3/agent mixtures are summarized in Table 5. The explanation of the content of the table is similar to that of Table 4. The values shown in Table 5 are the averages of at least two runs with their half range.

At about −60 °C, the final residual pressures in all cases were very low. This would make CHF_3 as a pressurization gas unfavorable if the vessels were to be discharged at low temperatures. The results also imply that a significant amount of CHF_3 was dissolved in the liquid agent at −60 °C.

When the agent/CHF_3 mixtures (except FC-116/CHF_3) were heated, the pressures exceeded 13.7 Pa by the time a temperature of 70 °C had been reached. Because CHF_3 is highly soluble in all the liquid agents and the initial amount of CHF_3 required to pressurize the vessel is very significant (see Section **2.3.3**), an increase in pressure at moderately elevated temperatures was caused by a decrease in solubility of CHF_3 in the liquid agent and a subsequent increase in the amount of CHF_3 in the ullage. As a result, if CHF_3 were to be selected as a pressurization gas, extreme care should be taken in the design of the bottle for the replacement agent, especially if the bottle is to be exposed to a high temperature environment.

2.3.3 Solubility of N_2 and CHF_3 in Agents.

2.3.3.1 Experimental Results. Table 6 summarizes the experimental results (averages of at least two runs ± half the range) for nitrogen. In all cases, the total amount of nitrogen required to pressurize the system to 4.1 MPa was less than 8% of the total mass of the agent.

Experimental results (averages of at least two runs ± half the range) from CHF_3/agent mixtures are shown in Table 7. The amount of CHF_3 needed to pressurize the vessel to ~ 4.1 MPa is as much as or greater than that of the agent in the vessel. This is not surprising because CHF_3 is readily soluble in all the agents. Since a significant amount of CHF_3 is dissolved in the liquid agent, subsequent heating of the vessel causes a steep rise in pressure due to decreasing solubility of CHF_3 in the liquid agent at high temperatures (see Section **2.3.2**).

2.3.3.2 Theoretical Predictions. In order to determine the solubility of nitrogen in the agent, measurements of nitrogen and agent concentrations in both phases are required. Solubility is normally defined as the mole fraction of nitrogen dissolved in the liquid agent. The present experimental set-up does not have the provision for sampling the liquid and gas phases, but the mass of nitrogen that is dissolved in the liquid agent can be estimated by applying mass balances on the agent and nitrogen. The calculation procedure is as follows.

Initially, the vessel is filled with a pre-determined amount of agent, $m_{a,t}$, at temperature T (K) (in this case room temperature); which is expressed as

$$m_{a,t} = m_{a,v} + m_{a,l} = \rho_{a,v} V_v + \rho_{a,l} V_l \tag{12}$$

where m is the mass, subscript t represents total, subscript a represent agent, subscripts v and l represent vapor and liquid phases respectively, ρ is the saturation density of the agent, and V is the volume. Since $m_{a,t}$, V_t, $\rho_{a,v}$, and $\rho_{a,l}$ are known and $V_l = V_t - V_v$, the masses of agent in both liquid and vapor phases can be calculated by substituting $V_t - V_v$ for V_l and solving for V_v in Equation (12).

Table 4. Initial pressures (P_i) at 23 ± 1 °C and final pressures ($P_{f,1}$) and ($P_{f,2}$) at −60 ± 1 °C and 150 ± 1 °C, respectively, for N_2/agent mixtures

Agent	Fill density (kg/m^3)	P_i (MPa)	$P_{f,1}$ (MPa)	$P_{f,2}$ (MPa)
HFC-236fa	468 ± 0.2	4.16 ± 0	2.72 ± 0	9.66 ± 0.02
FC-31-10	523 ± 0.1	4.15 ± 0.02	2.68 ± 0.01	8.82 ± 0.03
FC-318	524 ± 2.3	4.16 ± 0.04	2.80 ± 0.18	9.32 ± 0.28
HCFC-124	471 ± 0.5	4.16 ± 0.05	2.65 ± 0	9.96 ± 0.02
HFC-227ea	492 ± 2.0	4.14 ± 0.02	2.55 ± 0.02	9.99 ± 0.10
CF_3I	736 ± 1.0	4.17 ± 0.01	2.67 ± 0	10.25 ± 0.01
HFC-134a	430 ± 0.5	4.16 ± 0.01	2.50 ± 0.01	11.59 ± 0.02
FC-218	497 ± 2.9	4.24 ± 0.05	2.40 ± 0.06	10.16 ± 0.44
HCFC-22	433 ± 0.3	4.20 ± 0.02	2.46 ± 0.01	13.00 ± 0.03
HFC-125	458 ± 1.2	4.16 ± 0.05	2.11 ± 0.04	11.59 ± 0.71
HFC-32/125	390 ± 2.9	4.13 ± 0.02	2.04 ± 0.01	13.82[a] ± 0
CF_3Br	601 ± 1.8	4.20 ± 0	2.07 ± 0	12.30 ± 0.04
FC-116	371 ± 0.9	4.24 ± 0.04	1.24 ± 0.02	9.07 ± 0.08

[a]at 140 °C

$$V_v = \frac{m_{a,t} - \rho_{a,l} V_t}{\rho_{a,v} - \rho_{a,l}} \tag{13}$$

The vessel is then pressurized with nitrogen until an equilibrium pressure P_t at T is reached. Assuming that the dissolved nitrogen would not cause a significant change in the saturation liquid density of the agent and that the liquid agent is incompressible, the liquid mixture density can be approximated by the saturation liquid density of the pure agent. This approximation is reasonable if the amount of nitrogen dissolved in the liquid agent is much smaller than the mass of the liquid agent. If the vapor phase is further assumed to be ideal, then the total pressure P_t is given by

$$P_t = p_a + p_g \tag{14}$$

where p_a and p_g are the partial pressures of the agent and nitrogen respectively. From Raoult's law (Denbigh, 1984),

Table 5. Initial pressures (P_i) at 23 ± 1 °C and final pressures ($P_{f,1}$) and ($P_{f,2}$) at −60 ± 1 °C and $T_{f,2}$, respectively, for CHF_3/agent mixtures

Agent	Fill density (kg/m^3)	P_i (MPa)	$P_{f,1}$ (MPa)	$T_{f,2}$ (°C)	$P_{f,2}$ (MPa)
HFC-236fa	467 ± 1.0	4.19 ± 0.07	0.30 ± 0.01	48 ± 1	13.51 ± 0.01
FC-31-10	523 ± 0.4	4.31 ± 0.01	0.33 ± 0.01	56 ± 0	13.50 ± 0.01
FC-318	525 ± 0.6	4.21 ± 0.01	0.34 ± 0	53 ± 1	13.53 ± 0.02
HCFC-124	472 ± 0.5	4.11 ± 0.01	0.29 ± 0	48 ± 1	13.55 ± 0.02
HFC-227ea	495 ± 0.6	4.22 ± 0.02	0.29 ± 0	53 ± 1	13.51 ± 0.03
HFC-134a	426 ± 0.4	4.18 ± 0.05	0.27 ± 0	47 ± 1	13.55 ± 0.03
FC-218	498 ± 1.8	4.19 ± 0.02	0.44 ± 0.04	62 ± 0	13.54 ± 0.01
HCFC-22	433 ± 0.1	4.21 ± 0.05	0.29 ± 0.01	49 ± 1	13.53 ± 0.03
HFC-125	455 ± 0.5	4.23 ± 0.04	0.28 ± 0.01	52 ± 1	13.58 ± 0.01
HFC-32/125	391 ± 1.1	4.19 ± 0.02	0.27 ± 0.01	51 ± 3	13.59 ± 0.11
FC-116	376 ± 1.5	4.21 ± 0.08	0.39 ± 0.02	150 ± 0	11.22 ± 0.70

$$p_a = x_{a,l}\, p_{sat} = \frac{n_{a,l}}{n_{g,l} + n_{a,l}}\, p_{sat} \tag{15}$$

where $x_{a,l}$ is the mole fraction of the agent in the liquid phase, p_{sat} is the saturation vapor pressure of the agent at temperature T, $n_{g,l}$ is the number of moles of dissolved gas in the liquid phase, and $n_{a,l}$ is the number of moles of agent in the liquid phase. Furthermore, p_g can be calculated by

$$p_g = \frac{n_{g,v}RT}{V_v} = \frac{(n_{g,t} - n_{g,l})\ RT}{V_v} \tag{16}$$

where $n_{g,v}$ is the number of moles of pressurization gas in the vapor phase, $n_{g,t}$ is the total moles of pressurization gas required to pressurize the vessel to P_t at a temperature T, and R is the universal gas constant. Substituting Equations (15) and (16) into Equation (14), a quadratic equation for $n_{g,l}$ (unknown) is obtained.

$$n_{g,l}^2 + n_{g,l}\left(n_{a,l} - n_{g,t} + \frac{P_t V_v}{RT}\right) + n_{a,l}\left(\frac{P_t V_v}{RT} - \frac{p_{sat} V_v}{RT} - n_{g,t}\right) = 0 \tag{17}$$

Solving for $n_{g,l}$ (only one root is meaningful) and knowing $n_{g,v} = n_{g,t} - n_{g,l}$, the amount of nitrogen in both phases can be calculated. When no nitrogen is dissolved in the liquid agent (*i.e.*, $n_{g,l} = 0$), $P_t = p_g + p_{sat}$ is recovered from Equation (17).

Table 6. Amount of nitrogen required to pressurize mixture to total pressure, P_t at 23 ± 1 °C

Agent	P_t (MPa)	Nitrogen (g)	Agent (g)
HFC-236fa	4.27 ± 0.08	1.9 ± 0.1	24.8 ± 0.1
FC-31-10	4.15 ± 0.02	2.0 ± 0	27.8 ± 0.1
FC-318	4.16 ± 0.03	2.0 ± 0.1	28.0 ± 0
HCFC-124	4.16 ± 0.01	1.9 ± 0.1	25.2 ± 0.1
HFC-227ea	4.16 ± 0	1.8 ± 0	26.3 ± 0.1
CF_3I	4.28 ± 0.05	1.9 ± 0	39.0 ± 0
HFC-134a	4.18 ± 0.02	1.8 ± 0.1	22.8 ± 0.1
FC-218	4.15 ± 0.02	1.7 ± 0.1	26.6 ± 0.1
HCFC-22	4.12 ± 0.01	1.4 ± 0.1	21.4 ± 0.1
HFC-125	4.21 ± 0.14	1.5 ± 0.1	24.3 ± 0
HFC-32/125	4.17 ± 0.01	1.3 ± 0	20.7 ± 0.1
CF_3Br	4.17 ± 0.01	1.4 ± 0.1	32.0 ± 0.1

The results and the parameters that are required to perform the calculation are shown in Table 8. The conditions used for the calculations correspond to Table 6. The calculated solubilities ($x_{g,l}$) and mass fractions ($w_{g,l}$) are also tabulated in Table 8. Solubility is defined as follows:

$$x_{g,l} = \frac{n_{g,l}}{n_{g,l} + n_{a,l}} \tag{18}$$

and the mass fraction of nitrogen in the liquid agent is calculated by

$$w_{g,l} = \frac{x_{g,l} M_g}{x_{g,l} M_g + (1 - x_{g,l}) M_a} \tag{19}$$

where M_a and M_g are the molecular weights of agent and pressurization gas (nitrogen) respectively.

For all the agents studied, the amount of nitrogen dissolved in the liquid agent was calculated to be less than 25% of the total amount of nitrogen added, and less than 2% of the mass of the agent.

The solubility of nitrogen in liquid agent can also be estimated if the solution can be assumed regular. A correlating scheme based on the theory of regular solutions and the law of corresponding states to predict solubility of a gas in liquid was developed by Prausnitz and Shair (1961). The following equations form the basis of the correlation of gas solubilities:

Table 7. Amount of CHF_3 required to pressurize mixture to total pressure, P_t at 23 ± 1 °C

Agent	P_t (MPa)	CHF_3 (g)	Agent (g)
HFC-236fa	4.29 ± 0.04	32.8 ± 0	24.7 ± 0.1
FC-31-10	4.16 ± 0	28.8 ± 0.2	27.9 ± 0.1
FC-318	4.17 ± 0.01	30.3 ± 0	27.9 ± 0.1
HCFC-124	4.21 ± 0.05	32.0 ± 0.1	25.1 ± 0.1
HFC-227ea	4.16 ± 0.04	30.4 ± 0	26.3 ± 0.1
HFC-134a	4.17 ± 0.03	31.9 ± 0.1	22.7 ± 0
FC-218	4.23 ± 0.03	25 ± 0.1	26.4 ± 0
HCFC-22	4.33 ± 0.21	30.8 ± 0.4	22.8 ± 0
HFC-125	4.16 ± 0.01	28.2 ± 0	24.4 ± 0.1
HFC-32/125	4.20 ± 0.01	29.9 ± 0.1	20.7 ± 0.1
CF_3Br	4.12 ± 0.01	23.9 ± 0.1	31.8 ± 0.3

$$\frac{1}{x_{g,l}} = \frac{f^L_{pure,g}}{f^G_g} \exp\left[\frac{v^L_g (\delta_a - \delta_g)^2 \Phi^2_a}{RT} \right] \tag{20}$$

with

$$\Phi_a = \frac{x_{a,l} v^L_a}{x_{a,l} v^L_a + x_{g,l} v^L_g} \tag{21}$$

$$\delta_a \approx \sqrt{\frac{(h_{fg})_a - RT}{v^L_a}} \tag{22}$$

Table 8. Parameters used in the solubility calculations, calculated mass of nitrogen in liquid agents, calculated nitrogen solubility, and calculated nitrogen mass fractions in liquid agents (conditions shown in Table 6)

Agent	$\rho_{a,l}$ (kg/m^3)	$\rho_{a,v}$ (kg/m^3)	p_{sat} (MPa)	$m_{g,l}$ (g)	$x_{g,l}$	$w_{g,l}$
HFC-236fa	1371	15.8[a]	0.26	0.2	0.05	0.01
FC-31-10	1505	27.3	0.25	0.4	0.11	0.01
FC-318	1504	27.0	0.30	0.4	0.10	0.02
HCFC-124	1363	22.5	0.36	0.3	0.06	0.01
HFC-227ea	1400	36.3	0.45	0.3	0.07	0.01
CF_3I	2102	36.7[a]	0.46[b]	0.3	0.06	0.01
HFC-134a	1214	30.2	0.62	0.3	0.05	0.01
FC-218	1333	83.4	0.84	0.3	0.08	0.01
HCFC-22	1206	40.7	0.96	N.S.	-	-
HFC-125	1201	84.0	1.31	0.3	0.05	0.01
HFC-32/125	1045	59.3	1.63	0.2	0.02	0.01
CF_3Br	1556	126.6	1.53	0.3	0.05	0.01

[a]Estimated by using the ideal gas law
[b]Estimated by the method of Lee and Kesler (Reid *et al.*, 1987)
N.S.: not significant

and

$$\delta_g \approx \sqrt{\frac{(h_{fg})_g - RT}{v_g^L}} \tag{23}$$

where f is the fugacity, v^L is the molar "liquid" volume, δ_g is the solubility parameter of solute (nitrogen), δ_a is the solubility parameter of solvent (liquid agent), h_{fg} is the heat of vaporization, superscripts L and G represent liquid and vapor phases respectively, and subscripts a and g represent agent and pressurization gas respectively. In order to use Equation (20) to estimate solubility, the three parameters for the dissolved gas as a hypothetical liquid ($f^L_{pure,\ g}$, v^L_g, and δ_g) need to be specified. These parameters are all dependent on temperature; however, according to the theory of regular solutions the term $v^L_g\ (\delta_a - \delta_g)^2\ \Phi_a^2$ is not temperature-dependent. Therefore, any convenient reference temperature can be used for v^L_g and δ_g as long as the same reference temperature is also used for δ_a and v^L_a. Since the "liquid" molar volume and solubility parameters for gaseous solutes are normally tabulated at 25 °C in the literature, this temperature is used in the following calculation of

$v_g^L (\delta_a - \delta_g)^2 \Phi_a^2$. However, the dependence of the fugacity of the hypothetical liquid on temperature must be considered in the solubility estimation.

By applying the theorem of corresponding states, it can be shown that the reduced fugacity ($f^L_{pure,g}/P_{c,g}$) of the hypothetical pure liquid solute can be correlated as a universal function of the reduced temperature, $T/T_{c,g}$ (Prausnitz and Shair, 1961), where $P_{c,g}$, T and $T_{c,g}$ are the solute critical pressure, the solution temperature and the solute critical temperature respectively. The function can be represented by the following two equations (Walas, 1985):

$$\ln\left(\frac{f^L_{pure,g}}{P_{c,g}}\right) = 7.81 - \frac{8.06\,T_{c,g}}{T} - 2.94\,\ln\left(\frac{T}{T_{c,g}}\right) \qquad 0.7 \le \frac{T}{T_{c,g}} \le 2.5 \tag{24}$$

$$f^L_{pure,g} \approx 6.0 \qquad 2.5 < \frac{T}{T_{c,g}} \le 3.0 \tag{25}$$

The correlation given by Prausnitz and Shair (1961) is for a total pressure (P_t) of 0.101 MPa. To account for higher pressure, the Poynting correction (Prausnitz *et al.*, 1986) should be applied; thus

$$f^L_{pure,g}\ (@\ P_t) = f^L_{pure,g}\ (@ 0.101\ MPa)\ \exp\left[\ \frac{v_g^L (P_t - 0.101)}{RT}\ \right] \tag{26}$$

where P_t is in MPa.

Since Φ_a contains $x_{g,l}$, iteration is required to solve for $x_{g,l}$ in Equation (20). However, the iteration converges rapidly. If the solubility is small, a first approximation of $x_{g,l}$ can be obtained by setting Φ_a equal to unity.

The fugacity, f_g^G, is approximated by the partial pressure of nitrogen in the vapor phase and can be estimated as follows. From Equation (15),

$$f_g^G \approx p_g = P_t - p_a \tag{27}$$

$$f_g^G \approx P_t - (1 - x_{g,l}) p_{sat} \tag{28}$$

Table 9 lists the parameters used in the solubility estimation and the calculated solubilities ($x_{g,l}$). The solubility parameters of the agents were obtained from Daubert and Danner (1992) or were calculated by using Equation (22) with v_a^L assumed to be the molar liquid volume of pure agent at 25 °C. The solubility parameter of nitrogen and v_g^L were obtained from Prausnitz *et al.* (1986).

The third method for predicting solubility is to perform a detailed vapor-liquid equilibrium calculation by using an appropriate equation of state. Specifically, an isothermal flash calculation is required (Prausnitz *et al.*, 1980, 1986, and Walas, 1985). Such calculations involve the determination of vapor and liquid phase compositions, given the total system composition (in this case, the amount of pressurization gas and the agent in the vessel, total pressure, and temperature). The computer program PROZPER developed by Ely and Huber (1993), was used to calculate the solubility of nitrogen in agents. The Peng-Robinson equation of state was used in the calculation although other

Table 9. Parameters used in the estimation of solubilities, calculated solubilities of nitrogen in agents, and calculated mass fractions of nitrogen in agents

Agent	v^L (cm^3/mole) @ 25°C	δ $(J/cm^3)^{1/2}$ @ 25°C	$x_{g,l}$	$w_{g,l}$
HFC-236fa	111.4	12.9	0.18	0.04
FC-31-10	159.0	11.9	0.18	0.03
FC-318	133.4	13.0	0.18	0.03
HCFC-124	100.6	13.1	0.17	0.04
HFC-227ea	121.9	11.5	0.17	0.03
CF_3I	93.2	13.0	0.17	0.03
HFC-134a	84.6	13.5	0.16	0.05
FC-218	142.1	12.3	0.16	0.03
HCFC-22	72.4	17.3	0.14	0.05
HFC-125	100.9	10.2	0.14	0.04
HFC-32/125	64.7	13.0	0.12	0.05
CF_3Br	96.8	14.5	0.13	0.03
Nitrogen	32.4	5.3	-	-

equations of state could be used with some modification. Calculations were performed without taking the binary interaction coefficient into account.

Table 10 shows the input parameters used for the calculation by PROZPER and the calculated solubility. Agents that are not currently included in PROZPER have blank entries in the table. The column, $x_{g,t}$, represents the overall mole fraction of nitrogen in the vessel:

$$x_{g,t} = \frac{n_{g,t}}{n_{g,t} + n_{a,t}} \tag{29}$$

where $n_{g,t}$ and $n_{a,t}$ are the total moles of pressurization gas required and agent in the vessel, respectively, (given in Table 6), and $x_{a,t}$ $(= 1 - x_{g,t})$ is the overall mole fraction of agent.

Table 11 compares the three methods used to estimate nitrogen solubility in the agents studied. The solubilities obtained from the correlation scheme appear to be higher than those obtained by PROZPER, and the values calculated by the mass balance method are generally lower than those obtained by correlations and vapor-liquid equilibrium calculations. However, all three methods predict solubility on the same order of magnitude, and the calculated mass fractions of nitrogen in liquid agents in all cases are less than or equal to 0.05. The discrepancy could be due to the assumptions invoked in both mass balance and correlation techniques. In the mass balance approach, the density of the mixture is approximated by the density of pure agent. This assumption is only true if $x_{g,l} \rightarrow 0$. On the other hand, the correlation scheme may not work well if the pressure is high or if the solution is not regular.

Table 10. Experimental parameters, calculated solubilities of nitrogen, and mass fraction of nitrogen in liquid agents

Agent	T (K)	P_t (MPa)	$x_{g,t}$	$x_{g,l}$	$w_{g,l}$
HFC-236fa	296	4.27	0.29	-	-
FC-31-10	296	4.15	0.38	-	-
FC-318	297	4.16	0.34	0.13	0.02
HCFC-124	296	4.16	0.27	0.09	0.02
HFC-227ea	297	4.16	0.29	0.12	0.02
CF_3I	296	4.28	0.25	0.09	0.01
HFC-134a	296	4.18	0.22	0.09	0.03
FC-218	296	4.15	0.30	0.15	0.03
HCFC-22	295	4.12	0.17	0.07	0.02
HFC-125	296	4.21	0.21	0.11	0.03
HFC-32/125	297	4.17	0.13	-	-
CF_3Br	296	4.17	0.19	0.09	0.02

The first two approximate methods, discussed above, for estimating solubility are not appropriate for calculating solubility of CHF_3 in liquid agents because the assumptions made in the calculations become invalid. Given the amount of CHF_3 and that of the agent at a specified temperature and pressure, the solubility of CHF_3 in the liquid agent can, in principle, be estimated by performing an isothermal flash calculation. However, since the critical point of CHF_3 is very close to the experimental condition (at room temperature, and ~ 4.1 MPa), attempts to use PROZPER to estimate the solubility of CHF_3 in the agents were unsuccessful, the reason being that the Peng-Robinson equation of state may not be able to represent the region near the critical point well.

2.4 Summary and Recommendations

A vessel filled 1/3 with liquid agent initially at room temperature increased in pressure as it was heated to 150 °C to a value below 11 MPa (1600 psia), for all of the pure compounds studied. The HFC-32/125 mixture had the highest final pressure, 10.78 MPa. When cooled to −61 °C, the pressure of all the agents except FC-116 dropped below the ambient (0.101 MPa). The final pressure of FC-116 was 0.25 MPa (37 psia).

The amount of nitrogen required to pressurize the vessel to 4.1 MPa (600 psia) accounted for less than 8% of the total mass of the agent. The calculated mass fractions of nitrogen dissolved in the liquid agents in all cases was less than 0.05. For N_2/agent mixtures, the final pressure of the vessel at 150 °C was less than 14 MPa (2040 psia), with the HFC-32/125 mixture again yielding the highest final pressure (13.8 MPa). The nitrogen in the mixture maintained an appreciable residual pressure

Table 11. Comparison of the three methods used to calculate solubilities of nitrogen in agents (conditions shown in Table 6)

Agent	$x_{g,l}$ (Mass balance)	$x_{g,l}$ (Correlation)	$x_{g,l}$ (PROZPER)
HFC-236fa	0.05	0.18	-
FC-31-10	0.11	0.18	-
FC-318	0.10	0.18	0.13
HCFC-124	0.06	0.17	0.09
HFC-227ea	0.07	0.17	0.12
CF_3I	0.06	0.17	0.09
HFC-134a	0.05	0.16	0.09
FC-218	0.08	0.16	0.15
HCFC-22	-	0.14	0.07
HFC-125	0.05	0.14	0.11
HFC-32/125	0.02	0.12	-
CF_3Br	0.05	0.13	0.09

of 1.24 MPa (180 psia) even when the vessel was cooled to −60 °C. This residual pressure is essential when the vessel is discharged at a cold ambience.

Significant amounts of CHF_3 were needed to pressurize the vessel to 4.1 MPa because CHF_3 is readily soluble in all of the liquid agents studied. For all of the CHF_3/agent mixtures, pressures above 13.7 MPa (2000 psia) were reached for temperatures as low as 70 °C. At −60 °C, the final pressures dropped below 0.45 MPa (65 psia). This low pressure would make CHF_3 an unfavorable choice for a pressurization gas if discharge of the vessel happened at very cold temperatures.

The following recommendations are made to ensure the integrity of the storage vessel:

1. The current pressure vessels described in military specification MIL-C-22284A (proof pressure of 9.62 MPa and minimum burst pressure of 12.37 MPa) should not be used as drop-ins for any of the core alternative agents when the vessels are to be exposed to or stored at temperatures up to 150 °C.

2. Trifluoromethane, CHF_3, should not be used as a pressurization gas. If discharge of the vessel is to occur at cold ambience, a very low residual pressure will exist, and at temperature in excess of 70 °C, very high pressures could lead to rupture of the vessel.

2.5 References

Abu-Eishah, S.I., "Calculation of Vapor-Liquid Equilibrium Data for Binary Chlorofluorocarbon Mixtures Using the Peng-Robinson Equation of State," *Fluid Phase Equilibria 62*, 41 (1991).

Allied Signal Inc., *Selected Physical Properties: HCFC-123, HCFC-123a, HCFC-124, HFC-125, HFC-134, HFC-134a, and HFC-143a*, Allied Signal Inc., Buffalo Research Laboratory, Buffalo, New York, 1990.

Allied Signal Inc., *Genetron® Products Technical Bulletin: R-32/125 Azeotrope*, Allied Signal Inc., Genetron® Products, Morristown, New Jersey, July 1991.

ASHRAE Inc., *ASHRAE Thermodynamic Properties of Refrigerants*, ASHRAE Inc., New York, 1969.

Braker, W., and Mossman, A.L., *Matheson Gas Data Book*, 6th ed., Matheson Gas Products, New Jersey, 1980.

Brown, I.A., and Mears, W.H., "Physical Properties of n-Perfluorobutane," *J. Phys. Chem. 62*, 960 (1958).

Daubert, T.E., and Danner, R.P., *Physical and Thermodynamic Properties of Pure Chemicals, Data Compilation*, Hemisphere Publishing Corporation, New York, 1992.

Denbigh, K., *The Principles of Chemical Equilibrium*, Cambridge University Press, Cambridge, 1984.

Ely, J., and Huber, M.L., *PROZPER*, personal communication with M.L. Huber (1993).

Eng, E., and Joffe, J., "Thermodynamic Properties of Perfluoropropane," *J. Chem. Eng. Data 11*, 376 (1966).

Gallagher J., McLinden, M., Huber, M., and Ely, J., *NIST Standard Reference Database 23: Thermodynamic Properties of Refrigerants and Refrigerant Mixtures Database (REFPROP), Version 4.0*, U.S. Department of Commerce, Washington, DC 1993.

Great Lake Chemical Corporation, *FM-200™: Environmentally Superior Fire Extinguishant for Total Flooding Applications*, Great Lake Chemical Corporation, West Lafayette, Indiana, May 1993.

Kudchadker, A.P., Kudchadker, S.A., Shukla, R.P., and Patnaik, P.R., "Vapor Pressures and Boiling Points of Selected Halomethanes," *J. Phys. Chem. Ref. Data 8*, 499 (1979).

Morrison, G., and McLinden, M.O., *Application of a Hard Sphere Equation of State to Refrigerants and Refrigerant Mixtures*, NBS Technical Note 1226, U.S. Department of Commerce, Washington, DC 1986.

Peng, D.-Y., and Robinson, D.B., "A New Two-Constant Equation of State," *Ind. Eng. Chem. Fundam. 15*, 59 (1976).

Piao, C., Sato, H., and Watanabe, K., "Thermodynamic Charts, Tables, and Equations for Refrigerant HFC-134a," *ASHRAE Transactions 97*, 268 (1991).

Platzer, B., Polt, A., and Maurer, G., *Thermophysical Properties of Refrigerants*, Springer-Verlag, Berlin, 1990.

Prausnitz, J.M., and Shair, F.H., "A Thermodynamic Correlation of Gas Solubilities," *AIChE Journal 7*, 682 (1961).

Prausnitz, J.M., Anderson, T.F., Grens, E.A., Eckert, C.A., Hsieh,R., and O'Connell, J.P., *Computer Calculations for Multicomponent Vapor-Liquid and Liquid-Liquid Equilibria*, Prentice-Hall, New Jersey, 1980.

Prausnitz, J.M., Lichtenthaler, R.N., and Gomes de Azevedo, E., *Molecular Thermodynamics of Fluid Phase Equilibria*, 2nd ed., Prentice-Hall, New Jersey, 1986.

Reid, R.C., Prausnitz, J.M., and Poling, B.E., *The Properties of Gases and Liquids*, 4th ed., McGraw-Hill, New York, 1987.

Shankland, I.R., Basu, R.S., and Wilson, D.P., "Thermophysical Properties of HCFC-124: An Environmentally Acceptable Refrigerant," *ASHRAE Transactions 96*, 317 (1990).

Sladkov, I.B., and Bogacheva, A.V., "Critical Parameters of Mixed Carbon Halides," *Zhurnal Prikladnoi Khimii 64*, 2435 (1991); *64*, 2276 (1992) (English translation).

Smith, J.M., and Van Ness, H.C., *Introduction to Chemical Engineering Thermodynamics*, 3rd ed., McGraw-Hill, New York, 1975.

Walas, S.M., *Phase Equilibrium in Chemical Engineering*, Butterworth, Boston, 1985.

Yaws, C.L., Ni, H.M., and Chiang, P.Y., "Heat Capacities for 700 Compounds," *Chemical Engineering 95(7)*, 91 (1988).

3. FLUID DYNAMICS OF AGENT DISCHARGE

William M. Pitts, Jiann C. Yang, Grzegorz Gmurczyk,
Leonard Y. Cooper, William L. Grosshandler
Building and Fire Research Laboratory

William G. Cleveland, Cary Presser
Chemical Science and Technology Laboratory

3.1 Introduction

The extinguishment of a fire using gaseous agents is a very complicated process which is not completely understood. Current fire-fighting agents such as halon 1301 and halon 1211 are believed to function by a combination of chemical (catalytic removal of hydrogen atoms at the flame front due to the presence of bromine atoms) and physical (cooling and dilution of flame gases) actions. All of the proposed alternative agents are known to be less effective (*i.e.*, considerably higher molar concentrations of the agent are required) than halon 1301. This reduction in effectiveness is attributed to the absence of bromine atoms in these chemicals and thus the absence of a highly effective chemical means of fire extinguishment.

An aspect of fire extinguishment using halons which has not received a great deal of attention is the role that the dispersion and evaporation characteristics of the agent play in fire-fighting effectiveness. The reason for this lack of interest in the past was that these properties have been nearly optimized by the use of halon 1301 for total flooding applications and halon 1211 for spray applications. With regard to total flooding applications, which are of most interest for this study, the low boiling point of halon 1301 has ensured that, for the majority of applications, it can be dispersed and vaporized very rapidly into a space. Design of total flooding systems generally have focused on the use and placement of hardware designed to ensure all areas of an enclosure quickly receive concentrations of the agent sufficient to extinguish the fire.

The fire fighting applications--nacelle and dry bay fires on aircraft--which are the focus of the current investigation have different requirements with respect to these agent characteristics. Due to the nature of dry bay fires, detection and extinguishment is generally required within tens of milliseconds. On the other hand, nacelle fires tend to have burned for longer periods before extinguishment and a premium is placed on the achievement of extinguishing concentrations which can be maintained for a period of time following extinguishment to prevent relight on heated surfaces. Effective dispersion throughout the volume is required, but the dispersion can take place over longer periods of time than for the dry-bay application. Due to the more stringent requirements for dry bay fire extinguishment, much of the work which follows has focused on rapid release and dispersion of agents. It should be kept in mind, however, that the findings also have applications for nacelle fire-fighting.

Even though the physical mixing processes involved are not generally considered in designs of halon fire-fighting systems, they are crucial. The important processes can be characterized into three major categories--release rate, dispersion and mixing, and evaporation. The release rate determines the minimum time required to extinguish a fire. If the release is very slow it is possible that the fire may never be extinguished.

The release rate for an agent also generally, but not always, affects the subsequent dispersion and mixing behavior of the agent. Much of the dispersion and mixing is the result of the momentum imparted to the agent by its release. If sufficiently high, this momentum causes the development of turbulent flows which can effectively transport the released agent throughout a volume.

In order to be fully effective, gaseous agents must interact with the flame as a gas. All of the alternative agents considered here, with the exception of FC-116, are liquids when stored under pressure at room temperature. As will be shown shortly, the room-temperature agents are released from pressurized bottles into ambient atmospheres as superheated liquids, *i.e.*, the liquid has a vapor pressure which is above the ambient pressure. Therefore, the vaporization behavior of these liquids following release becomes an important characteristic for fire fighting effectiveness.

This chapter discusses experimental and modeling studies which were designed to rank the proposed alternative agents with respect to release rate, dispersion and mixing, and evaporation. The following section (Section 3.2) describes the development of a model for predicting the release behavior of pressurized liquids from a containment vessel. This effort provided guidance for the design of an experimental system for investigating the release behavior and subsequent mixing and evaporation of the proposed alternative agents and halon 1301. The vessel design is discussed in Section 3.3. Experimental characterizations of the release rates from the vessel and characterization of vessel interior conditions are summarized in Section 3.4 for all of the agents and halon 1301. Section 3.5 describes the development and use of an experimental system for characterizing the dispersion and evaporation behavior of the alternative agents and halon 1301 following release from the pressurized vessel. During the course of this study initial attempts were made to modify existing computer models for two-phase evaporating flows to allow computation of agent release behaviors. These efforts are discussed in Section 3.6. The final section of the report summarizes the major findings of the chapter and provides recommendations for future work as well as a ranking for the alternative agents based solely on their release rate, dispersion and mixing, and evaporation behaviors.

3.2 Model of Discharging Vessel

3.2.1 The Problem and the Objective. This work formulates a mathematical model to simulate the discharge of halon and halon-alternative fire extinguishment agents from N_2-pressurized vessels. The objective is to develop a mathematical model which simulates agent-discharge experiments.

The model is expected to have three applications. First, it was used to guide the development of the experimental design and procedure (see Section 3.3) which closely simulates discharge of field-deployed vessels while allowing for acquisition of data, including high speed photography, to characterize adequately the discharge process. Second, the model will be used to evaluate the discharge characteristics of a wide range of alternative-agent/pressure-vessel configurations, thereby extending the slow and relatively costly experimental method of making such evaluations. Finally, it will be used to determine the discharge vessel exit-flow conditions for use in the simulation of agent dispersal outside of the vessel. [See Section 3.6.3 and Cooper (1993b).] After presenting the mathematical model, this section will include results of example calculations which addressed the first of these applications. Descriptions of the model have been presented previously elsewhere (Cooper, 1993a).

The analysis is based on the experimental arrangement depicted in Figure 1.

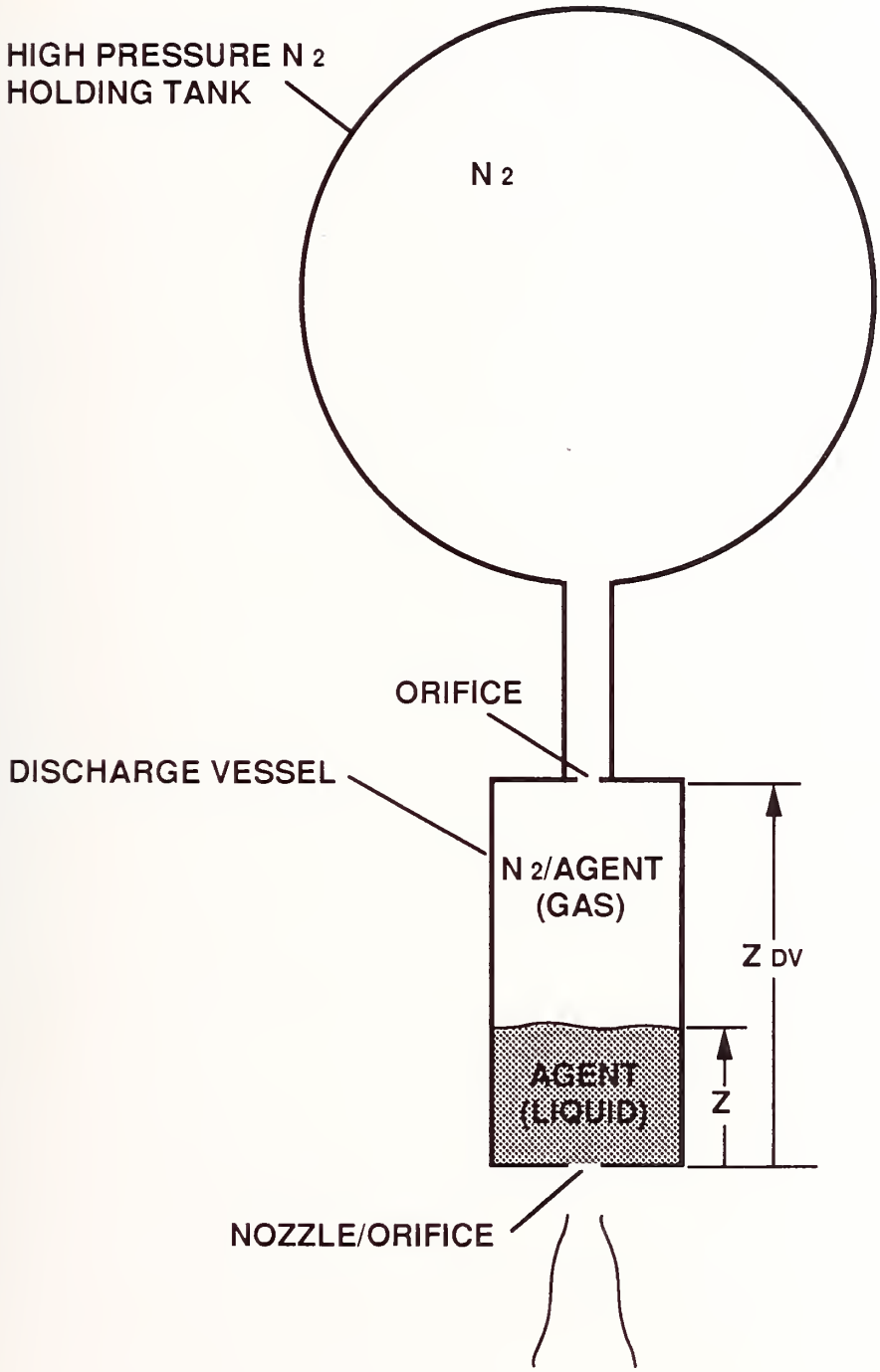

Figure 1. The experimental arrangement.

3.2.2 The Experiment and the Model Assumptions

3.2.2.1 The Experimental Arrangement. Refer to Figure 1. This represents generically the arrangement associated with the downward discharge experiments which were carried out at NIST. The Figure 1 arrangement can also be used to describe the phenomena of discharge from vessels under field conditions.

The experimental arrangement involves a right cylinder discharge vessel at pressure P_{DV}, which contains N_2-pressurized test agent, and a holding tank filled with mass $M_{HT,N2}$ of N_2 at pressure P_{HT}. The discharge vessel is of height Z_{DV} and cross-sectional area A_{DV}. The volume of the holding tank is V_{HT}.

The holding tank is connected *via* an orifice of area A_O to the discharge vessel. It is assumed that the flow path through the orifice can be opened or closed with a relatively fast-acting solenoid valve. If the path is open it is assumed that $P_{HT} \geq P_{DV}$, *i.e.*, the flow is always from the holding tank to the discharge vessel. In the case of a field-deployed system there is no holding tank and A_O is zero.

At the bottom of the vessel is a short-nozzle/orifice-type opening (note that the containment vessel exit will be referred to as the "nozzle/orifice" for the purposes of this section and Section 3.6.3) of area A_N. The agent will be discharged through this to the outside ambient environment which is at pressure $P_{AMB} < P_{DV}$. The discharge flow path is originally closed off by a cap or diaphragm. When the cap is removed, the test agent liquid is driven out of the discharge vessel by virtue of the cross-nozzle/orifice pressure difference.

3.2.2.2 The Procedure Prior to An Experimental Run or a Field-Deployed Discharge. The orifice and nozzle/orifice flow paths are closed and the discharge vessel is evacuated. The vessel is then filled completely with a known mass of test agent. There will be a volume of liquid agent below and a volume of gaseous agent above and the pressure will be P_{SAT}, the saturation pressure at the agent temperature. The vessel is then pressurized with N_2. This flows into the vessel from the holding tank or from some other relatively high-pressure N_2 source. In general, the upper gas volume is now a two-component mixture of N_2 and test agent gas. Although some N_2 may be dissolved in the liquid volume, it is assumed that the amount is always so small that throughout subsequent sequential (additional) pressurization and discharge processes to be studied here the properties of the liquid in the discharge vessel are well approximated by the liquid properties of the pure test agent.

Now consider the system at the time, $t = 0$, when an experimental run or a field-deployed discharge is initiated. The liquid/gas interface is a distance Z_1 above the bottom of the vessel. The mass of liquid in the vessel is $M_{DV,AL}$ (the subscript refers to that portion of Discharge Vessel test Agent in the Liquid state) and, throughout the experimental run or field-deployed discharge, the temperature and density of the liquid that remains in the vessel will be assumed to maintain their respective initial values, T_{AL} and $\rho_{AL} = \rho_{SAT}(T_{AL})$. As indicated, ρ_{AL} is estimated to be the density of saturated test agent liquid at the saturation temperature T_{AL}. The gas mixture is at an assumed uniform initial temperature $T_{DV,1}$ and the initial masses of gaseous test agent and N_2 in the discharge vessel are $M_{DV,AG}$ and $M_{DV,N2,1}$, respectively. Note that the prepressurization process, prior to $t = 0$, may have been so rapid that the liquid and gas are not in thermal equilibrium with each other. For this reason, $T_{DV,1}$ is not necessarily identical to T_{AL}. The discharge vessel and the holding tank are at the uniform pressures $P_{DV,1}$ and $P_{HT,1}$, respectively.

3.2.2.3 During an Experimental Run or Field-Deployed Discharge. During discharge of a Figure 1-type system, the flow path through the orifice is either open or closed at $t = 0^+$. When the orifice is closed the discharge will simulate discharge of a field-deployed system which does not involve a holding tank. When the orifice is open the discharge will simulate discharge of the experimental system where additional N_2 pressurization during the discharge is provided by the holding tank. The flow path through the nozzle/orifice at the exit of the discharge vessel is either opened at $t = 0^+$ (as in the field-deployed system, which uses an explosive cap to initiate discharge from an equilibrium state at the specified $P_{DV,1}$) or else it opens if and when P_{DV} rises to some specified diaphragm rupture/burst pressure, $P_{BURST} < P_{HT,1}$ (as in the experimental system). The time when this latter flow path is opened is designated as t_{BURST}.

3.2.2.4 Further Assumptions. For times and conditions of interest, it is assumed that as long as liquid remains in the vessel $P_{DV} > P_{SAT}(T_{AL})$, and there is no possibility of flashing (*i.e.*, spontaneous change from a thermodynamically unstable liquid state to an equilibrium, two-phase, liquid/gas state) in the liquid volume. Future work will address the problem of removing this latter constraint from the analysis. It is assumed that any N_2 dissolved in the liquid that may come out of solution during the discharge process is negligible.

The purpose of this work is to mathematically model the state of the system at any $t > 0$ up to t_D, where t_D is the smaller of 1) the time when the discharge vessel is emptied of test-agent liquid, and 2) the time when P_{DV} is reduced to $P_{SAT}(T_{AL})$. For experimental systems of interest here, t_{BURST} is expected to be of the order of 10 s and the time interval of the discharge process, $(t_D - t_{BURST})$, of the order of 10^{-2} s. Prior to t_D there is no gas mixture discharge from the vessel. The mass of gaseous agent in the vessel therefore remains constant at its initial value $M_{DV,AG}$.

In view of the relatively short times of interest it is assumed that during an experimental run or field-deployed discharge there is no heat or mass transfer across the liquid/gas interface. It is also assumed that there is no heat or mass transfer across the interface that contains the nitrogen and gaseous test agent in the combined holding-tank/discharge-vessel system, *e.g.*, there is negligible heat transfer to the walls of the vessel and holding tank. This is the basis of the assumption that both $M_{DV,AG}$ and the total mass of N_2 in the combined system, designated as M_{N2}, are constant for all t, $0 < t < t_D$. M_{N2} is determined from the initial conditions.

It is assumed that the gaseous test agent and the N_2 can be modeled as perfect gases with constant specific heats and gas constants, $C_{V,AG}$ $C_{P,AG}$, R_{AG} and $C_{V,N2}$ $C_{P,N2}$, R_{N2}. The values of the specific heats, which depend on temperature, are taken to be those which correspond to $T_{DV,1}$.

3.2.3 The Model Equations. Together with specified parameters, the unknown time-dependent variables of the problem that define the state of system at an arbitrary time are: P_{HT}, P_{DV}, $M_{HT,N2}$, $M_{DV,N2}$, $M_{DV,AL}$, T_{HT}, T_{DV}, and Z. Known/specified parameters would include: the initial values of these variables, $P_{HT,1}$, $P_{DV,1}$, $M_{HT,N2,1}$, $M_{DV,N2,1}$, $M_{DV,AL,1}$, $T_{HT,1}$, $T_{DV,1}$, and Z_1, respectively; the geometric parameters of the system, A_O, A_N, A_{DV}, Z_{DV}, and V_{HT}; material properties of the test agent and of N_2; the constant value $M_{DV,AG}$; and nozzle/orifice discharge coefficients, to be introduced below. The equations governing the variables are:

Equations of State in the Holding Tank and in the Discharge Vessel and the Law of Partial Pressure in the Discharge Vessel:

$$P_{HT} = \left(\frac{M_{HT,N2}}{V_{HT}}\right) R_{N2} T_{HT} \tag{1}$$

and

$$P_{DV} = \frac{(M_{DV,AG} R_{AG} + M_{DV,N2} R_{N2}) T_{DV}}{[(Z_{DV} - Z) A_{DV}]} \tag{2}$$

Conservation of Mass of N_2:

$$M_{DV,N2} + M_{HT,N2} = constant = M_{N2} = M_{DV,N2,1} + M_{HT,N2,1} \tag{3}$$

Relation of Z to $M_{DV,AL}$:

$$\frac{M_{DV,AL}}{\rho_{AL}} = A_{DV} Z \tag{4}$$

Reversible Adiabatic Expansion for N_2 in Holding Tank:

$$\frac{P_{HT}}{(M_{HT,N2})^{\gamma}} = constant = \frac{P_{HT,1}}{(M_{HT,N2,1})^{\gamma}} \; ; \quad \gamma = \frac{C_{P,N2}}{C_{V,N2}} = \frac{R_{N2}}{C_{V,N2}} + 1 \tag{5}$$

First Law of Thermodynamics for Entire Gas System:

$$\frac{d[(M_{DV,AG} C_{V,AG} + M_{DV,N2} C_{V,N2}) T_{DV} + M_{HT,N2} C_{V,N2} T_{HT}]}{dt} = P_{DV} A_{DV} \frac{dZ}{dt} \tag{6}$$

Flow Across the Orifice:

$$\frac{dM_{HT,N2}}{dt} = \begin{cases} -C_{D,O}A_O P_{HT}\left[\left[\frac{\gamma}{R_{N2}T_{HT}}\right]\left[\frac{2}{(\gamma+1)}\right]^{(\gamma+1)/(\gamma-1)}\right]^{1/2} \\ \qquad if\ \frac{P_{HT}}{P_{DV}} \geq \left[\frac{(\gamma+1)}{2}\right]^{\gamma/(\gamma-1)}\ (i.e.,\ choked\ flow) \\ -C_{D,O}A_O P_{HT}\left[\frac{P_{DV}}{P_{HT}}\right]^{1/\gamma}\left[\frac{2\gamma\left[1-\left[\frac{P_{DV}}{P_{HT}}\right]^{(\gamma-1)/\gamma}\right]}{[(\gamma-1)R_{N2}T_{HT}]}\right]^{1/2} \\ \qquad if\ \frac{P_{HT}}{P_{DV}} < \left[\frac{(\gamma+1)}{2}\right]^{\gamma/(\gamma-1)}\ (i.e.,\ un\text{-}choked\ flow) \end{cases} \tag{7}$$

where $C_{D,O}$ is the (compressible) flow coefficient for the orifice (Shapiro, 1953).

Flow Across the Nozzle/Orifice:

$$\frac{dM_{DV,AL}}{dt} = \begin{cases} -C_{D,N}A_N\left[2\rho_{AL}(P_{DV}-P_{AMB})\right]^{1/2} & if\ P_{AMB} \geq P_{SP} \\ -C_{D,N}A_N\left[2\rho_{AL}(P_{DV}-P_{SP})\right]^{1/2} & if\ P_{AMB} < P_{SP} \end{cases} \tag{8}$$

where $C_{D,N}$ is the flow coefficient for the nozzle/orifice and P_{SP} is defined below. Assuming that $A_N/A_{DV} << 1$ in discharge vessels of interest here, in Equation (8) the kinetic energy of the liquid upstream of the exit nozzle is neglected compared to the kinetic energy at, and immediately downstream of the nozzle.

3.2.4 Definition of P_{SP} and Comments on Equation (8). In Equation (8) it is assumed that the liquid in the discharge vessel, at state $[T, P] = [T_{AL}, P_{DV} > P_{SAT}(T_{AL})]$, flows into and through the exit nozzle/orifice while moving along state paths of constant entropy. When the pressure of the liquid drops below its saturation pressure, the liquid is assumed to initiate its movement into the "vapor dome" as a metastable superheated liquid.

For the generic pure material, the relevant *P-V* diagram which depicts the metastable states is sketched in Figure 2. This includes the region of metastable superheated liquid states and the corresponding region of metastable subcooled vapor states. For a pure material the metastable liquid or vapor state can only be maintained where $(\partial P/\partial V)|_T < 0$ (Modell and Reid, 1983), *i.e.*, only outside the locus of points, referred to as the spinoidal curve, where $(\partial P/\partial V)|_T = 0$. The spinoidal curve, sketched in Figure 2, passes through the critical state and has the superheated liquid region to its left and the subcooled vapor region to its right.

At any time during the discharge, P_{SP} is defined as the particular pressure along the liquid-leg of the spinoidal curve of the test agent associated with the intersection of the spinoidal curve and the

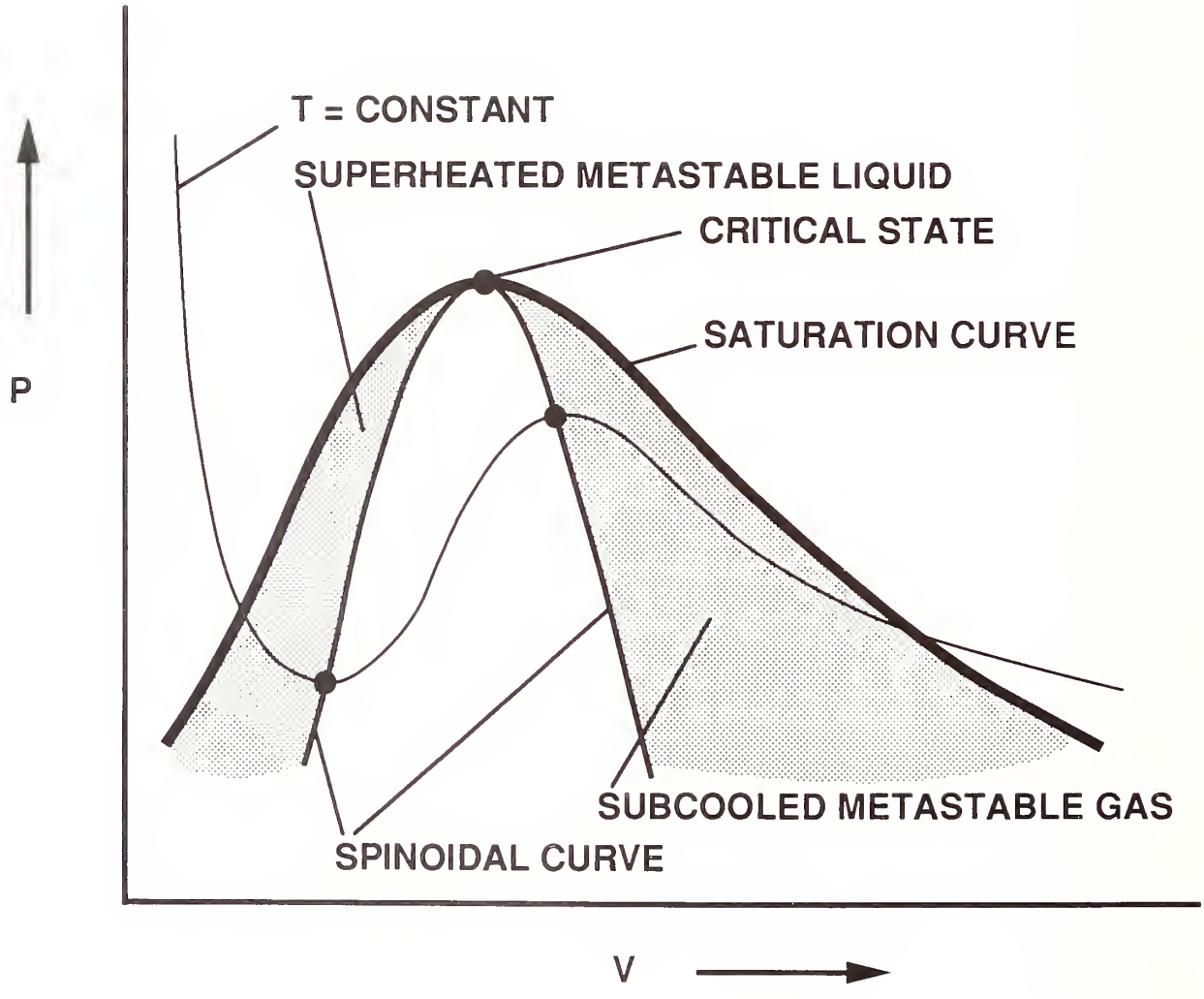

Figure 2. *P-V* diagram for a generic material; the spinoidal curve and regions of metastable liquid and vapor.

above-mentioned, instantaneous, constant-entropy paths. Since states along the spinoidal curve are states of unstable equilibrium where spontaneous nucleation will occur (Modell and Reid, 1983; Kim-E and Reid, 1983), *i.e.*, the constant-entropy metastable-state path of the liquid cannot be sustained at the state defined by the intersection point, it is conjectured that if $P_{SP} > P_{AMB}$ violent flashing of the liquid jet occurs where and when its pressure reaches P_{SP}. This would be upstream of a physically unachievable, *i.e.*, unstable, *vena contracta* at pressure P_{AMB}.

If P_{AMB} is achieved prior to the P_{SP} state then the top portion of Equation (8) is used. For this circumstance the constant-entropy state of the possibly metastable superheated liquid at P_{AMB} is a physically admissible endpoint to the liquid-jet development process. The situation is consistent with the idea that: 1) the endpoint state coincides with the *vena contracta* of the jet; 2) the jet is convected for some distance downstream of this endpoint without substantial changes and at the *vena contracta* diameter; and 3) the jet eventually breaks apart due to fluid-dynamic and/or thermodynamic (flashing) instabilities. Note that the upper Equation (8)-description of the nozzle flow rate of a superheated liquid as an incompressible, nonflashing fluid, is consistent with results reported in the literature, *e.g.*, (Benjamin and Miller, 1941) for flow through sharp-edge orifices and short nozzles.

If P_{SP} is achieved prior to P_{AMB} then flashing of the metastable liquid will be initiated immediately downstream of the position in space where the intercept occurs. In the latter case the incompressible flow calculation methodology is still applicable at and upstream of the spinoidal-curve intercept point. This is indicated by the use of the bottom portion of Equation (8).

The above discussion is illustrated with CO_2. For stable and metastable liquid CO_2, a sketch based on a drawing by Kim-E (1981, see his Figure 4) of constant-entropy paths in a P-T diagram is presented in Figure 3. In preparing his figure, Kim-E used the Peng-Robinson (1976) equation of state to describe the metastable liquid CO_2.

First assume that liquid CO_2 is in a Figure 1-type discharge vessel at $P_{DV} = 70 \times 10^5$ Pa and $T_{AL} = 288$ K. In Figure 3 this initial state is seen to lie on the $s = s2$ constant-entropy line, which has no positive P intercept with the spinoidal curve. As the liquid CO_2 flows toward and then out of the vessel's nozzle/orifice its state is assumed to move downward along the *s2* curve of Figure 3. As can be seen, the $P = P_{ATM} \approx 1 \times 10^5$ Pa intercept on this curve, corresponding to $T \approx 277$ K, represents an achievable metastable liquid state for the material. This is the metastable liquid state that is predicted by the present model. It would be expected at, and for some distance downstream of, the jet's *vena contracta*.

Now assume that liquid CO_2 in a discharge vessel is at $P = P_{DV} = 60 \times 10^5$ Pa and $T = T_{AL} = 291$ K. In Figure 3 this initial state is seen to lie on the $s = s3$ constant-entropy line, which intersects the spinoidal curve at approximately $P_{SP} = 10 \times 10^5$ Pa $>> P_{AMB}$. In this case, as the liquid CO_2 flows through and out of the vessel nozzle/orifice the model predicts that it will flash explosively when $P = P_{SP}$. This will occur upstream of the position at which a fluid jet *vena contracta* would otherwise occur; well within a distance of one nozzle/orifice diameter downstream of the vessel exit.

This nozzle/orifice flow model is consistent with a discharge process involving a smoothly time-varying P_{DV}, a constant T_{AL}, and an abrupt change in nozzle/orifice exit flow from a simple incompressible-fluid-jet type flow to an explosively flashing two-phase flow. Note that the idea of using the condition of the existence of $P_{SP} > P_{AMB}$ as a criterion for violent flashing of liquids flowing through sharp-edged orifices or very short nozzle-like openings does not seem to have been proposed previously. Nor has it been validated quantitatively.

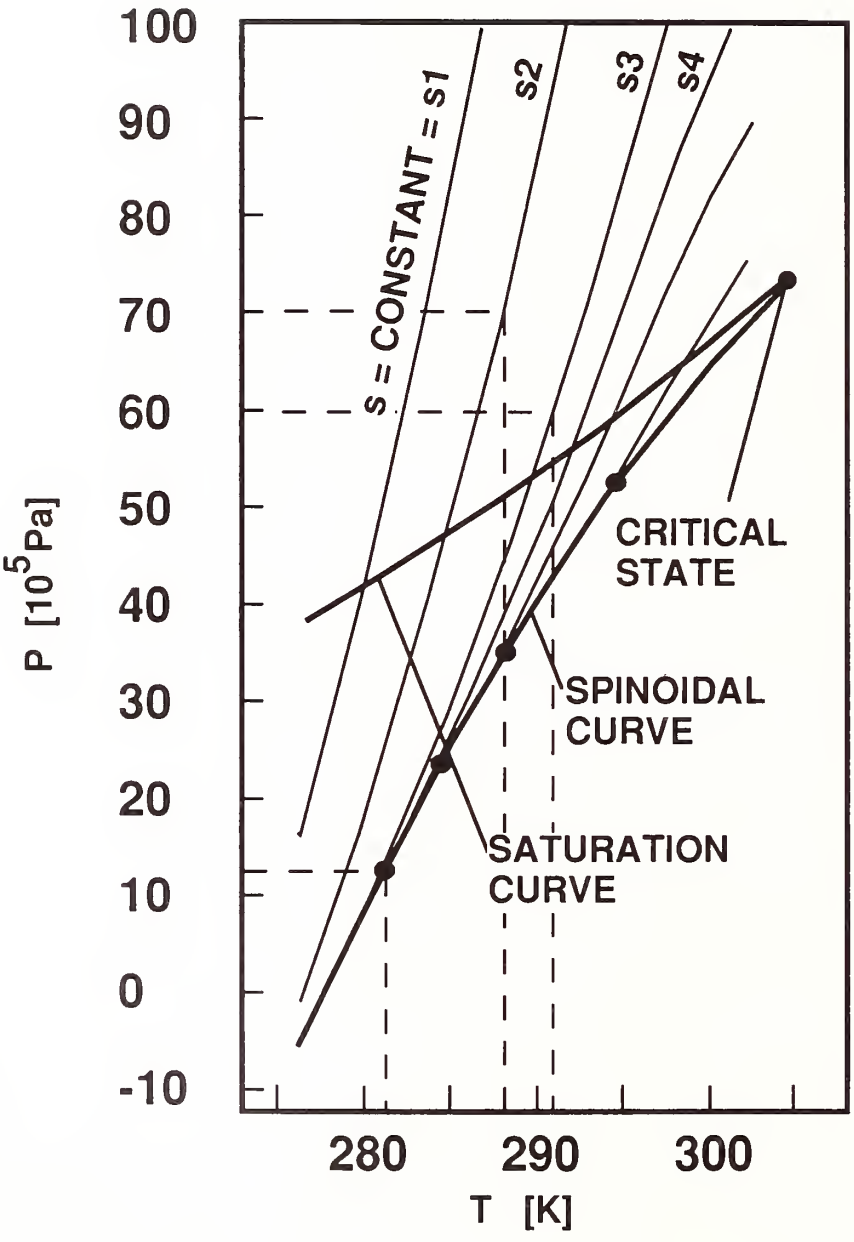

Figure 3. *P-T* diagram for metastable liquid CO_2.

3.2.5 Reduced Dimensionless Equation Set - The Initial Value Problem. Equations (1)-(8) are made dimensionless by introducing a dimensionless time, τ, dimensionless mass of N_2 and liquid agent in the discharge vessel, x_2 and x_3, respectively, and a combined variable, x_1.

$$x_1 = \frac{(1 + \lambda_3 x_2) P_{DV}}{(1 + \lambda_1 x_2) P_{DV,1}} \left[\frac{Z_{DV}}{Z_1} - x_3 \right] + \lambda_2 \lambda_4 (1 - x_2)^{\gamma}; \quad x_2 = \frac{M_{DV,N2}}{M_{N2}}; \quad x_3 = \frac{M_{DV,AL}}{M_{DV,AL,1}}$$
$$\tau = t C_{D,N} A_N \left[\frac{2 P_{DV,1}}{(M_{DV,AL,1} A_{DV} Z_1)} \right]^{1/2} \tag{9}$$

$$\lambda_1 = \frac{M_{N2}}{M_{DV,AG}} \frac{R_{N2}}{R_{AG}}; \quad \lambda_2 = \frac{\frac{P_{HT,1}}{P_{DV,1}}}{\left[\frac{M_{HT,N2,1}}{M_{N2}} \right]^{\gamma}}; \quad \lambda_3 = \frac{\lambda_1 (\gamma_{AG} - 1)}{(\gamma - 1)}; \quad \lambda_4 = \frac{(\gamma_{AG} - 1) V_{HT}}{(\gamma - 1) Z_1 A_{DV}} \tag{10}$$

The initial values of the x's are functions of the various parameters of the particular problem of interest. The dimensionless initial value problem for an arbitrary Figure 1-configuration is

$$\frac{dx_i}{d\tau} = \sigma_i; \quad x_i(0) \textit{ specified}, \; i = 1, 2, 3;$$
$$\sigma_i = \sigma_i(x_1; x_2; x_3; \textit{parameters of the problem}) \tag{11}$$

The reader is referred to Section 3.2.13 (Appendix) for definitions of the σ_i and for explicit equations to extract values of time-dependent dimensional variables from a solution of Equation (11).

3.2.6 N_2 Jet-Driven Mixing in the Discharge Vessel - Estimating the Resulting Disturbance of the Liquid/Gas Interface. The above model assumes that throughout the pressurization and discharge process the agent gas and the N_2 in the discharge vessel are fully mixed and in a state of thermodynamic equilibrium. It is also assumed that there is no significant heat or mass transfer interactions at the gas/liquid interface, *i.e.*, it is assumed that the interface is relatively quiescent.

In cases where there is no N_2 flow from the holding tank (*e.g.*, the orifice is closed) the initial fully-mixed state of the gases will persist throughout depressurization, the gas volume will be relatively quiescent, and the assumption of negligible interface interactions is expected to hold. This is the case for actual field-deployed systems.

When there is N_2 flow from the holding tank, it is the N_2 jet from the orifice that will drive gas mixing in the discharge vessel. Refer to Figure 4. If jet velocities are too large, the liquid/gas interface disturbance of the jet can be violent enough to invalidate the quiescent interface assumption.

For the configuration of Figure 1 and Figure 4, the significance of the effect of the N_2 jet impinging on the liquid surface can be determined from an estimate of the axial velocity of the orifice jet at the liquid/gas interface. Such an estimate is obtained here from the characteristics of an incompressible submerged jet (*i.e.*, analogous to the N_2 orifice jet) in an unconfined space (analogous to the gas volume of the discharge vessel). The estimate is also useful for other orifice orientations.

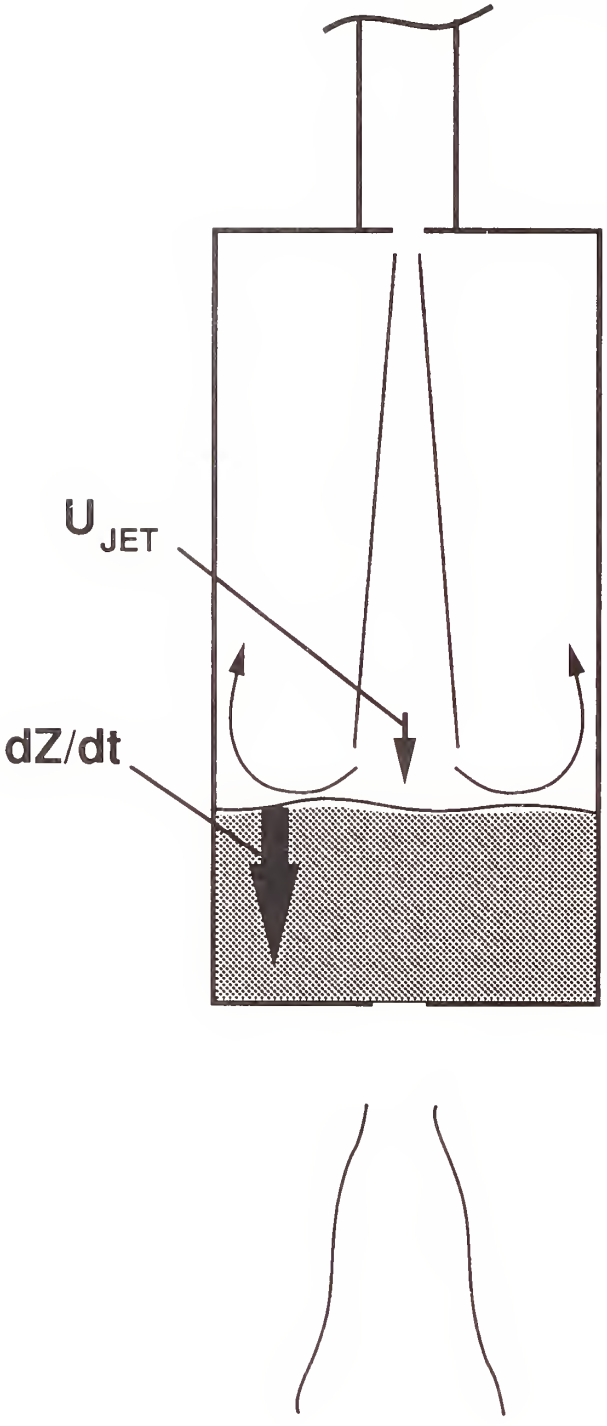

Figure 4. Sketch of the orifice-driven N_2 jet flow in the discharge vessel.

Let the velocity on the jet axis a distance $Z_{JET} = Z_{DV} - Z$ from the orifice (*i.e.*, at the elevation of the liquid/gas interface) be denoted by U_{JET} and assume a uniform velocity, U_O, across the orifice opening,

$$U_O = \frac{\frac{dM_{DV,N2}}{dt}}{\frac{A_O M_{HT,N2}}{V_{HT}}}. \tag{12}$$

From Abramowitz (1963),

$$\frac{U_{JET}}{U_O} = \frac{0.96}{\left[\frac{0.132 Z_{JET}}{D_O} + 0.29\right]} \quad for \quad \frac{Z_{JET}}{D_O} > 5 \tag{13}$$

When the time-dependent solution for $M_{DV,N2}$ is available, U_{JET} can now be estimated from Equations (12) and (13) and the significance of the jetting phenomenon can be assessed.

3.2.7 Solving the Model Equations. A computer program was developed to solve the initial value problem of Equation (11) corresponding to an arbitrary choice of geometric parameters, material properties, and initial conditions, and to determine the value of U_{JET} from Equations (12) and (13). The method of solution is based on the differential equation solver **RKQC** presented by Press (1986). The program was used in the example calculations to follow.

3.2.8 Example Calculations

3.2.8.1 An Experimental Procedure to Simulate the Discharge of Field-Deployed Vessels. As mentioned in Section 3.2.1, the example calculations to be presented here focused on providing guidance for the experimental design and procedure such that a vessel discharge of the experimental system closely simulates the discharge of a field-deployed vessel, while allowing for acquisition of data, including high-speed photography, to characterize the discharge process.

Field-deployed systems use an explosive device to remove, "on demand," a cap covering the exit nozzle/orifice of a prepressurized discharge vessel. Thus, the deployed system is characterized by a Figure 1-type configuration with no holding tank component, *i.e.*, with $A_O = 0$.

The nature of the experimental program at NIST precluded the use of an explosive cap device. The experimental procedure to be evaluated therefore involved a vessel discharge process which was initiated, instead, by the rupture of a nozzle/orifice diaphragm cap at a high cross-diaphragm pressure difference. The pressurization of the discharge vessel from $P_{DV,I}$ to the diaphragm burst pressure, P_{BURST}, was assumed to be achieved with the use of the holding-tank/orifice-flow feature of Figure 1.

As discussed earlier, an experimental run involves sequential processes of vessel pressurization and discharge. Initially, the diaphragm cap prevents flow from the vessel to the outside environment. At $t = 0^+$ the orifice connecting the vessel and the holding tank is opened and pressurization of the vessel is initiated. At the instant the pressure in the vessel reaches the diaphragm burst pressure, the diaphragm ruptures. Nozzle/orifice flow and discharge of the vessel are then initiated. As mentioned

earlier, the pressurization and discharge processes of interest here are expected to occur over time intervals of the order of 10 s and 10^{-2} s, respectively.

Prior to any particular test run, P_{BURST} is only known to an accuracy of approximately 10%. Also, the high-speed camera used to photograph the discharge process during the test procedure could record a total time interval no longer than the order of a few seconds, including an initial interval of approximately 1 s required to bring the camera up to its operating speed.

3.2.8.2 Criteria for Experimental Discharges to Closely Simulate Field-Deployed Discharges. One would hope to determine that an experimental discharge would closely simulate a field-deployed system discharge by obtaining good agreement between results of model simulations of the two processes. The basic criterion would be good reproduction of the predicted time-dependent values of P_{DV} and $M_{DV,AL}$.

Since field-deployed discharges involve no addition of N_2 and no significant heat or mass transfer at the liquid/gas interface, an acceptable Figure 1-type experimental procedure should similarly involve discharges with no significant addition of N_2. In view of this, in addition to the above criterion, two additional criteria must be satisfied if the experimental discharge is to simulate closely a field-deployed discharge: 1) the experiment must include a discharge process during which the total mass of N_2 delivered from the holding vessel to the discharge vessel is small compared to the mass of N_2 in the discharge vessel immediately prior to the onset of discharge, *i.e.*,

$$require \ \frac{(M_{N2} - M_{N2,B})}{M} << 1 \ for \ t > t_{BURST} \tag{14}$$

where $M_{N2,B}$ is the mass of N_2 in the discharge vessel at t_{BURST}; and 2) the addition of N_2 during the entire pressurization/discharge sequence does not lead to gas flows in the discharge vessel gas (where velocities will be of the order of U_{JET}) which are so vigorous as to lead to significant heat or mass transfer at the liquid/gas interface. It is reasonable to expect that interface surface interactions will not be significant if $U_{JET} - dZ/dt$ never exceeds the order of a few m/s. Thus

$$require \ U_{JET} - \frac{dZ}{dt} < 5\text{–}10 \ m/s \ for \ t \geq 0 \ s \tag{15}$$

3.2.8.3 Model Input Parameters. Sets of parameters representative of those for a Figure 1-type experimental design were selected to simulate discharge of a field-deployed system with a 0.5×10^{-3} m^3 discharge vessel half-filled with liquid HCFC-22 and pressurized with N_2 to 41.4×10^5 Pa. Parameters of the field-deployed system are included in Table 1.

The selected parameter sets of Table 1 defined simulations of 18 different experimental systems and the single simulation of the field-deployed system. The parameters sets were used to define and solve the model's initial value problem. Solution results provide time-dependent histories of all model variables and the information necessary to determine whether or not the criteria of Equations (14) and (15) are satisfied during the simulation.

As indicated, the model simulations involve the agent HCFC-22. In solving Equations (11) and (12) the thermodynamic properties listed in Table 2 and Table 3 were used for HCFC-22 and for N_2.

Table 1. Characteristics of Simulated Discharges - Model Input Parameters

agent material	HCFC-22						
$T_{DV,1}$ = $T_{HT,1}$ =	294 K						
diameter of discharge vessel = D_{DV} =	0.05 m						
volume of discharge vessel = V_{DV} =	0.5×10^{-3} m^3						
initial volume of liquid agent in discharge vessel	$V_{DV}/2 = 0.25 \times 10^{-3}$ m^3						
D_N =	0.0191 m						
V_{HT} =	2.5×10^{-3} m^3 (large holding tank)				2.5×10^{-5} m^3 (small holding tank)		field simulation (no holding tank)
$P_{HT,1}$ =	51.7×10^5 Pa				155×10^5 Pa		-
$P_{DV,1}$ =	34.5×10^5 Pa		9.38×10^5 Pa = $P_{SAT}(T_{DV,1})$		34.5×10^5 Pa		41.4×10^5 Pa
P_{BURST}=	37.9×10^5 Pa	44.8×10^5 Pa	37.9×10^5 Pa	44.8×10^5 Pa	37.9×10^5 Pa	44.8×10^5 Pa	41.3×10^5 Pa
D_O =	0.5 mm, 1 mm, and 5 mm	0.5 mm, 1 mm, and 5 mm	0.5 mm, 1 mm, and 5 mm	0.5 mm, 1 mm, and 5 mm	0.5 mm, 1 mm, and 5 mm	0.05 mm 1 mm, and 5 mm	-

Table 2. Properties of HCFC-22

Molecular Weight	86.47 kg/mole
Liquid Density [$\rho_{AL} = \rho_{SAT}(294\ K)$]	1209 kg/m^3
Constant Pressure Specific Heat [$C_{P,AG}$]	57×10^3 Jkg^{-1}mole^{-1}K^{-1}
Saturation Pressure [P_{SAT}]	$6895(T/R)^{-C} \times [F - (T/R)]^{E[F - (T/R)]/[F(T/R)]} 10^{A - B/(T/R) + D(T/R)}$ Pa where A=29.36, B=3845.1, C=7.861, D=0.002190, E=305.8, F=686.1

The following completes the information used to fully define the model equations.

The flow coefficient for the nozzle/orifice (flow of test agent liquid from the discharge vessel to the outside environment) was assigned a value of

$$C_{D,N} = 0.60. \tag{16}$$

The use of Equation (8) and the σ_1 and σ_3 components of Equation (11) require values of P_{SP} for isentropic paths from the time-dependent liquid states in the discharge vessel. For the present calculation it is assumed that throughout the discharge process $P_{SP} < P_{ATM} = 1.01 \times 10^5$ Pa, *i.e.*, spinoidal-curve type instabilities of the metastable exit liquid stream do not occur during the major portion of the discharge-process time interval. However, as seen above in the discussion of CO_2, this assumption can not be expected to hold in general, and actual estimates of P_{SP} will have to be included in more general applications of the mathematical model.

An expression for the flow coefficient, $C_{D,O}$, for the flow through a sharp-edged orifice (flow of N_2 from the holding tank to the discharge vessel) as a function of cross-orifice pressure ratio, P_{DV}/P_{HT}, is taken from Perry (1949). Data points for $C_{D,O}(P_{DV}/P_{HT})$ are plotted in Figure 5. In the present calculations, values of $C_{D,O}$ are estimated by linear interpolation between these data points.

To determine the constant mass of gaseous test agent in the discharge vessel it is assumed that the process of filling the vessel included a time when pure test agent filled the entire vessel with gas and liquid volumes in thermodynamic equilibrium with each other. The mass of gaseous agent at this time is taken to be $M_{DV,AG}$. In the present calculations it is assumed that at this time of equilibrium the agent temperature was 294 K. This is the value taken above for the initial temperatures $T_{DV,1}$ and $T_{HT,1}$.

3.2.9 Relatively Low-Pressure Large-Volume Holding Tank. This section presents results for the pressurization/discharge sequence using a relatively low-pressure large-volume holding tank. Note that experimental safety considerations motivate use of relatively low-pressures in the holding tank, especially when it is of relatively large volume.

$V_{HT} = 2.5 \times 10^{-3}$ m^3 is chosen to be ten times larger than the initial gas volume in the discharge vessel and $P_{HT,1} = 51.7 \times 10^5$ Pa is chosen to be 6.9×10^5 Pa greater than the maximum of the diaphragm burst pressure which can fall within the range 37.9×10^5 Pa $< P_{BURST} < 44.8 \times 10^5$ Pa.

Table 3. Properties of Nitrogen

Molecular Weight	28.01 kg/mole
Constant Pressure Specific Heat [$C_{P,N2}$]	[7.440 - 3.24 $\times$ 10^{-3}(T/K) + 6.400 $\times$ 10^{-6} $(T/K)^2$ - 2.790 $\times$ $10^{-9}$$(T/K)^3$] $\times$ 4186 J/(kg-mole·K)

The objective in using the present choice of parameters is to provide for a pressurization process which is slow enough to minimize disturbances of the liquid/gas interface, *i.e.*, satisfy Equation (15), but fast enough to be able to bracket clearly the time of the subsequent discharge process to a known time interval of the order of 1 s. The 1 s time interval is required to guarantee timely triggering of and photographic data acquisition from a high-speed camera during the discharge process. As mentioned above, the latter is expected to occur over a time interval of the order of 10^{-2} s.

The relatively large volume of the holding tank would allow the pressurization/discharge process to be initiated either: 1) from a relatively high-$P_{DV,1}$ state, somewhat below the minimum possible diaphragm burst pressure and with a relatively significant initial mass of N_2 in the discharge vessel; or 2) from a minimum-$P_{DV,1}$ state where there is no N_2 in the discharge vessel (i.e, the discharge vessel initially contains only pure test agent at the saturation pressure $P_{DV,1} = P_{SAT}$, where P_{SAT} is significantly below the P_{BURST} pressures under investigation).

3.2.9.1 Initiating the Pressurization/Discharge Sequence from the Agent's Saturation State; No N_2 in the Discharge Vessel at t = 0. Simulations were carried out for experiments where the pressurization/discharge processes were initiated at the test agent's saturation state, *i.e.*, at $P_{DV,1} = P_{SAT}(T_{DV,1} = 294\ K) = 9.38 \times 10^5$ Pa, *e.g.*, shortly after filling the evacuated vessel with the test agent. In such experiments there is no N_2 in the discharge vessel at t = 0, *i.e.*, $M_{DV,N2,1} = 0$. Results of the calculations are plotted in Figure 6 through Figure 11.

First the pressurization process will be considered. Figure 6 presents plots of P_{DV} and P_{HT} during vessel pressurization, $0 < t < t_{BURST}$. Results are presented for the three orifice diameters, D_O = 0.005 m, 0.001 m, and 0.0005 m.

As seen in Figure 6, for the smallest orifice, D_O = 0.0005 m, the pressurization process, when $P_{DV,1} \leq P_{DV} < P_{BURST}$, takes 4.2 s for $P_{BURST} = 37.9 \times 10^5$ Pa to 5.8 s for $P_{BURST} = 44.8 \times 10^5$ Pa. For the intermediate-size orifice, D_O = 0.001 m, the pressurization process takes 1.0 s for $P_{BURST} = 37.9 \times 10^5$ Pa to 1.4 s for $P_{BURST} = 44.8 \times 10^5$ Pa. For the largest orifice, D_O = 0.005 m, the entire process takes place within 0.1 s.

U_{JET} values corresponding to Figure 6 are presented in Figure 7. For the smallest orifice, D_O = 0.0005 m, U_{JET} starts out at approximately 4 m/s and drops to 2 - 3 m/s at t_{BURST}, the time of diaphragm bursting. For D_O = 0.001 m, U_{JET} starts out at approximately 8 m/s and drops to approximately 4 m/s at t_{BURST}. For D_O = 0.005 m, U_{JET} starts out at approximately 40 m/s and drops to as low as approximately 16 m/s for $P_{BURST} = 44.8 \times 10^5$ Pa at t_{BURST}.

Based on the above results it is concluded that during the pressurization process and relative to the criterion of Equation (15): 1) use of the large orifice would lead to conditions which do not satisfy

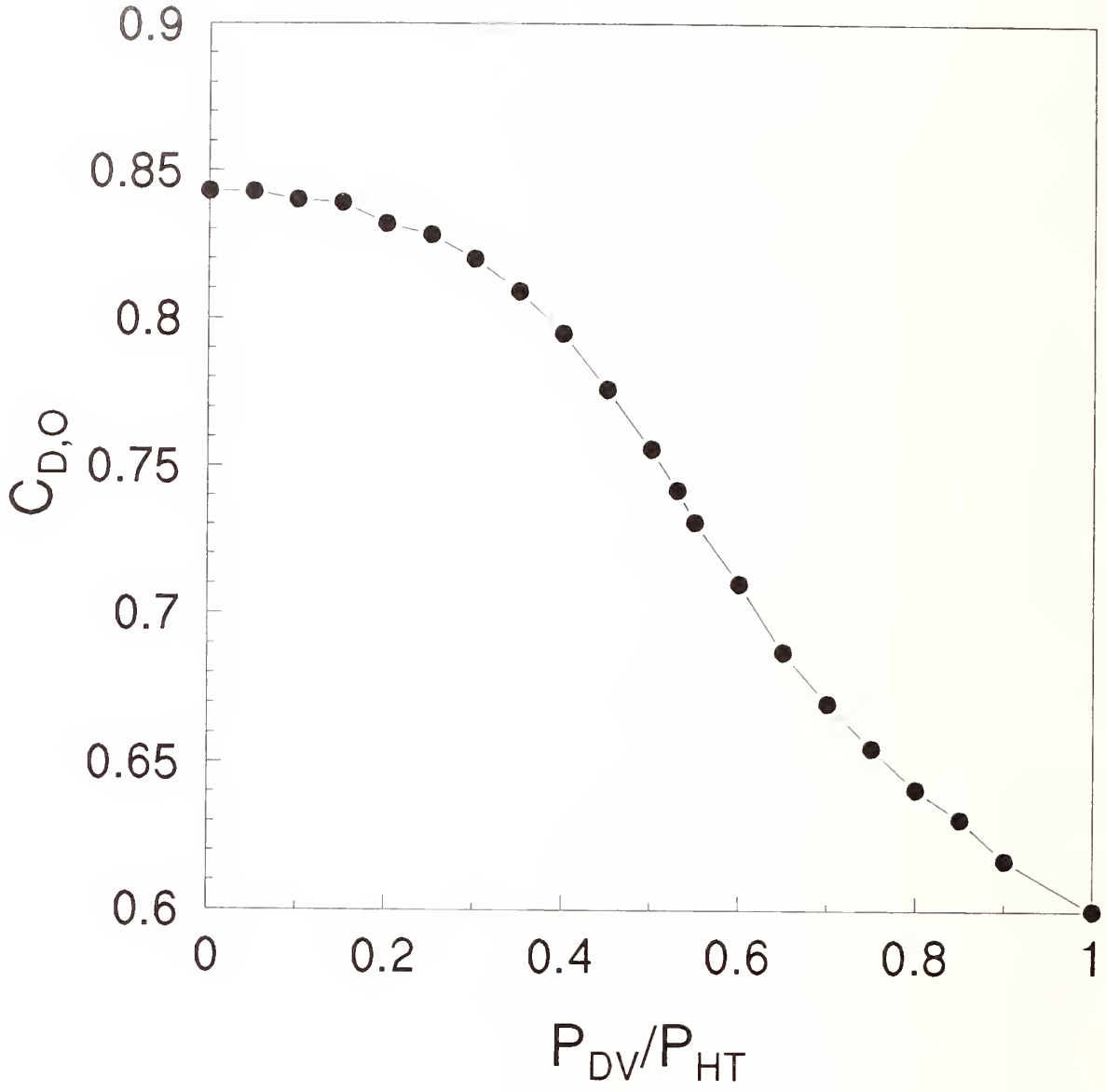

Figure 5. Discharge coefficient, $C_{D,O}$, for compressible flow through a sharp-edged orifice as a function of cross-orifice pressure ratio, P_{DV}/P_{HT} (Perry, 1949).

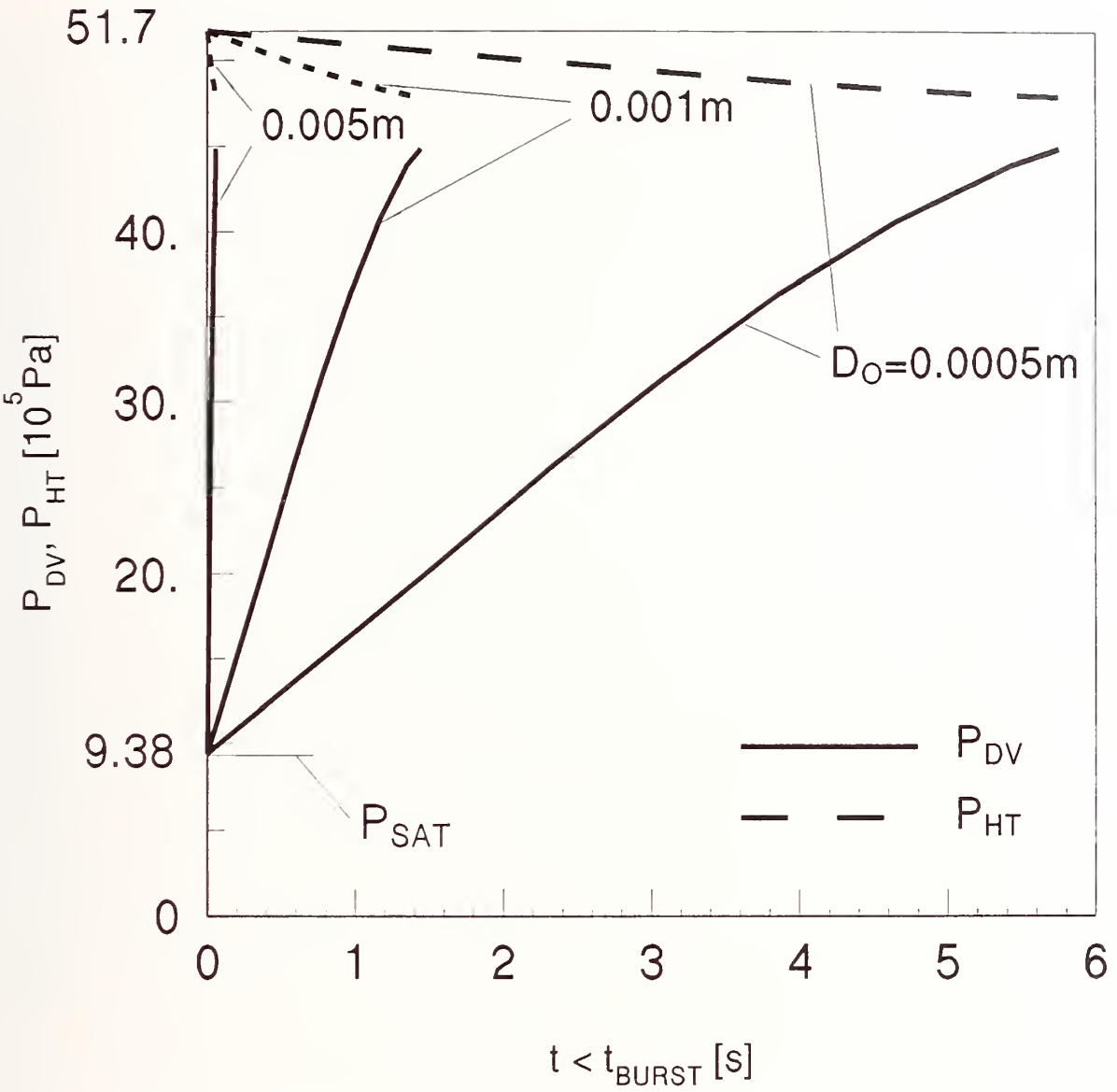

Figure 6. Pressures in the holding tank and discharge vessel for $0 \leq t \leq t_{BURST}$ for a large-volume, low-pressure holding tank and no N_2 in the discharge vessel at $t = 0$.

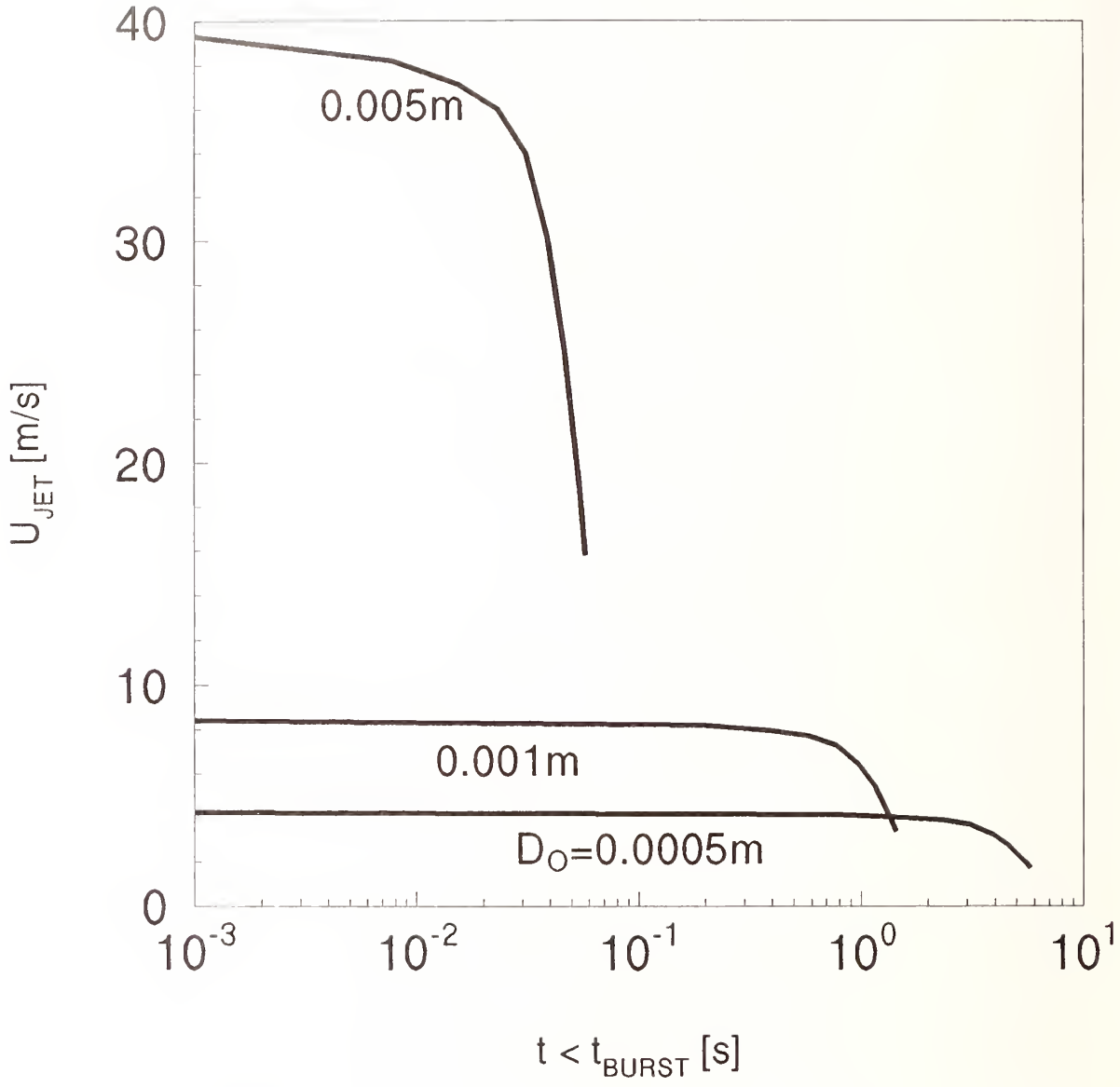

Figure 7. Plots of U_{JET} in the discharge vessel for $0 \leq t \leq t_{BURST}$ for a large-volume, low-pressure holding tank and no N_2 in the discharge vessel at $t = 0$.

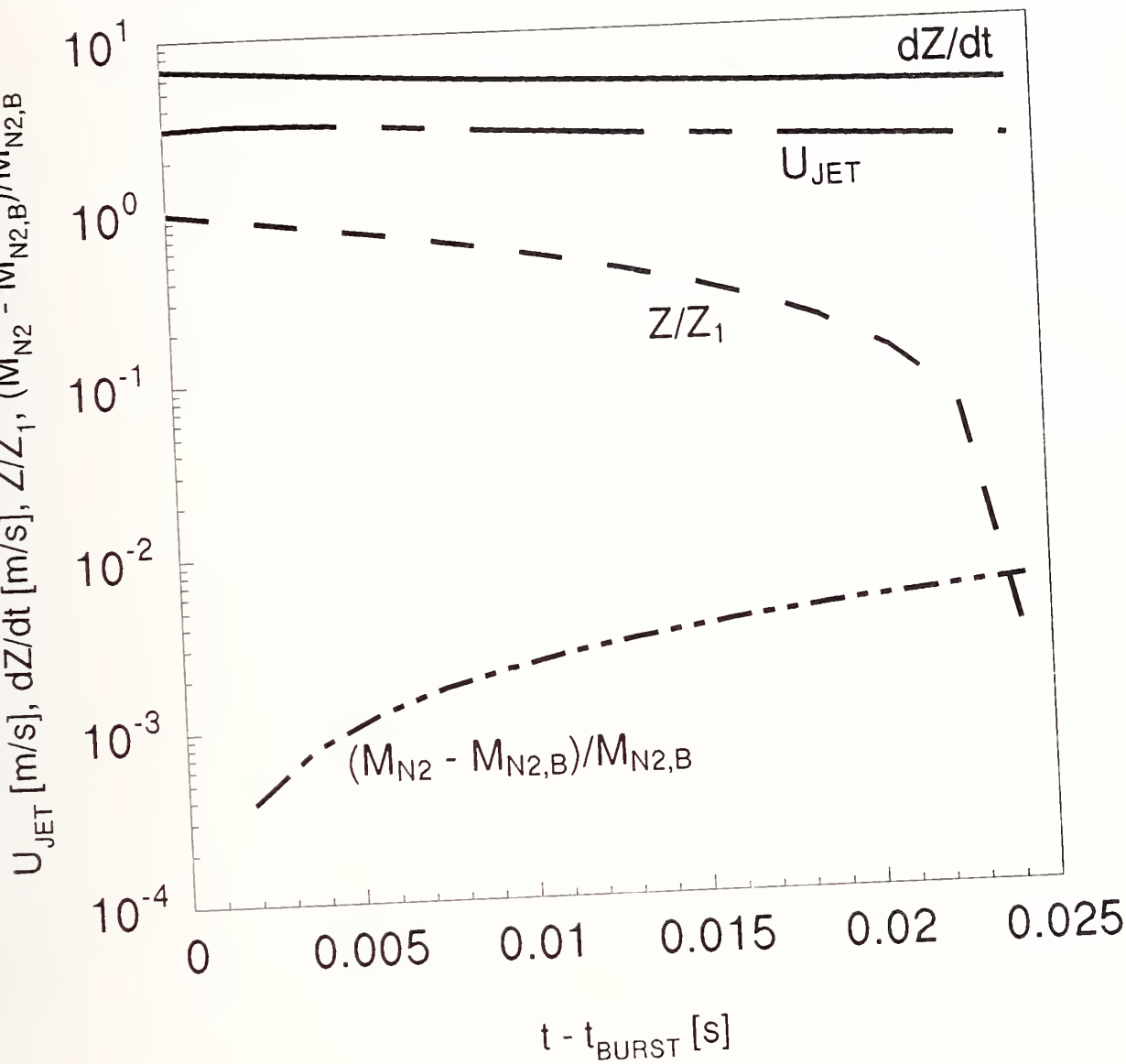

Figure 8. U_{JET}, dZ/dt, Z/Z_1, and $(M_{N2}-M_{N2,B})/M_{N2,B}$ for $t \geq t_{BURST}$; large-volume, low-pressure holding tank; no N_2 in vessel at t=0; D_o=0.5 mm; P_{BURST}=3.8 MPa.

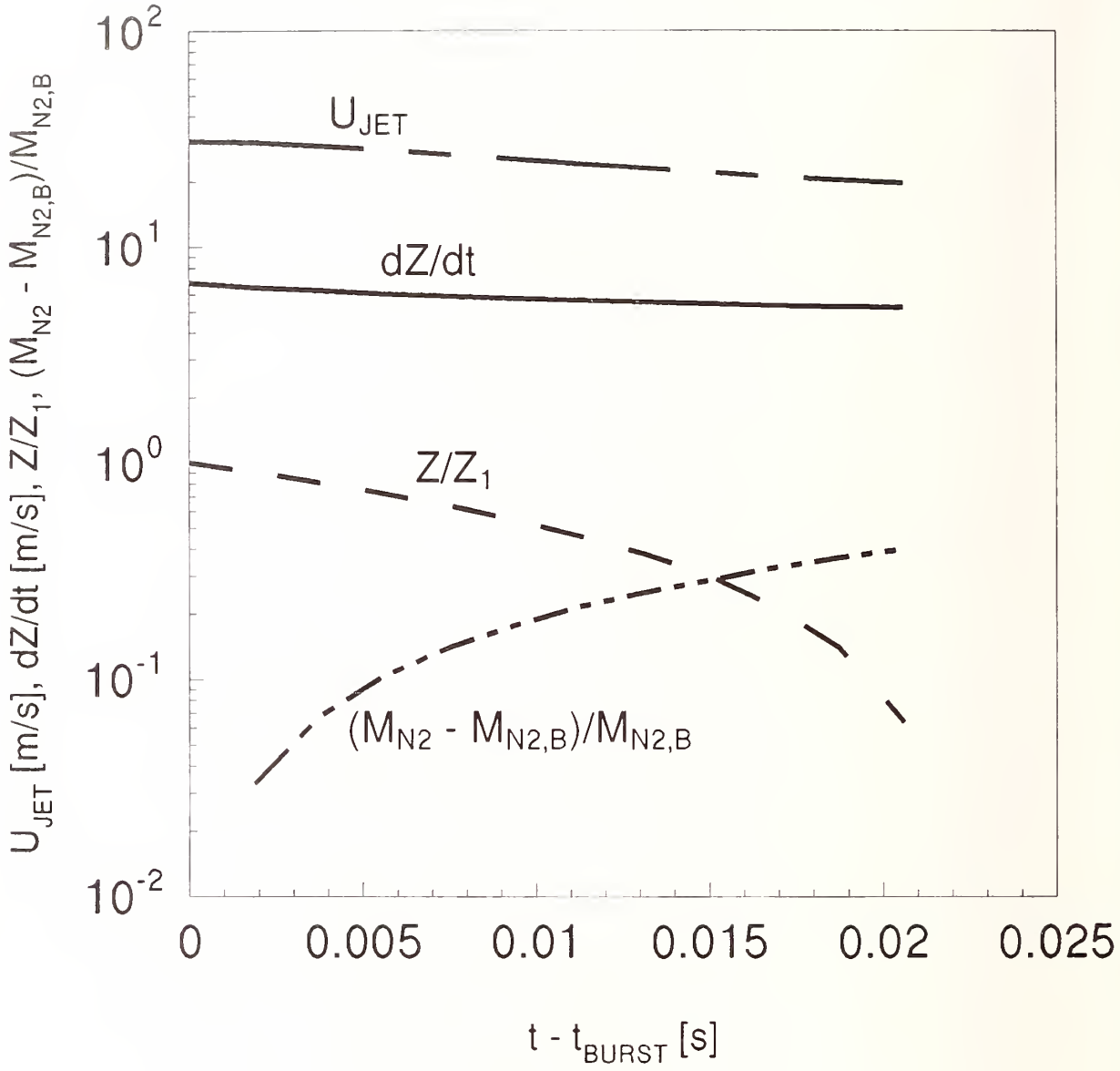

Figure 9. U_{JET}, dZ/dt, Z/Z_1, and $(M_{N2}-M_{N2,B})/M_{N2,B}$ for $t \geq t_{BURST}$; large-volume, low-pressure holding tank; no N_2 in vessel at $t=0$; $D_o=5$ mm, $P_{BURST}=3.8$ MPa.

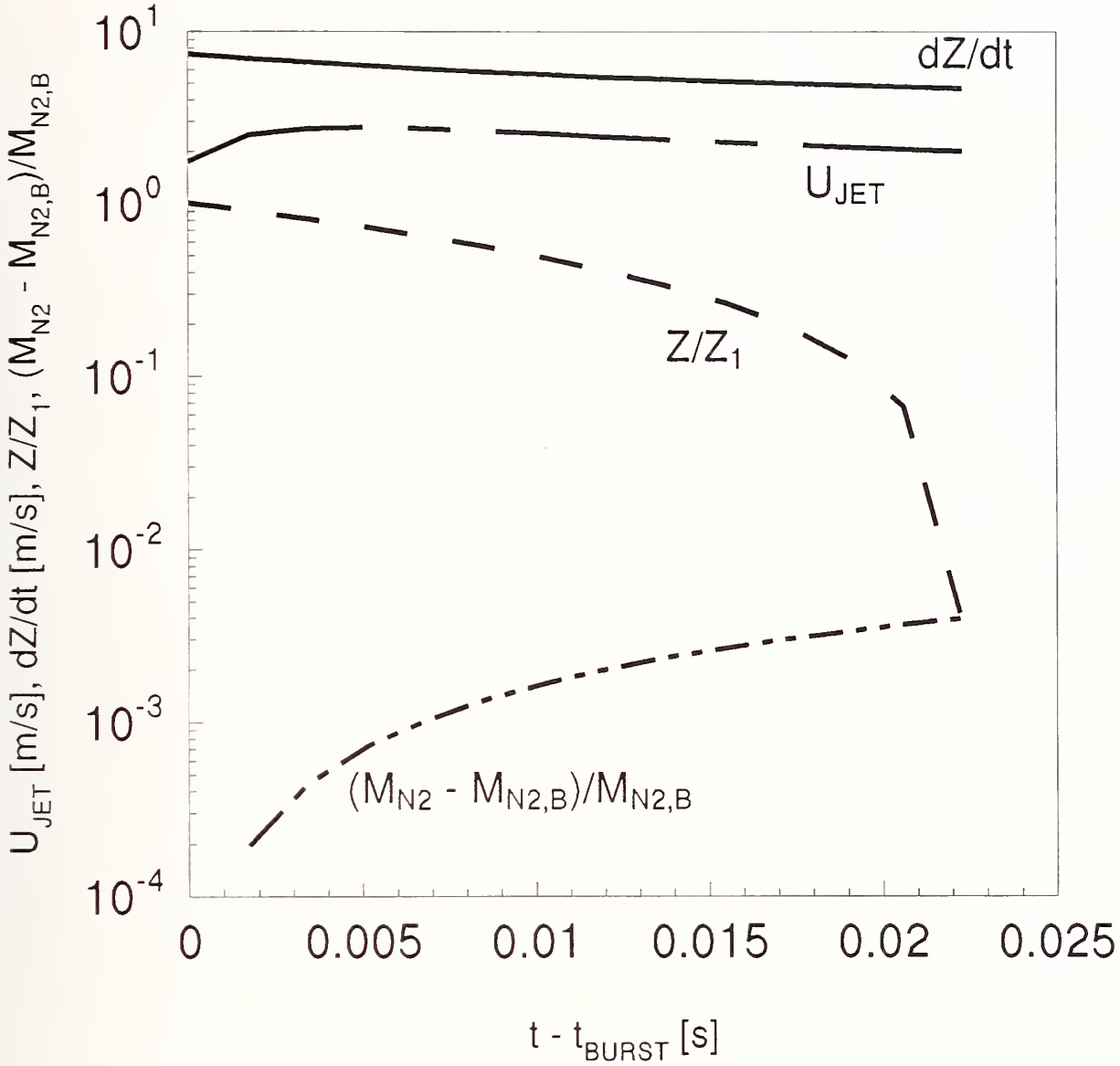

Figure 10. U_{JET}, dZ/dt, Z/Z_1, and $(M_{N2}-M_{N2,B})/M_{N2,B}$ for $t \geq t_{BURST}$; large-volume, low-pressure holding tank; no N_2 in vessel at $t=0$; $D_o=0.5$ mm, $P_{BURST}=4.5$ MPa.

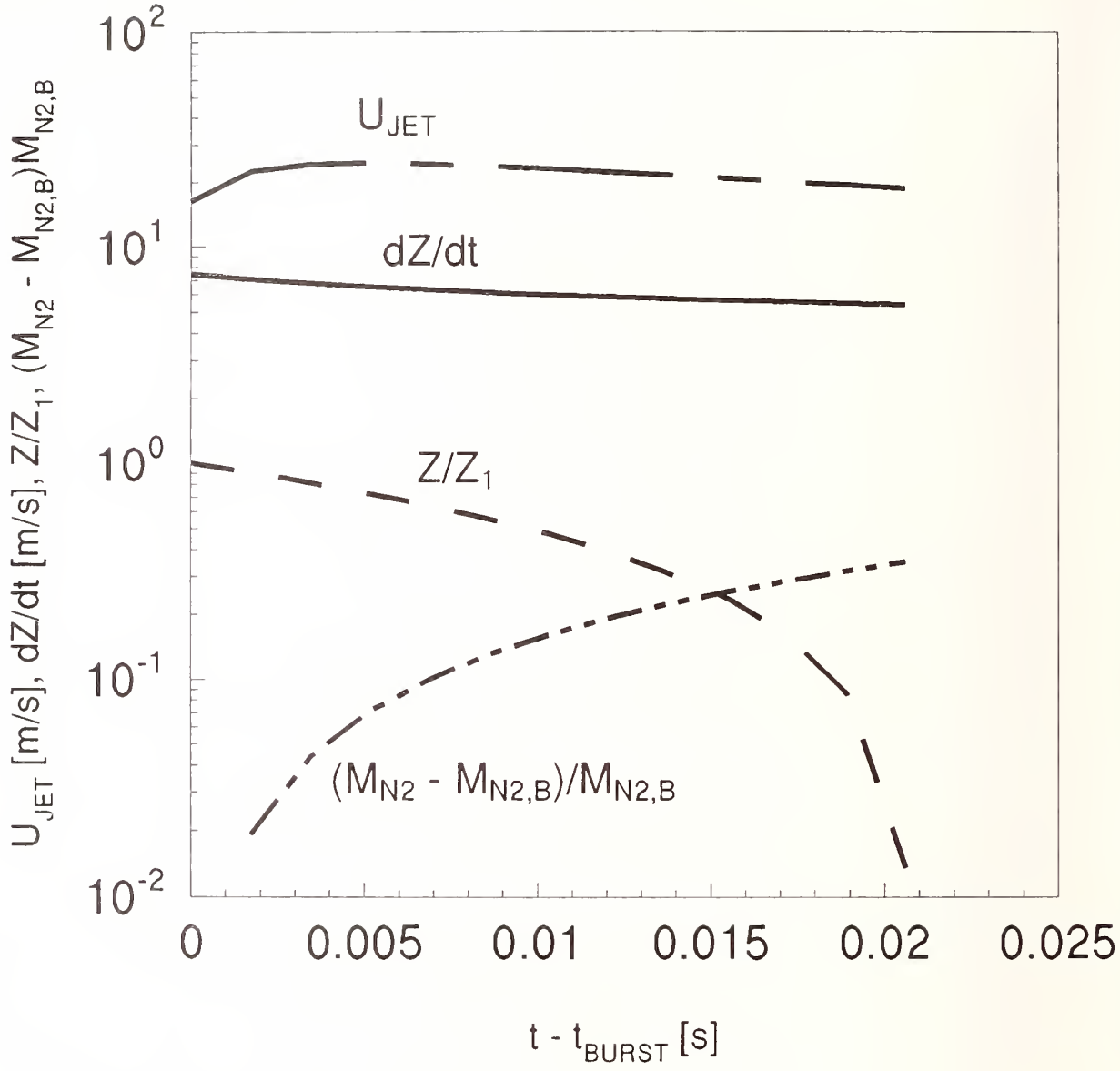

Figure 11. U_{JET}, dZ/dt, Z/Z_1, and $(M_{N2}-M_{N2,B})/M_{N2,B}$ for $t \geq t_{BURST}$; large-volume, low-pressure holding tank; no N_2 in vessel at $t=0$; $D_o=5$ mm, $P_{BURST}=4.5$ MPa.

the criterion; 2) use of the intermediate size orifice would lead to results which are barely acceptable; and 3) use of the small orifice would lead to acceptable performance, provided that pressurization times are consistent with timing requirements of the photographic data acquisition system.

Now the discharge behavior will be discussed. Figure 8 through Figure 11 present plots of U_{JET}, dZ/dt, Z/Z_1, and $(M_{N2} - M_{N2,B})/M_{N2,B}$ during the discharge process. For the limiting burst pressures, $P_{BURST} = 37.9 \times 10^5$ Pa and 44.8×10^5 Pa, results are presented for the small- and large-orifice designs.

Figure 8 presents results for $P_{BURST} = 37.9 \times 10^5$ Pa and $D_O = 0.0005$ m. Once the discharge process is initiated, the liquid is seen to drop from its initial elevation ($Z/Z_1 = 1$) and to be removed entirely from the vessel ($Z/Z_1 \rightarrow 0$) in approximately 0.024 s. Liquid discharge occurs at a relatively uniform rate with dZ/dt dropping from approximately 7.0 to 4.5 m/s during the emptying process. During discharge U_{JET} first rises slightly (because of relatively rapid reductions of P_{DV}, slow reductions of P_{HT}, and resulting increases in cross-orifice pressure difference) from approximately 3 m/s, and then drops (because of the significantly increased length along the jet axis between the source of the jet, at the orifice, and the elevation at the gas/liquid interface - refer to Figure 1 and Figure 4) to the final value of approximately 2 m/s. As can be seen from the plot of $(M_{N2} - M_{N2,B})/M_{N2,B}$, during the entire emptying process the total mass addition of N_2 from the holding tank to the discharge vessel is less than 1% of the initial N_2 mass in the discharge vessel.

Figure 9 presents results for $P_{BURST} = 37.9 \times 10^5$ Pa and $D_O = 0.005$ m. Based on an approximate extrapolation from $t - t_{BURST} = 0.020$ s, once the discharge process is initiated the liquid is seen to drop from its initial elevation and to be removed entirely from the vessel in approximately 0.023 s. Liquid discharge occurs at a relatively uniform rate with dZ/dt dropping from approximately 7.0 to 5.5 m/s during the emptying process. During discharge U_{JET} first rises slightly from approximately 30 m/s, and then drops to the final value of approximately 20 m/s. As can be seen from the plot of $(M_{N2} - M_{N2,B})/M_{N2,B}$, during the entire emptying process the total mass addition of N_2 from the holding tank to the discharge vessel is significant, approximately 45% of the initial N_2 mass in the discharge vessel.

Figure 10 presents results for $P_{BURST} = 44.8 \times 10^5$ Pa and $D_O = 0.0005$ m. Here the discharge is completed in 0.023 s. Liquid discharge occurs at a relatively uniform rate with dZ/dt dropping from approximately 7.5 to 5.0 m/s during the emptying process. During discharge U_{JET} first rises from approximately 1 to 2 m/s, and then drops back to the final value of approximately 1 m/s. During the discharge the total mass addition of N_2 from the holding tank to the discharge vessel is less than 1% of the initial N_2 mass in the discharge vessel.

Figure 11 presents results for $P_{BURST} = 44.8 \times 10^5$ Pa and $D_O = 0.005$ m. From this it is seen that discharge occurs in approximately 0.021 s. Liquid discharge occurs at a relatively uniform rate with dZ/dt dropping from approximately 7.5 to 5.5 m/s during the emptying process. During discharge U_{JET} first rises from approximately 17 to 25 m/s, and then drops to the final value of approximately 20 m/s. During the discharge the total mass addition of N_2 from the holding tank to the discharge vessel is approximately 40% of the initial N_2 mass in the discharge vessel.

Based on the above results it is concluded that during the discharge process and relative to the criteria of Equations (14) and (15) : 1) use of the large orifice would lead to conditions which violate both of the criterion; 2) use of the small orifice would lead to acceptable performance.

3.2.9.2 Initiating the Pressurization/Discharge Sequence From a $P_{DV,1}$ Slightly Below P_{BURST}. Simulations were carried out for experiments initiated from a $P_{DV,1}$ which is slightly below P_{BURST}. Since the minimum possible P_{BURST} is 37.9×10^5 Pa, $P_{DV,1}$ is selected to be 34.5×10^5 Pa.

Figure 12 presents plots of P_{DV} and P_{HT} during vessel pressurization. Results are presented for the three orifice diameters, D_O = 0.005 m, 0.001 m, and 0.0005 m.

As seen in Figure 12, for the smallest orifice, D_O = 0.0005 m, the pressurization process, $P_{DV,1} \leq P_{DV} < P_{BURST}$, takes 0.6 s for $P_{BURST} = 37.9 \times 10^5$ Pa to 1.9 s for $P_{BURST} = 44.8 \times 10^5$ Pa. For the intermediate-size orifice, D_O = 0.001 m, the pressurization process takes 0.1 s for $P_{BURST} = 37.9 \times 10^5$ Pa to 0.5 s for $P_{BURST} = 44.8 \times 10^5$ Pa. For the largest orifice, D_O = 0.005 m, the entire pressurization process takes place in less than 0.02 s.

U_{JET} values corresponding to Figure 12 are presented in Figure 13. For the smallest orifice, D_O = 0.0005 m, U_{JET} starts out at approximately 3.5 m/s and drops to 2.0 - 2.5 m/s at the time of diaphragm rupture. For D_O = 0.001 m, U_{JET} starts out at approximately 7 m/s and drops to approximately 4.5 m/s at the time of diaphragm rupture. For D_O = 0.005 m, U_{JET} starts out at approximately 33 m/s and drops to as low as approximately 21 m/s for $P_{BURST} = 44.8 \times 10^5$ Pa at the time of diaphragm rupture.

Based on the above results it is concluded that during the pressurization process and relative to the criterion of Equation (15), the present results for $P_{DV,1} = 34.5 \times 10^5$ Pa are similar to the earlier results for $P_{DV,1} = P_{SAT} = 9.38 \times 10^5$ Pa.

In the present case where $P_{DV,1} = 34.5 \times 10^5$ Pa, results for the discharge process are very similar to the earlier results where $P_{DV,1} = P_{SAT} = 9.38 \times 10^5$ Pa and are qualitatively well represented by the plots of Figure 8 through Figure 11 and the earlier discussion of these.

3.2.9.3 Comparing the Discharges of a Small-Orifice Test Configuration and a Field-Deployed System. The model equations were also used to simulate the discharge of a field-deployed vessel filled with HCFC-22 and pressurized with N_2. At the onset of discharge the temperature in the vessel was taken to be 294 K and, corresponding to the above calculations, the pressure in the vessel was taken to be 41.4×10^5 Pa, *i.e.*, a nominal $P_{BURST} = 41.4 \times 10^5$ Pa, where simulating tests would involve experiments where 37.9×10^5 Pa $\leq P_{BURST} \leq 44.8 \times 10^5$ Pa. In Figure 14 and Figure 15 calculated values of P_{DV} and Z/Z_1 for the deployed system simulation are compared with the values of these variables obtained in the above test simulations with D_O = 0.0005 m. The $P_{DV,1} = 9.38 \times 10^5$ Pa results are presented in the figures since these compare somewhat less favorably with the field-deployed system results than do the $P_{DV,1} = 34.5 \times 10^5$ Pa results.

As can be seen in the figures, simulated field-deployed system results and simulated test results compare favorably.

3.2.9.4 Summary of Results of Simulations Involving the Relatively Low-Pressure Large-Volume Holding Tank. A Figure 1-type test configuration with a 0.25×10^{-3} m^3 holding tank and a 0.0005 m, and possibly a 0.001 m diameter orifice will provide experimental discharges which can be expected to simulate accurately the discharge of field-deployed systems. Of the two orifice sizes, the smaller orifice is preferable. Use of a 0.005 m diameter orifice can not be expected to adequately simulate field-deployed system discharges under the conditions studied.

It is expected that this result can be extended to a wide range of test parameters and test agents.

3.2.10 Relatively High-Pressure Small-Volume Holding Tank. This section presents results for the pressurization/discharge sequence using a relatively high-pressure small-volume holding tank. $V_{HT} = 2.5 \times 10^{-5}$ m^3 is chosen to be one tenth of the initial gas volume in the discharge vessel and $P_{HT,1} = 155.1 \times 10^5$ Pa is chosen to be large enough to ensure that the amount of N_2 stored in the holding tank will rupture the diaphragm even when P_{BURST} is at its maximum value, 44.8×10^5 Pa.

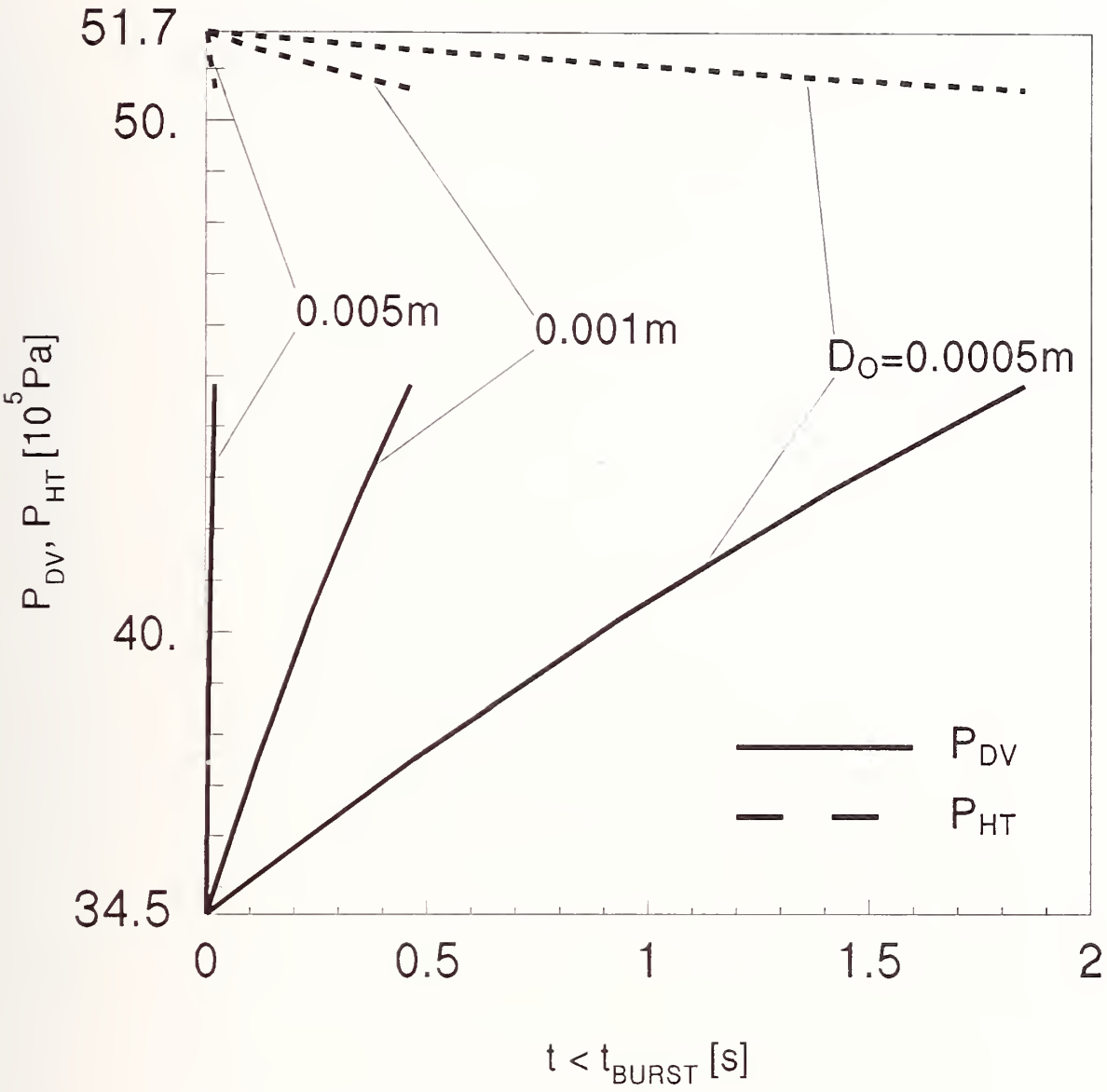

Figure 12. Pressures in the holding tank and discharge vessel for $0 \leq t \leq t_{BURST}$ for a large-volume, low-pressure holding tank; $P_{DV,1}$=3.4 MPa; $P_{HT,1}$=5.17 MPa; P_{BURST} =4.5 MPa.

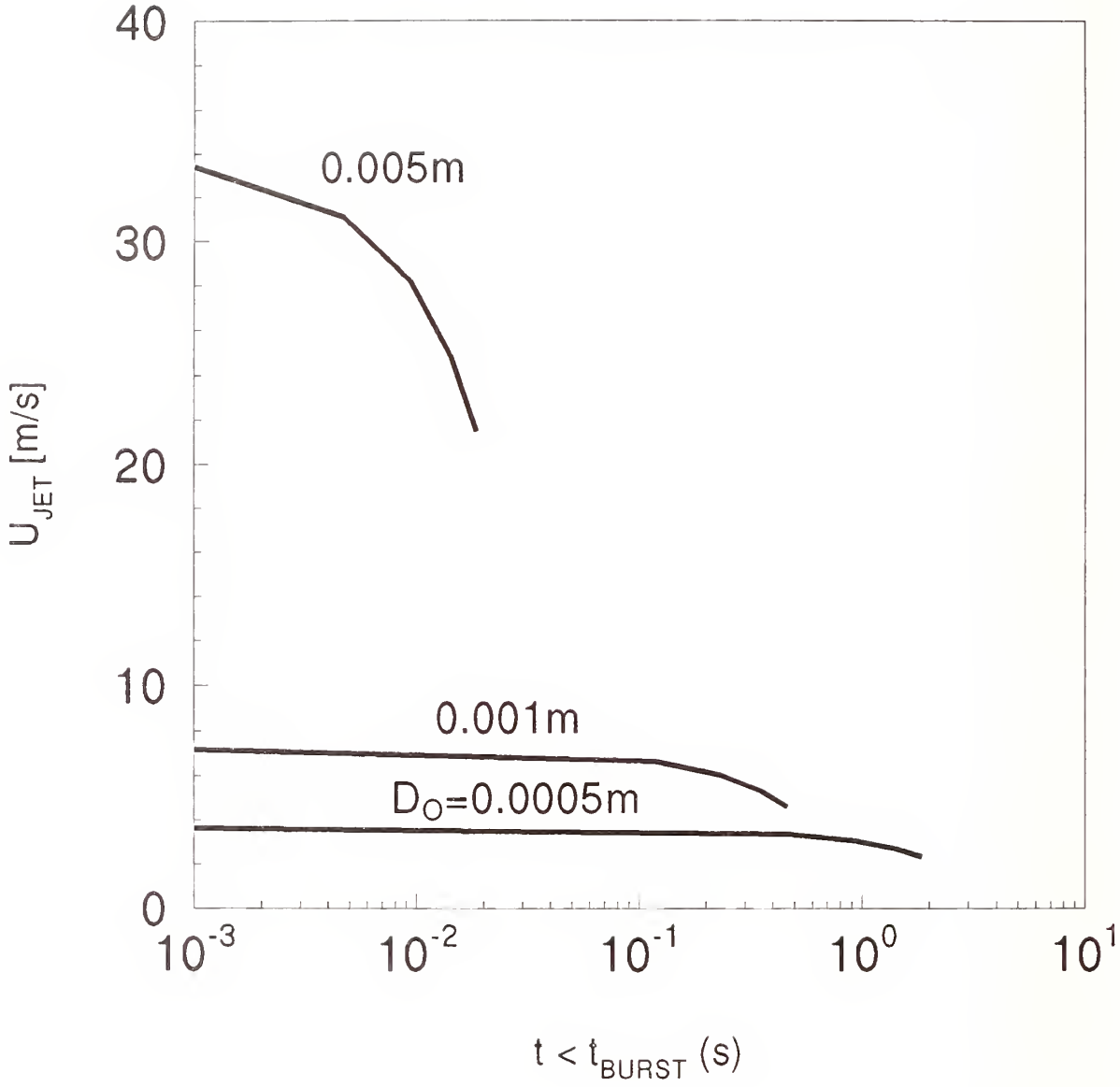

Figure 13. Plots of U_{JET} in the discharge vessel for $0 \leq t \leq t_{BURST}$ for a large-volume, low-pressure holding tank; $P_{DV,1}$=3.4 MPa; $P_{HT,1}$=5.17 MPa; P_{BURST}=4.5 MPa.

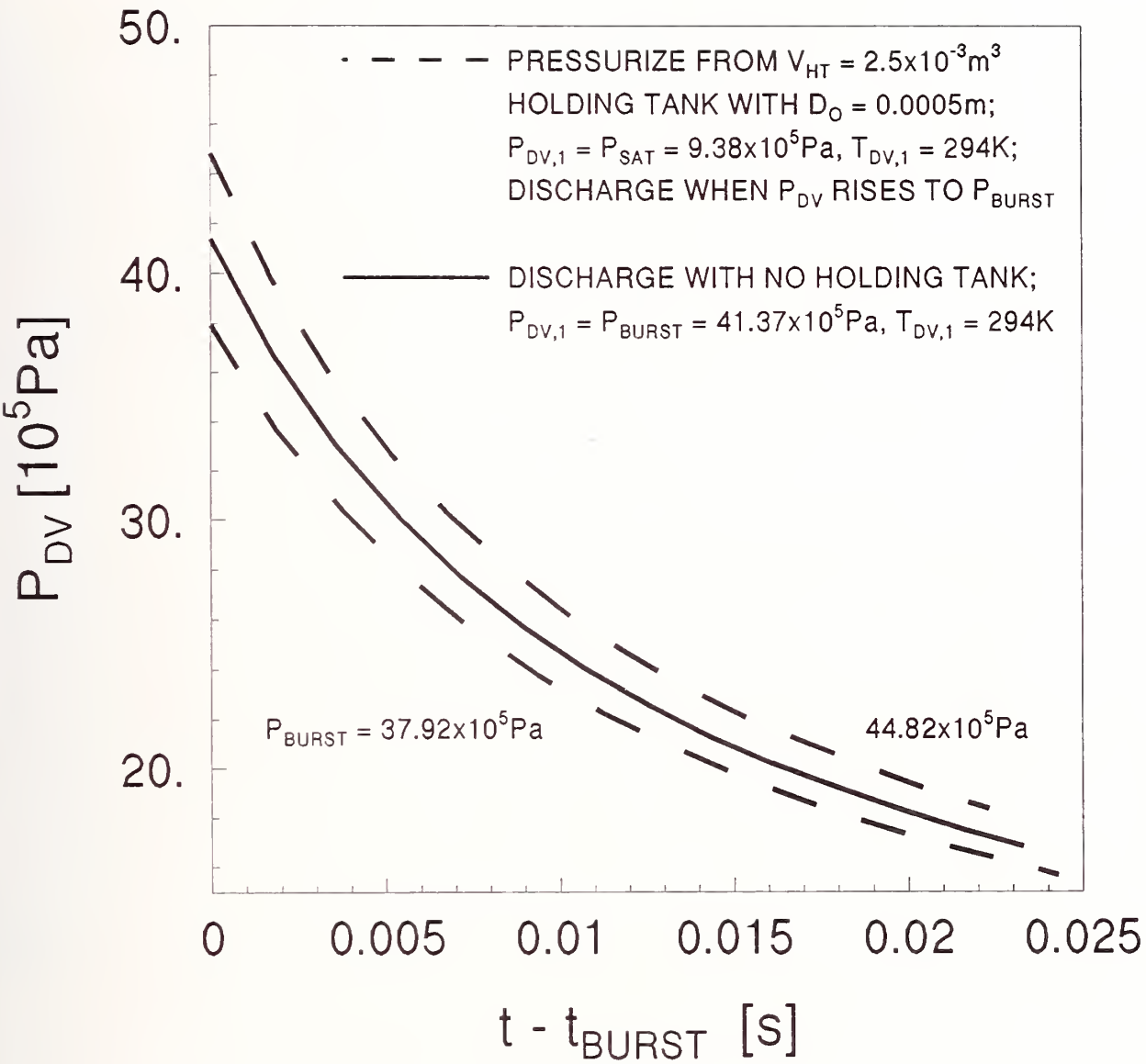

Figure 14. Pressure in the vessel during discharges of the field-deployed vessel and test configuration vessel with a large-volume, low-pressure holding tank and no N_2 in the discharge vessel at t = 0.

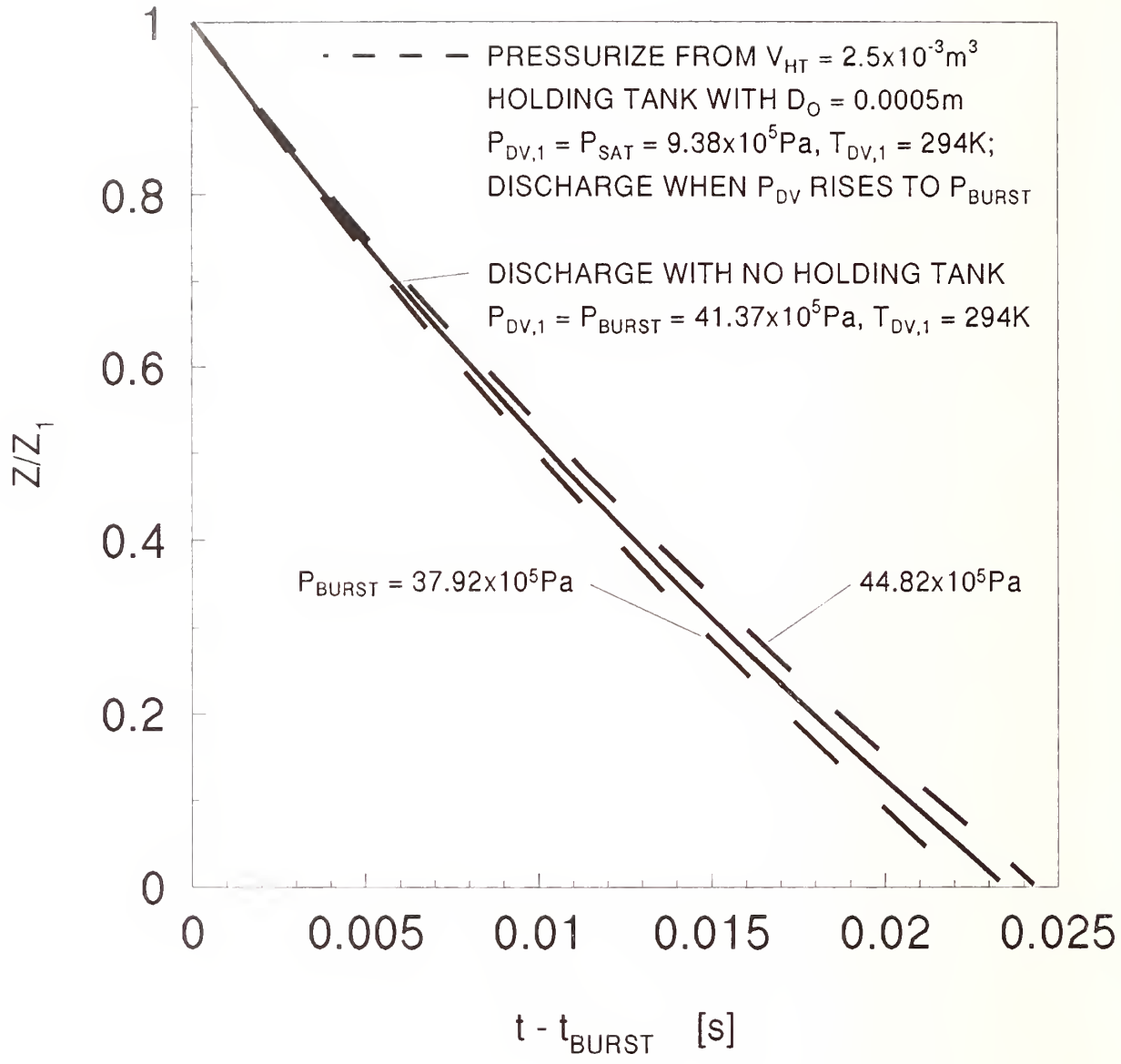

Figure 15. Plots of Z/Z_1 during discharges of the field-deployed vessel and test configuration vessel with a large-volume, low-pressure holding tank and no N_2 in the discharge vessel at t = 0.

The objective of choosing this combination of parameters is to attain a pressurization/discharge sequence which is so rapid, well within the above-mentioned 1 s time interval, as to guarantee, without any significant timing considerations, successful acquisition of high-speed photographic data of the discharge process. The feature of a relatively small initial volume and mass of N_2 in the holding tank is only consistent with test sequences with relatively high initial $P_{DV,1}$'s, values close to the minimum possible diaphragm burst pressure. Thus, the present test parameters would not be expected to be useful in initiating the pressurization/discharge process from an initial state where the vessel contained only pure test agent at its saturation pressure. Here, $P_{DV,1}$ is again chosen to be 34.5×10^5 Pa, slightly below 37.9×10^5 Pa, the minimum value for P_{BURST}.

3.2.10.1 Pressurization and Discharge for the Small Orifice, D_O = 0.0005 m. Simulation results for pressurization/discharge test using the small orifice design are presented in Figure 16 through Figure 20.

For $P_{BURST} = 37.9 \times 10^5$ Pa, plots of P_{DV} and P_{HT} are presented in Figure 16 and plots of U_{JET}, dZ/dt, Z/Z_1, and $(M_{N2} - M_{N2,B})/M_{N2,B}$ in Figure 17. Note that the latter variable is meaningful only during discharge when $t \geq t_{BURST}$. As can be seen in these figures, for this case t_{BURST} = 0.173 s, *i.e.*, this is the time it takes for P_{DV} to rise from $P_{DV,1} = 34.5 \times 10^5$ Pa to the diaphragm rupture pressure. From Figure 17 it is seen that the liquid is nearly all discharged from the vessel (*i.e.*, Z/Z_1 is approaching zero) at approximately t = 0.2 s. From Figure 17 it is also seen that during discharge: the rate of liquid outflow is reduced to about half of its original value, with dZ/dt being reduced from 7.0 m/s to 4.5 m/s; U_{JET} is reduced from an initial predischarge value of approximately 4 m/s to approximately 2 m/s; and $(M_{N2} - M_{N2,B})/M_{N2,B}$ rises from 0 to approximately 0.02, *i.e.*, at the end of the discharge the mass of N_2 in the vessel is increased from its value at t_{BURST} by a factor of approximately 0.02. The latter two results indicate that the criteria of Equations (14) and (15) are both satisfied and, in this sense, as with the relatively large holding tank, the small orifice design can be expected to adequately reproduce field-deployed discharges.

For $P_{BURST} = 44.8 \times 10^5$ Pa, plots of P_{DV} and P_{HT} are presented in Figure 18 and plots of U_{JET} and dZ/dt are presented in Figure 19. Plots of U_{JET}, dZ/dt, Z/Z_1, and $(M_{N2} - M_{N2,B})/M_{N2,B}$ for the times of the discharge process are highlighted in Figure 20. For this case t_{BURST} = 0.94 s. From Figure 18 it is seen that the P_{HT} has almost been reduced to P_{DV} at the time that discharge is initiated. Indeed, if the $P_{HT,1}$ had been much less than 155×10^5 Pa, P_{DV} would not have risen to P_{BURST} and the discharge process would never have occurred! From Figure 19 it is seen that during the pressurization process U_{JET} is reduced from approximately 4.0 m/s to 1.5 m/s. The liquid is nearly all discharged from the vessel at 0.962 s. During discharge: dZ/dt is reduced from 7.5 m/s to 5.0 m/s; U_{JET} rises to approximately 2.5 m/s from its initial value of 1.5 m/s and finally drops to approximately 2 m/s; and $(M_{N2} - M_{N2,B})/M_{N2,B}$ rises from 0 to approximately 0.005. The criteria of Equations (14) and (15) are again satisfied.

As noted, for both $P_{BURST} = 37.9 \times 10^5$ Pa and 44.8×10^5 Pa the above results indicate that both criteria of Equations (14) and (15) are satisfied with the small-holding-tank/small-orifice design and that, in this sense, this design can be expected to adequately reproduce field-deployed discharges. However, for the following three reasons the large-holding-tank design is significantly more robust than the small-holding-tank design: (1) For a given maximum value for P_{BURST} and discharge vessel volume, the minimum acceptable value for $P_{HT,1}$ (approximately 155×10^5 Pa for the present test parameters) is very sensitive to the original amount of liquid in the vessel. For example, in the present simulations the vessel was assumed to be one-half full; but if it were only one-quarter full, the minimum $P_{HT,1}$ that would lead to rupture of the 44.8×10^5 Pa diaphragm would have been approximately 207×10^5 Pa. (2) The small-volume-holding tank configuration does not allow for the

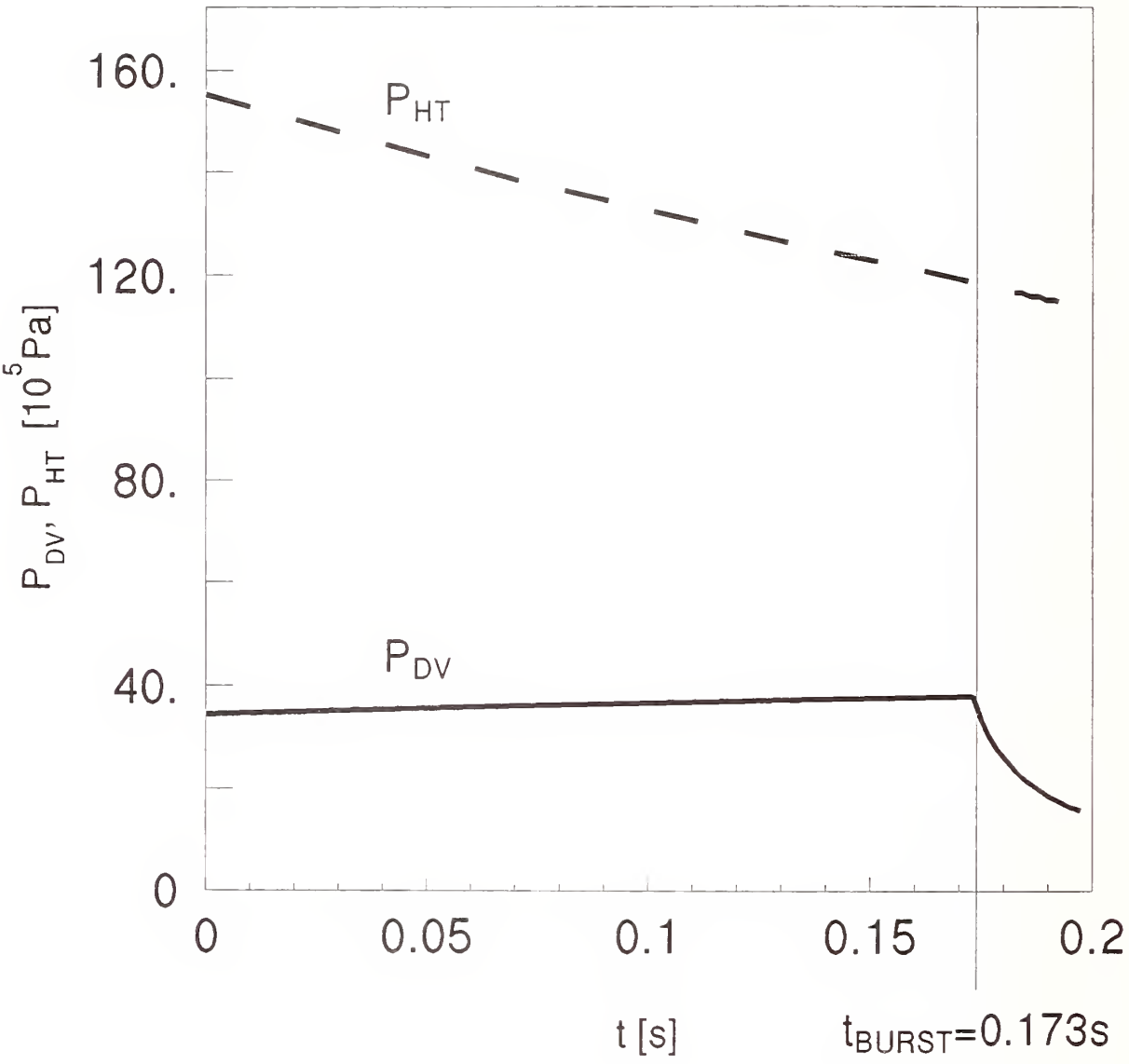

Figure 16. Pressures in the holding tank and discharge vessel for $t \geq 0$ for a small-volume, high-pressure holding tank; D_o = 0.5 mm; $P_{DV,1}$ = 3.45 MPa; $P_{HT,1}$ = 15.5 MPa; P_{BURST} = 3.79 MPa.

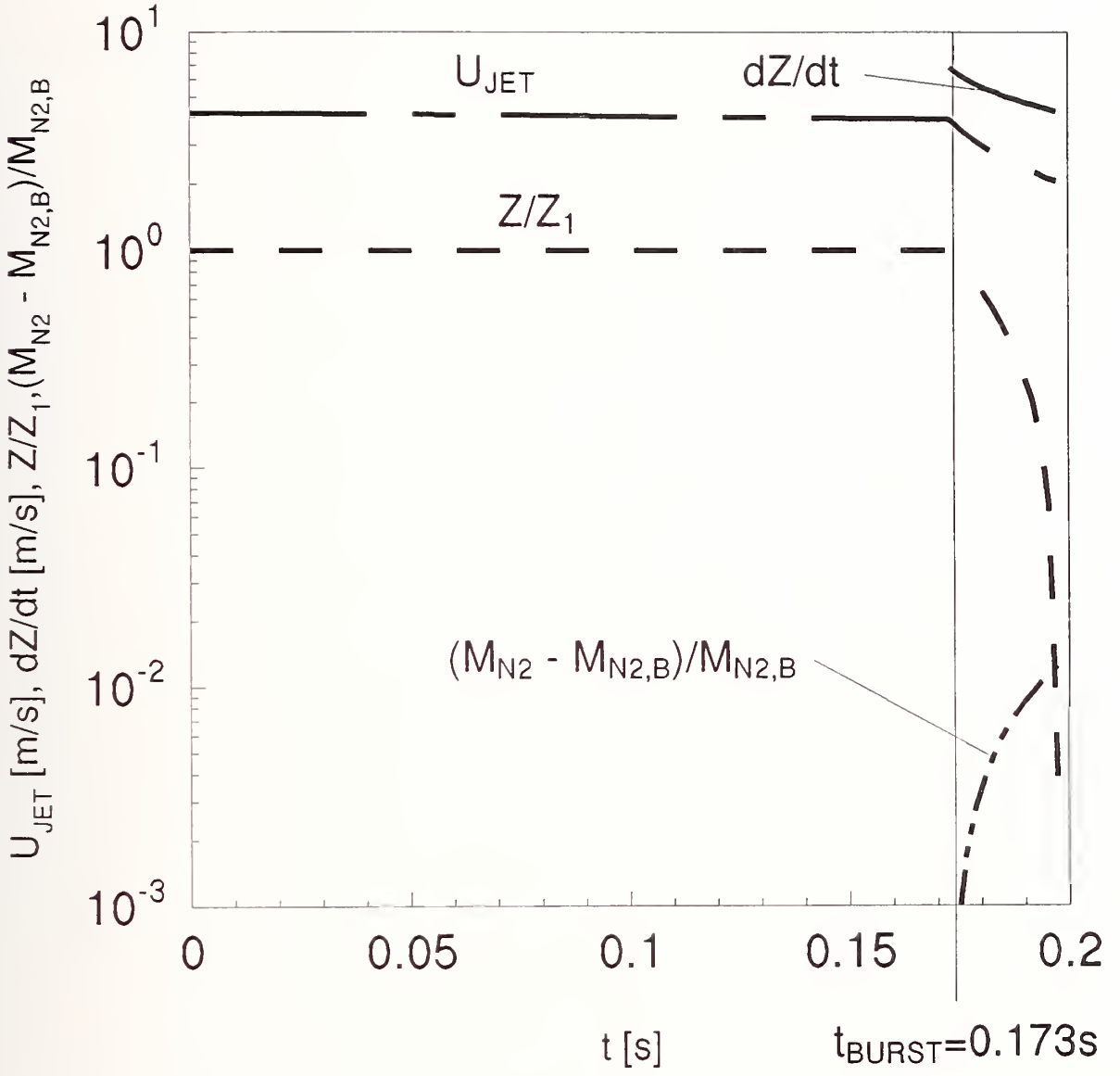

Figure 17. U_{JET}, dZ/dt, Z/Z_1, and $(M_{N2}-M_{N2,B})/M_{N2,B}$ for small-volume, high-pressure holding tank; D_o=0.5 mm; $P_{DV,1}$=3.45 MPa; $P_{HT,1}$=15.5 MPa; P_{BURST}=3.8 MPa.

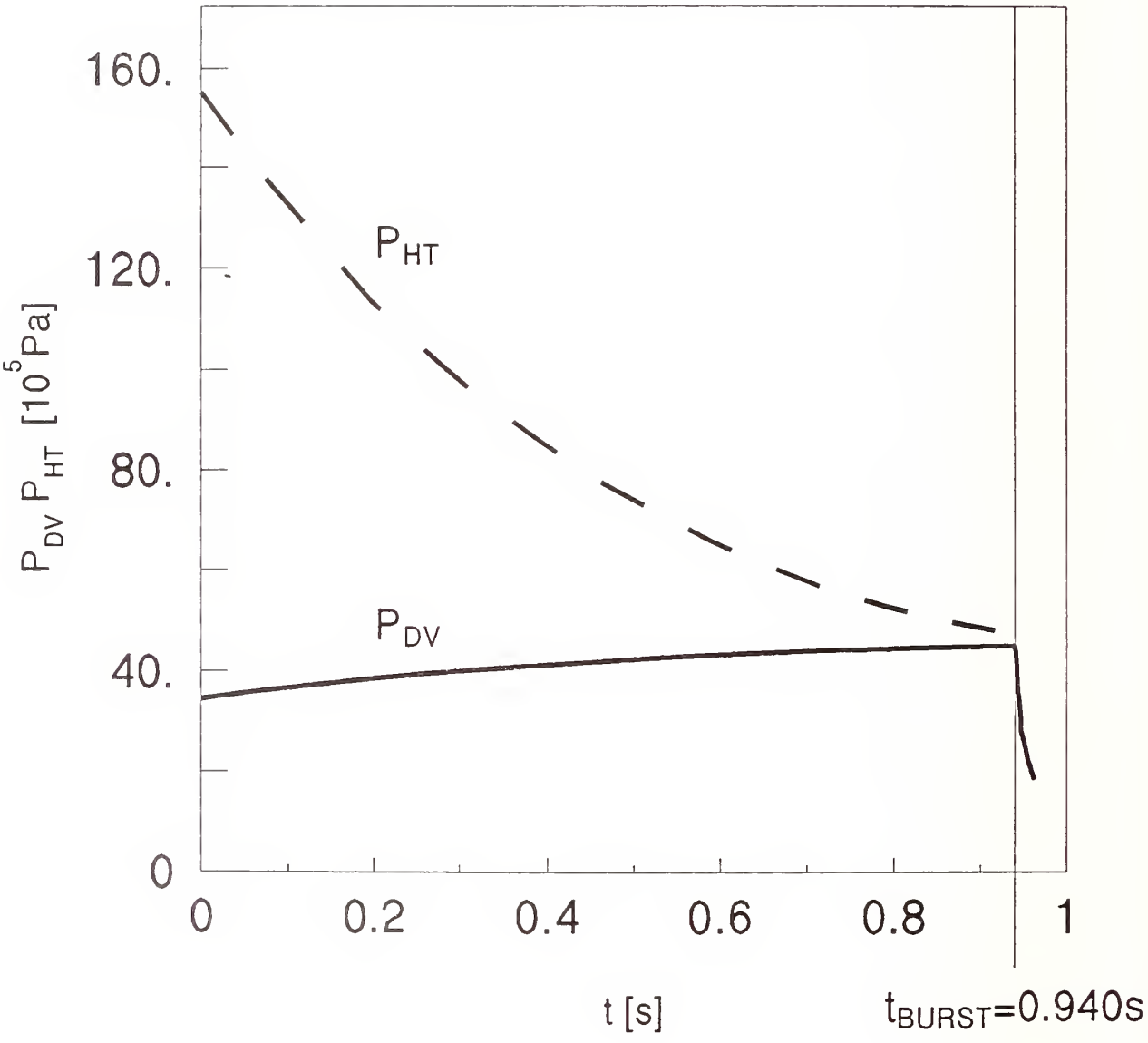

Figure 18. Pressures in the holding tank and discharge vessel for $t \geq 0$ for a small-volume, high-pressure holding tank; D_o = 0.5 mm; $P_{DV,1}$ = 3.45 MPa; $P_{HT,1}$ = 15.5 MPa; P_{BURST} = 4.48 MPa.

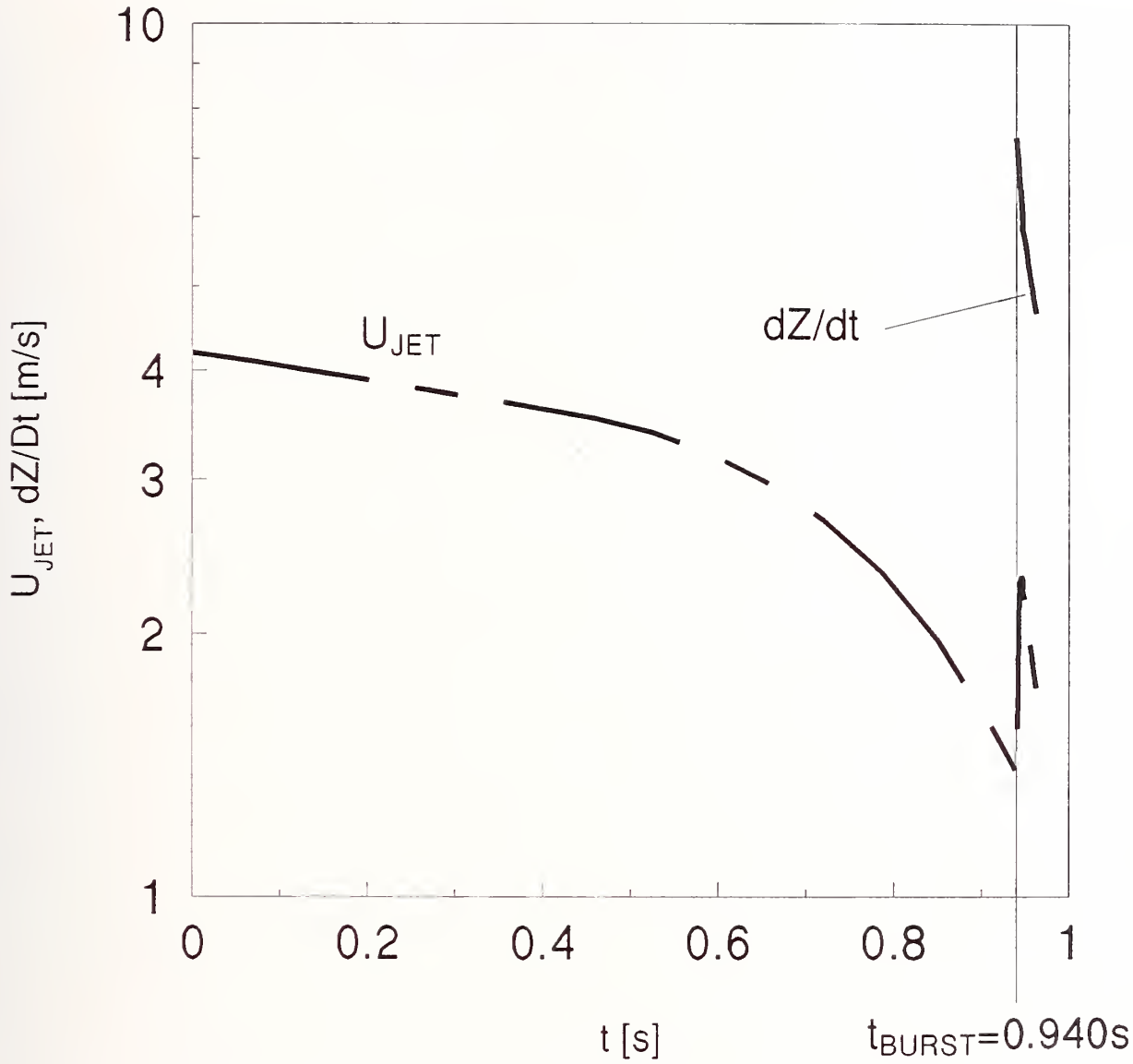

Figure 19. U_{JET} and dZ/dt for $t \geq 0$ for a small-volume, high-pressure holding tank; D_o = 0.5 mm; $P_{DV,1}$ = 3.45 MPa; $P_{HT,1}$ = 15.5 MPa; P_{BURST} = 4.48 MPa.

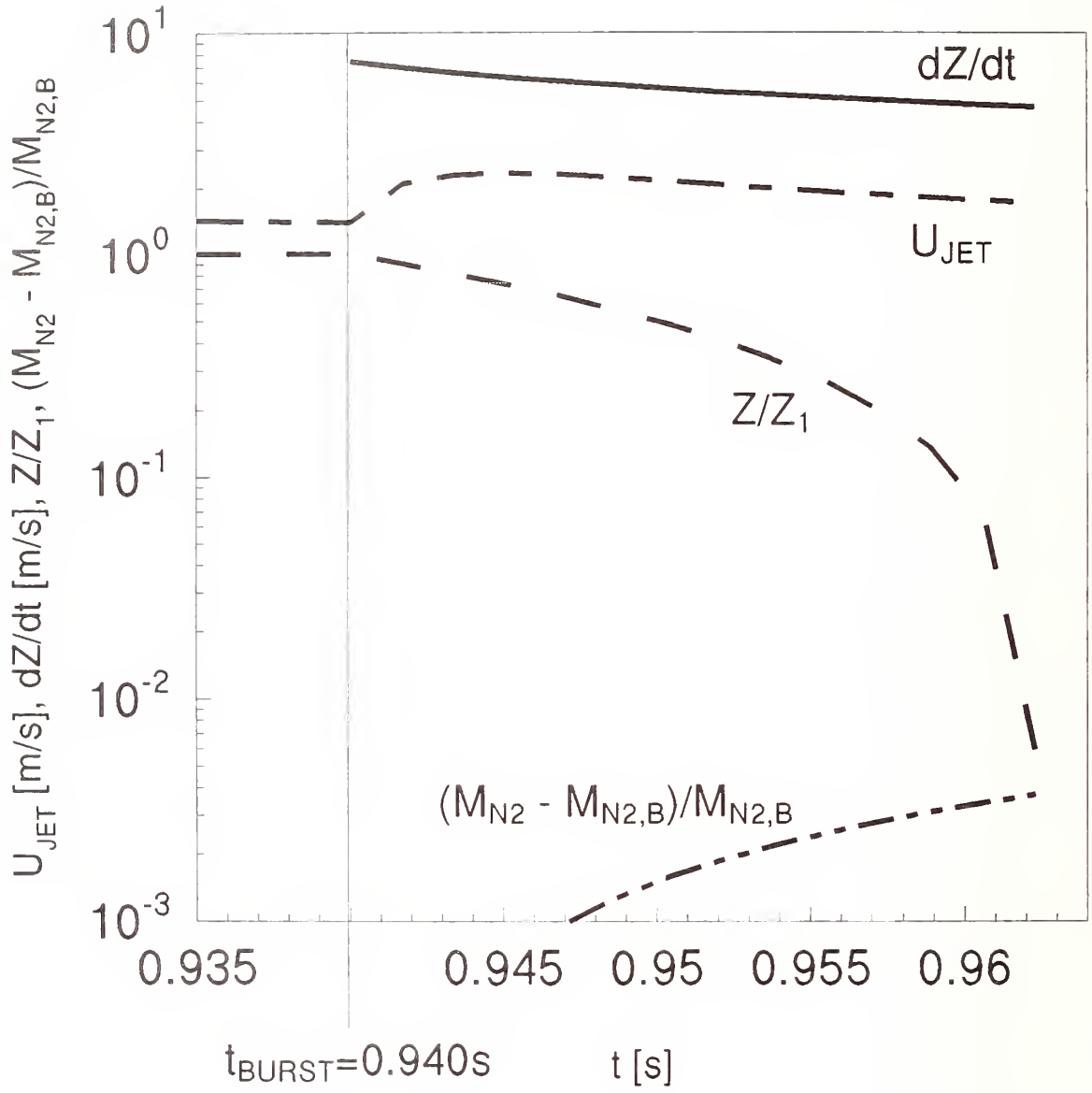

Figure 20. U_{JET}, dZ/dt, Z/Z_1, and $(M_{N2}-M_{N2,B})/M_{N2,B}$ for small-volume, high-pressure holding tank; D_o=0.5 mm; $P_{DV,1}$=3.45 MPa; $P_{HT,1}$ =16 MPa; P_{BURST}=4.48 MPa.

option of initiating tests from relatively-low values of $P_{DV,1}$, *e.g.*, immediately after filling the vessel with the test agent, when $P_{DV,1} = P_{SAT}$. To do so would once again require highly variable and unreasonably large values of $P_{HT,1}$. (3) The large-holding-tank design requires $P_{HT,1}$ values only slightly greater than the maximum P_{BURST} value and it suffers from neither of the above shortcomings.

3.2.10.2 Pressurization and Discharge for the Large Orifice, D_O = 0.005 m. Simulation results for pressurization/discharge test using the large-orifice design are presented in Figure 21 through Figure 24.

For $P_{BURST} = 37.9 \times 10^5$ Pa, plots of P_{DV} and P_{HT} are presented in Figure 21 and plots of U_{JET}, dZ/dt, Z/Z_1, and $(M_{N2} - M_{N2,B})/M_{N2,B}$ in Figure 22. Note that the latter variable is meaningful only during discharge when $t \geq t_{BURST}$. As can be seen in these figures, for this case t_{BURST} = 0.00173 s, *i.e.*, this is the time it takes for P_{DV} to rise from $P_{DV,1} = 34.5 \times 10^5$ Pa to the diaphragm rupture pressure. From Figure 21 is seen that the P_{HT} has almost been reduced to P_{DV} at t = 0.015 s, at which time approximately 40% of the original amount of liquid is still in the vessel, *i.e.*, Z/Z_1 = 0.4 (Figure 22). Also, from Figure 22 it is seen that the liquid is nearly all discharged from the vessel (*i.e.*, Z/Z_1 is approaching zero) at approximately t = 0.023 s. From Figure 22 it is seen that during discharge: the rate of liquid outflow is reduced to about half of its original value, with dZ/dt going from 8 m/s to 4 m/s; U_{JET} is always dropping, being reduced from an initially large predischarge value of approximately 40 m/s to approximately 4 m/s; and $(M_{N2} - M_{N2,B})/M_{N2,B}$ rises from 0 to 0.35, *i.e.*, at the end of the discharge the mass of N_2 in the vessel is increased from its value at t_{BURST} by a factor of approximately 0.35. The latter two results indicate that the criteria of Equations (14) and (15) are not satisfied and, as when used in conjunction with a relatively large holding tank, the large orifice design is not expected to adequately reproduce field-deployed discharges.

For $P_{BURST} = 44.8 \times 10^5$ Pa, plots of P_{DV} and P_{HT} are presented in Figure 23 and plots of U_{JET}, dZ/dt, Z/Z_1, and $(M_{N2} - M_{N2,B})/M_{N2,B}$ in Figure 24. The results are qualitatively similar to those discussed in the last paragraph for $P_{BURST} = 37.9 \times 10^5$ Pa. The quantitative differences can be easily determined from the figures. For this case t_{BURST} = 0.0094 s. From Figure 23 is seen that the P_{HT} has almost been reduced to P_{DV} at the time that discharge is initiated. Indeed, if the $P_{HT,1}$ had been much less than 155×10^5 Pa, P_{DV} would not have risen to P_{BURST} and the discharge process would never have occurred! The liquid is nearly all discharged from the vessel at 0.03 s. During the pressurization process U_{JET} drops from approximately 40 m/s to 15 m/s. During discharge: dZ/dt is reduced from 7 m/s to 5 m/s; U_{JET} is reduced from 15 m/s to 3.5 m/s; and $(M_{N2} - M_{N2,B})/M_{N2,B}$ rises from 0 to 0.1. Although the criterion in Equation (14) is satisfied, that of Equation (15) is not.

3.2.11 Summary and Conclusions. A mathematical model and associated computer program were developed to simulate the discharge of fire extinguishment agents from N_2-pressurized vessels. The model is expected to have three applications. First, to guide the development of an experimental procedure which both 1) simulates depressurization of a field-deployed discharge vessel and 2) allows for acquisition of data, including high speed photography, to characterize adequately the discharge process. Second, to evaluate the discharge characteristics of a wide range of alternative-agent/pressure-vessel configurations, thereby extending the slow and relatively costly experimental method of making such evaluations. Finally, to predict exit flow conditions to be used to solve the problem of agent dispersal outside of the discharge vessel.

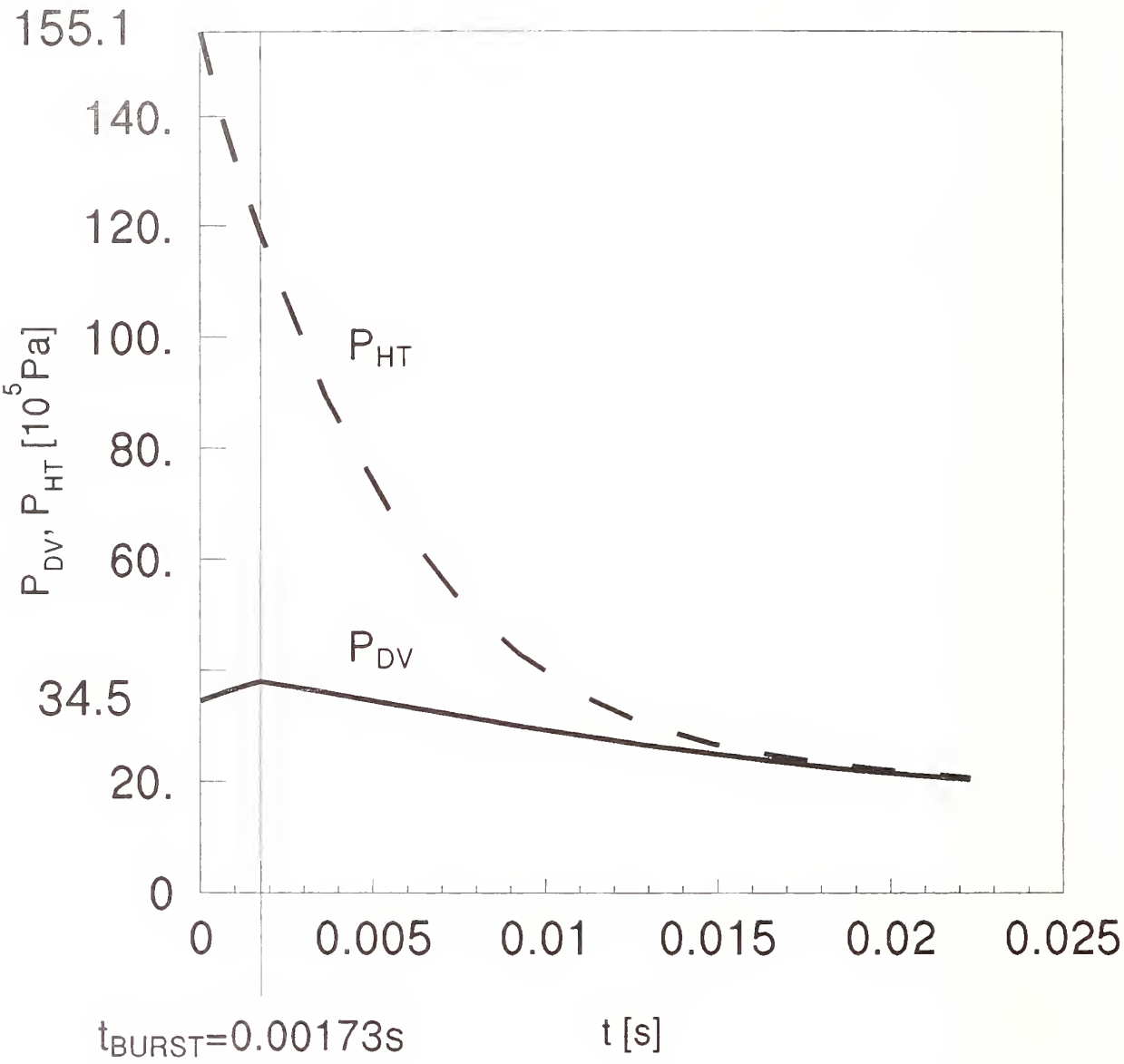

Figure 21. Pressures in the holding tank and discharge vessel for $t \geq 0$ for a small-volume, high-pressure holding tank; D_o = 5 mm; $P_{DV,1}$ = 3.45 MPa; $P_{HT,1}$ = 15.5 MPa; P_{BURST} = 3.79 MPa.

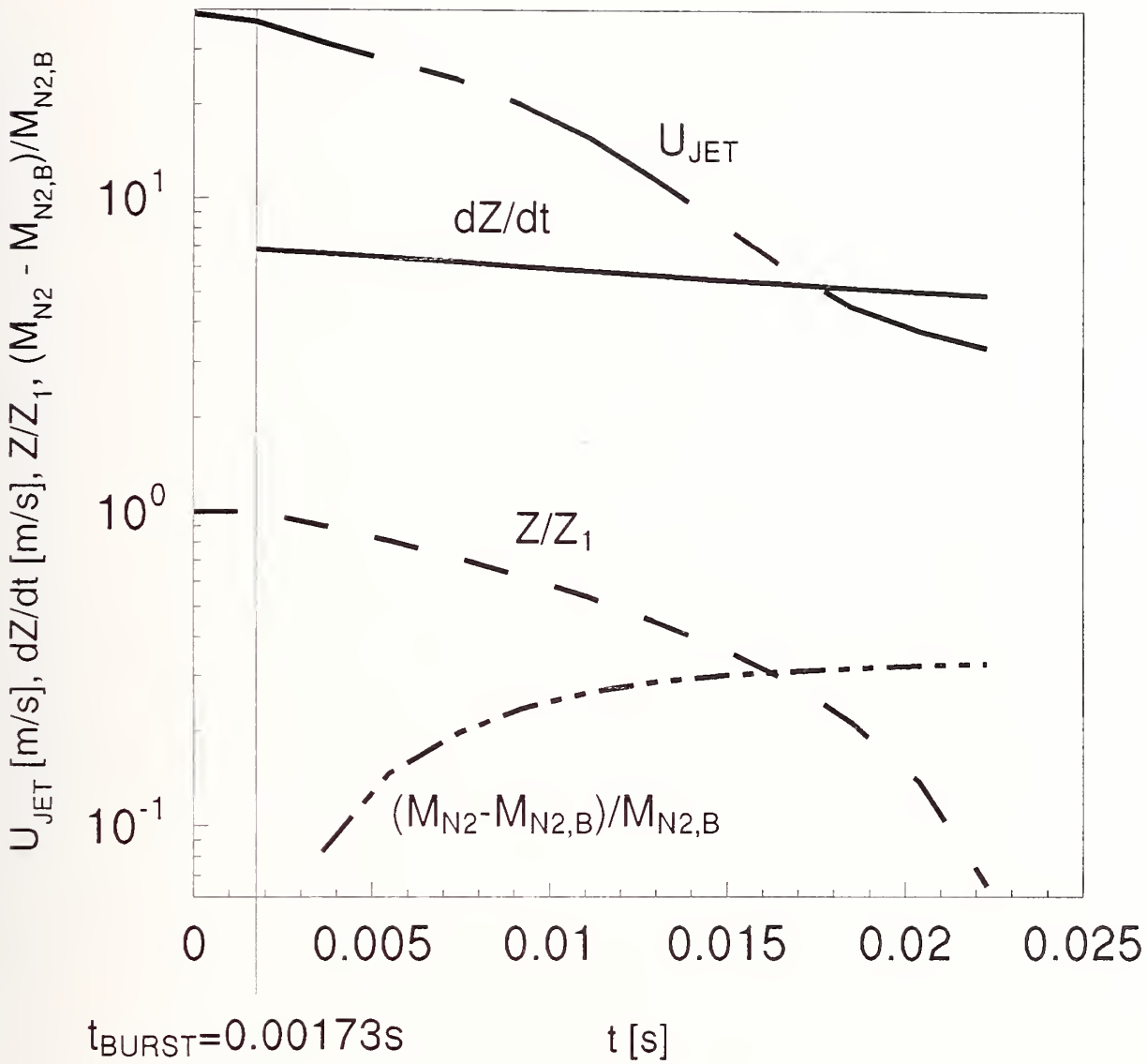

Figure 22. U_{JET}, dZ/dt, Z/Z_1, and $(M_{N2}-M_{N2,B})/M_{N2,B}$ for small-volume, high-pressure holding tank; D_o=5 mm; $P_{DV,1}$=3.45 MPa; $P_{HT,1}$=15.5 MPa; P_{BURST}= 3.79 MPa.

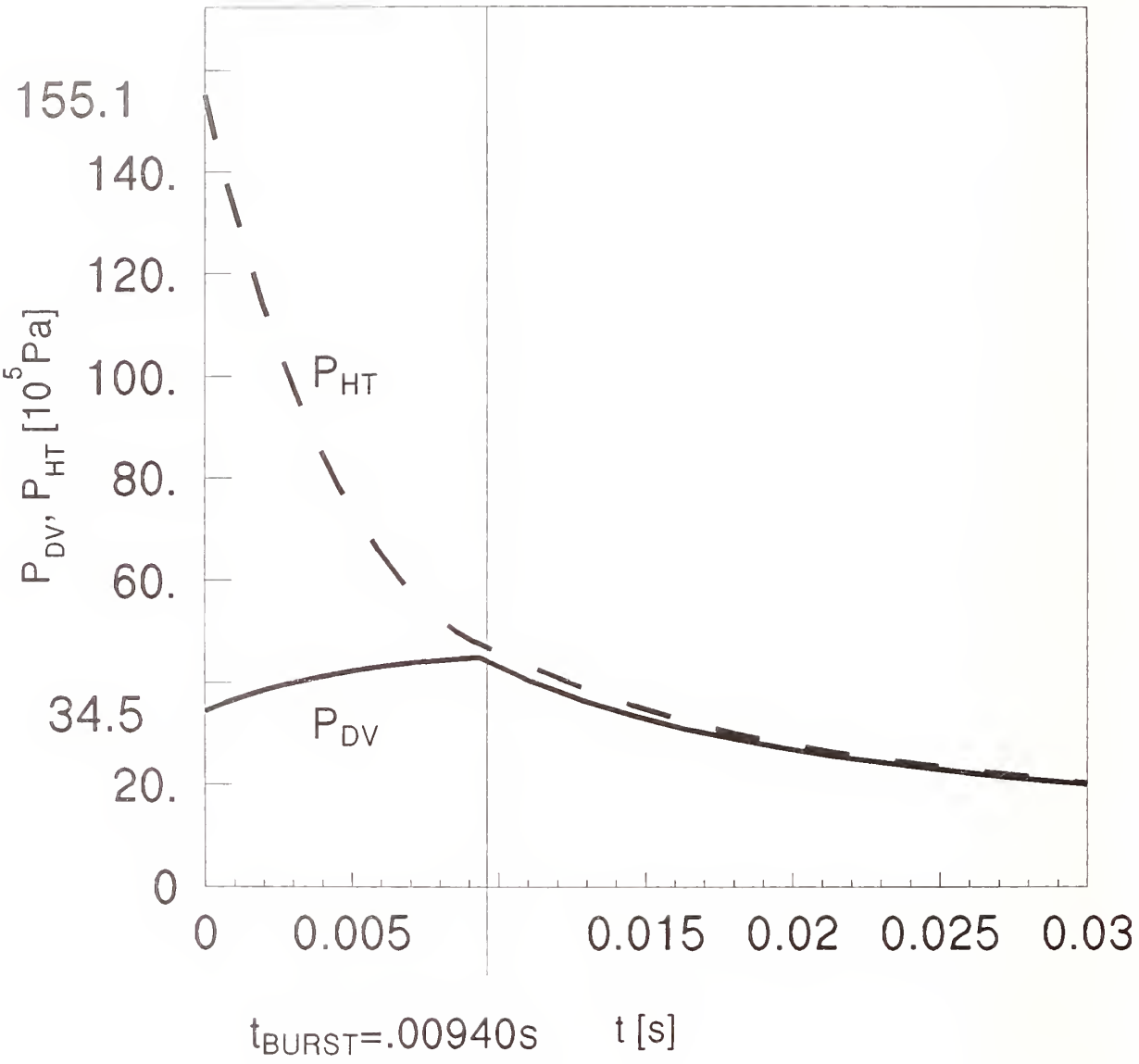

Figure 23. Pressures in the holding tank and discharge vessel for $t \geq 0$ for a small-volume, high-pressure holding tank; D_o = 5 mm; $P_{DV,1}$ = 3.45 MPa; $P_{HT,1}$ = 15.5 MPa; P_{BURST} = 4.48 MPa.

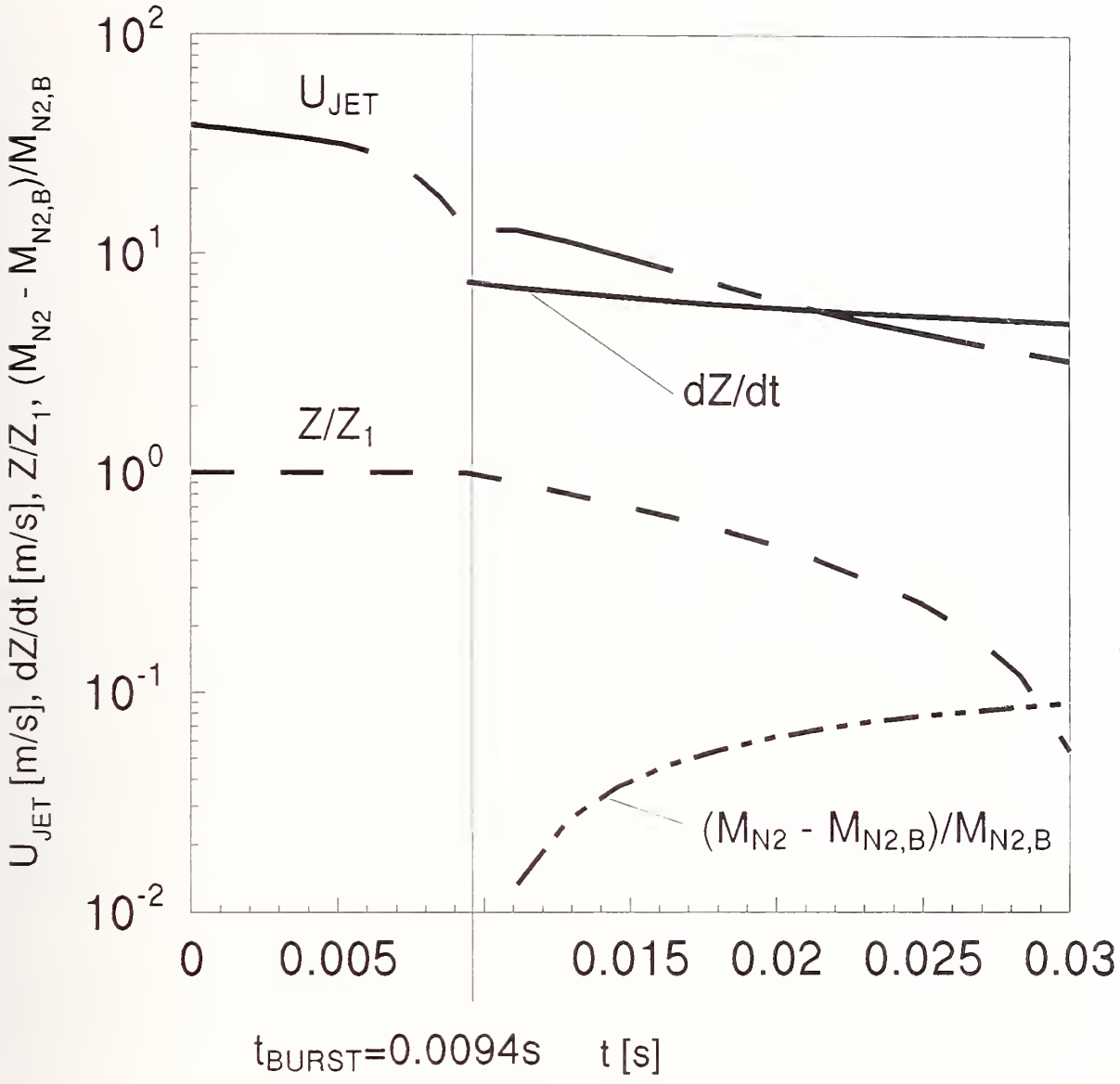

Figure 24. U_{JET}, dZ/dt, Z/Z_1, and $(M_{N2}-M_{N2,B})/M_{N2,B}$ for small-volume, high-pressure holding tank; D_o=5 mm; $P_{DV,1}$=3.45 MPa; $P_{HT,1}$=16 MPa; P_{BURST}=4.48 MPa.

The model is based on the experimental configuration depicted in Figure 1, and the solution method is capable of treating arbitrary choices of geometric parameters, material properties, and initial conditions.

The model was used in example calculations which address the first of the applications, viz., the establishment of a robust experimental design and procedure that would 1) simulate the discharge of field-deployed fire extinguishment systems useable in aircraft and 2) meet additional experimental constraints consistent with a program at NIST in support of aircraft fire safety issues.

In the example calculations, the fixed parameters which characterized the system were a 0.0005 m^3 discharge vessel with a circular exit nozzle/orifice of diameter 0.01905 m half-filled with HCFC-22 in the liquid phase at "room temperature," 294 K.

The deployed system was assumed to be pressurized with N_2 to a total pressure of 41.4×10^5 Pa, where the exit nozzle/orifice is closed with an explosive cap which is released "on demand." In the experimental system, the exit nozzle/orifice is capped with a disk which ruptures at an *a priori*-unknown pressure, between 37.9×10^5 Pa and 44.8×10^5 Pa.

The experimental system, is brought to the rupture/burst pressure, P_{BURST}, from an initial pressure $P_{DV,1}$ by a process of pressurization by flow from the holding tank which is initially filled with N_2 at some pressure, $P_{HT,1}$, higher than P_{BURST}. The holding tank communicates with the discharge vessel through a circular orifice of diameter D_O.

The model was used to simulate the discharge of the deployed system and of the experimental system. Experimental parameters that were varied were $P_{DV,1}$ (9.38×10^5 Pa, the saturation pressure of HCFC-22 at 294 K, or 34.5×10^5 Pa); $P_{HT,1}$ and the volume of the holding tank (51.7×10^5 Pa and 2.5×10^{-3} m^3, or 155.1×10^5 Pa and 2.5×10^{-5} m^3); and D_O (0.005 m, 0.001 m, or 0.0005 m).

Results of the simulations are presented in Figure 6 through Figure 24. Based on the model calculations it was determined that with $P_{DV,1} = 9.38 \times 10^5$ Pa or 34.5×10^5 Pa an experimental configuration/design using the relatively low-pressure (51.7×10^5 Pa), large-volume (2.5×10-3 m^3), holding tank and the smallest-diameter (0.0005 m) orifice would accurately simulate the discharge of the field-deployed system. Furthermore, it is expected that such a design is robust in the sense that it would also simulate well the field-deployed system even when extended to a range of parameters and agent materials well beyond the scope of the present calculations.

Model calculations also indicated that an experimental design which uses the large-diameter orifice (0.005 m) and/or the relatively high pressure small-volume holding tank (155.1×10^5 Pa and 2.5×10^{-5} m^3) would often not provide accurate simulations of field-deployed discharges and would never be expected to be "robust."

3.2.12 Nomenclature

A_{DV}	cross-sectional area of discharge vessel
A_N, A_O	area of discharge nozzle/orifice, orifice from holding tank
$C_{D,N}$, $C_{D,O}$	flow coefficient of discharge nozzle/orifice, orifice from holding tank
$C_{P,AG}$, $C_{P,N2}$	specific heat at constant pressure of agent gas, N_2
$C_{V,AG}$, $C_{V,N2}$	specific heat at constant volume of agent gas, N_2
D_O	diameter of the orifice between discharge vessel and holding tank
$M_{DV,AG}$, $M_{DV,AL}$	mass of gaseous, liquid agent in discharge vessel
$M_{DV,N2}$, $M_{HT,N2}$	mass of N_2 in discharge vessel, holding tank
$M_{DV,N2,1}$, $M_{DV,AL,1}$, $M_{HT,N2,1}$	$M_{DV,N2}$, $M_{DV,AL}$, $M_{HT,N2}$ at t = 0

M_{N2}	total mass of N_2 in discharge vessel and holding tank, see Equation (3)
$M_{N2,B}$	mass of N_2 in discharge vessel when the diaphragm ruptures
P	pressure
P_{AMB}	pressure of ambient environment
P_{BURST}	pressure in discharge vessel when the diaphragm ruptures
P_{DV}, P_{HT}	pressure in discharge vessel, holding tank
$P_{DV,1}$, $P_{HT,1}$	P_{DV}, P_{HT} at t = 0
P_{SAT}	pressure when liquid agent is at saturation
P_{SP}	pressure on agent spinoidal curve
R_{AG}, R_{N2}	gas constants for gaseous agent, N_2
T	temperature
T_{AL}	temperature of liquid agent
T_{DV}, T_{HT}	temperature of gaseous agent in discharge vessel, N_2 in holding tank
$T_{DV,1}$, $T_{HT,1}$	T_{DV}, T_{HT} at t = 0
t	time from beginning of experiment or from onset of discharge of field-deployed system
t_{BURST}	time when diaphragm ruptures
t_D	time at completion of liquid discharge or when P_{DV} reaches P_{SAT} during discharge
U_{JET}, U_O	axial velocity of orifice jet upstream of gas/liquid interface
V_{HT}	volume of holding tank
x_i	variables of dimensionless initial value problem, i = 1, 2, 3, Equation (9)
Z	elevation of gas/liquid interface above bottom of discharge vessel
Z_1	Z at $t = 0$
Z_{DV}	length of discharge vessel
Z_{JET}	$Z_{DV} - Z$
γ, γ_{AG}	ratio of specific heats for N_2, gaseous agent
ζ	dimensionless Z, Equation (A-1)
ζ_{DV}	dimensionless Z_{DV}, Equation (A-4)
θ_{DV}, θ_{HT}	dimensionless T_{DV}, T_{HT}, Equation (A-1)
$\theta_{DV,1}$, $\theta_{HT,1}$	dimensionless $T_{DV,1}$, $T_{HT,1}$, Equation (A-1)
ρ_{AL}	density of liquid agent
ρ_{SAT}	density of saturated liquid agent
λ_i	dimensionless parameters, i = 1 to 5, Equations (10) and (A-4)
$\mu_{DV,N2}$, $\mu_{HT,N2}$	dimensionless $M_{DV,N2}$, $M_{HT,N2}$, Equation (A-1)
$\mu_{DV,N2,1}$, $\mu_{HT,N2,1}$	dimensionless $M_{DV,N2,1}$, $M_{HT,N2,1}$, Equation (A-1)
π_{AMB}	dimensionless P_{AMB}, Equation (A-4)
π_{HT}, π_{DV}, $\pi_{HT,1}$	dimensionless P_{HT}, P_{DV}, $P_{HT,1}$, Equation (A-1)
π_{SP}	dimensionless P_{SP}, Equation (A-4)
σ_i	functions of x_i and parameters, i = 1, 2, 3, Equation (11)
τ	dimensionless t, Equations (9) and (A-1)

3.2.13 Appendix: The Dimensionless Initial Value Problem. Define the following dimensionless variables and their initial values:

$$\tau \equiv tC_{D,N}A_N[2P_{DV,1}/(M_{DV,AL,1}A_{DV}Z_1)]^{1/2}$$

$$\pi_{HT} \equiv P_{HT}/P_{DV,1};\ \ \pi_{HT}(\tau = 0) \equiv \pi_{HT,1} = P_{HT,1}/P_{DV,1} > 1$$

$$\pi_{DV} \equiv P_{DV}/P_{DV,1};\ \ \pi_{DV}(\tau = 0) = 1$$

$$\mu_{HT,N2} \equiv M_{HT,N2}/M_{N2};\ \ \mu_{HT,N2}(\tau = 0) = M_{HT,N2,1}/M_{N2} \equiv \mu_{HT,N2,1} = 1 - \mu_{DV,N2,1} \leq 1$$

$$\mu_{DV,N2} \equiv M_{DV,N2}/M_{N2};\ \ \mu_{DV,N2}(\tau = 0) = M_{DV,N2,1}/M_{N2} \equiv \mu_{DV,N2,1} = 1 - \mu_{HT,N2,1} \leq 1$$

$$\mu_{DV,AL} \equiv M_{DV,AL}/M_{DV,AL,1} = M_{DV,AL}/(\rho_{AL}A_{DV}Z_1);\ \ \mu_{DV,AL}(\tau = 0) = 1 \qquad \text{(A-1)}$$

$$\theta_{HT} \equiv T_{HT}R_{N2}M_{N2}/(V_{HT}P_{DV,1}) = (T_{HT}/T_{HT,1})(P_{HT,1}/P_{DV,1})/(M_{HT,N2,1}/M_{N2});$$

$$\theta_{HT}(\tau = 0) \equiv \theta_{HT,1} = (P_{HT,1}/P_{DV,1})/(M_{HT,N2,1}/M_{N2}) > 1$$

$$\theta_{DV} \equiv T_{DV}M_{DV,AG}R_{AG}/(Z_1A_{DV}P_{DV,1}) = T_{DV}M_{DV,AG}R_{AG}\rho_{AL}/(M_{DV,AL,1}P_{DV,1});$$

$$\theta_{DV}(\tau = 0) \equiv \theta_{DV,1} = T_{DV,1}M_{DV,AG}R_{AG}/(Z_1A_{DV}P_{DV,1})$$

$$\zeta \equiv Z/Z_1;\ \ \zeta(\tau = 0) = 1$$

Define the new variable x_1 and introduce x_2 and x_3 as new designations for $\mu_{DV,N2}$ and $\mu_{DV,AL}$, respectively:

$$x_1(\tau) \equiv [(1 + \lambda_3\mu_{DV,N2})/(1 + \lambda_1\mu_{DV,N2})]\pi_{DV}(\zeta_{DV} - \mu_{DV,AL}) + \lambda_2\lambda_4(1 - \mu_{DV,N2})^{\gamma};$$

$$x_1(0) = [(1 + \lambda_3\mu_{DV,N2,1})/(1 + \lambda_1\mu_{DV,N2,1})](\zeta_{DV} - 1) + \lambda_2\lambda_4(1 - \mu_{DV,N2,1})^{\gamma} \qquad \text{(A-2)}$$

$$x_2(\tau) \equiv \mu_{DV,N2};\ \ x_2(0) = \mu_{DV,N2,1}$$

$$x_3(\tau) \equiv \mu_{DV,AL};\ \ x_3(0) = \mu_{DV,AL,1}$$

Define also the following functions of the x_i:

$$f_1 \equiv [x_1 - \lambda_2\lambda_4(1 - x_2)^{\gamma}](1 + \lambda_1x_2)/[(1 + \lambda_3x_2)(\zeta_{DV} - x_3)];$$

$$f_2 \equiv \lambda_2(1 - x_2)^{(\gamma - 1)};\ \ f_3 \equiv \lambda_2(1 - x_2)^{\gamma};\ \ \ f_4 \equiv \lambda_2(1 - x_2)^{\gamma}/f_1; \qquad \text{(A-3)}$$

$$f_5(x_i) \equiv \begin{cases} \lambda_5 f_3 \{\gamma[2/(\gamma+1)]^{(\gamma+1)/(\gamma-1)}/f_2\}^{1/2}; & \text{if } f_4 \geq [(\gamma+1)/2]^{[\gamma/(\gamma-1)]} \\ \lambda_5 f_3 (1/f_4)^{1/\gamma} \{2\gamma[1-(1/f_4)^{(\gamma-1)/\gamma}]/[(\gamma-1)f_2]\}^{1/2}; & \text{if } f_4 < [(\gamma+1)/2]^{[\gamma/(\gamma-1)]} \end{cases}$$

$$f_6(x_i) \equiv \begin{cases} (f_1 - \pi_{AMB})^{1/2}; & \text{if } \pi_{AMB} \geq \pi_{SP} \\ (f_1 - \pi_{SP})^{1/2}; & \text{if } \pi_{AMB} < \pi_{SP} \end{cases}$$

where

$$\begin{aligned} &\lambda_1 = (M_{N2}/M_{DV,AG})(R_{N2}/R_{AG});\ \lambda_2 \equiv \pi_{HT,1}/(\mu_{HT,N2,1})^{\gamma}; \\ &\lambda_3 = (C_{V,N2}/C_{V,AG})(M_{N2}/M_{DV,AG}) = \lambda_1(\gamma_{AG}-1)/(\gamma-1); \\ &\lambda_4 = [(\gamma_{AG}-1)/(\gamma-1)][V_{HT}/(Z_1 A_{DV})]; \\ &\lambda_5 = (C_{D,O}/C_{D,N})(A_O/A_N)[(M_{DV,AL}/M_{N2})(A_{DV}Z_1/V_{HT})/2]^{1/2}; \\ &\zeta_{DV} = Z_{DV}/Z_1 = \text{constant} > 1;\ \gamma_{AG} = C_{P,AG}/C_{V,AG} = R_{AG}/C_{V,AG} + 1; \\ &\pi_{AMB} = P_{AMB}/P_{DV,1};\ \pi_{SP} = P_{SP}/P_{DV,1} \end{aligned} \tag{A-4}$$

Then the x_i can be determined from the solution of the following initial value problem

$$\begin{aligned} &dx_1/d\tau = -(\gamma_{AG}-1)f_1 f_6;\ dx_2/d\tau = f_5;\ dx_3/d\tau = -f_6 \\ &x_1(0) = [(1+\lambda_3\mu_{DV,N2,1})/(1+\lambda_1\mu_{DV,N2,1})](\zeta_{DV}-1) + \lambda_2\lambda_4(1-\mu_{DV,N2,1})^{\gamma}; \\ &x_2(0) = \mu_{DV,N2,1};\ x_3(0) = \mu_{DV,AL,1} \end{aligned} \tag{A-5}$$

and the solutions for the original dimensionless variables of Equation (A-1) can be retrieved from

$$\begin{aligned} &\pi_{DV} = f_1;\ \pi_{HT} = f_3;\ \mu_{HT,N2} = 1 - x_2;\ \mu_{DV,N2} = x_2;\ \mu_{DV,AL} = \zeta = x_3; \\ &\theta_{HT} = f_2;\ \theta_{DV} = (\zeta_{DV} - x_3)f_1/(1+\lambda_1 x_2) \end{aligned} \tag{A-6}$$

From the latter solutions the dimensional variables can be determined finally from the definitions of Equation (A-1).

The problem formulation of Equation (A-5) and its solution are valid up to the value of τ where $x_3 = 0$ (the last of the liquid is driven from the discharge vessel) or f_1 is reduced to $P_{SAT}/P_{DV,1}$ (the

liquid in the discharge vessel is subjected to a condition where an equilibrium state would lead to flashing).

3.3 Design of Experimental Release Vessel

3.3.1 Introduction. In a conventional halon 1301 bottle, a fixed amount of agent is initially dispensed to the bottle followed by pressurization with nitrogen to a fixed equilibrium pressure at room temperature. Depending upon the application, the amount of agent and the charged pressure can be varied accordingly. Release of the agent from the vessel is normally achieved by a squib or a solenoid valve, either manually or automatically, upon the detection of a fire. For fire protection of dry bays, the agent has to be released from the vessel and suppress the fire in less than 50 ms. The use of a squib or solenoid valve to study discharge dynamics in a laboratory is not appropriate because a squib is an explosive device and the flow path through a solenoid valve is too complex to analyze. In order to obtain fundamental understanding of the discharge processes, an experimental apparatus has to be designed such that it can eliminate the above shortcomings of using either a squib or a solenoid valve and at the same time closely simulate the actual discharge process.
There were two major design criteria that had to be considered: vessel size and release mechanism. Since the experimental condition was at high pressure, the size of the vessel had to be small enough to minimize weight for ease of mounting and handling of the vessel, but not so small that the size of the vessel became unrealistic and that the characteristic emptying time of the agent was so short that it was not possible to characterize the discharge process in sufficient detail. In addition, minimization of the amount of agents used in the discharge tests had to be considered because of the limited availability and high cost of some of the alternative agents. An internal volume of approximately 5×10^{-4} m^3 was selected. This volume was less than a factor of three smaller than the internal volume (14×10^{-4} m^3) of the smallest vessel (type CF-2) specified in the appropriate Military Specification (1965). In addition, this volume was large enough to hold a sufficient amount of agent to perform the discharge experiments. An aspect ratio (length/diameter) of about 5 was used in the vessel design. The selection of this aspect ratio was governed by the dimension of the rupture disk holder (to be discussed).

Since the intent was not to design an actual release mechanism for practical applications, but rather to design a release mechanism that could be used to compare the discharge dynamics of various alternative agents, the device had to have a simple geometry, a simple flow pattern, and quick action. Due to safety consideration in the laboratory, release mechanisms that utilized explosive cartridges to initiate the discharge of the vessel were not considered in the design of the discharge vessel. Solenoid valves were also not considered because of the complex flow path inside the valves (although some valves do have a straight-through design) and a slow response time compared to the emptying time of the vessel. Furthermore, solenoid valves are not designed to operate under extreme high and low temperatures. A rupture disk was chosen as a quick release mechanism because the bursting of the disk is almost instantaneous once a specified pressure has been reached and a simple straight-through and full opening of the non-fragmented burst disk can be obtained. This technique had been successfully used previously in a study of rapid venting of hot, high pressure liquids from a pressure vessel (Kim-E, 1981; Kim-E and Reid, 1983).

3.3.2 Release Vessel Design. A rupture disk (FDI FA scored) with a diameter of 19.1 mm was used as a rapid release mechanism for discharging agents from the pressurized vessel. The disk was

made of stainless steel (SS 316) with a nominal burst pressure of 4.12 MPa at room temperature (22 °C). The actual burst pressure varied less than ± 10% of the nominal burst pressure.

The vessel used in this study was made of either stainless steel or clear acrylic plastic (polymethyl methacrylate). The clear acrylic vessel was used for visualizing the internal behavior of the agents during discharge and for obtaining emptying rates of the agents from the vessel.

The stainless steel (SS 304) vessel was constructed from a tube with an internal diameter of 50.8 mm and a wall thickness of 6.4 mm. One end of the tube was welded with an end plate in which there were four tapped access holes for mounting a piezoelectric dynamic pressure transducer (Kistler Model 603B1), two thermocouples (K-type), and a needle valve (Whitey SS-1RS4) for dispensing the agent into the vessel and for subsequent nitrogen pressurization. The other end of the tube was welded to a flange with an O-ring seal for mounting a rupture disk holder (FDI Model FF). A tapped hole was also made on the lower side wall of the vessel so that a pressure transducer could be mounted to monitor the pressure of the liquid during downward discharge. The internal volume of the vessel was measured by filling the vessel with water and weighing and was found to be 4.97×10^{-4} m^3. The vessel was hydrostatically tested to 17.2 MPa. However, for safety reasons, the vessel was operated at pressures less than or equal to 8.2 MPa. Figure 25 is a schematic of the stainless steel vessel.

The plastic vessel was constructed from a clear acrylic tube with a nominal internal diameter of 50.8 mm and a nominal wall thickness of 9.5 mm. A schematic of the vessel is shown in Figure 26. The tube was sandwiched between two aluminum end plates equipped with O-ring seals using four threaded rods which passed through the plates. The rupture disk holder was attached to one of the end plates. Two tapped holes were drilled for mounting a dynamic pressure transducer and a needle valve on the other end plate. For those agents (all the HCFC's and HFC's) that were found to cause glazing or to dissolve into the wall of the plastic vessel, a new acrylic tube was used for each run. The internal diameter of the plastic tube was found to vary from tube to tube due to the manufacturing process of extruding the tube. The average internal volume of the all plastic vessels was 5.09×10^{-4} m^3 with a standard deviation of 0.15×10^{-4} m^3. Measurements were recorded for each tube used.

3.3.3 Design Validation. The experimental set-up used in this study (to be discussed) resembles closely the conceptual experimental configuration described in Section 3.2. In the conceptual design, a nitrogen holding tank was proposed, whereas in the actual experimental set-up the internal volume (3.38×10^{-4} m^3) of the supply line (not shown in Figure 25 and Figure 26) between the nitrogen cylinder and the pressure vessel acted like a holding tank. In addition, the needle valve used for regulating nitrogen flow into the vessel functioned in a similar way as an orifice plate placed between the holding tank and the pressure vessel. A holding tank was not used in the actual experimental set-up because the combined holding tank/vessel system could not be easily assembled due to the bulkiness of the system. The situation was more critical when changing of the orientation of the system was required in order to study the effect of orientation on the discharge (see Section 3.4).

In an actual discharge vessel, the vessel is a closed system; that is, there is no continuous flow of nitrogen into the vessel. However, the present experimental design depends on the inflow of nitrogen to raise the internal pressure of the vessel in order to rupture the disk (see Section 3.4.2). Furthermore, it was not possible to shut off the nitrogen flow to the vessel at the instant when the rupture disk burst due to the relatively slow response time (~ 35 ms) of the solenoid used to connect the vessel and nitrogen supply line.

A series of experiments were performed to access the effect of the continuous nitrogen inflow during discharge. It was found that by regulating (less than a 1/4 turn; equivalent to an orifice opening of less than 0.5 mm) the needle valve to minimize the inflow of nitrogen such that the

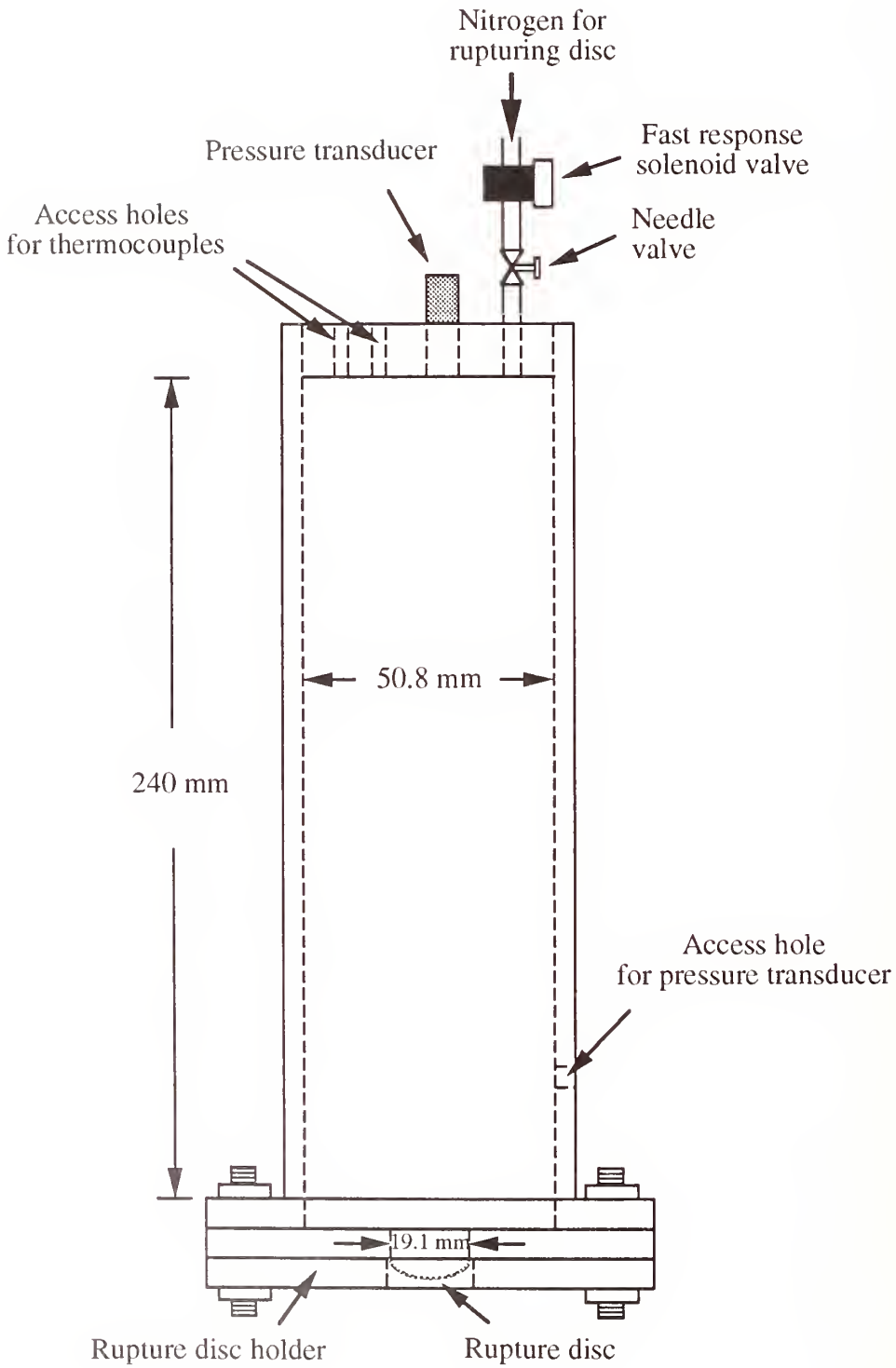

Figure 25. Schematic of the stainless steel vessel.

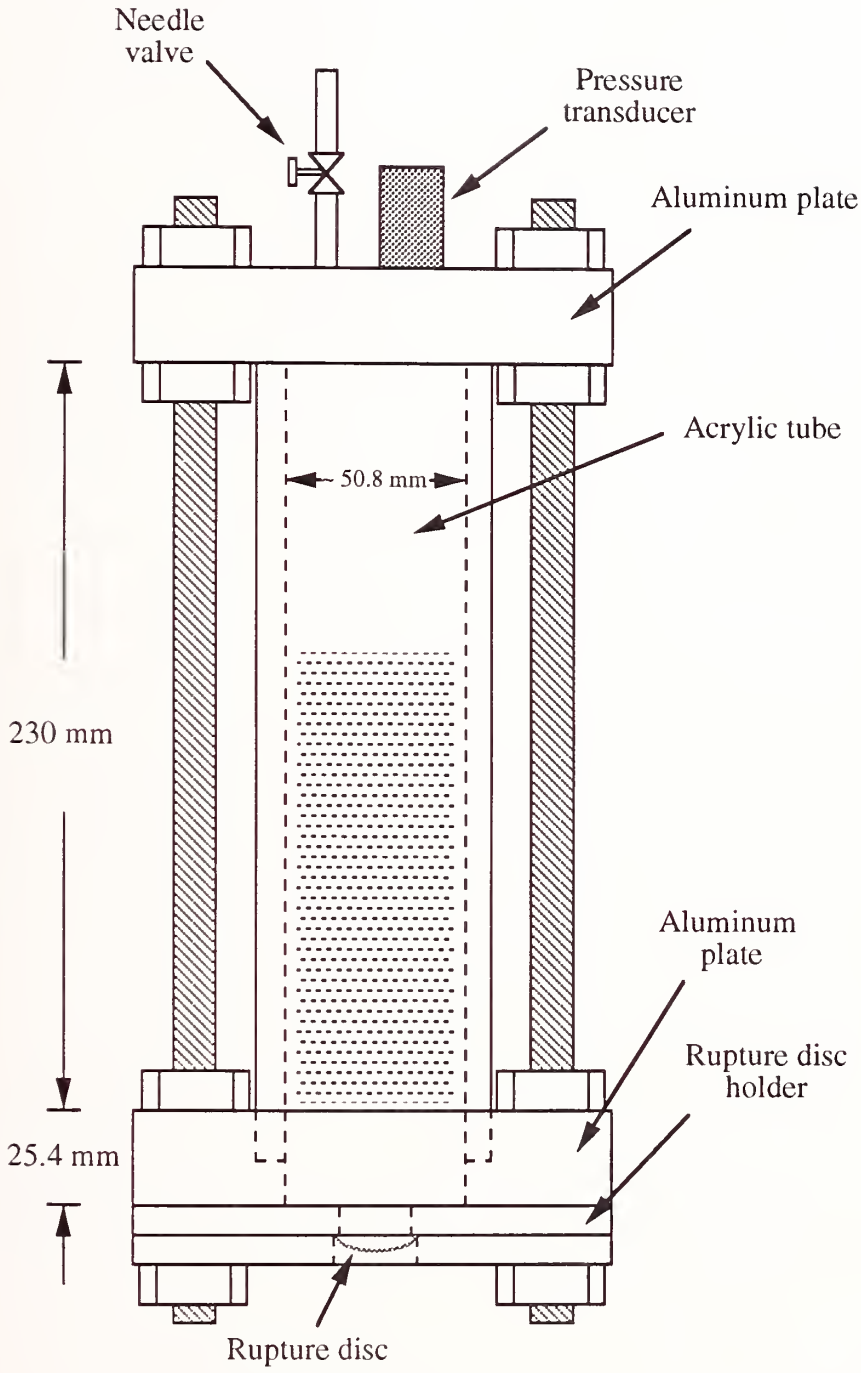

Figure 26. Schematic of the acrylic vessel.

duration from the initiation of nitrogen flow to the rupture of the burst disk was greater than one second, no appreciable differences (within the experimental uncertainty due to the actual burst pressure) were detected in the internal pressure traces during discharge. Therefore, it can be concluded that the continuous flow of nitrogen has an *insignificant* effect on the discharge behavior.

Based on the above discussion, the actual experimental configuration, in essence, incorporates the design recommendations made in Section 3.2 for a generic experimental set-up using a relatively low-pressure large-volume holding tank and a small orifice between the holding tank and the discharge vessel.

Since nitrogen is dissolved in liquid agent in an actual discharge vessel, the effect of dissolved nitrogen on the discharge process needs to be addressed. During discharge, rapid internal depressurization of the vessel could cause degassing of dissolved nitrogen from the liquid which could affect the dynamic behavior of the liquid agent inside the vessel and the flow rate through the vessel opening. Based on observed internal pressure-time histories during discharges of halon 1301, it has been conjectured (with no visual observations) that degassing of nitrogen occurs during the time interval from initiation of discharge to the complete depletion of the liquid (Williamson, 1976, Elliot *et al.*, 1984). However, the characteristic discharge times (order of seconds) for vertically downward release were much longer in these earlier studies than in our experiments ($\sim$ 30 ms). Based on the following argument, it is *hypothesized* that the characteristic discharge time in our experiments is much faster than the time required for degassing of dissolved nitrogen. The time for evolution of dissolved nitrogen in the liquid can be considered to be the sum of the waiting time for nucleation of nitrogen bubbles and the time for nitrogen bubbles to grow (Avedisian, 1985). If the waiting time is assumed to be very short even in the case of rapid discharge, the bubble growth time is then the dominant factor. Assuming the bubble growth is diffusion-controlled, *i.e.*, the growth is due to the diffusion of nitrogen into the bubble, the bubble growth velocity is of the order of 0.1 m/s (Bankoff, 1966). This growth velocity is about two orders of magnitude slower than the velocity of the depleting liquid level during rapid discharge (to be discussed later), implying that the discharge time of the liquid is much faster than that of degassing of dissolved nitrogen. Hence, the presence or absence of dissolved nitrogen would not affect the behavior of the liquid inside the vessel during very rapid discharge. In the experimental procedure used in this work (to be discussed in the next section), the dissolved nitrogen does not play a role due to the short contact time between the liquid and nitrogen in the vessel before initiation of discharge. The above argument is to ensure that the experimental procedure used in this study simulates closely the actual discharge process. Although dissolved nitrogen may not play a role in the behavior of the liquid inside the vessel during vertically downward discharge, it may affect the flashing behavior of the liquid external to the vessel as well as the behavior of the liquid inside the vessel during vertically upward and horizontal release due to longer characteristic discharge time. However, the solubilities of nitrogen in all the liquid agents used in this study were found to be very similar (see Section 2). Therefore, the differences in the overall external behaviors of the liquid agents could still be considered not to be attributable to differences in the solubility of nitrogen in the liquid agents.

3.4 Vessel Discharge Rate Measurements

3.4.1 Introduction. The events occurring inside and outside of a pressurized vessel containing alternative agent during discharge are extremely complicated due to the presence of two-phase flow. The discharge process addresses how the agent is delivered to a fire scene. The effectiveness of an agent in suppressing a fire depends on how fast and how it is transported to the fire. This part of the

task is designed to address the behavior of the proposed alternative agents inside the pressure vessel during *rapid* discharge. The characteristic discharge time is on the order of tens of milliseconds. Various parameters that could influence the discharge process will also be examined in this study. The parameters studied are: (1) orientation of discharge, (2) orifice diameter, (3) presence of an extension tube at the vessel exit, (4) vessel pressure at discharge, and (5) ambient temperature. The behaviors of the agents external to the vessel during discharge are discussed in Section 3.5.

3.4.2 Experimental Method. The experimental procedure involved the following steps. The vessel was evacuated for at least 15 min. The vessel was then connected to the agent supply bottle. For liquid agents, the vessel was filled approximately two-thirds full (by volume). For FC-116, which is a gas at room temperature, the vessel was filled until the pressure in the vessel equilibrated with the pressure in the supply bottle, and the amount of FC-116 in the vessel corresponded to an average fill density of 110 kg/m^3. This number was limited by the pressure of the agent in its supply bottle. The total mass of an agent dispensed to the vessel was obtained by weighing on an electronic scale with an accuracy of 1 g. The vessel was then pressurized with nitrogen to 75% of the nominal burst pressure of the rupture disk through a solenoid valve (Skinner 712X1D1B) and the needle valve (see Figure 25 and Figure 26). To initiate a discharge, the upstream nitrogen pressure in the nitrogen supply line was first raised to approximately 15% above the nominal burst pressure with the solenoid valve closed. The solenoid valve was then opened to start a flow of nitrogen into the vessel through the needle valve and initiate the experiment. The nitrogen flow continuously increased the internal pressure of the vessel to a point where the rupture disk could no longer sustain the rising internal pressure. Bursting and complete opening of the rupture disk followed, thus causing rapid release of the agent from the vessel.

A high-speed movie camera (Photec IV) operating at 2000 frames per second was used to document the events occurring inside the plastic vessel. Kodak Ektachrome high-speed daylight films (ASA 400), some front lighting, and intense backlighting were used. Emptying rates were obtained by using frame-by-frame analysis of the movies taken from the experiments. The high-speed motion picture film acquired for each discharge was analyzed using a slide scanner (Microtek ScanMaker 35t) to digitize the images and digital image processing software (Aldus PhotoStyler Version 1.1). Emptying rates were extracted from the digitized images of the liquid level of the agent in the vessel as a function of time during discharge.

The slide scanner is designed for use with 35 mm slides or film strips, both color and black and white, but is easily adapted for use with 16 mm movie film. It uses a linear array CCD (charge coupled device) and can digitize an image with a resolution of 3656 $\times$ 3656 dpi (dots per inch); twice the resolution (7312 x 7312 dpi) is possible with software interpolation. Dots can be represented by an 8-bit code indicating any one of 256 shades of gray, or by a 24-bit color code indicating any one of over 16 million colors. For this work, two frames per image were scanned as grayscale images with 3656 $\times$ 3656 dpi at 100% scale.

The scanning module incorporated in the digital image processing software (PhotoStyler) is Twain-compliant, which allows software applications and hardware imaging devices to communicate directly. This means that the scanner can be accessed directly from within the digital image processing software; after the scan, the image is placed inside the imaging software, where data processing is performed before the image is archived. The archival method used is to compress the image in JPEG format. In this way, an image that comprises 3.8 Mbyte of disk space can be saved in a file which is 144 kbyte without loss of image quality.

The process for computing the emptying rates is straightforward. The digital image processing software allows the measurement of the position of every pixel in the image, which is typically 2630 pixels wide by 1470 pixels high. Accurate measurements of timing and liquid level position, as seen

through the transparent vessel, allow the computation of volumetric flow rate when the vessel diameter is known.

The edge of the film strip contains a timing mark adjacent to the sprocket holes; the spot appears on the film at a rate of 1 kHz. When the high-speed movie camera is operated at 2000 frames per second, there is a timing spot every 2 frames (nominally 0.5 ms per frame). A more accurate framing rate can be computed by measuring the timing spot relative to the sprocket holes and using linear interpolation. It is estimated that the imprecision in the film speed for the data in this report is $\pm$ 0.001 ms per frame, or $\pm$ 0.2%.

The liquid level and a reference point are measured for each frame with a resolution of $\pm$ 0.5 pixels. Pixels are related to the physical length measurement scale by means of a 25.4 mm steel ball photographed at the beginning of each film reel. The uncertainty in the length calibration is $\pm$ 0.5 pixel, or 0.2 mm. Thus, the uncertainty in the liquid position measurements is typically $\pm$ 0.4 mm.

Two thermocouples, one placed in the ullage and one in the liquid, were used to record the temperature changes in both phases during discharge. The thermocouples used were K-type, fine gage (12 or 25 μm), and unsheathed. The thermocouple were constructed by arc-welding the fine thermocouple to the two bare ends (with the original bead junction removed) of a rugged unsheathed thermocouple (K-type) probe under a microscope. Attempts to record temperatures in the both phases (vapor and liquid) inside the vessel proved to be difficult, although some qualitative information could still be obtained from the temperature measurements. The difficulty lies in the response time and the fragility of the fine wire thermocouples. Even a fine 12 μm unsheathed thermocouple was found to have a time constant which was too slow to follow the events occurring inside the vessel.

The pressure transducer was a Kistler Model 603B1 piezoelectric dynamic pressure transducer which was regulated by a dual mode charge amplifier (Kistler Model 5004). The outputs from the charge amplifier and thermocouples were recorded using a high-speed data acquisition board (Strawberry Tree FLASH-12^{TM} Model 1) at a rate of 25 kHz and stored in a personal computer for subsequent data analysis.

Unless specified, discharge experiments were conducted by discharging vertically downward at room temperature with rupture disks having a nominal burst pressure of 4.12 MPa. This condition will be referred to as the standard discharge in the discussion. The agents studied were the eleven potential replacement agents: HFC-236fa, FC-31-10, FC-318, HCFC-124, HFC-227ea, HFC-134a, FC-218, HCFC-22, HFC-125, HFC-125 (40% by mass)/HFC-32 (60%) mixture, and FC-116. Halon 1301 was also included in the study as a reference agent.

The effect of the size of the opening on the discharge process was assessed by mounting various diameter orifice plates at the base of the discharge vessel to restrict the opening of the rupture disk at the exit of the disk holder. The orifice diameters used in this study were 19.1, 12.7 and 6.4 mm. The plates were 5.08 mm thick.

In order to simulate discharge through a pipe for engine nacelle fire protection applications, experiments were performed using an extension tube 0.5 m long with an internal diameter equal to that of the 19.1 mm rupture disk. The tube was attached to the vessel exit, and the effect of orientation on the discharge dynamics with an extension tube was also studied.

The effect of the initial charge pressure on the discharge was simulated and studied by performing a series of experiments at room temperature using rupture disks with different burst pressures. Rupture disks with nominal burst pressures of 2.76, 4.12, and 5.50 MPa were selected.

A few experiments were also conducted to evaluate the effect of temperature on the discharge characteristics. The temperature effect was evaluated only at -45 °C by using burst disks with nominal burst pressures of 2.76 MPa. Based on the measurements of thermodynamic properties of agent/nitrogen mixture (see Section 2), this burst pressure was chosen in order to simulate the residual pressure in an actual vessel as a result of exposing the vessel to a -45 °C environment. Two agents

(FC-31-10 and FC-218) were evaluated at this temperature. Cooling was achieved by immersing the vessel in dry ice. Due to its large thermal inertia, the stainless steel vessel and its contents could only be chilled to an equilibrium temperature of −45 °C. No experiments were conducted at 150 °C as originally planned because the final pressure exceeded the operating pressure of the vessel even when the vessel was 1/3 fill (see Section 2). However, some general comments will be made in Section 3.4.3.5 with regard to the discharge characteristics at elevated temperatures.

The study on effects of orientation on the discharge dynamics was carried out by discharging the vessel vertically downward and upward or horizontally. Since the horizontal and vertical upward-discharge processes were found experimentally to be slower than the downward discharge, the high-speed movie camera was operated at 500 or 1000 frames per second in these experiments.

Only three agents were used for studying the effect of various parameters on the discharge process. Two representative alternative agents (FC-31-10 and FC-218) and halon 1301 at room temperature. These two alternative agents were chosen among others because they represented the range of boiling points encompassed by most of the eleven proposed fluids. Halon 1301 was included as the baseline agent.

3.4.3 Results and Discussion

3.4.3.1 Standard Discharge. Visual observations of the events occurring inside the vessel during downward discharge are described as follows. Liquid agent is propelled out of the vessel when the rupture disk breaks. In some of the experiments, the inflow of nitrogen disturbs the liquid/vapor interface causing a wavy motion along the liquid surface in a manner similar to that described in Section 3.2. Apparently these disturbances did not affect the agent release behavior. At the end of the liquid discharge the vessel interior becomes foggy, possibly due to the condensation of vapor caused by a decrease in temperature in the ullage due to the adiabatic expansion of the vapor phase. As the discharge of the remaining vapor continues, the vessel becomes clear once again.

Figure 27 shows a photographic sequence of events during a downward discharge of FC-218 from a plastic vessel. The photographs were taken at 2000 frames per second. The frame which corresponds to the time t = 0.5 ms is the first frame where agent is observed outside the vessel. Due to the framing rate, there is a 0.5 ms uncertainty in the times. The dark grey horizontal shadow in the middle of the background was caused by the backlighting set-up. The first photograph shows the plastic vessel, which is located in the middle, the vessel mount, and the liquid level. In this sequence of photographs, the perturbation of the vapor/liquid interface caused by the inflow of nitrogen is evident from the wavy nature of the interface. The photographs also show the behavior (to be discussed in Section 3.5) of the agent outside the vessel during discharge.

Figure 28 through Figure 39 show results for the temporal variation of the internal pressure during downward discharges of all the agents evaluated in this study. Pressures reported in the figures are gauge pressures. The pressure is nondimensionalized by the actual burst pressure, P_i, which is taken to be the pressure at t (time) = 0 s. The time t = 0 s is defined as the time when the first laser (located at the immediate exit of the vessel) signal is attenuated (see Section 3.5) by the agent coming out from the vessel. For most agents (except FC-116, HFC-125/HFC-32 mixture, and halon 1301), there are two distinct regions, separated by an inflection point, in the pressure-time history. The first region corresponds to the time interval during which the liquid agent is being propelled from the vessel; the second region corresponds to the period when the remaining vapor (mostly nitrogen) is being vented from the vessel. Based on observations from the plastic vessel experiments, the inflection point corresponds very closely to the time at which the liquid agent has just been completely expelled from the vessel. Since the pressure-time histories obtained from the pressure transducer mounted on the stainless steel vessel wall in order to monitor the temporal change

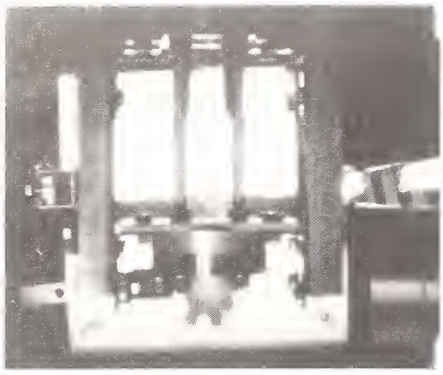

0.5 ms

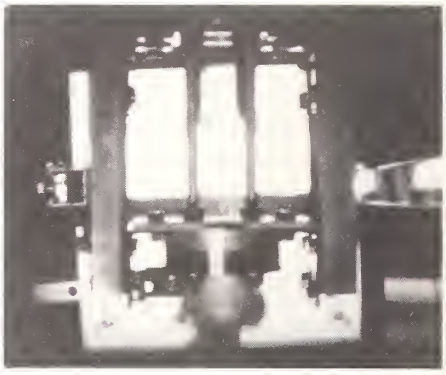

1.0 ms

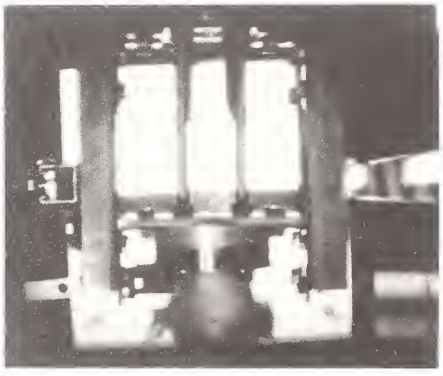

1.5 ms

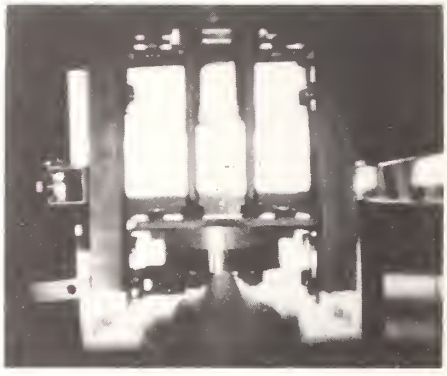

2.0 ms

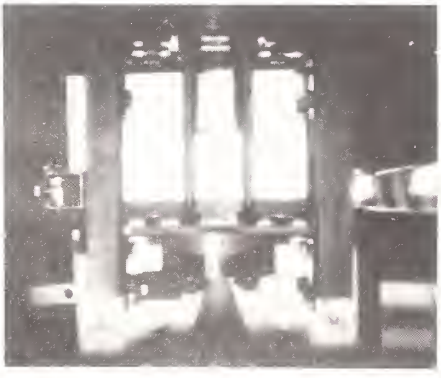

2.5 ms

3.0 ms

Figure 27. Photographic sequence of events showing a downward discharge of FC-218 from a plastic vessel.

10.0 ms

15.0 ms

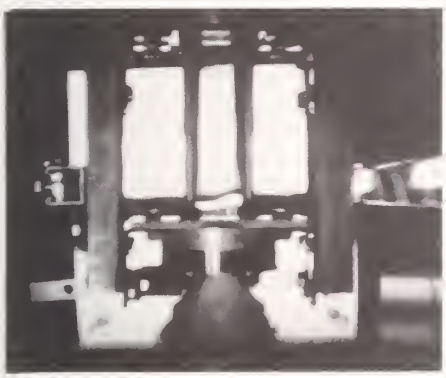

20.0 ms

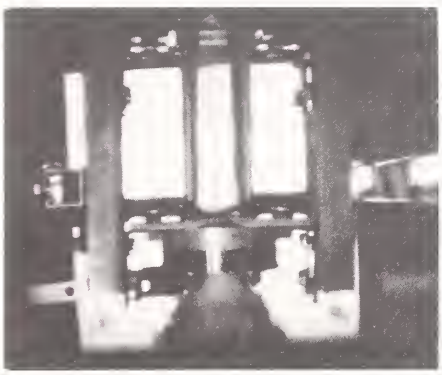

25.0 ms

30.0 ms

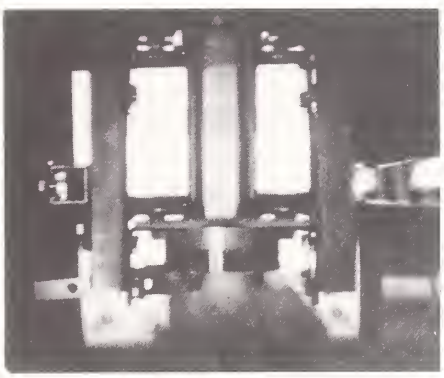

32.5 ms

Figure 27. (continued) Photographic sequence of events showing a downward discharge of FC-218 from a plastic vessel.

35.0 ms

40.0 ms

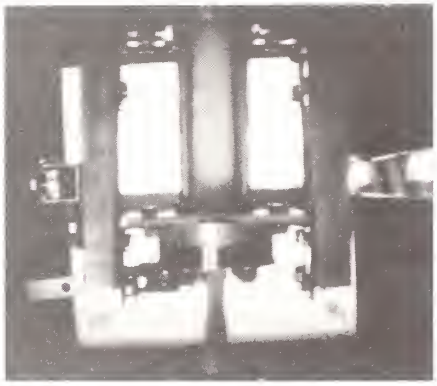

50.0 ms

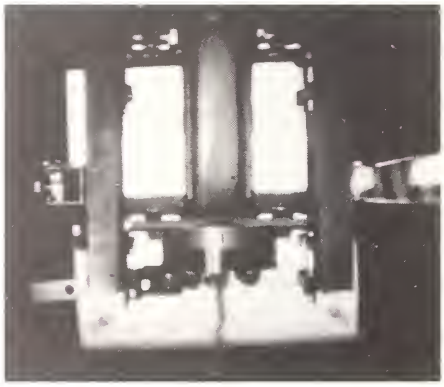

75.0 ms

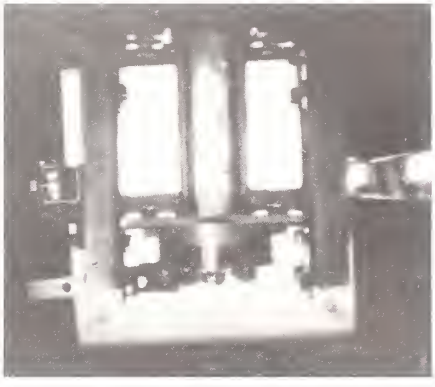

100.0 ms

125.0 ms

Figure 27. (continued) Photographic sequence of events showing a downward discharge of FC-218 from a plastic vessel.

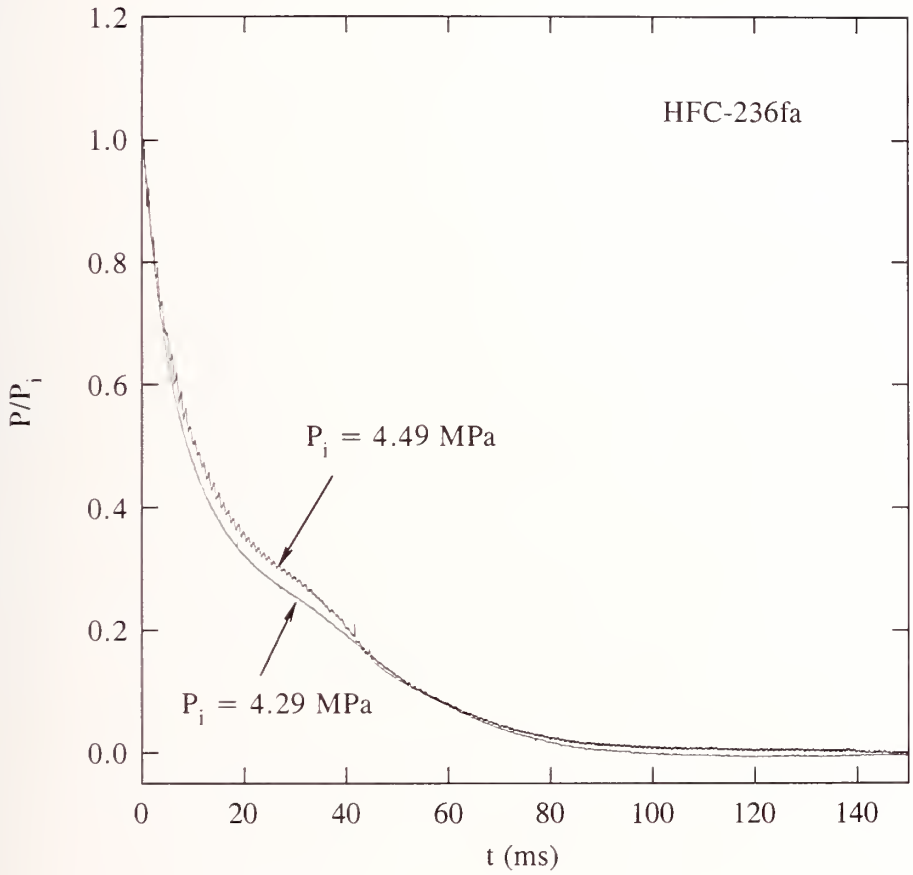

Figure 28. Temporal variations of internal pressure during downward discharges of HFC-236fa.

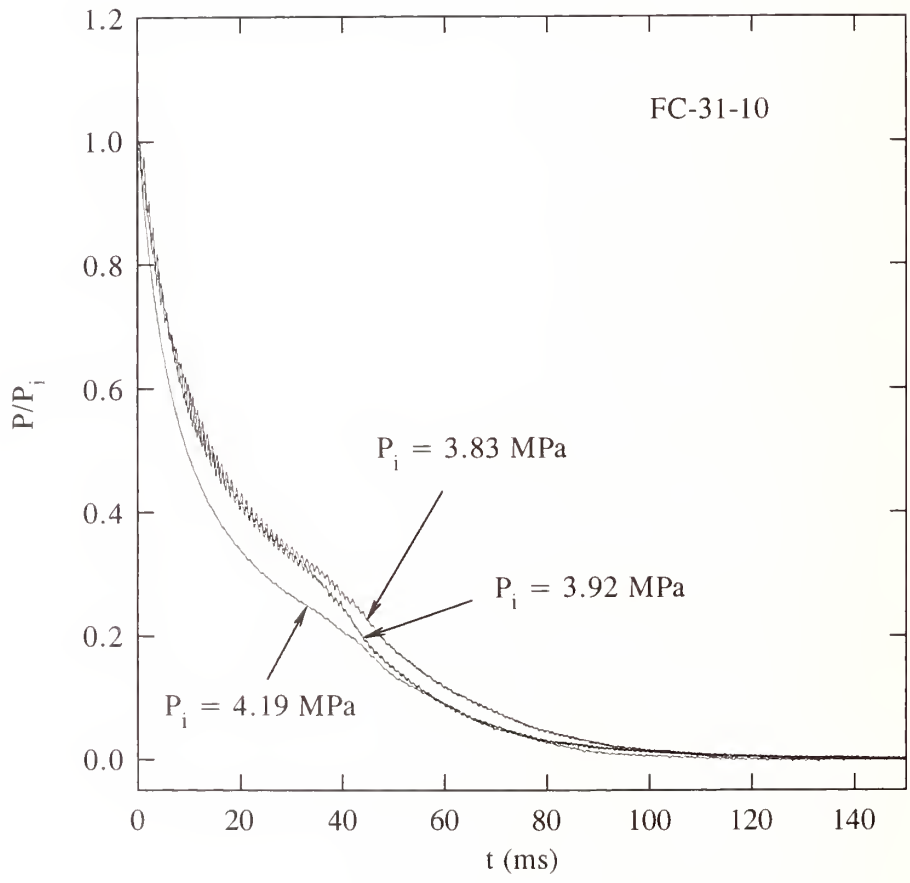

Figure 29. Temporal variations of internal pressure during downward discharges of FC-31-10.

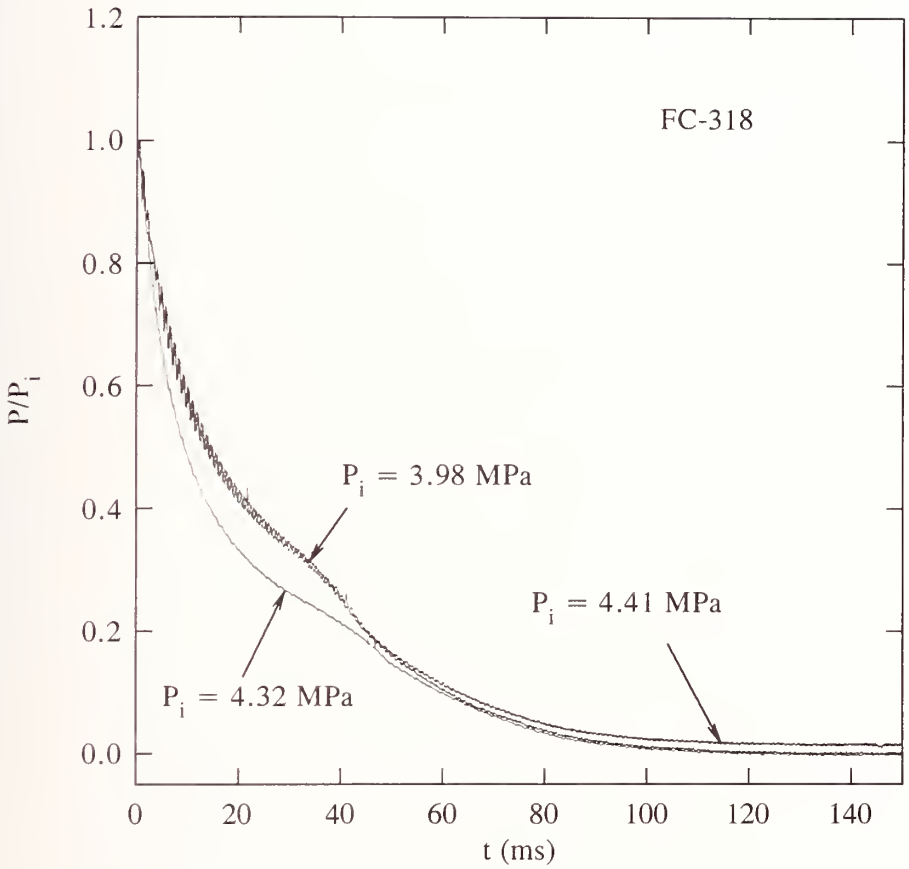

Figure 30. Temporal variations of internal pressure during downward discharges of FC-318.

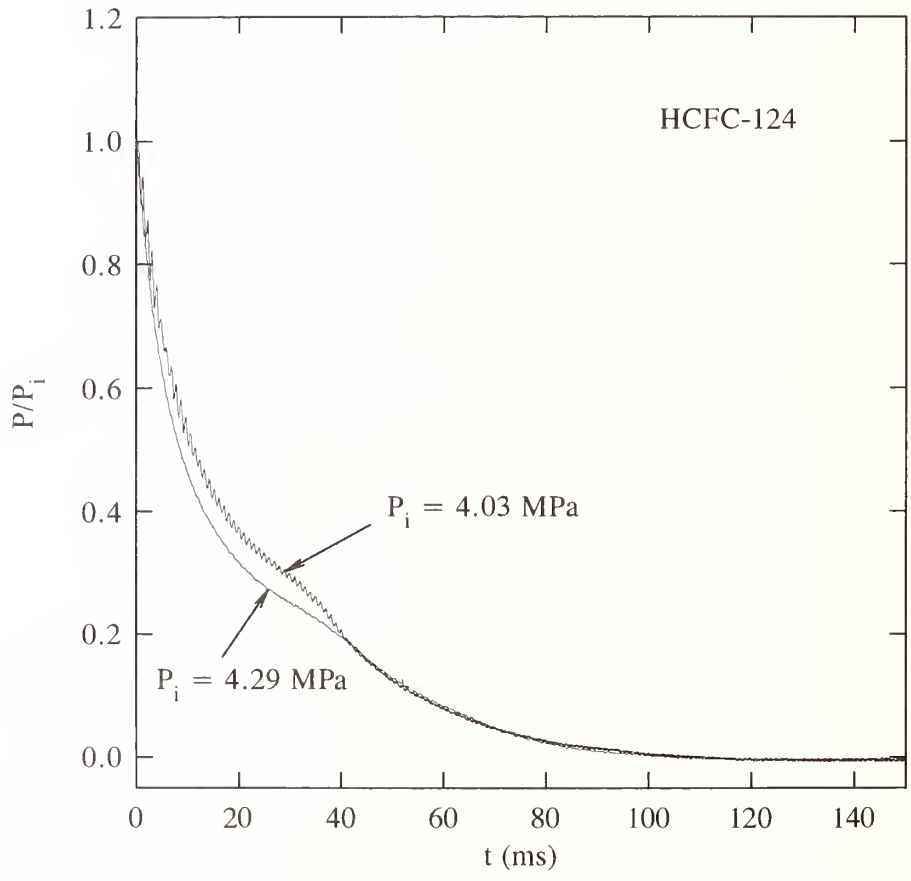

Figure 31. Temporal variations of internal pressure during downward discharges of HCFC-124.

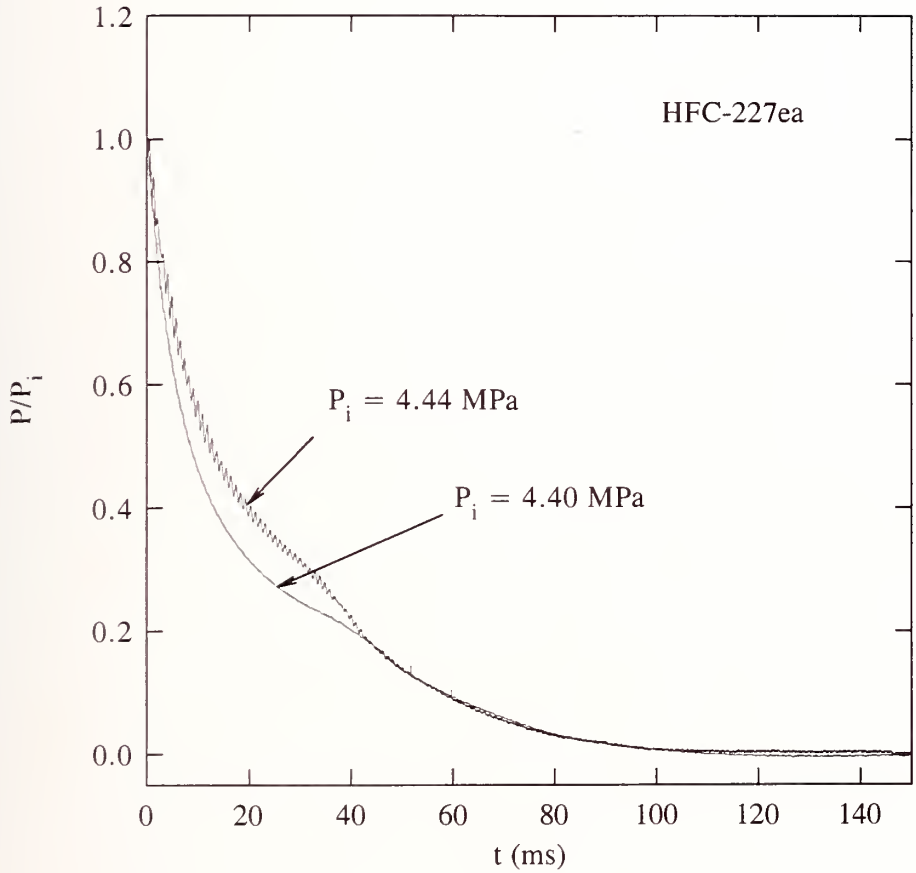

Figure 32. Temporal variations of internal pressure during downward discharges of HFC-227ea.

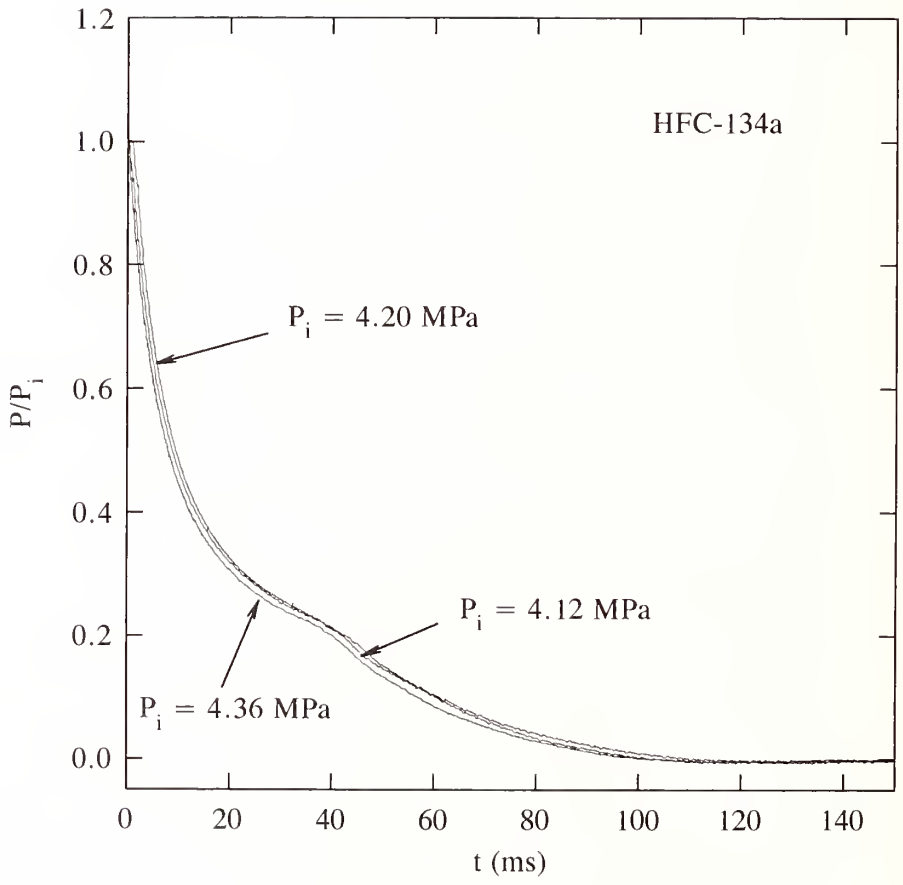

Figure 33. Temporal variations of internal pressure during downward discharges of HFC-134a.

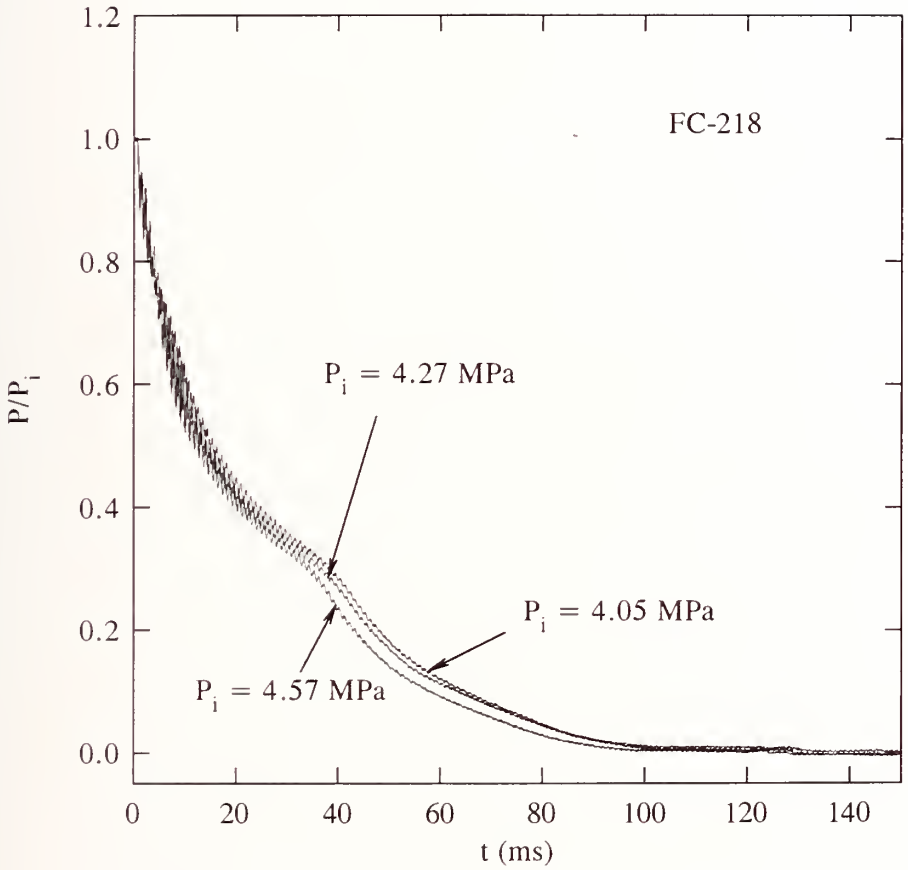

Figure 34. Temporal variations of internal pressure during downward discharges of FC-218.

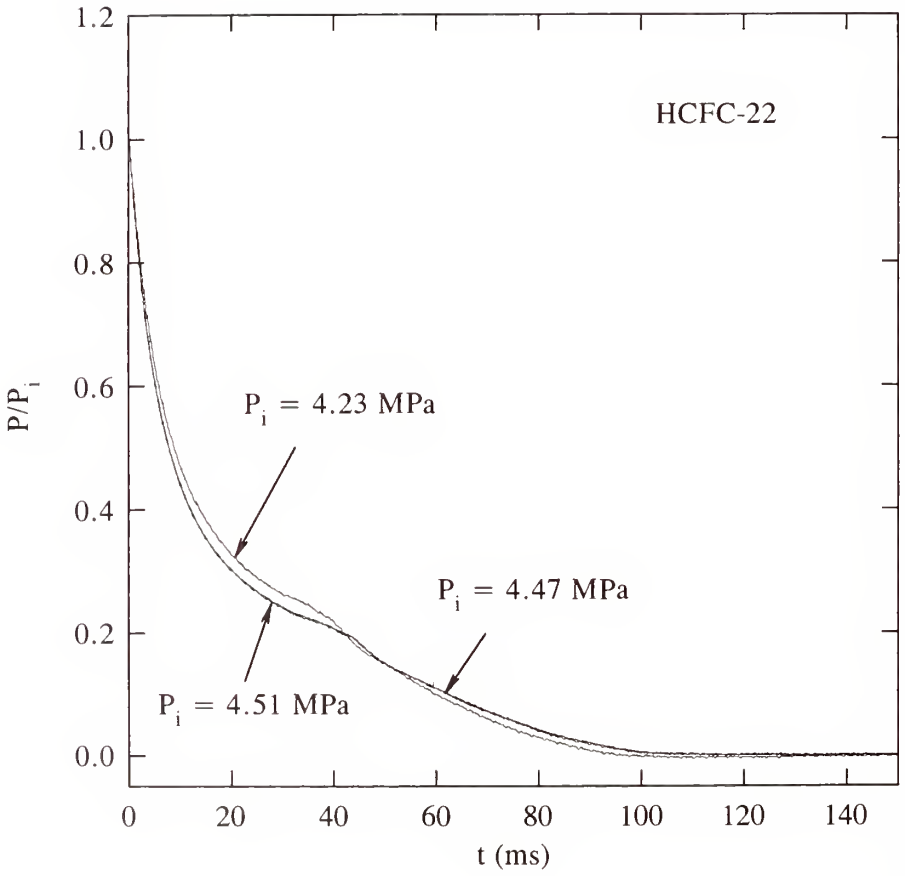

Figure 35. Temporal variations of internal pressure during downward discharges of HCFC-22.

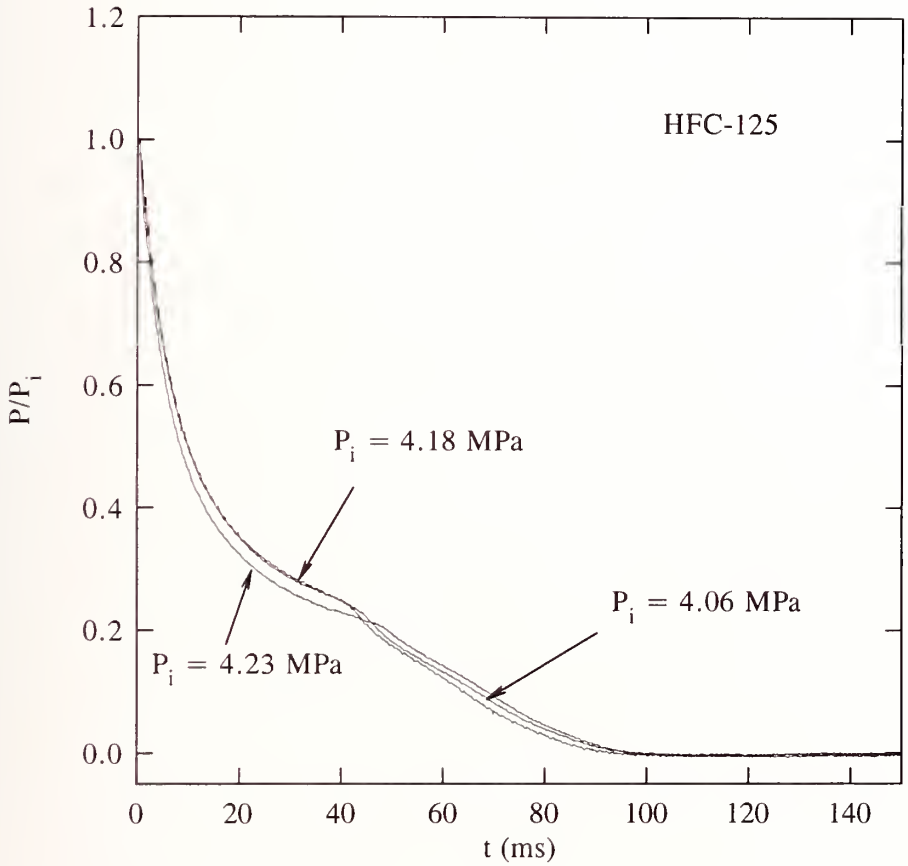

Figure 36. Temporal variations of internal pressure during downward discharges of HFC-125.

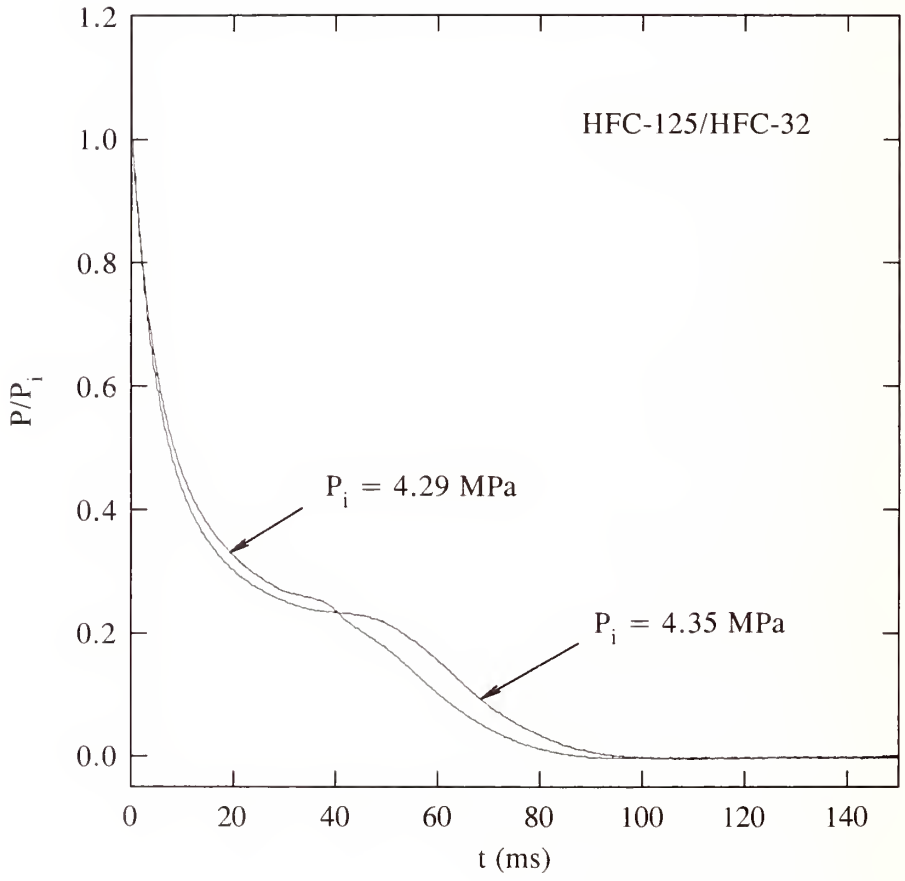

Figure 37. Temporal variations of internal pressure during downward discharges of the HFC-125/HFC-32 mixture.

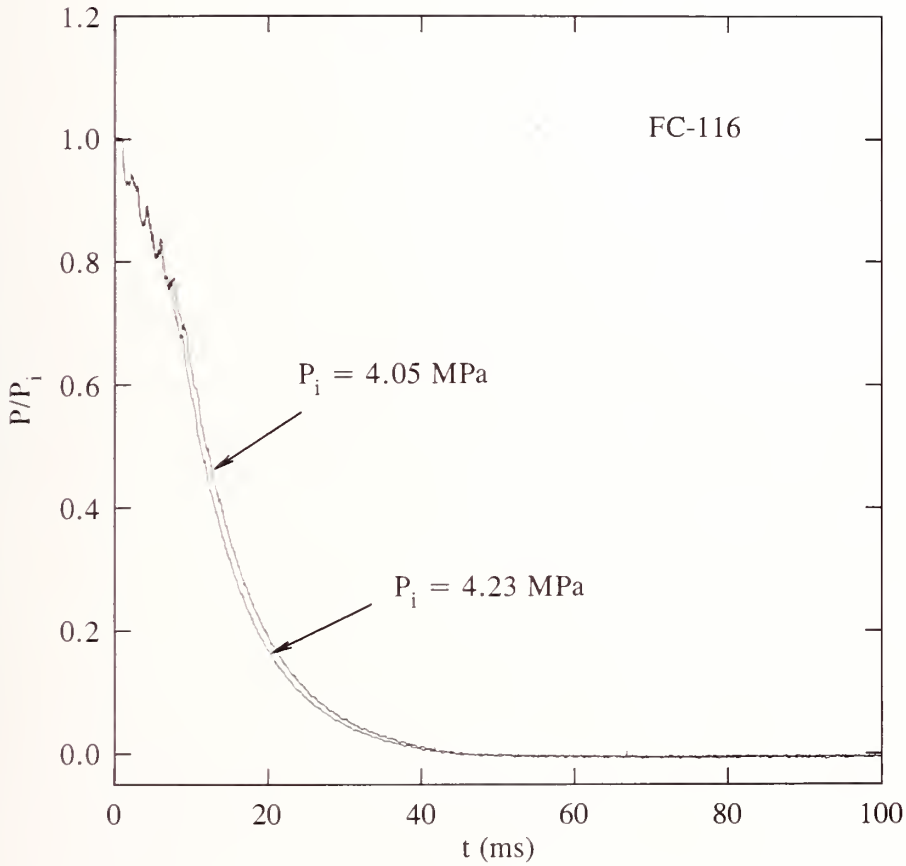

Figure 38. Temporal variations of internal pressure during downward discharges of FC-116.

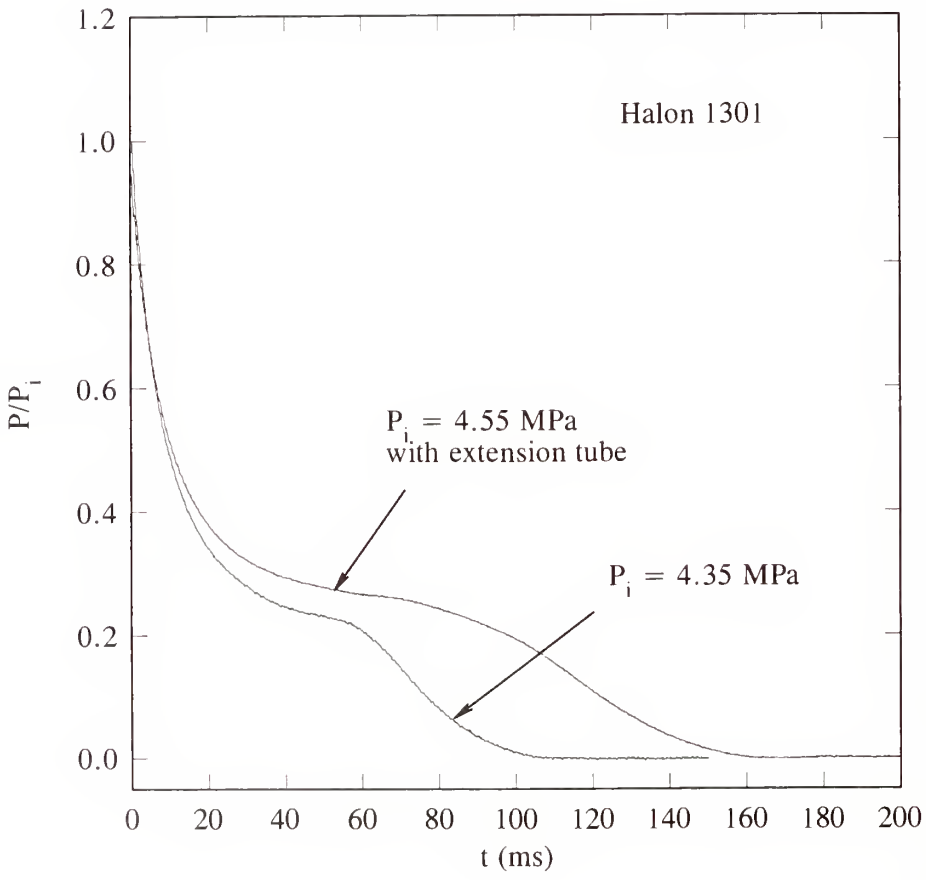

Figure 39. Temporal variations of internal pressure during downward discharges of halon 1301.

of the pressure in the liquid phase followed those obtained from the pressure transducer used to measure pressure change in the vapor phase, only the pressure-time histories from the vapor phase measurements are presented and discussed.

The pressure-time histories obtained using plastic vessels have an oscillatory nature and more noise. Such time traces are easily identified in the figures. This behavior is believed to have been caused by vibration of the vessel mount during discharge. The observed oscillatory frequency of the pressure traces corresponded closely to the natural frequency of the vessel mount, which was estimated by simulating the four threaded rods (see Figure 26) as four springs and the vessel as a mass attached to the springs. Since a different mount was used for the stainless steel vessel, no such oscillatory characteristic in the pressure-time histories was observed. The variations in the pressure-time histories from run to run reflect the nature of the rupture disk, that is, the actual burst pressure of each rupture disk used in the experiments deviated somewhat from its nominal burst pressure. Therefore, different P_i's are anticipated depending on the pressure at which the disk bursts. Differences in the pressure histories obtained from the stainless steel vessel and from plastic vessels are due to the differences in the internal volumes of the vessels.

The visual observation of the internal behavior of liquid agent during discharge from plastic vessels shows that during the time when the liquid level is visible (refer to Figure 26) no internal boiling of the liquid occurs during depressurization. This observation can be explained by examining the temporal variation of the internal pressure. From Figure 28 through Figure 36, for the nine agents with boiling points above -45 °C, the pressures at the time when the liquid empties (at the inflection point in the pressure-time history) is still well above the saturation vapor pressure for all of these agents at room temperature. Although the temperature of the ullage above the liquid is very low because of the expansion of the vapor phase, the characteristic time, t_c, for the interfacial heat transfer between the liquid and the vapor phases is much longer than the discharge time of the liquid, typically $O(10$ ms). The characteristic time for heat transfer can be estimated (Bird *et al.*, 1960) using

$$t_c \sim \frac{\delta^2}{\alpha}, \tag{17}$$

where α is the thermal diffusivity, typically $O(10^{-7}$ m^2/s) and δ is the thermal penetration distance in the liquid, in our case typically $O(10^{-2}$ m). Hence, t_c is on the order of tens of seconds. Therefore, the liquid agent remains at the initial room temperature and can be considered to undergo an isothermal depressurization during discharge. As shown in Figure 40, this argument is supported by the temperature-time histories in the liquid during discharge of HCFC-22. Figure 40 was obtained using a 25 μm fine wire thermocouple. Data were taken at a rate of 10 kHz.

For FC-116 (see Figure 38), the pressure-time histories show a relatively smooth decay of the internal pressure. Since FC-116 is a gas at room temperature, this behavior is typical of a gas vented from a pressurized vessel. The two regions in the temporal variation of the internal pressure observed for the liquid agents do not exist.

For HCFC-22, HFC-125, HFC-125/HFC-32 mixture, and halon 1301, only the pressure-time histories from the stainless vessel were recorded. Since some of these agents etch plastic and all have relatively high vapor pressures at room temperature, the plastic vessel was not used for fear of rupture of the vessel during its filling and handling.

The experimental results for HFC-125/HFC-32 mixture and halon 1301 deserve further discussion. The pressure-time histories in Figure 37 and Figure 39 show that the transition from the liquid discharge to the venting of the remaining vapor from the vessel is not distinct and abrupt. The transition appears to be gradual. Since no visual observations were made for these agents, the events

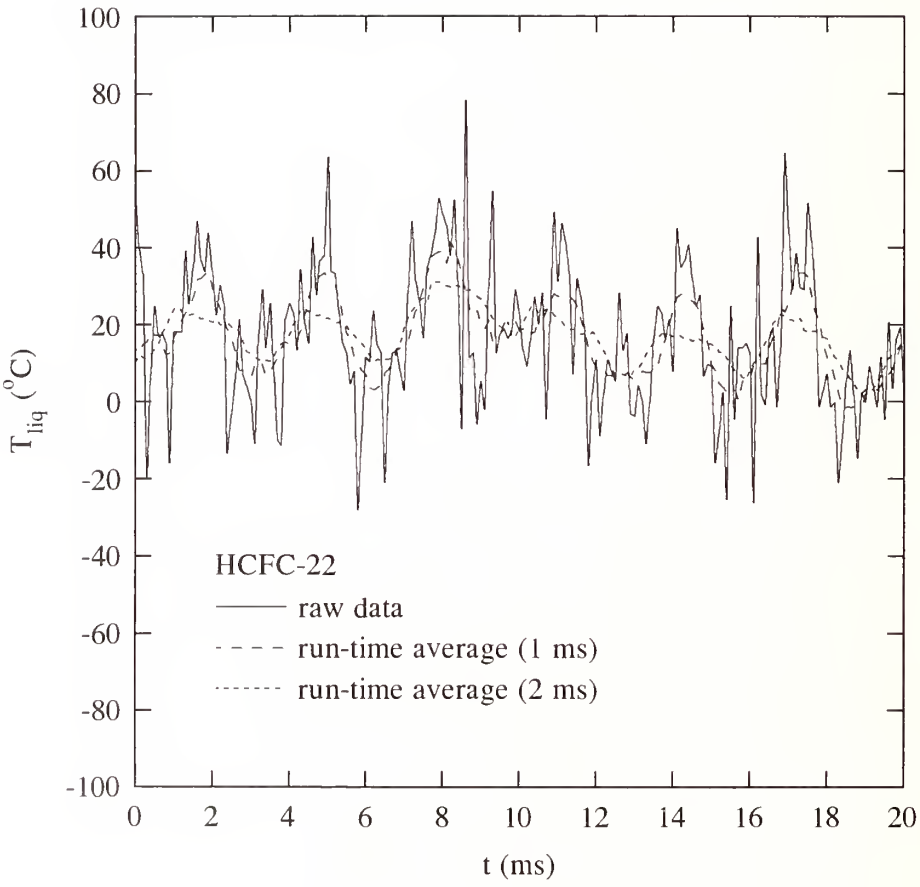

Figure 40. Temporal variation of temperature in the liquid phase during discharge of HCFC-22.

occurring inside the vessel could only be inferred from the experimental pressure-time traces. It can be seen that at some point during the release the internal pressure dropped below the saturation vapor pressure of the agent at room temperature (refer to Section 2). Therefore, it is conjectured that boiling of the liquid occurred near the end of the liquid discharge, thus causing a gradual transition until the remaining liquid had been discharged.

Based on visual observations of the discharges, a simple mathematical model can be formulated to simulate the pressure-time history. As mentioned above, there are two distinct regions, separated by an inflection point, in the pressure-time traces. The first region corresponds to the liquid discharge while the second region corresponds to the discharge of the remaining vapor after the liquid has been released from the vessel. The formulation of the model for liquid discharge will first be presented, followed by a discussion on the simulation of the discharge process of the remaining vapor.

Once the rupture disk bursts, the nitrogen above the liquid agent simply acts as a piston to drive the liquid out of the vessel. The control volume that is being considered is the ullage above the liquid. Since the discharge process is very rapid, the process occurring in the gas phase can be assumed to be adiabatic and reversible, *i.e.*, isentropic. Furthermore, for simplicity the control volume is assumed to be closed in the analysis because the inflow of nitrogen does not influence the discharge process (see Sections 3.2 and 3.3.3). Assuming the vapor phase to be ideal, from the first law of thermodynamics for an isentropic process,

$$PV^{\gamma} = constant \ , \tag{18}$$

where γ is the ratio of the constant pressure and volume heat capacities, P is the pressure, and V is the control volume. Since nitrogen is the dominant species in the vapor phase, the γ of nitrogen with a value of 1.4 is assumed. If a time derivative of Equation (18) is taken, then

$$\frac{dP}{dt} + \frac{P\gamma}{V}\frac{dV}{dt} = 0 \ . \tag{19}$$

Because of the design of the rupture disk holder, there is a short distance, L (25.4 mm), having a diameter of 19.1 mm through which the fluid has to pass before exiting from the release vessel assembly. Because of rapid depressurization, the liquid becomes superheated as it passes through the opening of the disk (Modell and Reid, 1983; Reid, 1976). Superheating of the liquid has been observed in previous studies on the discharge of saturated and subcooled liquid from orifices and nozzles (Benjamin and Miller, 1941; Burnell, 1947; Pasqua, 1953; Hesson and Peck, 1958; Henry, 1970; Prisco *et al.*, 1977; Celata *et al.*, 1983; Van den Akker *et al.*, 1983). If we assume the flow of metastable liquid through the disk opening (D) and the disk holder can be approximated by flow through a short tube ($0 < L/D < 3$) , then the volumetric flow rate of the liquid, expressed in terms of the volumetric expansion rate of the gas above the liquid agent, can be calculated by (Prisco *et al.*, 1977; Tong, 1965)

$$\frac{dV}{dt} = C_d A \sqrt{\frac{2(P - P_{sat})}{\rho_l}} \ , \tag{20}$$

where A is the cross sectional area of the disk opening, ρ_l is the liquid density, P_{sat} is the saturation vapor pressure of agent, and C_d is the discharge coefficient for the liquid, with measured values found

to be between 0.61 to 0.64 in the literature (Prisco *et al.*, 1977; Tong, 1965). Equations (19) and (20) were solved numerically using a fourth order Runge-Kutta method (Carnahan *et al.*, 1969) to obtain the pressure-time histories and the liquid level as a function of time.

Figure 41 through Figure 46 show the temporal variations of liquid level for agents obtained from experiments using plastic vessels. Also shown in the figures are predictions obtained using Equations (19) and (20). The liquid levels were measured from the upper edge of the lower aluminum plate (see Figure 26), and a zero liquid level does not correspond to complete depletion of liquid. The best curve fits were obtained by optimizing the values of C_d, which varied between 0.67 to 0.80. These C_d values are slightly higher than previous experimental values reported in the literature.

After complete depletion of liquid, the discharge process of the remaining vapor can be modeled as follows. If the vapor is assumed to be an ideal gas, the process is again assumed to be isentropic, and the pressure in the vessel is high enough that the flow can be assumed to be choked in the disk opening (which is approximated as a round, sharp-edged orifice), it can be easily shown that the following equation describes the rate of pressure decay in a vessel as a function of time (Kim-E, 1981).

$$\frac{P}{P_{el}} = \left(1 - \frac{C_a A}{V} \left(\frac{R T_{el} \gamma^3 K}{M} \right)^{1/2} \left(\frac{1 - \gamma}{2\gamma} \right) t \right)^{\frac{2\gamma}{1-\gamma}}, \tag{21}$$

with

$$K = \left(\frac{2}{\gamma + 1} \right)^{\left(\frac{\gamma + 1}{\gamma - 1} \right)}, \tag{22}$$

where P_{el} and T_{el} are the pressure and temperature in the vessel at the instant of complete depletion of liquid agent, respectively, C_a is the discharge coefficient for the gas, R is the universal gas constant, and M is the molecular weight of the vapor (assumed to be nitrogen). A choked flow is justifiable because P_e/P, where P_e is the exit pressure (0.101 MPa), is less than the critical pressure ratio most of the time during discharge of the remaining vapor. For an ideal gas undergoing an isentropic process, the critical pressure ratio is given by (Balzhiser *et al.*, 1972)

$$\left(\frac{P_e}{P} \right)_{critical} = \left(\frac{2}{\gamma + 1} \right)^{\frac{\gamma}{(\gamma - 1)}} \tag{23}$$

Optimum values of C_a were found to be between 0.26 and 0.31 (Kim-E, 1981) during depressurization of a vessel initially filled with nitrogen.

Figure 47 through Figure 52 compare the complete pressure-time histories with predictions from Equations (19), (20), (21), and (22). The best curve fits for the duration of vapor discharge were obtained by optimizing the values of C_a, which varied between 0.25 to 0.35. However, if instead of using the P_{el}'s from the liquid discharge calculations, one fits the experimental results of vapor discharge by optimizing both P_{el} and C_a, the values of C_a are found to be $\sim$ 0.6.

The average volumetric flow rates, defined as the initial volume of liquid in the vessel divided by the emptying time of the liquid, are summarized in Table 4. Knowing the framing rate of the high-

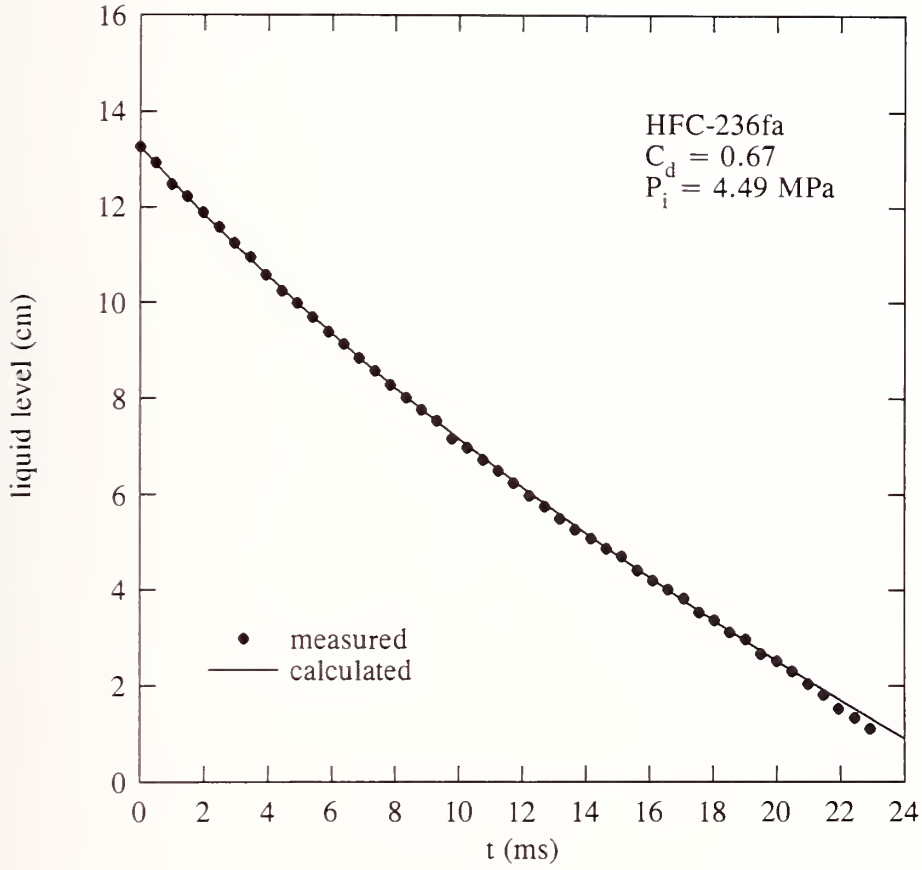

Figure 41. Temporal variation of liquid level obtained from a HFC-236fa discharge.

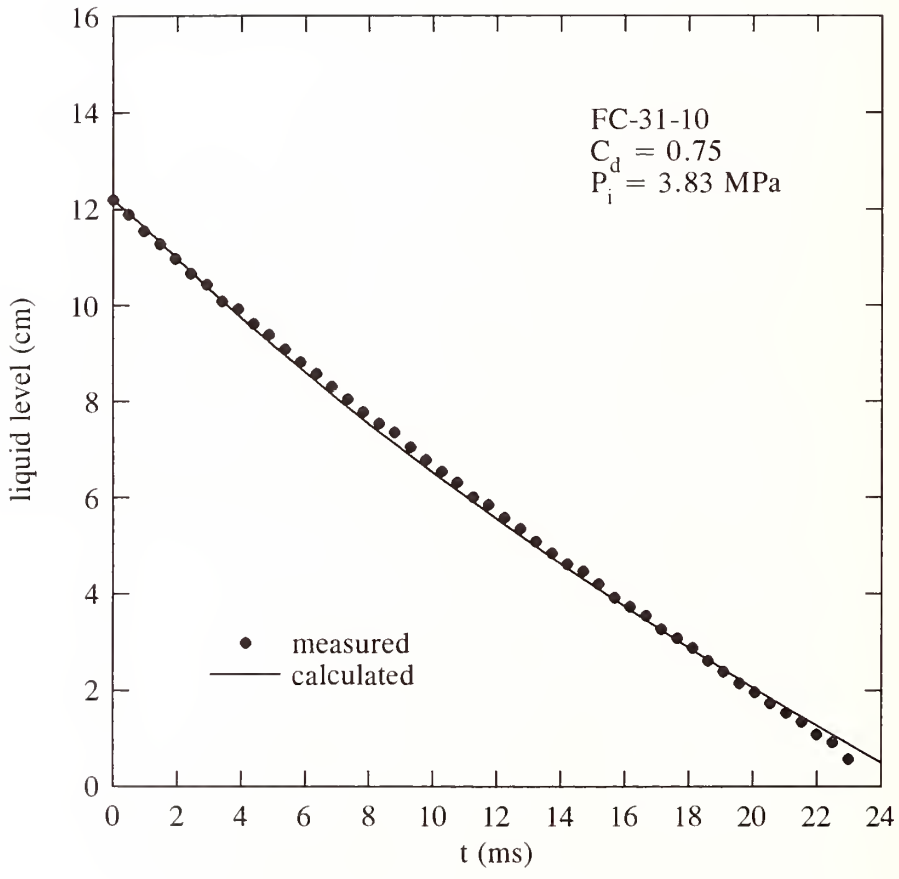

Figure 42. Temporal variation of liquid level obtained from a FC-31-10 discharge.

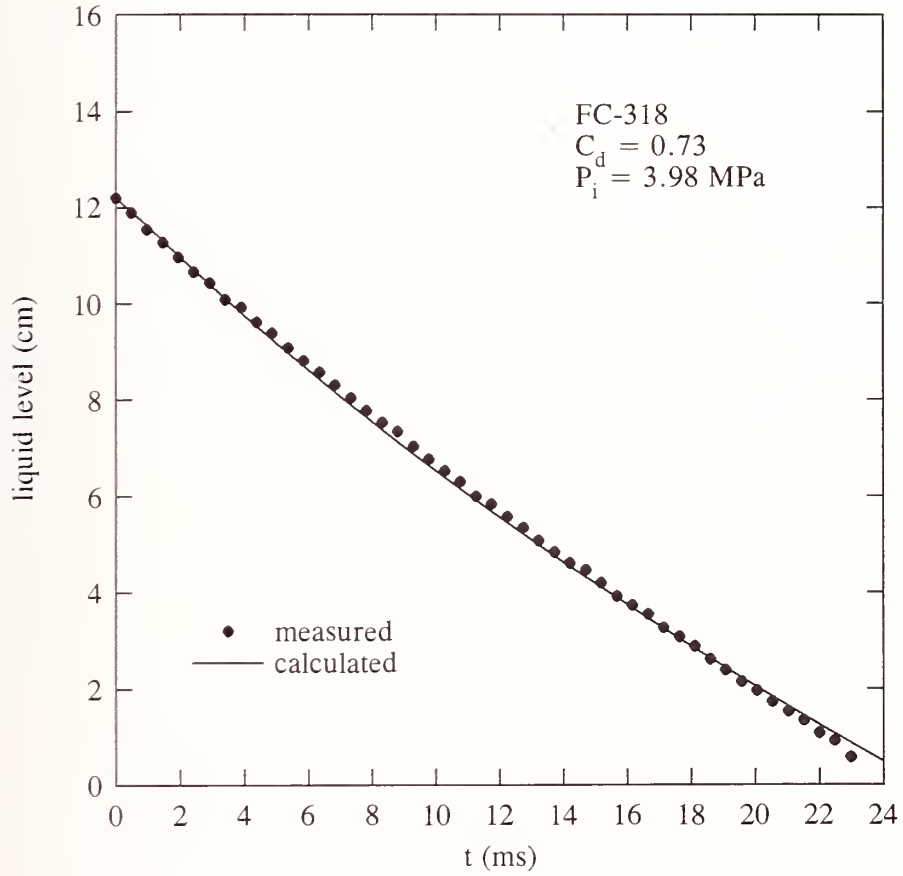

Figure 43. Temporal variation of liquid level obtained from a FC-318 discharge.

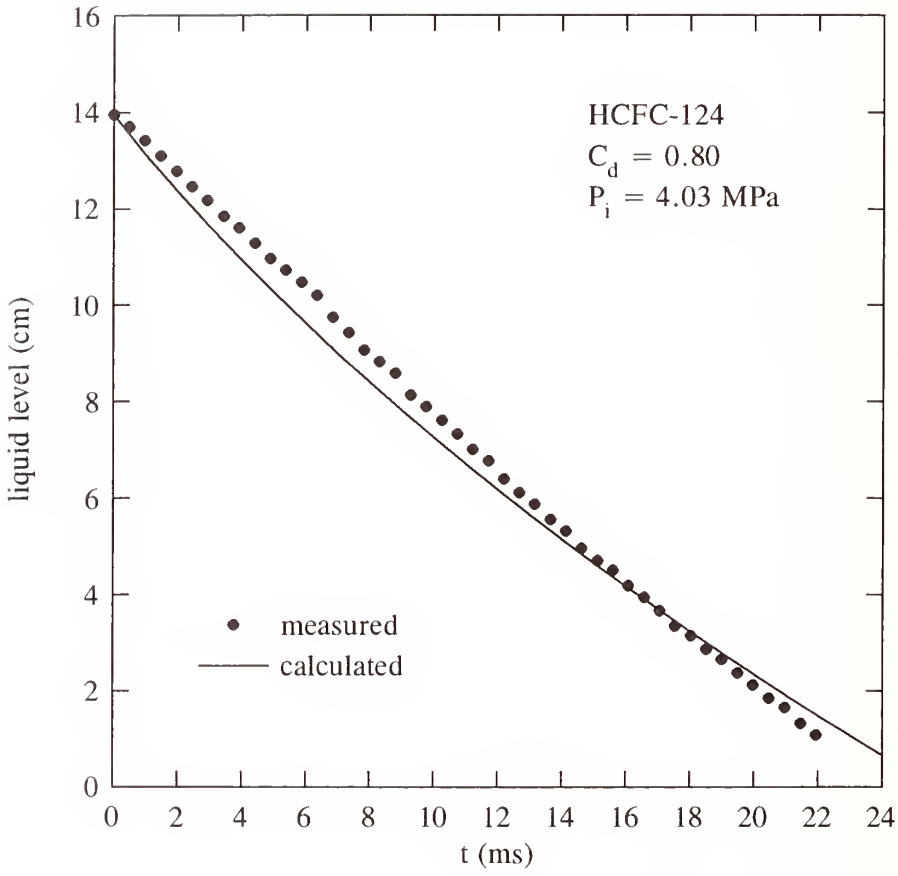

Figure 44. Temporal variation of liquid level obtained from a HCFC-124 discharge.

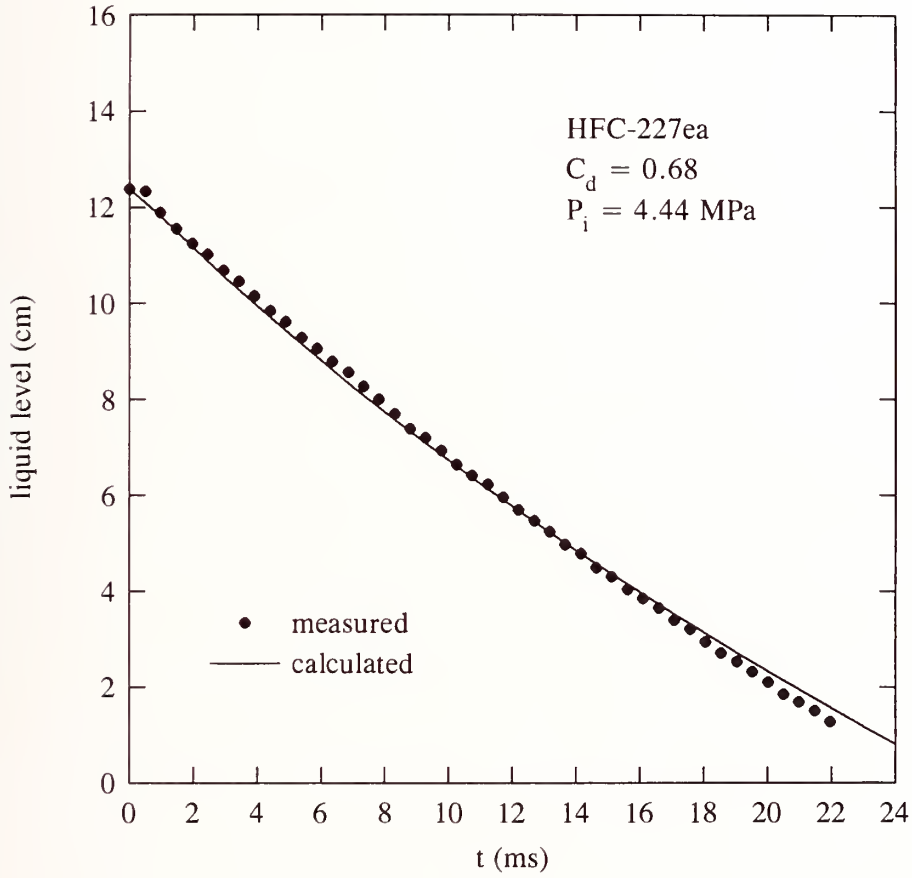

Figure 45. Temporal variation of liquid level obtained from a HFC-227ea discharge.

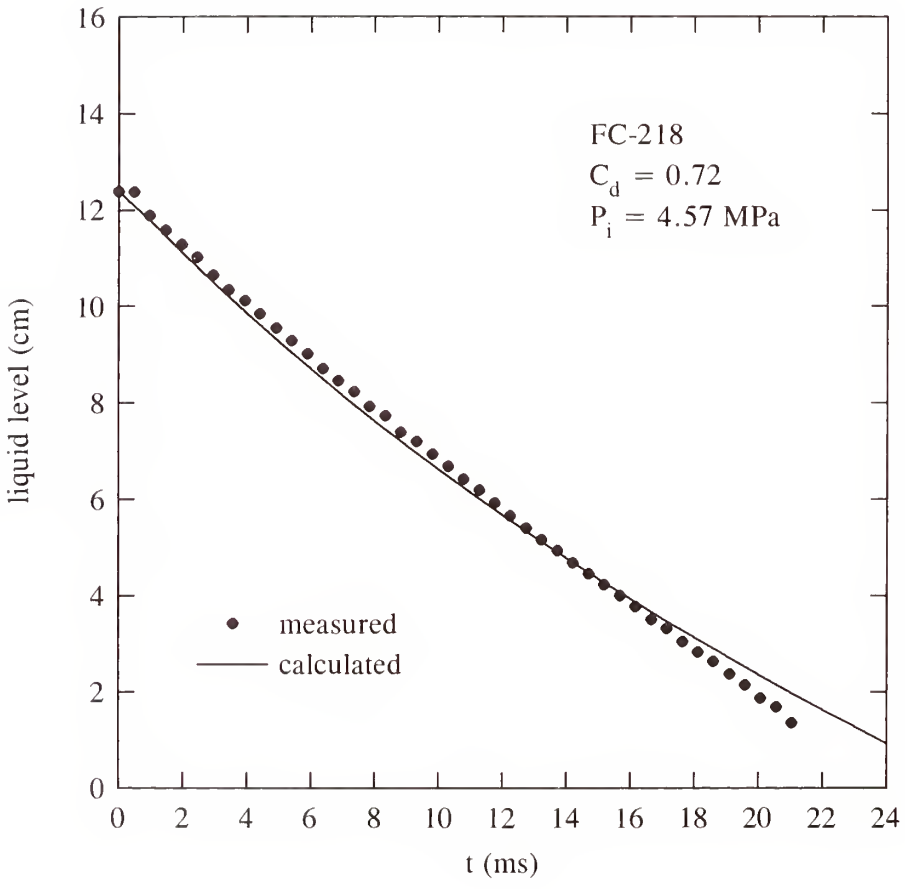

Figure 46. Temporal variation of liquid level obtained from a FC-218 discharge.

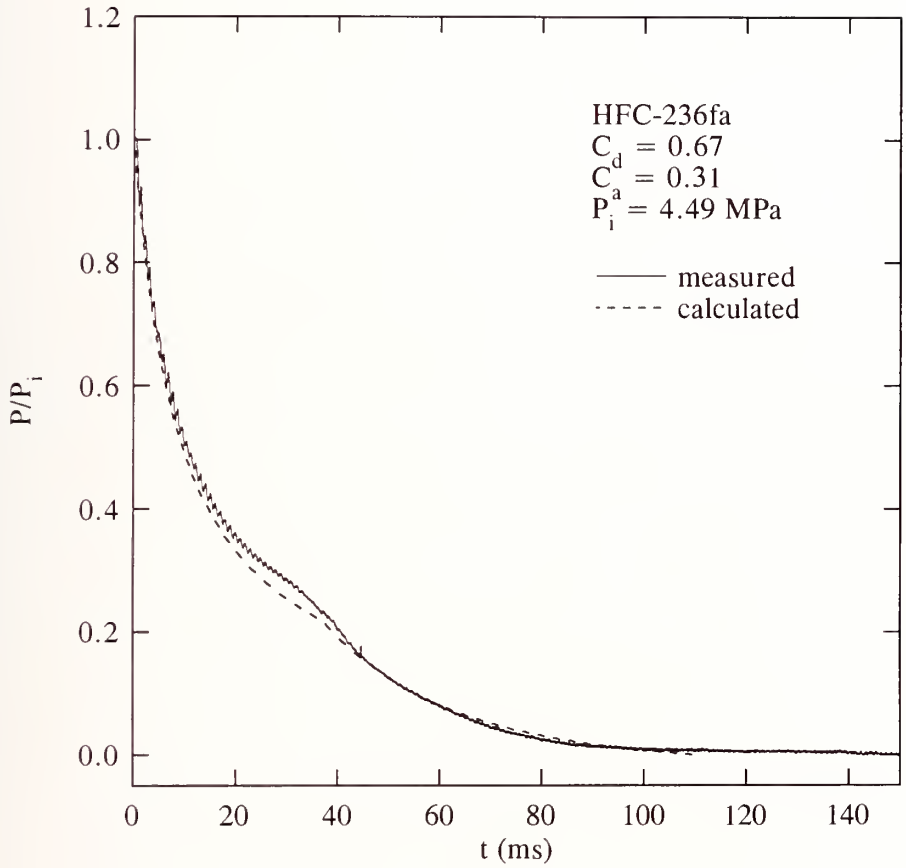

Figure 47. Comparison of measured pressure-time history of a HFC-236fa discharge with prediction.

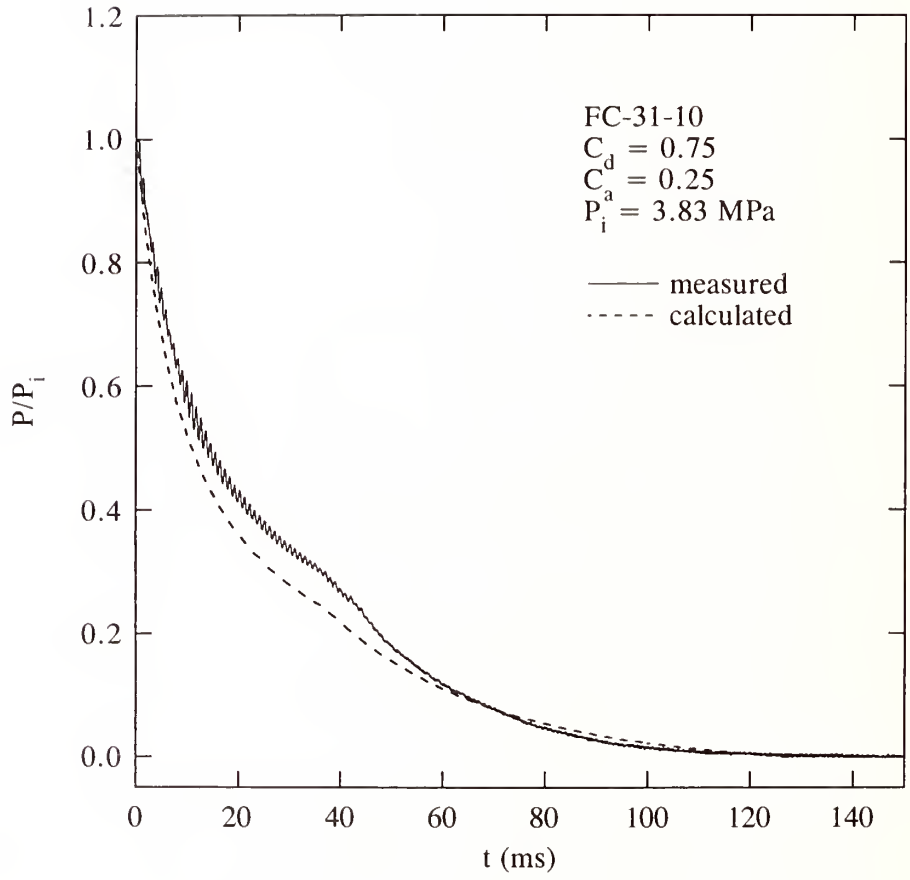

Figure 48. Comparison of measured pressure-time history of a FC-31-10 discharge with prediction.

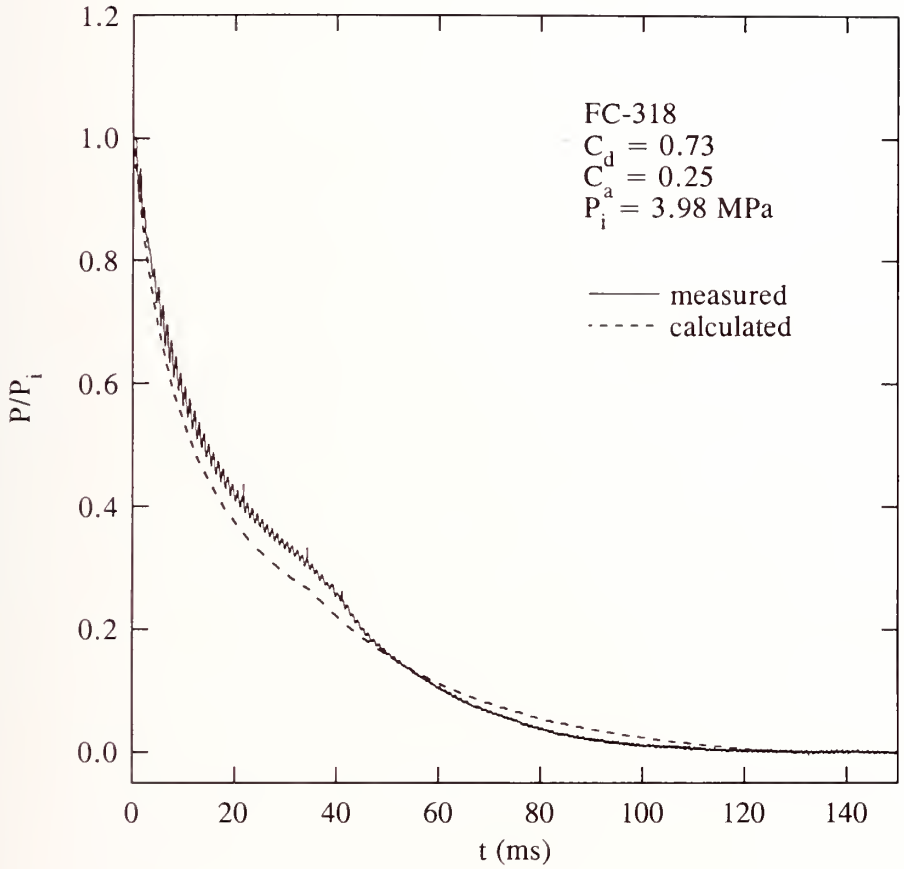

Figure 49. Comparison of measured pressure-time history of a FC-318 discharge with prediction.

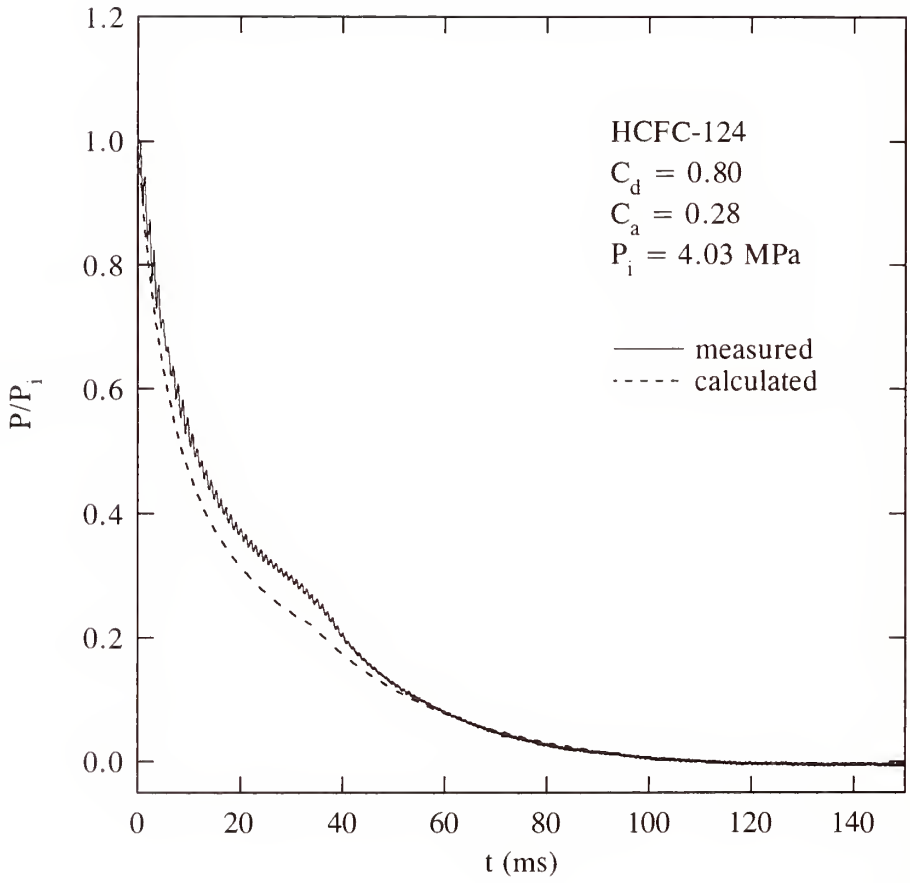

Figure 50. Comparison of measured pressure-time history of a HCFC-124 discharge with prediction.

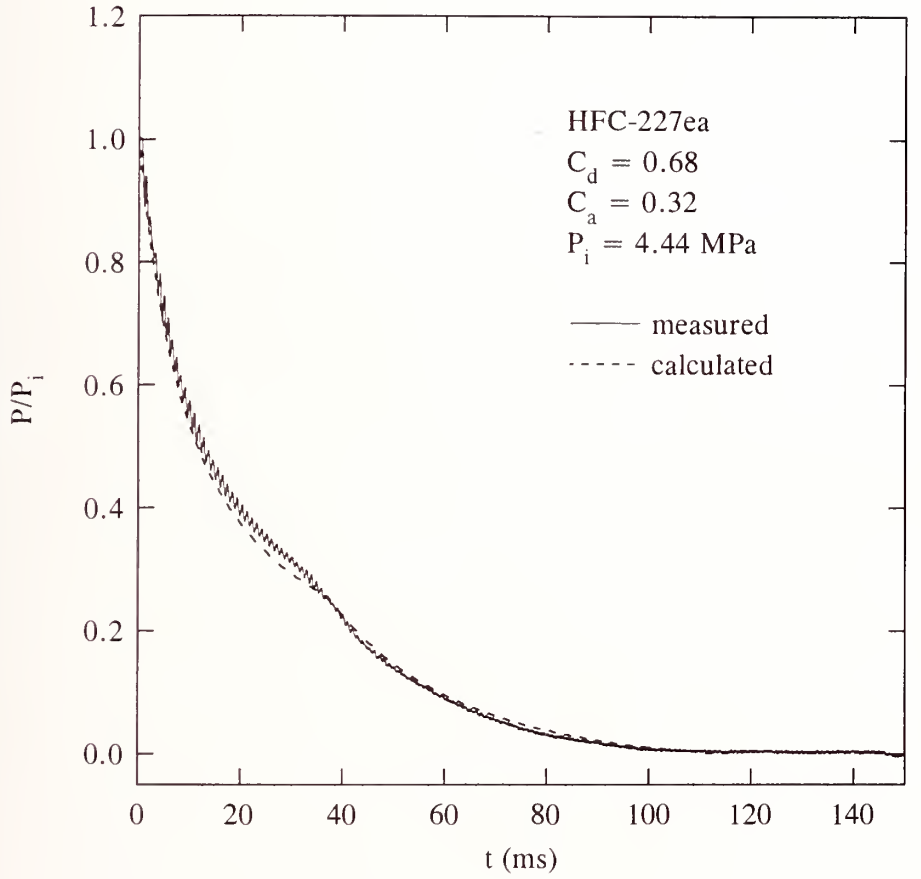

Figure 51. Comparison of measured pressure-time history of a HFC-227ea discharge with prediction.

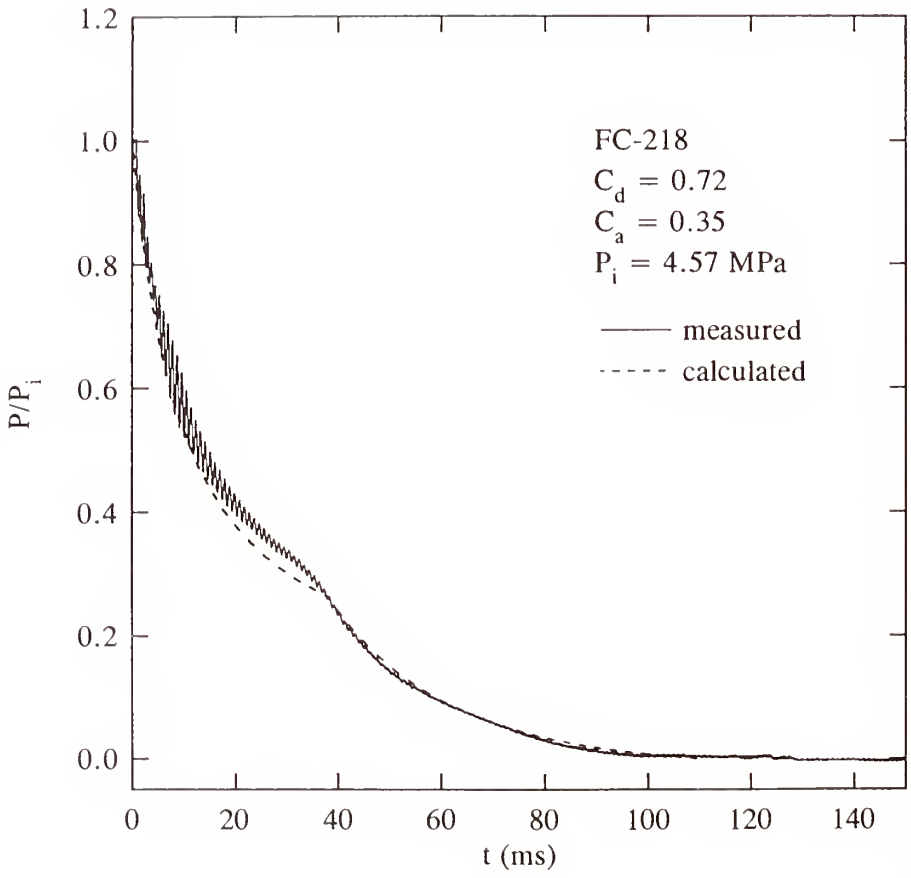

Figure 52. Comparison of measured pressure-time history of a FC-218 discharge with prediction.

Table 4. Initial burst pressures (P_i), initial agent masses (M_i), and average volumetric flow rates (Q) obtained from experiments using plastic and stainless steel vessel

Agent	P_i (MPa)	M_i (g)	Q (m^3/s) x 10^3
HFC-236fa	4.39 ± 0.14[a]	468 ± 5	10.8 ± 0.5
FC-31-10	3.88 ± 0.06	508 ± 18	10.3 ± 0.2
FC-318	4.20 ± 0.30	503 ± 3	10.8 ± 0.2
HCFC-124	4.16 ± 0.18	464 ± 2	10.9 ± 0.8
HFC-227ea[b]	4.44	476	11.1
HFC-134a	4.23 ± 0.12	416 ± 8	10.7 ± 0.9
FC-218	4.31 ± 0.37	462 ± 2	10.8 ± 0.7
HCFC-22	4.40 ± 0.15	411 ± 14	10.2 ± 0.1
HFC-125	4.16 ± 0.09	414 ± 10	9.8 ± 0.7
HFC-125/HFC-32 mixture	4.32 ± 0.04	367 ± 12	10.0 ± 0.8
CF_3Br[b]	4.35	554	7.6

[a]mean ± SD
[b]one run

speed movie camera, the emptying time was obtained by counting the number of frames of the movies for the second flashing of the spray (see Section 3.5) to occur at the vessel exit following the start of the release because the time for the appearance of the second flashing corresponded closely to the inflection point in the pressure-time histories. The scatter in the data reflects the uncertainty in identifying the exact emptying time of the liquid and variations in the initial burst pressure. Except for halon 1301, the average volumetric flow rates of the alternative liquid agents evaluated vary less than 10% among each other. Based on Equations (19) and (20) and given the same initial conditions, the emptying time or the volumetric flow rate of the liquid should be relatively independent of the agents studied because the terms under the square root in Equation (20) do not differ significantly among the agents. This is consistent with the experimental observations made in this work. However, the above simple analysis is only applicable when there is no internal boiling of liquid agent inside the vessel during discharge in a downward orientation; this may not be the case for liquid agents with low boiling points (*e.g.*, halon 1301).

Since FC-116 is a gas at room temperature, Equations (21) and (22) can be used to simulate the discharge of FC-116. In this case, $P_{el} = P_i$ and $T_{el} = T_i$. The predicted and measured pressure decays are given in Figure 53. The predicted values were calculated by assuming an average molecular weight of 83 based on the amount of FC-116 and nitrogen at $t = 0$ and a value of 1.2 for γ. There is a large discrepancy between the measured and predicted temporal variations of internal pressure during discharge. It is conjectured that the assumption of ideal gas behavior which underlies Equations (21) and (22) may not be applicable for FC-116. Support for this conjecture is obtained from studies on releases of nitrogen only (which should behave as an ideal gas). For nitrogen-only releases from the pressurized vessel, Equations (21) and (22) predicted reasonably well the temporal variation of the internal pressure as can be seen in Figure 54. Note that, for both cases

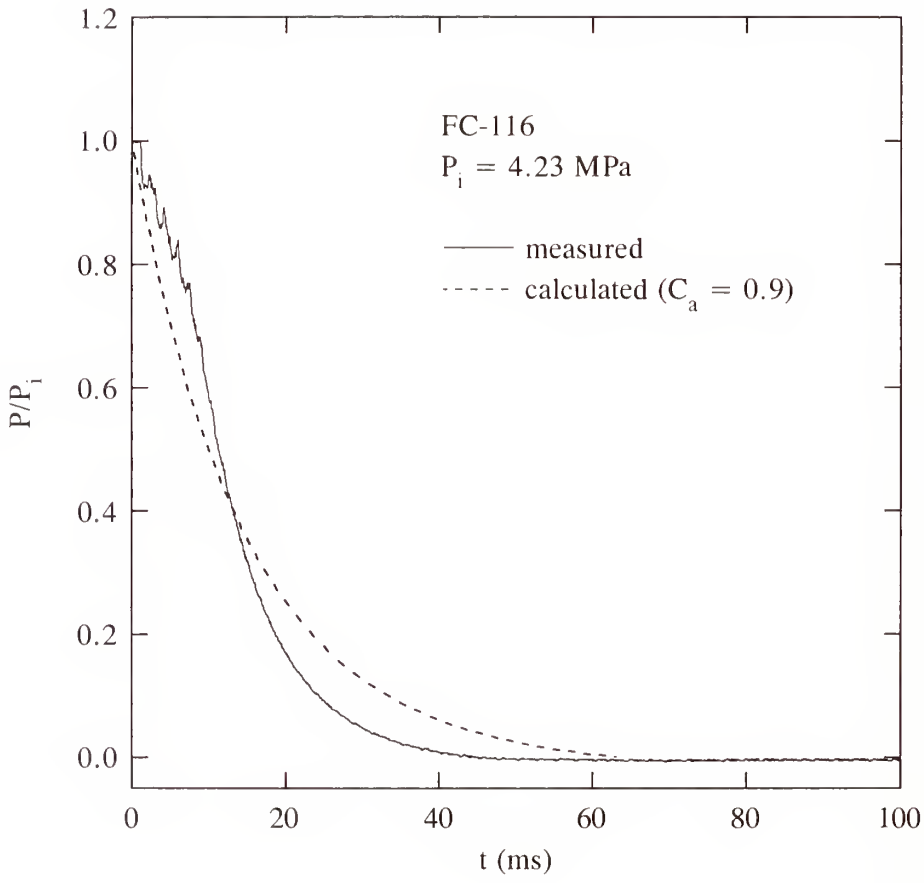

Figure 53. Comparison of a measured pressure-time history of FC-116 discharge with prediction.

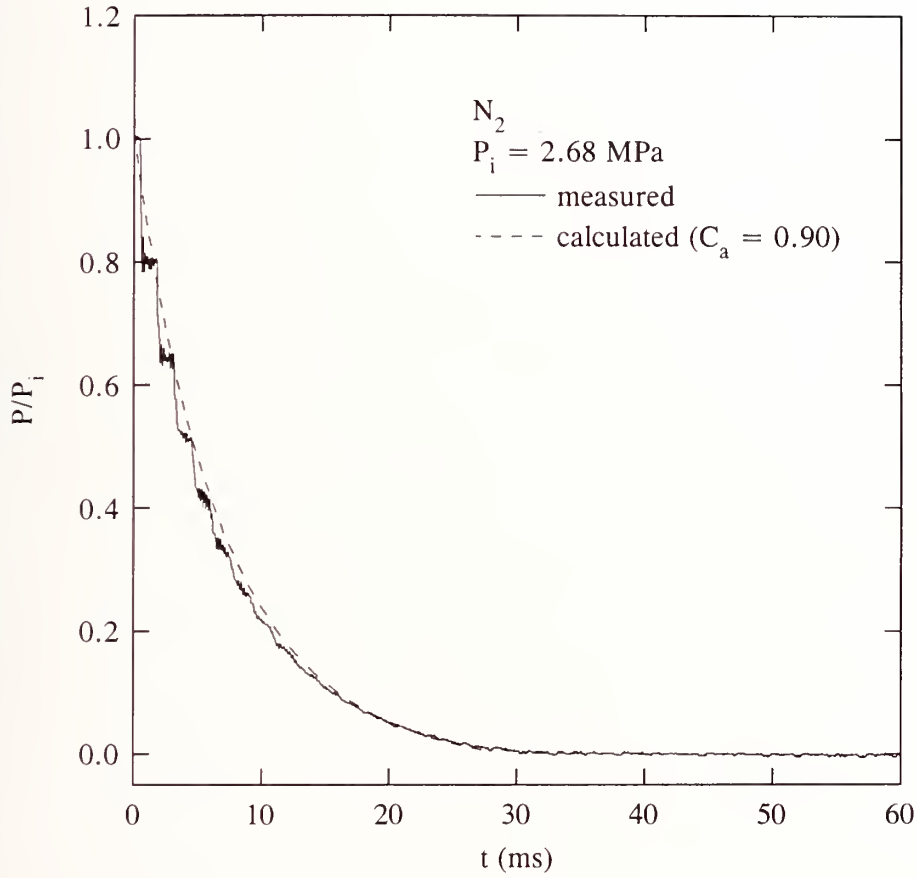

Figure 54. Comparison of a measured pressure-time history of pure nitrogen discharge with prediction.

FC-116 and nitrogen releases, the optimum values of C_a are much higher than the values found in other discharge experiments wherein a liquid agent is initially present and the values in the literature (Kim-E, 1981). The low values of C_a obtained by Kim-E (1981) are possibly due to obstruction of his flow path by a pneumatic plunger. In his experimental set-up, a rupture disk was used as a release mechanism. The plunger which was placed inside the vessel was used to break the rupture disk in order to initiate the discharge process. However, the reason for the low and high values obtained in this study is not known; the low values of C_a were obtained when gas discharge was preceded by liquid release, whereas the high values of C_a were found when liquid was not present initially in the vessel. The value for C_a normally centers around 0.6 (Perry *et al.*, 1984). It can only be conjectured that the edge roughness of the rupture disk opening (Perry *et al.*, 1984) and the transient effect due to the abrupt transition from the discharge of liquid to the release of the remaining vapor may have an effect on the discharge coefficient, and that the assumption of a round, sharp-edged orifice may not be valid because the flow through the disk holder resembles one through a short tube rather than through an orifice. The use of a single value of C_a may also be questionable because C_a can be a function of the pressure ratio across the opening (see Section 3.2). Since the pressure inside the vessel is changing with time during discharge, the pressure ratio is then a function of time. Therefore, it is conceivable that C_a may not be constant during the course of discharge.

3.4.3.2 Effect of an Orifice Plate. The experimental results for internal pressure obtained by restricting the disk opening by means of an orifice plate are shown in Figure 55 through Figure 57. The agent in the vessel remains as liquid during the observation period from the initiation of discharge to the time when the liquid level is no longer visible (see Figure 26) within the plastic vessel. The discharge process is very similar to that without the orifice plate. The key effect of decreasing the diameter of the orifice on the discharge process is to increase the emptying time of the contents, as indicated by the locations of the inflection points in Figure 55 through Figure 57. For the 12.7 mm plate, the average volumetric flow rates are 6.0×10^{-3}, 5.6×10^{-3}, and 3.2×10^{-3} m^3/s for FC-31-10, FC-218, and halon 1301, respectively. For the 6.4 mm plate, the average volumetric flow rates are 1.5×10^{-3}, 1.4×10^{-3}, and 1.3×10^{-3} m^3/s for FC-31-10, FC-218, and halon 1301, respectively. It is found that increasing the diameter of the plate from 6.4 to 12.7 mm increases the average volumetric flow rates of FC-31-10 and FC-218 by approximately fourfold, in accordance with Equation (20), *i.e.*, $dV/dt \sim A$ for a given P. The relationship between the average volumetric flow rate (Q) and the orifice area (A) is clearly seen in Figure 58 for FC-31-10 and FC-218 using burst disks with a nominal burst pressure of 4.12 MPa. Results discussed earlier for standard releases (orifice diameter of 19.1 mm) are included. The symbols in the figure are measured values. The dotted and solid lines in the figure are least-square fits of the data which are forced to pass through the origin. Figure 59 through Figure 62 show the comparisons of measured pressure-time histories of FC-31-10 and FC-218 discharge with predictions using Equations (19) through (22). For the experimental results obtained using a 6.4 mm restrictor plate, the model did not simulate the discharge process well because the flow field is more complicated when a smaller orifice plate is used to restrict the flow at the exit of the short tube section which was part of the rupture disk holder (see Figure 25 and Figure 26). Since it has been conjectured in Section 3.4.3.1 that boiling of liquid halon 1301 inside the vessel occurs near the end of liquid discharge, the above volumetric flow rate-area relationship is not applicable to halon 1301.

3.4.3.3 Effect of an Extension Tube. From visual observations, the presence of an extension tube did not affect the internal behavior of the liquid during discharge. Figure 63, Figure 64, and

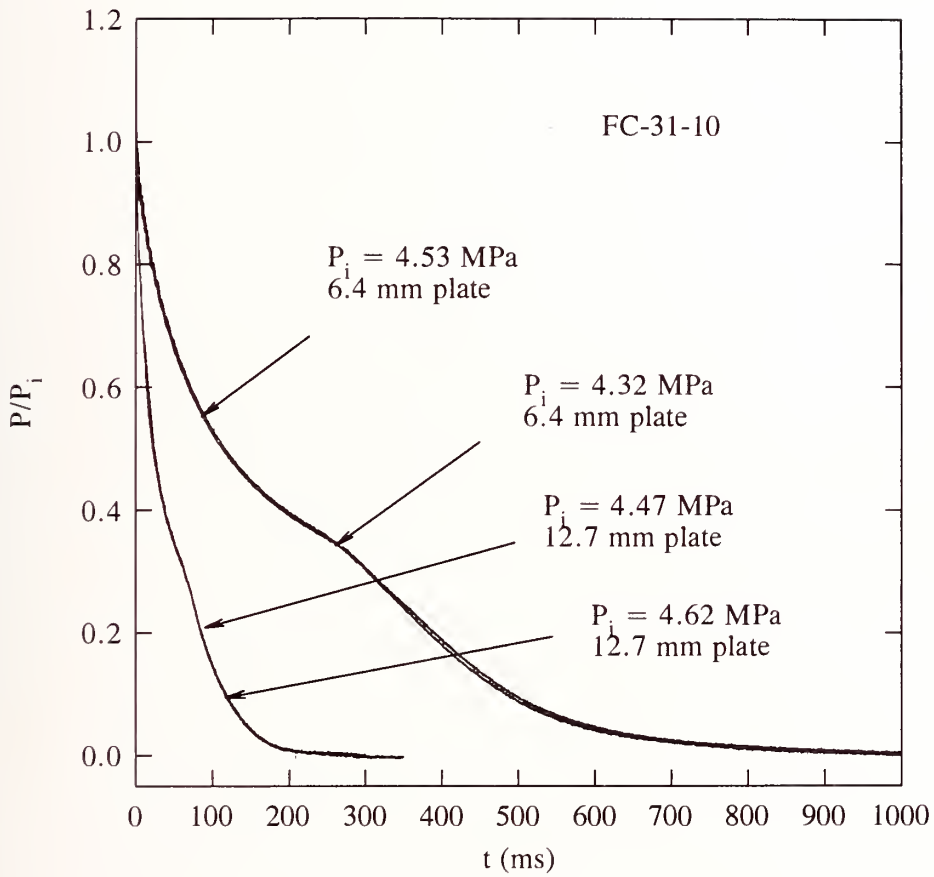

Figure 55. Temporal variations of internal pressure during discharges of FC-31-10 with a restricting orifice plate (6.4 or 12.7 mm).

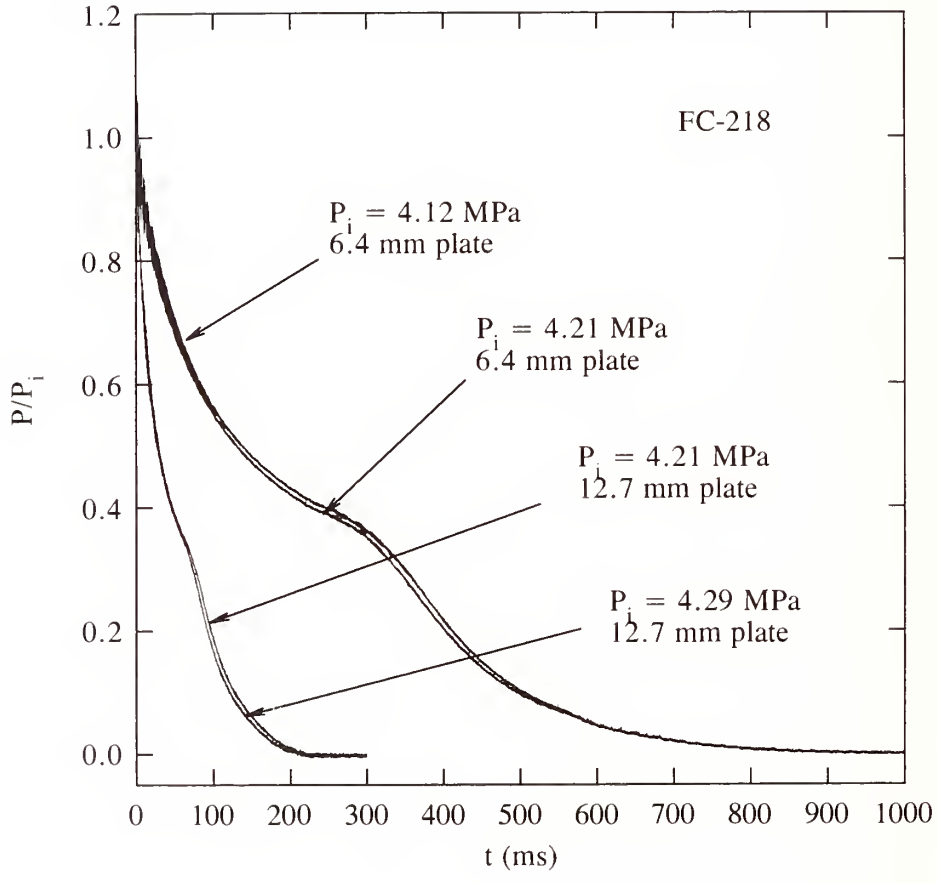

Figure 56. Temporal variations of internal pressure during discharges of FC-218 with a restricting orifice plate (6.4 or 12.7 mm).

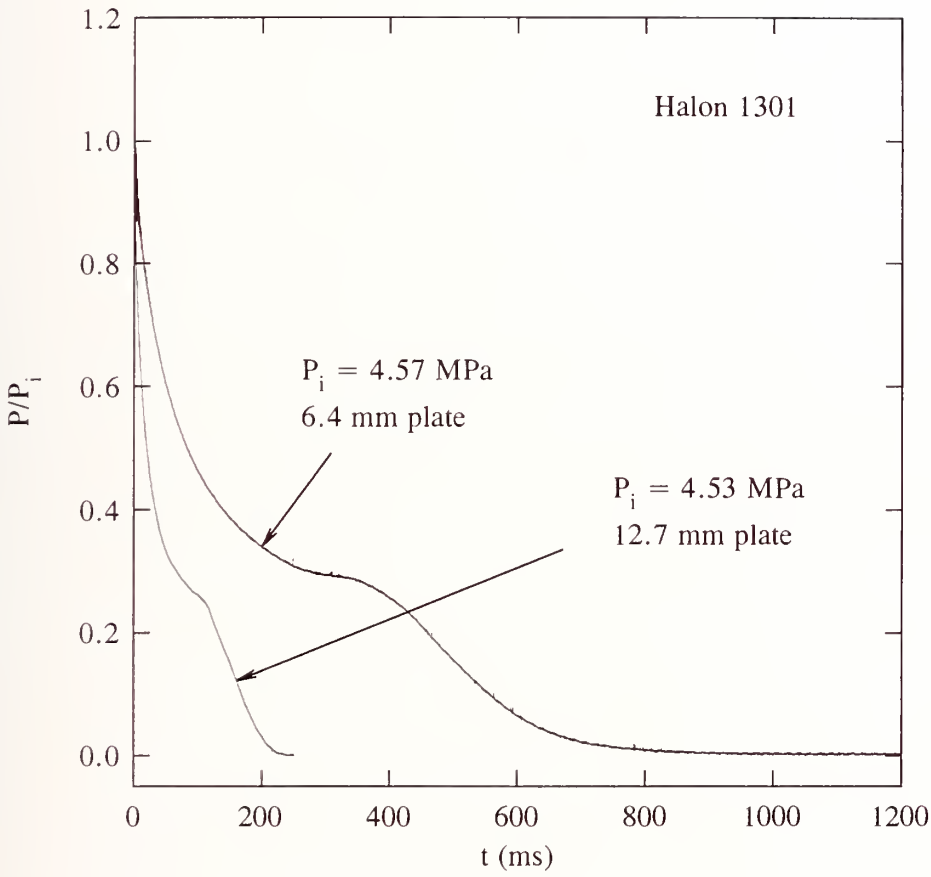

Figure 57. Temporal variations of internal pressure during discharges of halon 1301 with a restricting orifice plate (6.4 or 12.7 mm).

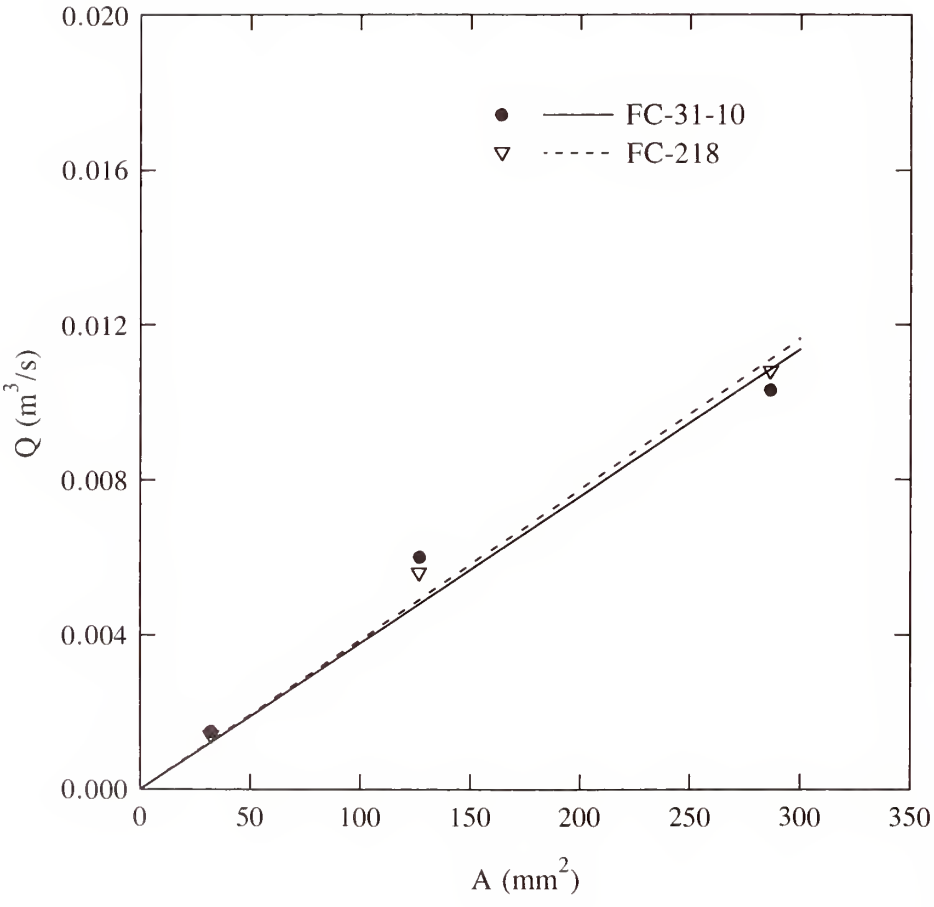

Figure 58. Relationship between average volumetric flow rate and orifice area.

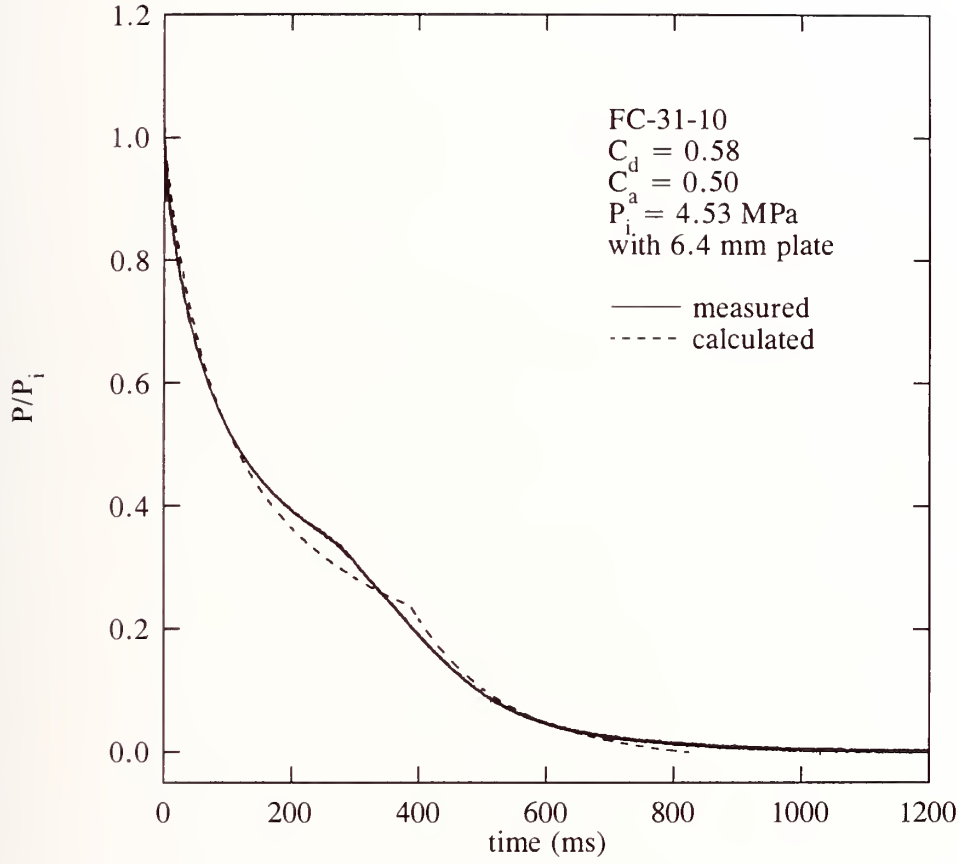

Figure 59. Comparison of a measured pressure-time history of FC-31-10 discharge using a 6.4 mm orifice plate with prediction.

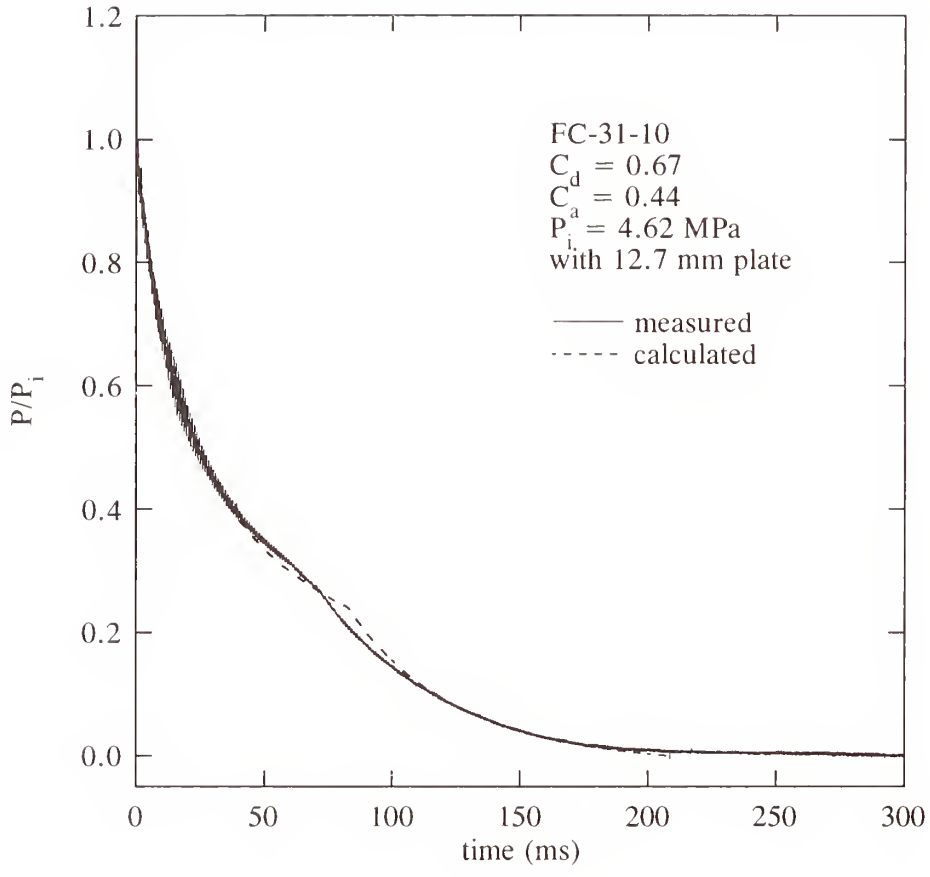

Figure 60. Comparison of a measured pressure-time history of FC-31-10 discharge using a 12.7 mm orifice plate with prediction.

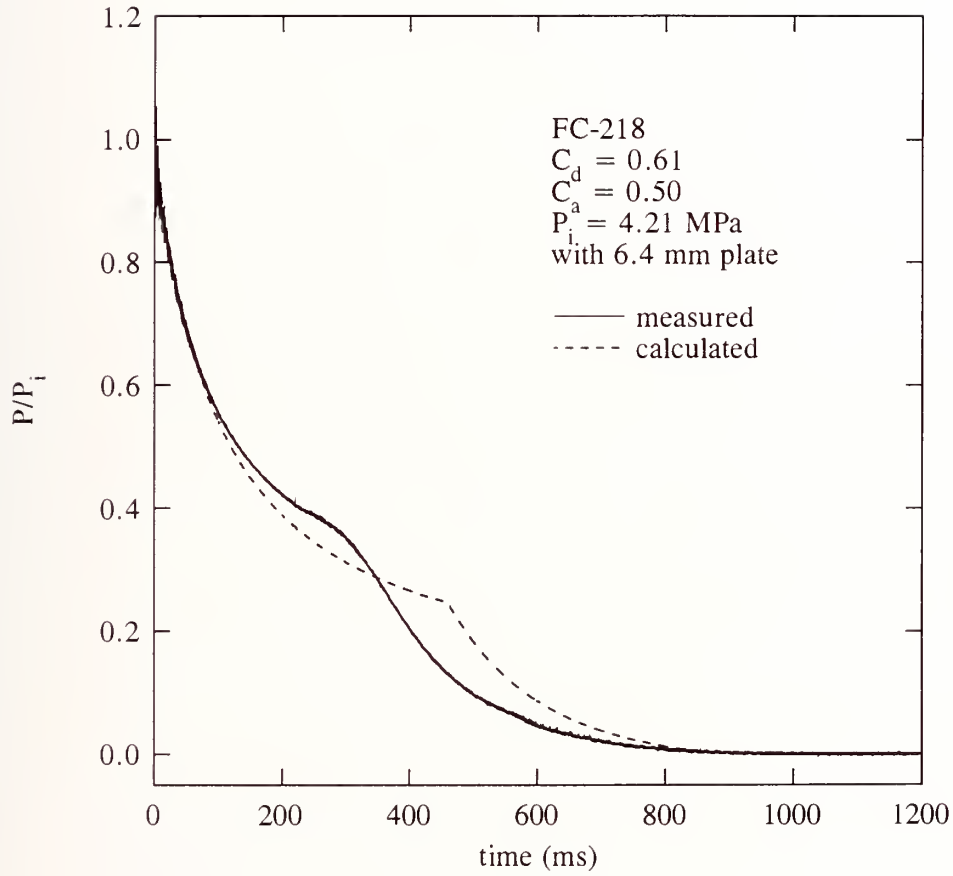

Figure 61. Comparison of a measured pressure-time history of FC-218 discharge using a 6.4 mm orifice plate with prediction.

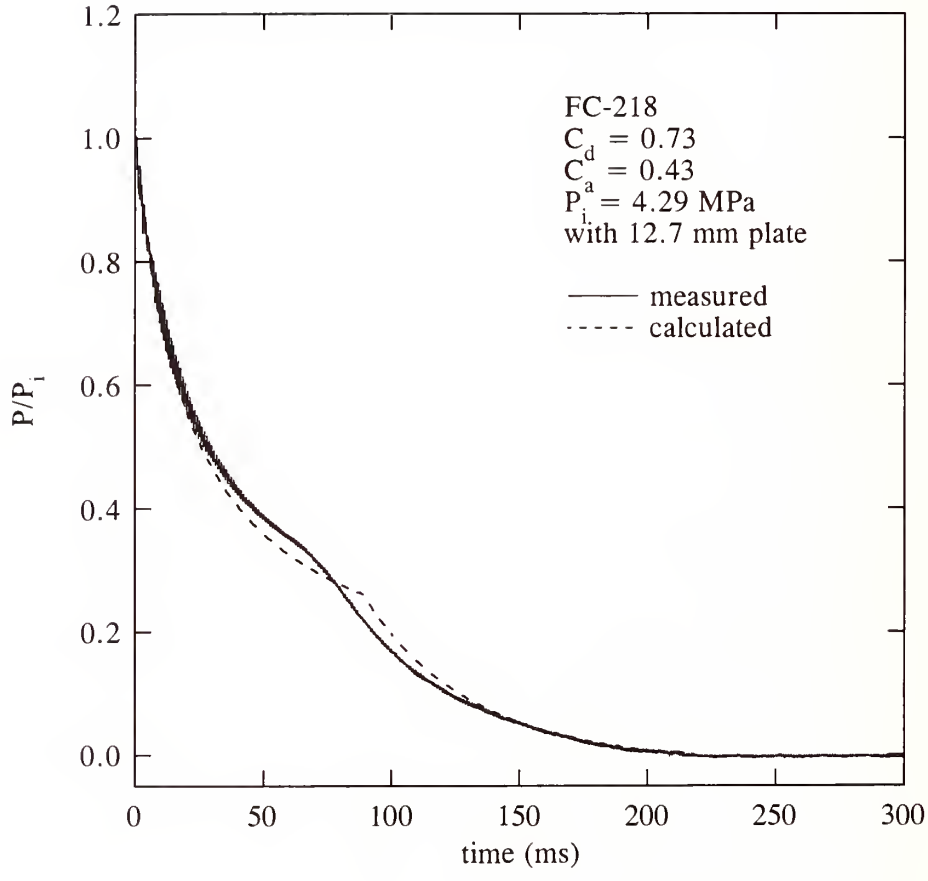

Figure 62. Comparison of a measured pressure-time history of FC-218 discharge using a 12.7 mm orifice plate with prediction.

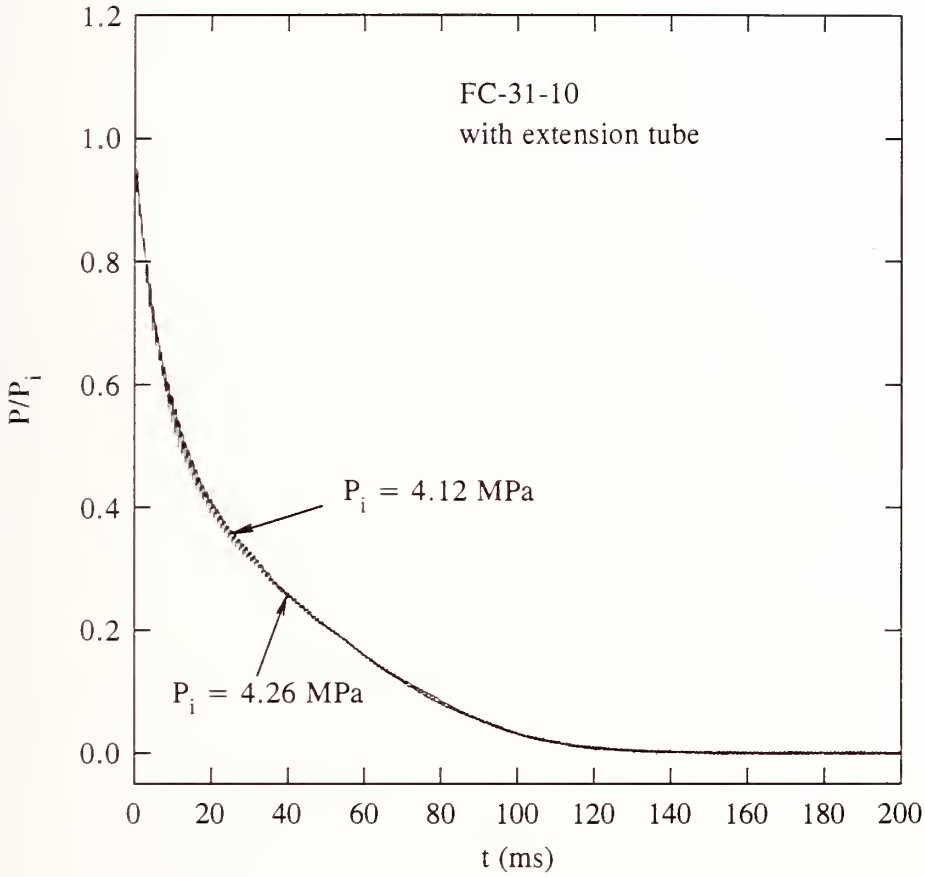

Figure 63. Temporal variations of internal pressure during discharges of FC-31-10 with a 0.5 m long extension tube.

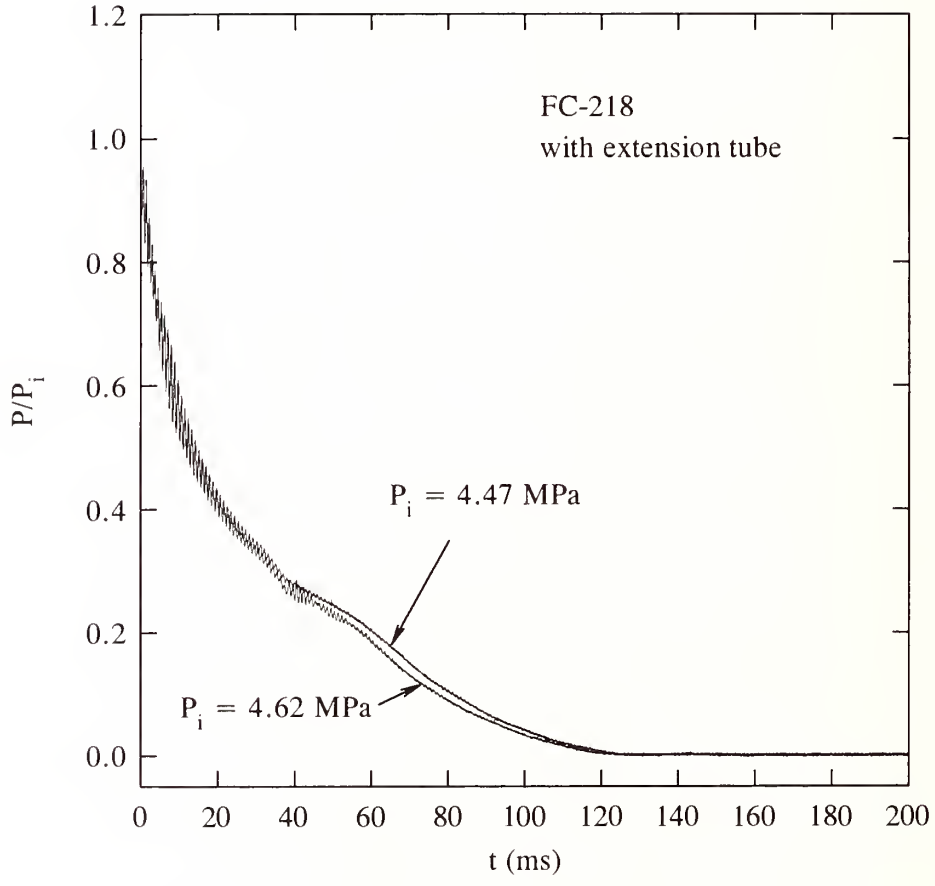

Figure 64. Temporal variations of internal pressure during discharges of FC-218 with a 0.5 m long extension tube.

Figure 39 show the internal pressure results for FC-31-10, FC-218, and halon 1301. For comparison, the results obtained with and without extension tube are shown in Figure 65, Figure 66, and Figure 39. It appears that the presence of an extension tube does not change the temporal behavior of the internal pressure during discharge of liquid FC-31-10 and FC-218. This is indicative of the existence of critical flow at the vessel orifice since the downstream geometry does not affect the pressure upstream (Prisco *et al.*, 1977). The presence of an extension tube slows down the discharge of the remaining vapor from the vessel after liquid depletion because of friction losses in the tube, as can be seen in Figure 65, Figure 66, and Figure 39. In the case of halon 1301, the presence of an extension tube makes the pressure-curve transition from liquid to gaseous discharge more gradual. Such gradual transition is indicative of initiation of boiling within the vessel or extension tube (see discussion in Section 3.4.3.1). Furthermore, when compared to the discharge behavior of halon 1301 without an extension tube, the discharge of the two-phase boiling halon 1301 in the presence of an extension tube is much slower due to additional frictional losses in the tube.

3.4.3.4 Effect of Initial Vessel Pressure. The above discussion is based on results obtained using rupture disks with nominal burst pressures of 4.12 MPa. In order to study the effect of initial pressure on the discharge dynamics, rupture disks with different nominal burst pressures (2.75 and 5.50 MPa) were used. Figure 67 shows pressure-time histories for FC-218 for three initial burst pressures. The oscillation seen in two of the pressure traces reflects the use of a plastic vessel. It is clear that the emptying time of the liquid decreases with increasing initial pressure in the vessel, and that a twofold increase in the initial burst pressure only increases the average volumetric flow rate by approximately a square root of 2. The measured average volumetric flow rates for these three runs are 8.4×10^{-3} m^3/s for $P_i = 2.60$ MPa, 11.3×10^{-3} m^3/s for $P_i = 4.57$ MPa, and 11.9×10^{-3} m^3/s for $P_i = 6.18$ MPa. The results are consistent with the model (Equation (20)), *i.e.*, $dV/dt \sim (P)^{1/2}$ for a given A. The relationship between the average volumetric flow rate (Q) and the initial charge pressure (P_i) is shown in Figure 68 for FC-218 using a 19.1 mm opening. The dotted line in the figure is a least-square fit through the origin, and the symbols represent measured values. The calculated and measured temporal variations of internal pressure for $P_i = 6.18$ MPa, as an example, are shown in Figure 69. The prediction matches the experiment quite well.

3.4.3.5 Effect of Vessel Temperature. The study of the effect of temperature on the discharge dynamics was carried out experimentally with FC-31-10 and FC-218 at −45 °C. Since similar trends were observed for FC-218, only the results for FC-31-10 are shown in Figure 70. The pressure-time histories are very similar to those obtained using the same burst disks but at room temperature. The internal behavior of the agent in the vessel, though not observed visually, should be similar. However, the dispersion characteristics of the agent external to the release vessel were observed to have a less-flashing nature when the agent was discharged at −45 °C (see Section 3.5.3.9). Figure 71 shows a comparison of the measured results with predictions from Equations (19) through (22).

Although no experiments were carried out at 150 °C, the discharge of an agent at this temperature may be characterized as a discharge of a supercritical fluid from the vessel because at this temperature, and its corresponding pressure, the agent/nitrogen mixture is in the supercritical region. If this indeed is the case, then the discharge process should be very similar to that of a FC-116/nitrogen mixture.

Some interesting but important events which may occur when the vessel is rapidly discharged at moderately high temperature and pressure will be discussed. These processes are also discussed in Section 3.2.4. The following is based on the hypothesis proposed by Reid (1979) in an attempt to

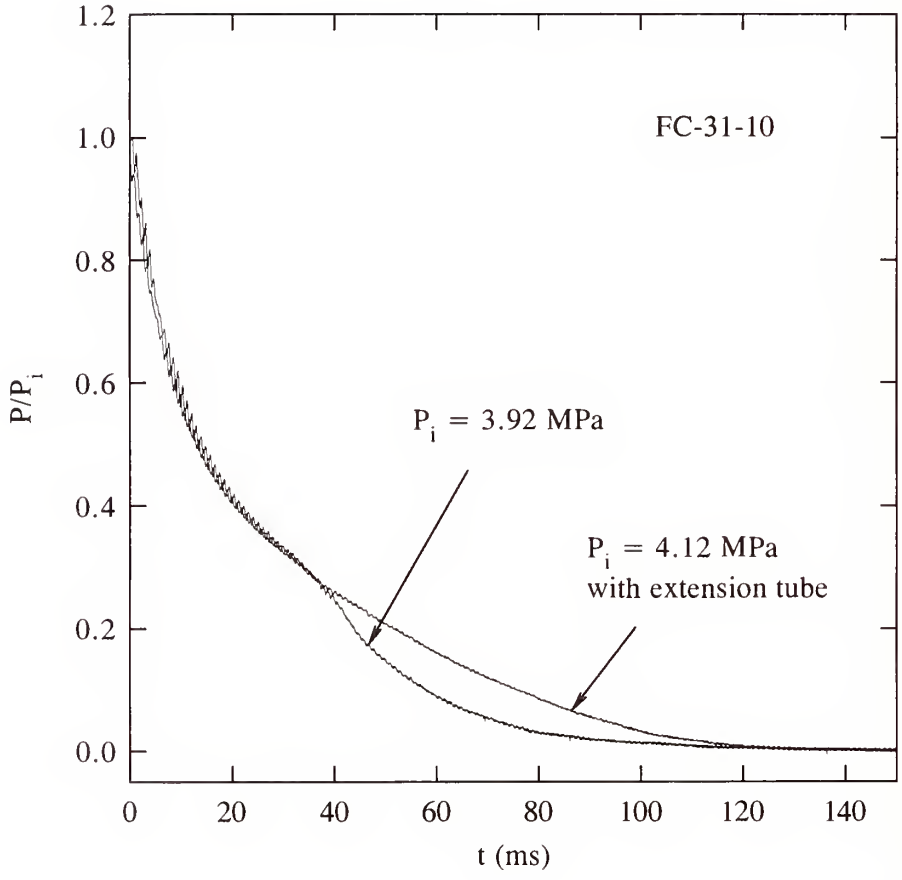

Figure 65. Temporal variations of internal pressure during discharges of FC-31-10 with and without an extension tube.

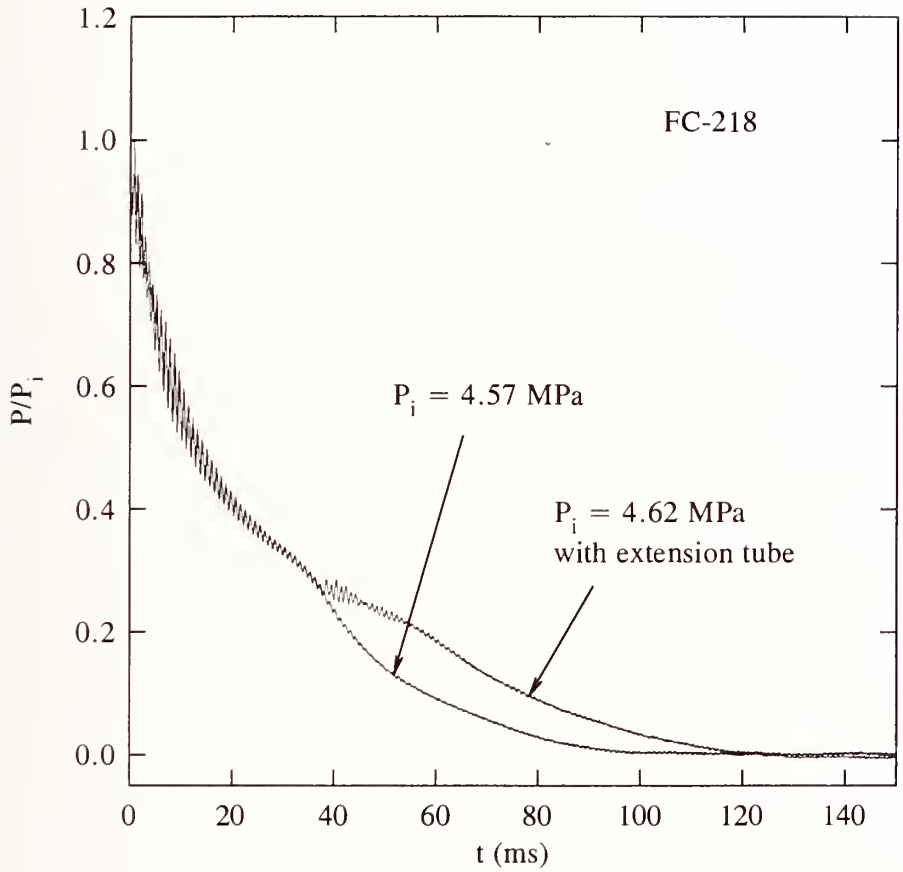

Figure 66. Temporal variations of internal pressure during discharges of FC-218 with and without an extension tube.

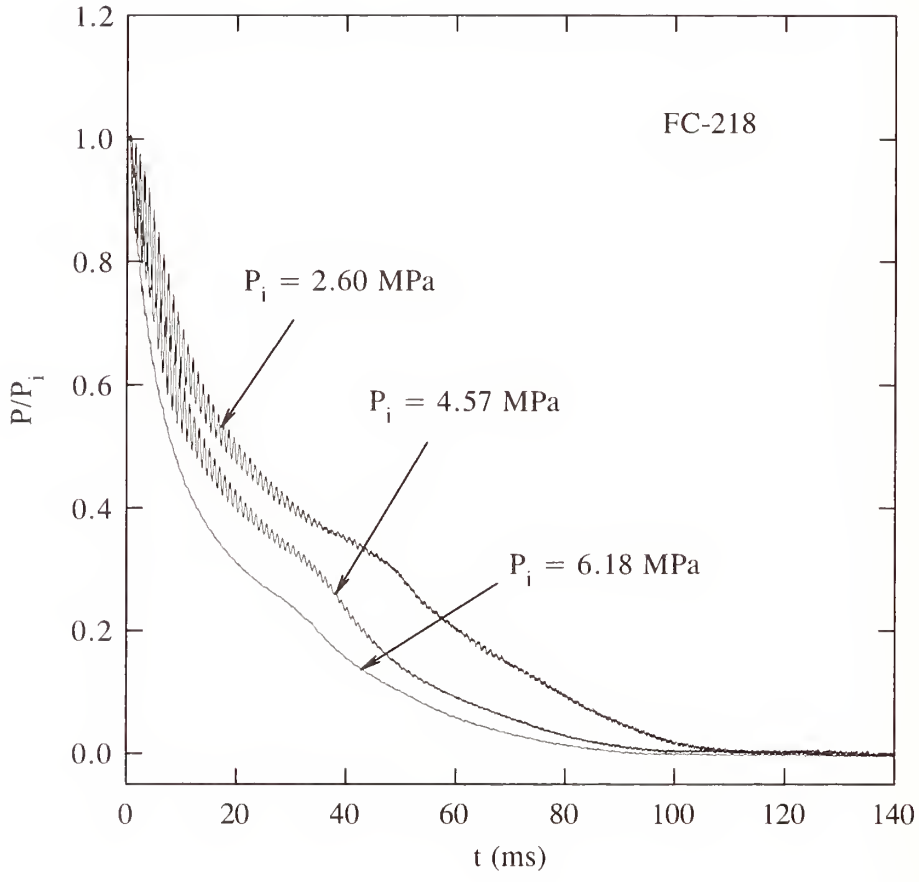

Figure 67. Temporal variations of internal pressure during discharges of FC-218 with different initial burst pressures.

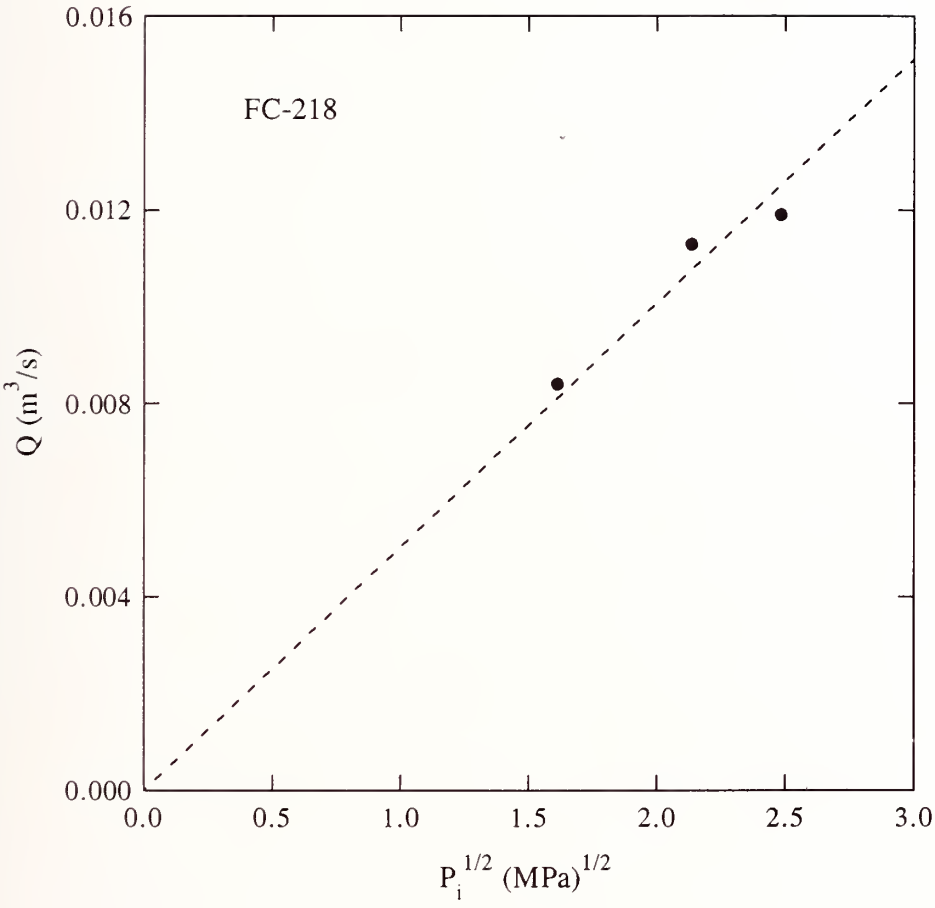

Figure 68. Relationship between average volumetric flow rate and initial charge pressure.

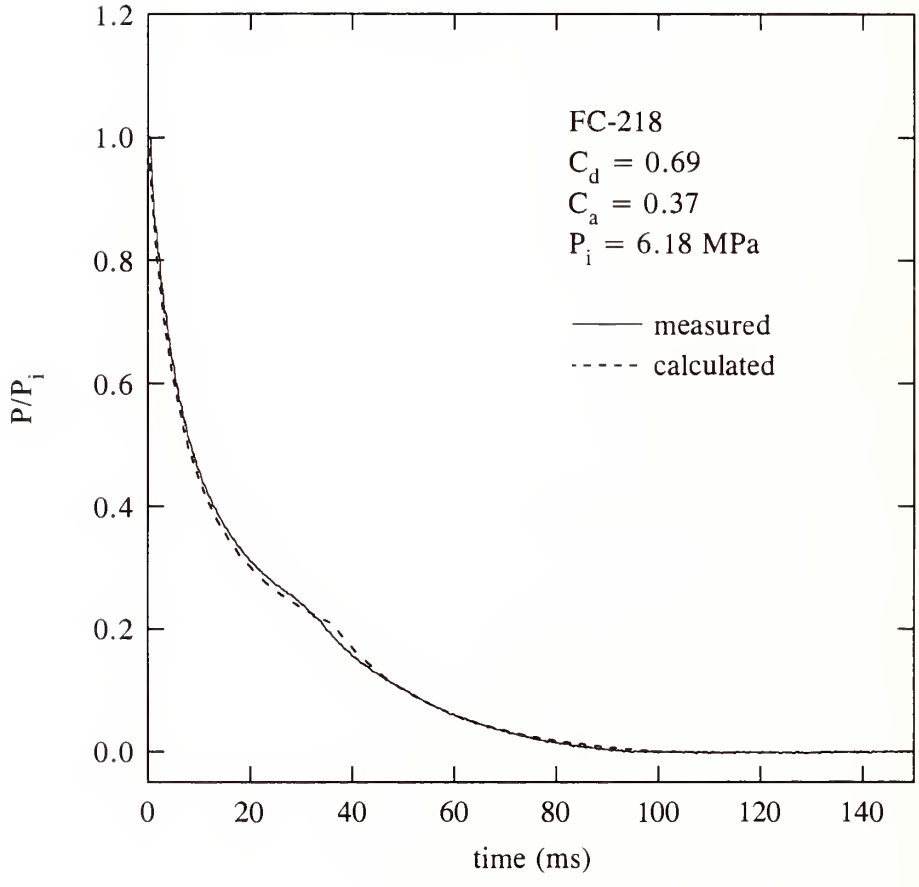

Figure 69. Comparison of measured pressure-time history of a FC-218 discharge at elevated pressure with prediction.

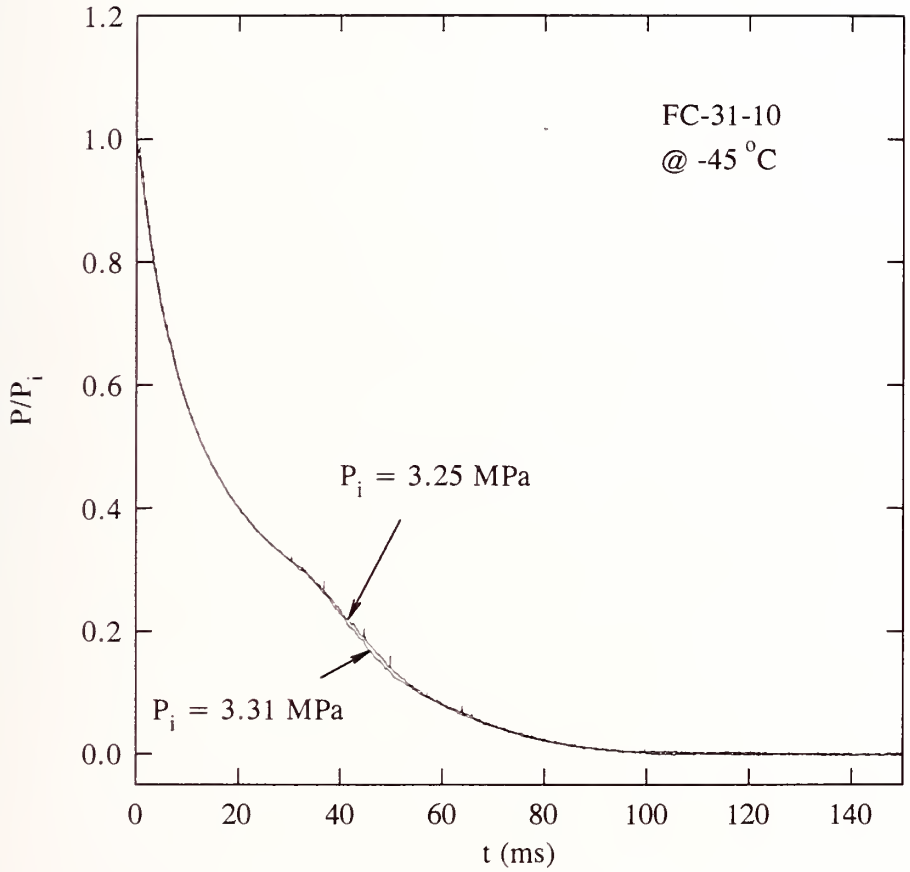

Figure 70. Temporal variations of internal pressure during downward discharges of FC-31-10 at −45 °C.

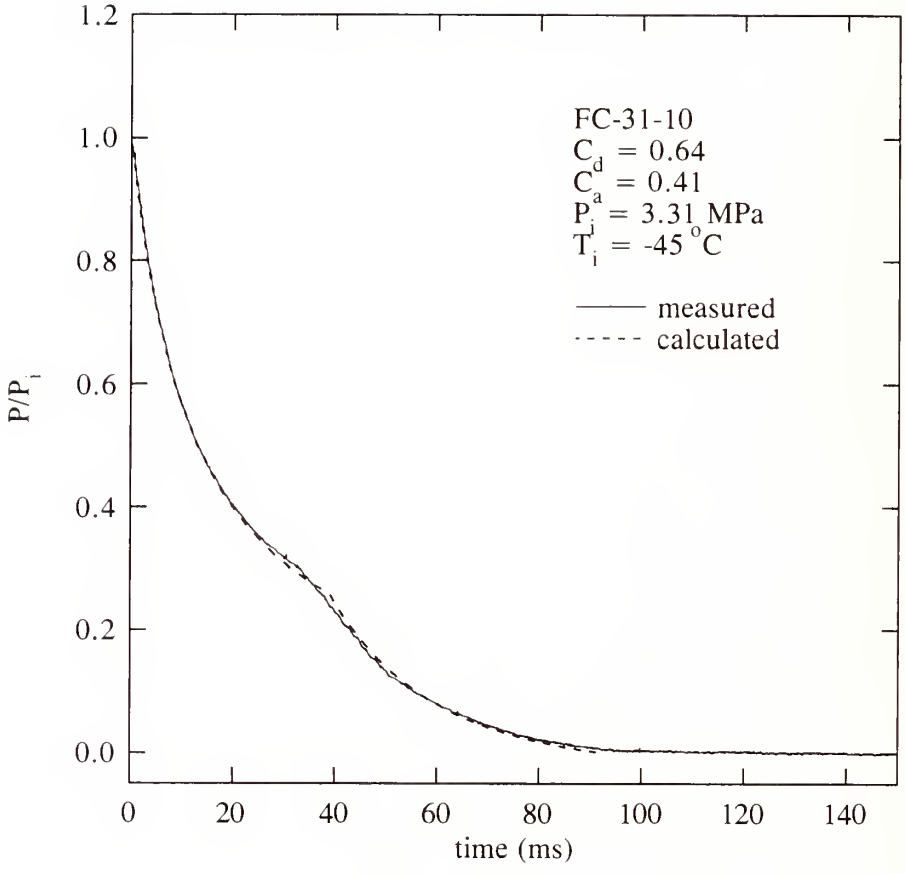

Figure 71. Comparison of measured pressure-time history of a FC-31-10 discharge at −45 °C with prediction.

provide a possible mechanism for pressurized-liquid tank explosions or boiling liquid expanding vapor explosions (BLEVEs).

In order to delineate the important features, and for simplicity and clarity, a fixed initial amount of pure agent in the vessel without pressurization of nitrogen will be considered. For example, say the vessel has an initial fill density (ρ_{fill}) of 0.5 kg of FC-31-10 per 5×10^{-4} m^3 (approximately 2/3 full) at room temperature (22 °C). The vessel is then heated to say T_f = 100 °C. The heating process of the vessel is illustrated in Figure 72 (point *A* to point *B*) which is a pressure-temperature diagram of pure FC-31-10 (Daubert and Danner, 1992). Point *A* represents the initial condition of the vessel, that is, liquid and vapor of FC-31-10 coexist in the vessel at T_i = 22 °C with a saturation vapor pressure of 0.24 MPa). The saturation curve in Figure 72 represents the conditions of pressure and temperature required for the coexistence of liquid and vapor phases. To determine the final state (point *B*) of the heating process, that is, whether point *B* will lie in the single phase (gas or liquid) region or on the saturation curve, one has to compare the saturation vapor and liquid densities at T_f ($\rho_{v,f}$ and $\rho_{l,f}$) with the initial fill density of the vessel (ρ_{fill}). If $\rho_{v,f} < \rho_{fill} < \rho_{l,f}$, then two phases (vapor and liquid) still coexist in equilibrium in the final state (Smith and Van Ness, 1975). In the case of FC-31-10, $\rho_{v,f}$ = 296 kg/m^3 and $\rho_{l,f}$ = 1002 kg/m^3 (Brown and Mears, 1958). Given an initial fill density of 1000 kg/m^3, the final state is still two-phase. Therefore, point *B* lies on the saturation curve, as shown in Figure 72. If the vessel is *rapidly* depressurized or discharged at the final temperature and pressure, the liquid will be superheated, that is, at a temperature higher than the saturation temperature at the corresponding existing pressure (Modell and Reid, 1983). The liquid is superheated as a result of crossing the saturation curve without concomitant phase change. However, there is a pressure limit for how far the metastable liquid can be sustained. This limit is the so-called spinodal curve (Modell and Reid, 1983). The superheated liquid thus lies in the region between the saturation curve and the spinodal curve. Once the superheated liquid reaches the spinodal curve, spontaneous, homogeneous nucleation will occur within the bulk of the liquid. Such rapid nucleation is expected to be accompanied by strong and damaging shock waves and huge pressure increases in the vessel. If this event happens, it is expected that substantial damage would be incurred by the vessel, or in the worst scenario, explosion of the vessel would occur if the vessel was not designed to withstand such a pressure surge.

For a pure agent, the spinodal curve can be calculated (Beegle *et al.*, 1974) by determining where the condition

$$\left(\frac{\partial P}{\partial v}\right)_T = 0 \tag{24}$$

is met. P is the pressure, v is the molar volume, and T is the temperature. The Peng-Robinson equation of state (Peng and Robinson, 1976) is used for illustration (see Section 2.3.1). By applying Equation (24) to the equation of state, the following quartic equation in v results:

$$-\frac{RT}{(v-b)^2} + \frac{2a(v+b)}{[v(v+b)+b(v-b)]^2} = 0 \tag{25}$$

or

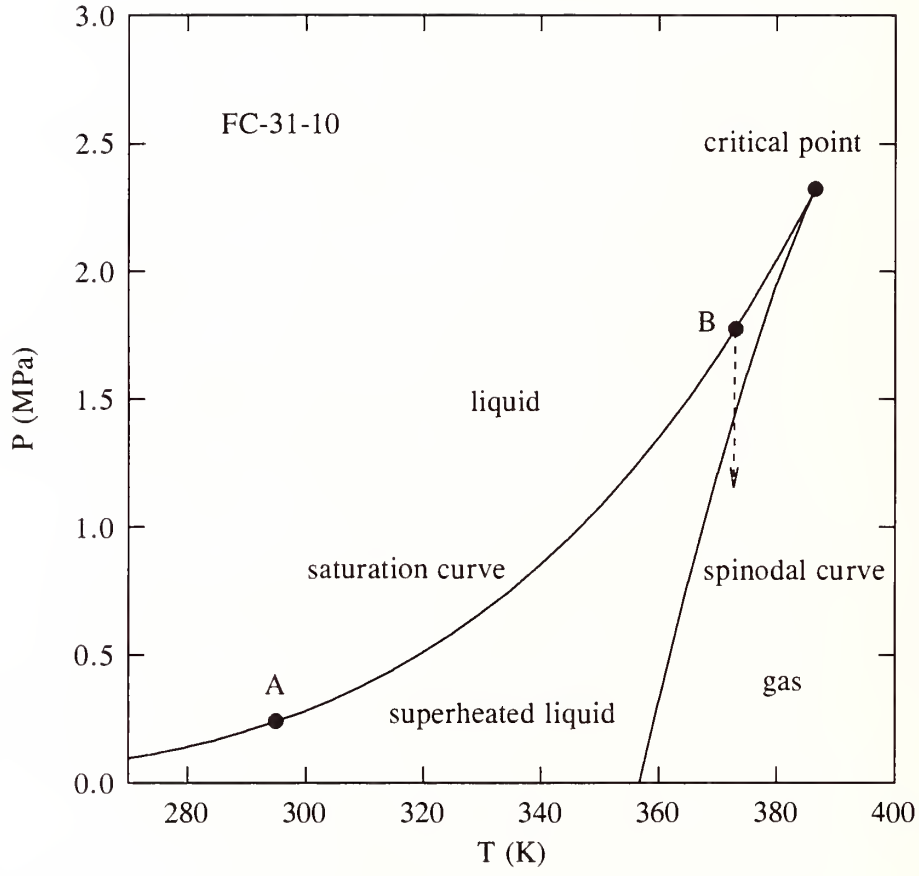

Figure 72. Vapor pressure and calculated spinodal curves for FC-31-10.

$$v^4 + (4b - \frac{2a}{RT})v^3 + 2b(b + \frac{a}{RT})v^2 + 2b^2(\frac{a}{RT} - 2b)v + b^4 - \frac{2ab^3}{RT} = 0 \qquad (26)$$

where a and b are the parameters of the equation of state (see Section 2.3.1). For given temperatures below the critical point, there are four real roots from Equation (26). Two of the roots, one less than the saturated liquid molar volume and the other greater than the saturated vapor molar volume, are nonphysical and are disregarded. The smallest of the remaining two roots corresponds to the v on the liquid spinodal curve, whereas the largest corresponds to the v on the vapor spinodal curve which is not relevant in this discussion. Once v is determined for a given T, P can be obtained from the equation of state. The calculated liquid spinodal curve for FC-31-10 is also shown in Figure 72.

If the vessel is rapidly discharged at the condition corresponding to point B in Figure 72, the discharge process can be approximated by that of an isothermal depressurization (see Section 3.4.3), as depicted by the vertical line in Figure 72. If the homogenous nucleation pressure (P_{hn}) at T_f, which is the pressure corresponding to the intersection of the vertical line and the spinodal curve, is greater than any instantaneous pressure during the interval when the liquid is being discharged, that is

$$P(t) < P_{hn} \qquad 0 < t < t_{el} \qquad (27)$$

where t_{el} represents the time at which complete depletion of liquid occurs, then homogeneous nucleation would be predicted. However, if $P(t) > P_{hn}$ for $0 < t < t_{el}$, then homogeneous nucleation would not occur.

The above discussion is based on a pure agent. If nitrogen is used to pressurize the vessel, nitrogen will be dissolved in the liquid agent. The homogeneous nucleation pressure will then depend not only on the temperature but also on the composition of the liquid mixture. The effect of dissolved gas on the homogeneous nucleation pressure of a liquid was found to raise the homogeneous nucleation pressure (Forest and Ward, 1977). In this case, homogeneous nucleation, if it occurs, would initiate sooner in the presence of the dissolved gas during rapid isothermal depressurization.

Although the hypothesis proposed by Reid (1979) can not be substantiated or disproved at present (Reid, 1979, Kim-E and Reid, 1983), it is prudent to recognize such a potentially hazardous event when the vessel is rapidly discharged at high temperature and pressure, and further study is warranted.

3.4.3.6 Vertically Upward Discharge. When the vapor above the liquid is vented first during depressurization, that is, in the case of upward discharge of the vessel, the discharge process is totally different from that of downward discharge. Visual observation of the discharge process from a plastic vessel reveals several stages. Once the rupture disk breaks, the vapor on top of the liquid is vented out rapidly, during which time the liquid in the vessel remains quiescent. The vapor ullage becomes foggy ($t \sim 10$ ms), possibly due to the condensation of the vapor as the result of cooling by adiabatic expansion. Then, following a delay time ($t \sim 25$ ms), boiling is initiated from the bottom of the vessel, and, because of bubble growth, the liquid-gas mixture level expands all the way through the disk opening. Frothing of the liquid continues for a period of time during which time a two-phase flow emerges from the vessel. The liquid level then settles down ($t \sim 500$ ms). The interior of the vessel becomes clear, and some liquid is observed at the bottom of the vessel. At this point, most of the liquid in the vessel has been expelled. Pool boiling of the liquid then continues until the remaining liquid is boiled off. The complete emptying time of the liquid agent in the vessel is on the order of seconds. The discharge process is much slower for FC-31-10 than for FC-218 because

FC-31-10 has a higher boiling point. The observations, in general, are very similar to those made by Gühler *et al.* (1979) and Fletcher (1982) although the discharge process in both earlier studies is much slower.

Figure 73 shows a photographic sequence of events during a vertically upward discharge of FC-218. The photographs were taken at 1000 frames per second. The frame which corresponds to t = 1 ms is the first frame where the agent first appears outside the vessel. Due to the framing rate, there is a 1 ms uncertainty in the time. The first photograph shows the plastic vessel, a stainless-steel tube inside the vessel for introducing nitrogen in order to burst the rupture disk, vessel mount, and the liquid level. The behavior of the agent inside and outside of the vessel during discharge can be seen in these photographs. The discharge characteristics of the agent outside of the vessel is discussed in Section 3.5.

In Figure 74 the results of pressure measurement for upward discharges of FC-31-10 are shown. In the upward discharge configuration, the pressure transducer measured the temporal variation of the pressure in the liquid phase. When the stainless steel vessel was used in the experiments, the pressure transducer mounted on the side wall of the vessel was used to monitor the pressure change in the vapor phase. Due to its relatively high boiling point, FC-31-10 does not show distinctly in the pressure-time histories the several stages occurring in the discharge process.

Pressure traces for FC-218 and halon 1301 are shown in Figure 75 and Figure 76. The several processes discussed above are clearly depicted. Upon initiation of discharge, the internal pressure decreases rapidly. The following small pressure rise corresponds to the expansion of the liquid. Then, the pressure decreases gradually over a period of time. This time interval corresponds to the continuous frothing of the liquid. Eventually, an abrupt decrease in pressure corresponds to the pool boiling of the remaining liquid in the vessel. The above interpretation is based on comparison of the pressure traces with high-speed movie records obtained from experiments on FC-218 using plastic vessels. Only the stainless steel vessel was used for experiments on halon 1301 due to safety considerations. However, it is conjectured that similar behaviors occurred for halon 1301 because similar pressure-time histories were noted.

When an extension tube was attached to the release vessel assembly exit, the behavior of the liquid agent inside the vessel during vertically upward discharge was very similar to that without an extension tube, as observed in the high-speed movies and noted in Figure 74 through Figure 76.

3.4.3.7 Horizontal Discharge. Observations regarding horizontal discharge of the vessel also show several stages. Once discharge is initiated, the vapor is vented very rapidly from the vessel. Some liquid also flows out of the vessel because the initial liquid level in the horizontally mounted vessel covers a portion of the rupture disk. The flow of vapor causes some wavy motion along the liquid/vapor interface. The sloshing of the liquid could also be caused by the vibration of the vessel mount. A foggy cloud is formed ($t \sim 15$ ms) above the liquid for a period of time. The vessel ullage then becomes clear ($t \sim 400$ ms), and pool boiling is initiated in the remaining liquid pool which still constitutes a significant amount of the initial liquid. Boiling continues until all the liquid is depleted. The emptying time is on the order of seconds. The complete discharge of the remaining liquid is much slower for FC-31-10 than for FC-218 because FC-218 has a lower boiling point.

Figure 77 shows a photographic sequence of events during a horizontal discharge of FC-218. The photographs were taken at 1000 frames per second. The frame which corresponds to t = 1 ms is the first frame where the agent first appears outside the vessel. Due to the framing rate, there is a 1 ms uncertainty in the time. The first photograph shows the plastic vessel (mounted horizontally) with its exit located to the far left and the liquid level. The photographs reveal the behavior of the agent internal and external to the vessel.

1 ms

2 ms

10 ms

15 ms

25 ms

30 ms

Figure 73. Photographic sequence of events showing a vertically upward discharge of FC-218 from a plastic vessel.

40 ms

60 ms

100 ms

150 ms

200 ms

250 ms

Figure 73. (continued) Photographic sequence of events showing a vertically upward discharge of FC-218 from a plastic vessel.

300 ms

350 ms

400 ms

450 ms

500 ms

550 ms

Figure 73. (continued) Photographic sequence of events showing a vertically upward discharge of FC-218 from a plastic vessel.

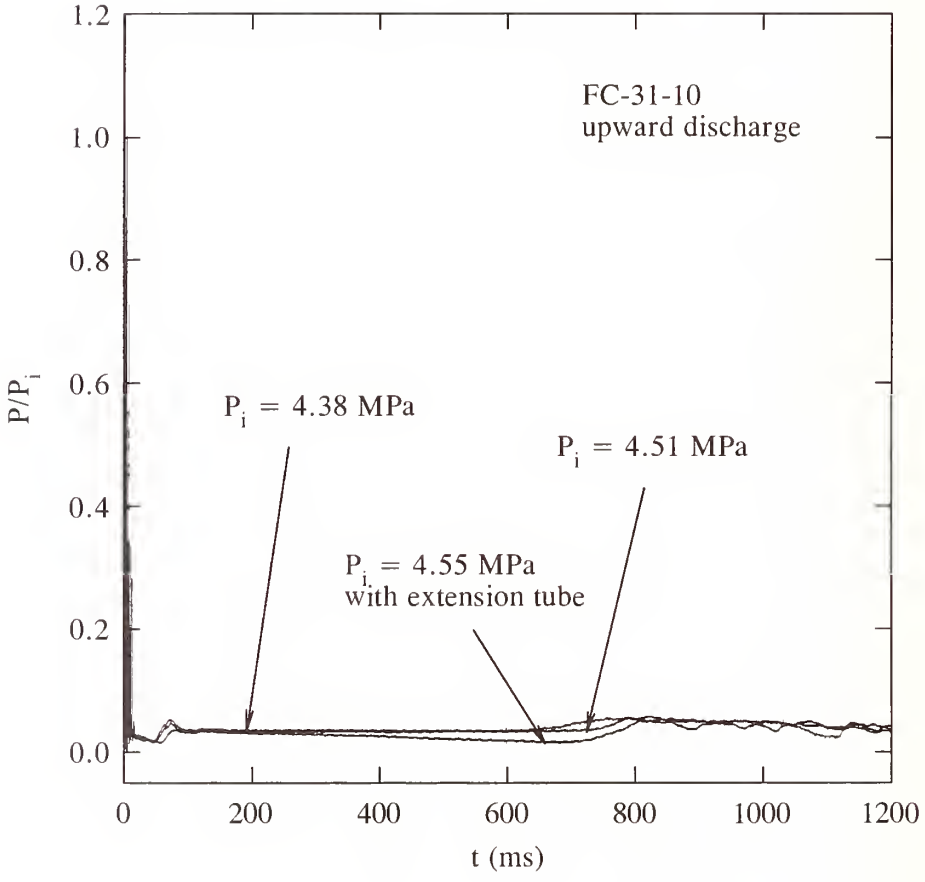

Figure 74. Temporal variations of internal pressure during upward discharges of FC-31-10 with and without an extension tube.

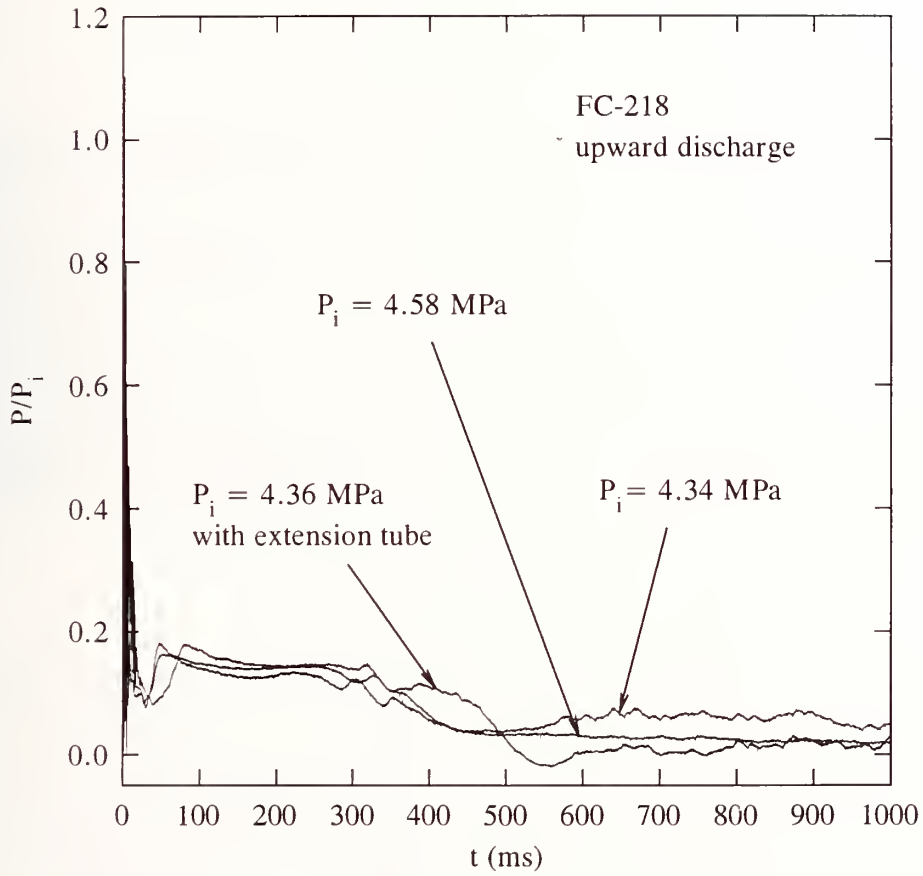

Figure 75. Temporal variations of internal pressure during upward discharges of FC-218 with and without an extension tube.

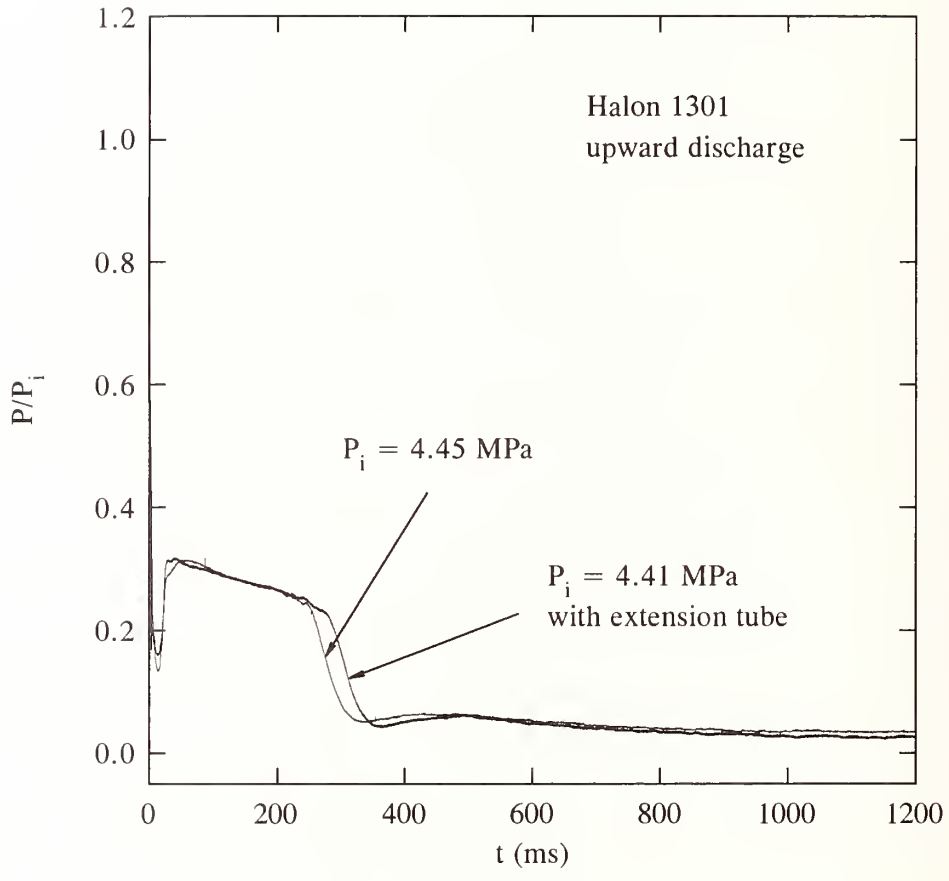

Figure 76. Temporal variations of internal pressure during upward discharges of halon 1301 with and without an extension tube.

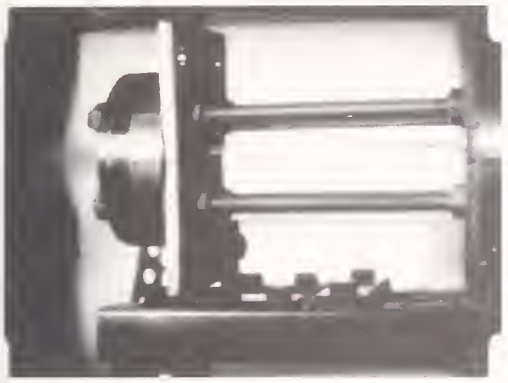

1 ms

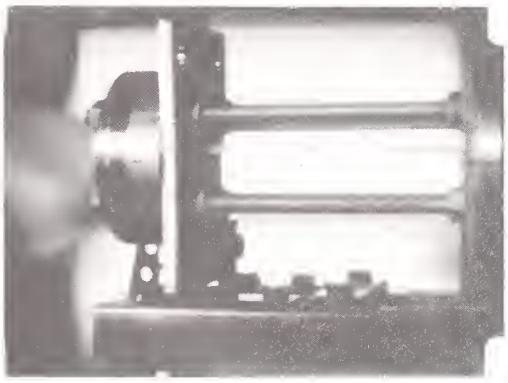

2 ms

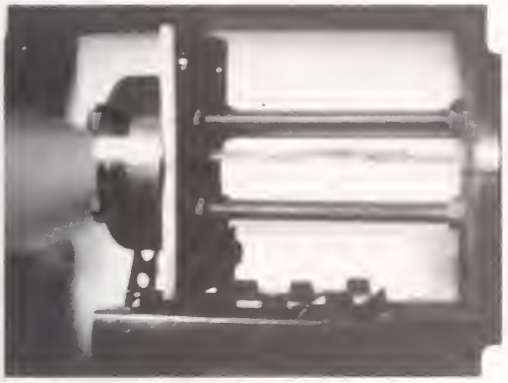

10 ms

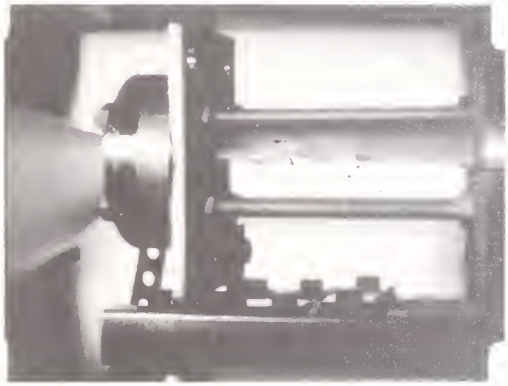

20 ms

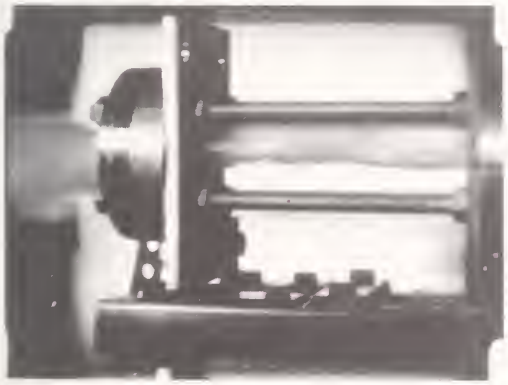

80 ms

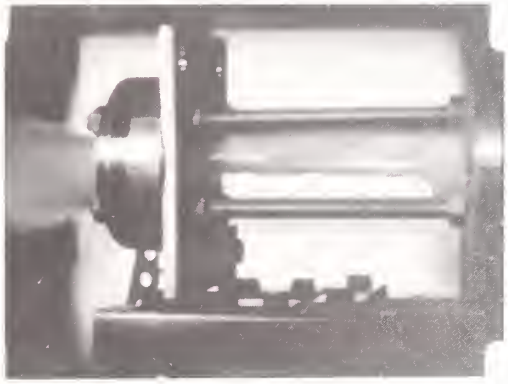

100 ms

Figure 77. Photographic sequence of events showing a horizontal discharge of FC-218 from a plastic vessel.

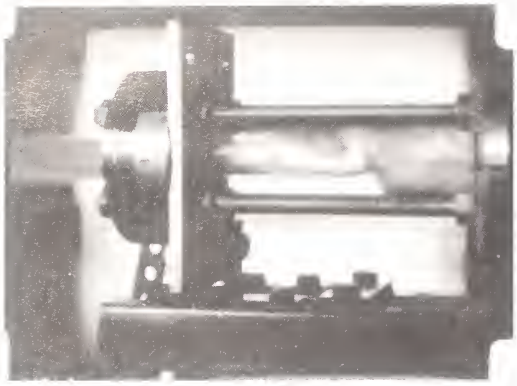

150 ms

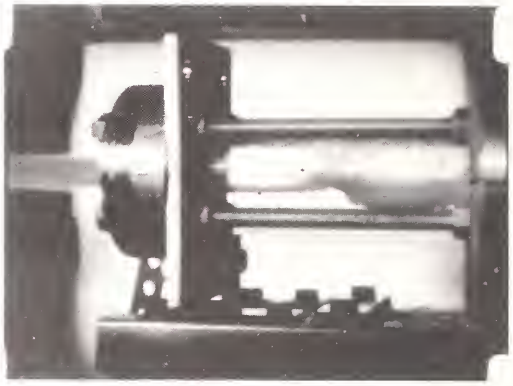

200 ms

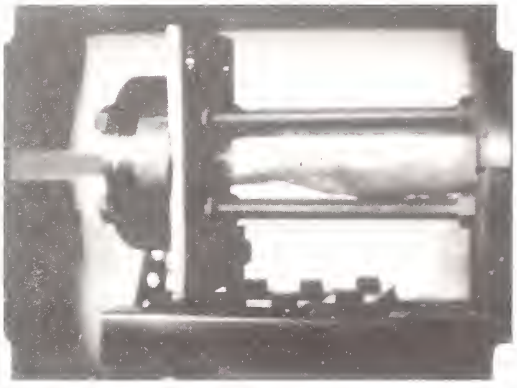

250 ms

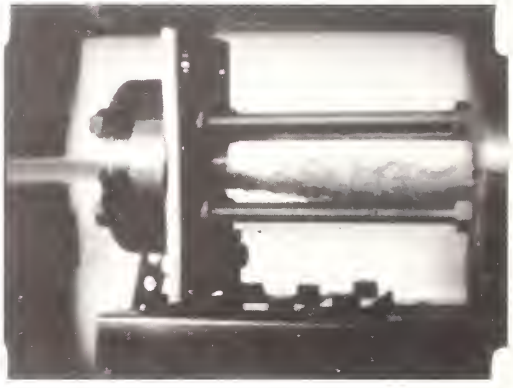

300 ms

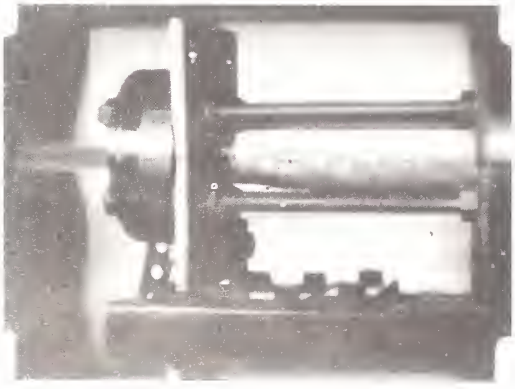

350 ms

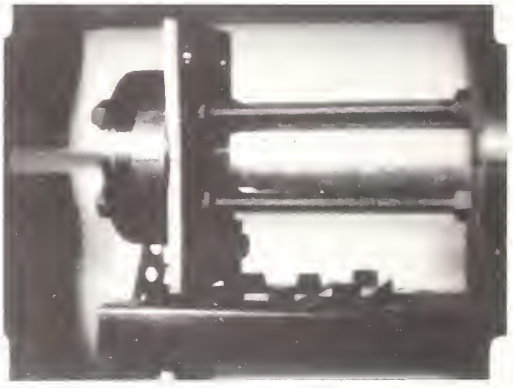

400 ms

Figure 77. (continued) Photographic sequence of events showing a horizontal discharge of FC-218 from a plastic vessel.

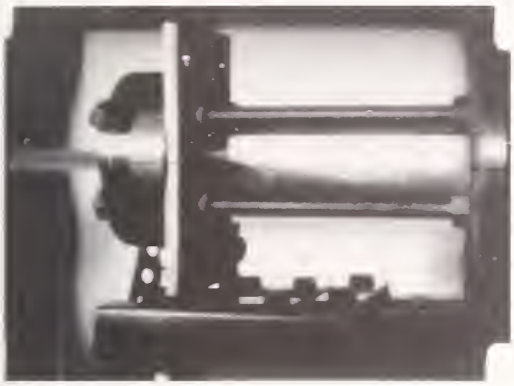

440 ms

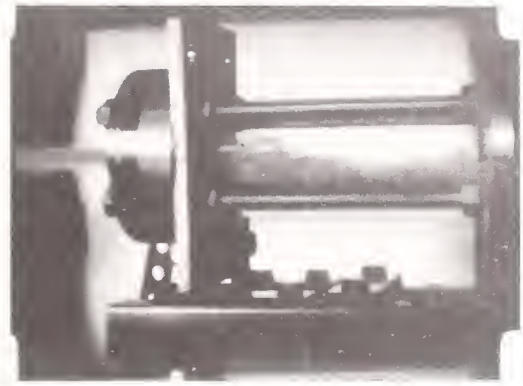

480 ms

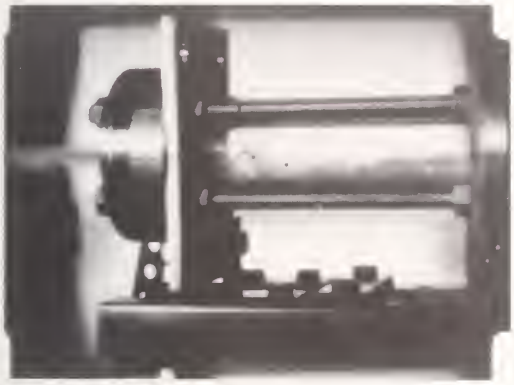

520 ms

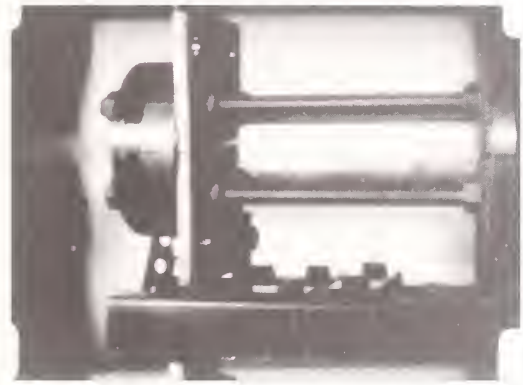

580 ms

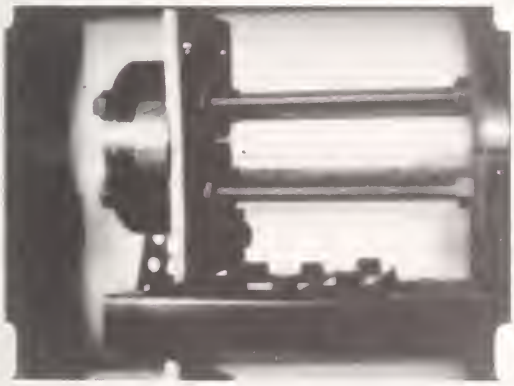

600 ms

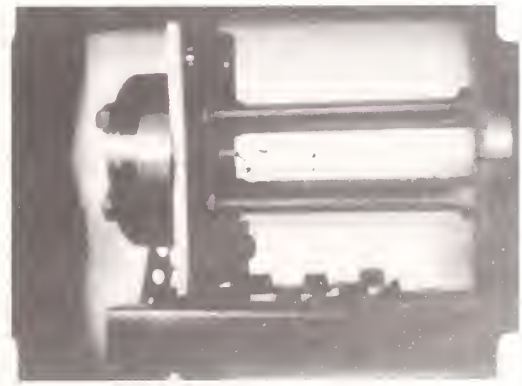

650 ms

Figure 77. (continued) Photographic sequence of events showing a horizontal discharge of FC-218 from a plastic vessel.

Figure 78 and Figure 79 show the pressure-time histories for horizontal releases of FC-31-10 and FC-218. The results were obtained from the pressure transducer that was initially positioned at a location below the liquid level. Therefore, the measured pressure traces represent a combination of the pressure change in two stages during discharge. In the first stage, the pressure measurements were made when the liquid level was still above the position where the transducer was located. In the second stage, the pressure measurements were obtained when the liquid level had dropped below the location of the pressure transducer. In other words, the pressure in the vapor phase was measured.

In Figure 78 and Figure 79, after the initial rapid decrease in pressure, the slight rebound in pressure due to initiation of boiling and bubble growth is not apparent in the case of FC-31-10, but is noticeable in the case of FC-218. Thereafter, the pressure decreases continuously until the liquid is completely boiled off. The reason for the presence of small humps in the pressure traces of FC-31-10 at 500 ms $< t <$ 1000 ms (Figure 78) is unclear. It is conjectured that the liquid level in the vessel during this time interval is still slightly below the location of the pressure transducer because of the relatively slow boiling process of FC-31-10, and that any sloshing of the liquid upon the transducer could raise the pressure reading. The shifting of the location of the hump in the two pressure traces may be indicative of such an event.

Figure 78 and Figure 79 also show results for temporal variations of pressure when an extension tube is connected to the exit of the rupture disk holder. The behaviors are very similar to that when no extension tube is present.

In the case of halon 1301, the results obtained with and without an extension tube are shown in Figure 80. Because a stainless steel vessel was used, no visual observations were made. Therefore, it is unclear at present why the small pressure rebound is apparent in the case of an extension tube but is not present when the extension tube is absent.

3.4.4 Conclusions. In downward discharge, the average volumetric flow rates for all the alternative liquid agents are very similar. No internal boiling was observed for downward discharge of HFC-236fa, FC-31-10, FC-318, HCFC-124, HFC-227ea, HFC-134a, FC-218, HCFC-22, and HFC-125. Based on results for FC-31-10 and FC-218, the behavior of the liquid inside the vessel during discharge was found to be very similar whether an extension tube was present or absent at the vessel exit. A twofold increase in the initial discharge pressure decreases the emptying time of the liquid approximately by half. The effect of a restrictor plate at the vessel exit on the discharge process is to increase the liquid emptying time. A twofold increase in the diameter of the orifice plate increases the average volumetric flow rate by approximately fourfold. Liquid discharged at cold temperature behaves very similarly to that at room temperature. However, when the vessel is discharged vertically upward or horizontally, the discharge process depends on the boiling point of the agent. Agents with higher boiling points remain in the vessel for a considerable amount time before they can be boiled off.

3.4.5 Recommendations. Based on the above findings, it is recommended that in order to empty the liquid contents from the pressure vessel within tens of milliseconds, the vessel should be discharged in a vertically downward position. If the vessel were to be designed to increase release rates and to withstand higher internal pressure, higher initial charge pressures are also recommended. In addition, further study of discharge at high temperatures is needed because of concern regarding boiling liquid expanding vapor explosion (BLEVE).

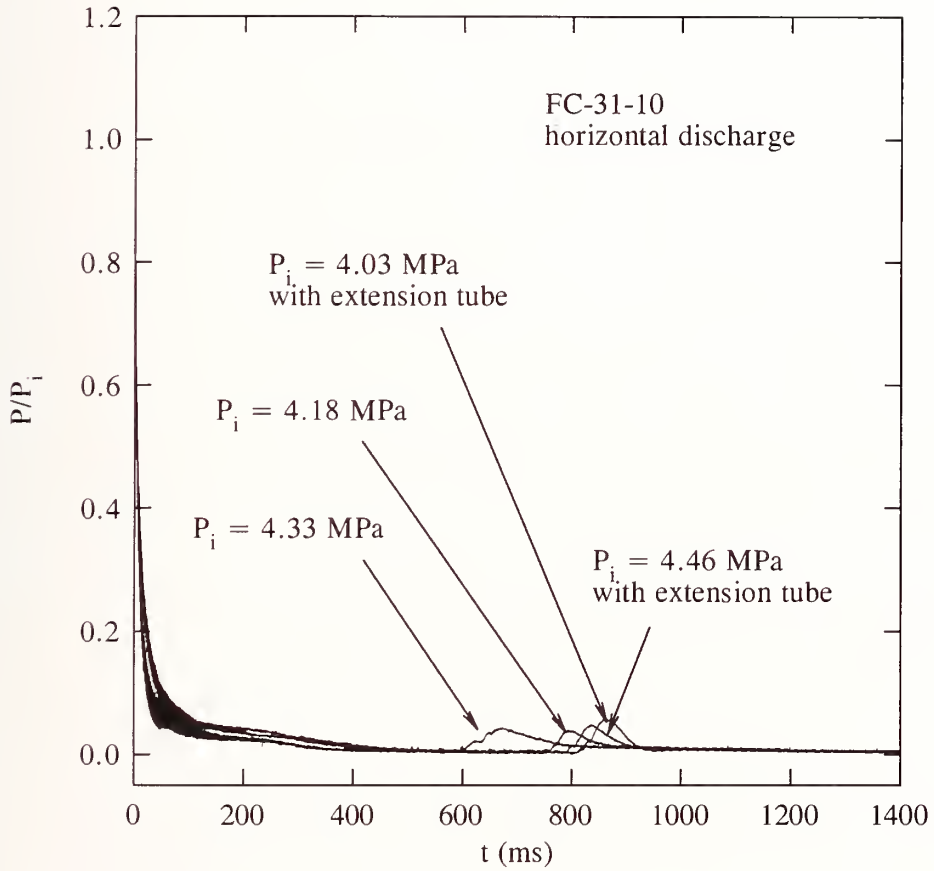

Figure 78. Temporal variations of internal pressure during horizontal discharges of FC-31-10 with and without an extension tube.

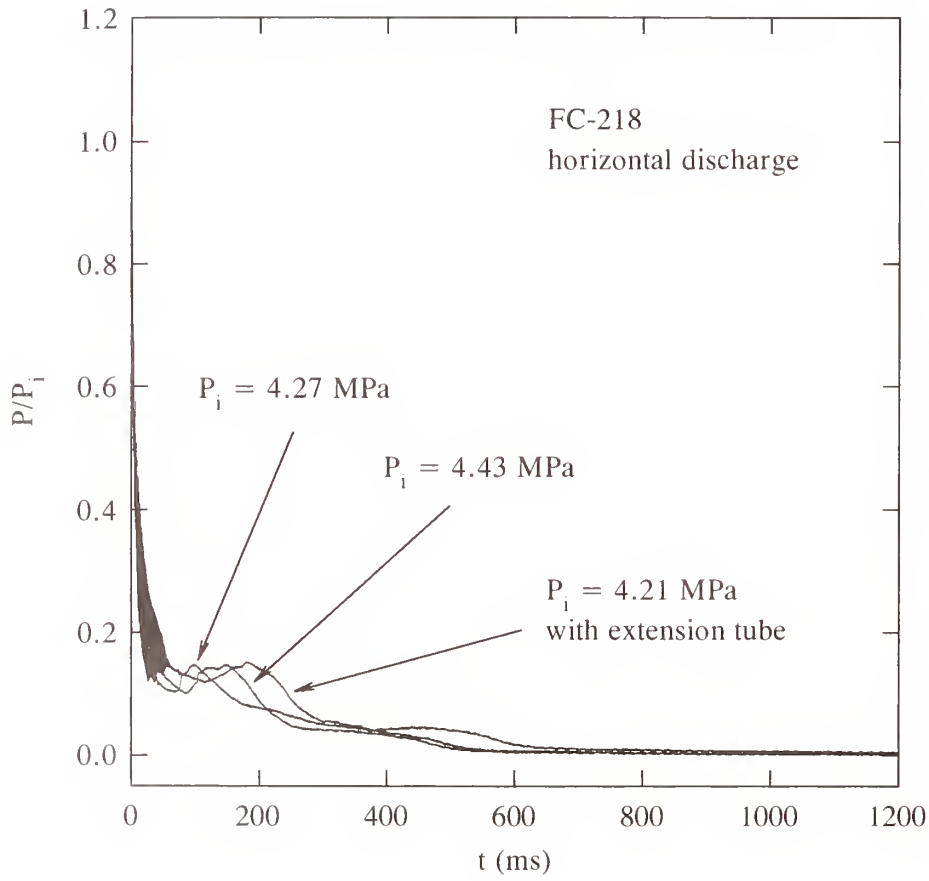

Figure 79. Temporal variations of internal pressure during horizontal discharges of FC-218 with and without an extension tube.

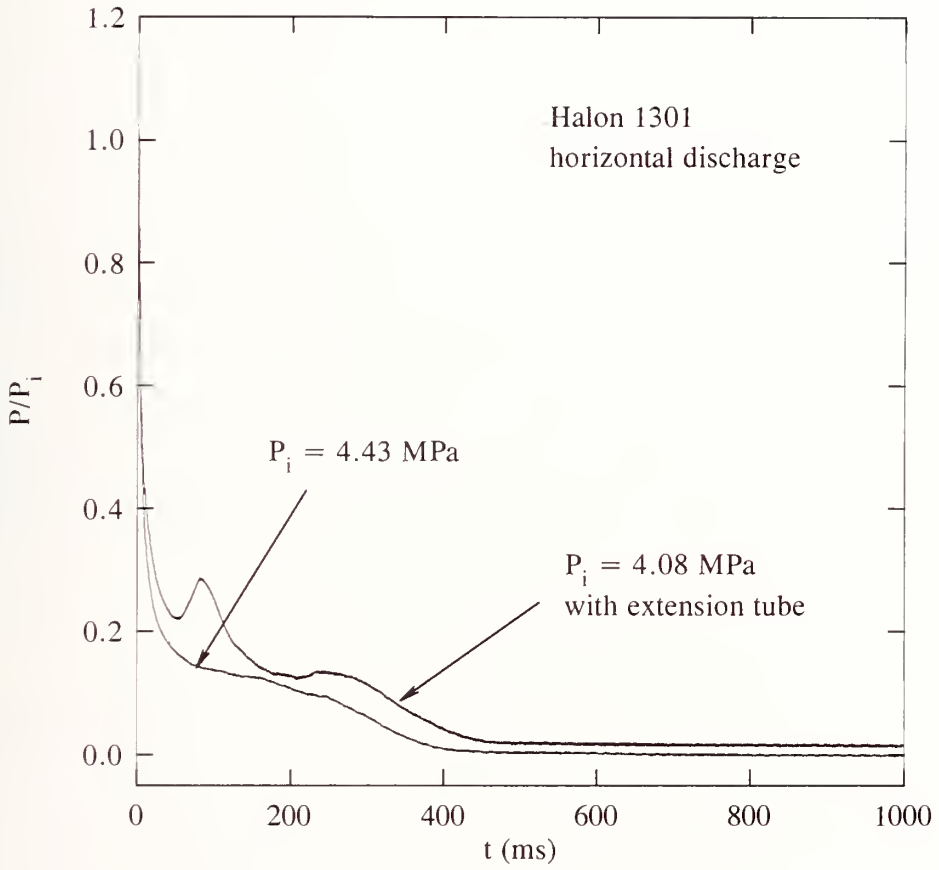

Figure 80. Temporal variations of internal pressure during horizontal discharges of halon 1301 with and without an extension tube.

3.5 Measurements of Agent Dispersion

3.5.1 Introduction. The purpose of this part of the research effort was to characterize experimentally the dispersion and evaporation behavior of the eleven potential replacement fire extinguishing agents. The design of the experiments was based on the reasonable hypothesis that effective fire extinguishment requires both rapid dispersion of the agent within a volume as well as rapid gasification following release of the agent from a pressurized bottle. These properties are expected to be crucial for both the dry bay and engine nacelle applications. However, they are particularly relevant for the dry bay application due to the extremely rapid fire suppression times (on the order of tens of milliseconds) required.

The agent must be dispersed throughout the volume to ensure that all regions of flame are suppressed. This requires that the agent not only be rapidly released from the bottle, but also that it be rapidly and effectively mixed with the surrounding gases. Rapid vaporization of the liquid is desirable for two reasons. While the liquid may, in some circumstances, be dispersed more rapidly as a two-phase mixture, it is also true that it is unlikely to be dispersed evenly throughout the volume. Since the fire location cannot be specified, it is necessary to have full vaporization to ensure a more uniform distribution. The proposed halon replacement agents are not expected to be as effective as halon 1301 for these fire fighting applications since they do not have the effective chemical suppression mechanism associated with the presence of bromine atoms. Principal mechanisms for extinguishment are therefore likely to be heat extraction and dilution as well as the physical effects associated with the rapid release of the agent (*i.e.*, flame extinction due to stretch). Complete vaporization ensures the maximum interaction between the agent and the fire zone.

With the exception of one of the chemicals (FC-116), all of the proposed alternatives are liquids when stored under pressure at room temperature and are superheated when released as liquids into the ambient atmosphere. As a result, partial rapid vaporization is to be expected when these agents are released into an ambient environment at room temperature. A review of the literature indicated that while there have been investigations of flashing liquids reported, none of these previous experiments dealt with the rapid, short-time releases which are characteristic of the current study. Here we summarize the literature which was reviewed during the course of this effort in order to provide an overview of the existing understanding and to provide a basis for later discussion.

One of the earliest investigations of released superheated liquids was the study of Brown and York (1962). These authors investigated sprays formed by the release of water, CFC-11 and water saturated with carbon dioxide. They noted that the flashing of a superheated liquid or a pressurized liquid with dissolved gases provides an additional mechanism for the breakup of a liquid stream (in addition to the classical mechanisms resulting from surface tension forces (Rayleigh, 1878) and aerodynamic forces (Weber, 1931)). They pointed out that for adiabatic conditions the flashing of a superheated liquid would occur by the extraction of latent heat from the liquid to provide the energy necessary to evaporate the liquid. Thermodynamic equilibrium is attained when the fraction of liquid converted to gas is sufficient to cool the remaining liquid to it saturation pressure.

Results reported included the distance required for the liquid jets to break up as well as characterization of the sprays generated. Several of their conclusions are relevant to the current investigation. They reported that a liquid jet does not "shatter" abruptly when the liquid just becomes superheated, but that a well defined amount of superheating is required for shattering to occur. A dependence of the flashing behavior on the jet diameter was characterized by correlating the liquid breakup times with the Weber number (We), defined as

$$We = \frac{\rho_g U_o D}{2\sigma}, \tag{28}$$

where ρ_g is the density of the gas surrounding the liquid jet, U_o is the jet velocity, D is the jet diameter, and σ is the liquid surface tension. The times required for jet breakup increased with decreasing D. A transition in the behavior was observed for $We = 12$.

Brown and York argued that the times required for flashing of pressurized liquid jets containing dissolved gases should be considerably longer than those for superheated jets due to molecular diffusivity considerations. Experimental evidence was provided which supports this conclusion.

Measurements of drop sizes generated by the flashing liquids showed that flashing provided an effective mechanism for atomizing the liquid. The flashing of the liquids resulted in a rapid expansion of the flow.

Lienhard and coworkers (Lienhard, 1964; Lienhard and Stephenson, 1966; Lienhard, 1966; Lienhard and Day, 1970) developed a model for predicting the time required for superheated liquids to flash and compared the findings with experiment. The first of these papers (Lienhard, 1964) considered the conditions for which bubbles growing in a liquid are stable to growth or collapse. Results were based on thermodynamic arguments. Lienhard and Stephenson (1966) considered the kinetics of bubble growth. Their analysis was based on equations for bubble growth developed earlier by Deragarabedian (1953), Forster and Zuber (1954), and Plesset and Zwick (1954). In order for bubbles to grow spontaneously they must attain a critical size. For smaller sizes, bubbles tend to redissolve into the liquid. Nuclei bubbles therefore arise due to fluctuations in the local environment which favor their formation. When such fluctuations result in a bubble with sufficient size to continue growth, a large bubble will form. Generally the formation of a larger bubble will "trigger" the growth of additional bubbles. Using arguments based on the distribution of disturbances in the liquid, Lienhard and Stephenson derived an approximate relation for the period required for a superheated liquid to flash which can be written as

$$t_d \sim \frac{1}{A(P_v - P_{amb})^{7/2}}, \tag{29}$$

where t_d is the delay time for bubble growth, A is the cross sectional area for the liquid flow, P_v is the vapor pressure for the liquid at its release temperature, and P_{amb} is the ambient pressure. Note that P_v-P_{amb} is a measure of the superheat based on pressure. Experimental results were presented for the flashing of superheated water which supported the use of this equation.

In the same paper these authors derived an expression for the amount of work that an isobaric expansion of a superheated liquid can do. For the case where the saturation temperature for the liquid, T_l, is much greater than the superheat expressed in temperature terms, T_l-T_{sat}, the resulting expression is

$$w = C_p \frac{(T_l - T_{sat})^2}{2T_{sat}}, \tag{30}$$

where w is the amount of work which can be done by the flashing and C_p is the constant pressure heat capacity which had been assumed to be constant.

The above analysis for the flashing time was extended by Lienhard and Day (1970) [see also Day (1969)] in order to derive a more general equation applicable to different superheated fluids. They

argued that the delay time for bubble growth should scale with the density of the saturated liquid, ρ_l, D, σ, and the superheat, P_v-P_{amb}. Using the Buckingham Pi-Theorem, they reduced these variables to two dimensionless variables which should correlate the experimental data. These were a dimensionless dwell time, Φ,

$$\Phi \equiv \frac{(P_v - P_{amb})^{5/2} D t_d}{\sigma^2 \sqrt{\rho_f}}, \tag{31}$$

where ρ_f is the liquid density, and a dimensionless jet diameter, Ψ,

$$\Psi \equiv \frac{D(P_v - P_{amb})}{\sigma}. \tag{32}$$

By using Equation (29) and eliminating t_d and $(P_v$-$P_{amb})$ from the equations one finds that

$$\Phi \Psi = constant \tag{32}$$

Once the constant in Equation (32) is determined experimentally, it should be possible to predict t_d for any superheated fluid. Based on measurements of delay times for jet flashing with water and liquid nitrogen, the constant in Equation (32) was found to equal 2.12×10^{13}. This paper also has a detailed discussion of the conditions under which liquid jet break up occurs as the result of capillary and aerodynamic instability.

In a brief paper, Lienhard (1966) considered how the spreading of a flashing liquid jet can be understood in terms of the amount of work which the flashing can do on the system (Equation (30)). The analysis was done in terms of the radial velocity, U_r, imparted to the spray by the flashing. The maximum such velocity, $U_{r,max}$, is

$$U_{r,\max} = \left(\frac{C_p}{T_{sat}} \right)^{1/2} (T_l - T_{sat}) \tag{33}$$

Lienhard argued that all of the available work would not be used to impart radial momentum and that only a fraction, C, would be available. Based on experimental spreading angles for flashing superheated water jets he estimated that $C \approx 0.04$.

Solomon *et al.* (1982) reported limited measurements for a flashing jet of CFC-11 and superheated fuels. They found that flashing due to small amounts of superheating was very effective in generating atomized liquid flows.

Celata *et al.* (1982) have provided a very brief description of experiments on the release of superheated water. They found that flashing took place very rapidly, and that the spreading angle of the two-phase flow increased with increasing superheat. Using a probe, they recorded dynamic pressures within the flow field. Unlike previous investigations, they concluded that evaporation was occurring on the outside of the flow and that there was a narrow liquid core in the center of the flow surrounded by a two-phase shell.

Moodie and Ewan (1990) provide a nice introduction to the release behavior of liquid jets. They discussed the behavior of flashing jets and showed a photograph of a flashing CFC-11 jet. The analysis was complicated because flashing seemed to occur within the vessel orifice. They measured

the peak droplet sizes which suggested that the droplet size decreased with increasing superheating. Time-averaged temperature measurements were also provided. The temperature profiles seem to suggest that the entire jet is flashing unlike the findings of Celata *et al.* (1982). The temperature measurements also indicate that the entrainment of air plays a critical role in the ultimate evaporation of the superheated liquid.

These authors also made mass fraction measurements of CFC-11 and air in the flow field. These measurements also suggest the two-phase flow covered a large extent of the flow. Velocity measurements were also reported. These measurements showed that measured flow velocities were considerably higher than expected based on liquid flow rates at the vessel exit. Radial velocity profiles in the region near the vessel were non Gaussian, but tended to attain a Gaussian profile as the measurement location was moved further downstream.

Superheated releases of CFC-11, chlorine, methylamine, and cyclohexane have been investigated by Johnson and Diener (1991). In these experiments the liquid fraction of the two-phase flow was captured. The data indicated that there were well defined superheat points for which the liquids flashed near the vessel exit. Under these conditions the amounts of liquid trapped decreased significantly. Comparisons were made with a model designed to predict the behaviors. In general, the agreement was not very good.

There are a variety of systems employed for the release of halon 1301 into dry bays and nacelles. It was beyond the scope of this study to investigate a wide range of release configurations. For this reason, the decision was made to characterize the spreading and mixing characteristics of the agents following release from a generic system based on the vessel developed to study the release rate of agents (see Section 3.3).

3.5.2 Experimental Methods. As mentioned above, there were very few investigations available in the literature to guide the design of a system for characterizing the dispersion and evaporation behavior of the agents. As a first step in the design process a high-speed video system[1] was used to record a downward release of HCFC-22 from the vessel at a rate of 1000 frames/s. A burst disk providing a nominal pressure of 4.1 MPa was employed and the 0.0005 m^3 vessel was filled one-third full. A series of sequential photographs from the high-speed video are reproduced in Figure 81. Lighting for the camera was provided from the rear and front of the release.

As can be seen from Figure 81, the mixing process is extremely complex. When the burst disk first opens, a flashing is observed which results in a rapid expansion of the agent in both the downward and radial directions. The lighting from behind the flow is attenuated by the flow. Shortly afterwards a vortex structure forms at the downstream edge of the release and the flow field looks very much like an impulsively started axisymmetric gas jet. Such structures have been observed in liquid jets (Shirakashi *et al.*, 1984) and combustion torch ignition experiments (Cattolica and Vosen, 1987). As the flow develops behind the leading edge it has a nearly linear spreading behavior. This is true near the orifice as well as the far field. The linear expansion seems to be initiated immediately at the orifice of the vessel. At 13 ms into the release a second flashing starts near the vessel orifice and one ms later this flashing has resulted in a very rapid radial expansion. Analysis of the emptying rate of the vessel for these conditions indicates that the second flashing occurred very close to the time when the liquid was completely released from the vessel. Following

---

[1]Kodak Ektapro 1000 Motion Analyzer. The authors thank Michael Howachyn of Kodak for arranging a demonstration of this instrument and for allowing us to record an initial series of high-speed images of the releases.

Figure 81. Sequence from a high-speed video (1000 frames/s) of the flow formed by a release of 245 g (1/3 full) of HCFC-22 from the 0.0005 m^3 test vessel. Time increases to the right and from top to bottom.

the second flashing, the release becomes obviously slower and within 30 ms the flow has cleared up and the backlighting is again transmitted.

Additional high speed films indicated that the double flashing behavior identified from Figure 81 was typical for downward releases of all of the agents, with the exception of FC-116 which was not investigated since this agent is not a liquid under the storage conditions. All of the agents resulted in nearly total attenuation of a laser beam when they were present in a two-phase state. This observation ultimately determined the type of diagnostics which could be employed to characterize the mixing and vaporization behavior.

Our initial intention was to record the concentration of agent as a function of time using either Rayleigh light scattering (gas concentrations only) (Pitts and Kashiwagi, 1984) or aspirated hot-film probes (Brown and Rebollo, 1972). However, the early visualization studies indicated that these techniques are inappropriate due to the two-phase nature of the flows and their high optical density. A consideration of possible diagnostics revealed that there were no techniques available which would allow quantitative concentration measurements or two-phase flow characterization over the short time periods required.

The discussion above indicates that the two most important flow properties determining the ability of an agent to extinguish a flame are rapid mixing and agent vaporization. A simple, but effective, experimental system was developed to characterize the agents with regards to these two variables. This system combined high speed flow visualization, laser attenuation measurements, dynamic pressure measurements, and an aspirated hot-film concentration probe. To our knowledge, this is the first time that such a system has been used to characterize the behavior of the short period, two-phase flow generated by a release from a pressurized bottle. Figure 82 shows a schematic of the overall system.

The system was used to characterize the flows formed by releases of the agents from the vessels developed to study their release rates (see Section 3.3). Data were recorded for the various release conditions performed during these investigations (see Section 3.4).

3.5.2.1 High-Speed Filming. The same high-speed camera which was used to record the fluid level inside the transparent vessel (see Section 3.4.2) simultaneously recorded the release of the agent in regions near the vessel exit. This was accomplished by placing the camera such that it recorded the liquid behavior inside the transparent vessel as well as locations immediately downstream of the vessel exit. The field of view imaged by the camera could be varied by adjusting the camera placement and distance from the vessel. Most data were recorded with a field of view of roughly 0.40 m width and 0.10 m height.

Selected frames of these films were used to estimate the axial and radial velocities of the agents immediately following release. The approach used image analysis (see Section 3.4.2) to locate the downstream and radial edges of the release at different times and calculate the corresponding velocity. The radial velocity was determined for the downstream location (13 mm from orifice) where the pressure transducer (see ahead) was located. Due to the relatively small area of the near-field release which was imaged, normally only two such measurements could be made before the agent covered an area larger than the field-of-view. Note that frame 1 is defined as the frame where it is clear that the release of the agent has begun. As a result, the time for frame 1 can be anywhere from 0 to 0.49 ms (for a framing rate of 2000 frames/s) following the bursting of the disk.

3.5.2.2 Laser Attenuation Measurements. This part of the system was designed to measure the rate at which the downstream edge of the released agent moved away from the vessel exit and to provide estimates for the period required for the agent to evaporate. Five laser beams were aligned downstream of the vessel exit and perpendicular to the flow direction. Simple helium neon lasers

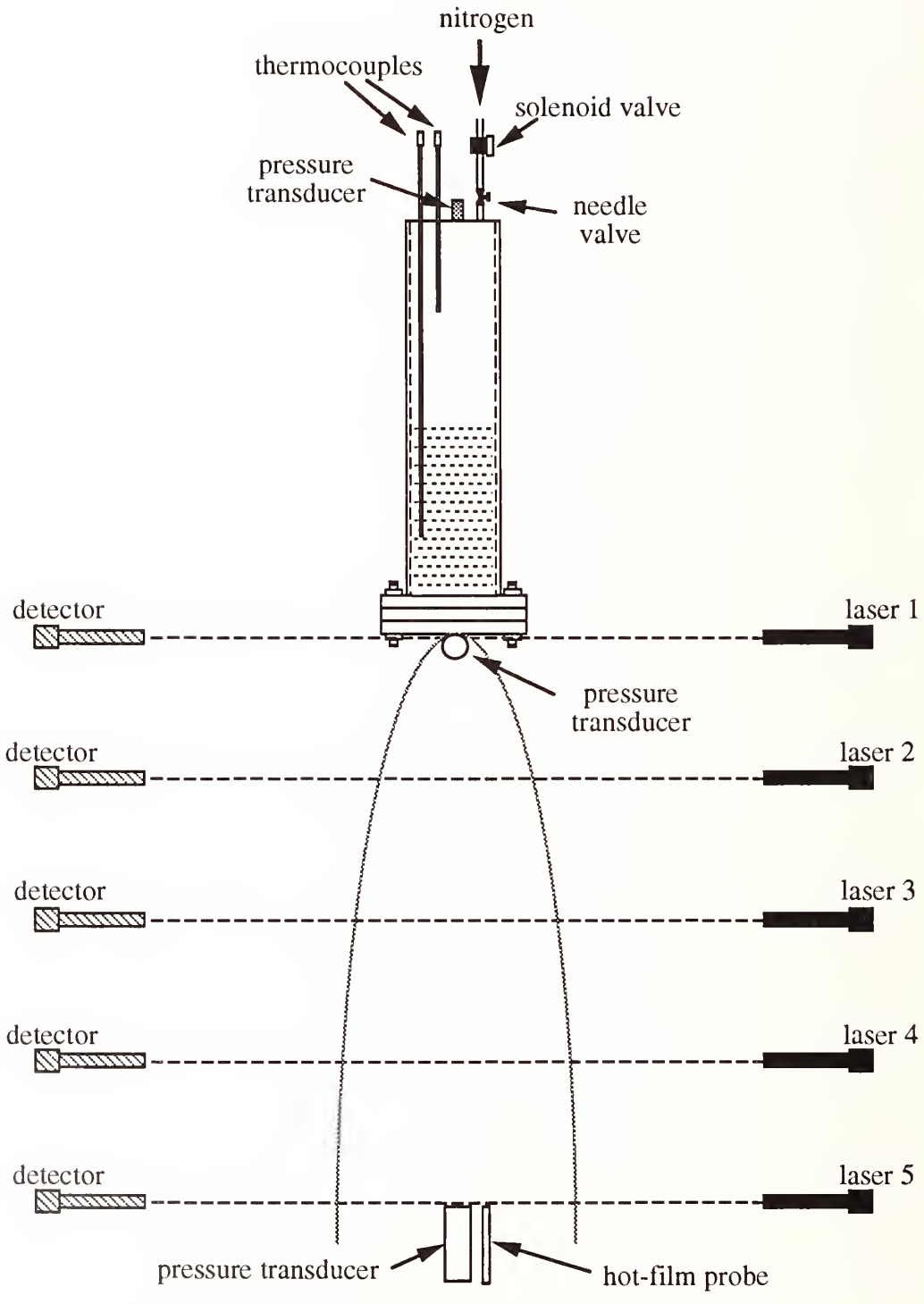

Figure 82. A schematic of the experimental system is shown. Helium-neon lasers and silicon photodiodes are used for the extinction measurements. The piezoelectric pressure transducers and aspirated hot-film probe are described in the text.

(Melles Griot 05-LLR) were mounted on a vertical strut located 1.3 m from the vessel such that the spacing between lasers was nominally 0.3 m. The laser closest to the vessel was positioned across the center of the orifice within 1 mm of the rupture disk holder.

After traversing the flow field the lasers were detected by a series of five photodiodes. The photodiode amplifier circuits and mountings were based on a design by Bryner (1993). Each detector was a silicon photodiode (Hamamatsu S1337-1010BQ) having an active surface area of 100 mm^2. An operational amplifier circuit (Figure 83) was used to generate a voltage proportional to the light intensity striking the photodiode. Each photodiode and amplifier was placed in a rigid mount with a connector for power input and signal extraction. The mount was drilled and tapped so that a rod could be attached for positioning the photodiode. A tube having an inside diameter of 22 mm and a length of 0.23 m was placed in front of the detector in order to shield the photodiode from ambient light in the room. In some cases neutral density filters were used to ensure that the outputs of the photodetectors were not saturated. Circuits housed in a single box were built to provide power for the photodiodes and signal outputs on BNC connectors for a maximum of eight detectors. For the experiments reported here only five detectors were used.

The photodetectors were mounted on a vertical strut located on the opposite side of the room from the lasers. Each photodiode system was aligned with one of the laser beams in such a way that the beam was centered on the active area. Figure 84 is a photograph of the photodiode detectors.

The voltage outputs for the photodiodes (numbered 1 to 5 with 1 closest to the vessel) were recorded using the data acquisition system described below. Tests showed that laser #1 was totally attenuated very rapidly (in less than 40 μs) when the disk burst. The attenuation of this laser beam was used to define time 0 for the experiments. It is interesting that this laser beam was normally found to be totally attenuated several hundred microseconds before a pressure drop was recorded by the pressure transducers within the vessel.

3.5.2.3 Dynamic Pressure Measurements. Two piezoelectric pressure transducers were used external to the vessel to record the dynamic pressure of the releases. The transducers were Kistler 603B1 models used with Model 5004 amplifiers. The amplifiers included 180 kHz frequency filters and were operated in the "long" integration mode to allow the pressure to be tracked over the relatively long time (generally several hundred milliseconds) of a release. The output of the amplifier is a voltage proportional to the pressure. Usually a range of 687 kPa/V was used.

One of the pressure transducers was located near the vessel exit at a distance 13 mm downstream of the rupture disk holder of the vessel and 46 mm from the centerline defined by the center of the orifice. It was oriented so that it was perpendicular to the centerline. Note that the orifice was nominally 19.1 mm in diameter, and the pressure transducer was located 4.8 orifice radii from the centerline.

The second pressure transducer was positioned along the centerline of the release at a downstream position just beyond the point where the fifth laser beam crossed the centerline (1.3 m downstream of the vessel exit). It was oriented perpendicular to the flow direction.

Both pressure transducers were mounted in the center of conically shaped pieces of aluminum designed to protect the transducers and, at the same time, minimize their interaction with the flow field. The near-field transducer and its mount were attached to a rod which allowed positioning of the transducer. This pressure transducer and its mount can be seen in the early frames of the high-speed films which are shown later. The downstream transducer and its mount were attached to a plate which was capable of surviving the large dynamics pressures sometimes generated by the flow fields at this position. Figure 85 is a photograph showing the pressure transducer mounted in the experimental system.

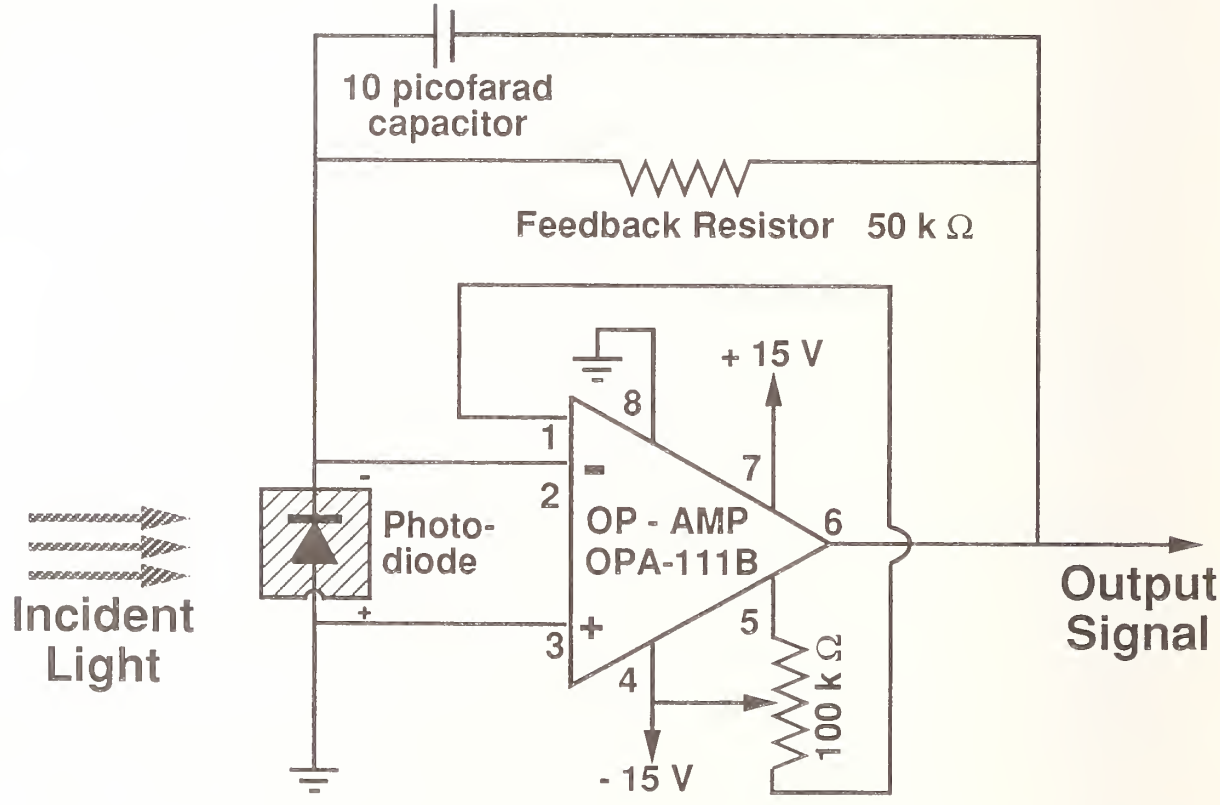

Figure 83. The circuit used to power a photodiode and generate a voltage proportional to the current generated by light striking the detector. The output is a signal proportional to the laser intensity reaching the detector.

Figure 84. A photograph of the array of five photodiodes and mounts used to record transmitted laser intensities across the flow. The nominal spacing between detectors is 0.3 m.

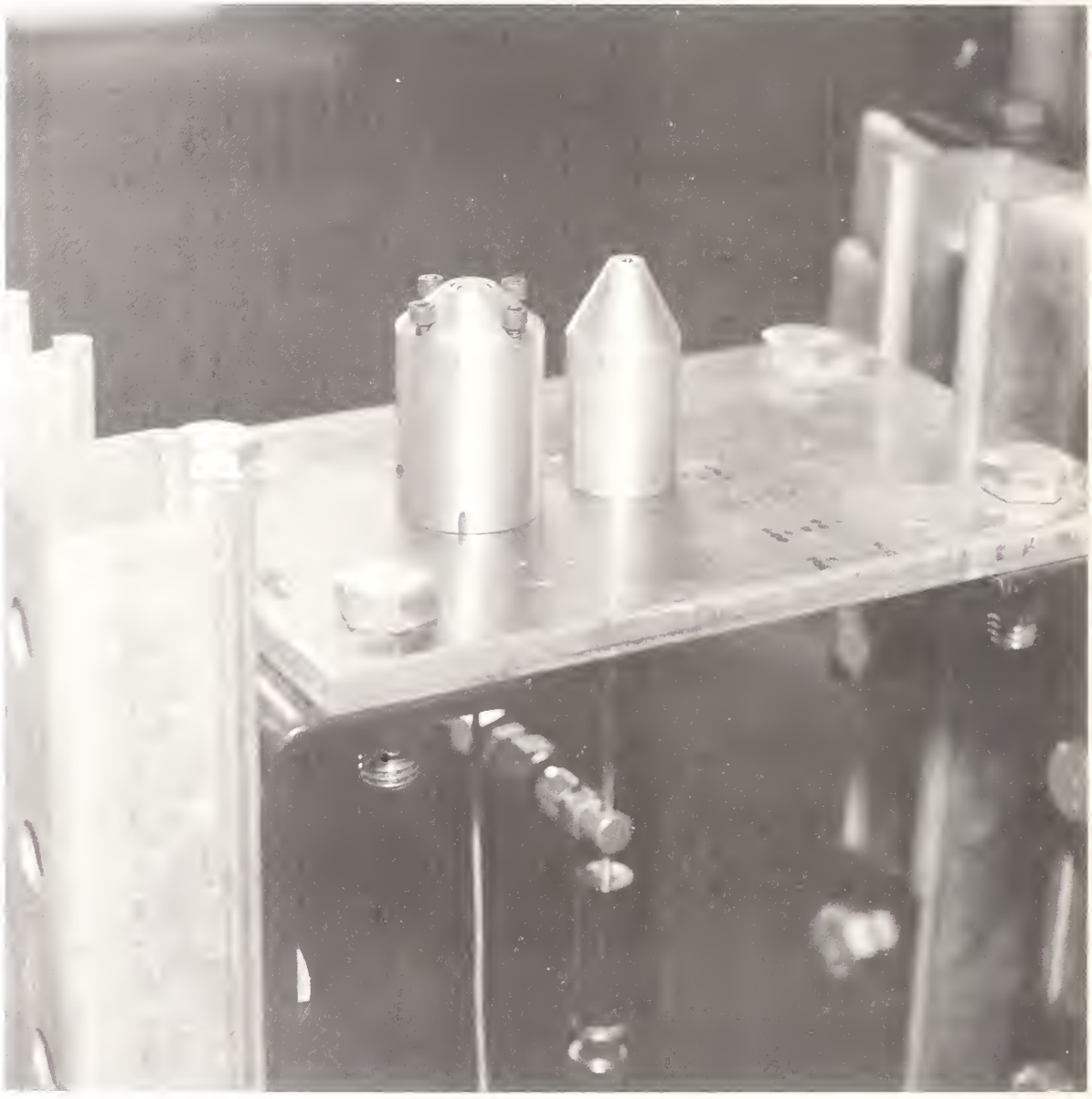

Figure 85. Photograph of the dynamic pressure transducer (left) and aspirated hot-film (right) located 1.3 m downstream of the agent vessel. Probes are placed in metal housings for protection and to provide a means for mounting to an aluminum plate.

An important point with regard to the use of these transducers is the expected response of the transducer to the flow. Davis (1980) used pitot tubes to make similar measurements of dynamic pressure in a gas-liquid mixture flow. He reported that pressure probes respond partially to the incident flow momentum flux with pressure rises of

$$P_m = \tfrac{1}{2}\varepsilon \rho_m U^2 \tag{34}$$

where P_m is the measured dynamic pressure, ε is a factor which varies between 1.0 and 1.85, ρ_m is the density of the mixture, and U is the local flow velocity. Note that Equation (34) reduces to the standard Bernoulli equation form for a pitot tube (Roberson and Crowe, 1980) when ε equals 1. Davis argues that the variation in ε is the result of the relative motion of the gas and liquid in the region of the probe tip. For the case of the piezoelectric transducers used in the current investigation, the stagnation point is very close to the probe and such effects should not be important. Equation (34) with $\varepsilon = 1$ will therefore be used.

3.5.2.4 Aspirated Hot-Film Probe. The aspirated hot-film probe is a device which is designed to record real-time concentrations in isothermal binary gas mixtures. The response time depends on a number of system parameters, but is generally less than 1 ms. The active part of the device consists of a thin quartz rod which is coated with platinum. A small current is passed through the platinum film and resistively heats the surface. The resistance of the device changes with temperature. Feedback electronics are provided which maintain the resistance, and hence the temperature, constant. This is known as the constant-temperature mode. A bridge circuit provides the current necessary to balance the heat losses from the rod. By monitoring this current it is possible to characterize these heat losses which vary with the flow velocity over the rod, the thermal conductivity of the gases surrounding the rod, and the fluid temperature. (Bradshaw, 1971)

The most common use of hot-films is for velocity measurement in a single fluid where proper calibration allows the measured heat losses to be related to velocity. Brown and Rebollo (1972) showed that these devices could be utilized for accurate concentration measurements in isothermal binary gas mixtures by placing the hot-film in the flow generated by extracting gases through a small orifice with a sufficient backing pressure that the gas becomes sonically choked. In this case the velocity only depends on the fluid properties. Since the flow velocity is always constant for a given composition, it is possible to calibrate the instrument with mixtures of the two gases having a range of concentration, and then make accurate concentration measurements in unknown mixtures.

The use of an aspirated hot-film for concentration measurements in the current investigation is complicated by the variations in temperature which occur as the result of the vaporization of the superheated agents and the presence of two-phase flow, which dramatically alters the heat loss behavior of the fluid. For this reason, in the current investigation, these probes were not used for quantitative measurements, but rather provided qualitative indications of the presence of an agent and whether or not a single or two phase fluid was present.

The system employed was commercially available from TSI, Inc. It consisted of a Model 1440-20 aspirating probe used in conjunction with a Model 1053B constant temperature anemometer and Model 1051-2 power supply. The necessary vacuum source for the probe (7 l/m @ 33 kPa) was provided by a small vacuum pump. The probe was placed in a conically shaped aluminum holder to protect it and allow easy mounting. It was positioned near the centerline just downstream of the fifth laser beam by mounting on a plate placed in the flow. It can be seen in the photograph in Figure 85. The voltage output of the anemometer circuit was recorded in the manner described below.

3.5.2.5 Data Acquisition System. The data acquisition requirements for this experiment were demanding. Counting the sensors employed within the vessel, a maximum of eleven sensors were used for a single run. The processes of interest occur at submillisecond time scales. A data acquisition rate of 25 kHz per channel was ultimately used. Note that this corresponds to a total maximum data rate of 275 kHz. Total data collection times varied up to a maximum of 2 s.

The design of the agent release vessel presented an additional difficulty. Due to variations in the pressure required to rupture the disk and the need to flow the pressurization nitrogen into the vessel at a reasonably slow rate, it was not possible to know exactly when the experiment would be initiated. This meant that it was necessary to "trigger" data acquisition using some property of the experiment itself. It was also desirable to record some data prior to the initiation of the experiment in order to provide baselines. This was done by continuously recording the data until a trigger was received and then saving a specified number of data points before and after the trigger signal. This type of data acquisition is referred to as "pretriggering."

The system chosen for the experiments was the Flash 12-Model 1 digitizer from Strawberry Tree. This system provides 16 channels of 12 bit data acquisition at a maximum total data rate of 1 MHz. Voltage ranges can be specified for each channel, and provisions are available for making thermocouple measurements. A daughter board was attached which provided a total high-speed memory of 1 Mbyte. The board was mounted in a 486 personal computer, and data acquisition functions were controlled using Workbench 4.0 software.

The system was operated in the pretrigger mode with the trigger signal provided by the near-total attenuation of laser #1 which was located immediately downstream of the vessel orifice. All of the transducer outputs described above as well as those internal to the vessel (see Section 3.4.2.) were connected to the digitizer, and the voltage ranges adjusted to match the expected signals. Following the conclusion of an experiment, the data was stored for later analysis using SigmaPlot 5.0 software.

3.5.2.6 Test Conditions. These experiments were performed in conjunction with the release experiments summarized in Section 3.4. The majority of these experiments were downward releases at room temperature using nominally 4.1 MPa burst disks and a vessel orifice of 19.1 mm. However, additional runs were performed with a cooled vessel exhausting into a room temperature environment, using burst disks set for higher and lower pressure, and smaller orifices. In a few cases, a half-meter extension tube was attached to the vessel. In this case, the near-field pressure measurements were not made, but the transmitted intensities of the three downstream lasers, the downstream dynamic pressure, and the aspirated hot-film response were recorded. Some measurements were also made for upward releases. In this case laser #5 was placed just above the vessel orifice and provided the timing for the experiment.

3.5.3 Experimental Results

3.5.3.1 High-Speed Filming. The high-speed films provide excellent qualitative insights into the behavior of the agents upon release from the pressure vessel. Figure 86 and Figure 87 show time series taken from films recorded at 2000 frames/s for releases of FC-31-10 and halon 1301. These films were recorded primarily to monitor the behavior of the released agent. The region imaged is 0.19 m (downstream) x 0.33 m (radial). Remarkable differences are observed in the mixing behaviors of the two agents.

The behavior of the FC-31-10 (Figure 86) is summarized as follows. At time 0 the disk bursts and the agent appears as a white plume. During the next 3 ms the agent spreads rapidly in both the radial (maximum of 0.14 m) and axial directions (0.17 m). The flow then develops a mushroom shape which is characteristic of an impulsively started axisymmetric jet. As the flow further

0.0 ms

0.5 ms

1.0 ms

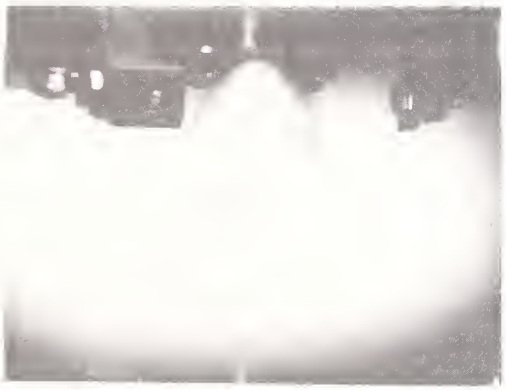

1.5 ms

2.0 ms

2.5 ms

Figure 86. A sequence from a high-speed film (2000 frames/s) of the flow formed by a release of 386 g of FC-31-10 from the vessel. The times indicate the period since the initiation of the release.

3.0 ms

3.5 ms

4.0 ms

4.5 ms

5.0 ms

5.5 ms

Figure 86. (continued) A sequence from a high-speed film (2000 frames/s) of the flow formed by a release of 386 g of FC-31-10 from the vessel. The times indicate the period since the initiation of the release.

6.0 ms

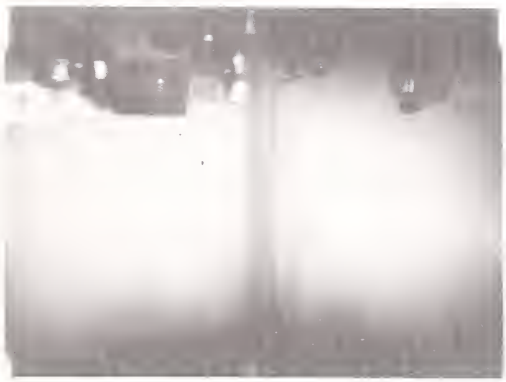

6.5 ms

7.0 ms

7.5 ms

8.0 ms

8.5 ms

Figure 86. (continued) A sequence from a high-speed film (2000 frames/s) of the flow formed by a release of 386 g of FC-31-10 from the vessel. The times indicate the period since the initiation of the release.

9.0 ms

9.5 ms

10.0 ms

10.5 ms

11.0 ms

11.5 ms

Figure 86. (continued) A sequence from a high-speed film (2000 frames/s) of the flow formed by a release of 386 g of FC-31-10 from the vessel. The times indicate the period since the initiation of the release.

12.0 ms

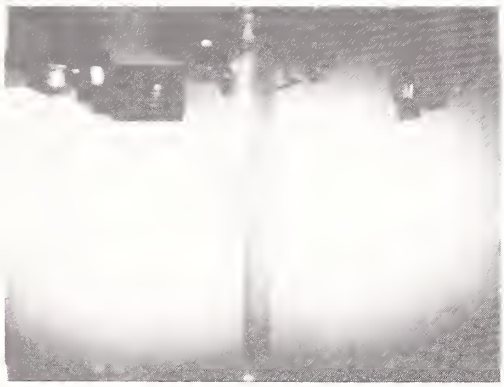

12.5 ms

13.0 ms

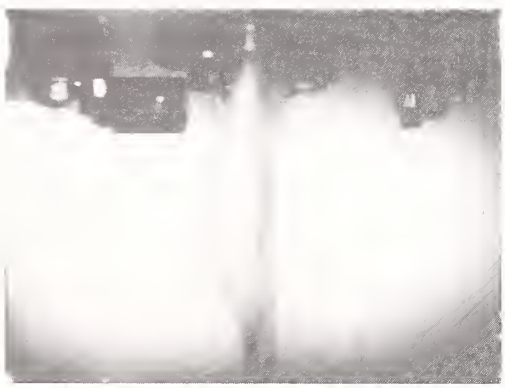

13.5 ms

14.0 ms

14.5 ms

Figure 86. (continued) A sequence from a high-speed film (2000 frames/s) of the flow formed by a release of 386 g of FC-31-10 from the vessel. The times indicate the period since the initiation of the release.

15.0 ms

15.5 ms

16.0 ms

16.5 ms

17.0 ms

17.5 ms

Figure 86. (continued) A sequence from a high-speed film (2000 frames/s) of the flow formed by a release of 386 g of FC-31-10 from the vessel. The times indicate the period since the initiation of the release.

18.0 ms

18.5 ms

19.0 ms

19.5 ms

20.0 ms

20.5 ms

Figure 86. (continued) A sequence from a high-speed film (2000 frames/s) of the flow formed by a release of 386 g of FC-31-10 from the vessel. The times indicate the period since the initiation of the release.

21.0 ms

21.5 ms

22.0 ms

22.5 ms

23.0 ms

23.5 ms

Figure 86. (continued) A sequence from a high-speed film (2000 frames/s) of the flow formed by a release of 386 g of FC-31-10 from the vessel. The times indicate the period since the initiation of the release.

24.0 ms

24.5 ms

25.0 ms

25.5 ms

26.0 ms

26.5 ms

Figure 86. (continued) A sequence from a high-speed film (2000 frames/s) of the flow formed by a release of 386 g of FC-31-10 from the vessel. The times indicate the period since the initiation of the release.

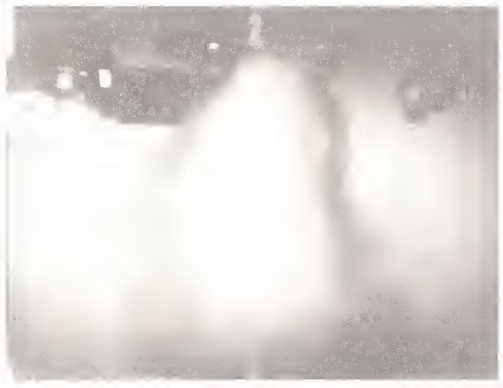

27.0 ms

27.5 ms

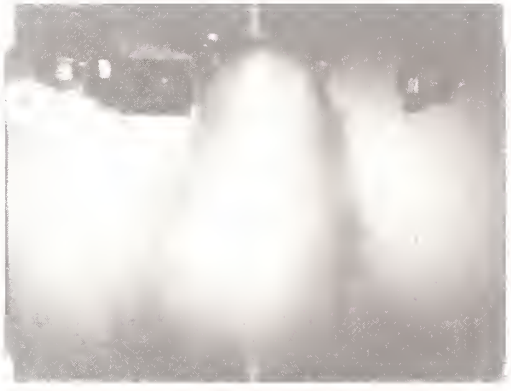

28.0 ms

28.5 ms

29.0 ms

29.5 ms

Figure 86. (continued) A sequence from a high-speed film (2000 frames/s) of the flow formed by a release of 386 g of FC-31-10 from the vessel. The times indicate the period since the initiation of the release.

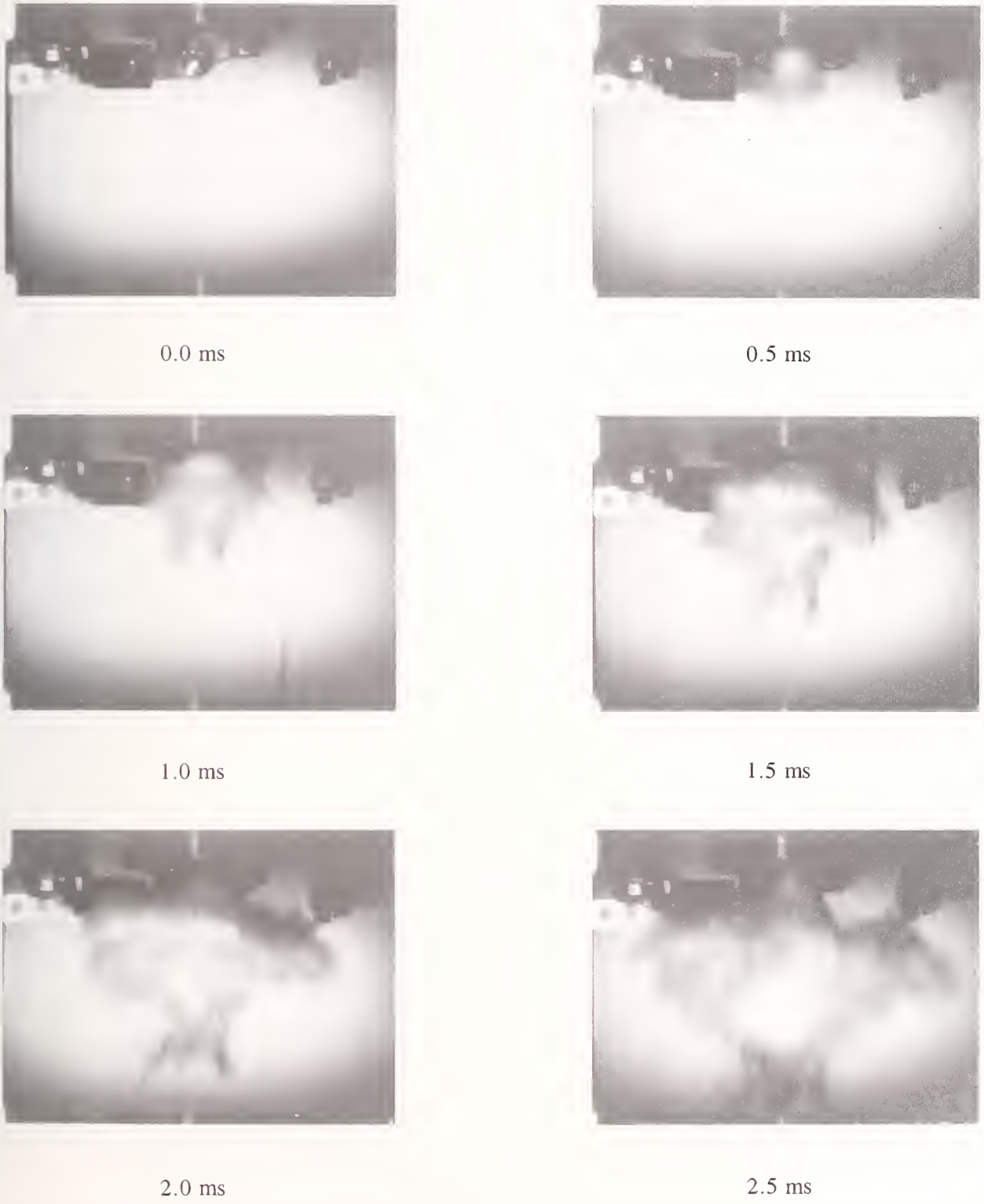

Figure 87. A sequence from a high-speed film (2000 frames/s) of the flow formed by a release of 270 g of halon 1301 from the vessel. The times indicate the period since the initiation of the release.

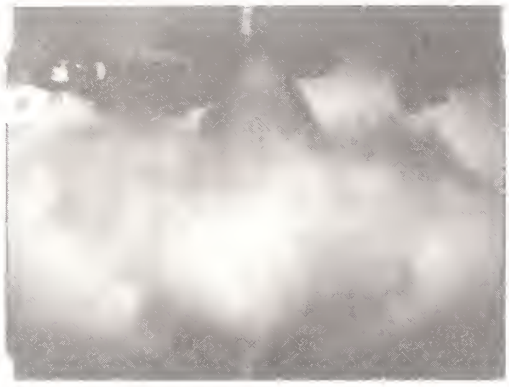

3.0 ms

3.5 ms

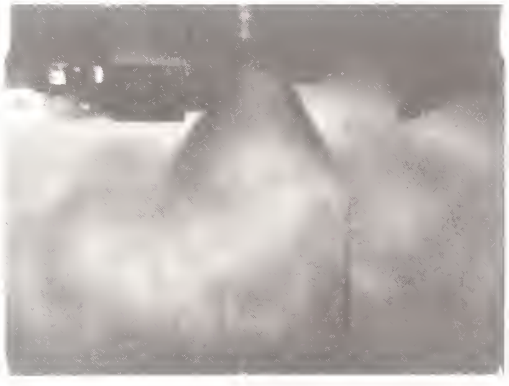

4.0 ms

4.5 ms

5.0 ms

5.5 ms

Figure 87. (continued) A sequence from a high-speed film (2000 frames/s) of the flow formed by a release of 270 g of halon 1301 from the vessel. The times indicate the period since the initiation of the release.

6.0 ms

6.5 ms

7.0 ms

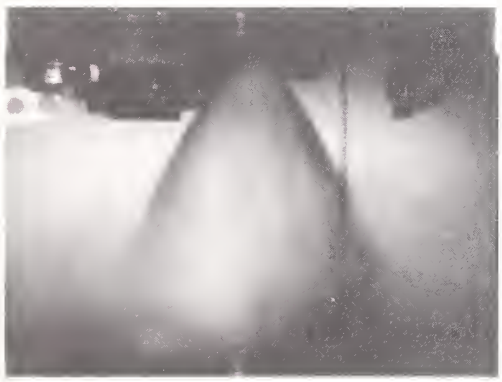

7.5 ms

8.0 ms

8.5 ms

Figure 87. (continued) A sequence from a high-speed film (2000 frames/s) of the flow formed by a release of 270 g of halon 1301 from the vessel. The times indicate the period since the initiation of the release.

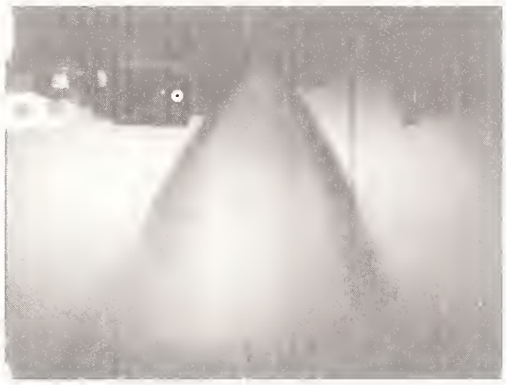

9.0 ms

9.5 ms

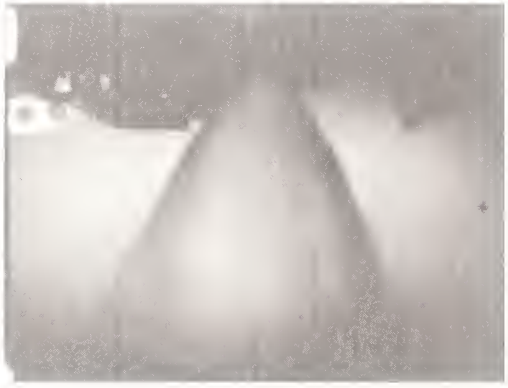

10.0 ms

10.5 ms

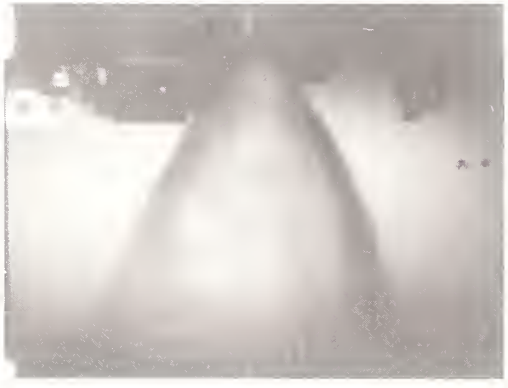

11.0 ms

11.5 ms

Figure 87. (continued) A sequence from a high-speed film (2000 frames/s) of the flow formed by a release of 270 g of halon 1301 from the vessel. The times indicate the period since the initiation of the release.

12.0 ms

12.5 ms

13.0 ms

13.5 ms

14.0 ms

14.5 ms

Figure 87. (continued) A sequence from a high-speed film (2000 frames/s) of the flow formed by a release of 270 g of halon 1301 from the vessel. The times indicate the period since the initiation of the release.

15.0 ms

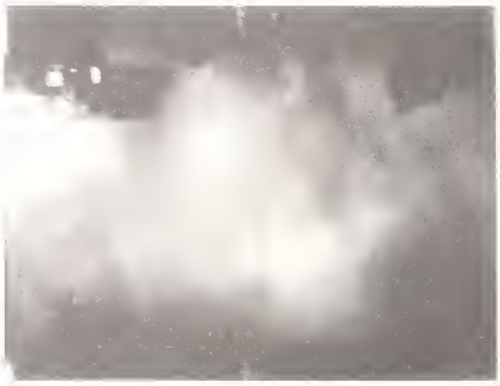

15.5 ms

16.0 ms

16.5 ms

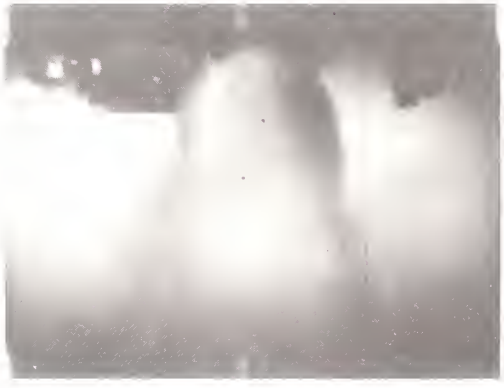

17.0 ms

17.5 ms

Figure 87. (continued) A sequence from a high-speed film (2000 frames/s) of the flow formed by a release of 270 g of halon 1301 from the vessel. The times indicate the period since the initiation of the release.

18.0 ms

18.5 ms

19.0 ms

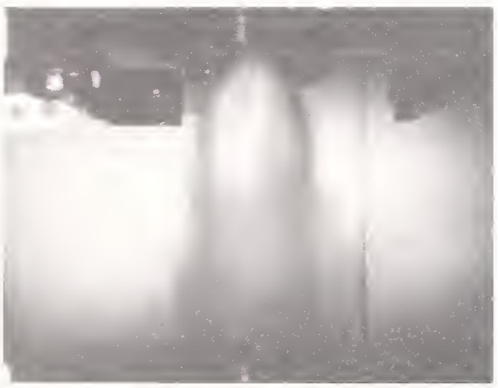

19.5 ms

20.0 ms

20.5 ms

Figure 87. (continued) A sequence from a high-speed film (2000 frames/s) of the flow formed by a release of 270 g of halon 1301 from the vessel. The times indicate the period since the initiation of the release.

21.0 ms

21.5 ms

22.0 ms

22.5 ms

23.0 ms

23.5 ms

Figure 87. (continued) A sequence from a high-speed film (2000 frames/s) of the flow formed by a release of 270 g of halon 1301 from the vessel. The times indicate the period since the initiation of the release.

24.0 ms

24.5 ms

25.0 ms

25.5 ms

26.0 ms

26.5 ms

Figure 87. (continued) A sequence from a high-speed film (2000 frames/s) of the flow formed by a release of 270 g of halon 1301 from the vessel. The times indicate the period since the initiation of the release.

27.0 ms

27.5 ms

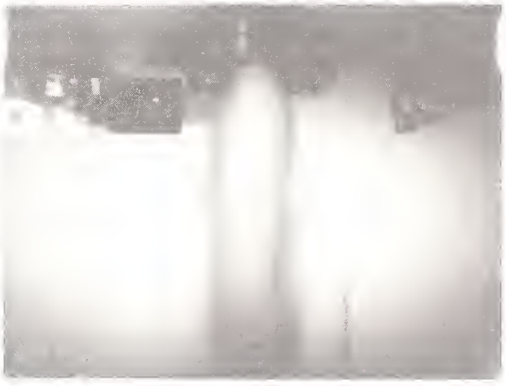

28.0 ms

28.5 ms

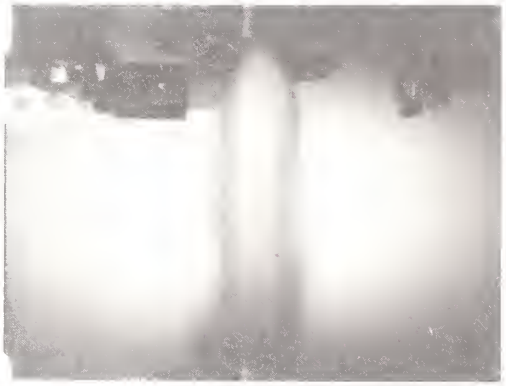

29.0 ms

29.5 ms

Figure 87. (continued) A sequence from a high-speed film (2000 frames/s) of the flow formed by a release of 270 g of halon 1301 from the vessel. The times indicate the period since the initiation of the release.

develops, the neck of the flow grows thinner until at roughly 6 ms following release the agent is exiting the vessel as a liquid stream which exists over the entire observed downstream length. At approximately 10 ms partial flashing of the liquid jet occurs near the orifice and subsequently grows in time and space. Even after 15 ms the two-phase flow is compact and has not spread substantially over the observed downstream distance. At later times the jet begins to spread slowly until a very strong expansion occurs 21 ms after release. This point corresponds closely to the emptying time estimated from pressure measurements recorded internal to the vessel. This strong flashing behavior lasts a few milliseconds before only condensed vapor in the nitrogen flow is observed to exit the vessel.

The halon 1301 (Figure 87) is released in a very different way. The initial release of the agent from the bottle is much more violent than observed for the FC-31-10. The flow develops fingers which look almost like an explosion. By 3.5 ms the agent covers a wider radial extent (approximately 0.29 m) than it has moved downstream. The flow near the nozzle seems to be assuming a conical shape. The jet continues to spread in the radial direction as the flow field moves beyond the farthest observed downstream position. For the next 8 ms the flow seems to settle down into a flow condition for which the flow leaves the nozzle and spreads rapidly with downstream distance. The spreading angle is roughly 60°. During this period the material ejected to large radial positions at earlier times seems to have evaporated. This behavior can be contrasted to that for FC-31-10 where the released agent appears to form a liquid stream during this phase of the release. Fourteen milliseconds after the release a very strong flashing is observed which disperses material over extremely wide radial distances for short downstream distances. Again, internal pressure measurements indicate that this is roughly the time when all of the liquid has been emptied from the vessel.

Films were recorded for all of the agents over the smaller 0.40 m × 0.10 m view area. Table 5 lists measured values of radial and axial velocities calculated from the films for the ten proposed alternative agents which are liquid at room temperature and halon 1301. Due to the limited number of measurements the data do not show definite trends. However, it is clear that the axial near-field velocities increase with decreasing boiling point (*i.e.*, the amount of superheating).

3.5.3.2 Near-Field Dynamic Pressure Measurements. These measurements were intended to test two aspects of the released agent behaviors. The first was whether or not there were shock waves generated by either the bursting of the disk or the sudden flashing of the liquid. The second was to detect the presence of the agent at the transducer and, if possible, estimate the degree of vaporization.

The high-speed films showed that during an agent release there were two flashings which might expel liquid to a distance where it could strike the pressure transducer. Time records of pressure traces all show signals corresponding to the second flashing near the end of the release. The lower boiling-point liquids also showed pressure rises shortly after the disk burst (recall that time 0 is defined as the time when laser #1 is strongly attenuated). Interestingly, no pressure changes were generally detected for the higher boiling-point liquids at short times.

Figure 88 shows a time plot of pressure from the near-field pressure transducer for two room temperature releases of HFC-236fa from a vessel which is 2/3 full of the liquid agent. The two sets of data are in good agreement. No pressure increases are observed until near the time when the fluid is emptied from the vessel. Apparently, the flashing observed in the high-speed films when the disk burst did not generate shock waves or impart sufficient momentum to the HFC-236fa to reach the pressure transducer which was 46 mm from the centerline. In contrast, the strong flashing observed near the ends of the releases generated a very large dynamic pressure at the transducer. Table 6 lists the maximum pressures observed for the two releases.

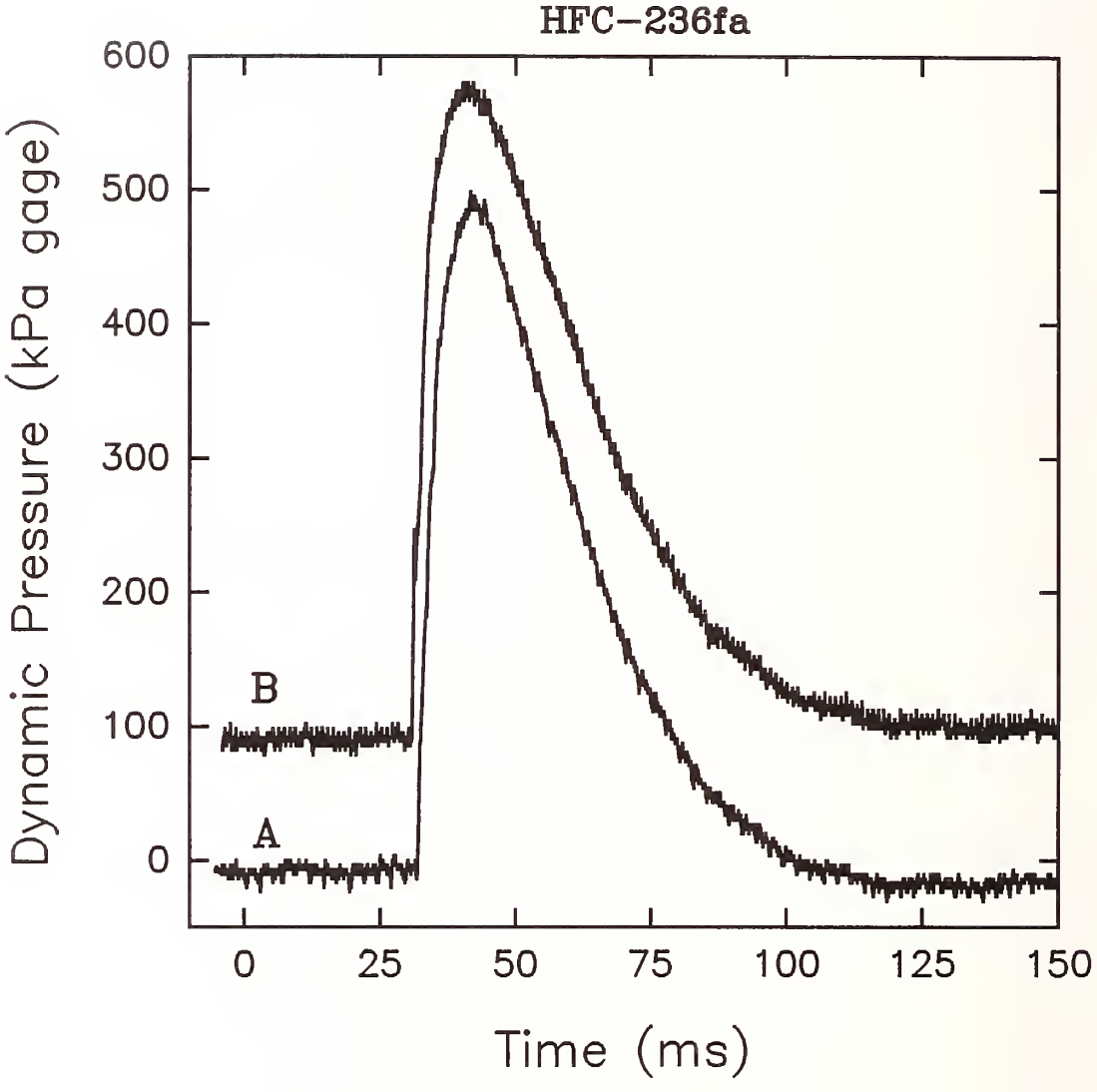

Figure 88. Two time traces of near-field dynamic pressure for releases of HFC-236fa. For clarity, trace B is offset by 100 kPa. Conditions are: A, 464 g of agent, release pressure of 4.30 Mpa; B, 471 g agent, release pressure of 4.51 MPa.

Table 5. Values of Velocity Determined from High Speed Films of Liquid Agents Released from Pressurized Vessels

AGENT	Radial Velocity Frame 2-3 (m/s)	Radial Velocity Frame 3-4 (m/s)	Axial Velocity Frame 2-3 (m/s)	Axial Velocity Frame 3-4 (m/s)
HFC-236fa	9	[a]	42	57
FC-31-10	12	2.4	49	[a]
FC-318	14	0	67	[a]
HCFC-124	10	0	57	[a]
HFC-227ea	[a]	2	55	57
HFC-134a	10	5	69	63
FC-218	6	11	86	[a]
HCFC-22	[a]	[a]	58.1	49.3
HFC-125	2.1	18	76	[a]
HFC-125/HFC-32 mixture	17	9	80	[a]
halon 1301	11	1.5	> 80	[a]

[a] Measurements could not be made for these conditions due to poor contrast in the images

A number of releases with various vessel fill levels have been made for FC-31-10. Figure 89 shows time plots of pressures from the near-field pressure transducer for three runs having initial vessel fill levels of 1/3, 1/2, and 2/3. The observed behaviors are very similar to those found for HFC-236fa. Table 6 summarizes the pressure increases observed during the second flashings for a number of experiments. There are no clear trends in the maximum pressure with burst pressure or the mass of agent in the bottle. A range of values are observed which are likely to be characteristic of run-to-run variations.

Figure 90 shows two pressure time traces for FC-318. The results are similar to those for HFC-236fa and FC-31-10 except that one of the pressure traces has a slight jump with a maximum of 41 kPa starting 3.48 ms after the agent release. This pressure rise indicates that for this release the initial flashing behavior was strong enough to eject material as far as the pressure transducer. A total of six experiments were run with this agent. Only one recorded the initial flashing behavior. Pressure increases associated with the second flashing are listed in Table 6. A fairly wide range of pressures is observed.

Two time traces for the near-field pressure behavior are shown in Figure 91 for HCFC-124. No signals were recorded immediately following the opening of the vessel orifice. The relevant data for observed dynamic pressures as a result of the second flashing are summarized in Table 6.

Table 6. Maximum Dynamic Pressures Observed by the Near-Field Transducer During the Second Flashings of Agent Releases

Agent	Mass of Agent (g)	Internal Pressure at Release (MPa)	Maximum Dynamic Pressure (kPa)
HFC-236fa	464	4.30	499
	471	4.51	480
FC-31-10	261	4.50	314
	262	4.45	293
	263	3.98	364
	266	4.33	314
	386	4.21	448
	387	4.52	397
	495	3.93	557
	515	4.20	312
	520	3.85	315
FC-318	257	3.90	487
	270	4.25	469
	404	3.92	516
	501	4.43	647
	505	3.99	561
	521	4.34	629
HCFC-124	465	4.30	708
	462	4.05	668
HFC-227ea	476	4.45	900
	489	4.41	792
HFC-134a	419	4.21	1176
	418	4.13	1101
	423	4.38	1317

Table 6. (continued) Maximum Dynamic Pressures Observed by the Near-Field Transducer During the Second Flashings of Agent Releases.

Agent	Mass of Agent (g)	Internal Pressure at Release (MPa)	Maximum Dynamic Pressure (kPa)
FC-218	468	4.28	559
	463	4.06	421
	460	4.58	579
HCFC-22	412	2.81	572
	421	4.48	1402
	417	4.52	1271
HFC-125	423	4.24	1047
	403	4.19	367
	416	4.07	566
HFC-125/HFC-32 mixture	375	4.36	1508
	358	4.31	1626
halon 1301	270	4.43	602
	554	4.36	113

Figure 92 and Table 6 contain similar results for HFC-227ea. One of the releases showed a quite substantial pressure increase starting 1.12 ms after the initial release of the agent. The pressure reached a maximum of 304 kPa.

Results for HFC-134a are given in Figure 93 and Table 6. Three sets of data were recorded for this agent. Two of these showed pressure increases (169, 102 kPa) shortly after (1.80 ms and 1.52 ms) the initiation of the experiments. The experiment which isn't shown in Figure 93 did not have a pressure increase at the short delay time.

Three sets of data were also recorded for FC-218. Figure 94 and Table 6 summarize the findings. As found for the HFC-134a, two of the releases resulted in small pressure increases (28 and 31 kPa) shortly following the release time (1.92 and 1.60 ms). As can be seen by comparing entries in Table 6, the pressure increases as a result of the second flashing observed for the FC-218 are considerably smaller than those found for the HFC-134a.

HCFC-22 generated pressure traces which were quite complicated and variable. Examples of two of the traces are shown in Figure 95. The pressure time histories are quite different than those for the agents discussed up to this point. Not only are pressure increases observed near the beginnings and ends of the releases, there also indications of some flashing behavior at intermediate times. Table 6 summarizes the findings for three releases of HCFC-22. The dynamic pressures observed for the releases using nominal 4.14 burst disks were the highest recorded during the study. The pressure increase was found to be considerably smaller for the one case using a lower-pressure burst disk (see Table 6).

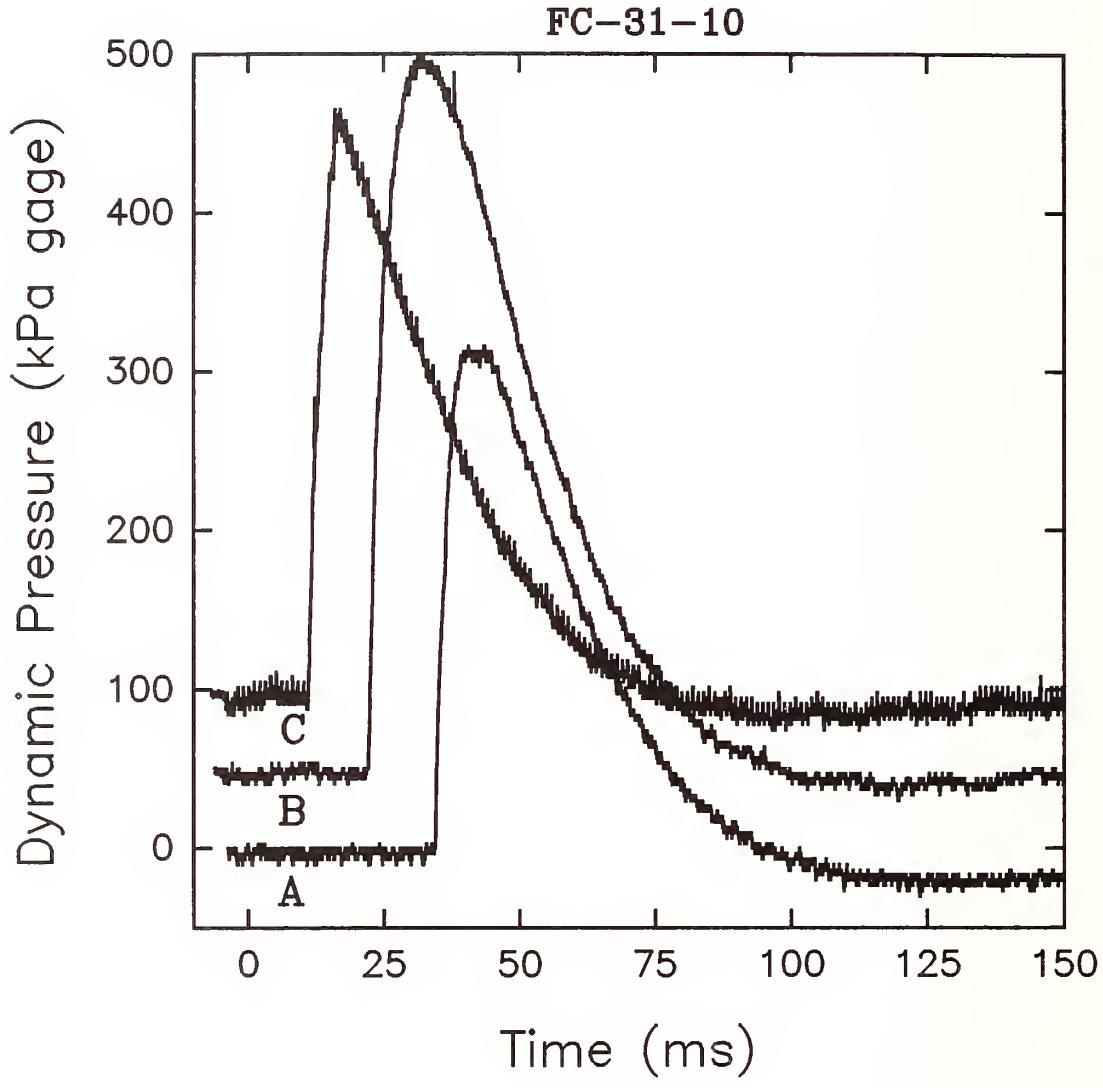

Figure 89. Three time traces of near-field dynamic pressure for releases of FC-31-10. Traces B and C are offset by 50 kPa. Conditions: A, 515 g, release pressure 4.20 MPa; B, 386 g, release pressure 4.21 MPa; C, 263 g, release pressure of 3.98 MPa.

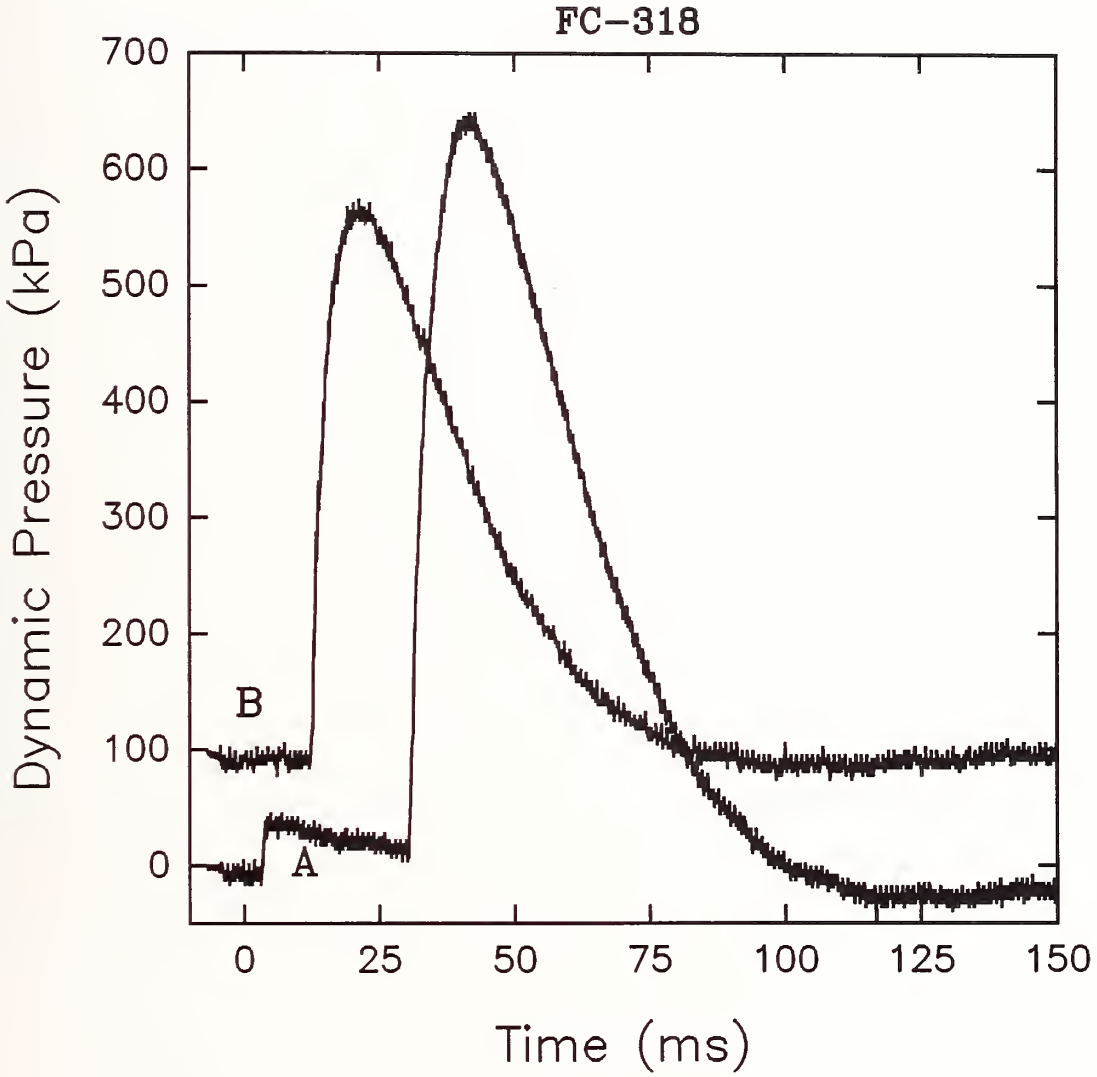

Figure 90. Two time traces of near-field dynamic pressure for releases of FC-318. Trace B is offset by 100 kPa. Conditions: A, 501 g, release pressure 4.43 MPa; B, 270 g, release pressure 4.25 MPa.

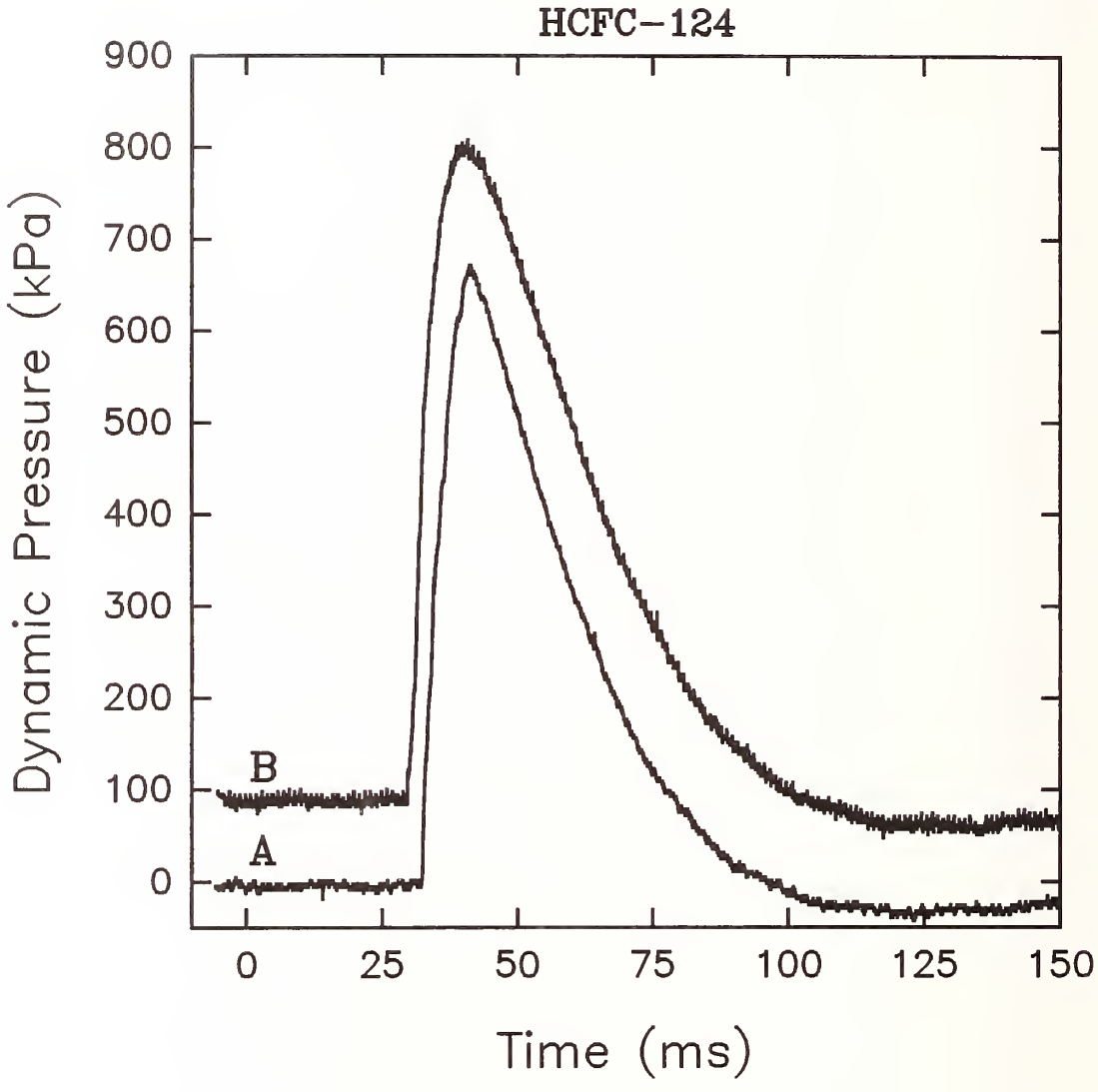

Figure 91. Two time traces of near-field dynamic pressure for releases of HCFC-124. Trace B is offset by 100 kPa. Conditions: A, 465 g, release pressure 4.30 MPa; B, 462 g, release pressure 4.05 MPa.

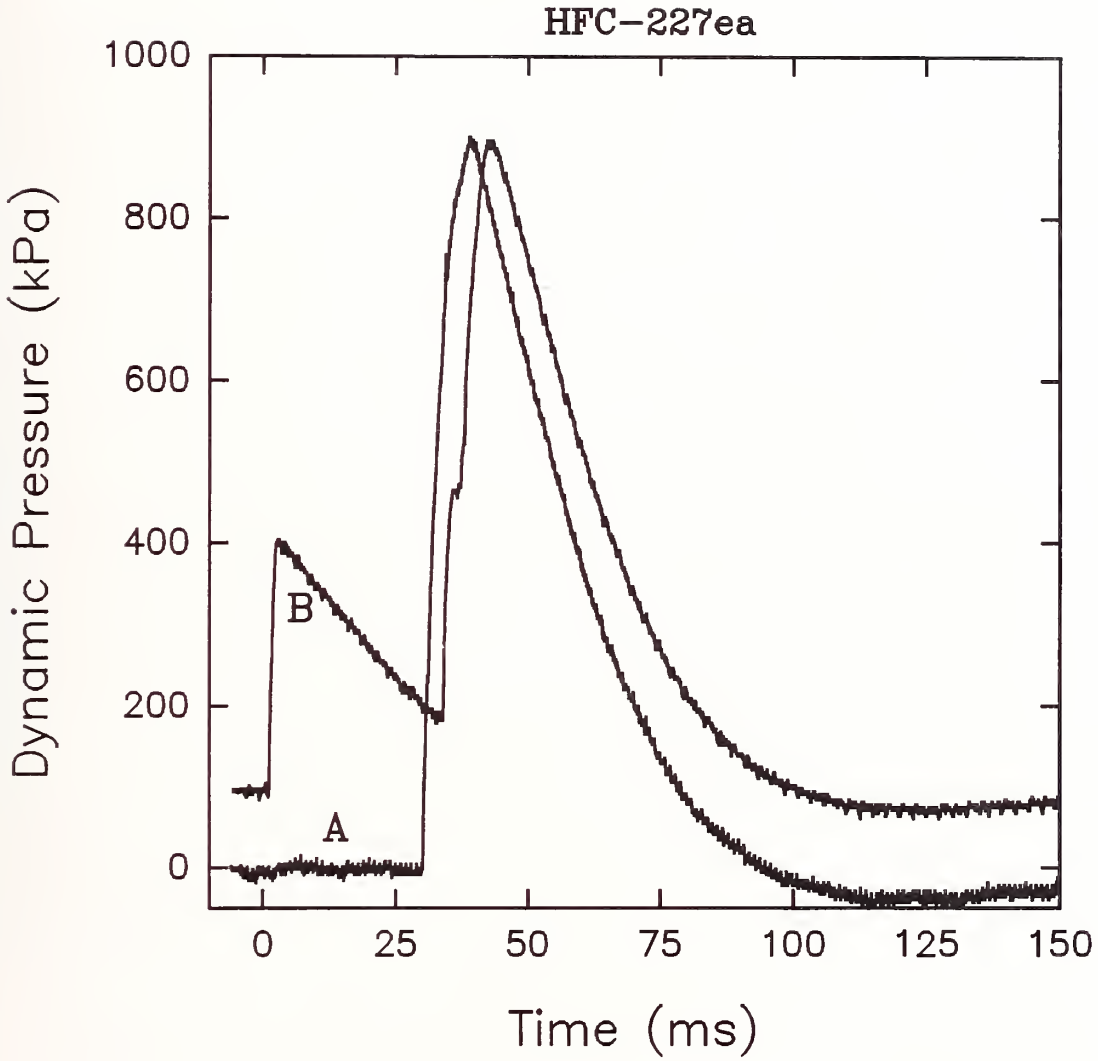

Figure 92. Two time traces of near-field dynamic pressure for releases of HFC-227ea. Trace B is offset by 100 kPa. Conditions: A, 476 g, release pressure 4.45 MPa; B, 489 g, release pressure 4.41 MPa.

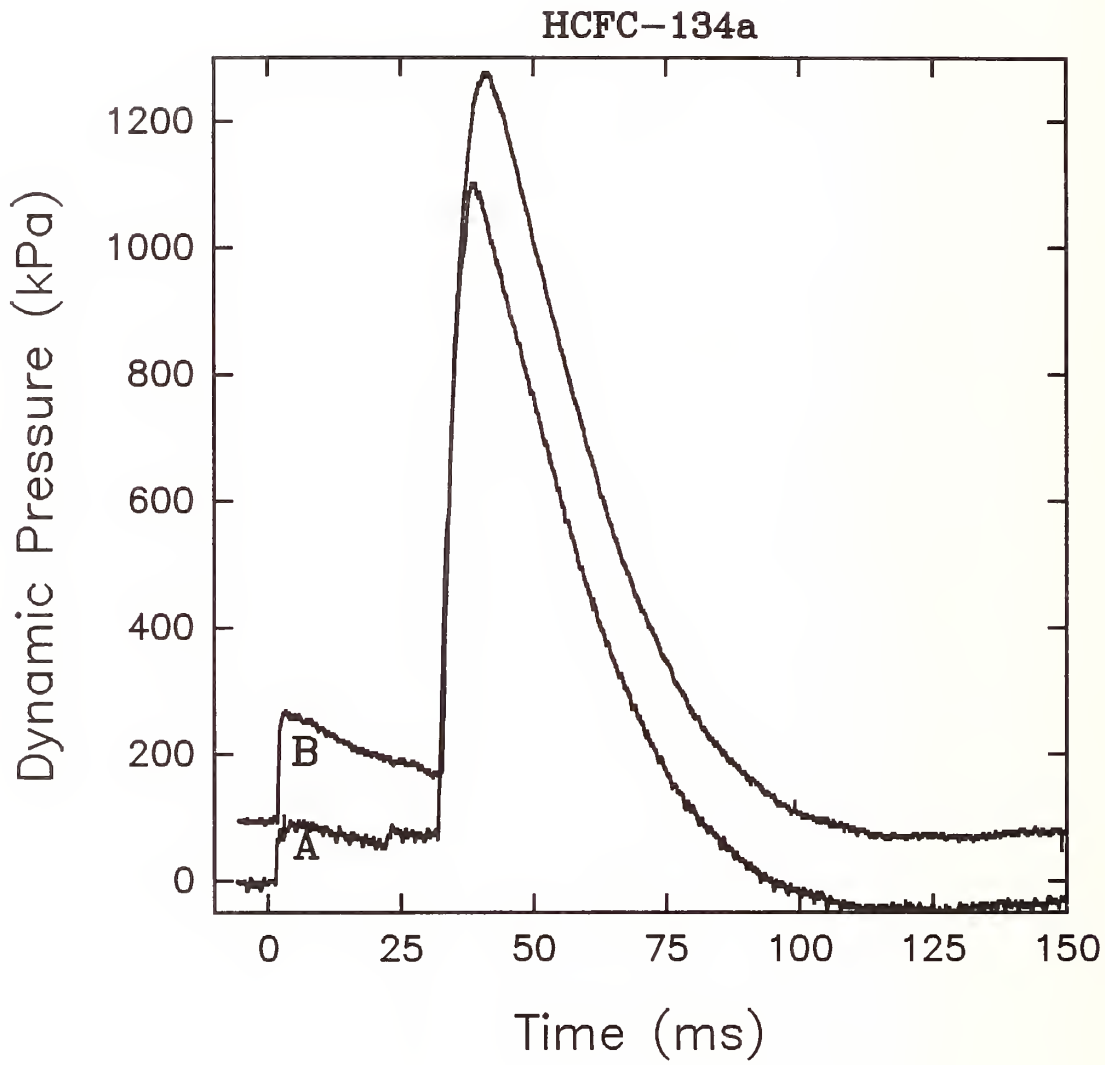

Figure 93. Two time traces of near-field dynamic pressure for releases of HFC-134a. Trace B is offset by 100 kPa. Conditions: A, 423 g, release pressure 4.38 MPa; B, 418 g, release pressure 4.13 MPa.

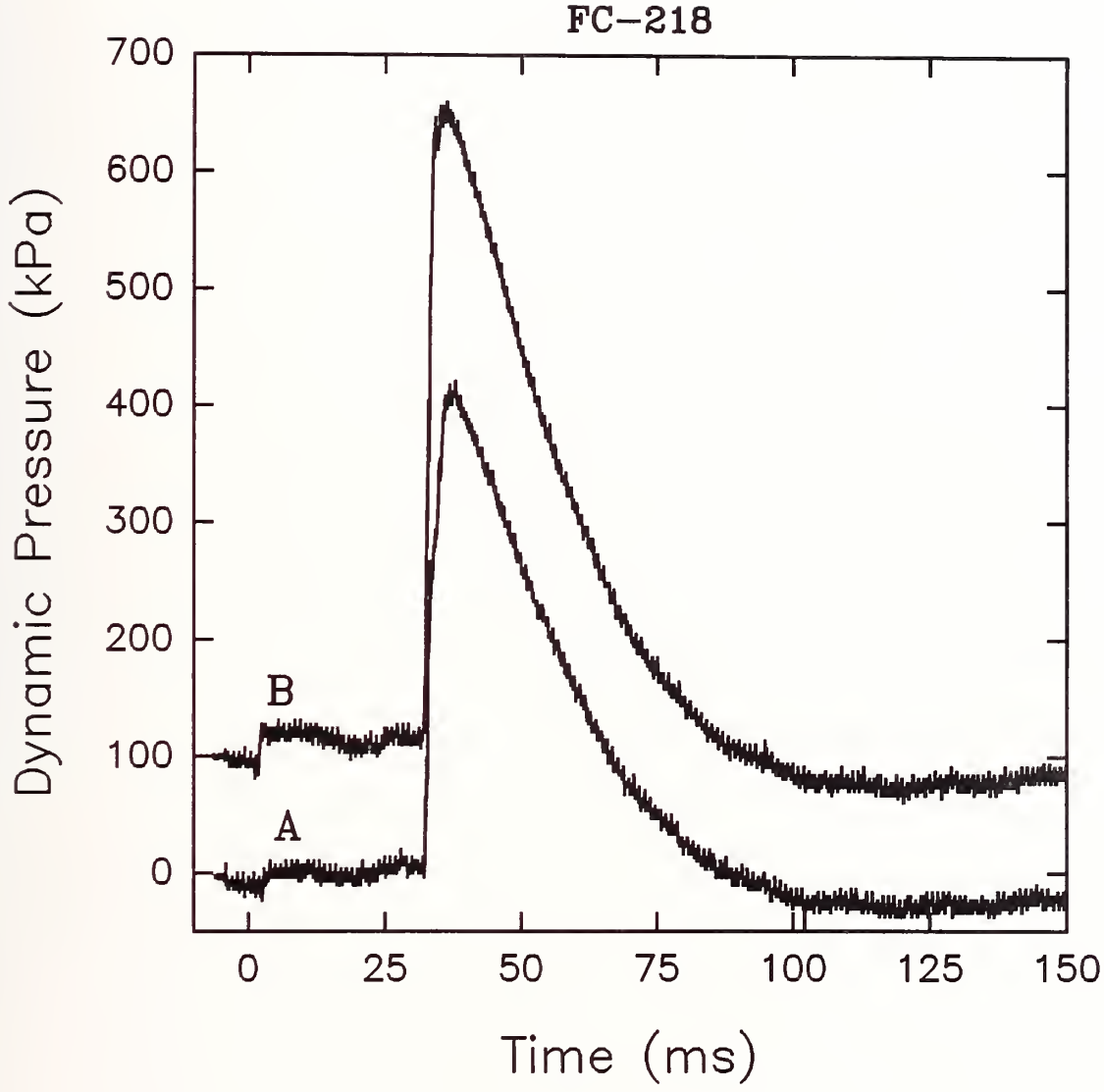

Figure 94. Two time traces of near-field dynamic pressure for releases of FC-218. Trace B is offset by 100 kPa. Conditions: A, 463 g, release pressure 4.06 MPa; B, 468 g, release pressure 4.28 MPa.

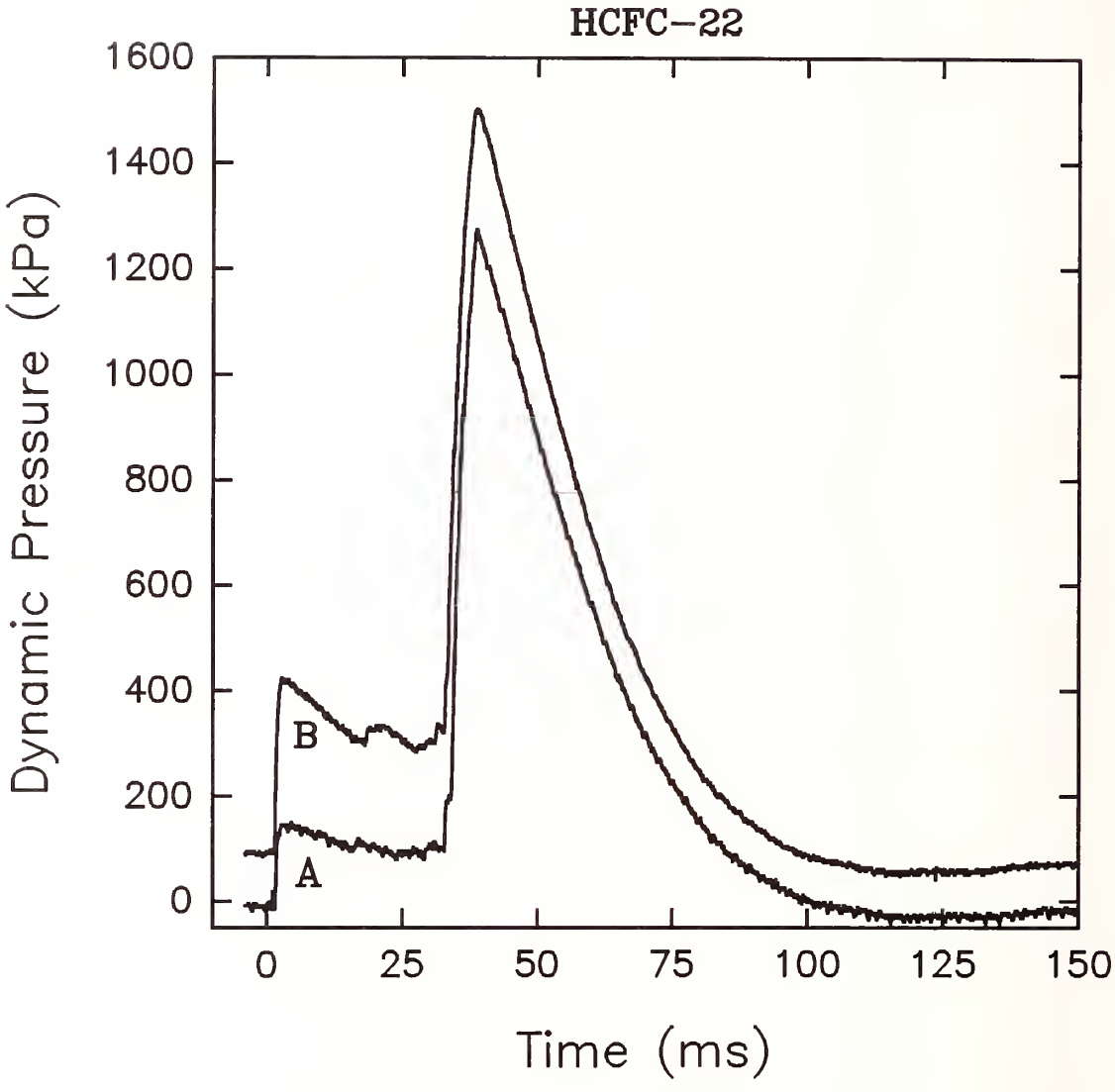

Figure 95. Two time traces of near-field dynamic pressure for releases of HCFC-22. Trace B is offset by 100 kPa. Conditions: A, 412 g, release pressure 4.52 MPa; B, 417 g, release pressure 4.48 MPa.

HFC-125 also generated pressure traces which varied from release to release. Figure 96 shows two examples. Both plots indicate that flashing occurred at the beginning and end of the releases, but there were indications that flashing also took place at intermediate times. The third set of data summarized in Table 6 was similar. Each release has a pressure rise at early times. The maximum pressures observed were 20, 81, and 122 kPa.

The HFC-125/HFC-32 mixture has the lowest boiling point of all of the potential replacement agents except FC-116. Time traces for two releases of this agent (see Figure 97) indicate that the liquid tends to flash strongly during most of time the liquid is exiting the vessel. Pressure increases (249 and 293 kPa) first appear immediately (1.24 and 1.12 ms) following the release. These are followed by a short quiet period before the dynamic pressure begins to increase rapidly. The maximum pressure readings occurred near the end of the releases, reaching values greater than 1500 kPa. Table 6 summarizes the findings.

For comparison purposes, releases of halon 1301 were also performed. Figure 98 and Table 6 summarize the findings. Note that trace B was recorded for a release in which the vessel was only 1/3 full of liquid. In both cases, the pressure traces indicate that flashing occurred immediately following (1.16 and 1.84 ms) the opening of the orifice. Early pressure increases of 91 and 43 kPa were observed. Trace A indicates that the liquid flashed near the orifice during most of the release. The flashing associated with the emptying of the vessel is also obvious. Despite the fact that the boiling point of halon 1301 is 20 K lower than for the HFC-125/HFC-32 mixture, the dynamic pressures measured are considerably lower for the halon 1301. The maximum pressures observed due to the second flashing are quite different for the two experiments shown in Figure 98.

These measurements will be discussed further in Section 3.5.4. However, a few general conclusions can be drawn from the results summarized in Table 6 and the figures. The data for the various agents have been presented in order of decreasing boiling point. Only for the lowest boiling-point agents are dynamic pressures generated by the flashing observed immediately following the opening of the burst disk. For agents having boiling points higher than HCFC-22 (232 K), flashing is only detected near the beginning and end of the releases. Pressure increases observed for HCFC-22 and agents having lower boiling points suggest that strong flashing is taking place at intermediate times as well. With the exceptions of FC-218, HFC-125, and halon 1301, the pressure increases observed near the time when the vessel empties increase with decreasing boiling point.

3.5.3.3 Laser Attenuation Measurements. Laser attenuation measurements were made at the five downstream positions listed in Table 7 for each of the agents investigated. Figure 99 through Figure 109 show examples of the laser signals recorded for releases of all of the alternative agents, with the exception of FC-116, and halon 1301. In each case the vessel was 2/3 full of the liquid agent and a nominal 4.14 MPa burst disk was used.

For the higher boiling-point agents, the arrival of the agent at a laser beam fully extinguishes the beam nearly instantaneously (within 40 μs). This is clearly seen in Figure 99 through Figure 104 where sharp drops are seen in the laser intensities at successively later times as the agent moves away from the vessel orifice. Recall that time 0 corresponds to the extinguishment of laser #1. The light extinguishment is the result of scattering by the two-phase flows generated by the releases. For the lower boiling-point agents, the fall off in light intensity with time is not as sharp. This is most clear for lasers #3, #4, and #5 for the halon 1301 release (see Figure 109). This observation is evidence that these liquid agents are evaporating at a sufficient rate on the leading edges of the releases that the two-phase flow is not optically dense enough to fully extinguish the laser beams. Even for the low boiling-point liquids, the laser beams are eventually fully attenuated as the flow develops further.

At varying times following the complete attenuation of the laser beams, the optical density of the flows decreases and the laser beams are partially transmitted. The exact nature of the optical density

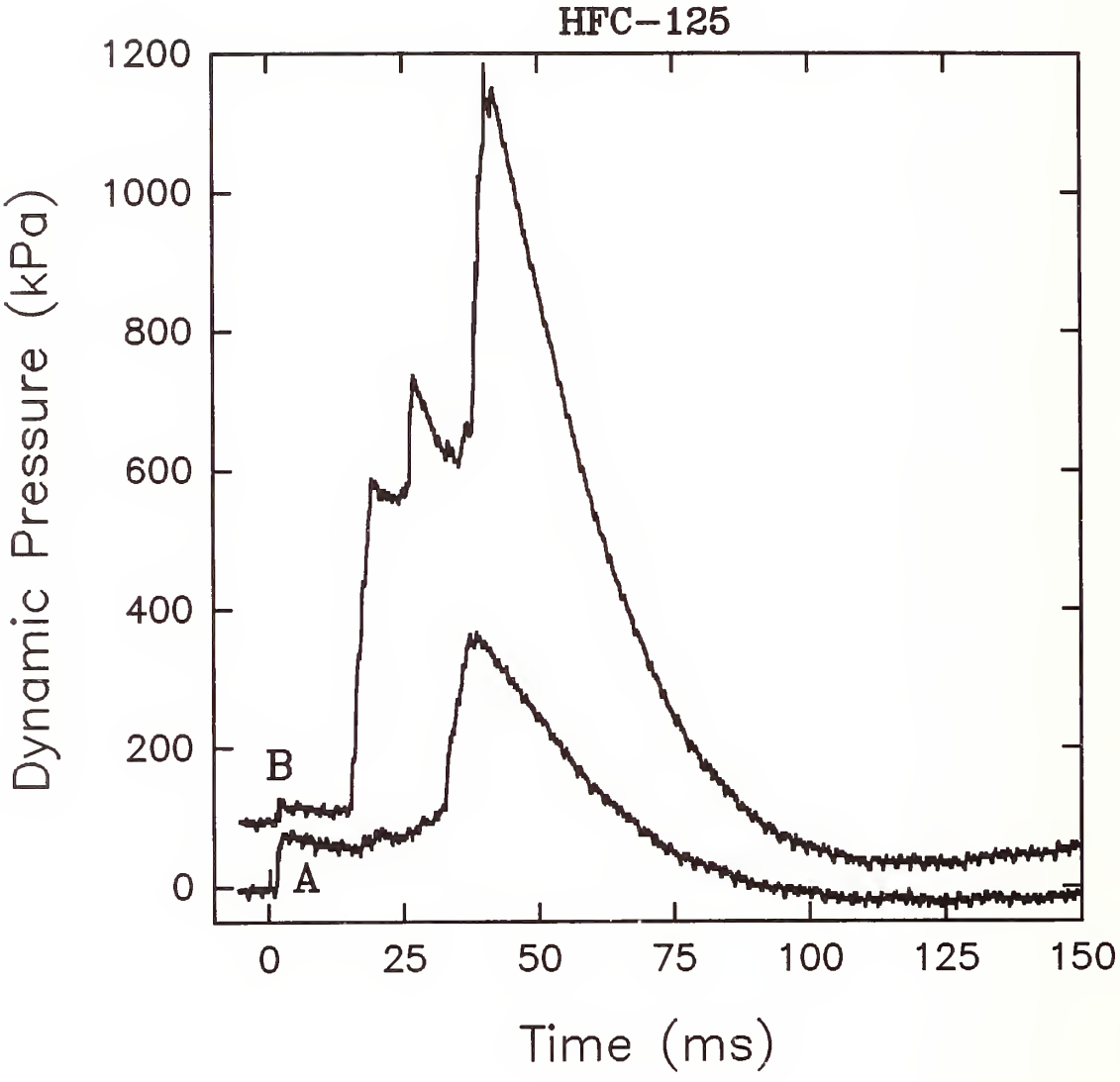

Figure 96. Two time traces of near-field dynamic pressure for releases of HFC-125. Trace B is offset by 100 kPa. Conditions: A, 416 g, release pressure 4.07 MPa; B, 423 g, release pressure 4.24 MPa.

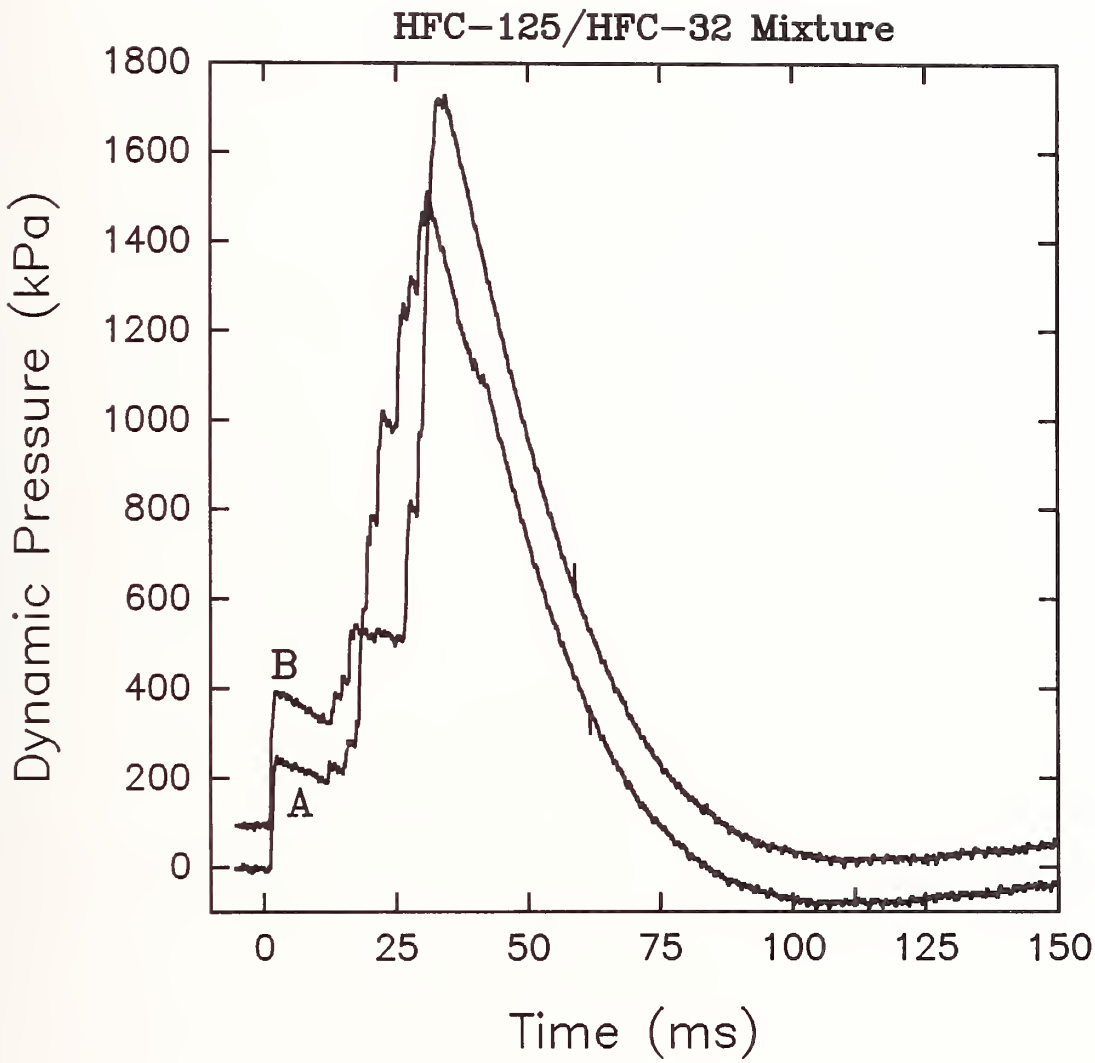

Figure 97. Two time traces of near-field dynamic pressure for releases of the HFC-125/HFC-32 mixture. Trace B is offset by 100 kPa. Conditions: A, 375 g, release pressure 4.36 MPa; B, 358 g, release pressure 4.31 MPa.

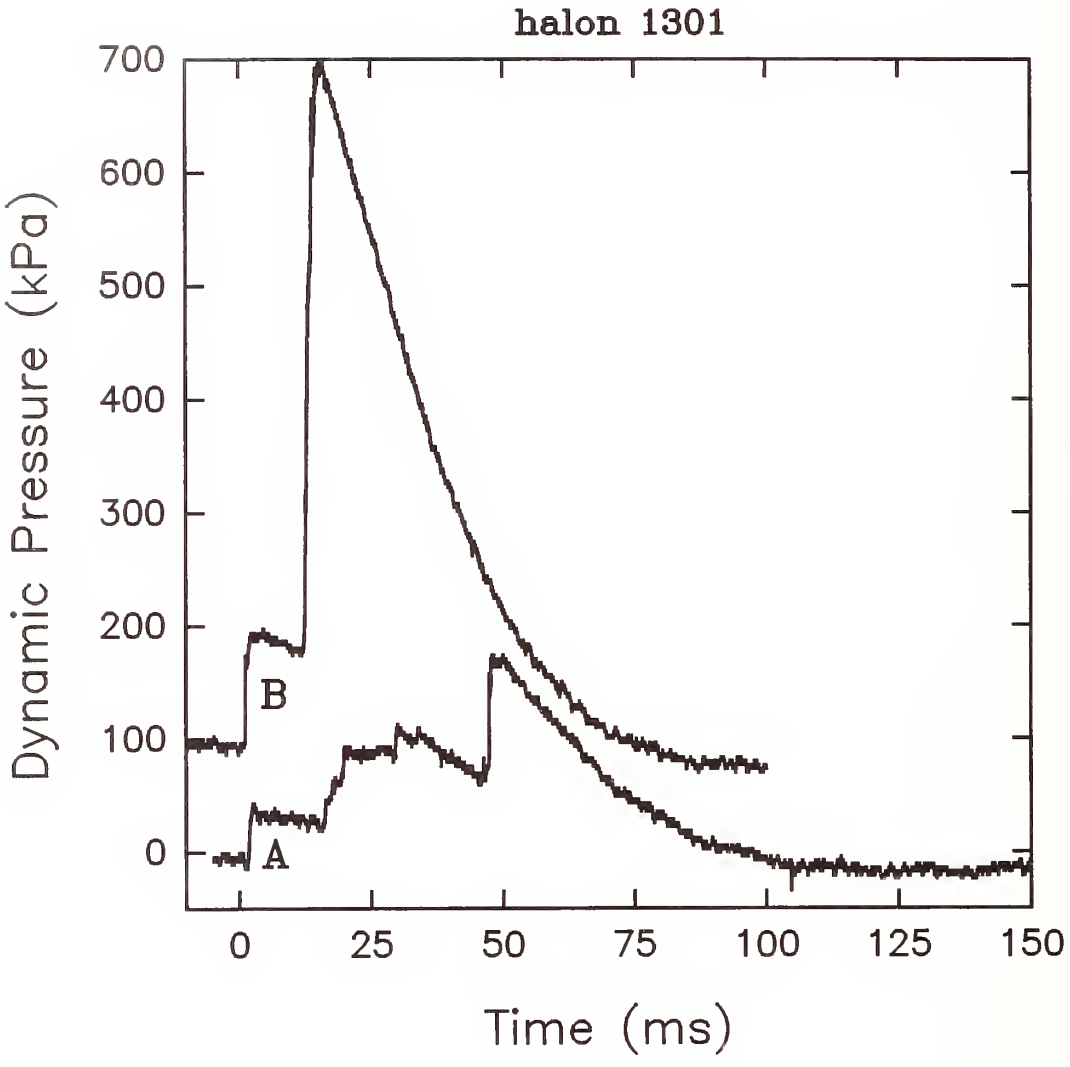

Figure 98. Two time traces of near-field dynamic pressure for releases of halon 1301. Trace B is offset by 100 kPa. Conditions: A, 554 g, release pressure 4.36 MPa; B, 270 g, release pressure 4.43 MPa.

Table 7. Downstream Distances from the Orifice of the Release Vessel for the Five Laser Beams. Distances Between the Laser Beams are also Indicated.

	Downstream Position (m)	Separation Distance (m)
Laser #1	0.0	0.320
Laser #2	0.320	0.335
Laser #3	0.655	0.305
Laser #4	0.960	0.340
Laser #5	1.300	

of a flow is expected to be quite complex. It should be a function of the total mass concentration of the agent, the degree of vaporization of the agent, the size of droplets in the liquid phase, and the degree to which the agent has cooled and condensed water vapor from the surrounding air entrained by the flow. Even so, there are clear trends in the data. The total attenuation of laser #1 lasts for much longer than the agent release time (30-40 ms). The explanation for this behavior is available from the high-speed films of the behavior of the agents inside the vessel (see Section 3.4.1). These show that agent condensation occurs in the nitrogen above the liquid in the vessel during a release. This is attributed to the cooling of the nitrogen and gaseous agent by the adiabatic expansion of the gas (see Section 3.4). Due to the gas used to pressurize the vessel, there is a slow flow of nitrogen even after a release is complete and eventually the condensed agent is swept from the vessel.

The time behaviors of laser #2 transmission for releases of different agents provide insight in the evaporation characteristics of the various agents. For all of the agents except FC-218, the time of total laser beam attenuation is on the order of 60 ms or roughly 50% longer than the total release time of the liquid. The total attenuation time for FC-218 is roughly the same as its release time. The total attenuation times of the beam for laser #3 tend to be somewhat shorter than for laser #2. The recovery of light transmission tends to be quicker for the lower boiling-point agents.

The periods of total light attenuation for lasers #4 and #5 are longer and the recovery of light transmission takes place more slowly. It is likely that this observation is the result of the condensation of water vapor which should require a longer period to evaporate than the agents.

As can be seen in Figure 99 through Figure 109, the arrival time of an agent release at a laser beam is easily detected as a rapid, near-total attenuation of the transmitted light. It is a simple exercise to accurately determine these arrival times. For example, for the data shown in Figure 99 the arrival times are 0, 5.88, 10.55, 15.31, and 20.01 ms for lasers #1-#5, respectively. Since the distances between the laser beams are known, four average velocities can be calculated from these results. Such calculations have been made for the series of releases from 2/3 filled vessels. In the figures which follow, the average velocities are plotted as a function of downstream distance defined as the midpoints of the laser beam locations.

Figure 110 through Figure 120 show results for the ten agents which are liquids at room temperature and halon 1301. There are dramatic differences among the results. HFC-236fa, FC-31-10, FC-318, HCFC-124, and HFC-227ea (Figure 110 through Figure 114) are similar. Average velocities measured at the first measuring station fall in a range of 50 to 60 m/s. As the

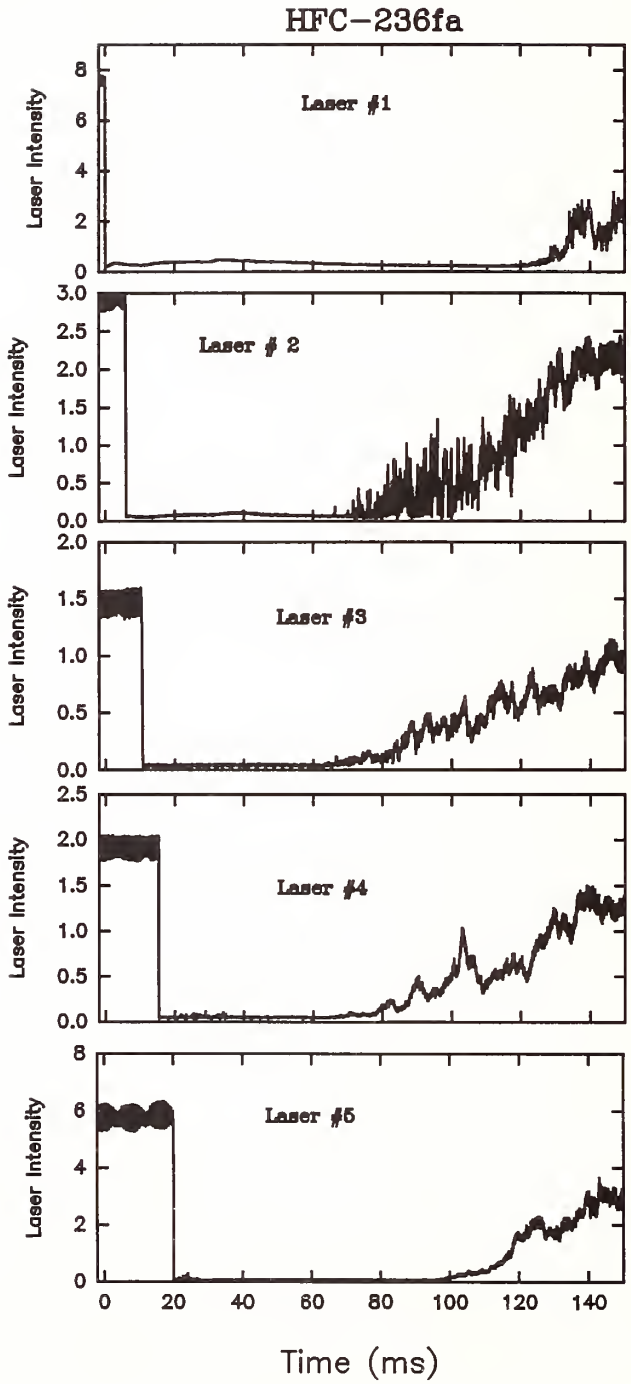

Figure 99. Time behaviors for transmission of laser beams #1-#5 spaced as shown in Table 7 following a release of HFC-236fa at 0 s. Conditions: 464 g agent, 4.30 MPa release pressure.

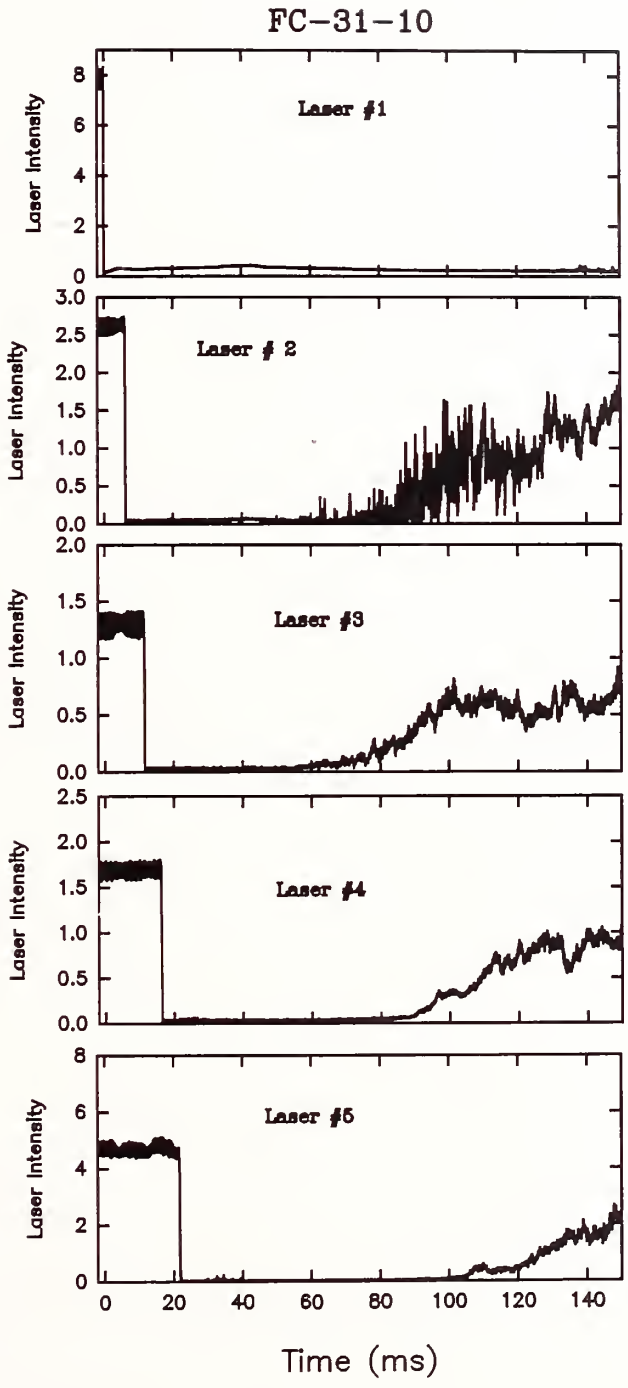

Figure 100. Time behaviors for transmission of laser beams #1-#5 spaced as shown in Table 7 following a release of FC-31-10 at 0 s. Conditions: 520 g agent, 3.85 MPa release pressure.

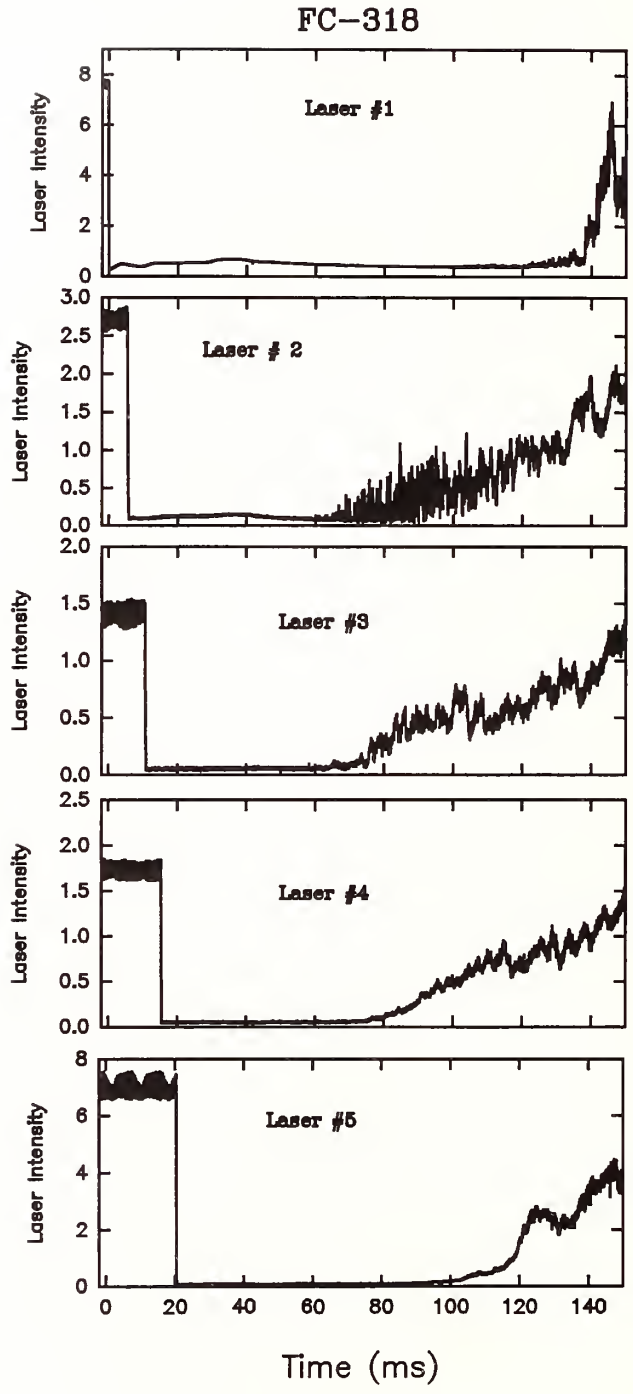

Figure 101. Time behaviors for transmission of laser beams #1-#5 spaced as shown in Table 7 following a release of FC-318 at 0 s. Conditions: 501 g agent, 4.43 MPa release pressure.

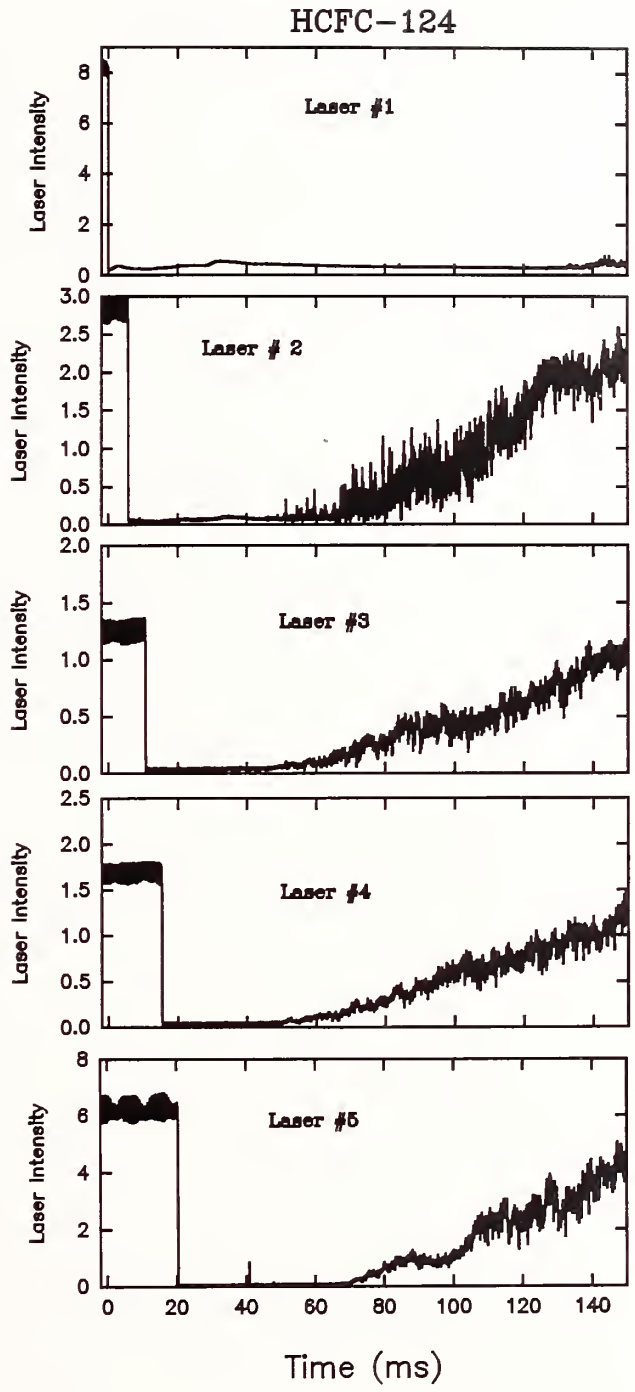

Figure 102. Time behaviors for transmission of laser beams #1-#5 spaced as shown in Table 7 following a release of HCFC-124 at 0 s. Conditions: 462 g agent, 4.05 MPa release pressure.

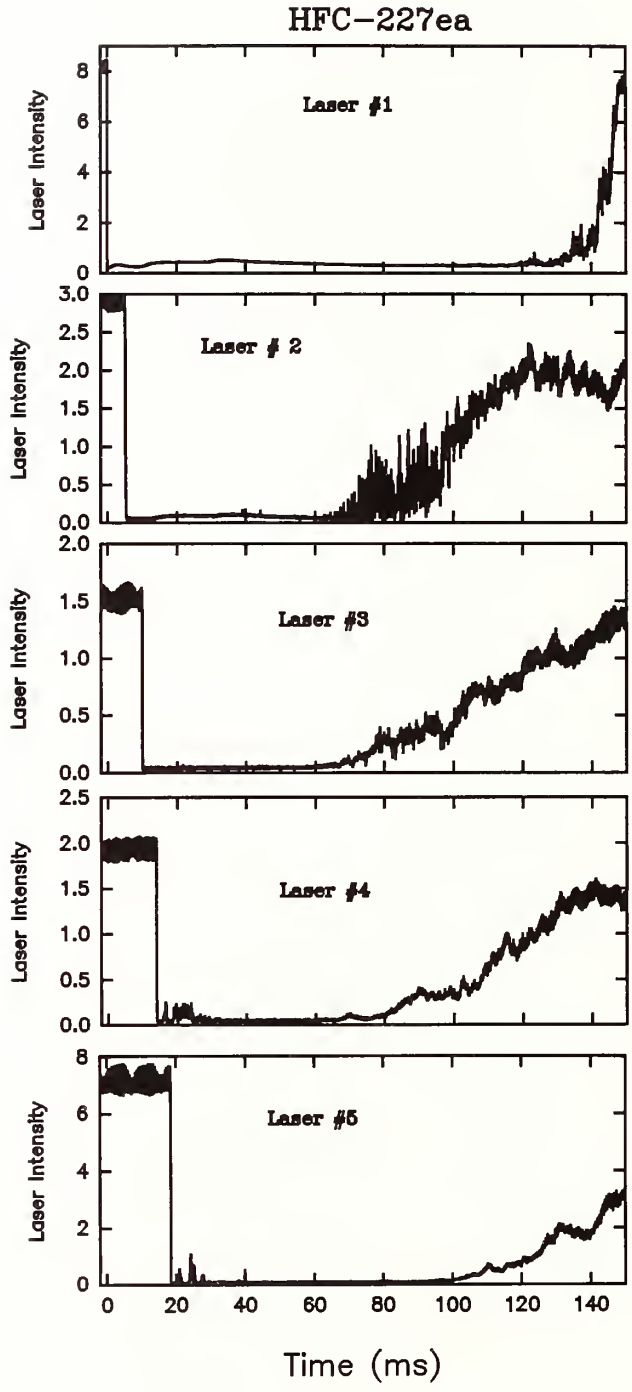

Figure 103. Time behaviors for transmission of laser beams #1-#5 spaced as shown in Table 7 following a release of HFC-227ea at 0 s. Conditions: 476 g agent, 4.45 MPa release pressure.

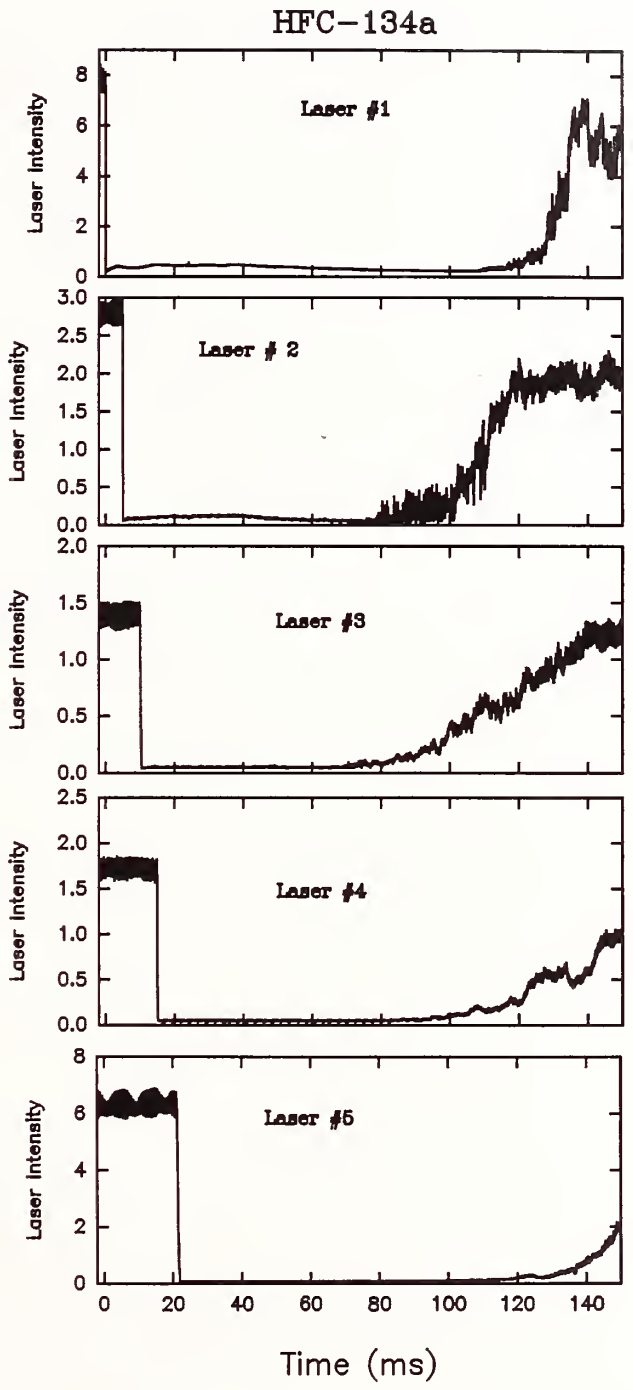

Figure 104. Time behaviors for transmission of laser beams #1-#5 spaced as shown in Table 7 following a release of HFC-134a at 0 s. Conditions: 418 g agent, 4.13 MPa release pressure.

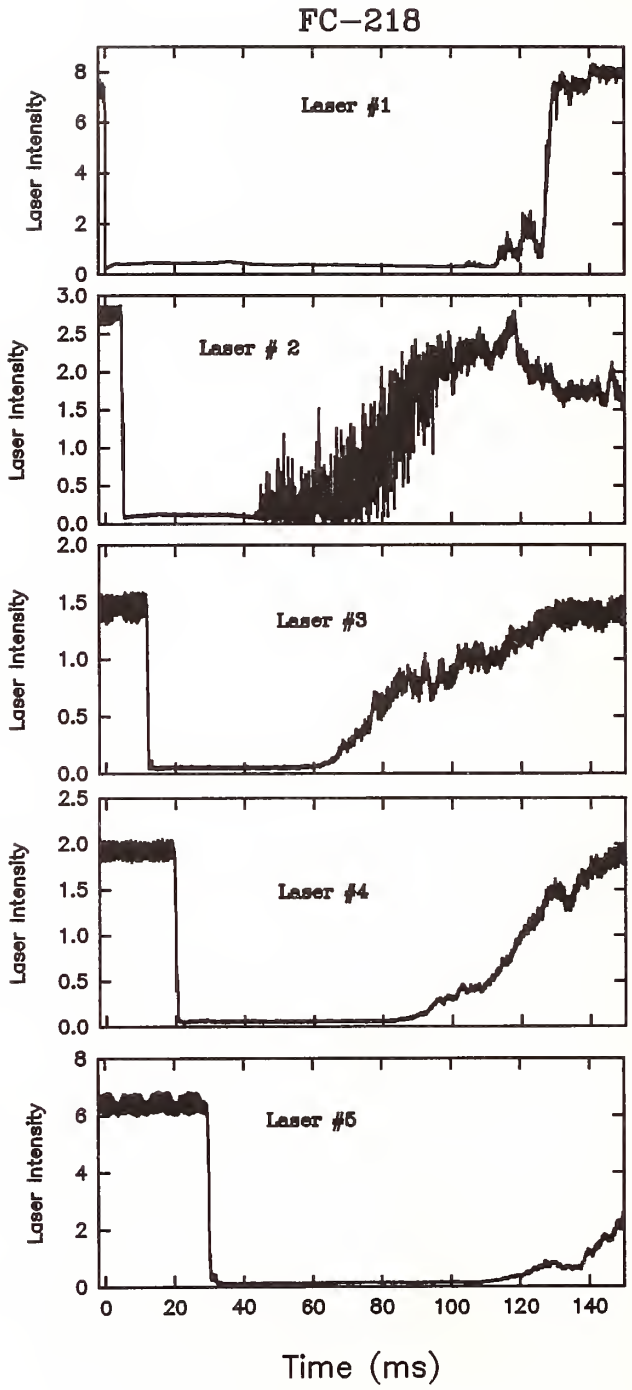

Figure 105. Time behaviors for transmission of laser beams #1-#5 spaced as shown in Table 7 following a release of FC-218 at 0 s. Conditions: 463 g agent, 4.06 MPa release pressure.

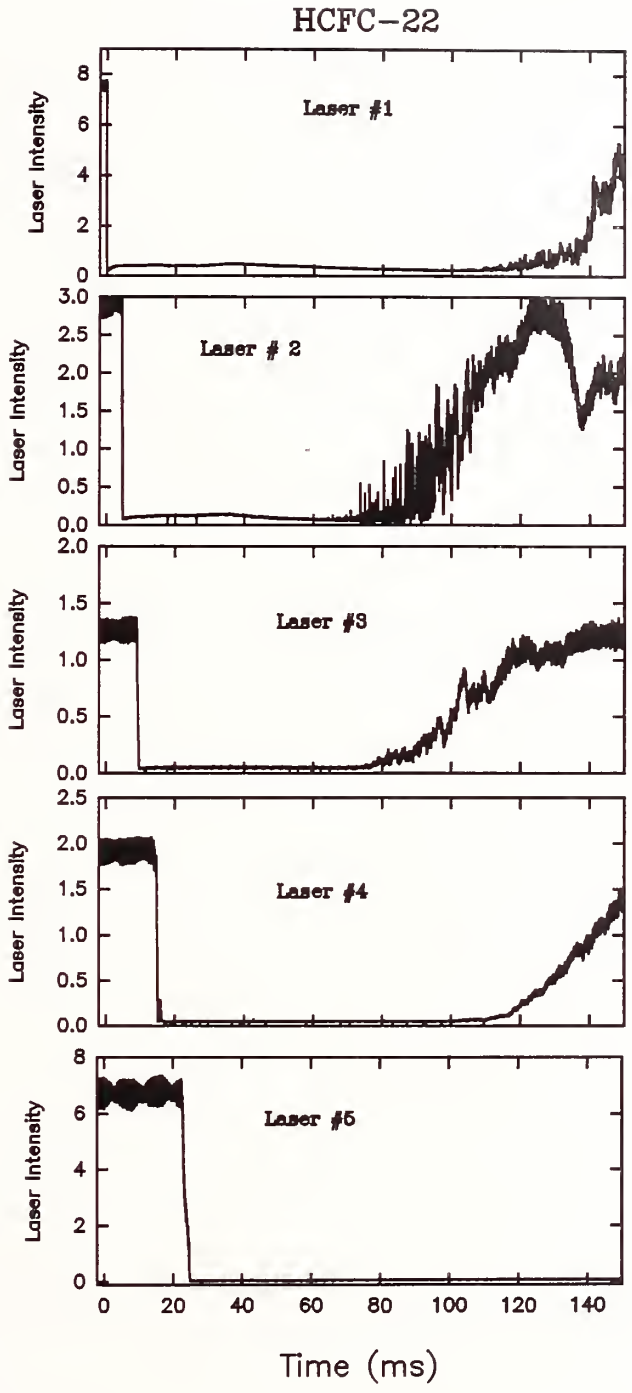

Figure 106. Time behaviors for transmission of laser beams #1-#5 spaced as shown in Table 7 following a release of HCFC-22 at 0 s. Conditions: 417 g agent, 4.52 MPa release pressure.

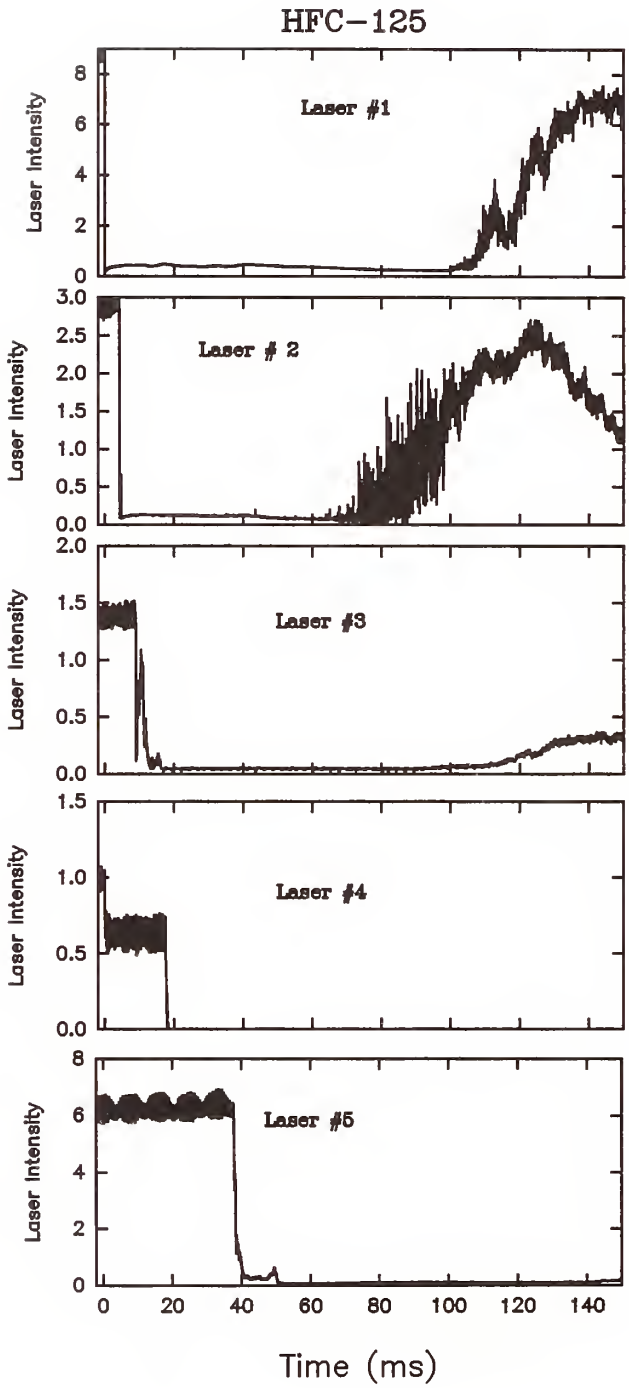

Figure 107. Time behaviors for transmission of laser beams #1-#5 spaced as shown in Table 7 following a release of HFC-125 at 0 s. Conditions: 423 g agent, 4.24 MPa release pressure.

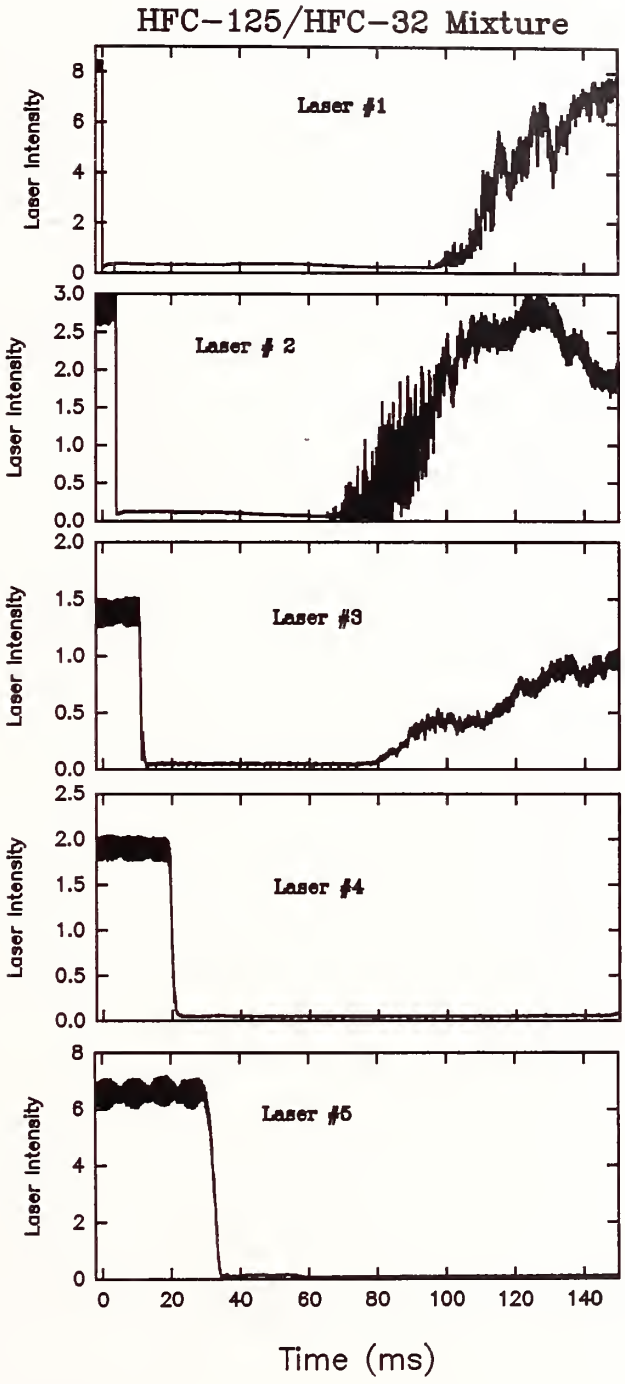

Figure 108. Time behaviors for transmission of laser beams #1-#5 spaced as shown in Table 7 following a release of the HFC-125/HFC-32 mixture at 0 s. Conditions: 375 g agent, 4.36 MPa release pressure.

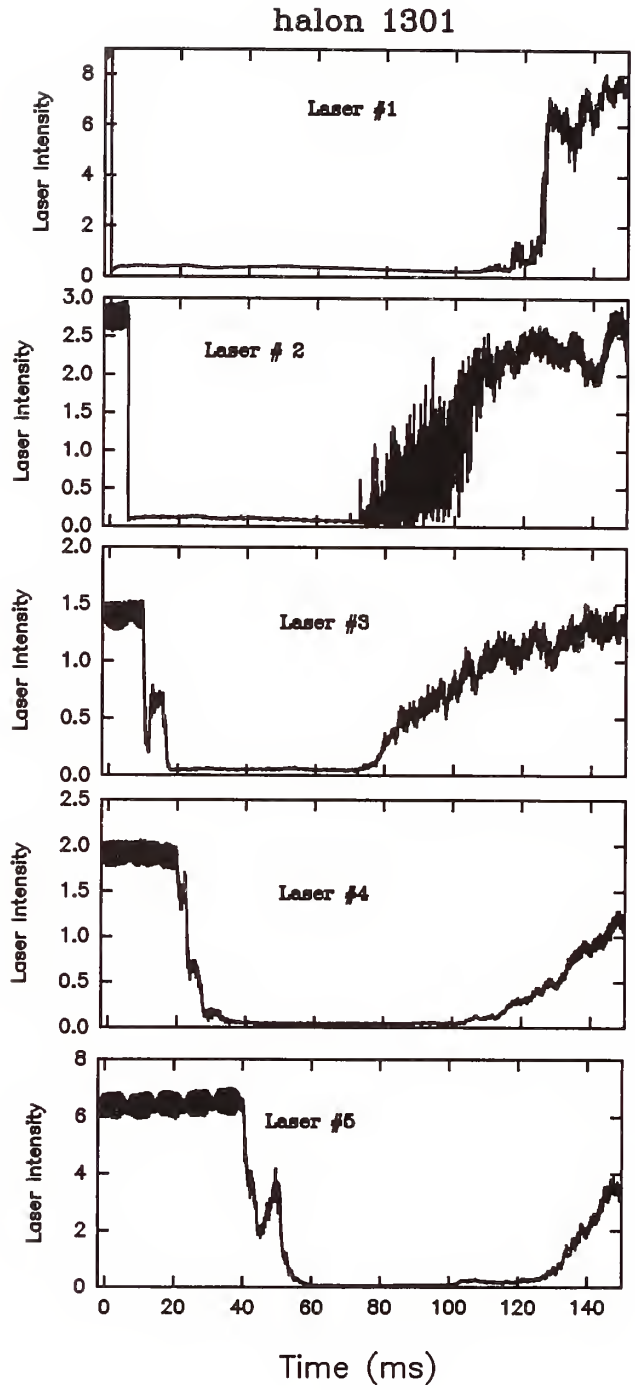

Figure 109. Time behaviors for transmission of laser beams #1-#5 spaced as shown in Table 7 following a release of halon 1301 at 0 s. Conditions: 554 g agent, 4.36 MPa release pressure.

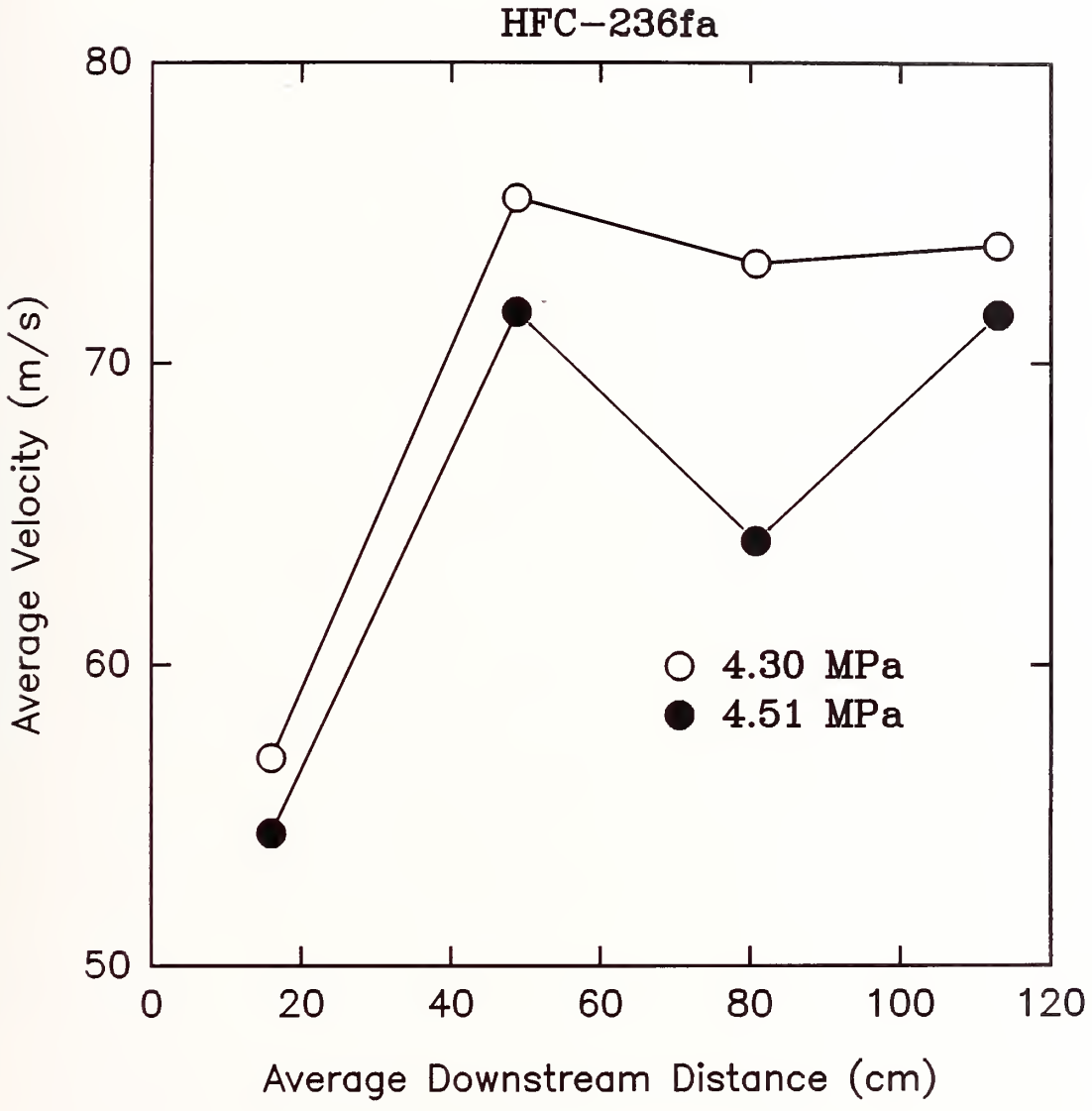

Figure 110. Average velocities for releases of HFC-236fa determined by the time of arrival at laser beams #1-#5 plotted as a function of average downstream distance. Pressures are those inside the vessel at disk bursting.

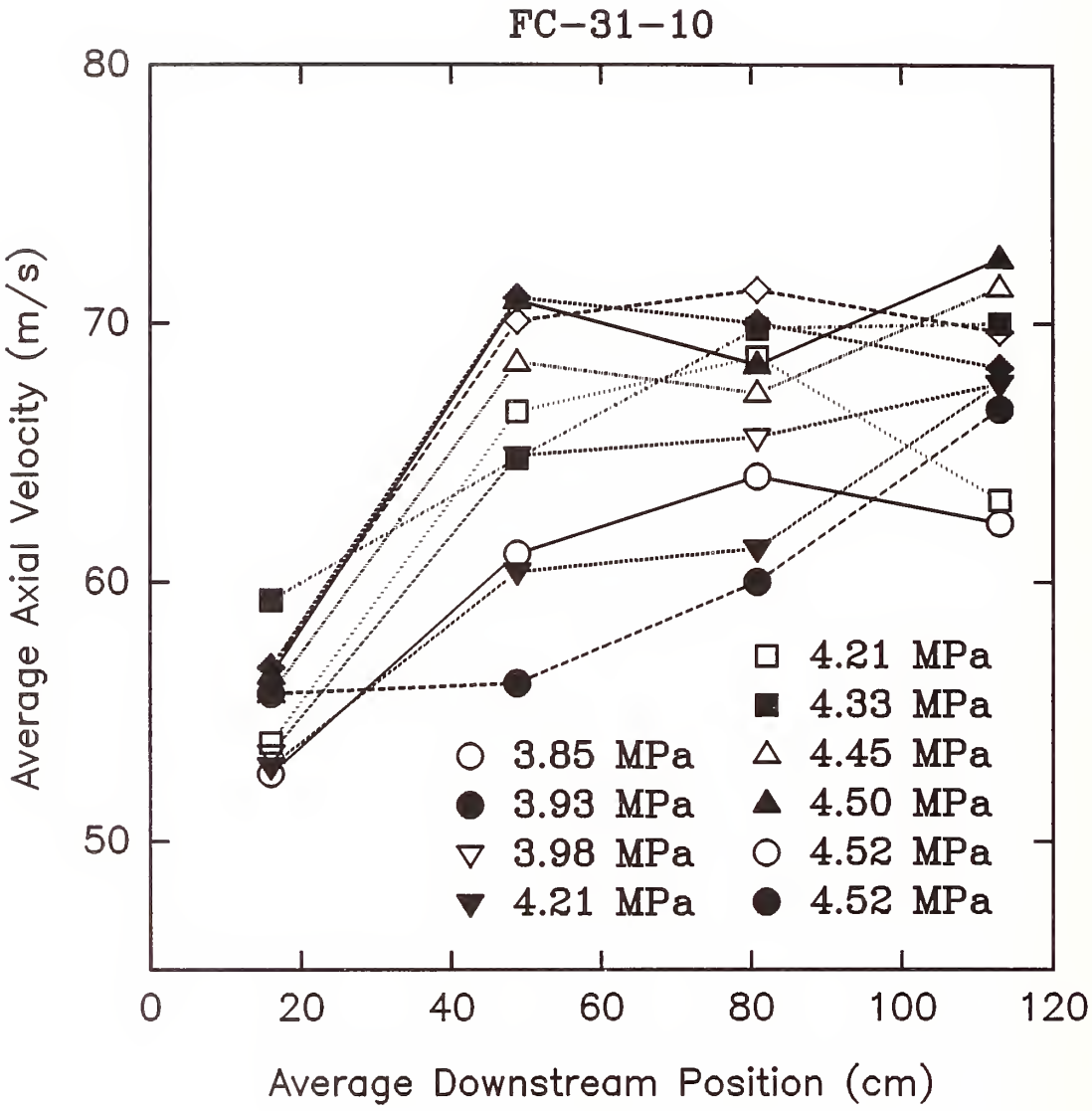

Figure 111. Average velocities for releases of FC-31-10 determined by the time of arrival at laser beams #1-#5 plotted as a function of average downstream distance. Pressures are those inside the vessel at disk bursting.

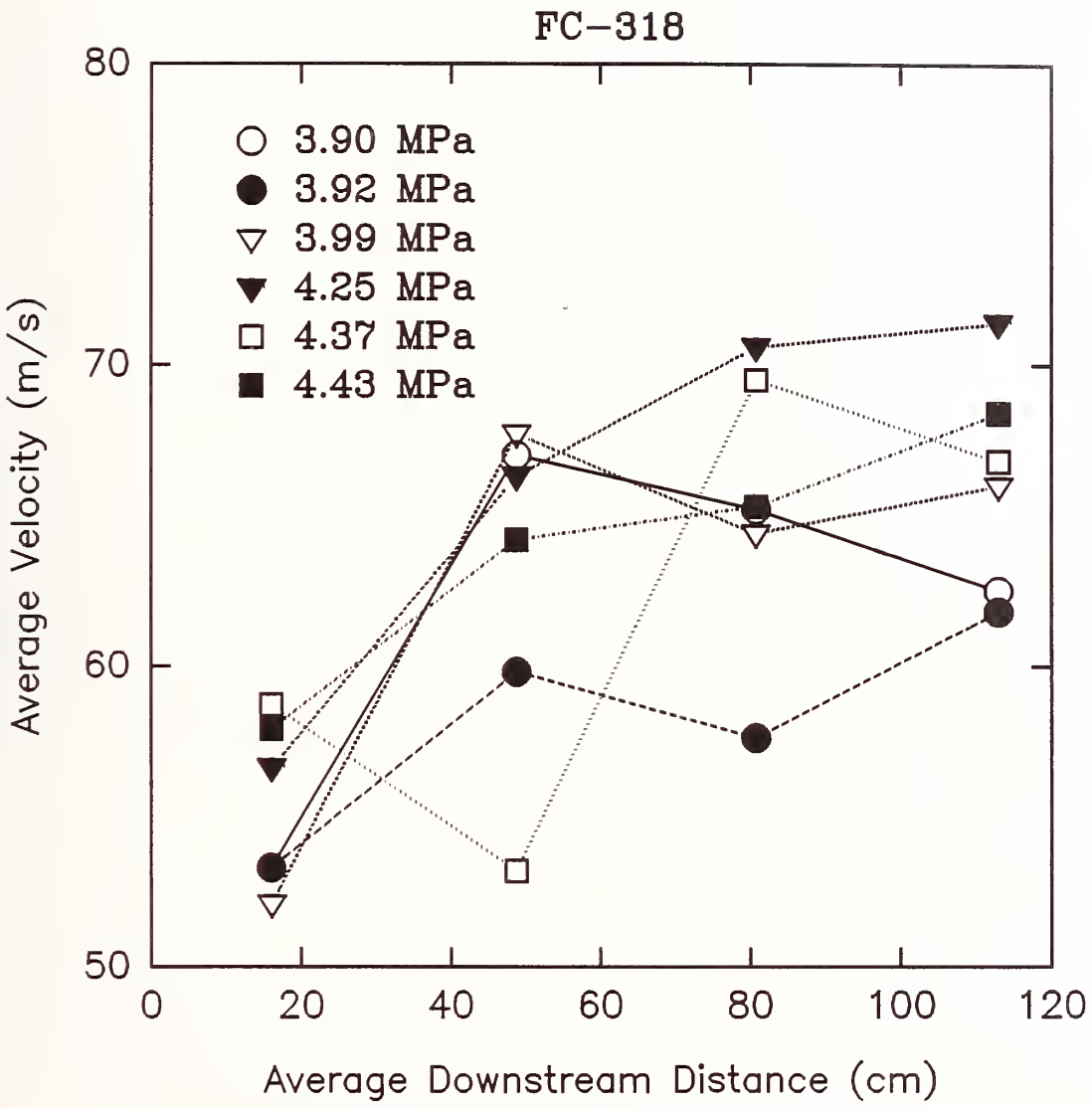

Figure 112. Average velocities for releases of FC-318 determined by the time of arrival at laser beams #1-#5 plotted as a function of average downstream distance. Pressures are those inside the vessel at disk bursting.

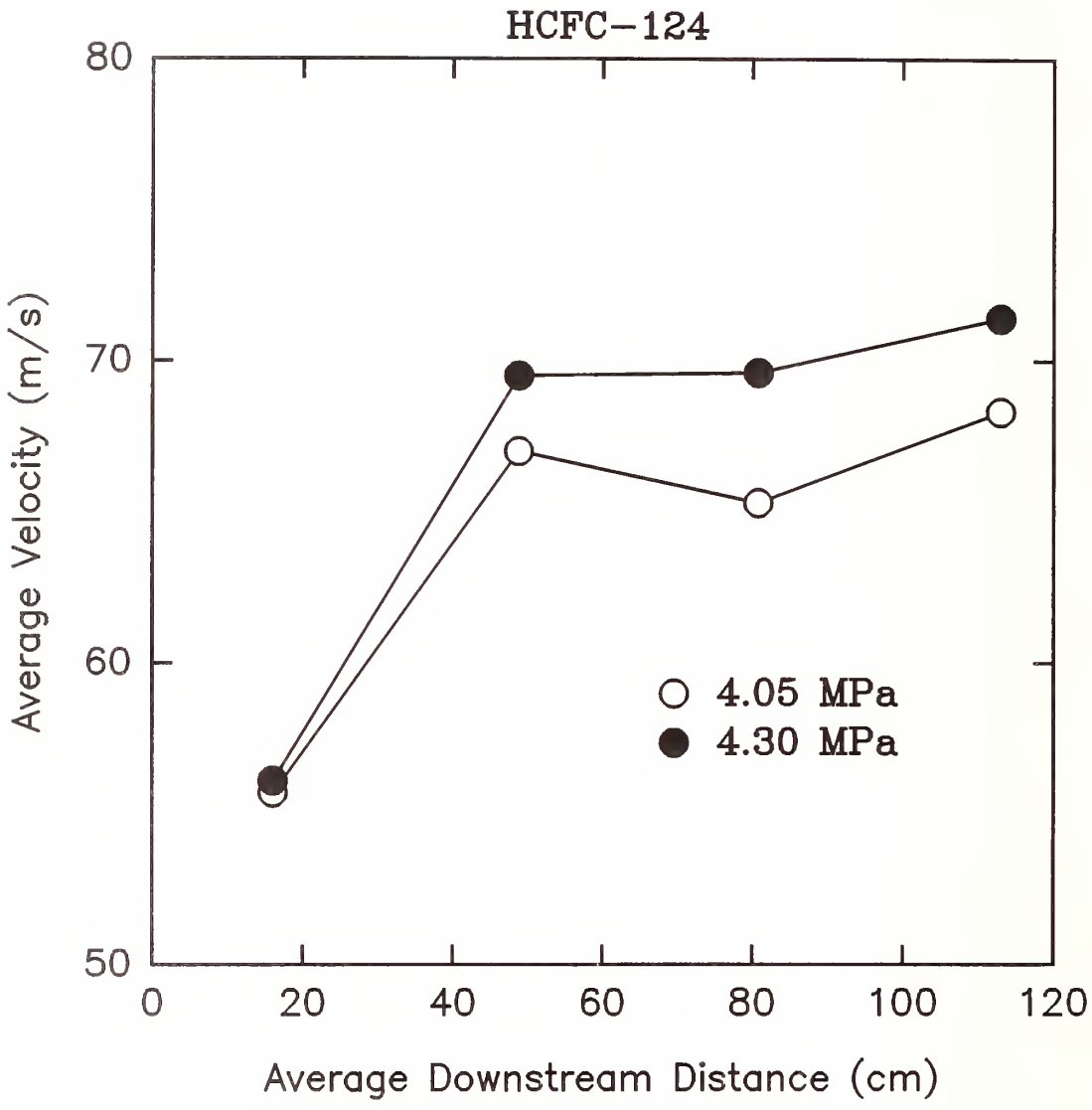

Figure 113. Average velocities for releases of HCFC-124 determined by the time of arrival at laser beams #1-#5 plotted as a function of average downstream distance. Pressures are those inside the vessel at disk bursting.

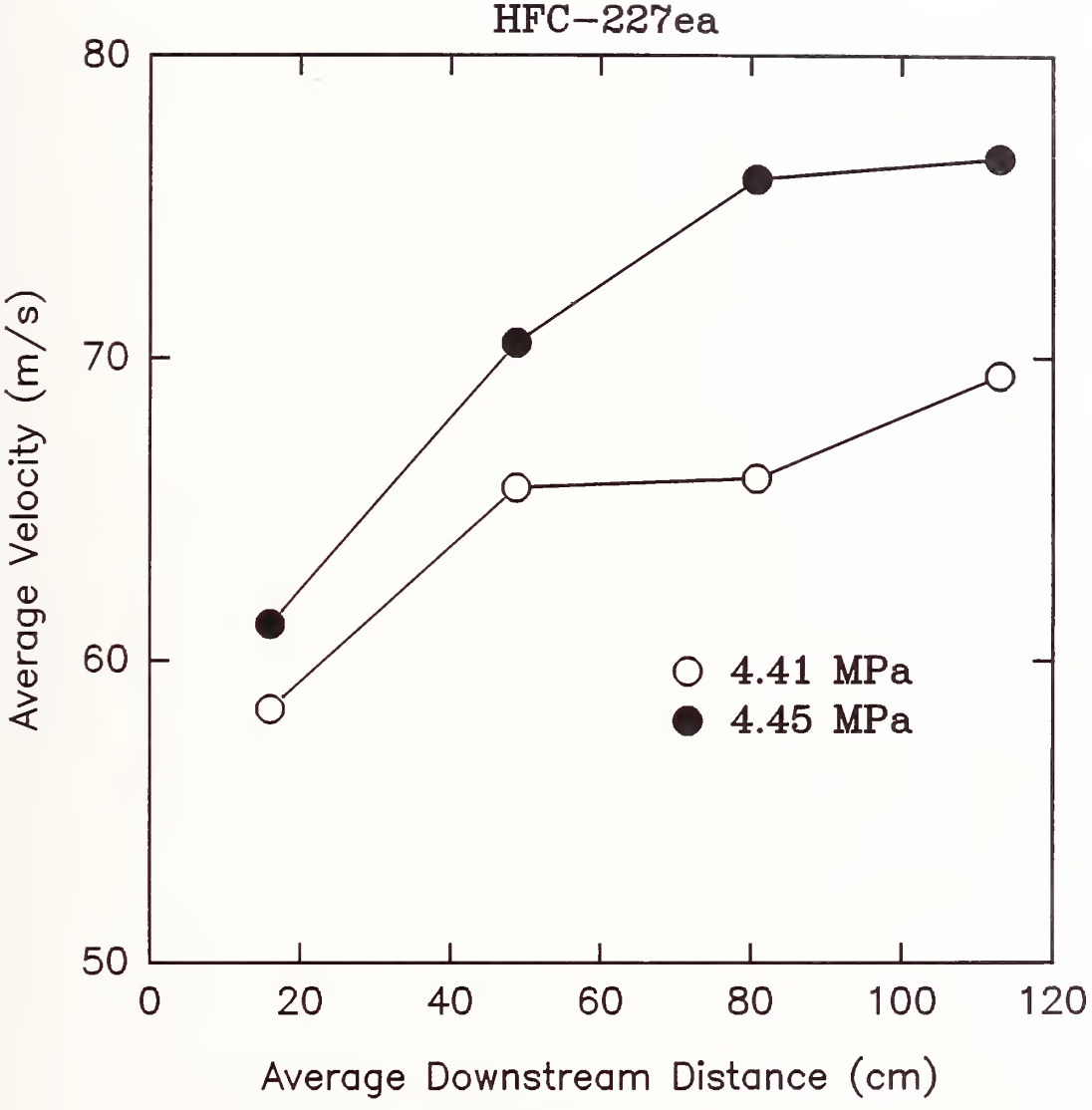

Figure 114. Average velocities for releases of HFC-227ea determined by the time of arrival at laser beams #1-#5 plotted as a function of average downstream distance. Pressures are those inside the vessel at disk bursting.

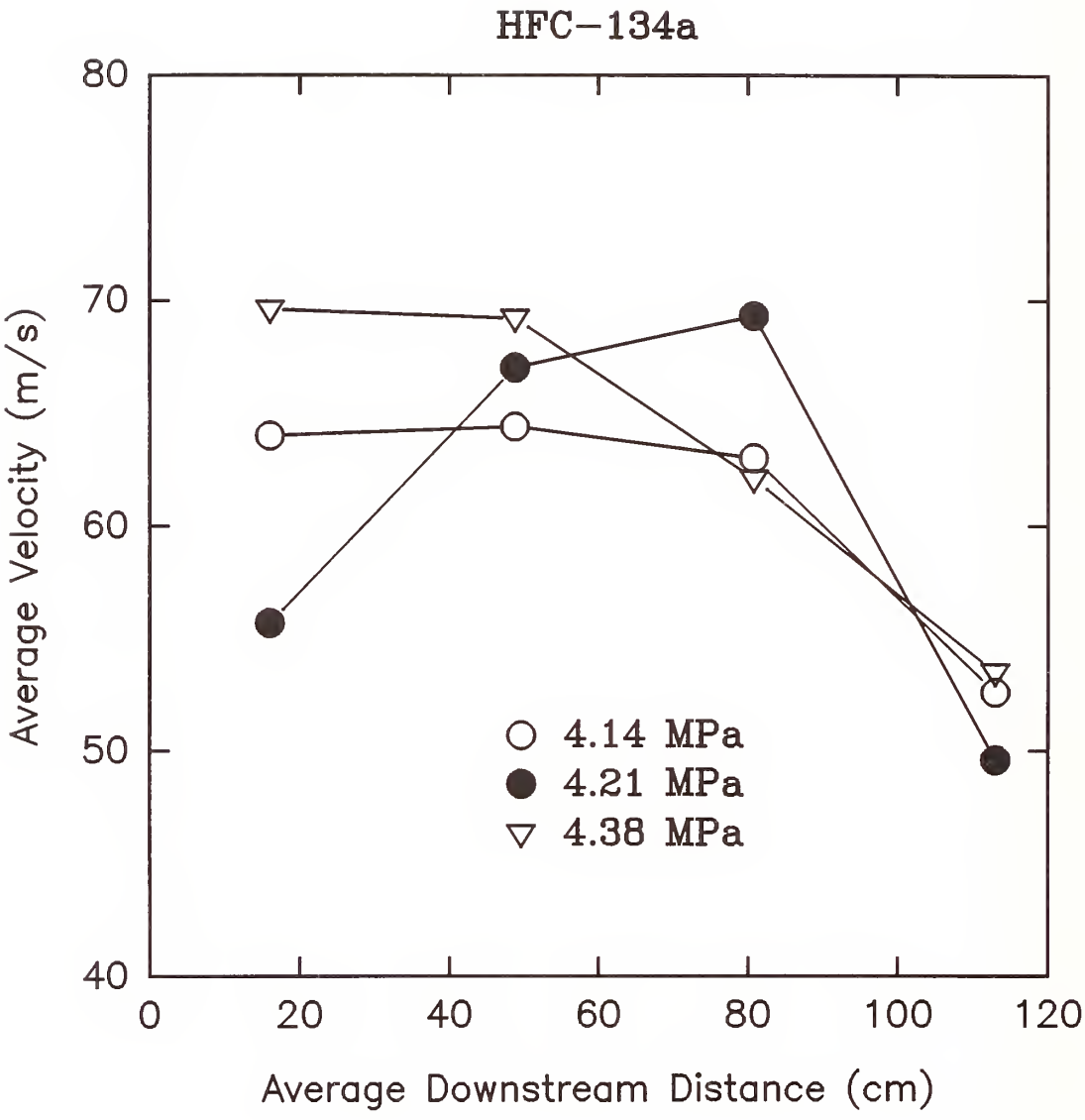

Figure 115. Average velocities for releases of HFC-134a determined by the time of arrival at laser beams #1-#5 plotted as a function of average downstream distance. Pressures are those inside the vessel at disk bursting.

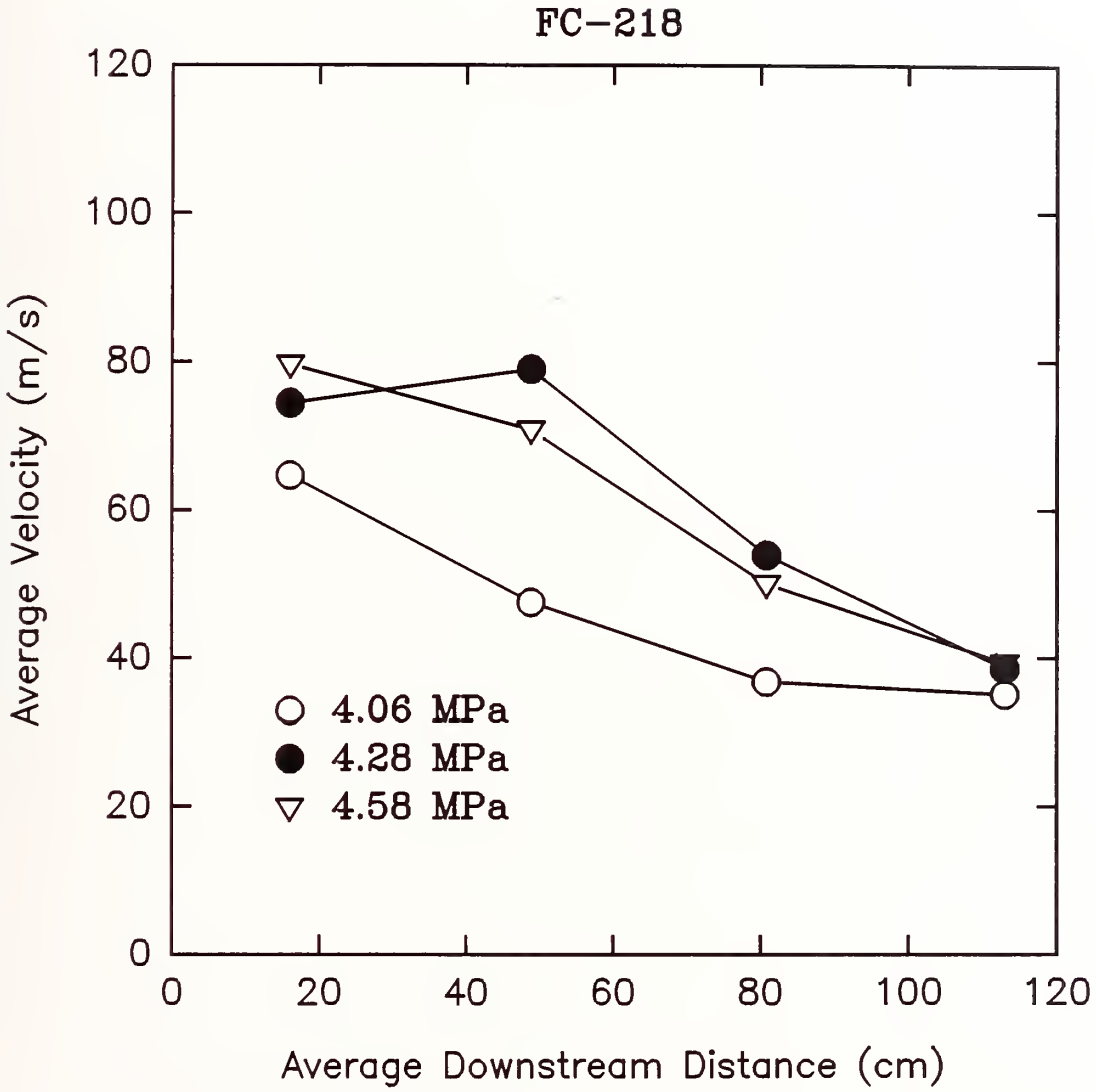

Figure 116. Average velocities for releases of FC-218 determined by the time of arrival at laser beams #1-#5 plotted as a function of average downstream distance. Pressures are those inside the vessel at disk bursting.

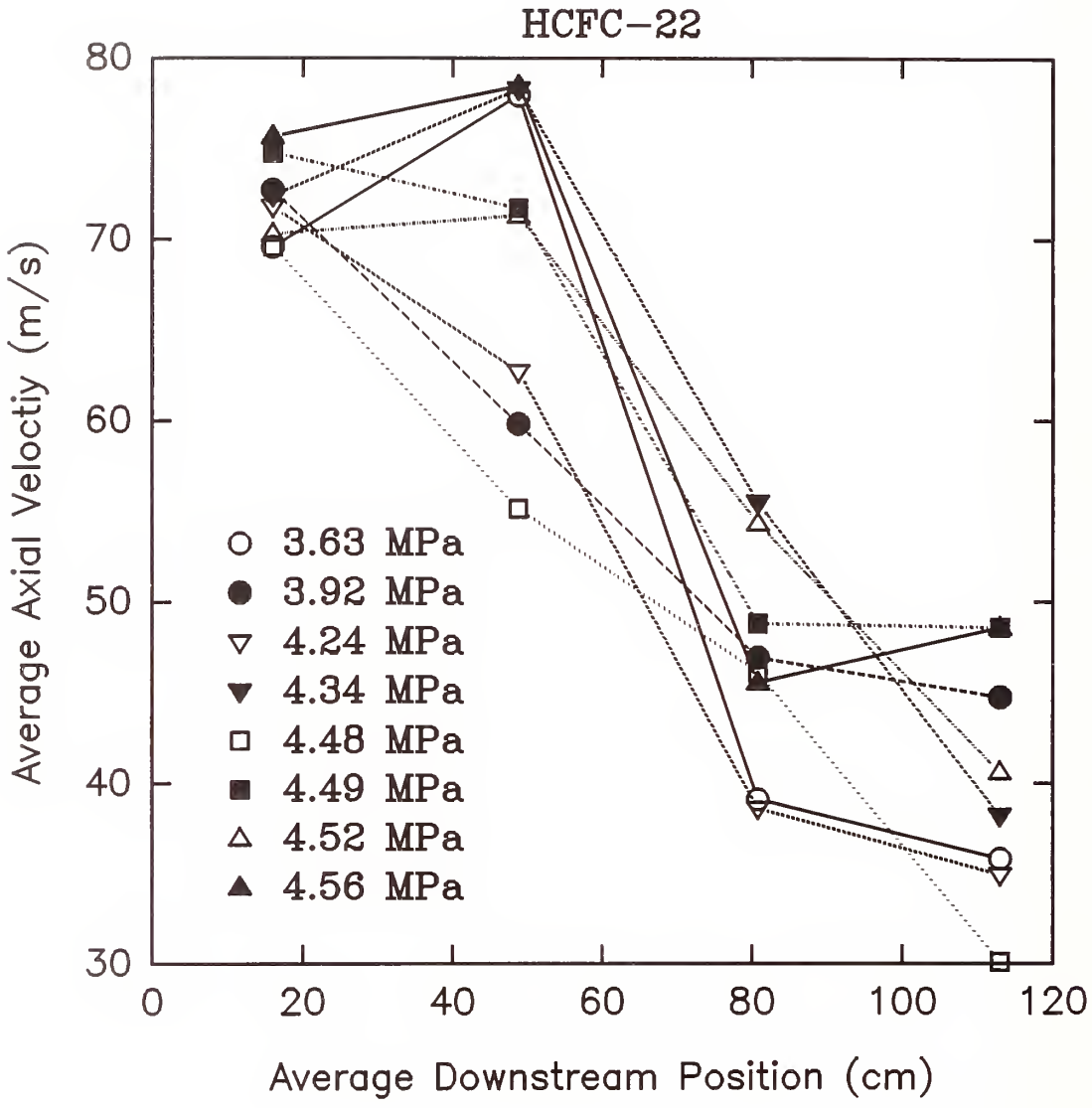

Figure 117. Average velocities for releases of HCFC-22 determined by the time of arrival at laser beams #1-#5 plotted as a function of average downstream distance. Pressures are those inside the vessel at disk bursting.

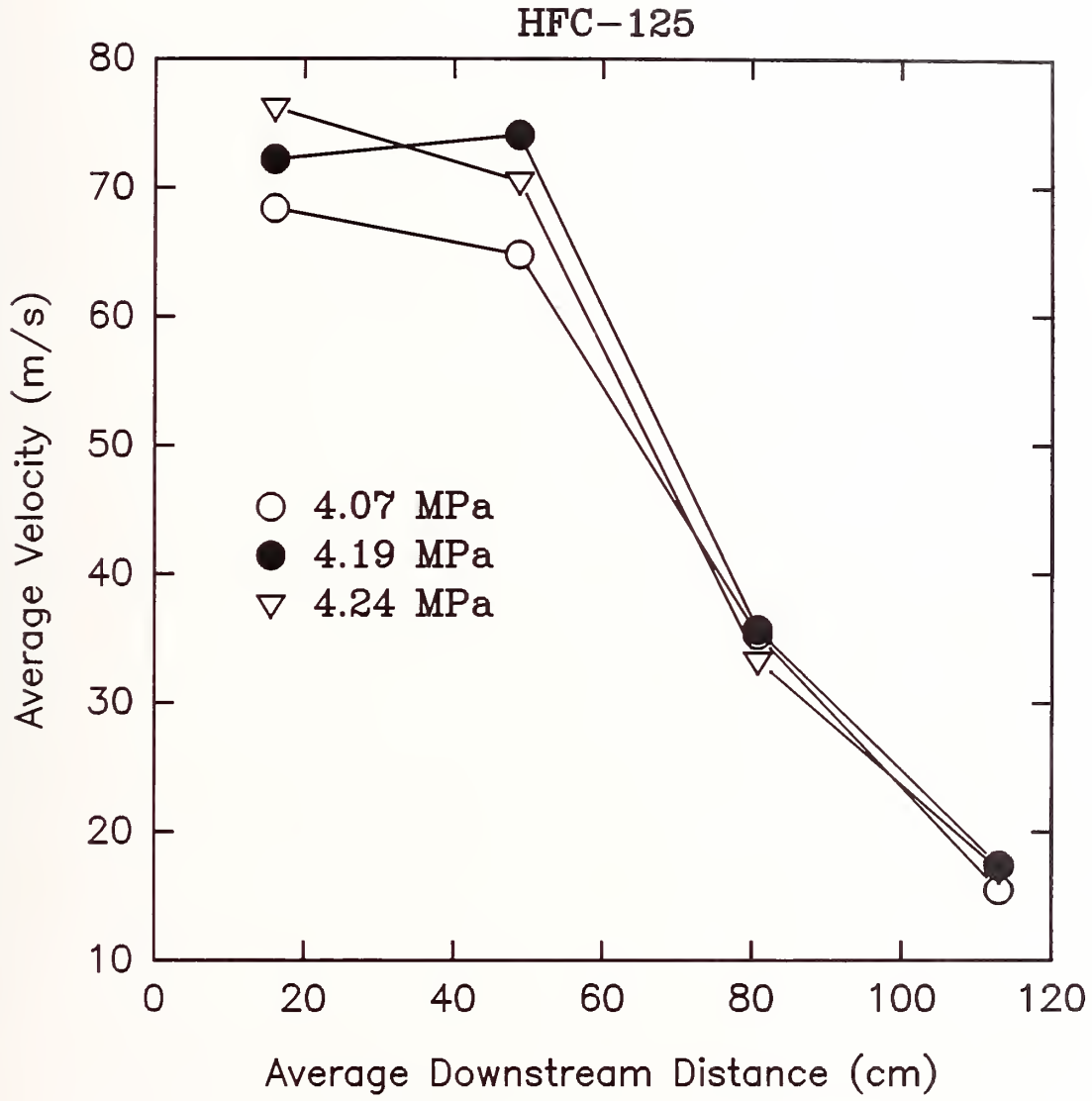

Figure 118. Average velocities for releases of HFC-125 determined by the time of arrival at laser beams #1-#5 plotted as a function of average downstream distance. Pressures are those inside the vessel at disk bursting.

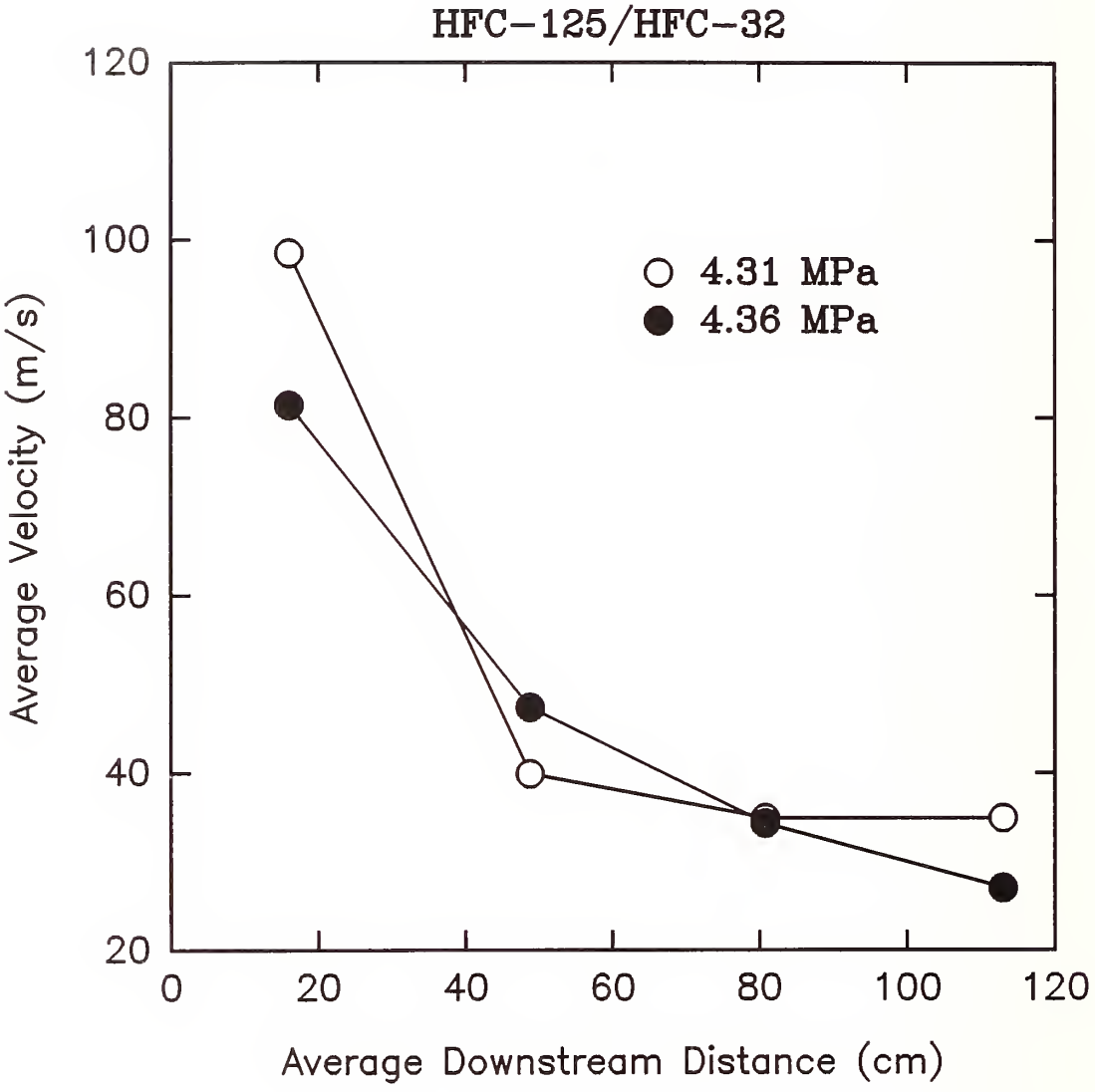

Figure 119. Average velocities for releases of the HFC-125/HFC-32 mixture determined by the time of arrival at laser beams #1-#5 plotted as a function of average downstream distance. Pressures are those inside the vessel at disk bursting.

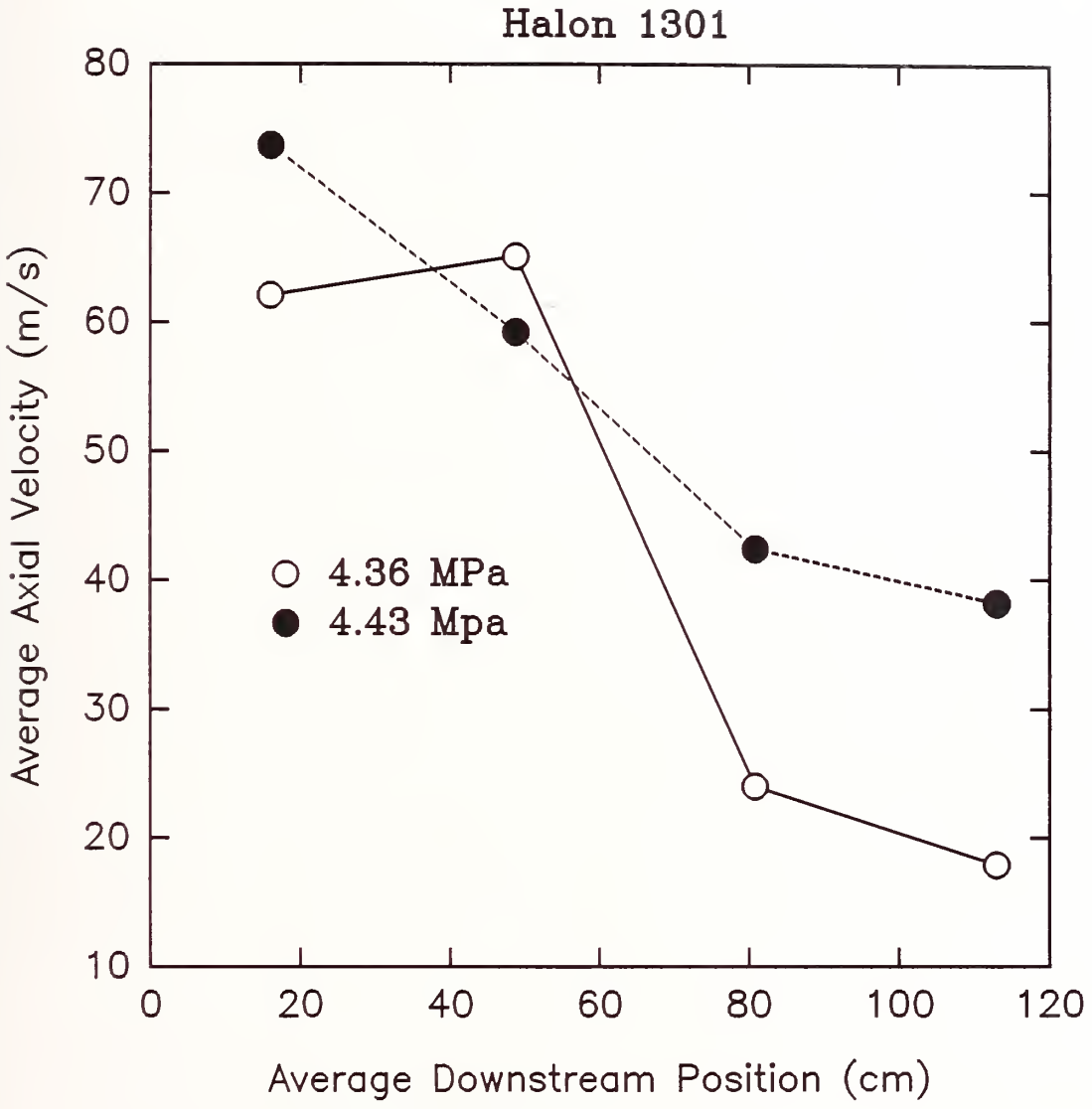

Figure 120. Average velocities for releases of halon 1301 determined by the time of arrival at laser beams #1-#5 plotted as a function of average downstream distance. Pressures are those inside the vessel at disk bursting.

agent moves further away from the vessel, the average velocities actually increase, remaining roughly constant at approximately 70 m/s.

HFC-134a (Figure 115) has a different velocity dependence on downstream distance. Two of the releases had high velocities (65-70 m/s) near the vessel which stayed roughly constant over the two nearest measurement locations. At the third and fourth locations the velocities actually decreased to values of roughly 50 m/s. Note that these results are nearly exactly the opposite of those for the higher boiling-point agents discussed above. A third release of HFC-134a looks similar to the higher boiling-point agents (*i.e.*, the measured velocity near the nozzle is roughly 56 ms/s and increases to roughly 70 m/s) except that the velocity again decreases at the furthest measuring station.

The velocity results for FC-218 (Figure 116) are similar to those for HFC-134a. Velocities for the two locations near the nozzle are on the order of 80 ms/s. As the agent moves further from the exit the velocity begins to fall off, decreasing to approximately 40 m/s for the last station. The results for HCFC-22 (Figure 117) are similar, but there is substantial scatter in the results.

For HFC-125 (Figure 118) the velocities near the vessel are again roughly 70 m/s. However, these velocities decrease faster with downstream distance becoming less than 20 m/s at the most distant location. The HFC-125/HFC-32 mixture (Figure 119) displays a similar, but enhanced behavior. Velocities near the vessel exit are very high, approaching 100 m/s. By the second measuring station the velocity has dropped rapidly and eventually falls to less than 30 m/s. Interestingly, the results for halon 1301 (Figure 120) are similar to those for FC-218 and HFC-125.

These measurements have been made for a range of pressures in the release vessel due to variations in burst disks. Close examination shows that the measured velocities depend somewhat on pressure, with higher pressures yielding higher velocities. However, for the range of pressures shown the dependence is relatively weak and on the order of experiment-to-experiment variation.

3.5.3.4 Far-Field Dynamic Pressure Measurements. These measurements were made on the centerline of the releases at a distance 1.3 m from the vessel exit. The pressure transducer was oriented such that it faced the release direction. Figure 121 through Figure 131 show examples of the dynamic pressures recorded as a function of time for the ten room-temperature liquid replacement agents as well as halon 1301.

Figure 121 shows time plots of downstream dynamic pressure for two releases of HFC-236fa. In both cases a rapid pressure rise is observed at approximately 20 ms following release. This agrees closely with the arrival of the agent at laser #5 as determined by strong beam attenuation (18.8 ms and 20.1 ms). The pressure jumps roughly 200 to 300 kPa immediately following the arrival of the agent at the transducer. The pressure then continues to increase over the next 25 ms. Maximum pressures observed in the two cases were 1,100 kPa and 1,420 kPa. As we will be discussed shortly, such pressure increases are indicative of a two-phase flow striking the transducer.

Similar pressure traces for FC-31-10 are shown in Figure 122. The behaviors are similar to those for HFC-236fa with maximum pressures reaching 820 and 1029 kPa. The pressure traces for FC-318 (Figure 123) also have a similar behavior except the initial pressure increase is somewhat higher (500 to 700 kPa) with maximum observed values of 1000 and 1200 kPa. Results for HCFC-124 are shown in Figure 124. This agent generates strong pressure increases (500 to 700 kPa) immediately upon arrival at the transducer which then grow to very high levels (1200 to 1500 kPa). The results for HFC-227ea (Figure 125) are very similar to those for HCFC-124. The pressure traces for HFC-134a (Figure 126) have very rapid and large increases ($>$ 1000 kPa) upon arrival at the transducer and reach the highest values (1900-2100 kPa) of any of the high boiling-point agents.

The dynamic pressure measurements for FC-218 (Figure 127) have a very different behavior than those discussed thus far. A rapid pressure increase is observed at roughly 25 ms corresponding to the time when the agent reaches the transducer. A maximum value is quickly reached. This maximum

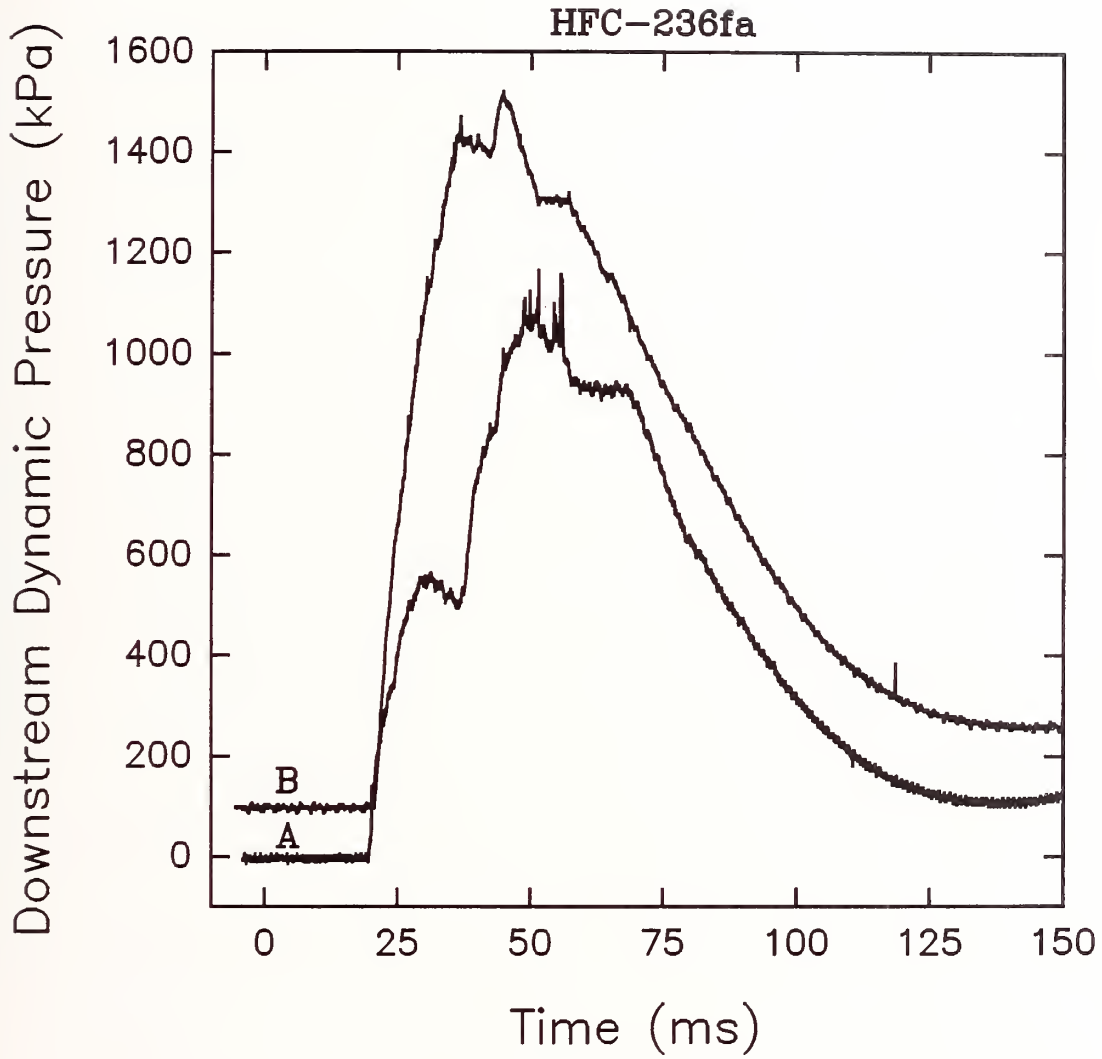

Figure 121. Dynamic pressure measured 1.3 m from the vessel for HFC-236fa. For clarity, trace B is offset by 100 kPa. Conditions are: A, 471 g agent, release pressure of 4.51 MPa ; B, 464 g of agent, release pressure of 4.30 MPa.

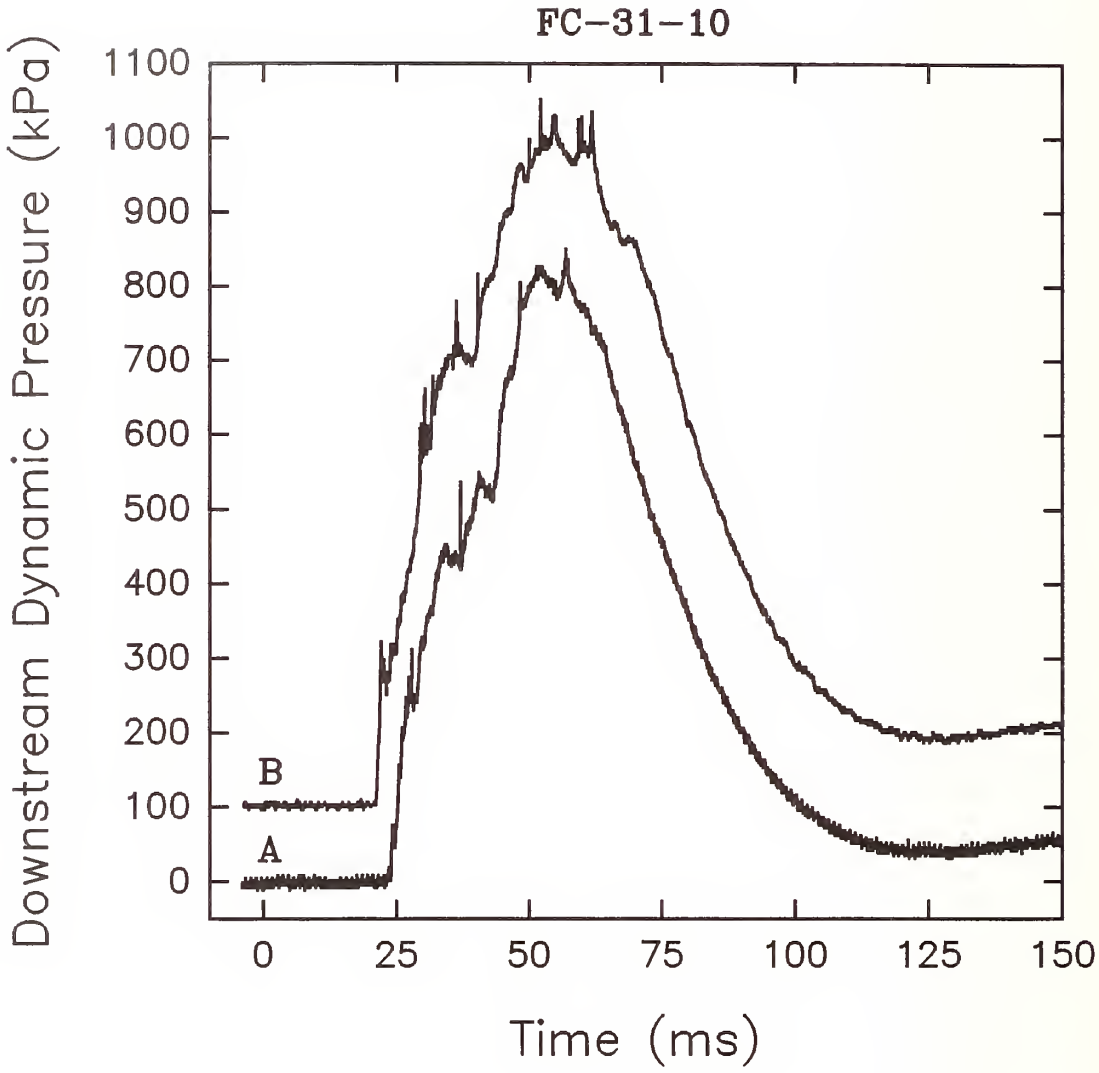

Figure 122. Dynamic pressure measured 1.3 m from the vessel for FC-31-10. For clarity, trace B is offset by 100 kPa. Conditions are: A, 495 g agent, release pressure of 3.93 MPa ; B, 515 g of agent, release pressure of 4.20 MPa.

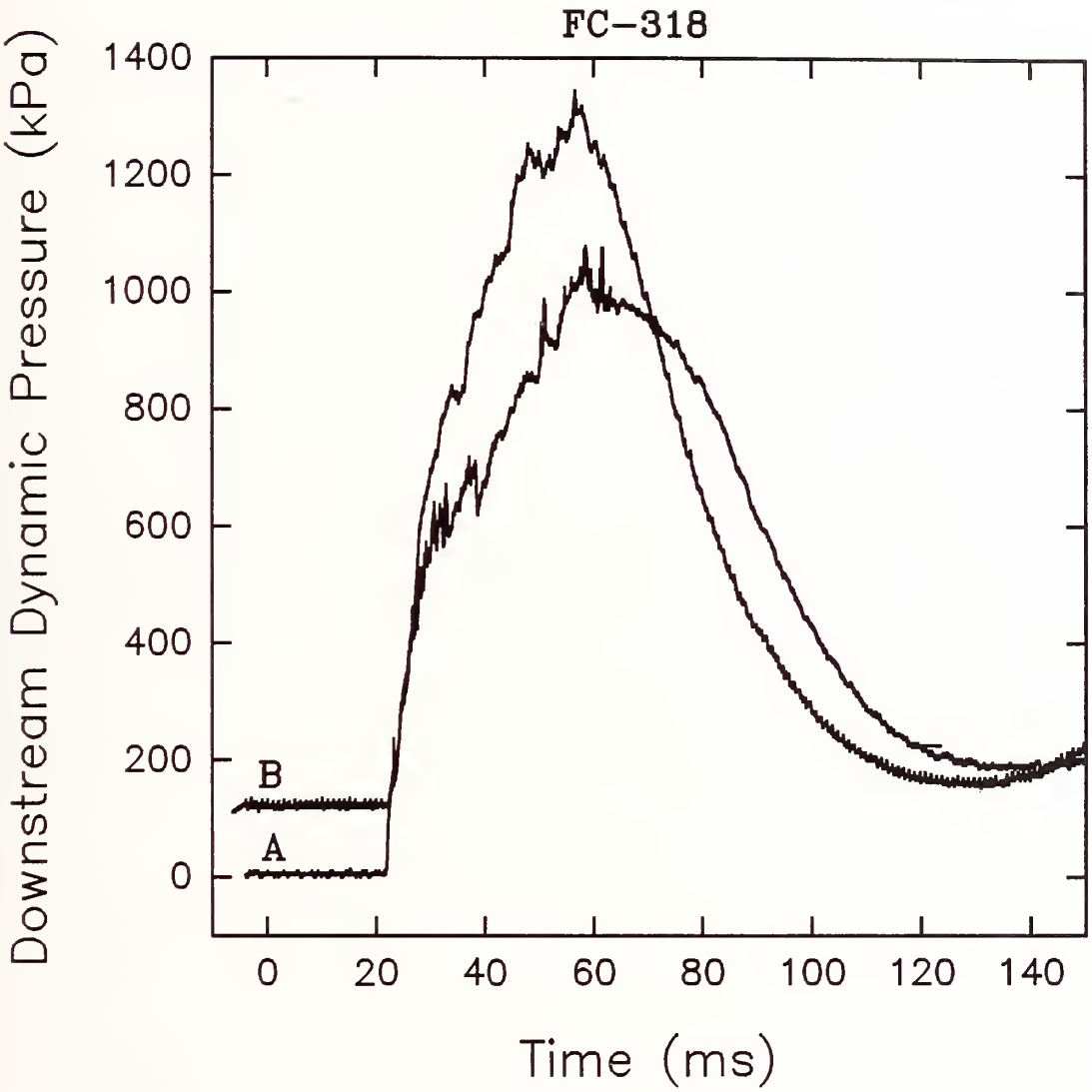

Figure 123. Dynamic pressure measured 1.3 m from the vessel for FC-318. For clarity, trace B is offset by 100 kPa. Conditions are: A, 521 g agent, release pressure of 4.34 MPa ; B, 505 g of agent, release pressure of 3.99 MPa.

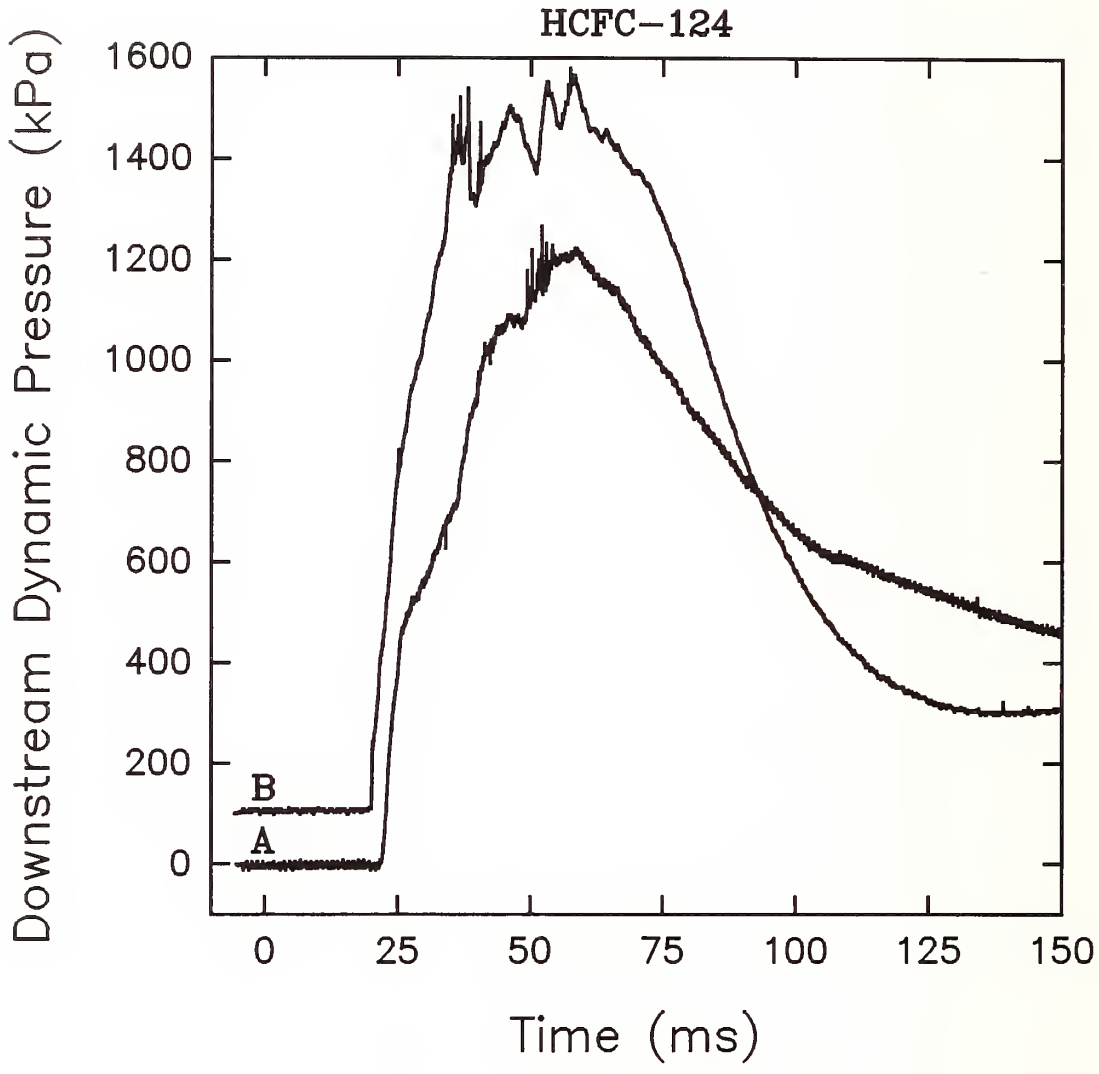

Figure 124. Dynamic pressure measured 1.3 m from the vessel for HCFC-124. For clarity, trace B is offset by 100 kPa. Conditions are: A, 462 g agent, release pressure of 4.05 MPa ; B, 465 g of agent, release pressure of 4.30 MPa.

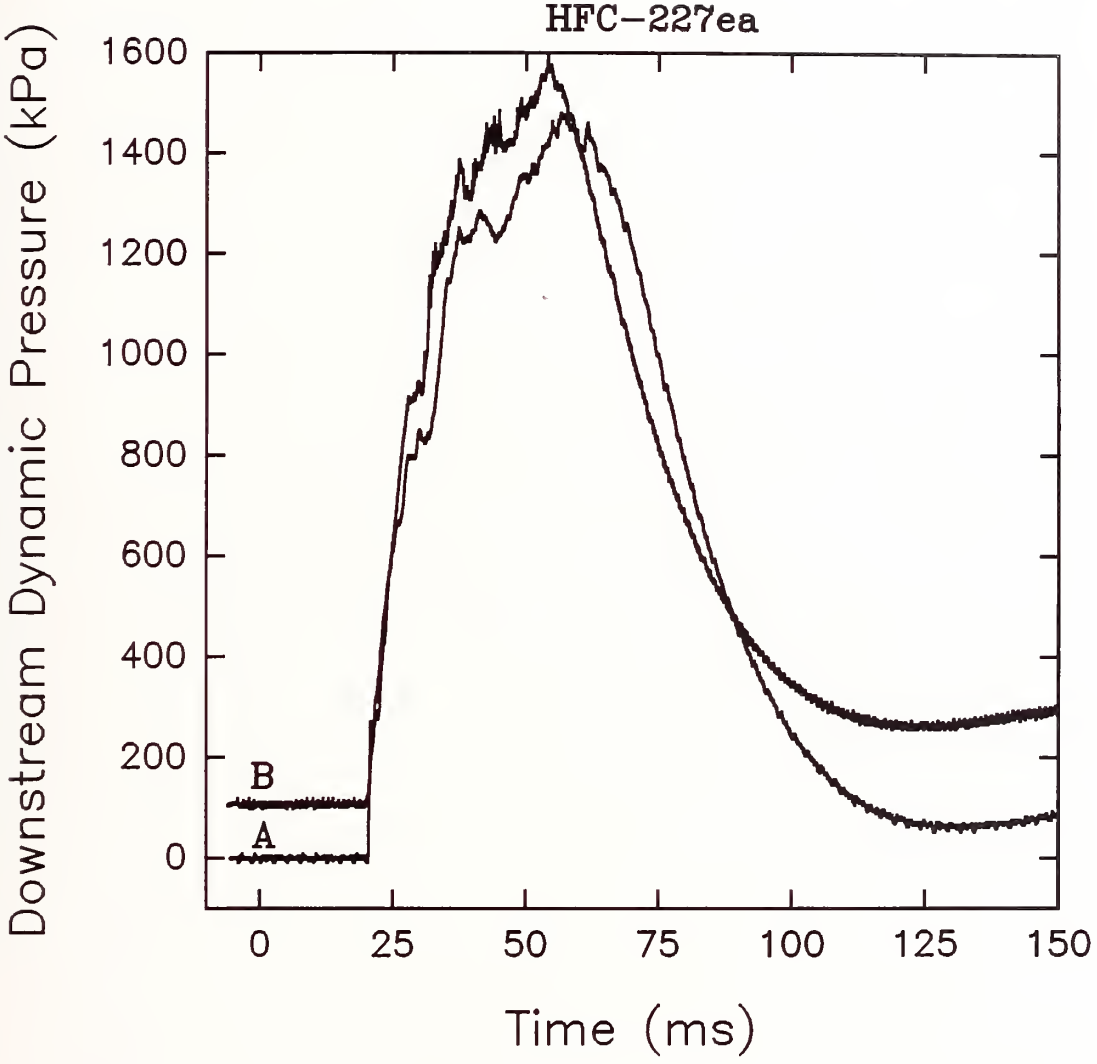

Figure 125. Dynamic pressure measured 1.3 m from the vessel for HFC-227ea. For clarity, trace B is offset by 100 kPa. Conditions are: A, 489 g agent, release pressure of 4.41 MPa ; B, 476 g of agent, release pressure of 4.45 MPa.

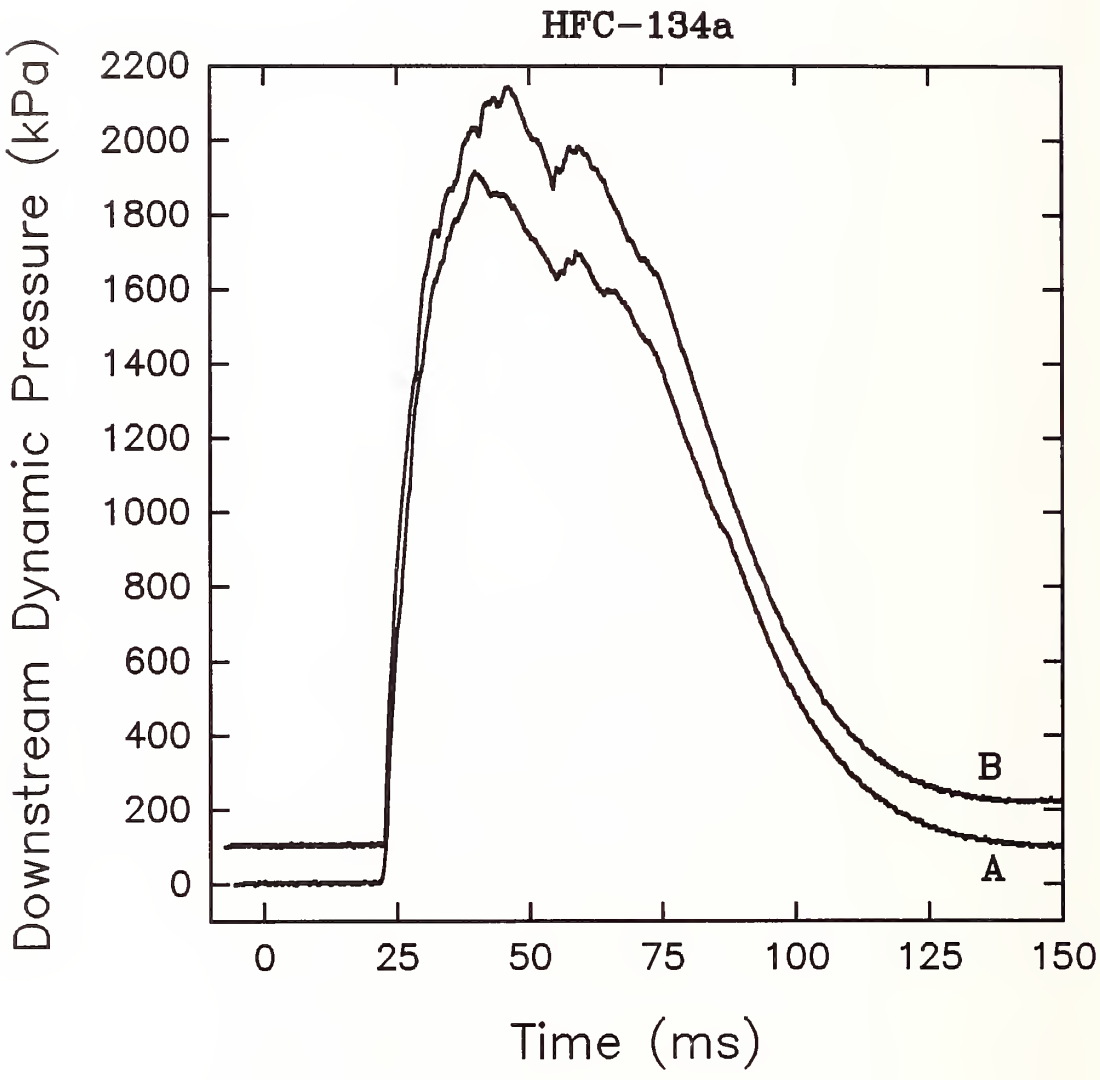

Figure 126. Dynamic pressure measured 1.3 m from the vessel for HFC-134a. For clarity, trace B is offset by 100 kPa. Conditions are: A, 418 g agent, release pressure of 4.13 MPa ; B, 419 g of agent, release pressure of 4.21 MPa.

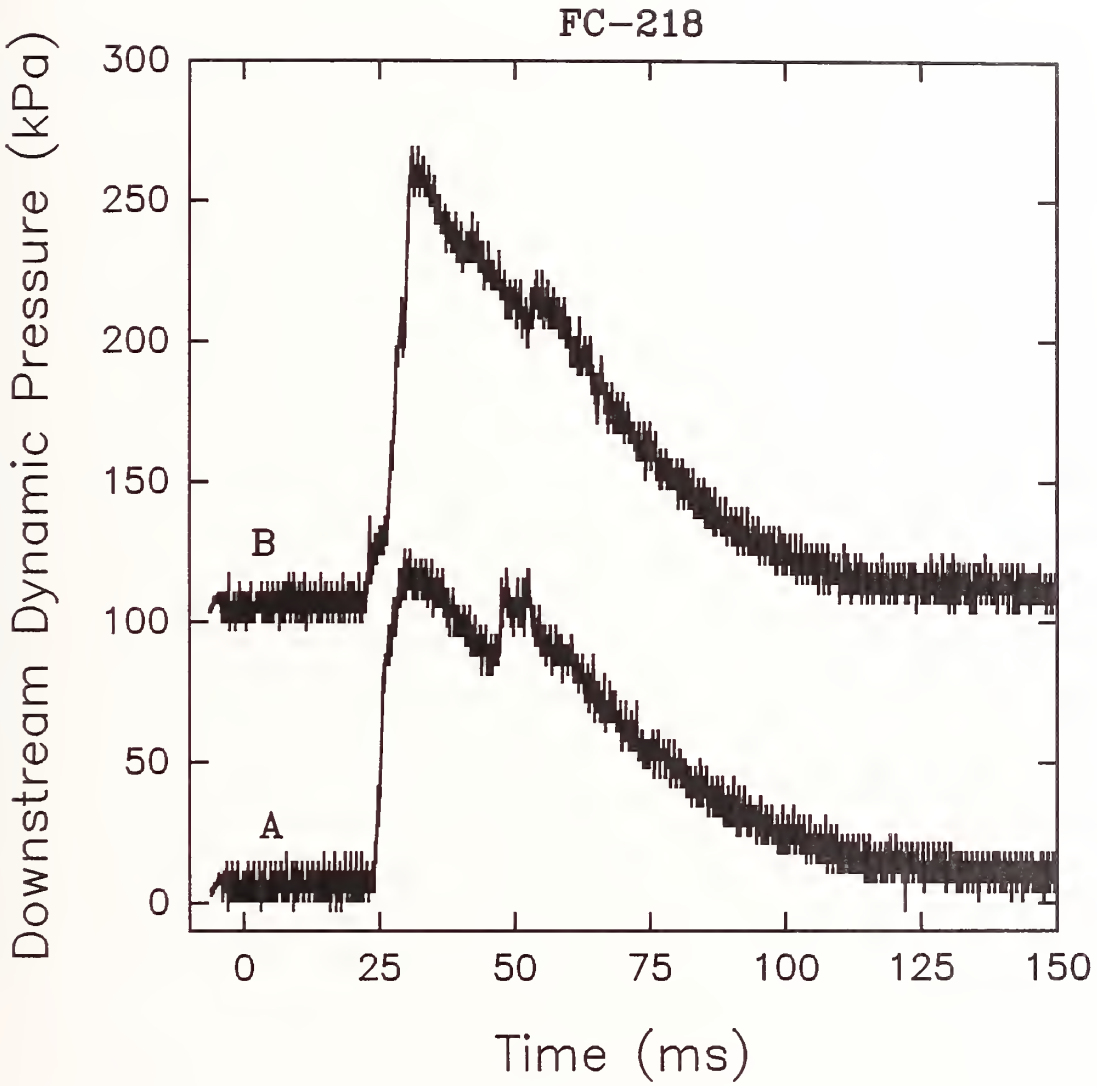

Figure 127. Dynamic pressure measured 1.3 m from the vessel for FC-218. For clarity, trace B is offset by 100 kPa. Conditions are: A, 460 g agent, release pressure of 4.58 MPa ; B, 468 g of agent, release pressure of 4.28 MPa.

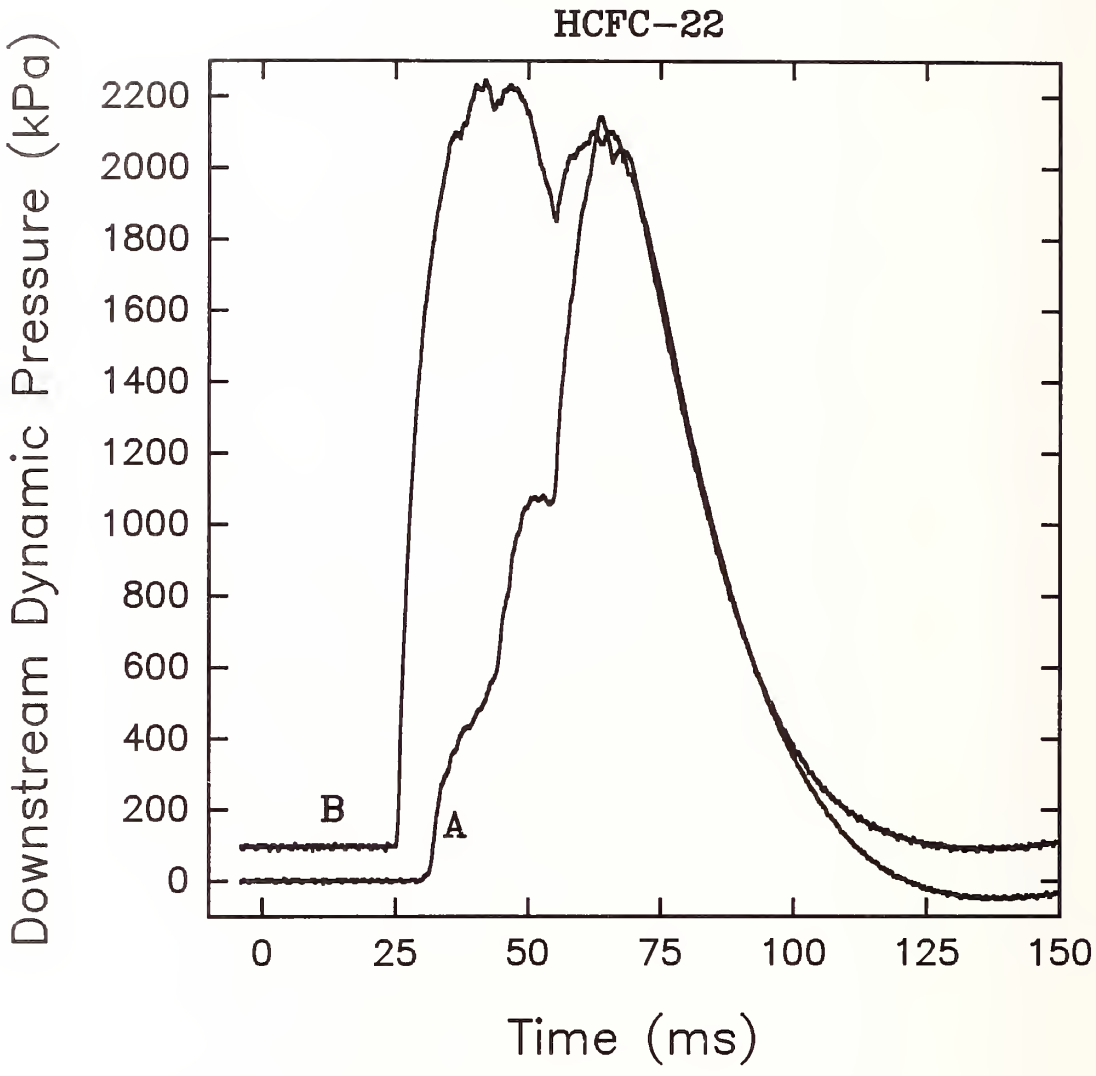

Figure 128. Dynamic pressure measured 1.3 m from the vessel for HCFC-22. For clarity, trace B is offset by 100 kPa. Conditions are: A, 421 g agent, release pressure of 4.48 MPa ; B, 417 g of agent, release pressure of 4.52 MPa.

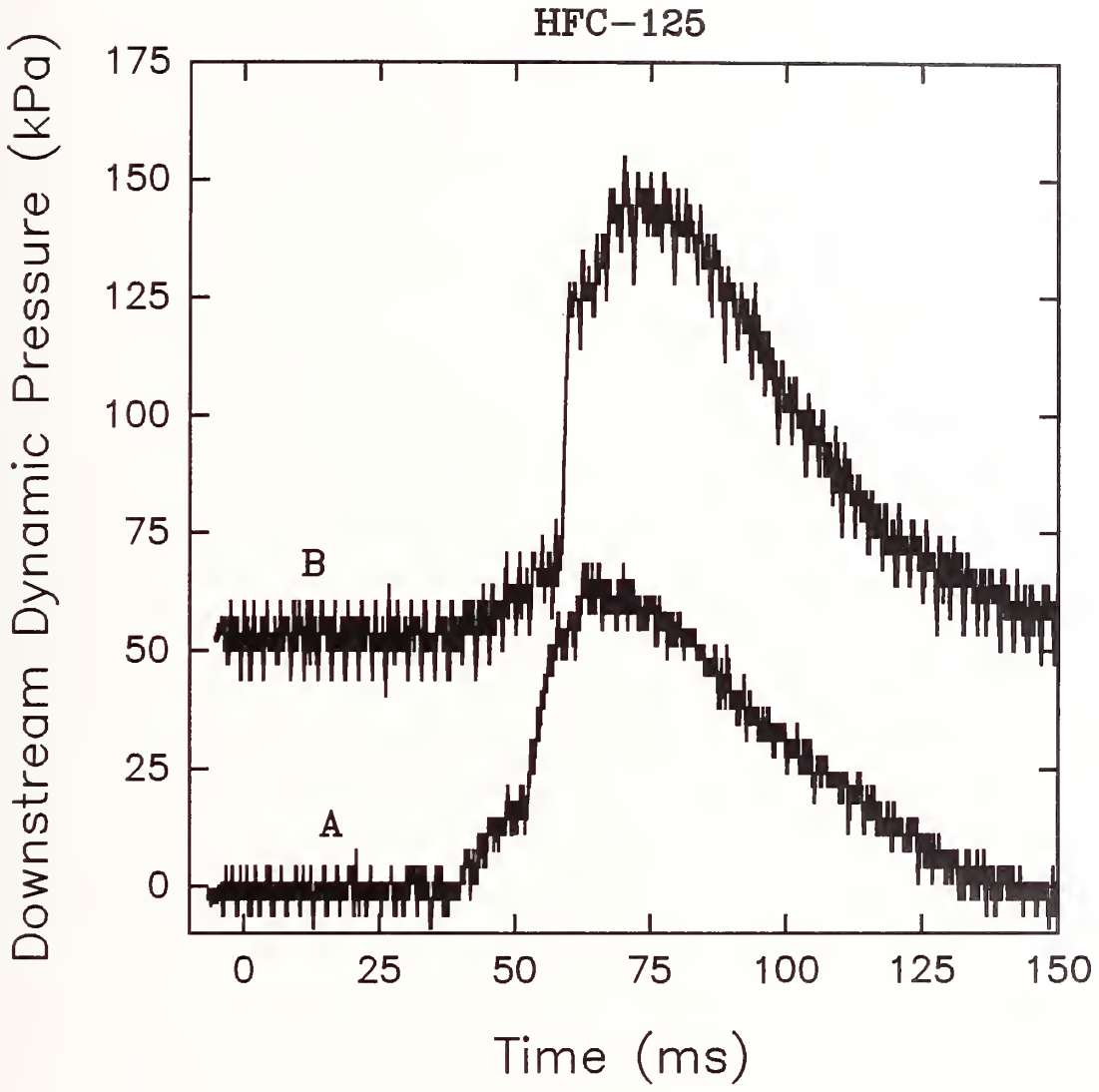

Figure 129. Dynamic pressure measured 1.3 m from the vessel for HFC-125. For clarity, trace B is offset by 50 kPa. Conditions are: A, 403 g agent, release pressure of 4.19 MPa ; B, 423 g of agent, release pressure of 4.24 MPa.

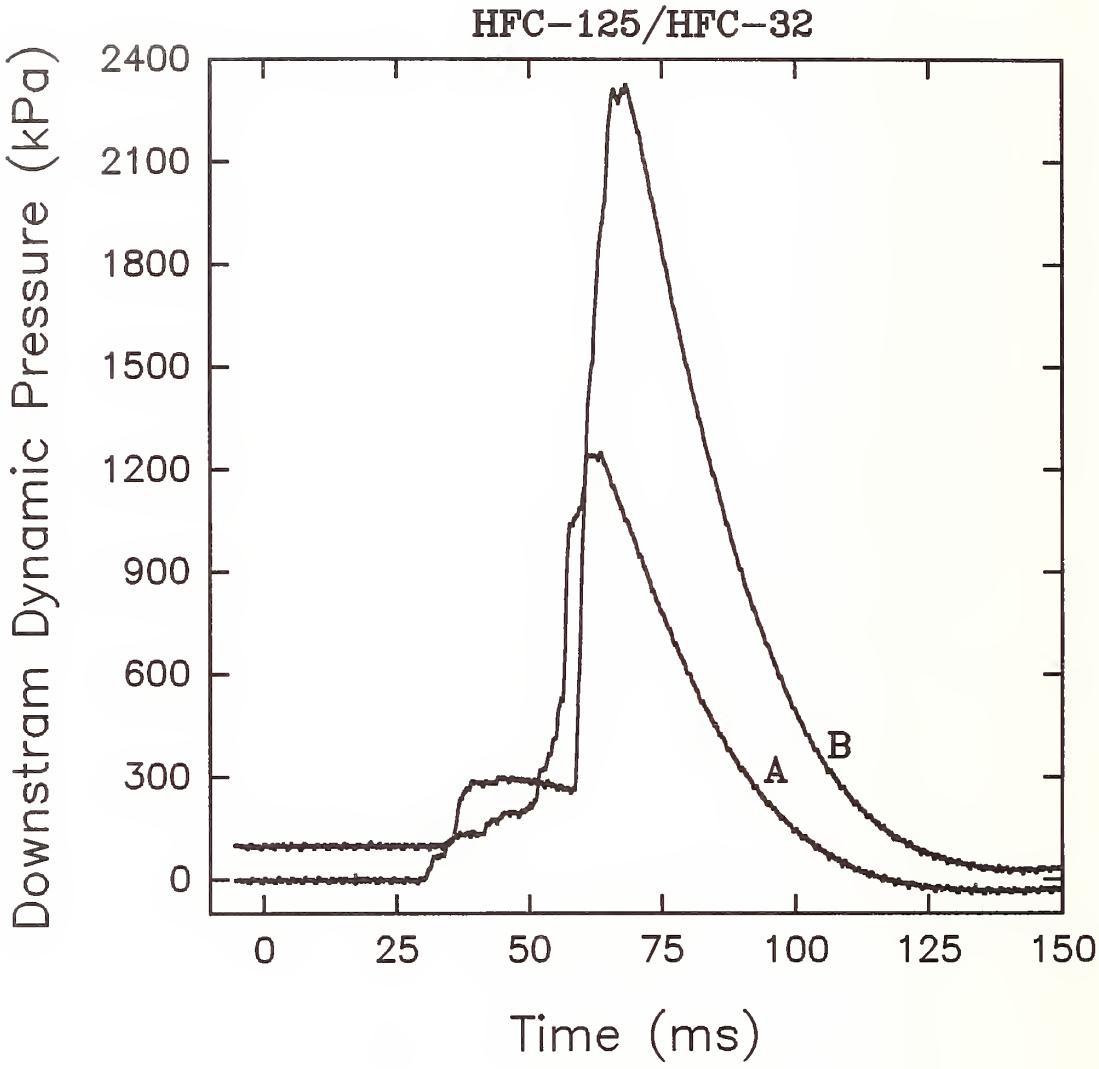

Figure 130. Dynamic pressure measured 1.3 m from the vessel for the HFC-125/HFC-32 mixture. For clarity, trace B is offset by 100 kPa. Conditions are: A, 358 g agent, release pressure of 4.31 MPa ; B, 375 g of agent, release pressure of 4.36 MPa.

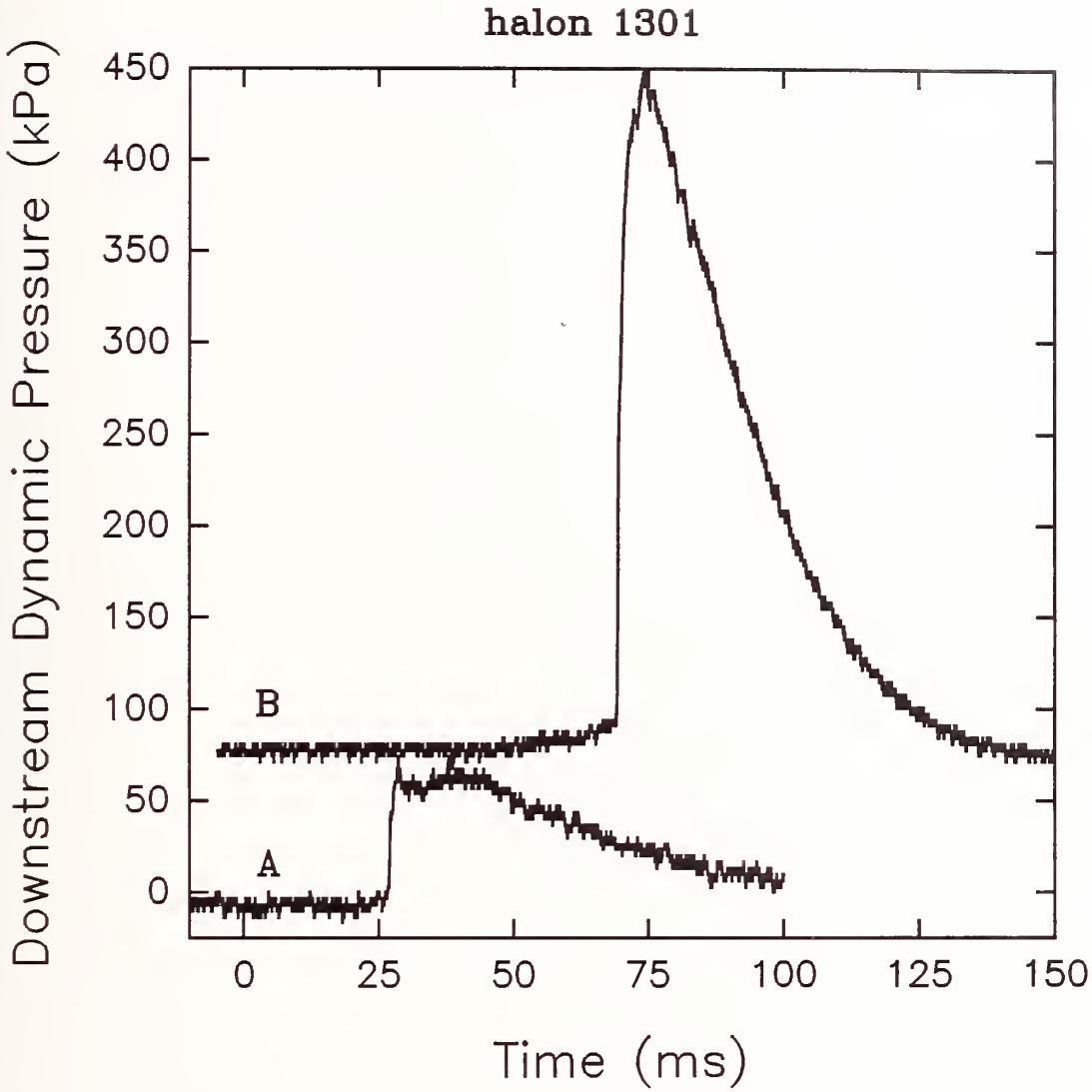

Figure 131. Dynamic pressure measured 1.3 m from the vessel for halon 1301. For clarity, trace B is offset by 75 kPa. Conditions are: A, 1/3 full, 270 g agent, release pressure of 4.43 MPa ; B, 554 g of agent, release pressure of 4.36 MPa.

value is considerably smaller (100-150 kPa) than observed for any of the higher boiling-point agents. The pressure time traces for HFC-125 (Figure 129) are similar except for the fact that the maximum observed pressures are even lower (on the order of 50 kPa). Dynamic pressures observed for halon 1301 (Figure 131) were also quite low, except near the end of one of the releases where a rapid increase to 375 kPa was observed.

While the pressure increases for the low boiling-point agents FC-218, HFC-125, and halon 1301 tended to be smaller than observed for higher boiling-point cases, the results were quite different for HCFC-22 (Figure 128) and the HFC-125/HFC-32 mixture (Figure 130). Both of these agents showed substantial variation between experiments. For HCFC-22 the time required for the pressure to reach its maximum value differed somewhat between releases, but the maximum values reached were greater, being on the order of 2100 kPa for both cases shown. The data for the mixture are also variable. In one case the maximum pressure was in excess of 2200 kPa, while in the other the maximum only reached 1200 kPa.

To summarize, the results for the high boiling-point liquids seem to be consistent and show that very high dynamic pressures are generated at a distance of 1.3 m from the vessel by the release of this type of agent. Two distinct types of pressure curves are found for the lower boiling-point liquids. HCFC-22 and the HFC-125/HFC-32 mixture generate maximum pressures which are similar to those observed for the higher boiling-point agents even though they have more complex time histories, and there are larger variations among experiments. FC-218, HFC-125, and halon 1301 releases generate maximum pressures which are considerably reduced from those observed for all of the other tested liquids.

3.5.3.5 Aspirated Hot-Film Measurements. The aspirated hot-film has only been used to characterize qualitatively the nature of the flows reaching the 1.3 m downstream position. It should be noted that the these probes can be calibrated to accurately measure concentration in isothermal binary mixtures of gases. If the temperature is changing, or if two phases are present the response of these probes is more complex. An ongoing project at NIST is evaluating the utility of aspirated hot-film probes for concentration measurements under these complex conditions.

Since the results are qualitative, only a few representative examples are reported here. Even so, it will become clear that the hot-film response provides useful information for detecting the present of an agent and for determining whether it is a single or two-phase flow.

Figure 132 shows an example of the aspirated hot-film output observed during the release of HFC-236fa. A nearly constant signal (roughly 6.3 V) is observed until 20 ms following release at which time an abrupt increase in voltage is observed. Figure 99 and Figure 121 show that 20 ms is the time when the agent first reaches the probe. Thus the constant signal is that representative of room temperature air. The signal induced by the arrival of the agent is very "spikey" and reaches values of nearly 10 V. Such voltages are much higher than would be expected for a 100% concentration of the gaseous agent (Pitts and McCaffrey, 1986). The large heat transfer from the hot-film probe which these voltages represent is attributed to the presence of two-phase flow in the probe. Evaporative cooling of the droplets requires large amounts of heat. The large voltage spikes are observed for roughly 40 ms. This period is on the order of the period required for release of the agent. Afterwards, much smaller voltages are observed which decay slowly toward that expected for air. This is taken as evidence that the mixture is becoming more gaseous due to evaporation of the agent as it mixes with the air. This is consistent with the transmission observed for laser #5 (Figure 99) which indicates that the flow becomes partially transmitting at roughly 100 ms following the release.

The hot-film responses for FC-31-10, FC-318, HCFC-124, HFC-227ea, and HFC-134a are very similar to those for HFC-236fa. During the period when the releases are passing the probe there are

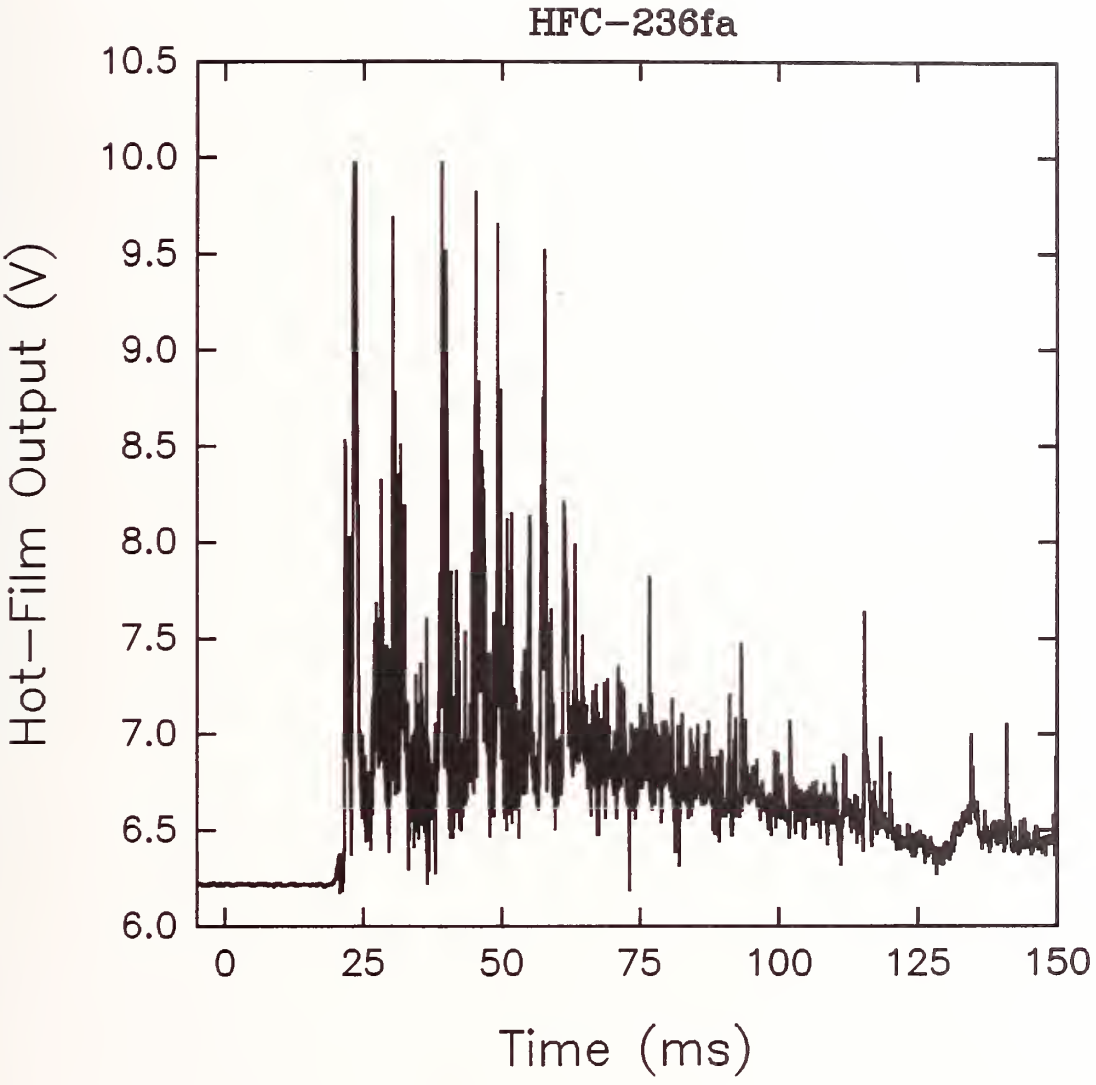

Figure 132. The voltage output of the aspirated hot-film located 1.3 m from the vessel is plotted as a function of time for a release of HFC-236fa. Conditions: 464 g of agent, release pressure of 4.30 MPa.

voltage signals which must be associated with two-phase flow. Afterwards, the voltages begin to fall and approach those for room-temperature air.

The hot-film response for FC-218 releases was quite different. Figure 133 shows an example of the hot-film voltage plotted as a function of time. The signal begins to rise at the time when laser beam #5 is strongly attenuated (Figure 105) and the downstream pressure transducer (Figure 127, curve A) detects the arrival of the agent. The signal changes rapidly with time indicating the presence of highly turbulent flow, but during the initial part of the signal following the arrival of the agent the voltage increases are relatively small and consistent with those expected for a binary gas mixture. At roughly 50 ms following the release, there is a rise in the hot-film voltage and spiking appears which suggests the presence of a two-phase flow. Interestingly, the downstream pressure transducer recorded a small rise in dynamic pressure at the same time. These results suggest that near the end of the release a small amount of two-phase fluid reached the 1.3 m downstream position, but the responses of the detectors suggest that the FC-218 was much more completely vaporized than the higher boiling-point agents.

Figure 134 shows simultaneous plots of downstream dynamic pressure and hot-film output as functions of time for a release of HFC-125. The flow of this agent results in relatively small increases in both dynamic pressure and hot-film voltage. Roughly 20 ms after the agent arrives at the measurement location there are sharp increases in both signals. It is difficult to determine whether this is the result of the arrival of two-phase flow or a higher concentration (*i.e.*, density) or velocity of gaseous agent. In either case, it is clear that this agent arrives nearly completely vaporized. Figure 135 shows a similar plot for halon 1301. Here there is a significant increase in dynamic pressure associated with the end of the release which appears to have two-phase behavior. However, it is clear from the traces that during most of the release primarily gas-phase agent is reaching this downstream position.

Recall that releases of HCFC-22 and the HFC-125/HFC-32 mixture resulted in large downstream dynamic pressures. Figure 136 and Figure 137 show time plots for the hot-film outputs for these two agents. In both cases there is evidence for two-phase flow near the beginning and ends of the releases. This conclusion is consistent with the observed dynamic pressure behaviors (see Figure 128 and Figure 130).

3.5.3.6 Effects of Orifice Diameter. Experiments were done for FC-31-10, FC-218, and halon 1301 using plates with orifices of 12.7 and 6.4 mm. The same flow characterizations recorded for the standard release conditions were used.

For the FC-31-10 the near-field pressure transducer recorded a pressure rise of roughly 450 kPa when the 12.7 mm orifice was used and no measurable increase when the 6.4 mm orifice was used. These results can be compared with the results in Table 6 for the 19.1 mm opening where maximum dynamic pressures were between 300-400 kPa. The pressure behavior for a release of FC-218 through the 12.7 mm orifice is shown in Figure 138. It can be seen that the transducer responded shortly after the start of the release and that the dynamic pressure remained high over the remaining release period of approximately 75 ms. Comparison with Figure 94 shows that the maximum pressures reached are lower for this orifice diameter than for the 19.1 mm opening, but that the pressures are sustained over a much longer period. For the 12.7 mm orifice, the fluid seems to be flashing continuously. For the smallest orifice no pressure increase was detected. The dynamic pressure time behaviors recorded for releases of halon 1301 had very similar behaviors to those for the FC-218.

The size of the orifice has a strong effect on flashing behavior. For the higher boiling-point FC-31-10 no flashing is observed for the smaller orifices. For the lower boiling-point liquids, the maximum dynamic pressure observed decreases when the 19.1 mm orifice is reduced to 12.7 mm, but

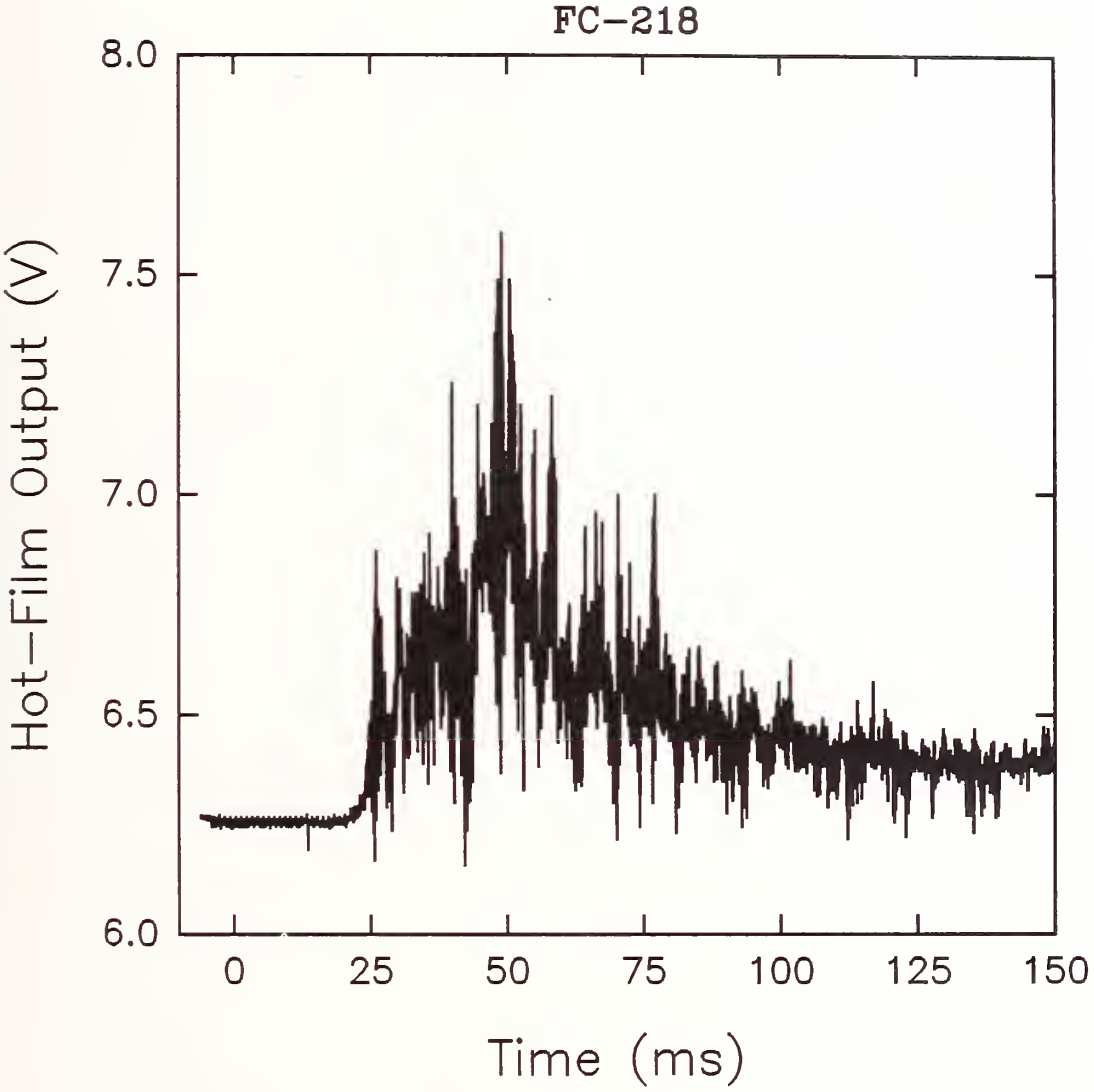

Figure 133. The voltage output of the aspirated hot-film located 1.3 m from the vessel is plotted as a function of time following a release of FC-218. Conditions: 460 g of agent, release pressure of 4.58 MPa.

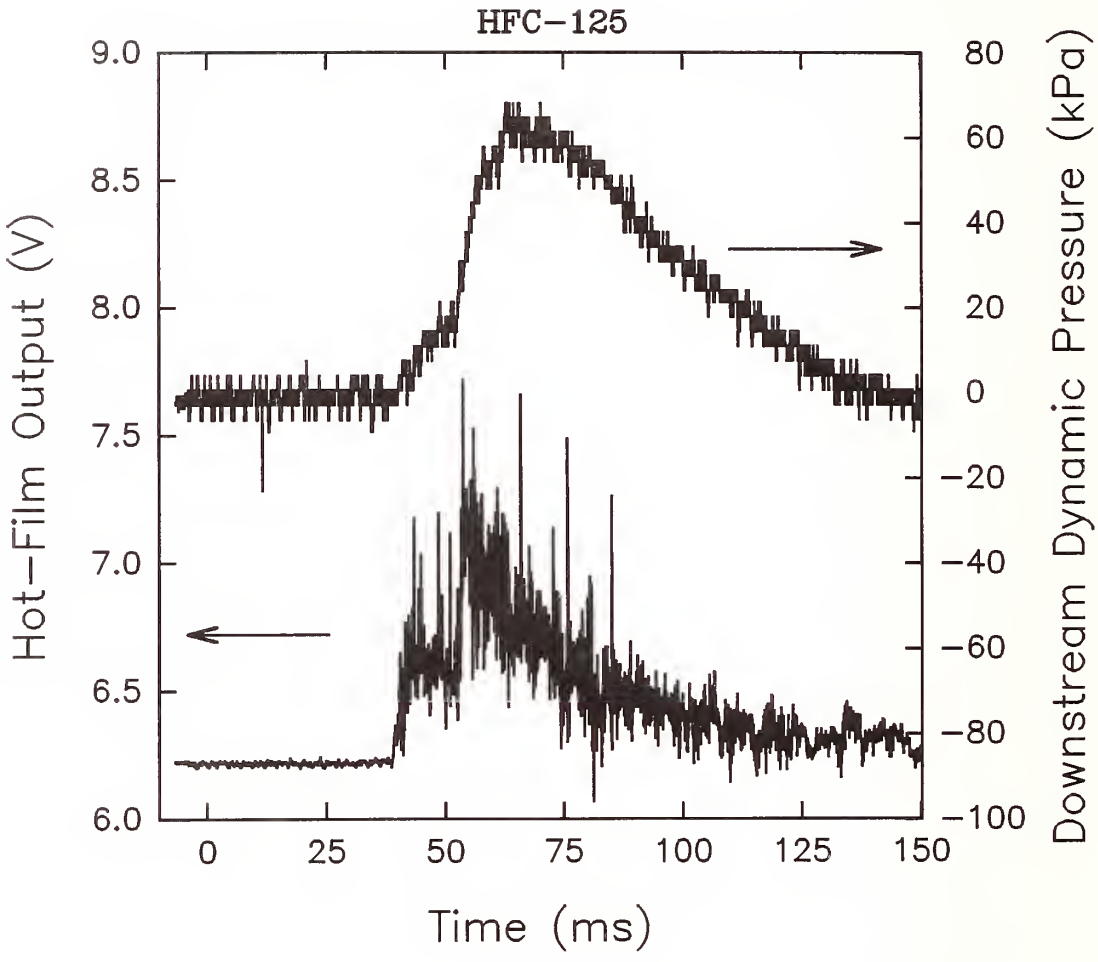

Figure 134. The voltage output of the aspirated hot-film and the dynamic pressure for probes located 1.3 m from the vessel are plotted as a function of time following a release of HFC-125. Conditions: 403 g of agent, release pressure of 4.19 MPa.

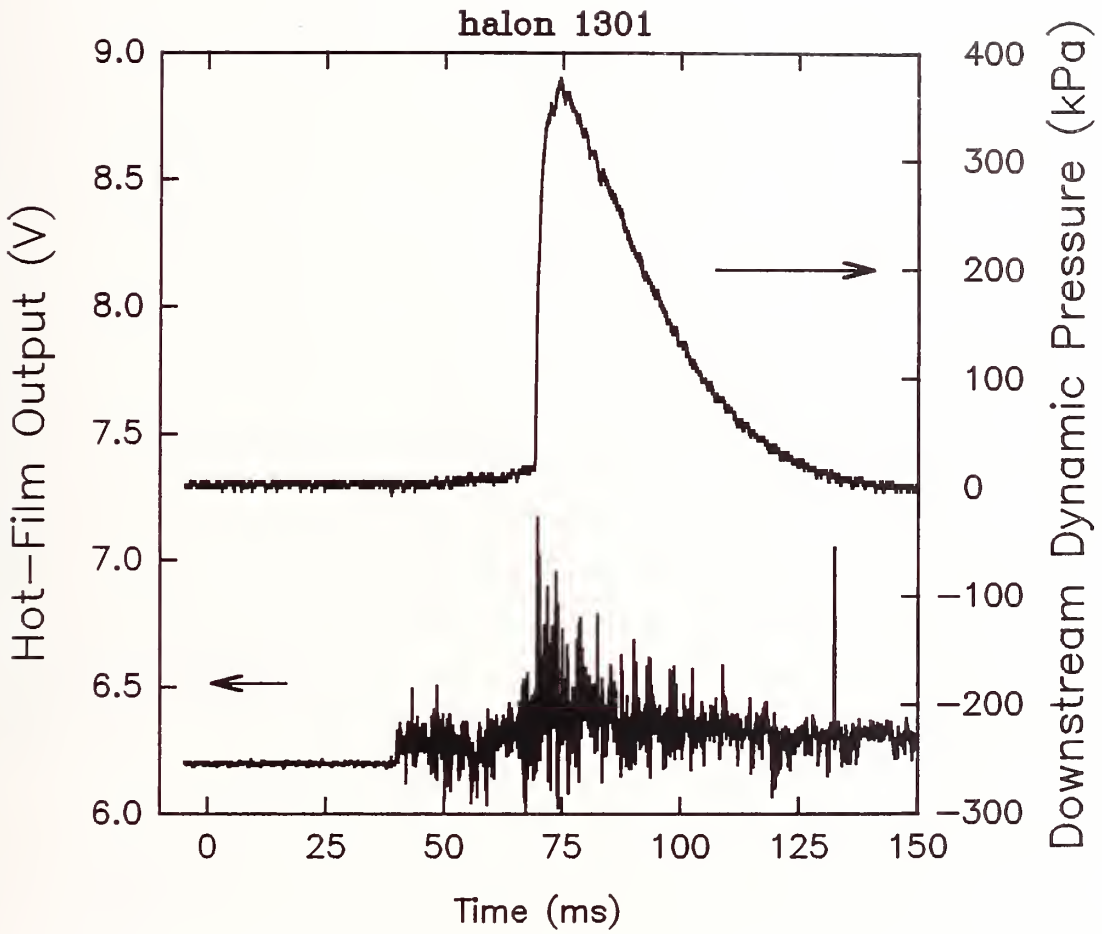

Figure 135. The voltage output of the aspirated hot-film and the dynamic pressure for probes located 1.3 m from the vessel are plotted as a function of time following a release of halon 1301. Conditions: 554 g of agent, release pressure of 4.36 MPa.

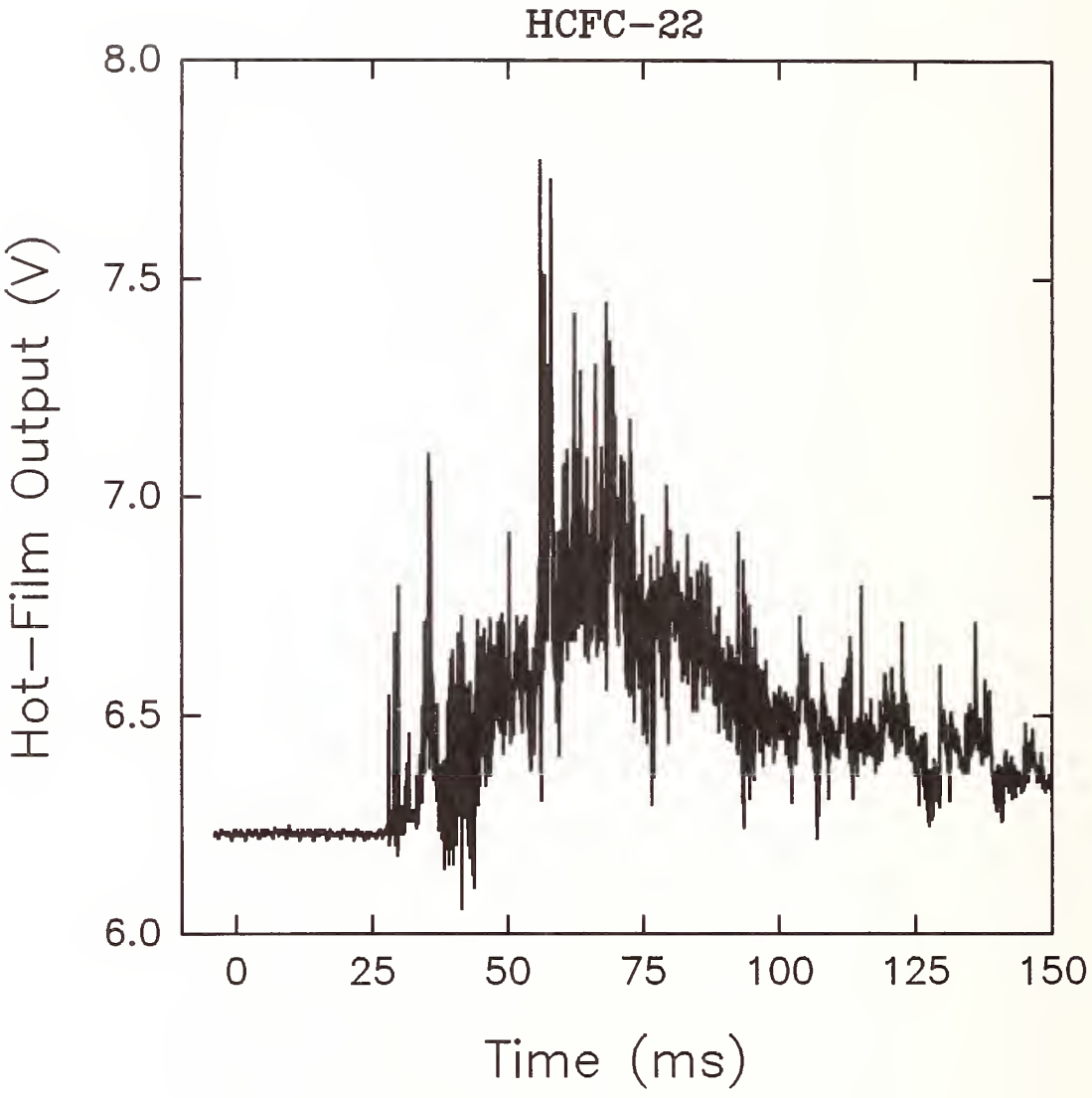

Figure 136. The voltage output of the aspirated hot-film located 1.3 m from the vessel is plotted as a function of time following a release of HCFC-22. Conditions: 421 g of agent, release pressure of 4.48 MPa.

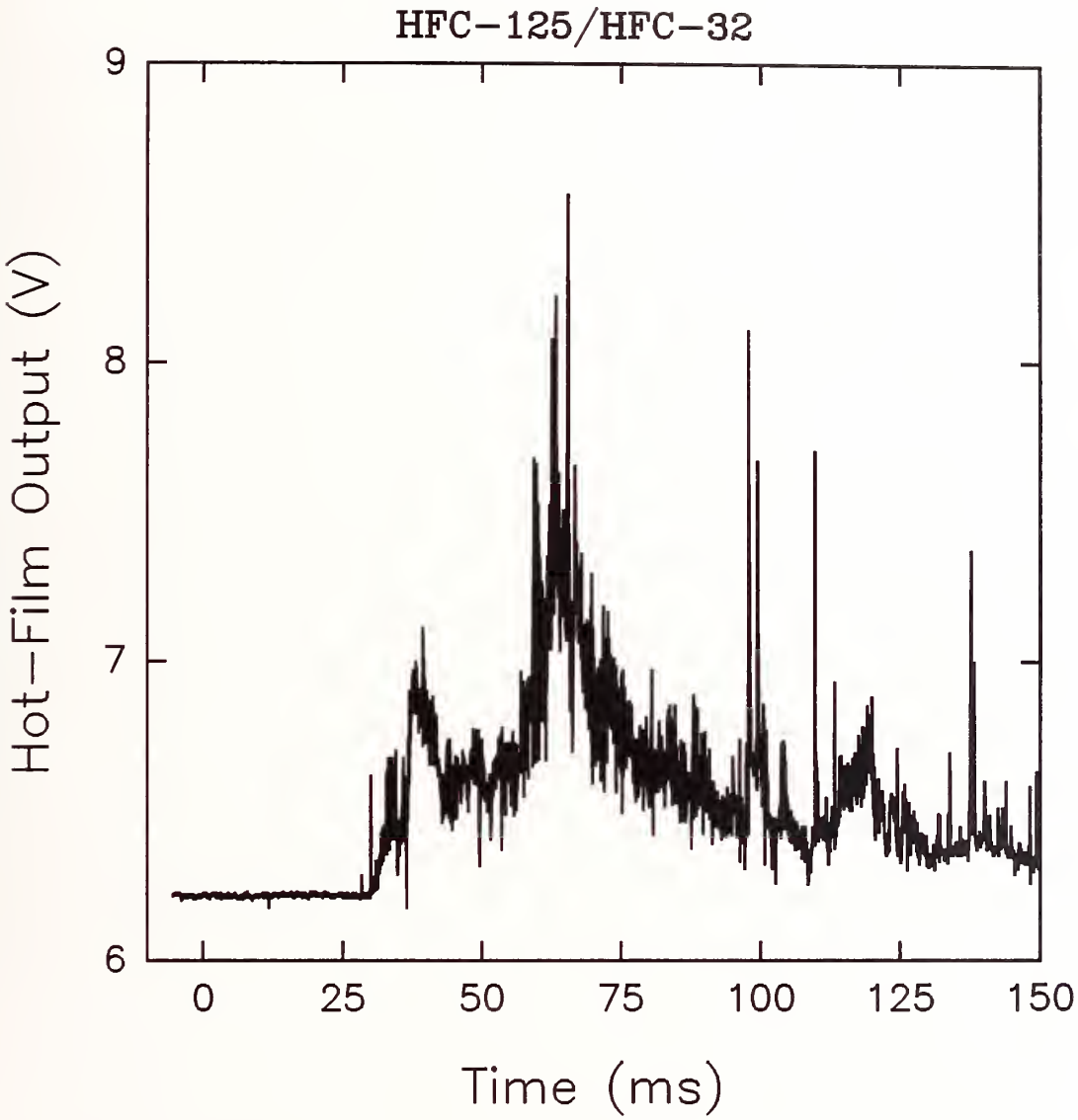

Figure 137. The voltage output of the aspirated hot-film located 1.3 m from the vessel is plotted as a function of time following a release of the HFC-125/HFC-32 mixture. Conditions: 375 g of agent, release pressure of 4.36 MPa.

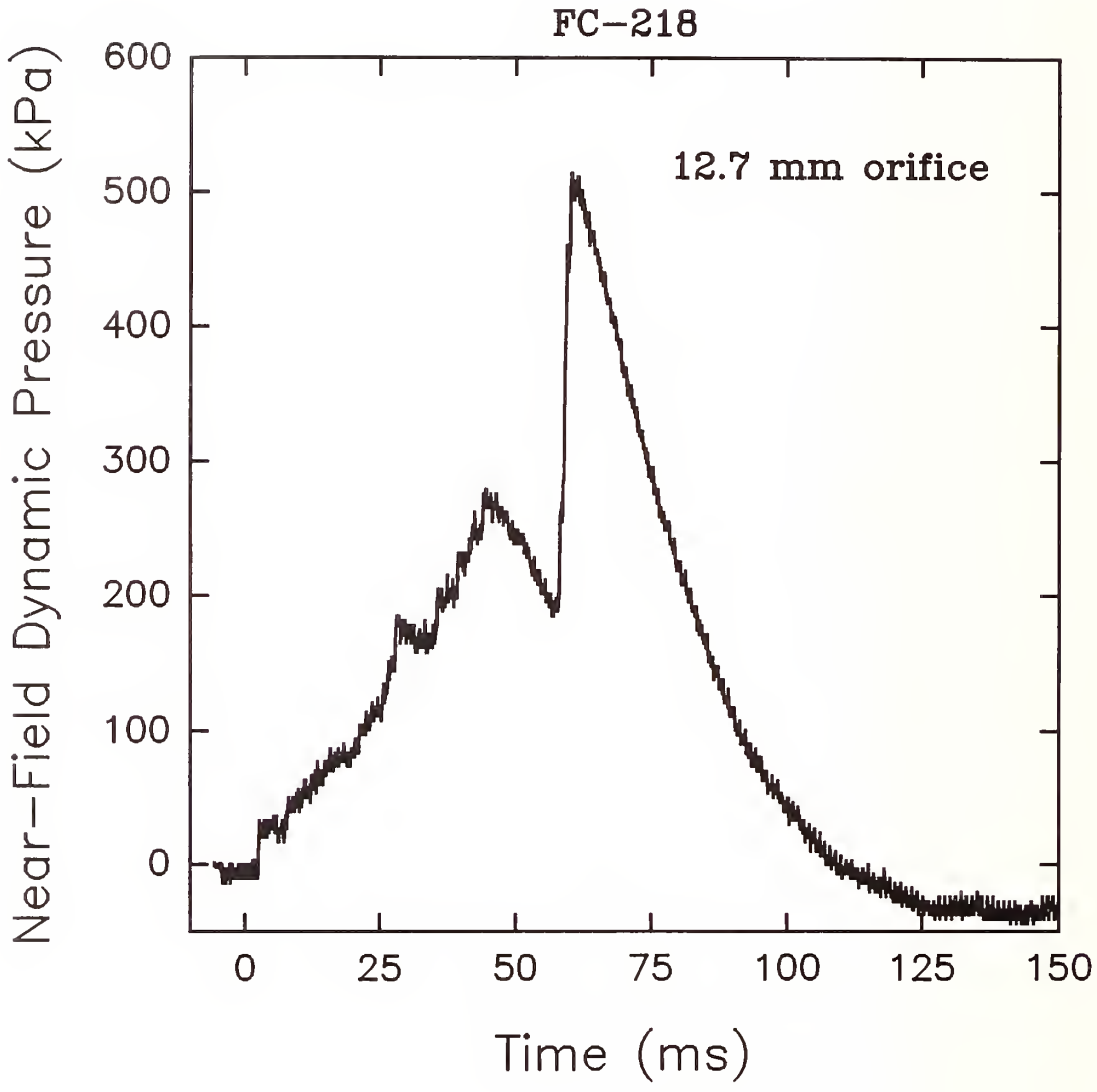

Figure 138. Time trace of near-field dynamic pressure for a release of FC-218 through a 12.7 mm orifice. Conditions: 457 g of agent, 4.30 MPa release pressure.

the period of flashing is substantially extended. No increases in dynamic pressure are observed for the smallest orifice.

Figure 139 through Figure 141 compare the average velocity variations with average downstream position for releases of FC-31-10, FC-218, and halon 1301 through the three orifices. For FC-31-10 releases, smaller orifices result in significant changes in the velocity development. With the 19.1 mm opening (Figure 111 and Figure 139) the velocity first increases and then levels off at values near 70 m/s. For the two smaller orifices the initial velocity is on this order, but it then decreases with increasing downstream distance. The smallest velocity is observed at the farthest position using the 6.4 mm orifice.

Velocities near the vessel exit are roughly the same for each orifice size when FC-218 is considered (Figure 140). The velocities drop off in each case with increasing downstream distance. Once again the smallest orifice results in the lowest velocity at the last measuring position.

The results for halon 1301 (Figure 141) are similar to those for FC-218 except that the velocities nearest the orifice vary somewhat with the smaller orifices producing higher velocities. Overall, the smaller orifices generate higher velocities near the vessel and lower velocities further downstream.

The evaporation characteristics of the flows for releases of the three agents are indicated by Figure 142 through Figure 145 where the time behaviors for the far-field pressure transducer and hot-film aspirated film voltages are plotted as functions of time. The responses for the release of FC-31-10 from the 12.7 mm orifice (Figure 142) indicate that this agent is a two-phase mixture 1.3 m from the vessel. This is clear from the high dynamic pressures and spikey nature of the hot-film signal. The period required to empty the bottle is roughly 65 ms. This is also roughly the length of the two-phase flow period at the downstream position. The plots for the release from the 6.4 mm orifice indicate that the agent first arrives in the gas phase and remains so throughout the release period.

The data for the release of FC-218 through the 12.7 mm orifice (Figure 143) suggest that this agent is fully vaporized when it reaches the sampling position, except, perhaps, at the very end of the release. Both the low dynamic pressures and small increases in hot-film voltages support this conclusion. Similar results were obtained for the 6.4 mm orifice.

Halon 1301 has a behavior which is very much like that for FC-218 except that a very strong two-phase component is observed near the end of the release when the 12.7 mm orifice is used (Figure 144). Both the dynamic pressure and hot-film signals indicate the presence of two-phases. It is possible that this change in flow composition is associated with the strong flashing which occurred near the vessel as the liquid emptied from the vessel. Figure 145 shows results for a release of halon 1301 through the 6.4 mm orifice. Here the signals from both transducers are small indicating that only gaseous agent is present 1.3 m from the orifice. A small pressure increase was recorded at the end of the release which may be associated with the presence of a small amount of liquid agent or a higher concentration or velocity of the gaseous agent. Note the long time period required for release through this small opening.

3.5.3.7 Effect of Vessel Pressurization Level. The effect of the vessel pressurization level on the mixing and dispersion behavior of an agent was investigated for releases of FC-218 using burst disks designed to break at nominal pressures of 2.76, 4.14, and 5.52 MPa. Figure 146 and Figure 147 show examples of the results for near-field dynamic pressure as a function of time for vessels having high and low internal pressures, respectively. Figure 94 shows two examples of results for releases having intermediate levels of pressurization. None of the releases indicated a pressure rise associated with the first flashing following the release of the FC-218. Interestingly, the highest dynamic pressure associated with the second flashing is observed for the release with an

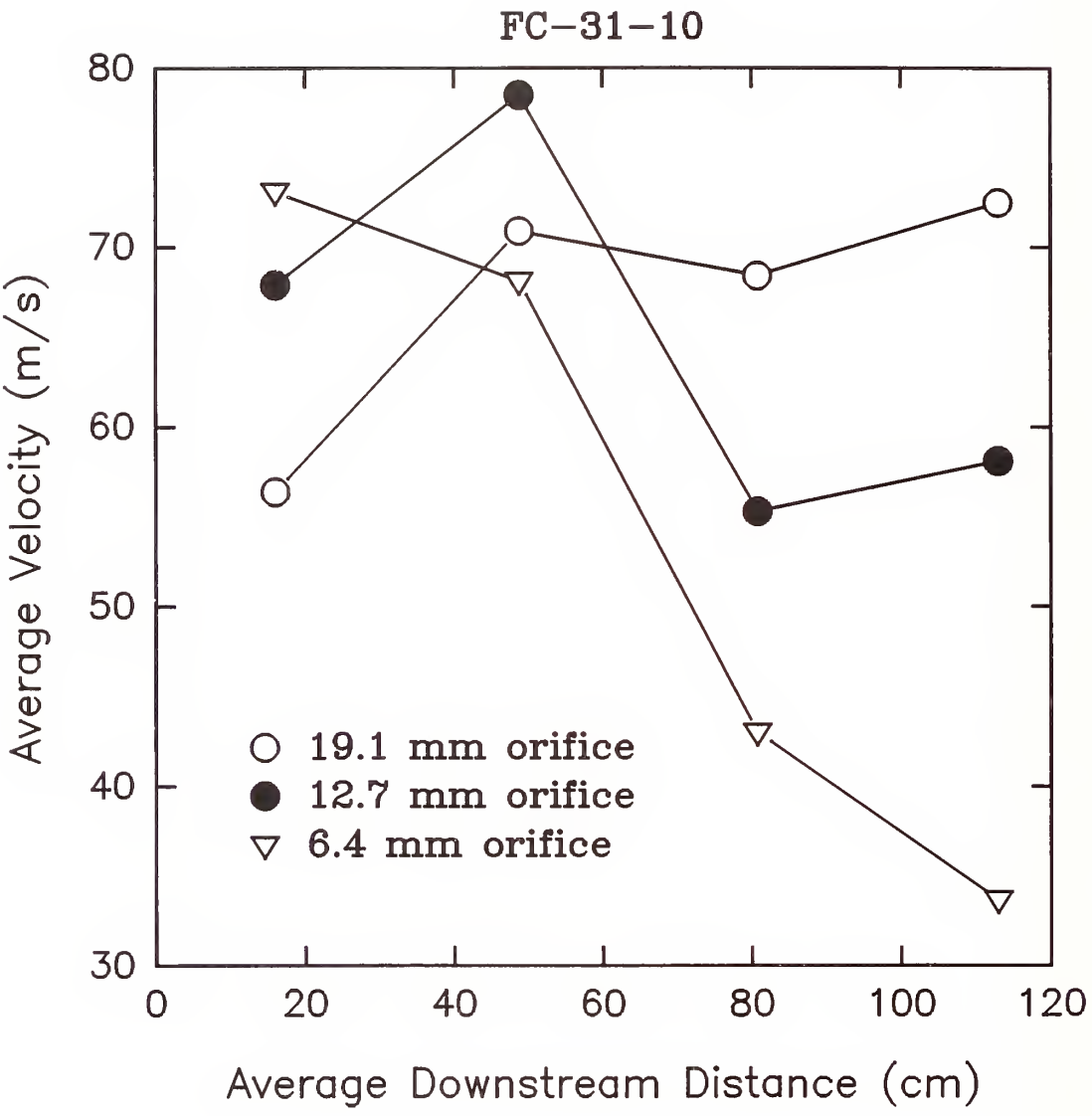

Figure 139. Average velocities determined by the time of arrival at laser beams #1-#5 plotted as a function of average downstream distance for releases of FC-31-10 through 19.1, 12.7, and 6.4 mm orifices.

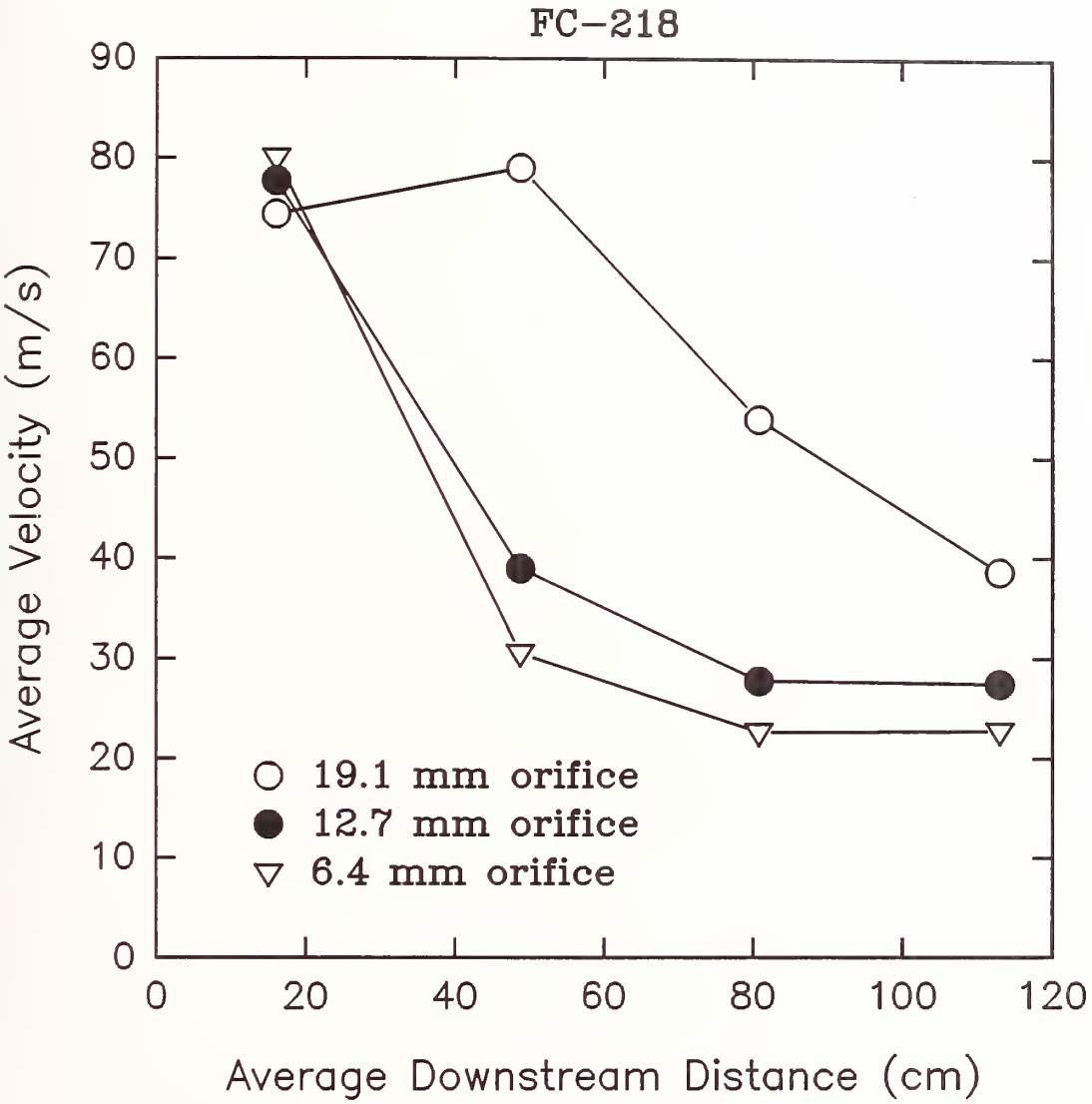

Figure 140. Average velocities determined by the time of arrival at laser beams #1-#5 plotted as a function of average downstream distance for releases of FC-218 through 19.1, 12.7, and 6.4 mm orifices.

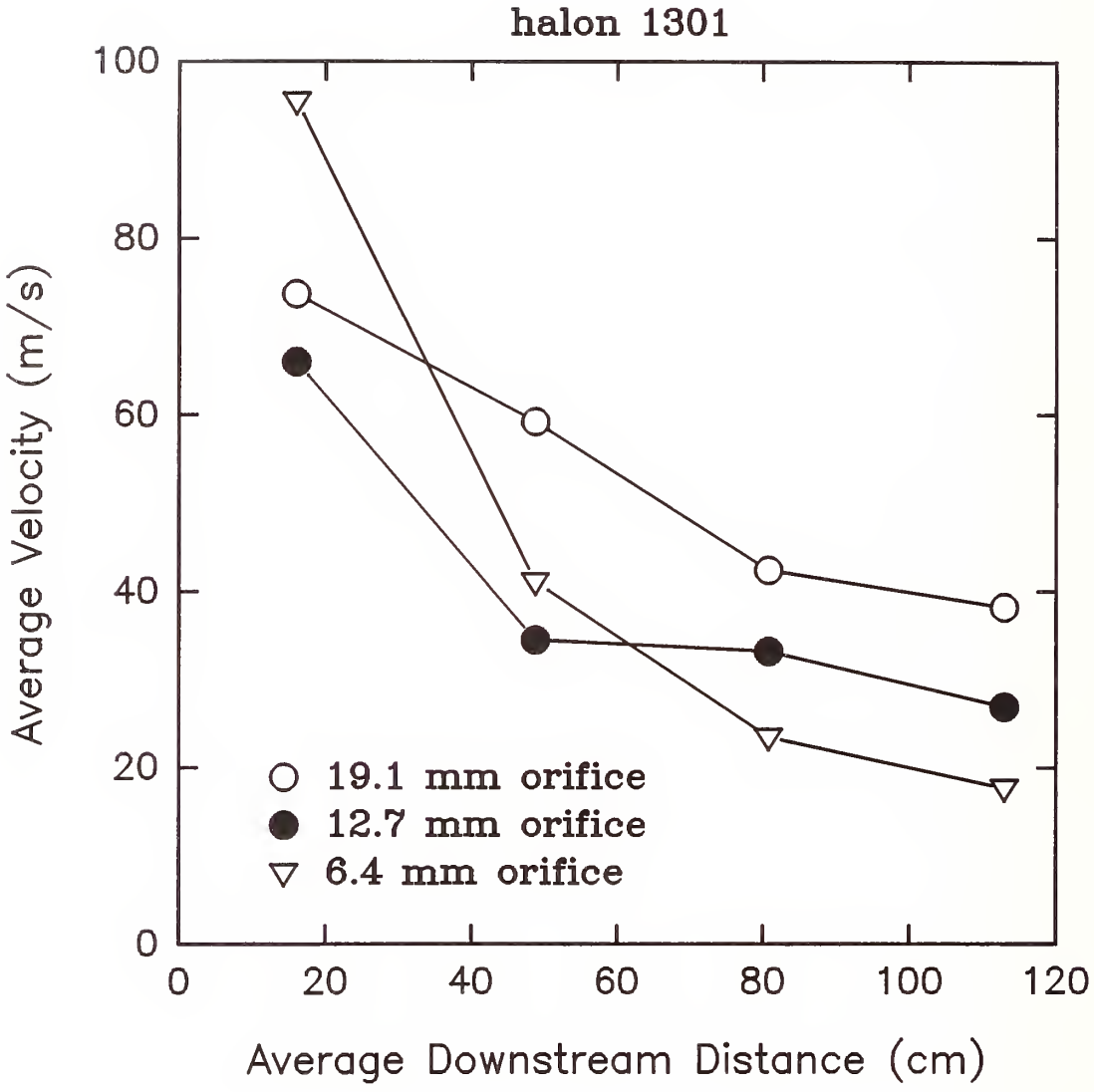

Figure 141. Average velocities determined by the time of arrival at laser beams #1-#5 plotted as a function of average downstream distance for releases of halon 1301 through 19.1, 12.7, and 6.4 mm orifices.

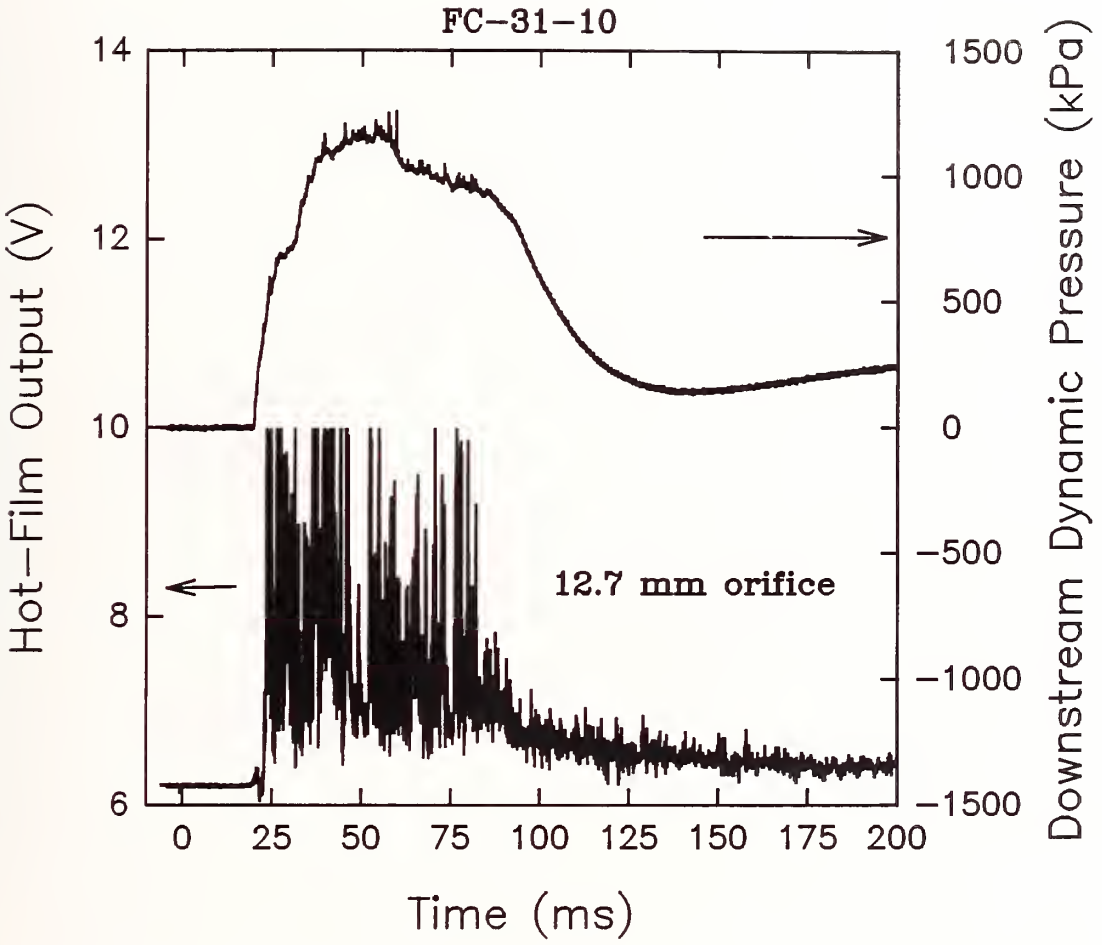

Figure 142. Voltage output of the aspirated hot-film and dynamic pressure for probes placed 1.3 m from the vessel as a function of time following a release of FC-31-10 through a 12.7 mm orifice. Conditions: 521 g of agent, release pressure of 4.48 MPa.

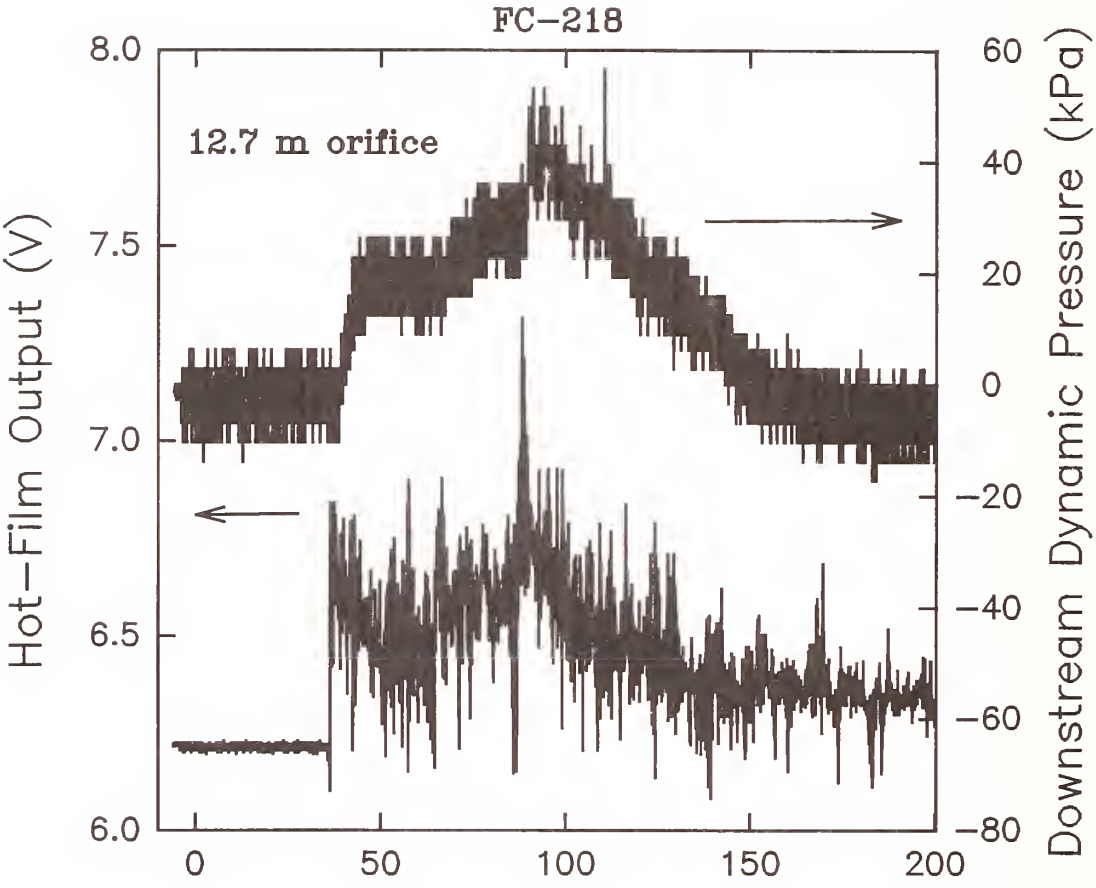

Figure 143. Voltage output of the aspirated hot-film and dynamic pressure for probes placed 1.3 m from the vessel as a function of time following a release of FC-218 through a 12.7 mm orifice. Conditions: 463 g of agent, release pressure of 4.23 MPa.

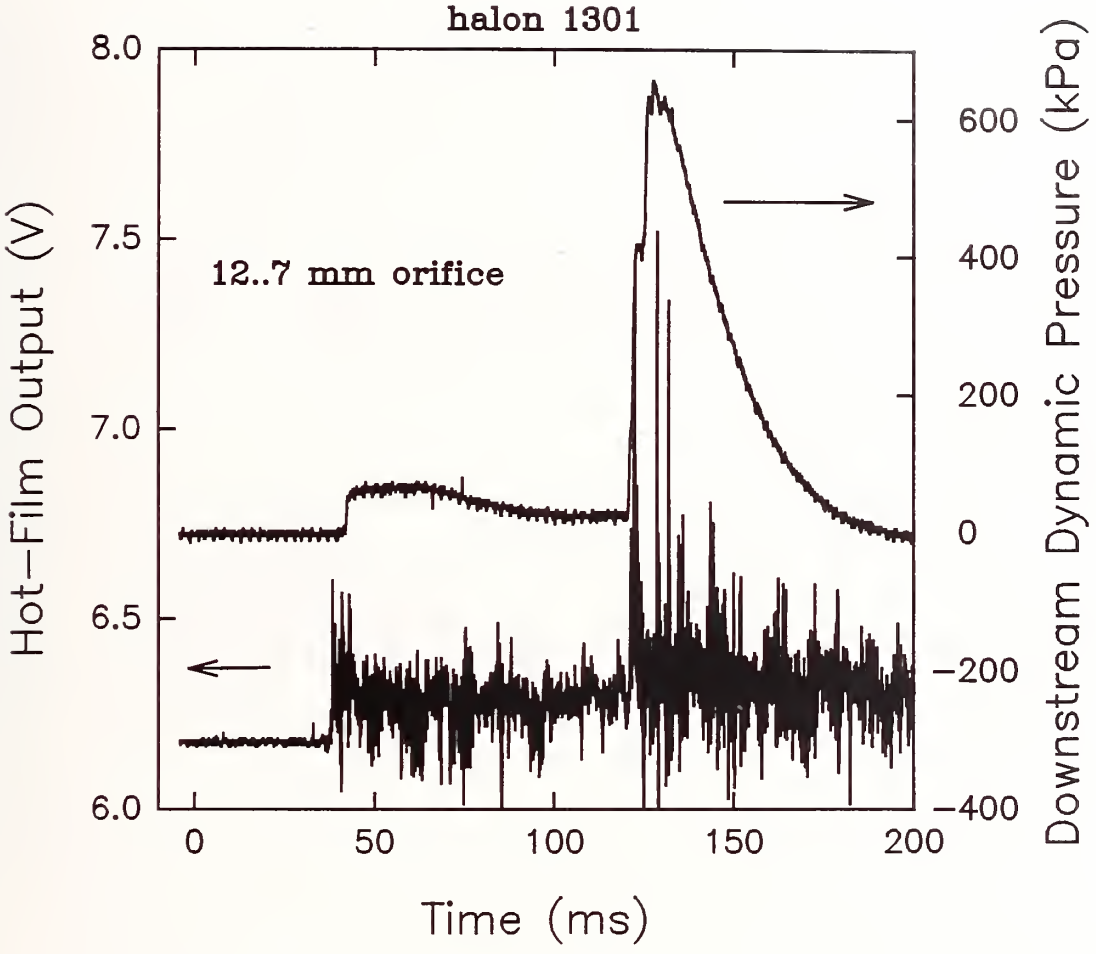

Figure 144. Voltage output of the aspirated hot-film and dynamic pressure for probes placed 1.3 m from the vessel as a function of time for a release of halon 1301 through a 12.7 mm orifice. Conditions: 537 g of agent, release pressure of 4.54 MPa.

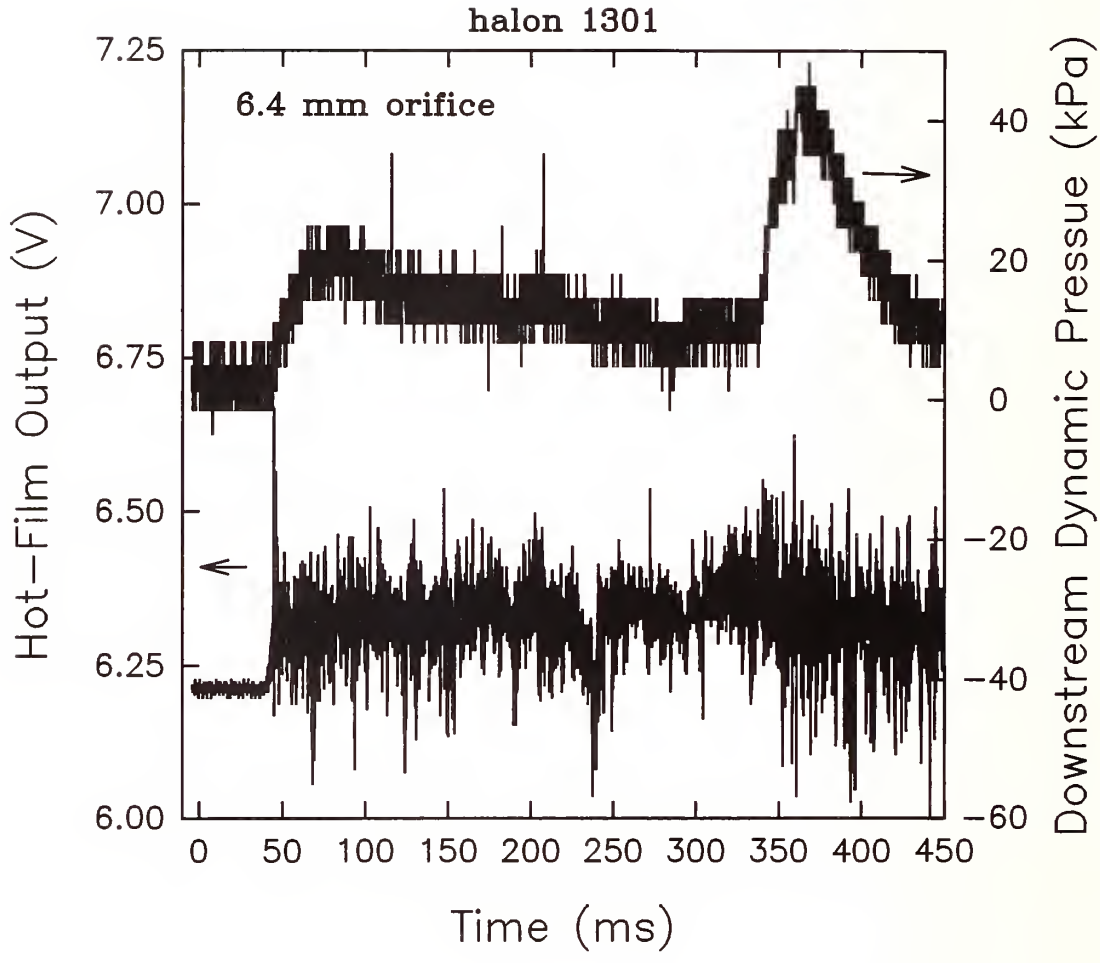

Figure 145. Voltage output of the aspirated hot-film and dynamic pressure for probes placed 1.3 m from the vessel as a function of time for a release of halon 1301 through a 6.4 mm orifice. Conditions: 546 g of agent, release pressure of 4.62 MPa.

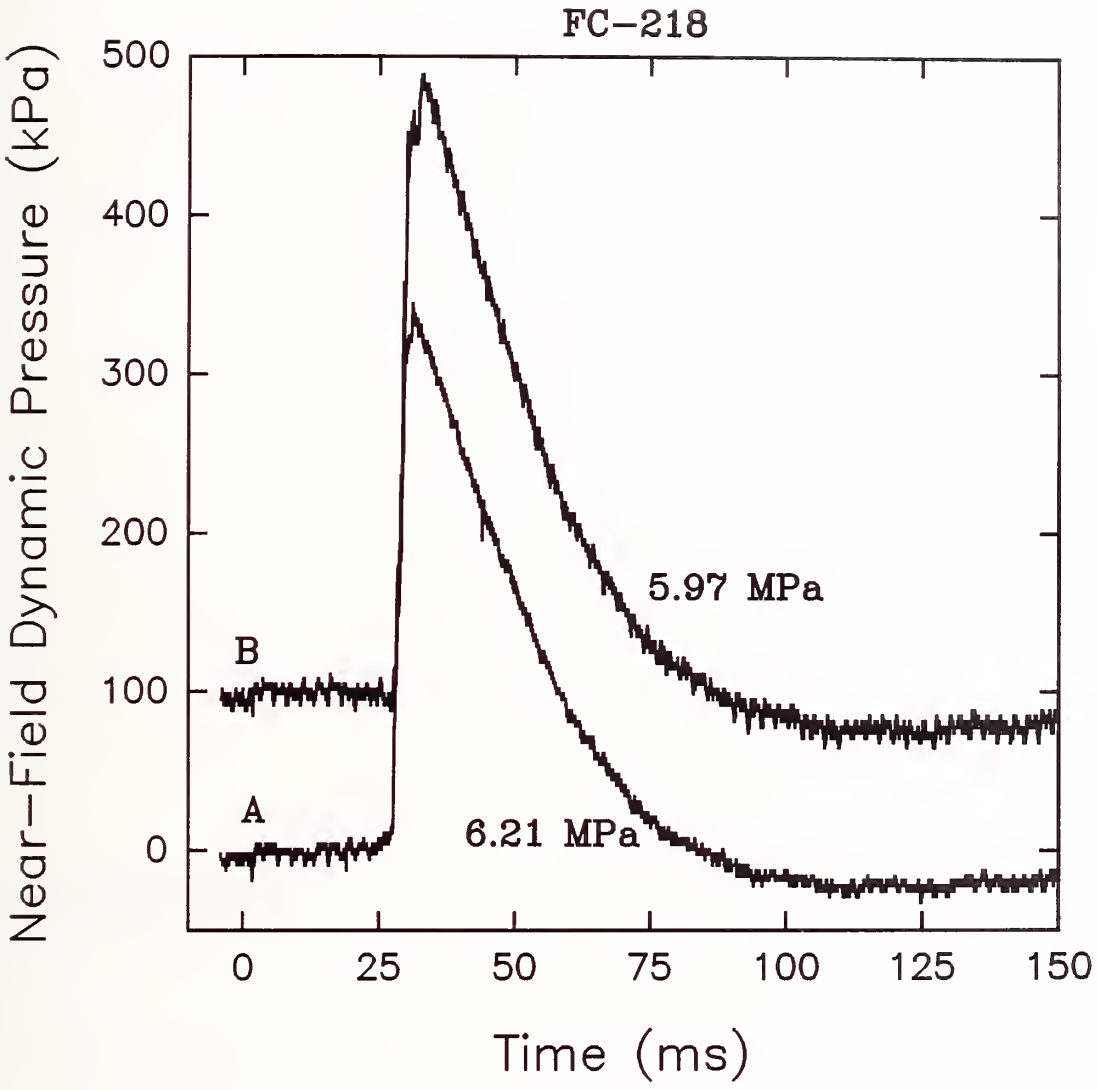

Figure 146. Two time traces of near-field dynamic pressure for releases of FC-218 using nominal 5.52 MPa burst disks. Trace B is offset by 100 kPa. Conditions: A, 455 g, release pressure 6.21 MPa; B, 457 g, release pressure 5.97 MPa.

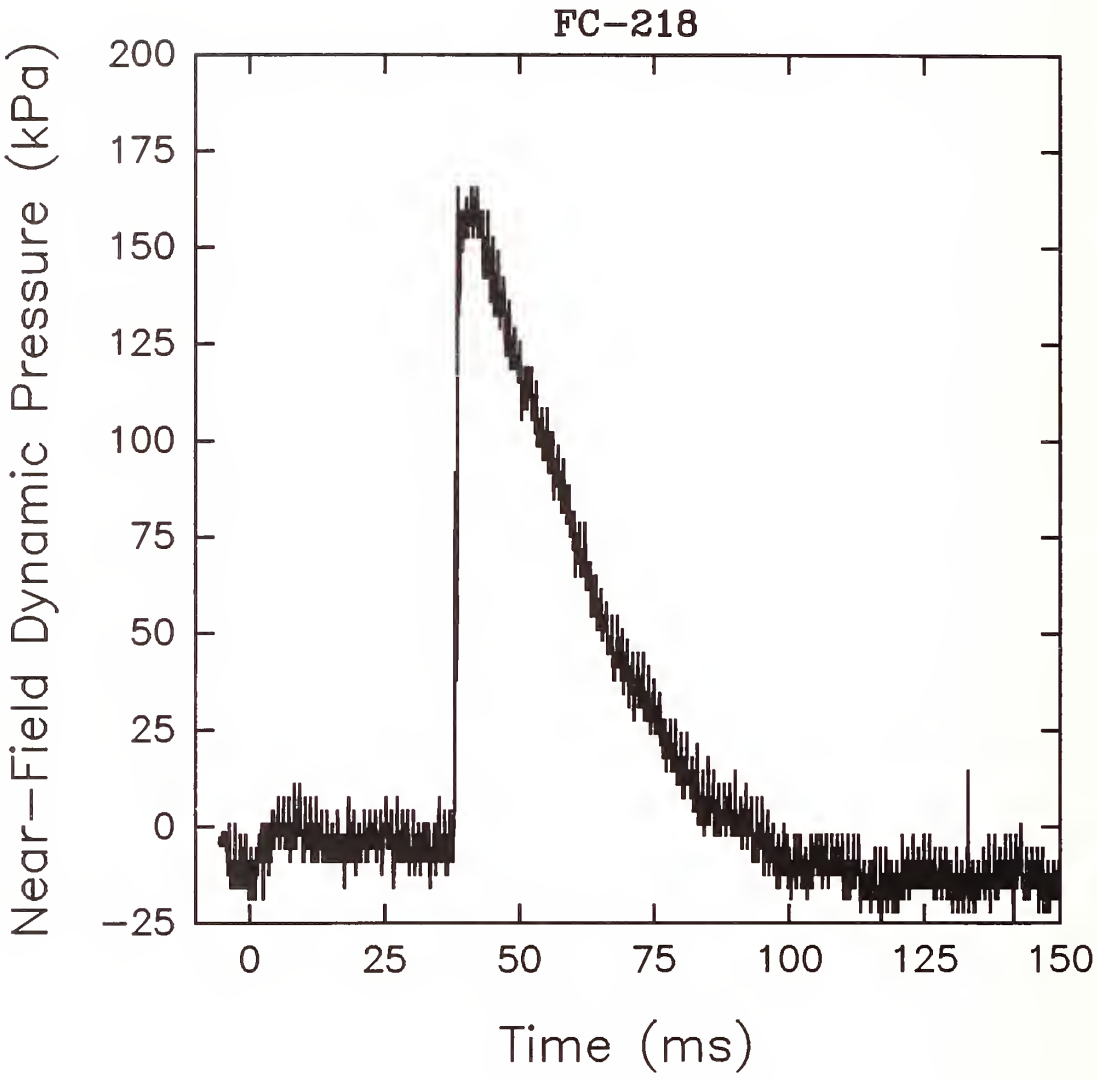

Figure 147. Time trace of the near-field dynamic pressure for a release of FC-218 using a nominal 2.76 MPa burst disk. Conditions: 436 g, release pressure 2.61 MPa.

internal pressure of 4.28 MPa. The releases at higher internal pressures resulted in somewhat lower dynamic pressures. The smallest pressure rise was observed when the vessel pressure was 2.61 MPa.

Measurements discussed in Section 3.4.3.4 showed that the agent was expelled from the vessel at higher rates as the internal pressure was increased. Figure 148 shows the average velocities measured for three releases of FC-218 subject to a range of vessel pressures. Consistent with the emptying rate measurements, the velocities increase with internal pressure. The largest difference is observed when reducing the internal vessel pressure from 4.28 MPa to 2.61 MPa.

3.5.3.8 Effect of Attaching a 0.5 m Extension Tube to the Vessel. A 0.5 m tube having a 19.1 mm inside diameter was attached to the orifice of the vessel. The near-field pressure transducer was not employed in these experiments. The tube blocked lasers #1 and #2. As a result, average velocity measurements are only available for the two measurement locations farthest from the vessel. Note that the exit for the tube was located 0.8 m from the downstream position of laser #5. Measurements were made for FC-31-10, FC-218, and halon 1301.

Figure 149 through Figure 151 show measurements of average velocities for the three agents with the tube in place. For comparison purposes the results for releases without the tube are also shown. In each case the velocities observed with the tube are considerably higher than when the tube is absent. For the higher boiling-point FC-31-10 the increase is only 20 to 30%. However, for the two lower boiling-point agents the increase is more than a factor of two.

The downstream dynamic pressures and hot-film responses recorded for releases of the three agents are shown in Figure 152 through Figure 154. In each case very high dynamic pressures are measured suggesting that the agents are arriving as two-phase flows. The spikey nature of the hot-film signals support this conclusion. For the two low boiling-point agents, FC-218 and halon 1301, the hot-film detects the presence of the agents before a large pressure increases is observed. This suggest that the initial agent reaching the detectors is primarily vapor. However, after only a few milliseconds, the flow displays two-phase character.

Comparison of Figure 154 with Figure 152 and Figure 153 shows that the two-phase flow period is considerably longer for the halon 1301 ($\sim$ 100 ms) than for the other two agents. This, in turn, implies that the time required for the release of the agent from the vessel is substantially longer. In the absence of the extension tube (see Section 3.4.3.1) the liquid release period for the three agents is on the order of 40 ms. The presence of the extension tube therefore more than doubles the liquid release period for halon 1301. The same conclusion was reached in Section 3.4.3.3 based on internal vessel pressure measurements. The longer liquid release period is attributed to the generation of a two-phase flow of halon 1301 in the tube.

3.5.3.9 Effect of Cooling the Agent Prior to Release. Two releases of FC-31-10 were studied in which the agent inside the vessel was cooled to 228 K, *i.e.*, a temperature far below its boiling point of 271 K. As would be expected, the high-speed films indicated that there was very little flashing of the liquid as it exited the vessel. No near-field dynamic pressure measurements were made, but no pressure increase would be expected due to the absence of flashing behavior.

Figure 155 is a plot of the measured average velocity as a function of distance from the vessel. These results can be compared with similar plots shown in Figure 111 for releases of FC-31-10 with the vessel at room temperature. The velocities near the vessel exit are much lower for the cooled agent as expected for the lower release pressure. There are small increases in these velocities with downstream distance, but the increases are much smaller than observed for the room temperature releases (roughly 10 m/s versus 15 m/s).

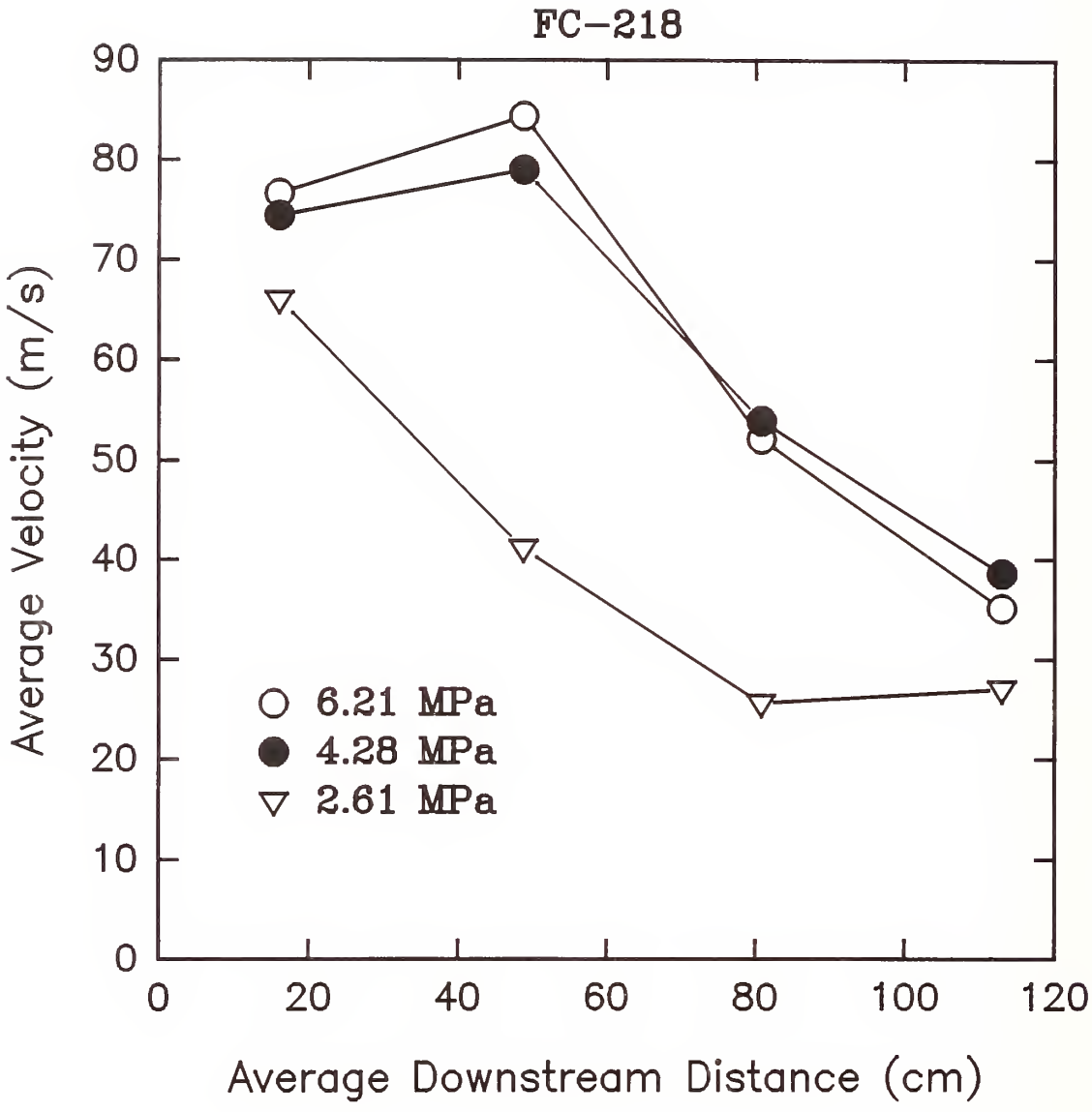

Figure 148. Average velocities as a function of downstream distance determined by time of arrival at laser beams #1-#5 for releases of FC-218 with burst disks covering a range of nominal pressures. Pressures are those inside the vessel at disk bursting.

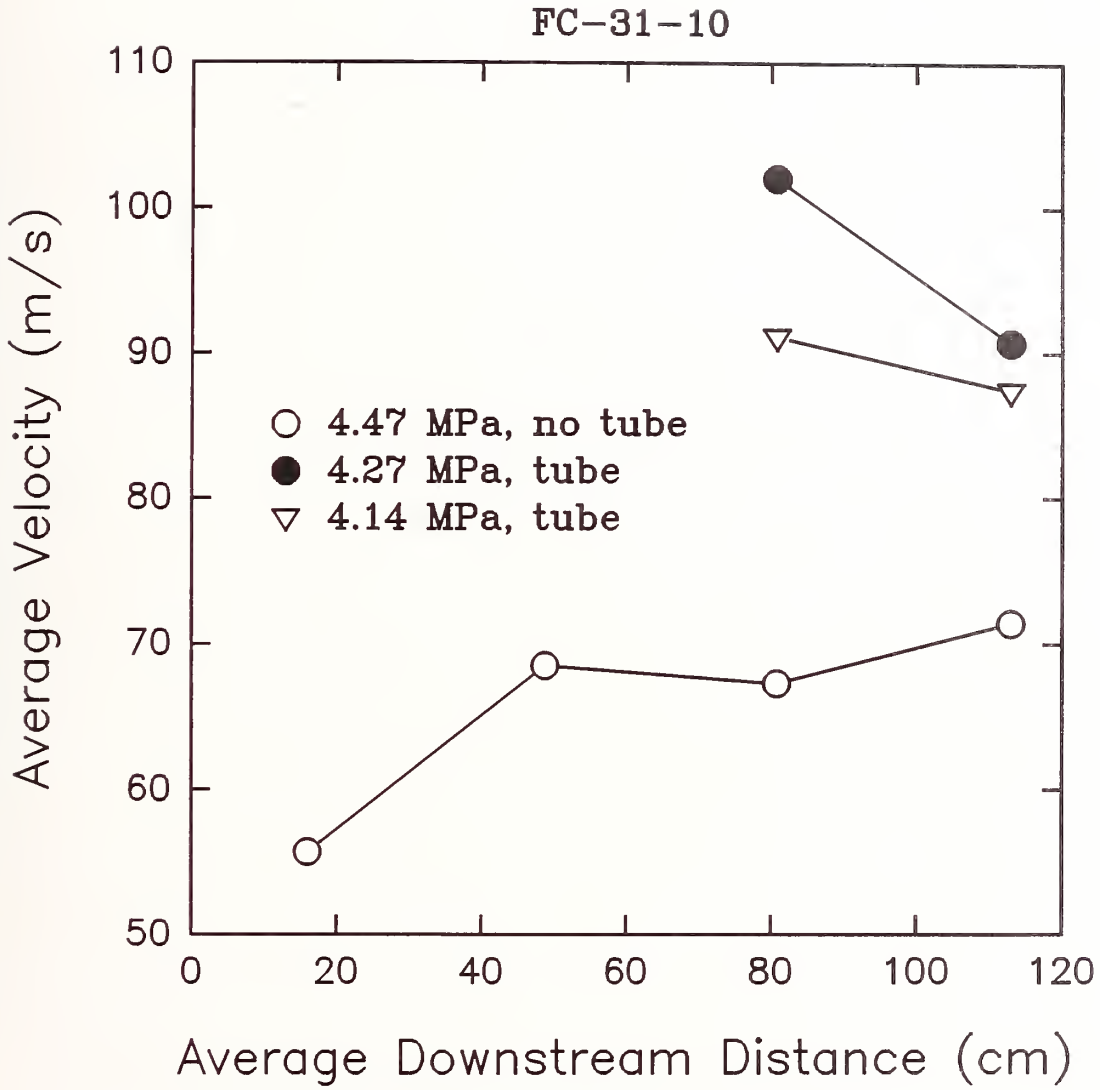

Figure 149. Average velocities determined by the time of arrival at laser beams #1-#5 as a function of downstream distance for releases of FC-31-10 with and without an extension tube. Pressures are those inside vessel at disk bursting.

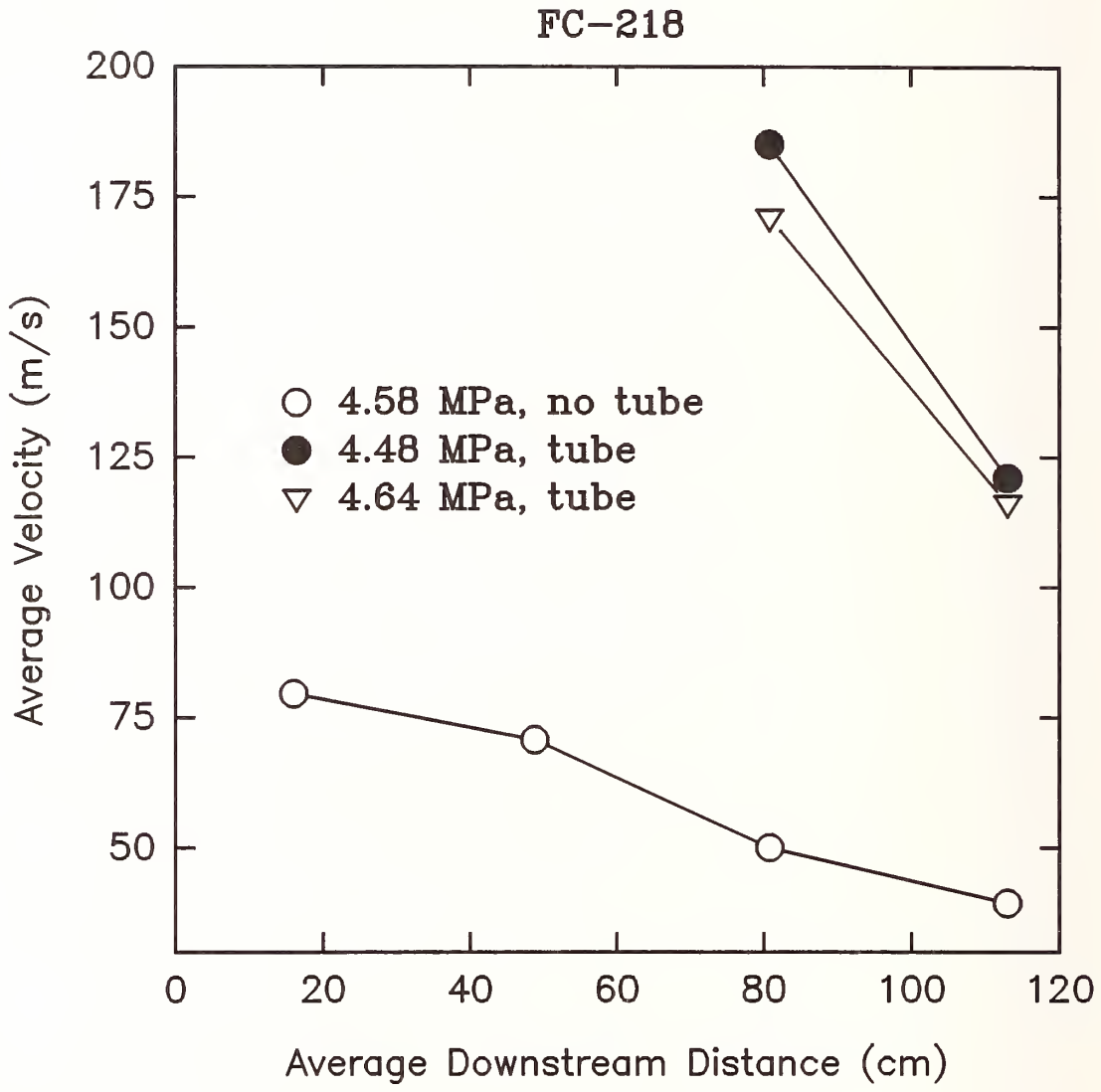

Figure 150. Average velocities determined by the time of arrival at laser beams #1-#5 as a function of downstream distance for releases of FC-218 with and without an extension tube. Pressures are those inside vessel at disk bursting.

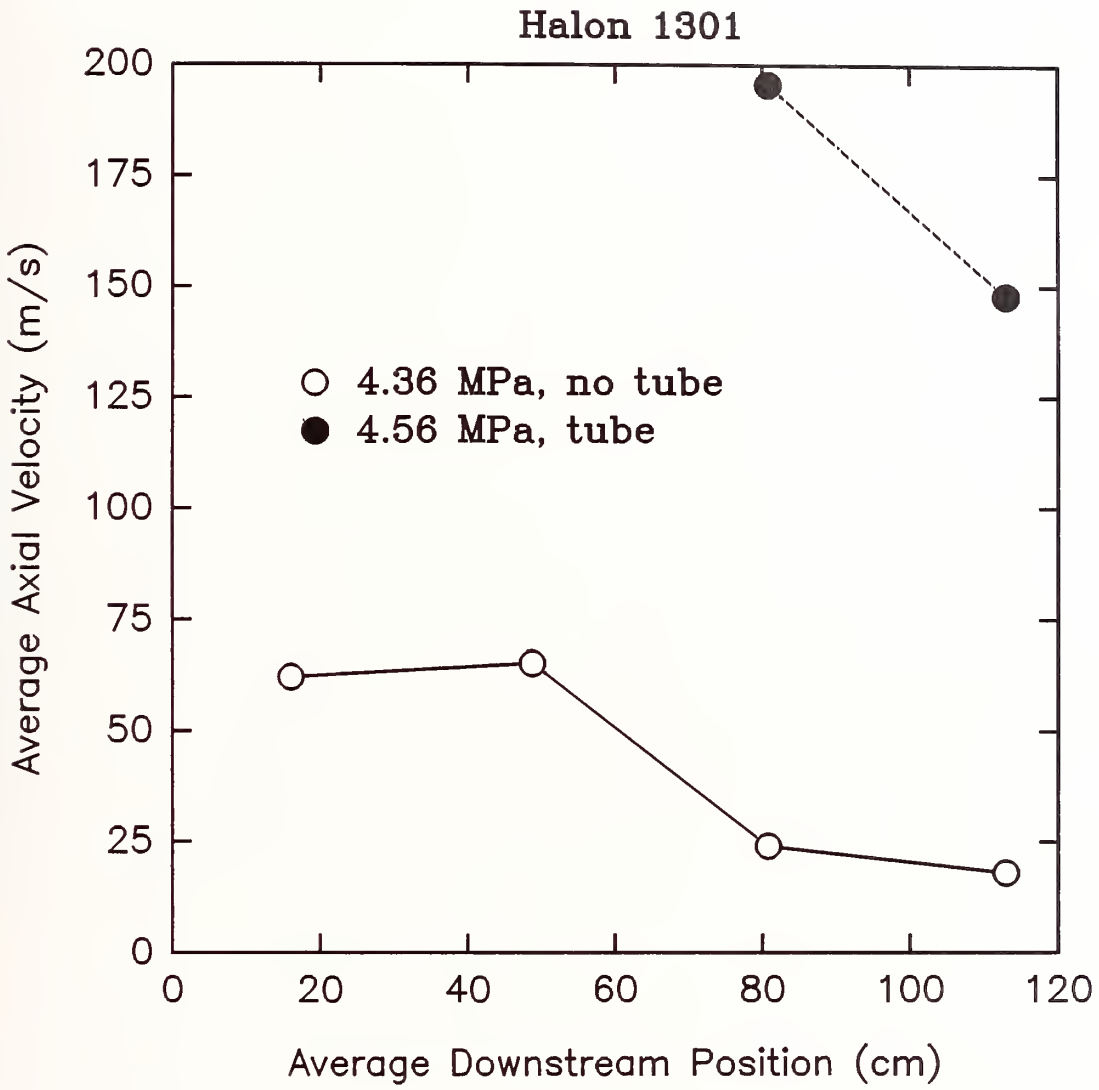

Figure 151. Average velocities determined by the time of arrival at laser beams #1-#5 as a function of downstream distance for releases of halon 1301 with and without an extension tube. Pressures are those inside vessel at disk bursting.

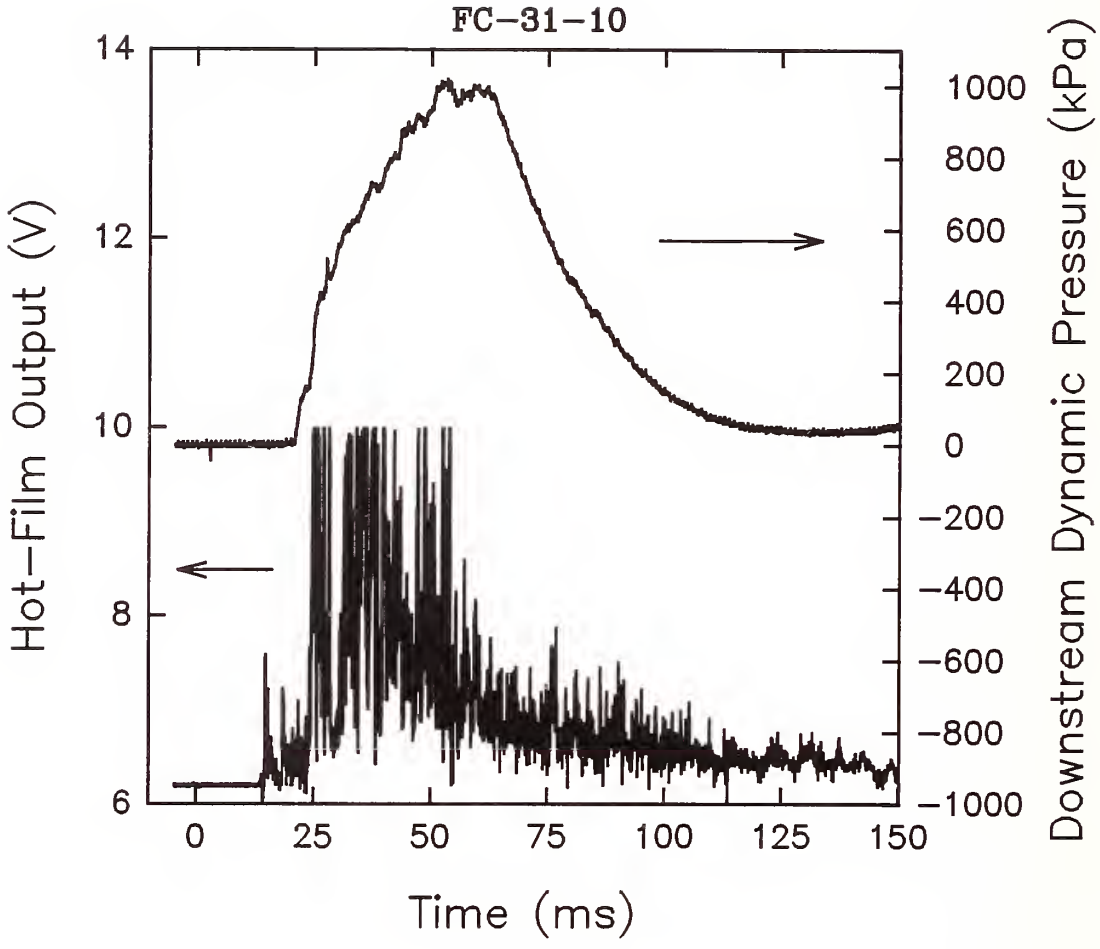

Figure 152. Aspirated hot-film voltage and dynamic pressure for probes located 1.3 m from the vessel with an attached 0.5 m tube plotted as functions of time following release of FC-31-10. Conditions: 513 g of agent, release pressure of 4.14 MPa.

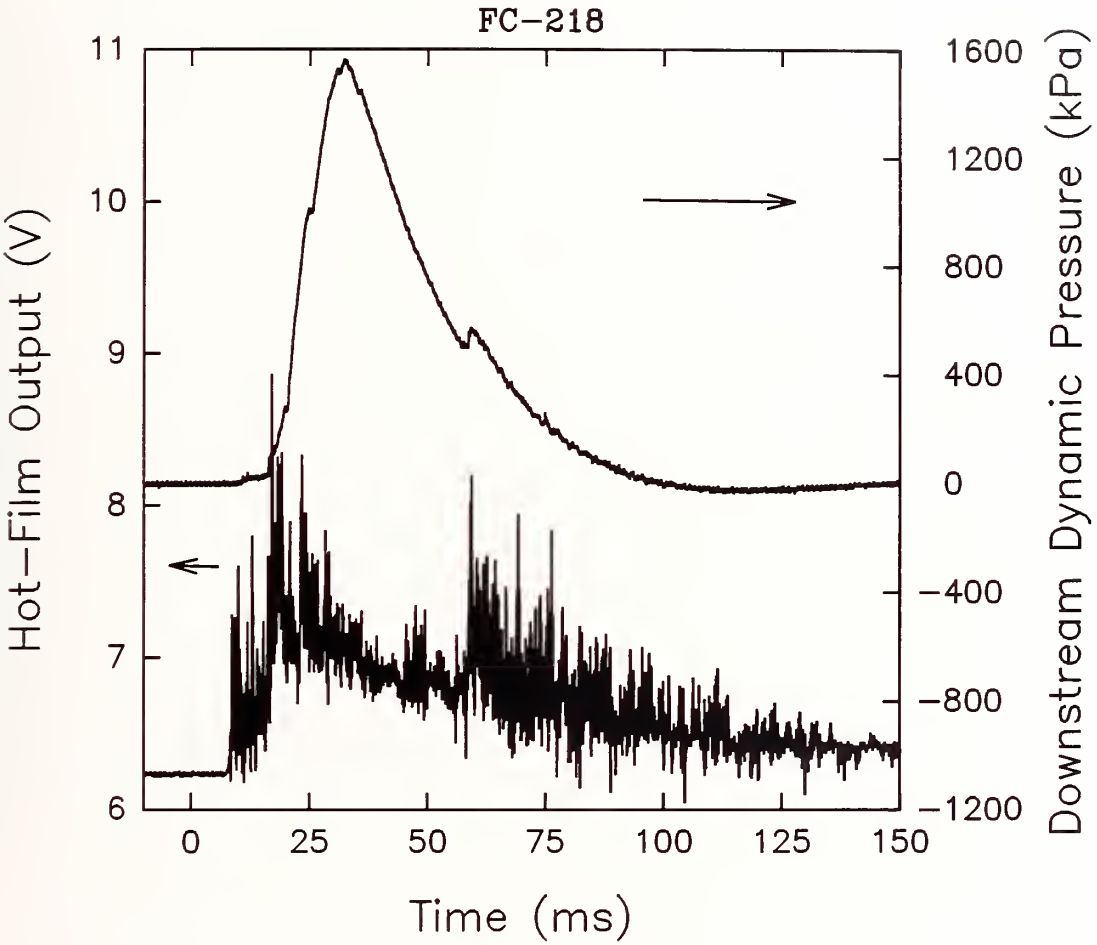

Figure 153. Aspirated hot-film voltage and dynamic pressure for probes located 1.3 m from the vessel with an attached 0.5 m tube plotted as functions of time following release of FC-218. Conditions: 465 g of agent, release pressure of 4.48 MPa.

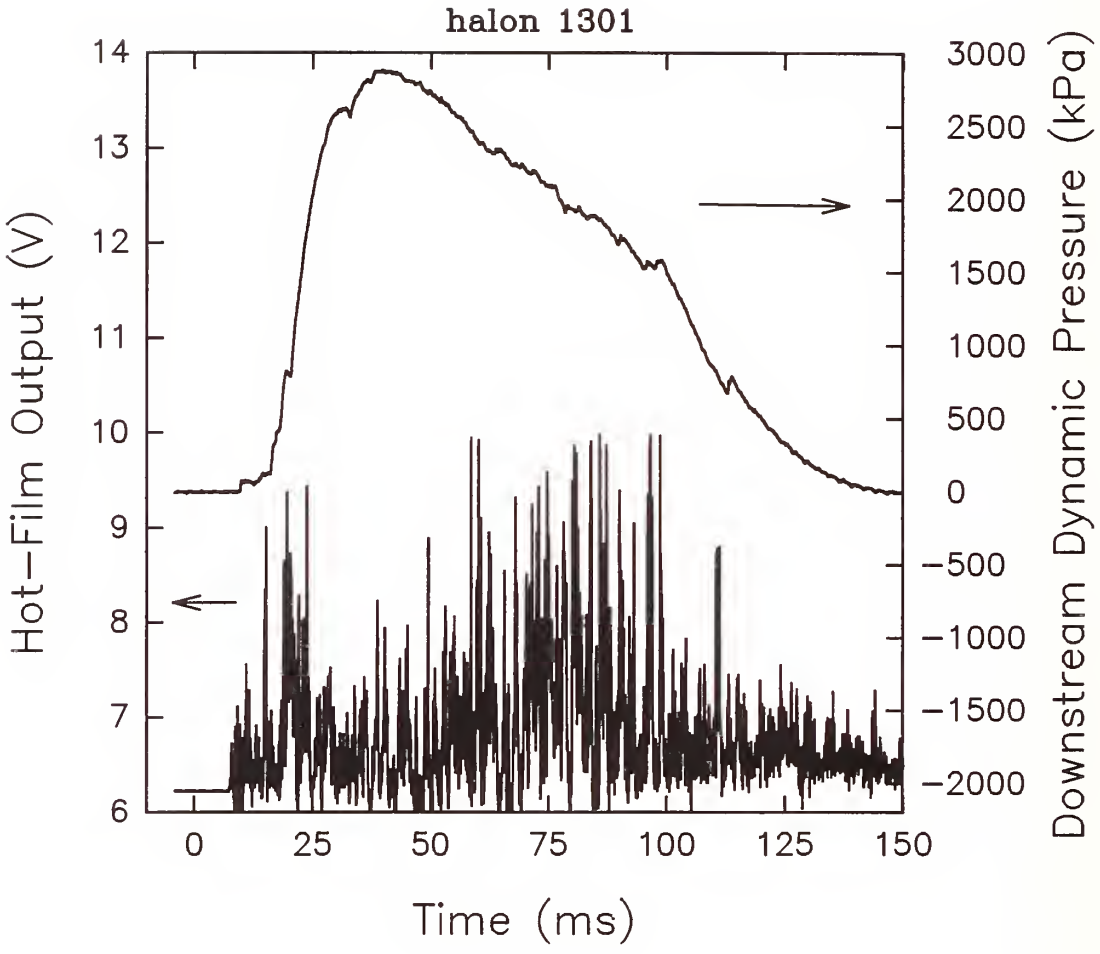

Figure 154. Aspirated hot-film voltage and dynamic pressure for probes located 1.3 m from the vessel with an attached 0.5 m tube as functions of time following release of halon 1301. Conditions: 523 g of agent, release pressure of 4.56 MPa.

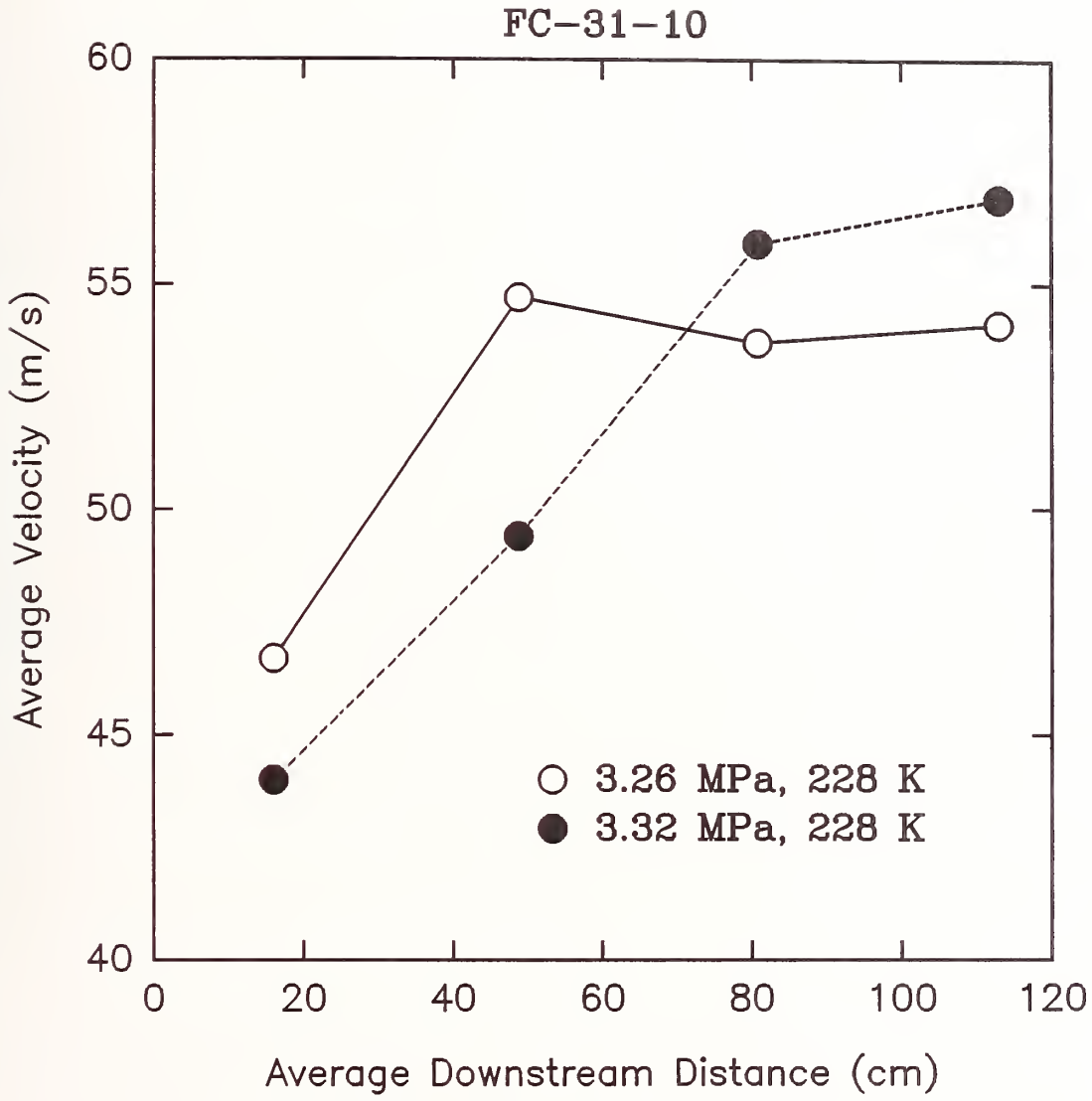

Figure 155. Average velocities for releases of cooled FC-31-10 determined by the time of arrival at laser beams #1-#5 plotted as a function of average downstream distance. Vessel internal temperatures and pressures are indicated.

The downstream dynamic pressure and aspirated hot-film voltage time plots shown in Figure 156 indicate that when the agent arrives at the 1.3 m sampling position it has a great deal of two-phase character. This is consistent with a slow evaporation due to its initial cold temperature.

A single release of FC-218 cooled to 228 K was run. At times during releases of agents which reached the downstream detectors as mostly liquid, a strong interference was recorded on all of the data channels. This was the case for the release of cold FC-218. For this reason, plots of the data are not shown. However, the results are discussed because they provide important insights as to the importance of superheating on the agent behavior. The release pressure was 3.34 MPa. Due to the positioning of the vessel, laser #1 was located 60 mm from the vessel orifice. The initial pressure drop inside the vessel was noted 1 ms before laser #1 detected any attenuation. This suggests agent began flowing immediately and achieved a near-vessel velocity on the order of 60 m/s. This estimate is consistent with measurements of the average velocity determined from laser beam attenuation measurements shown in Figure 157. For comparison, the results for a room temperature release are also included in the figure. The most remarkable finding from Figure 157 is the nearly constant flow velocity at positions removed from the vessel. A steady stream of fluid is detected with a velocity of 57 m/s.

Strong interferences in the signals were detected when the release reached the 1.3 m sampling position. The aspirated hot-wire signal was very large and saturated the digitizer. The dynamic pressure measurement was also quite noisy, however, it is possible to estimate that the dynamic pressure rose quickly and reached a level of roughly 1.4 MPa that persisted over the period of the release. Using the velocity of 57 m/s from the laser measurements, this dynamic pressure corresponds to a density of 860 kg/m^3. The room temperature density of the liquid is 1321 kg/m^3 suggesting that very little of the liquid was evaporated over the 1.3 m length of the flow.

Recall that for room temperature releases of FC-218, the degree of vaporization was quite high, approaching 100%. These results demonstrate the dramatic effect that the degree of superheating can have on the vaporization of these agents.

3.5.3.10 Effect of Orientation--Upward Releases. Releases of the agents were made with the vessel orifice oriented upward and horizontally. Measurements of the mixing behavior have only been recorded for the vessel oriented upwards. High-speed films, near-field dynamic pressure, laser attenuation, downstream dynamic pressure, and aspirated hot-film measurements have all been made. The experimental system was modified by moving the vessel to a location just below laser #5 and the downstream pressure transducer and aspirated hot-film to a location just upstream of laser #1. Keep in mind for the figures which follow that laser #5 is closest to the vessel exit. Releases of FC-31-10, FC-218, and halon 1301 were studied.

The high-speed films demonstrated that releases of the agents upward were quite different from downward releases. The behaviors of the agents within the vessel are described in Section 3.4.3.6 There it is noted that for an upward release the nitrogen first exited the vessel. During this period some gaseous agent was condensed. After a fairly substantial delay the agent in the bottle began to boil and froth, filled the vessel, and generated a two-phase flow exiting the vessel. Approximately 20 ms was required for the agent to begin to boil and a longer period to fill the vessel and generate the two-phase flow. The periods required to expel the agent completely were substantially longer for the upward releases than when the agents were released downward.

The films show related behaviors for the released agents near the vessel orifice (*e.g.*, see Figure 73). A plume is easily observed when the disk first opens. After a short period of time the plume seems to disappear, only to reappear when the fluid inside the vessel begins to boil.

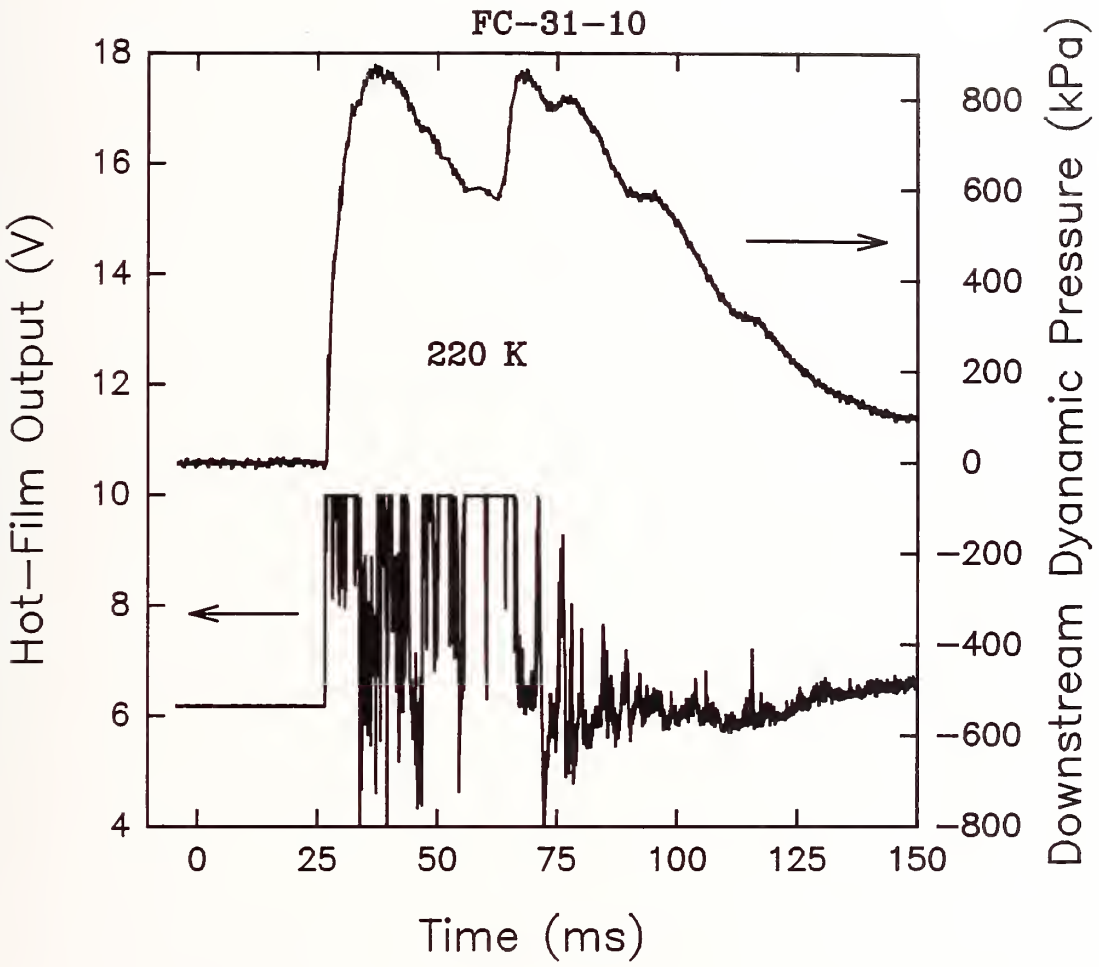

Figure 156. Aspirated hot-film voltage and dynamic pressure for probes located 1.3 m from the vessel plotted as functions of time following release of FC-31-10 cooled to 228 K. Conditions: 517 g of agent, release pressure of 3.34 MPa.

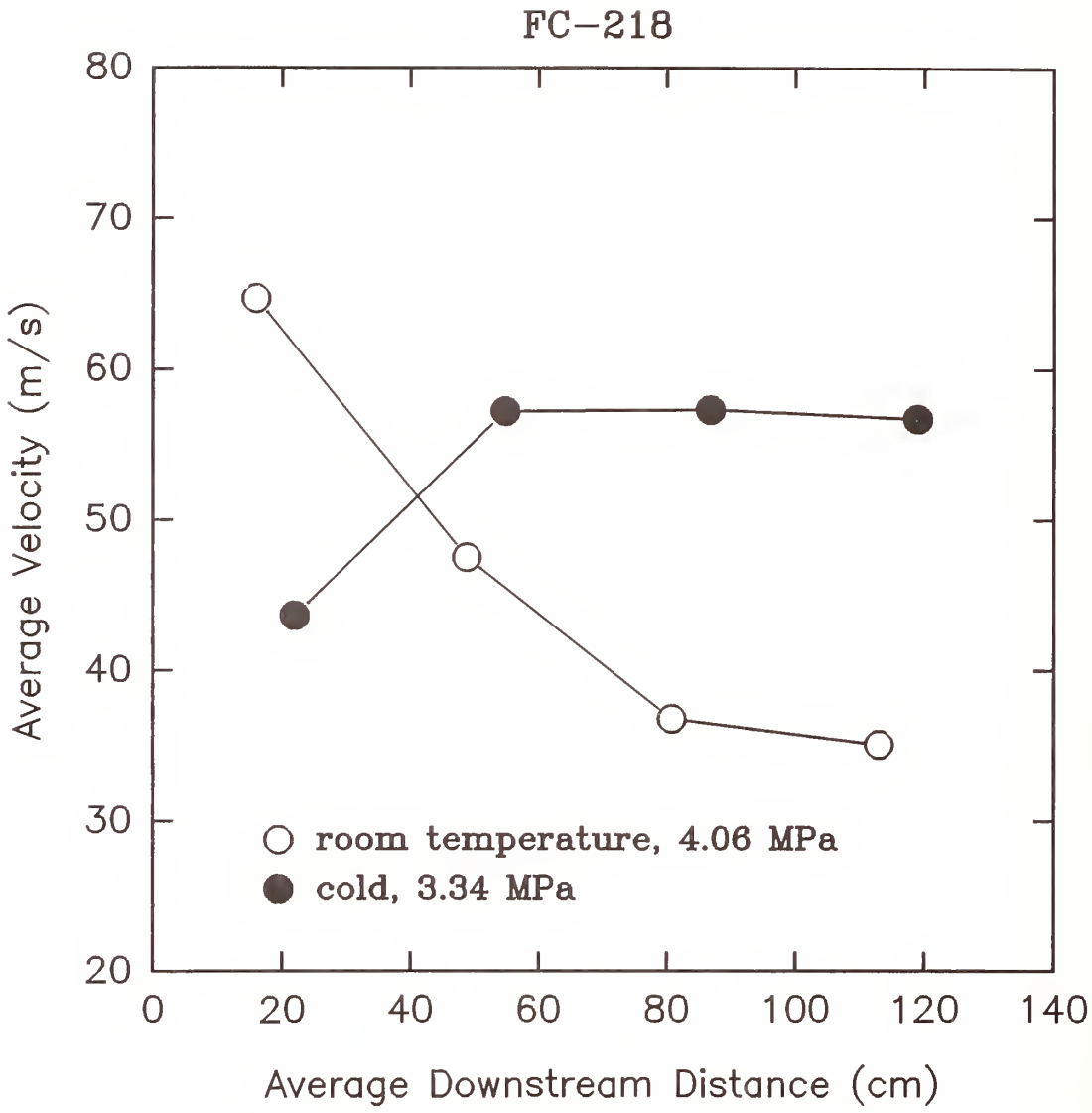

Figure 157. Average velocities for releases of room temperature and cooled FC-218 determined by the time of arrival at laser beams #1-#5 plotted as a function of average downstream distance. Vessel pressures are indicated.

None of the time plots of near-field dynamic pressure showed an increase following the bursting of the disk. This indicates that the disk bursting does not generate a shock wave, and that the strong flashing behaviors which are characteristic of downward releases do not occur for the upward cases.

Figure 158 shows the laser attenuation signals over the first 200 ms for a release of FC-31-10. Laser #5 is totally attenuated very rapidly when the disk bursts. The flow then allows light to pass for a very short period before extinguishing the beam once again. The high-speed film shows that the second attenuation occurs as the result of an increase in optical density in the gas within the vessel which is subsequently transported through the orifice. Presumably this is agent vapor which condensed as the nitrogen cooled during expansion. At roughly 18 ms the flow becomes partially transmitting for a brief period. The film shows the same behavior. It appears as if the nitrogen flow has ceased before the agent begins to boil in the vessel. At roughly 24 ms following release, the liquid begins to boil at the bottom of the vessel and vapor is once again forced through the orifice leading to total attenuation of laser #5. At approximately 54 ms after release the boiling liquid fills the vessel and the flow from the orifice begins to spread much more rapidly. Since laser #5 is already totally attenuated, no effect is observed on the laser signal.

Further downstream the lasers are attenuated in different ways. Laser #4 is nearly totally attenuated very shortly after the disk opens, but then is partially transmitted for a period before the two-phase flow arrives. The degree of laser beam attenuation due to the initial flow of nitrogen decreases with increasing distance from the nozzle, but is still observable at laser #1. The furthest laser detects the flow very shortly (approximately 5 ms) after the release indicating the flow velocity is quite high. Figure 159 shows the average velocities determined for the initial gas flow as a function of distance from the orifice. At progressively later times, lasers #4-#1 show a strong extinguishment which is attributed to the arrival of condensed agent from the vessel. Estimates of the arrival times for this flow have been made and used to calculate average velocities which are also included in Figure 159. Lasers #3-#1 become partially transmitting after the initial arrival of the two-phase flow. The flow continues to transmit light for periods of tens of milliseconds before all three lasers are again totally attenuated. The later attenuations are attributed to the arrival of the two-phase flow generated by the boiling liquid filling the vessel. The arrival times of this third flow at lasers #3-#1 have also been estimated and used to calculate average velocities. Results are shown in Figure 159.

Three points should be noted concerning Figure 159. First, the velocities of the two-phase flows are considerably less than the velocities associated with the nitrogen release. Second, the average two-phase flow velocities are much lower than observed for comparable downward releases of FC-31-10 (see Figure 111). Three, the velocities of the two two-phase flows are similar.

Figure 160 shows a similar time plot for the laser signals over a much longer period of time. It is now clear that an optically dense flow is present until roughly 800 ms after the disk opens and the period required for full release of the agent approaches 1 s. This result contrasts dramatically with the observed emptying times when this agent is released downward which are on the order of 40 ms for a two-thirds full vessel.

The signals recorded by the downstream pressure transducer and aspirated hot-film are consistent with the above conclusions. Results over short and longer time periods are shown in Figure 161 and Figure 162. The arrival of the released nitrogen at the position 1.3 m from the vessel is clearly detectable in the hot-film signal even though it causes only a very small dynamic pressure rise (Figure 161) despite the high velocity. The response of the hot-film requires that this initial gas flow either contains some of the agent, or that it is substantially cooled by the nitrogen. On the other hand, when the first flow identified as consisting of two phases arrives at 75 ms following release, there is a substantial increase in both the hot-film and pressure signals consistent with the presence of a two-phase flow. Note that the velocity of the two-phase flow is considerably lower than the flow

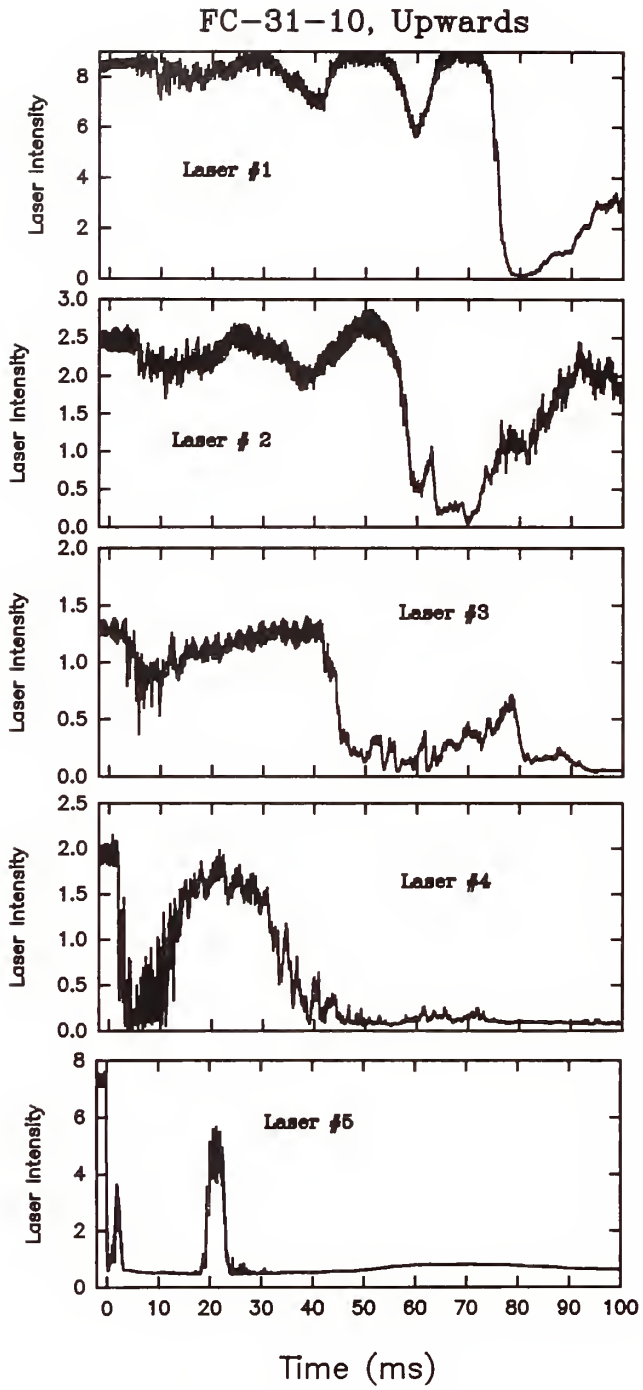

Figure 158. Short time behaviors for transmission of laser beams #5-#1 spaced as shown in Table 7 following an upward release of FC-31-10 at 0 s. Conditions: 505 g agent, 4.40 MPa release pressure.

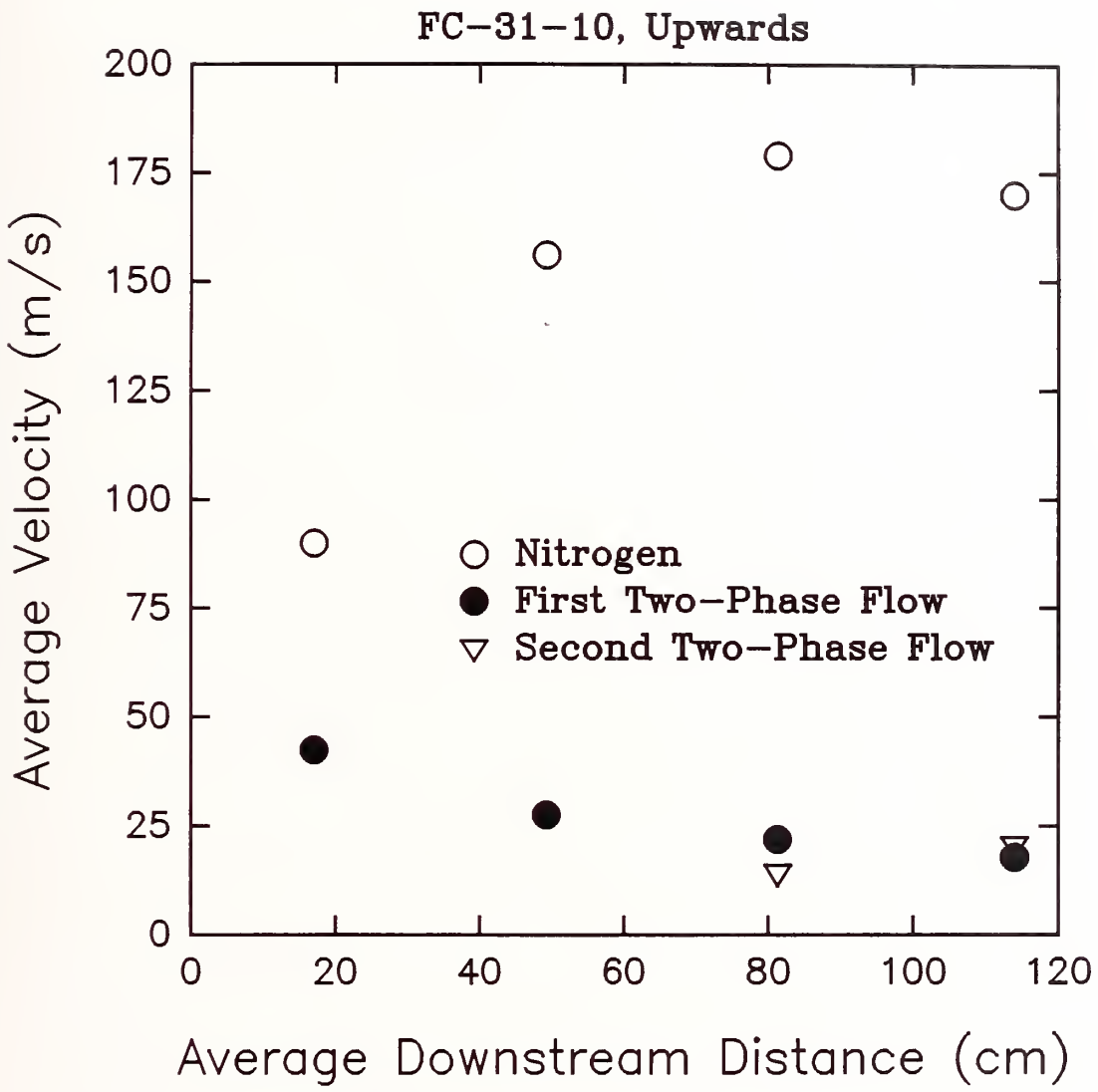

Figure 159. Average velocities for upward releases of FC-31-10 determined by the time of arrival at laser beams #5-#1 plotted as a function of average downstream distance. Results for arrival of nitrogen and two two-phase flows are indicated (see text).

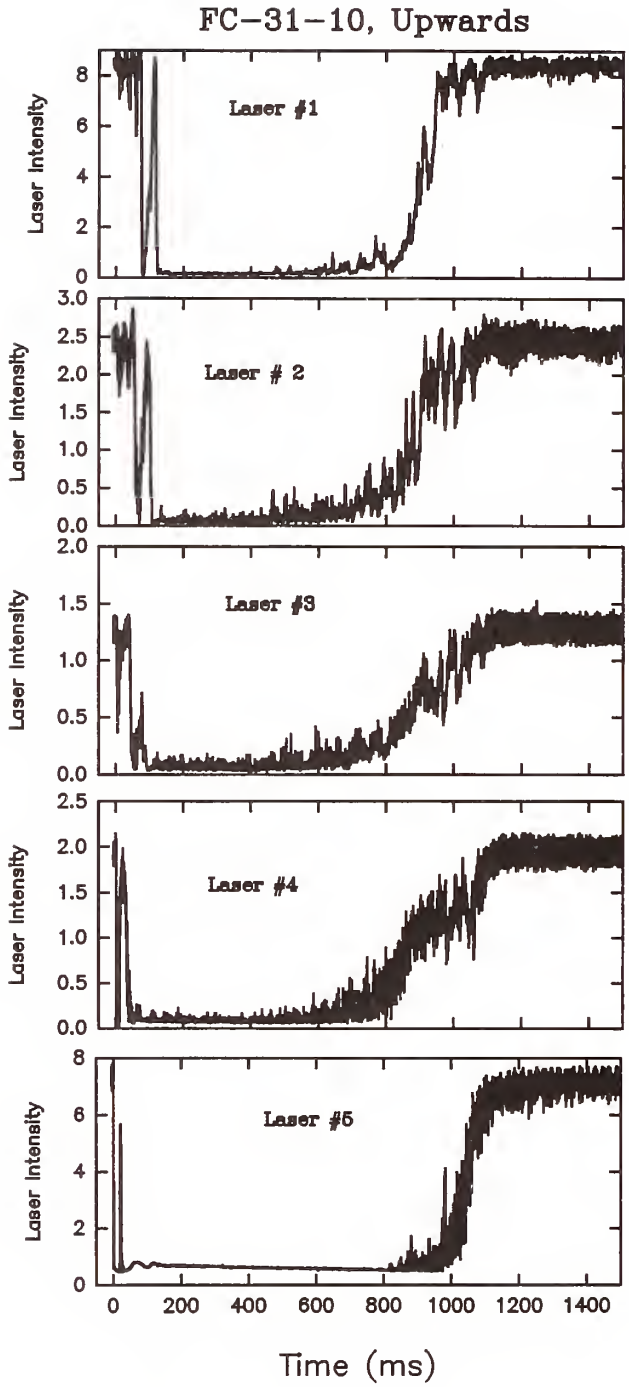

Figure 160. Long time behaviors for transmission of laser beams #5-#1 spaced as shown in Table 7 following an upward release of FC-31-10 at 0 s. Conditions: 505 g agent, 4.40 MPa release pressure.

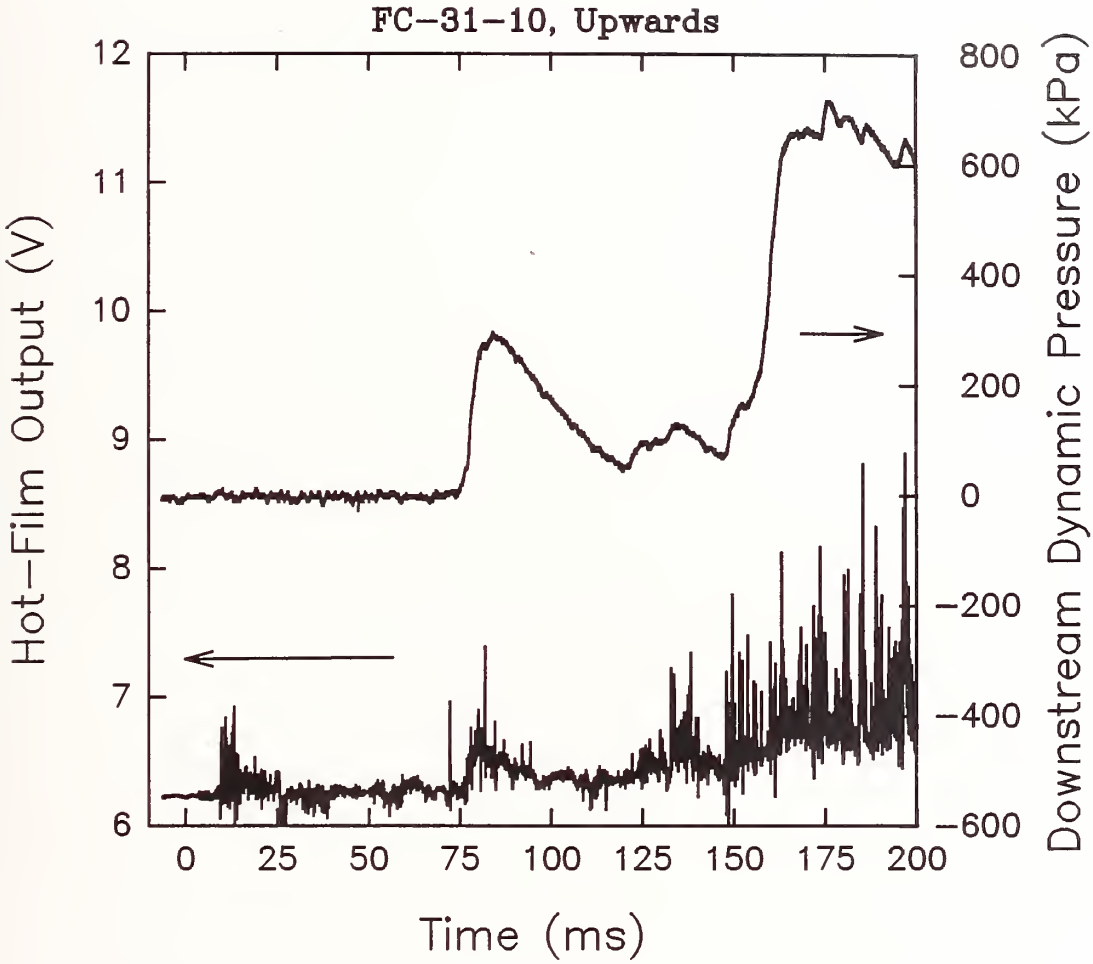

Figure 161. Voltage output of the aspirated hot-film and the dynamic pressure for probes located 1.3 m from the vessel are plotted for a short time period following an upward release of FC-31-10. Conditions: 505 g of agent, release pressure of 4.40 MPa.

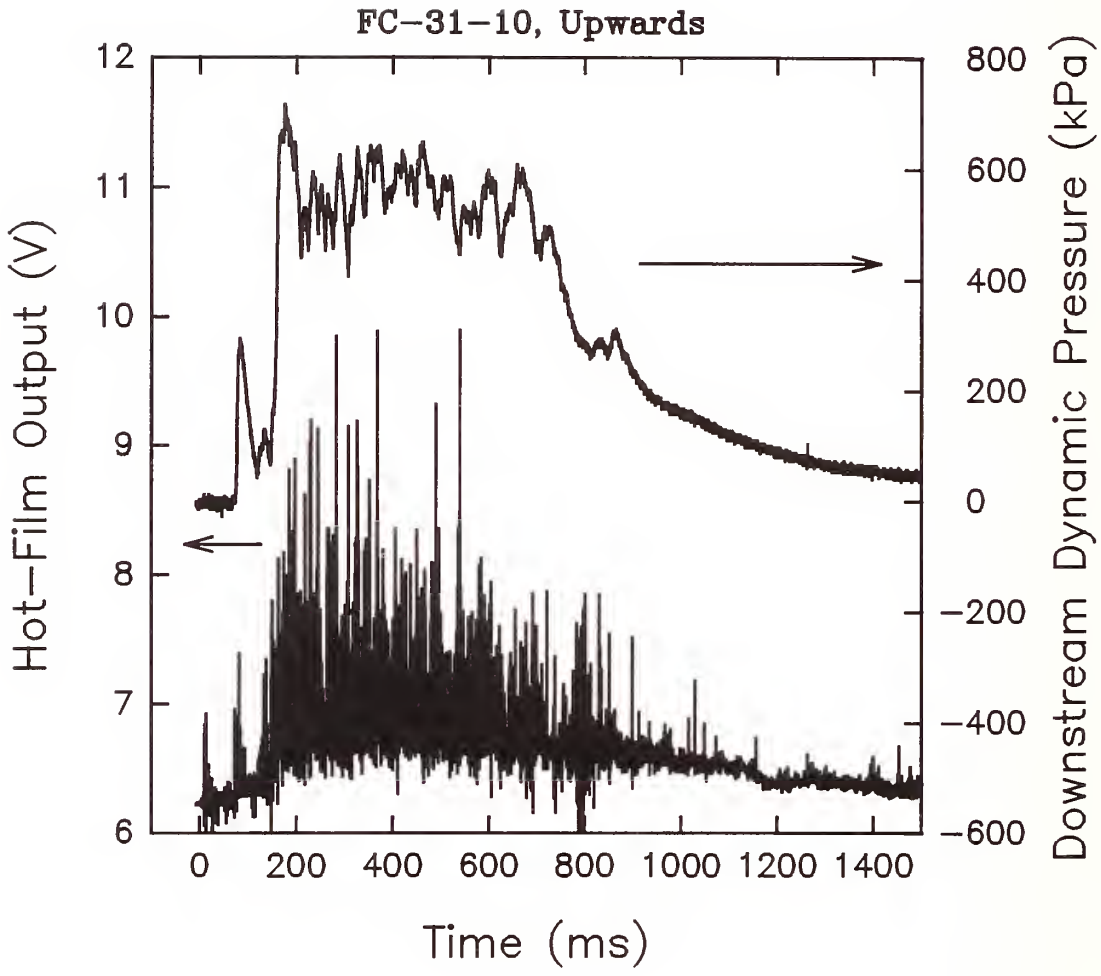

Figure 162. Voltage output of the aspirated hot-film and the dynamic pressure for probes located 1.3 m from the vessel are plotted for a long time period following an upward release of FC-31-10. Conditions: 505 g of agent, release pressure of 4.40 MPa.

resulting from the nitrogen release (see Figure 159). Following the first arrival of two-phase flow, both signals fall consistent with laser #1 being transmitted during this period. The arrival of the second two-phase flow is accompanied by a large dynamic pressure jump and much stronger indications of two-phase flow in the aspirated hot-film signal. Figure 162 shows that the later two-phase flow persists until roughly 800 ms, again consistent with the attenuation behavior of laser beam #1.

Figure 163 and Figure 164 show the laser intensity behaviors observed for upward releases of FC-218. For short times (Figure 163), the results are similar to those for the FC-31-10. When the disk bursts, laser #5 is immediately fully attenuated. Some transmission is then observed shortly after the disk opens before the laser is totally attenuated a few milliseconds later due to condensation of the agent vapor in the nitrogen. Transmission is observed for a period from roughly 12 to 20 ms following the nitrogen release. At this point, boiling in the vessel begins from the bottom and expulsion of gas from the vessel again extinguishes the laser beam. Note that the boiling begins at a somewhat shorter time than observed for the FC-31-10. High-speed films indicate the vessel is filled with boiling liquid at 39 ms following release and the more vigorous two-phase flow should form at this time.

The attenuation signals for lasers #4-#5 do not show the distinct arrival of two separate types of two-phase flow. However, it is possible to estimate roughly when the flow generated by the two-phase flow formed when the vessel is completely filled with boiling liquid reaches the lasers. For the position of laser #5 we have used the high-speed film to provide the starting time for the flow. The arrival times have been used to calculate the average velocities for the downstream edge of the two-phase flow shown in Figure 165. Velocities for the nitrogen release are also included in this figure. The results are very similar to those for FC-31-10 shown in Figure 159.

Figure 164 shows that the total attenuation of the laser beams lasts until roughly 250 ms after the release and that the laser beams are nearly completely transmitted at 500 ms. These results suggest that the upward release of FC-218 from the vessel requires only 1/3 as long as a similar release of FC-31-10.

Time plots of the downstream dynamic pressure and aspirated hot-film voltage for the FC-218 release are shown in Figure 166 and Figure 167. Figure 166 indicates that the two-phase flow reaches the sampling position roughly 55 ms following release. This is attributed to the two-phase flow which extinguishes laser #5 at 20 ms following release. A much higher pressure rise appears starting at roughly 80 ms. This time is consistent with the attenuation behavior seen for laser #1. The hot-film signal is consistent with the arrival of a strong two-phase flow. The plots of these signals over longer time periods (Figure 167) show that the two-phase flow is present until roughly 250 ms following release, consistent with the conclusion based on laser measurements.

The plastic vessel was not used for releases of halon 1301 so the internal behavior cannot be described. However, high-speed films of releases outside of the vessel indicated that the behaviors for halon 1301 were similar to those already described. The first two-phase flow appeared at 16 ms following release and the two-phase flow from the filled vessel appeared at approximately 30 ms. Figure 168 through Figure 171 show measurement results for a release of halon 1301. Short and long time plots of laser intensities are given in Figure 168 and Figure 169. For the short time data (Figure 168), the behaviors observed are similar to those described for FC-31-10 and FC-218. It is difficult to estimate arrival times for the two-phase flow at the positions nearer the orifice so velocities will not be reported. However, it is clear that two different two-phase flows reach laser #5 at roughly 30 and 50 ms. The effects of these flows are also evident in the hot-film and dynamic pressure signals shown in Figure 170. As found for the other agents, the second flow generates much higher dynamic pressures and hot-film response. This is attributed to the arrival of a two-phase flow generated by boiling when the vessel is totally filled with a two-phase mixture. Figure 169 and

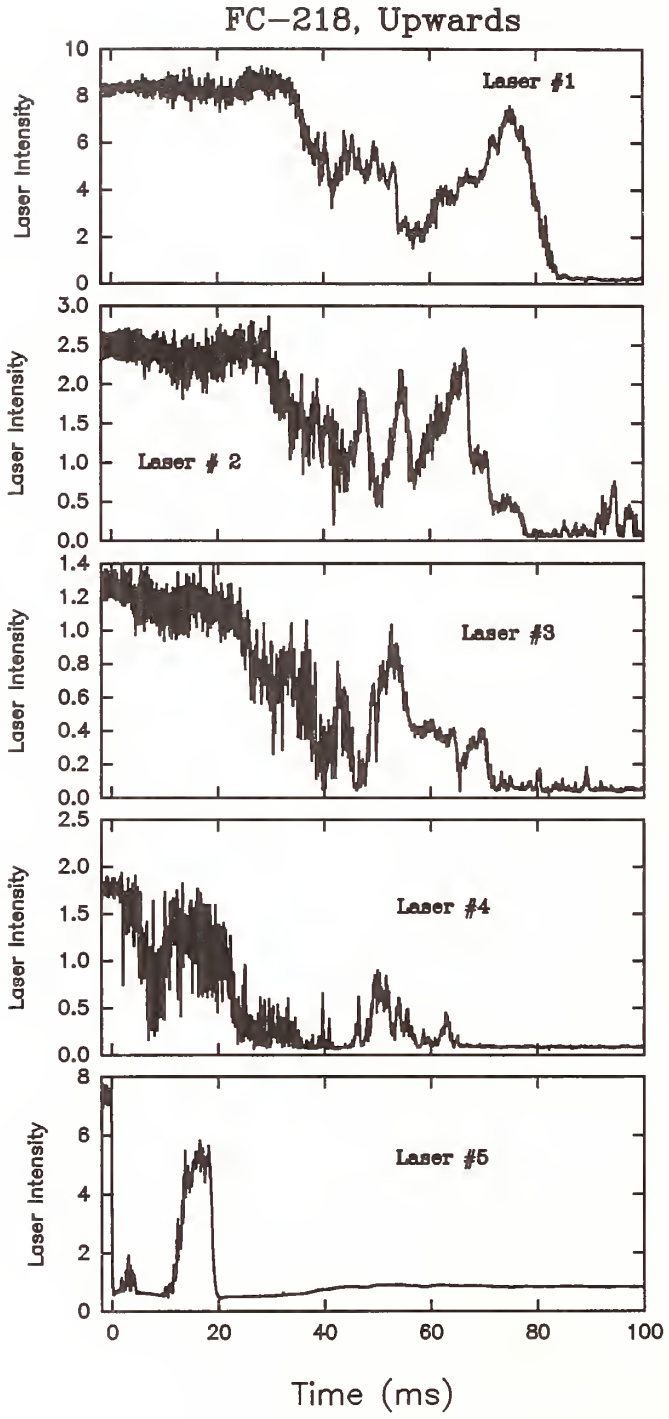

Figure 163. Short time behaviors for transmission of laser beams #5-#1 spaced as shown in Table 7 following an upward release of FC-218 at 0 s. Conditions: 461 g agent, 4.35 MPa release pressure.

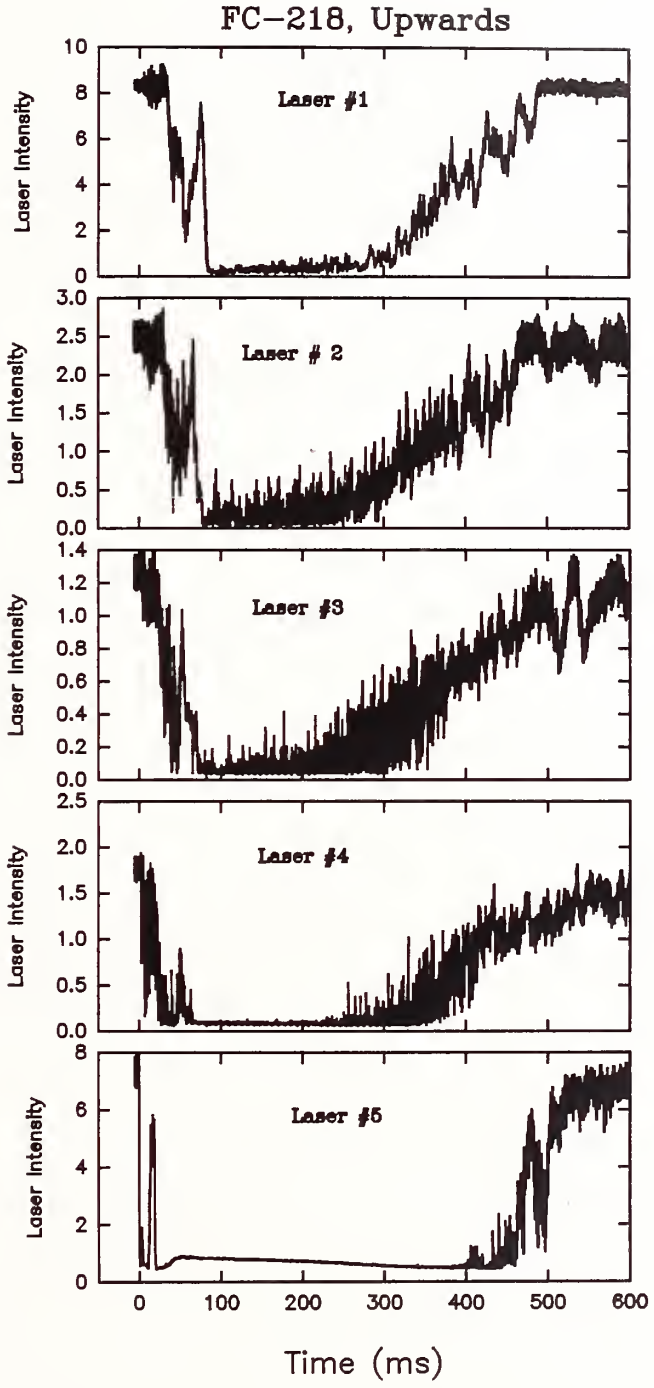

Figure 164. Long time behaviors for transmission of laser beams #5-#1 spaced as shown in Table 7 following an upward release of FC-218 at 0 s. Conditions: 461 g agent, 4.35 MPa release pressure.

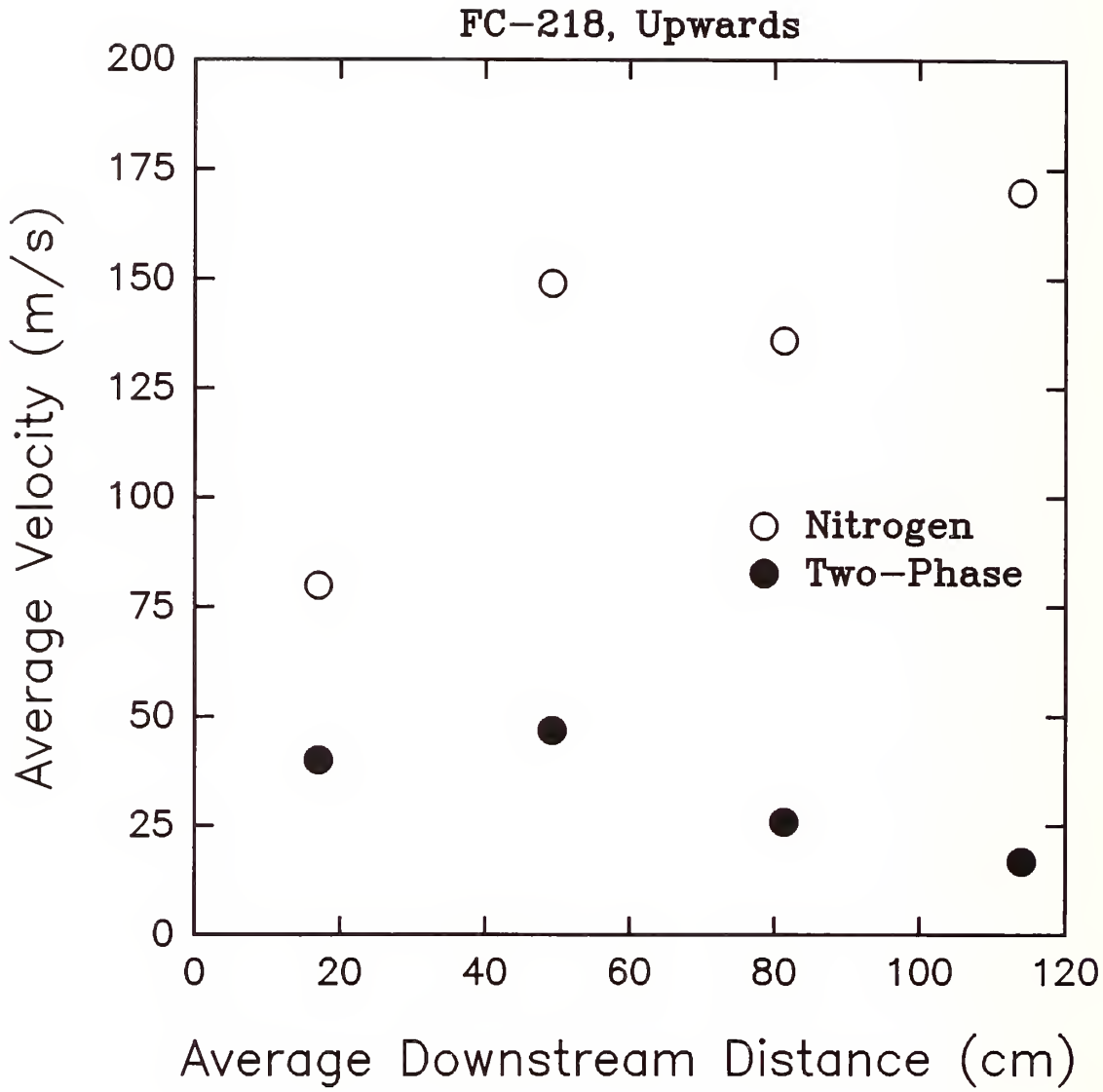

Figure 165. Average velocities for upward releases of FC-218 determined by the time of arrival at laser beams #5-#1 plotted as a function of average downstream distance. Results for arrival of nitrogen and the two-phase flow are indicated (see text).

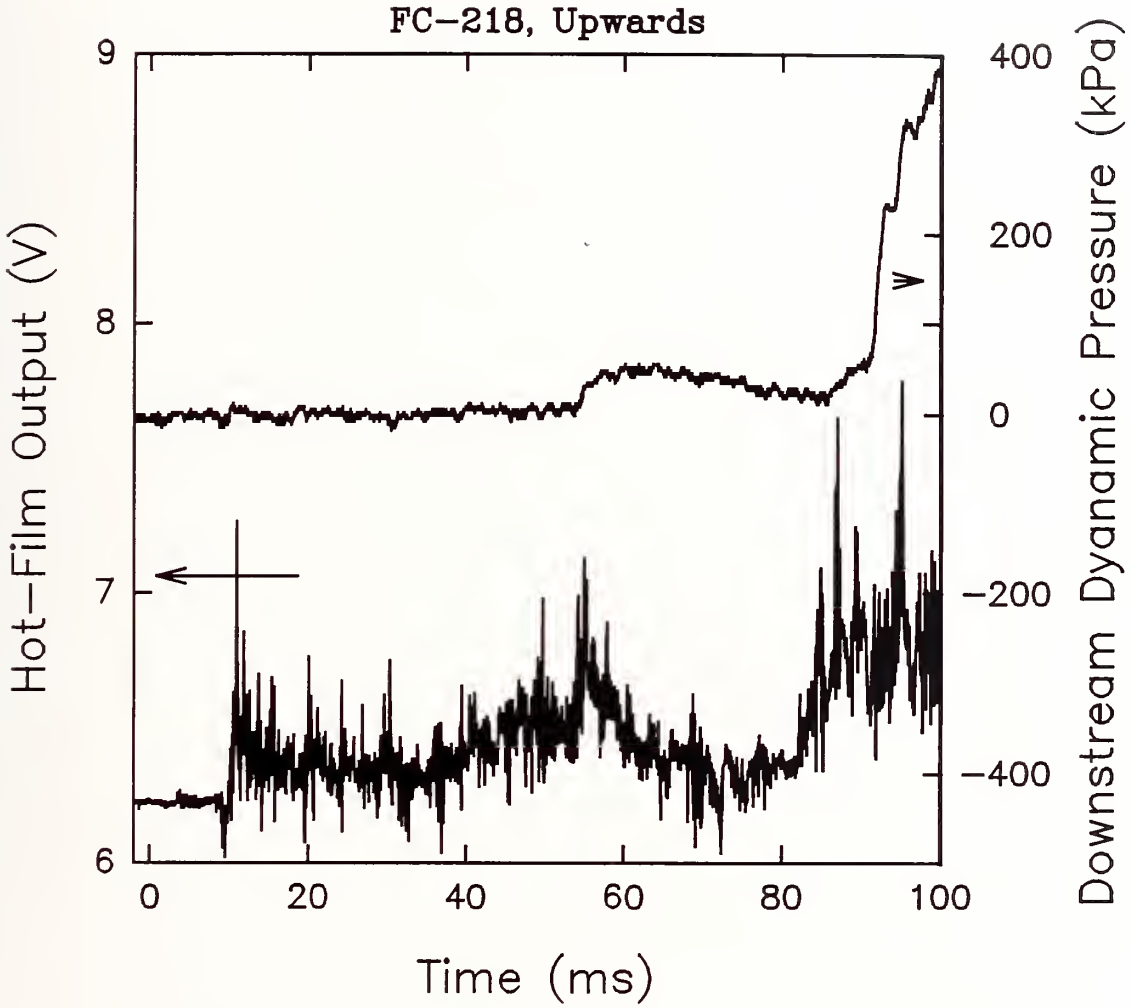

Figure 166. Voltage output of the aspirated hot-film and the dynamic pressure for probes located 1.3 m from the vessel are plotted for a short time period following an upward release of FC-218. Conditions: 461 g of agent, release pressure of 4.35 MPa.

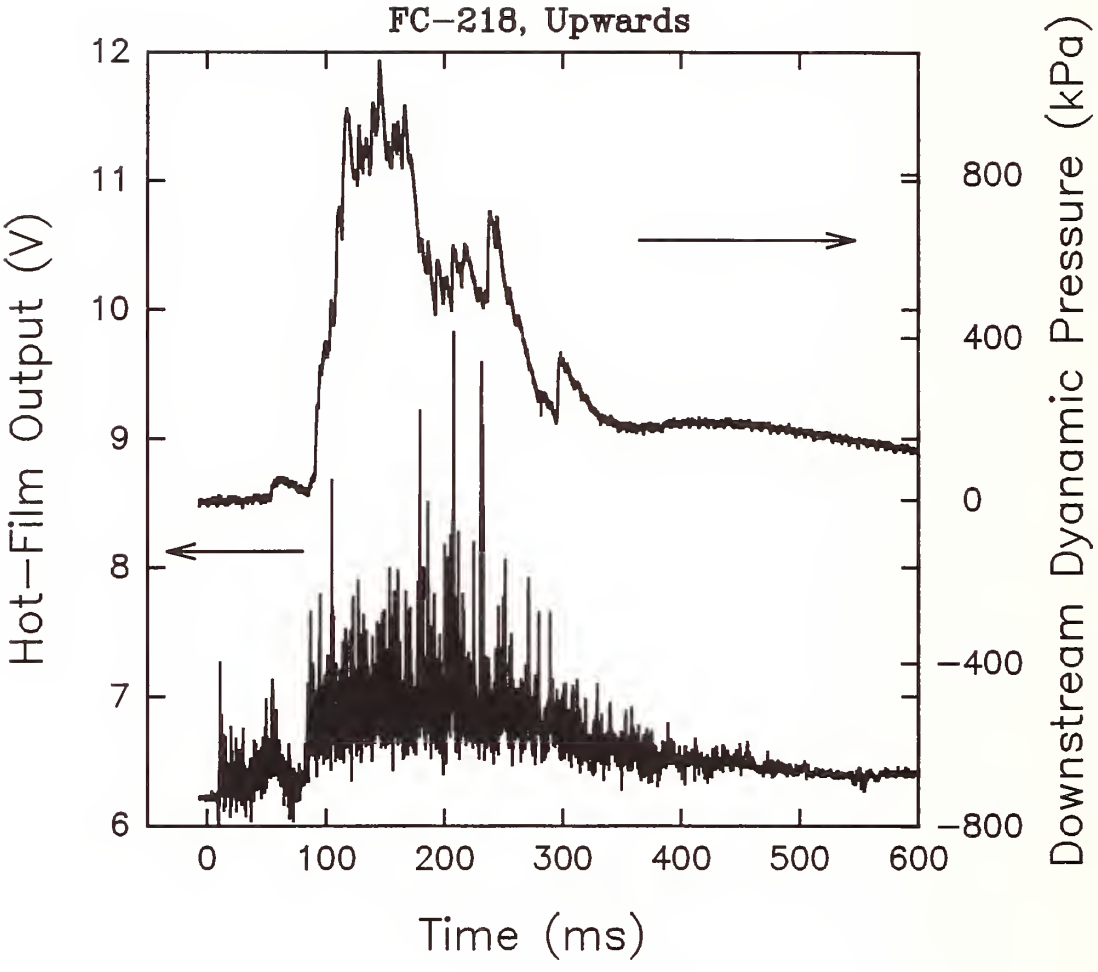

Figure 167. Voltage output of the aspirated hot-film and the dynamic pressure for probes located 1.3 m from the vessel are plotted for a long time period following an upward release of FC-218. Conditions: 461 g of agent, release pressure of 4.35 MPa.

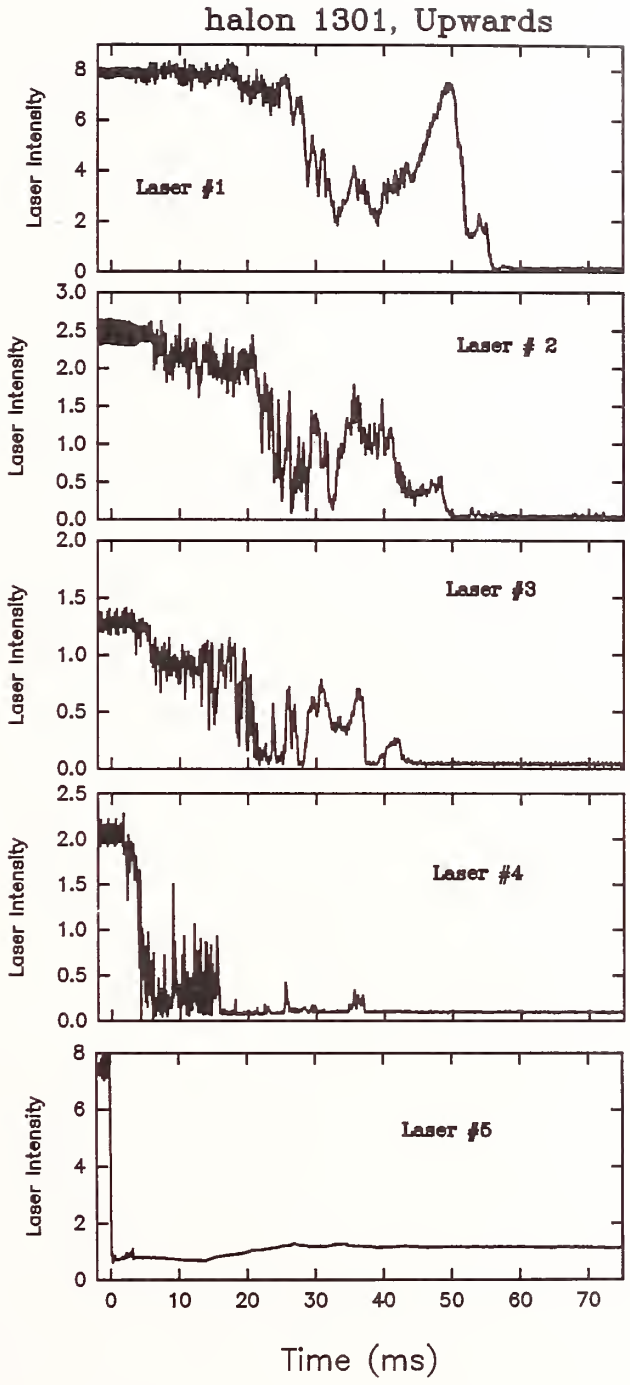

Figure 168. Short time behaviors for transmission of laser beams #5-#1 spaced as shown in Table 7 following an upward release of halon 1301 at 0 s. Conditions: 545 g agent, 4.46 MPa release pressure.

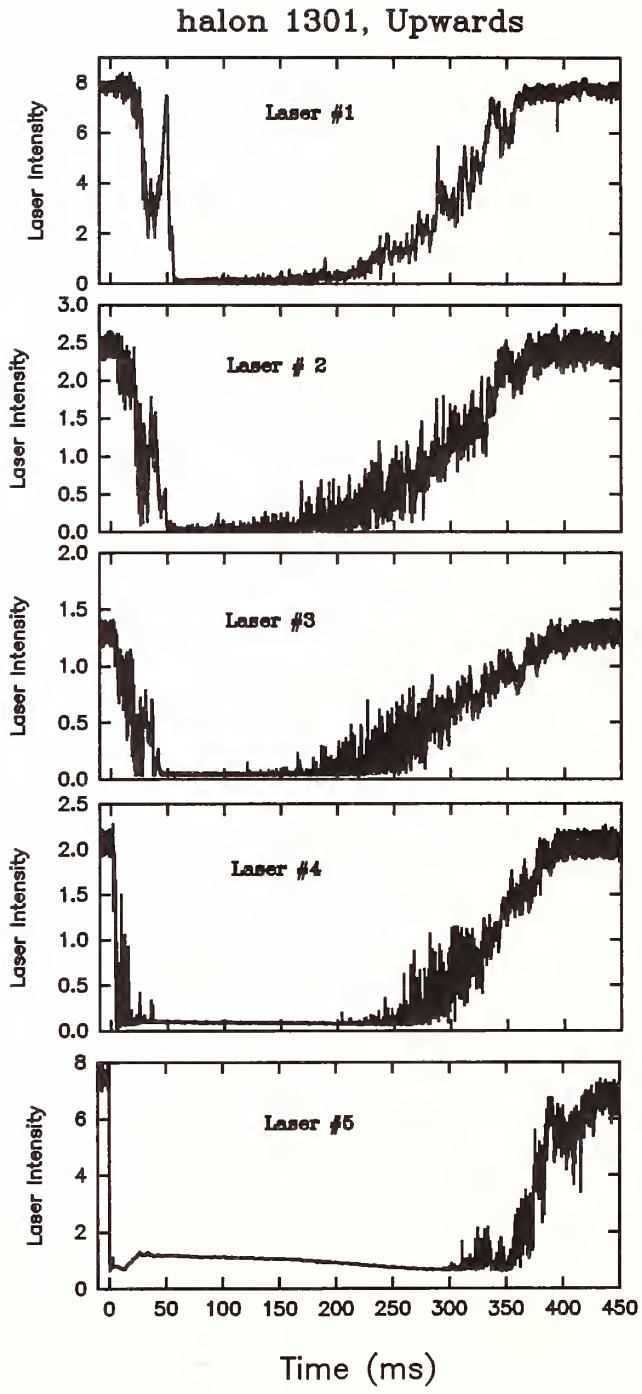

Figure 169. Long time behaviors for transmission of laser beams #5-#1 spaced as shown in Table 3 following an upward release of halon 1301 at 0 s. Conditions: 545 g agent, 4.46 MPa release pressure.

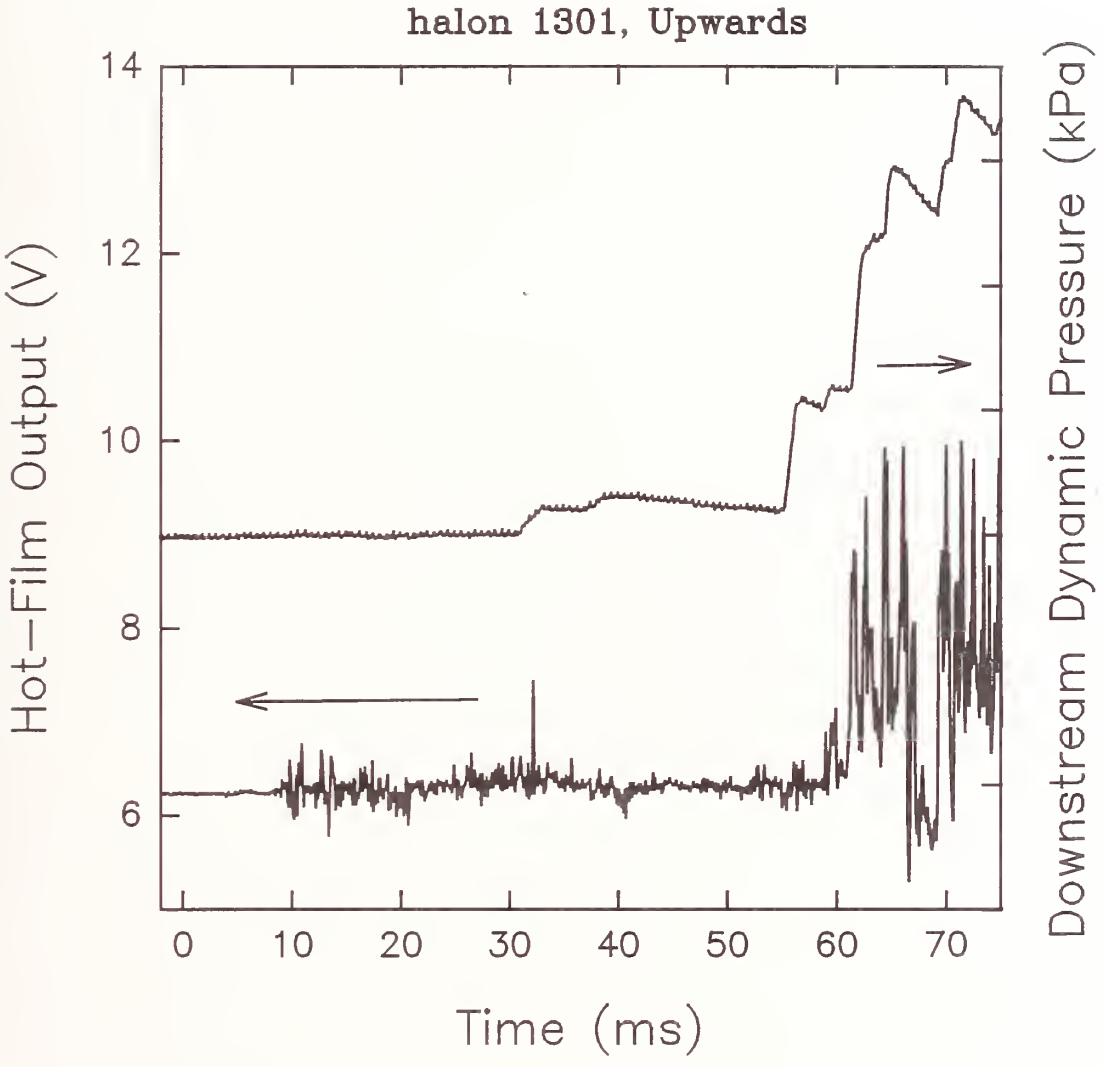

Figure 170. Voltage output of aspirated hot-film and dynamic pressure for probes located 1.3 m from the vessel are plotted for a short time period following an upward release of halon 1301. Conditions: 545 g of agent, release pressure of 4.46 MPa.

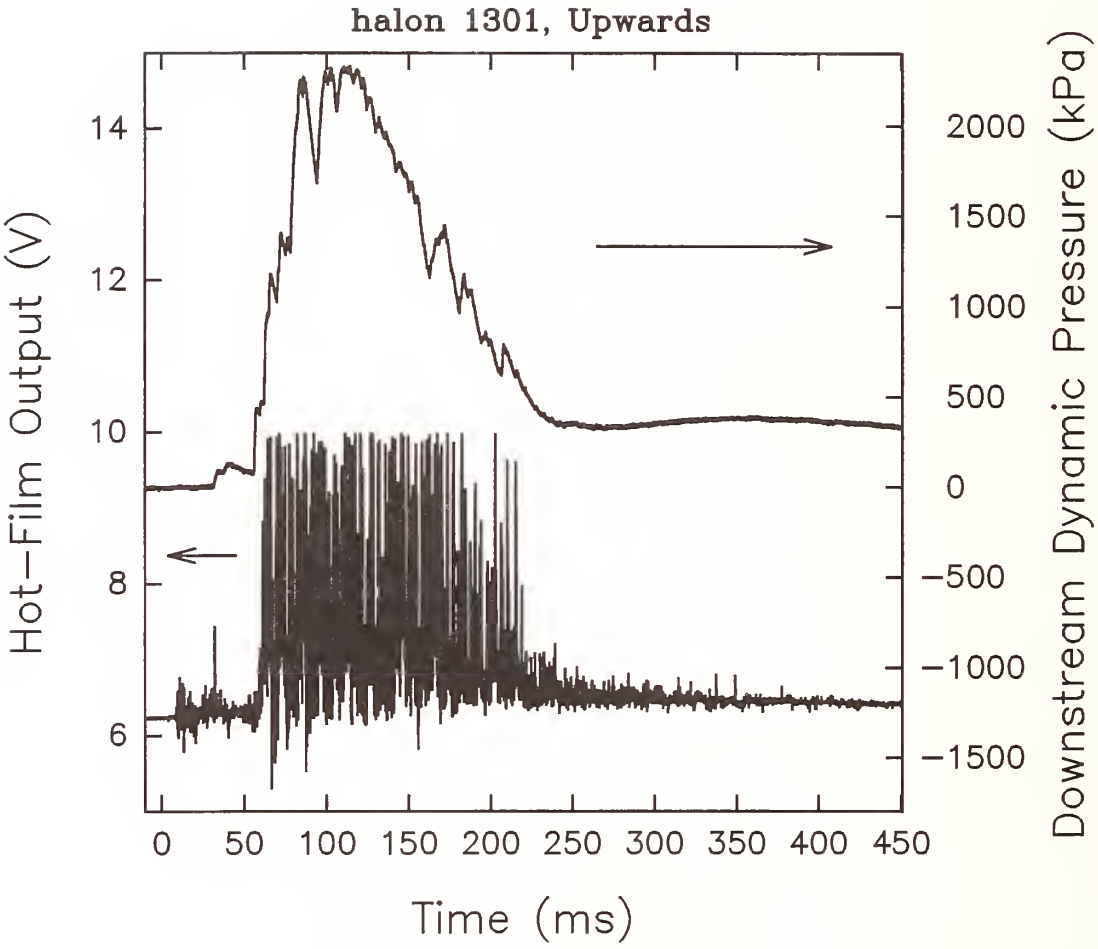

Figure 171. Voltage output of aspirated hot-film and dynamic pressure for probes located 1.3 m from the vessel are plotted for a long time period following an upward release of halon 1301. Conditions: 545 g of agent, release pressure of 4.46 MPa.

Figure 171 show that the two-phase flow from the vessel lasts until roughly 200 ms following the start of the release.

3.5.4 Discussion

3.5.4.1 Downward Release of Pressurized Superheated Liquids. The experimental findings provide a great deal of insight into the mechanisms responsible for the dispersion and vaporization of superheated liquids from pressurized bottles. To our knowledge, this investigation represents the first systematic investigation of these important physical processes which are expected to be crucial in the ability of an agent to extinguish a fire in a compartment. These findings are particularly relevant for the aircraft dry bay application. In the following we will summarize the important conclusions of the study and attempt to provide physical explanations for the observations.

The following discussion will be clearer if one considers the following figures which show calculated values of Jakob number (Figure 172) for each agent as a function of agent boiling point and the dynamic pressures (Figure 173 and Figure 174) expected for a given velocity and a range of densities chosen to span pure air to those typical of the liquid agents.

The Jakob number (*Ja*) is a dimensionless number which estimates the fraction of a superheated liquid which can be vaporized adiabatically. In other words, it is the ratio of the sensible heat within the liquid, which can be extracted from the liquid by cooling to its boiling point for the ambient pressure, and the heat of vaporization, ΔH_{vap}, for the liquid. Mathematically, it is defined as

$$Ja = \frac{\Delta h}{\Delta H_{vap}}, \tag{35}$$

where Δh is the change in enthalpy of the liquid on cooling from the ambient temperature (T_{amb}) to the boiling point of the liquid (T_{sat}) for the ambient pressure,

$$\Delta h = \int_{T_{amb}}^{T_{sat}} C_{p,l}(T)dT. \tag{36}$$

$C_{p,l}$ is the constant pressure heat capacity for the liquid which varies slightly with temperature. Values of *Ja* calculated for each of the potential replacement agents, with the exception of FC-116, and halon 1301 have been calculated. The results are plotted in Figure 172 and listed in Table 8.

In order to calculate the specific heats at a constant pressure of one atmosphere for temperatures ranging from room temperature to the liquid boiling point, the specific heat was assumed to be independent of pressure. The specific heats were fit to a second- or third-order polynomial and integrated from the boiling point to room temperature (293 K) to yield the change in internal energy. The specific heat was also fit by a spline fit technique. Results for the two approaches are included in Table 8. The two sets of calculations are in excellent agreement.

The required specific heats of HFC-227ea, HCFC-22, HFC-134a, HCFC-124, HFC-125, FC-218, FC-318, and halon 1301 were obtained from the PROZPER program (Ely and Huber, 1993). The values for FC-31-10 were estimated by the method of Tarakad, Danner, and Lee-Kesler (Daubert and Danner, 1992). The specific heat of the HFC-125/HFC-32 mixture was calculated using Rowlinson's corresponding states method (Reid *et al.*, 1987) coupled with the Genetron equation (Allied Signal, 1991) for the ideal heat capacity. Values for HFC-236fa were calculated using Rowlingson's corresponding states method and the method of Joback (Reid *et al.*, 1987). Heats of vaporization are those listed in Table 1 of Section 2.1.

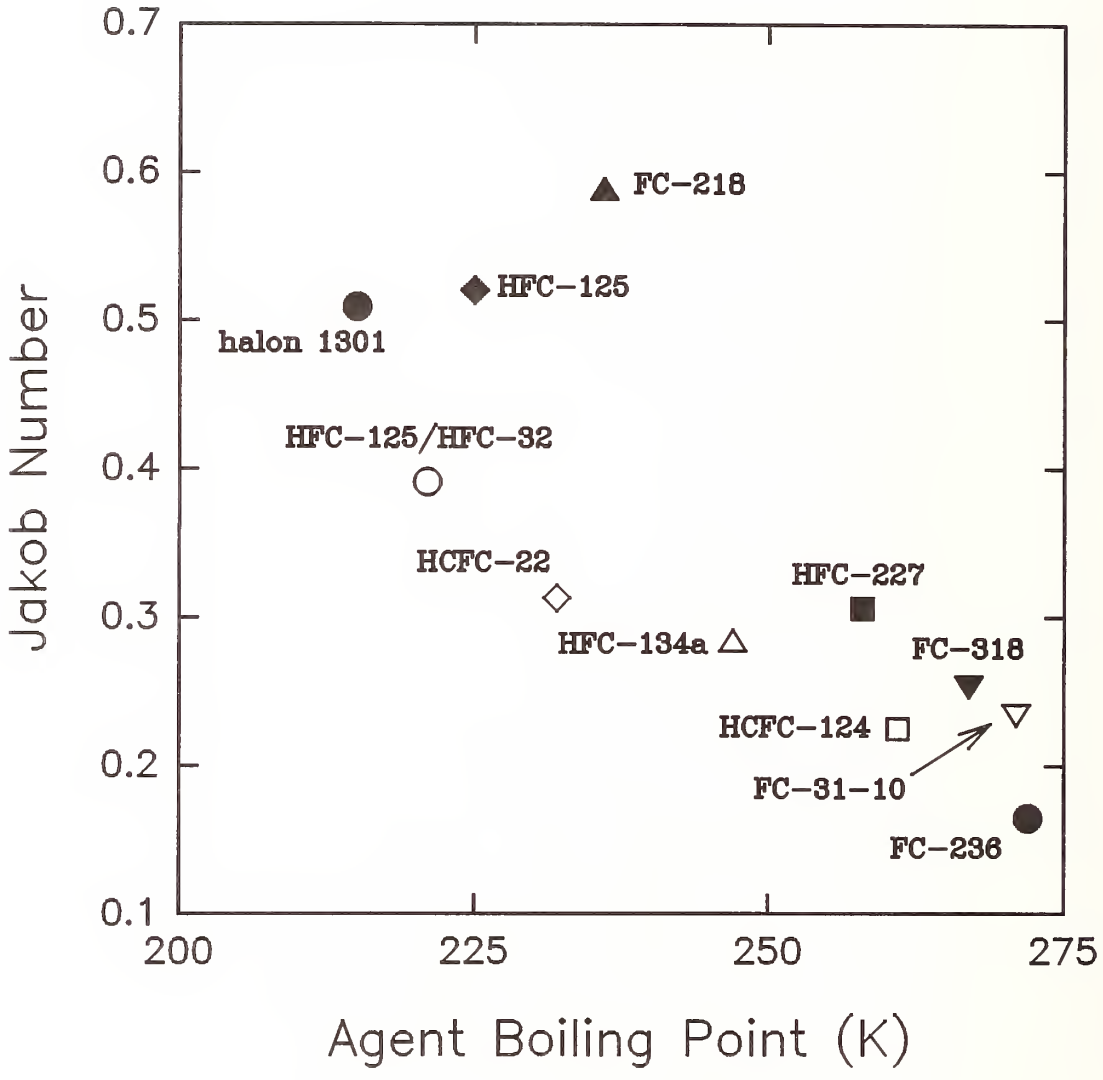

Figure 172. Values of Jakob number are plotted as a function of boiling point for each of the potential replacement agents, except FC-116, and halon 1301.

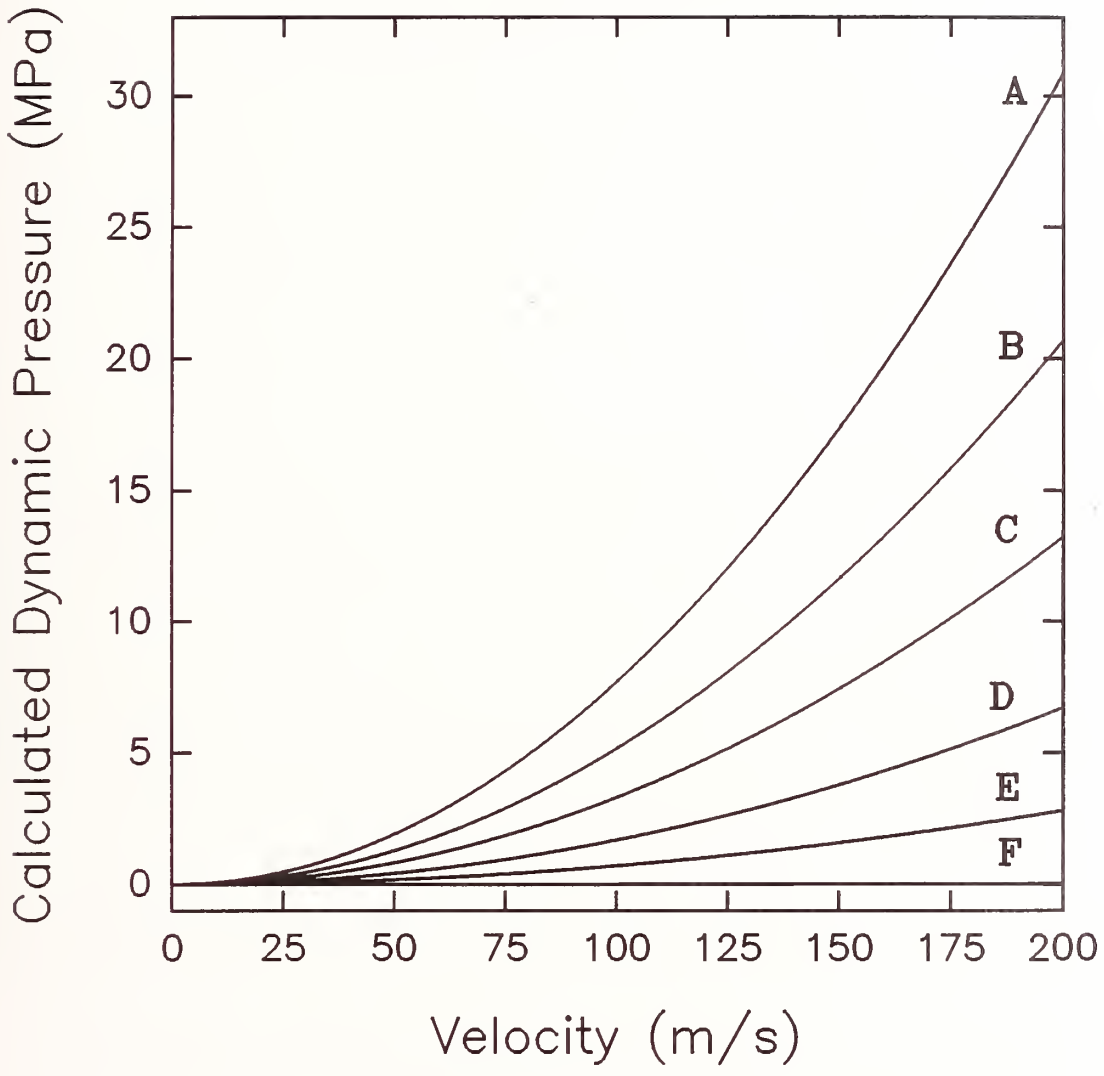

Figure 173. Calculated dynamic pressures for: A) liquid halon 1301, B) liquid HFC-125/HFC-32 mixture, C) 50% liquid/50% vapor mixture FC-218, D) 25% liquid/75% mixture FC-218, E) 10% liquid/90% gas mixture FC-218, and F) room-temperature air.

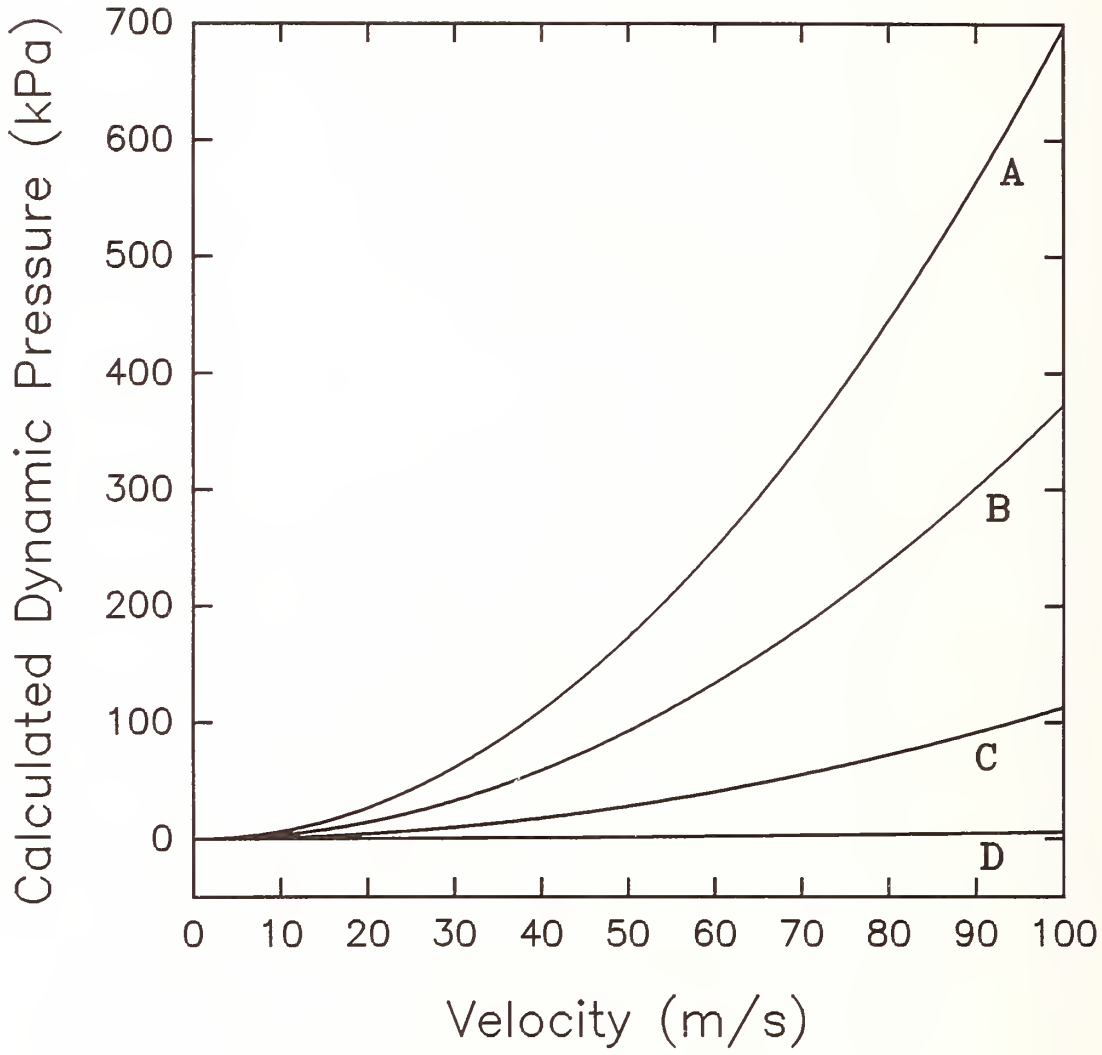

Figure 174. Calculated dynamic pressures for: A) 10% liquid/90% mixture FC-218, B) 5% liquid/95% mixture FC-218, C) 1% liquid/99% mixture FC-218, and D) room-temperature air.

Table 8. Jakob Numbers for Room Temperature (293 K) Releases of Ten Potential Replacement Agents and Halon 1301. Heat Capacity Temperature Dependencies have been Fit Using Polynomial and Spline Fits.

AGENT	*Ja* (Polynomial Fit)	*Ja* (Spline Fit)
HFC-236fa	0.165	0.165
FC-31-10	0.236	----
FC-318	0.255	0.255
HCFC-124	0.228	0.228
HFC-227ea	0.306	0.306
HFC-134a	0.283	0.283
FC-218	0.587	0.578
HCFC-22	0.313	0.313
HFC-125	0.520	0.520
HFC-125/HFC-32	0.391	0.391
halon 1301	0.509	0.509

Note that three of the agents, HFC-125, FC-218, and halon 1301, have higher *Ja* than the remaining agents. The value for the HFC-125/HFC-32 mixture is intermediate. All of the other agents have values which fall below 0.35.

During the course of this investigation dynamic pressures were recorded near the vessel exit and on the flow centerline 1.3 m from the vessel orifice. Since actual velocities or densities are not available, it is not possible to derive density or velocity information from these measurements using Equation (34). However, the magnitudes of the dynamic pressures do provide insights into the nature of the flows. This becomes clear when one considers Figure 173 and Figure 174.

Figure 173 shows the calculated dynamic pressure as a function of velocity for densities corresponding to those for liquid halon 1301 (1551 kg/m^3), liquid HFC-125/HFC-32 mixture (1040 kg/m^3), a 50% liquid/50% vapor mixture of FC-218 (665 kg/m^3) at its boiling point temperature, a 25% liquid/75% gas mixture of FC-218 (338 kg/m^3), a 10% liquid/90% gas mixture of FC-218 (141 kg/m^3), and room-temperature air (1.20 kg/m^3). The dependencies of the calculated dynamic pressures on density and velocity are clear. Note that for high velocities and densities, very large dynamic pressures are attained, while for air the pressures are relatively low for the entire velocity range.

Figure 174 is a similar plot of dynamic pressure, but the velocity and density ranges have been reduced. Results are for a 10% liquid/90% gas mixture of FC-218 (141 kg/m^3), a 5% liquid/95% gas mixture of FC-218 (75.3 kg/m^3), a 1% liquid/99% gas mixture of FC-218 (22.8 kg/m^3), and room-temperature air (1.20 kg/m^3). The effect of even a small fraction of liquid phase agent on measured dynamic pressures is obvious from this figure.

The two most dramatic events that were identified in the high-speed films of the releases were the violent mixing of agents with their surroundings observed at the initiation of a release and at times close to when the final liquid agent exits the containment vessel. These events were termed "flashings" even though it will become clear that term is most likely inappropriate for the later of these events.

The initial rapid spreading of the agent as the burst disk opens is fairly easy to explain qualitatively by considering the events when the disk opens, even though the actual behaviors are exceedingly complex to describe quantitatively. Immediately following the rupture of the disk, the liquid agent in proximity to the orifice experiences a rapid depressurization to the outside ambient pressure. At this point the liquid is not in motion. Pressure measurements in the liquid within the vessel indicate that this pressure drop is not transmitted into the vessel which means the drop must occur within the orifice. The liquid at the interface should undergo a rapid flashing. This flashing may be induced by local perturbations associated with the bursting of the disk or may even take place as a miniature boiling liquid expanding vapor explosion (BLEVE). Such processes have been discussed in Sections 3.2.4 and 3.4.3.5.

The first detectable pressure drops inside the vessel within the nitrogen occur 0.36 to 0.76 ms following the near-total attenuation of laser beam #1, with the majority requiring roughly 0.4 ms. Since pressure changes are expected to be transmitted at the speed of sound, less than 1 ms is required for pressure fluctuations to travel from the orifice to the internal pressure transducer at the top of the vessel. The observed delay is therefore attributable to the period required for the liquid to begin to accelerate through the orifice and thus drop the nitrogen pressure due to a volume increase of the ullage. The internal pressure fits discussed in Section 3.4.3.1 indicate that the liquid flow reaches a choked condition in a very short period of time.

Even though the initial flashing behavior is evident in all of the high-speed movies of the releases, it was only detected by the near-field pressure transducer for the lower boiling-point liquids. This demonstrates that shock waves are not generated by the disk bursting, and that any signals recorded by the transducer must either result from shock waves generated by liquid flashing or direct impingement of a two-phase flow on the transducer. The periods required for the near-field external pressure transducer to sense the releases varied from 1.28 to 1.84 ms. Such time delays are consistent with estimates for radial velocities listed in Table 5 based on high-speed-films measurements.

Once the pressure at the orifice is released, the liquid in the vessel begins to accelerate and flow through the orifice. The high-speed films indicate that the flows quickly form a liquid stream. Based on measurements given in Section 3.4.3.1, the flow velocities are on the order of 60 m/s.

The "flashing" near the conclusion of the release of the liquid agent is at first glance more difficult to understand. The films show a very vigorous event which appears to occur as the result of very rapid boiling of the agent. For all of the agents the near-field pressure transducer recorded sharp increases in dynamic pressure which varied from several hundred to 1600 kPa (see Figure 88 through Figure 98).

Reference to Figure 173 and Figure 174 shows that the fluid striking the pressure transducer must have high velocities and densities. Such a behavior is difficult to attribute simply to flashing of the liquid. The key is to recognize that a release of a vessel's contents is not complete once the liquid is expelled. A significant pressure of nitrogen and vaporized agent remains. These gases will now exit the vessel. The question is: How are the gases released from the vessel? The answer has already been provided in Section 3.4.3.1. The flow becomes that of a sonically choked gas flow through the orifice.

By assuming that there is only ideal-gas nitrogen in the vessel, it is straightforward to estimate a flow velocity for the gas. Assuming an initial pressure of 4.14 MPa and that the liquid fills two thirds of the vessel, the expression for the adiabatic expansion of a gas,

$$P_i V_i^{\gamma} = P_f V_f^{\gamma}, \tag{37}$$

allows the initial temperature for the gas release to be calculated. Here P and V are pressure and volume, the subscripts i and f refer to initial and final conditions, and γ is the ratio of constant pressure and constant volume heat capacities. Using the ideal gas law this becomes

$$T_f = T_i\left(\frac{P_f}{P_i}\right)^{\left(1-\frac{1}{\gamma}\right)}, \tag{38}$$

where T is the temperature. For $V_i = 0.000333$ m^3 and $V_f = 0.000500$ m^3, these equations yield $P_f = 2.40$ MPa and $T_f = 251$K. With these values, it is now possible to calculate the sonic velocity using

$$U_{sonic} = \sqrt{\gamma R T_f M}, \tag{39}$$

where R is the gas constant and M is the molecular weight for the gas. Substituting in Equation (39) gives $U_{sonic} = 323$ m/s.

It is now clear that the flow leaving the vessel will accelerate dramatically once the liquid has been expelled. This rapidly expanding gas quickly catches up with the slower moving, but much denser, liquid or two-phase jet. To the gas stream, the liquid will appear much as a solid body due to its much higher density. As a result, the gas should pass around the agent flow which explains the very rapid expansion of the jet observed in the films. The nitrogen flow is also expected to interact with the liquid or two-phase flow, both fragmenting it and mixing with it. As a result of this mixing, a two-phase mixture will be generated. It is presumably such mixtures which are detected by the dynamic pressure transducer. These flows can be both high speed and relatively high density due to their two-phase character, thus explaining the very high dynamic pressures which are observed.

To our knowledge, this is the first report of such an aerodynamic mechanism for rapidly dispersing releases of liquid agents. It is unclear how significantly this process will affect the overall dynamics for the mixing of an agent with its surroundings. However, it seems likely that for short-period releases, such as those investigated here, the effects can be substantial, and that the release of high pressure nitrogen can substantially augment the mixing of a released liquid agent as the result of its own velocity and flashing behavior.

The velocities measured from the extinguishment of the laser beams provide insights into the flashing behaviors of the various agents. The measured velocities nearest the vessel exit were between 50 and 60 m/s for HFC-236fa, FC-31-10, FC-318, and HCFC-124 (see Figure 110 through Figure 113). The results for HFC-227ea (Figure 114) are only slightly higher. These velocities are consistent with the flow velocity of the liquid stream from the vessel suggesting that for these agents the liquid stream extends at least 0.32 m downstream of the orifice. These observations are also consistent with the observation of a liquid stream in the high-speed films (*e.g.*, see Figure 86).

For each of these high boiling-point agents the velocity was higher at the second measurement position indicating that flashing had begun and the flow was accelerating due to the volume expansion associated with the flashing. Assuming an average liquid flow velocity of 60 m/s, this means that the period required for these agents to flash lies somewhere between 5 and 10 ms.

As noted earlier, the measured velocities for HFC-134a (Figure 115) suggested that this agent was an intermediate case. In two experiments the highest velocities were observed between lasers #1 and #2 suggesting that flashing of the liquid jet occurred somewhere in between. One case showed the flashing taking place between lasers #2 and #3. For the two cases where flashing occurred near the vessel, the velocity then fell off with increasing distance for distances beyond laser #3. This suggests that flashing is complete and the resulting two-phase flow is slowing down as it mixes with surrounding air as would be expected for a gas jet.

The remaining low boiling-point liquids, FC-218, HCFC-22, HFC-125, the HFC-125/HFC-32 mixture, and halon 1301 all have high velocities near the vessel exit, and then slow down significantly with increasing distance. Again, this is taken to mean that the agents rapidly expand near the exit due to rapid boiling and then spread more slowly as two-phase flows entraining air. The fact that all have increased velocities near the vessel exit indicates that the time required for flashing must be significantly less than 5 ms.

Additional evidence for this conclusion is found in the near-field pressure traces for FC-218, HCFC-22, HFC-125, the HFC-125/HFC-32 mixture, and halon 1301 (Figure 94 through Figure 98). These traces show that dynamic pressures are recorded not only at the start and end of a release, but during the release. This can only be the case if the fluid leaving the vessel is flashing over a very short flow distance. This flashing generates the two-phase flows necessary for the observed pressure increases. The pressure increases for the intermediate times are strongest for the HFC-125/HFC-32 mixture and halon 1301 consistent with their low boiling points. A very rapid expansion of halon 1301 is also consistent with the rapid spreading of this flow which can be seen in Figure 87.

The general trends observed for the flashing times are consistent with those discussed by Day (1969) and Lienhard and Day (1970). The times decrease with increasing superheat which is directly related to the difference in pressure between the ambient and saturated values. Using Equations (31)-(32), it is possible to derive the following expression for the flashing time,

$$t_d = 2.12X10^{13}(P_v - P_{amb})^{-7/2} D^{-2} \sigma^3 \sqrt{\rho_f} \tag{40}$$

This equation has been tested for those agents for which surface tension value estimates were available from Daubert and Danner (1992). Other values for the variables in Equation (40) are taken from Table 1 of Section 2. Table 9 lists the values of surface tension used along with calculated values of t_d.

It is clear that Equation (40) vastly underestimates the times required for the liquid streams to flash. At the present time we are unable to provide an explanation for this failure. On the basis of this finding, it is concluded that the prediction of flashing lengths for these agents is currently not possible.

The discussion thus far has shown how flashing of the agents leads to enhanced mixing of the two-phase flow with its surroundings. It is clear that the amount of superheating is crucial to the speed and violence of this flashing. As noted earlier, it is also necessary for the agents to be vaporized in order to be effective. The downstream dynamic pressure measurements and hot-film response provide insights here.

All of the high boiling-point agents show similar behaviors. When the agent first reaches the pressure transducer there is a rapid jump in the pressure. Following this jump the pressure continues to increase for a period roughly equal to the time required for release of the liquid agent from the containment vessel. This observation suggests that velocity measured from the propagation of the downstream edge of the release should provide a good estimate for the entire release period.

For HFC-236fa, FC-31-10, FC-318, HCFC-124, and HFC-227ea these velocities were on the order of 70 m/s. The maximum dynamic pressures observed for these agents were in range of 800 to

Table 9. Values of Time Required for Flashing of Superheated Liquid Streams Calculated Using Equation (40)

Agent	Surface Tension (N/m)	Calculated t_d (s)
FC-31-10	0.0153	4.0×10^{-6}
FC-318	0.0117	8.5×10^{-7}
HFC-134a	0.0230	2.7×10^{-8}
FC-218	0.0159	1.3×10^{-8}
HCFC-22	0.0184	1.1×10^{-8}
HFC-125	0.0171	3.3×10^{-8}
halon 1301	0.0156	2.1×10^{-9}

1600 kPa with a typical value being 1200 kPa. Using Equation (34), the density necessary to generate such a pressure rise is on the order of 430 kg/m^3. The densities of these liquids range from 1356 to 1499 kg/m^3. This suggests that roughly 30% of the mass for these agents reaching the 1.3 m downstream position on the centerline of the flow is not vaporized. As discussed in the experimental section, the aspirated hot-film responses were consistent with the presence of two-phase flows at this downstream location for all of the releases.

The HFC-134a results are somewhat different. The laser measurements (Figure 115) indicate the velocity for this flow at the 1.3 m position is on the order of 50 m/s, but the dynamic pressures observed were on the order of 2000 kPa yielding a density of roughly 1600 kg/m^3. This estimate is higher than the original density of the liquid which is 1209 kg/m^3. This suggests that this agent is only slightly evaporated over the flow distance and its velocity must be somewhat higher than estimated. It is difficult to understand this finding given the behavior of the other agents. However, the experimental results were repeatable.

The results for the low boiling-point liquids varied dramatically from agent to agent. When FC-218 reached the pressure transducer there was a fairly rapid increase in dynamic pressure to values on the order of 100 to 200 kPa (Figure 127). Figure 116 indicates the flow velocities are on the order of 40 m/s. This suggests that the local density is roughly 125-250 kg/m^3. Since the liquid density is 1321 kg/m^3, this suggests that 10-20% of the agent is present as liquid (also see Figure 173 and Figure 174).

For HFC-125 the dynamic pressures recorded when the agent first reached the pressure transducer (Figure 129) were very low, being less than 10 kPa. Measured velocities (Figure 118) were on the order of 18 m/s. This indicates that the flow density was less than 60 kg/m^3. Based on the liquid density for HFC-125 (1190 kg/m^3), this suggests that much less than 5% of the flow is in the liquid state.

The results for halon 1301 were variable. One of the releases (B in Figure 131) gave no measurable pressure increase when the agent first arrived. The pressure eventually began to rise slowly after 20 ms and then increased at the end of the release to almost 400 kPa. The hot-film response (Figure 135) indicates that two-phase flow is associated with the large pressure rise. Flow velocities are on the order of 30 m/s (Figure 120). These observations suggest that the flow initially

arrives nearly fully vaporized, but that near the end of the release the flow density increased to roughly 900 kg/m^3. This observation is difficult to understand until one realizes that the large dynamic pressure increase is likely associated with the flow generated by the release of nitrogen from the vessel. Flow velocities are expected to be much higher for this case. It seems likely that the high pressure results from a high-speed flow of nitrogen, which has entrained some two-phase halon 1301, striking the pressure transducer. Recall it was concluded that a two-phase mixture of halon 1301 is released from the vessel near the end of the liquid release due to flashing within the nozzle or vessel (see Section 3.4.3.1). The high-speed nitrogen flow would be likely to entrain the resulting two-phase flow.

The results for FC-218, HFC-125, and halon 1301 indicate that most of the liquid agent is vaporized over the 1.3 m flow length. This is in sharp contrast to HCFC-22 where very high dynamic pressures are generated during most of the time the agent flow is striking the transducer (Figure 128). Maximum dynamic pressures were on the order of 2000 kPa. Using an average velocity of 40 m/s (Figure 117), these pressures yield calculated densities on the order of 2500 kg/m^3 which can be compared to a liquid density of 1192 kg/m^3. This is another case where the flow velocity estimate must be low. However, it seems clear that a large fraction of the agent arrives in the liquid state at the 1.3 m location.

The HFC-125/HFC-32 mixture also generated complicated dynamic pressure time dependencies (Figure 130). When the agent first reached the transducer there were pressure increases on the order of several hundred kPa. Using an estimate for the flow velocity of 30 m/s from Figure 119, this yields densities on the order of 700 kg/m^3 or roughly 60% liquid. The aspirated hot-film response (Figure 137) for this agent also indicated the presence of a strong two-phase flow. Near the end of the releases there were strong pressure increases which are likely associated with an increase in flow velocity, perhaps as a result of the nitrogen release.

The conclusions from the above discussion can be summarized as:

- The high boiling-point agents generate flows which consist of roughly 30% liquid on the centerline at 1.3 m from the vessel.
- FC-218, HFC-125, and halon 1301 produce flows which have most of the agent ($> 90\%$) in the gas state.
- HCFC-22 and the HFC-125/HFC-32 mixture yield pressure traces which suggest that a large fraction of their mass is still liquid at the measurement location.

It is impossible to provide a detailed description of the physical processes which are occurring during the mixing following a high pressure release of a superheated liquid due to the complex and interactive nature of the physical processes which are taking place. Flashing generates a two-phase flow at some unknown position which has unknown velocity, temperature, and droplet size distributions. This two-phase flow then begins to entrain room-temperature air. For temperatures near 295 K, the entrained air will also introduce heat into the flow which can evaporate additional liquid. The short duration of the flows further complicates attempts to understand the behavior since flow development is likely to last for a large fraction of the total flow time. As an example, the impulsively started flow should immediately interact directly with room temperature air. However, as the flow develops, the flow volume will contain more and more agent and air will enter only from outer regions of the flow. As a result, the amount of agent which is vaporized as a function of downstream distance is expected to vary with time. This may explain some of the time dependencies observed in the downstream dynamic pressure measurements.

The lack of detailed measurements also makes a complete understanding impossible. Most of the downstream measurements are only valid for the centerline of the flow and the fraction of two-phase flow is only estimated for two locations. No information is available concerning the radial structure of the flow.

Despite the limitations of the measurements, it is possible to draw some general conclusions concerning the evaporation of the agents. The measurements suggest that the high boiling-point agents are only roughly 70% vaporized at the 1.3 m downstream position. Referring to Figure 172 it can be seen that these six agents, including HFC-134a, are clumped together at the lower right-hand side of the plot of *Ja* versus agent boiling point. The *Ja* numbers are all 0.3 or less indicating that the superheating of these agents is sufficient to vaporize only a small fraction of the agent. In order for the remainder of the agent to be vaporized, additional heat must be absorbed from the surroundings. The fact that these agents reach the pressure transducer as two-phase flows indicates that insufficient heat is available to fully vaporize the agents. Since it was estimated that roughly 30% of the agent flows was liquid at the transducer, this suggests that sufficient air was entrained to vaporize half of the remaining liquid.

It should be pointed out that the actual dynamic pressure which is measured will be a complicated function of flashing behavior and the degree of vaporization. This is due to the different dependencies of the dynamic pressure on density and velocity (see Equation (34)). Flashing of an agent increases its velocity and decreases it density due to the accompanying volume expansion. As a result, it is possible to either increase or decrease the measured dynamic pressure. This effect may explain the high densities calculated for some of the flows such HFC-134a.

Based on this discussion, it is now possible to gain some insight into the vaporization behaviors of the low boiling-point liquids. The three liquids which seemed to be nearly fully vaporized were FC-218, HFC-125, and halon 1301. Figure 172 shows that these three liquids have the highest *Ja* numbers of any of the agents tested. In each case, the agent can provide over 50% of the heat required for full evaporation. They also have quite high superheats, and, as a result, they tend to flash strongly near the vessel exit. The resulting two-phase flow has a relatively long distance over which to entrain air. The wide dispersion of the agent due to flashing also aids in the evaporation process. Apparently, sufficient air is entrained into these flows to provide the heat necessary to complete the evaporation for these agents.

HCFC-22 is an interesting case. Even though its boiling point is lower than that for FC-218, its *Ja* is only slightly more than 0.3. As a result, flashing vaporizes considerably less of the fluid than for the low boiling-point liquids just discussed. Another peculiarity of this agent is that for constant fill level in the vessel (generally 3.33×10^{-4} m^3), significantly higher number of moles of this agent are released during the same liquid flow period (4.6 moles versus 2.3, 3.3, and 3.6 for FC-218, HFC-125, and halon 1301, respectively). This means the amount of expansion and acceleration of the liquid will be higher for a given percentage of vaporization. This expansion will tend to shield the liquid from entrained air and may well contribute to a slower rate of agent evaporation. The combination of low *Ja* and high number of moles most likely accounts for the very high downstream dynamic pressures observed for this agent (see Figure 128).

The same arguments provide an explanation for the two-phase character of the HFC-125/HFC-32 mixture which was observed. Its *Ja* number is intermediate between that of halon 1301 and HCFC-22. The liquid itself only provides 40% of the heat necessary to vaporize all of the liquid. In addition, this agent provides, by far, more moles of agent (5.2 moles) than any other for a release from the 2/3 full vessel. Again, the degree of expansion and acceleration associated with this large number of moles is likely to limit the entrainment of air and complete vaporization of this agent.

On the basis of the mixing results, three parameters have been identified which control the degree of vaporization of an agent. These are the amount of superheat, Jakob number, and the number of moles contained in the liquid release. Efficient evaporation is favored by high superheat, high *Ja*, and a low number of moles of fluid in the vessel.

3.5.4.2 Effects of Orifice Diameter on Mixing and Evaporation. The orifice size affects the dynamic pressure measurements in the near field, the dispersion velocities, and the degree of evaporation at the far stream position. For FC-31-10 the maximum dynamic pressure associated with the release of the nitrogen using the 12.7 mm opening was roughly the same as for the 19.1 mm opening, while the 6.4 mm opening generated no pressure increase. For FC-218 and halon 1301 the intermediate size orifice yielded lower maximum overpressures, but also provided indications that flashing was taking place over much of the liquid release periods. Such an indication of continual flashing for the largest nozzle was not observed for FC-218. For both of the low boiling-point liquids no near-field pressure increases were observed when the smallest orifice was used.

These dynamic pressure results can be understood in terms of the expected flashing behavior of the agents and the effects of the released nitrogen. Due to the low superheat of the FC-31-10, this agent never flashes in the near field. The pressure rise detected for the 12.7 mm orifice is the result of high-speed nitrogen striking the slower moving liquid. For the smaller orifice, no pressure rise is detected due to the reduced mass flow of both the liquid and the nitrogen gas. The flow simply does not expand sufficiently to reach the pressure transducer.

The most interesting observation for the FC-218 was the flashing of the liquid for flow through the 12.7 mm opening, which was not observed when the 19.1 mm opening was used. This is likely due to a reduction in the flashing time for the smaller orifice which caused the flashing to occur nearer the nozzle with the result that two-phase flow struck the transducer. Such a behavior is consistent with the dependence of flashing time on liquid stream diameter reported by Lienhard and Day (1970). The reduction of the maximum dynamic pressure associated with the release of nitrogen on going from the 19.1 to 12.7 mm orifices and the absence of a pressure rise for the 6.4 mm orifice are explained by the reduction in mass flows of the liquid and nitrogen as discussed above for FC-31-10. The near-field pressure behaviors for halon 1301 are consistent with the conclusions for FC-218.

The average velocity measurements with downstream position shown in Figure 139 through Figure 141 indicate that, in general, the velocities nearest the vessel increase as the orifice size is decreased and that those at the farthest downstream position decrease. These higher velocities are consistent with the liquid flashing earlier and more strongly near the vessel when the liquid stream diameter is reduced as predicted by Lienhard and Day (1970). Due to the smaller diameters and lower mass flows of the liquid jet through the smaller orifices, the two-phase flows will mix with air and spread faster over shorter distances in a manner similar to turbulent axisymmetric jets (see Richards and Pitts (1993) and references therein). As a result of air entrainment they slow down as observed experimentally.

The measurements of downstream dynamic pressure and aspirated hot-film response confirm the above conclusions. Due to the low superheat of FC-31-10 it reached the 1.3 m downstream position as a two-phase flow for releases through both the 19.1 mm and 12.7 mm orifices. However, due to the shorter flow distance required for the entrainment of a sufficient mass of air to evaporate the agent, the 6.4 mm orifice release reached these detectors as a gas-phase flow. The FC-218 seems to be fully vaporized for each of the orifice sizes. Interestingly, halon 1301 showed (Figure 144) two-phase character near the end of the release when the intermediate orifice size was used. This was also the case for the 19.1 mm orifice. The smallest orifice yields single-phase flow due to the more efficient entrainment of air as can be seen in Figure 145.

3.5.4.3 Effects of Vessel Pressurization Level on Mixing and Evaporation. The effects of vessel pressurization are only available for FC-218. The near-field dynamic pressure traces are qualitatively similar when using nominal 5.51 MPa, 4.14 MPa, and 2.76 MPa burst disks. No pressure rise is observed until very near the time when liquid is completely expelled from the vessel.

In each case the pressure rise is attributed to the collision of high-speed nitrogen with the liquid stream. The actual magnitudes of the dynamic pressure increases are difficult to interpret physically due to the complex interactions involved.

The average flow velocities observed for the FC-218 as a function of downstream distance were very similar for overpressures of 6.21 MPa and 4.28 MPa (Figure 148). This suggests that the flashing behavior is similar for these two flows and that the velocities resulting from the flashing are dominating the flow behavior. On the other hand, the velocities were lower at each station for a release at the lowest pressure (2.61 MPa). It would appear that the significantly lower liquid velocities near the vessel exit in this case resulted in significantly slower mixing.

3.5.4.4 Effects of an Extension Tube on Mixing and Evaporation. The addition of a 0.5 m extension tube on the vessel had very little effect on the release behavior of the agents, but it significantly modified the mixing behavior. Figure 149 through Figure 151 show that measured velocities at the two locations furthest from the vessel exit were much higher when the tube was in place than when no tube was used for FC-31-10, FC-218, and halon 1301. These observation can be easily understood if one makes the reasonable assumption that each of these liquids flashed somewhere within the tube due to a reduction in pressure. The flashing liquids must expand. For a free expansion, the gas is free to expand in all directions. However, for the liquids in a tube the expansion is constrained to occur only along the tube direction. Much as for a bullet constrained within the barrel of a rifle, the mass of the fluid is highly accelerated down the tube. For flashing liquids with high *Ja* number, the accelerations are quite dramatic indeed. Velocities approaching 200 m/s were observed.

The dynamic pressures measured 1.3 m from the vessel opening were extremely high for each of the fluids (Figure 152 through Figure 154), and, in the case of halon 1301, approached 3 MPa. Even assuming very high velocities, this suggests that a significant amount of the liquid was unevaporated. The measured responses of the aspirated hot-films support this conclusion. To our knowledge, the extremely high velocities and overpressures generated by using a tube to dispense superheated fire-fighting agents have not been previously documented.

3.5.4.5 Effects of Agent Cooling on Mixing and Evaporation. Cooling of the agents has a very large effect on the dispersion and evaporation of the released liquid. FC-31-10 has a boiling point close to room temperature and, as a result, does not flash or evaporate rapidly. At the 1.3 downstream measurement position, the flow generated by a room temperature release of this agent has a large percentage of the agent in the liquid phase. Cooling will slow down the mixing and evaporation and increase the liquid fraction of the two-phase flow. In fact, very nearly 100% of the agent is expected to arrive at the 1.3 m position as liquid.

The effects of cooling FC-218 are considerably more dramatic than for FC-31-10. A room temperature release of FC-218 flashes very close to the vessel exit rapidly evaporating and dispersing the agent. By the time the agent reaches the 1.3 m downstream position the flow has entrained sufficient air to essentially evaporate all of the released agent. Upon cooling to a temperature of 228 K, which is below its boiling point of 236 K, these advantages of FC-218 for mixing disappear. Flashing no longer takes place and the agent reaches the downstream location mostly as a liquid flow. It should be noted that for these tests the agent entered room temperature air. If the ambient environment was also cooled, the liquid would not be expected to vaporize at all, and the release would be a liquid stream which would eventually pool somewhere within the space.

3.5.4.6 Effects of Release Orientation on Mixing and Evaporation The effects of releasing the agents upwards instead of downward are dramatic. The observations are easily understood in

terms of the changes in release behavior which were observed inside the vessel (see Section 3.4.3.6). It was noted that for downward releases the nitrogen acts on the liquid inside the vessel much as a pressure applied to a piston. It pushes the liquid rapidly from the vessel where it subsequently flashes if the liquid at the vessel temperature is superheated. The behavior for upward releases is completely different. Since the nitrogen is now at the top of the vessel next to the orifice, it is immediately released from the vessel upon the opening of the burst disk. The pressure within the vessel drops very rapidly to close to that of the ambient surroundings. There is no force to drive the liquid agent from the vessel. If the pressure in the vessel falls below the ambient saturation pressure of the agent, the agent will begin to boil, ultimately filling the vessel with a two-phase mixture. As the pressure rises due to expanding bubbles, this two-phase mixture is expelled from the vessel.

The measurements of nitrogen velocity shown in Figure 159 and Figure 165 show that downstream velocities are on the order of 175 m/s. These high velocities are due to the very large velocities (estimated to be on the order of 300 m/s) expected for choked flows of nitrogen through the 19.1 mm orifice. There is very little agent vapor in the nitrogen and the fraction of the total agent mass released initially is quite small. The very small laser attenuations (Figure 158, Figure 163, and Figure 168) observed downstream of the vessel when the nitrogen flows arrived are consistent with this conclusion.

Once the nitrogen was expelled from the vessel, delay times were observed before the liquid agent began to flow. For FC-31-10 this delay time was 24 ms and for FC-218 it was 19 ms. It was not possible to measure a time accurately for the halon 1301 release, but the behavior of laser #4 in Figure 168 suggests a value on the order of 16 ms. These initial releases of agent are attributed to the expulsion of condensed vapor above the liquid as the superheated liquids in the vessel begin to boil following depressurization. The decreasing delay times observed with increasing superheat are consistent with the behaviors expected for flashing of superheated liquids (see the discussion in Section 3.5.1). It is interesting that the observed delay times are significantly longer than those estimated for streams of liquid outside of the vessel, which were much less than 5 ms for the two low boiling-point liquids.

The initiation of boiling does result in the release of some agent from the vessel. However, the laser beam attenuation, downstream dynamic pressure, and aspirated hot-film measurements all indicated the mass of the agents released during these release periods were fairly low. Only when the two-phase mixture fully filled the vessel did significant agent begin to leave the bottle. These times were estimated as 54, 39, and 30 ms for FC-31-10, FC-218, and halon 1301, respectively. For FC-31-10 the time before significant mass of agent was released during an upward release was longer than required for the complete downward release of this agent. Even for the lower boiling-point agents the times required for release of a significant mass of the agents were quite long for upward releases as compared to downward releases.

The change in release mechanism for upward releases as compared to downward releases also has significant effects on the mixing and evaporation behavior of the agents. The results shown in Figure 159 and Figure 165 show that both of the two-phase flows have velocities which are significantly lower than observed for downward releases. As a result, much longer times are required for an agent to reach the 1.3 m downstream distance. Even though the two-phase flows are moving more slowly and therefore provide longer times for evaporation, the very high dynamic pressures and aspirated hot-film responses measured indicate that much of the agent mass is still liquid. Estimates of densities for FC-31-10 and FC-218 based on the measured velocities and dynamic pressures are significantly higher than the densities of the pure liquid agents. This suggests that velocities later during the flow period are somewhat higher than estimated based on the leading edge measurements. This does not contradict the conclusion that the flows must consist of large fractions of unevaporated liquid. For the low boiling-point liquids this result is completely the opposite to that for downward

releases, where it was observed the FC-218 and halon 1301 were nearly fully vaporized over this distance.

The change in evaporation behavior can be understood in terms of the release mechanism. The pressure necessary to expel the liquid from the vessel is generated by boiling of the liquid at a pressure close to atmospheric. As a result, the temperature of the liquid drops to levels close to it boiling point. The gas-liquid mixture leaving the vessel is expected to have a similar temperature. No additional flashing will occur to evaporate liquid. The only way that additional vaporization can occur is through entrainment of room temperature air into the flow with subsequent heat transfer to the agent mixture. The downward releases demonstrated that insufficient air is entrained to vaporize a large fraction of the agent.

The times required for complete release of the agents estimated from the laser beam attenuation measurements, 800 ms for FC-31-10, 500 ms for FC-218, and 250 ms for halon 1301, are consistent with estimates based on measurements within the vessel. (see Section 3.4.3.6).

These results demonstrate how detrimental the effects of changing the release direction of a pressurized agent from a downward to upward orientation can be on the time required for the start of the release, the release rate, the effectiveness of agent dispersion, and the degree of evaporation. It should be noted that while no tests were performed using cooled agents, it is extremely likely that essentially no agent would be expelled from the vessel by an upward release of one of these agents cooled below it boiling point.

3.5.5 Summary and Agent Ranking. The primary purpose of the work described in this section was to allow the proposed halon-alternative agents to be ranked with regard to their dispersion behaviors and evaporation rates following release from pressurized bottles. It has been argued that fire extinguishment capability is enhanced by efficient dispersion and mixing and rapid evaporation. The measurement techniques developed during the study provide sufficient data to allow the proposed alternative agents to be ranked based on these criteria.

It is significant that the current fire extinguishing agent, halon 1301, was found to be efficiently dispersed following release from a pressurized vessel at room temperature as the result of the rapid and strong flashing of the superheated liquid. Rapid vaporization was also observed due to its high Jakob number and relatively low number of moles per unit volume of the liquid. During the course of this investigation a workshop was held with a selected group of representatives of manufacturers (Walter Kidde Aerospace, Pacific Scientific, and Systron Donner) of fire-extinguishment systems for aircraft in an effort to obtain practitioners' viewpoints on desirable dispersion, mixing, and evaporation behaviors for alternative agents. Their conclusion was that the replacement agent's physical properties should resemble as nearly as possible those for halon 1301. This conclusion is consistent with our own, which is based on our understanding of the fire extinguishment process.

The experimental findings show that agents which are relatively high boiling--FC-236fa, FC-31-10, FC-318, HCFC-124, HFC-227ea, and HFC-134a--have dispersion, mixing, and evaporation properties following downward release which are not well suited for rapid fire extinguishment. This results from their relatively high-boiling points and low Jakob numbers. In the case of the lower boiling alternative agents--FC-218, HCFC-22, HFC-125, and the HFC-125/HFC-32 mixture--important differences were observed. HCFC-22 and the HFC-125/HFC-32 mixture were shown to have strong flashing behaviors due to their low boiling points, but also were found to vaporize relatively slowly due their low Jakob numbers and relatively high number of moles per unit volume of liquid. As a result, their mixing and vaporization behaviors are quite different than observed for halon 1301. On the other hand, FC-218 and HFC-125 were found to mix very efficiently by flashing and to vaporize rapidly since they have higher Jakob numbers and fewer moles per unit volume of the liquid than HCFC-22 and the mixture.

Table 10. Relative ranking of ten alternative agents based on dispersion, mixing, and evaporation behavior. Note that FC-116 has not been included since it is a critical fluid at room temperature.

Agent	Relative Ranking
FC-218	1
HFC-125	1
HFC-125/HFC-32 Mixture	3
HCFC-22	4
HFC-134a	5
HFC-227ea	6
HCFC-124	7
FC-318	8
FC-31-10	9
FC-236fa	10

On the basis of the above discussion it is possible to rank the alternative agents based on their dispersion, mixing, and evaporation behaviors as shown in Table 10. Boiling point alone has been used to rate agents having boiling points which are higher than FC-218. Note that FC-116 is not included in the table. This is because this agent is not a liquid at room temperature.

This investigation has yielded a number of findings which provide an improved understanding of the physical processes which are responsible for the dispersion, mixing, and evaporation behaviors of the agents and may be useful for the engineering design of practical fire extinguishment systems.

The importance of the boiling point, Jakob number, and number of moles of agent per unit volume of liquid for determining the behaviors during downward releases have already been discussed. To our knowledge, this is the first time that these parameters have been identified as the controlling physical properties for short-period releases of pressurized agents. Also for the first time, it has been shown that the release of the nitrogen pressurization gas following expulsion of an liquid agent from the vessel interacts strongly with the agent flow and provides an additional mechanism for dispersion and mixing of the agent. This mechanism is expected to be important for releases having very short periods.

The effects of variations in a variety of system parameters on the mixing behavior have been characterized. Modifications in dispersion and evaporation behaviors with changes in the pressurization level of the vessel and diameter of the vessel orifice for downward releases can be understood in terms of the understanding of these processes obtained during the current investigation. Higher vessel pressurization of the agents results in more rapid discharges of the liquids from the containment vessel and, therefore, more rapid mixing. The higher pressures of nitrogen present result in more intense mixing when the high-speed nitrogen exits the vessel following depletion of the liquid.

Changes in the mixing and evaporation behavior with orifice diameter result from a number of dependencies. Use of smaller diameters significantly reduces the mass flow rate of the liquids. As a result, the mixing times are increased. Reduction of the orifice diameter also reduces the time required for the liquid flow to flash. In some cases, this effect improves mixing even though the total release time has been increased. The known mixing behavior for gaseous axisymmetric jets indicates that downstream mixing behavior scales with jet diameter. For this reason, flows through smaller orifices mix over much shorter flow distances than flows from larger orifices. Keep in mind that this apparent advantage is offset by the reduced agent mass-flow rate.

The effects of adding an extension tube to the vessel are dramatic. When flashing occurs within the tube very high exit velocities are observed. The resulting two-phase flows are capable of generating quite high dynamic pressures. Even for the low boiling liquids, mixing and evaporation are inhibited in this configuration.

The system parameter which has been found to have the most profound effect on the mixing and evaporation behavior is the liquid temperature. This is a direct result of the dominant role of the degree of superheating on the flashing and evaporation. It is interesting that the role of agent temperature has been characterized as being underappreciated with regard to testing of halon 1301 dispersion in nacelles (Chamberlain, 1970). The current investigation has considered the effects of cooling the agent. Particularly for FC-218, the dispersion and evaporation were drastically degraded by cooling below the boiling point. It is likely that cooling drastically reduces the effectiveness of an agent for suppression of nacelle or dry bay fires.

As an example of the possible effects which might result from cooling, Figure 175 shows the calculated Jakob number for superheated FC-218 liquid for a range of liquid temperatures at atmospheric pressure. It is clear that Ja decreases rapidly with temperature. Most measurements for this investigation were for 294 K for which Ja $\approx$ 0.6. A decrease in temperature of less than 30 K results in a decrease of the Ja number to 0.3. This value is similar to those the high boiling liquids at room temperature which were found to vaporize very slowly. Clearly, relatively minor cooling will result is dramatic variations in flashing and evaporation behavior.

Effects of heating the liquid agent were not considered during this work. However, dramatic changes, which might aid or hinder fire-fighting effectiveness are to be anticipated.

The significance of these findings for designing fire extinguishment systems for aircraft are discussed further in Section 3.7.

Another parameter which significantly changes the mixing and evaporation behavior is the vessel orientation. In general, highly effective dispersion and evaporation is only observed for an orientation where the nitrogen pressurization gas is located such that the agent is expelled from the vessel as a liquid driven by the gas pressure. If an orientation allows the pressurization gas to exit the vessel before the liquid, the release rate is substantially reduced. Due to the slower release rates, mixing is less effective. Furthermore, in these cases the agent is generally expelled as a two-phase flow which does not flash on exiting the vessel. A significant mechanism for mixing and rapid evaporation is thus eliminated.

3.6 Transient Spray Computations

3.6.1 Introduction. Over the past three decades, an increasing acceptance of and reliance upon numerical solutions for transient fluid flow problems have taken place. In many cases, experimental studies are prohibitively expensive, whereas high-speed computers are comparatively economical and allow a wide range of parameters to be examined in a short time. As a result, computational fluid

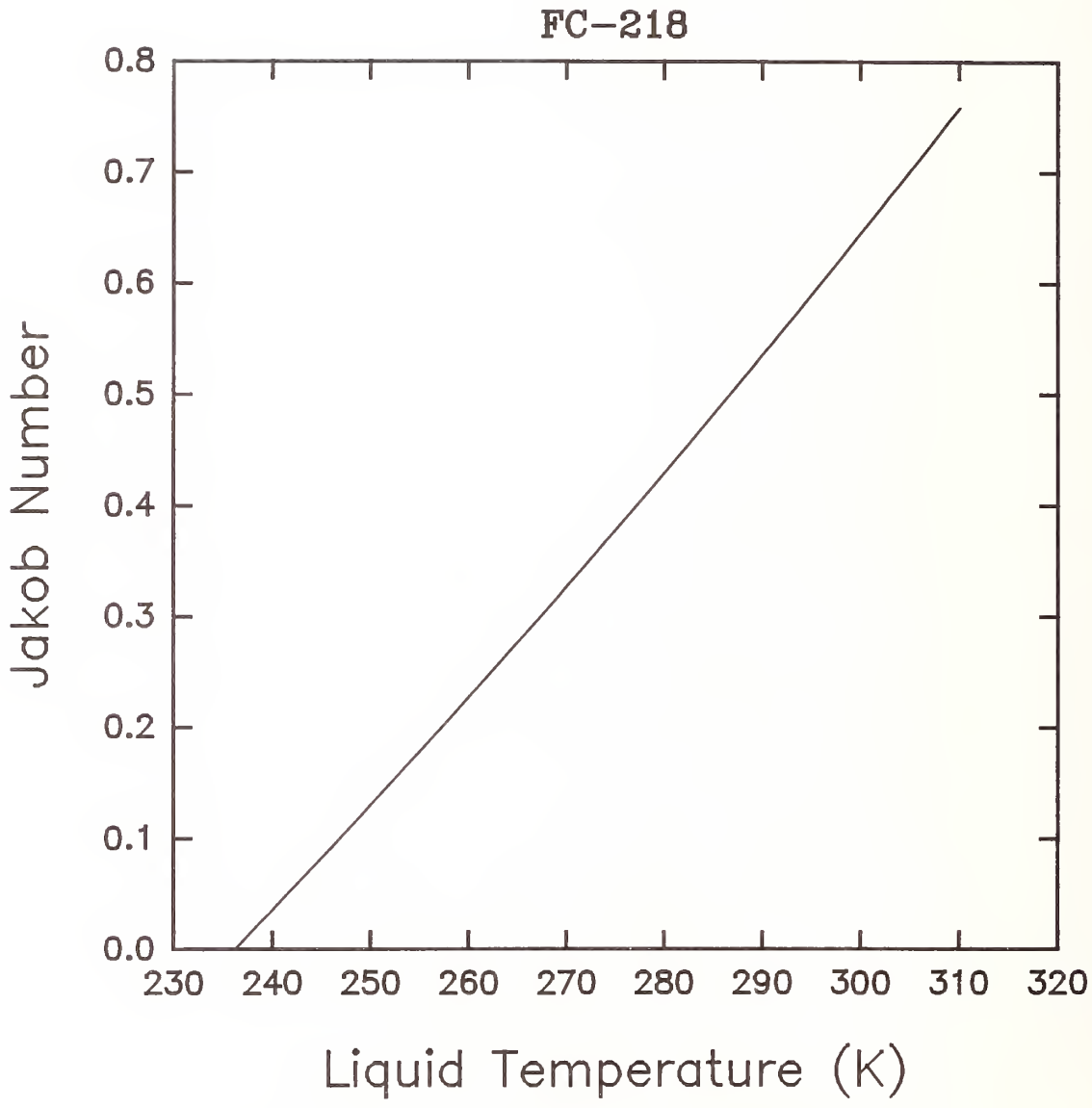

Figure 175. Calculated values of Jakob number for releases of FC-218 as a function of liquid temperature over a range of 310 to 235 K.

dynamics (CFD) has become a powerful tool for both basic and design studies in a broad range of physics and engineering problems. CFD refers mainly to the use of computers for numerically solving the nonlinear equations governing fluid motion. Pioneering work in this field first employed hand computations to demonstrate that nonlinear equations of fluid motion could be solved numerically. Computers have automated, improved, and dramatically sped up what was first done by hand.

The basic CFD equations express the balances of mass, momentum and energy of a fluid, and can be solved analytically for only a limited number of simplified situations. The success of CFD is often based on innovative numerical algorithms which discretize either the full set of equations or some simplified set derived from them, forming a large but finite number of algebraic or ordinary differential equations which can be solved by computers (Oran, 1988). The fundamental idea in CFD is that spatial dimensions are divided into discrete contiguous cells, usually called finite volumes or finite elements, and time is discretized in short intervals called timesteps. This discretization is forced by conventional computers having finite-sized memories segmented into floating-point words of data. The numerically determined values of the fluid variables in each cell are advanced from one timestep to the next using the nearby fluid variables determined at the previous timestep. While such marching techniques are developed with time-dependent problems in mind, they are also used to find steady-state solutions when appropriate.

The number of possible CFD algorithms is enormous and the correct choice depends on many properties of the problem being solved and the computer resources available. In all cases, however, only a finite number of discrete values comprise the representation, and each value is only specified to finite precision. This means that information is inevitably lost in the computational solution relative to the continuous problem being approximated. The result is uncertainty and errors in the computation arising from the discretization. The source of the uncertainty is the missing information about the detailed solution structure within the discrete spatial cells and timesteps. All approaches which use a finite number of values to represent a continuous profile have this problem. Nowadays, computers with hundreds of millions of high-precision floating-point calculations per second are readily available, and this translates into computations which can simulate some real fluid flows more accurately than can be validated by modern experimental diagnostic techniques. Three-dimensional simulations with several million cells are possible giving spatial resolution on the order of 1% of the size of the physical system. Two-dimensional solutions, where they are appropriate, can provide even higher spatial resolution.

In this section preliminary efforts to extend the use of existing CFD codes for the computation of the flows generated by the release of halon 1301 and alternative agents are summarized. Also included is an approach for predicting the initial conditions for the two-phase flow generated by the release of superheated liquids into an ambient environment.

3.6.2 Numerical Simulation of Discharge Sprays

3.6.2.1 Models Considered and General Capabilities. The fundamental CFD problem for an extinguishing agent discharge and dispersion is to develop the capability of qualitatively and quantitatively predicting the time evolution of the agent concentration field. It inherently involves a multidimensional analysis of a one- or two-phase, multi-component, compressible medium where thermodynamic effects and transport phenomena are important. This, in turn, imposes even more stringent requirements on the numerical algorithms used and computational times.

The dispersion of sprays of halon and halon-alternative fire extinguishing agents throughout a protected space is a very complex process involving many physical phenomena occurring simultaneously and affecting each other. The agent stored in the liquid state is discharged from nitrogen-pressurized vessels through a simple, nozzle/orifice-like exit. The systems under consideration

involve vessel volumes of the order of 10^{-3} m^3, with required discharge times of the order of 10^{-2} s. To achieve such rapid discharge times, the initial pressurization levels must typically be of the order of several megapascals. As the liquid agent exits from the vessel, thermodynamic and fluid-dynamic instabilities lead to flashing and break the agent into a two-phase droplet/gaseous jet mixture. This occurs in a short transition region which starts at the vessel exit and ends where thermodynamic and fluid-dynamic equilibrium has been achieved. If the temperature of the discharged liquid agent is far above its normal boiling point, the liquid very quickly evaporates and creates a cloud of agent vapors surrounding the moving spray with remaining liquid having a temperature equal to its boiling point. In the transition region the spray consists of a flowing mixture of liquid-agent fragments of various shapes and sizes and gaseous agent. This flow then entrains initially-quiescent air from the surrounding environment.

Downstream of the transition region the flow begins to develop as a mixed, two-phase, agent/air jet where thermodynamic equilibrium is maintained and where droplet collision and agglomeration do not play an important role in the ensuing jet dynamics and in the dispersal of the agent throughout the protected space. The entrainment, mixing and evaporation continue as the spray is dispersed throughout the space.

For advanced multi-dimensional mathematical models describing complex transient flow problems, numerical methods solving sets of nonlinear partial differential equations as well as relevant computer codes have been developed at the Los Alamos National Laboratory. Two of these codes--CONCHAS-SPRAY (Cloutman *et al.*, 1982) and KIVA-II (Amsden *et al.*, 1985a,b,c; 1987; 1989)--have been considered during the present study. The reader is referred to the cited references for complete details concerning these models.

CONCHAS-SPRAY was the first computer code developed at Los Alamos National Laboratory to solve the equations of transient, multi-component, dissipative, chemically reactive fluid dynamics, together with those for the dynamics of an evaporating liquid spray. It was a descendant of an earlier experimental code called CONCHAS (Butler *et al.*, 1979), which did not include the spray modeling capability. The code is quite general, but has been designed with applications to internal combustion engines specifically in mind. The formulation is spatially two-dimensional, which requires that the dependent variables depend on only two of the three spatial coordinates because of symmetry. The option is provided to select either rectangular or cylindrical coordinates, corresponding to linear or axial symmetry, respectively. All the transport coefficients such as dynamic viscosity, heat conductivity and mass diffusivity as well as heat capacities are assumed to be temperature dependent. The effects of turbulence are represented by an optional subgrid scale (SGS) turbulence model (Deardorff, 1971). This model was found to be very useful for parabolic flows which occur in, as an example, jet flows (*e.g.*, Gmurczyk *et al.*, 1992). The code allows a Lagrangian, Eulerian, or mixed description, and is particularly useful for representing curved or moving boundary surfaces.

Evaporating liquid sprays are represented by a discrete-particle technique (Dukowicz, 1980), in which each computational particle represents a number of similar physical particles. The radius and other attributes of a particle are statistically assigned using a Monte Carlo sampling technique. The evaporation rate is obtained from a quasi-steady model (Dukowicz, 1979). The particles and fluid interact by exchanging mass, momentum and energy. These interactions are treated by implicit coupling procedures to avoid the prohibitively small time steps that would otherwise often be necessary. The spray is assumed to be thin, as defined by O'Rourke (1981).

KIVA-II (a descendent of KIVA) is one of the latest in a sequence of multidimensional numerical models (Amsden *et al.*, 1985a,b,c; 1987; 1989) designed to solve the dynamics of evaporating fuel sprays interacting with flowing multicomponent gases undergoing mixing and heat transfer in a manner similar to CONCHAS-SPRAY, but extended into full three-dimensional situations, including droplet break-up/coalescence phenomena. Turbulence modeling is more sophisticated than in

CONCHAS-SPRAY. A standard k-ϵ model (Amsden *et al.*, 1989; Launder and Spaulding, 1972) extended to variable density flows is used to simulate turbulence effects in the calculations. Transport equations for the turbulence kinetic energy and turbulence dissipation rate are solved with appropriate source terms for the spray interaction.

The spray model is fundamentally based and, as such, has broad applicability. The dynamics of the atomized fuel spray are handled by a Monte Carlo based discrete-particle technique (Dukowicz, 1980). The spray is considered to be composed of discrete computational particles, each of which represents a group of droplets of similar physical properties. The distribution functions for droplet size, velocity, and spray pattern produced by the fuel injector are statistically sampled and the resulting Lagrangian parcels are followed as they locally interact and exchange mass, momentum, and energy with the surrounding gas. The model accounts for turbulence effects and interactions between droplets (O'Rourke, 1981) but other dense spray effects are neglected. When a computational parcel is selected to be injected into the flow field, its size is determined by sampling from a chi-squared distribution function (Bracco, 1985). The masses of the injected parcels are constant, thereby permitting each parcel to represent a different number of actual droplets depending on its size. The influence of droplet collisions on the spatial variation of the droplet mean size is taken into account by a sampling procedure. Collision frequency is then calculated and used to determine the probability that a droplet in a given parcel undergoes a collision with a droplet in a nearby parcel. All droplets in the given parcel behave in the same manner; either they do or do not collide and no new computational parcels are created. However, if a collision occurs and the resulting parcel has more than twice the original injection mass of the parcel, it is broken into two identical parcels with half the number of droplets as the original. Trajectories of these two parcels subsequently diverge because of their different interactions with the local turbulence field.

3.6.2.2 Calculational Approach and Code Modification. As a first step in the development of codes capable of modeling releases of halon 1301 and alternative agents, it was decided to focus on the use of CONCHAS-SPRAY. The two-dimensional axisymmetric variant of the generalized model was adapted as a subset of the KIVA-II code to accommodate the needs of the specific problem under consideration. The set of time-dependent equations is expressed in a two-dimensional form since the experimental discharges were designed to be axisymmetric. It should be noted, however, that the experiments discussed earlier in Section 3 were in a large rectangular room, while those which were modeled are for much smaller closed volumes. The choice to model a smaller closed volume was dictated by practical computational time limitations.

CONCHAS-SPRAY consists of a set of 26 primary subroutines controlled by a short main program. In addition to the primary subroutines there are thirteen supporting subroutines that perform tasks for the primaries. For various applications, all required geometrical specifications, initial and boundary conditions may be specified using input data alone. In other cases where the input data is inadequate to define the problem of interest, the required specifications must be inserted directly into the appropriate subroutines. The modular structure of the program enables such modifications.

The CONCHAS-SPRAY code was used almost as received from Los Alamos. However, the evaporation routine was judged to be inadequate. As a result, the following expression for the agent equilibrium vapor pressure, $P_a(T_l)$, at liquid temperature T_l suggested by Daubert and Danner (1992),

$$P_a(T_l) = \exp\left(A + \frac{B}{T_l} + C\ln T_l + DT_l^E\right), \tag{41}$$

was incorporated into the expression for the mass fraction of agent vapor, Y_l^*, at the droplet surface,

$$Y_l^* = M_a\left[\frac{PM_{air}}{P_a(T_l)} + M_a - M_{air}\right]^{-1}. \quad (42)$$

where M_{air} and M_a are the molecular weights for air and agent, respectively, and P is the total pressure in the gas. A, B, C, D, and E are empirical constants chosen to fit the temperature variation of a given agent. When the vapor pressure data of HCFC-22 were modeled, CONCHAS-SPRAY was unable to compute beyond the first timestep because the liquid vapor pressure exceeded 101 kPa for a temperature corresponding to the boiling point of HCFC-22. A different set of coefficients was chosen in subsequent calculations to maintain a vapor pressure below the ambient. Rather than a flashing spray, the results are more applicable to an evaporating spray. Special attention to this issue will be required to properly model the flashing process which was experienced by many of the agents in the experimental discharges.

Several other minor modifications to the code were necessary to ensure numerical stability. For instance, strong temperature and pressure gradients were generated by the rapid evaporation of the liquid that prevented convergence of the calculations. This type of numerical instability was removed by the introduction of a viscous pressure (Thompson, 1972), which was added to individual pressures within a computational cell and also to the pressure-volume work term appearing in the energy equation. Following these modifications, it was found that stable calculations could be carried out.

The situation investigated was the discharge of a hypothetical liquid agent through an orifice located on the centerline of a 0.42 m diameter cylindrically shaped volume. Agent inflow boundary conditions were derived from the results of the discharge vessel experiments (see Section 3.4), in which the agent mass flow rate was measured. The initial pressure was 101 kPa, and the liquid was assumed to be a mono-sized spray at a temperature of -41 °C. Computational parcels representing the droplets were introduced at the injector with an axial velocity of 61.4 m/s directed at an angle of 0° relative to the symmetry axis. The corresponding mass flow rate was 21.2 kg/s. A zero azimuthal component of velocity was assumed for the droplets at the injector. All of the gas and liquid parameters were taken as uniform across the orifice exit. The air in the compartment was specified to be quiescent and uniform in temperature at time equals zero. The surrounding walls were treated as solid, free-slip boundaries maintained at a constant temperature of 21 °C. The subsequent penetration and shape of the spray resulted solely from the interactions of the liquid droplets with the ambient air.

A zero-order model of the transitional region between the nozzle exit and a fully-developed spray is described in Section 3.6.4. Because the details of the actual fluid flow were not measured and are essentially unknown, it has been assumed that a spray of uniform droplet size is already established at the discharge orifice exit and is injected into the area at a prescribed rate. It should be noted that, due to these assumptions, the model does not reproduce many critical aspects of the discharge process, and cannot be directly compared to the experiments. The value of the calculations has been in the identification of the limitations of CONCHAS-SPRAY and the clarification of the experimental parameters which must be measured or controlled before a realistic representation of the discharge process can be expected. Six cases were chosen for the numerical simulations: a chamber length of 1.0 and 2.5 m, an initial air temperature of 21 and -30 °C, and an initial droplet diameter of 200 or 600 μm.

3.6.2.3 Sample Calculations and Results. All the computations were performed on a Convex supercomputer with a UNIX operating system. The wall clock computational time for one case (around 15 ms of the real process) required three hours on the average. The data were collected in

the form of large ASCII files (typically 12 Mb/file/case) which were converted subsequently into small graphics subfiles. The results were then plotted as contours of constant velocity, density, pressure, temperature, gas species mass fraction, vorticity, kinematic viscosity, mass flux, and liquid phase mass fraction. In order to demonstrate the types of effects which were observed, results for the vapor phase mass fraction of agent into the one meter long volume are described.

Figure 176 shows the time behavior of the agent vapor mass fraction distribution for four times following release. Assuming that the mass fraction of agent vapor follows the two-phase jet flow (likely to be an excellent assumption), it can seen that the downstream edge of the flow field moves away from the orifice with increasing time and that the jet spreads with increasing downstream distance. By 14.3 ms the flow has moved roughly 0.9 m from the source. An interesting feature is the "head" which grows on the downstream edge of the flow field. Recall that a similar structure was observed in high speed films of the experimental agent releases. Calculated velocity fields indicate that the head forms as the result of a vortical motion developed by the flow field. As a result, this is a region of efficient heat transfer from the air to the flow which evaporates the liquid droplets. The resulting agent evaporation causes a volume expansion which further enlarges the head.

Figure 177 shows the results of an identical calculation except that the diameter of the injected liquid droplets is increased from 200 μm to 600 μm. The downstream penetration of the two-phase flow is little changed from that found when smaller droplets are injected. However, the spreading rate of the jet is decreased and the head at the downstream edge of the flow is much narrower. Larger droplets are expected to result in lower evaporation of the liquid due to their smaller surface area. The reduction in spreading rates for Figure 177 is likely due to a combination of a smaller volume expansion and the lesser entrainment of air associated with fewer large rather than many small droplets.

The effect of the ambient temperature on the mixing behavior can be seen by comparing Figure 176 and Figure 178. The overall shapes of the mass fraction contours are very similar even though the air temperature has been decreased over 50 °C. At first glance this appears to be counter to what one would expect; *i.e*, a lower ambient temperature should diminish the vaporized agent mass fraction. The explanation is that the vapor pressure curve used in the calculation ensures that the agent pressure is less than the ambient pressure even for the higher temperature computation. For an agent like HCFC-22, an increase in temperature has a much more dramatic impact on the vapor pressure, which most likely would lead to a significantly higher vapor fraction when the ambient temperature is increased as much as 50 °C. This could not be verified, however, because of numerical instabilities which occurred under more realistic flashing conditions.

As noted above, the calculations generate two-dimensional predictions for a wide range of variables including velocity, pressure, temperature, density, species mass fraction and spray contours. A few additional characteristics of the results are summarized here to give an indication of what physical processes may be important in these systems. At certain regions in the flows very high velocities were calculated due to the rapid evaporation of the liquid droplets. These velocities were sufficient at times to generate shock waves which subsequently interacted with the two-phase flow and modified its mixing and evaporation behavior. It should be noted that shock waves were not detected in the experiments, but this may have been the result of differences in geometry between the experiment and calculation. Since the vessel was closed, major modifications were found when the vessel length was increased from 1.0 m to 2.5 m. This is to be expected due to the higher pressures and stronger shock waves which occur in the smaller volume.

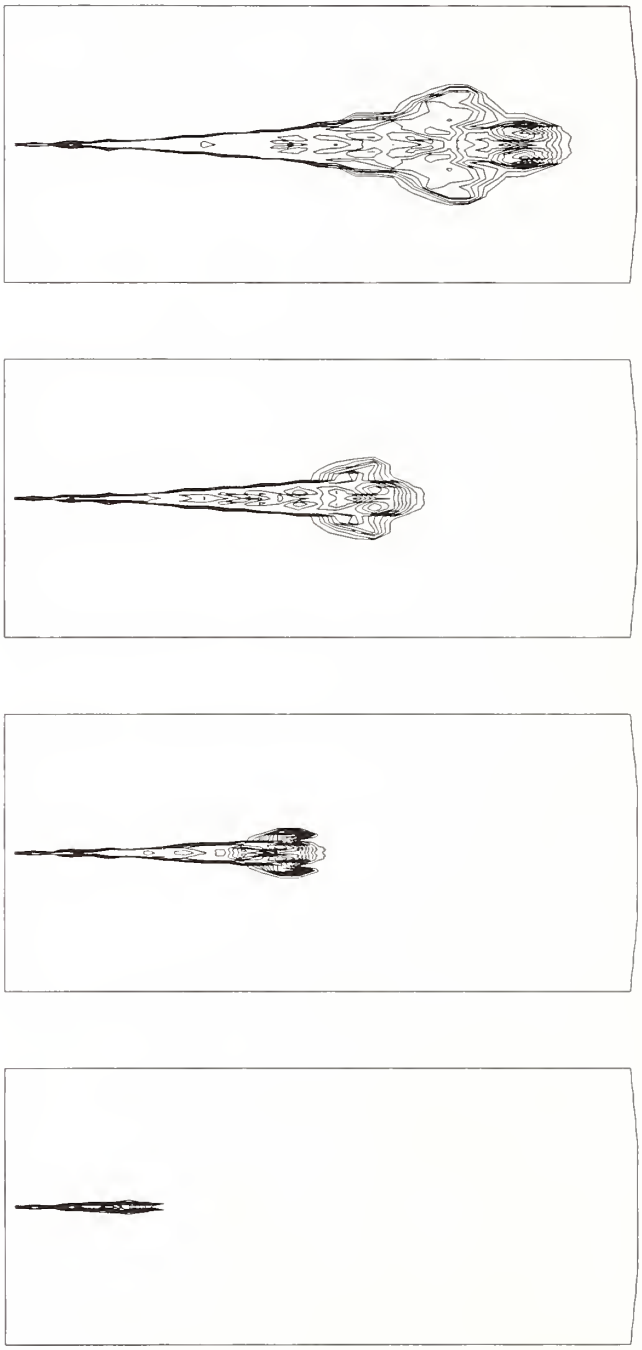

Figure 176. Agent vapor mass fraction contours at 3.5, 8.3, 10.7, 14.3 ms following spray release at 0 ms. Maximum mass fraction=0.15, contour interval=0.0188, spray mean Sauter diameter=200 μm, ambient T=294 K, P=101 kPa, compartment length=1 m.

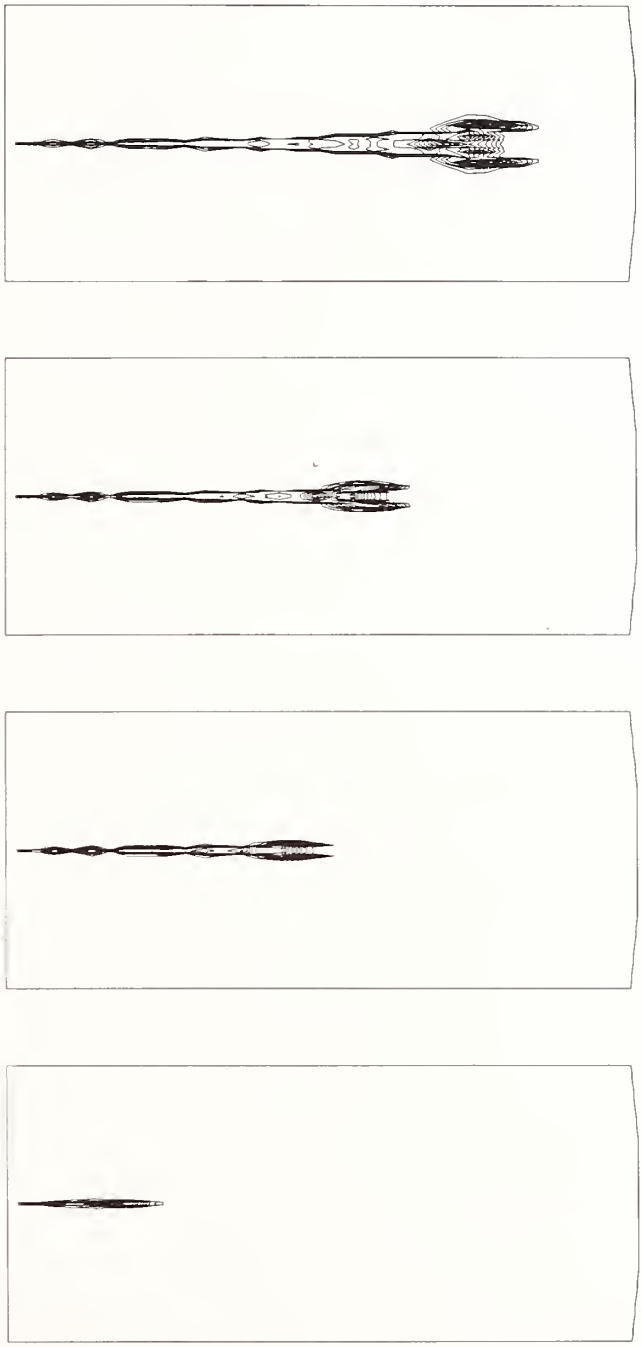

Figure 177. Agent vapor mass fraction contours at 3.5, 8.3, 10.7, 14.3 ms following spray release at 0 ms. Maximum mass fraction=0.14, contour interval=0.0175, spray mean Sauter diameter=600 μm, ambient T=294 K, P=101 kPa, compartment length=1 m.

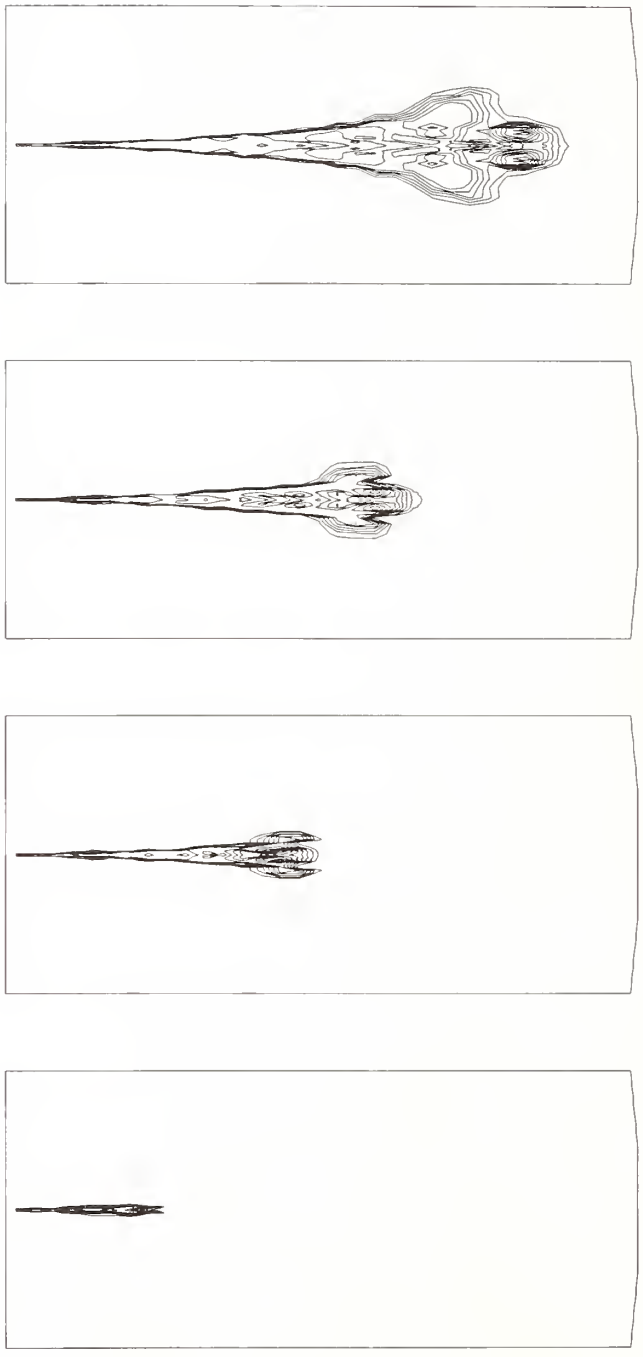

Figure 178. Agent vapor mass fraction contours at 3.5, 8.3, 10.7, 14.3 ms following spray release at 0 ms. Maximum mass fraction=0.209, contour interval=0.0261, spray mean Sauter diameter=200 μm, ambient T=243 K, P=101 kPa, compartment length=1 m.

3.6.3 Establishing Initial/Boundary Conditions from the Vessel Discharge Simulations

3.6.3.1 Overview. A critical element in exercising CONCHAS-SPRAY, KIVA, or any other computational fluid mechanics computer code, for the purpose of providing agent dispersion simulations, is the establishment of a set of initial/boundary conditions. Especially important and problematic is a determination of the characteristics of the agent jet at a location on the jet axis, near the exit section of the discharge vessel, as it enters the protected space. These initial/boundary conditions should be determined from results of a simulation of pressure vessel agent discharge. The purpose of this section is to present a method of estimating the required time-dependent initial/boundary conditions by expanding on the vessel discharge model described in Section 3.2. Although not used in the dispersion computations reported above, this new methodology is expected to be used and evaluated in future CONCHAS-SPRAY and KIVA simulations.

3.6.3.2 Modeling the Early Development of the Jet: From the Exit Section of the Discharge Vessel to a Nearby Section in a State of Thermodynamic Equilibrium and Completed Droplet Formation. It is assumed that within the discharge vessel and upstream of the exit nozzle/orifice the velocity of the liquid agent is so small that its kinetic energy can be neglected in defining its thermodynamic state. Therefore, the thermodynamic state upstream of the nozzle/orifice position can be estimated by the pressure in the discharge vessel, P_{DV}, and the temperature there of the liquid agent, $T_{DV,AL}$. Note that in most applications it is expected that $T_{DV,AL}$ is well approximated by T_{AMB}, the ambient temperature outside the vessel. A point representing the state of the liquid agent in the vessel is indicated in the pressure-enthalpy (P,h) diagram of Figure 179.

Because of the relatively short nozzle/orifice design under consideration, the time interval for the liquid to approach it, pass through it, and enter the outside environment is very small. For conditions of this study this time is of the order of 10^{-3} s. During this time interval the pressure of the traversing liquid is reduced from the high P_{DV} values inside the vessel, of the order of several MPa, to pressures of the order of P_{AMB}, 101 kPa.

As discharging liquid enters and traverses the region of the nozzle/orifice, it will enter and move along superheated metastable thermodynamic states. While dependent on its changing thermodynamic state in the vessel, (P_{DV}, $T_{DV,AL}$), and on its particular thermodynamic properties, as the agent material penetrates the ambient environment it approaches, and likely achieves the P_{AMB} pressure while still in its metastable liquid state. Thus, downstream of a vena contracta the liquid agent develops into a near-uniform-radius liquid jet, r_{LJ}, which can be predicted from traditional incompressible fluid-dynamic considerations. See Figure 180. For the relatively large-vapor-pressure agent materials of interest here, a combination of fluid-dynamic and thermodynamic instabilities will then lead to breakup into small droplets and flashing (*i.e.*, rapid evaporation to a two-phase equilibrium thermodynamic state) of the metastable liquid jet (Lienhard and Day, 1970).

Prior to the onset of breakup and/or flashing the metastable liquid is expected to move through thermodynamic states on near-isentropic paths. However, as discussed in Sections 3.2 and 3.4.3.4, for a given agent and initial-state condition, (P_{DV}, $T_{DV,AL}$), it is possible that the pressure along such a path will not reach P_{AMB} prior to an intersection with the agent's spinoidal curve. Moreover, if such an intersection does occur, then at that instant spontaneous nucleation in the liquid is to be expected (Reid, 1978; Modell and Reid, 1983). It is conjectured that this would lead to near-explosive breakup and flashing of the jet, all of this being initiated within a jet penetration depth (into the outside environment) of the order of a single nozzle/orifice diameter.

Whatever the thermodynamic-state path of the discharging metastable liquid, it is reasonable to assume that a relatively short distance downstream of the nozzle/orifice a thermodynamic equilibrium

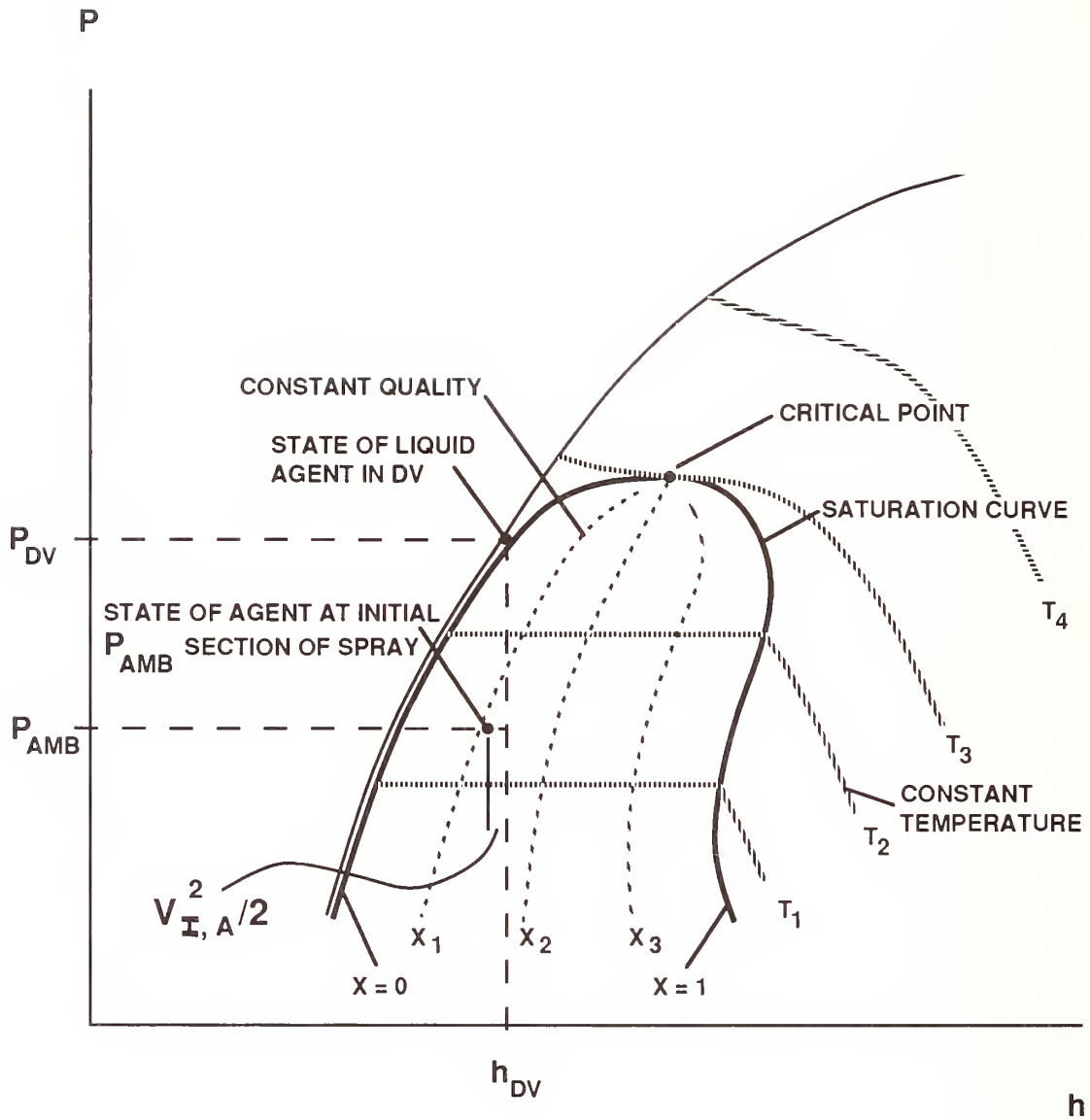

Figure 179. Path in the enthalpy - pressure plane of the thermodynamic state of the initially liquid agent as it flows from inside to outside the pressure vessel and achieves a stable two-phase state at the initial section.

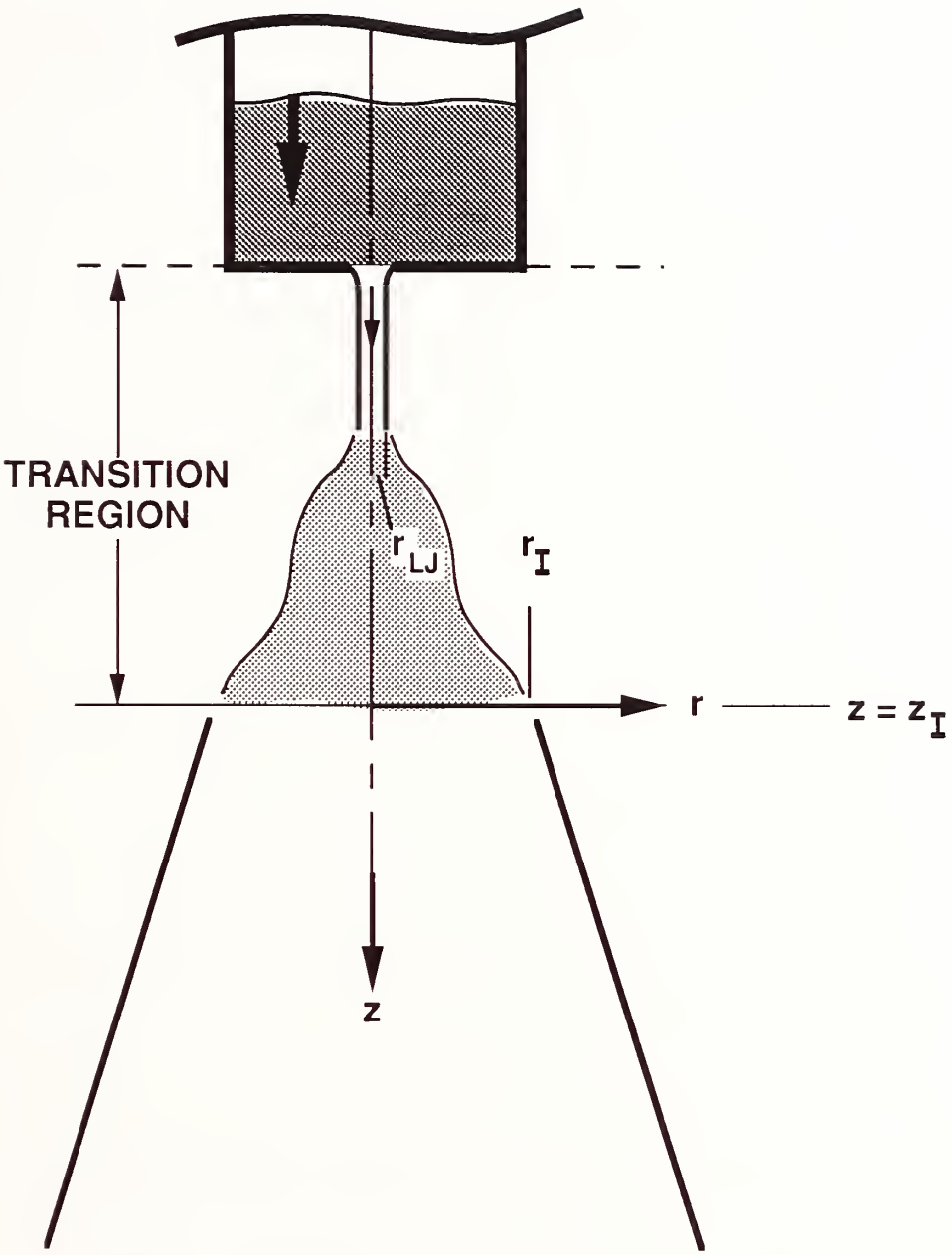

Figure 180. Sketch of the discharging agent, the transition region, and the initial section, $z = z_I$.

state and an end to the droplet-formation phenomenon will be achieved. It is also reasonable to assume that, as the agent flows further downstream, developing as a mixed, two-phase, agent/air jet, thermodynamic equilibrium will be maintained, and droplet collision and agglomeration will not play an important role in jet dynamics. These latter conditions are required if CONCHAS-SPRAY, KIVA, or similar CFD simulations are to be applicable.

The position along the jet axis where both approximate thermodynamic equilibrium and completion of droplet formation is first achieved will be denoted here as the *initial* position of the jet. Associated with this position is the plane section normal to the jet axis, called the *initial* section of the jet. Similarly, the thermodynamic state and properties of the jet at the initial position will be denoted as its *initial* state and *initial* properties. The region of the flow between the nozzle/orifice discharge section and the initial section will be referred to as the transition region of the jet. The *initial* section is a critical portion of the surface that bounds the protected space throughout which the agent is being dispersed.

A detailed description of the initial state and properties of the jet would be extremely complicated. This would include the variation across the initial section of air/gaseous-agent concentrations, temperature, and velocity, and of the size, velocity, and temperature distributions of the liquid agent droplets. Note also that in the present application all of these variables of the initial jet flow field would be time-dependent. In general, an accurate detailed description of the initial state of the jet, whether determined by theoretical or experimental means, is either impractical or beyond the current state of technology.

Although it is not possible to provide a detailed description of the initial state of the jet, it is reasonable to expect that an achievable approximate description, suitable for use in establishing boundary conditions for in the formulation the dispersing-agent-flow-field problem, would lead to good approximations of agent dispersal phenomena. It is the purpose of this work to provide such an approximate description of the initial state.

The dynamic processes that initiate breakup and flashing of the metastable liquid jet and bring it to its initial state are not completely understood. At one extreme, it is possible that the above-mentioned instabilities lead to violent breakup and flashing of the liquid jet immediately upon leaving the exit nozzle/orifice. Such behavior was observed, for example, in some experiments of Brown and York (1962). This was also observed in the current experiments described in Section 3.5 for low-boiling agents.

The metastable state can also persist even as the liquid jet penetrates relatively deeply into the ambient environment. For example, Brown and York (1962) described a liquid water jet of diameter $D = 7.6 \times 10^{-4}$ m, initially at 9.03×10^5 Pa and 415 K, which penetrated up to 0.0254 m, corresponding to $L/D \approx 32$, before initiation of violent breakup/flashing. Similar behaviors were observed for high-boiling agents in the current study. In this regard it is of interest to note that in the literature of the discharge of flashing liquids from high pressure vessels there is a degree of conventional wisdom that analyses of the two-phase flow phenomena, based on thermodynamic equilibrium states, tend to yield good results when the nozzle/piping from the inside to the outside of a high pressure discharge vessel is at least 0.1 m (Lueng and Nazario, 1990).

The initial section will be some incremental distance downstream of the penetration distance of the metastable liquid jet. The studies of Brown and York (1962) and the recent experiments at NIST suggest that this incremental distance will typically not exceed the order of the penetration distance itself. Whatever the distance, it is assumed here that the total length of the transition region is small enough, compared to the characteristic length of the overall agent dispersal problem of interest, that the processes within the transition region can be treated as quasi-steady.

In the transition region it is assumed that momentum transfer and any net work or heat transfer interactions between the penetrating agent jet and the ambient air environment are negligible. Thus,

consistent with the analysis of Epstein *et al.* (1983) for steady, two-phase, air/evaporating-liquid jets, it is assumed that the jet at the initial section can be approximated as consisting only of a two-phase mixture of agent, with no entrained air. Finally, in the transition section it is assumed that increases in the energy of the liquid due to mechanical work by surface tension forces to form the initial-section droplets are negligible compared to the energy transfers involved in phase-change processes.

The above assumptions are used with the following additional considerations to determine the initial state.

The initial section of the jet is defined by a characteristic initial radius r_I. The region $r \leq r_I$ consists of a pure mixture of saturated-agent vapor and liquid (droplets) in thermodynamic equilibrium at ambient pressure, $P_I = P_{AMB}$, and saturation temperature, $T_I = T_{SAT}(P_{AMB})$. The liquid-agent component of the jet consists of droplets of uniform-radius $r_{I,D}$, and these are uniformly dispersed over the region $r \leq r_I$. The agent droplets and gas have the same uniform axial jet velocity, $V_{I,A}$. There is no agent in $r > r_I$, and in the initial section, this outer region is assumed to consist of a uniform ambient-temperature/pressure environment (P_{AMB}, T_{AMB}) of quiescent air.

Conservation of mass and energy is invoked by assuming a quasi-steady state between the initial section and a section in the discharge vessel somewhat upstream of the exit nozzle/orifice. Conservation of mass yields

$$\pi r_I^2 V_{I,A} \rho_{I,A} = \frac{dM_{DV,AL}}{dt}, \tag{43}$$

where

$$\rho_{I,A} = \left[\frac{x_I}{\rho_{I,AG}} + \frac{(1-x_I)}{\rho_{I,AL}} \right]^{-1}. \tag{44}$$

and $\rho_{I,A}$, $\rho_{I,AL}$ and $\rho_{I,AG}$ are the average density of the agent, the density of the liquid agent (droplets), and the density of the agent gas at the initial section, respectively; x_I is the quality of the two-phase flow at the initial section, *i.e.*, the fraction of a mass of agent which is saturated gas; $M_{DV,AL}$ is the instantaneous mass of liquid agent in the discharge vessel; and the right side of Equation (43), determined previously from, *e.g.*, the discharge model of Section 3.2, is assumed to be specified.

When invoking conservation of energy, the kinetic energy at the section in the discharge vessel is assumed negligible compared to that at the initial section. The resulting expressions are

$$h_{DV,AL} = h_{I,AL} + x_I h_{ALG}(T_{sat}) + \frac{V_{I,AG}^2}{2} \tag{45}$$

and

$$h_{ALG}(T_{SAT}) = h_{I,AG} - h_{I,AL}, \tag{46}$$

where $h_{DV,AL}$ and $h_{I,AL}$ are the specific enthalpy of the agent liquid in the discharge vessel and at the initial section, respectively; $h_{I,AG}$ is the specific enthalpy of the agent gas at the initial section; and h_{ALG} is the heat of vaporization of the agent at the temperature T_{SAT}. In Equation (46),

$$h_{ALG} = h_{ALG}(T),\ T \leq T_{CR} \tag{47}$$

is a specified function of temperature, T, where T can not exceed the critical temperature, T_{CR}.

A point representing the state of the agent at the initial section is presented in the (P, h) diagram of Figure 179. Consistent with Equation (45), this reflects the fact that some of the original enthalpy of the liquid agent in its high pressure "near-rest" state, h_{DV}, was exchanged for its now-potentially-significant kinetic energy.

The sketch of the transition region, consistent with the all the above assumptions/ approximations, is presented in Figure 180.

The initial droplet radius is assumed to be specified. According to Brown and York (1962) it is expected that this will be in the range 10 μm - 100 μm. The sensitivity of the downstream agent concentrations to variations of this parameter should be evaluated from future dispersion computations.

The initial jet radius is assumed to be specified. Based on photographic data in Brown and York (1962), r_I/r_{LJ} seems to be of the order of ten to twenty. Thus, in (what is reasonable to construe visually in high speed photographs as) a region of breakup and flashing of the liquid jet to an initial equilibrium state, the radius of the jet increases by a factor between ten and 20. Again, the sensitivity of the downstream agent concentrations to variations of this ratio should be evaluated from future dispersion computations. One would hope that such sensitivity is not great.

In describing the thermodynamic properties of the agent, the liquid state is modeled everywhere as being incompressible, and the gaseous state at the initial section is modeled as a perfect gas. For problems of interest here, agent liquid temperatures are expected to be small enough compared to T_{CR} and vary in a small enough range to permit accurate modeling of the liquid as being incompressible, with density ρ_{AL}, and as having a constant specific heat, C_{AL}. Thus,

$$\rho_{I,AL} = \rho_{AL}. \tag{48}$$

The values of ρ_{AL} and C_{AL} will be taken as

$$\rho = \rho_{AL}(T_{AL});\quad C_{AL} = C_{AL}(T_{AL});\quad T_{AL} = (T_{SAT}+T_{DV,AL})/2, \tag{49}$$

where T_{AL} is taken to be the average temperature of the liquid in the discharge vessel and at the initial state, and where $\rho_{AL}(T)$ and $C_{AL}(T)$ are specified functions of T.
From the assumption of incompressibility it follows that

$$h_{DV,AL}-h_{I,AL} = C_{AL}(T_{DV,AL}-T_{SAT})+\frac{(P_{DV}-P_{AMB})}{\rho_{AL}}. \tag{50}$$

The agent gas is modeled as a perfect gas,

$$\rho_{I,AG} = \frac{P_I}{R_{AG}T_I} = \frac{P_{AMB}}{R_{AG}T_{SAT}}, \tag{51}$$

where R_{AG} is the gas constant.

As discussed above, it is expected that in most instances the liquid jet will achieve P_{AMB} prior to its breakup/flashing. Then, Bernoulli's equation leads to

$$\frac{dM_{DV,AL}}{dt} = \pi r_{LJ}^2 \rho_{AL} \left[\frac{2(P_{DV}-P_{amb})}{\rho_{AL}} \right]^{1/2}, \tag{52}$$

where r_{LJ} is determined from the radius of the exit nozzle/orifice, r_N, and its orifice discharge coefficient, C_D,

$$\left(\frac{r_{LJ}}{r_N} \right)^2 = C_D. \tag{53}$$

Substituting Equations (46) and (50) into Equation (45) leads to

$$\frac{V_{I,A}^2}{2} = C_{AL}(T_{DV,AL}-T_{SAT}) + \frac{(P_{DV}-P_{AMB})}{\rho_{AL}} - x_I h_{ALG}(T_{SAT}). \tag{54}$$

Substituting Equations (44) and (52) into Equation (43) leads to

$$\frac{V_{I,A}^2}{2} = \left(\frac{r_{LJ}}{r_I} \right)^4 \frac{(P_{DV}-P_{AMB})}{\rho_{AL}} \left(\frac{x_I(1-\epsilon)}{\epsilon} \right)^2, \tag{55}$$

where

$$\epsilon = \frac{\rho_{I,AG}}{\rho_{AL}}. \tag{56}$$

Comparing Equations (55) and (54) leads to

$$X^2 + \lambda_2 X - (\lambda_1 + 1) = 0, \tag{57}$$

where

$$X = \frac{x_I}{\epsilon}(1-\epsilon)\left(\frac{r_{LJ}}{r_I} \right)^2; \quad x_I = \frac{X\epsilon}{(1-\epsilon)\left(\frac{r_{LJ}}{r_I} \right)^2}, \tag{58}$$

$$\lambda_1 = \rho_{AL} C_{AL} \frac{T_{DV,AL}-T_{SAT}}{P_{DV}-P_{AMB}}, \tag{59}$$

and

$$\lambda_2 = \frac{\epsilon}{(1-\epsilon)} \frac{\rho_{AL} h_{ALG} T_{SAT}}{\left[P_{DV} - P_{AMB} \left(\frac{r_{LJ}}{r_I} \right)^2 \right]}. \tag{60}$$

The solution to Equation (57) is

$$X = -\frac{\lambda_2}{2} + \left[\left(\frac{\lambda_2}{2} \right)^2 + \lambda_1 + 1 \right]^{1/2}. \tag{61}$$

With Equation (58) and other previous definitions, Equation (61) provides the solution for x_I. This would be used, in turn, to obtain $V_{I,A}$ from Equation (54) or (55), thereby completing the description of the initial state,

$$V_{I,A} = 2X \left(\frac{P_{DV} - P_{AMB}}{\rho_{AL}} \right)^{1/2}. \tag{62}$$

A sketch of the velocity distribution and the mass flux distributions of gaseous and liquid agent at the initial section are presented in Figure 181.

3.6.3.3 Algorithm for Determining the Initial State. The above solution can be implemented with the following algorithm:

1. Specify agent and its thermodynamic properties, including $T_{SAT}(P)$ and $h_{ALG}(T)$, $\rho_{AL}(T)$, and $C_{AL}(T)$.

2. Specify r_I/r_{LJ} (expected range 10 - 20).

3. Specify P_{AMB}, T_{AMB}, and $T_{DV,AL}$. (In most cases expect to specify $T_{DV,AL} = T_{AMB}$.)

4. Specify $T_I = T_{AMB}$ for r > r_I. Compute $T_{SAT}(P_{AMB})$ and then specify $T_I = T_{SAT}$ for $0 \leq r \leq r_I$.

5. Compute $h_{ALG}(T_{SAT})$ from Equation (47).

6. Compute T_{AL} according to Equation (49) and then ρ_{AL} and C_{AL} according to Equation (49) and $\rho_{AL}(T)$ and $C_{AL}(T)$, respectively.

7. Compute $\rho_{I,AG}$ according to Equation (51) and then ε according to Equation (56).

8. Use a component-1 model, *e.g.*, that of Section 3.2, to find the time-dependent values of P_{DV} for a particular Figure 1-configuration of interest.

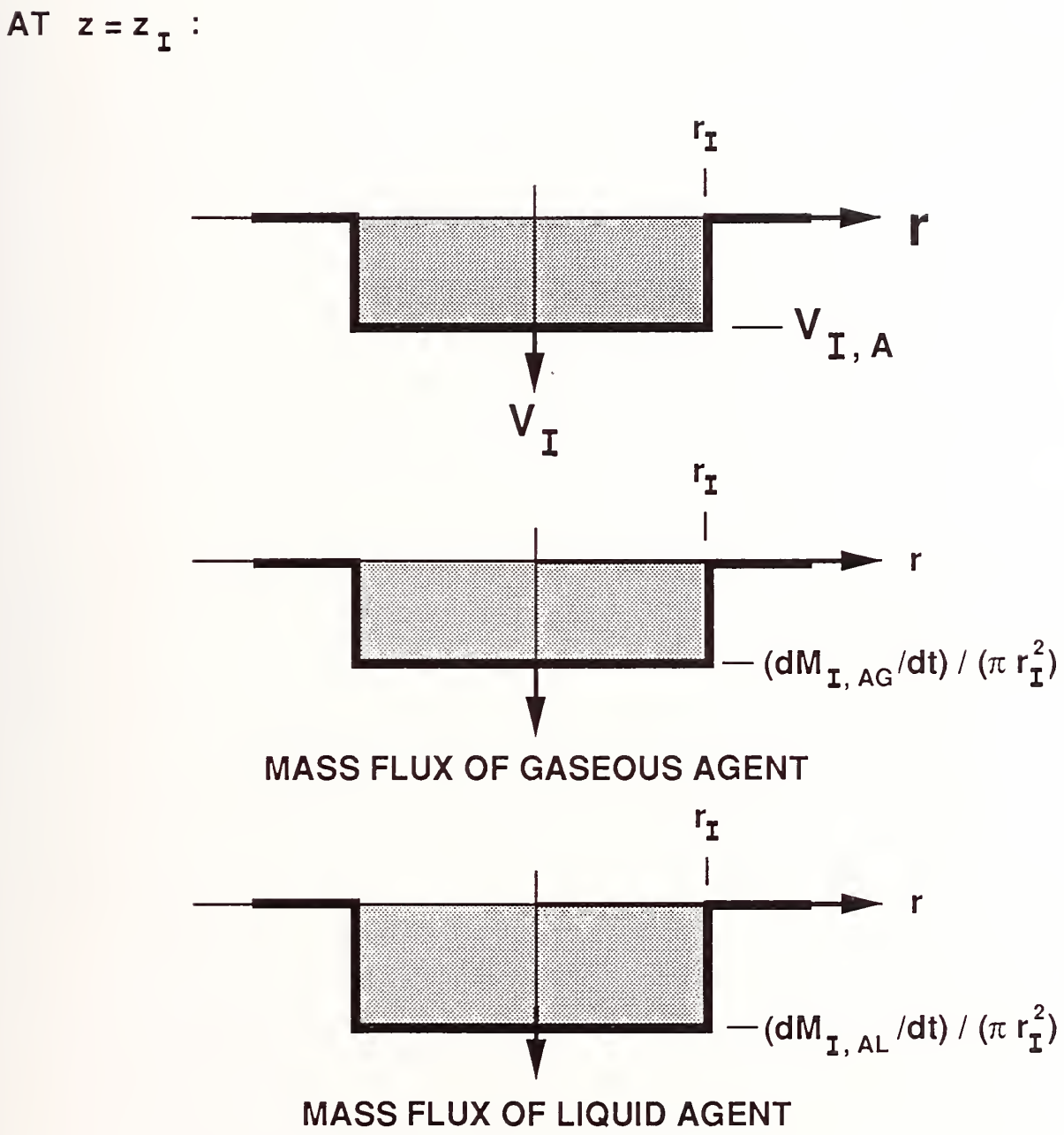

Figure 181. Sketch of the velocity and mass fluxes of agent gas and agent liquid droplets at the initial section, $z = z_I$.

9. For a particular value of P_{DV} compute λ_1 and λ_2 from Equations (59) and (60), and then X from Equation (61).

10. Find x_I from Equation (58) and $V_{I,A}$ from Equation (62).

3.6.3.4 Example Applications of the Initial State Algorithm. The initial-state algorithm was applied in four example simulations. These involve the potential replacement agent HCFC-22 and halon 1301 and two different r_I values, 0.074 m and 0.148 m, corresponding to $r_I = 10r_{LJ}$ and $20r_{LJ}$ and to a value r_{IJ} of 0.0074 m which corresponds, in turn, to a discharge vessel nozzle radius of 0.0095 m and a discharge coefficient of 0.6. The examples involve time-dependent discharges of room-temperature agent from a Figure 1-type configuration with no holding tank. The geometric parameters, orifice coefficient, and initial conditions assumed in the simulated example discharge calculations are presented in Table 11. These are the same parameters used in the example calculations of Section 3.2. During the discharge, the time-dependent value of P_{DV} was computed using the component-1-type model of Section 3.2.

The material property functions for HCFC-22 and halon 1301 which were used in the example calculations are taken from the prescriptions given in Table 12 (Daubert and Danner, 1992).

T_{SAT} was obtained as the root of $P(T_{SAT}) = P_{AMB}$. Then T_{AL} was calculated using Equation (49). Finally, $h_{ALG}(T_{SAT})$, $\rho_{AL}(T_{AL})$, and $C_{AL}(T_{AL})$ were calculated from the property functions of Table 12. Results are presented in Table 13.

The results of the example calculations are tabulated in Table 14 (HCFC-22, $r_I = 10r_{LJ} = 10C_D^{1/2}r_N = 0.0738$ m), Table 15 (halon 1301, $r_I = 10r_{LJ} = 10C_D^{1/2}r_N = 0.0738$ m), Table 16 (HCFC-22, $r_I = 20r_{LJ} = 20C_D^{1/2}r_N = 0.148$ m), and Table 17 (halon 1301, $r_I = 20r_{LJ} = 20C_D^{1/2}r_N = 0.148$ m). Included in the tables are computed values of the variable ζ,

$$\zeta = \frac{M_{DV,AL}}{M_{DV,AL}(t=0)} = \frac{Z}{Z(t=0)} \tag{63}$$

which is the dimensionless mass of liquid agent, $M_{DV,AL}$, or dimensionless elevation of the liquid agent in the discharge vessel, Z.

The tabulated results of Table 14 for the discharge of HCFC-22 ($r_I = 10r_{LJ} = 0.0738$ m) are plotted in Figure 182 through Figure 185. These include plots of the time-dependent values of P_{DV} (Figure 182), $V_{I,A}$ (Figure 183), ζ and x_I (Figure 184), and $dM_{I,AL}/dt$ and $dM_{I,AG}/dt$ (Figure 185).

A study of the results leads to the following observations:

1. For both HCFC-22 and halon 1301, the times to complete the discharge of liquid agent from the pressure vessel are almost identical at 0.024 ± 0.001 s (Table 14 through Table 17).

2. At the initial section, the quality of the two-phase agent flow, x_I, is significantly different for the two agents considered, but for a given agent x_I is relatively independent of t and r_I, for the two initial-section radii values considered ($r_I = 0.0738$ m and 0.148 m). Thus, for the cases considered, $x_I = 0.31 \pm 0.01$ for HCFC-22 (Table 14 and Table 16) and $x_I = 0.54 \pm 0.02$ for halon 1301 (Table 15 and Table 17).

Table 11. Geometric parameters, orifice coefficient, and initial conditions for example discharges from a Figure 1-type configuration with no holding tank

Length of discharge vessel (Z_{DV})	0.255 m
Cross-sectional area of discharge vessel (A_{DV})	0.196×10^{-2} m^2
Volume of discharge vessel (V_{DV})	0.500×10^{-3} m^3
Area of exit nozzle/orifice (A_O)	0.285×10^{-3} m^2
Radius of exit nozzle/orifice (r_O)	0.953×10^{-2} m
Discharge coefficient of exit nozzle/orifice (C_D)	0.6
Initial volume of agent liquid in discharge vessel ($M_{DV,AL,1}$)	0.250×10^{-3} m^3
Initial temperature of gas in the discharge vessel ($T_{DV,1}$)	21 °C
Initial pressure in discharge vessel ($P_{DV,1}$)	41.4×10^5 Pa
Temperature of agent liquid in discharge vessel ($T_{DV,AL}$)	21 °C

3. At the initial section, for a given agent, and for the two initial-section radii values considered, the mass flow rates of liquid or gaseous agent are almost identical at any particular time during the discharge. (For example: for HCFC-22, approximately half-way through the discharge at t = 0.0125 s, values of $dM_{I,AL}/dt$ for r_I = 0.0738 m and r_I = 0.148 m are 8.59 kg/s (Table 14) and 8.49 kg/s (Table 16), respectively; and for halon 1301, approximately half-way through the discharge at t = 0.0122 s, values for $dM_{I,AL}/dt$ for r_I = 0.0738 m and r_I = 0.148 m are 6.95 kg/s (Table 15) and 8.59 kg/s (Table 17), respectively.) However, over the course of the discharge, these mass flow rates are reduced to approximately two thirds of their initial value. (For example: for HCFC-22 and r_I = 0.0738 m, the values of $dM_{I,AL}/dt$ at t = 0 and t = 0.233 s (near the end of the liquid discharge) are 11.78 kg/s and 7.34 kg/s, respectively (Table 14 and Table 16); and for halon 1301, and r_I = 0.0738 m, the values of $dM_{I,AL}/dt$ at t = 0 and t = 0.244 s (near the end of the liquid discharge) are 9.26 kg/s and 5.88 kg/s, respectively (Table 15)).

Table 12. Material Property Functions for HCFC-22 and halon 1301

	HCFC-22	halon 1301
Molecular Weight (kg/mole)	86.47	148.9
$P(T_{SAT})$/Pa = exp[$A + B/(T_{SAT}/R) + C\ln(T_{SAT}/R) + D(T_{SAT}/R)^2$]; $T_1 \le T_{SAT} \le T_2$		
A	9.78×10^{1}	6.28×10^{1}
B	-4.77×10^{-3}	-3.38×10^{3}
C	-1.23×10^{1}	-6.75
D	2.42×10^{-5}	1.44×10^{-5}
T_1	116 K	105 K
T_2	369 K	340 K
$h_{ALG}(T_{SAT})$/(J/kg-mole) = $A(1 - T_{SAT}/T_{CR})^{B}$; $T_1 \le T_{SAT} \le T_2$		
A	2.96×10^{7}	2.51×10^{7}
B	3.86×10^{-1}	3.57×10^{-1}
T_{CR}	369 K	340 K
T_1	116 K	105 K
T_2	369 K	340 K
$\rho_{AL}(T)$/(kg-mole/m^3) = A/B^{F}; $F = \{1 + [1 - (T/R)/C]^{D}\}$; $T_1 \le T \le T_2$		
A	1.60	1.34
B	2.66×10^{-1}	2.70×10^{-1}
C	3.69×10^{2}	3.40×10^{2}
D	2.81×10^{-1}	2.80×10^{-1}
T_1	116 K	105 K
T_2	369 K	340 K
$C_{AL}(T)$/[J/(kg-mole·K)] = $A + B(T/R) + C(T/R)^2 + D(T/R)^3$; $T_1 \le T \le T_2$		
A	9.47×10^{4}	1.14×10^{5}
B	3.93×10^{1}	-1.32×10^{2}
C	-8.17×10^{-1}	6.12×10^{-1}
D	2.79×10^{-3}	0
T_1	116 K	193 K
T_2	369 K	298 K

Table 13. Constant properties of the initial state for the example calculations

	HCFC-22	halon 1301
T_{SAT}	-41 °C	-58 °C
T_{AL}	-10 °C	-18.5 °C
$h_{ALG}(T_{SAT})$	0.234×10^6 J/kg	0.118×10^6 J/kg
$\rho_{AL}(T_{AL})$	0.132×10^4 kg/m^3	0.180×10^4 kg/m^3
$C_{AL}(T_{AL})$	0.115×10^4 J/(kg·K)	0.809×10^3 J/(kg·K)

3.6.3.5 Nomenclature

D	diameter of a liquid jet
h	specific enthalpy
h_{DV}	h of agent liquid in the discharge vessel
L	length of liquid jet
P	pressure
P_{AMB}	pressure of the ambient environment
P_{DV}	pressure in the discharge vessel
P_I	pressure at the initial section
R_{AG}	gas constant for the agent gas
r	radius
r_I	radius of two-phase agent jet at the initial section
$r_{I,D}$	radius of agent droplets at initial section
r_{LJ}	radius of the liquid jet outside the discharge vessel
T	absolute temperature
T_{AMB}	temperature of the ambient environment
$T_{DV,AL}$	temperature of liquid agent in the discharge vessel
T_I	temperature at the initial section
T_{SAT}	saturation temperature of the agent
t	time
V_I	velocity at the initial section
$V_{I,A}$	V_I of agent
x_I	quality of the two-phase agent flow at the initial section
z	distance along the jet axis from exit nozzle/orifice
z_I	z at the initial section

3.6.4 Concluding Remarks on Modeling the Discharge Spray. Realistic numerical modeling of the spray discharge process requires an accurate knowledge of the initial conditions surrounding the release of the agent. The conditions prior to bursting the rupture disc in the agent storage vessel are fully established, but a mathematical description of the disintegration of the disc and the motion of the

Table 14. HCFC-22 Jet Behavior for $r_I = 10r_{LJ} = 0.148$ m; $\rho_{AL} = 1320$ kg/m^3; $\rho_{I,AG} = 3.58$ kg/m^3; $T_{I,A} = 232$ K

t (s)	P_{DV} (Pa)	ζ	$V_{I,A}$ (m/s)	x_I	$dM_{I,AG}/dt$ (kg/s)	$dM_{I,AL}/dt$ (kg/s)
0.00000	0.4135×10^7	1.0000	32.21	0.3172	5.36	11.53
0.00179	0.3663×10^7	0.9030	30.13	0.3158	5.01	10.86
0.00358	0.3299×10^7	0.8117	28.45	0.3148	4.73	10.30
0.00537	0.3008×10^7	0.7248	27.05	0.3139	4.50	9.83
0.00716	0.2769×10^7	0.6417	25.86	0.3132	4.30	9.43
0.00895	0.2570×10^7	0.5620	24.83	0.3126	4.13	9.08
0.01073	0.2401×10^7	0.4851	23.92	0.3121	3.98	8.77
0.01252	0.2255×10^7	0.4108	23.12	0.3117	3.85	8.49
0.01431	0.2128×10^7	0.3389	22.40	0.3113	3.73	8.24
0.01610	0.2016×10^7	0.2690	21.75	0.3109	3.62	8.02
0.01789	0.1917×10^7	0.2010	21.16	0.3107	3.52	7.81
0.01968	0.1829×10^7	0.1347	20.62	0.3104	3.43	7.62
0.02147	0.1749×10^7	0.0701	20.12	0.3102	3.35	7.44
0.02326	0.1677×10^7	0.0069	19.67	0.3099	3.27	7.28

liquid agent through the exit plane and for several orifice diameters downstream is far beyond the state of the art for even the simple geometry chosen for the discharge experiments. What is known are the size of the orifice and the emptying rate of the storage vessel, both from the experimental measurements and the model of the emptying process described in Section 3.2. The first-order analysis in the previous section provides a starting point for the droplet enthalpy, but because prediction and/or measurement of droplet size have not yet been developed for these conditions, the droplet size distribution can only be hypothesized.

The general approach for numerically simulating a developing, two-phase, multi-component, compressible, evaporating spray has been presented, and two different Los Alamos computer codes have been described. KIVA-II is the most versatile because it can deal with fully three dimensional flow and boundary conditions, it has a more sophisticated description of the turbulent interactions between the droplets and the gas phase, and it accounts for droplet breakup. There is a severe computational penalty paid for this increased versatility, however. Because the discharge experiments were close to axisymmetric, and because the initial droplet diameter was unknown anyway, the long computational times required for KIVA-II convinced us to chose the more efficient CONCHAS-SPRAY code for our initial parametric study. It was felt that at this stage of our knowledge of the

Table 15. HCFC-22 Jet Behavior for $r_I = 10r_{LJ} = 0.074$ m; $\rho_{AL} = 1320$ kg/m^3; $\rho_{I,AG} = 3.58$ kg/m^3; $T_{I,A} = 232$ K

t (s)	P_{DV} (Pa)	ζ	$V_{I,A}$ (m/s)	x_I	$dM_{I,AG}/dt$ (kg/s)	$dM_{I,AI}/dt$ (kg/s)
0	0.4135×10^7	1.000	122.73	0.3022	5.10	11.78
0.00179	0.3663×10^7	0.9031	115.46	0.3025	4.80	11.07
0.00358	0.3299×10^7	0.8117	109.49	0.3028	4.55	10.48
0.00537	0.3008×10^7	0.7248	104.46	0.3030	4.34	9.99
0.00716	0.2769×10^7	0.6417	100.14	0.3032	4.16	9.57
0.00895	0.2570×10^7	0.5620	96.37	0.3033	4.01	9.20
0.01073	0.2401×10^7	0.4851	93.05	0.3034	3.87	8.88
0.01252	0.2255×10^7	0.4108	90.08	0.3035	3.75	8.59
0.01431	0.2128×10^7	0.3389	87.41	0.3036	3.63	8.33
0.01610	0.2016×10^7	0.2690	84.99	0.3037	3.53	8.10
0.01789	0.1917×10^7	0.2010	82.78	0.3038	3.44	7.89
0.01968	0.1829×10^7	0.1347	80.76	0.3039	3.36	7.69
0.02147	0.1749×10^7	0.0701	78.88	0.3039	3.28	7.51
0.02326	0.1677×10^7	0.0069	77.15	0.3040	3.21	7.34

phenomena, the penalty for using a less sophisticated axisymmetric code would be offset by the increased number of parameters which could be varied.

Sample computations were carried out to evaluate the potential of CONCHAS-SPRAY to provide qualitative understanding of agent spray dispersion. The input data for the calculations were based on the agent discharge experiments described earlier. The geometrical dimensions of the computational domain were smaller than the dimensions of the actual compartment in which the discharges were performed to ensure enough spatial resolution to resolve the controlling parameters.

The calculations have demonstrated that the Los Alamos computer code CONCHAS-SPRAY can be used to analyze the dynamics of halon-alternative agent dispersion and mixing in a space designed for fire protection. Within its physical limitations, it can perform the necessary computations of the discharge process quickly and relatively cheaply, aiding one's understanding and indicating directions for future experiments.

The numerical analysis based on the full fluid dynamics equations as well as a description of the heat and mass transfer leads to the time dependance of the two-dimensional field of all parameters characterizing the agent dispersion phenomena, including velocity, pressure, temperature, density, species mass fraction, mass flux and spray contour. Much of these data are difficult or impossible to measure in experiments.

Table 16. Halon 1301 Jet Behavior for $r_I = 10r_{LJ} = 0.074$ m; $\rho_{AL} = 1800$ kg/m^3; $\rho_{I,AG} = 6.17$ kg/m^3; $T_{I,A} = 215$ K

t (s)	P_{DV} (Pa)	ζ	$V_{I,A}$ (m/s)	x_I	$dM_{I,AG}/dt$ (kg/s)	$dM_{I,AL}/dt$ (kg/s)
0	0.4135×10^7	1.0000	142.83	0.5181	9.95	9.26
0.00204	0.3687×10^7	0.9030	135.28	0.5205	9.43	8.69
0.00407	0.3338×10^7	0.8111	128.99	0.5224	8.99	8.22
0.00611	0.3057×10^7	0.7236	123.64	0.5239	8.62	7.83
0.00814	0.2826×10^7	0.6397	118.99	0.5252	8.29	7.50
0.01018	0.2631×10^7	0.5590	114.91	0.5263	8.01	7.21
0.01222	0.2465×10^7	0.4812	111.28	0.5273	7.76	6.95
0.01425	0.2322×10^7	0.4058	108.03	0.5281	7.53	6.73
0.01629	0.2197×10^7	0.3327	105.08	0.5289	7.32	6.52
0.01832	0.2086×10^7	0.2616	102.40	0.5295	7.14	6.34
0.02036	0.1988×10^7	0.1924	99.94	0.5301	7.97	6.17
0.02240	0.1899×10^7	0.1248	97.67	0.5307	6.81	6.02
0.02443	0.1820×10^7	0.0588	95.58	0.5311	6.66	5.88

A comparison between KIVA-II and CONCHAS-SPRAY for the same set of conditions is needed to determine the impact of the turbulence and droplet breakup model on the results. If the outcome is independent of the code, additional analyses with CONCHAS-SPRAY could be conducted. If the turbulence and droplet models influence the results, KIVA-II (or better yet, KIVA-III, (Amsden *et al.*, 1993)) should be used for future calculations. KIVA has the additional advantage that fully three dimensional spaces can be handled. Extended resources on the NIST Cray computer would be required for these investigations. The spectrum of parameters influencing the spray dynamics needs to be broadened to include additional compartment geometries, discharge orifice geometry, thermodynamic and gas dynamic parameters of the agent and ambient air, agent injection and atomization parameters as well as consideration of the transition region of the spray.

3.7 Summary and Recommendations

The proposed alternative agents are ranked based on their release, mixing and dispersion, and evaporation behavior. Measurements of the release behaviors for the alternative agents have demonstrated that when the liquid agents are initially at room temperature, all of the agents are released as superheated liquids. Theory predicts that only very small differences in release rates are

Table 17. Halon 1301 Jet Behavior for $r_I = 10r_{LJ} = 0.148$ m; $\rho_{AL} = 1800$ kg/m^3; $\rho_{I,AG} = 6.17$ kg/m^3; $T_{I,A} = 215$ K

t	P_{DV}	ζ	$V_{I,A}$	x_I	$dM_{I,AG}/dt$	$dM_{I,AL}/dt$
0.00000	0.4135×10^7	1.0000	38.48	0.5583	10.73	8.49
0.00204	0.3687×10^7	0.9030	36.17	0.5566	10.08	8.03
0.00407	0.3338×10^7	0.8111	34.28	0.5552	9.56	7.66
0.00611	0.3057×10^7	0.7236	32.69	0.5541	9.11	7.33
0.00814	0.2826×10^7	0.6397	31.33	0.5532	8.73	7.05
0.01018	0.2631×10^7	0.5590	30.15	0.5524	8.41	6.81
0.01222	0.2465×10^7	0.4812	29.11	0.5518	8.12	6.59
0.01425	0.2322×10^7	0.4058	28.19	0.5512	7.86	6.40
0.01629	0.2197×10^7	0.3327	27.36	0.5507	7.63	6.22
0.01832	0.2086×10^7	0.2616	26.60	0.5503	7.42	6.06
0.02036	0.1988×10^7	0.1924	25.92	0.5499	7.23	5.91
0.02240	0.1899×10^7	0.1248	25.29	0.5496	7.05	5.78
0.02443	0.1820×10^7	0.0588	24.71	0.5492	6.89	5.65

to be expected between agents when this is the case. In fact, experiments indicate that all of the agents have comparable volume release rates. The only indication of a different behavior was observed for halon 1301 for which the liquid apparently flashed just upstream of or in the orifice. As a result of the formation of a two-phase flow, the flow rate of halon 1301 was substantially reduced.

Since the room-temperature release rates are essentially identical for all of the proposed alternative agents, this parameter does not provide a means to differentiate between the agents. As a result the ranking is based solely on their behaviors once released. The results summarized in Section 3.5.5 thus provide the final ranking of the agents based on release behavior, mixing and dispersion, and evaporation rate. The final ratings on these criteria are summarized in Table 10. Note once again that FC-116 has not been included since it is not a liquid at room temperature.

Table 10 presents the result which represent the primary goal of the investigation to rank the alternative agents with regard to release rate, dispersion and mixing, and evaporation rate. However, during the course of the research program a number of observations and secondary conclusions have been obtained which have important implications for the design and engineering of systems for suppression of nacelle and dry bay fires using the proposed alternative agents. During the discussion it should be kept in mind that the experimental system developed for this investigation was designed solely to allow a ranking of the proposed alternative agents. Actual commercial systems designed for suppression of fires on aircraft are likely to be significantly different. On the other hand, many of the findings and conclusions of this work should be applicable to more complicated vessels and flow

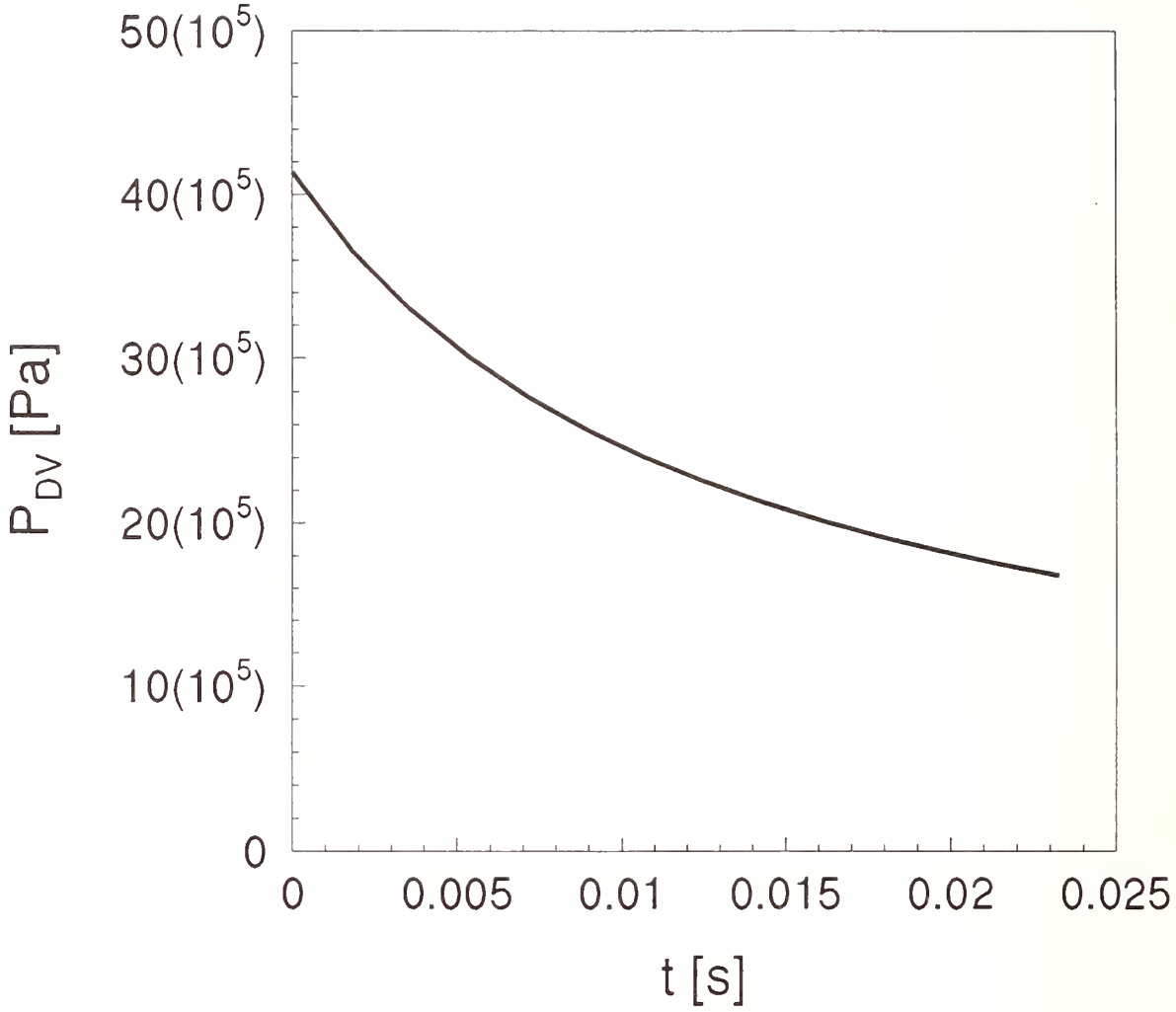

Figure 182. Plot of Table 14 results for P_{DV} as a function of time during vessel discharge of HCFC-22.

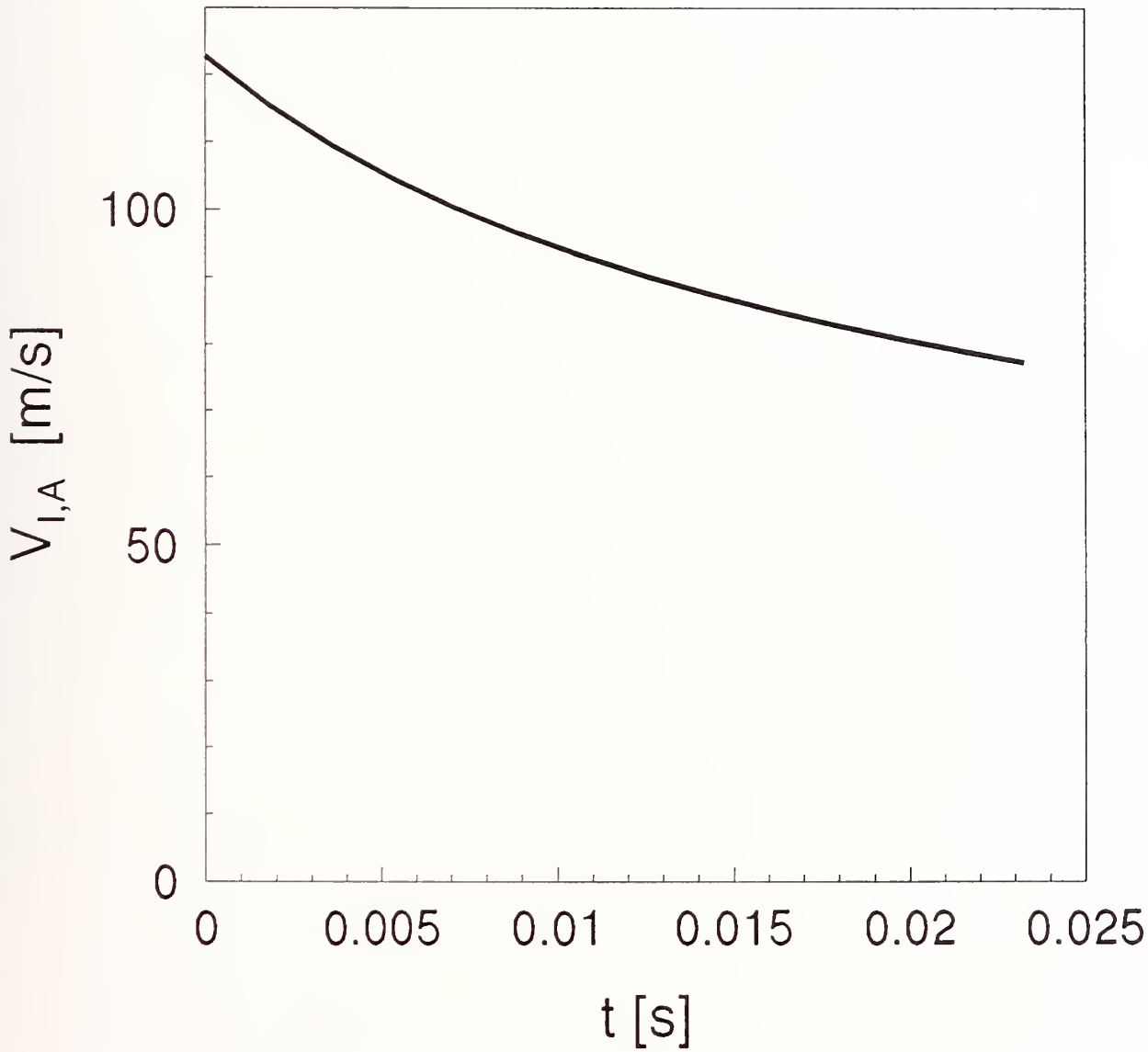

Figure 183. Plot of Table 14 results for $V_{I,A}$ as a function of time during vessel discharge of HCFC-22.

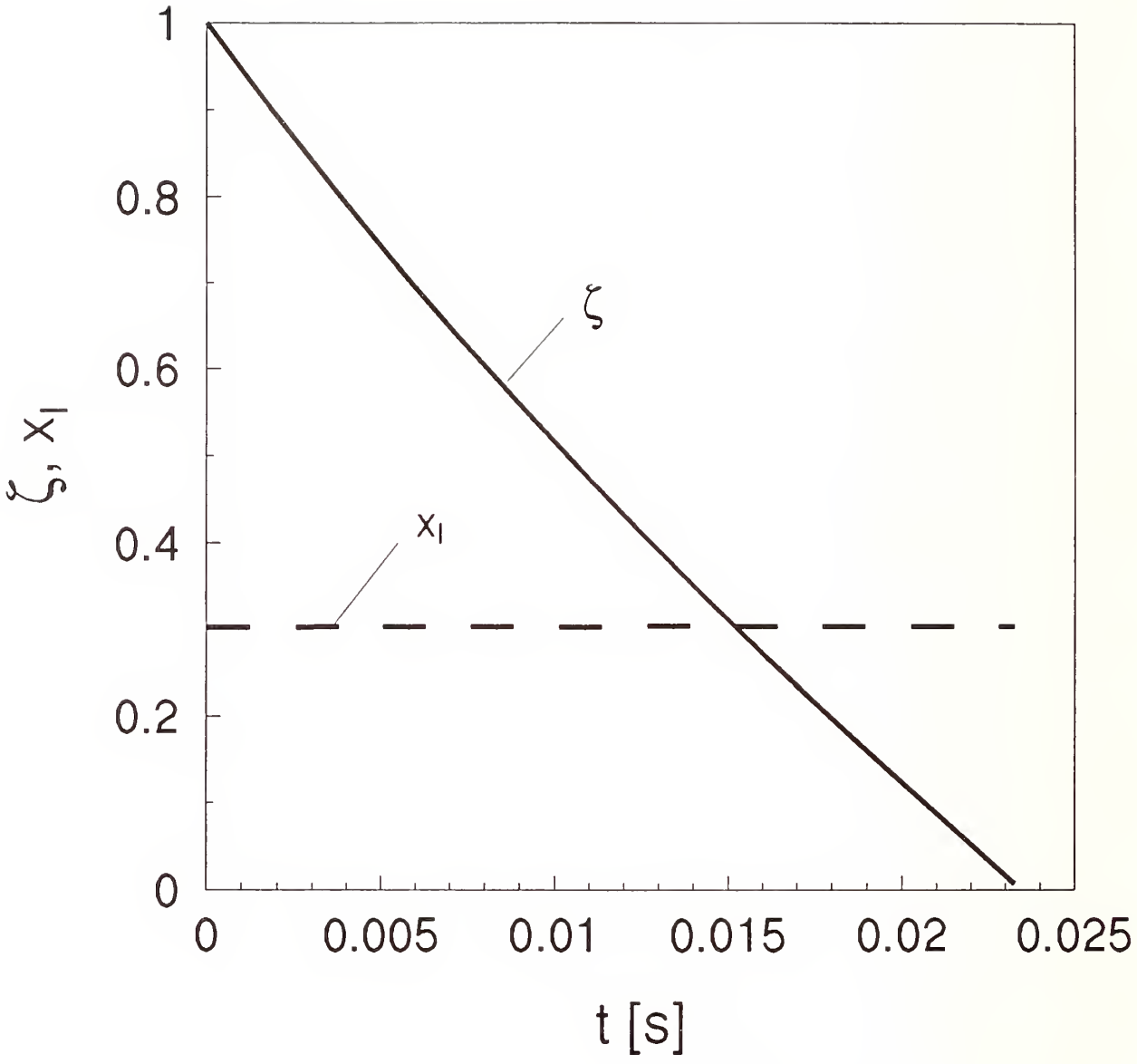

Figure 184. Plots of Table 14 results for ζ and x_l as functions of time during vessel discharge of HCFC-22.

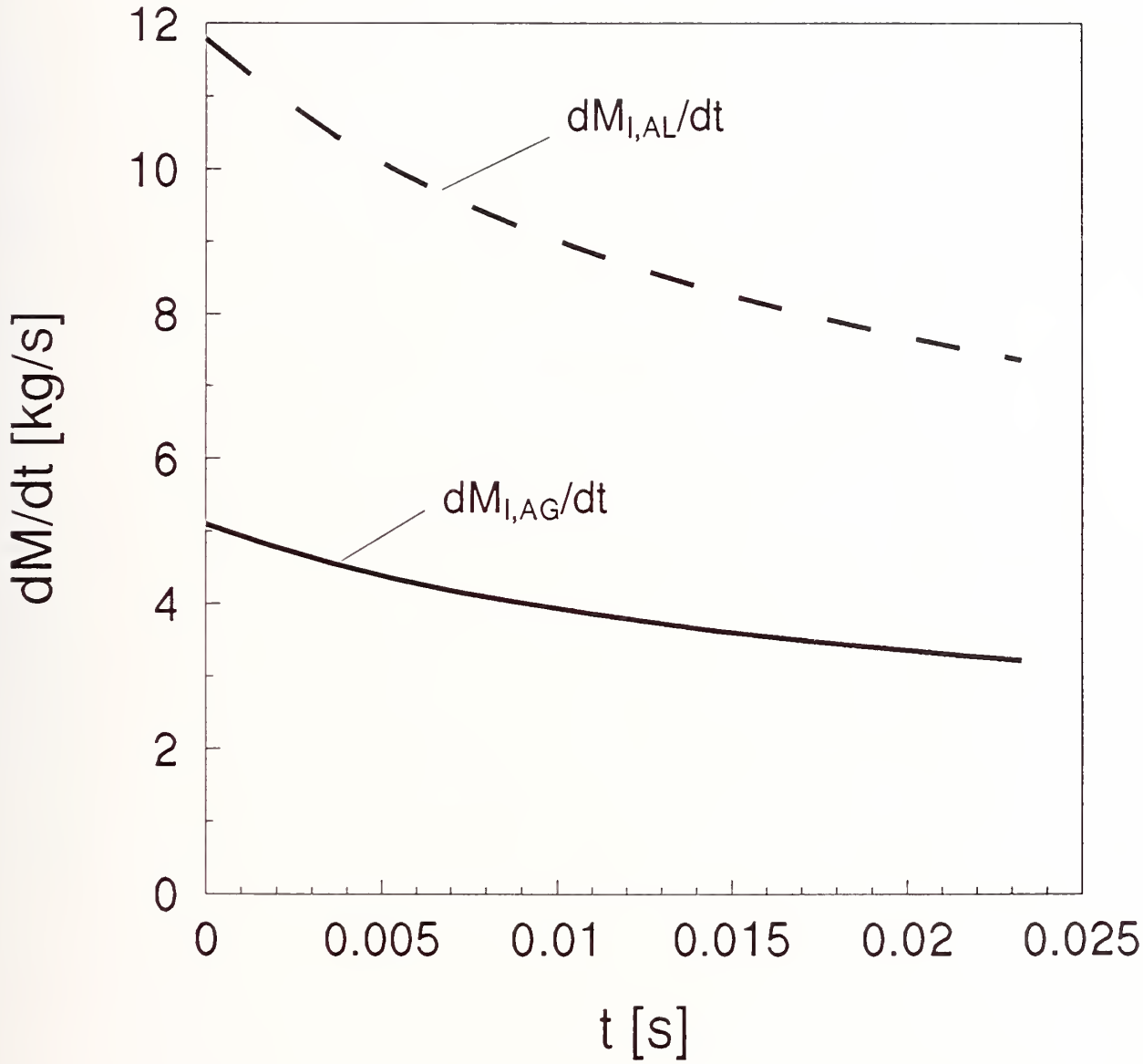

Figure 185. Plots of Table 14 results for $dM_{I,AL}/dt$ and $dM_{I,AG}/dt$ as functions of time during vessel discharge of HCFC-22.

geometries. Where appropriate, suggestions are provided for additional studies which should be considered.

Downward releases of agents will be considered first. Results discussed in Sections 4.2 and 4.4 demonstrate that when agents are released from pressurized vessels as liquids, it is possible to predict release rates and pressure time histories within the vessel quite accurately. The effects of changing a vessel orifice size or degree of pressurization are easily predictable. The only case where premature flashing within the vessel or orifice was found to result in a reduction in release rate was for halon 1301. This agent has the lowest boiling and therefore the highest superheat of the liquids tested. The potential replacement agents may be exposed to ambient temperatures higher than standard room temperature. These higher temperatures result in higher overheats which may ultimately lead to flashing which disrupts the liquid flow. As a result, the release of an agent may require a longer period than predicted based on the assumption of a liquid flow. If this occurs, the agent's fire-fighting effectiveness could be reduced. It would be worthwhile to determine more carefully the conditions for which flashing of a superheated liquid can reduce the release rate. Recall also that it has been hypothesized that a superheated liquid which is rapidly depressurized might reach its spinodial condition and undergo a boiling liquid expanding vapor explosion. Such an event has not been characterized experimentally, but due to the dire consequences which could result, it would be prudent to investigate the possibility further.

The primary effect on the release rate of cooling a vessel containing an agent below room temperature is to reduce the pressure of the driving gas within the vessel. It should be possible to predict these effects using the models developed during the course of this project.

The effects of various system parameters on the dispersion and mixing and evaporation behavior following release of the liquid agents from a pressurized vessel are complex. During the course of this effort several major influencing parameters have been identified. The parameter which has the largest effect on the initial mixing behavior following a room-temperature release of an agent is the degree of superheating. The higher the superheat, the more likely the agent is to flash near the vessel exit. Flashing also appears to occur more rapidly with higher superheats. As a result of flashing the agent is accelerated in multiple directions and is mixed with it surroundings. The velocity measurements also demonstrate that the agent spreading is accelerated by flashing leading to enhanced and more rapid dispersion and better mixing. If the ambient temperature is raised, a liquid will become more superheated and it dispersion and mixing behavior should be enhanced. Cooling of the vessel should have an opposite effect. Measurements with FC-218 demonstrated that the latter was indeed the case.

For the experimental system investigated here only the vessel was cooled. If an agent release occurred into an environment which was also cooled it would be expected that the dispersion and mixing would be hindered even more. It would be useful to investigate release of agents into cooled environments in order to fully characterize these effects. It would also be useful to run flame extinguishment tests such as the Wright-Patterson dry bay test facility under cold conditions to assess the effects on flame-extinguishment effectiveness.

The effects of changes in the degree of vessel pressurization and orifice size on the dispersion and mixing and vaporization behavior are understandable in terms of the flashing and vaporization behavior of the agents once discharged.

Orientation of the release vessel is a parameter which strongly influences the liquid-agent release mechanism and subsequent mixing and agent evaporation. If the bottle is oriented such that the pressurization gas is located next to the release orifice it is released first and release of the liquid agent occurs by boiling and subsequent release of a two-phase flow. Experiments show that not only are the release times for an agent substantially increased, but the dispersion and evaporation behavior are significantly degraded as compared to a downward release. If cooled sufficiently, release of agent

may not occur at all. Designers of extinguisher systems should assess the probability of a pressure vessel being oriented incorrectly as a result of aircraft flight profiles. If such events are probable it may be necessary to design pressure vessels in such a way that nitrogen will always expel liquid from the vessel.

Initial efforts have been described which are aimed at modeling the dispersion and mixing and evaporation of agents following their release as superheated liquids from pressurized bottles. Considerable work remains to be done, but this initial work suggests that simulations sufficiently accurate for engineering design work can be developed. It should be possible to calculate behaviors for releases of agents into complex three-dimensional compartments such as dry bays and engine nacelles. Similar models are widely employed in a wide range of engineering disciplines to reduce design times and limit expensive testing. Efforts to develop effective models for agent releases should be pursued.

The experimental diagnostics which have been used to investigate the release behavior of agents following discharge of the potential fire-fighting agents have provided sufficient characterization to allow a ranking. However, there are a number of characteristics of these releases which have not been addressed. Many of these are expected to be crucial for effective fire fighting. Such properties as the flow fields, the concentration fields, temperature fields, droplet sizes, entrainment rates, and degree of vaporization in the space are required before true models of flame extinction can be developed. Such experimental measurements should be performed to provide a data base for validating models of mixing behavior and flame extinction. Such information would also be very useful for future efforts to develop new and improved flame suppression processes.

3.8 References

Abramowitz, G.N., *The Theory of Turbulent Jets*, MIT Press, Cambridge, MA, 1963.

Allied Signal, Inc., *Genetron® Products Technical Bulletin: R-32/125 Azeotrope*, Allied Signal Inc., Genetron® Products, Morristown, NJ, July, 1991

Amsden, A.A., Ramshaw, J.D., O'Rourke, P.J., and Dukowicz, J.K., *KIVA: A Computer Program for Two- and Three-Dimensional Fluid Flows with Chemical Reactions and Fuel Sprays*, Los Alamos National Laboratory Report No. LA-10245-MS, 1985a.

Amsden, A.A., Butler, T.D., O'Rourke, P.J., and Ramshaw, J.D., *KIVA: A Comprehensive Model for 2D and 3D Engine Simulations*, SAE Technical Paper No. 850554 (1985b).

Amsden, A.A., Ramshaw, J.D., Cloutman, L.D., and O'Rourke, P.J., *Improvements and Extensions to the KIVA Computer Program*, Los Alamos National Laboratory Report No. LA-10534-MS, 1985c.

Amsden, A.A., Butler, T.D., and O'Rourke, P.J., *The KIVA-II Computer Program for Transient Multi-Dimensional Chemically Reactive Flows with Sprays*, SAE Paper 872072; also appears in SAE Transactions (1987).

Amsden, A.A., O'Rourke, P.J., and Butler, T.D., *KIVA-II: A Computer Program for Chemically Reactive Flows with Sprays*, Los Alamos National Laboratory Report No. LA-11560-MS, 1989.

Amsden, A.A., Butler, T.D., O'Rourke, P.J., *KIVA-III: A KIVA Program with Block-Structured Mesh for Complex Geometries*, Los Alamos National Laboratory Report No. LA-12503-MS, 1993.

Avedisian, C.T., "The Homogeneous Nucleation Limits of Liquids," *J. Phys. Chem. Ref. Data 14*, 695 (1985).

Balzhiser, R.E., Samuels, M.R., and Eliassen, J.D., *Chemical Engineering Thermodynamics, The Study of Energy, Entropy, and Equilibrium*, Prentice-Hall, Englewood Cliffs, NJ, 1972.

Bankoff, S.G., "Diffusion-Controlled Bubble Growth," in *Advances in Chemical Engineering, Vol. 6*, Drew, T.B., Hoopes, Jr., J. W., Vermeulen, T., and Cokelet, G. R., Eds., pp. 1-60, Academic Press, New York, 1966.

Beegle, B.L., Modell, M., and Reid, R.C., "Thermodynamic Stability Criterion for Pure Substances and Mixtures," *AIChE Journal 20*, 1200 (1974).

Benjamin, M.W., and Miller, J.G., "The Flow of Saturated Water through Throttling Orifices," *Transactions ASME 63*, 419 (1941).

Bird, R.B., Stewart, W.E., and Lightfoot, E.N., *Transport Phenomena*, John Wiley & Sons, New York, 1960.

Bracco, F.V., *Modeling of Engine Sprays*, SAE Technical Paper No. 850394 (1985).

Bradshaw, P., *An Introduction to Turbulence and Its Measurement*, Pergamon, New York, 1971.

Brown, J.A., and Mears, W.H., "Physical Properties of n-Perfluorobutane," *J. Phys. Chem. 62*, 960 (1958).

Brown, G.L., and Rebollo, M.R., "A Small, Fast-Response Probe to Measure Composition of a Binary Gas Mixture," *AIAA J. 10*, 649 (1972).

Brown, R., and York, J.L., "Sprays Formed by Flashing Liquid Jets," *A.I.Ch.E. Journal 8*, 149 (1962).

Bryner, N.P., personal communication, 1993.

Burnell, J.G., "Flow of Boiling Water through Nozzles, Orifices, and Pipes," *Engineering 164*, 572 (1947).

Butler, T.D., Cloutman L.D., Dukowicz J.K., and Ramshaw J.D., *CONCHAS: An Arbitrary Lagrangian-Eulerian Computer Code for Multicomponent Chemically Reactive Fluid Flow at All Speeds*, Los Alamos Scientific Laboratory Report No. LA-8129-MS, 1979.

Carnahan, B., Luther, H.A., and Wilkes, J.O., *Applied Numerical Methods*, John Wiley & Sons, New York, 1969.

Cattolica, R., and Vosen, S., "Combustion-Torch Ignition: Fluorescence Imaging of OH Concentration," *Combust. Flame 68*, 267 (1987).

Celata, G.P., Cumo, M., Farello, G.E., and Incalcaterra, P.C., "On the Critical Flows of Subcooled Liquids," in *Heat Transfer 1982, Proceedings of the Seventh International Heat Transfer Conference*, Grigull, U., Hahne, E., Stephan, K., and Straub, J., Eds., Hemisphere, New York, 1982.

Celata, G.P., Cumo, M., Farello, G.E., Incalcaterra, P.C., and Naviglio, A., "Thermodynamic Disequilibrium in the Critical Flow of Subcooled Liquids," *Nuclear Technology 60*, 137 (1983).

Chamberlain, G., *Criteria for Aircraft Installation and Utilization of an Extinguishing Agent Concentration Recorder*, Federal Aviation Administration Report NO. FAA-DS-70-3, March, 1970.

Cloutman, L.D., Dukowicz J.K., Ramshaw J.D., and Amsden A.A., *CONCHAS-SPRAY: A Computer Code for Reactive Flows with Fuel Sprays*, Los Alamos National Laboratory Report No. LA-9294-MS, 1982.

Cooper, L.Y., *Discharge of Fire Suppression Agents From a Pressurized Vessel: A Mathematical Model and Its Application to Experimental Design*, National Institute of Standards and Technology Internal Report, NISTIR 5181, 1993a; see also Cooper, L.Y., "Discharge of Fire Suppression Agents From a Pressurized Vessel: A Mathematical Model and Its Application to Experimental Design," *Proceedings of Halon Alternatives Technical Working Conference 1993*, University of New Mexico, New Mexico Engineering Research Center for Global Environmental Technologies, Albuquerque NM, pp. 530-549, 1993a.

Cooper, L.Y., *The Dispersion of Fire Suppression Agents From High Pressure Vessels: Establishing Initial/Boundary Conditions for the Flow Outside the Vessel*, National Institute of Standards and Technology Internal Report, NISTIR 5219, 1993b.

Daubert, T.E., and Danner, R.P., *Physical and Thermodynamic Properties of Pure Chemicals, Data Compilation*, Hemisphere, New York, 1992.

Davis, M.R., "Response of Small Pitot Tubes in Gas-Liquid Flows," *Int. J. Multiphase Flow 6*, 369 (1980).

Day, J.B., *Combined Effects of Superheat and Dynamical Instability on the Breakup of Liquid Jets*, Masters Thesis, University of Kentucky, 1969.

Deardorff, J.W., "On the Magnitude of the Subgrid Scale Eddy Coefficient," *J. Comput. Physics 7*, 120 (1971).

Deragarabedian, P., "The Rate of Growth of Vapor Bubbles in Superheated Water," *J. Applied Mech. 20*, 537 (1953).

Dukowicz, J.K., *Quasi-Steady Droplet Phase Change in the Presence of Convection*, Los Alamos Scientific Laboratory Report No. LA-7997-MS, 1979.

Dukowicz, J.K., "A Particle-Fluid Numerical Model for Liquid Sprays," *J. Comput. Physics 35*, 229 (1980).

Elliot, D.G., Garrison, P.W., Klein, G.A., Moran, K.M., and Zydowicz, M.P., *Flow of Nitrogen-Pressurized Halon 1301 in Fire Extinguishing Systems*, Jet Propulsion Laboratory, JPL Publication 84-62, 1984.

Ely, J., and Huber, M.L., *PROZPER*, Personal Communication with M. L. Huber (1993).

Epstein, M., Henry, R., Midvidy, W., and Pauls, R., "One-Dimensional Modeling of Two-Phase Jet Expansion and Impingement, in *Thermal-Hydraulics of Nuclear Reactors, Vol. II*, 2nd International Topical Meeting on Nuclear Reactor Thermal Hydraulics, Santa Barbara, CA, Jan. 11-14, 1983.

Fletcher, B., "Sudden Discharge of a Superheated Fluid to Atmosphere," *IChemE Symposium Series No. 71*, 25 (1982).

Forest, T.W., and Ward, C.A., "Effect of a Dissolved Gas on the Homogeneous Nucleation Pressure of a Liquid," *J. Chem. Phys. 66*, 2322 (1977).

Forster, H.K, and Zuber, N., "The Growth of a Vapor Bubble in a Superheated Liquid," *J. Appl. Phys. 25*, 474 (1954).

Gmurczyk, G., Lezanski, T., Kesler, M., Chomiak, T., Rychter, T., and Wolanski, P., "Single Compression Machine Study of a Pulsed Jet Combustion (PJC)," *Twenty-Fourth Symposium (International) on Combustion*, pp.1441-1448, Combustion Institute, Pittsburgh, 1992.

Gühler, M., Hannemann, R.J., and Sallet, D.W., "Unsteady Two-Phase Blowdown of a Flashing Liquid from a Finite Reservoir," in *Two-Phase Momentum, Heat and Mass Transfer in Chemical, Process, and Energy Engineering Systems, Vol. 2*, Durst, F., Tsiklauri, G.V., and Afgan, N.H., Eds., pp. 781-795, Hemisphere Publishing Co., Washington, 1979.

Henry, R.E., "The Two-Phase Critical Discharge of Initially Saturated or Subcooled Liquid," *Nuclear Science and Engineering 41*, 336 (1970).

Hesson, J.C., and Peck, R.E., "Flow of Two-Phase Carbon Dioxide through Orifices," *AIChE Journal 4*, 207 (1958).

Johnson, D.W., and Diener, R., "Prediction of Aerosol Formation from the Release of Pressurized, Superheated Liquids to the Atmosphere," *IChemE Symposium Series No. 124*, 87 (1991).

Kim-E, M.E., *The Possible Consequences of Rapidly Depressurizing a Fluid*, M.S. Thesis, Department of Chemical Engineering, Massachusetts Institute of Technology, 1981.

Kim-E, M.E., and Reid, R.C., "The Rapid Depressurization of Hot, High Pressure Liquids or Supercritical Fluids," in *Chemical Engineering at Supercritical Fluid Conditions*, Paulaitia, M.E., Penninger, J.M.L., Gray, Jr., R.D., and Davidson, P., Eds., pp. 81-100, Ann Arbor Science, Ann Arbor, MI, 1983.

Launder, B.E., and Spaulding, D.B., *Mathematical Models of Turbulence*, Academic Press, New York, 1972.

Leung, J.C. and Nazario, F.N., "Two-Phase Flashing Flow Methods and Comparisons," *Journal Loss Prevention Process Industry 3*, 253, (1990).

Lienhard, J.H., "Some Generalizations of the Stability of Liquid-Gas-Vapor Systems," *Int. J. Heat Mass Trans. 7*, 813 (1964).

Lienhard, J.H., "An Influence of Superheat Upon the Spray Configuration of Superheated Liquid Jets," *J. Basic Eng. 88*, 685 (1966).

Lienhard, J.H., and Day, J.B., "The Breakup of Superheated Jets," *J. Basic Eng. 92*, 515 (1970).

Lienhard, J.H., and Stephenson, J.M., "Temperature and Scale Effects Upon Cavitation and Flashing in Free and Submerged Jets," *J. Basic Eng. 88*, 525 (1966).

Military Specification, "Container, Aircraft Fire Extinguishing System, Bromotrifluoromethane, CF_3Br," *Mil-C-22284A(WP)*, September, 1965.

Modell M., and Reid, R.C., *Thermodynamics and Its Applications, 2nd Ed.*, Prentice-Hall, Englewood Cliffs, NJ, 1983.

Moodie, K., and Ewan, B.C.R., "Jets Discharging to Atmosphere," *J. Loss Prev. Process Ind. 3*, 68 (1990).

O'Rourke, P.J., *Collective Drop Effects in Vaporizing Liquid Sprays*, Ph.D. Thesis 1532-T, Princeton University, 1981.

Oran, E.S., "Current Status of Computational Fluid Dynamics in Combustion Modeling," *Eastern States Section Technical Meeting*, Clearwater Beach, FL, December 5-7, 1988.

Pasqua, P.F., "Metastable Flow of Freon-12," *Refrigerating Engineering 61*, 1084A (1953).

Peng, D.-Y., and Robinson, D.B., "A New Two-Constant Equation of State," *Ind. Eng. Chem. Fundam. 15*, 59 (1976).

Perry, Jr., J.A., "Critical Flow Through Sharp-Edged Orifices," *Trans. ASME 71*, 757 (1949).

Perry, R.H., Green, D.W., and Maloney, J.O., *Perry's Chemical Engineers' Handbook*, 6th ed., McGraw-Hill, New York, 1984.

Pitts, W.M., and Kashiwagi, T., "The Application of Laser-Induced Rayleigh Light Scattering to the Study of Turbulent Mixing," *J. Fluid Mech. 141*, 391 (1984).

Pitts, W.M., and McCaffrey, B.J., "Response Behaviour of Hot Wires and Films to Flows of Different Gases," *J. Fluid Mech. 169*, 465 (1986).

Plesset, M.S., and Zwick, S.A., "The Growth of Vapor Bubbles in Superheated Liquids," *J. Appl. Physics 25*, 493 (1954).

Press, W.H., Flannery, B.P., Teukolsky, S.A., and Vetterling, W.T., *Numerical Recipes - The Art of Scientific Computing*, Cambridge University Press, Cambridge, 1986.

Prisco, M.R., Henry, R.E., Hutcherson, M.N., and Linehan, J.L., "Nonequilibrium Critical Discharge of Saturated and Subcooled Liquid Freon-11," *Nuclear Science and Engineering 63*, 365 (1977).

Rayleigh, Lord, "On the Instability of Jets," *Proc. London Math. Soc. 10*, 7 (1878).

Reid, R.C., "Superheated Liquids," *American Scientists 64*, 146 (1976).

Reid, R.C., "Superheated Liquids - A Laboratory Curiosity and, Possibly, an Industrial Curse," *Chemical Engineering Education*, 60 (1978).

Reid, R.C., "Possible Mechanism for Pressurized-Liquid Tank Explosions or BLEVE's," *Science 203*, 1263 (1979).

Reid, R.C., Prausnitz, J.M., and Poling, B.E., *The Properties of Gases and Liquids, 4th Ed.*, McGraw-Hill, New York, 1987.

Richards, C.D., and Pitts, W.M., "Global Density Effects on the Self-Preservation Behaviour of Turbulent Free Jets, *J. Fluid Mech. 254*, 417 (1993).

Roberson, J.A., and Crowe, C.T., *Engineering Fluid Mechanics*, Houghton Mifflin Company, Boston, 1980.

Shapiro, A.H., *The Dynamics and Thermodynamics of Compressible Fluid Flow, Volume 1*, Ronald Press, New York, 1953.

Shirakashi, M., Arakawa, T., and Wakiya, S., "The Turbulent Structure and the Diffusion of the Nozzle Fluid in an Impulsively Started Axisymmetrical Jet," in *Turbulence and Chaotic Phenomena in Fluids*, Tatsumi, T., Ed., pp. 385-390, North-Holland, New York, 1984.

Smith, J.M., and Van Ness, H.C., *Introduction to Chemical Engineering Thermodynamics, 3rd Ed.*, McGraw-Hill, New York, 1975.

Solomon, A.S.P., Chen, L.-D., and Faeth, G.M., *Investigation of Spray Characteristics for Flashing Injection of Fuel Containing Dissolved Air and Superheated Fluids*, NASA Contractor Report 3563, 1982.

Thompson, P.A., *Compressible-Fluid Dynamics*, McGraw-Hill, New York, 1972.

Tong, L.S., *Boiling Heat Transfer and Two-Phase Flow*, John Wiley and Sons, New York, 1965.

Van den Akker, H.E.A., Snoey, H., and Spoelstra, H., "Discharge of Pressurized Liquefied Gases through Apertures and Pipes," *IChemE Symposium Series No. 80*, E23 (1983).

Weber, C., "Zum Zerfall eines Flüssigkeitsstrahles," *Zeit. fur Angew. Math. 11*, 106 (1931).

Williamson, H.V., "Halon 1301 Flow in Pipelines," *Fire Technology 13*, 18 (1976).

4. FLAME SUPPRESSION EFFECTIVENESS

Anthony Hamins, Grzegorz Gmurczyk, William Grosshandler,
R. Gregory Rehwoldt, Isaura Vazquez, and Thomas Cleary
Building and Fire Research Laboratory

Cary Presser
Chemical Sciences and Technology Laboratory

and Kalyanasundaram Seshadri
AMES Department, University of California at San Diego, La Jolla, CA

4.1 Overview

A flame will be extinguished when the time required for the chain reaction which sustains combustion exceeds the time it takes to replenish the necessary heat and reactants. A characteristic time for reaction, t_{chem}, can be estimated from the inverse of a global kinetic rate coefficient, k, expressed in Arrhenius form as

$$t_{chem} \sim k^{-1} = B^{-1} \exp\left(\frac{E_0}{RT}\right), \ (seconds) \tag{1}$$

where B is a molecular collision frequency factor, E_0 is a global activation energy, R is the ideal gas constant, and T is the gas temperature. Assuming reactant species and heat are transported at about the same rate (*i.e.,* unity Lewis number), a characteristic time, t_{flow}, for replenishing both can be estimated from a convective flow velocity, U, and a length scale, L, by

$$t_{flow} \sim \frac{L}{U} \ (seconds). \tag{2}$$

The Damköhler number is the ratio of the characteristic flow time to the characteristic chemical reaction time, *i.e.,* $D_n \equiv t_{flow}/t_{chem}$. Liñan (1974) showed that as the maximum flame temperature and the fuel burning rate decrease, a critical value Damköhler number is reached, D_n*, where the flame abruptly extinguishes. The Damköhler number criteria suggests a number of strategies for extinguishing fires that include increasing the strain rate or flame stretch (to decrease t_{flow}), or cooling, reactant removal, and chemical inhibition (to increase t_{chem}).

A large number of studies have been conducted on fire suppression. Williams (1980) summarizes the fundamental processes of flame extinction. The suppression effectiveness of a number of inert, halogenated, and metal agents been studied phenomenologically in counterflow flames (Milne *et al.*, 1970; Kent and Williams, 1974; Seshadri and Williams, 1975; Mitani, 1983) and in co-flowing cup burner flames (Simmons and Wolfhard, 1956; Creitz, 1961, 1972; Bajpai, 1974a; Hirst and Booth, 1977; Tucker *et al.*, 1981; and Sheinson *et al.*, 1989). A number of investigators have studied the structure of inhibited flames in order to learn about the mechanisms of flame inhibition. A global measure of the chemical effectiveness of an agent has been quantified through heat capacity considerations (Tucker *et al.*, 1981; Sheinson *et al.*, 1989). Pitts *et al.* (1990) outline current understanding

of fire suppression, incorporating a comprehensive review of the relevant literature, in addition to a discussion of agent effectiveness, test methods, and the role of different suppression mechanisms.

The objective of this part of the study was to rank experimentally the effectiveness of various chemicals for suppressing different laboratory-scale flames, and to project the relative effectiveness to the performance one would expect in the Wright Laboratory simulated full-scale fire suppression facilities.

4.1.1 Comparison of Experimental Configurations. Fundamental studies have shown that the character of the fluid mechanical flow field is a key parameter in controlling flame extinction. A discussion of the importance of the flow field strain rate or flame stretch is given by Williams (1980). As the strain rate increases, t_{flow} in Equation 2 decreases and a flame becomes weaker and easier to extinguish by agent addition. In order to understand the chemical effectiveness of an agent, other parameters such as fluid mechanics which influence flame extinction must be well-controlled. For the applications considered here, an engine nacelle and a dry bay, the fluid mechanics and thus the strain rate is not well defined due principally to variability in the flowfield geometry. Observation in the Wright Laboratory simulated fire suppression facilities, however, indicate that the fires of interest are turbulent and thereby characterized by a range of strain rates. The configurations listed in Table 1 were designed to improve our understanding of the suppression effectiveness of agents under a variety of possible combustion scenarios.

Four experimental configurations were used to rank the relative effectiveness of suppression agents. They are listed in Table 1 and include the laminar opposed flow diffusion flame burner (OFDF), the cup burner, the turbulent spray flame burner, and the deflagration tube. Table 1 also lists differences in the parameters which characterize combustion in each of the test configurations including the nature of the flow field and the pressure regime. In a typical fire the fuel and air are nonpremixed, as represented by the cup burner and the OFDF burner.

Opposed flow and coflow systems provide two fundamental approaches for studying diffusion flame extinction. Past experience has shown the OFDF configuration to be a convenient geometry for detailed fundamental studies of the structure and mechanisms of extinction of diffusion flames (Hamins, 1985; Hamins and Seshadri, 1984a, 1984b, 1986, 1987; Hamins *et al.*, 1985; Seshadri and Williams, 1975, 1978a). The critical conditions of flame extinction measured in the opposed flow configuration, can be readily interpreted using currently available asymptotic theories of flame extinction (Fendell, 1965; Peters, 1982, 1984; Williams, 1985), and the results can also be extended to turbulent nonpremixed combustion (Peters, 1982, 1984). Interpretation of experimental results of flame extinction using asymptotic theories requires knowledge of the characteristic flow time in the flame, t_{flow}. In the opposed flow configuration, the value of t_{flow} is related to the velocity of the reactant streams or the flow field strain rate (Seshadri and Williams, 1978b), which is an independently controlled experimental parameter.

This is not the case for a coflow system like the cup burner. In the coflowing configuration, the shape of the flame is approximately conical and the value of t_{flow} cannot be related easily to the flow velocities of the reactant streams. It has been recently shown that in the coflowing configuration the value of t_{flow} at the flame varies with height above the exit of the burner (Seshadri *et al.*, 1990). Therefore, interpretation of extinction data obtained in the coflowing configuration is not straightforward. Also, in the coflowing configuration premixing of the fuel and oxidizer can occur near the vicinity of the surface of the liquid fuel and the exit of the oxidizer duct where the fuel vapors and the oxidizer initially come into contact. This premixing can influence the mechanisms of flame extinction. However, in the opposed flow configuration, premixing, other than that resulting directly from diffusion of reactants through the flame, is eliminated completely. A significant advantage of the opposed flow configuration is that there are numerous computer programs available for predicting the

Table 1. Experimental Configurations

Configuration	Type of Combustion and Flow Field	Pressure	Agents	Fuels
Opposed Flow Diffusion Flame	laminar non-premixed	ambient	13 gaseous agents & $NaHCO_3$	heptane, JP-8
Cup Burner	quasi-laminar non-premixed	ambient	14 gaseous agents, $NaHCO_3$, & 18 additional agents	JP-5, JP-8, 5606, 83282, heptane, propane
Spray Burner	turbulent spray	ambient	14 gaseous agents & $NaHCO_3$	83282, JP-8
Deflagration Tube	turbulent premixed	variable	14 gaseous agents	ethene

structure and critical conditions of flame extinction (Bui and Seshadri, 1992; Chelliah, 1992; Smooke *et al.*, 1986). Although, such programs have also been developed for predicting the structure of flames stabilized in the coflowing configuration, these programs require considerably more computational time. Careful interpretation of the data, however, show that there exists a correspondence between the results obtained in the opposed flow and coflow configurations.

Consideration of in-flight fire scenarios in engine nacelles and dry bays prompted the development of two unique test configurations, the deflagration tube and the spray flame burner. Although it is not possible to estimate the value of t_{flow} for the spray burner or the deflagration tube, extinction experiments in these configurations are of interest because they mimic combustion behavior in engine nacelle and dry bay fires, where t_{flow} is also not well characterized.

In contrast to all of the other configurations listed in Table 1, combustion is premixed in the deflagration tube. In the spray burner, although the fuel and oxidizer are initially nonpremixed, combustion occurs in the form of a turbulent two-phase spray which is neither purely premixed nor nonpremixed, but can be thought of as an ensemble of partially premixed flames. Whereas the flames are laminar in the OFDF and are nearly laminar in the cup burner, they are highly turbulent in the other two configurations. Atmospheric combustion occurs in all of the configurations except the deflagration tube, where final pressures can be much larger than atmospheric.

The differences in the structure of the flames in each of the test configurations is likely to have a large impact on the relative suppression effectiveness of the agents. The introduction of an inert or chemical inhibitor to a flame impacts the stability of the flame by influencing the flame structure through changes in the temperature and species concentration fields. At the same time, the structures of premixed and nonpremixed flames are distinct. The mechanism for suppression may be distinct in detonations and diffusion flames because the chemistry may take place at different pressures, and chemical rate constants are pressure sensitive which could enhance or diminish the importance of particular chemical reactions. In non-premixed flames, combustion can be limited by the rate at which the reactants are brought together, whereas in premixed flames, combustion is limited by the chemical kinetics. Spray flames represent a complicated combustion situation where fuel droplets vaporize and react with the oxidizer, which can be composed of either pure air, air mixed with combustion products or air mixed with fuel vapor. Because of the inherent differences in the

structure of the combustion zone in each of the configurations, it would be very surprising if the agents displayed identical agent suppression effectiveness in the different test configurations.

4.1.2 Fuels and Agents Tested. In the four configurations, a number of different fuels were tested. Table 1 lists these fuels. They consisted of gaseous fuels (propane and ethene), multi-component liquid fuels (JP-5 and JP-8 jet fuels, and 5606 and 83282 hydraulic fluids) and a single component liquid fuel (heptane). The jet fuels and hydraulic fluids contain many components and can vary in composition from batch to batch. Thus, the heats of combustion (Gascoyne Laboratories, 1993) and elemental composition (Galbraith Laboratories, 1993) for the fuel batch used in the experiments reported here were determined as listed in Table 2.

4.1.3 Agents. Thirteen gaseous agents were tested in all configurations. The agents included nitrogen; four perfluorinated compounds, C_2F_6, C_3F_8, C_4F_{10}, and cyclo-C_4F_8; four hydrogen/fluorine compounds, CF_3HFCF_3, $CF_3H_2CF_3$, C_2HF_5, and CFH_2CF_3; the mixture 60% CH_2F_2/40% C_2HF_5; the chlorinated agents CHF_2Cl and $CHFClCF_3$; and CF_3Br. In addition, CF_3I and sodium bicarbonate powder ($NaHCO_3$) were tested in all configurations except the OFDF burner and the deflagration tube, respectively.

Eighteen additional agents were tested in the cup burner including inert gases, other halocarbons, a silicon compound, and a nitrogen compound. In addition, several liquid agents were tested. A detailed explanation for the selection of additional agents for cup burner testing is given in Section 5.

In addition to the gaseous and liquid agents described above, sodium bicarbonate, a solid powder, was also tested in the first three configurations listed in Table 1. The objective of these tests was to quantitatively compare the suppression effectiveness of sodium bicarbonate to CF_3Br and the other gaseous agents.

Sodium bicarbonate powder is currently a popular fire suppressant and its effectiveness is well known. Because of its zero ozone depletion potential, it deserves consideration for a wider range of applications. Few flame extinction measurements have been conducted with powders in test devices where the effectiveness of the powder could be directly compared with gaseous agents, and where flow field effects were minimized.

Some previous studies indicated that particle size is an important parameter in flame extinction using dry powders. Milne *et al.*, (1970) studied the extinction of methane/air opposed flow diffusion flames using $NaHCO_3$ powders with different diameters and found that smaller powders were more effective flame suppression agents. Measurements were reported by Dodding *et al.*, (1977) for extinction of methane/air opposed flow diffusion flames with 10 to 20 μm sodium bicarbonate particles added to the oxidizer. However, a key experimental parameter, the strain rate, was not reported. Others have tested the effectiveness of powders in less fundamental geometries. Ewing *et al.*, (1989) reported that approximately 4% (by mass) of $NaHCO_3$ (≈ 10 μm particles) was needed to extinguish heptane pan fires.

In order to study the impact of particle size, the powder was milled and then silica (SiO_2) was added to the powder to improve flow behavior and to prevent agglomeration. The particles were then sized using a centrifuge by VORTEC Industries into several fractions, hereafter referred to as nominally 0-10, 10-20, 20-30, 30-40, 40-50, and 50+ μm. The powder was stored in sealed plastic bags until use.

Particle size distribution was measured using optical microscopy and an average (equivalent sphere) diameter is listed in Table 3. Table 3 also lists the density of the $NaHCO_3/SiO_2$ mixtures which was measured using helium pycnometry (Lum, 1993) and the (mass based) percentage of SiO_2 in each size fraction as measured by X-ray fluorescence (Dow-Corning, 1993).

Table 2. Fuel Properties

Fuel Type	Heat of Combustion (MJ/kg)	Elemental Analysis		
		Mass Percent H	Mass Percent C	Mass Percent O
JP-5	46.3	13.3	85.4	< 0.5
JP-8	46.5	13.9	86.2	< 0.5
5606	44.0	12.6	80.5	2.03
83282	45.1	13.2	79.5	4.78
ethene	50.3	14.3	85.7	0
propane	50.3	18.2	81.8	0
heptane	48.1	16.0	84.0	0

Table 3. Particle Characterization

Nominal Particle Size (μm)	Equivalent Particle Diameter (μm)	SiO_2 % (kg/kg)	Measured Density (kg/m^3)
0 - 10	4.5 $\pm$ 0.5	1.34	2220
10 - 20	7.0 $\pm$ 0.5	0.67	2220
20 - 30	[a]	0.46	2220

[a] Not measured

The remainder of this Section is broken into four parts which include detailed descriptions of the experimental apparatus listed in Table 1. For each configuration, experimental methods, results, and discussion are included. Key findings of the work are compiled in Section 4.6 and reference are listed in Section 4.7.

4.2 Opposed Flow Diffusion Flames

4.2.1 Introduction. An experimental study was conducted to characterize the relative influence of various inhibiting agents in extinguishing diffusion flames burning the liquid hydrocarbon fuels heptane and JP-8. Thirteen gaseous inhibiting agents and $NaHCO_3$ were tested, and their effectiveness in extinguishing diffusion flames burning liquid fuels was compared to CF_3Br. The experimental configuration employed in the study was a diffusion flame stabilized in the mixing layer produced by directing an oxidizing gas stream downward on the burning surface of a liquid fuel. This is referred to in the literature as the OFDF configuration and is a convenient geometry for detailed fundamental studies of the structure and mechanisms of extinction of diffusion flames. In the OFDF configuration,

shown in Figure 1, there exists a stagnation plane, and the stoichiometry of the overall combustion processes is such that the flame (defined as the position where the temperature attains a maximum value) is stabilized on the oxidizer side of the stagnation plane. The oxidizing gas used in the experiments was a mixture of air and the inhibiting agent. To test the influence of the initial temperature of the oxidizing gas stream on the critical conditions of flame extinction, the experiments were performed with the oxidizing stream at temperatures of 25 °C and 150 °C.

Milne *et al.*, (1970) employed the opposed flow technique to evaluate the influence of gaseous inhibiting agents, including CF_3Br and powdered agents, on the critical conditions of extinction of methane-air, propane-air and n-butane-air diffusion flames. These experiments employed the "Tsuji" type opposed flow configuration, where the diffusion flame is stabilized in the vicinity of the forward stagnation line of a porous cylinder from which the gaseous fuel is introduced into the reaction zone. From the experimental measurements it was concluded that on a mass basis some powder agents are approximately ten times more effective than CF_3Br in extinguishing diffusion flames. Kent and Williams (1974) and Seshadri and Williams (1975) studied the inhibiting effect of CF_3Br on opposed flow diffusion flames stabilized over the surface of pools of heptane. The velocity and composition of the oxidizer stream at extinction were measured (Kent and Williams, 1974 and Seshadri and Williams, 1975). The concentration of CF_3Br in the oxidizing stream at flame extinction was compared to the amount of the inert diluent N_2 which must be added to the air stream to extinguish the flame. At selected conditions the flame temperature near extinction was also measured. As mentioned in Section 4.1, interpretation of experimental results of flame extinction using asymptotic theories requires knowledge of the characteristic residence time in the flame, t_{flow}. At a fixed value of the flow velocity of the oxidizer stream, or at a fixed value of t_{flow}, the concentration of CF_3Br in the air stream at extinction was found to be considerably lower than the concentration of N_2 added to the air stream at extinction. In addition, the value of the measured temperature in the vicinity of extinction was higher or the value of the characteristic chemical-reaction time t_{chem} was lower when CF_3Br was added to the oxidizer stream than for nitrogen dilution. Since nitrogen is an inert compound, these results imply that inhibition of chemical reactions by CF_3Br may be responsible for extinguishing the flame at a lower value of t_{chem}. These previously developed techniques (Kent and Williams, 1974; Seshadri and Williams, 1975) are used to interpret the experimental results obtained in the present study.

4.2.2 Experimental Apparatus. Figure 2 shows a schematic illustration of the OFDF burner. The burner consisted of a fuel cup which had a diameter of 50 mm and a depth of 18 mm, and an oxidizer duct through which the oxidizing stream containing the gaseous inhibitor or $NaHCO_3$ powder was introduced into the flame. The fuel cup was cooled by water at the bottom in order to prevent the fuel from boiling, but was not cooled at the rim as that would establish a radial temperature gradient within the liquid fuel. A narrow annulus surrounded the wall of the cup near the rim to catch any overflow of the fuel and prevent it from entering into the exhaust duct. Since, the flame sheet was very sensitive to surface movements, the fuel height in the cup was accurately controlled by a device similar to that designed by Bajpai (1974b). A fine pointer projecting up through the liquid pool was used as an aid in adjusting the height of the fuel surface. Satisfactory repeatability had been obtained by setting the pool at the level at which the pointer just forms a discernible dimple on the fuel surface. The oxidizer duct had an inner diameter of 50.1 mm. For experiments with gaseous inhibitors approximately five layers of fine wire screens (80 mesh/cm) with each layer of the screen separated by a 1 mm split ring were placed in the duct to reduce the scale of turbulence and to ensure a flat velocity profile at the exit of the duct. For experiments with $NaHCO_3$ powder, only two layers of coarse wire screen (8 mesh/cm) were employed to prevent accumulation of the powder on screens. Also, in the experiments with $NaHCO_3$ powder, it was necessary to replace the screens frequently.

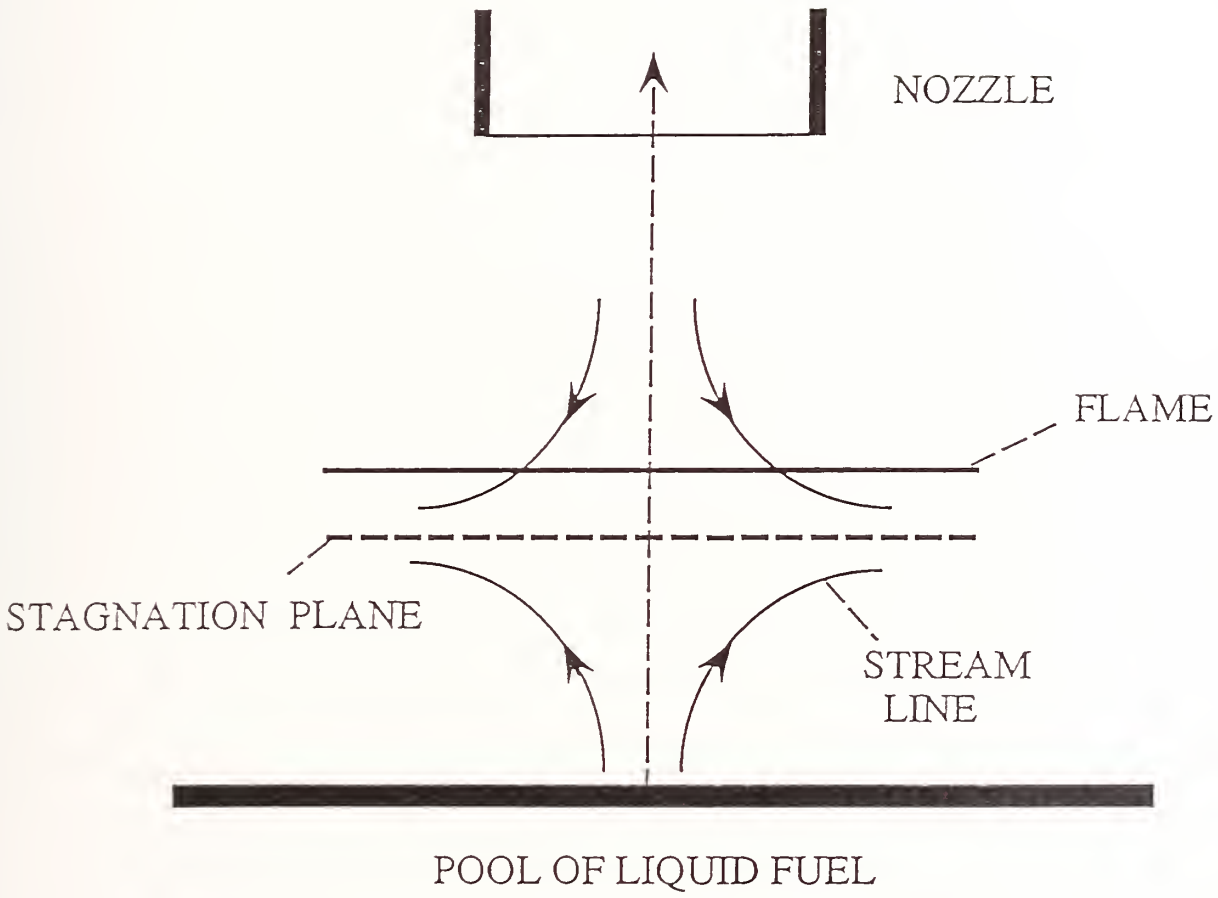

Figure 1. Schematic illustration of the counterflow configuration.

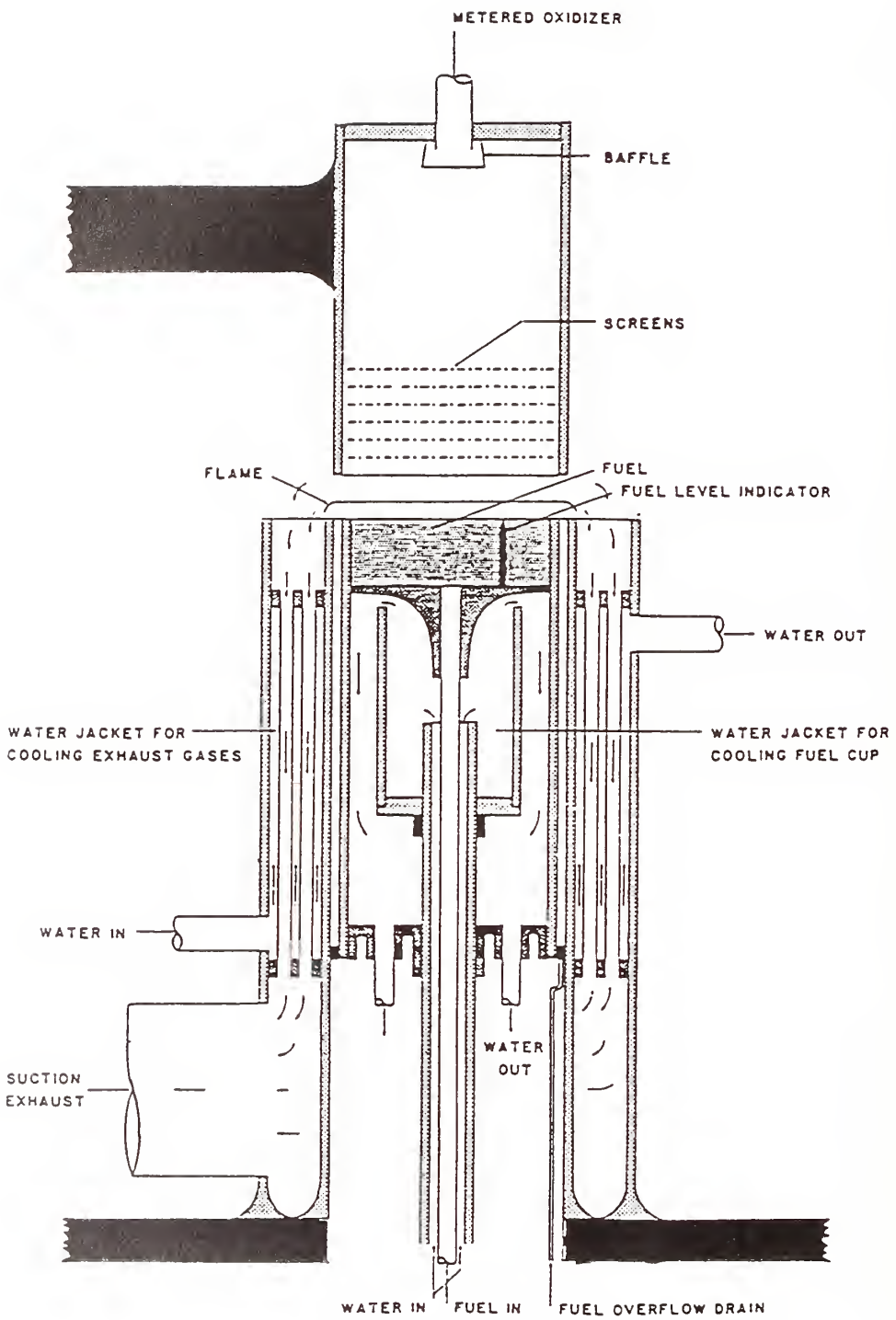

Figure 2. Schematic illustration of the OFDF burner.

The distance between the oxidizer duct and the fuel cup was adjustable and the oxidizer duct could be swivelled to allow access to the fuel cup. Experiments were performed with the separation distance, L, between the surface of the liquid pool and the exit of the oxidizer duct equal to 10 mm. Mild suction was used to pull the products of combustion from the flame into a heat exchanger surrounding the fuel-overflow rim. The cooled gases then flowed into the exhaust. The suction minimized the influence of the ambient air currents on the flame, and prevented after-burning in the heat exchanger. A steady flame like that shown in Figure 3 could be indefinitely stabilized in this apparatus. Measurements were made with the burner enclosed within a plexiglass box with an outlet directly connected to the exhaust to minimize operator exposure to the products of combustion.

The volumetric flow of air, nitrogen and the gaseous inhibitors were measured to $\pm 3\%$ by use of variable area flowmeters. Pressure gauges were arranged in parallel with the flowmeters to insure that the volumetric flow of the gas stream was not affected by fluctuations in the output pressure from compressed gas cylinders or from variations in stagnation pressure caused by adjusting the volumetric gas flows. The flowmeters were calibrated using wet-test meters. The uncertainty in the concentration of agent at extinction are estimated as approximately 10%.

Figure 4 shows a schematic illustration of the device employed to introduce $NaHCO_3$ powder into the flame. This device, originally designed by Williams and Peters (1982), was made of plexiglass and consisted of a bed of powder resting on a porous disk. Air was introduced from the bottom fluidizing tube and passed through a bed of glass beads which distributed the flow in the region between the glass beads and the porous disk. The air passed through the porous disk, lifted the particles and formed a fluidized bed in the region above the bed of powder. The air mixed with powder was removed from the exit tube and introduced into the oxidizing duct of the OFDF burner. The jet ring shown in Figure 4 was used to prevent agglomeration of the particles. The jet ring consisted of a thin tube closed on one end and bent to form a ring. A number of holes were punched along the periphery of the ring and air was introduced from the open end of the tube to raise the particles out of the fluidized bed. The mass fraction of the powder in the mixture of air and the particles flowing out of the exit tube was altered by adjusting the volumetric flows of air in the fluidizing tube and the jet ring.

Particle analysis was done by isokinetic sampling and weighing of the samples. After completion of the experiments, the portion of the OFDF burner containing the fuel cup was removed and a probe with a 10 mm diameter was placed under the oxidizer duct at nearly the same position as that of the fuel cup. A filter was placed inside the probe to collect the particles. The volumetric flows of air in the fluidizing tube and the jet ring were adjusted such that they were identical to those used in the extinction experiments. A wet-test meter was placed downstream to measure the volumetric flow rate of air in the probe. Mild suction was used such that the velocity of the mixture of air and the particles entering into the probe was approximately equal to that at the exit of the oxidizer duct. The flow into the probe was maintained until a measurable amount of powder was collected in the filter. The probe together with the powder was then removed and its weight was measured accurately. The weight of the powder in the probe was calculated from the difference between the weight of the probe with and without the powder. The total weight of the air flowing through the probe was calculated from the measured total volume of air recorded by the wet-test meter. The mass fraction of the particles in the air stream was then calculated from the ratio of the weight of the powder collected in the probe to the sum of the total weight of air and the weight of the particles. An average of three such runs was made at each measured extinction point to determine the mass fraction of powder in the oxidizing stream. The uncertainties in the amount of powder determined using this method was estimated to be approximately 15%.

Figure 3. Photograph of uninhibited flame stabilized above heptane pool in OFDF burner.

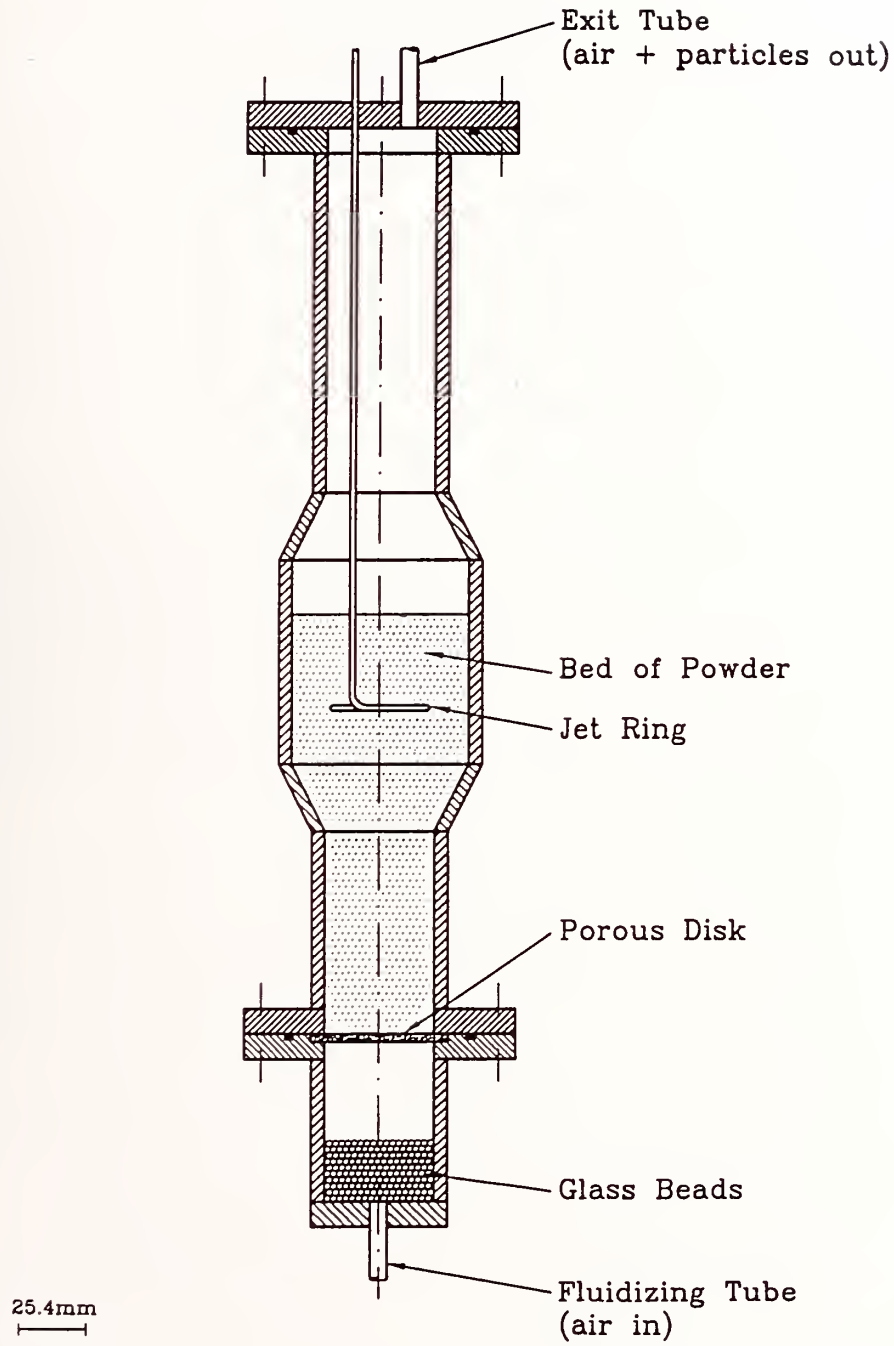

Figure 4. Schematic illustration of the powder dispensing device.

4.2.3 Experimental Procedure. For experiments with gaseous agents the volumetric flow of air through the oxidizer duct was maintained at some predetermined value and the liquid pool was ignited. The inhibitor was then added gradually to the oxidizer stream until the flame extinguished. Care was taken to ensure that the flame attained a steady state after each incremental addition of the inhibitor. The volumetric flows of air and inhibitor at extinction were recorded. The experiments were repeated with a different air flow. The velocity of the oxidizer stream at the exit of the duct, U, was presumed to be equal to the ratio of the total volumetric flow of air and the inhibitor to the cross-sectional area of the oxidizer duct. Following the analysis of Seshadri and Williams (1978b), the strain rate, a, is equal to the ratio of U to L, where L is the separation distance between the surface of the liquid pool and the exit of the oxidizer duct.

For experiments with $NaHCO_3$ powder, the uniformity of the concentration of powder in the oxidizing stream was monitored using the optical arrangement shown in Figure 5. For a given level of powder in the oxidizing gas stream, the attenuation of the He-Ne laser radiation was recorded by the oscilloscope and the strip-chart recorder. For experiments with $NaHCO_3$ powder, two separate air streams flowed into the oxidizer duct. One stream of air, termed the primary air, flowed directly from the flowmeters into the oxidizer duct, and the other stream of air flowed into the fluidizing and jet-ring tube of the powder dispensing device shown in Figure 4.

Initially the volumetric flow of primary air was maintained at some predetermined value and the liquid pool was ignited. Secondary air was then introduced through the fluidizing tube of the powder dispensing device until a sufficient amount of powder was observed to flow through the oxidizer tube. The uniformity of powder concentration in the oxidizer stream was monitored by recording the output of the strip-chart recorder. The flow of air was slowly increased until the flame was extinguished. Care was taken to ensure that the flame attained a steady state after each incremental addition of powder by monitoring the output of the strip-chart recorder. The flowmeter readings for the primary and secondary air as well as the fractions of the secondary air flowing through the fluidizing tube and the jet-ring were recorded. The amount of powder in the oxidizing stream was then determined as described in the previous section. The experiment was then repeated at a different volumetric flow of the primary air.

4.2.4 Experimental Results. Figure 6 shows the mass fraction of the agents as a function of the strain rate, a, at extinction. The fuel was heptane and the initial temperature of the oxidizer stream was 25 °C. For a given agent, the region below the curve represents flammable mixtures. For any value of the strain rate the value of the mass fraction of CF_3Br required to extinguish the flame is lower than the mass fraction of all other agents. Therefore on a mass basis CF_3Br is considerably more effective in extinguishing the flame than all the other agents tested. Figure 6 shows that the relative effectiveness of some of the agents in extinguishing the flame varies with the strain rate. This becomes more clear by examining the results shown in Figure 7, where the data are replotted with an expanded vertical scale. At low strain rates HFC-236 is most effective and FC-116 least effective in extinguishing the flame, whereas at high strain rates HCFC-22 is most effective and FC-318 least effective in extinguishing the flame. In fact at high strain rates only CF_3Br and HCFC-22 are more effective than N_2 in extinguishing the flame. However, the results plotted in Figures 6 and 7 show that with the exception of CF_3Br, the differences in the mass-based effectiveness of the various agent are not large.

Figure 8 is a plot of the same data shown in terms of the mole fraction of the agents. The fuel was heptane and the initial temperature of the oxidizer stream was 25 °C. For any given value of the strain rate the value of the mole fraction of CF_3Br required to extinguish the flame was lower than the mole fraction of all other agents. On a mole basis, at low and high strain rates FC-31-10 was most effective and HFC-32/125 least effective in extinguishing the flame. Note that on a mole basis, all

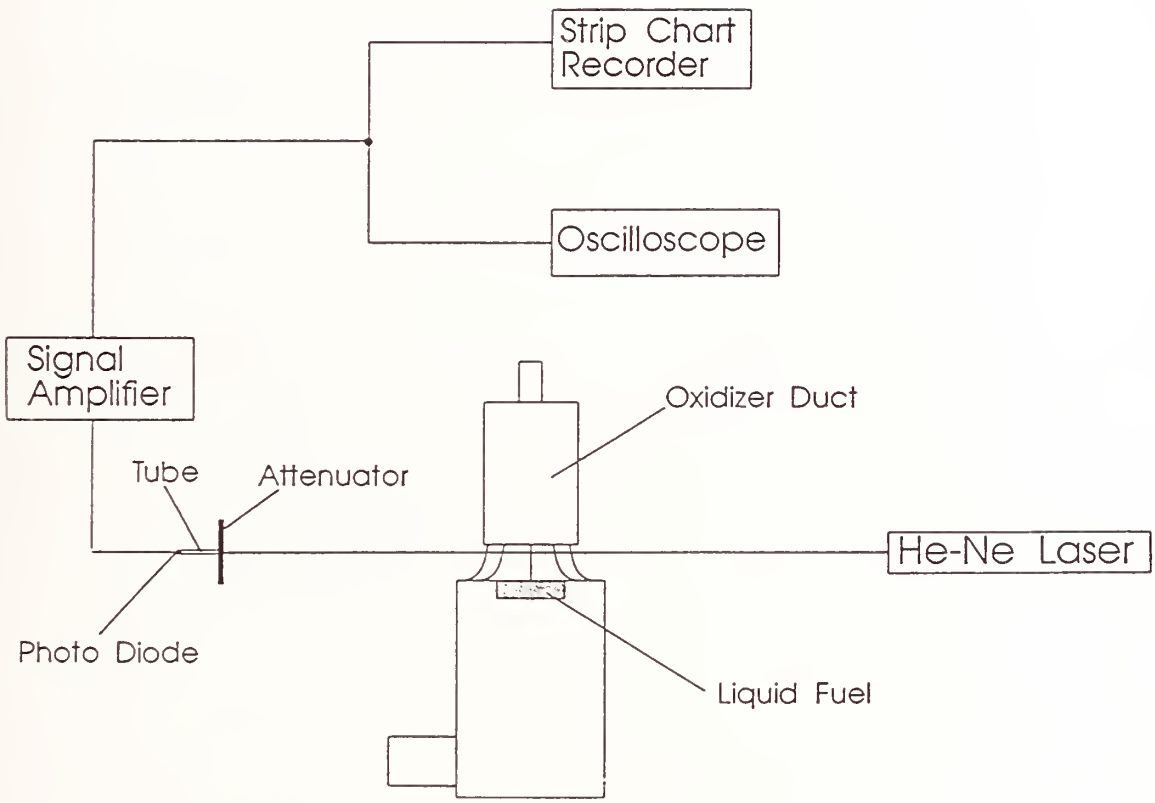

Figure 5. Schematic of the optical arrangement employed for monitoring powder concentration.

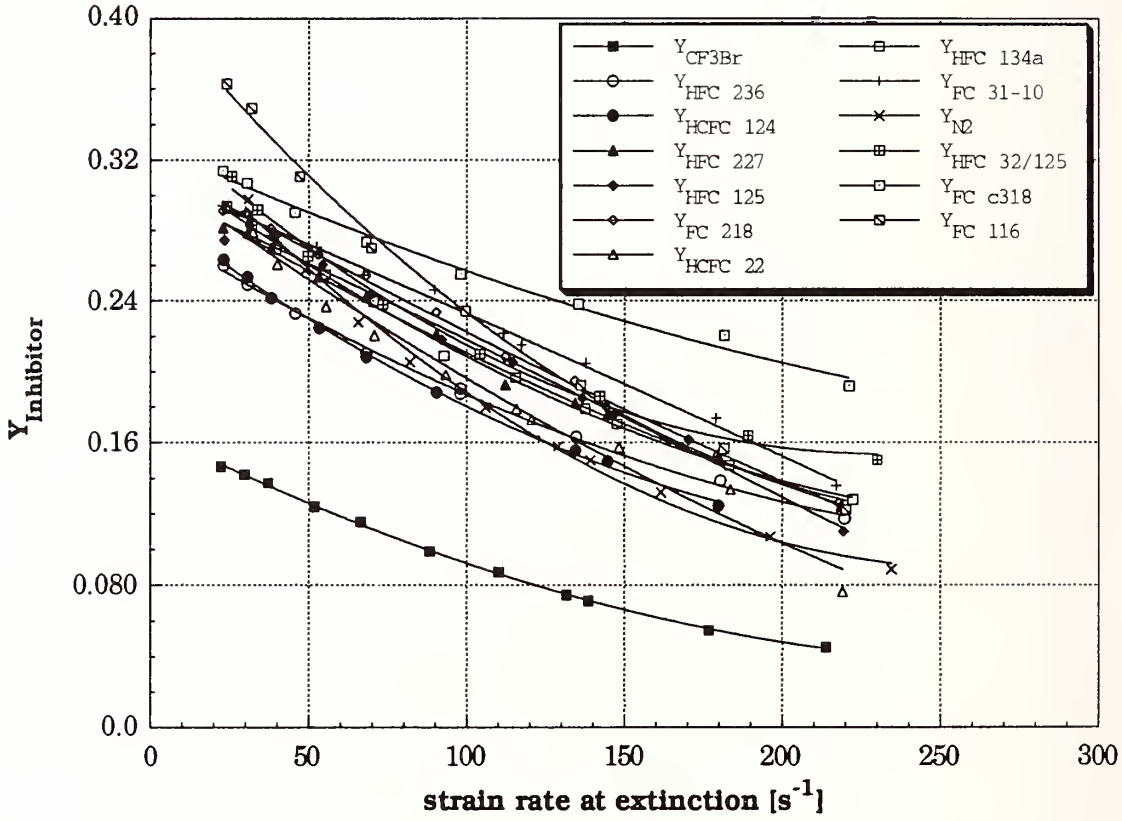

Figure 6. Mass fraction of various agents as a function of the strain rate for heptane flames at extinction, with an oxidizer temperature of 25 °C.

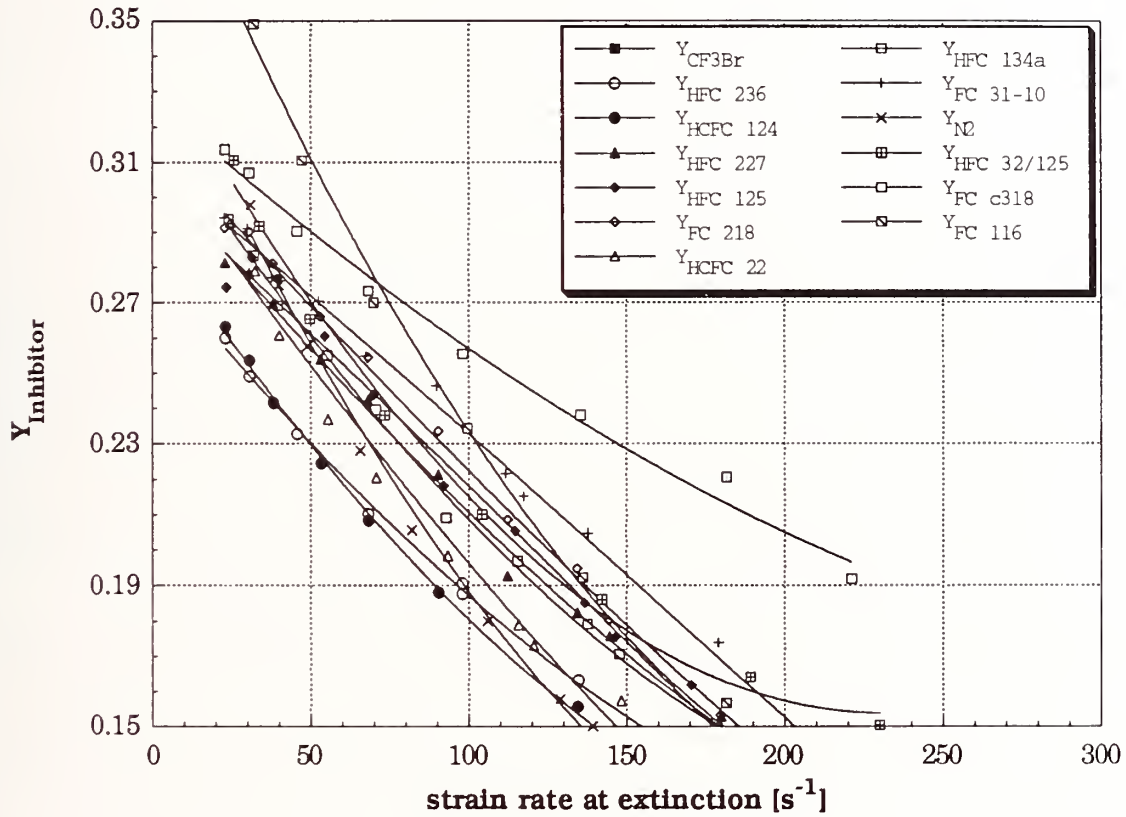

Figure 7. Mass fraction of various agents as a function of strain rate for heptane flames at extinction (expanded vertical scale), with an oxidizer temperature of 25 °C.

the agents tested were more effective than N_2 in extinguishing the flame, which is the inverse of the results when plotted versus mass fraction.

4.2.4.1 Impact of Fuel Type. Figures 9 and 10 show, respectively, the mass and mole fractions of the agents as a function of the strain rate at extinction for JP-8 flames. The oxidizer stream temperature was 25 °C. A comparison of Figures 8 and 10 shows that the JP-8 flames were somewhat easier to extinguish than the heptane flames. The average agent extinction concentration for the JP-8 flames was 65% to 93% of that required to extinguish the heptane flames over the range of strain rates, with the differences being greatest at the highest values of strain rate. The reasons for the variation of this value with strain rate is not clear.

4.2.4.2 Impact of Air Temperature. To clarify the influence of the initial temperature of the oxidizer on the critical conditions of flame extinction experiments were performed with the initial temperature of the air equal to 150 °C. Prior to performing these experiments, radial temperature profiles were measured in the apparatus without igniting the flame using thermocouples in the region between the exit of the gas duct and the surface of the liquid pool. The results are plotted in Figure 11, where the quantity DT refers to the difference between 150 °C and the measured value of the temperature, and *r* refers to the radial distance in millimeters from the axis of symmetry. Four sets of measurements were made: at the exit of the duct, 2 mm below the exit of the duct, and at approximately the position where the flame was stabilized above the surface of the liquid pool. The latter measurements were made with and without the pool covered with a thin metal sheet. All measurements were made with liquid heptane in the cup. The profiles near the exit of the duct show that the temperature is roughly 18 °C lower than 150 °C in the region near the walls of the duct. However, over a radius of approximately 15 mm from the axis of symmetry, the temperature was nearly uniform and differed from 150 °C by amounts less than 5 °C. The measurements made at the approximate location where the flame would stabilize showed that the radial temperature profile was relatively uniform. The values of the temperature measured with the pool covered were found to be lower than those measured with the uncovered pool, which was attributed to heat losses to the metal sheet. The temperature measurements clearly show the profile to be nearly uniform at the approximate position of the flame, and the value to differ from 150 °C by an amount less than 5 °C.

The relative mass-based effectiveness of the various agents differed slightly for different oxidizer stream temperatures. Figures 12 and 13 show the mass fraction of agent as a function of strain rate for heptane and JP-8, respectively, with an oxidizer temperature of 150 °C. A comparison of the results in Figures 12 and 13 with Figures 6 and 9, shows that an enhanced oxidizer temperature leads to flames which require somewhat more agent to extinguish. This result is consistent with theories of flame extinction. As more enthalpy is added to a flame, it is more difficult to extinguish. Figures 14 and 15 replot the data from Figures 12 and 13 in terms of agent mole fraction.

4.2.4.3 Powder Agent: Impact of Size. Figure 16 shows the mass fraction of $NaHCO_3$ powder with a nominal particle size of 10-20 μm in the oxidizer stream as a function of the strain rate at extinction. The fuel was heptane and the oxidizer stream temperature was 25 °C. For comparison the critical conditions of extinction measured with CF_3Br and N_2 added to the air stream are also shown. For measurements with $NaHCO_3$ powder, the experimental uncertainties are expected to be less than 30%. For any given value of *a,* the value of the mass fraction of $NaHCO_3$ required to extinguish the flame is lower than the mass fraction of CF_3Br and N_2. Therefore on a mass basis $NaHCO_3$ was more effective in extinguishing the flame than all the agents tested including CF_3Br. Figure 16 shows that at all values of the strain rate tested, the mass of $NaHCO_3$ powder required to extinguish the flame was a factor of three lower than that of CF_3Br. Figure 16 shows the mass

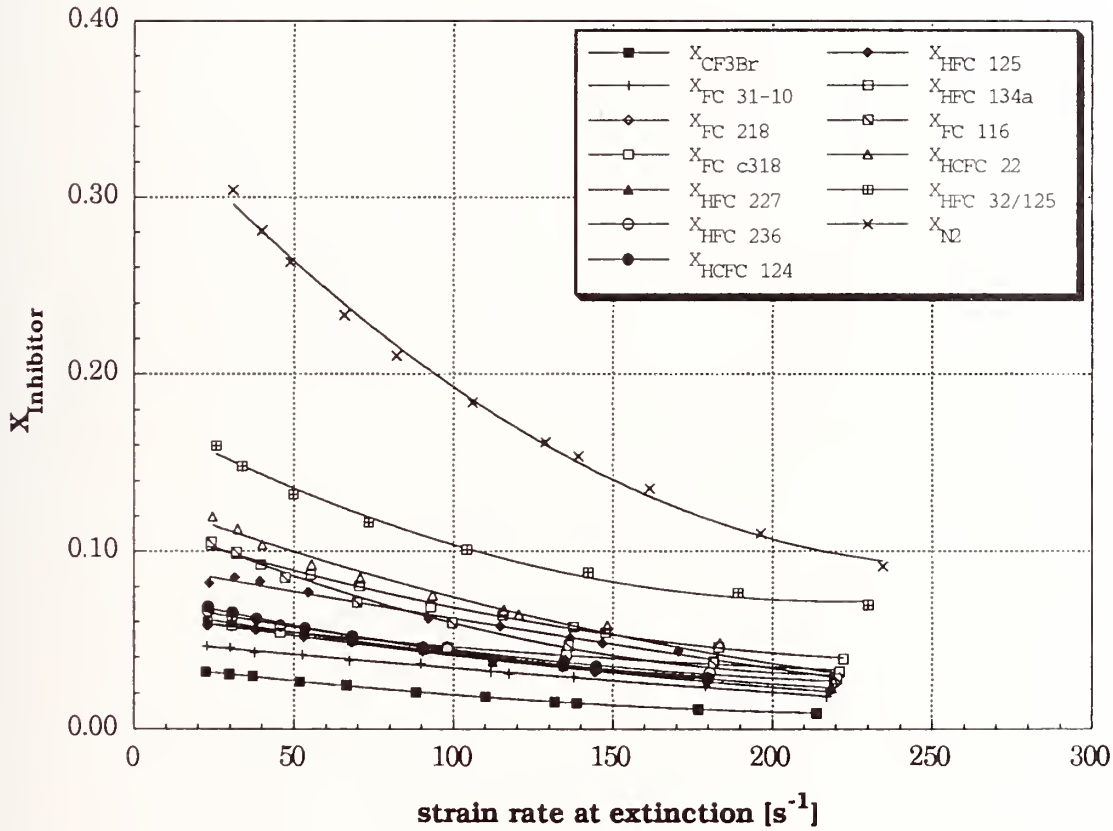

Figure 8. Mole fraction of various agents as a function of strain rate for heptane flames at extinction, with an oxidizer temperature of 25 °C.

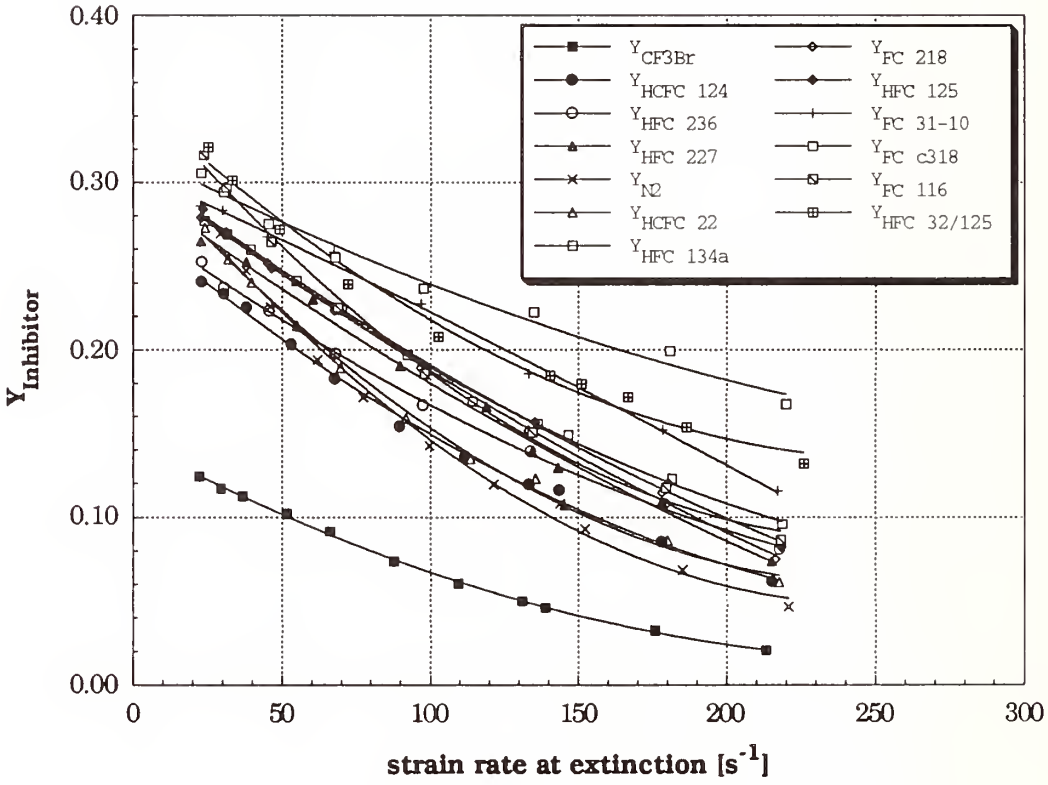

Figure 9. Mass fraction of various agents as a function of strain rate for JP-8 flames at extinction with an oxidizer temperature of 25 °C.

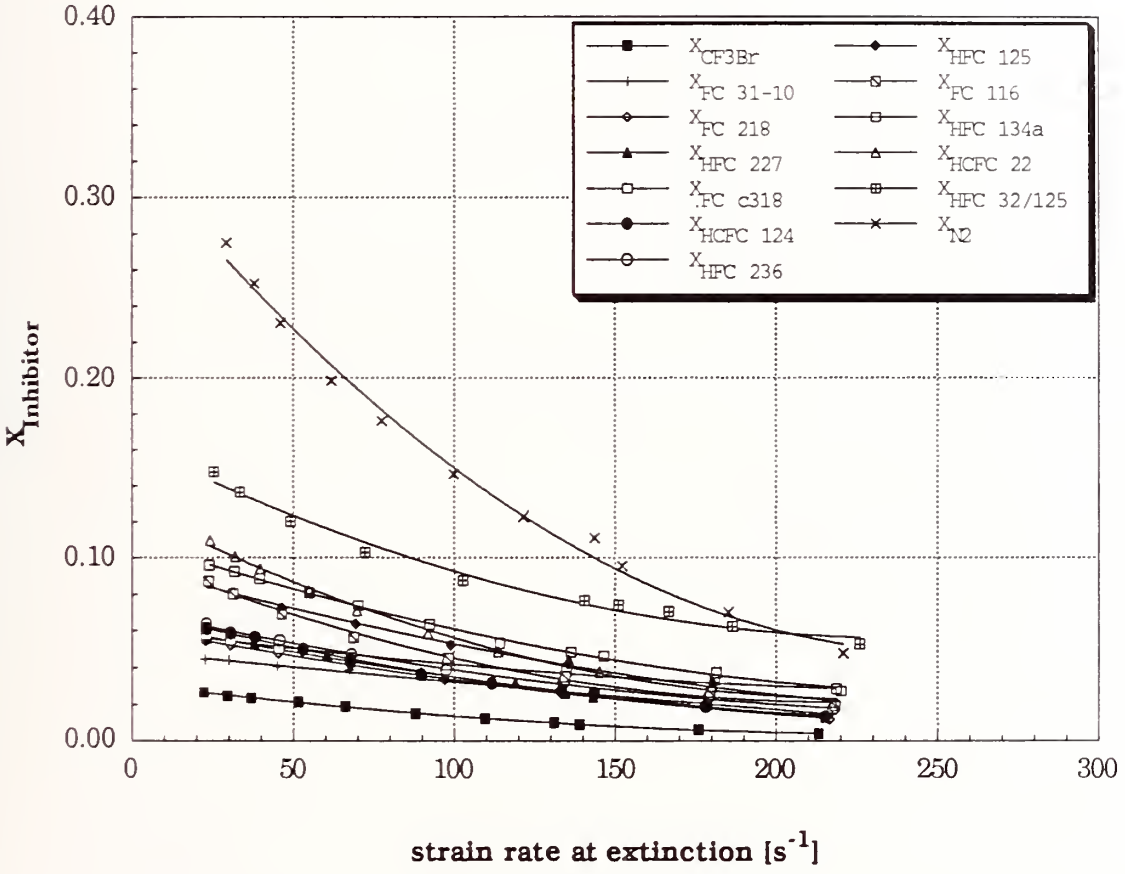

Figure 10. Mole fraction of various agents as a function of strain rate for JP-8 flames at extinction with an oxidizer temperature of 25 °C.

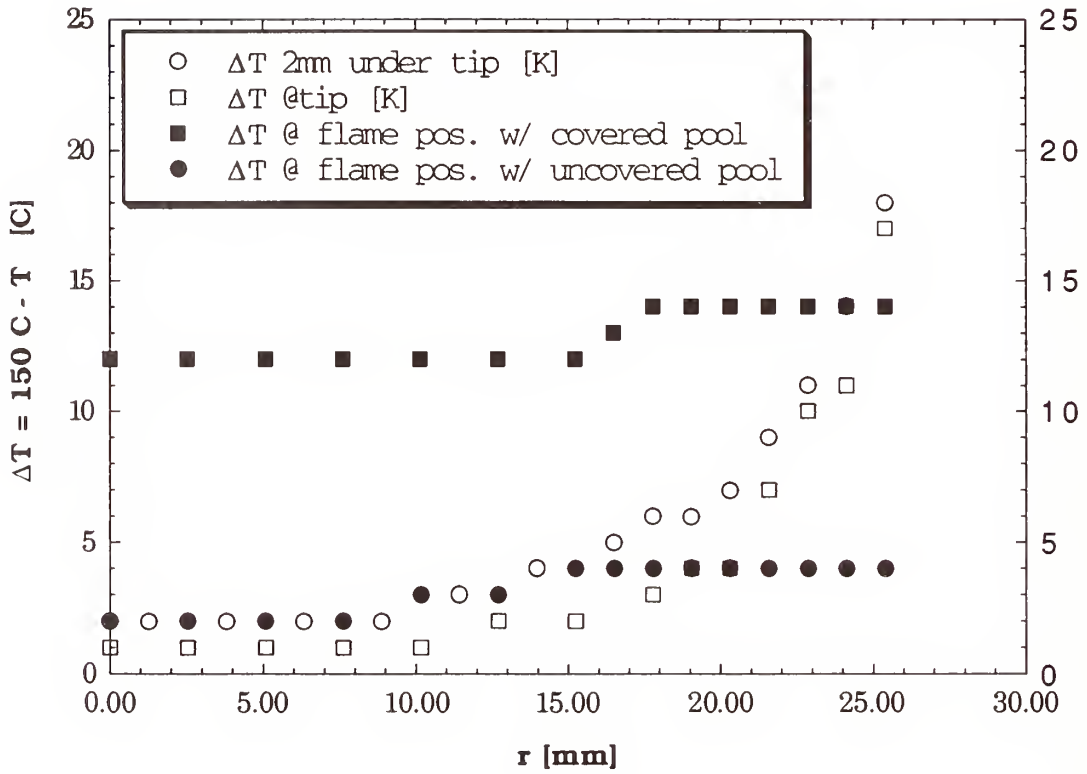

Figure 11. Radial temperature profiles measured without the flame at various locations at the region between the exit of the gas duct and the surface of the liquid pool for an oxidizer stream temperature of 150 °C.

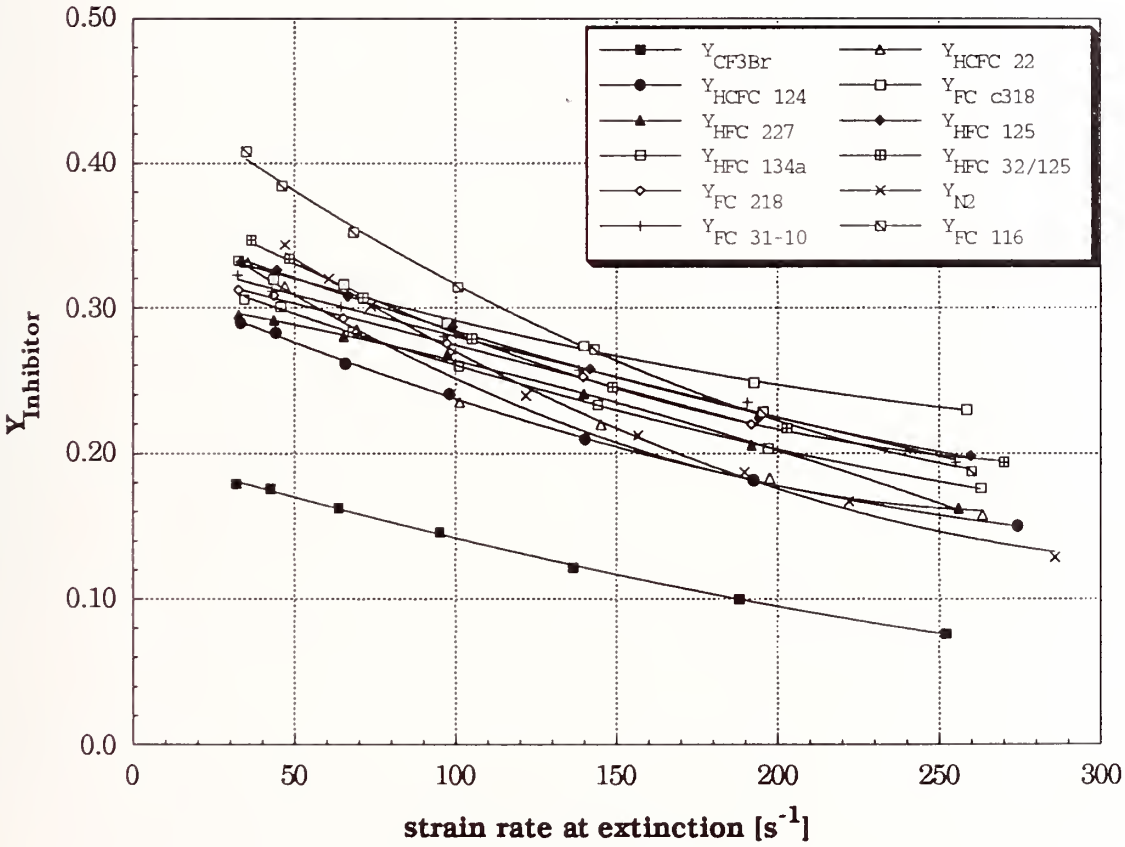

Figure 12. Mass fraction of various agents as a function of strain rate at extinction for heptane flames with an oxidizer temperature of 150 °C.

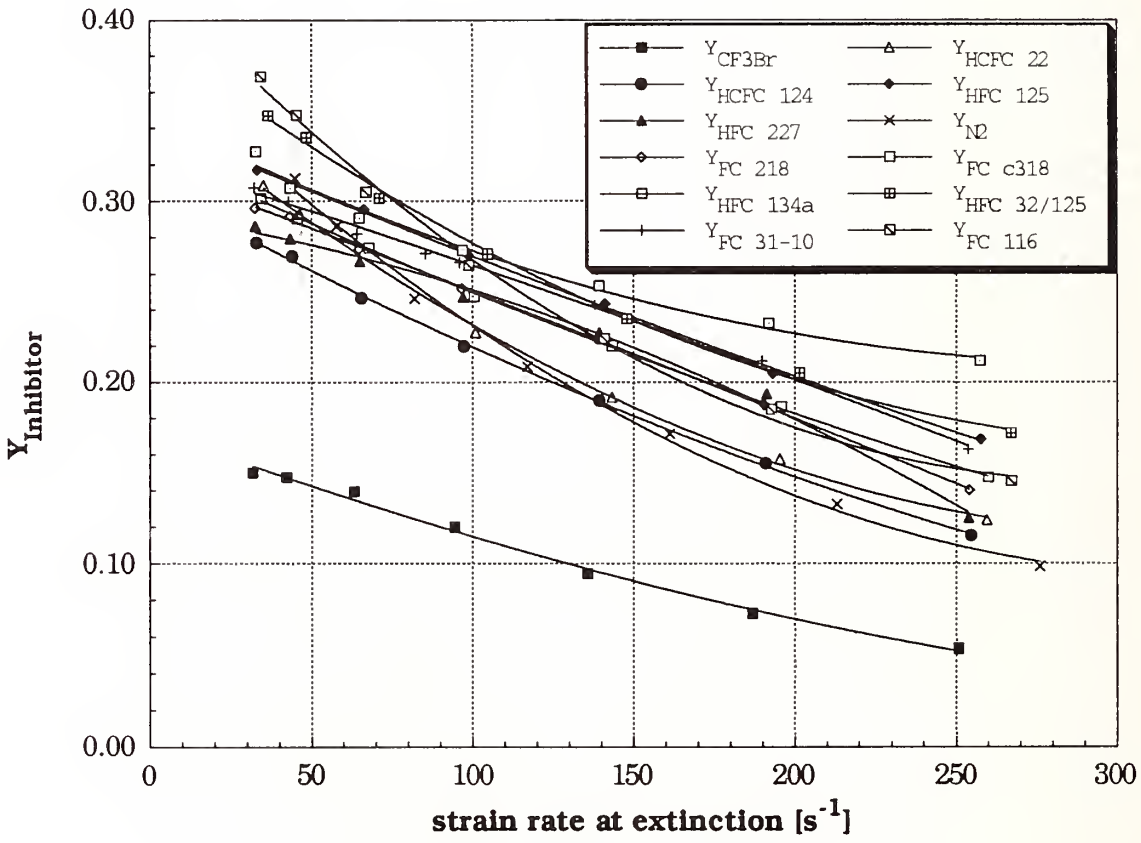

Figure 13. Mass fraction of various agents as a function of strain rate at extinction for JP-8 flames with an oxidizer temperature of 150 °C.

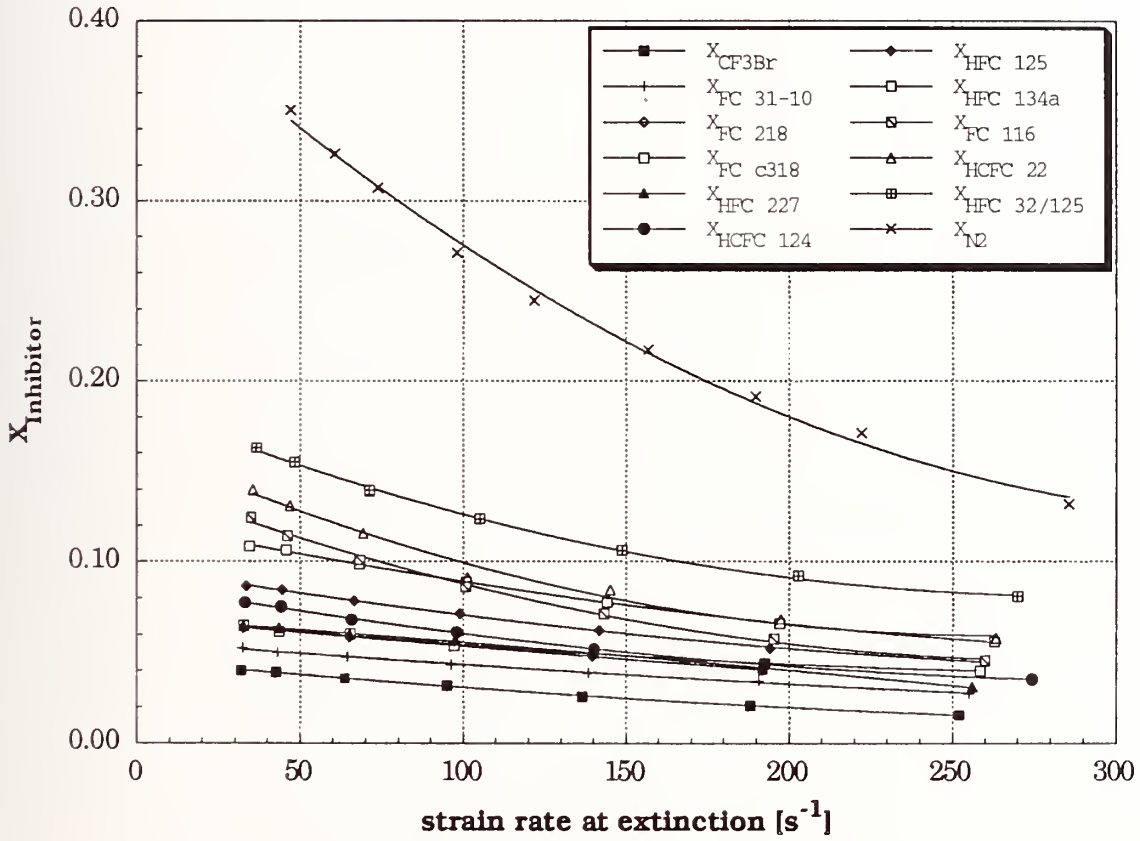

Figure 14. Mole fraction of various agents as a function of strain rate at extinction for heptane flames with an oxidizer temperature of 150 °C.

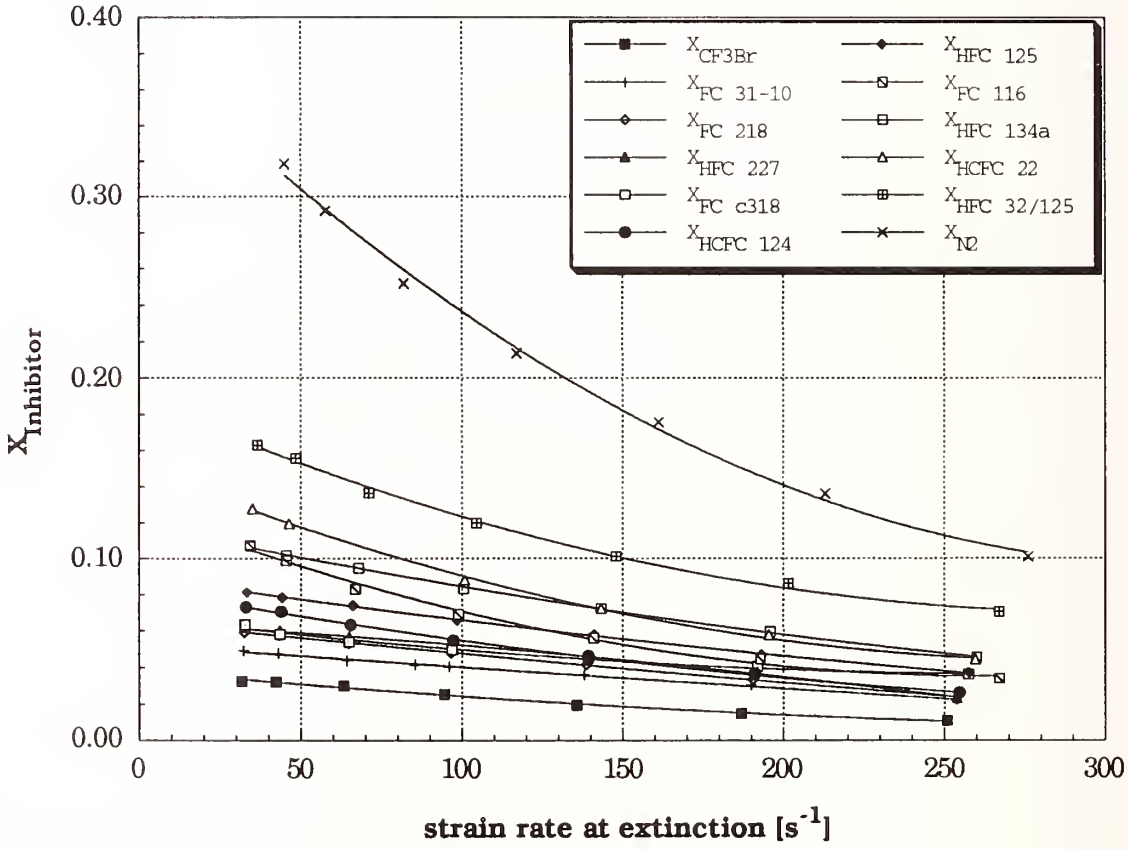

Figure 15. Mole fraction of various agents as a function of the strain rate at extinction for JP-8 flames with an oxidizer temperature of 150 °C.

fraction of $NaHCO_3$ powder (10 - 20 μm) in the oxidizer stream required to extinguish diffusion flames burning heptane and JP-8 as a function of the strain rate. The oxidizer stream temperature was 25 °C. Consistent with extinction data measured using gaseous agents, Figure 17 shows that at any value of the strain rate, the mass of $NaHCO_3$ required to extinguish JP-8 flames was less than that required to extinguish a heptane flame.

Figure 18 shows the influence of initial particle size of $NaHCO_3$ in extinguishing heptane flames. The initial temperature of the oxidizer stream was 25 °C and the nominal particles sizes tested were 0-10, 10-20, and 20-30 μm. The results show that particles between 0-10 μm were more effective than those between 10-20 and 20-30 μm. However, the results show that 20-30 μm particles were more effective than those 10-20 μm. Further studies are required to explain this observation.

4.2.5 Interpretation of the Experimental Results. As mentioned at the beginning of Section 4, in fundamental theories of flame extinction where the gas-phase chemical reaction can be approximated as a one-step process, changes in the value of the Damköhler number, D_n, can be used to qualitatively explain the results of the OFDF suppression experiments. For a given chemical system, flame extinction is predicted to occur at a well defined and experimentally reproducible value of the critical Damköhler number D_n* (Fendell, 1965; Liñan, 1974; Peters, 1982, 1984). The value of t_{chem} (and, hence, D_n) will depend on the relative concentrations of the various reactants including that of the agent and the local gas temperature, and the value of t_{flow} will depend inversely on the strain rate a. In the absence of temperature measurements at conditions close to flame extinction, the calculated adiabatic flame temperature T_f, can be used in Equation (1) to provide a rough measure of the characteristic chemical time. For flames near extinction, the value of t_{chem} decreases with increasing values of T_f for a fixed global activation energy.

The concentration of fuel, air, and agent at extinction in a heptane flame were used (from Figure 6) to calculate the adiabatic flame temperature, assuming complete combustion to stoichiometric amounts of CO_2 and H_2O, and frozen levels of inert agent. Figure 19 is a plot of T_f as a function of strain rate for each of the gaseous agents. The temperatures at extinction concentrations of CF_3Br are higher than the value of T_f calculated using the measured mass fractions of all other agents. Therefore for any value of t_{flow}, the critical conditions of extinction measured with CF_3Br yield values of t_{chem} which are smaller than those for the other agents. Hence the values of D_n* with CF_3Br is higher than the corresponding values of D_n* from the other agents. The values of T_f for N_2 suppression are 100 to 300 K lower than for CF_3Br. The temperatures for agents without chlorine are below nitrogen, and the two containing chlorine have slightly higher calculated temperatures. Since the nitrogen data are representative of a purely thermally acting agent, T_f can be used as a qualitative measure of the thermal versus chemical influence of the agent on the flame.

A global activation energy can be estimated from the theoretical value of D_n* found by performing an asymptotic analysis (Liñan, 1974; Peters, 1982, 1984; Krishnamurthy *et al.*, 1976) of the flame. Knowing the value of D_n at extinction from the analysis, and the flame temperature and strain rate from Figure 19, Equation (1) can be used to estimate the global rate coefficient k. Figure 20 is a plot of the natural log of a function (Krishnamurthy *et al.*, 1976) which is directly proportional to k (see Equation 1), versus $1/T_f$. (The value of T_f was calculated assuming that the agents were chemically inert.) The value of the E_0 for each of the agents can be estimated from the slope of the respective curves. For N_2, E_0 is 167 kJ/mole. Deviations of E_0 from this value for the other agents is a rough measure of the chemical influence of these agents. The value of E_0 calculated using extinction data with CF_3Br is equal to 894 kJ/mole, an unrealistically high value. Clearly the

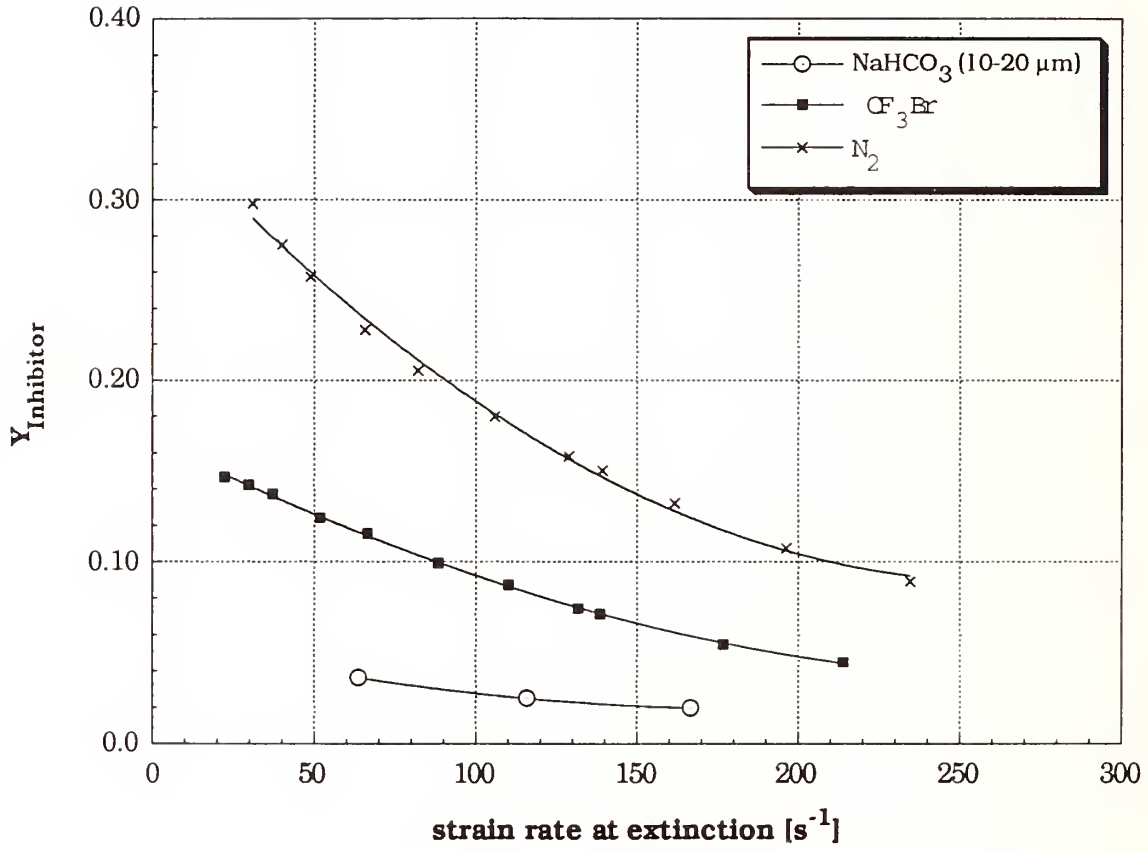

Figure 16. Mass fraction of $NaHCO_3$ (10 - 20 μm) powder in air as a function of the strain rate at extinction for heptane flames with an oxidizer temperature of 25 °C.

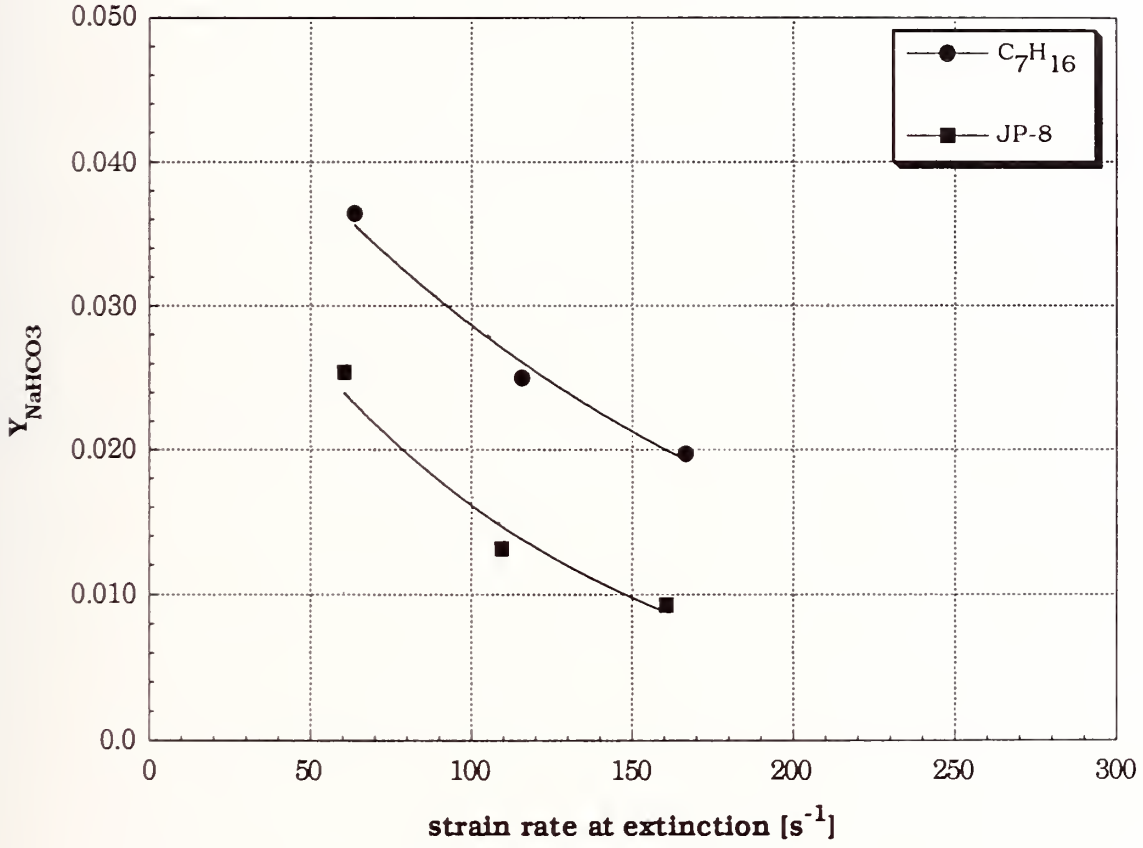

Figure 17. Mass fraction of $NaHCO_3$ (10 - 20 μm) powder in air as a function of the strain rate at extinction for heptane and JP-8 flames with oxidizer temperatures of 25 °C.

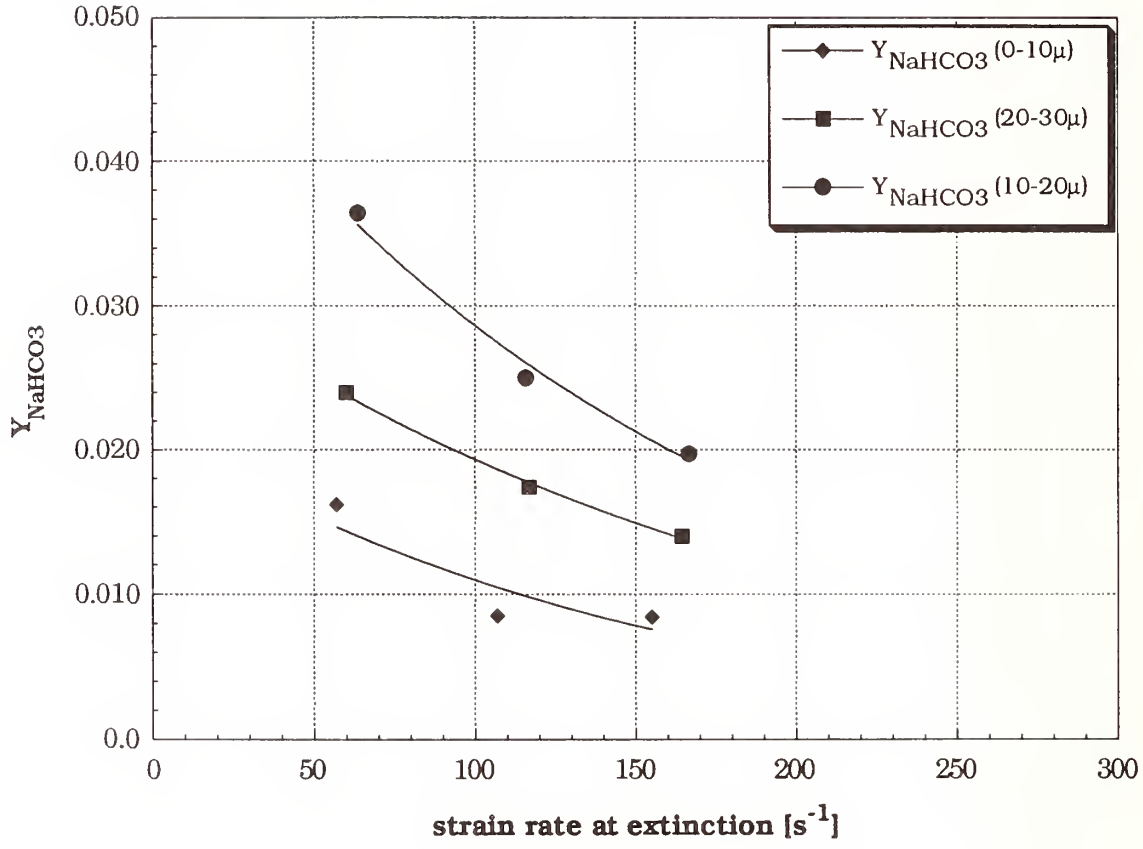

Figure 18. Mass fraction of $NaHCO_3$ (0-10, 10-20, and 20-30 μm) powder in air as a function of the strain rate at extinction for heptane flames with an oxidizer temperature of 25 °C.

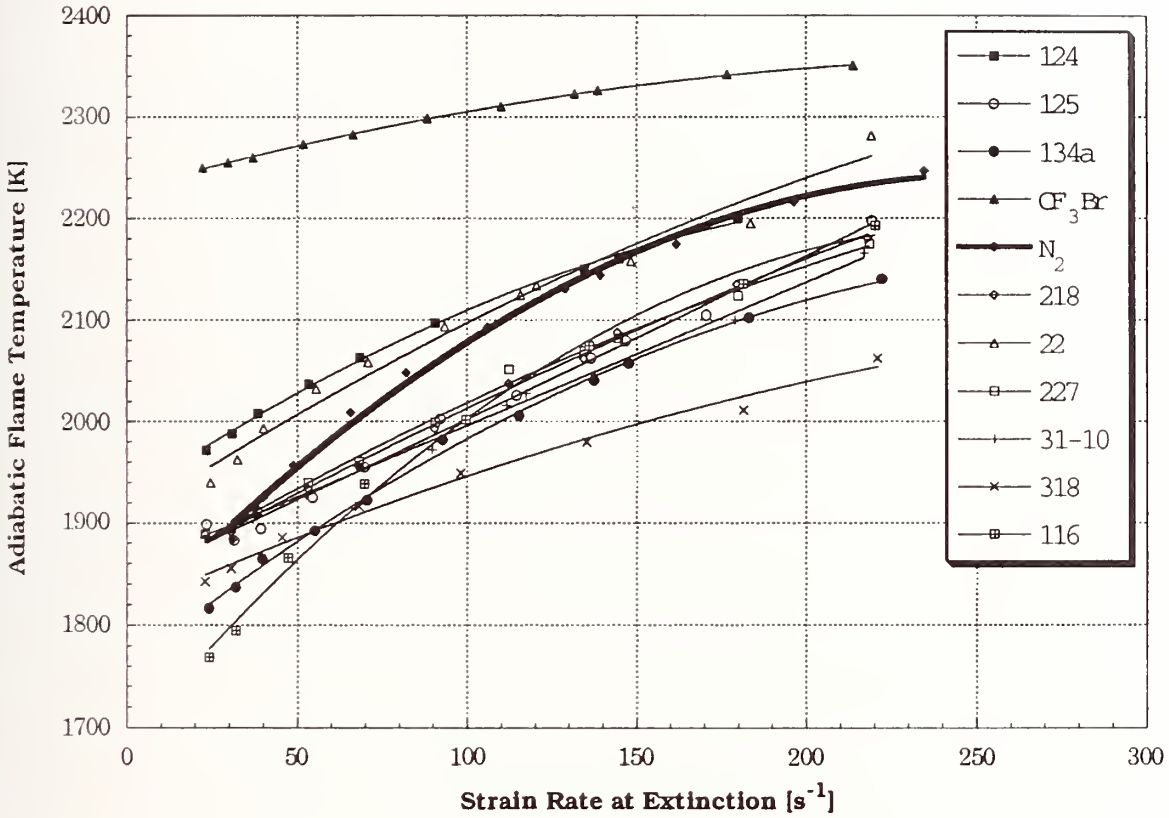

Figure 19. Calculated adiabatic flame temperatures at extinction assuming complete combustion of fuel and frozen composition of agent.

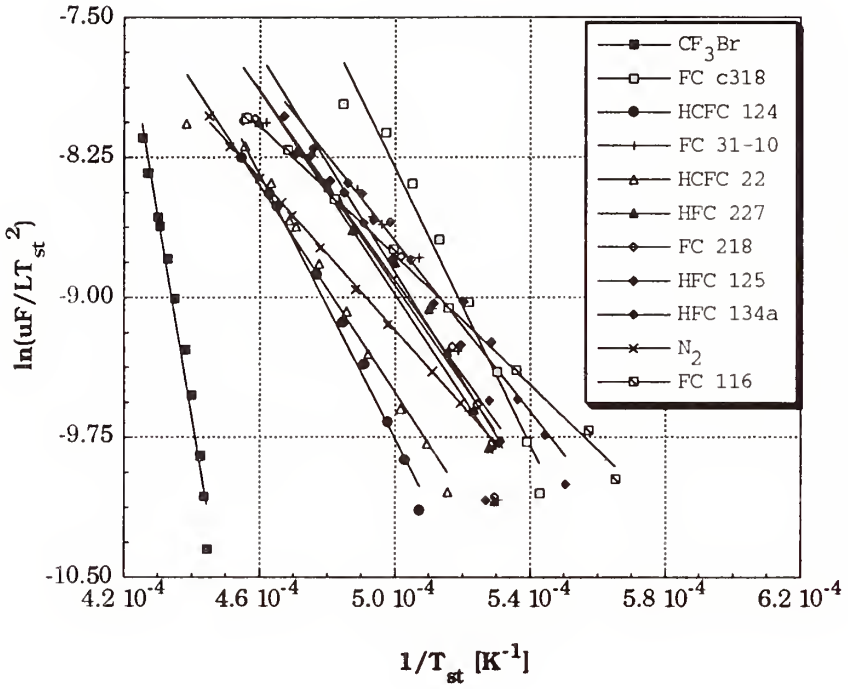

Agent	E_0 [kJ/mol]
CF_3Br	896
FC c318	310
HCFC 124	293
FC 31-10	243
FC 22	230
HFC 227	226
FC 218	218
HFC 125	214
HFC 134a	189
N_2	168
FC 116	142

Figure 20. Arrhenius plots obtained using the extinction data shown in Figure 6. The agents were considered to be chemically inert.

one-step approximation is not valid, and CF_3Br appears to be having a significant influence on the flame chemistry.

Figure 21 shows the adiabatic flame temperatures at different strain rates calculated assuming that the agents and stoichiometric fuel/air mixture react completely to N_2, CO_2, H_2O, HF, HBr, and HCl. The halogenated agents tend to have higher calculated temperatures in Figure 21 as compared to Figure 19 due to the enthalpy associated with conversion to the relatively stable acid gases, which implies that at least part of the chemical behavior exhibited by the agents may be related to simple conversion to equilibrium combustion products, HF and HCl. It is difficult to distinguish between the chemical and thermal influences of these agents on the flame because of possible differential transport effects. These effects are not accounted for in the current analysis.

4.2.6 Conclusions from OFDF Study. The opposed flow configuration was employed to determine the relative effectiveness of various inhibiting agents in extinguishing diffusion flames burning liquid heptane and JP-8. Eleven gaseous inhibiting agents and $NaHCO_3$ powder were tested. The oxidizing gas used in the experiments was a mixture of air and the inhibiting agent at initial temperatures of 25 °C and 150 °C. The following remarks summarize the major conclusions of the study:

1. The OFDF burner can be used to measure accurately the amount of a powdered agent required to suppress a variable strain-rate, laminar flame.

2. The strain rate, agent, fuel type and oxidizer temperature (in decreasing order of significance) all affect the amount of agent necessary to extinguish the opposed-flow diffusion flame.

3. The ranking of relative effectiveness of the various gaseous agents in quenching diffusion flames on a mole basis differs substantially from ranking on a mass basis, due to variation in molecular weight.

4. The rankings of relative mass- and mole-based effectiveness of the various agents are affected somewhat by the strain rate at which the tests are run, but only slightly by the fuel type (JP-8 or heptane) and the oxidizer temperature (25 °C and 150 °C).

5. On a mass or mole basis CF_3Br is considerably more effective in extinguishing the flame than all of the other gaseous agents tested.

6. On a mass basis at low strain rate HFC-236fa is most effective and FC-116 least effective of the gaseous alternatives, whereas at high strain rates HCFC-22 is most effective and FC-318 least effective.

7. On a mole basis, at low and high strain rates FC-31-10 is most effective and HFC-32/125 least effective of the gaseous alternatives.

8. Interpretation of the gaseous agent results based on one-step activation energy asymptotic theories shows that CF_3Br has a significant influence on the flame chemistry, and that the one-step approximation is not realistic. The results also show that all the agents except CF_3Br have a significant thermal influence on the flame. However, it is difficult to distinguish between the two influences accurately because preferential diffusion has not been considered. Further studies using detailed and reduced mechanisms are required to clarify the influence of the gaseous agents on the flame.

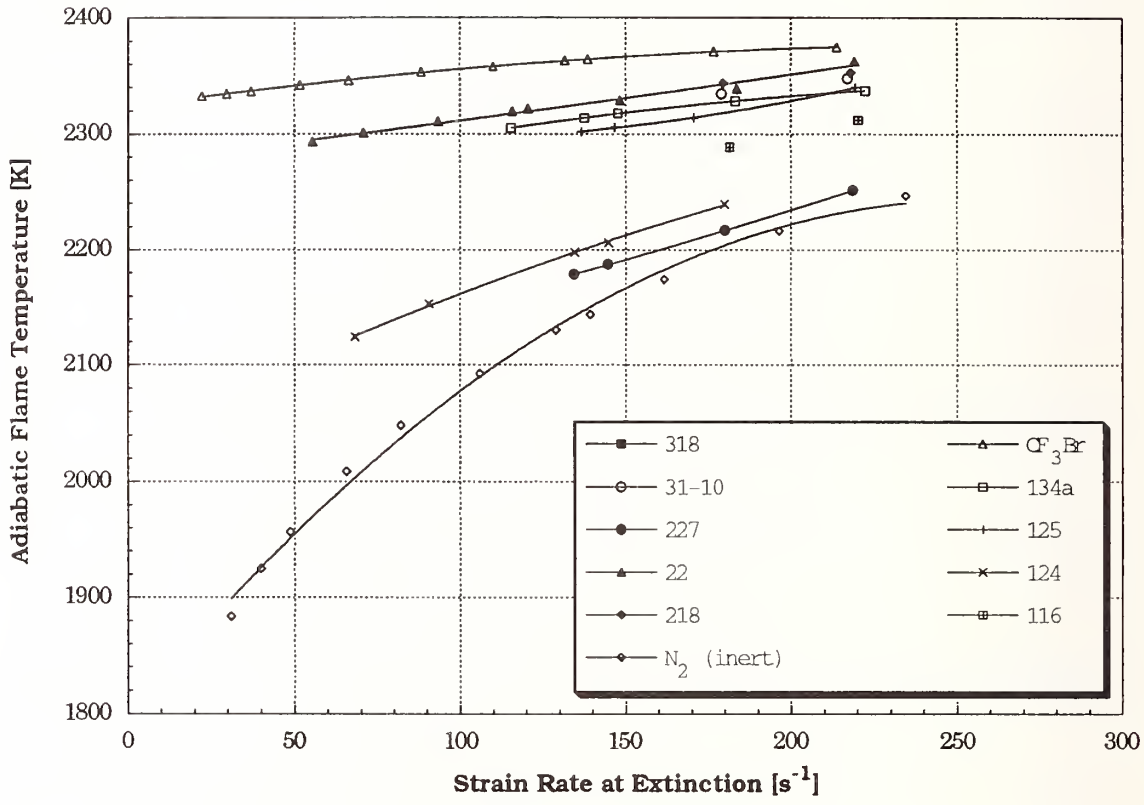

Figure 21. Calculated adiabatic flame temperatures as a function of extinction concentrations and strain rates assuming complete conversion of agents to CO_2, H_2O, HF, HCl, and HBr.

9. The effectiveness of $NaHCO_3$ powder on a mass basis is greater than that of CF_3Br; powder with 0-10 μm particles is more effective than the 20-30 μm, which in turn is more effective than the 10-20 μm. The mechanisms of flame extinction by powders are not well understood and merit further investigation.

4.3 Coflowing Nonpremixed Flames

4.3.1 Apparatus. An experimental study was conducted to rank the relative suppression effectiveness of various inhibiting agents on nonpremixed flames stabilized in a cup burner. The cup burner is a very common test apparatus for screening of suppressants. It is not, however, a standardized test method. A number of different size apparatus exist and various fuels and different air flows have been used (Gann *et al.*, 1990). Nevertheless, the experimental results from the different investigators have shown general agreement. The cup burner was selected as a test apparatus not to determine absolute extinction concentration data, but to rank the relative suppression effectiveness of the various agents. As such, it is an adequate test apparatus.

The concentration of gaseous agent in the oxidizer stream needed to obtain extinction was measured in the cup burner shown in Figure 22. The oxidizer, a mixture composed of dry air and agent, flowed through a 96 mm diameter chimney around a fuel cup. The cup had a 45° ground inner edge (28 mm diameter) and was used for both liquid and gaseous fuels. The ground inner edge minimized heat losses from the flame to the Pyrex cup. A fine wire mesh screen (40 mesh/cm) and small glass beads ($\approx$0.5 mm diameter) were placed inside the fuel cup for the gaseous fuel to flatten the velocity profile. The liquid fuel was gravity fed from a reservoir using a previously developed technique which facilitated an adjustable and constant level in the cup (Bajpai, 1974b).

Figure 23 is a schematic of the oxidizer flow control system. Compressed breathing air was dried by passing it through a two-stage filtering system composed of a silica gel water vapor trap followed by a particle trap. The flows of air and agent were monitored by rotameters which were calibrated with a dry test meter. Rotometer float and pressure readings were both measured. When sufficient agent was available, direct calibration was performed with that agent. Otherwise, an indirect calibration method was performed with dry air. Correction for density and viscosity differences were then applied to determine the flow. A series of tests were conducted with HCFC-22 to compare the precision of the two calibration methods. On average, the indirect method, calibrating with dry air, was within 3% of the direct calibration method. The values of gas viscosity (at 23 °C) for a number of test agents are listed in Table 4 (Reid *et al.*, 1977). For gases where data were not available (HFCs -125, -134a and -227, and HCFC-124) Reichenberg's corresponding states method was utilized. This method is described by Reid *et al.*, (1977). The method requires a number of physical parameters including the critical temperature, molecular weight and group contributions. For the mixture (HFC-32/HFC-125), Wilke's approximation was used. The critical temperatures are listed in Table 1 of Section 2.

4.3.2 Experimental Method

4.3.2.1 Gaseous Agents. A detailed experimental protocol was developed based on previous studies (Gann *et al.*, 1990). The fuel level was carefully set such that the ground lip of the pyrex cup was completely covered with fuel. The air flow was initiated and the flame was ignited with a torch.

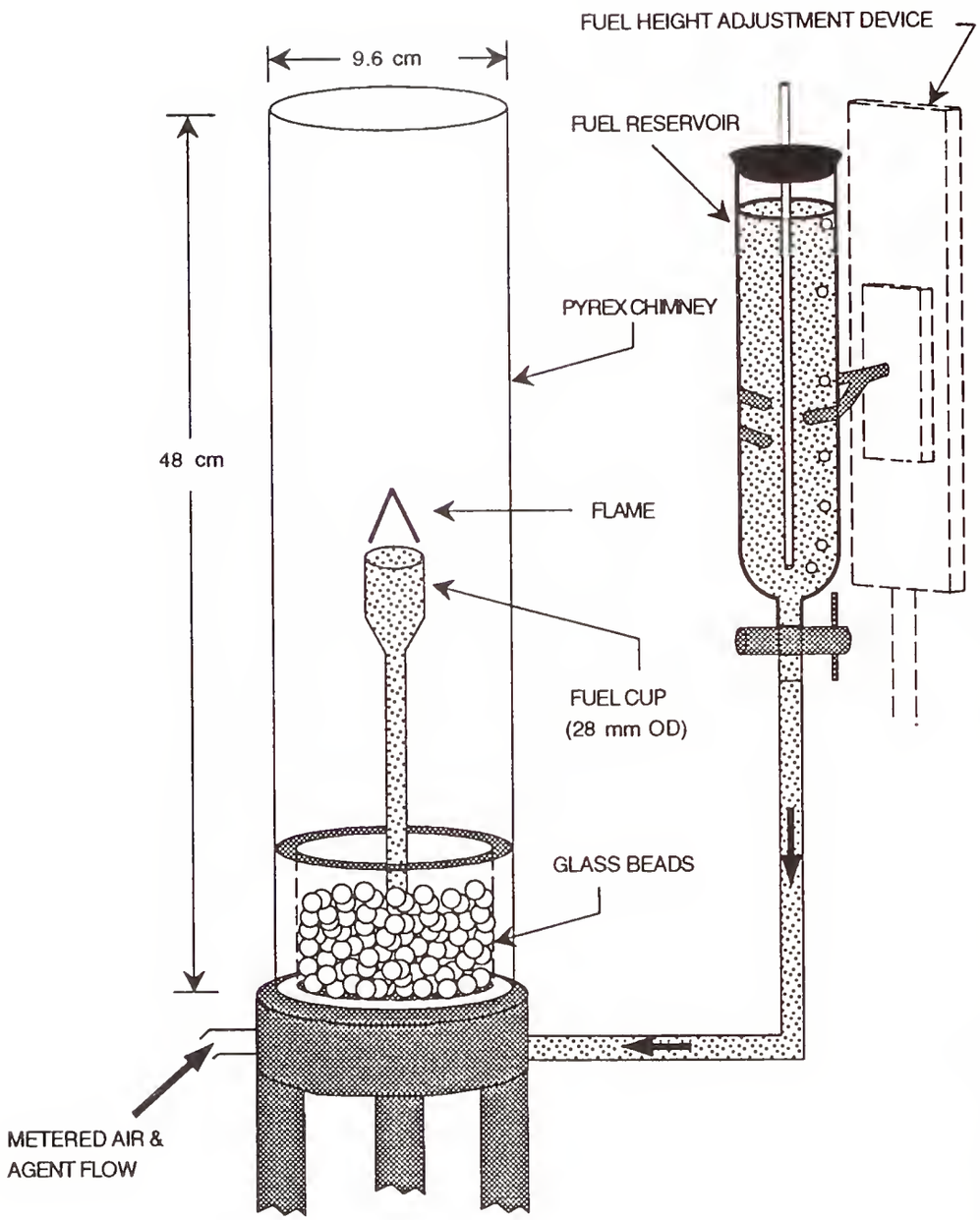

Figure 22. Schematic drawing of the cup burner.

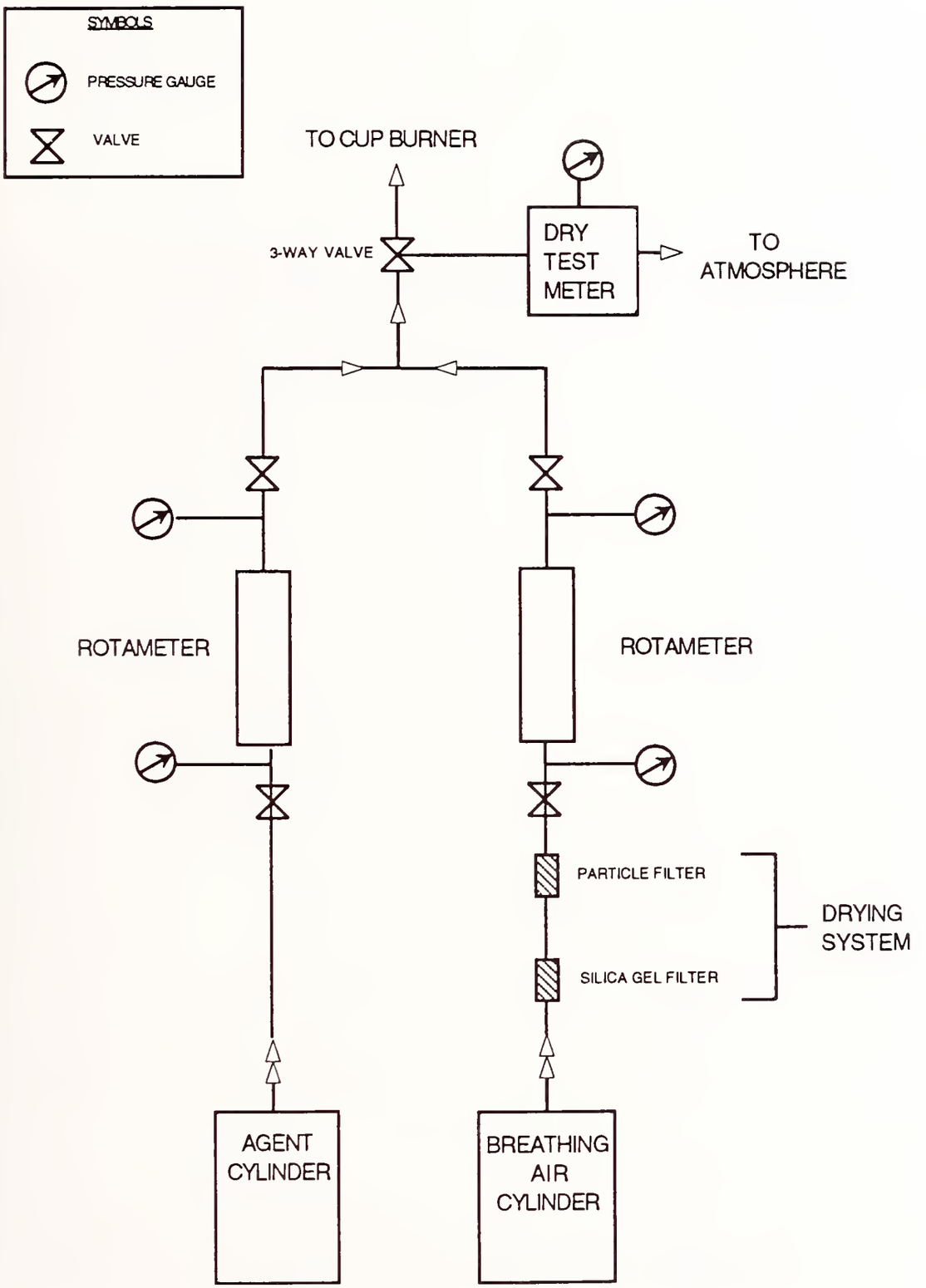

Figure 23. Schematic drawing of the oxidizer flow control system.

Table 4. Absolute Viscosity of Some Agents

Agent	Molecular Weight, g/mole	Absolute Viscosity @ 23 °C, N-s/m^2
HFC-32 (CH_2F_2)	52.1	1.20×10^{-5}
HFC-32/HFC-125 (CH_2F_2/C_2HF_5)	67.3	1.32
HFC-227 (C_3HF_7)	170.0	1.59
HCFC-22 (CHF_2Cl)	86.5	1.29
HFC-134a ($C_2H_2F_4$)	102.0	1.30
FC-116 (C_2F_6)	138.0	1.44
HCFC-124 (C_2HClF_4)	136.5	1.20
HFC-125 (C_2HF_5)	120.0	1.39
FC-128 (C_3F_8)	188.0	1.35
FC-31-10 (C_4F_{10})	238.0	1.25
1301 (CF_3Br)	148.9	1.55
1211 (CF_2ClBr)	165.4	1.36
FC-318 (c-C_4F_8)	200.3	1.18
CO_2	44.0	1.50
N_2	28.0	1.76
Ar	40.0	2.23
He	4.0	1.96
C_3F_6	150.0	1.36
HFC-236 ($CF_3H_2CF_3$)	152.0	1.22
SiF_4	104.1	1.60
C_2BrF_3	160.9	1.36
C_2F_3Cl	116.4	1.28
CF_4	88	1.72

Tests showed that the jet fuels and hydraulic fluids did not readily ignite without the use of a micro-torch. Once ignition occurred, the torch was immediately removed to prevent excess preheating of the Pyrex cup. The chimney was placed about the fuel cup. Figure 24 is a photograph of the flame in the cup burner. A 100 second warm up period was used prior to agent addition to minimize variation in apparatus heat-up during ignition. With the flame established, the agent concentration in the oxidizer stream was incrementally increased until the flame was extinguished. Agent was added to the oxidizer stream in small amounts ($< 1\%$ of flow needed to attain flame extinction), with a waiting a period from five to ten seconds between increases in the agent flow. This allowed time for the changing oxidizer flow to reach the burner and to impact flame stability. The flame was observed

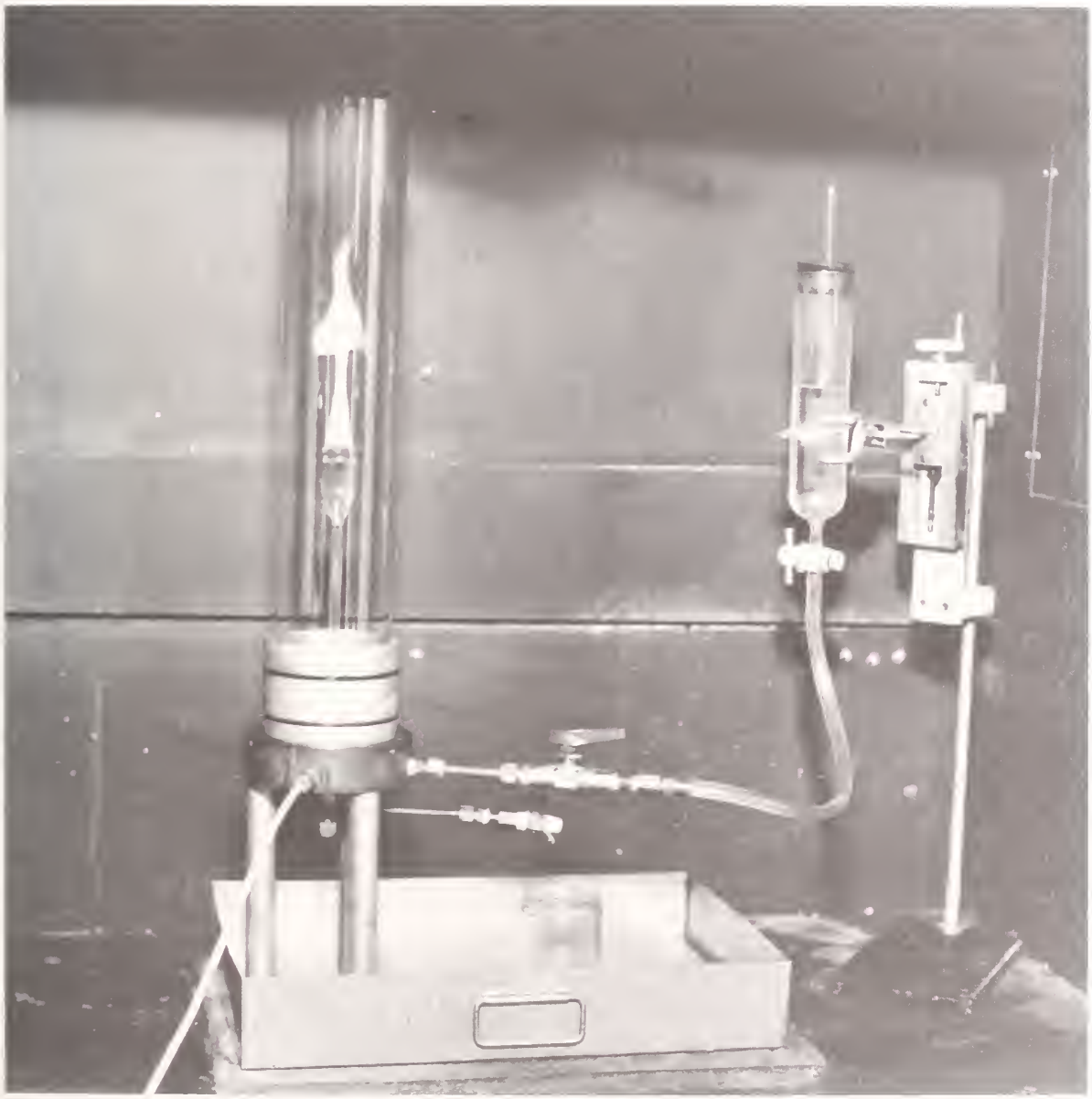

Figure 24. Photograph of cup burner and liquid fuel supply.

during this waiting period. After flame extinction was achieved, the used fuel was drained and the test was repeated several times (with fresh fuel each time) to insure experimental precision. Extinction tests were conducted on six fuels including one gas (propane) and five liquid fuels, which were heptane, two jet fuels (JP-5 and JP-8) and two hydraulic fluids (5606 and 83282) as shown in Table 1.

4.3.2.2 Liquid Agents. A liquid agent was introduced into the oxidizer stream using the delivery system shown in Figure 25. A regulated nitrogen stream flowed into a beaker containing the liquid agent, displacing the agent from the beaker into the heated oxidizer stream. The beaker holding the agent was situated in an ice-water bath. The flow of nitrogen was monitored using a calibrated flowmeter and a pressure gauge above the agent was observed. The liquid density at the bath temperature was needed to calculate the mass of agent addition to the oxidizer stream. The liquid agents CF_2Br_2 and CH_2BrCF_3 had densities of approximately 2.46 and 1.79 g/ml, respectively. A variable voltage regulator allowed control of the temperature of the heated oxidizer lines. A thermocouple above the glass beads inside of the chimney monitored the oxidizer temperature which was typically 10 to 15 °C above ambient. A test, described in Section 4.3.3, was conducted to substantiate the viability of the agent delivery method.

4.3.2.3 Sodium Bicarbonate Powder. The cup burner shown in Figure 22 was modified to foster a controlled, homogeneous flow of powder and to facilitate repeatable extinction measurements using powder agents. Figure 26 is a schematic diagram of the modified cup burner system. the system had five components: the cup burner, the air drying and control system, the powder feed system, the powder monitoring system, and the iso-kinetic sampling system used for calibration of the powder concentration.

A series of wire mesh screens (10 mesh/cm) functioned as flow straighteners. They were placed across the entire cross sectional area of the chimney, below the fuel duct, after cutting the chimney into several sections. Without these screens, non-homogeneous powder flow and recirculation zones were observed near the fuel cup. Flow visualization under non-combusting conditions showed that uniform upward flow was achieved for the powder/oxidizer dispersion for velocities greater than $\approx$ 9 cm/s.

The powder was introduced into the air stream by turning a 9 mm drill bit through a closed container of powder. The drill bit carried the powder through a 12.7 mm tube. The powder was fed into the oxidizer stream via a tee located just below the base of the cup burner where it was swept into the oxidizer flow. The delivery rate was controlled by a variable speed motor and a voltage regulator. Flow visualization showed that the 0-10 and 10-20 μm powder traveled through the chimney as a uniform bulk flow, whereas the 20-30 μm size fraction did not, for flows achievable in our laboratory. Thus, no powder testing was conducted with the larger size fraction. For the powder experiments, the air stream flow was maintained at 40 l/min (in the 96 mm diameter chimney).

The concentration of powder in the flow field at the time of extinction for locations near the flame was quantified by a laser transmission measurement in combination with iso-kinetic vacuum sampling and a wet chemistry technique - sodium ion analysis. The method assumes a uniformly seeded flow field. A 10 mW helium-neon laser beam (632.8 nm) was directed across a $\approx$7 cm chord of the pyrex chimney which traversed the flow field. The beam was positioned $\approx$ 2 cm below the fuel duct to avoid light attenuation by soot particles or other combustion products. The laser signal was monitored by a silicon photo-detector with a 10 nm bandwidth line filter and connected to a data acquisition system (4 Hz sampling rate). This allowed monitoring of the line-of-sight integrated $NaHCO_3$ concentration as a function of time. Increased powder concentration in the flow field was indicated by increased laser attenuation as represented by the following equation:

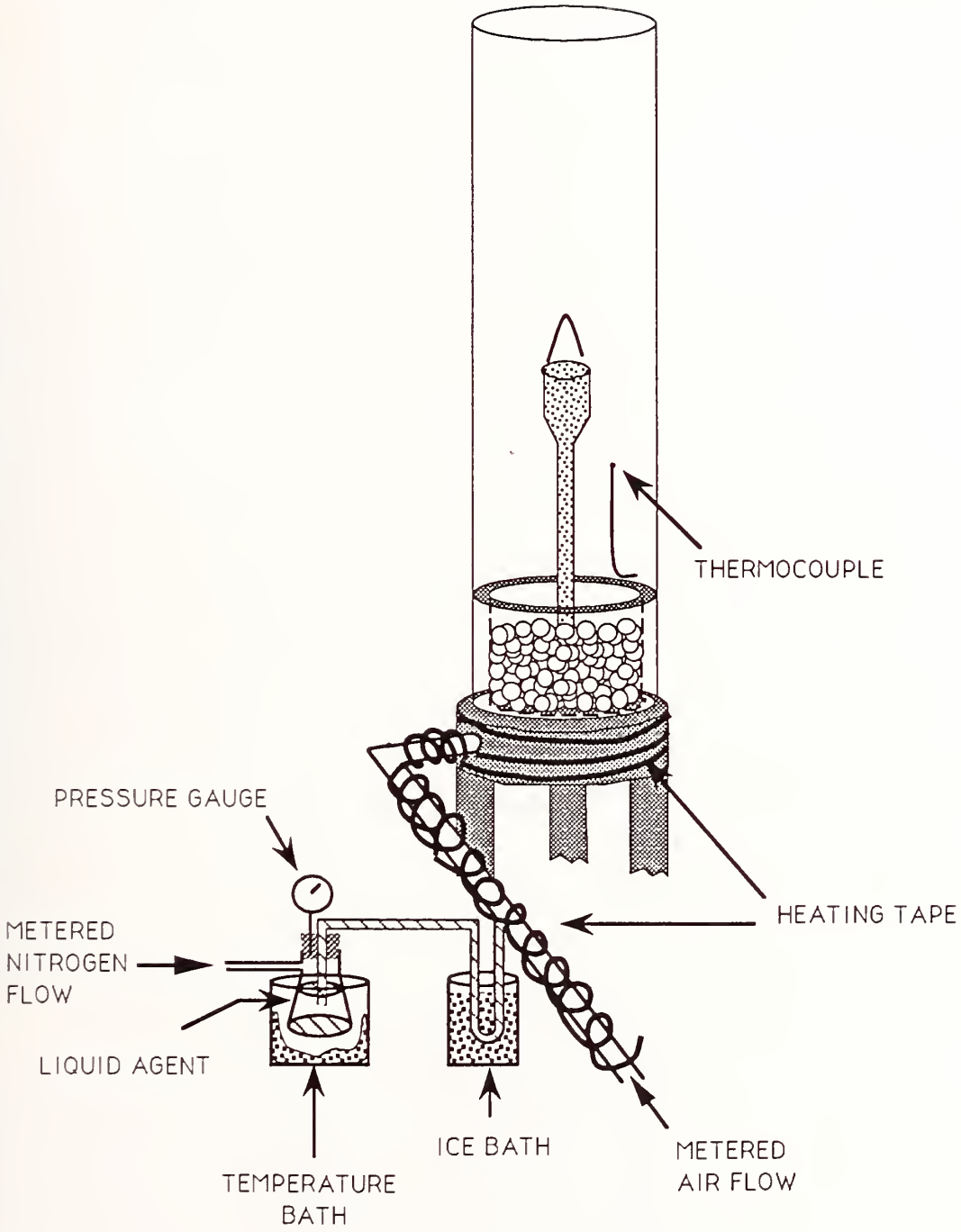

Figure 25. Schematic drawing of the cup burner modified for delivery of liquid agents.

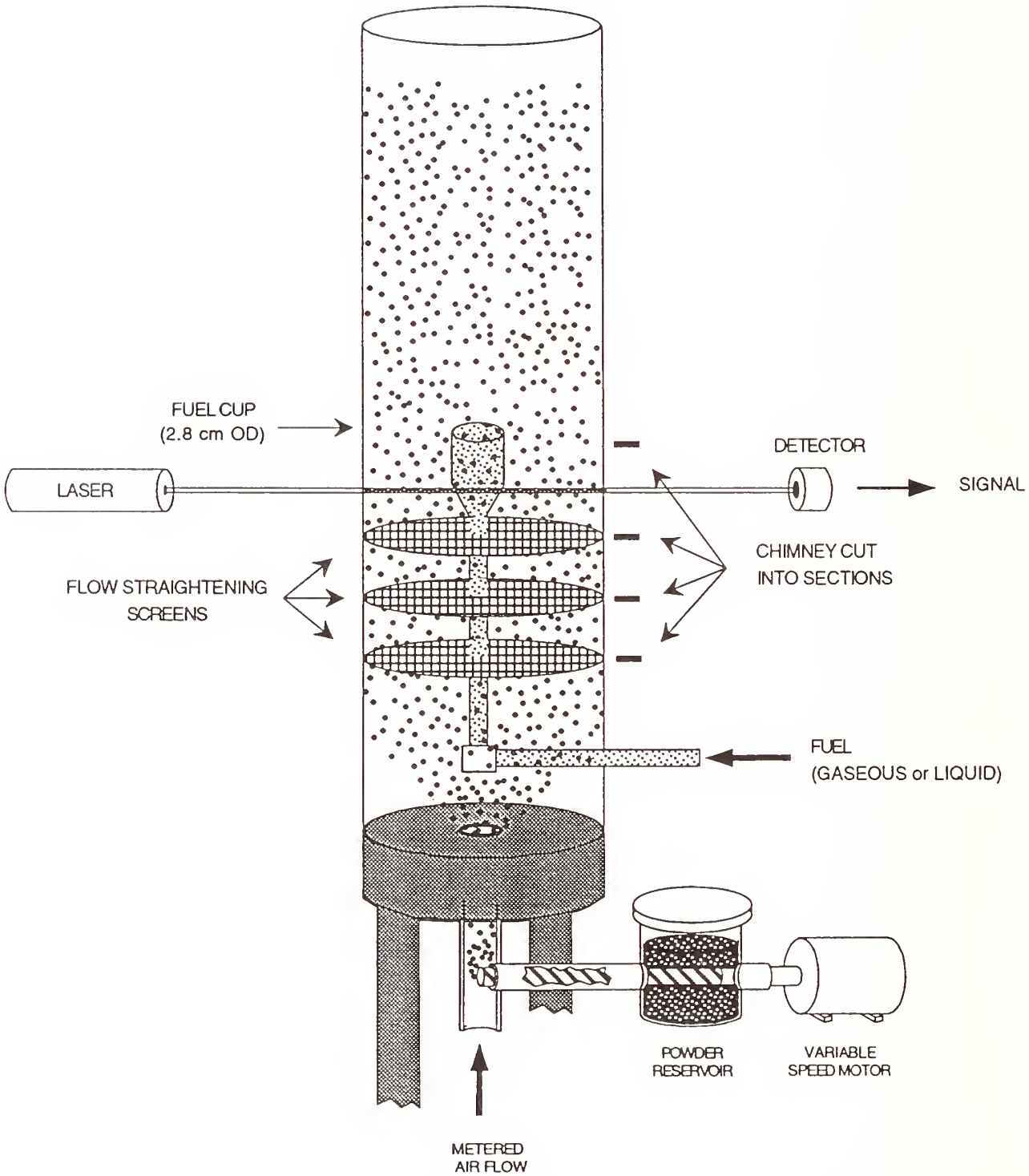

Figure 26. Schematic drawing of the cup burner modified for delivery of a solid powder.

$$\frac{I}{I_o} = \exp(-K \cdot [NaHCO_3] \cdot L) \quad (3)$$

where I_0 is the unattenuated laser signal, I is the attenuated signal, [$NaHCO_3$] is the powder concentration, L is the path length, and K is an absorption/scattering coefficient which is dependent on particle diameter, and shape as well as a number of other parameters. At the moment of flame extinction, a signal was sent to the data acquisition system, the laser transmission was monitored and the flow system was immediately shut off. This prevented further powder agglomeration on the chimney walls and allowed determination of the laser signal (I_0), unattenuated by powder in the flow field. Laser attenuation was related to mass percent of powder in the oxidizer by iso-kinetic vacuum sampling in combination with a sodium ion electrode/analysis system.

For calibration, small holes (2 mm) were drilled in the chimney for passage of the laser beam, eliminating the possibility of laser attenuation due to powder adsorption on the chimney walls. Flow visualization showed that a negligible amount of powder escaped through the orifices. During calibration, the top section of the chimney was removed and the probe/collection system was positioned at the plane defined by the rim of the fuel cup, where the flame was typically anchored. This avoided possible losses of powder to the chimney walls, which would have occurred if the sample was extracted at the top of the chimney.

Calibration of the $NaHCO_3$ mass flow in the oxidizer stream was determined by iso-kinetically sampling a portion of the $NaHCO_3$/air dispersion into a vacuum collection system while simultaneously monitoring the laser signal (I) for different powder loadings as shown in Figure 27. The absorption/scattering coefficient K was assumed to be invariant during the extinction and calibration measurements. The powder/oxidizer dispersion was iso-kinetically collected through a 20 mm diameter tube connected to a 20 l/min vacuum pump. The sample passed through $\approx$25 cm of polyvinyl tubing into a 200 ml glass impinger filled with deionized water which captured the water soluble powder particles. After approximately a 30 second sampling time, the sample probe and lines were washed with deionized water, combined with the impinger contents, and diluted with deionized water to 500 ml. A calibrated sodium ion-selective electrode was then used to determine the ion concentration in the powder/water solution. In this manner, a calibration curve was developed covering an appropriate range. Typically, 0.5 to 2 g of powder were collected over the sampling period, which was completely salable in the 500 ml water solution.

4.3.3 Assessment of Operating Parameters. A series of preliminary measurements tested the effect of a number of parameters on the agent concentration in the oxidizer stream at extinction. The parameters tested include the fuel cup diameter, the oxidizer flow, the chimney diameter, and the preburn time. The oxidizer flow was found to have a negligible effect on the concentration of agent at extinction, once a minimum flow was achieved, as seen in Figures 28 and 29 for N_2 and HCFC-22 suppressing JP-5, JP-8, 5605, and 83282 flames. The effect of varying chimney diameter (96 and 113 mm diameters) was also tested. The chimney size was found to have a negligible effect once a minimum flow velocity was achieved as shown in Figure 30 for HCFC-22 extinguishing 5606 and JP-8 flames. Two fuel cup diameters (12 and 28 mm) were tested as shown in Figure 31 and found to have a negligible impact on the agent concentration (HCFC-22) at extinction of JP-8 flames. Because fuel consumption in the two cups was expected to be different, this implies that the fuel burning rate had a minimal impact on the measured extinction concentration. In order to directly test this, flames burning a gaseous fuel (propane), where the fuel flow was an independently controlled experimental parameter, were used. The results presented in Figure 32 show only a small variation in

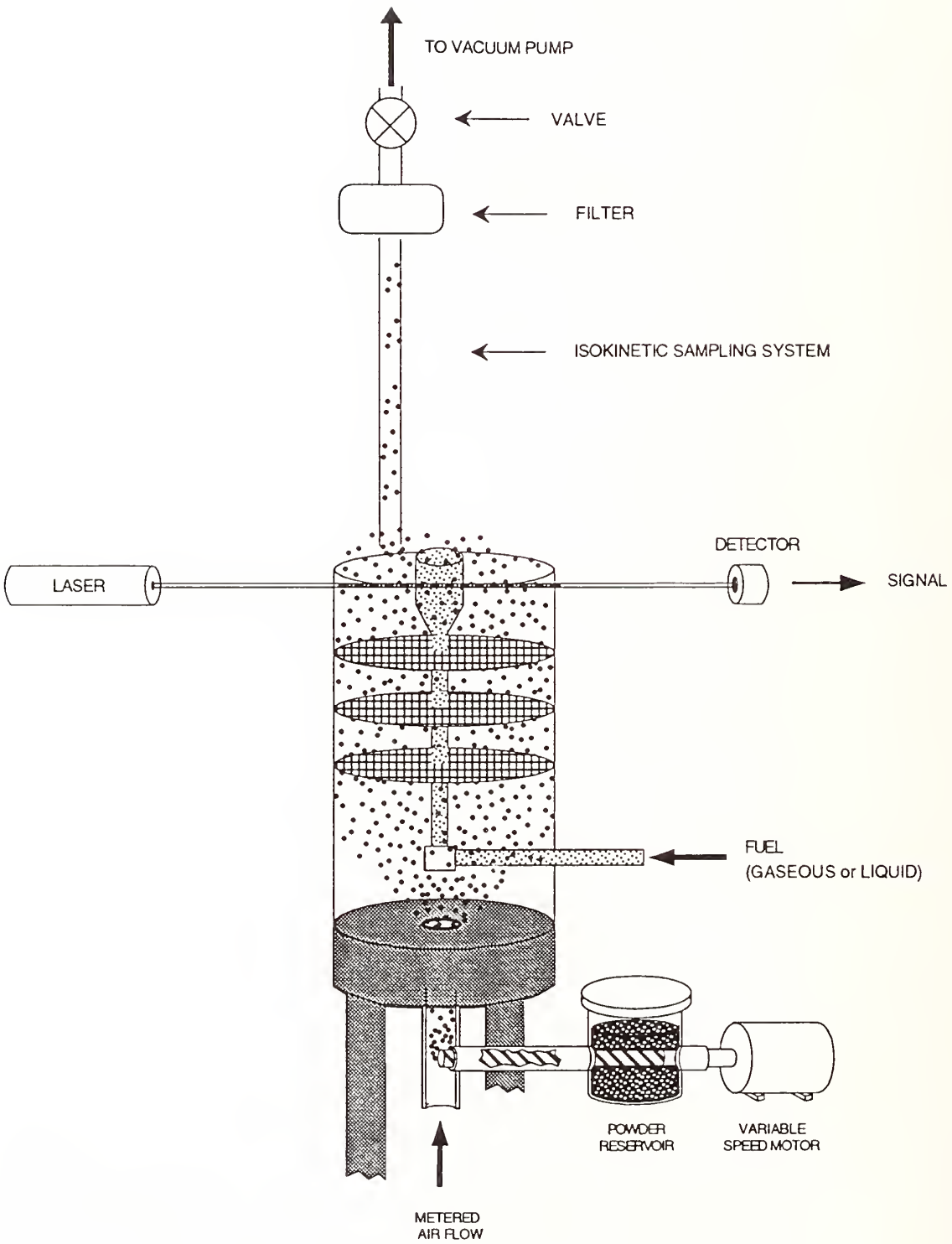

Figure 27. System used to calibrate powder flow in cup burner.

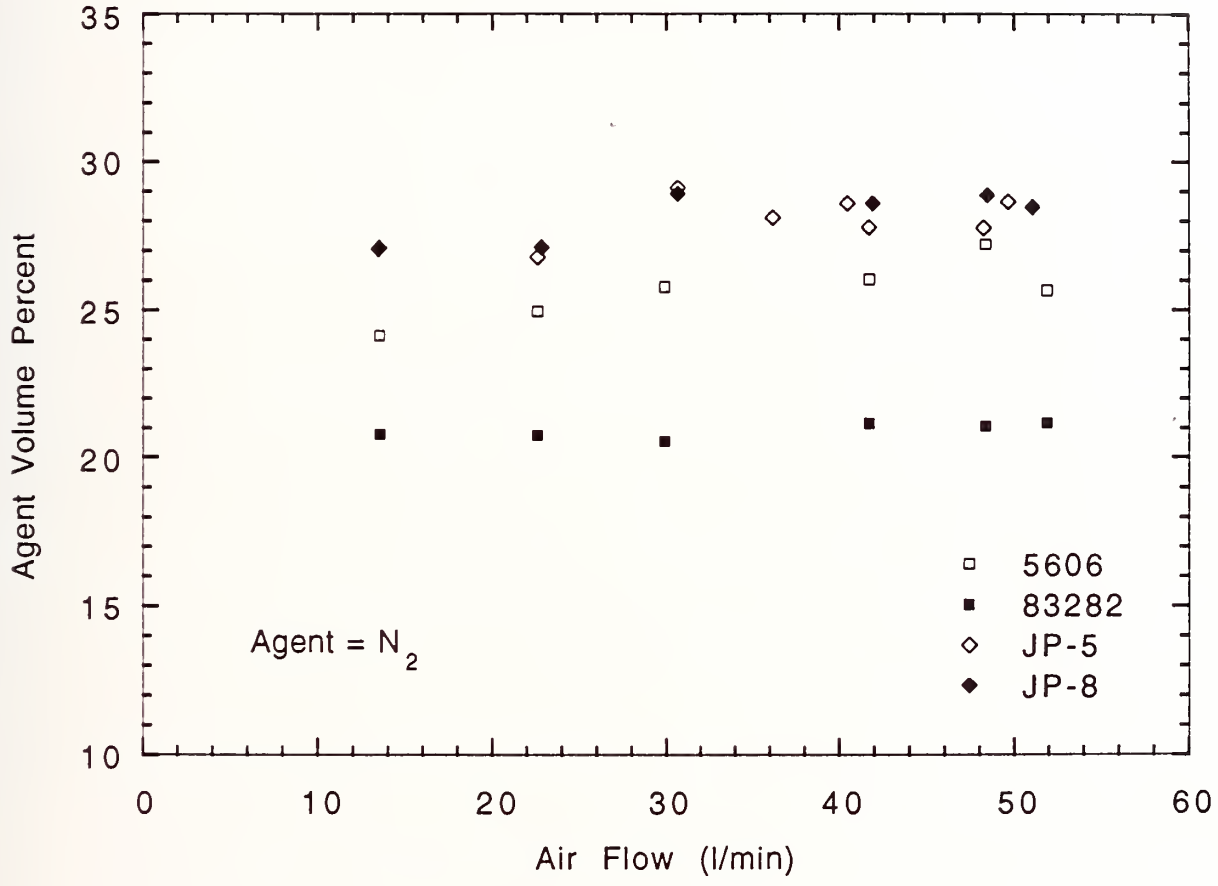

Figure 28. N_2 concentration at extinction as a function of air flow.

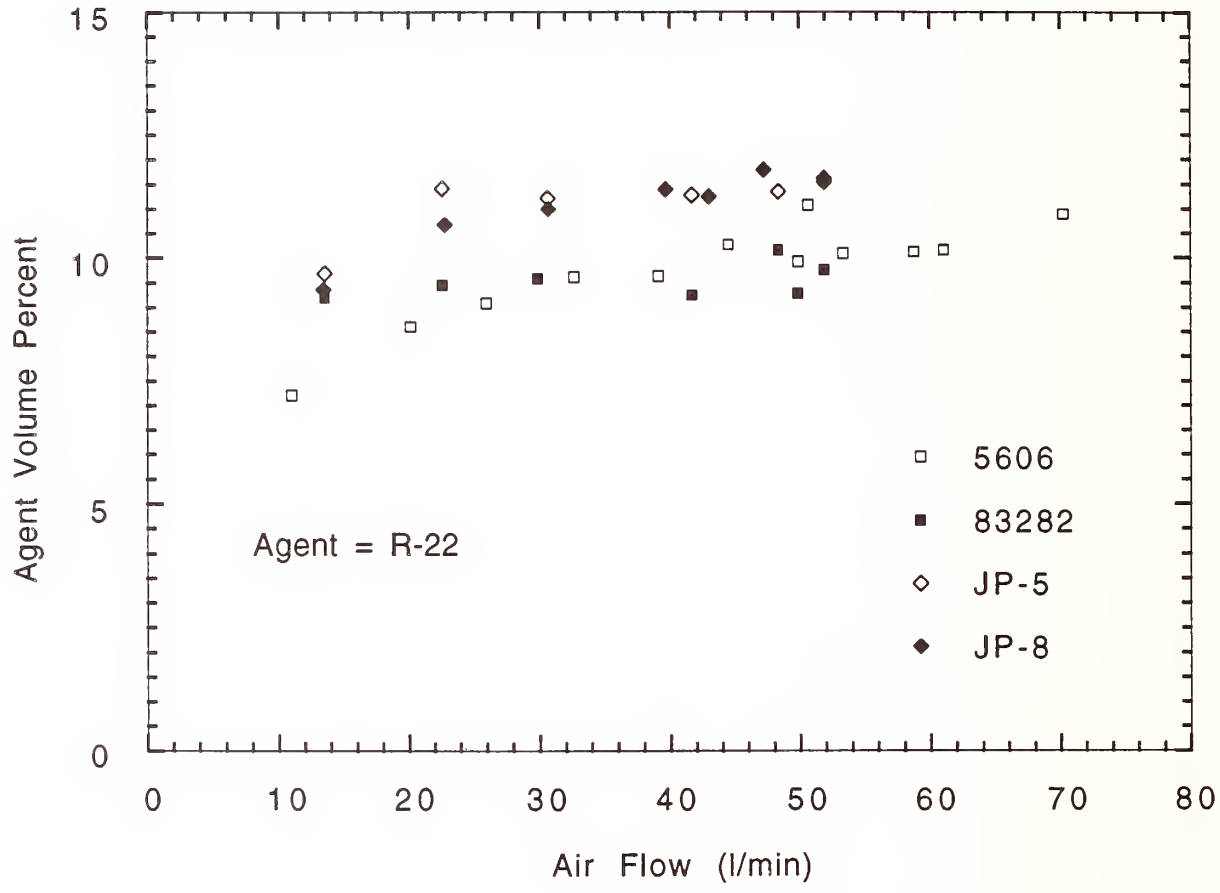

Figure 29. CHF_2Cl concentration at extinction as a function of air flow.

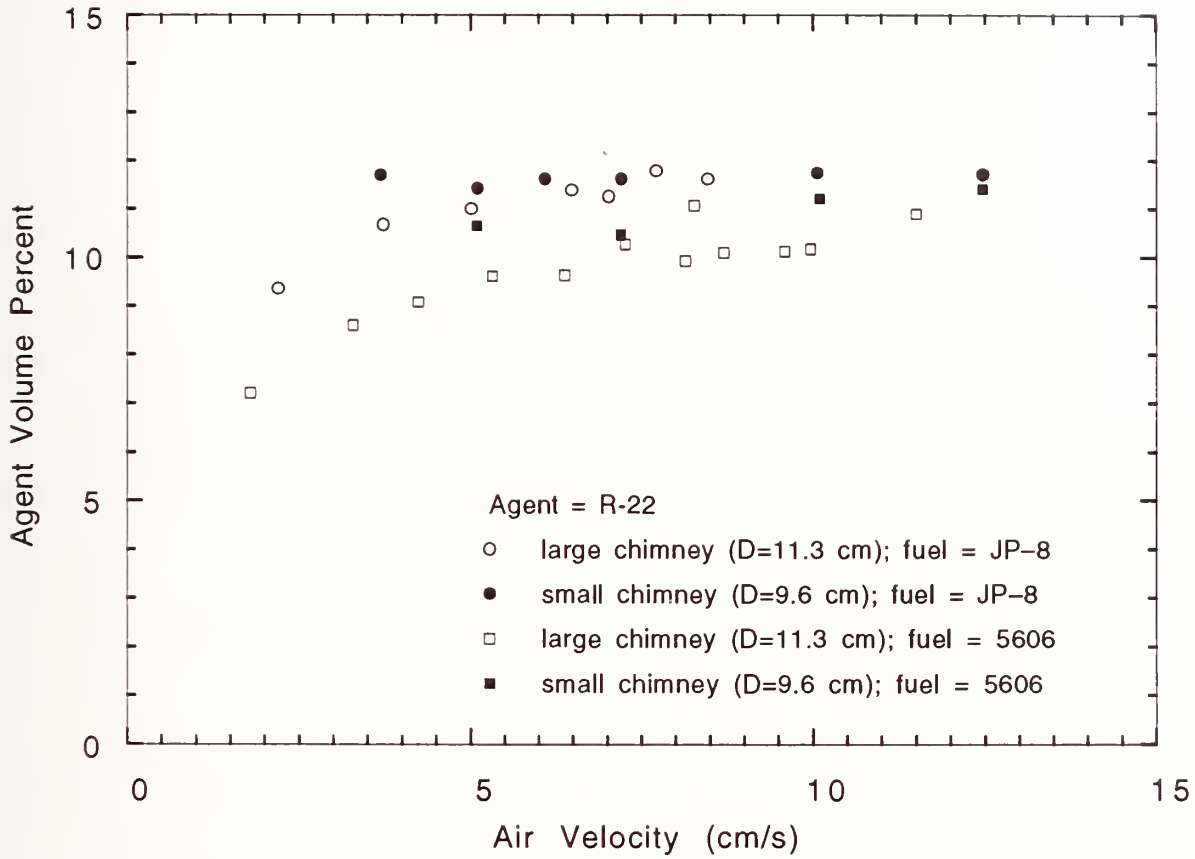

Figure 30. CHF_2Cl extinction concentration as a function of air velocity for different chimney sizes.

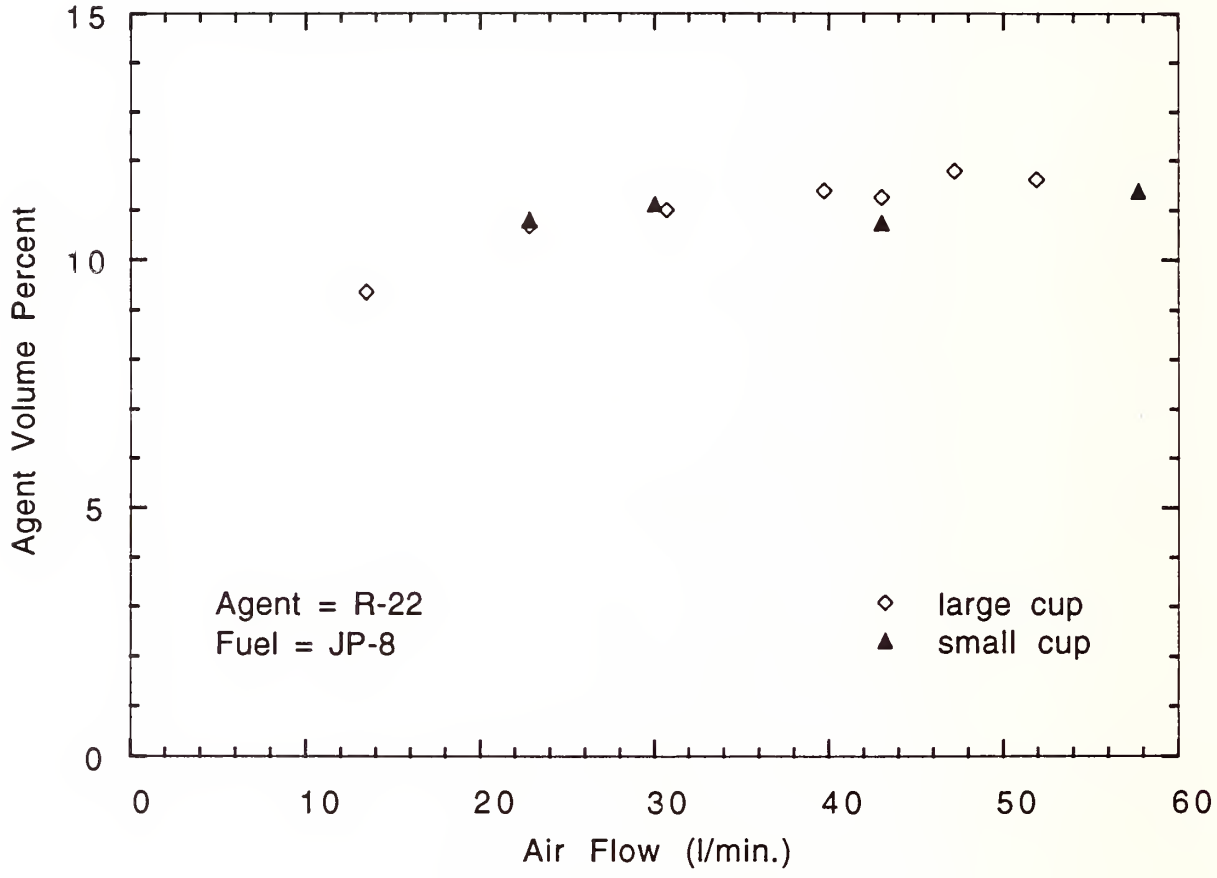

Figure 31. CHF_2Cl extinction concentration as a function of air flow for different fuel cup sizes.

the N_2 and HCFC-22 extinction concentration with the propane flow. In order to test if the global equivalence ratio was a factor in these results, a particular fuel flow (0.11 l/min) was used and the effect of increasing air flow on the agent extinction concentration was tested and found to be negligible. Thus, the fuel flow had only a small effect on the agent concentration at extinction. This effect may be related to flame liftoff and air/agent premixing with the fuel near the lip of the fuel cup. Further study is needed to investigate the mechanism responsible for these effects.

A number of the fuels contained multiple components. Thus, preferential distillation effects might have led to differences in the agent extinction concentration as a function of time after ignition. This effect was tested and found to be negligible for preburn times from 50 to 400 s. However, because the fuel burning rate was found to be unsteady at times less than 100 s, the experimental protocol required a 100 s preburn time after ignition and before agent was added. In addition, all extinction experiments were completed in less than 300 seconds. For all measurements, the 96 mm chimney was used. For the gaseous and liquid agents, an air velocity in the chimney of approximately 5 cm/s was used. For the extinction measurements with $NaHCO_3$, an air velocity of approximately 10 cm/s was used to insure that the powder travelled uniformly through the chimney.

Measurement variance and a propagation of error calculation considering the air and agent flows, yielded an estimate of the combined standard uncertainty in the gaseous agent concentration at extinction as $\pm$ 10%. The combined standard uncertainty in the measurement of the $NaHCO_3$ concentration at extinction was found to be approximately 25% on average and was always less than 40%. This value was dominated by measurement variance.

In order to test the impact of heating the liquid agent delivery system, the concentration of N_2 needed for extinction of a propane flame was tested with and without a heated (to 35 °C) oxidizer stream. The extinction concentration showed negligible difference.

As agents were added to the oxidizer stream the color of the flame changed. With the addition of an inert non-halogenated agent such as He or N_2, the flame lifted off the burner, became narrower and blue in color. With the addition of halogenated agents, the flame lifted off the burner, and became more intensely yellow in color for all of the fuels studied. At large agent concentrations, copious amounts of soot were produced, covering the pyrex chimney. A greenish luminosity was emitted from the flame when a chlorinated agent was used.

4.3.4 Experimental Results

4.3.4.1 Core Agents. Figure 33 shows the cup burner extinction results for N_2, CF_3Br and the core gaseous agents on a mole basis for flames burning propane, heptane, JP-8, JP-5 and the hydraulic fluids 5606 and 83282. The propane flames were the most difficult to extinguish, followed by heptane, the jet fuels, and the hydraulic fluids. The measurements compare favorably to previous results as shown in Table 5 for heptane flames. Consistent with our results, Hirst and Booth (1977) also found propane more difficult to extinguish than heptane. Cup burner extinction measurements using the jet fuels and the hydraulic fluids have not been previously reported.

The different agents in Figure 33 had dissimilar suppression effectiveness. For all fuels, CF_3Br was a highly effective suppressant as compared to the other gaseous agents, being approximately an order of magnitude more effective than N_2 in extinguishing the cup burner flames. Other agents had intermediate effectiveness as compared to halon 1301 and N_2. On a mole basis, the larger molecular weight FC, HFC, and HCFC compounds had a higher suppression effectiveness. The most efficient agent was C_4F_{10}, followed by cyclo-C_4F_8, C_3F_8, and C_3HF_7. The chlorinated agents (CHF_2Cl and $CHFClCF_3$) did not exhibit flame suppression behavior superior to the non-chlorinated agents.

Figure 34 replots the mole based results shown in Figure 33 on a mass basis. The most efficient gaseous agent was halon 1301 requiring approximately 15% by mass in the oxidizer stream to

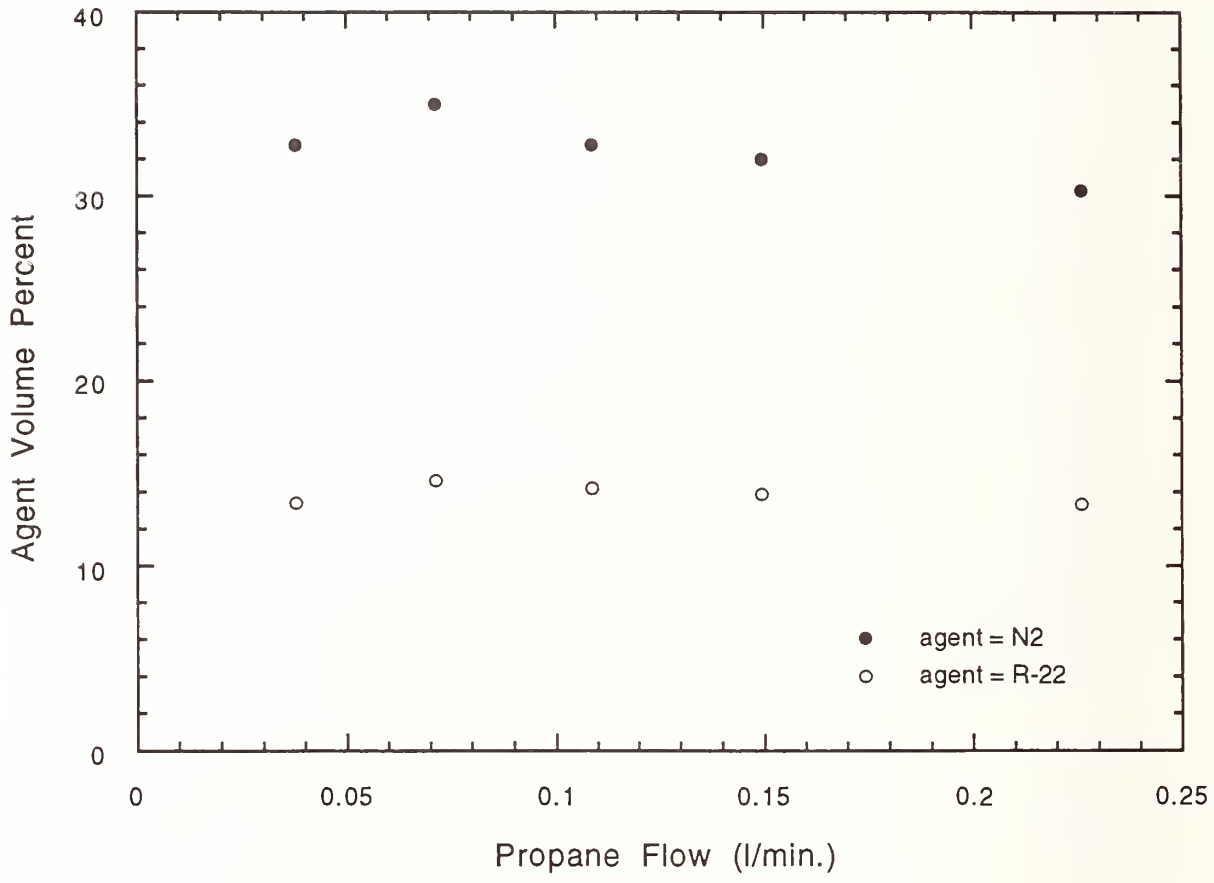

Figure 32. N_2 and CHF_2Cl extinction concentration as a function of the propane fuel flow rate.

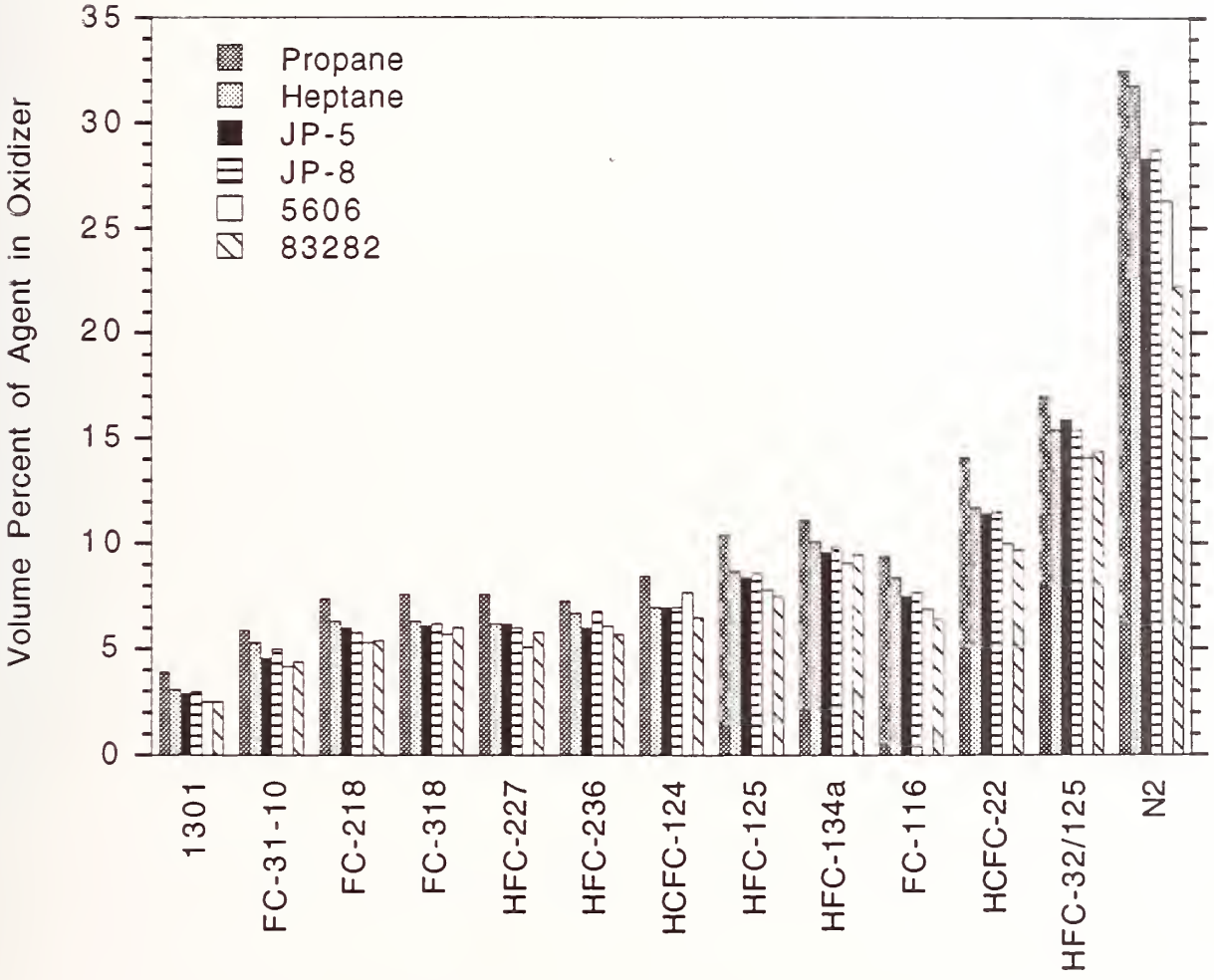

Figure 33. Agent (volume percent) concentration at extinction.

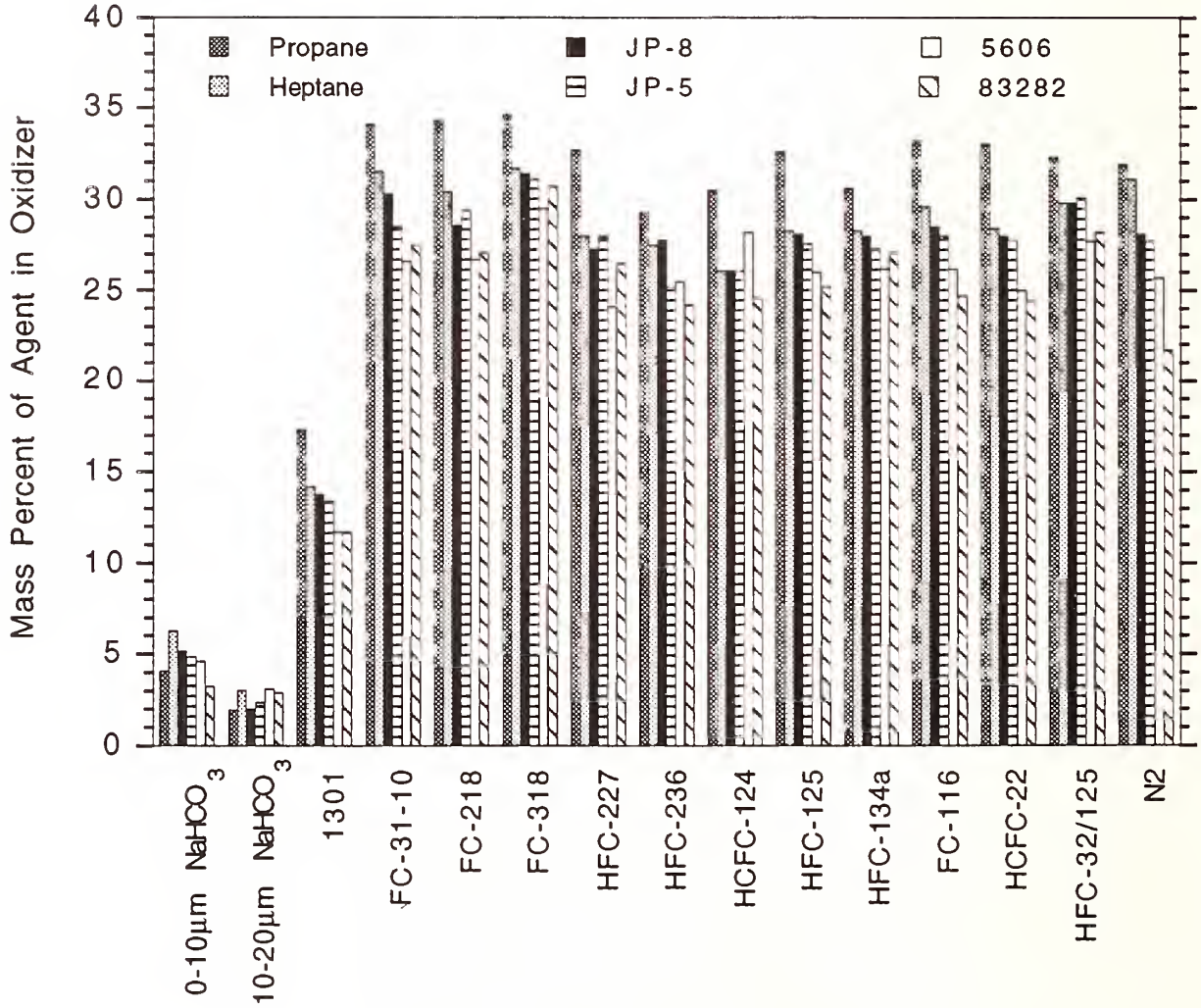

Figure 34. Agent (mass percent) concentration at extinction.

Table 5. Comparison of (mole based) Extinction Measurements with Previous Work. Fuel is Heptane.

Agent	Halon 1301	CF_3I	C_2F_6	N_2
this study	3.2%	3.2%	8.1%	32%
Hirst and Booth, 1977	3.5%	[a]	[a]	30.2%
Harrison, 1992	3.5%	[a]	[a]	[a]
Bajpai, 1974a	3.3%	[a]	[a]	[a]
Sheinson *et al.*, 1978	3.1%	3.2%	7.9%	30%

[a] Not measured

extinguish the cup burner flames. The perfluorinated agents all had approximately the same effectiveness as N_2 on a mass basis. This is directly related to the agent heat capacity, as listed in Table 6, which shows that all of the perfluorinated agents have approximately the same heat capacities at flame temperatures.

4.3.4.2 Sodium Bicarbonate Powder. The color of the flame became bright yellow with the addition of even minute amounts of $NaHCO_3$ into the flame. Equilibrium calculations (Gordon and McBride, 1970) indicate that at flame temperatures, the sodium containing species in the flame with the highest concentrations are Na^+ and NaOH. The intense yellow luminosity was likely due to high temperature Na^+ ion emission in the flame. As the powder concentration in the oxidizer stream was increased, the flame became thinner and less luminous. Near extinction only a small luminous region was apparent.

For suppression of the liquid fuel flames, some powder was observed to accumulate inside of the fuel cup and submerge. The effect of $NaHCO_3$ powder on the extinction resistance of the fuels was tested by measuring the extinction concentration of N_2 in the oxidizer stream for flames burning fuels with and without powder sprinkled on the fuel surface. No differences were determined for any of the five liquid fuels tested.

Experiments showed that flame extinction using SiO_2 was not possible for powder loadings achievable with our delivery system. With as much silica as could be delivered by our apparatus, the cup burner flames appeared unaltered. The SiO_2 concentration attainable by the delivery system was not quantified.

Figure 34 shows that the concentration of $NaHCO_3$ required to extinguish the cup burner flames for two powder size fractions. Approximately 4% by mass of $NaHCO_3$ in the oxidizer stream was necessary to extinguish the heptane cup burner flames. A comparison shows that in general, $NaHCO_3$ was a factor of three to five times more efficient than halon 1301 on a mass basis depending on fuel type and powder size. Unlike the gaseous agents, propane flames were less difficult to extinguish than heptane for both powder sizes. The reason for this warrants further study.

There were some inconsistencies between the 0-10 and the 10-20 μm powder results. Ewing *et al.*, (1992) observed enhanced extinction effectiveness with decreasing powder size in heptane pool

Table 6. Agent Heat Capacity in the Oxidizer Stream and Calculated Adiabatic Temperature near Extinction for Heptane Cup Burner Flames

Agent	C_p[1627 °C] (J/g-°C)	T_f (°C)
CF_3Br (1301)	0.0406	1981
CO_2	0.0779	1567
N_2	0.0731	1586
C_3HF_7 (HFC-227)	0.0822	1614
CHF_2Cl (HCFC-22)	0.0678	1689
CH_2FCF_3 (HFC-134a)	0.0946	1567
C_2F_6 (FC-116)	0.0726	1628
$CHFClCF_3$ (HCFC-124)	0.0717	1706
CHF_2CF_3 (HFC-125)	0.0836	1615
C_3F_8 (FC-218)	0.0764	1597
C_4F_{10} (FC-31-10)	0.0764	1569
cyclo-C_4F_8 (FC-318)	0.0798	1560
Ar	0.0296	1607
He	0.296	1747
CF_3H	0.0831	1685
CF_4	0.0683	1522

fires, until a critical powder size (≈ 30 μm for $NaHCO_3$), when the effectiveness was nearly a constant. The results reported here are not consistent with these findings. Figure 34 shows that the larger diameter particles were more efficient than the small size fraction. It is possible that the 0-10 μm size fraction was exposed to heat or water vapor under preparation or storage, causing the $NaHCO_3$ to react and form Na_2CO_3, a reaction which is known to begin at 50 °C. This possibility is being currently investigated. In any case, $NaHCO_3$ is three to five times more efficient than halon 1301 on a mass basis.

4.3.4.3 Additional Agents. The mole and mass-based heptane extinction results for all gaseous agents tested are shown in Table 7, grouped by molecular type (inert, a silicon containing compound, a sodium containing compound, perfluorinated agents, and chlorine, bromine, and iodine containing compounds). On a mass basis, the most efficient agent was the solid powder, $NaHCO_3$. The most efficient gaseous agent was He, followed by $CHCl_2F$, CF_3Br, and CF_3I. The most efficient gaseous agent on a mole basis was the liquid agent CF_2Br_2, followed by CF_3Br, CF_3I, CH_2BrCF_3, and $CHCl_2F$.

A number of agents, especially those with a large percentage of hydrogen atoms, proved to be flammable. As CF_2H_2, for example, was added to the oxidizer stream, an independent premixed

flame was established in the pyrex chimney. The location of the premixed flame in the chimney depended on the oxidizer flow velocity which was related to the flame speed of the CF_2H_2-air mixture.

One agent, NF_3, behaved as an oxidizer, creating an intensely luminous flame with increasing agent concentration. A simple thermodynamic analysis shows that stoichiometric combustion of NF_3 in conjunction with a hydrocarbon fuel and air yields rather than demands O atoms. Thus, NF_3 should act as a hydrocarbon oxidizer.

A detailed discussion of the results for the additional agents can be found in Section 5 of this publication.

4.3.5 Discussion of Results. The heat capacities of the agents are approximately equal on a mass basis as shown in Table 6. Table 7 and Figure 34 show that on a mass basis, CF_3Br and CF_3I were very effective compared to the other gaseous agents tested. The remainder of the agents exhibited essentially the same suppression performance, which was not significantly more efficient than N_2. Some investigators have found that interpretation of the results are facilitated by flame temperature calculations (Tucker *et al.*, 1981; Sheinson *et al.*, 1989).

Table 7 shows the results of such calculations assuming (a) that the agents behave as an inert, (b) that the combustion process is stoichiometric, with only H_2O and CO_2 as products, (c) that there is no dissociation, and (d) that the agent and O_2 diffuse into the flame at the same rate. Both of the inert non-halogenated agents, CO_2 and N_2, had adiabatic flame temperatures approximately 1587 °C. All of the fluorinated agents had calculated adiabatic flame temperatures near 1590 °C, actually between 1557 and 1617 °C. Halon 1301 had a very high calculated temperature, suggesting an amount of chemical suppression by this compound. The chlorinated agents, HCFC-22 and HCFC-124, also had relatively high calculated temperatures compared to the inert agents and to the perfluorinated agents, indicating some measure of chemical activity. From an energy balance it is possible to quantify the percentage of physical and chemical action associated with each of these agents.

This interpretation of the data, however, is problematic when considering results for the inert monatomic gases (helium and argon). The high calculated flame temperature associated with helium in Table 6 is likely due to large preferential diffusion or Lewis Number effects. An interpretation of Lewis Number effects on coflow extinction studies has not been addressed. Understanding preferential diffusion effects could be an important parameter for predicting the effectiveness of a replacement agent and understanding the relative importance of an agent's chemical activity to its transport properties.

Figure 35 compares the mole fraction of agent needed for extinction of heptane flames burning in the cup (from Figure 33) and OFDF burners (from Figure 8). The relative agent suppression ranking and even the absolute values of agent concentration at extinction show excellent agreement between the low strain rate OFDF results and the cup burner results. It is conjectured that the strain rate near extinction in the cup burner flame is characterized by a low strain rate.

Table 8 shows the results of a statistical analysis considering all of the agents tested which indicates that propane flames were the most difficult to extinguish, followed by heptane, the jet fuels, and the hydraulic fluids.

4.3.6 Summary and Recommendations. An apparatus and methodology were developed to test the suppression effectiveness of gaseous, liquid and solid powder agents in a simple, coflowing flame burning gaseous and liquid fuels. The major findings were:

Table 7. Agent Fraction in the Oxidizer Stream at Extinction of Heptane Cup Burner Flames

Agent Type	Agent	Mass Percent	Volume Percent
inert	N_2	31	32
	CO_2	32	23
	He	6.0	31
	Ar	38	41
nitrogen containing	NF_3	[a]	[a]
silicon containing	SiF_4	36	13
sodium containing	$NaHCO_3$ (10-20 μm)	3.0	[b]
HFC	CF_3H	25	12
	CF_2H_2	[c]	[c]
	CF_2H_2/C_2HF_5	30	15
	CH_2FCF_3	29	10
	CHF_2CF_3	29	8.7
	$CF_3CH_2CF_3$	27	6.5
	C_3HF_7	28	6.2
FC	CF_4	37	16
	C_2F_6	30	8.1
	C_3F_6	29	7.3
	C_3F_8	30	6.3
	c-C_4F_8	32	6.3
	C_4F_{10}	32	5.3
chlorine containing	CHF_2Cl	28	12
	$CHCl_2F$	32	11
	CH_3CF_2Cl	[c]	[c]
	CF_2=$CHCl$	[c]	[c]
	CF_2=$CFCl$	31	10
	$CHFClCF_3$	26	7.0
bromine containing	CF_3Br	14	3.1
	CF_2Br_2 (l)	16	2.6
	CH_2BrCF_3 (l)	17	3.5
	CH_2=$CHBr$	[c]	[c]
	CF_2=$CFBr$	27	6.3
	CF_2=$CHBr$	24	6.0
iodine containing	CF_3I	18	3.2

[a] acted as an oxidizer, promoted flame stability
[b] solid powder not expressed in volume percent
[c] agent observed to be flammable

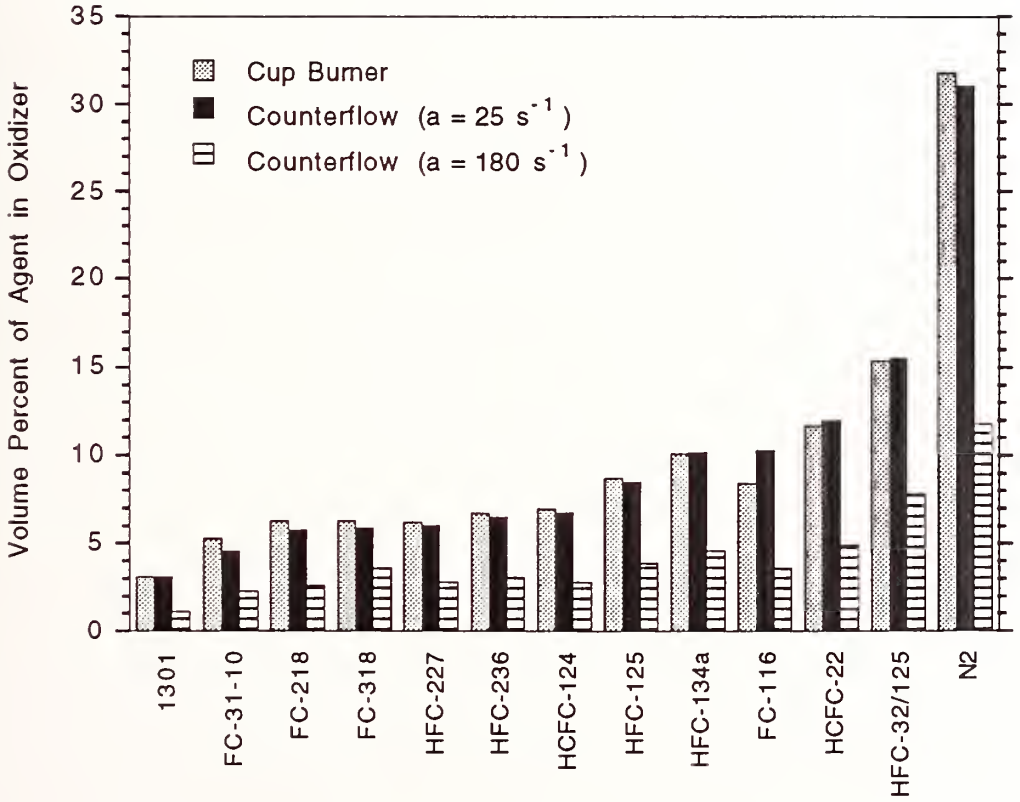

Figure 35. Comparison between the volume percent of agent required to suppress heptane flames in the OFDF and the cup burner.

Table 8. Relative Difficulty in Extinguishing Different Fuels in the Cup Burner

Fuel	Resistance to Extinction
Propane	1.00
Heptane	0.87
JP-8	0.84
JP-5	0.82
5606	0.76
83282	0.74

1. The measurements showed that a mass-based agent ranking of agent suppression effectiveness significantly differed from a mole based ranking. On a mass basis the FC, HFC, and HCFC compounds had essentially the same suppression effectiveness, whereas on a mole basis the higher molecular weight compounds were more effective.

2. Propane flames were most difficult to extinguish (required highest agent concentration), followed by heptane, the jet fuels, and the hydraulic fluids.

3. The relative extinction effectiveness of the agents was essentially unchanged for all fuels tested.

4. $NaHCO_3$ powder was the most effective of all agents tested on a mass basis.

5. Several agents (CF_2H_2, CH_3CF_2Cl, $CF_2{=}CHCl$, and $CH_2{=}CHBr$) behaved like fuels, as characterized by the appearance of an independently stabilized premixed flame inside the burner. Another agent (NF_3) behaved like an oxidizer.

6. CF_3I and the bromine containing compounds were generally very effective on both a mole and a mass basis.

7. The relative rankings of the effectiveness of various gaseous agents in extinguishing the opposed flow diffusion flame burner at low strain rates agree with the cup-burner studies. In addition, at low strain rates, the absolute agent concentration at extinction was found to agree well with measurements made in the cup-burner. Although it is very likely that flame stretch in the cup burner is similar to the low strain rate generated in the OFDF, a systematic study to show this correspondence should be undertaken.

4.4 Turbulent Spray Flames

4.4.1 Background. A fuel spray provides a unique opportunity for a fire. Small droplets quickly evaporate and the momentum from the spray efficiently entrains the air necessary for combustion. A ruptured high pressure fuel, lubricant or hydraulic fluid line can supply a steady flow of fuel for a fire stabilized behind obstacles in the engine nacelle, or create a cloud of droplets from a punctured fuel tank adjacent to a dry bay. Extinguishment of the burning spray will occur when the critical level of agent is mixed with the air that gets entrained into the primary reaction zone. The process is affected by the velocity of the flow, the rate of mixing, the system temperature, and the agent and fuel concentrations and properties.

Neither the cup burner nor the OFDF can simulate the combined droplet evaporation and turbulent mixing which occur in a realistic spray flame. The objective of this portion of the investigation was to develop a laboratory facility which could capture some of the additional critical elements that could exist within an engine nacelle or dry bay fire. The apparatus is useful as a screening device only if the flame and agent injection process can be precisely controlled and operated in a reliable and repeatable manner. In addition to the flexibility offered by a reduced scale facility, the laboratory spray burner provides an opportunity to separate the effects of agent transport and vaporization from flame suppression effectiveness, and to control independently the rate at which the agent enters the flame.

No standard laboratory setup for evaluating the effectiveness of an agent for extinguishing an aircraft in-flight spray fire existed when this study was initiated. The design described in the next section was based upon the desire to maintain flame stability over a reasonable dynamic range, and to accommodate the application of gaseous and powdered agents. A coaxial jet with a spray nozzle typical of a simple oil furnace or gas turbine combustor was chosen for the spray flame apparatus.

4.4.2 Experimental Facility. The spray burner facility consisted of an air delivery system, a fuel delivery system, an agent injection system, and a combustion zone, as laid out in Figure 36. Figure 37 shows a cross-sectional view through the combustion zone. Air at atmospheric pressure co-flowed around a 6 mm diameter fuel tube within a 0.5 m long, 50 mm diameter stainless steel pipe. A pyrex tube with a 65 mm inner diameter, supported on a Teflon ring, contained the flame for 75 mm beyond the outer steel casing. The fuel was injected along the centerline through a pressure-jet nozzle (Delevan model 0.5-45-B) that formed a 45° solid-cone spray. The exit of the nozzle was flush with the open end of the surrounding pipe. The flame was stabilized on a 35 mm diameter steel disk attached to the nozzle body.

The air was supplied by a high capacity compressor at 800 kPa, and its flow was monitored with a sonic-orifice. Temperatures from ambient to in excess of 150 °C, measured with a type-K thermocouple 1.1 m upstream of the fuel outlet, could be obtained using a 60 kW electric air heater. Average velocities across the burner cross-sections reached 50 m/s. The fuel (JP-8 or hydraulic fluid MIL-H-83282C) was stored in an 18 liter tank and delivered to the burner with an electric pump at pressures controllable to 1.0 MPa-g. The nozzle was designed to deliver fuel oil at a rate of 0.5 ml/s when the fuel line gauge pressure is 687 kPa. The flow was calibrated at the actual operating temperatures and pressures for each of the fuels.

The gaseous agents were injected impulsively into the air 0.54 m upstream of the nozzle. Uniform dispersion across the air stream was enhanced by injecting the gas in a radial direction into a reduced diameter (25 mm) section of the air pipe through two 6 mm diameter tubes. Screens with 50% open area were placed 40 and 80 mm downstream of the injection point to ensure complete mixing between the air and agent prior to encountering the flame zone.

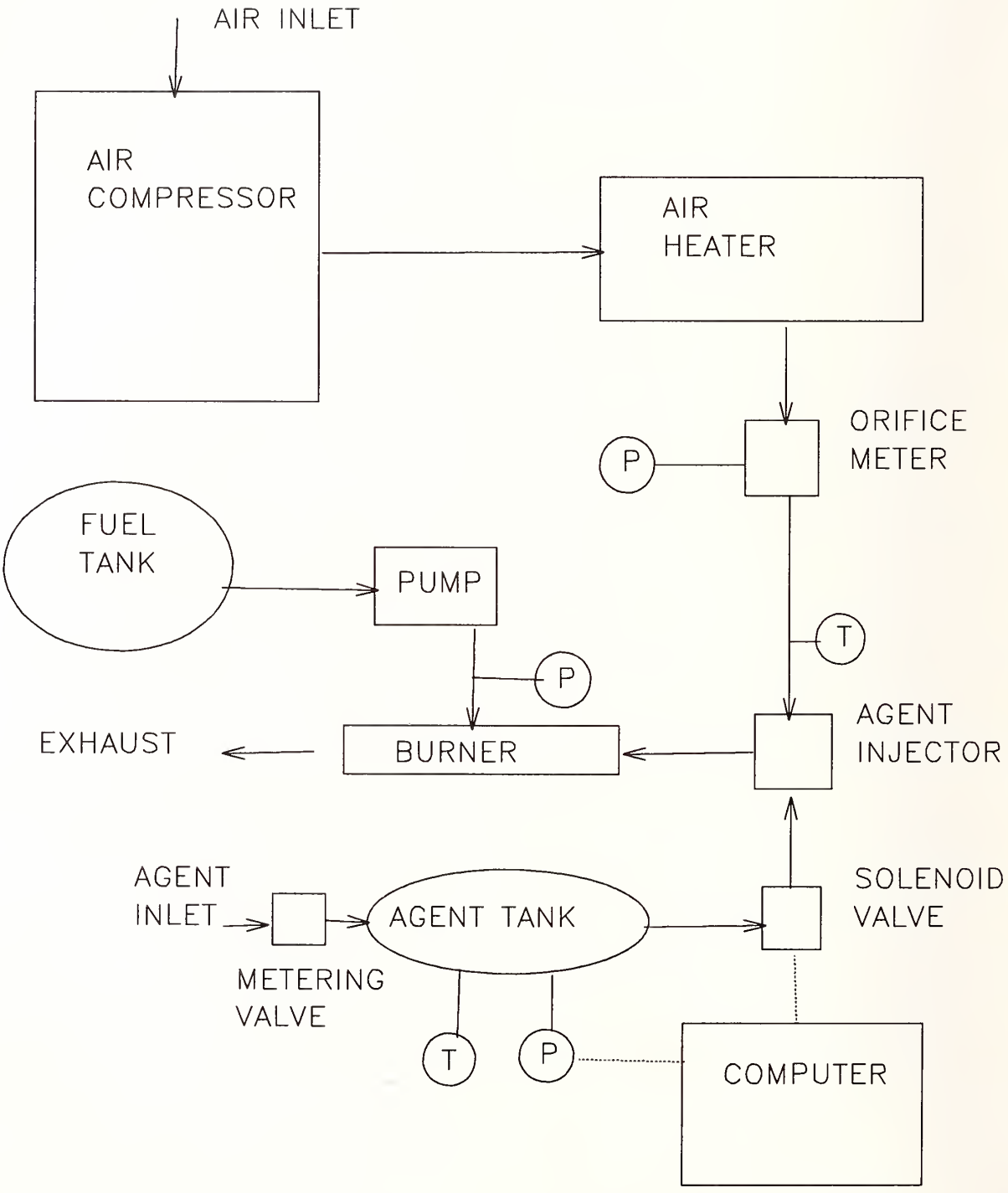

Figure 36. Block diagram of turbulent spray burner facility.

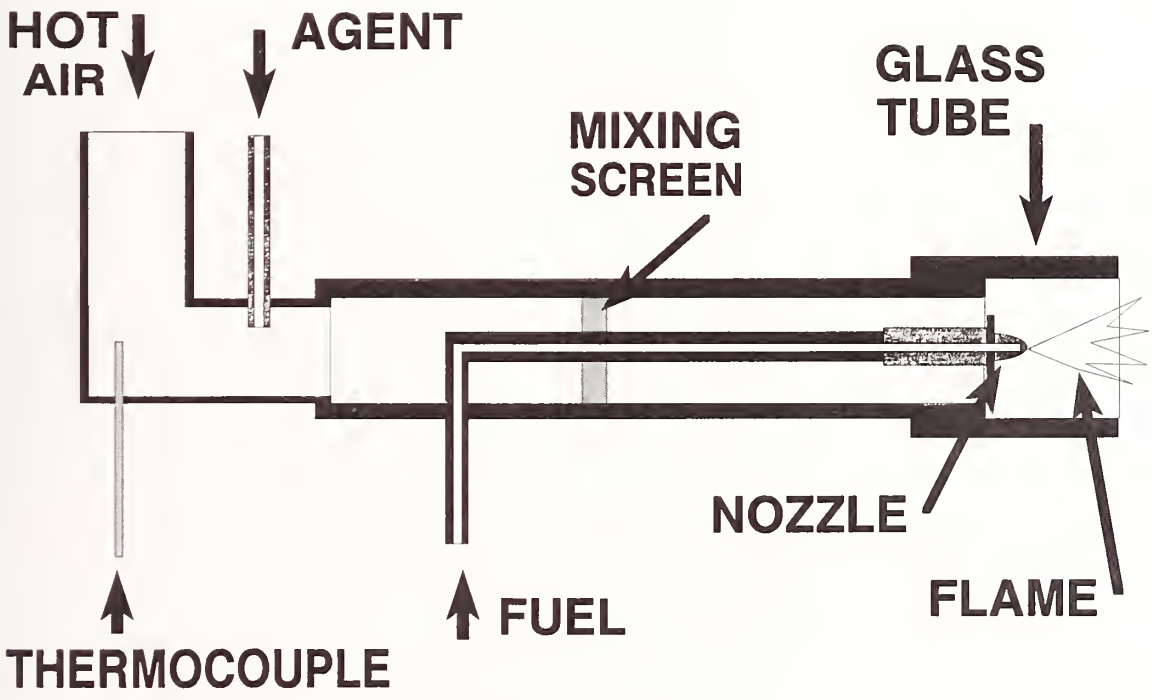

Figure 37. Cross-section of combustion zone of spray burner facility.

A photograph of the overall facility is shown in Figure 38.

The injection mechanism, shown in Figure 39 (a), consisted of the agent supply bottle connected to a stainless steel storage vessel through a metering valve, and to the burner through a computer controlled solenoid valve. The storage volume, including the one liter pressure vessel and associated plumbing, was 1040 $\pm$ 10 ml and the agent pressure was adjustable up to 687 kPa-g. The agent temperature and pressure in the storage vessel were measured with a type-K thermocouple and a pressure transducer located upstream of the solenoid valve. The amount of injected agent was controlled by varying the initial pressure and the time that the valve was open. The controlling computer acquired the digital signal from the pressure transducer at 700 Hz. The actual mass delivered was determined from the difference between the initial and final pressures in the storage vessel using the Redlich-Kwong equation of state (Van Wylen and Sonntag, 1978).

Figure 39 (b) shows how the gaseous injection system was modified to accommodate powders. The powder was loaded into two nylon tees downstream of the computer-controlled solenoid valve. Straight-through ball valves isolated the powder from the burner to minimize back-flow and powder loss during loading. Aluminum caps were machined to reduce any excess volume within the storage tees. Compressed air stored in the agent vessel was used to propel the powder into the burner.

4.4.3 Experimental Parameters and Procedures. The independent parameters which were controlled in the spray burner facility were the air flow and temperature, the fuel flow and type, the agent composition, and the mode of injection (fixed time or fixed pressure). For powder agents there were two additional independent parameters: the particle size distribution and the transport gas pressure. The primary dependent parameters were the mass and the rate of injection required for suppression. Table 9 lists the range of independent parameters investigated, and other relevant operating conditions derived therefrom.

The air and JP-8 fuel flows were varied to ascertain how flame stability was affected by the operating conditions. The fuel pressure was fixed at 687 $\pm$ 10 kPa-g (corresponding to a mass flow rate of around 0.42 g/s). The spray was ignited without the air flowing using a propane torch. The flame extended well beyond the exit of the pyrex tube and was highly luminous under these conditions. As the air flow was increased, the flame attached itself to the stabilizing disc and the plume length decreased until the flame was stationed within the horizontal tube passage. At high air flows little soot radiation was observed beyond the exit plane, although the flame itself maintained some luminosity. A moderate amount of soot formed on the nozzle face in a matter of minutes. A stable flame was sustainable until the air flow rate exceeded 73 g/s. The average gas velocity across the air duct was about 33 m/s at the above-mentioned mass flow, which translated to an estimated residence time in the recirculation zone behind the stabilizing disc of 5 ms. Blowout experiments were repeated for fuel nozzle pressures of 515 and 858 kPa-g. At the reduced pressure the fuel flow rate decreased by about 14%, which resulted in an equivalent decrease in the amount of air necessary to extinguish the flame. The higher nozzle pressure had no appreciable affect on the blowout limit. The operating conditions chosen for baseline measurements were a mass flow of JP-8 equal to 0.42 g/s and an ambient temperature and pressure air flow of 33 g/s, resulting in an average inlet air velocity of 14 m/s. This produced an 18 kW flame with an overall equivalence ratio of about 0.17.

4.4.3.1 Gaseous Agents. The injection system under idealized conditions (incompressible flow, massless valves, no pressure losses) was designed to deliver a square-wave pulse of agent to the burner for the amount of time programmed by the computer controller. The actual flow deviated substantially from this scenario. There was a 15 ms delay between when the solenoid was triggered and the flow of agent actually began. When the valve started to close, pressure waves were created which reverberated in the injection system at the acoustic velocity, causing the flow rate to modulate.

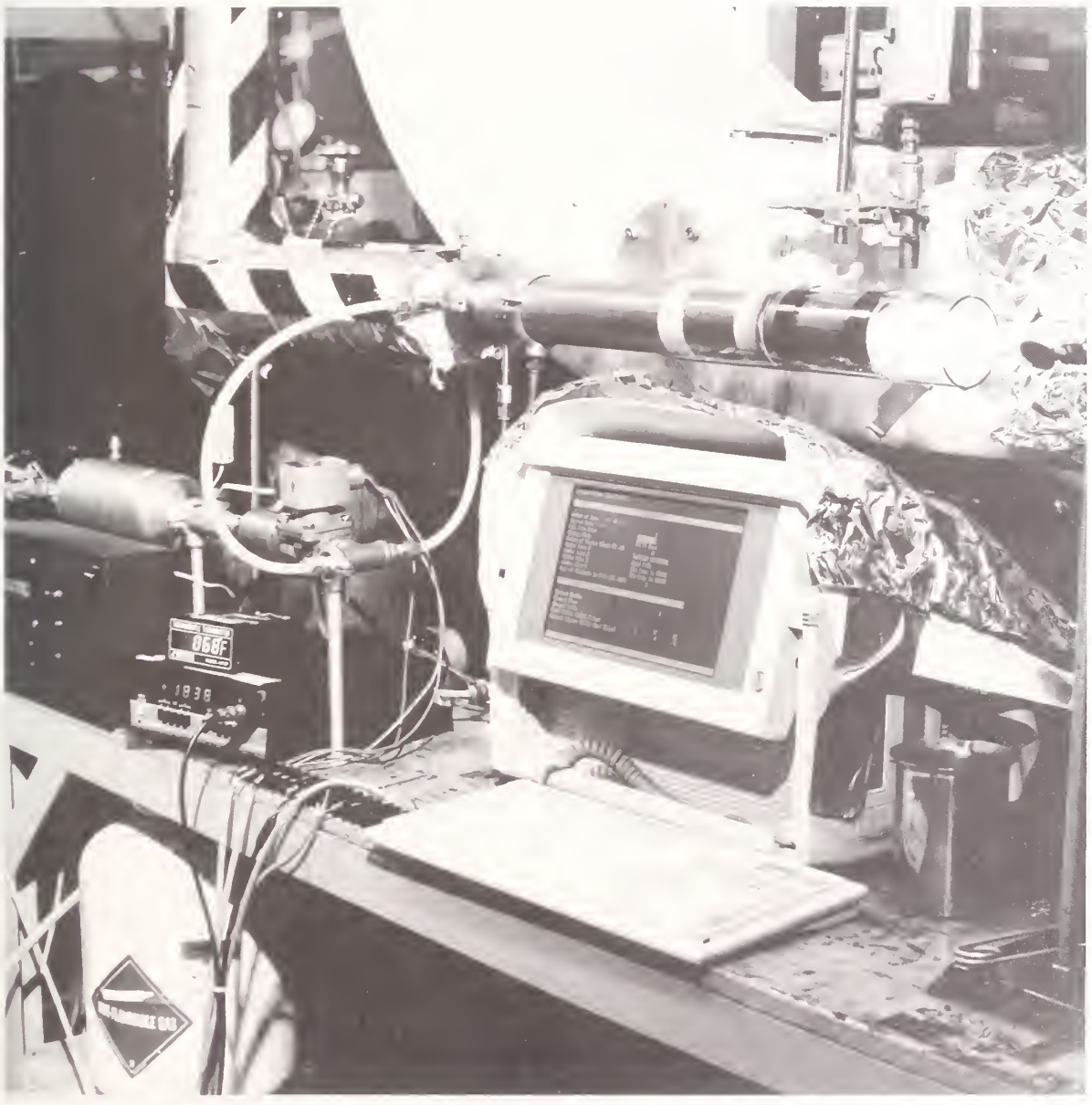

Figure 38. Photograph of turbulent spray burner facility.

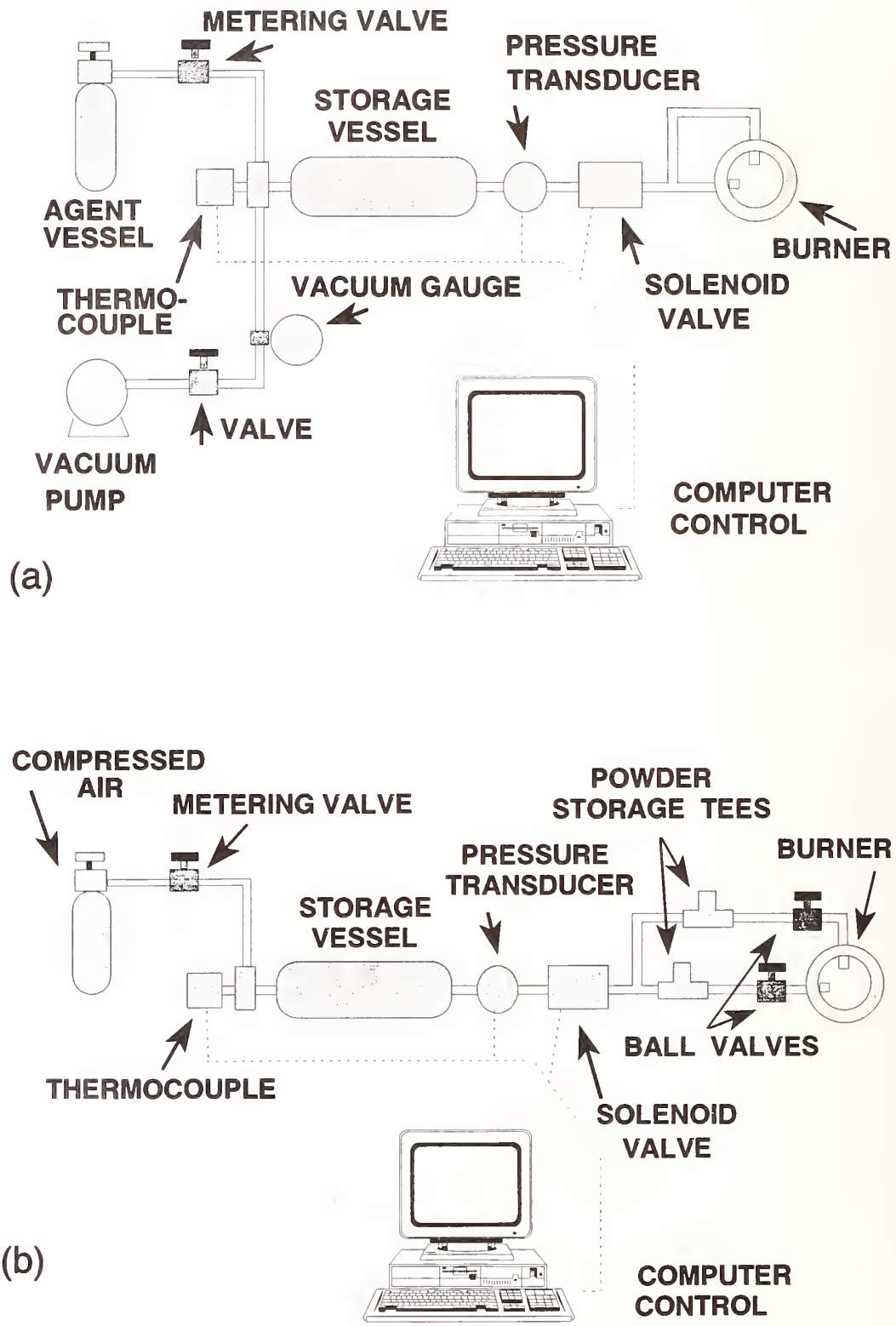

Figure 39. Schematic of agent injection mechanism for (a) gases, and (b) powders.

Table 9. Operating conditions in turbulent spray burner

Parameter	Fuel		
	JP-8		MIL-H-83282C
Air Temperature	19 - 25 °C	146 - 153 °C	118 - 123 °C
Air Pressure	ambient	ambient	ambient
Air Flow	22 to 73 g/s	33±1 g/s	30±1 g/s
Nominal Air Velocity	10 to 33 m/s	20 m/s	18 m/s
Fuel Temperature	19 - 25 °C	< 150 °C	< 120 °C
Fuel Pressure	515 to 858 kPa-g	1034±10 kPa-g	896±10 kPa-g
Fuel Flow	0.43 to 0.55 ml/s	0.46±.05 ml/s	0.65±.05 ml/s
Thermal Input	15 to 20 kW	16±2 kW	[a]
Equivalence Ratio	0.14 to 0.19	0.15	[a]
Gaseous Agents	core 11, N_2, CF_3Br, CF_3I	core 11, N_2, CF_3Br	core 11 (except FC-31-10), N_2, CF_3Br
Powder	$NaHCO_3$ + silica (0-10 μm, +50 μm)	none	none
Agent Temperature	20 - 25 °C	20 - 25 °C	20 - 25 °C
Agent Pressure	20 - 687 kPa-g	20 - 60 kPa-g	20 - 60 kPa-g
Injection Interval	20 to 900 ms	75±10 ms	75±10 ms

[a] molecular composition and enthalpy of formation not provided

An example of these pressure modulations and the injection timing sequence is seen in Figure 40. The curve labeled P2 is the voltage from the pressure transducer between the solenoid valve and the metering orifice and P1 relates to the pressure upstream of the orifice.

The mass of agent, m, contained in the vessel of volume V, at pressure P and temperature T, was determined from the Redlich-Kwong equation of state,

$$m = \frac{PVM}{RT}\left[\frac{1}{1-bm/V} - \frac{am/(VRT^{3/2})}{1+bm/V}\right]^{-1} \quad (4)$$

M is the molecular weight of the gaseous agent, R is the gas constant, and a and b are constants dependent upon the critical properties of the agent (Van Wylen and Sonntag, 1978). The initial temperature was measured, and the final temperature was determined by assuming that the expansion occurred isentropically following the relation

$$\frac{T_f}{T_i} = \left(\frac{P_f}{P_i}\right)^{\frac{\gamma-1}{\gamma}}. \tag{5}$$

Gamma is the specific heat ratio for the gas. Thus, by measuring the change in pressure, Equation (4) can be used in an iterative fashion to determine the total amount of mass injected into the burner. Equation (5) assumes the gas is ideal. (From Equation (4) the deviation from ideal gas behavior was found to be a maximum of 7% for the gaseous agents.) The pressure data were collected at a rate of 700 Hz, with the initial and final conditions found from the average of at least 100 points measured one-half second prior to the release of the agent, and one second after the solenoid valve closed, respectively. Figure 41 presents an example under minimum suppressing conditions of the calculated mass delivered as a function of time using Equations (4) and (5) for six different trials at the same computer setting.

A figure of merit for extinguishing the flame, ß, can be defined in terms of the mass flows of agent, m_i, and air, m_{Air}:

$$\beta \equiv \frac{\dot{m}_i}{\dot{m}_i + \dot{m}_{Air}}. \tag{6}$$

A small value for ß is desirable. The mass of agent added to the flame is determined from Equation (4), and the actual time interval of agent injection into the burner is estimated from the linear portion of the slope in the mass-time curve. (*e.g.*, see Figure 40).

The storage vessel was pressurized with air to 687 kPa-g, and the solenoid valve was opened for successively longer periods of time, up to a maximum of 910 ms. Figure 42 presents the cumulative increase in mass delivery with set time. The results indicate that the mass of air (solid symbols) increased almost linearly with time in the range between about 25 and 250 ms. For short time settings, less mass was delivered because the valve did not have sufficient time to fully open. The deviation from linear behavior when the valve was open for a long period resulted from depletion of the entire mass ($\approx$ 10 g) contained in the injector storage vessel. Figure 42 also presents the time over which the pressure decreased in the vessel (open symbols). There was a minimum time for the solenoid valve to respond due to inertia, which explains the greater measured time for settings below 25 ms.

A number of experiments were carried out with the burner operating at baseline conditions and with air as the extinguishing agent to ensure that the flame could not be suppressed simply by blowing it out. When air was injected into the burner, the flame was observed to fluctuate momentarily, but was never extinguished even when the storage pressure and injection period were at their maximum values (*viz.*, 687 kPa-g and 910 ms, respectively).

The protocol used in the experiments with the gaseous agents was to ignite the fuel spray and set the air flow to the desired level. The flame was allowed to burn for several minutes to ensure steady operation. If the air was at an elevated temperature, it was necessary to wait until the temperature of the air at the burner stabilized, which took as long as 20 minutes in some cases. The storage vessel was evacuated and then flushed several times with the agent under investigation to purge contaminating gases from the system. The pressure in the vessel was adjusted with the solenoid valve closed using the inlet metering valve. Initially a pressure was chosen which was expected to be insufficient to extinguish the flame. The computer control/data acquisition was begun and the response of the flame to the injection process was observed. If the flame was not extinguished, the pressure in the agent vessel was increased and the experiment was repeated immediately. Eventually a pressure was

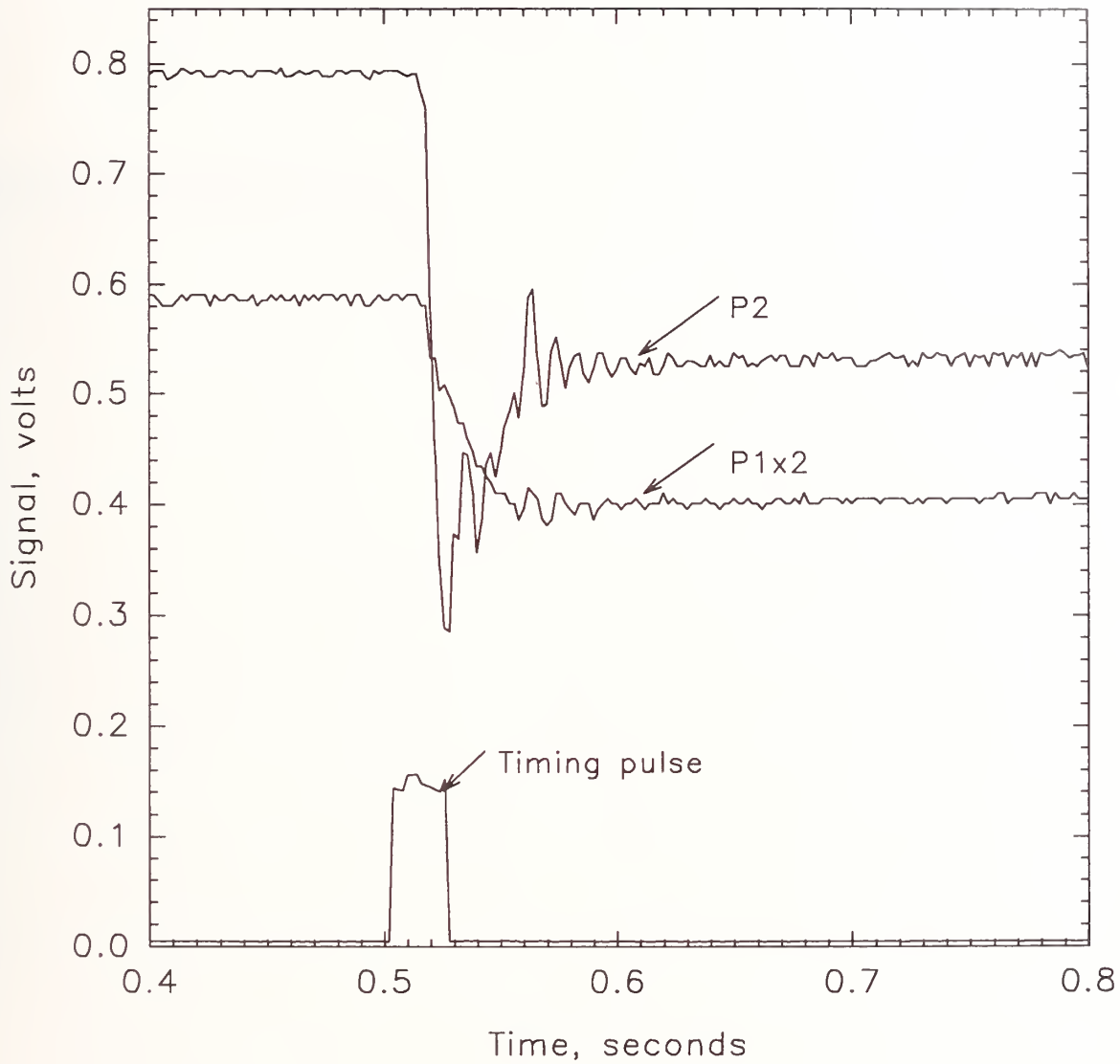

Figure 40. Pressure during injection of nitrogen; 6.4 mm metering orifice, time = 23 ms.

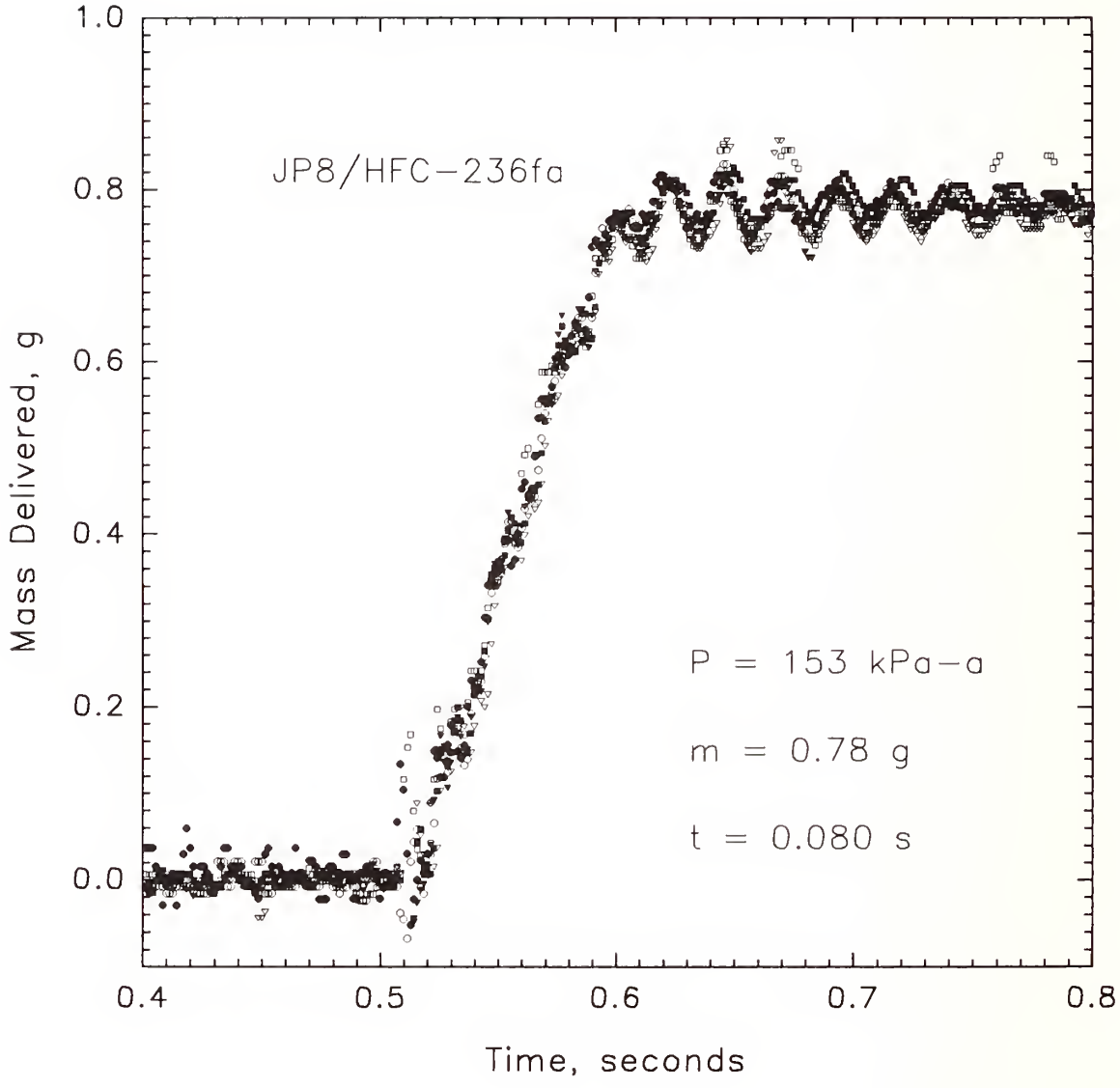

Figure 41. Mass delivered to burner as a function of time; HFC-236fa/hydraulic fluid flame.

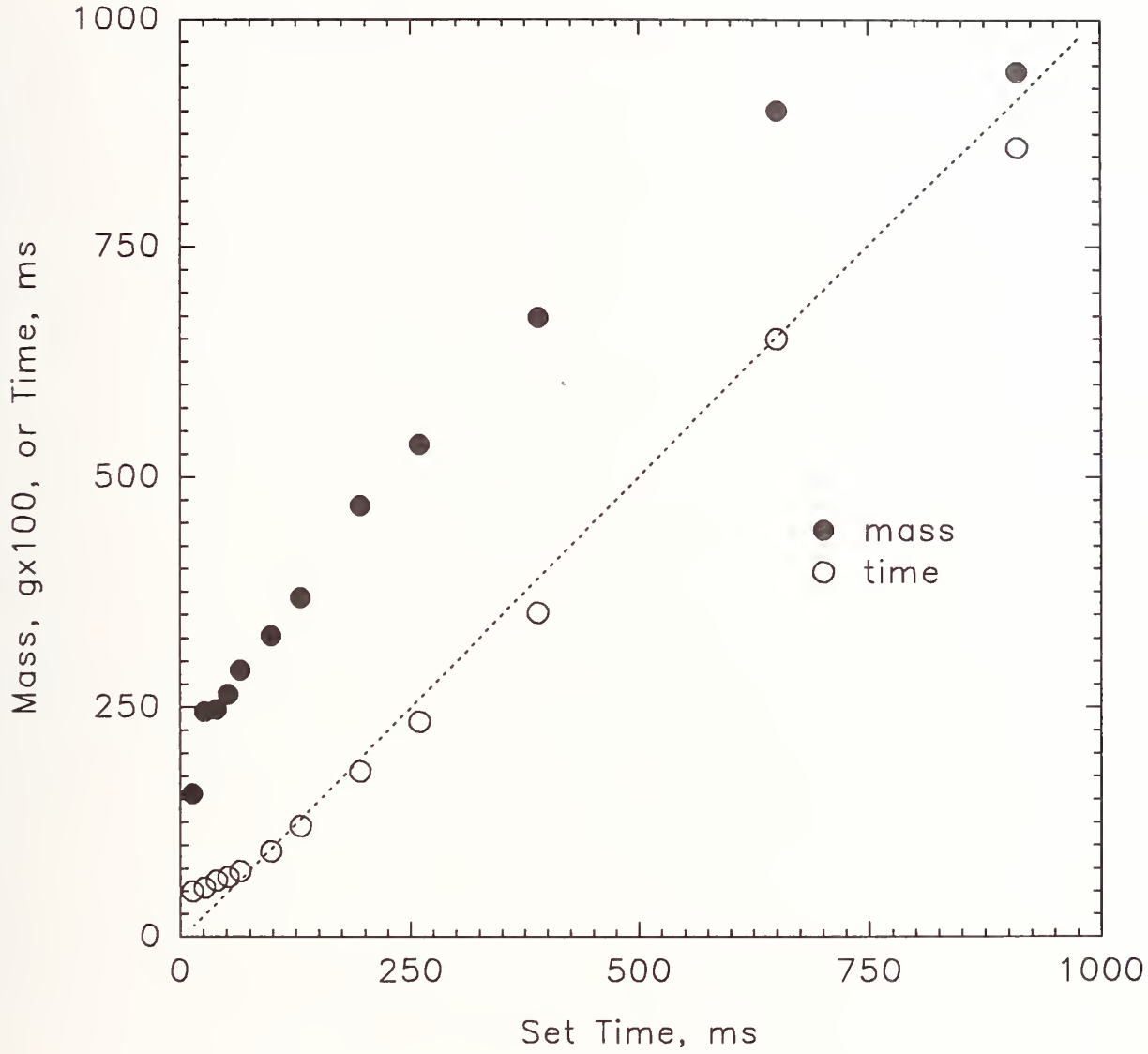

Figure 42. Injection period (open circles) and mass of air delivered (solid circles) as a function of set time. Initial pressure is 687 kPa-g.

found which was sufficient to suppress the flame. This procedure was normally repeated four times for each agent.

4.4.3.2 Powder Agents. Two powder samples and two different pressures were used to determine the effects of particle size and pressure on suppression performance. $NaHCO_3$ powder was mixed with silica gel and classified by size as described earlier in Section 4. The two distributions used were 0-10 μm and +50 μm. Two air pressures were selected for powder delivery, 172 and 241 kPa-g. Lower pressures were avoided because of poor delivery performance in preliminary testing.

The storage vessel was filled to the desired air pressure with the solenoid valve closed using the inlet metering valve. With both downstream ball valves closed, a preweighed amount of powder, expected to be insufficient to extinguish the flame, was loaded into the storage tees (see Figure 39 (b)). Once loading was complete, both ball valves were opened, the computer control/data acquisition was begun, and the flame response to the injection process was observed. The nominal injection period was set for 65 ms in all the experiments presented here. If the flame was not extinguished, any powder accumulation within the injection mechanism and the burner was removed. Total removal was accomplished by using a minimum of five high pressure air injections ($>$ 240 kPa-g) and by increasing the burner air flow to at least 60 g/s for approximately 20 minutes. Preliminary testing showed that this procedure was necessary to properly clean the injection mechanism. The storage vessel was again pressurized to the same injection pressure, a larger preweighed amount of powder was loaded into the storage tees, and the experiment was repeated. Eventually an amount of powder was found which was sufficient to suppress the flame. This procedure was normally repeated three times for each powder sample and pressure.

Once the powder suppression mass was determined the delivery tubes were disconnected from the burner and a series of tests were run to determine powder injection efficiency. This was done by loading a preweighed amount of powder into the storage tees and injecting it into a one liter plastic bag. The injection was performed according to the previously discussed experimental procedure. The plastic bag was weighed before and after the injection to determine the weight gain. Five air injections at 240 kPa-g were also performed in a different plastic bag to determine the amount of residue left in the injection mechanism after the first injection. This procedure was repeated a minimum of five times to determine reproducibility. The percentage of powder injected was determine by dividing the plastic bag weight gain by the preweighed amount of powder loaded into the injection mechanism. The percentage of powder residue was calculated in the same manner, using the plastic weight gain from the five high pressure injections. The results are summarized in Table 10. Powder losses within the burner itself were not quantified; however, inspection of the burner walls and mixing screens showed almost no powder accumulation beyond a very thin layer of dust.

4.4.4 Experimental Results

4.4.4.1 Characterization of Facility. The influence of air velocity, injection period, and injection pressure on the amount of N_2 required to extinguish the JP-8 spray flame and on the value of ß was investigated as a means to validate the operation of the experimental facility. The storage vessel was pressurized with nitrogen to 113 kPa-g and the turbulent burner set to baseline conditions (ambient temperature, air flow equal to 33 g/s). The fuel flow was kept constant at 0.42 g/s. The injection interval was increased one millisecond at a time until the flame was extinguished. Flame extinguishment occurred between 23 and 26 ms for five different runs, delivering an average of 0.33 $\pm$ 0.03 g nitrogen at a mean flow rate of 11.2 $\pm$ 0.5 g/s. From Equation (6), the figure of merit

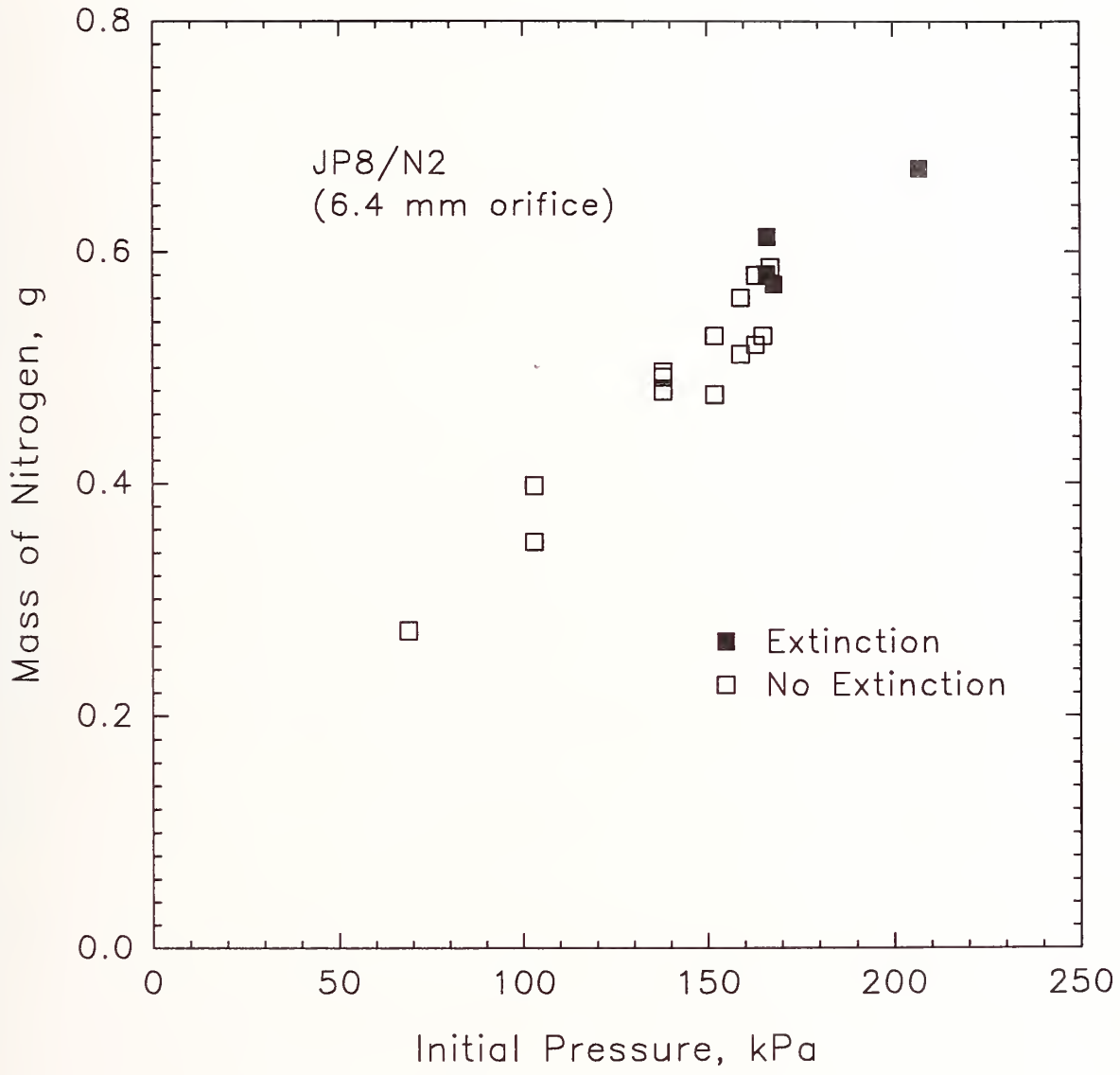

Figure 43. Effect of vessel pressure on extinguishment of JP-8 spray flame by nitrogen. Solid symbols indicate extinction; open circles indicate no extinction.

Table 10. Powder injection efficiency

Particle Size (μm)	Powder Injected (%)	Powder Residue (%)	Air Injection Pressure (kPa)
0-10	81.2 ± 3.0	17.8 ± 3.4	172
0-10	88.8 ± 1.2	10.7 ± 1.7	240
+50	82.3 ± 3.4	17.9 ± 4.4	172
+50	93.8 ± 1.5	7.5 ± 0.1	240

varied between 0.24 and 0.26. This value compares to a figure of merit for nitrogen of 0.28 measured in the cup burner apparatus with JP-8 as the fuel.

Additional experiments were carried out for air flows of 44 g/s and 22 g/s. The high velocity (19 m/s) required an average total nitrogen mass of 0.29 g at a rate of 11.5 g/s. The amount of nitrogen required to extinguish the lower air velocity flame was 0.32 g, with an average flow of 10.7 g/s. In this case, doubling the air flow reduced the mass of nitrogen required by 10%. The high air flow case yielded ß = 0.21 and the low air flow case yielded ß = 0.33.

A series of experiments was carried out with the air and fuel flow rates at baseline conditions, and the time interval was fixed as the nitrogen pressure was increased. Figure 43 is a plot of the mass of nitrogen delivered to the burner as a function of initial vessel pressure for an injection interval set to 65 ms. The open squares indicate that the flame remained lit; the solid squares correspond to successful extinguishments. The minimum vessel pressure necessary to extinguish the flame 100% of the time was 167 kPa-g. The amount of nitrogen delivered at this pressure and time interval was 0.58 ± .03 g.

The injection time interval had an effect on the minimum amount of nitrogen required to extinguish the flame. The open squares plotted in Figure 44 illustrate this effect. For these experiments, the pressure was fixed and the injection time interval was gradually increased until extinction occurred. The minimum mass of nitrogen was about 0.32 g, for a set injection period of 23 ms. Reducing the set time to 6 ms had no impact on the amount of nitrogen required to quench the flame because, as shown in Figure 42, the actual period of injection did not change appreciably. Injection times longer than 23 ms lead to delivering greater amounts of N_2, with more than three times as much N_2 required when the injection time was set to 260 ms. A limit was reached at long time intervals where the transient mass addition was insufficient to extinguish the flame.

Nitrogen was allowed to flow continuously in one experiment, with the rate increasing until the flame was extinguished. The figure of merit was found from Equation (6) to be 0.11, and is indicated by the continuous flow arrow in Figure 44. This compares to a value of 0.28 found in the cup burner with the same fuel/agent combination. Less nitrogen was required for extinguishment of the spray flame because of the greater turbulence levels and reduced time available for the combustion to occur. The solid squares also plotted in the figure are values of ß that correspond to the different injection time intervals. As the time was shortened, ß increased, reaching a limiting value of about 0.28. (It is a coincidence that this value is identical to the value of ß measured in the cup burner.)

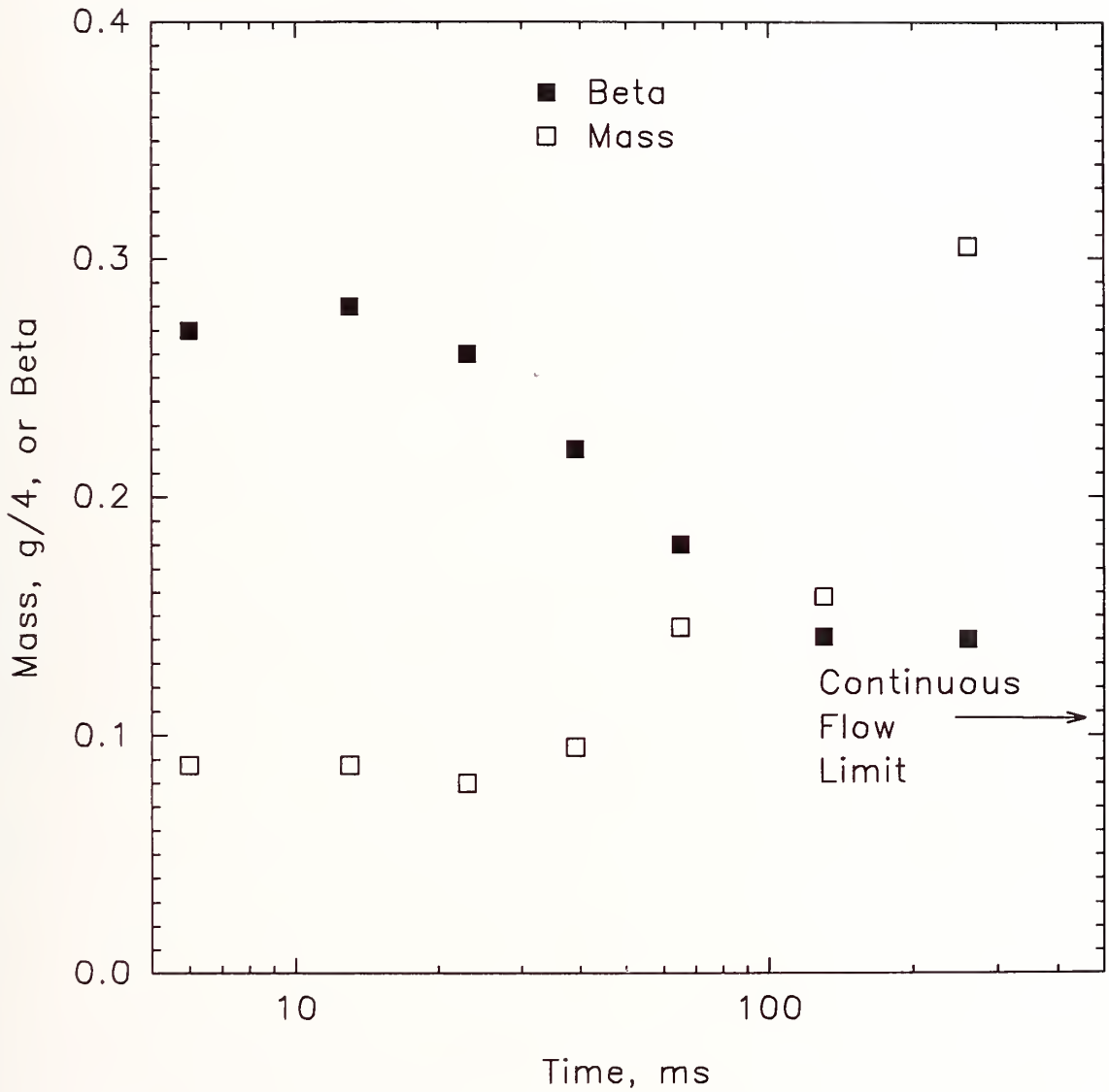

Figure 44. Effect of injection time interval on mass of nitrogen (open squares) required to extinguish JP-8 spray flame; solid squares: β.

If the value of ß were the sole criterion for evaluating an extinguishing strategy, one would chose to inject the agent over an extended period of time. However, as seen in Figure 44, this has the undesirable effect of greatly increasing the amount of agent required to put out the flame. For an agent that is to be used in a transient manner, the total mass must also be considered. This is distinct from the quasi-steady state measurements taken with the cup burner apparatus, for which ß is a reasonable measure of performance for a total flooding agent.

4.4.4.2 Gaseous Agents/JP-8/Ambient Air Test Series. A fixed injection time of 65 ms was chosen to compare the performance of the alternative agents. This value is intermediate between the estimated residence time in the spray flame (5 ms) and a typical time interval for injection in an actual engine nacelle (500 ms). At this setting, an initial pressure of 167 kPa-g was necessary to extinguish the flame with nitrogen. Nitrogen is considered chemically inert during suppression, and has a much lower molecular weight than halon 1301 and the alternative gaseous agents that were evaluated. As a result, the initial pressure in the vessel required for flame extinction was much less for the alternative agents. The 6.4 mm flow-metering orifice was therefore replaced with a 4.8 mm orifice to increase the required pressure and reduce the per cent uncertainty in the pressure change measurement. Extinguishment experiments were performed using halon 1301 to establish a performance reference (Grosshandler *et al.*, 1993). An average over five experiments led to a required initial CF_3Br pressure of 24 kPa-g to extinguish the flame, which translates to a mass of 0.44 $\pm$ .04 g and a β of 0.15.

The repeatability of the experimental technique is demonstrated in Figure 41, which is a plot of the mass of agent delivered to the burner as a function of time for six different trials where the mass of the agent, HFC-236fa, was just above the extinction threshold. The average mass injected was 0.78 g with a range of $\pm$0.02 g. The initial pressure needed to cause extinction was 52 $\pm$ 2 kPa-g, and the calculated injection interval was 80 $\pm$ 8 ms, as compared to the set time of 65 ms. The difference between the average injection interval and the computer setting was slightly larger than that found using nitrogen. This was attributed to the lower initial pressure used in the HFC-236fa experiments, which was less effective in causing the solenoid valve to close.

The results of the ambient temperature air/JP-8 flame suppression experiments for all of the gaseous chemicals examined are summarized in Table 11. The CF_3I required the least mass (0.54 g) and had a figure of merit of β = 0.16, close to that of CF_3Br. Nitrogen was only slightly less effective. Of the core agents, HCFC-22 required the least (0.65 g) and FC-31-10 required the most (1.00 g) material to extinguish the flame. FC-31-10 had the poorest figure of merit, 0.27.

4.4.4.3 Effect of Air Temperature and Fuel Type. The air was preheated to 150 °C (+3/-5 °C) and the experiments were repeated with all of the gaseous agents except for CF_3I (Vazquez *et al.*, 1994). The increase in temperature affected the flame stability in several ways. First, since the mass flow of air remained fixed, the average velocity across the air duct increased about 50% because of the drop in density. The JP-8 in the line was also heated as it flowed through the heated air annulus. The higher temperatures and lower fuel density required the fuel pressure to be increased to deliver the same amount. However, even at a maximum fuel line pressure of 1.03 MPa-g, the mass of fuel was only 90% of the ambient temperature condition, resulting in a slightly leaner flame. The increase in air velocity and decrease in equivalence ratio destabilized the flame; but this was counteracted by the increase in enthalpy of the reactants due to the higher initial temperature.

As seen in Table 11, increasing the temperature, on average, increased the amount of alternative agent required to suppress the JP-8 spray flame by 0.04 g. The halon 1301 remained the most effective, but in relative and absolute terms, required the largest increase in mass of all the chemicals investigated. The nitrogen remained better than the other halogenated compounds, and FC-31-10

Table 11. Amount of agent required to suppress turbulent spray flames

	JP-8, T_{air}=20 °C		JP-8, T_{air}=150 °C		Hydraulic Fluid T_{air}=120 °C	
Agent	mass	β	mass	β	mass	β
halon 1301	0.44	0.15	0.53	0.19	0.44	0.16
CF_3I	0.54	0.16	[a]	[a]	[a]	[a]
nitrogen	0.58	0.18	0.63	0.19	0.42	0.16
HCFC-22	0.65	0.20	0.70	0.23	0.70	0.24
HFC-125	0.73	0.22	0.77	0.24	0.78	0.26
HCFC-124	0.74	0.22	0.75	0.22	0.70	0.23
FC-116	0.75	0.22	0.74	0.23	0.73	0.23
HFC-134a	0.76	0.24	0.78	0.23	0.79	0.26
HFC-236fa	0.78	0.23	0.84	0.25	0.78	0.24
HFC-227	0.80	0.24	0.81	0.24	0.82	0.26
HFC-32/125	0.81	0.24	0.89	0.26	0.82	0.25
FC-218	0.89	0.24	0.87	0.25	0.86	0.28
FC-318	0.97	0.25	0.99	0.26	1.08	0.30
FC-31-10	1.00	0.27	1.02	0.25	[a]	[a]

[a] not measured

remained the least effective. It can be speculated that the relatively poorer behavior of the halon 1301 is attributable to the decreased residence time of the agent in the flame, such that the bromine has less opportunity to scavenge the chain carrying radicals.

A flame could not be stabilized using Mil-H-83282C hydraulic fluid and ambient temperature air. By increasing the fuel volume flow by 27% over the JP-8 flame and the air temperature to 120 °C (±3 °C), sufficient stability could be maintained. A bluish appearance of the hydraulic fluid spray flame suggested that less soot was being formed.

There was little difference in the amount of halogenated agent necessary to suppress the hydraulic fluid spray when compared to the JP-8 flames. (See Table 11, and note that neither FC-31-10 nor CF_3I was tested with the hydraulic fluid.) In particular, the amount of halon 1301 was identical to the unheated jet fuel experiments. About 10% more FC-318 was used to suppress the hydraulic fluid. By contrast, 28% less nitrogen extinguished the hydraulic fluid flame. An explanation for this unique behavior is not available.

4.4.4.4 Sodium Bicarbonate Powder Experiments. There was a definite particle size effect on the efficiency of the powder as a fire suppression agent. Table 12 summarizes the results. The smallest particle size powder was 2.4 to 3.0 times more effective in its fire suppression capability than the large particle size powder. There was no significant difference in performance created by changing injection pressure in the small size range. On the other hand, increasing pressure increased the effectiveness of the large particle size by more than 20%. The β values indicate a very effective agent for small particles, and a rather average agent for the large particle size.

High speed movies of injection of the 0-10 μm particles showed what appears to have been a uniform powder cloud passing through the burner in about 80 ms. This compared to an injection interval equal to 75 ms based upon the recorded air pressure in the storage vessel. The photographs also showed that flame extinction happened within the first 50 ms from the time the powder reached the flame. This time was independent of injection pressure, and was close to the 40 ms estimated from high speed photographs of HCFC-22 suppressing a similar flame.

4.4.5 Discussion of Results. If the agents are ranked according to the mass required to inhibit the flame, the order does not change by more than plus or minus one position for the three series of experiments. The exception is HFC-125, which drops two positions in both of the high temperature tests. Expressing the results in terms of the flame suppression number (FSN) is a convenient way to compare the performance of the different agents in the three series of experiments. The FSN is defined as the mass of agent relative to the mass of halon 1301 used to suppress the equivalent flame. Figure 45 summarizes the results in this fashion, using (a) ambient temperature air and JP-8 (open bars), (b) 150 °C air and JP-8 (cross-hatch bars), and (c) 120 °C air and hydraulic fluid (solid bars). The superior performance of the 0-10 μm $NaHCO_3$ powder is evident in the figure.

A flame suppression number also can be defined in terms of β, the mass fraction of agent in the flowing mixture, with β for halon 1301 used to normalize the results. The FSN computed on a mass flow basis can be seen in Figure 46. For the ambient temperature JP-8 flame, the cup burner mass flow FSN is about 2.0 ($\pm$0.15) for the various agents, which is about 0.5 greater than the FSNs plotted in Figure 46. The implication is that it takes a significantly lower mass fraction of agent to extinguish the turbulent spray flame than the cup burner flame. The cup burner was not operated at elevated temperatures, but one series of tests were run using ambient temperature hydraulic fluid. The same trend was observed when the cup and turbulent spray extinguishing mass fractions were compared: a measurable decrease in agent concentration was required for the turbulent spray flame (in spite of the fact that the higher reactant temperatures were expected to stabilize the spray flame, everything else being equal).

Minimizing the storage volume on board the aircraft is as critical as minimizing the mass of agent. There are a number of densities which one could use to convert the required mass of agent to the required volume, including the dispersed gas density and the density of the saturated liquid agent at ambient temperature. The former scales with molecular weight. The latter density also has practical significance. It provides a logical conversion from the mass required to the storage volume because the saturated liquid condition at ambient temperature is close to the condition maintained when the fire bottle is filled (assuming negligible solubility of the pressurizing gas). The volume factor, VF, is defined as the volume of the agent, computed with either of the above densities, normalized by the equivalent volume of halon 1301. Figure 47 compares the dispersed volumes. Figure 48 displays the volume factors under storage conditions. Nitrogen requires a storage volume 36 times that of halon 1301, and is off the scale in Figure 48 because it does not liquify under typical bottle conditions. The FC-116 also rates poorly on volume factor because its critical temperature is less than the ambient. In the figure, the density of FC-116 was calculated at 20 °C and 4.1 MPa, a typical bottle pressure. The remainder of the agents have storage volume factors between 1.5 and

Table 12. Sodium bicarbonate powder results

Particle Size, μm	Air Injection Pressure, kPa	Powder Mass, g	β
0-10	172	0.20	0.08
0-10	240	0.19	0.07
+50	172	0.59	0.20
+50	240	0.46	0.16

2.5, depending on the agent, fuel and temperature. Of these, the HFC-32/125 mixture has the highest volume factor, and HFC-227, HCFC-124 and HCFC-22 have the lowest. The powdered agent was not compared on a volume basis since the volume depends upon the pressurizing method as much as on the volume of the powder.

4.4.6 Conclusions from Turbulent Spray Burner Study. The turbulent spray burner has been found to be suitable for comparing the performance of gaseous and fine powder extinguishing agents in transient operation. The facility is not overly sensitive to the air or fuel flows, and the agent delivery system is able to control accurately the injection period between 20 and 910 ms.

The following conclusions can be made regarding the ability of different agents to extinguish the spray flame:

1. The mass fraction, total mass, and minimum volume of agent required to extinguish a given flame must all be considered when ranking the performance of different fire fighting agents.

2. Of the chemicals evaluated in the turbulent spray burner, $NaHCO_3$ was the only compound more effective than halon 1301. CF_3I required the least mass and volume of the gaseous agents to extinguish the flame, followed by nitrogen (FSN only) and the chlorinated agents, HCFC-22 and 124.

3. The larger perfluorocarbons, FC-31-10 and 318, required the greatest mass. On a volume basis, nitrogen was the poorest performer. The mixture of HFC-32 and HFC-125 had the largest volume factor of the condensible agents.

4. No statistically significant difference in agent performance was found between the room temperature JP-8 and hydraulic fluid flame testing, indicating little fuel effect.

5. The majority of the agents required slightly more mass to extinguish the higher temperature JP-8 flame, indicating a small temperature effect. This trend is not completely unexpected since a higher enthalpy flame is normally more stable. However, the temperature effect did not alter the ranking on agent performance, with the exception of HFC-125.

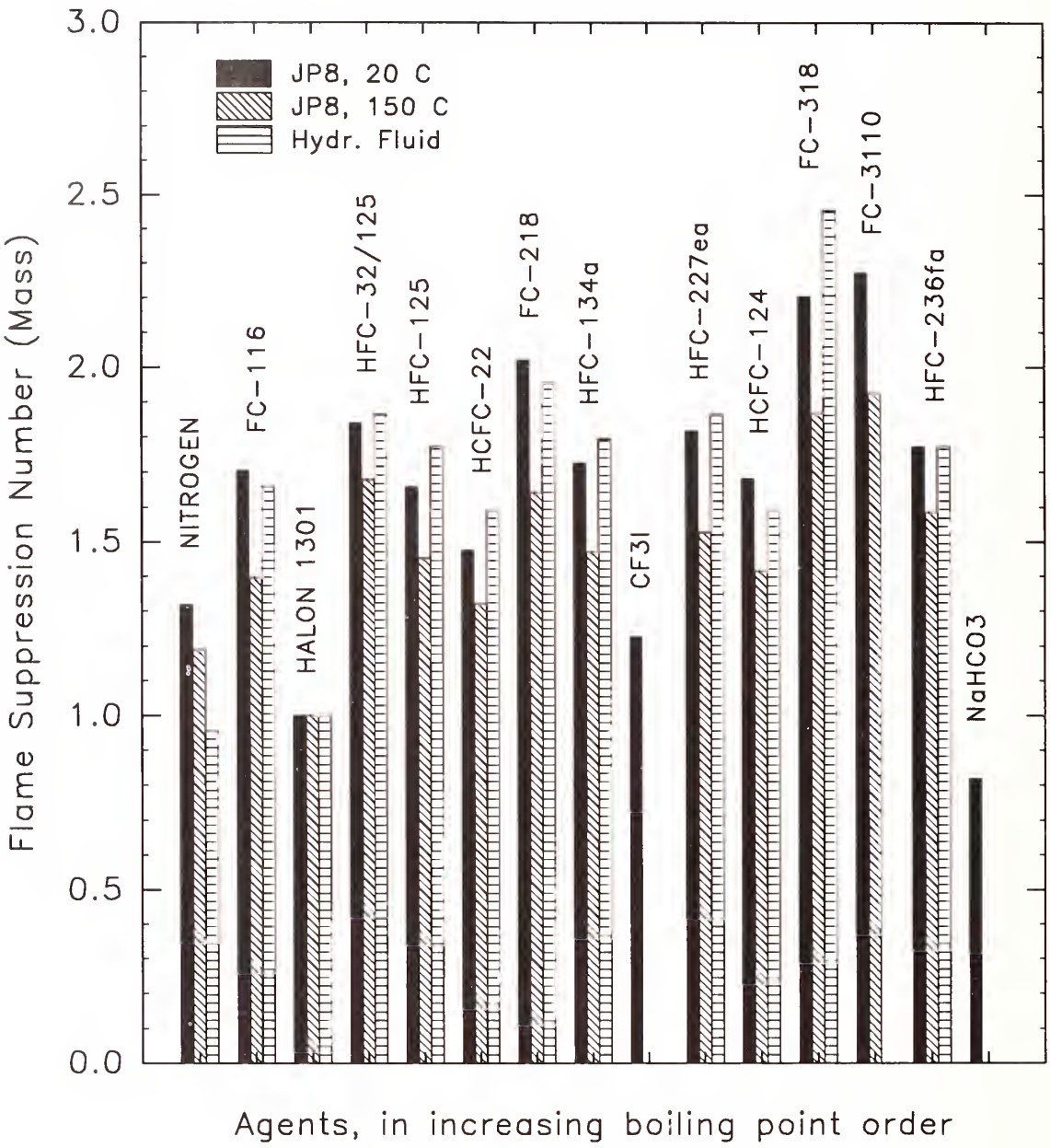

Figure 45. Flame suppression number (FSN) computed on a relative mass basis.

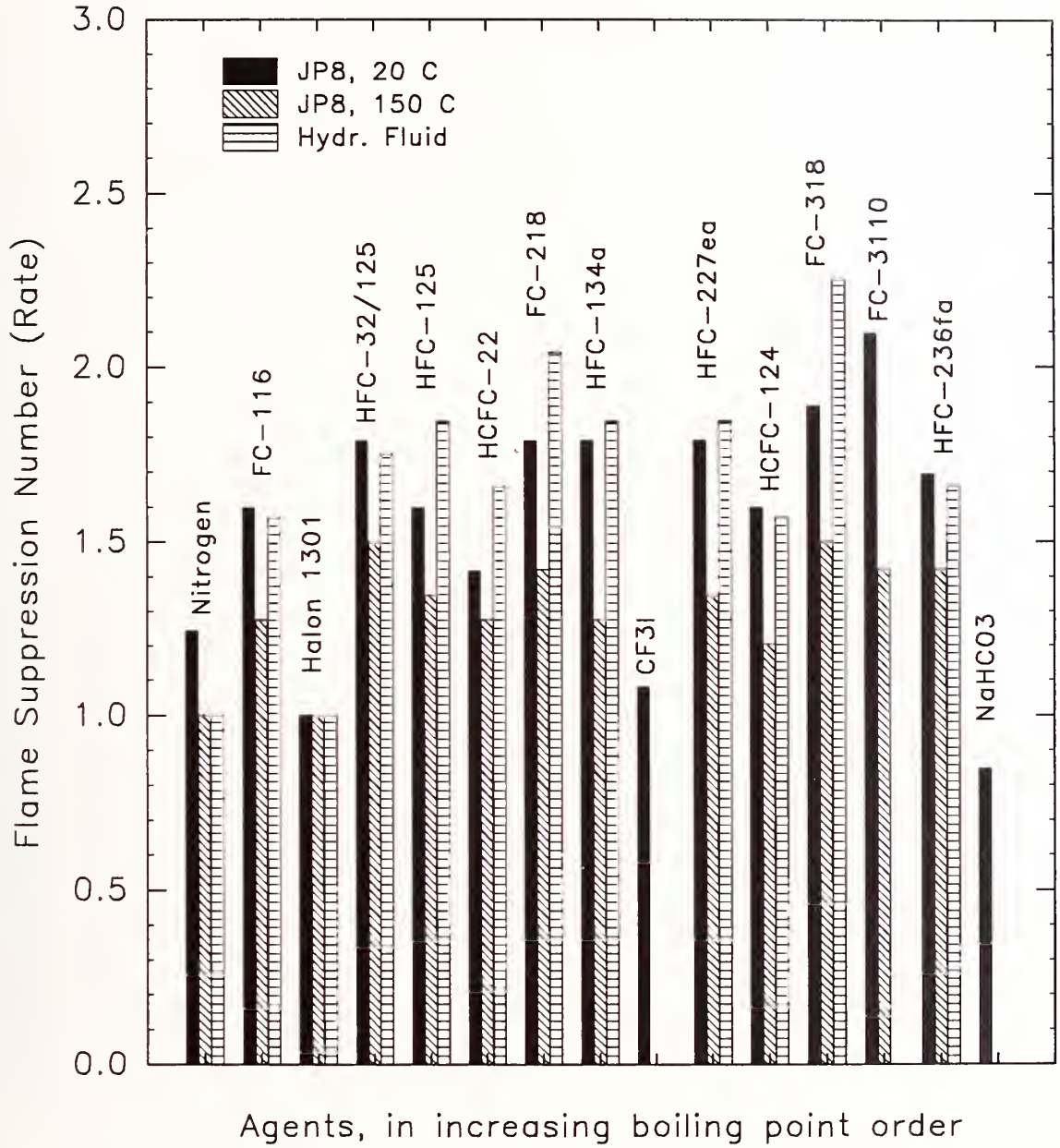

Figure 46. Agent flame suppression number (FSN) based upon relative rate of mass injected.

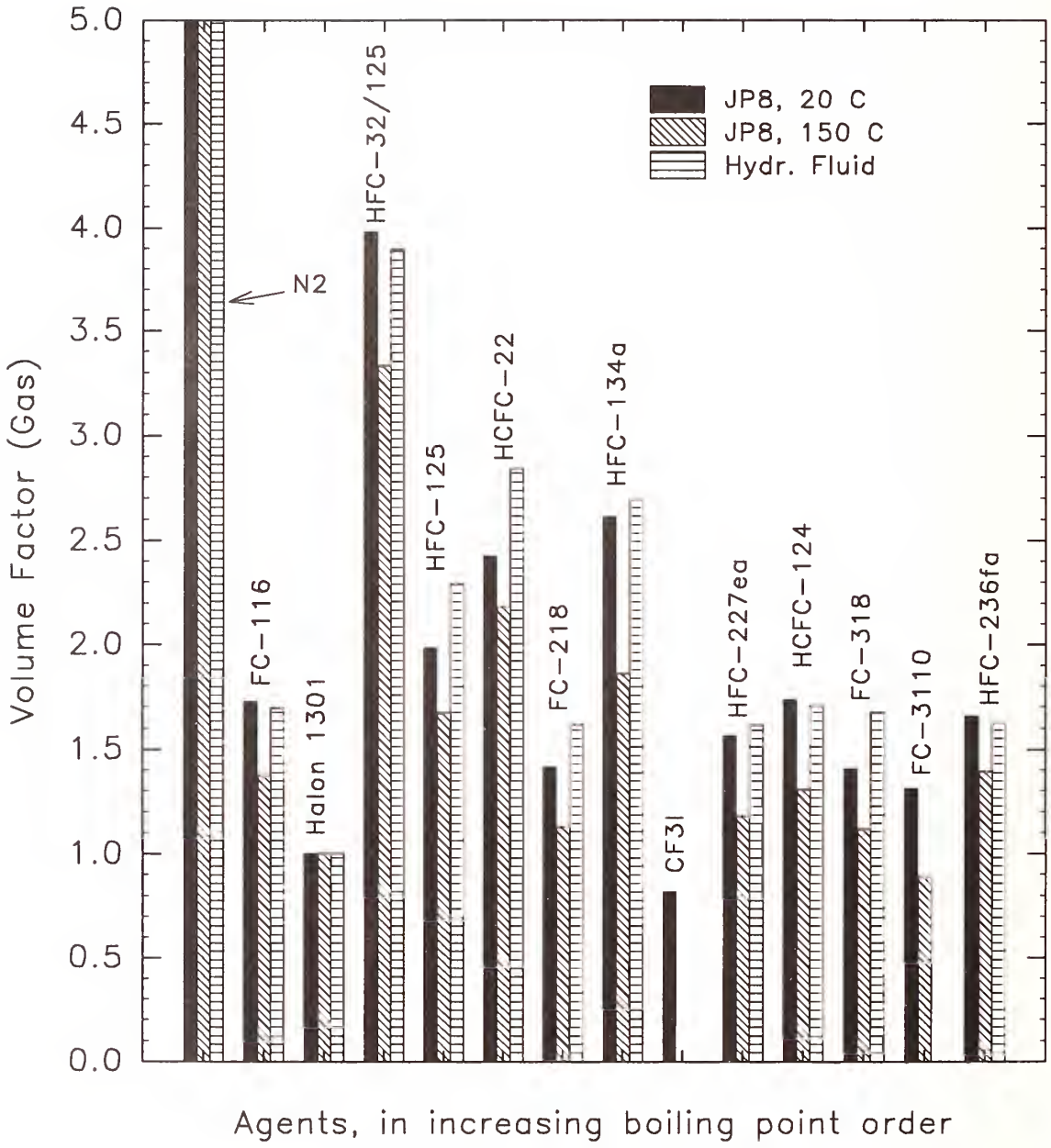

Figure 47. Dispersed gas volume factor (based upon 101 kPa and 22 °C air).

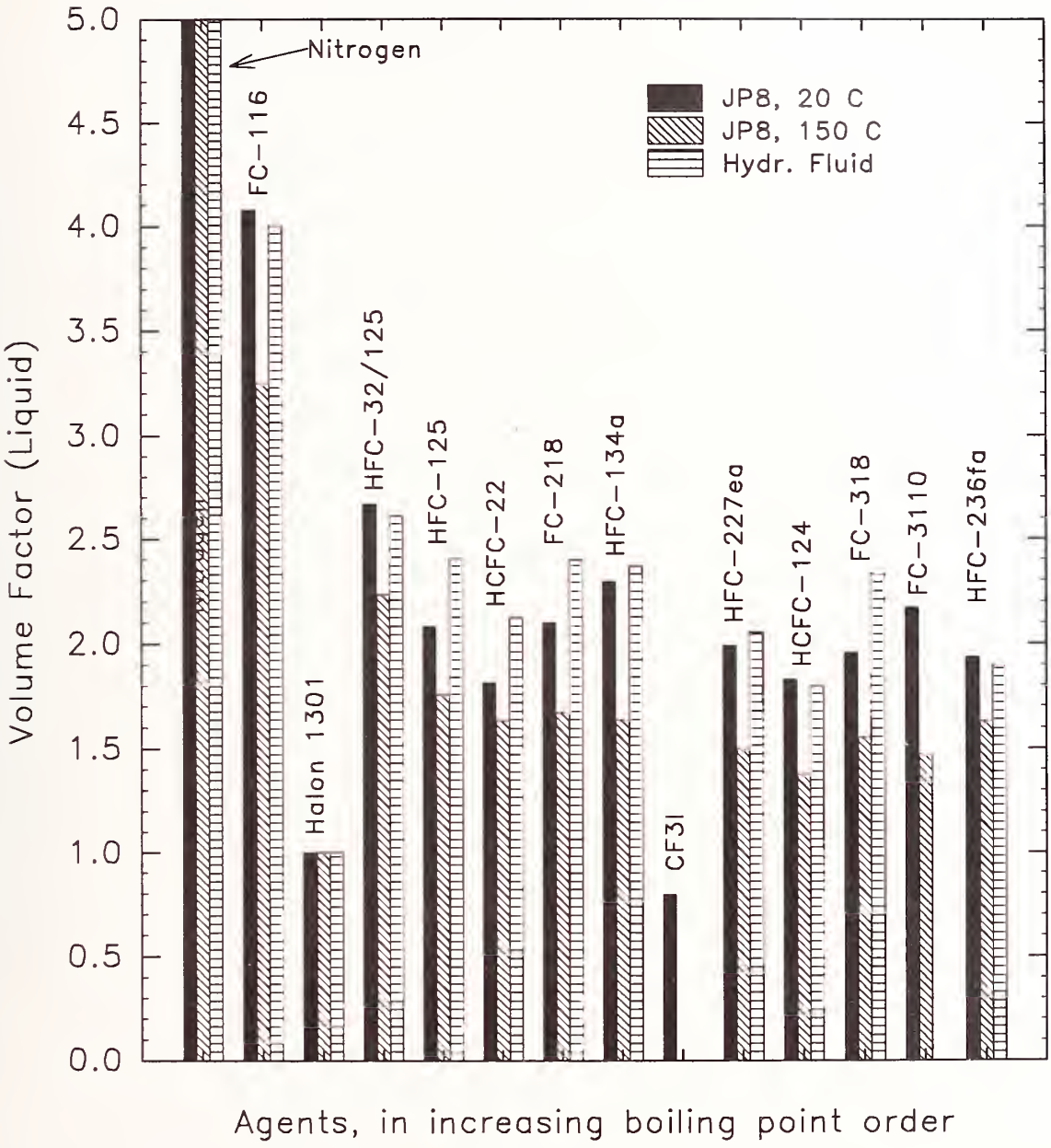

Figure 48. Storage volume factor of different agents based upon saturated liquid conditions at 20 °C.

6. The core gaseous agents all performed better in the turbulent spray burner relative to halon 1301 than was predicted from cup burner measurements. Generally speaking, about twice as much mass and volume were needed to suppress the spray flame using the core alternative agents when compared to halon 1301.

4.5 High Speed Premixed Flames and Quasi-detonations

4.5.1 Introduction. An anti-aircraft device entering a dry bay could lead to a situation in which a vaporizing fuel spray produces a combustible mixture which is then ignited by a glowing fragment. If the space were confined, the pressure would increase behind the reaction front, accelerating the flame. A transition to turbulence would likely occur as the flame encounters clutter in the dry bay. If the ventilation is insufficient to relieve the pressure build up, the possibility of a supersonic detonation would exist, leading to destructive over-pressures in the dry bay.

A supersonic flame is distinct from the flames simulated in the cup, OFDF and spray burners. As a result, the effectiveness of an agent in preventing a detonation depends upon different chemical and physical mechanisms. A shock wave precedes the supersonic flame. Obstructions in the flow promote intense mixing of the fresh reactants with the combustion products and cause the pressure waves to interact with the mixing region. Given enough distance, the flame can accelerate dramatically, increasing the temperature of the reaction zone behind the shock and further adding to the heat release rate. Depending upon the geometric details, the wave can approach its theoretical Chapman-Jouguet velocity and accompanying high pressure ratio. Even a slight variation in composition of the reactants near the limit of detonation can cause a dramatic change in the wave velocity and cause destructive pressures to be attained.

There exists an extensive literature describing the kinetics and dynamics of flame/shock wave systems formed within classical detonation tubes (*e.g.,* Lefebvre *et al.,* 1992; Nettleton, 1987; Lee, 1984; Baker *et al.*, 1983; Westbrook, 1982). Chapman and Wheeler (1926) were the first to note that a methane/air flame could be accelerated to a terminal velocity in a shorter distance within a circular tube by placing obstacles into the flow. Lee *et al.,* (1984) built on this observation to study quasi-detonations in hydrogen/air and hydrocarbon/air mixtures. A quasi-detonation propagates more slowly than a true detonation due to pressure losses in the flow, but its structure is more complex than a true detonation, and the mechanism of its propagation is not fully understood. Although an obstructed flow is more difficult to analyze than the flow in a smooth-walled tube, the complex arrangement was chosen for the current study because it more closely simulates a potentially damaging condition in the dry bay. The desire to rapidly suppress a flame and the associated pressure build up in such a situation is the primary motivation behind this study.

4.5.2 Experimental Facility. The effectiveness of a fire fighting agent in suppressing a high speed, premixed flame or quasi-detonation can be rated by the extent to which it decelerates the propagating wave and simultaneously attenuates the hazardous shock which is always ahead of the flame. Because the fire extinguishant is unlikely to be released prior to the establishment of a turbulent flame, the traditional experiment in which the flame inhibitor is premixed with the fuel and air prior to ignition (*e.g.*, Das, 1986) does not replicate the chemistry critical to the actual situation. Each dry bay on an aircraft has a different geometry, and the release of the agent once a fire is detected is highly variable. Heinonen *et al.,* (1991) injected suppressant into a chamber shortly following the ignition of a fuel spray in air, but had difficulty controlling the mixing and in duplicating the process. The

complexities and biases associated with the fluid dynamics of release can be avoided by premixing the agent with the fuel and air in a portion of the tube distinct from where the flame is initiated.

The two-section, deflagration/detonation tube shown in Figures 49 and 50 was designed to produce the desired environment for both the flame initiation and flame suppression regimes. A repeatable, uninhibited turbulent flame was fully established in the driver section, the design of which was based directly upon the work of Peraldi *et al.*, (1986). They found that a 50 mm inner diameter tube with a blockage ratio of 0.43 could be used to create repeatable, high-speed flames and quasi-detonations within the first several meters of an 18 m tube. By varying the equivalence ratio of ethene/air mixtures from 0.5 to 2.1, they were able to produce flame velocities between about 600 and 1300 m/s.

The driver section was 5 m long and was equipped at the closed end with a spark plug. This section was filled with the combustible mixture of ethene and air. The gas handling system consisted of a vacuum pumping network; pressurized gas cylinders for the fuel, oxidizer and agent; and a dual circulating pump. The ignition energy was delivered in a microexplosion of a tin droplet short-circuiting the tips of nichrome electrodes connected to an 80 V power supply. Spiral-shaped obstructions made of 6.4 mm stainless steel rods with a pitch equal to the inner diameter of the tube were inserted into the tube, to produce an area blockage ratio of 44%, close to the value shown by Lee *et al.* (1984) to promote a quasi-detonation in their facility. The second section of the deflagration/detonation tube contained the gaseous agent along with the same fuel/air mixture used in the driver section. The diameter was the same and its length was 2.5 m. An identical spiral insert was used to maintain a high level of mixing. The two sections were separated from each other by a 50 mm inner diameter, stainless steel, high vacuum gate valve, which remained closed until just before ignition.

Pressure transducers and photodiodes were located along the test section to monitor the strength and speed of the combustion wave. Their output was recorded on a multi-channel, digital storage oscilloscope. The pressure transducer mounting is depicted in Figure 51 and a schematic of the photodiode mounting is shown in Figure 52. A logic diagram of the photodiode sequencing system is shown in Figure 53.

4.5.3 Operating Procedure. The whole system was evacuated to 10^{-1} Pa before filling the two sections separately with the desired mixtures, which were attained through the method of static partial pressures. The fuel/air ratio and total pressures were held constant across the gate valve. The initial temperature was the ambient value, 22 $\pm$ 3 °C. The oxidizer used in all experiments was breathing grade air. Ethene (CP grade, 99.5% volume purity) was chosen as the fuel because it had been demonstrated (Lee *et al.*, 1984) that subsonic flames, quasi-detonations, and full detonations all could be obtained in a tube of this geometry simply by varying the stoichiometry. After filling, the gases were homogenized independently using a double, spark-free circulating pump, recirculating the entire tube volume a total of 20 times. The mixtures were left for five minutes to become quiescent. About ten seconds prior to ignition, the gate valve was opened manually.

After ignition, the flame propagated into the driver section and accelerated quickly due to the intense turbulence created by the interactions of the flow with the obstacles, generating a shock wave ahead of it. After passing through the open gate valve the flame/shock system encountered the same combustible mixture and a certain amount of agent in the test section. A rendering of the flame/shock system passing through the gate valve is shown in Figure 54. Depending on the concentration of the agent, the flame was or was not extinguished and the pressure wave attenuated.

Experiments using 5% ethene in air mixtures were run under a variety of conditions to assess the operation of the system. Figure 55 is an example of the pressure trace when the N_2 partial pressure is (a) insufficient to extinguish the flame radiation, and (b) sufficient for suppression of an air/ethene

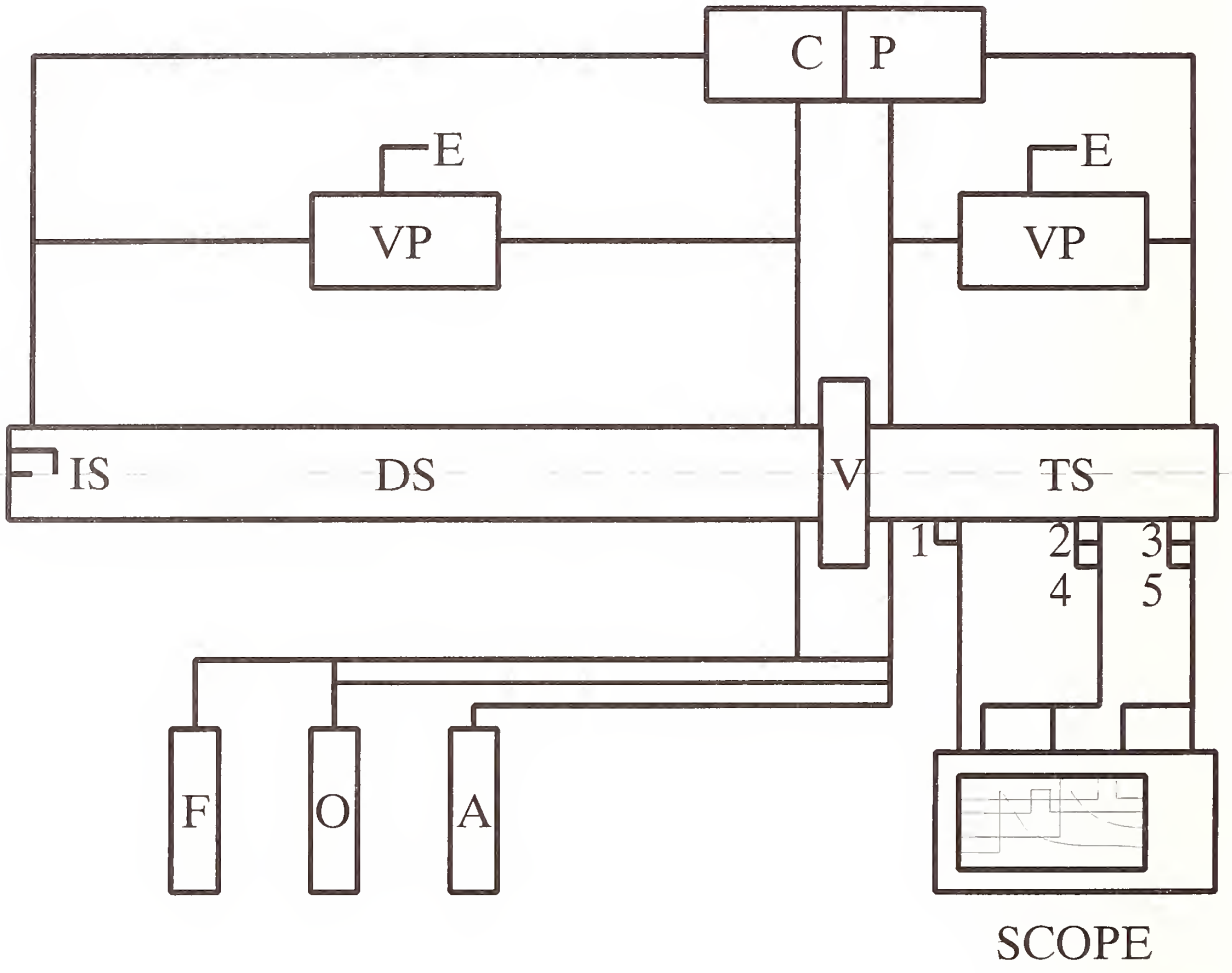

DS - Driver Section, TS - Test Section, V - High Vacuum Gate Valve, IS - Ignition Source, CP - Dual Circulating Pump, VP - Rotary Vacuum Pump, E - Exhaust, F - Fuel, O - Oxidizer, A - Agent, 1 - Triggering Transducer, 2,3 - Piezo-electric Pressure Transducers, 4,5 - Fast Photodiodes, SCOPE - Collects Four Pressure and Visible Radiation Signals

Figure 49. Schematic diagram of detonation/deflagration tube facility.

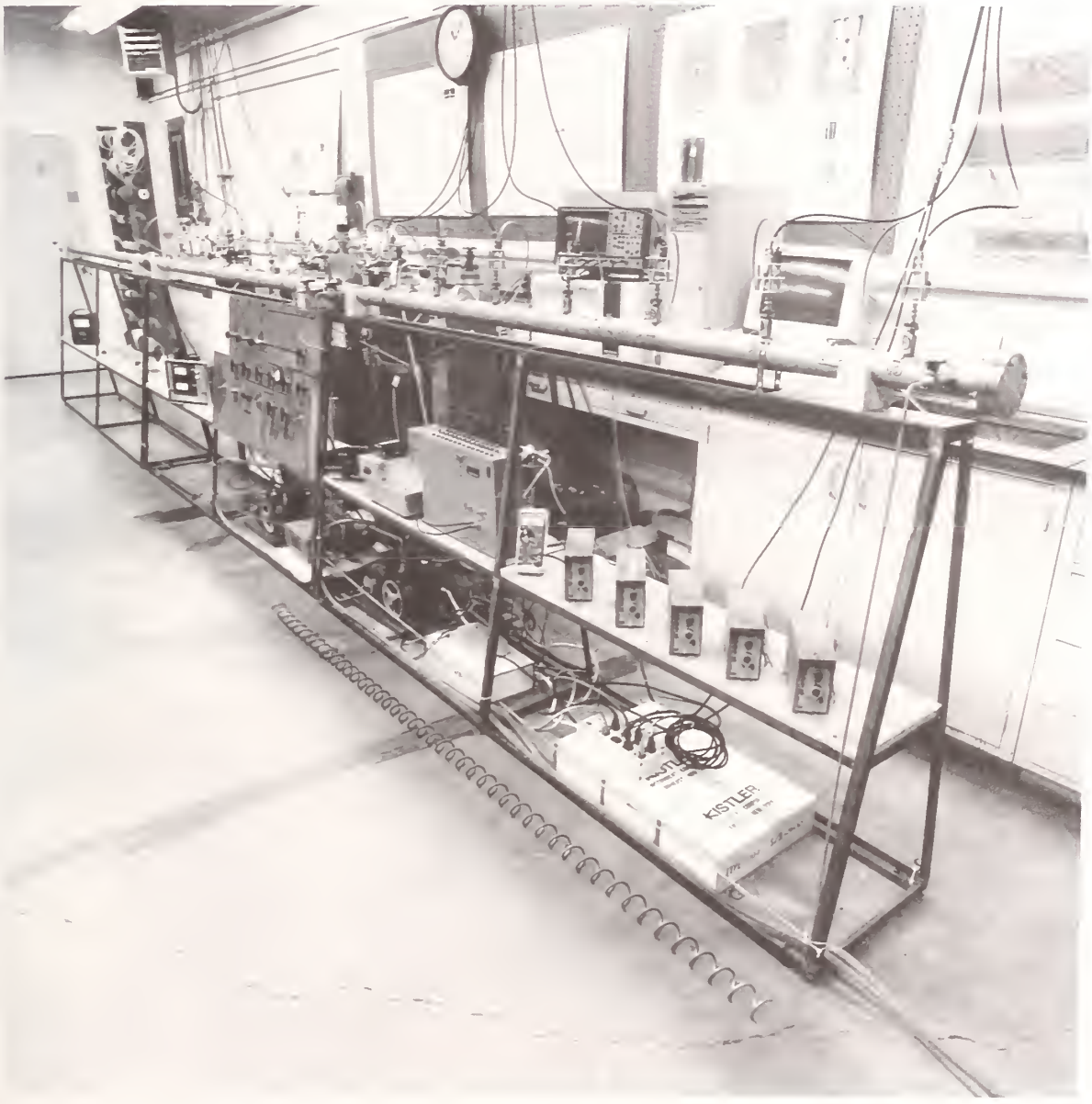

Figure 50. Photograph of detonation/deflagration tube facility.

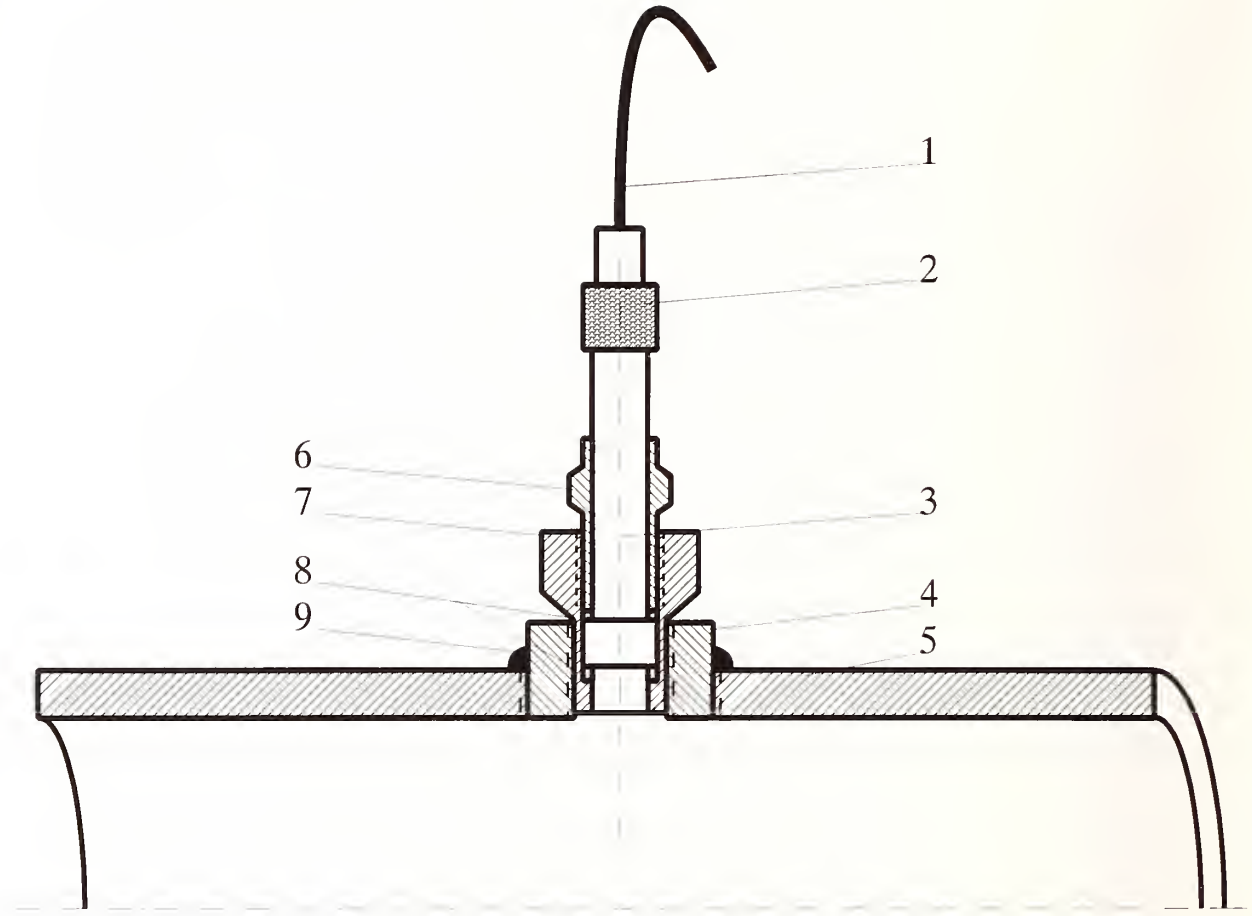

1 - Low-noise Cable, 2 - Cable Connector, 3 - Piezo-electric Pressure Transducer, 4 - Stub, 5 - Tube, 6 - Retaining Nut, 7 - Holder, 8 - Seals, 9 - Seal Weld

Figure 51. Pressure transducer mounting.

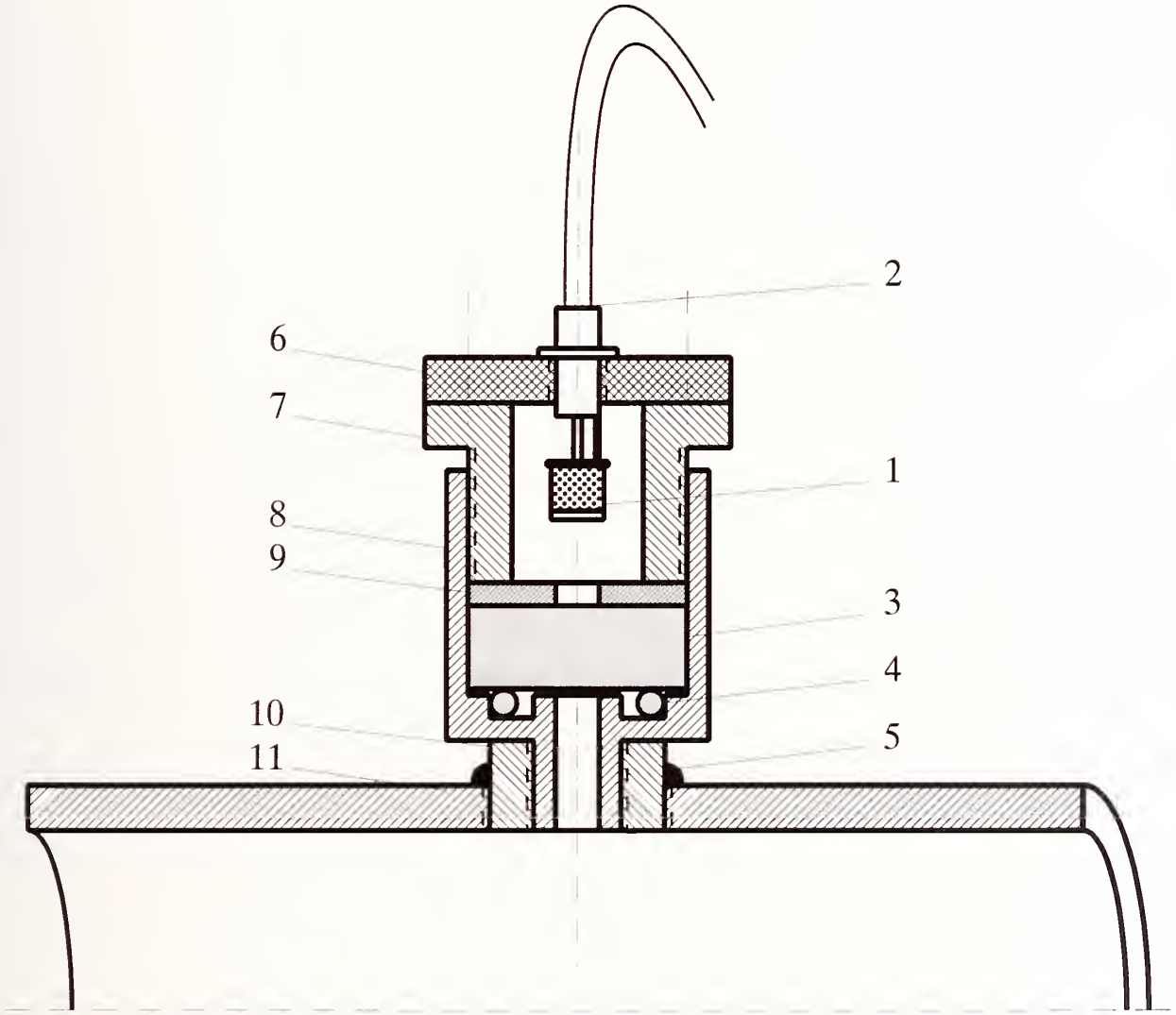

1 - Fast Photodiode, 2 - BNC Cable, 3 - Quartz Window,
4 - "O" Ring, 5 - Seal Weld, 6 - Plexiglas Cover, 7 - Barrel,
8 - Holder, 9 - Washer, 10 - Stub, 11 - Tube

Figure 52. Photodiode mounting.

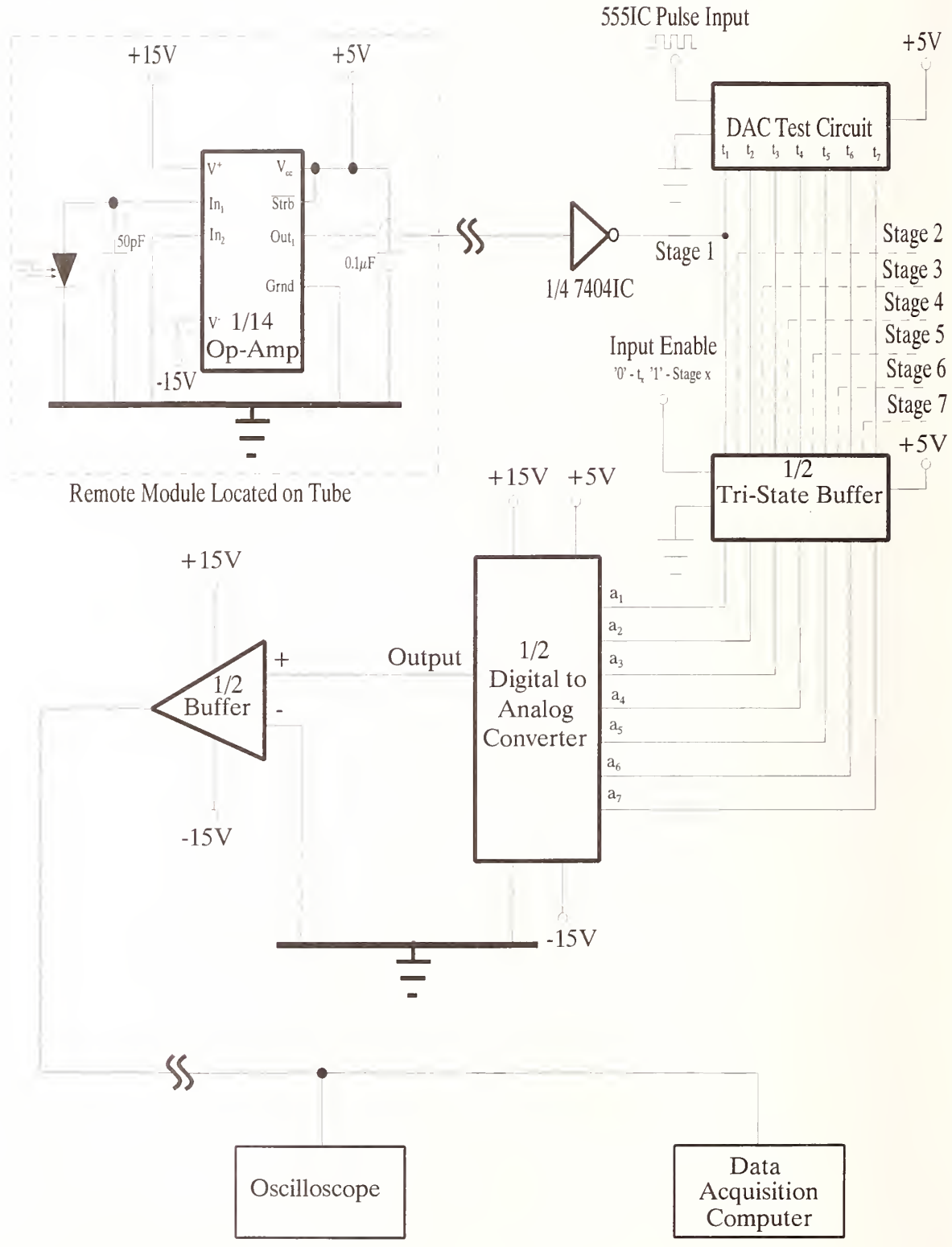

Figure 53. Logic diagram of photodiode sequencing system.

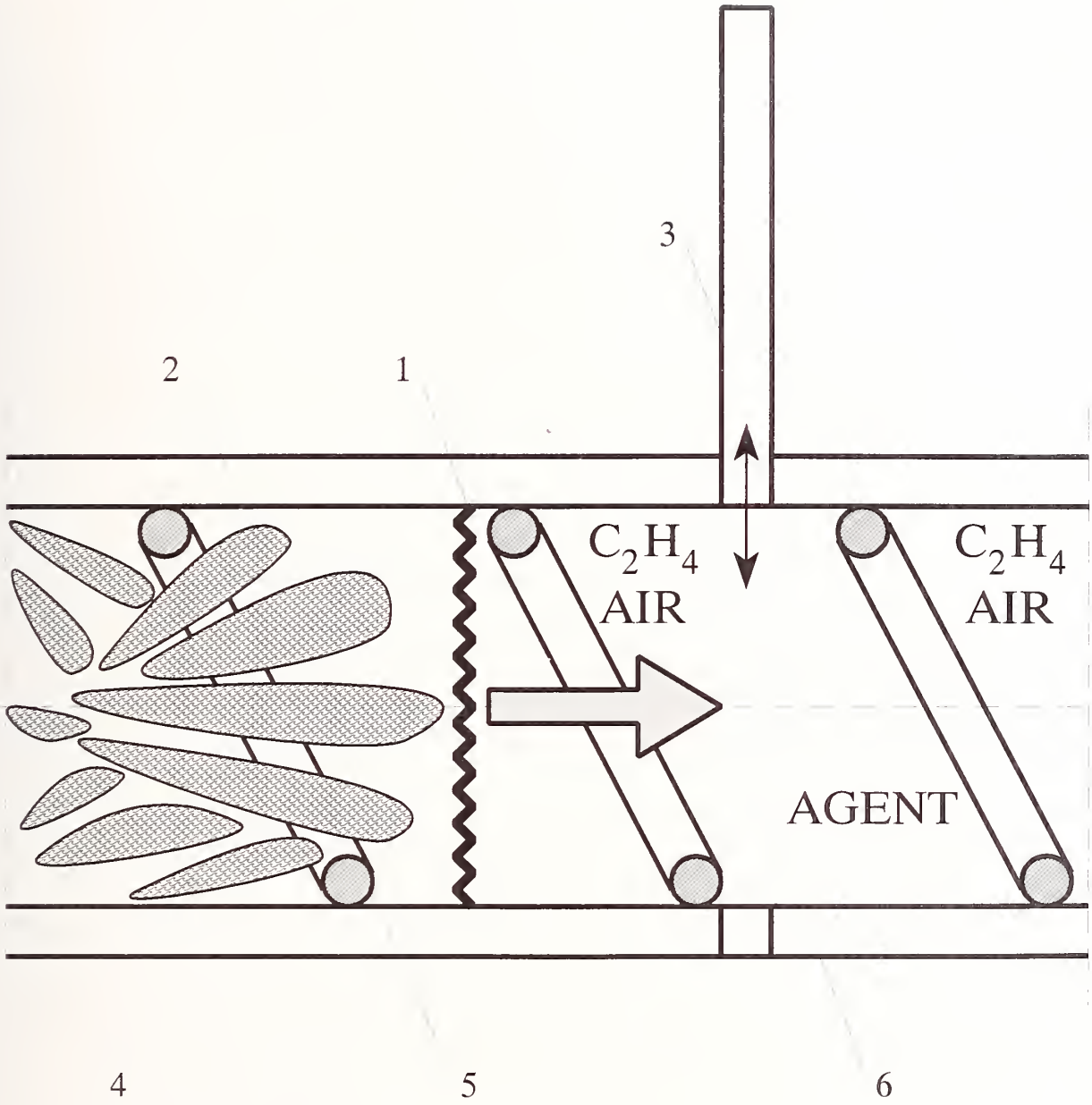

1 - Shock Wave, 2 - Turbulent Premixed Flame, 3 - Gate Valve,
4 - Driver Section, 5 - Spiral Obstruction, 6 - Test Section

Figure 54. Rendering of high-speed turbulent flame entering test section.

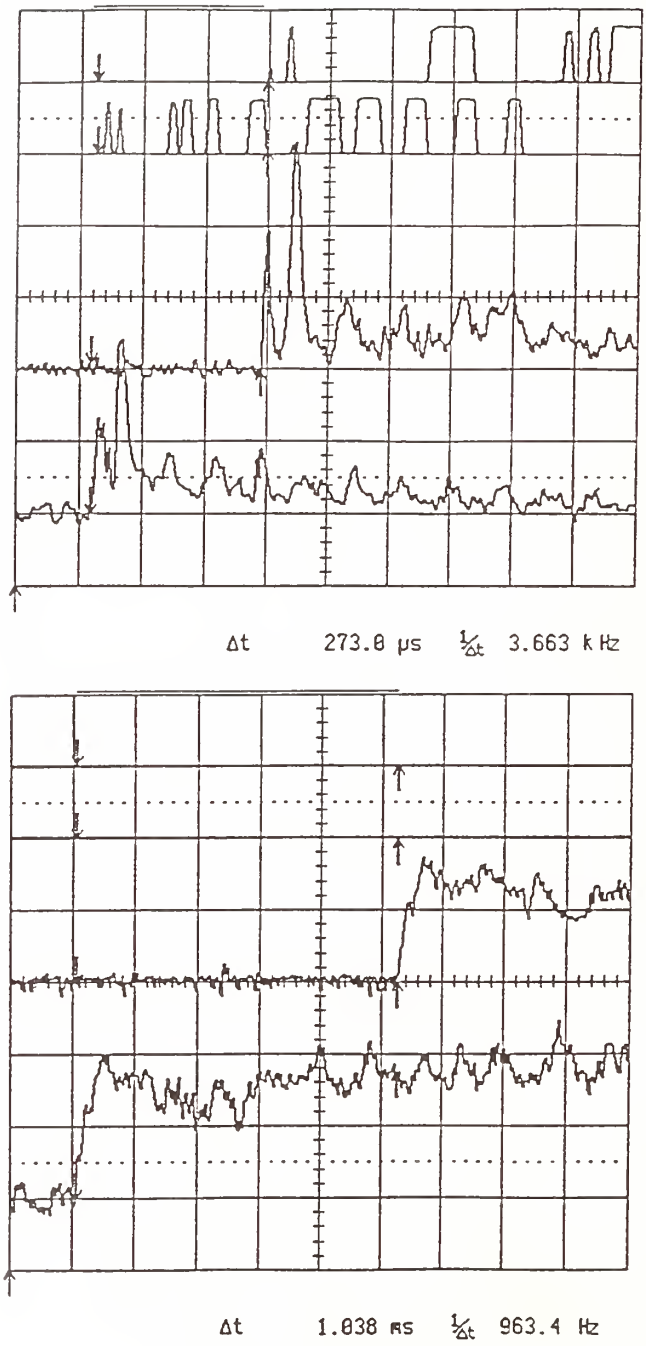

Figure 55. Pressure traces comparing (a) non-suppressed and (b) suppressed flames using FC-31-10.

mixture at a total pressure of 100 kPa. Knowing the distance between the two pressure transducers, the shock speed was determined from the time lag between the pressure rises. The pressure ratio was tabulated from the initial pressure in the tube and either the first peak or the maximum pressure increase. The sensitivity of the flame speed and pressure ratio to the voltage of the ignition system, the mixing time of the components before ignition, the presence or absence of the gate valve, the speed of opening the gate valve, and cleaning the tube between runs were all investigated.

Experiments were conducted with 100% nitrogen in the test section, a 5% ethene in air mixture in the driver section, and the total pressure equal to 20, 50 and 100 kPa. The incident shock wave velocity measured 2.2 m beyond the gate valve and 0.3 m from the end of the tube was 420 $\pm$ 8 m/s at all three total pressures. The pressure ratio based upon the initial pressure rise was 2.5 $\pm$ 0.5, and about 3.0 $\pm$ 1.0 based upon the peak increase.

As can be seen in Figure 56, no significant changes in shock speed occurred for a partial pressure fraction (which is approximately equal to the mole fraction) of nitrogen in air greater than 40%. The region of no change was extended down to 30% for the 20 kPa case. When no suppressing nitrogen was added to the test section the shock velocities attained values of 780 and 1170 m/s, respectively, for the 20 kPa and 100 kPa experiments. The pressure ratio based upon the initial rise is plotted in Figure 57. P_1/P_0 increased dramatically at the same point as the velocity when the partial pressure of nitrogen was decreased, reaching maxima of 26 and 18, respectively, for the 20 kPa and 100 kPa initial conditions when no nitrogen was added to the ethene/air mixture. The peak pressure ratio, which normally did not correspond to the initial pressure pulse, exceeded 50:1 for the 20 kPa and 50 kPa experiments. The 100 kPa experiments generated peak pressure ratios around 30:1.

The results of the preliminary parameter assessment led to an experimental protocol which yielded flame speeds which were reproducible from run to run within about $\pm$ 2%. Pressures downstream of the shockwave had a higher variability ($\pm$ 20%) because of the complex shock structures created by interactions with the spiral rod inserts.

4.5.5 Results and Analysis. Mach number and pressure ratio were the two dependent parameters which were measured as a means to characterize the extent of flame suppression. The Mach number was based upon the time it took for the pressure wave to travel the distance between the two pressure transducers, normalized by the sonic velocity of the reactant gases in the test section. The pressure ratio was evaluated from the average amplitude of the first pressure pulse to be recorded by each transducer, normalized by the initial pressure. Consecutive pressure jumps occurred, as can be seen in Figure 55, indicating that localized explosions in the mixing region between the spirals were present. Individual runs were concluded before the shock wave reflected from the end plate arrived back at the pressure transducers. The distance between the leading shock wave and the flame front was measured in some of the experiments from the time lag between the photodiode and pressure transducer response at the same location. The primary independent variables were agent type and concentration. The fuel/air equivalence ratio and the system absolute pressure were also varied for a number of agent experiments.

Table 13 summarizes the results with no suppressant in the test section, and compares the Mach number, pressure ratio, and flame spacing to the situation in a "fully suppressed" flame, in which pure nitrogen was located in the test section. Note that neither the Mach number nor pressure ratio go to zero for the fully suppressed case because total dissipation of the shock wave would require a substantially longer tube. On the other hand, the flame radiation disappears entirely; hence, the infinite separation distance.

The bromine atom in CF_3Br is known to inhibit laminar flames by scavenging active radicals from the chain-branching reactions. Experiments using halon 1301 were run to compare to an

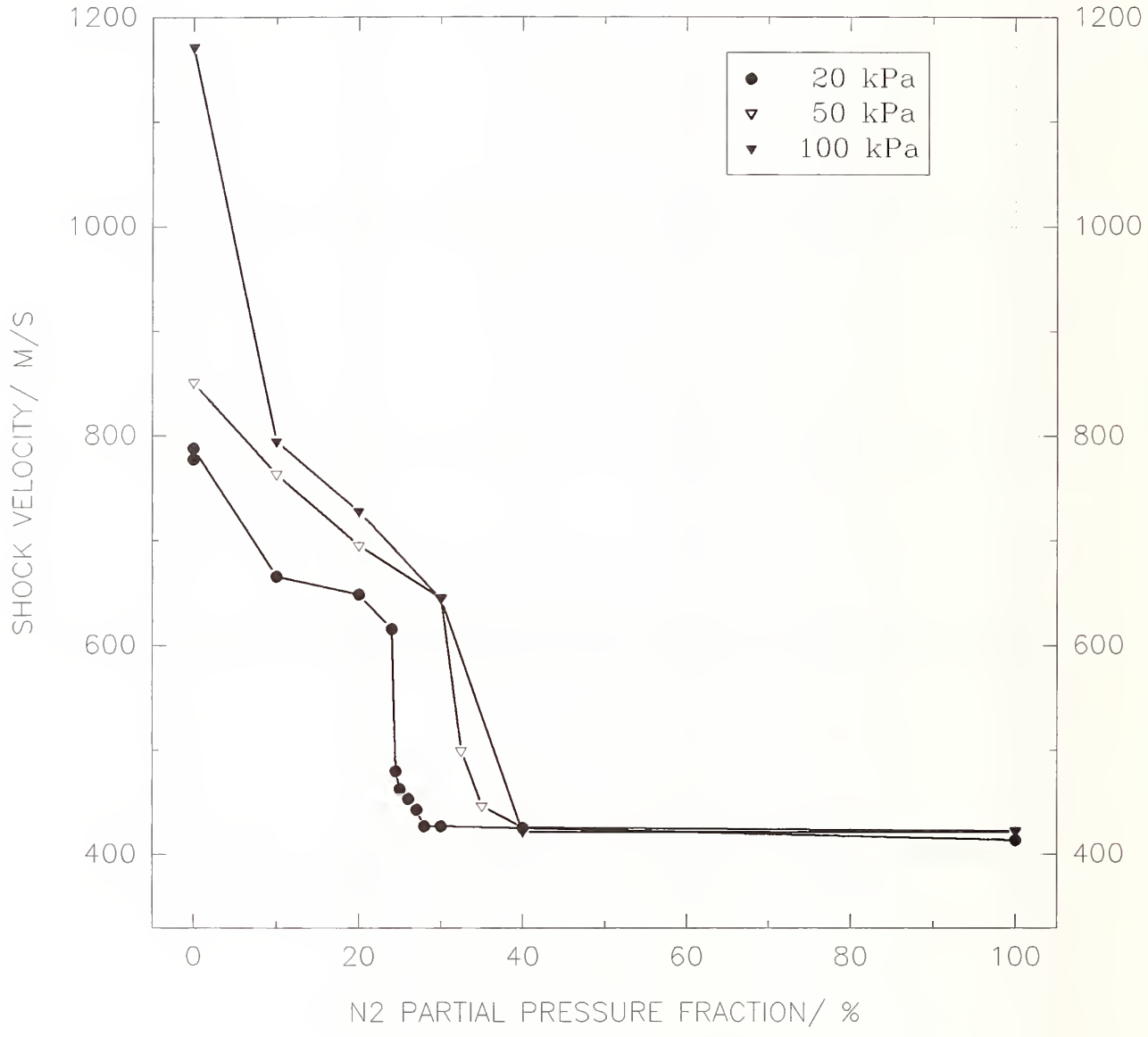

Figure 56. Effect of initial pressure on the reduction of shock wave velocity by nitrogen.

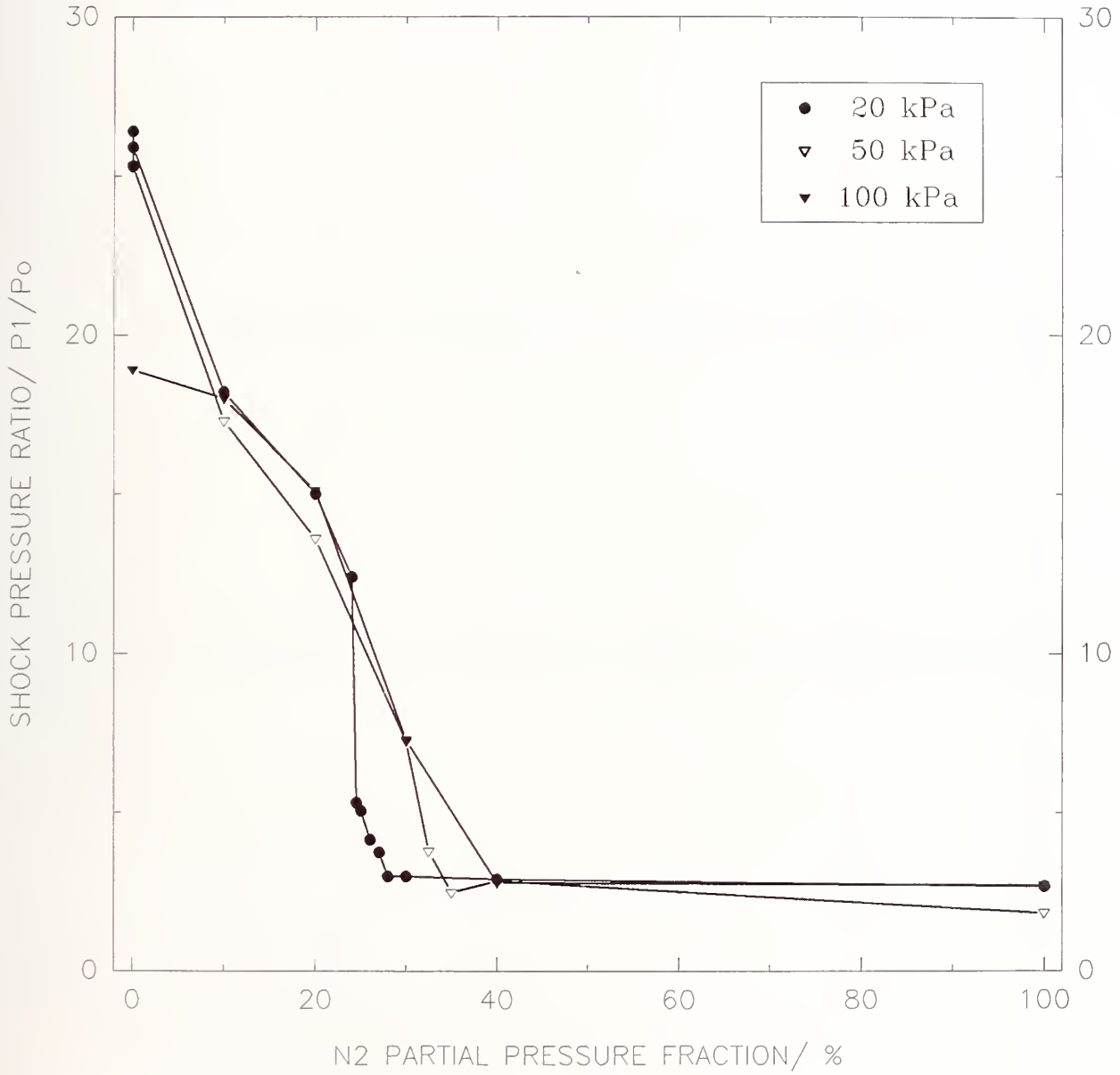

Figure 57. Effect of initial pressure on the reduction in pressure ratio by nitrogen.

Table 13. Summary of flame parameters for ethene/air mixtures under suppression extremes

Amount of N_2 added to Test Section	Initial Pressure	Equivalence Ratio	Mach Number	Pressure Ratio	Flame/Shock Separation Distance, mm
0%	20 kPa	0.75	2.4 ± 0.1	26 ± 1	[a]
	50 kPa	0.75	2.6 ± 0.1	26 ± 1	[a]
	100 kPa	0.75	3.4 ± 0.1	18 ± 2	3 ± 1
	100 kPa	1.00	4.1 ± 0.1	26 ± 2	2 ± 1
	100 kPa	1.25	4.5 ± 0.1	35 ± 3	[a]
100%	20 kPa	0.75	1.25 ± 0.05	2.5 ± 0.5	∞
	50 kPa	0.75	1.25 ± 0.05	2.0 ± 0.5	∞
	100 kPa	0.75	1.25 ± 0.05	2.5 ± 0.5	∞
	100 kPa	1.00	1.3 ± 0.1	3.5 ± 0.5	∞

[a] quantity not measured

inerting agent like N_2, and to determine the suitability of the facility for assessing the effectiveness of a wide range of agents for suppressing high speed turbulent flames and detonations. Figures 58 and 59 show the shock Mach numbers and the respective pressure ratios measured at three different total pressures as a function of the partial pressure fraction of CF_3Br in the test section. The largest effect of total pressure occurred between 50 and 100 kPa for halon, compared to between 20 and 50 kPa for N_2. Halon 1301 suppressed the flame at a partial pressure fraction of 10% to the same extent as if the test section had been completely filled with nitrogen. An unusual behavior occurred in the 100 kPa experiments when the concentration was between 2% and 3%. Both the Mach number and pressure ratio increased with the amount of CF_3Br, followed by the expected decrease for large concentrations. The reversal, while small, was greater than the uncertainty in the data.

Halocarbons, unlike nitrogen, are known to promote the production of soot. To determine the sensitivity of the shock velocity to soot contamination, a series of experiments with a 5% ethene/air mixture at a total pressure of 20 kPa was run for CF_3Br partial pressure fractions between 0 and 10% with and without cleaning the tube and spirals in the test section. The performance was similar, with the maximum deviation between the cleaned and uncleaned results amounting to less than 35 m/s.

4.5.5.1 Lean Mixtures at 100 kPa. Attenuation of the shock speed and pressure increase by the core agents and CF_3I was measured with the ethene/air equivalence ratio fixed at 0.75 (5.0% by volume C_2H_4), an initial absolute pressure of 100 kPa, and an initial temperature of 22 °C. It was found that the amplitude and speed of the pressure wave, and the speed of the trailing flame, were all strongly dependent on the agent type and concentration. The flame always followed the shock wave in such a way that both speeds were equal. However, when the amount of the agent in the mixture was increased, the distance between the shock and flame increased as well, up to around 100 mm as

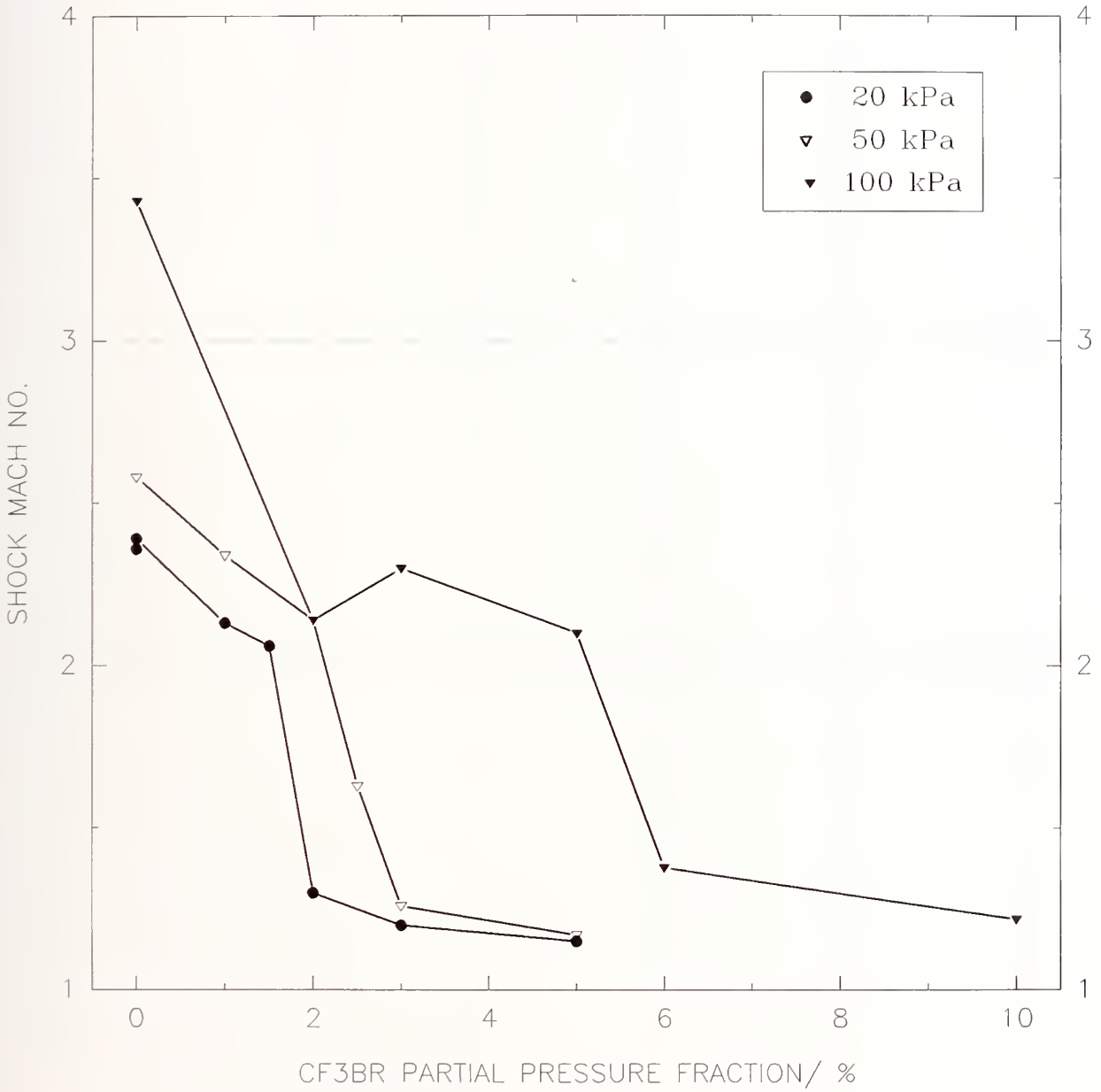

Figure 58. Effect of initial pressure on the reduction in shock wave Mach number by CF_3Br.

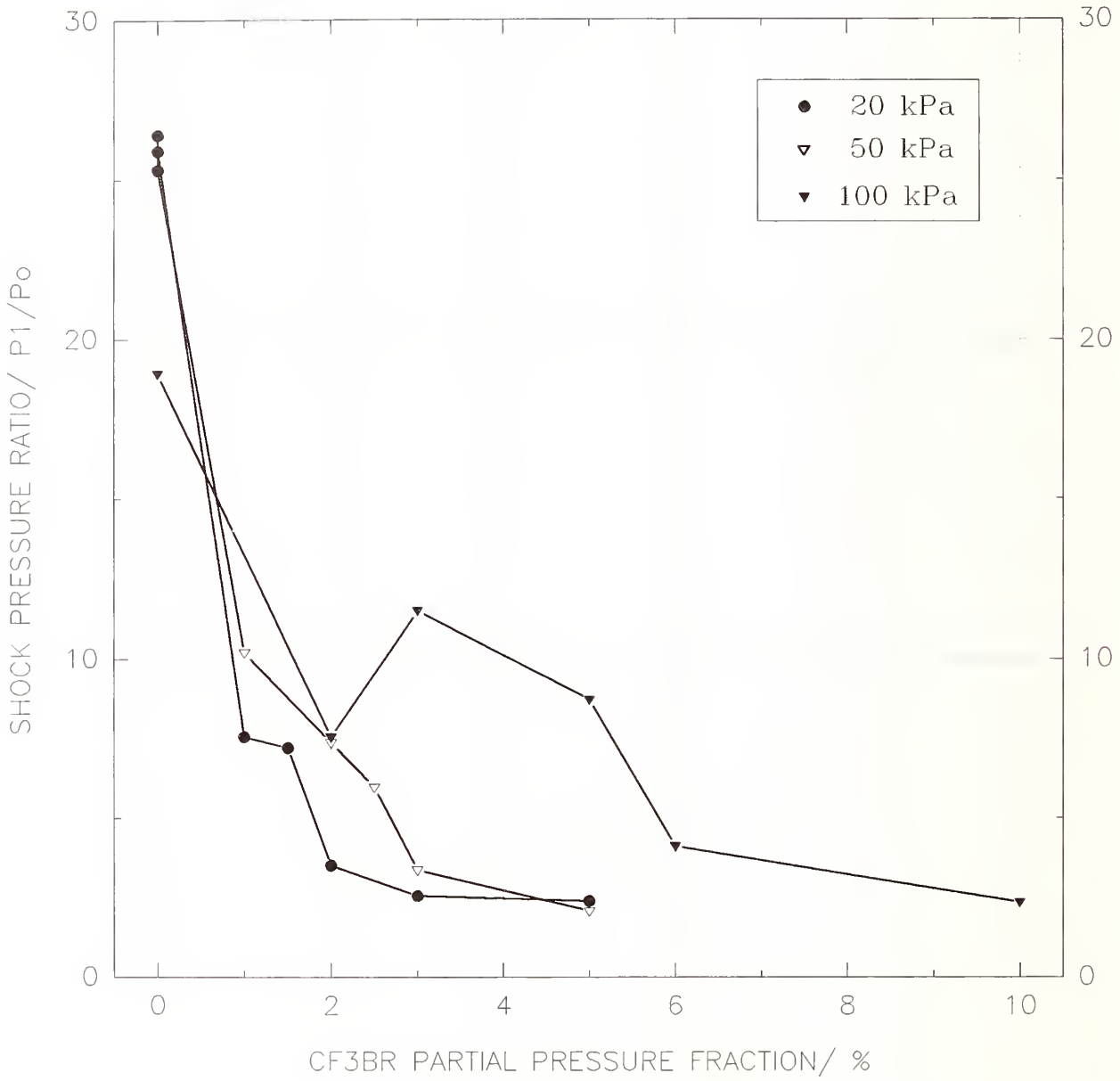

Figure 59. Effect of initial pressure on the reduction in pressure ratio by CF_3Br.

full suppression was approached. At the extinguishing concentration the radiation disappeared, which indicated the absence of the flame. In that situation the pressure wave amplitude was attenuated by a factor of eight and the wave speed by a factor of three, similar to the results for nitrogen (see Table 13).

The results for all the alternative agents are compared in Figures 60-63. The amount of agent is expressed both as a mass fraction and as a partial pressure fraction. The Mach numbers and pressure ratios at zero represent the pure combustible mixture with no flame suppressing agent present. One can see that the concentrations necessary for total extinguishment for all the compounds are between 40 and 50% by mass. However, at low concentrations the Mach numbers and pressure ratios are higher for some agents than even the value for the pure combustible mixture. Because of the sheer number of data, it is instructive to examine the results by the class of compound; *i.e.*, FCs, HFCs, HCFCs and the IFC (CF_3I).

The FCs, as a class, were generally the best performers on both a partial pressure and mass fraction basis. In fact, FC-116 was superior to CF_3Br, and FC-318 was about equivalent. FC-218 and FC-31-10 slightly enhanced the pressure ratio in low concentration. This can be seen in Figures 64 and 65. FC-218 reduced the pressure ratio to less than 5:1 at a mass fraction of 0.29, which was better than with CF_3Br.

Adding hydrogen to the molecule had a significant effect on the performance of the HFCs, shown in Figures 66 and 67. The HFC-32/125 mixture produced peak pressures more than double the value for no suppressant. The Mach number was increased to its highest value of 4.1 when the mass fraction was 11%. It wasn't until the mass fraction exceeded 38% that the HFC-32/125 mixture became as effective as nitrogen in reducing the speed and pressure build-up of the shock wave. The two fluoropropanes, HFC-227ea and HFC-236fa produced the lowest pressure build-up of the HFCs and did a good job of suppressing the shock speed.

The chlorine atom in the two HCFCs created an additional complexity because chlorine is a strong oxidizer. From Figure 68, one can see that HCFC-22 was the least effective on a mass basis of all of the agents in fully suppressing the combustion wave Mach number, requiring a mass fraction of over 50% in the test section. The maximum pressure ratio for HCFC-124 was 32:1 at a 23% mass fraction (see Figure 69), which was exceeded only by HFC-125 and the HFC-32/125 mixture (Figure 67).

The one IFC tested was CF_3I. The Mach number and pressure build-up, shown in Figure 70, were cut about in half with partial pressure fractions in the test section of only 15 to 20%. None of the other chemicals, including CF_3Br, was able to accomplish that. Unfortunately, when the mass fraction was increased to 30%, the Mach number shot back up and the pressure ratio attained a value of 21:1, which was greater than when no CF_3I was present. This reversal, which was slight in the bromine-containing halon 1301, changed what at first appeared to be the most effective suppressing agent into one of the least effective agents. It is known that iodine atoms can cause a catalytic effect in some reactions by lowering the overall activation energy. At intermediate concentrations the possibility also exists that the iodine (and bromine) recombined, reducing their impact on the combustion process. It is not out of the question that in the cases under consideration both of these effects became important.

4.5.5.2 Stoichiometric Mixtures. Changing the fuel/air mixture (*i.e.*, the equivalence ratio) changes the flame temperature and radical concentration significantly. Figure 71 demonstrates the impact of equivalence ratio on the shock Mach number and pressure ratio with no agent in the test section. To see if the relative performance of the agents was dependent upon the fuel/air ratio a number of experiments were run under stoichiometric conditions. The equivalence ratio was based upon the amount of ethene in the mixture and was not adjusted to account for the contribution of the

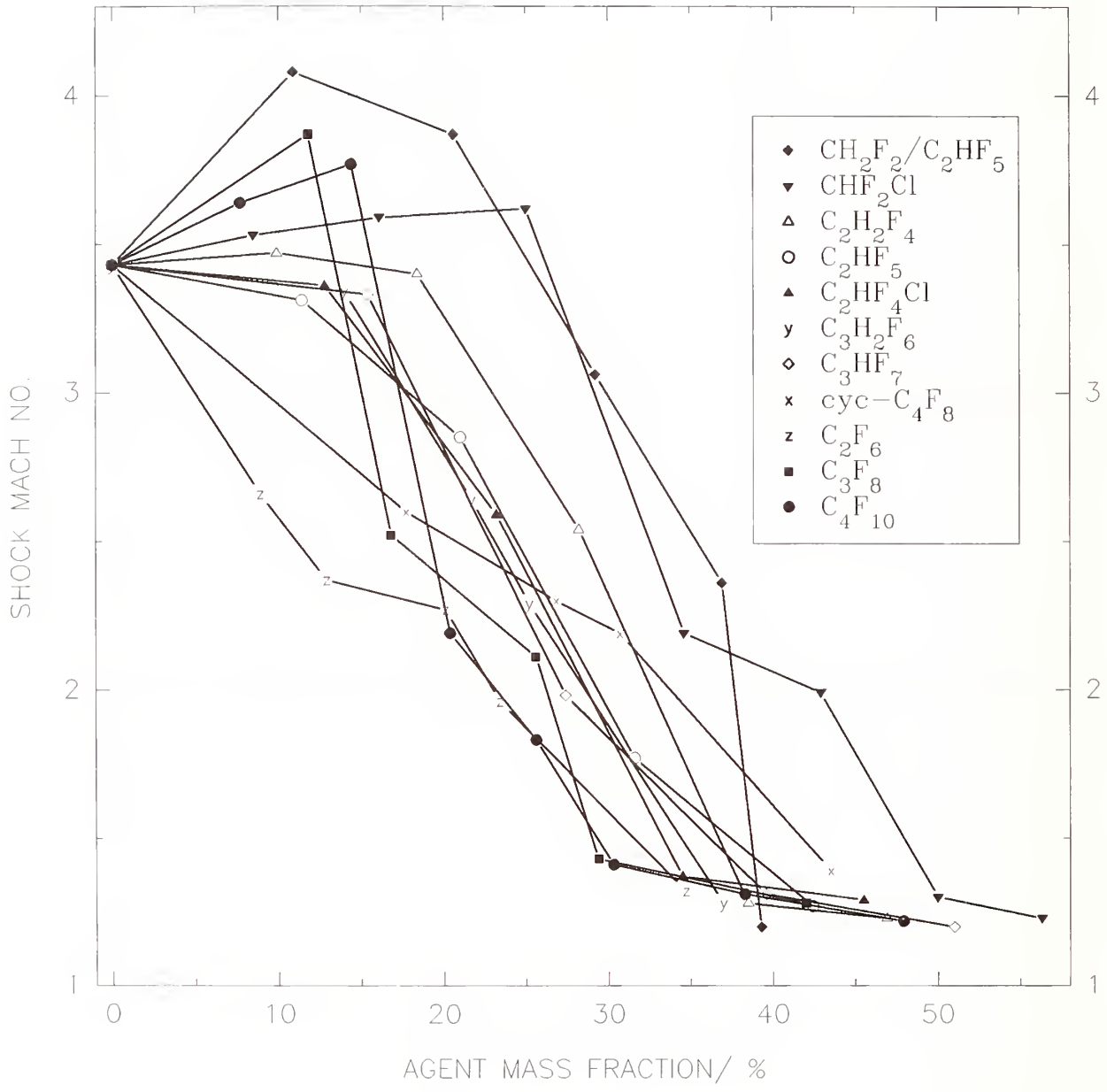

Figure 60. Reduction in shock Mach number as a function of mass fraction for all agents tested.

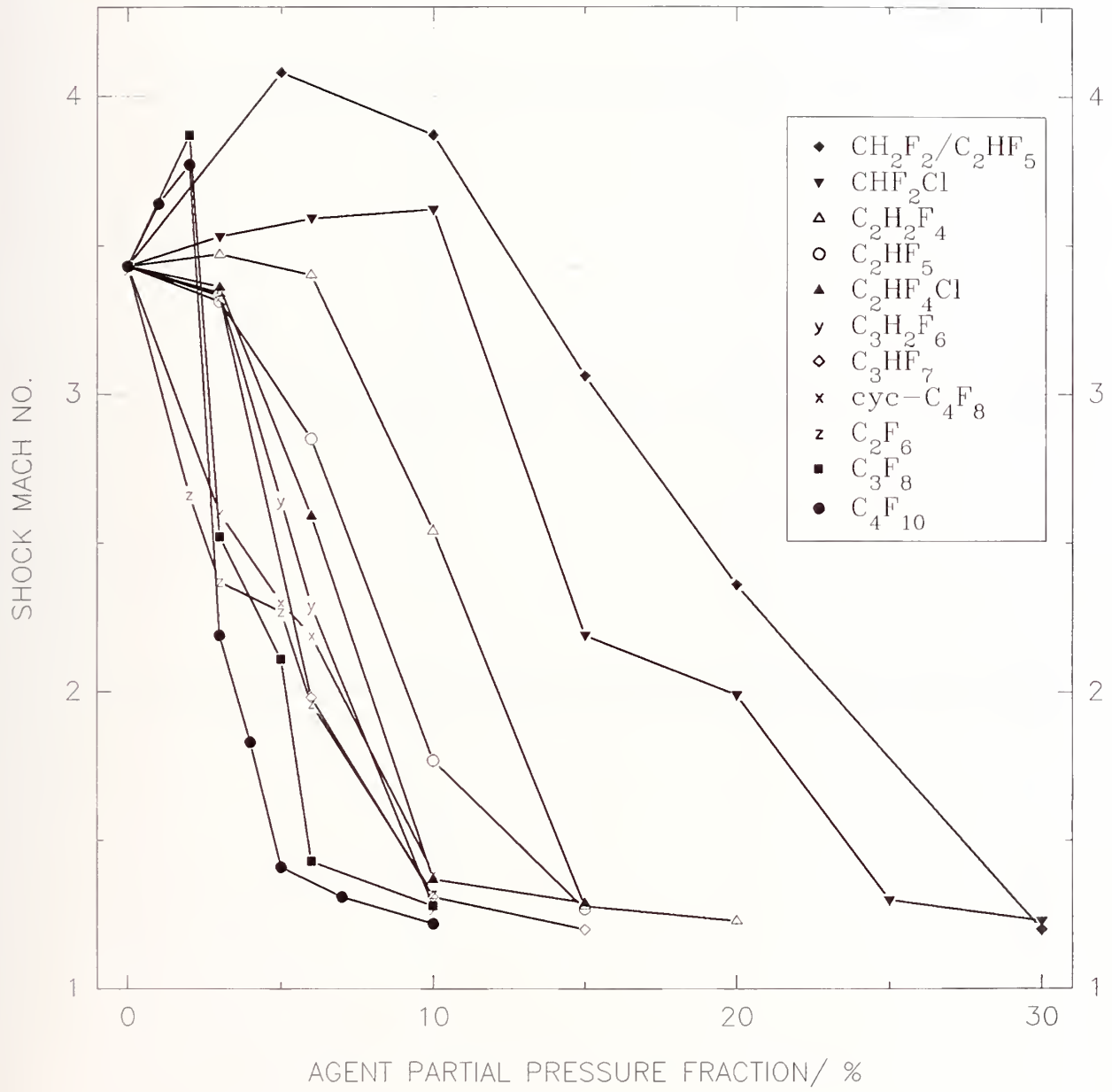

Figure 61. Reduction in shock Mach number as function of partial pressure for all agents tested.

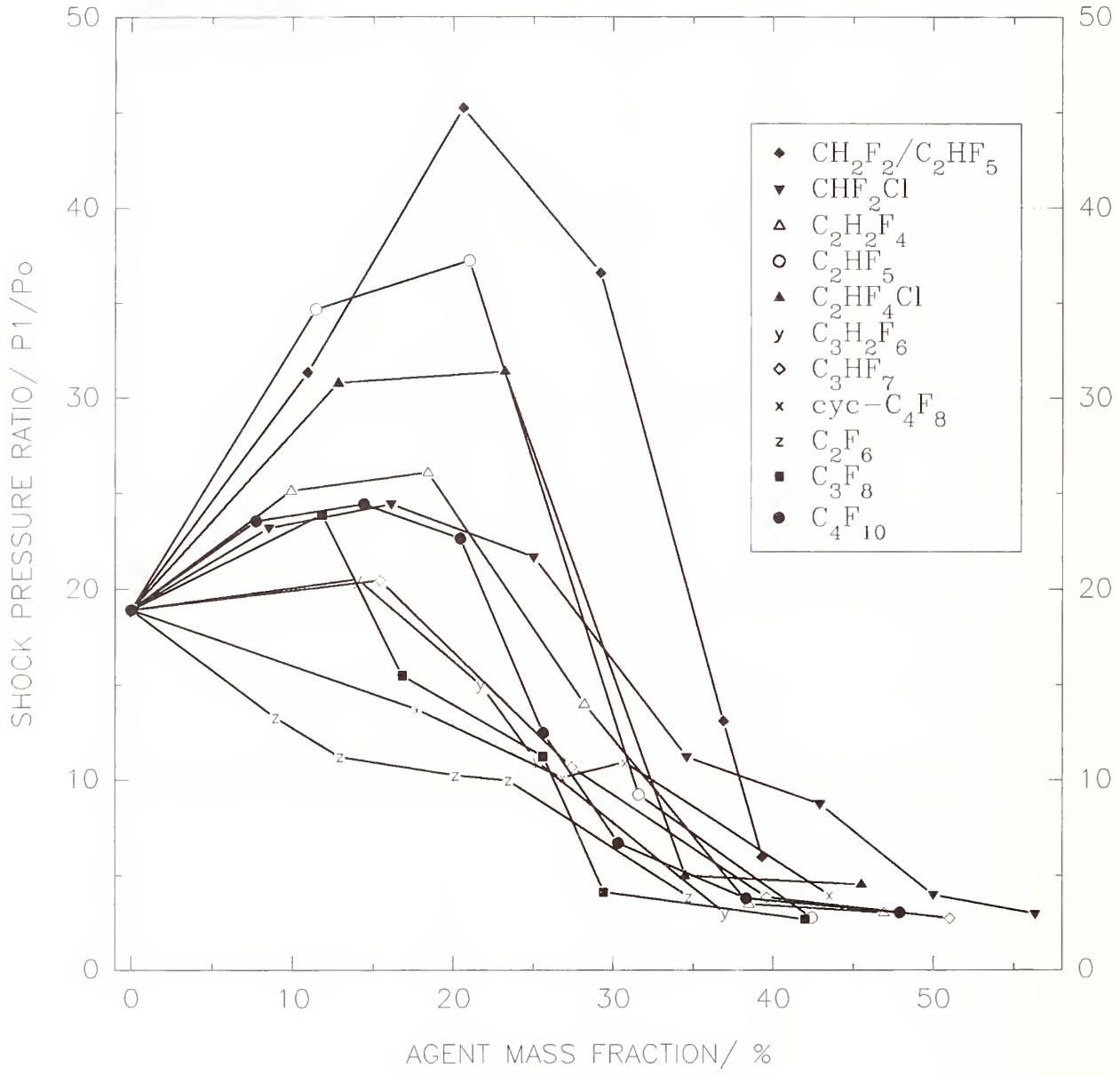

Figure 62. Reduction in pressure ratio as a function of mass fraction for all agents tested.

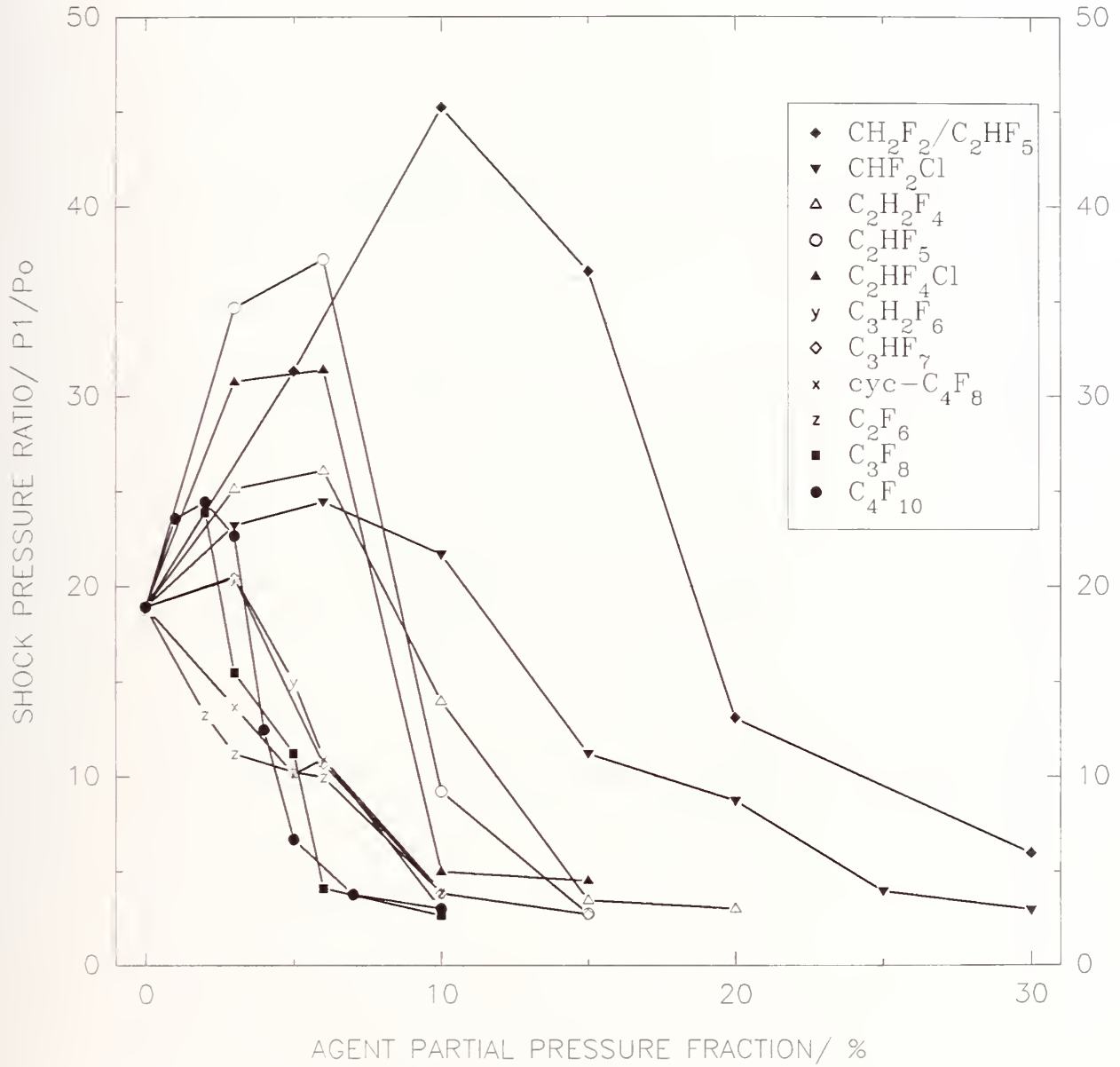

Figure 63. Reduction in pressure ratio as a function of partial pressure for all agents tested.

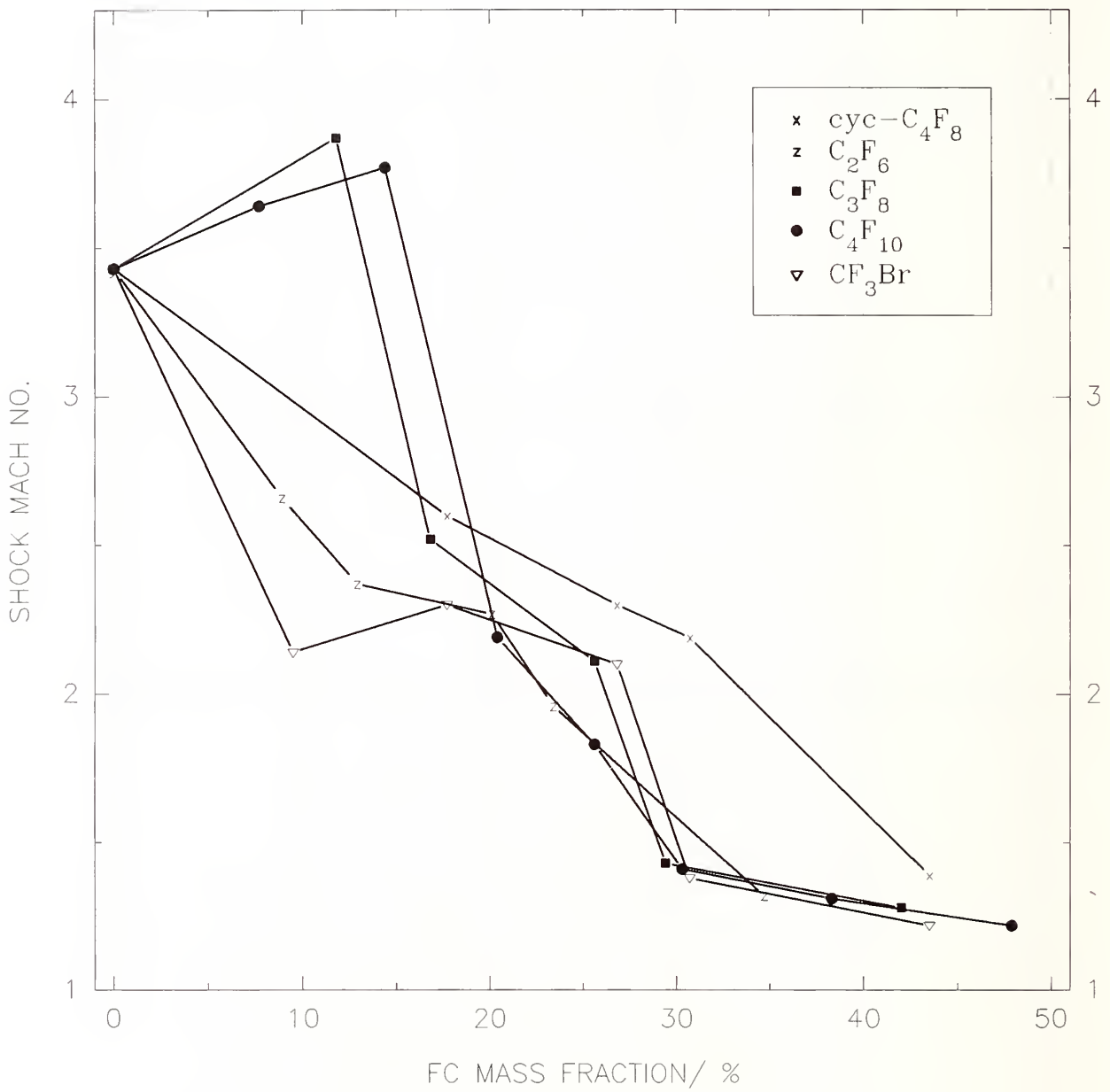

Figure 64. Reduction in shock Mach number vs mass fraction of FCs compared to CF_3Br.

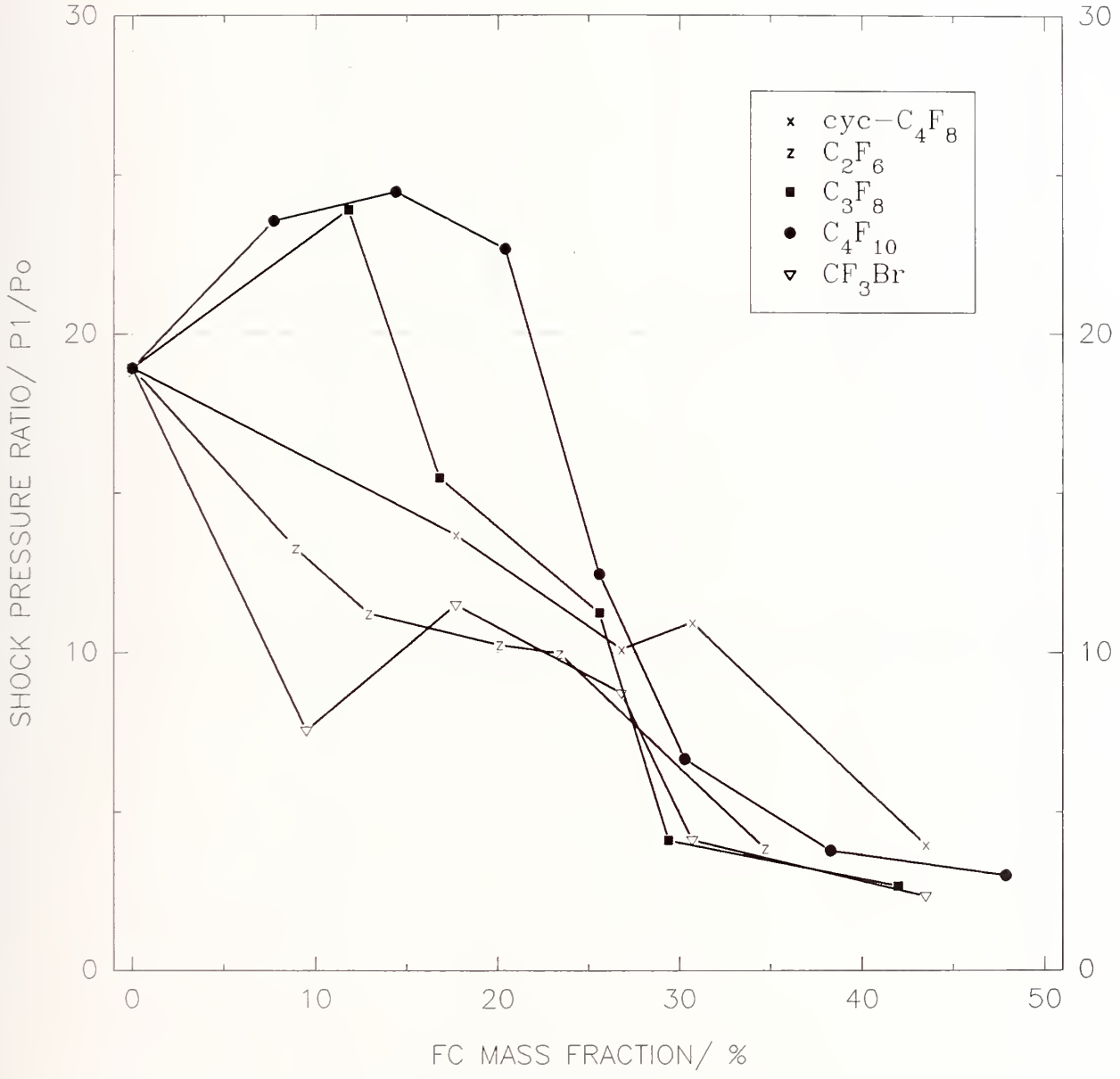

Figure 65. Reduction in pressure ratio as function of FC mass fraction compared to CF_3Br.

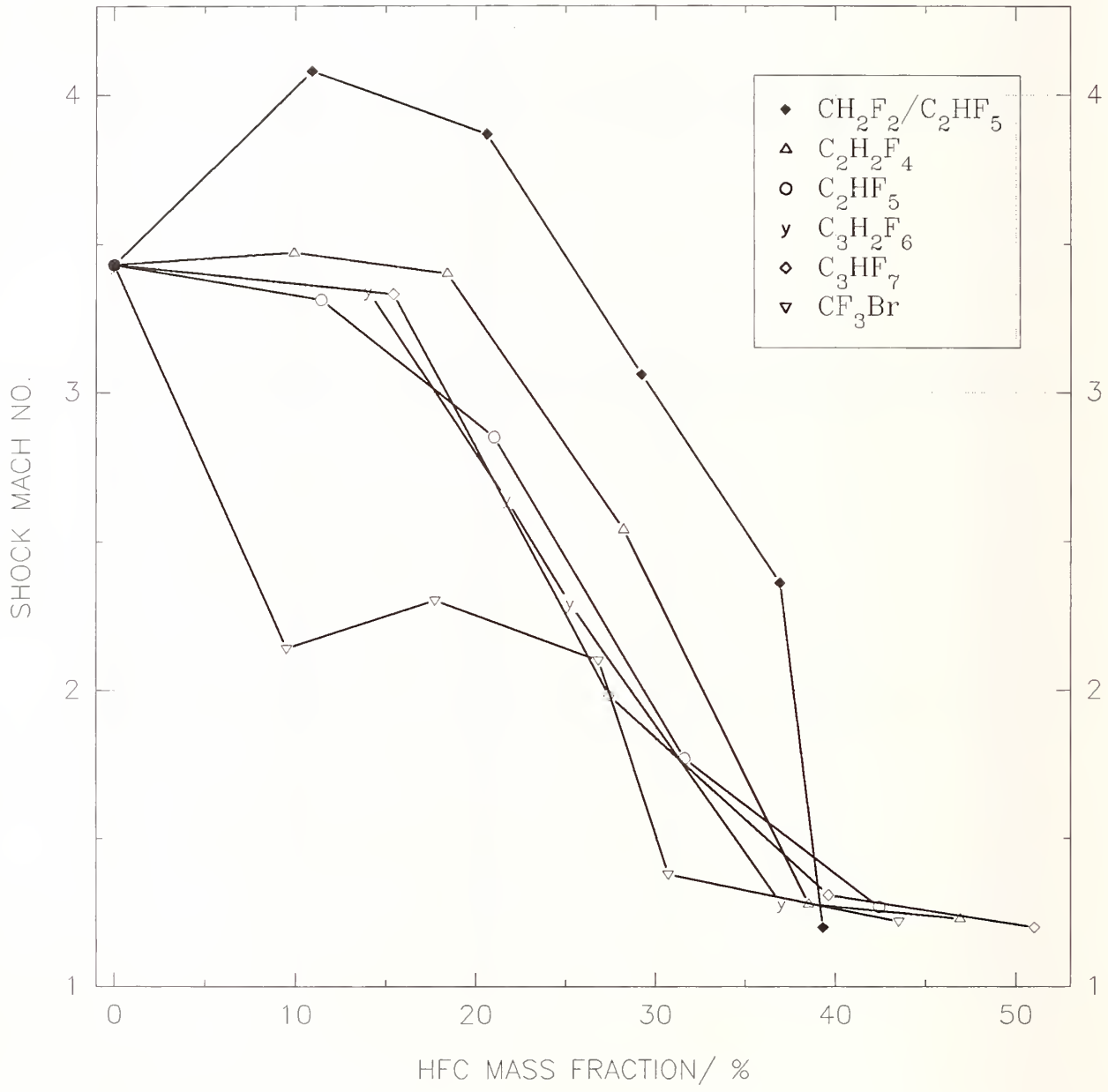

Figure 66. Reduction in shock Mach number as function of HFC mass fraction, compared to CF_3Br.

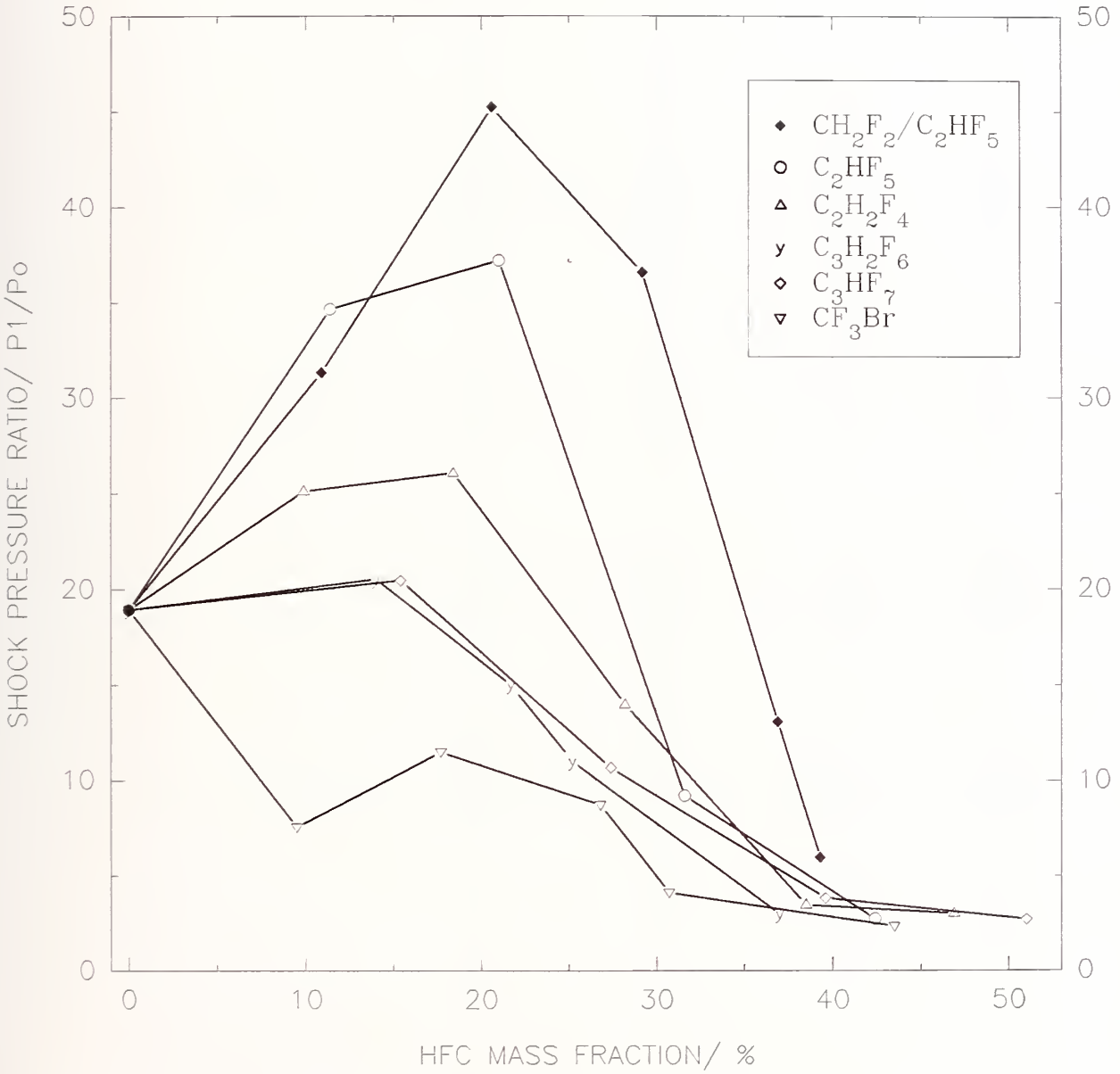

Figure 67. Reduction in pressure ratio as a function of hydrofluorocarbon mass fraction, compared to CF_3Br.

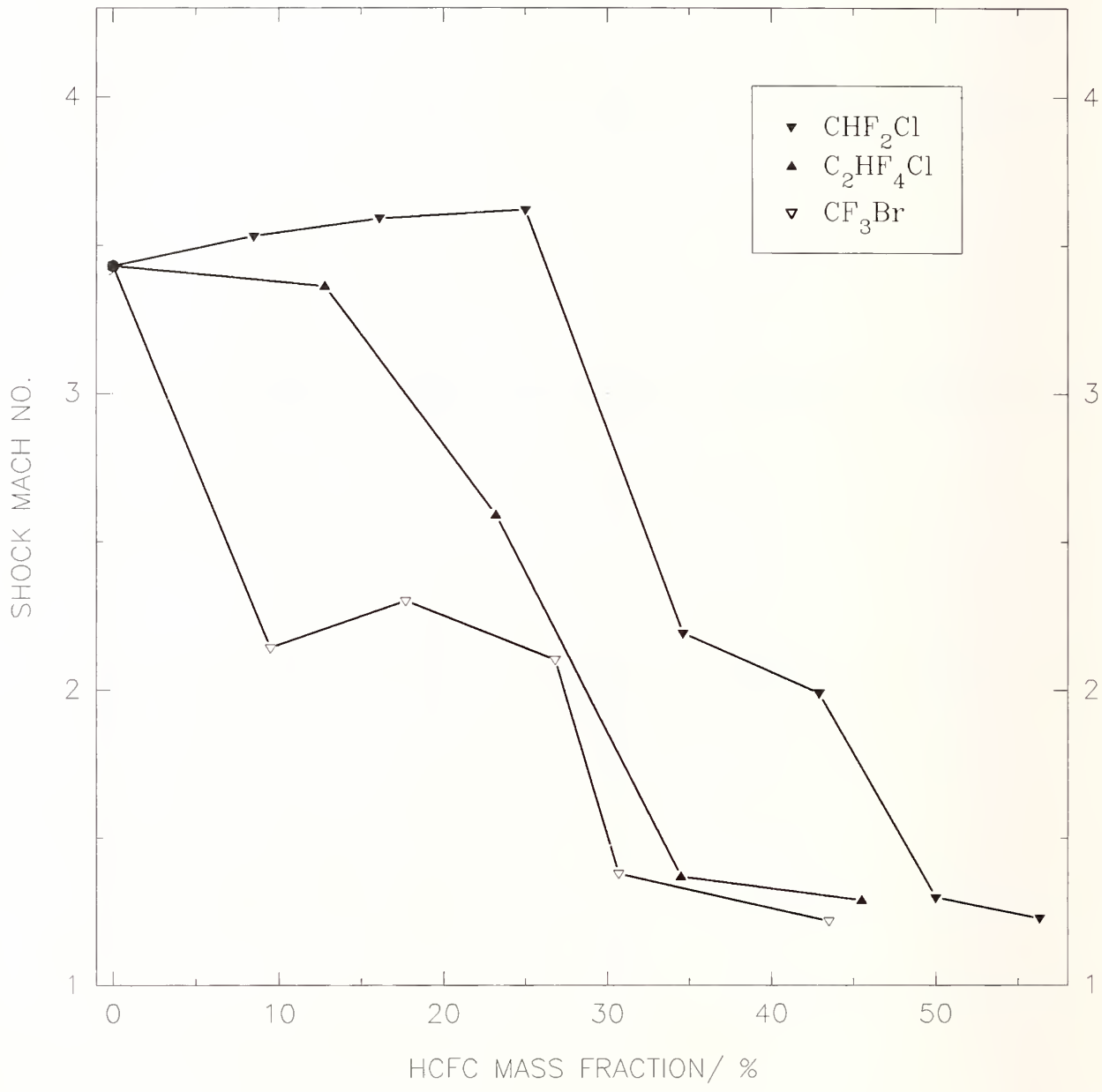

Figure 68. Reduction in shock Mach number as a function of hydrochlorofluorocarbon mass fraction, compared to CF_3Br.

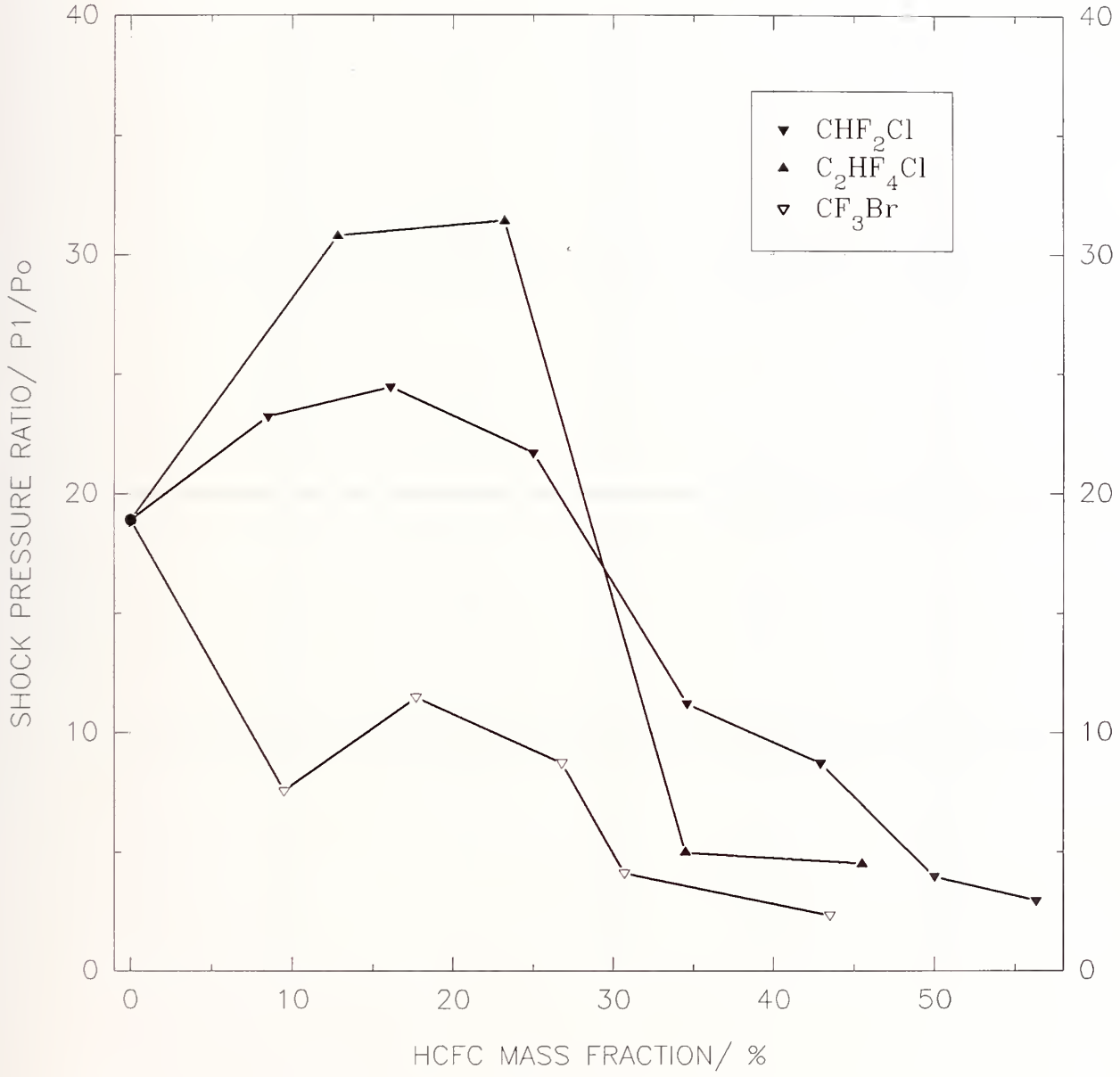

Figure 69. Reduction in pressure ratio as a function of hydrochlorofluorocarbon mass fraction, compared to CF_3Br.

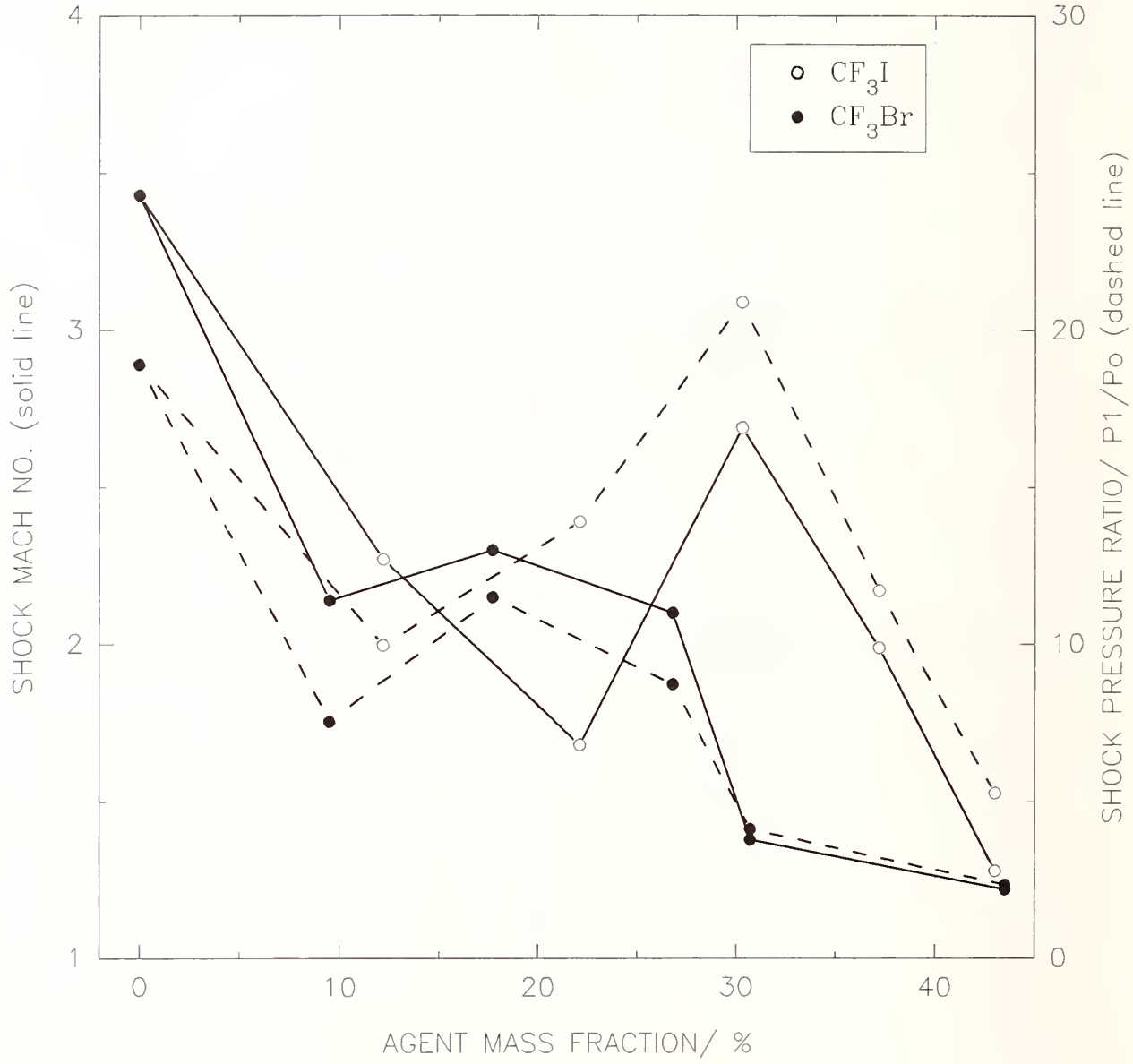

Figure 70. Reduction in shock wave Mach number and pressure ratio as a function of CF_3I mass fraction, compared to CF_3Br.

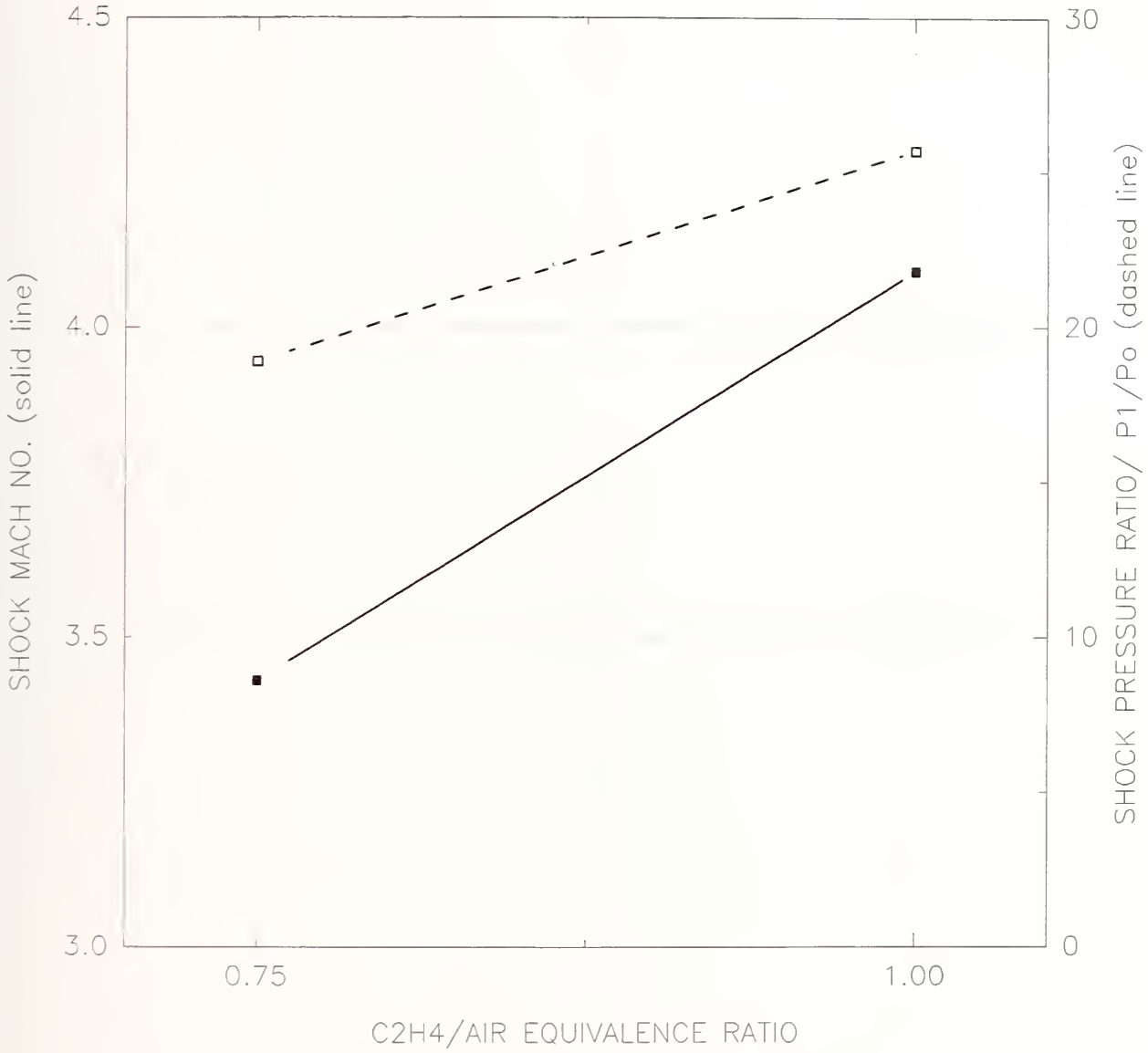

Figure 71. Effect of fuel/air equivalence ratio on shock wave Mach number and pressure ratio.

agent to the fuel or oxidizer pool. The initial pressure and temperature remained the same for the stoichiometric experiments: 100 kPa and 22 °C.

The results for the FCs are plotted in Figures 72-74. In all cases, the Mach number and pressure ratio increased as the fuel/air mixture was changed from lean to stoichiometric. The shapes of the curves, in the most part, were not significantly altered. The impact was greatest at low concentrations, decreasing as the partial pressure fraction reached 8%. For FC-116, the biggest difference occurred at a partial pressure fraction of 3%.

A distinctly different behavior occurred with the two HFCs shown in Figures 75 and 76. The hydrogen atoms attached to the agent molecules had less of an enhancing effect under stoichiometric conditions. The over-pressure was greatly reduced when the equivalence ratio was increased, leading to a cross-over condition where both the Mach number and pressure ratio became less for the stoichiometric condition. The implication of these data is that HFC-125 and the HFC-32/125 mixture increase in relative effectiveness under stoichiometric conditions.

Trifluoroiodomethane behaved no differently in suppressing the shock speed and pressure ratio under lean and stoichiometric conditions. From the data in Figure 77 it can be seen that the Mach number and pressure ratio increased uniformly over the range of partial pressure fractions investigated at an equivalence ratio of 1.0. The reversal of suppression effectiveness at partial pressure fractions between 3% and 6% observed at an equivalence ratio of 0.75 also occurred for stoichiometric combustion.

4.5.5.3 Ranking the Agents. The results which were gathered indicated the complexity of the suppression process in the deflagration/detonation tube. Because one does not know *a priori* the conditions in an actual dry bay fire zone, and because different initial conditions (*i.e.*, pressure, temperature and fuel/air ratio) affect the amount of agent required for suppression to varying degrees, a specific set of initial conditions was chosen at which all the agents were compared: 100 kPa, 22 °C, and 0.75 ethene/air equivalence ratio. The reduction in pressure ratio rather than the Mach number was chosen as the measure of suppression because of its direct impact on the structural integrity of the dry bay. The amount of halon 1301 required to reduce the pressure (a) to 10% and (b) to one-half the maximum increase was used to normalize the results.

Figure 78 displays three different performance parameters calculated under these conditions. The flame suppression number (FSN) is defined as the mass fraction of an agent required for suppression divided by the required mass fraction of halon 1301. The volume factor (VF) is defined as the storage volume of the alternative agent necessary for suppression divided by the storage volume of the CF_3Br. The saturated liquid density of the agents at 20 °C was used to convert mass to volume. Halon 1301 has a VF and FSN of unity by definition. For the other chemicals, the smaller these values the better is the agent.

While there were some reversals depending upon the basis of evaluation (*i.e.*, 90% reduction FSN, 50% reduction FSN, or VF), Figure 78 shows that FC-218 was clearly the best performer under the conditions tested, and that the HFC-32/125 mixture and HCFC-22 were the worst. The FSN of FC-116 based upon a 50% reduction in pressure build-up was the lowest of all agents, even performing better than halon 1301. However, because hexafluoroethane does not condense at room temperature its density is low, leading to a volume factor which is undesirably high. Nitrogen, which is also a gas at room temperature, had a VF of 32. On a mass basis nitrogen performed almost as well as 1301. The CF_3I had the third lowest volume factor of the alternative agents, although its FSN values were close to the highest.

4.5.6 Conclusions and Recommendations from the Premixed Deflagration/Detonation Study. It is necessary to emphasize that the experimental conditions in the deflagration/detonation tube differed

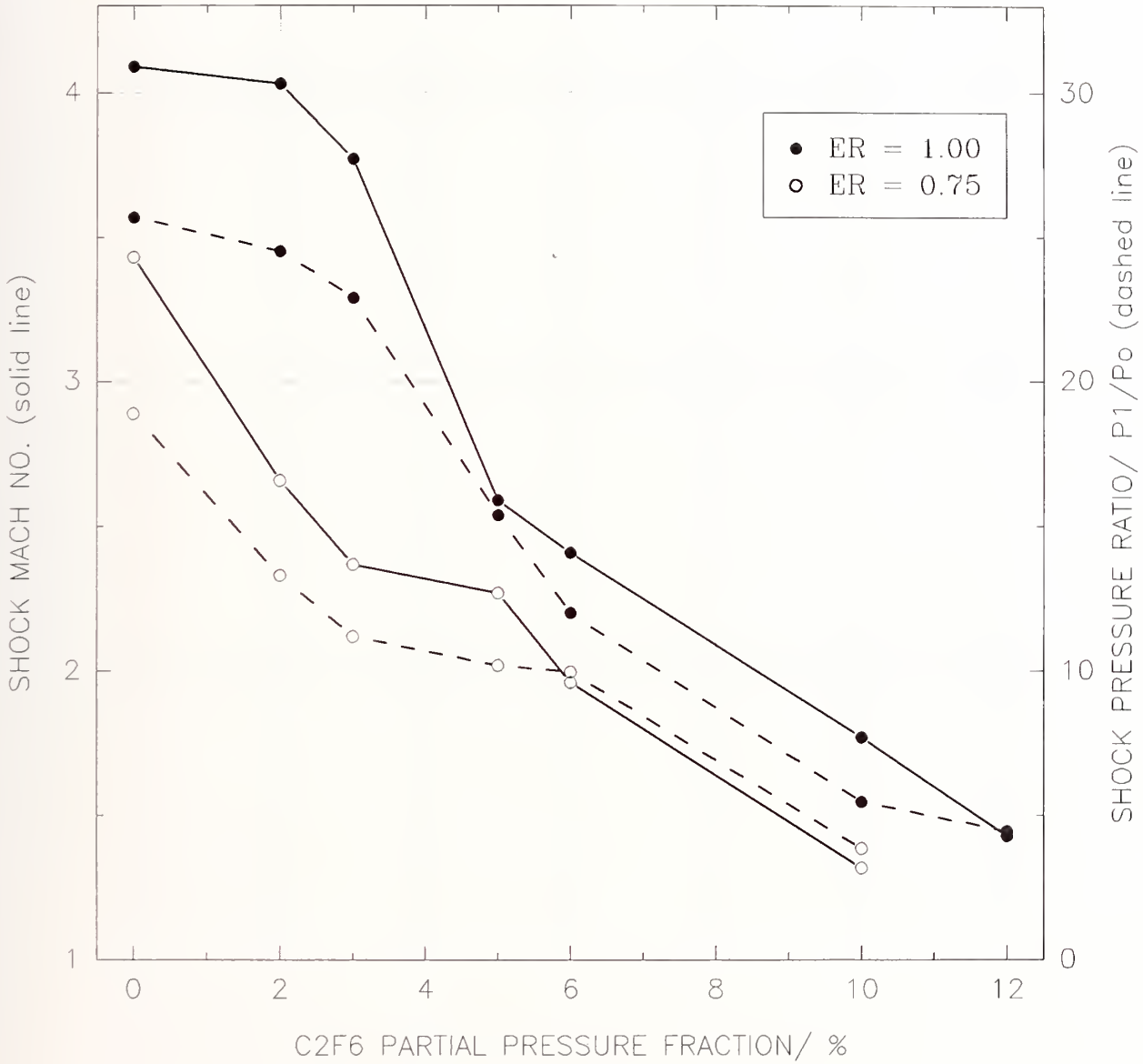

Figure 72. Effect of equivalence ratio on the reduction in Mach number by partial pressure of FC-116.

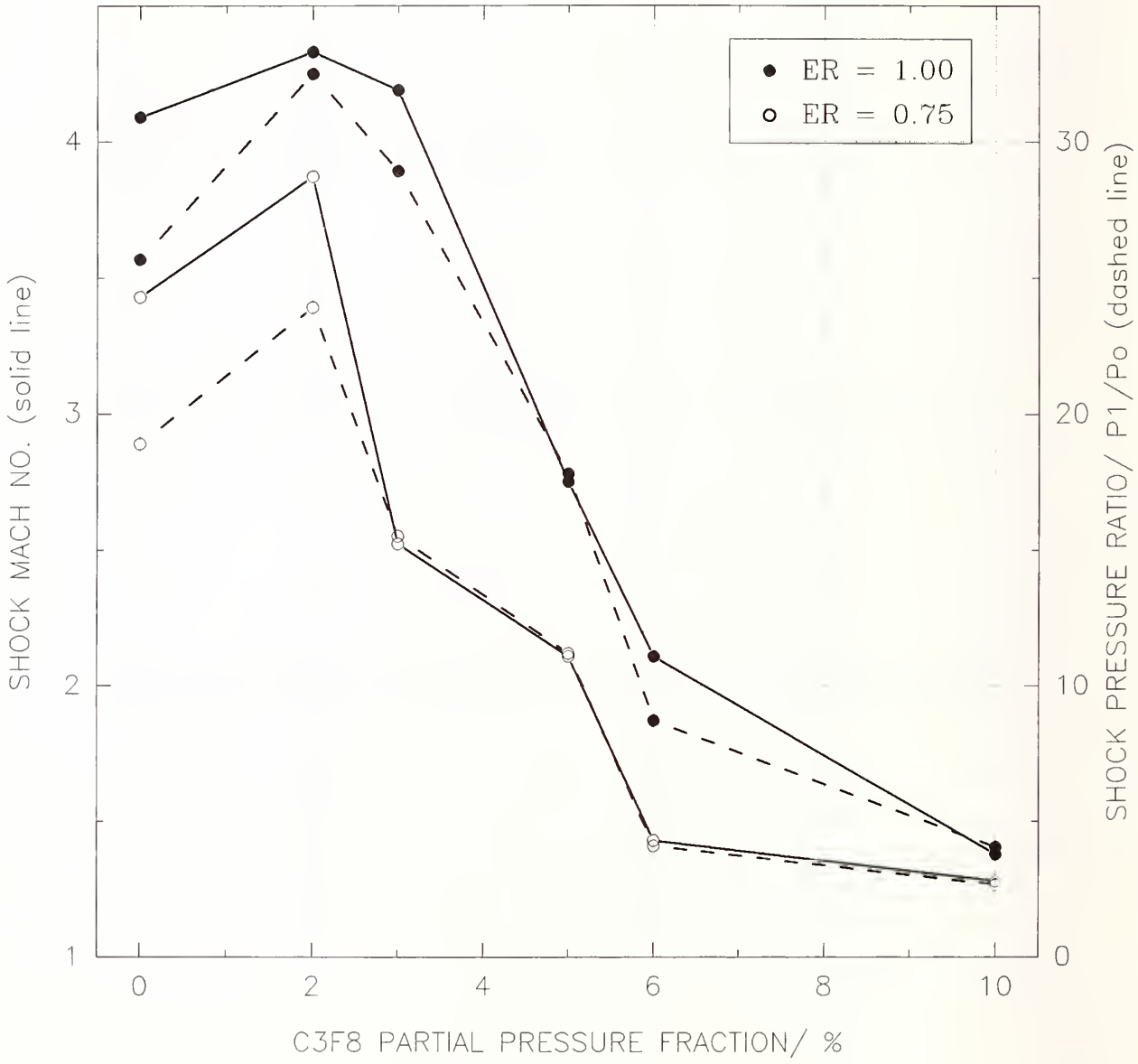

Figure 73. Effect of equivalence ratio on the reduction in shock Mach number and pressure ratio by partial pressure of FC-218.

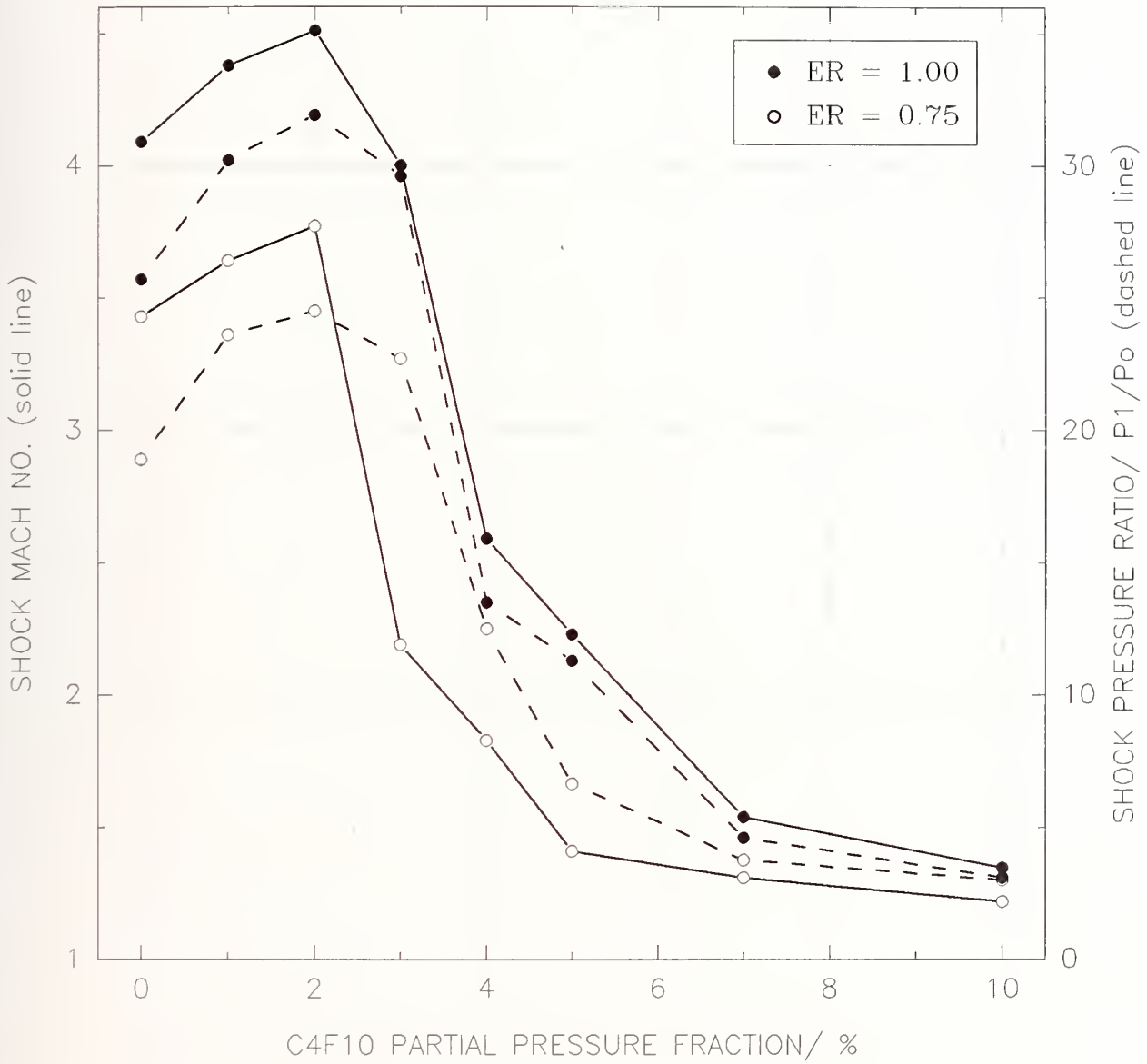

Figure 74. Effect of equivalence ratio on the reduction in shock Mach number and pressure ratio by partial pressure of FC-31-10.

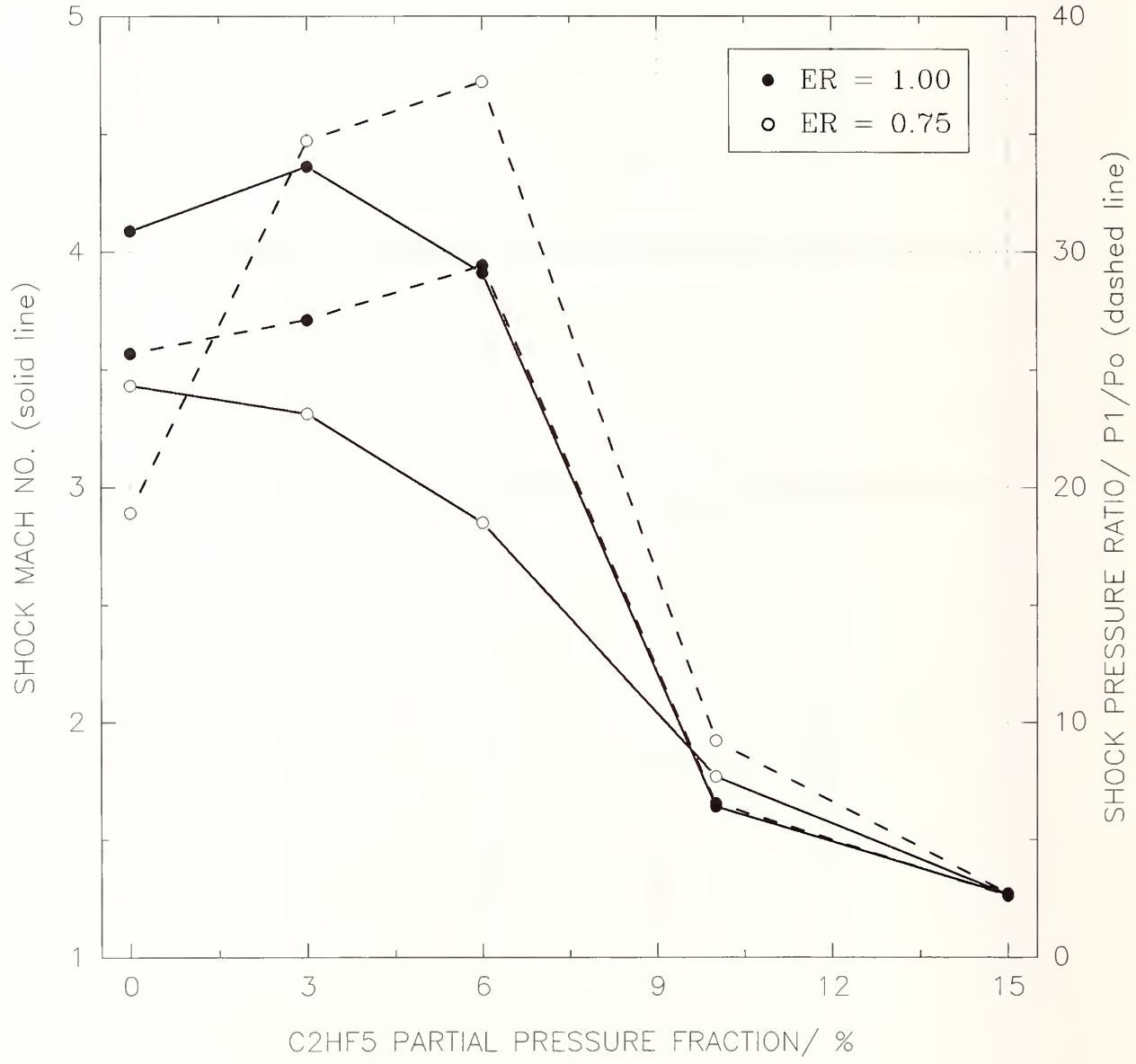

Figure 75. Effect of equivalence ratio on the reduction in shock wave Mach number and pressure ratio by partial pressure of HFC-125.

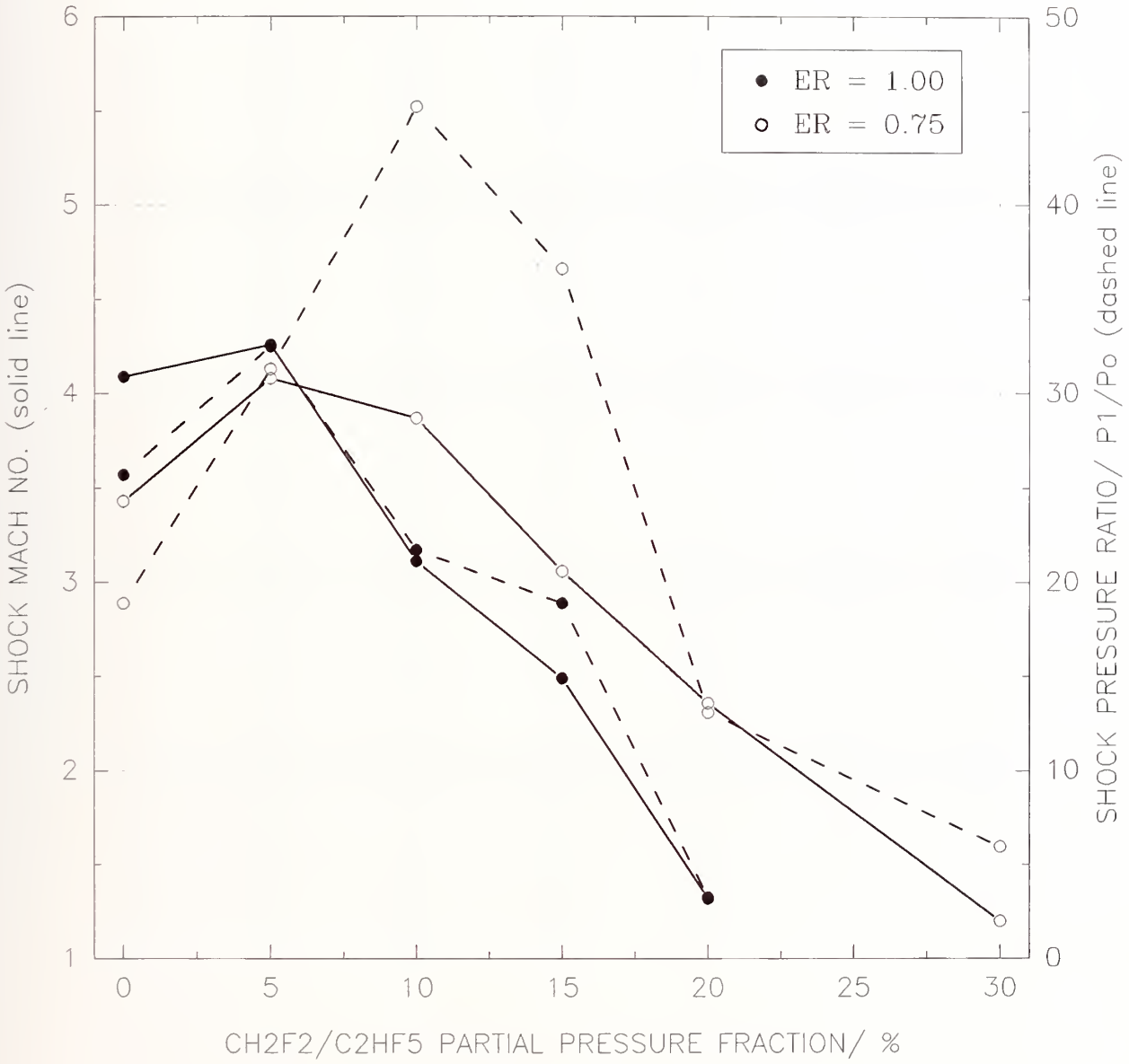

Figure 76. Effect of equivalence ratio on the reduction of shock wave Mach number and pressure ratio by partial pressure of HFC-32/125 mixture.

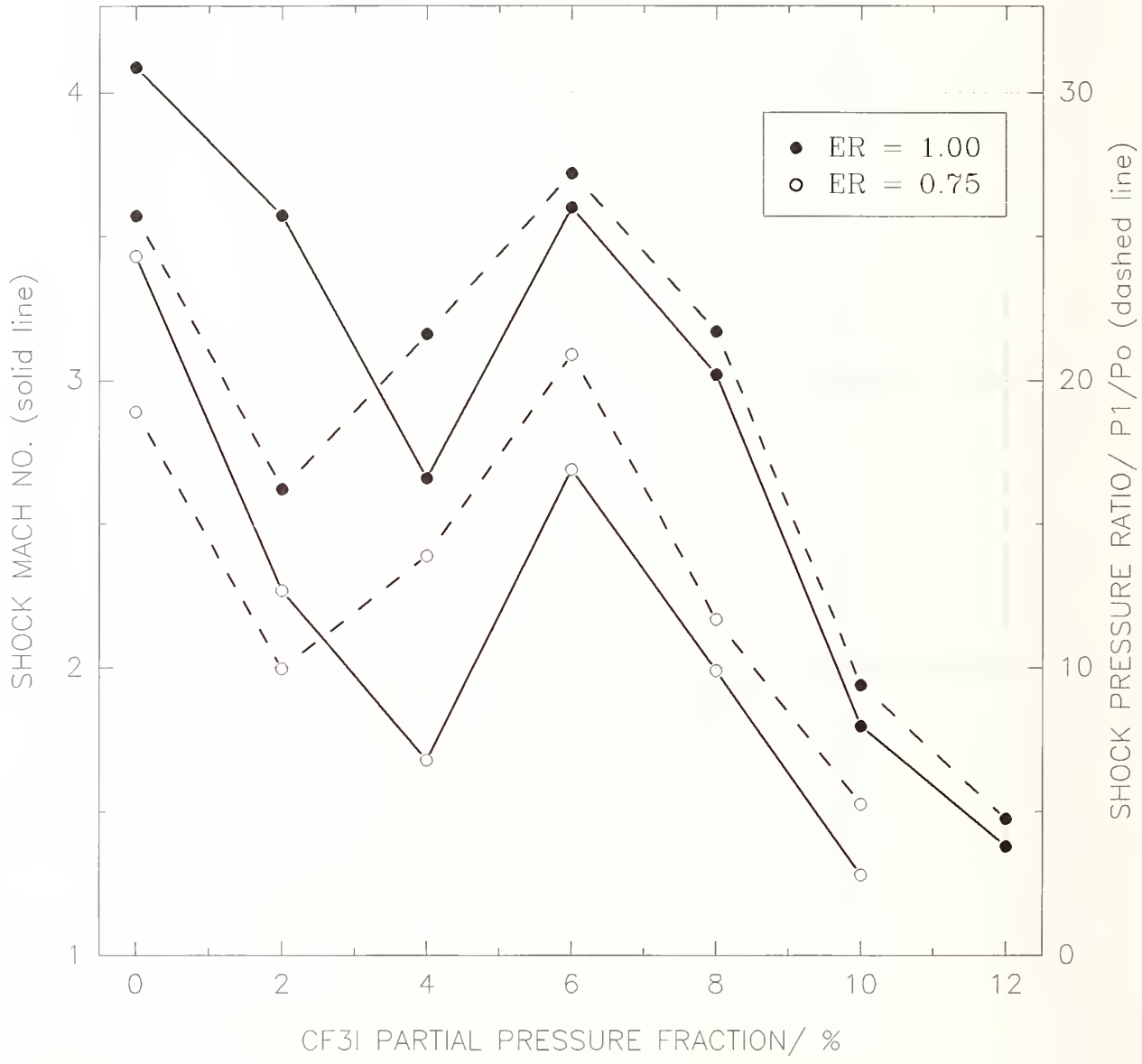

Figure 77. Effect of equivalence ratio on the reduction of shock wave Mach number and pressure ratio by partial pressure of CF_3I.

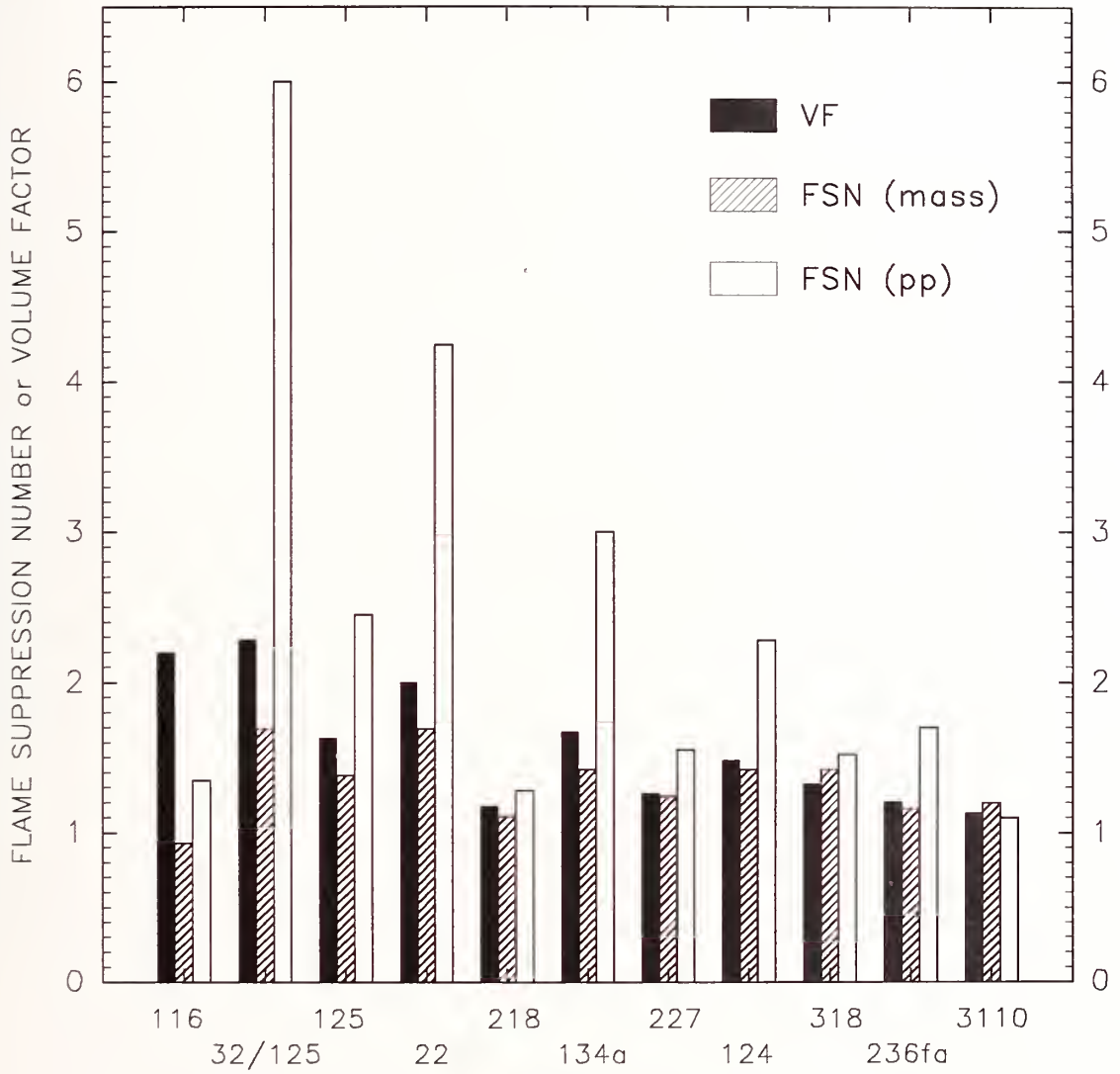

Figure 78. Flame suppression numbers and volume factors of the agents examined in the detonation/deflagration tube.

significantly from those used in the cup burner, opposed-flow diffusion flame burner and turbulent spray flame burner. The main qualitative difference was the occurrence of a strong shock wave ahead of the flame. That wave influenced the gasdynamic, thermodynamic and chemical state of the pure combustible mixture in the driver section and the mixture containing an agent in the test section. Another feature was a high level of turbulence within the flame due to its high speed and the interactions with the spiral obstruction. The quantitative difference was a supersonic regime (relative to the undisturbed mixture) of flame/shock propagation and strong pressure changes (due to confinement and shock) during the process. Thus the oxidizer, fuel and agent molecules underwent preliminary processes before entering the flame zone.

4.5.6.1 Conclusions. The following conclusions can be drawn based on the results obtained:

1. Suppression of highly dynamic flames can be effectively studied in the two-sectional tube, permitting clear discrimination of performance among various alternative extinguishing agents.

2. The high-speed turbulent flame and the flame in the quasi-detonation wave under suppression strictly follows the shock wave which is always ahead of it in such a way that its velocity is the same as the shock velocity. The distance between the flame and the shock increases with the amount of an extinguishing agent. At extinguishment the flame disappears while the residual shock still exists.

3. The suppression process of the lean ethene/air mixture is pressure dependent both for chemically inert nitrogen and chemically active halon 1301. That may be related to the fact that the oxidation mechanism of ethene is known to be pressure dependent.

4. The analysis of the suppression data for the lean ethene/air mixture leads to the division of the alternative compounds into four general categories. These are, in order of decreasing effectiveness: CF_3Br and CF_3I; perfluorocarbons; hydrofluorocarbons; and hydrochlorofluorocarbons. Within each of the categories the agents can be ordered (on a mole fraction basis) approximately inversely according to the molecular weight of the molecule.

5. The extinguishing concentrations of the more effective agents are around 10% by volume and 40% by weight, while less effective ones are 15-30% by volume and 40-50% by weight. The least effective agent is the HFC-32/125 mixture, giving unusually high pressure ratios. HCFC-22 requires the highest extinguishing concentration of all the alternatives.

6. The presence of a hydrogen-containing suppressant in the combustible mixture results in a significant increase in pressure ratio relative to that for the pure combustible mixture. The phenomenon occurs also for the compounds not containing hydrogen atoms at relatively lower concentrations but the impact is not so dramatic. The impact is generally weaker for stoichiometric relative to lean mixtures. That may be related to the fact that the agent acts as an extra fuel, causing the mixture to be richer. It is suspected that the effect may be associated with the release of hydrogen during the process which enhances the branching steps in the ethene oxidation mechanism. It is also not out of the question that a homogeneous autocatalysis occurs lowering the overall activation energy and enhancing the oxidation mechanism.

7. The behavior of CF_3I is different from the other agents. At lower concentrations (2-3% by volume) the performance is the best of all the alternatives. However, at intermediate concentrations (3-7% by volume) the performance is worsened significantly. Eventually at higher concentrations, up to the extinguishing value of 10%, the performance is comparable with the perfluorocarbons and CF_3Br. The phenomenon is independent of the equivalence ratio of the combustible mixture. The behavior at the intermediate concentrations may be attributed to the catalytic effect caused by the iodine atoms.

4.5.6.2 Recommendations. The relative ranking of the agents in Figure 78 can be used as a guide to choose a replacement for halon 1301 for suppressing high-speed turbulent flames and quasi-detonations. The influence of rich equivalence ratios up to 1.5, of other gaseous fuels, and of various tube geometries on the performance of the selected agents should be explored to determine the generality of the rankings. A more fully instrumented apparatus would allow the evolution of the flame and shock all along the length of the tube to be followed, and the key intermediate species and products of combustion to be ascertained.

The unusual behavior of CF_3I in lean and stoichiometric ethene/air mixtures indicates a critical need for further research into the kinetics of the compound. It is recommended that a shock tube be designed to investigate the dynamic and kinetic characteristics under high pressure and temperature conditions as well as various mixture compositions. The set-up should include a special dump chamber for collecting combustion products and optical access for spectroscopic measurements of important species.

In general, the application of this unique experimental apparatus for studying fire suppression processes under highly dynamic conditions should provide the information necessary to establish a physical/chemical model of the phenomena, contributing to the fire safety of facilities exposed to fast flames, explosions and detonations.

4.6 Summary of Conclusions on Flame Suppression Effectiveness

1. The relative ranking of the agents depends upon whether one uses a mass basis or a volume basis.

2. The relative ranking of the agents varies only slightly among the three non-premixed burners, but a substantially different ranking results from the premixed deflagration/detonation apparatus.

3. The relative ranking of the agents is not much affected by the fuel type or air temperature.

4. The quantity of agent required to suppress a flame varies with the type of burner generally in the following order:

   cup burner $\approx$ low strain OFDF $>$ spray burner $>$ high strain OFDF $>$ deflagration tube

5. The quantity of agent required to suppress a non-premixed flame varies somewhat with the type of fuel in the following order:

   propane $>$ heptane $>$ JP-8 $>$ JP-5 $>$ HF-5606 $>$ HF-83282

6. The quantity of agent required to suppress the turbulent spray flame increases with decreasing rate of agent injection.

7. The quantity of agent required to attenuate the shock wave speed and pressure ratio in the deflagration/detonation tube varies with equivalence ratio, sometimes increasing as one goes from lean to stoichiometric and sometimes decreasing.

8. Sodium bicarbonate was the most effective suppressant of the three non-premixed flames, requiring less mass than halon 1301. In general, the smaller size particles were more effective.

9. Iodotrifluoromethane was more effective than halon 1301 in suppressing the spray burner flame, had a similar effectiveness with the cup burner flames, and was less effective in attenuating the shock speed and pressure in the detonation/deflagration apparatus.

10. None of the core agents performed as well as halon 1301 in any of the four flame suppression studies, requiring from approximately one and a half to four times the storage volume as halon 1301 to suppress the different flames.

11. HCFC-124 was the generally the best performer of the core agents in suppressing the non-premixed flames, and FC-218 was judged the best for attenuating the shock speed and pressure in the detonation/deflagration tube.

12. FC-116 was the poorest performer (on a liquid storage volume basis) of all the core agents evaluated in the flame suppression tests; the HFC-32/125 mixture was the second poorest performer, and led to the highest over-pressures in the lean detonation/deflagration tube study.

4.7 References

Baker, W.E., Cox, P.A., Westine, P.S., Kulesz, J.J. and Strehlow, R.A., *Explosion Hazards and Evaluation,* Elsevier, 1983.

Bajpai, S.N., "An Investigation of the Extinction of Diffusion Flames by Halons," *Journal of Fire and Flammability 5*, 255 (1974a).

Bajpai, S.N., "Extinction of vapor fed diffusion flames by Halons 1301 and 1211-Part I," *ser No. 22430, Factory Mutual research Corporation*, Norwood, Massachusetts, November (1974b).

Bui, M. and Seshadri, K. "Comparisons between experimental measurements and numerical calculations of the structure of heptane-air diffusion flames," *Combust. Sci. Tech. 79*, No 4-6, 293 (1991).

Chapman, W.R. and Wheeler, R.N.V., "The Propagations of Flame in Mixtures of Methane and Air. Part IV. The Effect of Restrictions in the Path of the Flame," *Journal of the Chemical Society*, London, 1926.

Chelliah, H., Bui-Pham, M., Seshadri, K. and Law, C. K., "Numerical description of the structure of counterflow heptane-air flames using detailed and reduced chemistry with comparisons to experiments," *Twenty-Fourth Symposium (International) on Combustion*, The Combustion Institute, Pittsburgh, Pennsylvania, p. 851 (1992).

Creitz, E.C., "Inhibition of Diffusion Flames by Methyl Bromide and Trifluoromethyl Bromide Applied to the Fuel and Oxygen sides of the reaction zone," *Journal of Research of the National Bureau of Standards (U.S.) 65A*, 389, (1961).

Creitz, E.C., "Extinction of Fires by Halogenated Compounds - A Suggested Mechanism," *Fire Technology 8*, 131 1972.

Das, A., *Relationship Between Ignition Source Strength and Design Inerting Concentration of Halon 1301*, M.S. Thesis, Fire Protection Engineering Department, Worcester Polytechnic Institute, 1986.

Dodding, R.A., Simmons, R.F. and Stephens, A., "The Extinction of Methane - Air Diffusion Flames by Sodium Bicarbonate Powders," *Combustion and Flame 15*, 313 (1977).

Dow-Corning, Midlane, MI, Communication of Test Results, 1993.

Ewing, C.T., Faith, F.R., Hughes, J.T. and Carhart, H.W., "Flame Extinguishment Properties of Dry Chemicals: Extinction Concentrations for Small Diffusion Pan Fires," *Fire Technology 25*, 134 (1989).

Fendell, F. E., "Ignition and extinction in combustion of initially unmixed reactants," *J. Fluid Mechanics 21*, 281 (1965)

Galbraith Laboratories, Knoxville, TN, *Communication of Test Results*, 1993.

Gann, R.G., Barnes, J.D., Davis, S., Harris, J.S., Harris, R.H., Herron, J.T., Levin, B.C., Mopsik, F.I., Notarianni, K.A., Nyden, M.P., and Ricker, R.E., "Preliminary Screening Procedures and Criteria for Replacements for Halons 1211 and 1301," National Institute of Standards and Technology, NIST Technical Note 1278, U.S. Government Printing Office, Washington, DC (1990).

Gmurczyk, G., Grosshandler, W., Peltz, M. and Lowe, D., "A Facility for Assessing Suppression Effectiveness in High Speed Turbulent Flames," Eastern States Section Conference/The Combustion Institute, Princeton, 1993.

Gorden, S. and McBride, B.J., "Computer Program for the Calculation of Complex Chemical Equilibrium Compositions, Rocket Performance, Incident and Reflected Shocks, and Chapman-Jouget Detonations," NASA, NASA SP-273,(1976).

Goscoyne Laboratories, Baltimore, MD, *Communication of Test Results*, 1993.

Grosshandler, W.L., Lowe, D., Rinkinen, W., and Presser, C., "A Turbulent Spray Burner for Assessing Halon Alternative Fire Suppressants," ASME Winter Annual Meeting, December, 1993.

Hamins, A., *The Structure and Extinction of Diffusion Flames,* Ph.D. Thesis, University of California, San Diego, 1985.

Hamins, A., and Seshadri, K., "Prediction of overall chemical kinetic rate parameters for extinction of diffusion flames above multicomponent fuels," *Combust. Sci. Tech. 38*, 89 (1984a).

Hamins, A., and Seshadri, K., "Structure of counterflow diffusion flames burning multicomponent fuels," *Twentieth Symposium (International) on Combustion*, The Combustion Institute, Pittsburgh, Pennsylvania, p. 1905 (1984b).

Hamins, A., and Seshadri, K., "The influence of alcohols on the combustion of hydrocarbon fuels in diffusion flames," *Combust. Flame 64*, 43 (1986).

Hamins, A., and Seshadri, K., "The structure of diffusion flames burning pure binary, and ternary solutions of methanol, heptane, and toluene," *Combust. Flame 68*, 295 (1987).

Hamins, A., Thridandam, H., and Seshadri, K., "Structure and extinction of a partially premixed diffusion flame," *Chem. Eng. Sci. 40*, 2027 (1985).

Heinonen, E.W., Kirst, J.A. and Moussa, N.A., *Fire/Explosion Protection Characterization and Optimization: Alternative Dry Bay Fire Suppression Agent Screening, Medium-Scale Test Results*, Final Report, NUMERI OC 91/16, Report JTCG/AS-91-VR-005, 1991.

Hirst, R. and Booth, K., "Measurements of Flame-Extinguishing Concentrations," *Fire Technology 13*, No. 4, (1977).

Kent, J.H., and Williams, F.A., "Extinction of Laminar Diffusion Flames for Liquid Fuels," *Fifteenth Symposium (International) on Combustion*, pp. 315-325, The Combustion Institute, Pittsburgh, 1974.

Krishnamurthy, L., Williams, F.A., and Seshadri, K., "Asymptotic Theory of Diffusion Flame Extinction in the Stagnation-Point Boundary Layer," *Combust. Flame 26*, 363 (1976).

Lee, J.H.S., "Fast Flames and Detonations," *Chemistry of Combustion Processes*, The American Chemical Society, 1984.

Lee, J.H., Knystautas, R. and Chan, C.K., "Turbulent Flame Propagation in Obstacle-filled Tubes," *Twentieth Symposium (International) on Combustion*, The Combustion Institute, 1984.

Lefebvre, M.H., Nzeyimana, E., Van Tiggelen, P.J., *Progress in Astronautics and Aeronautics*, AIAA, 1992.

Liñan, A., "The Asymptotic Structure of Counterflow Diffusion Flames for Large Activation Energies," *Acta Astronautica 1*, 1007 (1974).

Lum, L., National Institute of Standards and Technology, Gaithersburg, MD, Personal Communication, 1993.

Miller, E. and McMillion, L.G., "The Suppression of Opposed-Jet Methane-Air Flames by Methyl Bromide," *Combustion and Flame 84*, 37 (1992).

Milne, T.A., Green, C.L., and Benson, D.K.,"The Use of the Counterflow Diffusion Flame in Studies of Inhibition Effectiveness of Gaseous and Powder Agents," *Combustion and Flame 15*, 255 (1970).

Mitani, T., "Flame Retardant Effects of CF3Br and NaHCO3," *Combustion and Flame 50*, 177 (1983).

Nettleton, M.A., *Gaseous Detonations, Their Nature, Effects and Control,* Chapman and Hall, 1987.

Peraldi, O., Knystautas, R. and Lee, J.H., "Criteria for Transition to Detonation in Tubes," *Twenty-first Symposium (International) on Combustion*, The Combustion Institute, p. 1629, 1986.

Peters, N., "Local premixing due to flame stretch and nonpremixed turbulent combustion," *Combust. Sci. Tech. 30*, 1 (1982).

Peters, N., "Laminar diffusion flamelets in nonpremixed turbulent combustion," *Prog. Energy Combust. Sci. 10*, 319 (1984).

Pitts, W.M., Nyden, M.R., Gann, R.G., Mallard, W.G. and Tsang, W., "Construction of an Exploratory List of Chemicals to Initiate the Search for Halon Alternatives," *NIST Technical Note 1279*, U.S. Government Printing Office, Washington, DC, 1990.

Reid, R.C., Prausnitz, J.M., and Sherwood, T.K., *The Properties of Gases and Liquids*, Third Edition, pp. 404-411, McGraw/Hill, New York, 1977.

Seshadri, K., Mauss, F., Peters, N. and Warnatz, J., " A flamelet calculation of benzene formation in coflowing laminar diffusion flames," *The Twenty-Third Symposium (International) on Combustion*, The Combustion Institute, Pittsburgh, Pennsylvania, 463 (1990).

Seshadri, K., and Williams, F.A., "Effect of CF_3Br on counterflow combustion of liquid fuel with diluted oxygen," *ACS Symposium Series, No. 16, Halogenated Fire Suppressants*, R.G. Gann (Ed.), American Chemical Society, Washington, DC, p. 149 (1975).

Seshadri, K., and Williams, F.A., "Structure and extinction of counterflow diffusion flames above condensed fuels: comparison between poly(methylmethacrylate) and its liquid monomer, both burning in nitrogen-air mixtures," *J. Polymer Sci. 16*, 1755 (1978a).

Seshadri, K., and Williams , F. A., "Laminar flows between parallel plates with injection of a reactant at high Reynolds number," *Int. J. Heat Mass Transfer 21*, 251 (1978b)

Sheinson, R.S., Penner-Hahn, J.E., and Indritz, D., "The Physical and Chemical Action of Fire Suppressants," *Fire Safety Journal 15*, 43 (1989).

Simmons, R.F., and Wolfhard, H.G., *Transactions of the Faraday Society, 52*:53-59 (1956).

Smooke, M.D., Puri, I.K., and Seshadri, K., "A comparison between numerical calculations and experimental measurements of the structure of a counterflow diffusion flame burning diluted methane in diluted air," *Twenty-First Symposium (International) on Combustion*, The Combustion Institute, Pittsburgh, Pennsylvania, p. 1783 (1986).

Strasser, A., Liebman, I., and Kuchta, J.M., "Methane Flame Extinguishment with Layered Halon or Carbon Dioxide," *Fire Technology 10*, 25 (1974).

Tucker, D.M., Drysdale, D.D. and Rasbash, D.J., "The Extinction of Diffusion Flames Burning in Various Oxygen Concentrations by Inert Gases and Bromotrifluormethane," *Combustion and Flame 41*, 293 (1981).

Van Wylen, G.J., and Sonntag, R.E., *Fundamentals of Classical Thermodynamics*, Second Edition, John Wiley and Sons, p. 400, 1978.

Vazquez, I., Grosshandler, W., Rinkinen, W., Glover, M., and Presser, C., "Suppression of Elevated Temperature Hydraulic Fluid and JP-8 Spray Flames," *Fourth International Symposium on Fire Safety Science*, Ottawa, June, 1994.

Westbrook, C.K., *Nineteenth Symposium (International) on Combustion*, The Combustion Institute, p. 127, 1982.

Westbrook, C.K., "Chemical Kinetics of Hydrocarbon Oxidation in Gaseous Detonations," *Combustion and Flame 46*, 191, 1982.

Williams, F.A., "A Unified View of Fire Suppression," *Journal of Fire and Flammability 5*, 54 (1974).

Williams, F.A., *Combustion Theory*, Second Edition, Addison Wesley, 2nd Edition, (1985).

Williams, F.A. and Peters, J.W., "Studies of Dry Powder Extinguishment of Diffusion Flames for Condensed Fuels," *Final Technical Report, National Bureau of Standards*, NBS Grant No. NB81NADA, June 15, 1982.

5. FLAME INHIBITION CHEMISTRY AND THE SEARCH FOR ADDITIONAL FIRE FIGHTING CHEMICALS

Marc R. Nyden, Gregory T. Linteris,
Building and Fire Research Laboratory

Donald R.F. Burgess, Jr., Phillip R. Westmoreland, Wing Tsang and Michael R. Zachariah
Chemical Science and Technology Laboratory

Replacements for the current commercial halons should posses a diverse set of properties which are rarely found together in the same molecule. Thus, the ideal candidate for the replacement of halon 1301 would be a nontoxic gas which is reactive in flames and in the troposphere, yet at the same time, inert in the stratosphere and in its storage environment. The present generation of replacements, as typified by the core candidates listed in Section 1, were selected on the basis of a compromise, whereby fire suppression efficiency was sacrificed to ensure acceptable environmental properties. The research reported in this section was directed at developing the capability to predict the fire suppression effectiveness, propensity to generate corrosive combustion products, and environmental impact of a molecule on the basis of its structure. This is essential to the development of a rational approach to the search for new and more effective fire fighting chemicals.

The immediate objective of the research described in Section 5.1 was to provide a chemical basis for understanding the relative fire suppression efficiencies of the core candidates. In this pursuit, a kinetic mechanism, accounting for the interactions of substituted fluoromethanes and fluorethanes in hydrocarbon flames, was developed and incorporated into a computer model. The expectation is that fire scientists will some day be able to use this model to predict the performance of replacement candidates, thereby reducing the time and expense involved in laboratory screening.

The fire suppression efficiencies of the core candidates are poor compared to halon 1301. This implies that much higher concentrations will be required to put out a fire. The levels of corrosive by-products, particularly HCl and HF, generated in the extinction process are likely to be considerably higher, as well. The empirical study summarized in Section 5.2 was undertaken to identify the factors which determine the potential of an agent to form acid gases in a combustion environment so that the worst offenders can be eliminated from further consideration

Additional research was conducted to expand the scope of agent screening beyond the core candidates. This effort is described in Section 5.3. Structure/activity relationships (SARs) for ozone depletion and global warming were tested and developed. These were used, in conjunction with experimental measurements of fire suppression efficiency and considerations of the commercial availability and suitability for total flooding, to identify the most promising candidates from an exhaustive list of possibilities.

5.1 Kinetics of Fluorine-Inhibited Hydrocarbon Flames

5.1.1 Project Objectives. The major objective of this subtask was to provide a chemical basis for rationalizing the relative degree of effectiveness of each candidate agent. A fundamental understanding of the chemistry of these agents in hydrocarbon flames should facilitate identification of desired characteristics of effective agents. That is, utilization of simple chemical concepts should enable

screening and selection of potential agents with minimal time and human resources. In order to accomplish the objective of this subtask, it was necessary to develop a chemical mechanism based on elementary reaction steps for their destruction, their participation in and influence on hydrocarbon flame chemistry, as well as for prediction of potential by-products of incomplete combustion. Unfortunately, neither such a mechanism nor a review of the relevant chemistry existed prior to this study. Consequently, a significant effort was required in order to "simply" construct such a comprehensive mechanism prior to its utilization in any simulations.

The focus of this task was restricted to the chemistry involving only fluoromethanes and fluoroethanes. This includes both those candidate agents specifically being considered as replacements (CH_2F_2, CF_3-CH_2F, CF_3-CHF_2, CF_3-CF_3), as well as for all of the other possible fluoromethanes (CH_3F, CHF_3, CF_4) and fluoroethanes (CH_3-CH_2F, CH_3-CHF_2, CH_3-CF_3, CH_2F-CH_2F, CH_2F-CHF_2, CHF_2-CHF_2). The two chlorine-substituted agents (CHF_2Cl, CF_3-CHF_2Cl) and the larger fluorinated hydrocarbon agents (C_3F_8, C_3F_7H, C_4F_{10}, cyclo-C_4H_8) were not specifically considered. Including these additional candidate agents would significantly increase the complexity of the chemistry that must be considered. However, the effectiveness of each can be estimated to some degree by analogy to the other agents that were studied. This can be done by using the qualitative trends observed and the fundamental understanding of the chemistry as developed as part of this subtask.

The complete set of fluoromethanes and fluoroethanes were studied for two basic reasons. First, when the four specific candidate agents being considered decompose in the flame, they generate a pool of fluorinated hydrocarbon stable species and radicals, which results in the formation of many of the other fluoromethanes and fluoroethanes. Consequently, in order to describe the decomposition of the four specific agents (and resultant chemistry) adequately, it is necessary to describe the chemistry of all of the many intermediates and products that are created, including most of the other fluoromethanes and fluoroethanes.

For example, the lowest energy and primary decomposition pathway for one of the candidate agents, CF_3-CF_3, involves dissociation of the C-C bond to form (two) $\bullet CF_3$ radicals. These $\bullet CF_3$ radicals will then react with methyl radicals, $\bullet CH_3$, which are present in significant concentrations in hydrocarbon flames. This radical-radical combination reaction has two decomposition channels whose relative importance is dependent upon temperature and pressure. One channel results in the formation of a fluoroethylene, $CH_2{=}CF_2$ (and HF by-product). The other channel results in the formation of another fluoroethane, CH_3-CF_3. In order to predict the products in the flame correctly, the magnitude and rate of heat release in the flame, and ultimately the effectiveness of the added agent, it is also necessary to describe correctly the decomposition of these two additional stable fluorinated hydrocarbon species (CH_3-CF_3, $CH_2{=}CF_2$). When the decomposition channels for these two molecules are considered and for all of the other reaction channels for $\bullet CF_3$, as well as for all of the relevant chemistry for the other three specific candidate agents, very quickly most of the possible fluoromethanes and fluoroethanes must be considered.

Second, given that as part of the overall project there was, unfortunately, no directly related experimental task to these simulations, it was imperative to provide a level of self-consistency to this work by considering a range of modeling parameters, including different reactor/flame geometries, different fuels, different (potential) agents, and many other conditions. In doing so, it allowed us to develop confidence in the validity of the qualitative trends that we observed. Quantitative prediction of the absolute or even relative effectiveness of the specific agents will require benchmarking of the simulations with experimental measurements.

5.1.2 Background. There has been a significant amount of work over many years investigating the effectiveness of halogenated fire suppressants (Ellis, 1948; Simmons and Wolfhard, 1955; Rosser

et al., 1958; Friedman and Levy, 1963; Fenimore and Jones, 1963; Halpern, 1966; McHale *et al.*, 1971; Day *et al.*, 1971; Creitz, 1972; Biordi *et al.*, 1973; Larsen, 1974; Brown, 1975; Gann, 1975; Larsen, 1975; Skinner, 1975; Biordi *et al.*, 1976; Biordi *et al.*, 1978; Fristrom and Van Tiggelen, 1979; Dixon-Lewis, 1979; Westbrook, 1980; Safieh *et al.*, 1982; Westbrook, 1983; Vandooren *et al.*, 1988; Masri, 1992; Morris *et al.*, 1992), as well as other types of fire suppressants (Jorrissen and Meuwissen, 1924; Jorissen *et al.*, 1932; Lask and Wagner, 1962; Ibiricu and Gaydon, 1964; Fristrom, 1967; McHale, 1969; Creitz, 1970; Cotton and Jenkins, 1971; Hastie, 1973; Jensen and Jones, 1978; Jensen and Jones, 1982). We will not review this body of work, but refer the reader to those relevant sources. However, in the following sections we will provide a brief overview of the most relevant work relating to the agents being considered as part of this project. For the most part, this means the chemistry of CF_3Br flame suppression. We will also describe the general and specific physical and chemical processes that are most important in influencing flame suppression and other effects (*e.g.*, ignition, promotion, by-products) in hydrocarbon flames. This will include those factors specifically related to the candidate agents.

The chemistry of CF_3Br and its role in flame suppression has been reviewed in detail by others. A number of these works are referenced in the prior section. A large part of our work is based on the pioneering work in this area by Biordi and coworkers (Biordi *et al.*, 1978) and Westbrook (1983). In earlier experiments on a range of candidates, CF_3Br was identified as being very effective for extinguishing flames. However, its mechanism was not understood. Biordi and coworkers constructed the first flame-sampling molecular beam mass spectrometer in order to understand how CF_3Br inhibited combustion in hydrocarbon flames. In this work, they measured both stable and radical species in methane flames that were doped with CF_3Br. Many of the relevant elementary reactions describing the decomposition of CF_3Br, its chemistry, and its influence on hydrocarbon flames were determined in this work. Westbrook developed the first comprehensive chemical mechanism to described in detail the chemistry of CF_3Br. This mechanism was then used to model the inhibition of CF_3Br in hydrocarbon flames. As a result of this work and other work, it is generally agreed that flame suppression by bromine-containing compounds is a result of catalytic destruction of H atoms by Br atoms in the flame. The ability of bromine to recycle in the chemical system in the flame is directly related to the weak molecular bonds formed by bromine. Thus, bromine when complexed in molecules such as CF_3Br, CH_3Br, HBr, and Br_2, can through a number of reactions regenerate Br atoms. It was also determined in these studies that $\bullet CF_3$, formed by decomposition of CF_3Br, also removes H atoms by competition with radicals important to combustion (*e.g.*, H, O, OH, HO_2).

There are a variety of ways in which fire suppressants act in inhibiting hydrocarbon flames. Most of these effects are intimately related. For example, a heat loss means a temperature decrease, which causes the chemistry to slow, which means fewer radicals leading to product formation, which means less heat generated, which results in a temperature decrease and so on. One can separate suppression effects into two general categories: physical and chemical (although there is overlap). We prefer a definition where chemical effects are directly related to the characteristics of the specific molecule, such a H or F or Cl substitution, and physical effects are not. For example, heat capacity to a first approximation is largely a function of the number of atoms in the molecule and their connectivity, but not the identity of the molecule. Consequently, heat capacity can be considered an effect of more of a physical nature than a chemical one.

There are a number of physical effects that relate to fluid mechanics, mass transport, and heat transport processes that were not specifically studied as a part of our task (largely dealing with the chemistry of these agents). Physical effects were addressed by other tasks in the overall project that consisted of measurements of PVT properties, discharge dynamics, dispersion mechanics, as well as measurements of extinction effectiveness for a number of more realistic geometries than can be

considered in this modeling task. We will not discuss these in any detail here and refer the reader to the sections dealing with other tasks. However, it is necessary to understand the impact of these effects as they relate to our results in order to provide a framework for transfer of the results of our simulations to more realistic conditions. Some of the fluid mechanics and mass transport effects include dilution, turbulent mixing, diffusive mixing, thermal diffusion, and buoyancy. Heat related effects, which we could not directly address in our simulations, include the latent heat of vaporization and non-adiabatic effects, such as radiative cooling or heat losses for flames attached to a cold surface.

There are a number of different types of chemical effects. Most of these involve different competing factors. First, all of the fluorinated hydrocarbons will eventually decompose and then burn (forming CO_2, H_2O, and HF). This liberates heat and increases flame temperatures (which of course speeds flame chemistry). On the other hand, the agents are large molecules with many atoms. Consequently, their high heat capacities may result in a decrease in temperature in the flame prior to complete combustion (which of course slows flame chemistry). The competition between these two factors will be strongly dependent upon conditions; most important of which will probably be the mechanics of mixing of the fuel and oxidizer (including diffusion processes).

Another set of competing effects involves the fluorinated radicals produced by decomposition of the agents. These radicals are slower to burn than their pure hydrocarbon analogues, because the C-F bond is significantly stronger than the C-H bond. Consequently, reactions involving these radicals may effectively compete with analogous pure hydrocarbon chemistry by creating less "flammable" intermediates, thereby inhibiting combustion of the hydrocarbon fuel. For example, since the agents are added to the air stream, their immediate decomposition products (radicals) are formed in oxygen rich, relatively cold regions (preheat) of the flame. Consequently, these radicals may be involved in termination steps, such as $\bullet CHF_2 + HO_2\bullet \rightarrow CH_2F_2 + O_2$, slowing radical chain reactions and inhibiting the flame. These radicals will also simply compete with hydrocarbon radicals for important H, O, and OH radicals. On the other hand, these radicals can also react with stable molecules in the colder air stream, such as O_2, generating more radicals, such as O atoms, and thereby initiating chemistry or promoting combustion of the fuel.

These and other chemical effects (and the relative importance of each) are being considered as part of this work.

5.1.3 Reaction Engineering Approach

5.1.3.1 Species Thermochemistry. We have constructed a large comprehensive reaction set or "mechanism" for fluorinated hydrocarbon chemistry involving C_1 and C_2 stable and radical hydrocarbon species, including partially oxidized fluorinated hydrocarbons. Existing thermochemical data was compiled and evaluated. Where little or no data existed for potential species of interest (most of the radicals), we have estimated that thermochemistry using both empirical methods, such as group additivity (Benson, 1976), and also through application of *ab initio* molecular orbital calculations (Frisch *et al.*, 1992; Curtiss *et al.*, 1991; Melius, 1990). Where heat capacity data existed, but only over a limited temperature range, these data were fit to two splined polynomials which extrapolated to the theoretical high temperature limit and were well-behaved at intermediate temperatures (*e.g.*, Figure 1). In all cases (experimental, empirical, and *ab initio*), significant effort was made to utilize thermochemical data for each which was consistent (correct relative values) with data for all other species. Figure 1 shows a typical fit to heat capacity data for one of the fluoroethanes. This figure is a (black & white) "screen dump" of the (color) display window of the interactive, graphics program "NIST FITCP," which was developed as part of this subtask.

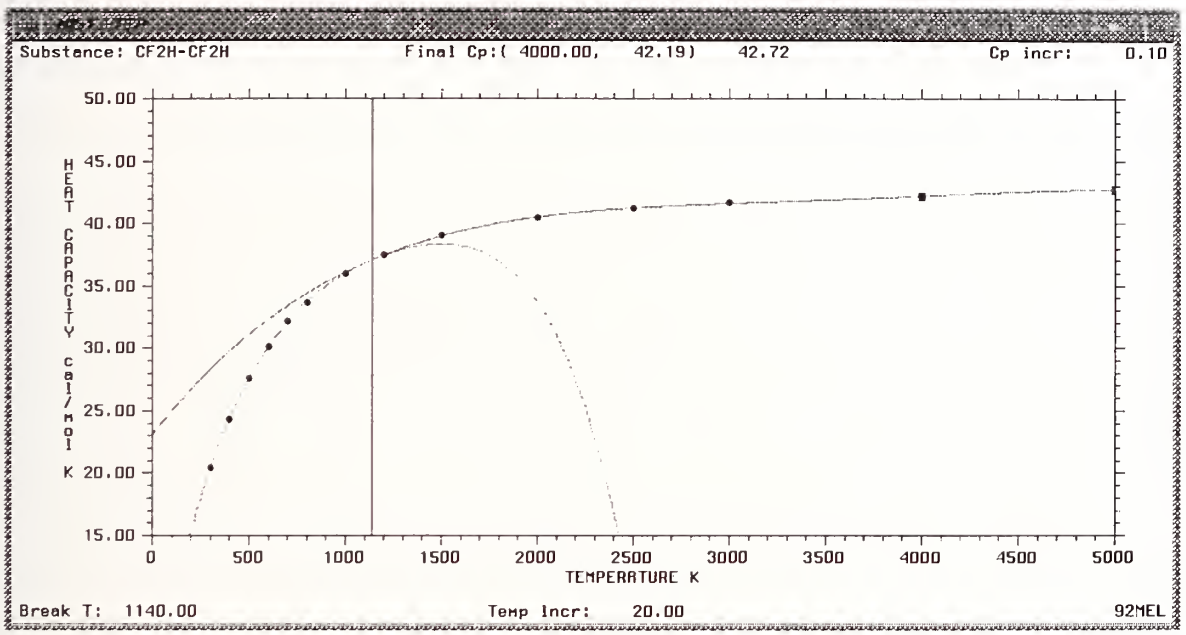

Figure 1. NIST FITCP. Typical fit to heat capacity data for a fluoroethane. This is a (black & white) "screen dump" of the (color) display window of the interactive, graphics program "NIST FITCP" developed as part of this subtask.

There are a number of general sources of relevant compiled and evaluated thermochemical data. These include *The Chemical Thermodynamics of Organic Compounds* (Stull *et al.*, 1969), *JANAF Thermochemical Tables* (Stull and Prophet, 1971), *Thermochemical Data of Organic Compounds* (Pedley *et al.*, 1986), *TRC Thermodynamic Tables* (Rodgers, 1989), *Physical and Thermodynamic Properties of Pure Chemicals* (Daubert and Danner, 1985), *NIST Structures and Properties Database and Estimation Program* (Stein *et al.*, 1991). There are two compilations/evaluations of fluorinated hydrocarbons in the *Journal of Physical and Chemical Reference Data*: "Ideal Gas Thermodynamic Properties of Six Fluoroethanes" (Chen *et al.*, 1975) and "Ideal Gas Thermodynamic Properties of Halomethanes" (Kudchadker and Kudchadker, 1978). There are a few individual sources of more recent data for thermochemistry that are relevant. These include "Thermochemistry of Fluorocarbon Radicals" (Rodgers, 1978), "Hydrocarbon Bond Dissociation Energies" (McMillen and Golden, 1982), and "Halomethylenes: Effects of Halogen Substitution on Absolute Heats of Formation" (Lias *et al.*, 1985). There are a numerous other references with thermodynamic data for fluorinated hydrocarbons that we have compiled as part of this work and will be discussed in more detail in a later publication. It should be noted that for most of the radicals, we have relied upon recent *ab initio* calculations of thermochemical data. This includes both *ab initio* calculations done as part of this subtask of the project and those done previously by other workers. Tschuikow-Roux and coworkers have calculated thermochemistry for the fluoroethyl radicals (Chen *et al.*, 1990a, 1990b; Chen *et al.*, 1991a, 1991b). Melius has calculated thermochemistry for many stable and radical fluorinated species (Melius, 1993). Nyden (1993) has used *ab initio* calculations to obtain thermochemical data for a number of the fluoroethanes and fluoroethyl radicals. Details of our *ab initio* calculations will be given in a subsequent section.

A listing of the thermochemistry that was used for fluorinated hydrocarbon species is given in Table 1, consisting of enthalpies of formation and entropies (at standard state) and temperature-dependent heat capacities. Standard thermochemistry for hydrocarbon, hydrogen/oxygen, and hydrogen/fluorine/oxygen species was used and is not included in this table.

5.1.3.1.1 Hydrocarbon and H/O/F Thermochemistry. We have used standard hydrogen/oxygen and hydrocarbon thermochemistry, most of which can be found in the JANAF tables (Stull and Prophet, 1971). More recent thermochemistry for C_2H_3 and HCO has been utilized. Further refinement of this mechanism should include re-adjustment of any other thermochemistry or rate constants that are based upon the older values for the heat of formation of these two species.

Thermochemistry for F, F_2, and HF can be found in the JANAF tables as can data for FO•, FOO•, FOF, and HOF. (The latter species were eventually excluded from the reaction set as the simulations showed that their concentrations were negligible at high temperatures under hydrocarbon flame conditions). The thermochemical data for F, F_2, and HF are very well established. Although there is a more recent value for the heat of formation of HF, the values contained in the JANAF table were used for consistency. This is because there are many thermochemical and rate data for fluorinated species that are based on the current JANAF recommendation for HF. Further refinement of this mechanism should include evaluation of this new value for HF and re-adjustment of any other thermodynamic or kinetic data that are based on HF thermochemistry.

5.1.3.1.2 C_1 Fluorinated Hydrocarbon Thermochemistry. Thermochemical data for the fluoromethanes: CH_3F, CH_2F_2, CHF_3, and CF_4 can be found in the JANAF tables (Stull and Prophet, 1971). The thermodynamic properties of these fluoromethanes have also been re-examined subsequently (Rodgers *et al.*, 1974). As part of this subtask of the project, we have also calculated this data using the BAC-MP4 *ab initio* method (Melius, 1990). Details of our *ab initio* calculations

will be given in a subsequent section. Melius (1993) has also calculated this thermochemical data for the fluoromethanes. It is necessary to have *ab initio* calculated values for these molecules with well known thermochemical data in order to adequately benchmark *ab initio* calculations for those molecules with unknown or uncertain thermochemistry. Entropy and heat capacity data for the fluoromethanes are derived from spectroscopic data and are known to a very good level of certainty (less than 0.5 J/mol/K for entropies). Heats of formation for CH_2F_2 and CF_4 are the best known, with levels of uncertainty of less than 1.5 kJ/mol. The values for CH_2F_2 and CF_4 are derived from their heats of combustion (which are dependent on the heat of formation of HF). These data also correlate well with heats of formation for other fluorine-containing molecules. Heats of formation of CH_3F and CHF_3 have somewhat higher uncertainties of less than 10 kJ/mol. The heat of formation of CH_3F is derived from appearance potential measurements (high level of uncertainty) and also from bond additivity correlations with heats of formation for CH_4 and the other fluoromethanes. The heat of formation of CHF_3 is obtained from heat of combustion data for CHF_3, equilibrium data with other compounds, and some kinetic data. The data derived from heat of combustion appear to be complicated by competing reactions. Heats of formation for the fluoromethanes calculated using BAC-MP4 are within 1-3 kJ/mol of the experimentally derived values (except for CF_4, the reference compound). A better BAC correction should be possible using correlations with all experimental data for fluoromethanes and fluoroethanes rather than just one compound (CF_4).

Thermochemical data for the perfluoromethyl radical ($\bullet CF_3$) can be found in the JANAF tables. More recent experimentally derived values for the heat of formation of $\bullet CF_3$ can be found elsewhere (Rodgers, 1978; McMillen and Golden, 1982; Tsang, 1986). These suggest a value that is about 4 kJ/mol higher than the JANAF recommendation. All of these heat of formation data are derived from kinetic experiments for the forward and reverse rates of several reaction. The JANAF recommendation is also based in part of correlations with heats of formation (and bond strengths) for other fluorine-containing compounds. The entropy and heat capacity data for $\bullet CF_3$ in the JANAF table are derived from spectroscopic measurements with an uncertainty of about 5 J/mol/K in the entropy. The other fluoromethyl radicals ($\bullet CH_2F$, $\bullet CHF_2$) are not in the JANAF tables. However, reliable, experimentally derived values for these two compounds can be found in other evaluated sources (McMillen and Golden, 1982; Pickard and Rodgers, 1983).

As part of this subtask of the project, we have also calculated thermochemical data for the fluoromethyl radicals using the BAC-MP4 *ab initio* method. These data have also been calculated by Melius (1993). We have used the entropies and heat capacities for $\bullet CH_2F$ and $\bullet CHF_2$ from the *ab initio* calculations in the kinetic simulations part of this subtask, since there does not exist (to our knowledge) experimental values for these two radical species. Heats of formation for $\bullet CH_2F$, $\bullet CHF_2$, and $\bullet CF_3$ calculated by this method are within 1-2 kJ/mol of the experimentally derived values. Although there are the experimentally derived values for $\bullet CH_2F$ and $\bullet CHF_2$, we have used the *ab initio* values in order to be consistent with other *ab initio* calculations. Undoubtedly, these data should be critically evaluated in further refinements of the mechanism. This may consist of using *ab initio* calculations benchmarked appropriately to experimental values.

Thermochemical data for the fluoromethylenes, :CHF and $:CF_2$, can be found in the JANAF tables. Unfortunately (since :CHF and $:CF_2$ are very important species), there are significant uncertainties in their heats of formation. The values for $:CF_2$ are the best and are derived from appearance potential, ionization potentials, kinetic data, and heats of reactions with heats of formation for related molecules. The best value based on ionization potential data is -186($\pm$10) kJ/mol. The kinetic data appear to provide the most consistent values. The JANAF recommendation is -182($\pm$6) kJ/mol (with a range of -172 to 190 kJ/mol). More recently Rodgers (1978) has recommended a

value based largely upon kinetic data of -187(±4) kJ/mol. Subsequently, Lias and coworkers (Lias *et al.*, 1985) have recommended a significantly lower value of -205(±13) kJ/mol. This recommendation was based solely on appearance potential and ionization data. Depending on what data were used, values ranged from -172 to -213 kJ/mol could be obtained. Given the large uncertainty in values derived from appearance and ionization potentials and given that it is essential to use a heat of formation for $:CF_2$ that is consistent with kinetic data, we believe that the JANAF recommendation or possibly the more recent value of Rodgers should be used. To date we have employed the JANAF recommendation until all of the experimental and *ab initio* data have been critically evaluated.

The uncertainty in the heat of formation for :CHF is even greater due to the lack of direct, reliable data (heat of reaction, kinetic, or otherwise). The recommended JANAF value of 126(±29) kJ/mol is based very roughly on bond energies from other molecules. More recently, Lin and coworkers (Hsu *et al.*, 1978) and Pritchard and coworkers (Pritchard *et al.*, 1984) have independently recommended 163(±8) kJ/mol based upon heat of reaction and kinetic data. However, Lias and coworkers again considered the kinetic and heat of reaction data to be unreliable and have used proton affinity values to make a recommendation of 108(±13) kJ/mol, which is much lower than all other recommendations. Again, since it is necessary to use a value that is consistent with kinetic data for neutral thermal species (not ionic species), we believe that either the JANAF value or the Lin and Pritchard value should be used. To date we have employed the JANAF recommendation until all of the experimental and *ab initio* data have been critically evaluated.

As part of this subtask of the project, we have also calculated thermochemical data for :CHF and $:CF_2$ using the BAC-MP4 *ab initio* method. These data have also been calculated by Melius (1993). The calculated value for $:CF_2$ is about 10-15 kJ/mol lower than the best experimentally derived values. For :CHF, the BAC-MP4 *ab initio* value is about 25 kJ/mol higher than the JANAF value and 10 kJ/mol lower than the value determined by Lin and coworkers (Hsu *et al.*, 1978) and Pritchard and coworkers (Pritchard *et al.*, 1984). We have also calculated heats of formation for :CHF and $:CF_2$ using G2 *ab initio* theory (Curtiss *et al.*, 1991) and obtain better agreement with the experimentally-derived values (within 5-10 kJ/mol of the JANAF recommendations).

Thermochemical data for most of the other possible C_1 fluorinated hydrocarbons can be found in the JANAF tables. These include •CF, CHF=O, CF_2=O, and •CF=O. The biggest uncertainties here are for CHF=O and •CF=O where no direct experimental data are available and, consequently, their heats of formation were calculated using average bond dissociation energies from other related compounds. We have calculated thermochemistry for these carbonyl fluorides using the BAC-MP4 *ab initio* method, as well using the G2 *ab initio* method. For •CF=O and CHF=O, the *ab initio* values are about 10 kJ/mol and 20 kJ/mol lower than their respective JANAF recommendations. For CF_2=O, the *ab initio* values are about 20-40 kJ/mol higher than the JANAF recommendation. Given the importance of these species and the uncertain thermochemistry, further refinement of this mechanism will require these values be re-examined. To date, we have used the JANAF values for consistency. There is an experimentally derived value for the heat of formation of CF_3O• (Batt and Walsh, 1982). However, we have used our BAC-MP4 *ab initio* value for the sake of consistency because we have relied solely on *ab initio* values for the other fluoromethoxy radicals and for a number of reactions involving CF_3O•. Undoubtedly, all of these data should be re-evaluated in order to provide the best values.

5.1.3.1.3 C_2 Fluorinated Hydrocarbon Thermochemistry. The thermochemical data for C_2 fluorinated hydrocarbons that were used in this work are given in Table 1.

Thermodynamic properties for most of the fluoroethanes are derived from experimental data. This work is compiled and evaluated in the *Journal of Physical and Chemical Reference Data* (Chen *et al.*, 1975). These data and data for other fluoroethanes can be also found in the DIPPR compilation (Daubert and Danner, 1985).

There are experimentally derived thermochemical data (Rodgers, 1978) for a few of the fluoroethyl radicals (CH_3-CH_2•, CF_3-CH_2•, CF_3-CF_2•). Thermochemistry for all of the fluoroethyl radicals have been calculated through the application of *ab initio* molecular orbital theory by Tschuikow-Roux and coworkers (Chen *et al.*, 1990a, 1990b; Chen *et al.*, 1991a, 1991b). Thermochemistry for a number of the fluoroethyl radicals have also been calculated using the BAC-MP4 and the G2 *ab initio* methods. We have used experimentally derived data, calculated some values using group additivity, and also calculated some of the values using the BAC-MP4 *ab initio* method. To date, we have chosen to use those values for the complete set calculated by Tschuikow-Roux and coworkers for consistency. In their work, the experimental heat of formation data for the three fluoroethyl radicals were employed. For the other fluoroethyl radicals, they determined heat of formations by benchmarking their *ab initio* values to experimental data using a series of isodesmic reactions. Future refinement of this mechanism will need to consider all of the *ab initio* calculations with the relevant experimental data using bond additivity and group additivity methods, as well as using isodesmic reactions. This would yield the best, consistent thermochemistry for all of the fluoroethyl radicals which are, whole or in part, experimentally derived.

Thermochemistry for $CF_2=CF_2$ can be found in the JANAF tables and data for $CH_2=CHF$ and $CH_2=CF_2$ in DIPPR (Daubert and Danner, 1985). For the three other fluoroethylenes (CHF=CHF(*E*), CHF=CHF(*Z*), $CHF=CF_2$), we have used thermochemistry from our *ab initio* calculations. Melius (1993) has also calculated this data. Again, as in the case of the fluoroethyl radicals, future refinement of this mechanism would involve benchmarking the *ab initio* calculations with the experimental data to provide a consistent set. There are not experimentally derived thermochemical data (to our knowledge) for the fluorovinyl radicals. Consequently, we have used values that we have calculated as part of this subtask the BAC-MP4 *ab initio* method.

The thermochemistry of the fluoroacetylenes (C_2HF, C_2F_2) can be found in the JANAF tables. We have used these values. However, there are relatively large uncertainties in these data: ± 60 kJ/mol and ± 20 kJ/mol in the heats of formation of C_2HF and C_2F_2, respectively. Further refinement of this mechanism should critically evaluated the sensitivity of the simulations to these data. Fluoroketenes and the fluoroketyl radical can be formed through a number of channels (analogous to simple hydrocarbon chemistry). To assess the importance of these species and relevant reactions, we have included these species in the mechanism. There are not experimentally derived data for these species. Consequently, we have had to rely upon values which we have calculated as part of this task using the BAC-MP4 *ab initio* method.

5.1.3.1.4 *Ab Initio* Thermochemistry. As part of this subtask, we have calculated thermochemistry for many fluorinated species through the application of *ab initio* molecular orbital theory. In this work, the GAUSSIAN series of programs was used (Frisch *et al.*, 1992). In the BAC-MP4 *ab initio* method (Melius, 1990), the geometries are optimized at the Hartree-Fock level, the relative energies are then calculated at the MP4 level, and finally the absolute energies are calculated by applying a Bond Additivity Correction (BAC). The BAC is based on the type of bond (*e.g.*, C-H, C-F), its bond length, the identity of all next nearest neighbors, and the bond length between the nearest neighbor and the next nearest neighbor. Both calculated and experimental derived (where available) heats of formation for these compounds are summarized in Table 2 and Table 3. A discussion of the

comparison between experimental heats of formation for these fluorinated hydrocarbons and the *ab initio* values is presented elsewhere in sections dealing with each class of compounds. It is necessary to have *ab initio* calculated values for molecules with well known thermochemical data in order to adequately benchmark *ab initio* calculations for those molecules with unknown or uncertain thermochemistry.

Thermochemical data for all of the species that we have calculated are given in Appendix A in a "JANAF style" tabular format. Values for moments of inertia, vibrational frequencies, bond distances, bond angles, heat of formation at 0 K, heat of formation at standard state, and entropy at standard state are given for each species. Heat capacity, free energy of formation, and other thermochemical quantities as a function of temperature are also given for each species. Many of the species included in Appendix A were initially considered in the chemical mechanism, but subsequently eliminated to keep the reaction set to a manageable level, because the simulations indicated they did not significantly contribute to the overall chemistry. Consequently, many of the species are not found in Table 1, which contains only those species employed in the final chemical kinetic mechanism used in the premixed flame simulations. The importance of some of the species, such as perfluoromethanol (CF_3OH) or the fluoroacetaldehydes (*e.g.*, CHF_2-CHO), should be reexamined in future refinements of this chemical mechanism. For example, they would undoubtedly play larger roles at lower temperatures.

We have calculated thermochemical data using the BAC-MP4 *ab initio* method for all of the possible C_1 fluorinated hydrocarbons. This work includes the fluoromethanes (CH_3F, CH_2F_2, CHF_3, CF_4), fluoromethyls ($\bullet CH_2F$, $\bullet CHF_2$, $\bullet CF_3$), fluoromethylenes (:CHF, $:CF_2$), and fluoromethylidyne ($\bullet$CF). We have also calculated thermochemistry for most of the possible oxidized C_1 fluorinated hydrocarbons. This includes all of the carbonyl fluorides (CF_2=O, CHFO, $\bullet$CFO), one of the fluoromethanols (CF_3OH), all of the fluoromethoxy radicals ($CH_2FO\bullet$, $CHF_2O\bullet$), $CF_3O\bullet$), one of the hydroxyfluoromethyl radicals ($\bullet CF_2OH$), one of the fluoromethylperoxy radicals ($CF_3OO\bullet$), one of the fluoromethylperoxides (CF_3OOH), and fluoroformic acid (FCO_2H). We note that there are energetically different, configurational isomers for the hydroxyfluoromethyl radicals and we calculated values for each. Melius (1993) has also calculated thermochemistry for some of the species and for a number of related species including the other fluoromethanols (CH_2FOH, CHF_2OH) and the other fluoromethylperoxy radicals ($CH_2FOO\bullet$, $CHF_2OO\bullet$), including the energetically different, configurational isomers when possible.

Thermochemical data for some of the fluoroethanes (CH_3-CH_2F, CH_3-CHF_2, CH_3-CF_3, CHF_2-CHF_2, CHF_2-CF_3), some of the fluoroethyl radicals (CHF_2-$CH_2\bullet$, CH_3-$CF_2\bullet$, CF_3-$CH_2\bullet$, CHF_2-$CF_2\bullet$, CF_3-$CF_2\bullet$), all of the fluoroethylenes (CH_2=CHF, CHF=CHF, CH_2=CF_2, CHF=CF_2, CF_2=CF_2), and all of the fluorovinyl radicals (CH_2=CF$\bullet$, CHF=CH$\bullet$, CHF=CF$\bullet$, CF_2=CH$\bullet$, CF_2=CF$\bullet$), have been calculated by Melius (1993) using the BAC-MP4 *ab initio* method. We note that CHF=CHF and two of the fluorovinyl radicals each have two energetically different, configurational isomers (*Z* and *E*). In addition, Melius (1993) has calculated thermochemistry for oxidized C_2 fluorinated hydrocarbon species, including the fluoroacetaldehydes (CH_2F-CHO, CHF_2-CHO, CF_3HO) and the fluoroacetyl radicals (CH_2F-CO$\bullet$, CHF_2-CO$\bullet$, CF_3-CO$\bullet$); In addition to these calculations, there have been *ab initio* calculations for the fluoroethanes and fluoroethyl radicals by other workers using other methods. As indicated previously, Tschuikow-Roux and coworkers have calculated thermochemistry for all of the fluoroethyl radicals in a series of papers (Chen *et al.*, 1990a, 1990b; Chen *et al.*, 1991a, 1991b). In addition, Nyden (1993) has used G2 *ab initio* calculations (Curtiss *et al.*, 1991) to obtain thermochemistry for a number of the fluoroethanes and fluoroethyl radicals.

As part of this task, we have replicated the calculations of Melius using the BAC-MP4 method for a number of these molecules. We have also calculated thermochemical data for a number of other related species, which were necessary to have either to include directly in the chemical mechanism or to benchmark (in combination with experimental data) other *ab initio* calculations. These include some of the other fluoroethanes (CH_2F-CH_2F, CH_2F-CHF_2, CH_2F-CF_3), the two fluoroacetylenes (C_2HF, C_2F_2, $\bullet C_2F$), the two fluoroketenes/ethenones ($CHF{=}C{=}O$, $CF_2{=}C{=}O$), and the fluoroketyl radical ($\bullet CF{=}C{=}O$).

Using both the experimentally derived and the *ab initio* calculated thermochemistry values presented in Tables 2 and 3, group additivity values (for heats of formation) for the fluoroethanes were determined which were consistent with the majority of the data. These values are relatively useful, since employing the group additivity method of Benson (1976), one can obtain relatively good thermochemistry in the absence of experimental or calculated data. For a complicated system such as being considered in this project (fluorinated-hydrocarbons), this is an extremely valuable tool. In determining group additivity values consistent with the majority of the data, the best correlations were obtained when a correction for repulsive interactions between fluorines on adjacent carbons was included. It was observed that the *ab initio* values often differed from the experimentally derived values in a consistent fashion. In general, with increasing number of C-F bonds in the molecules, the difference between the *ab initio* and the experimentally derived heats of formation also increased. This *ab initio* values were, in general, lower than the experimentally derived values in the range of 5-15 kJ/mol (depending on the *ab initio* method) per C-F bond. This trend was used to benchmark the *ab initio* values when determining group additivity values consistent with all the data. Group values were also determined for chloroethanes for reference. All of these data are shown in Figure 2.

5.1.3.2 Reaction Kinetics. Utilizing the species identified as potentially important, a grid of possible reactions was constructed. Existing chemical rate data involving these fluorinated species was then compiled and evaluated. Where rate data were available, but only over limited temperature ranges or at different pressures (for unimolecular or chemically activated steps), RRKM (Robinson and Holbrook, 1972) and QRRK (Dean and Westmoreland, 1987) methods were used to estimate the temperature dependencies (at 1 atmosphere pressure) of the rates and to predict relative rates where multiple product channels were possible. Where no rate data were available for potential reactions, the rate constants were estimated by analogy to other hydrocarbon or substituted hydrocarbon reactions. The rate constant prefactors were adjusted for reaction path degeneracy and the rate constant activation energies were adjusted empirically based on relative heats of reaction or relative bond energies (*i.e.*, Evans-Polanyi relationships).

Initially, upper limits were used for estimated rate constants. If as a result of simulation under a variety of conditions (using different agents, flame geometries, etc.), it was observed that a specific reaction with an upper limit rate constant did not significantly contribute to the destruction or creation of any of the species in the "mechanism," then that estimate continued to be used. If however, a specific reaction contributed to the chemistry and its rate constant was an upper-limit estimate, then its value was re-examined and possibly refined. For important contributing reactions where no good analogy was available, where significant uncertainty existed in the barrier (generally reactions with tight transition states and modest-to-large barriers), or where multiple energetically similar product channels were possible, *ab initio* methods were used to calculate the geometries and energies of the transition states. RRKM methods were then applied to obtain the temperature (and pressure) dependence of the rate constant. The procedure used for iterative development of the mechanism is schematically shown in Figure 3.

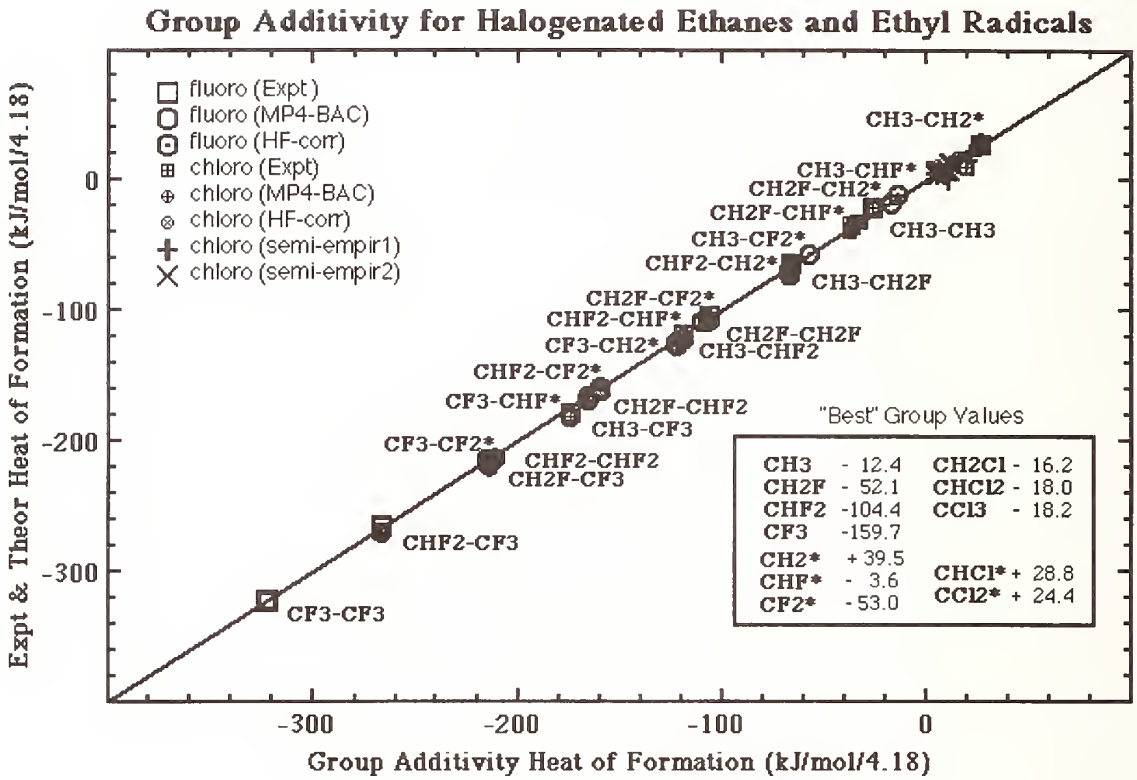

Figure 2. Empirically-Determined Halocarbon Thermochemistry. Group values were determined for predicting heats of formation of fluorinated and chlorinated ethanes consistent with the majority of experimental and *ab initio* data.

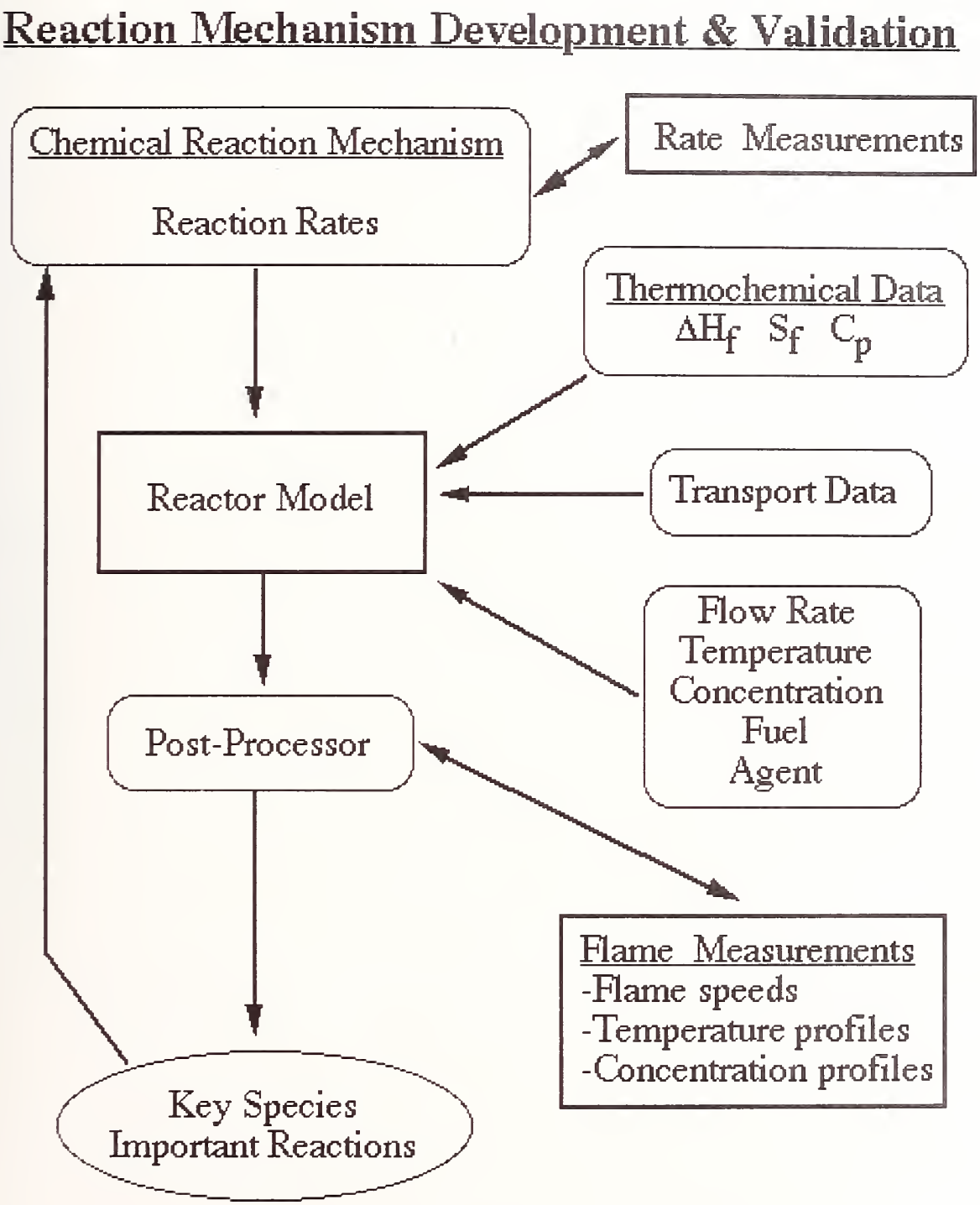

Figure 3. Reaction Mechanism Development and Validation.

Table 1. Fluorinated Hydrocarbons: Enthalpy of Formation, Entropy, Heat Capacities

Fluorocarbon	$\Delta H_f^o(298)$	$S^o(298)$	$C_p^o(T)$						ref
			300	500	800	1000	1200	1500	
CH_3F	-234.3	222.8	37.50	51.26	68.90	77.30	83.34	90.21	a
CH_2F_2	-450.6	246.6	42.96	58.91	76.33	83.55	88.84	94.35	a
CHF_3	-697.0	259.6	51.15	69.26	85.10	91.01	94.89	98.83	a
CF_4	-933.2	261.3	61.30	80.67	94.49	98.73	101.41	103.67	a
$\bullet CH_2F$	-31.5	234.4	38.71	48.67	59.29	64.20	67.92	72.02	b
$\bullet CHF_2$	-247.3	256.0	42.21	54.10	65.33	69.66	72.60	75.69	b
$\bullet CF_3$	-470.3	265.0	49.94	63.30	73.24	76.37	78.27	79.92	a
:CHF	125.5	223.2	34.63	39.25	45.21	47.93	50.05	52.43	a
$:CF_2$	-182.0	240.7	39.01	46.45	52.35	54.18	55.28	56.31	a
$\bullet CF$	255.2	212.9	30.05	32.24	34.79	35.77	36.32	36.96	a
$CF_3O\bullet$	-628.3	275.2	56.44	73.91	86.83	90.89	93.40	95.56	b
CHF=O	-376.6	246.7	40.50	51.65	63.12	67.92	71.20	74.70	a
$CF_2=O$	-638.9	258.8	47.41	60.49	70.82	74.39	76.71	78.78	a
$\bullet CF=O$	-171.5	248.4	38.99	45.06	50.63	52.76	54.14	55.44	a
CHF=C=O	-147.2	270.5	56.75	71.49	84.93	90.34	94.31	98.24	c
$CF_2=C=O$	-290.4	288.8	68.30	81.79	92.56	96.66	99.61	102.48	c
$\bullet CF=C=O(E)$	69.0	276.2	56.8	65.85	73.77	76.59	94.38	98.22	c
$CH_3\text{-}CHF_2$	-493.7	282.5	68.72	97.11	124.65	136.47	145.39	154.49	d
$CH_2F\text{-}CHF_2$	-643.5	311.7	75.31	107.53	133.47	143.93	151.98	159.92	e
$CH_3\text{-}CF_3$	-745.6	287.4	78.81	108.32	133.82	144.08	151.47	158.99	d
$CHF_2\text{-}CHF_2$	-890.1	314.8	85.23	115.25	141.25	150.60	156.64	163.29	b
$CH_2F\text{-}CF_3$	-895.8	316.2	86.58	118.04	143.15	152.09	158.17	164.43	d
$CHF_2\text{-}CF_3$	-1104.6	333.8	96.09	127.53	151.13	158.85	164.06	168.60	d
$CF_3\text{-}CF_3$	-1343.9	332.1	106.79	139.13	160.34	166.68	169.89	172.97	a
$CH_3\text{-}CHF\bullet$	-72.4	274.0	58.79	79.75	103.33	114.06	122.34	130.91	e
$CH_2F\text{-}CHF\bullet$	-235.5	293.4	69.59	91.24	111.69	119.75	125.52	131.33	f
$CHF_2\text{-}CH_2\bullet$	-277.2	297.8	67.06	90.20	111.94	121.10	128.00	135.04	e
$CH_3\text{-}CF_2\bullet$	-302.5	290.4	67.34	89.22	111.30	120.80	127.83	135.52	e
$CH_2F\text{-}CF_2\bullet$	-446.0	311.1	74.07	97.38	118.86	127.24	133.22	139.11	f
$CHF_2\text{-}CHF\bullet$	-451.9	310.7	76.14	99.54	119.95	127.91	133.70	139.35	f
$CF_3\text{-}CH_2\bullet$	-517.1	302.6	77.37	101.75	121.27	128.88	134.26	139.75	e
$CHF_2\text{-}CF_2\bullet$	-660.2	328.4	84.32	107.31	127.04	134.10	138.83	143.26	f
$CF_3\text{-}CHF\bullet$	-688.3	326.3	85.84	109.68	128.34	135.01	139.45	143.76	f
$CF_3\text{-}CF_2\bullet$	-891.2	340.5	92.84	118.29	136.19	141.80	145.18	148.11	f
$CH_2=CHF$	-138.9	262.3	50.61	71.66	91.80	100.57	107.42	114.10	d
CHF=CHF(Z)	-301.2	268.6	58.06	79.62	99.16	107.13	112.47	118.31	b

Table 1. Fluorinated Hydrocarbons: Enthalpy of Formation, Entropy, Heat Capacities

Fluorocarbon	$\Delta H_f^o(298)$	$S^o(298)$	$C_p^o(T)$						ref
			300	500	800	1000	1200	1500	
CHF=CHF(*E*)	-302.2	267.8	59.82	80.44	99.61	107.53	112.83	118.70	b
$CH_2=CF_2$	-336.8	265.2	59.33	81.55	100.20	107.74	113.14	118.70	d
$CHF=CF_2$	-495.8	292.7	69.45	90.32	107.48	113.93	118.67	124.16	b
$CF_2=CF_2$	-658.5	299.9	80.70	100.40	115.53	120.89	123.89	126.87	a
CHF=CH•(*E*)	124.3	258.0	50.61	67.10	81.56	87.66	92.21	97.15	c
CHF=CH•(*Z*)	123.0	257.0	50.74	67.33	81.76	87.92	92.44	97.29	c
$CH_2=CF•$	109.2	256.8	50.22	66.10	80.71	86.89	91.30	96.37	c
CHF=CF•(*E*)	-41.0	279.3	59.30	74.51	87.79	92.80	96.05	99.66	c
CHF=CF•(*Z*)	-42.7	279.3	59.30	74.51	87.79	92.80	96.05	99.66	c
$CF_2=CH•$	-67.8	277.0	59.20	76.36	89.73	94.73	97.78	100.81	c
$CF_2=CF•$	-216.3	300.5	68.26	83.42	95.36	99.41	101.77	104.39	c
C_2HF	125.5	231.5	52.48	62.17	69.69	73.22	75.83	78.82	a
C_2F_2	20.9	244.0	57.07	67.96	76.67	79.74	81.54	83.46	a

NOTATION

$\Delta H_f^o(298)$: enthalpy of formation (kJ/mol) at standard state (1 atmosphere; 298.15 K)

$S^o(298)$: entropy (kJ/mol) at standard state (1 atmosphere; 298.15 K)

$C_p^o(T)$: heat capacity (J/mol/K) at constant pressure
at standard state (1 atmosphere; T = 300, 500, 800, 1000, 1200, and 1500 K)

REFERENCES

a. Stull and Prophet, 1971
b. Melius, 1993
c. this work
d. Daubert and Danner, 1985
e. Chen *et al.*, 1990a; Chen *et al.*, 1990b
f. Chen *et al.*, 1991a; Chen *et al.*, 1991b

Table 2. BAC-MP4 Thermochemical Computations (C_1): Enthalpy of Formation (kJ/mol)

FLUOROCARBON	BAC-MP4	ref	G2	ref	expt	ref
CH_3F	-233.9	a,b	-246.4	c	-234.3	d
CH_2F_2	-451.0	a,b	-456.6	c	-450.6	d
CHF_3	-699.6	a,b	-716.6	c	-697.1	d
CF_4	-934.3	a,b	-962.7	c	-933.0	d
$\bullet CH_2F$	- 31.4	a,b			- 32.6	e
$\bullet CHF_2$	-247.3	a,b	-252.9	c	-247.7	e
$\bullet CF_3$	-471.5	a,b	-483.0	c	-470.3	d
:CHF	152.7	b	131.8	a	125.5	d
$:CF_2$	-203.3	a,b	-190.0	a	-182.0	d
$\bullet CF$	236.4	b			255.2	d
CHF=O	-395.0	a,b			-376.6	d
CF_2=O	-598.3	a,b	-620.1	a	-638.9	d
$\bullet$CF=O	-182.8	a,b			-171.5	d
$CH_2FO\bullet$	-194.6	b				
$CHF_2O\bullet$	-405.8	b				
$CF_3O\bullet$	-628.4	a,b			-655.6	f
CF_3OH	-219.8	a,b				
$CH_2FOH(E)$	-412.1	b				
$CHF_2OH(E)$	-684.5	b				
$\bullet CF_2OH(E)$	-456.5	a,b	-455.2			
$\bullet CF_2OH(G)$	-463.2	a,b				
CF_3OOH	-807.5	a				
$CH_2FOO\bullet$	-172.8	b				
$CHF_2OO\bullet$	-401.2	b				
$CF_3OO\bullet$	-627.6	a,b				
CF(O)OH	-615.0	a				

Enthalpy of Formation (kJ/mol) at standard state (1 atmosphere; 298.15 K)
BAC-MP4: calculated (BAC-MP4 *ab initio* method: Melius, 1990)
G2: calculated (G2 *ab initio* method: Curtiss *et al.*, 1991)
expt: experimentally derived

REFERENCES
a: this work
b: Melius, 1993
c: Nyden, 1993
d: Stull and Prophet, 1971
e: McMillen and Golden, 1982
f: Batt and Walsh, 1982

Table 3. BAC-MP4 Thermochemical Computations (C_2): Enthalpy of Formation (kJ/mol)

FLUOROCARBON	BAC-MP4	ref	TSC	ref	G2	ref	expt	ref
CH_3-CH_2F	-272.4	a,b			-284.1	c	-263.2	f
CH_2F-CH_2F	-446.9	b			-489.9	c	-431.0	f
CH_3-CHF_2	-505.4	b			-518.5	c	-493.7	f
CH_2F-CHF_2	-671.5	a					-643.5	g
CH_3-CF_3	-755.2	b			-777.0	c	-745.6	f
CHF_2-CHF_2	-890.4	a,b						
CH_2F-CF_3	-913.4	b					-895.8	f
CHF_2-CF_3	-1124.2	b					-1104.6	f
CF_3-CF_3							-1343.9	d
CH_2F-CH_2•	- 56.2	a	-44.8	i		c		
CH_3-CHF•			-72.4	i	- 79.1	c		
CH_2F-CHF•			-235.6	j	-255.8	c		
CHF_2-CH_2•	-280.7	b	-277.4	i	-294.2	c		
CH_3-CF_2•	-300.0	b	-302.5	i	-309.7	c	-302.5	h
CH_2F-CF_2•			-446.0	j				
CHF_2-CHF•			-451.9	j				
CF_3-CH_2•	-527.2	b	-517.1	i			-517.1	h
CHF_2-CF_2•	-673.2	b	-660.2	j				
CF_3-CHF•			-688.3	j				
CF_3-CF_2•	-907.5	b	-891.2	j			-891.2	h
CH_2=CHF	-139.3	a,b					-138.9	f
CHF=CHF(*Z*)	-301.2	a,b						
CHF=CHF(*E*)	-302.1	a,b						
CH_2=CF_2	-340.2	a,b					-336.8	f
CHF=CF_2	-485.8	a,b						
CF_2=CF_2	-653.5	a,b					-658.6	d
CHF=CH•(*Z*)	124.3	a,b						
CHF=CH•(*E*)	123.0	b						
CH_2=CF•	109.2	a,b						
CHF=CF•(*Z*)	- 41.0	b						

Table 3. BAC-MP4 Thermochemical Computations (C_2): Enthalpy of Formation (kJ/mol)

FLUOROCARBON	BAC-MP4	ref	TSC	ref	G2	ref	expt	ref
CHF=CF•(*E*)	- 42.7	b						
CF_2=CH•	- 67.8	a,b						
CF_2=CF•	-216.3	a,b						
C_2HF	118.0	a					125.5	d
C_2F_2	31.8	a					20.9	d
•C_2F	454.0	a						
CHF=C=O	-147.3	a						
CF_2=C=O	-290.4	a						
•CF=C=O(*E*)	69.0	a						
CH_2F-CHO(*Z*)	-322.6	b						
CH_2F-CHO(*E*)	-328.9	b						
CHF_2-CHO(*E*)	-525.1	b						
CHF_2-CHO(*Z*)	-538.9	b						
CF_3-CHO	-774.5	b						
CH_2F-CO•(*Z*)	-169.9	b						
CH_2F-CO•(*E*)	-172.8	b						
CHF_2-CO•(*Z*)	-377.4	b						
CF_3-CO•(*Z*)	-610.0	b						
CF_3-CO•(*E*)	-611.3	b						

Enthalpy of Formation (kJ/mol) at standard state (1 atmosphere; 298.15 K)
BAC-MP4: calculated (BAC-MP4 *ab initio* method: Melius, 1990)
TSC: calculated (*ab initio* method of references i,j)
G2: calculated (G2 *ab initio* method: Curtiss *et al.*, 1991)
expt: experimentally derived

REFERENCES
a: this work
b: Melius, 1993
c: Nyden, 1993
d: Stull and Prophet, 1971
e: McMillen and Golden, 1982
f: Daubert and Danner, 1985
g: Pedley, 1986
h: Rodgers, 1978
i: Chen *et al.*, 1990a; Chen *et al.*, 1990b
j: Chen *et al.*, 1991a; Chen *et al.*, 1991b

A listing of the rate constants in the reaction set or mechanism used in the simulations is given in Appendix B. In addition, other reactions were also considered, but were observed not to contribute under the conditions tested. The hydrocarbon and hydrogen/oxygen reaction subsets of the mechanism were derived from the Miller-Bowman mechanism (Miller and Bowman, 1989). Some modifications to this accepted mechanism were made. Many of the relevant rate constants can be found in the "NIST Chemical Kinetics Database" (Mallard *et al.*, 1993).

5.1.3.1.1 Hydrocarbon/H/O/F Kinetics. The hydrogen/oxygen and hydrocarbon reaction subsets of the mechanism are derived from the Miller-Bowman mechanism (Miller and Bowman, 1989) and consists of about 30 species and 140 reactions. Some modifications to this accepted mechanism were made. All N-containing species (except N_2) and reactions were removed. A number of the rich species (*e.g.*, C_2H, C_4H_2) were eliminated from the mechanism in order to keep the number of species in the mechanism to a manageable level. Eliminating these species is valid, since the agent is (in general) added to the air (fuel lean). A number of species (*e.g.*, CH_3OH) were also added to the mechanism. In addition to these addition and deletions, a number of rate constants for a number of reactions (*e.g.*, CH_3+OH) were adjusted to provide correct falloff and product-channel ratios.

Most of the reactions involving F and HF with hydrogen- and oxygen-containing species have been measured and the uncertainties in these values are relatively low. There are three reactions of this type which were determined to participate in the chemistry under a variety of conditions. These reactions are the combination of H and F to form HF (and the reverse decomposition) and the hydrogen abstractions by F atoms from H_2 and H_2O. The rate expressions used for these contributing reactions are given in Appendix B.

The HF decomposition reaction has been measured only at temperatures above about 4000 K (Jacobs *et al.*, 1965; Blauer, 1968, Blauer *et al.*, 1971). Although this reaction in the decomposition direction is unimportant at typical flame temperatures, the reverse H + F = HF combination must be considered. Extrapolating the recommended value (Baulch *et al.*, 1981) for decomposition to 1000 K may result in an uncertainty of as much as a factor of ten, especially when considering non-simple Arrhenius dependence to the rate and different third-body efficiencies. However, since many other reactions (F + H_2, H_2O, RH) contribute to F atom destruction, the uncertainty in the absolute rate of the forward or reverse reaction is most likely unimportant.

The hydrogen abstraction reactions of F atoms with H_2 and H_2O have been measured only near room temperature (Wurzberg and Houston, 1980; Stevens *et al.*, 1989; Walther and Wagner, 1983). These values were extended to higher temperatures by fitting the reported values to extended Arrhenius expressions. For the H_2 reaction, an expression with $T^{0.5}$ dependence was chosen consistent with the recommended value (Cohen and Westberg, 1983). For the H_2O reaction, an expression with $T^{1.5}$ dependence was chosen by analogy to other reactions.

There are a number of other reactions which were included in the mechanism, but were never observed to contribute to the chemistry. These reactions include the combination of F atoms to form F_2 and the hydrogen abstractions by F atoms from OH, HO_2, and H_2O_2. The oxy-fluoro-species FO•, HOF, FOO•, and F_2O were also initially considered in the mechanism. However, given the very low concentration of F atoms at high temperatures in the hydrocarbon/air flame, these species are present in extremely low concentrations and do not contribute to the overall chemistry. The rate constants used for reactions involving these species will be detailed later in another publication.

5.1.3.2.2 C_1 Fluorinated Hydrocarbon Kinetics. The C_1 reaction subset of the mechanism consists of about 15 species (fluorocarbons) and 200 reactions (including reactions with H, O, OH, etc.). Both thermally and chemically activated decompositions are considered (*e.g.*, $CH_2F_2 \rightarrow :CHF$

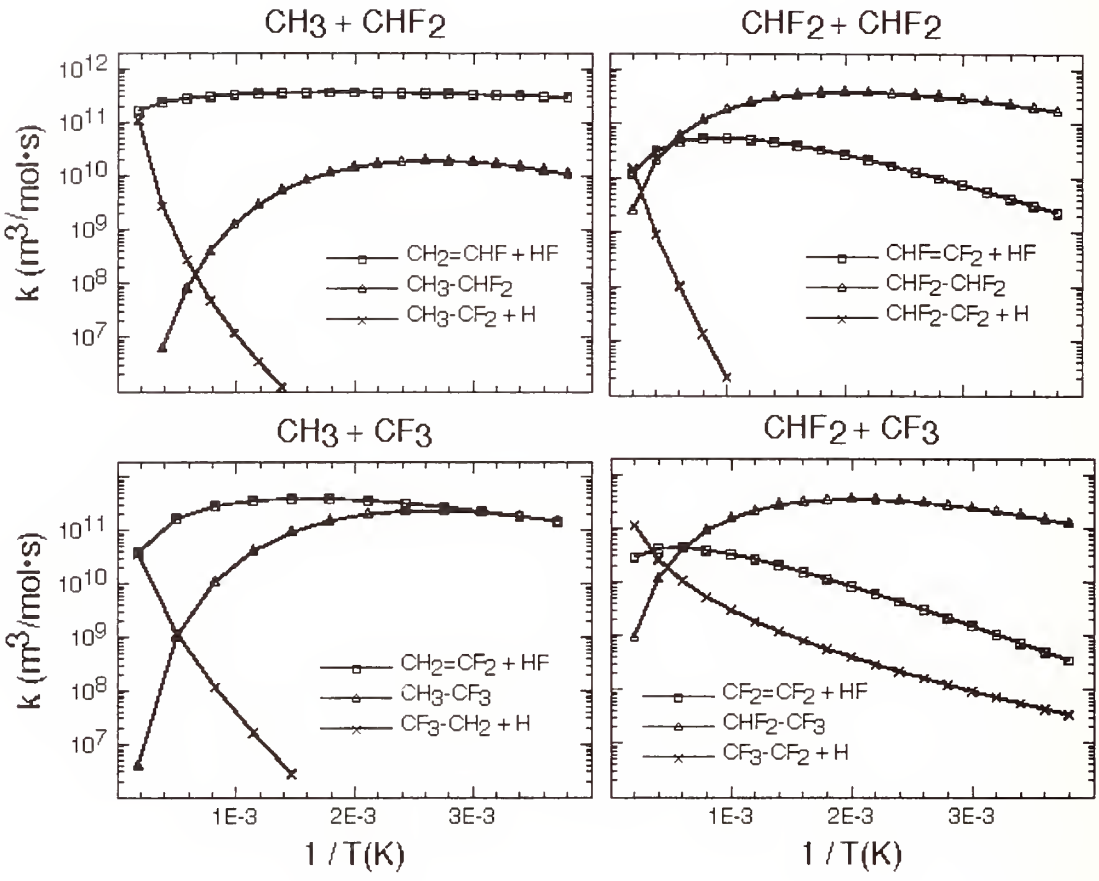

Figure 4. RRKM Predictions of Product Channels for Fluoromethyl Combinations.

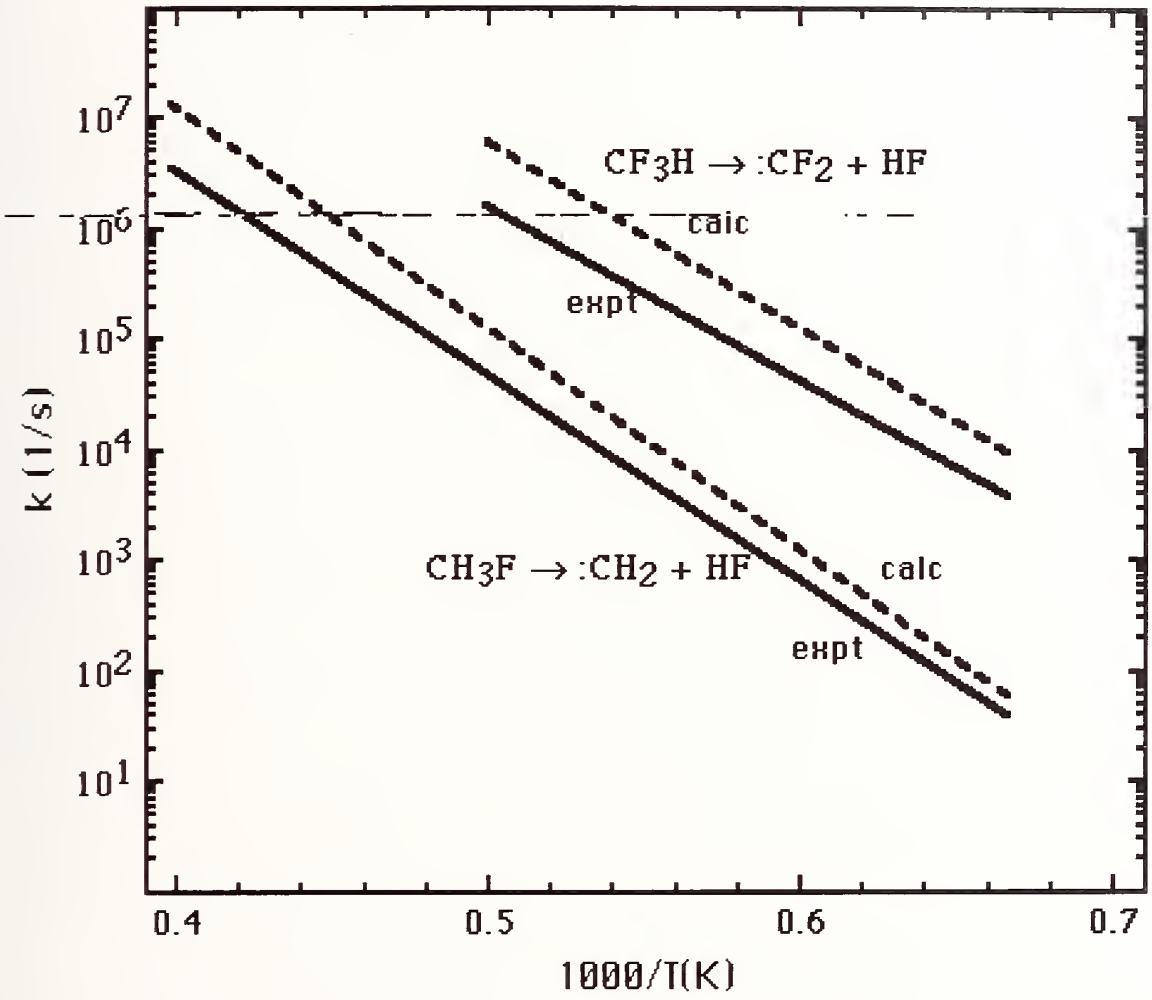

Figure 5. Comparison between Experimental and Calculated Rate Constants. *Ab initio* and RRKM methods for calculating rate constants must be validated by comparison to known, experimentally-derived values.

+ HF and $\bullet CHF_2$ + H → :CHF + HF). Fluoromethane decompositions via abstraction of H atoms by H, O, and OH radicals are also considered.

There have been a number of measurements of the unimolecular decomposition of fluoromethanes (with HF elimination): at least two for CH_3F (Politanskii and Shevchuk, 1967; Schug and Wagner, 1973), at least one for CH_2F_2 (Politanskii and Shevchuk, 1968), and several for CHF_3 (Tschuikow-Roux, 1965; Tschuikow-Roux and Marte, 1965; Modica and LaGraff, 1966; Politanskii and Shevchuk, 1968; Biordi *et al.*, 1978; Schug *et al.*, 1979; Hidaka *et al.*, 1991). In addition, there have been quite a few measurements of the unimolecular decomposition of other halomethanes (eliminating HF, HCl, or HBr) such as CHF_2Cl (Norton, 1957; Edwards and Small, 1964; Gozzo and Patrick, 1964; Edwards and Small, 1965; Gozzo and Patrick, 1966; Barnes *et al.*, 1971; Kushina *et al.*, 1972; Schug *et al.*, 1979; Zhitnev *et al.*, 1990; Zhitnev *et al.*, 1991), CHF_2Br (Cox and Simmons, 1971) , $CHFCl_2$ (Kushina *et al.*, 1972), and $CHCl_3$ (Shilov and Sabirova, 1960; Schug *et al.*, 1979). All of these halomethane decomposition reactions have a small-to-moderate barrier in the reverse direction (*i.e.*, carbene insertion into HF, HCl, or HBr) of 10-40 kJ/mol. Consequently, all of the halomethane measurements are important from the point of evaluating the fluoromethane values (both experimental and calculated) for consistency. Furthermore, the barriers-to-insertion of :CHF and $:CF_2$ in these reactions can be used to benchmark reactions of :CHF and $:CF_2$ with many other important molecules where there is no or little information available (*i.e.*, the reactions of :CHF and $:CF_2$ with H_2, H_2O, CH_4, C_2H_6, fluoromethanes, fluoromethyls, etc.).

In this work, we have employed rate expressions for HF elimination from CH_3F and CHF_3 that are fits to extended Arrhenius form to the experimental data of Schug and Wagner (1973) for CH_3F and to the experimental data of Hidaka *et al.* (1991) for CHF_3. These data were obtained, in general, at different temperatures and pressures than are relevant to the atmospheric flame conditions considered here. The experimental data were interpolated or extrapolated and fit using temperature dependencies (T^b) that were consistent with the experimental data and our RRKM calculations (using our BAC-MP4 barriers) for these systems. For HF elimination from CH_2F_2, we have employed a rate expression from our RRKM/BAC-MP4 calculations, although there is reasonable experimental data by Politanskii and Shevchuk (1968) that could be used. For the H_2 elimination channels for CH_3F and CH_2F_2 decompositions, we have used rate expressions from our RRKM calculations using our BAC-MP4 *ab initio* barriers. The H_2 elimination pathways are minor channels and were included for completeness. F atom eliminations from the fluoromethanes are negligible decomposition channels, except for CF_4, where it is the only possible pathway. For this reaction, we have used a rate expression that is a fit to extended Arrhenius form to the room temperature value of Plumb and Ryan (1986a, 1986b) using a reasonable temperature dependence ($T^{-1.0}$). Further refinement of this mechanism should include critical evaluation of all of the experimental data (for the HF elimination channels) and the *ab initio* barriers. RRKM methods should be used to obtain rate expressions that are consistent with both rate and (especially) thermochemical data. Although there is some uncertainties in the rate expressions for pyrolysis of the fluoromethanes due to extrapolation of measurements from other temperatures and pressures, these uncertainties are most likely acceptable since the primary decomposition pathways in atmospheric flames are by H atom abstraction by H and OH radicals and not by pyrolysis.

There have been no measurements to our knowledge for reactions involving chemically activated or "hot" fluoromethanes other than the room temperature measurements of the rate of reaction for CF_3 + H → Products by Ryan and Plumb (1984) and Tsai and McFadden (1989). This class of reactions is simply the radical combination of fluoromethyls and H atoms to form two product channels, HF or H_2 elimination, when the hot fluoromethane is not stabilized or returned to reactants.

We have used RRKM methods with the BAC-MP4 *ab initio* barriers to insertion for :CHF and $:CF_2$ into HF and H_2 and the energetics of the reactions pathways to estimate values for these various reactions, as well as for the stabilized fluoromethane channels. The barriers to insertion for :CHF and $:CF_2$ into HF are derived from the experimental measurements for the unimolecular decomposition of the fluoromethanes. A example of a similar set of RRKM calculations for fluoroethane decompositions (both thermal and chemically activated decompositions) is shown in Figure 4. These RRKM calculations were done for all of the fluoromethanes and fluoroethanes (only four for the fluoroethanes are shown in Figure 4).

We have also used the BAC-MP4 *ab initio* method (Melius, 1990) to provide estimates of the energy and structure of the transition state for some of these reactions, which agree well with the experimental values for the HF reactions. For insertion into H_2, where there are no experimental data, *ab initio* calculations were used to estimate the energy and structure of each transition state. Comparisons between experimental and *ab initio* calculated values for a few of these reactions are shown in Figure 5. Although there are no experimental measurements at flame temperatures for chemically activated fluoromethane decompositions and these are primary pathways for destruction of fluoromethyl radicals, the corresponding uncertainties in the rate expressions are small since these combinations are barrierless and occur nearly on every collision.

There have been a quite a number of measurements for H atom abstractions from fluoromethanes by H radicals, but only a few for H atom abstraction by O or OH radicals. For H atom abstraction by H radicals, there have been at least 3 measurements for CH_3F (Hart *et al.*, 1974; Westenberg and deHaas, 1975; Aders *et al.*, 1975), at least one measurement for CH_2F_2 (Ridley *et al.*, 1972), and quite a few for CHF_3 (Ayscough and Polanyi, 1956; Pritchard *et al.*, 1956; Skinner and Ringrose, 1965; Amphlett and Whittle, 1967; Arthur and Bell, 1968; Fagarash and Moin, 1968, Kibby and Weston, 1968; Berces *et al.*, 1972; Kondratiev, 1972; Arthur *et al.*, 1975; Arthur and Bell, 1978). We should note that many of the measurements for the CHF_3 reactions are actually measurements of the reverse rate or $CF_3 + H_2 \rightarrow CHF_3 + H$. Two of the citations (Kondratiev, 1972; Arthur and Bell, 1978) are evaluations of the experimental data. We have also calculated the structure and energy of each transition state for these H atom abstraction reactions from the fluoromethanes using the BAC-MP4 *ab initio* method. The energy barriers are included in Table 4 and compare well with the experimental values.

For the $CH_3F + H$ reaction, all of the workers cited above incorrectly identified the reaction as abstraction of F atoms instead of H atoms. These workers only measured the disappearance of the reactants and simply assigned the product channel by analogy to the $CH_3Br + H$ reaction, where it is known that the halogen atom (Br) is abstracted. However, the C-F bond is much stronger than the C-Br bond or even the C-H bond. Consequently in CH_3F, the H atom instead of the F atom, is abstracted. Our *ab initio* calculations (see Table 4) also support this argument where abstractions of H atoms from the fluoromethanes by H radicals were calculated to have energy barriers of 49.4, 40.6, 53.6 kJ/mol for the CH_3F, CH_2F_2, CHF_3 series, respectively. These same calculations yield barriers-to-abstraction of F atoms of 131.4, 142.7, 168.6, 171.1 kJ/mol for the CH_3F, CH_2F_2, CHF_3, CF_4 series, respectively. This is a significant difference and clearly supports assignment of H atom abstraction has the dominant channel.

In this work, we have used our fits to extended Arrhenius form to the experimental data of Westenberg and deHaas (1975), Ridley *et al.* (1972), and Arthur and Bell (1978) for H atom abstraction from CH_3F, CH_2F_2, and CHF_3, respectively. A temperature dependence of $T^{3.0}$ was used in analogy to the recommended value (Tsang and Hampson, 1986) for H atom abstraction from methane (CH_4). The experimental data were all obtained at modest temperatures (600-900 K). The uncertainties in extrapolation of this data to flame decomposition temperatures is most likely

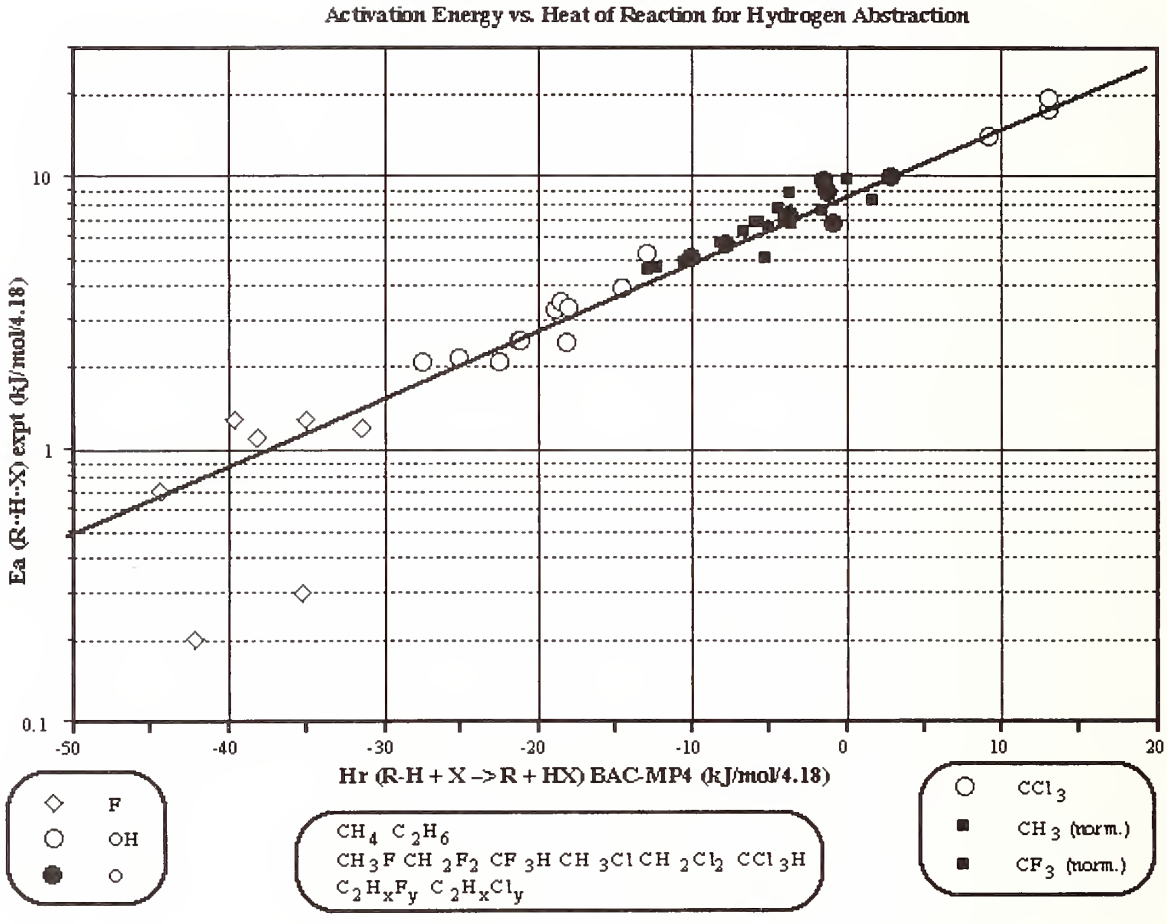

Figure 6. Empirically-Determined Activation Energies. In the absence of experimental data, the rate constant for a reaction can be estimated relatively well using its heat of reaction and known rate constants for other similar reactions.

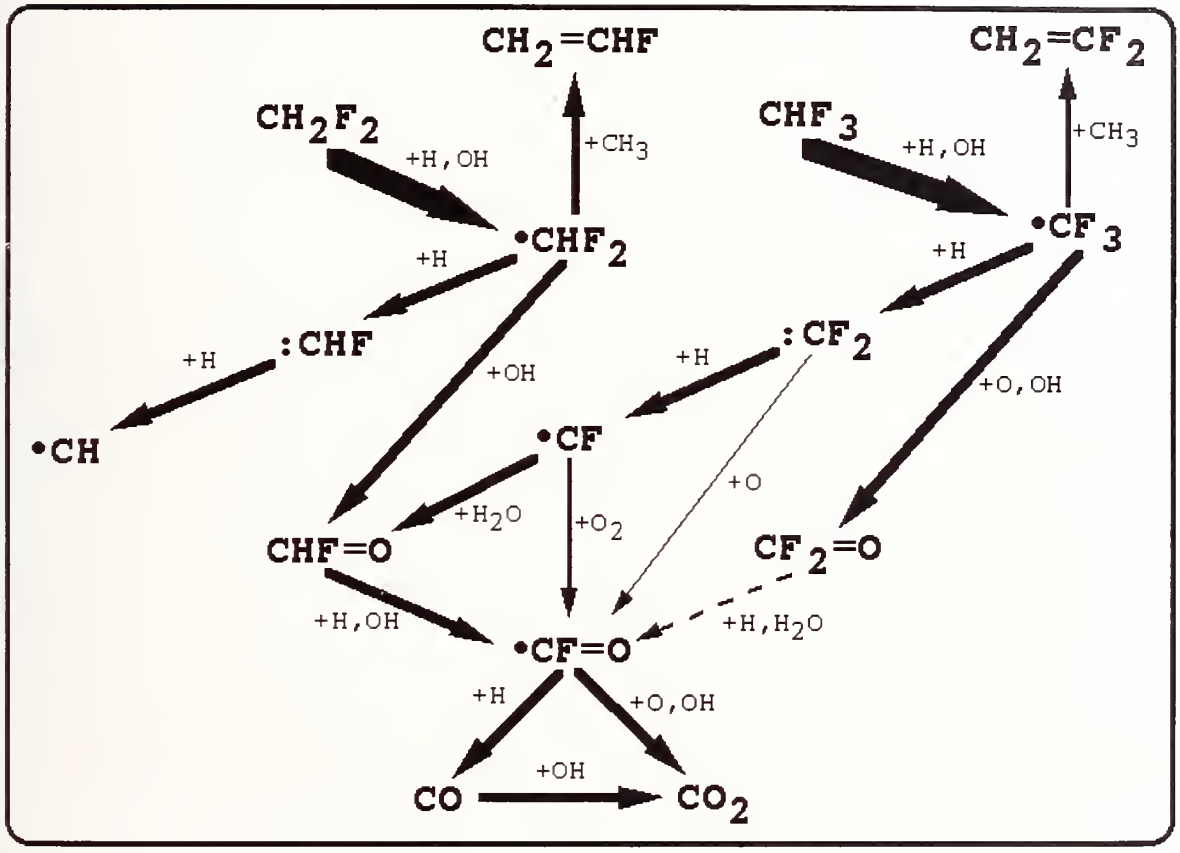

Figure 7. Typical Reaction Pathways for CH_2F_2 and CHF_3.

acceptable. We note that based on our limited evaluation, the trends in the rate expressions for this homologous series appear to be consistent with changes in the number of H atoms and the C-H bond strengths or heats of reaction (*e.g.*, Figure 6).

For the F atom abstraction reactions from CH_3F, CH_2F_2, and CHF_3 by H radicals, we have employed rate expressions derived from our BAC-MP4 *ab initio* calculations. The F atom abstraction pathways are negligible channels and these reactions were included simply for completeness in development of this reaction set. However, for reaction of H atoms with CF_4, the only possible pathway is F atom abstraction. For this reaction, we have used the experimentally derived rate expression of Kochubei and Moin (1969, 1971).

There have only been a few measurements of H atom abstractions from fluoromethanes by O radicals. Parsamyan and coworkers have measured the rate of reaction for CH_3F (Parsamyan *et al.*, 1967) and for CH_2F_2 (Parsamyan and Nalbandyan, 1968). Jourdain *et al.* (1978) and Miyoshi *et al.* (1993) have measured the rate of reaction for CHF_3. In our work, we have used our fits to extended Arrhenius form to the experimental data using a temperature dependence of $T^{1.5}$ in analogy to the recommended value (Tsang and Hampson, 1986) for H atom abstraction from methane (CH_4). We note that we have not used the more recent value for CHF_3 + O by Miyoshi *et al.* (1993), because it appears that this data may be complicated by the $CHF_3 \rightarrow :CF_2 + HF$ decomposition reaction at the highest temperatures. This should be examined in more detail, since our conclusion was based on a limited evaluation of the data.

There have been a few measurements of H atom abstractions from fluoromethanes by OH radicals. Cohen and Benson (1987a, 1987b) have used transition-state-theory calculations to analyze and predict rate coefficients for a series of halogen-substituted methanes and ethanes. Much of their analysis is based on the experimental data of Jeong and Kaufman (1982), but is also consistent with other measurements for fluoromethanes (Howard and Evenson, 1976; Clyne and Holt, 1979; Nip *et al.*, 1979; Talukdar *et al.*, 1991). In our work, we have used the recommendations of Cohen and Benson (1987a, 1987b). Since these recommendations are based on experimental measurements are relatively low temperatures (about 300-500 K) and these reactions are primary decomposition pathways for the fluoromethanes and significantly higher temperatures, it would be valuable to have experimental measurements of these rates near flame temperatures. We note that based on our limited evaluation, the trends in the rate expressions for this homologous series appear to be consistent with changes in the number of H atoms and the C-H bond strengths or heats of reaction (*e.g.*, Figure 6).

There have been quite a few measurements of H atom abstraction from methane (CH_4) by F atoms at or near room temperature (Wagner *et al.*, 1971; Pollock and Jones, 1973; Williams and Rowland, 1973; Manning *et al.*, 1975; Smith *et al.*, 1977; Clyne and Hodgson, 1983; Pagsberg *et al.*, 1988). In our work, we have used a fit to extended Arrhenius form to the recommended rate constant of Atkinson *et al.* (1992) using a reasonable temperature dependence ($T^{0.5}$) in order to extend the rate expression to flame temperatures. Although there is some uncertainty in extrapolating the rate constant to flame temperatures, this uncertainty is most likely unimportant since this reaction occurs on almost every collision and there are many other reactions (*e.g.*, F + H_2, F + H_2O, and F + other hydrocarbons) that contribute to F atom destruction. For completeness in the reaction set (although it is unlikely that they will contribute), we have also included the reactions for H atom abstractions from the fluoromethanes by F atoms. There have also been a number of measurements for these reactions at or near room temperature for CH_3F (Pollock and Jones, 1973; Smith *et al.*, 1977; Manocha *et al.*, 1983), for CH_2F_2 (Pollock and Jones, 1973; Smith *et al.*, 1977; Manocha *et al.*, 1983, Clyne and Hodgson, 1985; Nielsen *et al.*, 1992), and for CHF_3 (Pollock and Jones, 1973; Goldberg and Schneider, 1976; Smith *et al.*, 1977; Clyne and Hodgson, 1983; Maricq and Szente, 1992). For these reactions, rate expressions were used where the rate constant prefactor relative to

that recommended for CH_4 + F (Atkinson *et al.*, 1992) was adjusted to account for reaction path degeneracy (*i.e.*, fewer number of H atoms) and the activation energy was adjusted such that the rate was consistent with the measurements at room temperature. Use of extended Arrhenius form in these cases is not justified, because of the lack of temperature-dependent experimental measurements.

There have been quite a few measurements of metathetical reactions of methyl/fluoromethyl radicals with methane/fluoromethanes. These will not be reviewed here. In our work, we have used the recommendations of Kerr and Parsonage (1976) which are consistent with the majority of the experimental data and empirical relationships for barriers to reactions (such as shown in Figure 6). The recommended values are largely based on the pioneering work in this area by Pritchard and coworkers (*e.g.*, Pritchard *et al.*, 1965), Whittle and coworkers (*e.g.*, Chamberlain and Whittle, 1972), and Arthur and coworkers (*e.g.*, Arthur and Bell, 1978). We note that based on our limited evaluation, the trends in the rate expressions for this homologous series appear to be consistent with changes in the number of H atoms and the C-H bond strengths or heats of reaction (*e.g.*, Figure 6).

Although there have been no experimental measurements of metathetical reactions of vinyl radicals (C_2H_3) with the fluoromethanes, one can estimate their rates by analogy to the methyl radical (CH_3) reactions. We have used rate expressions for these reactions where the activation energy was reduced by 10% (due to the roughly 6 kJ/mol decrease in the heat of reaction) consistent with the empirical relationship demonstrated in Figure 6.

Given the abundance of H and OH radicals in hydrocarbon flames and the somewhat higher barrier for H atom abstraction by methyl/fluoromethyl and vinyl radicals, these are secondary reaction pathways. However, under pyrolytic conditions they may contribute (especially the C_2H_3 reactions which have the lowest barriers) and, consequently, for completeness should be retained in the reaction set. The experimental measurements for H atom abstractions by the methyl/fluoromethyl radicals were all made at relatively low temperatures (about 300-600 K). Extrapolation of these measurements to flame decomposition temperatures may introduce significant uncertainty in the rates especially since these reactions should have considerable non-simple Arrhenius temperature dependencies. In further refinement of this mechanism, these data should be critically evaluated. Experimental measurements at significantly higher temperatures would also be extremely valuable.

Fluoromethyl radicals are destroyed by three general pathways whose relative importance are sensitive to conditions. 1) Fluoromethyl radicals can combine with H atoms forming chemically activated fluoromethanes which may either be stabilized or eliminate HF or H_2 (creating methylene/fluoromethylenes). This class of reactions was discussed with the fluoromethane chemistry. 2) Fluoromethyl radicals can react with oxygen-containing species (*i.e.*, O_2, O, OH) resulting in the formation of fluoromethoxy radicals and carbonyl fluoride species (as well as elimination by-products). 3) Fluoromethyl radicals can also combine with methyl (CH_3) or fluoromethyl radicals forming chemically activated fluoroethanes which may either be stabilized or eliminate HF (creating ethylene/fluoroethylenes). This class of reactions will be discussed with the fluoroethane chemistry.

There have been a number of measurements of the reaction of CF_3 with O_2 at or near room temperature (Vedeneev *et al.* 1978; Ryan and Plumb, 1982; Caralp *et al.*, 1986; Cooper *et al.*, 1988; Orlando and Smith, 1988), but none (to our knowledge) for reaction of the other fluoromethyl radicals with O_2. At low temperatures the only possible product pathway is formation of the fluoromethylperoxy radical. These type of radical species are known to play a role in atmospheric chemistry. At high temperatures in a flame, these species will be present in significantly smaller concentrations and there are other possible product pathways for the fluoromethyl + O_2 reactions. By analogy to the CH_3 + O_2 reaction, fluoromethoxy radicals (and O atom by-product) can be formed upon dissociation of the O-O bond. The fluoromethylperoxy radical complex may also rearrange and undergo a internal abstraction reaction (of H atoms) creating fluoroformaldehyde species ($CHF{=}O$ or $CF_2{=}O$) and OH. In contrast to that assumed for the analogous chloromethyl

radical + O_2 → (chloro)formaldehyde + ClO reactions (Ho *et al.*, 1992), abstraction of F atoms is not possible because of the much stronger C-F bond. In our work we have assumed that at flame temperatures, the primary product channel is dissociation of the complex to fluoromethoxy radicals and O atoms. This assumption should be examined in more detail in further refinements of this mechanism. There are not any measurements (to our knowledge) for these reactions. For the flame chemistry, this is a minor channel. However, at lower temperatures and/or under ignition conditions, this class of reactions should be pathways which contribute to the chemistry.

The other various existing data and our many estimations, calculations, and evaluations for other reactions involving C_1 fluorocarbon species will not be discussed in further detail here. In many homologous series of reactions, missing rate constants (*i.e.*, no experimental data) were estimated by analogy to other reactions. For example, an empirical relationship between the activation energy and the heat of reaction for H atom abstraction reactions was determined. This is shown in Figure 6. As a result, in the absence of experimental data, the rate constant for a reaction can be estimated relatively well using its heat of reaction and known rate constants for other similar reactions.

Typical reaction pathways for the decomposition of two potential agents, CH_2F_2 and CHF_3, are shown in Figure 7. Briefly, fluoromethane decompositions via abstraction of H atoms by O and OH radicals are also considered with abstractions by OH and H the major decomposition pathways. The fluoromethyls produced via these reactions are destroyed by several pathways whose relative importance are sensitive to conditions. These pathways include reactions with H radicals, CH_3 radicals, and oxygen-containing species (O_2, O, OH). The products of the latter reactions consist of carbonyl fluorides (*i.e.*, $CF_2{=}O$, $CHF{=}O$, $\bullet CF{=}O$) and HF or other elimination products (*e.g.*, $\bullet CHF_2 + OH \rightarrow CHF{=}O + HF$). In the simulations, it was observed almost exclusively that any reaction channel with an HF product was the dominant channel. The fluoromethylenes ($:CHF$, $:CF_2$) were largely created by combination of fluoromethyls and H radicals via chemically activated fluoromethanes (and HF elimination). The fluoromethylenes were predominantly destroyed similarly by combination with H radicals via chemically activated fluoromethylenes (and HF elimination creating •CH and •CF). •CF radicals created here were largely consumed by reactions with H_2O and O_2 resulting in $CHF{=}O$ and $\bullet CF{=}O$ formation.

5.1.3.2.3 C_2 Fluorinated Hydrocarbon Kinetics. The C_2 reaction subset consisted of about 40 species and 400 reactions. This reaction set will not be described here in detail. Briefly, the fluoroethane destruction pathways (like fluoromethanes) consist of thermally and chemically activated decompositions and H atom abstraction reactions. Fluoroethyl radicals can react with H radicals (like fluoromethyls) creating fluoroethylenes (via chemically activated fluoroethanes and HF elimination). Fluoroethyl radicals can also react with oxygen-containing species (O_2, O, OH) resulting in the formation of oxidized fragments (*e.g.*, $CF_3\text{-}CF_2\bullet + O \rightarrow \bullet CF_3 + CF_2{=}O$). Fluoroethylenes (produced from thermally and chemically activated fluoroethane decompositions) are predominantly destroyed via reaction with O radicals resulting in the formation of oxidized fragments (*e.g.*, $CH_2{=}CF_2 + O \rightarrow \bullet CH{=}O + \bullet CHF_2$). Fluoroethylenes are also destroyed to a lesser degree through H atom abstraction by radicals such as OH, resulting in formation of fluorovinyl radicals (*e.g.*, $CH_2{=}CF_2 + OH \rightarrow CF_2{=}CH\bullet + H_2O$). Fluorovinyl radicals (like fluoromethyl and fluoroethyl radicals) are destroyed via reactions with H radicals, as well as with oxygen-containing species. However, it was observed that the fluorovinyl radicals established a dynamic equilibrium with the parent fluoroethylenes, irrespective of the specific creation and destruction pathways.

The kinetics of decomposition of most of the fluoroethanes (HF elimination) has been measured in a comprehensive series of work by Tschuikow-Roux and coworkers (Tschuikow-Roux *et al.*, 1970; Tschuikow-Roux and Quiring, 1971; Tschuikow-Roux *et al.*, 1971; Millward *et al.*, 1971; Millward

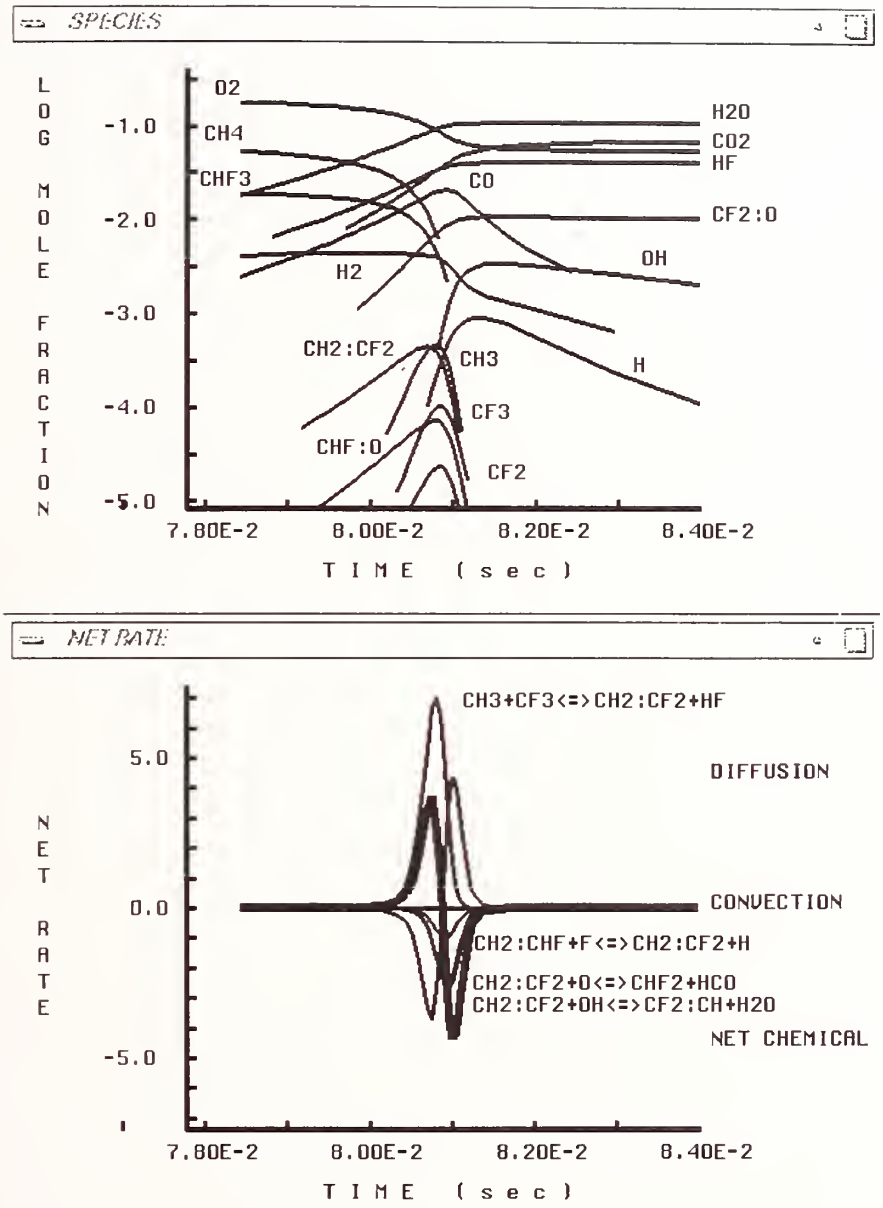

Figure 8. Typical concentration profiles of an agent (1.9% CHF3) and its decomposition intermediates and products in a lean (ϕ=0.65), premixed methane/air flame.

and Tschuikow-Roux, 1972; Sekhar and Tschuikow-Roux, 1974). Data for HF elimination from the other fluoroethanes have been obtained by Kerr and Timlin (1971) and Trotman-Dickenson and coworkers (Cadman *et al.*. 1970). Fluoroethane decomposition kinetics have also been measured by a few other workers (Kochubei *et al.*, 1980; Mitin *et al.*, 1988). In our work, we have used the rate expressions for these reactions as reported. However, the measurements by Tschuikow-Roux and coworkers were at significantly higher pressures (3-5 atm.). Consequently, our rates should be considered as upper limits to the rates in flames at atmospheric conditions. Future refinement of this mechanism should use RRK methods benchmarked to the experimental data to provide better values for the temperature (and pressure) dependencies of these unimolecular decomposition reactions.

There have been quite a few measurements of H atom abstractions from fluoroethanes by OH radicals. Cohen and Benson (1987a, 1987b) have used transition-state-theory calculations to analyze and predict rate coefficients for a series of halogen-substituted methanes and ethanes. Much of their analysis is based on the experimental data of Clyne and Holt (1979) and Jeong *et al.* (1984). Other experimental data included in their analysis was from the measurements by Howard and Evenson (1976), Handwerk and Zellner (1978), Nip *et al.* (1979), and Martin and Paraskevopoulos (1983). In our work to date, we have used the recommendations of Cohen and Benson (1987a, 1987b). For the three asymmetric fluoroethanes (CH_3-CH_2F, CH_3-CHF_2, CH_2F-CHF_2) where there are different functional H substitutions, we have estimated the relative branching ratios. Recently there have been a number of good measurements for these reactions for a number of the fluoroethanes by Huie and coworkers (Liu *et al.*, 1990; Zhang *et al.*, 1992), by Ravishankara and coworkers (Talukdar *et al.*, 1991; Gierczak *et al.*, 1991), and by Nielsen (1991). Based on some of the more recent measurements there are newer recommendations by Cohen and Westberg (1991) for some of these reactions. The biggest changes are for reactions involving CH_3-CHF_2 and CHF_2-CF_3. However, the changes in the rate expressions are only significant at temperatures well below flame temperatures (because T^b dependence). Since these recommendations are based on experimental measurements are relatively low temperatures (about 300-500 K) and these reactions are primary decomposition pathways for the fluoroethanes at significantly higher temperatures, it would be valuable to have experimental measurements of these rates near flame temperatures. We note that based on our limited evaluation, the trends in the rate expressions for this homologous series appear to be consistent with changes in the number of H atoms and the C-H bond strengths or heats of reaction (*e.g.*, Figure 6).

There have been no measurements (to our knowledge) for abstraction of H atoms from the fluoroethanes by H and O radicals. We have estimated the rates for these reactions by analogy to those for H atom abstraction from the fluoroethanes by OH radicals. Each prefactor and activation energy was scaled relative its OH reaction by the same amount as in series of H atom abstraction from the unsubstituted-ethane (C_2H_6) by H, O, and OH radicals.

There have been quite a few measurements of the reactions of O atoms with fluoroethylenes. These will not be reviewed here. In our work, we have used our fits to extended Arrhenius form to the recommendations of Cvetanovic (1987) in order to extrapolate the low temperature values (300-500 K) to flame temperatures. A temperature dependence of $T^{1.0}$ was used in analogy to other reactions. The recommended values by Cvetanovic are largely based on work in this area by Herron and Huie (1973), Jones and Moss (1974), Atkinson and Pitts (1977), and Gutman and coworkers (Park *et al.*, 1984). Typical creation and destruction paths for CH_2=CHF are shown in Figure 8.

For this class of reactions, it is generally understood that the dominant pathway is where the products are the fluoromethyl and (fluoro)formyl radical (*e.g.* CH_2=CHF + O → HCO + •CH_2F) following dissociation of the chemically activated fluoroethylene oxide formed by O atom attack on the double bond; that is, the O atom "adds" to the side with the least number of electronegative substitutions (*i.e.*, F) and the H atom "migrates" to the other side. The numerous other possible

channels are generally considered to be minor pathways: fluorine-substitute analogs of 1) stabilized ethylene oxide, 2) stabilized acetaldehyde, 3) formaldehyde + methylene, 4) acetyl radical + H, 5) ketene + H_2, and 6) vinyl radical + OH. The latter, abstraction of H atom, is a separate reaction from the first four (addition/elimination). For completeness in the reaction set, we have included the latter abstraction reaction using rate expressions based on analogy to the value estimated by Fontijn and coworkers (Mahmud *et al.*, 1987) for the unsubstituted ethylene reaction. It should be noted that for pefluoroethylene, the only possible channel is $CF_2{=}CF_2 + O \rightarrow CF_2{=}O + {:}CF_2$ (*i.e.*, no H migration possible). It should also be noted that for $CH_2{=}CHF$ there are two possible channels ("addition" of the O atom to one side or the other). We have used an estimated additional 4 kJ/mol for "addition" of the O atom to the fluorinated carbon. This is consistent with a upper limit measurement at room temperature for this reaction by Gutman and coworkers (Slagle *et al.*, 1974). Given that this is a primary decomposition pathway for the fluoroethylenes and that the rate expression we are using are based on experimental measurements at low temperatures (300-500 K), it would be very valuable to have measurements of these reactions and product channels at near flame temperatures.

Most of the rate expressions used in our work for reactions involving fluoroethyl radicals, fluoroethylenes, fluorovinyl radicals, and fluoroacetylenes were estimated by analogy to the reactions for the unsubstituted hydrocarbon species. The rate constant prefactors were adjusted to account for reaction path degeneracy (*i.e.*, number of H atoms). To date, we have not adjusted the activation energies. Clearly, for H atom abstraction reactions, the barriers should change with C-H bond strengths and for unimolecular and chemically activated reactions, the rates should be very sensitive to changes in stabilization with different number of F atom substitutions. Future modifications of this mechanism should address this issue.

In our work, we have used rate expressions for the fluorovinyl radicals by analogy to that for $C_2H_5 + O_2 \rightarrow C_2H_4 + HO_2$ measured by Bozzelli and Dean (1990). We have used the recommendation of Baulch *et al.* (1992) for $C_2H_5 + O \rightarrow CH_2O + CH_3$ to estimate the analogous reactions for fluorovinyl radicals. In our work, we have used rate expressions for the reactions of fluoroethylenes with H atoms by analogy to the recommendations of Tsang and Hampson (1986) for the two pathways $C_2H_4 + H \rightarrow C_2H_5$ and $C_2H_4 + H \rightarrow C_2H_3 + H_2$. For abstraction of H atoms from the fluoroethylenes by OH radicals, we have used our fit (with an estimated $T^{2.0}$ dependence) to the recommendation of Baulch *et al.* (1992) for $C_2H_4 + OH \rightarrow C_2H_3 + H_2O$, which is based on a measurement by Tully (1988). Westmoreland (1992) has calculated the temperature (and pressure) dependencies of the rate for the chemically activated reaction $C_2H_3 + O_2 \rightarrow CH_2O + HCO$. We have used these values for the analogous fluorovinyl radical reactions. In our work, we have used the recommendations of Warnatz (1984) and Tsang and Hampson (1986) for the $C_2H_3 + O \rightarrow$ Products and $C_2H_3 +$ OH → Products reactions, respectively, for the analogous fluorovinyl radical reactions. The recommendation for the first reaction by Warnatz is based on measurements by Heinemann *et al.* (1988). For reaction of H atoms with the two fluoroacetylenes (C_2HF, C_2F_2), have used rate expressions derived from the recommendation of Warnatz (1984) for $C_2H_2 + H \rightarrow C_2H_3$, which is based on measurements by Payne and Stief (1976).

5.1.3.3 Reactor Models. This large set of rate constants or "mechanism" was used to model the fluorinated hydrocarbon chemistry under a variety of conditions including different fuels, equivalence ratios, different agents, agent concentrations, and for a variety of reactor geometries. Since it is not yet possible to model a turbulent, chemically reacting flow, we relied upon employing a number of geometries in order to provide a good picture of realistic conditions. Simple plug flow conditions (1-D/time, no diffusion) were used to test a wide variety of conditions and to "debug" the mechanism since these types of calculations can be performed relatively quickly. The plug flow

Table 4. BAC-MP4 Transition State Calculations: Activation Energy for Reaction (kJ/mol)

TRANSITION STATE				ΔH_f^o	E_a
CH_3F		→ $:CH_2$	+ HF	120.8	368.6
		→ :CHF	+ H_2	*182.4	418.8
CH_2F_2		→ :CHF	+ HF	-121.8	327.2
		→ $:CF_2$	+ H_2	-51.9	406.7
		→ $:CH_2$	+ F_2	*346.4	792.0
CHF_3		→ $:CF_2$	+ HF	-388.3	313.8
		→ :CHF	+ F_2	*52.3	754.4
CF_3OH		→ CF_2=O	+ HF	-741.8	180.3
$CH_2FO•$		→ •CH=O	+ HF	-109.6	87.4
$CH_2FO•$		→ CF_2=O	+ F	-19.2	177.8
$CHF_2O•$		→ •CF=O	+ HF	-94.6	311.3
$CHF_2O•$		→ CF_2=O	+ H	-328.9	77.0
$•CF_2OH(E)$		→ •CF=O	+ HF	-300.0	156.5
		→ CF_2=O	+ H	-315.2	141.3
		→ $CHF_2O•$		-301.9	154.6
CH_3-CH_2F		→ CH_2=CH_2	+ HF	-4.6	270.3
CHF_2-CHF_2		→ CH_2F_2	+ $:CF_2$	-375.5	514.9
CH_4	+ $:CF_2$	→ CH_3-CHF_2		39.7	317.9
CH_3F	+ H	→ $•CH_2F$	+ H_2	28.9	50.2
		→ $•CH_3$	+ HF	110.9	131.4
CH_2F_2	+ H	→ $•CHF_2$	+ H_2	-189.1	40.6
		→ $•CH_2F$	+ HF	-87.0	142.7
CHF_3	+ H	→ $•CF_3$	+ H_2	-431.0	53.6
		→ $•CHF_2$	+ HF	-317.6	168.6
CF_4	+ H	→ $•CF_3$	+ HF	-545.2	171.1
CF_2=O	+ H	→ •CF=O	+ HF	-229.7	150.6
		→ $•CF_2OH$		-315.1	65.3
			(G2)	-368.2	33.9
		→ $CHF_2O•$		-302.1	78.2

Table 4. BAC-MP4 Transition State Calculations: Activation Energy for Reaction (kJ/mol)

TRANSITION STATE				ΔH_f^o	E_a
$CF_2=O$	+ H_2O	→ FC(O)OH	+ HF	-718.8	121.3
			(G2)	-710.4	151.5
CH_3-CHF•		→ CH_2=CH•	+ HF	216.7	289.1
CH_2F-CH_2•		→ CH_2=CHF	+ H	98.3	154.4

BAC-MP4 *ab initio* calculations (Melius, 1990)
G2 *ab initio* calculations (Curtis *et al.*, 1991)

ΔH_f^o: enthalpy of formation (kJ/mol) at standard state (1 atmosphere; 298.15 K)

E_a: activation energy (kJ/mol) at 298.15 K

*: spin contaminated

calculations provide essentially the limit of maximum concentration gradients since diffusion or the interaction between reactant-like and product-like molecules is neglected. A limited set of freely propagating, premixed flame calculations (1-D/time and distance, axial diffusion) were done to provide more realistic concentration and temperature gradients in the model. This was the primary method of calculating the effects of agents on flame speed and extinction.

In addition, a limited set of continually stirred tank reactor (CSTR), burner-stabilized premixed flame, and opposed-flow diffusion flame (OFDF) calculations was also done. The CSTR calculations can be considered as providing an upper limit to the importance of diffusion since reactants, intermediates, and products chemically interact or are completely mixed. This is a case of essentially minimal concentration gradients and may provide some analogies to turbulent reacting flows. The burner-stabilized, premixed flame more closely mimics a number of realistic burning geometries such as a flame near a fuel line leak or possibly a pool fire where the surfaces in these cases can provide a large heat sink to the flame. The opposed-flow diffusion flame geometry provides a somewhat realistic model of flame conditions which exist where a burning fuel jet or rapidly heated expanding fuel vapor comes in contact with the surrounding air. Unfortunately, these calculations which provide the most realistic picture of diffusion-dominated conditions, are also the most time-consuming computationally. Consequently, only a limited number of these have been done. It is expected that more calculations will be performed when a greater degree of certainty has been developed in the reaction mechanism or when experimental measurements in the OFDF geometry become available.

Schematic representations of these reactor geometries are shown in Figure 9.

5.1.4 Fluorinated Hydrocarbon Chemistry and Flame Suppression

5.1.4.1 Reaction Path Analysis. The fluoromethanes decomposed primarily through H atom abstraction by OH radicals in the premixed flame with H atom abstraction by H radicals the major secondary pathway (on the order of 10-20%). H atom abstraction by O radicals and unimolecular decomposition eliminating HF are the next important minor decomposition channels (generally contributing less than 10%). These minor pathways only begin to contribute as secondary channels at the highest temperatures in the premixed flame and the unimolecular decomposition channel at high

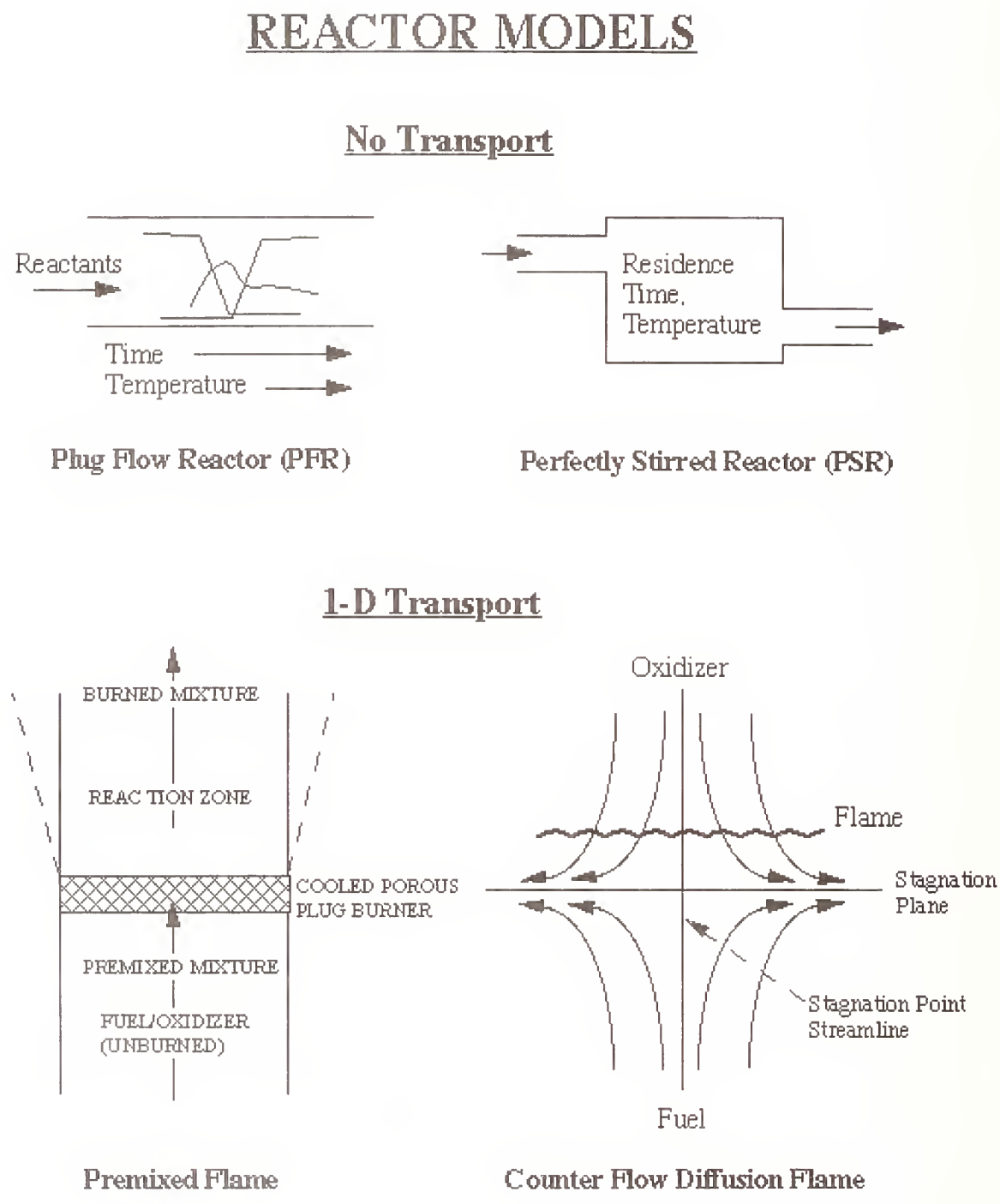

Figure 9. Reactor Models.

temperatures/short residence times under plug flow conditions. It is likely that the unimolecular decomposition channel also plays a role in a diffusion flame due to the lack of fuel (and consequently H and OH radicals) in the preheat, oxygen side of the flame. Abstraction by methyl, fluoromethyl, and vinyl radicals are negligible in the premixed flame although they may be minor channels in plug flow or diffusion flames. Abstraction of F atoms by H radicals is negligible for CH_3F, CH_2F_2, and CHF_3, since the H atom abstraction channel has a significant lower barrier (30-50 kJ/mol) than the F atom abstraction channel (120-160 kJ/mol). However, in the case of CF_4, F atom abstraction by H radicals is the only possible abstraction channel. Similarly, since there is no HF elimination channel, the only possible unimolecular decomposition pathway for CF_4 is elimination of F atoms.

There are two possible channels for production of fluoromethanes. The first involves the insertion of methylene ($:CH_2$) into HF (reverse reaction of the unimolecular decomposition) and the second is disproportionation between fluoromethyl radicals to form fluoromethanes and $:CF_2$. Although latter channel has significant experimental basis (Pritchard *et al.*,), there is some uncertainty with regard to this reaction, because there is also evidence to suggest that the reverse reaction or insertion of $:CF_2$ (a closed shell species) should have a modest barrier. Channels of the first type can contribute small amounts to "recycling" of F mass in the system. For example, CH_2F_2 can decompose via H atom abstraction reactions to form $\bullet CHF_2$, which can react with H radicals to create :CHF and HF (by elimination from chemically activated CH_2F_2). The :CHF formed via this pathway can then insert into HF (which is present in large concentrations in the system) and consequently reform CH_2F_2. However, in the cases we have tested, this channel contributes generally less than 10% to the net rate of reaction for CH_2F_2. On the other hand, this channel may be significant in predicting by-products of incomplete combustion. For example, CH_3F and the intermediates and products of its decomposition will always be formed in hydrocarbon flames irrespective of fluorocarbon starting material simply because the HF (always present in the fluorinated hydrocarbon-doped flame) will react with singlet methylene ($^1:CH_2$) (always present in hydrocarbon flames). The latter channel involving the disproportionation between fluoromethyl radicals to form fluoromethanes and $:CF_2$ should be investigated further.

There are three general channels for the destruction of the fluoromethyl radicals: (1) reaction with H radicals creating (fluoro)methylenes and HF - via chemically activated fluoromethanes; (2) reaction with O and OH radicals creating elimination products (*i.e.*, H, HF) and (fluoro)formaldehydes (CH_2O, $CHF{=}O$, $CF_2{=}O$) - via both thermal and chemically activated fluoromethoxy radicals; and (3) reaction with CH_3 radicals creating (fluoro)ethylenes and HF - via chemically activated fluoroethanes.

The relative importance of these three general channels depends upon fuel, agent, flame geometry, and other conditions. For example, under more realistic conditions in a diffusion flame where the agent is added to the air stream, the importance of the CH_3 combination route should be substantially diminished (as should the H combination to some degree), because of the lack of fuel (mixed) in the air. On the other hand the OH combination route should significantly increase in importance due to its high dispersion in the flame due to the abundance of H_2O in the flame. Similarly, the O atom reaction route should decrease in importance. Furthermore, other otherwise minor oxidative routes such as $\bullet CH_2F + O_2$ and $\bullet CH_2F + HO_2$ may begin to contribute in the preheat, oxygen rich side of the flame. For ignition delays under plug flow conditions these oxidative routes should be very important as contributors (like analogous reactions for pure hydrocarbons systems).

At high agent concentrations, autocombination of fluoromethyl radicals are contributing reactions. For $CF_3 + CF_3$, there is no HF elimination channel possible and, consequently, CF_3-CF_3 is the sole product (at the highest temperatures this rate falls-off slightly). For $\bullet CHF_2 + \bullet CHF_2$, the elimination channel is diminished somewhat in importance, since the CHF_2-CHF_2 with four heavy F

atoms can effectively stabilized the heat of reaction and compete as a product channel. This trend can be seen in Figure 4 (RRKM calculations).

The fluoromethyl radicals are primarily formed by H atom abstractions from the fluoromethanes. However, there are several other channels which can contribute to their formation and should be discussed in detail with reactions classified as C_2 chemistry. For example, the reactions $CH_2=CHF + O \rightarrow \bullet CH_2F + HCO$ or $CHF_2\text{-}CF_2\bullet + H \rightarrow \bullet CHF_2 + \bullet CHF_2$ contribute to the formation of fluoromethyl radicals. Similarly, there are a number of other decomposition channels which can be classified as C_2 or C_3 chemistry such as $\bullet CH_2F + C_2H_4 \rightarrow \bullet CH_2\text{-}CH_2\text{-}CH_2F$. These should be investigated further.

5.1.4.2 Freely Propagating, Premixed Flame Simulations. Adiabatic, freely propagating, premixed flame calculations (Kee *et al.*, 1985) were performed utilizing the reaction mechanism outlined above. Typically, fuel lean CH_4/air mixtures were simulated in order to be most sensitive to flame speed changes and (in a practical sense) since agents are added to the air supply. It would be more realistic to simulate agent effects in a diffusion flame. We have performed a few opposed flow diffusion flame calculations; however, those results are preliminary.

A summary of the effects on adiabatic flame temperature and speed are shown in Figure 10 and Figure 11 for addition of a variety of "agents" to a CH_4/air flame (equivalence ratio of 0.65). In addition to potential fluorinated hydrocarbon agents (CF_4, CHF_3, CH_2F_2, $CF_3\text{-}CF_3$, $CF_3\text{-}CF_2H$, $CF_3\text{-}CFH_2$), other species were added to investigate the effect of heat capacity and heat release on changes in flame speed and temperature. These reference "agents" include N_2, H_2O, CO_2, HF, and CH_4. In order to correct for differences in heat capacities for the different "agents", the amount of added "agent" was normalized to an equivalent amount of N_2, adjusting for relative heat capacities at 1500 K. For example, addition of 1% CF_4 (with $C_p=105$ J/mol/K) would be roughly equivalent to addition of 3% N_2 (with $C_p=35$ J/mol/K). Using heat capacities at other temperatures (1000-2000 K) had little impact on the relative normalized mole fractions.

In Figure 10, it can be seen that the effect of the various agents on flame temperature can be bracketed by addition of inert molecules (N_2, H_2O, CO_2, HF), where there is a decrease in flame temperature, and by addition of more fuel (CH_4), where there is a large increase in flame temperature. The decrease in flame temperature upon addition of the inerts is due to dilution and increased heat capacity of the mixture. The increase in flame temperature upon addition of more fuel is due to increased heat release as the fuel lean mixture becomes more rich. Addition of agents which are more fuel-like results in larger increases in flame temperature. All of the fluorinated hydrocarbons are fuels since they all eventually decompose, burn, and form CO_2, H_2O, and HF (liberating heat). At one extreme is CF_4, very little of which decomposes in the flame, and consequently, there is only a small increase in flame temperature relative to addition of inerts. On the other extreme is CH_2F_2, which completely burns forming highly exothermic products CO_2 and HF. In Figure 11, a range of effects on flame speed for the various added agents can be observed. For the inert molecules and the nearly inert fluorinated hydrocarbons (CF_4, $CF_3\text{-}CF_3$), a decrease in flame speed is observed consistent with dilution of the mixture. On the other extreme, for CH_4 (the fuel) and CH_2F_2 (a slightly poorer fuel), an increase in flame speed is observed. Of the various agents considered, only CHF_3 was seen to have any chemical effect in flame suppression. Figure 10 and Figure 11 show that although there is an increase in flame temperature upon CHF_3 addition, there is also a decrease in flame speed relative to inert molecule addition. Inspection of reaction pathways for CHF_3 and other agents (see Figure 7) reveals that a significant amount of decomposed CHF_3 results in the formation of a relatively unreactive perfluorocompound, carbonyl fluoride ($CF_2=O$). Decomposition of $CF_2=O$ occurs only very slowly via reaction with either H radicals (H addition + HF elimination) or

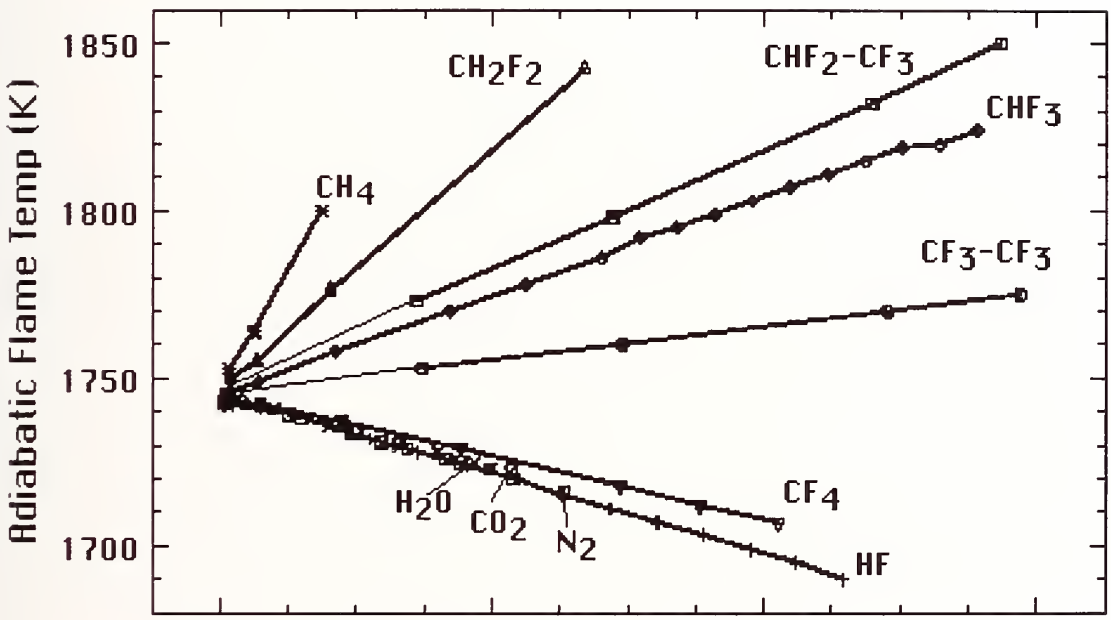

Figure 10. Effect of Agents on Flame Temperature.

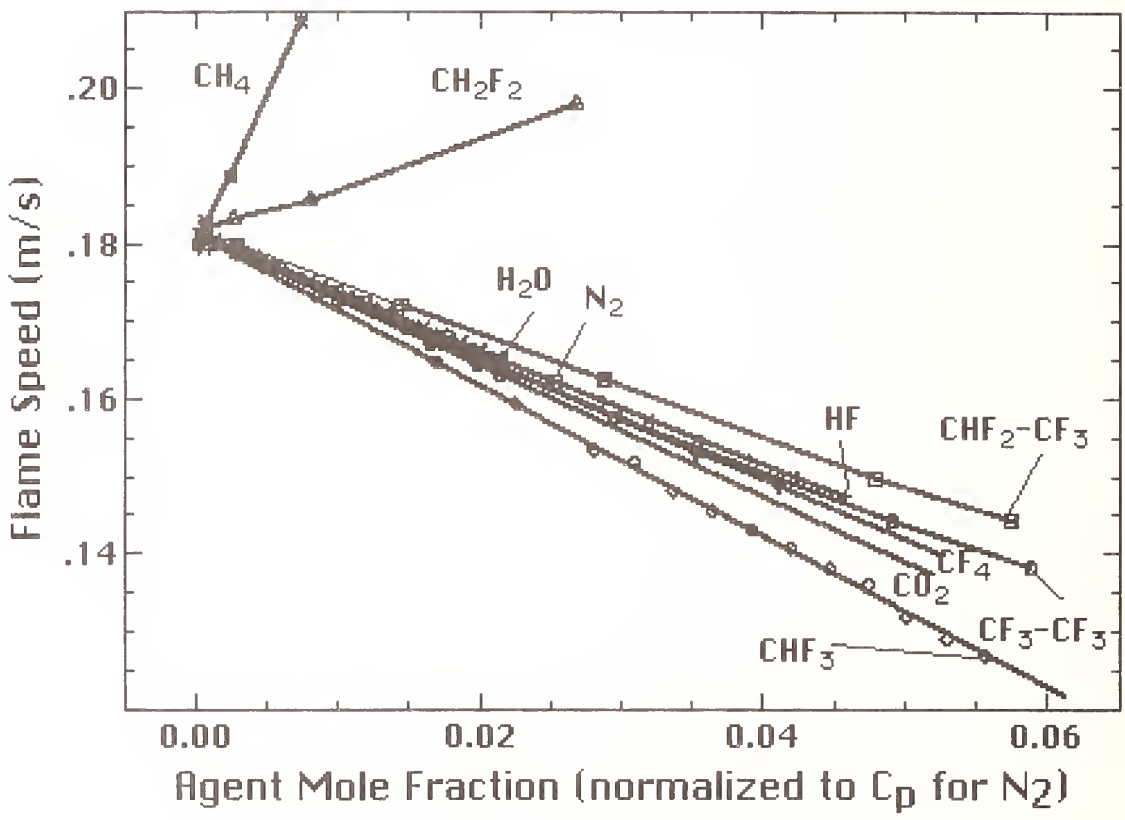

Figure 11. Effect of Agents on Flame Speed.

with H_2O (through a hot fluoroformic intermediate). For all other agents, this $CF_2=O$ bottleneck is avoided.

5.1.5 Discussion. These simulations are consistent with qualitative trends observed in experimental measurements of agent effectiveness in the work by others in other parts of the overall project at NIST. However, in order to quantitatively predict agent effectiveness, experimental validation of the mechanism will be necessary.

As indicated in the last section, the premixed flame simulations demonstrate that differences in the relative influence of candidate agents on hydrocarbon flames can be explained largely by simple differences in their relative heat capacities and relative amounts of heat release due to agent combustion. That is, flame extinction upon addition of each of the potential agents is only due to simple dilution of the flame by increased heat capacity of the mixture (consequently, reduced flame temperatures). This result is not surprising and was the expected behavior in the absence of any simulations or experimental measurements of agent effectiveness.

The majority of the candidate agents are perfluorocarbons, which are essentially inert relative to the fuel, and therefore by definition, cannot (chemically) inhibit flames. These inert "agents" can extinguish flames by dilution; however, so can equivalent amounts of completely inert molecules, such as N_2 or CO_2, as well as sufficient excess oxygen (O_2) in premixed flames.

In contrast to completely inert molecules, the nearly inert perfluorocarbons will eventually decompose (at least partially) under flame conditions (at the highest temperatures and long times), resulting in exothermic products CO_2 and HF (liberating heat) and increasing flame temperatures. However, since the perfluorocarbons decompose much slower than the hydrocarbon fuels, their decomposition intermediates and products cannot participate in the hydrocarbon combustion chemistry. Consequently, these "agents" cannot directly influence flame chemistry, but can only increase flame temperatures; that is, relative to inert molecules these agents can only indirectly promote combustion (through heat release) and cannot suppress flame processes.

This expected behavior was observed in the simulations (i.e., Figures 10 and 11). For example, addition of CF_3-CF_3 increases both flame temperature and speed relative to addition of inert molecules. Inspection of concentration profiles and reaction pathways in the premixed flame simulations for the perfluorocarbons CF_4 and CF_3-CF_3 reveal that the small fraction of these compounds that decompose, do so in the post-flame zone (subsequent to the important combustion chemistry). The larger the perfluorocarbon, the more readily it decomposes; that is, a larger fraction of it decomposes for a given set of conditions. Consequently, more heat is released and more enhancement of the flame is expected. This trend can be seen in Figures 10 and 11, where both flame temperature and speed are increased relative to inert molecules, going from CF4 to the larger and less stable CF_3-CF_3. It should be noted that in accordance with this behavior, one of the perfluorocarbons, cyclo-C_4F_8, is expected to have a larger enhancement than the corresponding alkane, because it is likely to decompose more rapidly (to two molecules of $CF_2=CF_2$) and have more combustible intermediates (thereby liberating more heat, increasing flame temperature and speed). In our work, we did not simulate the effect of agents with three or more carbons atoms, because of the additional complexity of the chemistry that must be considered. Consequently, we have no simulations to quantitatively support the above predicted qualitative behavior of the large molecules.

The influence of addition of the hydrofluorocarbon agents to hydrocarbon flames can best be described in reference to the related perfluorocarbons. The perfluorocarbons are relatively inert molecules, because they are relatively slow to decompose even under flame conditions. Hydrogen atom substitution of these molecules will significantly increase their reactivity and enable them to decompose prior to or during combustion (as opposed to in post-flame zones). However, for the

same reason, hydrogen atom substitution should significantly increase their fuel characteristics. That is, the hydrofluorocarbons will contribute excess heat when they decompose and their products react further to form exothermic products CO_2 and HF. Of course, these agents will also contribute hydrogen atoms (fuel) to the chemistry. These hydrofluorocarbon agents may also decompose sufficiently "early" that the radicals they produce may enhance ignition chemistry (promotion). However, the fluorinated radicals, which are less combustible than the corresponding hydrocarbon radicals, may also compete for important radicals in the flame, thereby slowing flame propagation (inhibition). In order for the hydrofluorocarbons to inhibit flames, these competitive reactions must be sufficient to counteract both the enhancement of flame chemistry due the hydrogen atom-substitution and the heat release due to combustion of the added agent. The simulations indicate that this radical scavenging effect is never dominant.

The influence of addition of the hydrochlorofluorocarbon agents to hydrocarbon flames can best be described in reference to their hydrofluorocarbon analogues (*e.g.*, CF_3-CHFCl versus CF_3-CHF_2). The primary decomposition pathway for the hydrofluorocarbons is through H atom abstraction by H or OH radicals in the flame. In general, HF elimination is a minor contributing pathway except under pyrolytic conditions where it may be dominant. However, for the hydrochlorofluorocarbons, decomposition by HCl elimination is an energetically feasible pathway. Consequently, these molecules may have a different chemical effect on the flame, if HCl (or other Cl-substituted molecules) influence the chemistry. One of the primary reasons for the effectiveness of CF_3Br is that HBr that is formed is recycled to Br atoms (which scavenge H atoms in the flame) through the energetically favorable reaction $HBr + OH \rightarrow Br + H_2O$ (ΔH_{rxn}=-130 kJ/mol). On the other hand F atoms do not catalytically destroy H atoms because HF, once formed, is never consumed. This is because the reaction $HF + OH \rightarrow F + H_2O$ (ΔH_{rxn}=+75 kJ/mol) is essentially energetically prohibited. However, the analogous reaction $HCl + OH \rightarrow Cl + H_2O$ (ΔH_{rxn}=-65 kJ/mol) is energetically favorable. Therefore, Cl atoms may catalytically destroy H atoms in the flame (like Br atoms) and consequently, the hydrochlorofluorocarbon agents may be more effective than their hydrofluorocarbon analogues. The one exception to this may be CHF_2Cl. In this case, HCl elimination yields $:CF_2$ (relatively reactive), while for CF_3-CHFCl, HCl elimination should yield $CF_2=CF_2$ (relatively unreactive). The $:CF_2$ species may be formed sufficiently "early" in the flame that it may enhance ignition chemistry (potential source of radicals). If this is the case, CHF_2Cl could promote, rather than inhibit the flame. In our work, we did not simulate the effect of agents with chlorine atoms (simultaneous with fluorine atoms), because of the additional complexity of the chemistry that must be considered. Consequently, we have no simulations to quantitatively support this predicted qualitative behavior for the hydrochlorofluorocarbon agents.

We did not perform any substantial number of simulations with other fuels. However, as discussed above, the differences in the relative influence of candidate agents on hydrocarbon flames can be explained largely by simple differences in their relative heat capacities and relative amounts of heat release due to agent combustion. That is, flame extinction upon addition of each of the potential agents is only due to simple dilution of the flame by increased heat capacity of the mixture and consequently, reduced flame temperatures. Therefore, a fuel with a higher adiabatic flame temperature should require more added agent in proportion with its higher energy content to slow the flame speed by a given amount (or completely extinguish the flame). We did not perform a sufficient number of simulations to quantitatively support this predicted qualitative behavior between fuels.

5.1.6 Recommendations. Of all the potential agents considered, only trifluoromethane (CHF_3) was observed in the simulations to inhibit hydrocarbon flames to any degree. All of the other potential agents either had no influence (inert molecules), were promoters (H atom substituted), or were fuels themselves (such as CH_2F_2). Consequently, we would recommend CHF_3 (although it was not one of

the 12 candidate agents). However, there may be other properties that would preclude its use such as toxicity or corrosiveness.

Of all of the specific candidate agents, we would recommend perfluoroethane (CF_3-CF_3), since our simulations indicate that it will extinguish flames through dilution on a par with N_2 based on their relative heat capacities. CF_3-CF_3 may be preferable to N_2 because it is denser than air or because of other properties. Based on our simulations, the single H atom-substituted hydrofluorocarbons should always be less effective than their perfluorocarbon analogues (*e.g.*, CF_3-CF_2H versus CF_3-CF_3) because their fuel-like characteristics (heat release) will always dominate any radical scavenging.

Based on the effectiveness of CHF_3 in the simulations and knowledge of its mechanism for inhibition, there are other potential agents which should be considered. Any molecule that decomposes readily to yield perfluoromethyl radicals ($\bullet CF_3$) could provide some degree of chemical inhibition of flame processes. That is, any molecule CF_3-X which has a weak bond (C-X) between the CF_3 group and any other group (denoted by X). CF_3-Br is the best example (although undesirable because of its ODP). CF_3-I is another simple example. We would also recommend perfluoroacetone (CF_3-C(O)-CF_3) and hexafluoroazomethane (CF_3-N=N-CF_3). These potential agents are known to be good sources of perfluoromethyl radicals ($\bullet CF_3$) and may decompose sufficiently "early" in the flame that the $\bullet CF_3$ radicals generated could participate in ignition chemistry. The $\bullet CF_3$ radicals can be a sink for terminating radical production through the reaction $\bullet CF_3 + HO_2 \rightarrow CHF_3 + O_2$, which is a contributing reaction (but not the dominant one) in the effectiveness of CF_3Br flame inhibition. The $\bullet CF_3$ radicals will also simply compete for all radicals in the flame. These molecules are amenable to simulations, since their decomposition products ($\bullet CF_3$, CO, and N_2) are already contained in the mechanism which has been developed. These agents should also be readily available for use in experimental determinations of their potential effectiveness. However, there may be other properties that would preclude their use such as toxicity, corrosiveness, or instability.

5.2 Acid Gas Formation in Halogenated Hydrocarbon-Inhibited Flames

5.2.1 Objective and Background. The objective of this part of the research project was to obtain an understanding of the chemical and physical process of acid gas formation in inhibited flames in order to predict the amount of acid gas formed in suppressed dry bay and engine nacelle fires. This is a continuing project, and this section of the report describes results of preliminary work to date.

The halogen acid or hydrogen halide HX (where X represents the halogen) is a thermodynamically stable product in mixtures containing hydrogen and halogen atoms. Since the halogenated hydrocarbon molecules of the present inhibitors can decompose in flames through thermal decomposition or radical attack, formation of the stable halogen acid is likely. The proposed alternatives to halon 1301 (CF_3Br), primarily fluorinated and chlorinated hydrocarbons, are required in much higher concentrations than 1301 (Section 4). Consequently, they have the potential to have correspondingly higher concentrations of decomposition by-products. The acid gases hydrogen fluoride (HF) and hydrogen chloride (Hcl) are believed to be the most corrosive of these products.

In order to understand the formation rates of acid gases in dry bay and engine nacelle fires it is necessary to examine the thermodynamics and chemical kinetics relevant to the formation of the acid gases as well as the effects of the flow field and mixing on the chemistry. An engine nacelle fire may be similar to a steady turbulent spray diffusion flame, whereas a dry bay fire may resemble a rapidly advancing turbulent premixed flame. Because suppression of the dry bay fires is rapid, occurring in a time of under 100 ms, it is also be necessary to consider transient effects on the acid gas formation process.

Formation of acid gases in inhibited hydrocarbon flames has been studied for many years. The research can be categorized as either global measurements of HF produced in suppressed fires, or detailed flame structure measurements. Burdon *et al.*, (1955) ignited mixtures of fuel, air, and CH_3Br in flasks, analyzed the products and found copious amounts of HBr. Numerous premixed low pressure flame studies (*e.g.* Wilson, 1965; Biordi *et al.*, 1973; Safieh *et al.*, 1982;, and Vandooren *et al,*. 1988) used mass spectroscopy to measure the profiles of hydrogen halides and other products in hydrogen, carbon monoxide, and hydrocarbon flames inhibited by CH_3Br, CF_3Br, and CF_3H. These studies indicated conversion efficiencies of the halogens in the inhibitor into halogen acids on the order of unity. Acid gas formation in hydrocarbon-air pool fires suppressed by CF_3Br has been studied by Sheinson *et al.* (1981, 1982). These studies, in test volumes of 1.7 and 650 m^3, stressed the difficulties in probe sampling for acid gases. The latter study described an *in situ* IR absorption method for measuring HBr and HF. To overcome these limitations and also provide time-resolved acid gas concentration data, Smith *et al.* (1993) developed a new HX sampling technique and obtained HX and inhibitor concentrations as functions of time for discharge of CF_3Br into a 56 m^3 space. In a series of experiments with a variety of fuels and halogenated inhibitors, Yamashika (1973) showed that the extinction time for a compartment fire sprayed with inhibitor is dependent upon the discharge rate and room volume. He then showed (Yamashika, 1974) that the amounts of hydrogen halides and carbonyl halides are also dependent upon the discharge rate. Using a simple model of acid gas formation based on the steady-state rates, he developed a model of transient acid gas formation to explain his results.

In more recent studies, Ferreira *et al.* (1992a,b) injected CF_3Br, C_3HF_7, and C_4F_{10} into an enclosure fire and measured the HF produced using ion-selective electrodes. Di Nenno *et al.* (1993) introduced halon alternatives into compartment fires and measured the HF, HCl, and COF_2 produced using Fourier transform infrared spectroscopy. These studies again confirmed the importance of injection rate and fuel consumption rate on the amount of acid gas produced. Filipczak (1993) introduced CF_2ClBr and CF_3Br into a methane flame and measured the O_2, CO_2, H_2O, HF, HCl, HBr, and unreacted inhibitor using a mass spectrometer. Hoke and Herud (1993) are currently developing a fast-response ion-selective electrode for measuring HF and HCl produced in extinguished fires in crew compartments of combat vehicles.

Previous research related to understanding acid gas formation in inhibited flames can be seen to include both detailed flame structure measurements and global measurements of HF produced in suppressed fires. The inhibited low-pressure premixed flame studies provide detailed data on the concentration profiles of major species as a function of position in the flame for inhibition by CH_3Br, CF_3Br, and CF_3H. These results provide the basis for obtaining a good understanding of the underlying chemical kinetics of the formation of acid gases. The second category of experiments is global measurements of the amount of acid gas formed in suppressed diffusion flames. These studies provide important information on the magnitude of the acid gases produced and allow a comparison of the relative amount of acid gases formed by new halon alternatives. In addition, some progress has been made (Yamashika, 1974; Smith *et al.*, 1993) in developing engineering models of acid gas formation in suppressed flames. There remains a need to develop a fundamental basis for interpreting the data on acid gas formation in flames suppressed by halon alternatives, and to understand the chemical kinetic rates of acid gas formation in flames inhibited by these alternative agents. In particular, there exists a need to understand the relationship between fuel and inhibitor type, flame characteristics, and the concentrations of by-products formed.

5.2.2 Experimental Approach. The formation of toxic and corrosive by-products in flames suppressed by halogenated hydrocarbons may be controlled by transport rates of the inhibitor into the

flame, chemical kinetic rates, and equilibrium thermodynamics. These phenomena in turn will be affected by the fuel type, local stoichiometry, inhibitor type and concentration, and the characteristics of the flow field (mixing rates, strain, and stabilization mechanisms). The approach in this research is to study the influence of key parameters (including the fuel type, inhibitor type and concentration, rate of inhibitor injection, and flame type) through systematic experiments on laboratory-scale flames. Inhibitor will be added to the fuel or air stream of co- and counter-flow diffusion flames and premixed flames under steady-state and transient conditions. Inhibitor type, concentration, and injection rates will be varied as will fuel type. The diffusion flames will be operated under both laminar and turbulent conditions to vary the mixing rates, and premixed flames will be studied over a range of fuel-air equivalence ratios. This is an ongoing project. At this point, the measurements of steady-state acid gas formation rates in inhibited co-flow propane-air diffusion flames have been completed. The apparatus used to obtain these data, the results, and their interpretation are presented below.

The experiments were performed with a propane-air co-flow diffusion flame. Two burner types were used. The first was modelled after the cup burner described by Booth *et al.* (1973) and Bajpai (1974). The experimental arrangement is shown in Figure 12. The burner consists of a 28 mm diameter pyrex cup positioned concentrically in a 120 mm diameter 450 mm tall chimney at about 150 mm from the base. In these experiments with propane, the cup burner was modified for use with a gaseous fuel (liquid fuels will be tested in future experiments). The cup was filled with 1 mm diameter glass beads and covered with a stainless steel screen. The second burner consisted of a 25 cm long pyrex tube with a 0.50 mm diameter opening positioned concentrically and at the same height as the cup burner, with the same chimney. The cold flow Reynolds number based on the exit velocity in the tube was 10,500. This second burner, referred to here as the jet burner, was designed to provide turbulent mixing of the inhibitor in the air stream with the fuel.

The air used was shop compressed air (filtered and dried) which was passed through an 0.01 micron filter to remove aerosols and particulates, a carbon filter to remove organic vapors, and a desiccant bed to remove water vapor. The fuel gas was propane (Matheson, CP grade) at flow rate of 0.114 l/min at 21 °C. Gas flows were measured with rotameters (Matheson 1050 series) which were calibrated with bubble and dry (American Meter Co. DTM-200A and DTM-325) flow meters. Inhibitor gases were of different purities from various suppliers.

Before measuring HF in the product gases, the concentration of inhibitor in the air stream necessary to extinguish the flame was determined. The inhibitor was then added to the co-flowing air stream at a concentration of either 50 or 90% of the extinguishing concentration, and the product gases were sampled for acid gas. In one series of experiments with the cup burner, the inhibitor was added to the gaseous propane stream at 70% of the concentration which was found to extinguish the flame.

A wet chemistry technique was used to measure the HF and HCl concentrations in the exhaust gases from the co-flow diffusion flames. A glass funnel was placed over the chimney and the exhaust gases passed through the 4.0 cm diameter neck. A quartz probe, centered in the neck, extracted a measured fraction of the product gases (approximately 0.5%), and directed the gases through polyethylene sample lines to polyethylene impingers filled with water which trapped the acid gases. The sample flow was continued for a total collection time of sixty seconds. The quartz probe and sample lines were washed with water which was returned to the impinger. The sample was tested for F^- and Cl^- using ion-selective electrodes (Orion models 96-09 and 96-17B). It should be noted that since COF_2 is know to hydrolyze rapidly in the presence of water, this technique for acid gas measurement includes F^- from both HF and COF_2. To reduce the effects of sampling losses reported by other investigators, a quartz probe and polyethylene sample lines were used, the distance from the

chimney top to the bubbler was kept small (~ 10 cm) and the sample lines were washed with the bubbler fluid immediately after the sample was collected.

5.2.3 Model for Acid Gas Formation. A model for the amount of acid gas formed in an inhibited diffusion flame can be developed in a manner analogous to the determination of the local equivalence ratio and structure for diffusion flames. In the classic Burke-Schumann analysis (Burke and Schumann, 1928), the chemical reaction is assumed to occur at a sheet. This location serves as a sink for the fuel and oxidizer which are assumed to diffuse there in stoichiometric proportions based on complete reaction to the most stable products (i.e., HF formation is assumed to be controlled by equilibrium thermodynamics rather than chemical kinetics). This model will be referred to as the stoichiometric model.

In the case of a flame inhibited by halogenated hydrocarbons, a thermodynamic analysis shows that in equilibrium, the inhibitor readily breaks down to CO_2, HX, and H_2O. Consequently, the inhibitor is assumed to be consumed like a fuel and form the most stable products. The assumptions used in the stoichiometric model are:

1. there is complete reaction of the inhibitor molecule with fuel and air to the most stable products;
2. the inhibitor in the air stream which by-passes the flame sheet does not decompose through interaction with the post-combustion product gases;
3. there is no loss of acid gases to the chimney walls; and
4. the product gases are perfectly mixed.

An equation for the reaction of an arbitrary hydrocarbon with air and arbitrary halogenated hydrocarbon inhibitor is:

$$\begin{aligned} &\alpha C_aH_b + \beta C_cH_dF_eCl_f + \gamma'(O_2 + 3.76N_2) \rightarrow \\ &\delta CO_2 + \lambda H_2O + \eta HF + \phi HCl + \epsilon COF_2 + \pi COCl_2 + \xi O_2 + 3.76\gamma' N_2 \end{aligned} \tag{1}$$

In this equation α is specified as is β when inhibitor is present only in the fuel stream. For inhibitor present in the air stream, β is determined by the concentration of inhibitor in the air stream and the ratio of the diffusion rates for oxygen and inhibitor.

$$\beta = \frac{\alpha\,(a + b/4)}{1/(\rho r) - [c + 1/4(d - e - f)]} \tag{2}$$

Where ρ is the ratio of the binary diffusion coefficient of the inhibitor in nitrogen to that of oxygen with nitrogen and r is the ratio of the concentration of inhibitor to oxygen in the air stream. An atom balance for all species provides all of the unknown coefficients, and an estimate of amount of acid gas formed per mole of fuel $(\eta + \phi)/\alpha$ is then readily found.

5.2.4 Results and Discussion. The acid gases produced were measured at inhibitor concentrations of 50 and 90% of the concentration of inhibitor found to extinguish the flame when the inhibitor was added to the co-flowing air stream in the cup burner and jet burner, and at 70% of the extinction concentration for inhibitor added to the propane fuel stream for the cup burner. Table 5 lists the extinction concentrations for each agent for inhibitor added to the air stream of both burners, and for

inhibitor added to the fuel stream of the cup burner. As the table indicates, the jet burner flame typically requires about 50% less inhibitor in the air stream to extinguish the flame than the cup burner, even for identical fuel and air flows, although there are notable exceptions: CF_3Br, which required about one fifth as much inhibitor in the jet burner than in the cup burner, and C_2HF_5 and the $CH_2F_2/C_2H_2F_4$ mixture which had nearly the same extinction concentrations. In addition to providing the necessary extinction conditions for specification of inhibitor flows at 50 and 90% of extinction, these results also demonstrate the sensitivity of the extinction conditions to the burner geometry.

The measured HF for these diffusion flames is shown in Figures 13 and 14. These figures present the HF produced (moles/min) for each inhibitor for the five burner/inhibitor combinations. The total flow was about 1 mole/min. For each inhibitor, the measured HF is plotted for the cup burner and for the turbulent jet burner with inhibitor present in the air stream at 50 and 90% the extinction value, and for inhibitor added to the fuel stream in the cup burner at 70% of the value necessary to cause extinction. The figure indicates that the amount of HF varies with both the flame type and the inhibitor type by about a factor of five for each. Note that the fuel and air flows are held constant in these data. Hydrogen chloride was also measured in these experiments and the results are qualitatively the same as for HF. For clarity of presentation, however, only the HF results are presented.

In order to provide insight into the controlling parameters in inhibited diffusion flames, the data of Figures 13 and 14 are presented in an alternative form in Figures 15 to 26. In these figures, the amount of HF produced is plotted as a function of the inhibitor concentration in air. The symbols represent the experimental data, while the lines marked F and H represent estimates of the fluxes of fluorine and hydrogen into the reaction zone based on the stoichiometric model described above.

Figure 15 shows the measured and estimated HF production rates in a propane-air diffusion flame for C_2F_6 in the cup and jet burners. The squares are the experimental data for the cup (c) and jet (j) burners at 50 and 90% of extinction, and with inhibition addition to the fuel stream (f) of the cup burner of 70% of the extinction concentration. The estimated uncertainty on the HF are $\pm$ 10% of the value for each data point. The curve labeled F in Figure 15 is the maximum fluoride atom mass flux into the reaction sheet of the diffusion flame calculated using the stoichiometric model described above. The curve labeled F' in Figure 15 is the fluoride mass flux when the diffusion rate of the inhibitor relative to oxygen is modified to account for preferential diffusion of oxygen relative to the inhibitor using the molecular weight correction factor

$$\sqrt{W_i + W_{N_2} / W_{N_2} W_i} \; / \sqrt{W_{O_2} + W_{N_2} / W_{O_2} W_{N_2}} \quad .$$

In this equation, W_{N_2}, W_{O_2}, and W_i are the molecular weights of nitrogen, oxygen, and inhibitor.

The predicted fluorine and hydrogen fluxes are based on actual experimental flows which vary slightly from run to run. The slight variations in flows cause the slight discontinuities in the F and H curves as in Figure 16.

Qualitatively, the curves F and F' are seen to increase with increasing inhibitor concentration in air, and the mass flux of inhibitor into the reaction zone is lower when a lower rate of diffusion is used for the inhibitor. The curves labeled H and H' (coincident for C_2F_6) show the estimated hydrogen atom flux into the reaction zone as a function of inhibitor concentration in the air stream. Since this inhibitor does not contain hydrogen, all of the hydrogen is from the propane, and

Table 5. Extinction concentrations in percent for halon alternatives added to a co-flow propane-air cup burner and jet burner flame

Inhibitor	Extinction Concentration in air (%)	
	cup	jet
CF_3Br	4.3 (± 0.1)	0.8 (± 0.02)
$C_3H_2F_6$	7.2 (± 0.2)	4.0 (± 0.1)
$CH_2F_2/C_2H_2F_4$	15.2 (± 0.5)	15.5 (± 0.5)
C_4F_{10}	5.0 (± 0.2)	3.2 (± 0.1)
C_2HClF_4	8.6 (± 0.3)	4.2 (± 0.1)
$C_2H_2F_4$	11.1 (± 0.3)	9.5 (± 0.3)
C_2HF_5	10.2 (± 0.3)	6.2 (± 0.2)
$CHClF_2$	13.8 (± 0.4)	6.7 (± 0.2)
C_3HF_7	7.6 (± 0.2)	4.2 (± 0.1)
C_2F_6	9.4 (± 0.3)	3.8 (± 0.1)
C_3F_8	7.5 (± 0.2)	3.8 (± 0.1)
C_4F_8	7.6 (± 0.2)	5.1 (± 0.2)

increasing inhibitor in the air stream does not increase the hydrogen flux into the flame. One would expect that the HF production rate would not be greater than the estimated flux of F or H into the reaction zone. For this inhibitor, the flame appears to be hydrogen limited above about 5% C_2F_6 in the air stream; however, when there is not enough hydrogen, the most stable product is COF_2, which is know to rapidly hydrolyze in the presence of water, and would also appear as F^- in the bubbler. Consequently, the hydrogen limit may or may not exist (depending upon whether the kinetics are fast enough to form COF_2 in the hydrogen-limited case).

Also shown in the figure are the experimentally measured HF production rates for the jet and cup burners (labeled c and j respectively) at 50 and 90% of the extinction concentration of C_2F_6. As indicated, the measured quantities of HF are lower than both the fluorine and hydrogen limits, and the measured values are closer to the estimated limits when the effects of preferential diffusion are included as described above. The results for the inhibitor addition to the fuel stream in the cup burner (labeled f) are plotted at an inhibitor concentration of zero so that they can be included in the figure.

When viewed in this manner, the behavior of the alternative inhibitors falls into three categories. In the first category are those inhibitors (C_2F_6, C_3F_8, C_4F_{10}, C_3F_8, C_2HF_5, and C_3HF_7; Figures 15 to 20) where, at the highest inhibitor concentration tested (cup burner at 90% of extinction), the estimated hydrogen flux into the reaction zone is lower than the fluorine flux, and is not a strong function of the inhibitor concentration. For these inhibitors, the HF produced does not increase significantly when the inhibitor concentration in the air stream increases above that necessary for a hydrogen/fluorine ratio in the reaction zone of about unity (the region of where the lines marked F and H or F' and H' cross in Figures 15 to 26). The second category includes those inhibitors

($C_2H_2F_4$, C_2HClF4, $C_3H_2F_6$, and $CH_2F_2/C_2H_2F_4$; Figures 21 to 24) for which the estimated H and F fluxes are about equal. For these inhibitors, the amount of HF produced increases with increasing inhibitor concentration in the air, but the highest concentration tested corresponds roughly to a unity F/H ratio in the reaction zone. The last category consists of CF_3Br and $CHClF_2$ (Figures 25 and 26) for which the estimated hydrogen flux is much higher than fluorine flux, and there is estimated always to be more hydrogen than fluorine in the reaction zone. For these inhibitors, the HF produced is always increasing with higher agent concentration in the air stream.

Although the stoichiometric model is very simple and is only expected to provide an upper limit on the amount of HF formed, it is instructive to investigate the possible reasons that the measured HF production rates might be lower than the estimates. Lower HF may be measured in the experiments due to experimental difficulties, for example: loss of HF to the chimney walls, loss in the sampling system, HF undetected by the ion-selective electrodes, or imperfect mixing in the product gases. Based on exploratory parametric tests, these loss mechanisms are considered to be of secondary importance. The predicted values of the HF production do not include chemical kinetic limitations and the estimates of transport rates into the reaction zone are only approximate. Additional experiments will be performed to allow examination of these important parameters.

5.2.5 Future Work. In order to eliminate the error associated with the estimates of the inhibitor transport rate into the reaction zone, experiments will be performed with inhibitor added to the reactant stream in a premixed burner. Adding known concentrations of inhibitor to a premixed flame and measuring the HF production rates will eliminate the need to estimate transport rates of inhibitor into the flame and allow a better assessment of kinetic limitations to HF formation. The premixed flame will also be used to perform measurements of the burning rate reduction with addition of inhibitor. These measurements will be used to validate chemical kinetic mechanisms of the reaction of hydrocarbons, halogens, and air. Measurements of the final product species in inhibited flames will provide insight into the kinetic mechanisms and can be used for comparison with kinetic modeling results. Finally, detailed flame structure measurements in inhibited counterflow diffusion flames will allow comparison with the results of detailed numerical calculations of the flame structure to provide a sound fundamental basis for estimates of HF production rates in suppressed dry bay and engine nacelle fires. The approach to be used in developing a model for HF production in these fires is similar to that of Yamashika (Yamashika, 1974). The experimentally determined steady-state production rates for HF will be used to predict the time-dependent production rate of HF. The important parameters then become the value of the extinction concentration for a given fire and the time it takes the concentration to reach this concentration. Since chemical kinetic limitations appear to affect HF formation rates, detailed flame structure measurements together with numerical modelling of the kinetics are necessary to provide the background for development of a global model of HF formation.

Although results on acid gas production in JP8 cup burner flames have not yet been obtained, it is possible to use the propane results and the model described above to obtain estimates of the amount of acid gas (HF and HCl) that would be formed in a turbulent JP8 flame suppressed by the proposed alternative agents, and use this estimate as a basis for ranking the agents with respect to acid gas formation. The quantity of HX (sum of HF and HCl) formed is estimated from the steady state production rates predicted by the stoichiometric model for JP8 fuel with suppressant present at 50% of the extinction value. Kinetic limitations are estimated from those indicated by the propane results. Table 6 provides the rank ordering of the agents and gives the fraction of acid gas the agent forms in

Table 6. Relative ranking of alternative inhibitors with respect to steady state hydrogen halide production rates

Inhibitor	Relative Steady State Acid Gas Production
CF_3Br	0.05 (± 0.01)
C_2HClF_4	0.16 (± 0.03)
C_2F_6	0.21 (± 0.03)
C_4F_{10}	0.27 (± 0.04)
$CHClF_2$	0.31 (± 0.05)
C_4F_8	0.32 (± 0.05)
C_3F_8	0.34 (± 0.05)
C_3HF_7	0.35 (± 0.05)
C_2HF_5	0.41 (± 0.06)
$C_3H_2F_6$	0.43 (± 0.06)
$C_2H_2F_4$	0.74 (± 0.10)
$CH_2F_2/C_2H_2F_4$	1.0 (± 0.10)

steady state compared to the agent which has the highest acid gas formation rate (CH_2F_2/C_2HF_5). The agent CF_3Br is listed for comparison. In practice, the amount of acid gas formed in a suppressed fire will be dependent upon the time it takes the agent to reach the extinction concentration. For example, the rank ordering in the list below (which is based on steady-state results) can be greatly affected by the injection system used and the mixing characteristics of the particular agent once it is released.

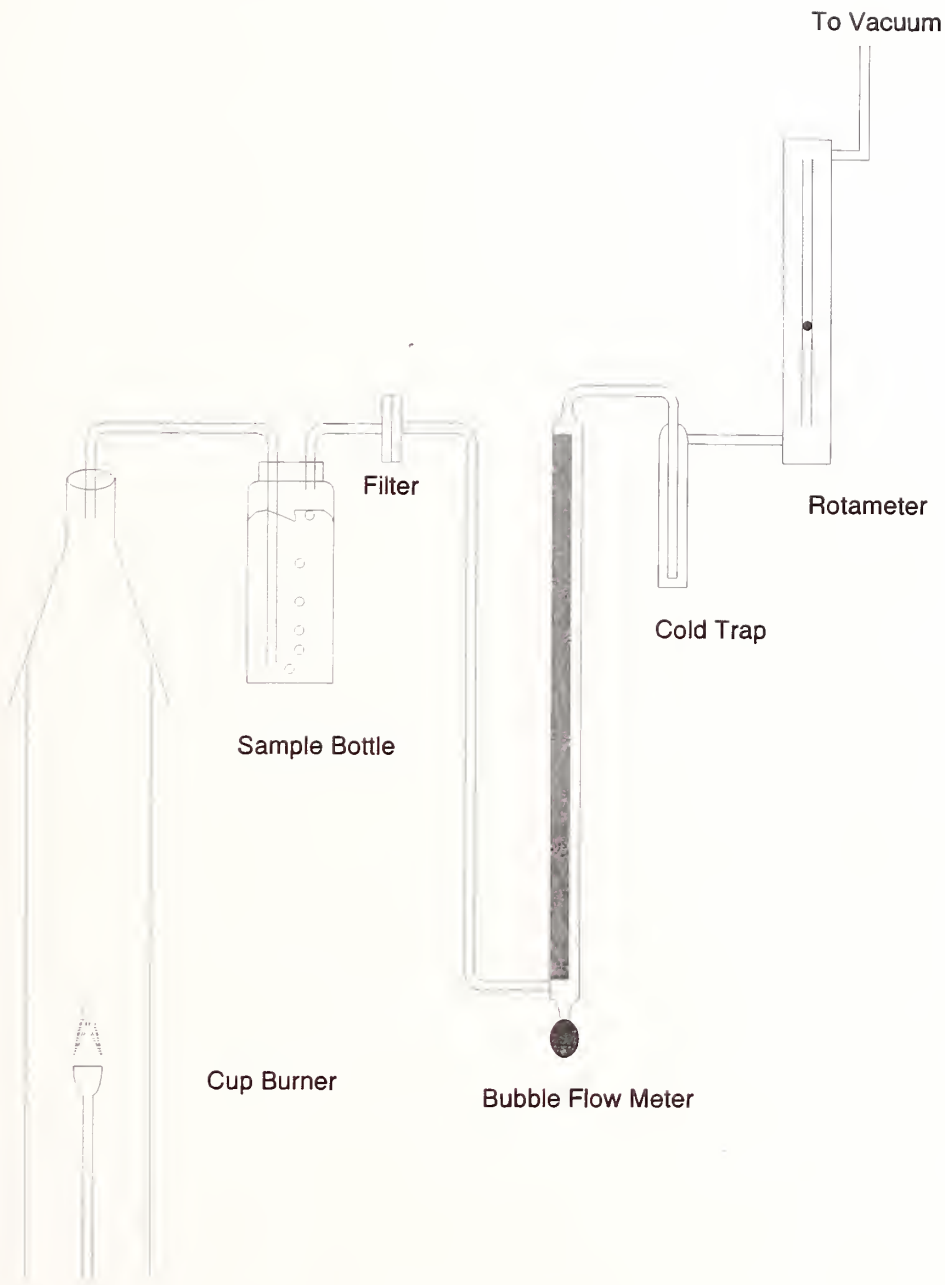

Figure 12. Experimental apparatus for co-flow diffusion flame studies of acid gas formation in inhibited propane-air flames.

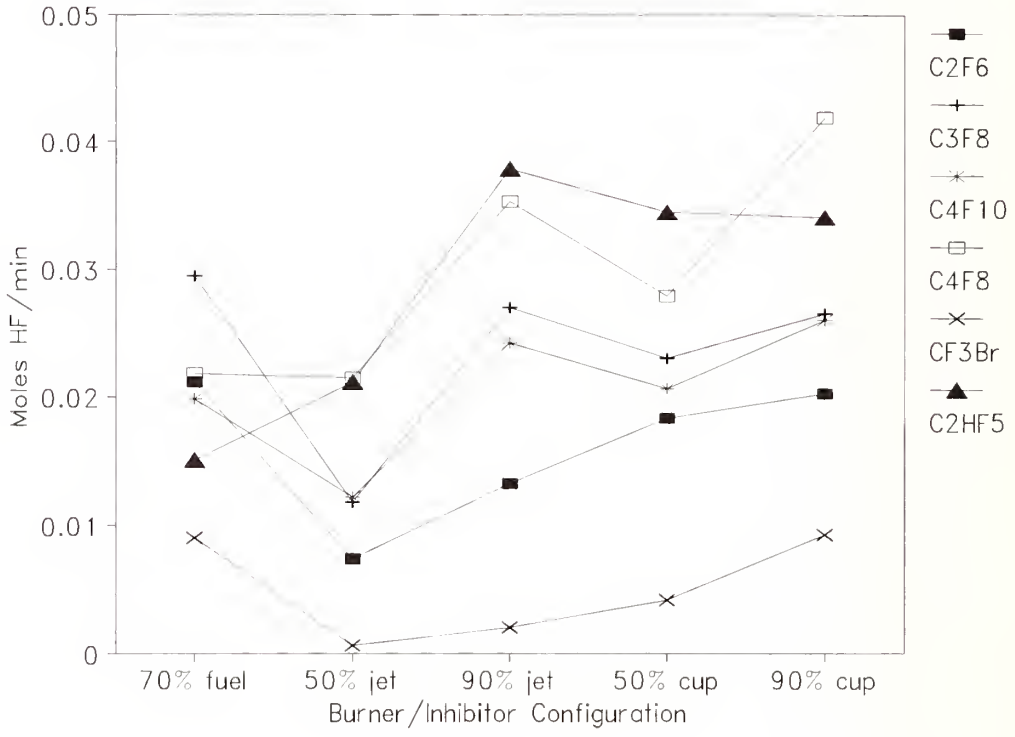

Figure 13. Measured HF production rates in co-flow propane-air diffusion flames. Data are shown for cup and jet burners at 50 and 90% of the extinction concentration for agent added to the air stream, and at 70% in the fuel stream in the cup burner.

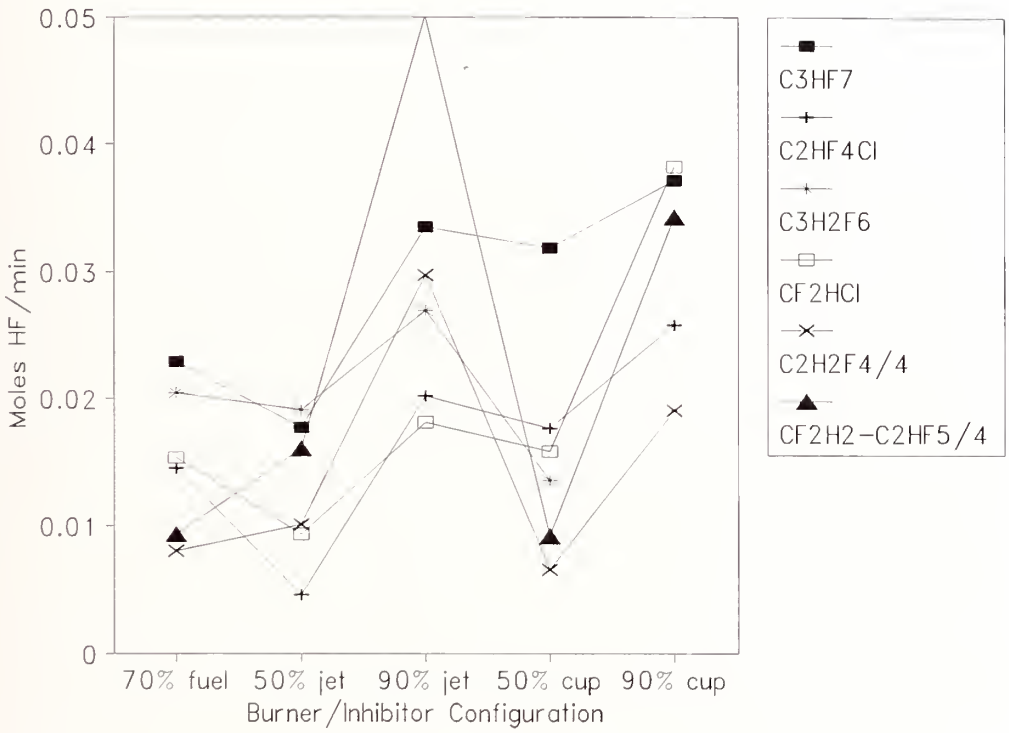

Figure 14. Measured HF production rates in cup and jet burners. Note that the curves for CF_2H_2/C_2HF_5 and $C_2H_2F_4$ are reduced by a factor of 4.

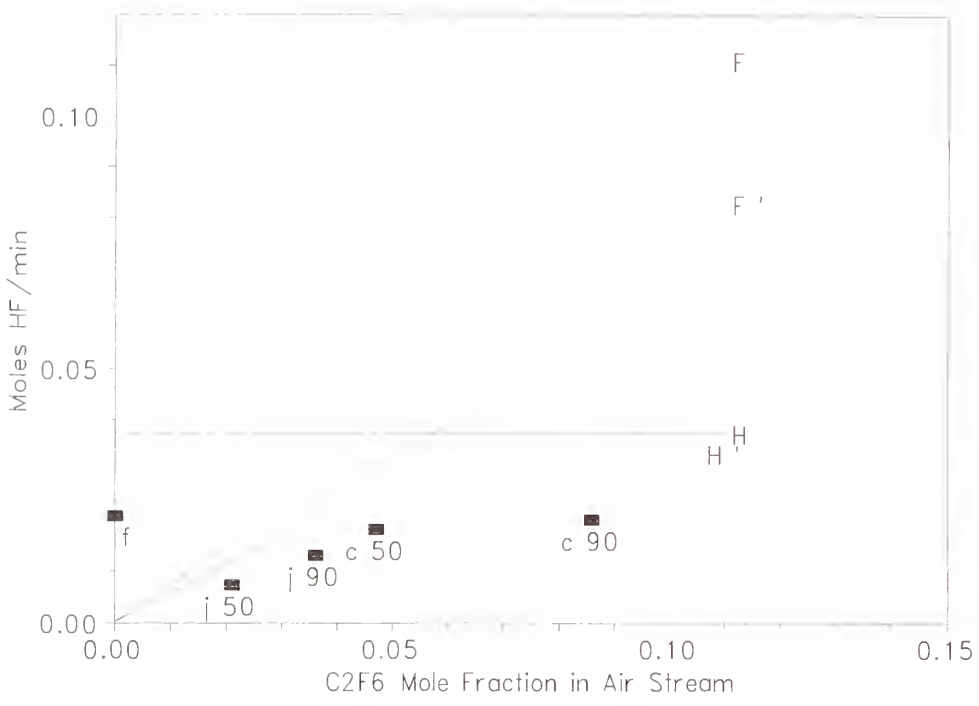

Figure 15. HF produced vs. C_2F_6 mole fraction for cup (c) and jet (j) burners at 50 and 90% of extinction, and with inhibitor addition to the fuel stream (f) of cup burner at 70% of extinction.

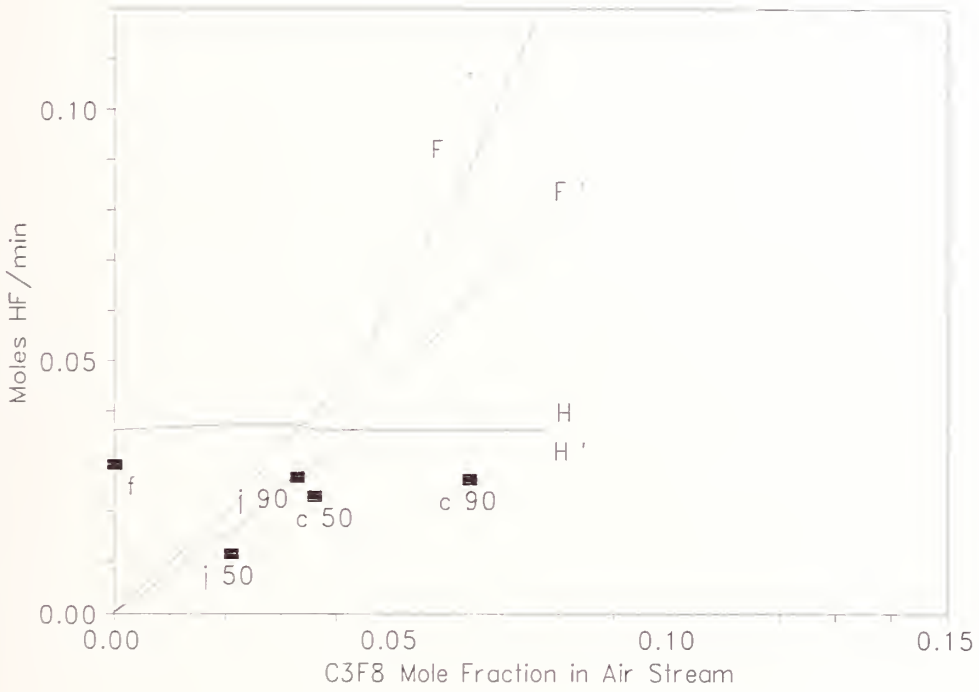

Figure 16. HF produced as a function of C_3F_8 mole fraction in air stream. Label definitions as in Figure 15. Discontinuities in curves are due to slight variations in flows from run to run.

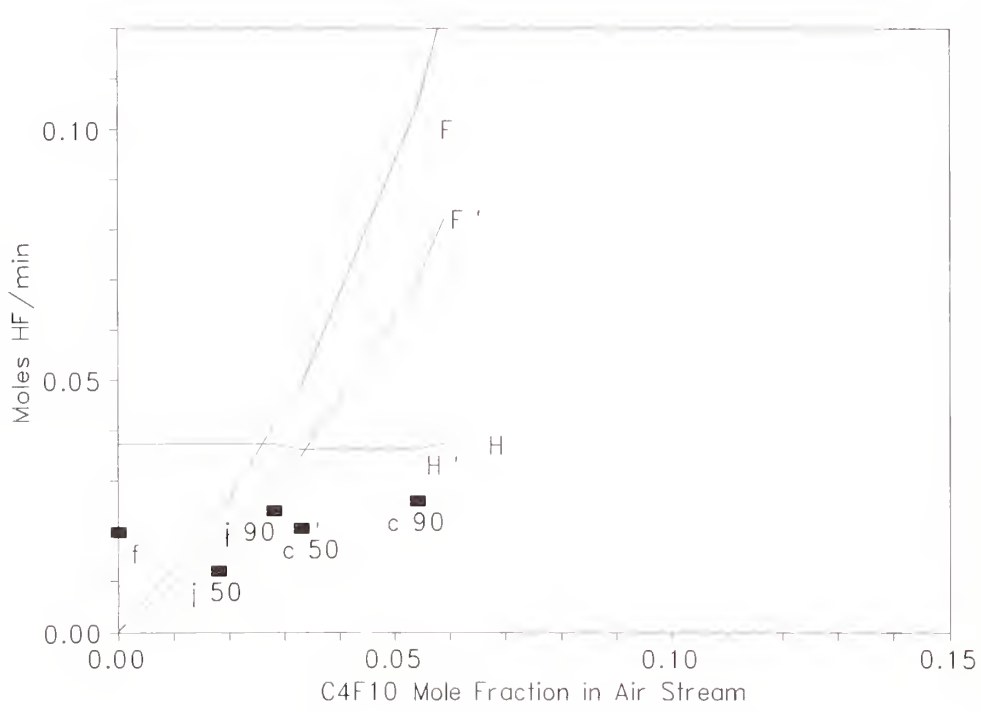

Figure 17. Moles of HF produced as a function of the C_4F_{10} mole fraction in the air stream. Label definitions as in Figure 15.

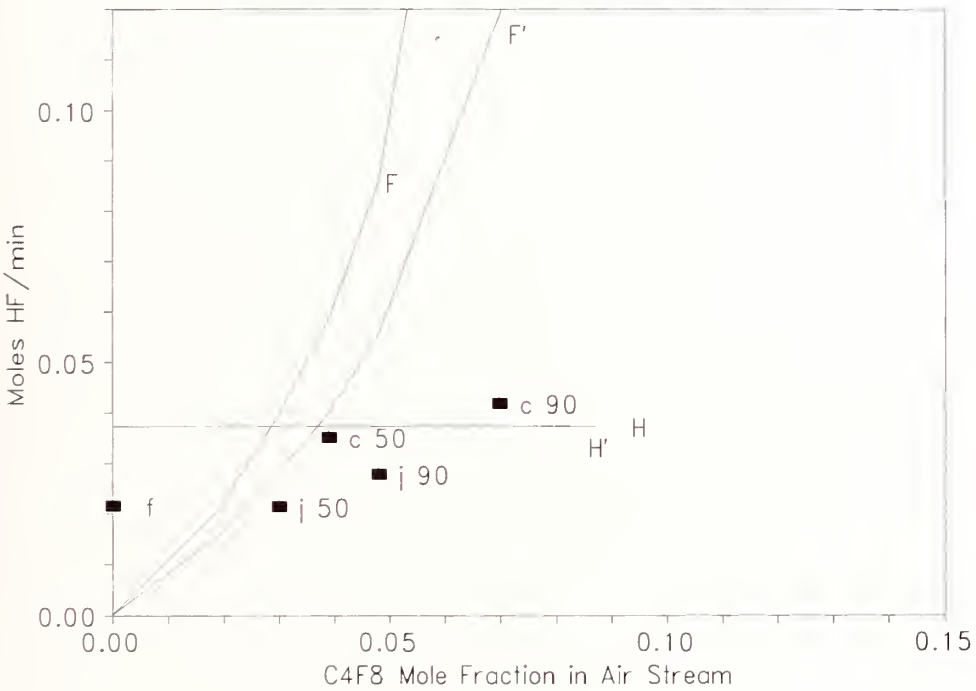

Figure 18. Moles of HF produced as a function of the C_4F_8 mole fraction in the air stream. Label definitions as in Figure 15.

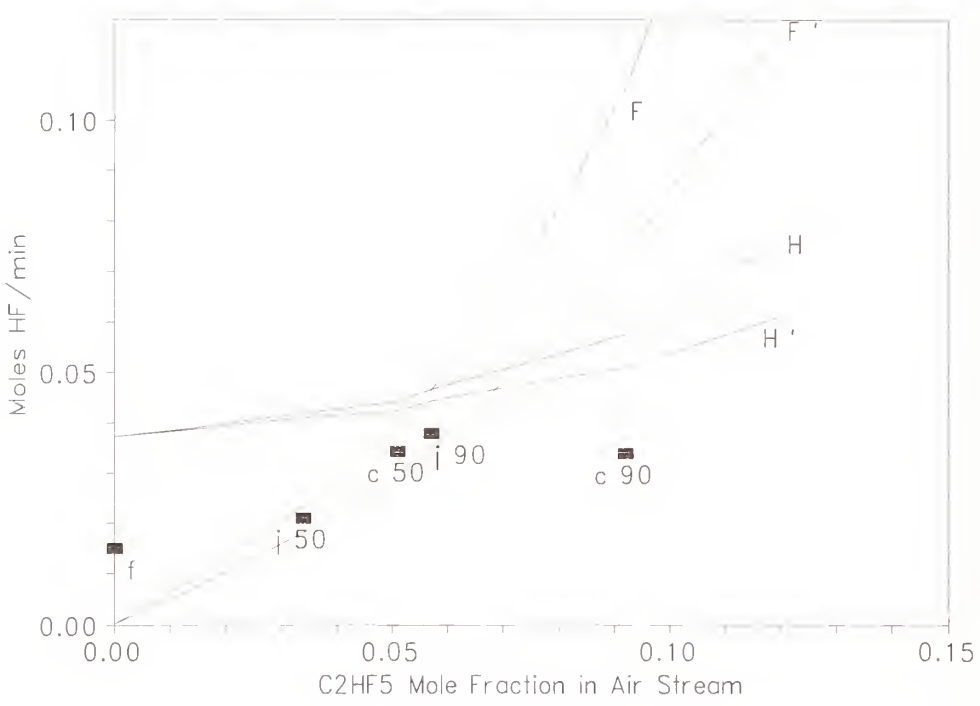

Figure 19. Moles of HF produced as a function of the C_2HF_5 mole fraction in the air stream. Label definitions as in Figure 15.

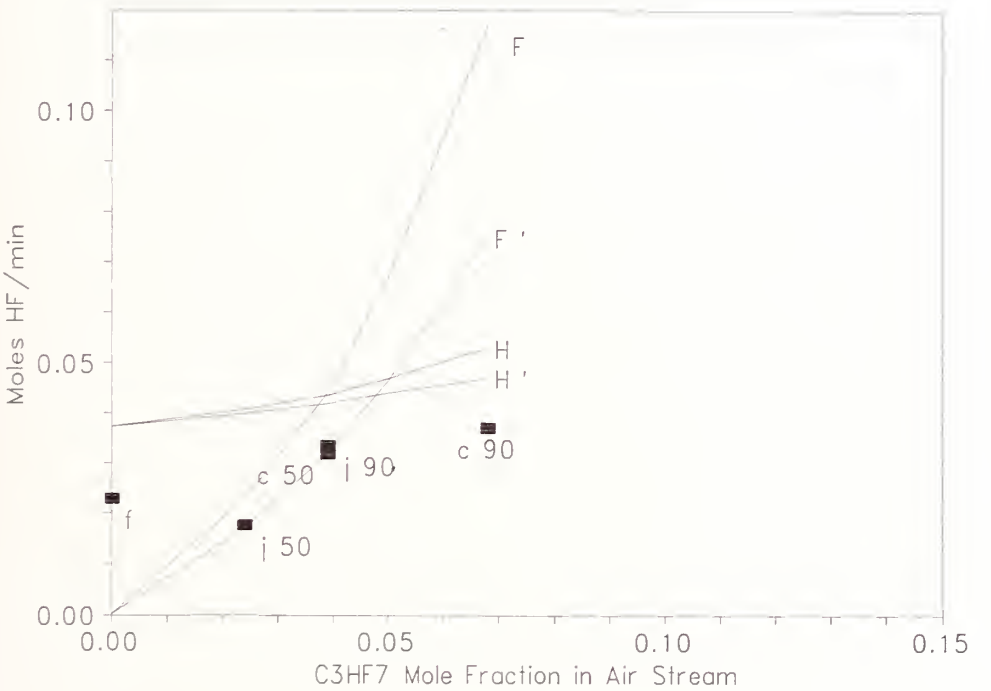

Figure 20. Moles of HF produced as a function of the C_3HF_7 mole fraction in the air stream. Label definitions as in Figure 15.

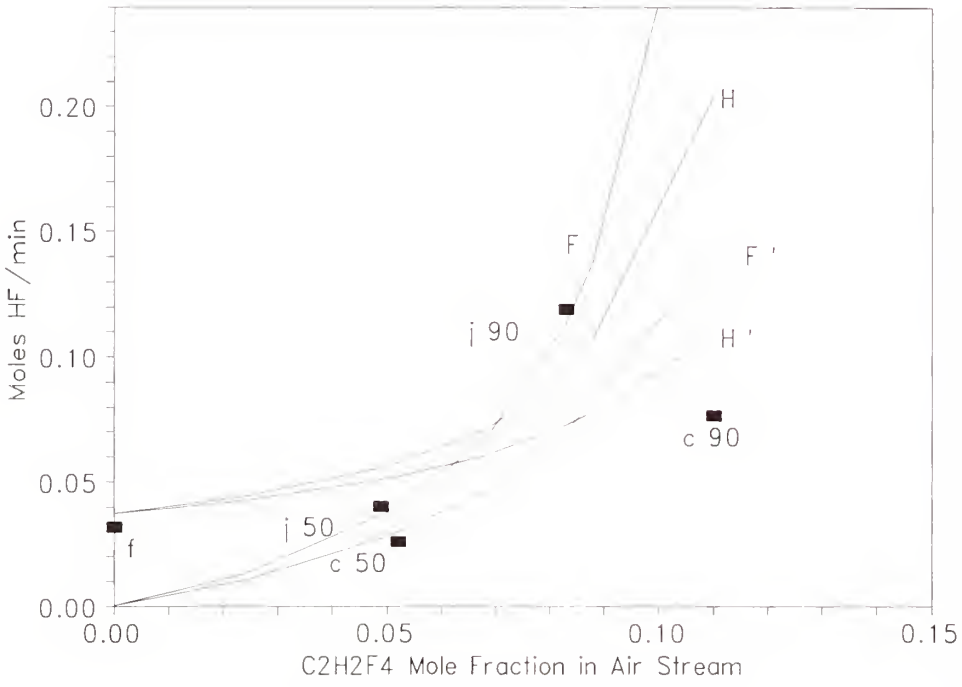

Figure 21. Moles of HF produced as a function of the $C_2H_2F_4$ mole fraction in the air stream. Label definitions as in Figure 15.

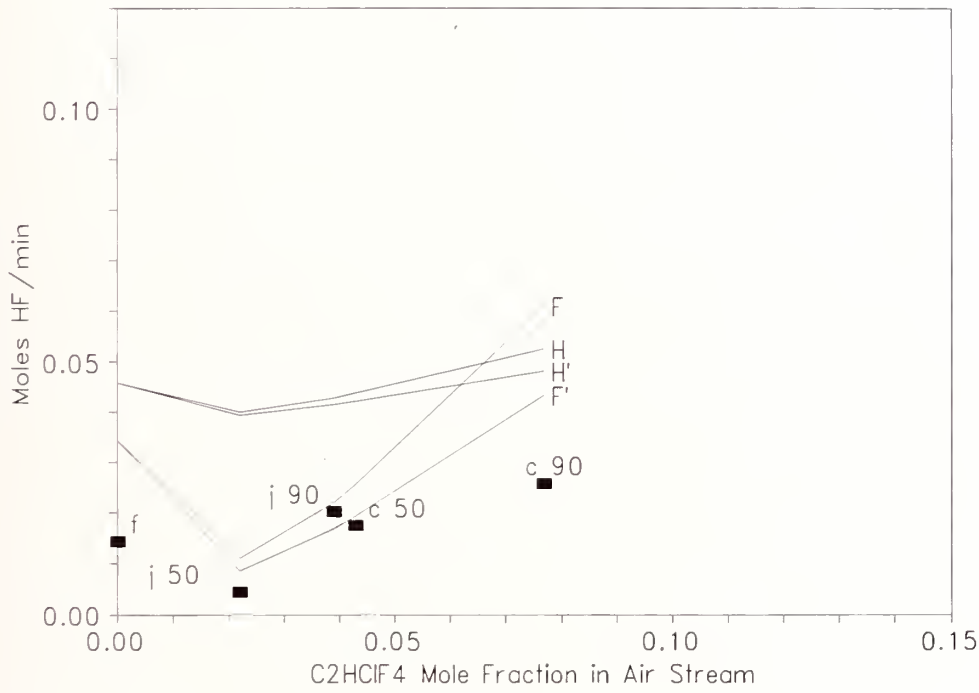

Figure 22. Moles of HF produced as a function of the C_2HClF_4 mole fraction in the air stream. Label definitions as in Figure 15.

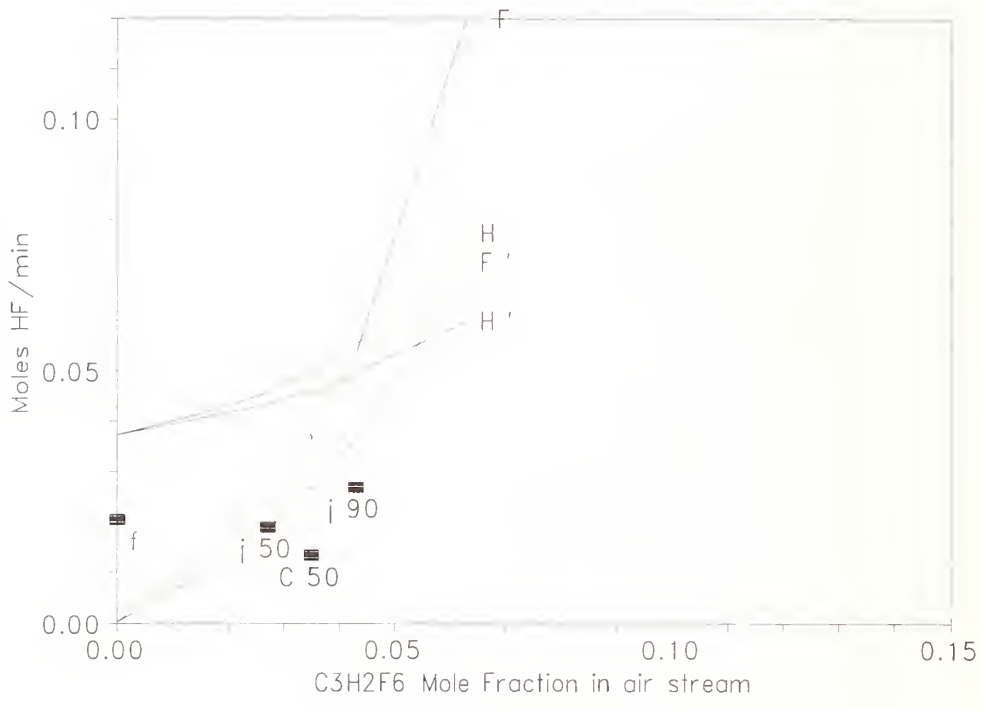

Figure 23. Moles of HF produced as a function of the $C_3H_2F_6$ mole fraction in the air stream. Label definitions as in Figure 15.

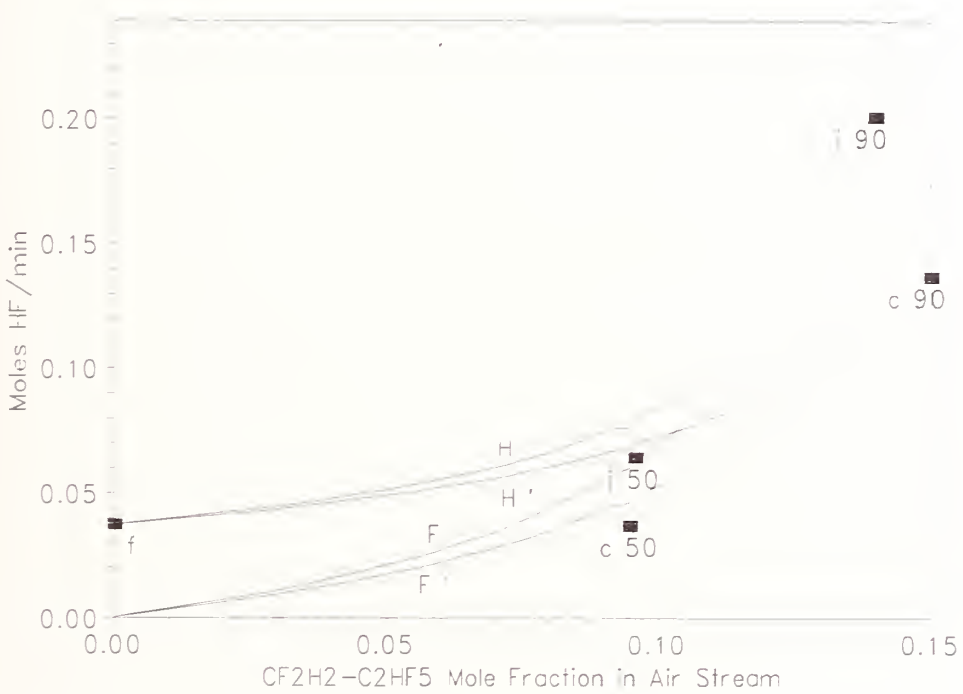

Figure 24. Moles of HF produced as a function of the CF_2H_2/C_2HF_5 mole fraction in the air stream. Label definitions as in Figure 15.

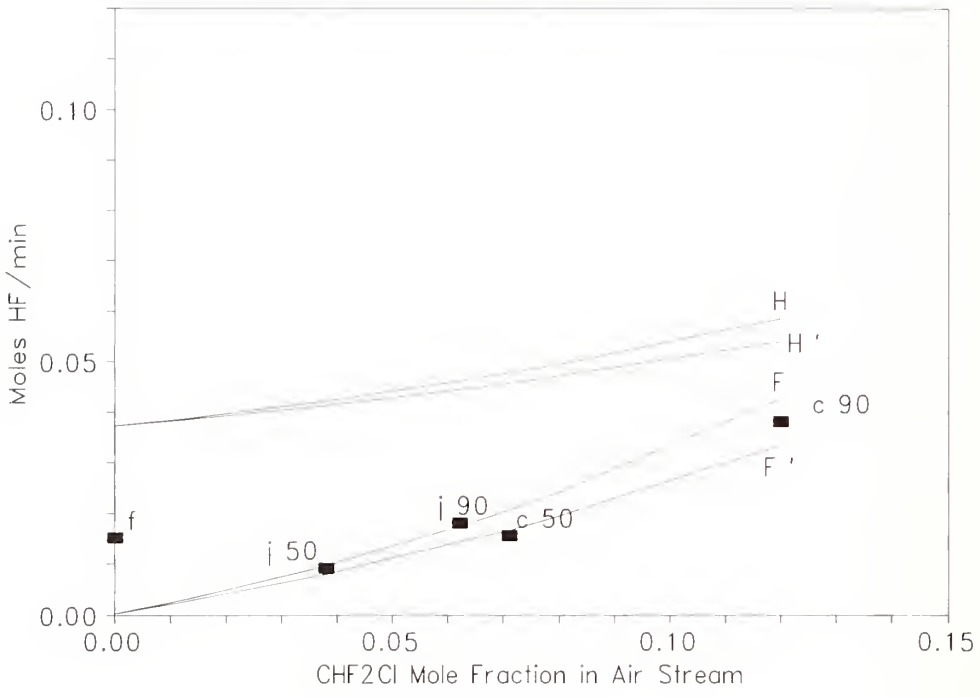

Figure 25. Moles of HF produced as a function of the CHF_2Cl mole fraction in the air stream. Label definitions as in Figure 15.

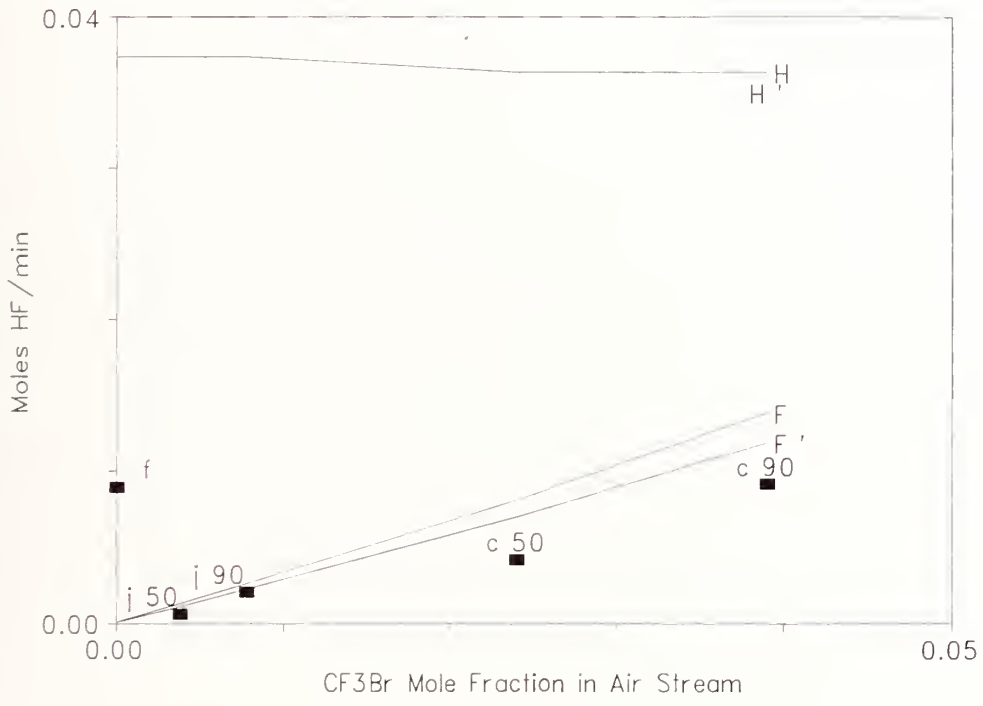

Figure 26. Moles of HF produced as a function of the CF_3Br mole fraction in the air stream. Label definitions as in Figure 15.

5.3 Alternative Low ODP Chemicals with High Fire Suppression Effectiveness

The major objectives of this research were to broaden the scope of alternative agent screening beyond the core candidates listed in Section 1 and to develop and test structure/activity relationships for environmental impact. The motivation for this pursuit was supplied by the following considerations which could be expected to affect the outcome of the alternative agents program:

1. the original list of compounds might not include a viable candidate;
2. guidelines for environmental impact might change without warning; and
3. a new class of environmentally safe fire extinguishants might be identified.

5.3.1 Background. The mechanism by which halons extinguish fires is thought to involve both chemical and physical processes (Sheinson *et al.*, 1989 and Pitts *et al.*, 1990). Simulations using detailed kinetic models (Westbrook, 1983) indicate that hydrogen halides (HX), which form when halons are introduced into flames, promote radical recombination via HX + H (OH) → H_2 (H_2O) + X. This inhibits the combustion process by reducing the concentration of radicals in the reaction zone. At some point, the rate of recombination exceeds the rate of propagation and the flame is extinguished. Physical suppression results from the removal of thermal energy from the flame by the vibrational excitation of the agent. This mechanism is universal in the sense that all molecules absorb heat, however, it is much less efficient than chemical suppression for the low molecular weight compounds which are most suitable for total flooding applications. Those halocarbons which contain Br or I are chemically active and are considerably more effective (per unit mass) than the corresponding F and Cl-containing compounds which act predominantly as physical suppressants (see Table 7 in Section 4).

The current commercial halons pose a serious threat to the ozone layer. The determining factor is whether they are sufficiently stable to make it into the stratosphere where over 90% of the column height of atmospheric ozone is located (Finlayson-Pitts and Pitts, 1986). Once they enter the stratosphere, halon molecules are photolyzed by short wavelength UV radiation. The halogen atoms released in this process are capable of catalyzing the destruction of ozone through the following mechanism:

$$\begin{aligned} X + O_3 &\rightarrow XO + O_2 \\ XO + O &\rightarrow O_2 + X, \end{aligned} \tag{4}$$

where X is Cl, Br or I.

The precise definition of ozone depletion potential (ODP) (Wuebbles, 1983) is

$$ODP(RX) = \frac{\Delta O_3(RX)}{\Delta O_3(CFCl_3)}, \tag{5}$$

where ΔO_3 is the amount of ozone destroyed by emission of compound RX over its entire atmospheric lifetime. This quantity is computed by modeling molecular transport, typically as a function of both latitude and altitude, through the troposphere and into the stratosphere. Chemical and photolytic processes, which can remove the compound from the atmosphere, are accounted for by kinetic

mechanisms which are parameterized on the basis of measured rate constants. The computed ODP depends on the following critical factors:

1. the fraction of molecules which reach the stratosphere, which in turn, depends on how long the molecule survives before it is oxidized or otherwise destroyed in the troposphere;
2. the number of Cl, Br and I atoms in the molecule; and
3. their relative efficiencies in catalyzing the destruction of O_3 according to the mechanism summarized in Equation (1).

The catalytic efficiency of Br is approximately 40 times greater than that of Cl (Pyle *et al.*, 1991). The conversion of halogen oxides into free halogen atoms via

$$BrO + ClO \rightarrow Cl + Br + O \tag{6}$$

is responsible for a large part of this enhancement. The kinetic constants for the analogous reactions of IO with ClO and BrO have not been measured. There is an indication, however, that low levels of I may greatly enhance the ozone destruction efficiencies of both Cl and Br (Huie, 1993), which are far more prevalent than I in the stratosphere.

The ozone depletion potential of fluorocarbons is essentially zero because, unlike the other halogens, atomic F is quickly converted to the hydrogen halide, HF, which is chemically and photolytically inert. On the other hand, any organic molecule which contains F will absorb infrared radiation in the atmospheric window region between 800 and 1400 cm^{-1} and will, therefore, have a nonzero global warming potential (GWP). Differences in the GWPs of these compounds are determined primarily by how long they survive in the troposphere.

On the basis of this analysis it is apparent that the most effective suppressants will contain the ozone depleting halogens Br or I. These compounds will almost certainly contain F, as well, since the substitution of F for H atoms is usually necessary to reduce flammability and increase volatility. On this basis, it is clear that low values of both ODP and GWP will be realized only in compounds which have short tropospheric lifetimes (τ_l). Thus, in the process of identifying replacement agents, their propensity to engage in one or more of the following processes which can remove these chemicals from the troposphere was a major concern:

1. reaction with OH radicals;
2. photolysis by long wavelength ($>$ 290 nm) UV-VIS radiation; and
3. hydrolysis and/or solvation in H_2O.

5.3.2 Methods. An exploratory list of 103 potential halon alternatives representing 10 distinct chemical families was cited in NIST TN 1279 (Pitts *et al.*, 1990). This document served as the point of departure and was augmented as new possibilities arose during the course of this investigation.

A short list was constructed from the most promising exploratory compounds. These candidates were selected on the basis of fire suppression effectiveness , suitability for total flooding applications in aircraft dry bays and engine nacelles, commercial availability and ODP. Other properties, including GWP and acute toxicity were also taken into consideration.

The results of cup burner and other fire suppression measurement techniques were available for many of the exploratory compounds (Purdue Research Foundation, 1950; Sheinson, *et al.* 1989; Zallen, 1992). Additional cup burner measurements (see Table 7 of Section 4) were conducted on representative compounds from chemical families which were rated highly with respect to the other

Table 7. ODP, GWP and τ_1 of Selected HCFCs

Formula	HCFC	τ_1	ODP	GWP
$CHCl_2CF_3$	123	1.6	0.016	0.19
CH_3CCl_3	NA	6.3	0.11	0.024
$CHClFCF_3$	124	6.6	0.019	0.10
CH_3CCl_2F	141b	7.8	0.080	0.092
$CHClF_2$	22	15.3	0.051	0.36
CH_3CClF_2	142b	19.1	0.056	0.37

Values taken from Fischer *et al.*, 1989.

selection criteria but for which there were no data relating to their effectiveness as flame suppressants. Compounds requiring suppression concentrations significantly higher than the core candidates were eliminated from further consideration.

Volatility is a critical factor in agent dispersal. Compounds having boiling points above ambient temperature (25 °C), with the possible exception of powders, are not suitable for total flooding applications and were not considered any further.

This investigation was primarily directed at finding near-term solutions to the urgent problem created by the production phaseout of halon 1301. The time and expense involved in developing the capability to produce a new agent was considered prohibitive. Consequently, any compound appearing on the exploratory list which could not be purchased from a commercial vendor was eliminated from further consideration. It will be beneficial to remove this limitation in future investigations directed at identifying second-generation halon replacement candidates.

The hypothesis that τ_1 is a reasonable predictor of both ODP (Herron, 1990) and GWP (Herron, 1990) is confirmed by the data listed in Table 7 and plotted in Figures 27 and 28. Qualitative assessments of τ_1, and consequently of environmental impact, can be made on the basis of SARs pertaining to the specific chemical family under consideration. Thus, for example, saturated halocarbons (SH) can react with OH if they have a labile C-H bond. The presence of certain functional groups, such as an ether (HE) or carbonyl (HK) oxygen, increase the absorption cross-section for UV-VIS radiation and can activate C-H bonds for abstraction of H by OH (Zhang *et al.*, 1992a). Similarly, OH radicals are known to attack π bonds in unsaturated halocarbons (UH). Many inorganic compounds, including the silicon, germanium (SG), sulfur (S) and phosphorous (P) halides have a tendency to hydrolyze, while metallic compounds (M) are frequently water soluble. The presence of a heavy halogen, particularly I (HI), shifts the absorption spectrum of the compound to the red and thereby increases the likelihood that these compounds will photolyze in the troposphere. This is especially true if there are multiple halogens bonded to the same carbon.

More reliable assessments of τ_1 can be made on the basis of laboratory measurements. At NIST, rate constants for reaction with OH (k_{OH}) have been measured by flash photolysis resonance fluorescence (Kurylo and Braun, 1976). In this technique, a small fraction of the OH radicals generated by photolysis of H_2O are excited by exposure to a high intensity lamp. The time dependent concentrations are monitored by detecting the emissions of resonant radiation from OH at 308 nm with a photomultiplier. A discharge flow technique coupled with electron paramagnetic resonance detection of OH has also been used to measure the OH rate constants for many halogen-containing compounds (Orkin and Khamaganov, 1993a). In either case, the rate constants for the pseudo first-order reaction (*i.e.* [RX] > > [OH]) are given by

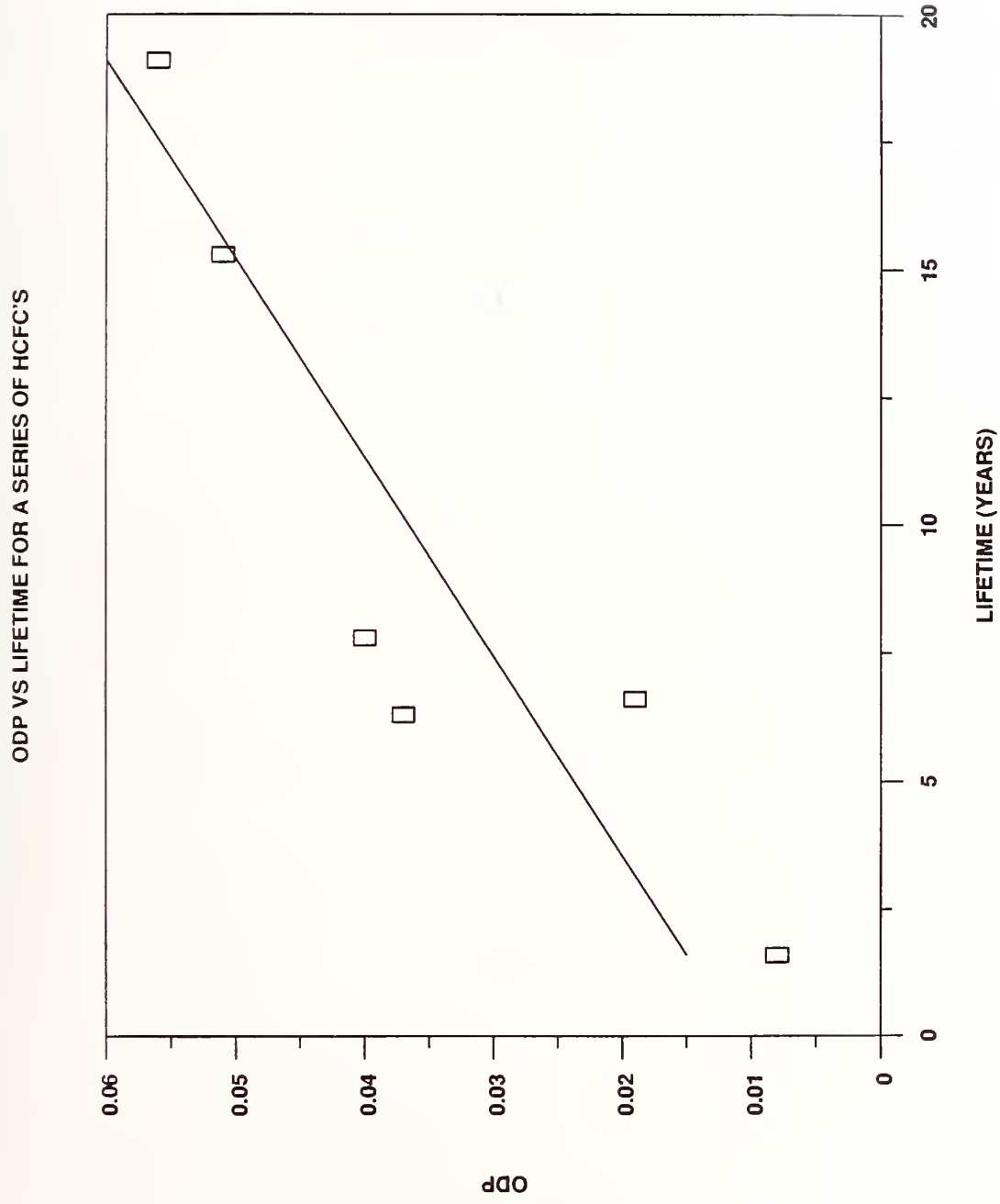

Figure 27. ODP, normalized by dividing the computed value by the number of Cl atoms in the molecule, plotted as a function of tropospheric lifetime.

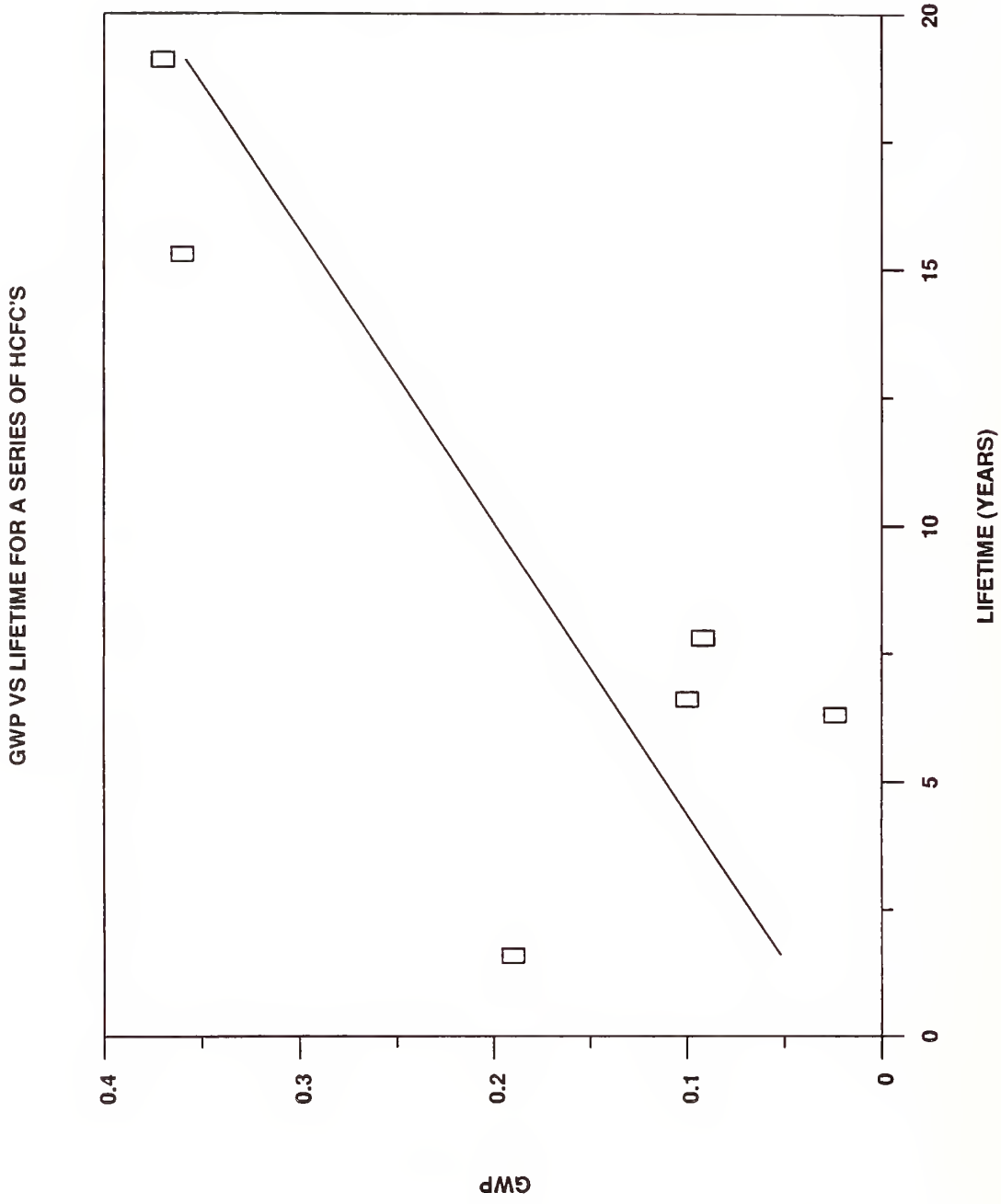

Figure 28. GWP plotted as a function of tropospheric lifetime.

$$k_{OH} = -\frac{1}{[RX]}\frac{dln[OH]}{dt}, \tag{7}$$

where RX denotes the compound under investigation and square brackets are used to indicate concentrations. According to Ahrrenius theory, the temperature dependence of the rate constant is given in Equation (8).

$$k = A\ \exp(\frac{-E_a}{RT}), \tag{8}$$

where R is the gas constant and T is the temperature in Kelvins. The kinetic constants, A and E_a, are the bimolecular collision frequency and activation energy (energy barrier for the reaction), respectively.

In lieu of performing simulations with an atmospheric model, tropospheric lifetimes were estimated from

$$\tau_l = 7.0\frac{k_{MC}(277)}{k_s(277)}, \tag{9}$$

where $k_{MC}(277)$ and $k_s(277)$ are the rate constants for the reactions of methyl chloroform (CH_3CCl_3) and the alternative agent with OH at 277 K and 7.0 is the lifetime (in years) of CH_3CCl_3 (Zhang *et al.*, 1992b). Methyl chloroform is used as a standard because it has an intermediate τ_l, which is useful for modeling the atmospheric transport of a wide range of compounds, and it is known to have only anthropogenic sources. Kinetic constants for some representative compounds are listed in Table 8.

Experimental measurements of OH reactivity are very expensive. Painstaking efforts have to be taken to ensure sample purity because trace amounts of a reactive contaminant will invalidate the results. In the present investigation, measured rate constants were supplemented with values obtained from correlations between τ_l and C-H bond dissociation energies (BDEs). The basis of these correlations is the hypothesis that the rate determining step in the reaction between OH and saturated halocarbons is the abstraction of a H to form H_2O. This process requires breaking a C-H bond in the halocarbon. The natural logarithm of τ_l (Fischer *et al.*, 1989) is plotted as a function of the smallest C-H BDE (McMillan and Golden, 1982) in the molecule for a series of HFCs in Figure 29. The linearity of this plot confirms the validity of this hypothesis.

Experimental determinations of BDEs are difficult to make and are subject to large errors, however, recent advances in the theory and application of molecular quantum mechanics have made the calculation of chemically accurate BDEs in small halocarbons almost routine (Curtiss *et al.*, 1991). The C-H and C-X BDEs were computed for some small molecules using a variety of *ab initio* methods including: local (LDA) and nonlocal density functional approximations (NLDA); Hartree-Fock (HF) and HF corrected to fourth order in the Moller-Plesset perturbation expansion of the energy (MP4); and the Gaussian-G1 (G1) and -G2 (G2) procedures. The results of these calculations are listed in Tables 9 and 10. The rms error from the experimental BDEs (McMillan and Golden, 1982) for the fluoro- and chloromethanes corresponding to the most accurate calculations (G2) are less than 5 kJ/mole and 10 kJ/mole, respectively.

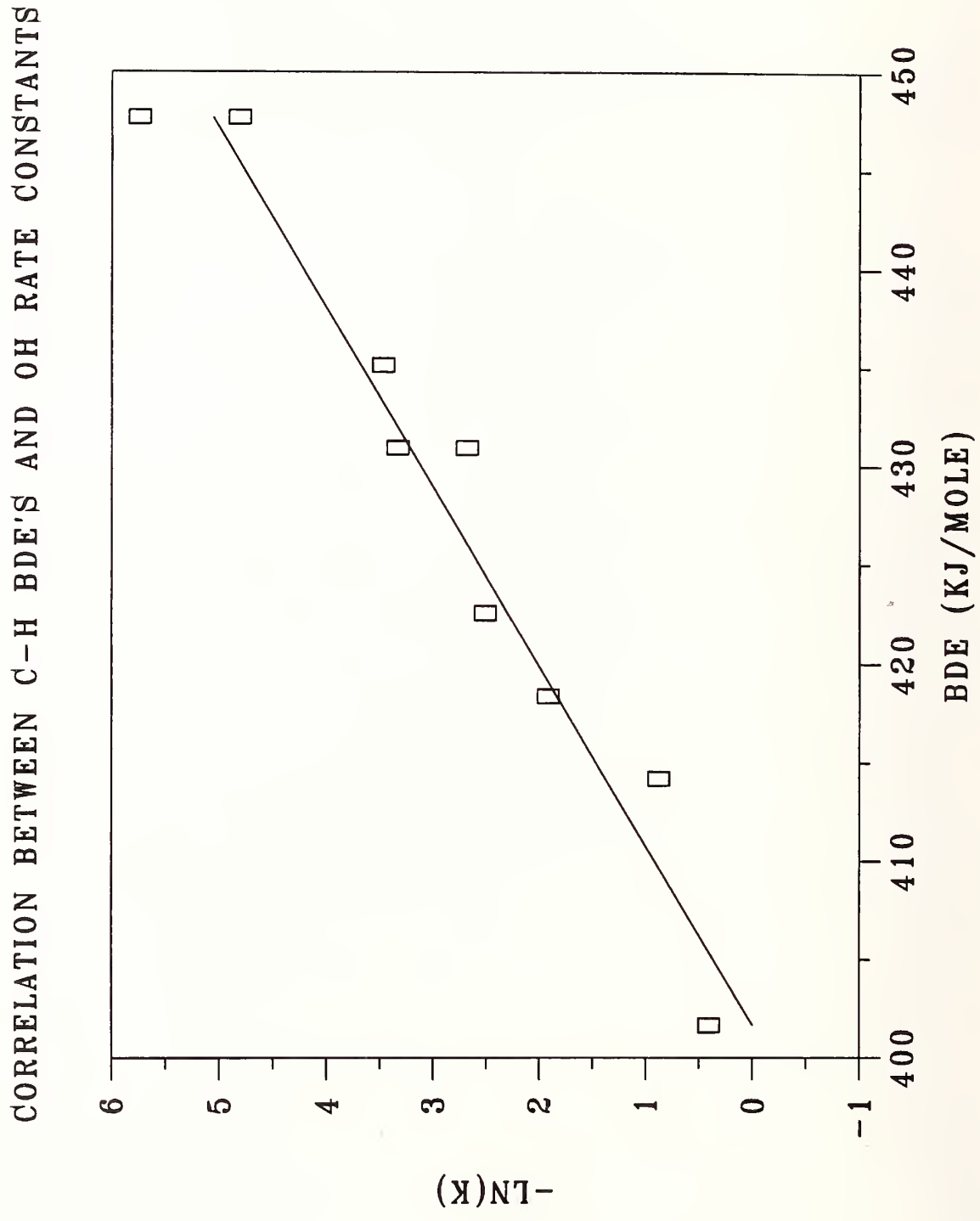

Figure 29. Tropospheric lifetime plotted as a function of C-H BDE.

Table 8. OH Kinetic Constants and τ_1's of Selected Compounds

Compound	A (x 10^{12})[a]	E_a/R (K)	τ_1(years)[b]
Substituted Methanes			
CH_4	7.0	2061	12.8
CHF_3	0.49	2115	192
CHF_2Cl	0.81	1516	14.0
CHF_2Br	0.93	1326	6.8
Substituted Ethanes[c]			
CH_3CH_3	7.8	1020	0.27
CH_2FCF_3	1.03	1588	14.3
CH_2BrCF_3	0.85	1113	3.4
$CHClBrCF_3$	1.28	995	1.6
Substituted Ethenes			
$CH_2=CH_2$	2.03	-411	0.0047
$CH_2=CHBr$	1.8	-405	0.0068
$CF_2=CCl_2$	1.5	-480	0.0062

a. In units of cm^3 $molecule^{-1}$ s^{-1}.
b. From Equation 9.
c. Orkin and Khamaganov, 1993a and 1993b.

Table 9. C-H and C-F BDEs in the Fluoromethanes, kJ/mol

Bond	LDA[a]	NLDA[a]	HF[b]	MP4[b]	G1[b]	G2[b]	Exp.[c]
CH_3-H	494	464	362	458	434	435	440
CH_2F-H	464	447	353	440	422	424	424
CHF_2-H	458	496	354	441	422	424	432
CF_3-H	482	461	462	462	443	445	447
CH_3-F	570	478	273	447	462	463	460
CH_2F-F	599	502	322	488	503	505	500
CHF_2-F	621	565	359	520	535	537	534
CF_3-F	629	510	374	533	548	551	546

aBiosym Technologies, Inc., 1992.
bFrisch, M.J., *et al* , 1992.
cMcMillan and Golden., 1982.

Table 10. C-H and C-Cl BDEs in the Chloromethanes, kJ/mol

Bond	LDA[a]	NLDA[a]	HF[b]	MP4[b]	G1[b]	G2[b]	Exp.[c]
CH_3-H	494	464	362	458	434	435	440
CH_2Cl-H	4654	4444	3513	4184	4164	4164	4224
CH_2Cl-H							
$CHCl_2$-H	431	419	338	401	401	401	414
CCl_3-H	415	401	322	385	390	390	401
CH_3-Cl	376	351	226	340	349	347	354
CH_2Cl-Cl	334	320	200	318	337	334	335
$CHCl_2$-Cl	304	286	165	291	321	315	325
CCl_3-Cl	272	247	128	265	301	297	306

[a]Biosym Technologies, Inc., 1992.
[b]Frisch, M.J. *et al.*,992.
[c]McMillan and Golden, 1982.

Table 11. Photolytic Rate Constants and τ_1's of Selected Compounds[a]

Compound	k_p	τ_1 (years)[b]
CF_2ClBr	2.2×10^{-9}	14
CF_2Br_2	2.3×10^{-8}	1.3
CF_3I	6.4×10^{-6}	0.0047

[a]Herron, 1990 and references therein.
[b]From Equation 11.

Rate constants for photolysis were obtained from

$$k_p = \int f\sigma d\lambda, \tag{10}$$

where the integral is over the wavelength range of atmospherically accessible solar radiation, f is the solar flux of photons, and σ is the measured UV-VIS absorption cross-section. Values for representative compounds are listed in Table 11. In this approximation, the quantum yield for photodissociation is assumed to be unity. Tropospheric lifetimes were estimated from

$$\tau_l = \frac{3 \times 10^{-8}}{k_p}, \tag{11}$$

where the factor in the numerator converts from seconds to years.

5.3.2.2 Exploratory List. The plan of work for this task was based on a strategic organization of the candidates into four working categories. The first of these, hereafter referred to as Category I, comprise the 41 halocarbons identified in NIST TN 1279 which contain at least one Cl, Br or I atom. These compounds are listed in Table 12. Unfortunately, all Category I compounds have some potential for ozone depletion and global warming. The expectation was, however, that the environmental impact of some of these compounds would be acceptable due to their reactivity with OH radicals, or their tendencies to undergo photolysis in the troposphere.

The Category II candidates, which are listed in Table 13, are the complementary set of halocarbons which contain F as the only halogen. As a group, fluorocarbons are much less effective as fire suppressants than are the analogous compounds containing Br or I (see Table 7 of Section 4). All of the compounds in this category are considered to have zero ODP; however, GWP was an important consideration.

Category III consists of the halogen-containing inorganic compounds identified in NIST TN 1279 (Table 14). Many of these compounds, for example CrO_2Cl_2 and $SnCl_4$, are highly toxic and are, therefore, not viable halon replacement candidates. The justification for their further consideration was that some are extremely effective flame inhibitors. The expectation was that new and important principles would be learned in the process of evaluating and comparing their effectiveness as fire suppressants and that these insights could be immediately applied to further the primary objectives of this project.

The non-halogenated inorganic compounds identified in NIST TN 1279 were placed in Category IV. They are listed in Table 15. All have zero ODP and minimal GWP.

5.3.3 Results. The selection process was carried out in two steps. First, compounds were eliminated from the exploratory list on the basis of boiling point (BP), commercial availability (CA), and other readily available data. Core candidates (indicated by the presence of an asterisk) were evaluated elsewhere in this report (see Section 10.2) and were not explicitly included in this process.

Table 12. Category I Compounds

Compound Formula	Chemical Family	Basis for Elimination or Further Consideration
CBr_2F_2	SH	ODP[a]
$C_2Br_2F_4$	SH	BP[b]
$CHClF_2$*	SH	see Section 10.2
$C_2H_3Cl_3$	SH	BP
$C_2HCl_2F_3$	SH	BP
C_2HClF_4*	SH	see Section 10.2
$C_2H_3Cl_2F$	SH	BP
$C_2H_3ClF_2$	SH	FSN[c]
$CHBrF_2$	SH	ODP
CHBrClF	SH	BP
$C_2HBrClF_3$	SH	BP
$C_2HBrClF_3$	SH	BP
C_2HBrF_4	SH	CA[d]
$C_2H_2BrF_3$	SH	BP
$C_2HBr_2F_3$	SH	BP
$C_2H_2Br_2F_2$	SH	BP
$C_2H_2Br_2F_2$	SH	BP
C_3HBrF_6	SH	BP
$C_3H_2Br_2F_4$	SH	BP
$C_3H_2Br_2F_4$	SH	BP
$C_3H_2BrF_5$	SH	BP
CF_3COCH_2Br	HK	BP
$BrCF_2COOCF_3$	HK	BP
CF_3COOCH_2Br	HK	BP
$BrCF_2CF=CF_2$	UH	BP
$CF_3CF=CFBr$	UH	BP
$CF_3BrC=CHCF_3$	UH	BP
CHF_2OCF_2CHFCl	HE	BP
$CF_3CHClOCHF_2$	HE	BP
CF_2BrOCF_2Br	HE	CA
CF_2BrOCF_3	HE	CA
$CBrF_2OCF_2CHFCl$	HE	BP

Table 12. Category I Compounds

Compound Formula	Chemical Family	Basis for Elimination or Further Consideration
BrC_4F_7O	HE	BP
CF_3I	HI	short list
CF_2ClI	HI	CA
CF_2BrCF_2I	HI	BP
CF_2ICF_2I	HI	BP
CH_3I	HI	BP
CH_3CH_2I	HI	BP
$CH_3CH_2CH_2I$	HI	BP
$CF_3CF_2CF_2I$	HI	BP

a. ozone depletion potential
b. boiling point
c. fire suppression number (see the definition given in Section 4.5.5.3)
d. commercial availability
* core candidate

Table 13. Category II Compounds

Compound	Family	Basis for Elimination or Further Consideration
CF_4	SH	FSN
C_2F_6*	SH	see Section 10.2
C_3F_8*	SH	see Section 10.2
C_4F_{10}*	SH	see Section 10.2
C_4F_8*	SH	see Section 10.2
CHF_3	SH	FSN
C_2HF_5*	SH	see Section 10.2
$C_2H_2F_4$*	SH	see Section 10.2
CF_3COCF_3	HK	FSN
$CF_3COOCOCF_3$	HK	BP
$(iC_3F_7)_2CO$	HK	BP
CF_3COOCH_3	HK	BP
C_3F_6	UH	short list
C_4F_8	UH	FSN
$CF_3C_6H_5$	UH	BP
$CF_3CH=CF_2$	UH	short list
$CF_2CH=CHCF_3$	UH	FSN
$CF_3CH=CH_2$	UH	FSN
$(C_4F_9)CH=CH(C_4F_9)$	UH	BP
$(CF_3)_2C=C(CF_3)_2$	UH	BP
CHF_2OCHF_2	HE	FSN
CHF_2OCF_3	HE	FSN
$C_4F_9C_4F_7O$	HE	BP
C_4F_8O	HE	BP
CF_3SCF_3	HE	CA
$(CF_3)_3N$	HE	CA

Table 14. Category III Compounds

Compound	Chemical Family	Basis for Elimination or Further Consideration
SF_6	S	FSN
SF_5Cl	S	FSN
SF_5Br	S	CA
PF_3	P	hazardous
PCl_3	P	BP
PF_2Br	P	CA
POF_3	P	hazardous
$POCl_3$	P	BP
POF_2Br	P	BP
$SiCl_4$	SG	BP
$SiCl_3F$	SG	CA
SiF_4	SG	short list
$SiBrF_3$	SG	CA
$SiBr_{3F}$	SG	BP
$Si(CH_3)_3Cl$	SG	BP
$SiCH_3Cl_3$	SG	BP
$Si(CH_3)_3CH_2Cl$	SG	BP
$GeCl_4$	SG	BP
CrO_2Cl_2	M	BP
$SnCl_4$	M	BP
$TiCl_4$	M	BP

The major reason for the elimination of each exploratory compound is noted next to its chemical formula in Tables 12-15. Although values for ODP and relative fire suppression efficiency, as indicated by fire suppression number (FSN) (Section 4.5.5.3), could not be found for every compound on the exploratory list, a reasonable assessment could usually be made on the basis of measured values obtained for other members from the same chemical family. Those candidates which were considered to merit further study, as well as, a few additional possibilities which arose during the course of this investigation, were included in a short list of compounds. These compounds were evaluated in the second step of the search process.

Table 15. Category IV Compounds

Compound	Chemical Family	Basis for Elimination or Further Consideration
$Si(CH_3)_4$	SG	BP
$Ge(CH_3)_4$	SG	CA
$NaHCO_3$	M	see Section 10.2
$NaC_2H_3CO_2$	M	BP
$KHCO_3$	M	BP
$K_2C_2O_4 \bullet H_2O$	M	BP
$KC_2H_3CO_2$	M	BP
$K_2C_5H_7O_2 \bullet \frac{1}{2}H_2O$	M	BP
$Cr(C_5H_7O_2)_3$	M	BP
$Pb(C_2H_5)_4$	M	BP
$Fe(CO)_5$	M	BP
N_2	I	FSN
CO_2	I	FSN
Ar	I	FSN

5.3.3.1 Development of the Short List. The fire suppression characteristics of the chlorocarbons are comparable to their fluorocarbon analogs (see Table 7 of Section 4). Two of these compounds, $CF_2=CClF$ and $CHFCl_2$, appeared to offer promising atmospheric properties, as well. The ozone destruction efficiency of Cl is significantly less than that of Br. Thus, for example, the ODP of CHF_2Cl is only 0.055, whereas the ODP of CHF_2Br is 1.4 (Pyle *et al.*,991). The presence of a π bond ensures that the τ_1 of $CF_2=CClF$ will be short (see Table 8) which suggests that both the ODP and GWP will be low. The computed BDE for the C-H bond in $CHFCl_2$ is 398 kJ/mole which is 17 kJ/mole less than the C-H BDE in CHF_2Cl. On the basis of the correlation in Figure 29, this effect should correspond to an order of magnitude reduction in τ_1. Consequently, the ODP of $CHFCl_2$ should be significantly lower than 0.055 even though it contains twice as many ozone depleting halogens as CHF_2Cl.

The brominated methanes, particularly CF_2Br_2 and $CFBr_3$, were of further interest. The presence of multiple Br atoms ensures a low FSN and imparts a significant cross-section for the absorption of long wavelength UV-VIS radiation which, in turn, increases the likelihood that these compounds will be photolyzed in the troposphere (see Table 13). The possibility that one of the brominated ethanes might be viable was raised by recent results obtained for $CF_3CHBrCl$ (Orkin and Khamaganov, 1992b). The best estimate ODP for this compound is 0.14 (Pyle *et al.*,1991) which is almost at the upper limit of acceptability. The brominated ethenes, $CF_2=CFBr$ and $CF_2=CHBr$, are reactive with OH and were also expected to have acceptable ODPs.

Table 16. The Short List of Candidates

Family	Chemical Formula	Basis for Elimination or Further Consideration
Category I		
Chlorinated Methanes	$CHFCl_2$	FSN (2.9)
Chlorinated Ethenes	$CF_2=CClF$	FSN (2.8)
Brominated Methanes	CHF_2Br, CF_2Br_2, $CFBr_3$	ODP (1.4, 1.25) BP (107 °C)
Brominated Ethanes	CH_2BrCF_3	BP (26 °C)
Brominated Ethenes	$CF_2=CFBr$, $CF_2=CHBr$	FSN (2.3, 1.9)
Iodocarbons	CF_3I	recommended
Category II		
Fluorinated Ethenes	$CF_2=CFCF_3$	FSN (2.5)
Category III		
Silicon Compounds	SiF_4	FSN (3.3)
Nitrogen Compounds	NF_3	FSN (oxidizer)

The iodocarbons are effective suppressants (Nimitz and Lankford, 1993) and they are known to be light sensitive, which suggests that they will be photolyzed in the troposphere. The iodine analog of halon 1301, CF_3I, was considered particularly attractive because it also has a low boiling point (-22.5 °C) which makes it suitable for total flooding applications.

All of the compounds in Category II have zero ODP; however, the high GWP of the saturated fluorocarbons on the exploratory list might play an important role in determining whether they can be used as fire extinguishants. Many of these compounds are core candidates and were already undergoing thorough testing. Thus, in an effort to avoid a duplication of effort, the decision was made to focus on the unsaturated fluorocarbons. Particular attention was placed on compounds, such as $CF_2=CHCF_3$ and $CF_2=CFCF_3$, where the C-F bond might be weakened by resonance stabilization in the radical. The rationale was the hypothesis that the exceptionally strong C-F bonds, which characterize most of the fluorocarbons, might have an adverse effect on their effectiveness as flame suppressants.

Similar reasoning was used to justify the further consideration of two inorganic halides, SiF_4 and NF_3. The former compound readily hydrolyzes to HF and silanol in the atmosphere, whereas the N-F bonds in the latter molecule are exceptionally weak.

5.3.3.2 Recommendations. The short list is presented in Table 18 along with the primary reason for the elimination of each candidate. The FSNs of the chlorinated methanes and ethenes, the fluorinated ethenes, and SiF_4 were noticeably worse than the corresponding values obtained for the leading candidates from the core list. The brominated ethenes were a little better, but not enough to warrant the recommendation of a Br-containing compound. NF_3 was disqualified because it behaved

as an oxidizer resulting in a visible increase in the intensity of the cup burner flame. Two of the compounds on the short list, CHF_2Br and CF_2Br_2, were eliminated because their ODPs were unacceptably high, as were the boiling points of $CFBr_3$ and CH_2BrCF_3. The boiling point of the former compound was mistakenly reported as 10.7 °C in some of the relevant literature (Zallen, 1992). The actual boiling point of $CFBr_3$ is 107 °C. On the basis of the reasoning presented in this section, it was determined that CF_3I is the only candidate which merits further consideration with respect to the near term applications of the sponsor.

The concentration of CF_3I required to extinguish the cup burner flame was 3.2 $\pm$ 0.3% by volume. This is almost identical to the value obtained for halon 1301 (3.1%). The UV-VIS cross-section for CF_3I is displayed in Figure 30. The short τ_1 of this molecule is attributable to the tail of this curve which extends to wavelengths beyond 290 nm where there is an appreciable solar flux at ground-level.

Detonation and deflagration suppression tests (see Section 4.5) have indicated that CF_3I is the most effective agent tested (including halon 1301) at mole fractions less than about 3%. Its effectiveness in suppressing detonation, however, diminished at higher concentrations, eventually becoming one of the least effective agents at concentrations exceeding 6%. The C-I bond in CF_3I is very weak. The results obtained from photofragmentation translational spectroscopy indicate that the corresponding BDE is about 223 kJ/mole (Felder, 1992). This suggests that reactivity, particularly when in the presence of metals which can function as heterogeneous catalysts, may present a significant problem. Indeed, the results of coupon corrosion tests have indicated the possibility of aggressive interactions between CF_3I and both AM355 and CD172 (see Section 7.2).

Atmospheric modeling of CF_3I was performed by the Atmospheric and Geophysical Sciences Division at Lawrence Livermore National Laboratory. This effort was intended to be a first attempt at a solution to a difficult problem. Computed values for the ODP of CF_3I , particularly for releases at altitude, should be considered as preliminary estimates due to the presence of a number of serious data gaps in the stratospheric chemistry of iodine. These include (Miziolek, 1993):

1. the absence of rate constants and branching ratios for the critical reactions of IO with BrO and ClO;
2. no measurements of the rate of photolysis of IO; and
3. no studies of the temperature dependencies of the reactions of IO with HO_2 and O.

The calculations performed at LLNL were based on the extended IOx chemistry which uses bromine analog rate constants for the reactions of IO with ClO, OH and NO_3, as well as, for the reaction of HI with O. The values obtained for the ODP and tropospheric lifetime corresponding to a ground-level release were 0.011 and 1.15 days, respectively. These findings are consistent with the previous estimates made by Susan Solomon. The LLNL group also performed a simulated high altitude release of CF_3I at 19.5 km (over latitudes extending from 23.5 to 58.2 degrees N). They calculated an ODP of 13.7 and a lifetime of 9.05 hours. Please note that the ODP value for the release of CF_3I at altitude is very close to the ground level ODP of CF_3Br ($\sim$ 16). This is an artifact of the extended IOx chemistry used in the LLNL model which assumes that the stratospheric chemistry of I is essentially identical to that of Br.

5.3.4 Conclusions. CF_3I is a viable candidate for the replacement of halon 1301. This is the first iodine-containing compound to be seriously considered. Other members of this family may have applications as fire extinguishants, and as refrigerants and foam blowing agents, as well. Every effort should be made to resolve the uncertainties in the stratospheric chemistry of iodine so that there is a clear path to examine all of the potential uses of these compounds.

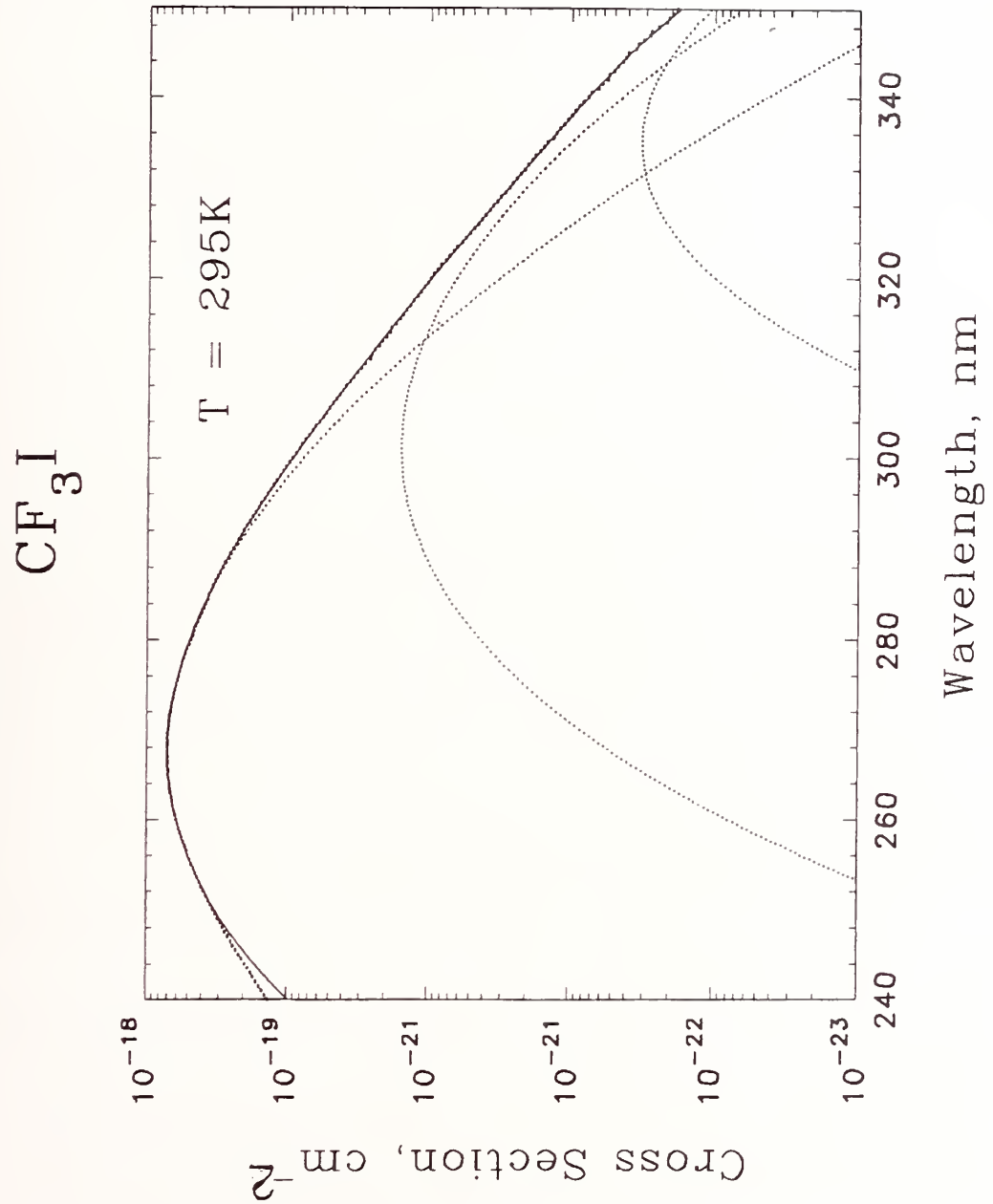

Figure 30. Absorption Cross-Section for CF_3I. The smooth curve was obtained by fitting the discrete absorption data to 3 Gaussians (dotted lines).

The research reported in this section is the first step in a rationale approach to the search for new and more effective fire fighting chemicals. Additional research, directed at developing the capability to predict key properties on the basis of molecular structure, is ongoing and will determine the prospects for identifying a new generation of zero ODP, low GWP fire suppressants.

5.4 References

Aders, W.-K., Pangritz, D., and Wagner, H.Gg., "Untersuchungen zur reaktion von wasserstoffatomen mit methylfluorid, methylchlorid und methylbromid," *Ber. Bunsenges. Phys. Chem.* 79, 90-94 (1975).

Amphlett, J.C. and Whittle, E., "Reactions of trifluoromethyl radicals with iodine and hydrogen iodide," *Trans. Faraday Soc.* **63**, 2695 (1967).

Arthur, N.L. and Bell, T.N., *Can. J. Chem.* **44**, 1445 (1966).

Arthur, N.L. and Bell, T.N., "An evaluation of the kinetic data for hydrogen abstraction from the gas phase," *Rev. Chem. Intermed.* **2**, 37-74 (1978).

Arthur, N.L., Donchi, K.F., and McDonell, J.A., "BEBO calculations. Part 4. - Arrhenius parameters and kinetic isotope effects for the reactions of CH_3 and CF_3 radicals with H_2 and D_2," *J. Chem. Soc. Faraday Trans.* **71**, 2431 (1975).

Atkinson, R., Baulch, D.L., Cox, R.A., Hampson, R.F., Jr., Kerr, J.A., and Troe, J., "Evaluated kinetic and photochemical data for atmospheric chemistry. Supplement IV. IUPAC subcommittee on gas kinetic data evaluation for atmospheric chemistry," *J. Phys. Chem. Ref. Data* **21**, 1125-1568 (1992).

Atkinson, R. and Pitts, J.N., Jr., "Rate constants for the reaction of $O(^3P)$ with $CH_2{=}CHF$, $CH_2{=}CHCl$, and CH_2CHBr over the temperature range 298-442 K," *J. Chem. Phys.* **67**, 2488-2491.

Ayscough, P.B. and Polanyi, J.C., "The reactions of trifluoromethyl radicals with hydrogen isotopes," *Trans. Faraday Soc.* **52**, 961 (1956).

Bajpai, S.N., "An investigation of the extinction of diffusion flames by halons," *J. Fire and Flammability* **5**, 255 (1974).

Barnes, G.R., Cox, R.A., and Simmons, R.F., "The kinetics of the gas-phase thermal decomposition of chlorodifluoromethane," *J. Chem. Soc (B).*, 1176 (1971).

Batt, L. and Walsh, R., "A reexamination of the pyrolysis of bis-trifluoromethyl peroxide," *Int. J. Chem. Kin.* **14**, 933-944 (1982).

Baulch, D.L., Cobos, C.J., Cox, R.A., Esser, C., Frank, P., Just, Th., Kerr, J.A., Pilling, M.J., Troe, J., Walker, R.W., and Warnatz, J., "Evaluated kinetic data for combustion modeling," *J. Phys. Chem. Ref. Data* **21**, 411-429 (1992).

Baulch, D.L., Duxbury, J., Grant, S.J., and Montague, D.C., "Evaluated kinetic data for high temperature reactions. Volume 4 Homogeneous gas phase reactions of halogen- and cyanide-containing species," *J. Phys. Chem. Ref. Data* **10**, Suppl. 1, (1981).

Benson, S.W., *Thermochemical Kinetics*, Wiley, New York, 1976.

Berces, T., Marta, F., and Szilagyi, I., "Reactions of CF_3 radicals with benzotrifluoride and the C-H bond strength in $C_6H_5CF_3$ and C_6H_6," *J. Chem. Soc. Faraday Trans.* **68**, 867 (1972).

Biordi, J.C., Lazzara, C.P., and Papp, J.F., "Flame-structure studies of CF_3Br-inhibited methane flames," *Fourteenth Symposium (International) on Combustion*, The Combustion Institute, Pittsburgh, PA, 367-381 (1973).

Biordi, J.C., Lazzara, C.P., and Papp, J.F., "Flame structure studies of CF_3Br-inhibited methane flames. II," *Fifteenth Symposium (International) on Combustion*, The Combustion Institute, Pittsburgh, PA, 917-931 (1974).

Biordi, J.C., Lazzara, C.P., and Papp, J.F., "Mass spectrometric observation of difluorocarbene and its reactions in inhibition," *J. Phys. Chem.* **80**, 1042-1048 (1976).

Biordi, J.C., Lazzara, C.P., and Papp, J.F., "Flame structure studies of CF_3Br-inhibited methane flames. III," *J. Phys. Chem.* **81**, 1139-1145 (1977).

Biordi, J.C., Lazzara, C.P., and Papp, J.F., "Flame structure studies of bromotrifluoromethane-inhibited methane flames. 4. Reactions of inhibitor species in flames containing initially 1.1% bromotrifluoromethane," *J. Phys. Chem.* **82**, 125 (1978).

Blauer, J.A., "The kinetics of dissociation of hydrogen fluoride behind incident shock waves," *J. Phys. Chem.* **72**, 79 (1968).

Blauer, J., Engleman, V.S., and Solomon, W.C., *Thirteenth Symposium (International) on Combustion*, The Combustion Institute, Pittsburgh PA, 109 (1971).

Booth, K., Melina, B.J., and Hirst, R., "Critical concentration measurements for flame extinction of diffusion flames using a laboratory 'cup burner' apparatus," Imperial Chemical Industries Limited, Mond Division, Cheshire UK, 31 August, 1973.

Brown, N.J., "Halogen kinetics pertinent to flame inhibition: a review," *ACS Symp. Ser.* **16**, 341-375 (1975).

Bozzelli, J.W. and Dean, A.M., "Chemical activation analysis of the reaction of C_2H_5 with O_2," *J. Phys. Chem.* **94**, 3313 (1990).

Burdon, M.C., Burgoyne, J.A., and Weinberg, F.J., "Effect of methyl bromide on combustion of some fuel-air mixtures," *Fifth Symposium (International) on Combustion*, Reinhold Publishing Corp., New York, 647 (1955).

Burke, S.P. and Schumann, T.E.W., *Ind. Eng. Chem.* **20**, 998 (1928).

Cadman, P., Day, M., and Trotman-Dickenson, A.F., "Shock tube pyrolyses. Part I. The thermal decomposition of iso-propyl chloride, ethyl fluoride, and n-propyl fluoride," *J. Chem. Soc. A*, 2498-2503 (1970).

Caralp, F., Lesclaux, R., and Dognon, A.M., "Kinetics of the reaction of CF_3 with O_2 over the temperature range 233-273 K," *Chem. Phys. Lett.* **129**, 433 (1986).

Chamberlain, G.A. and Whittle, E., "Photochemistry of anhydrides. Part 1. Photolysis of perfluoroacetic anhydrides vapour: A new source of CF_3 radicals," *J. Chem. Soc. Faraday Trans. 1* **68**, 88 (1972).

Chen, S.S., Rodger, A.S., Chao, J., Wilhoit, R.C., and Zwolinski, B.J., "Ideal gas thermodynamic properties of six fluoroethanes," *J. Phys. Chem. Ref. Data* **4**, 441-456 (1975).

Chen, Y., Rauk, A., and Tschuikow-Roux, E., "Structures, barriers for rotation and inversion, vibrational frequencies, and thermodynamic function of ethyl, α-fluoroethyl, and α,α-difluoroethyl radicals: an *ab initio* study," *J. Chem. Phys.* **93**, 1187-1195 (1990).

Chen, Y., Rauk, A., and Tschuikow-Roux, E., "Structures, barriers for internal rotation, vibrational frequencies, and thermodynamic function of CH_2FCH_2, CHF_2CH_2, and CF_3CH_2 radicals: an *ab initio* study," *J. Chem. Phys.* **93**, 6620-6629 (1990).

Chen, Y., Rauk, A., and Tschuikow-Roux, E., "Structures, barriers for internal rotation and inversion, vibrational frequencies, and thermodynamic functions of CH_2FCF_2, CHF_2CF_2, and CF_3CF_2 radicals: an *ab initio* study," *J. Chem. Phys.* **95**, 2774-2786 (1991).

Chen, Y., Rauk, A., and Tschuikow-Roux, E., "Structures, barriers for internal rotation, vibrational frequencies, and thermodynamic functions of CH_2FCHF, CHF_2CHF, and CF_3CHF radicals: an *ab initio* study," *J. Chem. Phys.* **94**, 7299-7310 (1991).

Clyne, M.A.A. and Hodgson, A., "Kinetics and detection of $F(^2P)$ atoms in a discharge flow system," *Chem. Phys.* **79**, 351 (1983).

Clyne, M.A.A. and Hodgson, A., "Absolute rate constants for the reaction of fluorine atoms with H_2, CH_2Cl_2, CH_2ClF, CH_2F_2 and $CHCl_2$," *J. Chem. Soc. Faraday Trans. 2* **81**, 443 (1985).

Clyne, M.A.A. and Holt, P.M., "Reaction kinetics involving ground and excited hydroxyl radicals. Part 2 - Rate constants for reactions of ground state OH with halogenomethanes and halogenoethanes," *Ber. Bunsenges. Phys. Chem.* **75**, 582 (1979).

Cohen, N. and Benson, S.W., "Transition-state-theory calculations for reactions of OH with haloalkanes," *J. Phys. Chem.* **91**, 162-170 (1987).

Cohen, N. and Benson, S.W., "Empirical correlations for rate coefficients for reactions of OH with haloalkanes," *J. Phys. Chem.* **91**, 171-175 (1987).

Cohen, N. and Westberg, K.R., "Chemical kinetic data sheets for high-temperature chemical reactions," *J. Phys. Chem. Ref. Data* **12**, 531 (1983).

Cohen, N. and Westberg, K.R., "Chemical kinetic data sheets for high-temperature reactions. Part II," *J. Phys. Chem. Ref. Data* **20**, 1211-1311 (1991).

Cooper, R., Cumming, J.B., Gordon, S., and Mulac, W.A., "The reactions of the halomethyl radicals CCl_3 and CF_3 with oxygen," *Radiat. Phys. Chem.* **16**, 169 (1980).

Cotton, D.H. and Jenkins, D. R., "Catalysis of radical-recombination reactions in flames by alkali earth metals," *Trans. Faraday Soc.* **67**, 730 (1971).

Cox, R.A. and Simmons, R.F., "The kinetics of the gas-phase thermal decomposition of bromodifluoro-methane," *J. Chem. Soc. B (London)*, 1625-1631 (1971).

Creitz, E.C., "A literature survey of the chemistry of flame inhibition," *J. Res. NBS* **74A**, 521-530 (1970).

Creitz, E.C., "Extinction of fires by halogenated compounds - a suggested mechanism," *Fire Technol.* **8**, 131-141 (1972).

Curtiss, L.A., Raghavachari, K., Trucks, G.W., and Pople, J.A., "Gaussian-2 theory for molecular energies of first- and second-row compounds," *J. Chem. Phys.* **94**, 7221 (1991).

Cvetanovic, R.J., "Evaluated chemical kinetic data for the reactions of atomic oxygen $O(^3P)$ with unsaturated hydrocarbons," *J. Phys. Chem. Ref. Data* **16**, 261-302 (1987).

Daubert, T.E. and Danner, R.P., "DIPPR Data Compilation of Pure Compound Properties," *NIST Standard Reference Database 17*, 1985.

Day, M.J., Stamp, V., Thompson, K., and Dixon-Lewis, G., "Inhibition of hydrogen-air and hydrogen-nitrous oxide flames by halogen compounds," *Thirteenth Symposium (International) on Combustion*, The Combustion Institute, Pittsburgh PA, 705-712 (1971).

Dean, A.M. and Westmoreland, P.R., "Bimolecular QRRK analysis of methyl radical reactions," *Int. J. Chem. Kin.* **19**, 207 (1987).

Di Nenno, P.J., Forssell, E.W., Peatross, M.J., Wong, J.T., and Maynard, M., "Thermal decomposition testing of halon alternatives," *Halon Alternatives Technical Working Conference*, Albuquerque, NM, May 11-13, 1993.

Dixon-Lewis, G., "Mechanism of inhibition of hydrogen-air flames by hydrogen bromide," *Combust. Flame.* **36**, 1-14 (1979).

DMOL, Biosym Technologies Inc., San Diego, CA, 1992.

Edwards, J.W. and Small, P.A., "Pyrolysis of chlorodifluoromethane and the heat of formation of chlorodifluoromethane and difluoromethylene," *Ber. Bunsenges. Phys. Chem.* **202**, 1329 (1964).

Edwards, J.W. and Small, P.A., "Kinetics of the pyrolysis of chlorodifluoromethane," *Ind. & Eng. Chem.* **4**, 396 (1965).

Ellis, O.C., "Extinction of petrol fires by methyl iodide," *Nature* **161**, 402-403 (1948).

Fagarash, M.B. and Moin, F.B., "Kinetics of the reaction of the CF_3 radical with ammonia," *Kinet. Catal.* **9**, 1135 (1968).

Felder, P., "The influence of the molecular beam temperature on the photodissociation of CF_3I at 308 nm," *Chem. Phys. Lett.* **197**, 425 (1992).

Fenimore, C.P. and Jones, G.W., "Flame inhibition by methyl bromide," *Combust. Flame* **7**, 323-329 (1963).

Ferreira, M.J., Hanauska, C.P., and Pike, M.T., "Thermal decomposition product results utilizing PFC-410," *Halon Alternatives Technical Working Conference*, New Mexico Engineering Research Institute, Albuquerque, NM, May 1992.

Ferreira, M.J., Hanauska, C.P., and Pike, M.T., "An update on thermal decomposition product results utilizing PFC-410," *Halon Alternatives Technical Working Conference*, New Mexico Engineering Research Institute, Albuquerque, NM, October 1992.

Filipczak, R.A., "Relative extinguishment effectiveness and agent decomposition products of halon alternative agents," *Halon Alternatives Technical Working Conference*, Albuquerque, NM, May 11-13, 1993.

Finlayson-Pitts, B.J. and Pitts, J.N., *Atmospheric Chemistry: Fundamentals and Experimental Techniques*, Wiley, New York, 1986.

Fischer, D.A., Hales, C.H., Filkin, D.L., Ko, M.K.W., Sze, N.D., Connel, P.S., Wuebbles, D.J., Isaksen, I.S.A., and Stordal, F., "Relative Effects on Stratospheric Ozone of Halogenated Methanes and Ethanes of Social and Industrial Interest," in World Meteorological Organization, Global Ozone Research and Monitoring Project - Report No. 20, *Scientific Assessment of Stratospheric Ozone: 1989* (1989).

Friedman, R. and Levy, J.B., "Inhibition of opposed-jet methane-air diffusion flames. The effects of alkali metal vapours and organic halides," *Combust. Flame* **7**, 195-201 (1963).

Frisch, M.J., Trucks, G.W., Head-Gordon, M., Gill, P.M.W., Wong, M.W., Foresman, J.B., Johnson, B.G., Schlegel, H.B., Robb, M.A., Repogle, E.S., Gomperts, R., Andres, J.L., Raghavachari, K., Binkley, J.S., Gonzalez, C., Martin, R.L., Fox, D.J., Defrees, D.J., Baker, J., Stewart, J.J.P., and Pople, J.A., Gaussian, Inc., Pittsburgh, PA, 1992.

Fristrom, R.M., "Combustion Suppression (a literature survey with commentary)," *Fire Res. Abs. Rev.* **9**, 125-152 (1967).

Fristrom, R.M. and Van Tiggelen, P., "An interpretation of the inhibition of C-H-O flames by C-H-X compounds," *Seventeenth Symposium (International) on Combustion*, The Combustion Institute, Pittsburgh, PA, 773-785 (1979).

Gann, R.G., "Initial reactions in flame inhibition by halogenated hydrocarbons," *ACS Symp. Ser.* **16**, 318-340 (1975).

Gierczak, T., Talukdar, R., Vaghjiani, G.L., Lovejoy, E.R., and Ravishankara, A.R., "Atmospheric fate of hydrofluoroethanes and hydrofluorochloroethanes: 1. Rate coefficients for reactions with OH," *J. Geophys. Res.* **96**, 5001-5011 (1991).

Goldberg, I.B. and Schneider, G.R., "Kinetic study of the reaction of F with H_2 and CF_3H by ESR methods," *J. Chem. Phys.* **65**, 147 (1976).

Gozzo, F. and Patrick, C.R., *Nature* **202**, 1329 (1964).

Gozzo, F. and Patrick, C.R., *Tetrahedron* **22**, 3329 (1966).

Halpern, C., "Effect of some halogenated hydrocarbons on the flame speed of methane," *J. Res. NBS* **70A**, 133-141 (1966) .

Handwerk, V. and Zellner, R., "Kinetics of the reactions of OH radicals with some halocarbons ($CHClF_2$, CH_2ClF, CH_2ClCF_3, CH_3CClF_2, CH_3CHF_2) in the temperature range 260-370 K," *Ber. Bunsenges. Phys. Chem.* **82**, 1161 (1978).

Hart, L.W., Grunfelder, C., and Fristrom, R.M., "The 'point source' technique using upstream sampling for rate constant determinations in flame gases," *Combust. Flame* **23**, 109-119 (1974).

Hastie, J.W., "Mass spectrometric studies of flame inhibition: analysis of antimony trihalides," *Combust. Flame* **21**, 49-54 (1973).

Heinemann, P., Hofmann-Sievert, R., and Hoyerman, K., "Direct study of the reactions of vinyl radicals with hydrogen and oxygen atoms," *Twenty-First Symposium (International) on Combustion*, The Combustion Institute, Pittsburgh, PA, 865 (1988).

Herron, J.T., "Ozone Depletion Potential," in *Preliminary Screening Procedures and Criteria for Replacements for Halons 1211 and 1301*, TN 1278, National Institute of Standards and Technology, Gaithersburg, MD, 74, 1990.

Herron, J.T., "Global Warming Potential," in *Preliminary Screening Procedures and Criteria for Replacements for Halons 1211 and 1301*, TN 1278, National Institute of Standards and Technology, Gaithersburg, MD, 74, 1990.

Herron, J.T. and Huie, R.E., "Rate constants for the reactions of atomic oxygen with organic compounds in the gas phase," *J. Phys. Chem. Ref. Data* **2**, 467-518 (1973).

Hidaka, Y., Nakamura, T., and Kawano, H., "High temperature pyrolysis of CF_3H in shock waves," *Chem. Phys. Lett.* **187**, 40-44 (1991).

Ho, W.-P., Barat, R.B., and Bozzelli, J.W., "Thermal reactions of CH_2Cl_2 in H_2/O_2 mixtures: implication for chlorine inhibition of CO conversion to CO_2," *Combust. Flame* **88**, 265-295 (1992).

Hoke, S.H. and Herud, C., "Real-time analysis of Halon degradation products," *Halon Alternatives Technical Working Conference*, Albuquerque NM, May 11-13, 1993.

Homann, K.H. and Poss, R., "The effect of pressure on the inhibition of ethylene flames," *Combust. Flame,* **18**, *300-302* (1972).

Howard, C.J. and Evenson, K.M., "Rate constants for the reactions of OH with CH_4 and fluorine, chlorine, and bromine substituted methanes at 296 K," *J. Chem. Phys.* **64**, 197 (1976).

Hsu, D.S, Umstead, M.E., and Lin, M.C., *ACS Symp. Ser.* **66**, 128 (1978).

Huie, R.E., personal communication, October, 1993.

Ibiricu, M.M. and Gaydon, A.G., "Spectroscopic studies of the effect of inhibitors on counter-flow diffusion flames," *Combust. Flame* **3**, 51-62 (1964).

Jacobs, T.A., Giedt, R.R., and Cohen, N., "Kinetics of decomposition of HF in shock waves," *J. Chem. Phys.* **43**, 3688 (1965).

Jensen, D.E. and Jones, G.A., "Alkaline earth flame chemistry," *Proc. Roy. Soc. London A* **364**, 509 (1978).

Jensen, D.E. and Jones, G.A., "Kinetics of flame inhibition by sodium," *J. Chem. Soc. Faraday Trans.* **78**, 2843 (1982),.

Jeong, K.-M., Hsu, K.-J., Jeffries, J.B., and Kaufmann, F.J., "Kinetics of the reactions of OH with C_2H_6, CH_3CCl_3, $CH_2ClCHCl_2$, $CH_2ClCClF_2$, and CH_2FCF_3," *J. Phys. Chem.* **83**, 1222 (1984).

Jeong, K.-M. and Kaufmann, F., "Kinetics of the reaction of hydroxyl radical with methane and with nine Cl- and F-substituted methanes. 1. Experimental results, comparisons, and applications," *J. Phys. Chem.* **86**, 1808 (1982).

Jones, D.S. and Moss. S.J., "Arrhenius parameters for reactions of oxygen atoms with the fluorinated ethylenes," *Int. J. Chem. Kin.* **6**, 443 (1974).

Jorrissen, W.P., Booy, J., and Van Heiningen, J., "On the prevention of explosive reactions in gas and vapour mixtures by small amounts of various substances," *Rec. Trav. Chim.* **51**, 868-877 (1932).

Jorrissen, W.P. and Meuwissen, J.C., "On the influence of some noninflammable vapours of organic liquid on the limits of inflammability of methane air mixtures. II.," *Rec. Trav. Chim.* **38**, 589-597 (1924).

Jourdain, J.-L., Le Bras, G., and Combourieu, J., "Etude cinetique des reactions du 1,1,1-trifluoro, 2-chloroethane avec les atomes de chlore et d'oxygene," *J. Chim. Phys.* **75**, 318 (1978).

Keating, E.L. and Matula, R.A., "The high temperature oxidation of tetrafluoroethylene," *J. Chem. Phys.* **66**, 1237 (1977).

Kee, R.J., Grcar, J.F., Smooke, M.D., and Miller, J.A., "A Fortran Program for Modeling Steady Laminar One-Dimensional Premixed Flames," *SAND85-8240*, Sandia National Laboratories, 1985.

Kerr, J.A. and Parsongage, M.J., *Evaluated Kinetic Data on Gas Phase Hydrogen Transfer Reactions of Methyl Radicals*, Butterworths, London, 1976.

Kerr, J.A. and Timlin, D.M., "Hydrogen abstraction from organosilicon compounds. The reactions of fluoromethyl radicals with tetramethylsilane. Polar effects in gas phase reactions," *Int. J. Chem. Kin.* **3**, 69-84 (1971).

Kibby, C.L. and Weston, R.E., Jr., "Photolysis of hexafluoroacetone in the presence of H_2, D_2, and HD. Kinetic isotope effects in the reaction of CF_3 with molecular hydrogen," *J. Chem. Phys.* **49**, 4825 (1968).

Kochubei, V.F. and Moin, F.B., *Kinet. Catal.* **10**, 405 (1969).

Kochubei, V.F. and Moin, F.B., "Kinetics of high-temperature reaction of atomic hydrogen with CO_2 and CF_4," *Kinet. Catal.* **11**, 712-721 (1971).

Kochubei, V.F., Gavriliv, A.P., Moin, F.B., and Pazderskii, Yu. A., "Reaction kinetics of thermal 1,1-difluoroethane decomposition," *Kinet. Catal.* **21**, 558 (1980).

Kondratiev, V.N., "Rate Constants of Gas Phase Reactions," *NBS COM-72-10014*, (1974).

Kudchadker, S.A. and Kudchadker, A.P., "Ideal gas thermodynamic properties of $CH_{4-(a+b+c+d)}F_aCl_bBr_cI_d$ halomethanes," *J. Phys. Chem. Ref. Data* **7**, 1285-1307 (1978).

Kushina, I.D., Bel'ferman, A.L., and Shevchuk,V.U., "Kinetic regularities of the thermal transformation of dichlorofluoromethane," *Kinet. Catal.* **13**, 758-764 (1972).

Kurylo, M.J. and Braun, W., "Flash Photolysis Resonance Fluorescence Study of the Reaction $Cl + O_3 \rightarrow ClO + O_2$ Over the Temperature Range 213 - 298 K," *Chem. Phys. Lett.* **37**, 232 (1976).

Larsen, E.R., "Mechanism of flame inhibition I: The role of halogens," *JFF/Fire Retardant Chem.* **1**, 4-12 (1974).

Larsen, E.R., "Mechanism of flame inhibition II: A new principle of flame suppression," *JFF/Fire Retardant Chem.* **2**, 5-20 (1975).

Lask, G. and Wagner, H.G., "Influence of additives on the velocity of laminar flames," *Eighth Symposium (International) on Combustion*, The Combustion Institute, Pittsburgh, PA, 432-438 (1962).

Lias, S.G., Karpas, Z., and Liebman, J.F., "Halomethylenes: effects of halogen substitution on absolute heats of formation," *J. Am. Chem. Soc.* **107**, 6089-6096 (1985).

Liu, R., Huie, R.E., and Kurylo, M.J., "Rate constants for the reactions of the OH radical with some hydrochlorofluorocarbons over the temperature range 270-400 K," *J. Phys. Chem.* **94**, 3247 (1990).

Mahmud, K., Marshall, P., and Fontijn, A., "A high-temperature photochemistry kinetics study of the reaction of $O(^3P)$ atoms with ethylene from 290-1510 K," *J. Phys. Chem.* **91**, 1568 (1987).

Mallard, W.G, Westley, F., Herron, J.T., Hampson, R.F., and Frizzell, D.H., "NIST Chemical Kinetics Database - Ver. 5.0," *NIST Standard Reference Database 17*, 1993.

Manning, R.G., Grant, E.R., Merrill, J.C., Parks, N.J., and Root, J.W., "Hydrogen abstraction by fluorine atoms under conditions of thermal initiation: Hydrocarbons and fluorinated hydrocarbons," *Int. J. Chem. Kinet.* **7**, 39 (1975).

Manocha, A.S., Setser, D.W., and Wickramaaratchi, M.A., "Vibrational energy disposal in reactions of fluorine atoms with hydrides of groups III, IV, and V," *J. Chem. Phys.* **76**, 129 (1983).

Maricq, M.M. and Szente, J.J., "Flash photolysis-time-resolved UV absorption study of the reactions $CF_3H + F \rightarrow CF_3 + HF$ and $CF_3 + O_2 \rightarrow CF_3O_2 \rightarrow$ Products," *J. Phys. Chem.* **96**, 4925-4930 (1992).

Martin, J.-P. and Paraskevopoulos, G., "A kinetics study of the reactions of OH radicals with fluoroethanes. Estimates of C-H bond strength in fluoroalkanes," *Can. J. Chem.* **61**, 861 (1983).

Masri, A.R., "Structure of laminar nonpremixed flames of methane inhibited with CF_3Br," *Twenty-fourth Symposium (International) on Combustion*, The Combustion Institute, Pittsburgh, PA, (1992).

McHale, E.T., "Survey of vapor phase chemical agents for combustion suppression," *Fire Res. Abs. Rev.* **11**, 90-104 (1969).

McHale, E.T., Geary, R.W., von Elbe, G., and Huggett, C., "Flammability limits of H_2-O_2-fluorocarbon mixtures," *Combust. Flame* **16**, 167-175 (1971).

McMillan, D.F. and Golden, D.M., "Hydrocarbon bond dissociation energies," *Ann. Rev. Phys. Chem.* **33**, 493 (1982).

Melius, C.F., "Thermochemistry of Hydrocarbon Intermediates in Combustion: Application of the BAC-MP4 Method," in *Chemistry and Physics of Energetic Materials*, Kluwer Academic Publishers, Dorderecht, 1990.

Melius, C.F., personal communication, January, 1993.

Miller, J.A. and Bowman, C.T., "Mechanism and modeling of nitrogen chemistry in combustion," *Prog. Energy Comb. Sci.* **15**, 287-338 (1989).

Milne, T.A., Green, C.L., and Benson, D.K., "The use of the counterflow diffusion flame in studies of inhibition effectiveness," *Combust. Flame* **15**, 255-264 (1970).

Millward, G.E. and Tschuikow-Roux, E., "A kinetic analysis of the shock wave decomposition of 1,1,1,2-tetrafluoroethane," *J. Phys. Chem.* **76**, 292-298 (1972).

Millward, G.E., Hartig, R., and Tschuikow-Roux, E., "Kinetics of the shock wave thermolysis of 1,1,2,2-tetrafluoroethane," *J. Phys. Chem.* **75**, 3195 (1971).

Mitin, P.V., Barabanov, V.G., Volkov, G.V., "Kinetics of the thermal decomposition of 1,1-difluoro-1-chloroethane and 1,1,1-trifluoroethane," *Kinet. Catal.* **29**, 1279 (1988).

Miyoshi, A., Ohmori, K., Tsuchiya, K., and Matsui, H., "Reaction rates of atomic oxygen with straight chain alkanes and fluoromethanes at high temperatures," *Chem. Phys. Lett.* **204**, 241-247 (1993).

Miziolek, A.W., personal communication, October, 1993.

Modica, A.P. and LaGraff, J.E., "Decomposition and oxidation of C_2F_4 behind shock waves," *J. Chem. Phys.* **43**, 3383-3392 (1966).

Morris, R.A., Brown, E.R., Viggiano, A.A., Vandoren, J.M., Paulson, J.F., Motevalli, V., "Positive ion chemistry related to hydrocarbon flames doped with CF_3Br," *Int. J. Mass Spectrom. Ion Proc.* **121**, 95-109 (1992).

Morrison, M.E., Scheller, K., "The effect of burning velocity inhibitors on the ignition of hydrocarbons," *Combust. Flame* **18**, 3-12 (1972).

Nielsen, O.J., "Rate constants for the gas-phase reactions of OH radicals with CH_3CHF_2 and $CHCl_2CF_3$ over the temperature range 295-388 K," *Chem. Phys. Lett.* **187**, 286-290 (1991).

Nielsen, O.J., Ellmermann, T., Bartkiewicz, E., Wallington, T.J., and Hurley, M.D., "UV absorption spectra, kinetics and mechanisms of the self-reaction of CHF_2O_2 radicals in the gas phase at 298 K," *Chem. Phys. Lett.* **192**, 82-88 (1992).

Nimitz, J. and Lankford, L., "Fluoroiodocarbons as Halon Replacements," *Halon Alternatives Conference*, Washington DC, October 20-22, 1993.

Nip, W.S., Singleton, D.L., Overend, R., and Paraskevopoulos, G., "Rates of OH radical reactions with CH_3F, CH_2F_2, CHF_3, CH_3CH_2F, and CH_3CHF_2 at 297 K," *J. Phys. Chem.* **19**, 2440 (1979).

Noda, S., Fujimoto, S., Claesson, O., and Yoshida, H., "ESR studies of Bunsen-type methane-air flames. II. The effects of the additives," *Bull. Chem. Soc. Jpn.* **56**, 2562-2564 (1983).

Norton, F.J., *Refrig. Eng.* **65**, 33 (1957).

Nyden, M.R., personal communication, November, 1993.

Orkin, V.L. and Khamaganov, V.G., "Determination of rate constants for reactions of some halocarbons with OH radicals and their atmospheric lifetimes," *J. Atmos. Chem.* **16**, 157 (1993).

Orkin, V.L. and Khamaganov, V.G., "Rate Constants for Reactions of OH with Some Br-Containing Haloalkanes," *J. Atmos. Chem.* **16**, 169 (1993).

Olando, J.J. and Smith, D.R., "Time-resolved tunable diode laser detection of products of the infrared multi-photon dissociation of hexafluoroacetone: A line-strength and band-strength measurement for CF_3," *J. Phys. Chem.* **92**, 5147 (1988).

Pagsberg, P., Munk, J., and Sillesen, A., " UV spectrum and kinetics of hydroxymethyl radicals," *Chem. Phys. Lett.* **146**, 375 (1988).

Park, J.-Y., Sawyer, P.F., Heaven, M.C., and Gutman, D., "Chemical branching in the oxygen-atom-reaction with vinyl fluoride. Pressure dependence of the route $O + C_2H_3F \rightarrow CH_2F + HCO$," *J. Phys. Chem.* **88**, 2821 (1984).

Parsamyan, N.I., Azatyan, V.V., and Nalbandyan, A.B., "Determination of the rate constant for reaction of atomic hydrogen and oxygen with methyl fluoride," *Arm. Kim. Zh.* **20**, 1 (1967).

Parsamyan, N.I. and Nalbanddyan, A.B.; "Determination of the rate constants for reactions of hydrogen and oxygen atoms with difluoromethane," *Arm. Khim. Zh.* **21**, 1 (1968).

Payne, W.A. and Stief, L.J., "Absolute rate constant for the reaction of atomic hydrogen with acetylene over an extended pressure and temperature range," *J. Chem. Phys.* **64**, 1150 (1976).

Pedley, J.B., Naylor, R.D., and Kirby, S.P., *Thermochemical Data of Organic Compounds*, Chapman and Hall, New York (1986).

Pickard, J.M. and Rodgers, A.S., "Kinetics of the gas phase reaction $CH_3F + I_2 = CH_2FI + HI$: The C-H bond dissociation energy in methyl and methylene fluorides" *Int. J. Chem. Kinet.* **15**, 569-577 (1983).

Pitts, W.M., Nyden, M.R., Gann, R.G., Mallard, W.G, and Tsang, W., *Construction of an Exploratory List of Chemicals to Initiate the Search for Halon Alternatives*, TN 1279, National Institute of Standards and Technology, Gaithersburg, MD, 1990.

Plumb, I.C. and Ryan, K.R., "Gas-phase reactions of CF_3 and CF_2 with atomic and molecular fluorine: their significance," *Ber. Bunsenges. Phys. Chem.* **6**, 11 (1986).

Plumb, I.C. and Ryan, K.R., "A model of the chemical processes occurring in CF_4/O_2 discharges used in plasma etching," *Plasma Chem. Plasma Process* **6**, 205 (1986).

Politanskii, S.F. and Shevchuk, U.V., "Thermal conversions of fluoromethanes. II. Pyrolysis of difluoromethane and trifluoromethane," *Kinet. Catal.* **9**, 411-417 (1968).

Pollock, T.L. and Jones, W.E., "Gas phase reactions of fluorine atoms," *Can. J. Chem.* **51**, 2041-2046 (1973).

Pritchard, G.O., Bryant, J.T., and Thommarson, R.L., "The reaction of methyl radicals with methyl and methylene fluoride," *J. Phys. Chem.* **69**, 664 (1965).

Pritchard, G.O., Pritchard, H.O., Schiff, H.I., and Trotman-Dickenson, A.F., "The reactions of trifluoromethyl radicals," *Trans. Faraday Soc.* **52**, 848 (1956).

Purdue Research Foundation and Department of Chemistry, *Final Report on Fire Extinguishing Agents for the Period September 1, 1947 to June 30, 1950*, Purdue University, West Lafayette, IN, 1950.

Pyle, J.A., Solomon, S., Wuebbles, D., and Zvenigorodsky, S., "Ozone Depletion and Chlorine Loading Potentials," in World Meteorological Organization, Global Ozone Research Monitoring Project - Report No. 25, *Scientific Assessment of Ozone Depletion: 1991*, 1991.

Ridley, B.A., Davenport, J.A., Stief, L.J., and Welge, K.H., "Absolute Rate Constant for the Reaction H + H_2CO," *J. Chem. Phys.* **57**, 520 (1972).

Robinson, P.J. and Holbrook, K.A., *Unimolecular Reactions*, Wiley Interscience, New York, 1972.

Rodgers, A.S., "Thermochemistry of fluorocarbon radicals," *ACS Symp. Ser.* **66**, 296 (1978).

Rodgers, A.S., *TRC Thermodynamics Tables*, Texas A&M University, College Station, TX, 1989.

Rodgers, A.S, Chao, J., Wilhoit, R.C., and Zwolinski, B.J., "Ideal gas thermodynamic properties of eight chloro- and fluoromethanes," *J. Phys. Chem. Ref. Data* **3**, 117-140 (1974).

Rosser, W.A., Wise, H., and Miller, J., "Mechanism of combustion inhibition by compounds containing halogens," *Seventh Symposium (International) on Combustion*, The Combustion Institute, Pittsburgh, PA, 175-182 (1958).

Ryan, K.R. and Plumb, I.C., "Kinetics of the reactions of CF_3 with $O(^3P)$ and O_2 at 295 K," *J. Phys. Chem.* **86**, 4678 (1982).

Ryan, K.R. and Plumb, I.C., "Gas-phase reactions of CF_3 and CF_2 with hydrogen atoms: Their significance in plasma processing," *Plasma Chem. Plasma Proc.* **4**, 141 (1984).

Safieh, H.Y., Vandooren, J., and Van Tiggelen, P.J. "Experimental study of inhibition induced by CF_3Br in a CO-H_2-O_2-Ar flame," *Nineteenth Symposium (International) on Combustion*, The Combustion Institute, Pittsburgh, PA, 117 (1982).

Saito, K., Kuroda, H., Kakumoto, T., Munechika, H., and Murakami, I., "Thermal unimolecular decomposition of formyl fluoride in Ar," *Chem. Phys. Lett.* **113**, 399 (1985).

Schug, K.P. and Wagner, H.Gg., "Zum thermischen zerfal von CH_3F," *Z. Phys. Chem.* **86**, 59-66 1973.

Schug, K.P., Wagner, H.Gg., and Zabel, F., "Gas phase elimination of hydrogen halides from halomethanes. I. Thermal decomposition of chlorodifluoromethane, trifluoromethane, and trichloromethane behind shock waves," *Ber. Bunsenges. Phys. Chem.* **83**, 167 (1979).

Sekhar, M.V.C. and Tschuikow-Roux, E., "Kinetics of the shock-induced competitive dehydrofluorinations of 1,1,2-trifluoroethane," *J. Phys. Chem.* **78**, 472-477 (1974).

Sheinson, R.S. and Alexander, J.I., "HF and HBr from Halon 1301 extinguished pan fires," *Fall Meeting, Eastern States Section Meeting/The Combustion Institute*, Pittsburgh, PA, Paper 62, 1982.

Sheinson, R.S., Musick, J.K., and Carhart, H.W., "HF and HBr production from full scale CF_3Br (Halon 1301) fire suppression tests," *Journal of Fire and Flammability*, **12**, 229-235 (1981).

Sheinson, R.S., Penner-Hahn, J.E., and Indritz, D., "The physical and chemical action of fire suppressants," *Fire Safety Journal* **15**, 437 (1989).

Shilov, A.E. and Sabirova, R.D., "The mechanism of the first stage in the thermal decomposition of chloromethanes. II. The decomposition of chloroform," *Russ. J. Phys. Chem.* **34**, 408-411 (1960).

Simmons, R.F. and Wolfhard, H.G., "The influence of methyl bromide on flames," *Trans. Farad. Soc.* **51**, 1211-1217 (1955).

Skinner, G.B., "Inhibition of the hydrogen-oxygen reaction by CF_3Br and CF_2BrCF_2Br," *ACS Symp. Ser.* **16**, 295-317 (1975).

Skinner, G.B. and Ringrose, G.H., "Ignition delays of a hydrogen-oxygen-argon mixture at relatively low temperatures," *J. Chem. Phys.* **42**, 2190 (1965).

Slagle, I.R., Gutman, D., and Gilbert, J.R., "Direct identification of products and measurement of branching ratios for the reactions of oxygen atoms with vinylfluoride, vinylchloride, and vinylbromide," *Fifteenth Symposium (International) on Combustion*, The Combustion Institute, Pittsburgh, PA, 785-793 (1974).

Smith, D.J., Setser, D.W., Kim, K.C., and Bogan, D.J., "HF infrared chemiluminescence. Relative rate constants for hydrogen abstraction from hydrocarbons, substituted methanes, and inorganic hydrides," *J. Phys. Chem.* **81**, 898 (1977).

Smith, W.D., Sheinson, R.S., Eaton, H.G., Brown, R., Salmon, G., Burchell, H., and St. Aubin, H.J., "Halogen acid production evaluation in an intermediate-scale Halon 1301 replacement suppressant test," *Proceedings of the Sixth International Fire Conference* (INTERFLAM 93), 757 (1993).

Stein, S.E., Rukkers, J.M., and Brown, R.L., "NIST Structures and Properties Database and Estimation Program," *NIST Standard Reference Database 25*, 1991.

Stevens, P.S., Brune, W.H. and Anderson, J.G., "Kinetic and mechanistic investigations of F + H_2O/D_2O and F + H_2/D_2 over the temperature range 240-373 K," *J. Phys. Chem.* **93**, 4068 (1989).

Stull, D.R. and Prophet, H., "JANAF Thermochemical Tables," *NSRDS-NBS 37*, 1971.

Stull, D.R., Westrum, E.F., Jr., and Sinke, G.C., *The Chemical Thermodynamics of Organic Compounds*, John Wiley, New York (1969).

Talukdar, R., Mellouki, A., Gierczak, T., Burkholder, J.B., McKeen, S.A., and Ravishankara, A.R., "Atmospheric fate of CF_2H_2, CH_3CF_3, CHF_2CF_3, and CH_3CFCl_2: Rate coefficients for reactions with OH and UV absorption cross sections of CH_3CFCl_2," *J. Phys. Chem.* **95**, 5815-5821 (1991).

Tsang, W. and Hampson, R.F., "Chemical kinetic data base for combustion chemistry. Part I. Methane and related compounds," *J. Phys. Chem. Ref. Data* **15**, 1087 (1986).

Tsai, C., Belanger, S.M., Kim, J.T., Lord, J.R., and McFadden, D.L., "Gas-phase atom-radical kinetics of elementary CF_3 reactions with O and N atoms," *J. Phys. Chem.* **93**, 1916, 1989.

Tsai, C. and McFadden, D.L., "Gas-phase atom-radical kinetics of atomic hydrogen reactions with CF_3, CF_2, and CF radicals," *J. Phys. Chem.* **93**, 2471 (1989).

Tsai, C.-P. and McFadden, D.L., "Gas-phase atom-radical kinetics of N and O atoms reactions with CF and CF_2 radicals," *Chem. Phys. Lett.* **173**, 241-244 (1990).

Tsai, C. and McFadden, D.L., "Gas-phase atom-radical kinetics of atomic hydrogen, nitrogen, and oxygen reactions with CHF radicals," *J. Phys. Chem.* **94**, 3298-3300 (1990).

Tsang, W.T., "Single pulse shock tube study on the stability of perfluorobromoethane," *J. Phys. Chem.* **90**, 414-418 (1986).

Tschuikow-Roux, E., "Thermal decomposition of fluoroform in a single-pulse shock tube. II. Pressure dependence of rate," *J. Chem. Phys.* **42**, 3639-3642 (1965).

Tschuikow-Roux, E. and Marte, J.E., "Thermal decomposition of fluoroform in a single pulse shock tube. I.," *J. Chem. Phys.* **42**, 2049-2056 (1965).

Tschuikow-Roux, E., Millward, G.E., and Quiring, W.J., "Kinetics of the shock wave pyrolysis of pentafluoroethane," *J. Phys. Chem.* **75**, 3493-3498 (1971).

Tschuikow-Roux, E., Quiring, W.J., and Simmie, J.M., "Kinetics of the thermal decomposition of 1,1-difluoroethane in shock waves. A consecutive first-order reaction," *J. Phys. Chem.* **74**, 2449-2455 (1970).

Tschuikow-Roux, E. and Quiring, W.J., "Kinetics of the thermally induced dehydrofluorination of 1,1,1-trifluoroethane in shock waves," *J. Phys. Chem.* **75**, 295-300 (1971).

Tully, F.P., "Hydrogen-atom abstraction from alkenes by OH. Ethene and 1-butene," *Chem. Phys. Lett.* **143**, 510 (1988).

Vandooren, J. F., da Cruz, N., and P. Van Tiggelen, "The Inhibiting Effect of CF_3H on the Structure of a Stoichiometric $H_2/CO/O_2/Ar$ Flame," *Twenty-Second Symposium (International) on Combustion*, The Combustion Institute, 1587 (1988).

Vedeneev, V.I., Teitel'boim, M.A., and Shoikhet, A.A., "The photolysis of CF_3I in the presence of O_2 and Br_2. 1. The mechanism of the elementary step in the reaction of CF_3 radicals with O_2," *Bull. Acad. Sci. USSR, Div. Chem. Sci.* **8**, 1534-1537 (1978).

Wagner, H.Gg., Warnatz, J., and Zetzsch, C., "On the reaction of F atoms with methane," *An. Asoc. Quim. Argent.* **59**, 169 (1971).

Walther, C.D. and Wagner, H.G., "Uber die reaktionen von F-atomen mit H_2O, H_2O_2 und NH_3," *Ber. Bunsenges. Phys. Chem.* **87**, 403 (1983).

Warnatz, J., "Rate coefficients in the C/H/O system," in *Combustion Chemistry* (ed. W.C. Gardiner, Jr.), Springer-Verlag, New York, 1984, p. 197.

Westbrook, C.K., "Inhibition of laminar methane-air and methanol-air flames by hydrogen bromide," *Combust. Sci. Technol.* **23**, 191-202 (1980).

Westbrook, C.K., "Inhibition of hydrocarbon oxidation in laminar flames and detonations by halogens," *Nineteenth Symposium (International) on Combustion*, The Combustion Institute, Pittsburgh, PA, 127-141 (1982).

Westbrook, C.K., "Numerical Modeling of Flame Inhibition by CF_3Br," *Combust. Sci. Technol.* **34**, 201 (1983).

Westbrook, C.K. and Dryer, F.L., *Combust. Sci. Technol.* **20**, 125 (1979).

Westenberg, A.A. and deHaas, N., "Rates of H + CH_3X reactions," *J. Chem. Phys.* **62**, 3321-3325 (1975).

Williams, R.L. and Rowland, F.S., "Hydrogen atom abstraction by fluorine atoms," *J. Phys. Chem.* **77**, 301-307 (1973).

Wilson, W.E., Jr., "Structure, kinetics, and mechanisms of a methane-oxygen flame inhibited with methyl bromide," *Tenth Symposium (International) on Combustion,* The Combustion Institute, Pittsburgh, PA, 47-54 (1965).

Wuebbles, D.J., "The relative Efficiency of a Number of Halocarbons for Destroying Stratospheric Ozone," *Report UCID-18 924*, Lawrence Livermore National Laboratory, Livermore, CA, 1983.

Wurzberg, E. and Houston, P.L., "The temperature dependence of hydrogen abstraction reactions: F + HCl, F + HBr, F + DBr, and F + HI," *J. Chem. Phys.* **72**, 5915 (1980).

Yamashika, S., "Dependence of the extinction time and decomposition of halogenated extinguishing agent on its application rate," *Report of Fire Research Institute of Japan*, **36**, 7, (1973).

Yamashika, S., Hosokai, R., and Morikawa, T., "Poisonous halogenated gases produced by the thermal decomposition of halons applied on fires," *Report of Fire Research Institute of Japan*, **38**, 1-8 (1974).

Zallen, D.M., *Halon Replacements Study*, report to Aeronautical Systems Division (ASD), Wright-Patterson AFB, Ohio (1992).

Zhang, Z., Saini, R.D., Kurylo, M.J., and Huie, R.E., "Rate constants for the reactions of the hydroxyl radical with $CHF_2CF_2CF_2CHF_2$ and $CF_3CHFCHFCF_2CF_3$," *Chem. Phys. Lett.* **200**, 230 (1992).

Zhang, Z., Saini, R.D., Kurylo, M.J., and Huie, R.E., "Rate constants for the reactions of the hydroxyl radical with several partially fluorinated ethers," *J. Phys. Chem.* **96**, 9301 (1992).

Zhitnev, Y.N., Mordkovich, N.Y., Tveritinova, E.A., Timofeev, V.V., Zakharchenko, A.V., and Nugaav,T .B.K., "Pulse laser pyrolysis - mathematical model and investigation of difluorochloromethane conversion kinetics," *Vestn. Mosk. Univ. Ser. Khim.* **31**, 329 (1990).

Zhitnev, Y.N., Zakharchenko, A.V., Mordkovich, N.Y., Nugaev, T.B.H., Tveritinova, E.A., and Timofeev, V.V., "The pulsed homogenous laser pyrolysis: determination of arrhenius parameters of $CHClF_2$ destruction basing on the model of physical and chemical processes," *Laser Chem.* **11**, 71-81 (1991).

Appendix A. Tabulation of *Ab Initio* Thermochemical Data for Fluorinated Hydrocarbons.

Thermochemical data calculated using the BAC-MP4 *ab initio* method for fluorinated hydrocarbons (and a few other reference species) are presented in a "JANAF style" tabular format. Values for principal moments of inertia (I_a, I_b, I_c in kg m^2), fundamental vibrational frequencies (ν_i in cm^{-1}), equilibrium bond distances (R_e in 10^{-10} m), equilibrium bond angles (θ_e in degrees), heat of formation at 0 K (ΔH_f^o: 0 K, 1 atmosphere in kJ mol^{-1}), heat of formation at standard state (ΔH_f^o: 298.15 K, 1 atmosphere in kJ mol^{-1}), and entropy at standard state (S^o: 298.15 K, 1 atmosphere in J K^{-1} mol^{-1}) are given for each species. Heat capacity (C_p^o in J K^{-1} mol^{-1}), free energy of formation (ΔG_f^o in kJ mol^{-1}), equilibrium constant for formation (Log K_f, dimensionless), and other ideal gas phase thermal functions (as a function of temperature) are also given for each species.

HF

ΔH_f°(0 K) = -273.22 kJ mol^{-1}
ΔH_f°(298.15 K) = -273.29 kJ mol^{-1}
S°(298.15 K) = 173.37 J K^{-1} mol^{-1}

Moments of Inertia (10^{-47} kg m^2)
1.32 1.32

Vibrational Frequencies (cm^{-1})
3890.2

Bond Distances (10^{-10} m)		**Bond Angles** (°)	**Dihedral Angles** (°)
F1-H1	0.911		

Enthalpy Reference Temperature = T_r = 298.15 K
Standard State Pressure = p_o = 1 atmosphere

	¦- J K^{-1} mol^{-1} -¦		¦-------- kJ mol^{-1} ---------¦			
T/K	**C_p°**	**S°**	**H°-$H^\circ(T_r)$**	**ΔH_f°**	**ΔG_f°**	**Log K_f**
150	29.10	153.38	-4.31	-273.22	-274.30	95.52
200	29.10	161.75	-2.86	-273.22	-274.68	71.74
250	29.10	168.25	-1.40	-273.26	-275.06	57.47
300	29.10	173.55	0.05	-273.30	-275.39	47.95
350	29.10	178.04	1.51	-273.34	-275.77	41.15
400	29.10	181.92	2.96	-273.42	-276.10	36.05
450	29.10	185.35	4.42	-273.51	-276.44	32.09
500	29.12	188.42	5.87	-273.63	-276.73	28.91
600	29.17	193.73	8.79	-273.88	-277.36	24.14
700	29.28	198.23	11.71	-274.18	-277.90	20.74
800	29.47	202.16	14.65	-274.47	-278.40	18.18
900	29.74	205.64	17.61	-274.81	-278.86	16.18
1000	30.07	208.79	20.60	-275.10	-279.32	14.59
1100	30.45	211.68	23.62	-275.39	-279.70	13.28
1200	30.84	214.34	26.69	-275.68	-280.08	12.19
1300	31.24	216.83	29.79	-275.93	-280.45	11.27
1400	31.63	219.16	32.94	-276.19	-280.79	10.48
1500	32.01	221.35	36.12	-276.44	-281.12	9.79
1600	32.38	223.43	39.34	-276.65	-281.42	9.19
1700	32.71	225.40	42.59	-276.86	-281.71	8.66
1800	33.03	227.28	45.88	-277.02	-281.96	8.18
1900	33.33	229.07	49.20	-277.23	-282.25	7.76
2000	33.60	230.79	52.54	-277.40	-282.50	7.38
2100	33.85	232.44	55.91	-277.52	-282.75	7.03
2200	34.08	234.02	59.31	-277.69	-283.01	6.72
2300	34.29	235.54	62.73	-277.82	-283.26	6.43
2400	34.48	237.00	66.17	-277.94	-283.47	6.17
2500	34.66	238.41	69.63	-278.07	-283.72	5.93
2600	34.83	239.78	73.10	-278.15	-283.93	5.70
2700	34.98	241.09	76.59	-278.28	-284.14	5.50
2800	35.12	242.37	80.10	-278.36	-284.39	5.30
2900	35.25	243.60	83.62	-278.45	-284.60	5.13
3000	35.37	244.80	87.15	-278.53	-284.80	4.96

F_2

ΔH_f°(0 K) = 1.21 kJ mol^{-1}
ΔH_f°(298.15 K) = 1.13 kJ mol^{-1}
S°(298.15 K) = 201.42 J K^{-1} mol^{-1}

Moments of Inertia (10^{-47} kg m^2)
28.53 28.53

Vibrational Frequencies (cm^{-1})
1111.7

Bond Distances (10^{-10} m) **Bond Angles** (°) **Dihedral Angles** (°)
F1-F2 1.345

Enthalpy Reference Temperature = T_r = 298.15 K
Standard State Pressure = p_o = 1 atmosphere

	- J K^{-1} mol^{-1} -		-------- kJ mol^{-1} ---------			
T/K	C_p°	S°	H°-$H^\circ(T_r)$	ΔH_f°	ΔG_f°	Log K_f
150	29.12	181.18	-4.37	1.21	1.34	-0.47
200	29.28	189.58	-2.92	1.17	1.38	-0.36
250	29.67	196.15	-1.44	1.17	1.42	-0.30
300	30.25	201.61	0.05	1.13	1.51	-0.26
350	30.94	206.32	1.59	1.09	1.55	-0.23
400	31.63	210.50	3.15	1.05	1.63	-0.21
450	32.28	214.26	4.75	0.96	1.72	-0.20
500	32.87	217.69	6.38	0.92	1.80	-0.19
600	33.85	223.78	9.72	0.84	1.97	-0.17
700	34.58	229.05	13.14	0.75	2.13	-0.16
800	35.12	233.71	16.62	0.71	2.34	-0.15
900	35.53	237.87	20.16	0.63	2.55	-0.15
1000	35.85	241.63	23.73	0.59	2.80	-0.15
1100	36.09	245.06	27.33	0.54	3.01	-0.14
1200	36.29	248.21	30.94	0.50	3.22	-0.14
1300	36.44	251.12	34.58	0.46	3.47	-0.14
1400	36.57	253.82	38.23	0.46	3.68	-0.14
1500	36.67	256.35	41.89	0.42	3.93	-0.14
1600	36.76	258.72	45.57	0.42	4.14	-0.14
1700	36.83	260.95	49.25	0.38	4.39	-0.14
1800	36.89	263.06	52.93	0.38	4.64	-0.13
1900	36.94	265.05	56.62	0.38	4.85	-0.13
2000	36.99	266.95	60.32	0.33	5.10	-0.13
2100	37.02	268.76	64.02	0.33	5.36	-0.13
2200	37.06	270.48	67.72	0.33	5.56	-0.13
2300	37.09	272.13	71.43	0.29	5.82	-0.13
2400	37.12	273.70	75.14	0.29	6.07	-0.13
2500	37.14	275.22	78.86	0.29	6.32	-0.13
2600	37.16	276.68	82.57	0.29	6.53	-0.13
2700	37.17	278.08	86.29	0.29	6.78	-0.13
2800	37.19	279.43	90.01	0.25	7.03	-0.13
2900	37.21	280.74	93.73	0.25	7.28	-0.13
3000	37.22	282.00	97.45	0.25	7.49	-0.13

CH_3F

ΔH_f°(0 K) = -225.48 kJ mol^{-1}
ΔH_f°(298.15 K) = -233.83 kJ mol^{-1}
S°(298.15 K) = 231.46 J K^{-1} mol^{-1}

Moments of Inertia (10^{-47} kg m^2)

5.25	31.84	31.84

Vibrational Frequencies (cm^{-1})

1059.4	1171.3	1171.4	1474.7	1476.1
1476.1	2886.7	2958.1	2958.6	

Bond Distances (10^{-10} m)		**Bond Angles** (°)		**Dihedral Angles** (°)	
C1-H1	1.082				
C1-F1	1.365	H1-C1-F1	109.13		
C1-H2	1.082	H1-C1-H2	109.84	F1-C1-H2	119.54
C1-H3	1.082	H1-C1-H3	109.84	F1-C1-H3	-119.54

Enthalpy Reference Temperature = T_r = 298.15 K
Standard State Pressure = p_o = 1 atmosphere

	|- J K^{-1} mol^{-1} -|		|-------- kJ mol^{-1} ---------|			
T/K	**C_p°**	**S°**	**H°-$H^\circ(T_r)$**	**ΔH_f°**	**ΔG_f°**	**Log K_f**
150	33.32	207.76	-5.15	-229.33	-221.79	77.24
200	33.82	217.40	-3.47	-230.79	-219.07	57.22
250	35.22	225.07	-1.75	-232.34	-216.02	45.13
300	37.59	231.69	0.07	-233.89	-212.63	37.02
350	40.67	237.71	2.03	-235.39	-208.99	31.19
400	44.14	243.37	4.14	-236.81	-205.14	26.79
450	47.73	248.77	6.44	-238.20	-201.12	23.34
500	51.27	253.99	8.92	-239.41	-196.94	20.57
600	57.91	263.93	14.38	-241.58	-188.28	16.39
700	63.81	273.31	20.47	-243.34	-179.24	13.38
800	68.99	282.18	27.12	-244.76	-170.00	11.10
900	73.49	290.57	34.25	-245.85	-160.58	9.32
1000	77.41	298.52	41.80	-246.65	-151.00	7.89
1100	80.81	306.06	49.71	-247.27	-141.38	6.71
1200	83.75	313.22	57.94	-247.69	-131.67	5.73
1300	86.30	320.03	66.45	-247.94	-121.92	4.90
1400	88.52	326.51	75.19	-248.07	-112.17	4.18
1500	90.44	332.68	84.14	-248.07	-102.38	3.57
1600	92.12	338.57	93.27	-248.03	-92.63	3.02
1700	93.59	344.20	102.56	-247.86	-82.89	2.55
1800	94.88	349.59	111.98	-247.69	-73.14	2.12
1900	96.01	354.75	121.53	-247.40	-63.47	1.74
2000	97.02	359.70	131.19	-247.11	-53.81	1.41
2100	97.91	364.46	140.93	-246.77	-44.22	1.10
2200	98.70	369.03	150.76	-246.40	-34.64	0.82
2300	99.40	373.43	160.67	-245.98	-25.15	0.57
2400	100.04	377.68	170.64	-245.56	-15.65	0.34
2500	100.60	381.77	180.67	-245.10	-6.23	0.13
2600	101.11	385.73	190.76	-244.60	3.18	-0.06
2700	101.58	389.55	200.89	-244.09	12.51	-0.24
2800	102.00	393.25	211.07	-243.59	21.84	-0.41
2900	102.38	396.84	221.29	-243.05	31.17	-0.56
3000	102.73	400.32	231.55	-242.50	40.46	-0.70

CH_2F_2

ΔH_f°(0 K) = -443.25 kJ mol^{-1}
ΔH_f°(298.15 K) = -451.06 kJ mol^{-1}
S°(298.15 K) = 252.16 J K^{-1} mol^{-1}

Moments of Inertia (10^{-47} kg m^2)

16.51	77.17	88.30

Vibrational Frequencies (cm^{-1})

509.7	1105.4	1122.6	1164.4	1258.4
1463.6	1529.2	2941.9	3006.3	

Bond Distances (10^{-10} m)		**Bond Angles** (°)		**Dihedral Angles** (°)	
C1-H1	1.078				
C1-F1	1.338	H1-C1-F1	108.93		
C1-F2	1.338	H1-C1-F2	108.91	F1-C1-F2	118.26
C1-H2	1.078	H1-C1-H2	112.48	F1-C1-H2	-120.89

Enthalpy Reference Temperature = T_r = 298.15 K
Standard State Pressure = p_o = 1 atmosphere

	- J K^{-1} mol^{-1} -		- kJ mol^{-1} -			
T/K	C_p°	S°	H°-$H^\circ(T_r)$	ΔH_f°	ΔG_f°	Log K_f
150	34.84	226.11	-5.69	-447.06	-436.85	152.12
200	36.88	236.40	-3.90	-448.40	-433.25	113.15
250	39.63	244.91	-1.99	-449.78	-429.36	89.70
300	43.09	252.43	0.08	-451.12	-425.18	74.02
350	47.01	259.36	2.33	-452.37	-420.74	62.79
400	51.07	265.90	4.78	-453.55	-416.18	54.35
450	55.07	272.15	7.43	-454.63	-411.45	47.76
500	58.86	278.15	10.28	-455.64	-406.64	42.48
600	65.63	289.50	16.52	-457.27	-396.73	34.54
700	71.32	300.06	23.38	-458.57	-386.52	28.84
800	76.08	309.90	30.75	-459.57	-376.18	24.56
900	80.09	319.10	38.57	-460.28	-365.68	21.22
1000	83.48	327.72	46.75	-460.78	-355.10	18.55
1100	86.35	335.81	55.25	-461.16	-344.47	16.36
1200	88.81	343.43	64.01	-461.33	-333.80	14.53
1300	90.90	350.63	72.99	-461.41	-323.09	12.98
1400	92.70	357.43	82.18	-461.37	-312.42	11.66
1500	94.26	363.88	91.53	-461.29	-301.71	10.51
1600	95.60	370.01	101.02	-461.08	-291.00	9.50
1700	96.77	375.84	110.64	-460.87	-280.37	8.61
1800	97.80	381.40	120.37	-460.57	-269.70	7.83
1900	98.69	386.71	130.20	-460.24	-259.12	7.12
2000	99.48	391.79	140.11	-459.86	-248.57	6.49
2100	100.18	396.66	150.09	-459.49	-238.07	5.92
2200	100.80	401.34	160.14	-459.07	-227.61	5.40
2300	101.36	405.84	170.25	-458.61	-217.19	4.93
2400	101.85	410.16	180.41	-458.15	-206.82	4.50
2500	102.29	414.32	190.61	-457.65	-196.52	4.11
2600	102.69	418.35	200.87	-457.14	-186.23	3.74
2700	103.05	422.23	211.15	-456.64	-175.98	3.40
2800	103.38	425.98	221.48	-456.10	-165.77	3.09
2900	103.68	429.61	231.83	-455.55	-155.56	2.80
3000	103.95	433.14	242.21	-455.01	-145.35	2.53

CHF_3

ΔH_f°(0 K) = -692.49 kJ mol^{-1}
ΔH_f°(298.15 K) = -699.45 kJ mol^{-1}
S°(298.15 K) = 268.72 J K^{-1} mol^{-1}

Moments of Inertia (10^{-47} kg m^2)
78.94 79.02 144.03

Vibrational Frequencies (cm^{-1})
491.7 492.1 680.7 1126.9 1185.7
1186.0 1413.4 1413.6 3036.6

Bond Distances (10^{-10} m)		**Bond Angles** (°)		**Dihedral Angles** (°)	
C1-H1	1.074				
C1-F1	1.316	H1-C1-F1	110.44		
C1-F2	1.316	H1-C1-F2	110.44	F1-C1-F2	120.03
C1-F3	1.316	H1-C1-F3	110.44	F1-C1-F3	-120.03

Enthalpy Reference Temperature = T_r = 298.15 K
Standard State Pressure = p_o = 1 atmosphere

	- J K^{-1} mol^{-1} -		---------- kJ mol^{-1} ----------			
T/K	**C_p°**	**S°**	**H°-$H^\circ(T_r)$**	**ΔH_f°**	**ΔG_f°**	**Log K_f**
150	37.19	239.03	-6.52	-696.22	-682.54	237.67
200	41.66	250.32	-4.55	-697.39	-677.85	177.02
250	46.48	260.13	-2.35	-698.48	-672.83	140.57
300	51.40	269.04	0.10	-699.48	-667.64	116.24
350	56.25	277.33	2.79	-700.36	-662.29	98.83
400	60.86	285.14	5.72	-701.15	-656.80	85.76
450	65.11	292.56	8.87	-701.87	-651.24	75.59
500	68.96	299.62	12.22	-702.45	-645.59	67.44
600	75.48	312.80	19.46	-703.33	-634.17	55.21
700	80.63	324.84	27.27	-703.96	-622.62	46.46
800	84.73	335.88	35.55	-704.38	-610.95	39.89
900	88.01	346.05	44.19	-704.59	-599.23	34.78
1000	90.70	355.47	53.13	-704.67	-587.52	30.69
1100	92.90	364.23	62.31	-704.63	-575.72	27.34
1200	94.74	372.39	71.70	-704.50	-563.96	24.55
1300	96.28	380.03	81.25	-704.33	-552.20	22.19
1400	97.58	387.22	90.94	-704.08	-540.45	20.16
1500	98.69	393.99	100.76	-703.75	-528.69	18.41
1600	99.64	400.39	110.68	-703.41	-516.98	16.88
1700	100.46	406.45	120.68	-703.04	-505.30	15.53
1800	101.17	412.22	130.77	-702.62	-493.67	14.32
1900	101.79	417.71	140.91	-702.20	-482.04	13.25
2000	102.33	422.94	151.12	-701.74	-470.49	12.29
2100	102.81	427.94	161.38	-701.24	-458.98	11.42
2200	103.23	432.74	171.68	-700.74	-447.56	10.63
2300	103.61	437.33	182.02	-700.23	-436.14	9.90
2400	103.94	441.75	192.40	-699.69	-424.80	9.25
2500	104.24	446.00	202.81	-699.15	-413.50	8.64
2600	104.51	450.09	213.25	-698.60	-402.25	8.08
2700	104.75	454.04	223.71	-698.06	-391.04	7.56
2800	104.97	457.86	234.20	-697.47	-379.82	7.09
2900	105.17	461.55	244.71	-696.89	-368.65	6.64
3000	105.35	465.11	255.23	-696.30	-357.48	6.22

CF_4

ΔH_f°(0 K) = -928.60 kJ mol^{-1}
ΔH_f°(298.15 K) = -934.37 kJ mol^{-1}
S°(298.15 K) = 273.27 J K^{-1} mol^{-1}

Moments of Inertia (10^{-47} kg m^2)
142.60 142.61 142.61

Vibrational Frequencies (cm^{-1})
422.0 422.0 609.8 609.8 609.8
895.5 1314.2 1314.2 1314.2

Bond Distances (10^{-10} m)		**Bond Angles** (°)		**Dihedral Angles** (°)	
C1-F1	1.302				
C1-F2	1.302	F1-C1-F2	109.47		
C1-F3	1.302	F1-C1-F3	109.47	F2-C1-F3	120.00
C1-F4	1.302	F1-C1-F4	109.47	F2-C1-F4	-120.00

Enthalpy Reference Temperature = T_r = 298.15 K
Standard State Pressure = p_o = 1 atmosphere

	¦- J K^{-1} mol^{-1} -¦		¦-------- kJ mol^{-1} ---------¦			
T/K	**C_p°**	**S°**	**H°-$H^\circ(T_r)$**	**ΔH_f°**	**ΔG_f°**	**Log K_f**
150	40.79	238.66	-7.64	-932.20	-913.07	317.94
200	48.23	251.41	-5.42	-933.12	-906.55	236.76
250	55.45	262.96	-2.82	-933.83	-899.85	188.00
300	61.97	273.66	0.11	-934.37	-893.03	155.48
350	67.73	283.65	3.36	-934.79	-886.13	132.24
400	72.75	293.03	6.87	-935.08	-879.18	114.80
450	77.09	301.85	10.62	-935.25	-872.20	101.24
500	80.83	310.18	14.57	-935.33	-865.21	90.38
600	86.78	325.47	22.97	-935.38	-851.19	74.10
700	91.16	339.19	31.88	-935.21	-837.22	62.47
800	94.40	351.59	41.17	-934.87	-823.24	53.75
900	96.85	362.85	50.73	-934.50	-809.27	46.97
1000	98.72	373.16	60.51	-934.08	-795.34	41.54
1100	100.17	382.64	70.46	-933.58	-781.45	37.11
1200	101.32	391.40	80.54	-933.07	-767.60	33.41
1300	102.25	399.56	90.72	-932.57	-753.75	30.28
1400	103.00	407.16	100.98	-932.03	-739.94	27.61
1500	103.62	414.29	111.32	-931.48	-726.18	25.29
1600	104.13	420.99	121.70	-930.90	-712.45	23.26
1700	104.56	427.32	132.14	-930.35	-698.77	21.47
1800	104.93	433.30	142.61	-929.77	-685.13	19.88
1900	105.24	438.99	153.12	-929.18	-671.57	18.46
2000	105.51	444.39	163.66	-928.60	-658.06	17.19
2100	105.74	449.55	174.22	-927.97	-644.59	16.03
2200	105.94	454.47	184.80	-927.38	-631.20	14.99
2300	106.12	459.18	195.41	-926.76	-617.85	14.03
2400	106.28	463.70	206.03	-926.17	-604.55	13.16
2500	106.42	468.04	216.66	-925.54	-591.28	12.35
2600	106.54	472.22	227.31	-924.92	-578.10	11.61
2700	106.65	476.24	237.97	-924.29	-564.92	10.93
2800	106.75	480.12	248.64	-923.62	-551.79	10.29
2900	106.84	483.87	259.32	-922.99	-538.69	9.70
3000	106.92	487.49	270.01	-922.36	-525.59	9.15

•CH_2F

ΔH_f°(0 K) = -27.57 kJ mol^{-1}
ΔH_f°(298.15 K) = -31.44 kJ mol^{-1}
S°(298.15 K) = 234.32 J K^{-1} mol^{-1}

Moments of Inertia (10^{-47} kg m^2)
3.15 26.82 29.53

Vibrational Frequencies (cm^{-1})
771.2 1134.2 1143.5 1443.5 2962.3
3087.6

Bond Distances (10^{-10} m)		**Bond Angles** (°)		**Dihedral Angles** (°)	
C1-F1	1.331				
C1-H1	1.073	F1-C1-H1	113.95		
C1-H2	1.073	F1-C1-H2	113.95	H1-C1-H2	144.84

Enthalpy Reference Temperature = T_r = 298.15 K
Standard State Pressure = p_o = 1 atmosphere

	J K^{-1} mol^{-1}		kJ mol^{-1}			
T/K	C_p°	S°	H°-$H^\circ(T_r)$	ΔH_f°	ΔG_f°	Log K_f
150	33.58	210.04	-5.28	-29.25	-30.29	10.55
200	34.60	219.82	-3.58	-29.96	-30.54	7.98
250	36.40	227.72	-1.80	-30.71	-30.63	6.40
300	38.74	234.56	0.07	-31.46	-30.59	5.32
350	41.31	240.72	2.07	-32.22	-30.42	4.54
400	43.90	246.41	4.20	-32.89	-30.12	3.93
450	46.37	251.72	6.46	-33.56	-29.75	3.45
500	48.68	256.73	8.84	-34.18	-29.33	3.06
600	52.76	265.97	13.92	-35.27	-28.28	2.46
700	56.25	274.38	19.37	-36.19	-27.07	2.02
800	59.25	282.09	25.15	-37.03	-25.69	1.68
900	61.88	289.22	31.21	-37.70	-24.23	1.41
1000	64.17	295.86	37.51	-38.28	-22.64	1.18
1100	66.18	302.08	44.03	-38.79	-21.00	1.00
1200	67.94	307.91	50.74	-39.20	-19.33	0.84
1300	69.47	313.41	57.61	-39.54	-17.57	0.71
1400	70.81	318.61	64.63	-39.83	-15.82	0.59
1500	71.99	323.54	71.77	-40.12	-14.02	0.49
1600	73.02	328.21	79.02	-40.33	-12.22	0.40
1700	73.93	332.67	86.37	-40.50	-10.42	0.32
1800	74.73	336.92	93.81	-40.67	-8.62	0.25
1900	75.44	340.98	101.31	-40.79	-6.86	0.19
2000	76.07	344.87	108.89	-40.92	-5.10	0.13
2100	76.63	348.59	116.52	-41.05	-3.35	0.08
2200	77.12	352.17	124.21	-41.09	-1.63	0.04
2300	77.57	355.61	131.95	-41.17	0.08	0.00
2400	77.97	358.92	139.72	-41.21	1.76	-0.04
2500	78.33	362.10	147.54	-41.25	3.39	-0.07
2600	78.66	365.18	155.39	-41.30	5.02	-0.10
2700	78.95	368.16	163.27	-41.34	6.65	-0.13
2800	79.22	371.03	171.18	-41.34	8.28	-0.15
2900	79.46	373.82	179.11	-41.34	9.87	-0.18
3000	79.68	376.52	187.07	-41.34	11.51	-0.20

•CHF_2

ΔH_f°(0 K) = -243.76 kJ mol^{-1}
ΔH_f°(298.15 K) = -247.27 kJ mol^{-1}
S°(298.15 K) = 255.94 J K^{-1} mol^{-1}

Moments of Inertia (10^{-47} kg m^2)
12.20 74.78 85.62

Vibrational Frequencies (cm^{-1})
521.4 1041.3 1150.0 1180.8 1343.1
3005.3

Bond Distances (10^{-10} m)		**Bond Angles** (°)		**Dihedral Angles** (°)	
C1-H1	1.076				
C1-F1	1.314	H1-C1-F1	113.77		
C1-F2	1.314	H1-C1-F2	113.77	F1-C1-F2	128.66

Enthalpy Reference Temperature = T_r = 298.15 K
Standard State Pressure = p_o = 1 atmosphere

	|- J K^{-1} mol^{-1} -|		|-------- kJ mol^{-1} ---------|			
T/K	**C_p°**	**S°**	**H°-$H^\circ(T_r)$**	**ΔH_f°**	**ΔG_f°**	**Log K_f**
150	34.75	230.08	-5.64	-245.35	-244.01	84.97
200	36.72	240.33	-3.86	-246.02	-243.51	63.59
250	39.27	248.79	-1.96	-246.65	-242.80	50.73
300	42.25	256.21	0.08	-247.27	-242.00	42.13
350	45.43	262.96	2.27	-247.90	-241.08	35.98
400	48.55	269.23	4.62	-248.45	-240.12	31.35
450	51.48	275.12	7.12	-248.95	-239.07	27.75
500	54.15	280.68	9.77	-249.41	-237.94	24.86
600	58.70	290.98	15.41	-250.20	-235.64	20.51
700	62.33	300.31	21.47	-250.83	-233.17	17.40
800	65.25	308.83	27.86	-251.33	-230.62	15.06
900	67.63	316.65	34.51	-251.75	-227.99	13.23
1000	69.60	323.89	41.37	-252.13	-225.27	11.77
1100	71.24	330.60	48.41	-252.42	-222.51	10.57
1200	72.63	336.86	55.61	-252.63	-219.74	9.56
1300	73.80	342.72	62.93	-252.84	-216.94	8.72
1400	74.80	348.23	70.36	-253.01	-214.10	7.99
1500	75.65	353.41	77.89	-253.17	-211.25	7.36
1600	76.39	358.32	85.49	-253.30	-208.36	6.80
1700	77.03	362.97	93.16	-253.38	-205.52	6.31
1800	77.59	367.39	100.89	-253.47	-202.67	5.88
1900	78.08	371.60	108.68	-253.55	-199.87	5.49
2000	78.51	375.62	116.51	-253.59	-197.07	5.15
2100	78.89	379.46	124.38	-253.63	-194.30	4.83
2200	79.22	383.14	132.29	-253.68	-191.54	4.55
2300	79.53	386.66	140.22	-253.72	-188.82	4.29
2400	79.79	390.05	148.19	-253.76	-186.10	4.05
2500	80.03	393.32	156.18	-253.76	-183.43	3.83
2600	80.24	396.46	164.19	-253.76	-180.79	3.63
2700	80.44	399.49	172.23	-253.76	-178.11	3.45
2800	80.62	402.42	180.28	-253.76	-175.48	3.27
2900	80.78	405.25	188.35	-253.76	-172.84	3.11
3000	80.92	407.99	196.43	-253.72	-170.21	2.96

•CF_3

ΔH_f°(0 K) = -469.24 kJ mol^{-1}
ΔH_f°(298.15 K) = -471.90 kJ mol^{-1}
S°(298.15 K) = 264.64 J K^{-1} mol^{-1}

Moments of Inertia (10^{-47} kg m^2)
75.31 75.31 145.53

Vibrational Frequencies (cm^{-1})
490.6 490.6 676.5 1086.2 1285.9
1285.9

Bond Distances (10^{-10} m)		**Bond Angles** (°)		**Dihedral Angles** (°)	
C1-F1	1.301	X1-C1-F1	107.60		
C1-F2	1.301	X1-C1-F2	107.60	F1-C1-F2	120.00
C1-F3	1.301	X1-C1-F3	107.60	F1-C1-F3	-120.00

Enthalpy Reference Temperature = T_r = 298.15 K
Standard State Pressure = p_o = 1 atmosphere

	¦- J K^{-1} mol^{-1} -¦		¦-------- kJ mol^{-1} ---------¦			
T/K	**C_p°**	**S°**	**H°-$H^\circ(T_r)$**	**ΔH_f°**	**ΔG_f°**	**Log K_f**
150	37.22	235.13	-6.47	-470.74	-464.76	161.84
200	41.58	246.43	-4.51	-471.20	-462.71	120.84
250	46.02	256.19	-2.31	-471.62	-460.57	96.23
300	50.22	264.95	0.09	-471.91	-458.36	79.80
350	54.09	272.99	2.70	-472.16	-456.10	68.07
400	57.57	280.45	5.49	-472.33	-453.80	59.26
450	60.64	287.41	8.45	-472.50	-451.50	52.41
500	63.32	293.94	11.55	-472.62	-449.19	46.92
600	67.62	305.88	18.11	-472.75	-444.51	38.70
700	70.80	316.56	25.04	-472.79	-439.82	32.82
800	73.16	326.17	32.24	-472.83	-435.14	28.41
900	74.94	334.90	39.65	-472.79	-430.41	24.98
1000	76.31	342.87	47.22	-472.75	-425.68	22.23
1100	77.37	350.19	54.91	-472.71	-420.91	19.99
1200	78.22	356.96	62.68	-472.71	-416.14	18.11
1300	78.89	363.25	70.54	-472.67	-411.37	16.53
1400	79.44	369.12	78.46	-472.62	-406.56	15.17
1500	79.89	374.61	86.42	-472.58	-401.79	13.99
1600	80.26	379.78	94.43	-472.58	-397.02	12.96
1700	80.58	384.66	102.47	-472.54	-392.25	12.05
1800	80.84	389.27	110.55	-472.50	-387.52	11.24
1900	81.07	393.65	118.64	-472.50	-382.79	10.52
2000	81.27	397.81	126.76	-472.46	-378.11	9.87
2100	81.43	401.78	134.90	-472.42	-373.42	9.29
2200	81.58	405.57	143.05	-472.42	-368.78	8.76
2300	81.71	409.20	151.21	-472.37	-364.18	8.27
2400	81.83	412.68	159.39	-472.33	-359.61	7.83
2500	81.93	416.02	167.57	-472.29	-355.05	7.42
2600	82.01	419.24	175.77	-472.25	-350.54	7.04
2700	82.10	422.34	183.98	-472.21	-346.02	6.69
2800	82.17	425.32	192.19	-472.16	-341.50	6.37
2900	82.24	428.21	200.41	-472.12	-336.98	6.07
3000	82.30	431.00	208.64	-472.08	-332.46	5.79

:CHF (singlet)

ΔH_f°(0 K) = 152.59 kJ mol^{-1}
ΔH_f°(298.15 K) = 152.77 kJ mol^{-1}
S°(298.15 K) = 222.83 J K^{-1} mol^{-1}

Moments of Inertia (10^{-47} kg m^2)
1.72 22.40 24.12

Vibrational Frequencies (cm^{-1})
1189.2 1404.2 2732.5

Bond Distances (10^{-10} m)		**Bond Angles** (°)		**Dihedral Angles** (°)
C1-F1	1.295			
C1-H1	1.104	F1-C1-H1	102.80	

Enthalpy Reference Temperature = T_r = 298.15 K
Standard State Pressure = p_o = 1 atmosphere

	J K^{-1} mol^{-1}		kJ mol^{-1}			
T/K	**C_p°**	**S°**	**H°-$H^\circ(T_r)$**	**ΔH_f°**	**ΔG_f°**	**Log K_f**
150	33.27	199.73	-4.99	153.09	145.35	-50.61
200	33.41	209.32	-3.33	153.09	142.72	-37.28
250	33.84	216.81	-1.64	152.97	140.16	-29.28
300	34.62	223.04	0.06	152.76	137.57	-23.95
350	35.66	228.46	1.82	152.51	135.02	-20.15
400	36.85	233.30	3.63	152.21	132.55	-17.31
450	38.09	237.71	5.51	151.92	130.08	-15.10
500	39.33	241.78	7.44	151.59	127.65	-13.33
600	41.66	249.17	11.49	150.92	122.88	-10.70
700	43.72	255.74	15.77	150.25	118.24	-8.82
800	45.53	261.70	20.23	149.58	113.72	-7.42
900	47.08	267.16	24.86	148.95	109.29	-6.34
1000	48.41	272.19	29.64	148.32	104.93	-5.48
1100	49.56	276.86	34.53	147.70	100.71	-4.78
1200	50.54	281.21	39.54	147.11	96.48	-4.20
1300	51.38	285.29	44.64	146.52	92.38	-3.71
1400	52.10	289.13	49.81	145.94	88.28	-3.29
1500	52.72	292.74	55.06	145.35	84.27	-2.93
1600	53.26	296.16	60.35	144.77	80.25	-2.62
1700	53.73	299.41	65.71	144.18	76.27	-2.34
1800	54.14	302.49	71.10	143.59	72.34	-2.10
1900	54.50	305.43	76.53	143.05	68.41	-1.88
2000	54.81	308.23	82.00	142.47	64.48	-1.68
2100	55.09	310.91	87.49	141.92	60.50	-1.51
2200	55.33	313.48	93.01	141.34	56.57	-1.34
2300	55.56	315.94	98.56	140.79	52.63	-1.20
2400	55.75	318.31	104.12	140.21	48.70	-1.06
2500	55.93	320.59	109.71	139.66	44.77	-0.94
2600	56.08	322.79	115.31	139.08	40.84	-0.82
2700	56.22	324.91	120.93	138.53	36.90	-0.71
2800	56.35	326.95	126.55	137.99	32.97	-0.62
2900	56.47	328.93	132.19	137.40	29.08	-0.52
3000	56.58	330.85	137.85	136.86	25.23	-0.44

:CF_2 (singlet)

ΔH_f°(0 K) = -203.84 kJ mol^{-1}
ΔH_f°(298.15 K) = -203.33 kJ mol^{-1}
S°(298.15 K) = 240.43 J K^{-1} mol^{-1}

Moments of Inertia (10^{-47} kg m^2)
9.35 64.95 74.30

Vibrational Frequencies (cm^{-1})
651.0 1155.5 1240.8

Bond Distances (10^{-10} m)		**Bond Angles** (°)		**Dihedral Angles** (°)
C1-F1	1.283			
C1-F2	1.283	F1-C1-F2	104.47	

Enthalpy Reference Temperature = T_r = 298.15 K
Standard State Pressure = p_o = 1 atmosphere

	¦- J K^{-1} mol^{-1} -¦		¦-------- kJ mol^{-1} ---------¦			
T/K	C_p°	S°	H°-$H^\circ(T_r)$	ΔH_f°	ΔG_f°	Log K_f
150	33.91	215.80	-5.35	-203.30	-208.07	72.45
200	35.20	225.72	-3.63	-203.26	-209.66	54.76
250	36.96	233.76	-1.82	-203.30	-211.29	44.15
300	38.94	240.67	0.07	-203.34	-212.92	37.07
350	40.97	246.82	2.07	-203.43	-214.51	32.02
400	42.90	252.42	4.17	-203.51	-216.15	28.22
450	44.66	257.58	6.36	-203.59	-217.74	25.27
500	46.23	262.37	8.63	-203.68	-219.33	22.91
600	48.79	271.04	13.39	-203.93	-222.46	19.37
700	50.71	278.70	18.37	-204.18	-225.56	16.83
800	52.14	285.57	23.51	-204.43	-228.61	14.93
900	53.22	291.78	28.78	-204.76	-231.58	13.44
1000	54.04	297.43	34.15	-205.14	-234.51	12.25
1100	54.69	302.62	39.58	-205.52	-237.40	11.27
1200	55.20	307.39	45.08	-205.94	-240.20	10.46
1300	55.61	311.83	50.62	-206.40	-242.96	9.76
1400	55.94	315.97	56.20	-206.86	-245.68	9.17
1500	56.22	319.83	61.81	-207.36	-248.40	8.65
1600	56.45	323.47	67.44	-207.86	-251.04	8.20
1700	56.64	326.90	73.10	-208.36	-253.72	7.79
1800	56.80	330.14	78.77	-208.87	-256.35	7.44
1900	56.94	333.21	84.46	-209.41	-258.95	7.12
2000	57.06	336.14	90.16	-209.95	-261.58	6.83
2100	57.16	338.92	95.87	-210.50	-264.18	6.57
2200	57.25	341.59	101.59	-211.04	-266.81	6.33
2300	57.33	344.13	107.32	-211.58	-269.45	6.12
2400	57.40	346.57	113.06	-212.13	-272.04	5.92
2500	57.46	348.92	118.80	-212.67	-274.68	5.74
2600	57.52	351.18	124.55	-213.22	-277.32	5.57
2700	57.56	353.35	130.30	-213.76	-279.95	5.42
2800	57.61	355.44	136.06	-214.30	-282.55	5.27
2900	57.65	357.46	141.82	-214.85	-285.10	5.14
3000	57.68	359.42	147.59	-215.39	-287.65	5.01

CHF=O

ΔH_f°(0 K) = -378.57 kJ mol^{-1}
ΔH_f°(298.15 K) = -382.28 kJ mol^{-1}
S°(298.15 K) = 246.15 J K^{-1} mol^{-1}

Moments of Inertia (10^{-47} kg m^2)
8.84 68.99 77.83

Vibrational Frequencies (cm^{-1})
659.1 1050.8 1115.1 1374.1 1876.5
2996.9

Bond Distances (10^{-10} m)		**Bond Angles** (°)		**Dihedral Angles** (°)
C1-O1	1.164			
C1-F1	1.314	O1-C1-F1	123.03	
C1-H1	1.081	O1-C1-H1	126.96	

Enthalpy Reference Temperature = T_r = 298.15 K
Standard State Pressure = p_o = 1 atmosphere

	|- J K^{-1} mol^{-1} -|		|-------- kJ mol^{-1} ---------|			
T/K	**C_p°**	**S°**	**H°-$H^\circ(T_r)$**	**ΔH_f°**	**ΔG_f°**	**Log K_f**
150	33.92	221.26	-5.42	-380.20	-377.40	131.41
200	35.38	231.20	-3.69	-380.91	-376.35	98.29
250	37.57	239.32	-1.87	-381.62	-375.14	78.38
300	40.21	246.40	0.08	-382.29	-373.80	65.08
350	43.03	252.81	2.15	-382.96	-372.38	55.57
400	45.86	258.74	4.38	-383.59	-370.83	48.42
450	48.57	264.29	6.74	-384.13	-369.24	42.86
500	51.12	269.55	9.23	-384.68	-367.56	38.40
600	55.64	279.28	14.58	-385.60	-364.09	31.69
700	59.43	288.15	20.33	-386.35	-360.45	26.90
800	62.61	296.30	26.44	-386.98	-356.69	23.29
900	65.26	303.83	32.84	-387.52	-352.88	20.48
1000	67.49	310.83	39.48	-387.98	-348.95	18.23
1100	69.37	317.35	46.33	-388.36	-344.97	16.38
1200	70.96	323.45	53.34	-388.69	-340.95	14.84
1300	72.32	329.19	60.51	-388.94	-336.94	13.54
1400	73.47	334.59	67.80	-389.20	-332.84	12.42
1500	74.47	339.69	75.20	-389.40	-328.74	11.45
1600	75.32	344.53	82.69	-389.57	-324.64	10.60
1700	76.07	349.12	90.26	-389.74	-320.54	9.85
1800	76.72	353.49	97.90	-389.87	-316.44	9.18
1900	77.28	357.65	105.60	-389.95	-312.38	8.59
2000	77.78	361.63	113.35	-390.07	-308.32	8.05
2100	78.22	365.43	121.16	-390.16	-304.26	7.57
2200	78.61	369.08	129.00	-390.20	-300.24	7.13
2300	78.96	372.58	136.88	-390.28	-296.27	6.73
2400	79.27	375.95	144.79	-390.33	-292.29	6.36
2500	79.55	379.19	152.73	-390.37	-288.32	6.02
2600	79.80	382.32	160.69	-390.41	-284.43	5.71
2700	80.02	385.33	168.69	-390.41	-280.50	5.43
2800	80.22	388.25	176.70	-390.45	-276.60	5.16
2900	80.41	391.07	184.73	-390.45	-272.67	4.91
3000	80.58	393.79	192.78	-390.45	-268.74	4.68

$CF_2=O$

ΔH_f°(0 K) = -595.34 kJ mol^{-1}
ΔH_f°(298.15 K) = -598.38 kJ mol^{-1}
S°(298.15 K) = 258.58 J K^{-1} mol^{-1}

Moments of Inertia (10^{-47} kg m^2)
68.97 69.00 137.97

Vibrational Frequencies (cm^{-1})
563.3 610.1 779.0 976.6 1305.5
1953.0

Bond Distances (10^{-10} m)		**Bond Angles** (°)		**Dihedral Angles** (°)
C1-O1	1.157			
C1-F1	1.290	O1-C1-F1	125.86	
C1-F2	1.290	O1-C1-F2	125.86	

Enthalpy Reference Temperature = T_r = 298.15 K
Standard State Pressure = p_o = 1 atmosphere

	- J K^{-1} mol^{-1} -		---------- kJ mol^{-1} ----------			
T/K	**C_p°**	**S°**	**H°-$H^\circ(T_r)$**	**ΔH_f°**	**ΔG_f°**	**Log K_f**
150	35.51	230.72	-6.11	-596.93	-590.11	205.49
200	39.15	241.41	-4.25	-597.52	-587.77	153.50
250	43.37	250.60	-2.18	-597.98	-585.30	122.29
300	47.51	258.88	0.09	-598.40	-582.75	101.46
350	51.30	266.49	2.56	-598.73	-580.15	86.58
400	54.69	273.57	5.21	-598.98	-577.48	75.41
450	57.68	280.18	8.02	-599.23	-574.80	66.72
500	60.31	286.40	10.97	-599.40	-572.12	59.76
600	64.64	297.80	17.23	-599.65	-566.68	49.33
700	67.98	308.02	23.87	-599.82	-561.16	41.87
800	70.58	317.27	30.80	-599.94	-555.64	36.28
900	72.61	325.71	37.97	-600.07	-550.07	31.92
1000	74.22	333.45	45.31	-600.11	-544.46	28.44
1100	75.51	340.59	52.80	-600.15	-538.86	25.59
1200	76.55	347.20	60.40	-600.24	-533.25	23.21
1300	77.40	353.36	68.10	-600.28	-527.60	21.20
1400	78.11	359.13	75.88	-600.28	-521.91	19.47
1500	78.69	364.54	83.72	-600.32	-516.26	17.98
1600	79.18	369.63	91.61	-600.36	-510.62	16.67
1700	79.60	374.44	99.55	-600.36	-504.97	15.51
1800	79.95	379.00	107.53	-600.40	-499.32	14.49
1900	80.26	383.33	115.54	-600.40	-493.71	13.57
2000	80.53	387.46	123.58	-600.40	-488.11	12.75
2100	80.76	391.39	131.65	-600.40	-482.54	12.00
2200	80.96	395.15	139.73	-600.45	-477.02	11.33
2300	81.14	398.76	147.84	-600.45	-471.49	10.71
2400	81.29	402.21	155.96	-600.40	-466.01	10.14
2500	81.43	405.53	164.10	-600.40	-460.57	9.62
2600	81.55	408.73	172.24	-600.40	-455.14	9.14
2700	81.67	411.81	180.41	-600.36	-449.70	8.70
2800	81.77	414.78	188.58	-600.36	-444.26	8.29
2900	81.86	417.66	196.76	-600.32	-438.86	7.90
3000	81.94	420.43	204.95	-600.28	-433.42	7.55

•CF=O

ΔH_f°(0 K) = -183.43 kJ mol^{-1}
ΔH_f°(298.15 K) = -182.87 kJ mol^{-1}
S°(298.15 K) = 248.32 J K^{-1} mol^{-1}

Moments of Inertia (10^{-47} kg m^2)
4.19 70.99 75.18

Vibrational Frequencies (cm^{-1})
632.0 1081.1 1915.2

Bond Distances (10^{-10} m)		**Bond Angles** (°)		**Dihedral Angles** (°)
C1-O1	1.152			
C1-F1	1.304	O1-C1-F1	128.26	

Enthalpy Reference Temperature = T_r = 298.15 K
Standard State Pressure = p_o = 1 atmosphere

	|- J K^{-1} mol^{-1} -|		|-------- kJ mol^{-1} ---------|			
T/K	**C_p°**	**S°**	**H°-$H^\circ(T_r)$**	**ΔH_f°**	**ΔG_f°**	**Log K_f**
150	34.00	223.66	-5.36	-182.88	-188.66	65.70
200	35.33	233.61	-3.63	-182.84	-190.62	49.78
250	36.97	241.66	-1.82	-182.84	-192.59	40.24
300	38.67	248.55	0.07	-182.88	-194.56	33.87
350	40.30	254.64	2.05	-182.92	-196.52	29.33
400	41.84	260.12	4.10	-182.97	-198.49	25.92
450	43.27	265.14	6.23	-183.05	-200.46	23.26
500	44.57	269.76	8.43	-183.13	-202.38	21.14
600	46.85	278.10	13.00	-183.38	-206.23	17.95
700	48.71	285.46	17.78	-183.64	-210.08	15.67
800	50.22	292.07	22.73	-183.97	-213.80	13.96
900	51.44	298.06	27.82	-184.35	-217.48	12.62
1000	52.42	303.53	33.01	-184.77	-221.12	11.55
1100	53.22	308.57	38.29	-185.23	-224.68	10.67
1200	53.88	313.23	43.65	-185.69	-228.20	9.93
1300	54.43	317.56	49.07	-186.15	-231.67	9.31
1400	54.88	321.61	54.53	-186.69	-235.10	8.77
1500	55.25	325.41	60.04	-187.19	-238.45	8.30
1600	55.57	328.99	65.58	-187.74	-241.79	7.89
1700	55.84	332.36	71.15	-188.28	-245.14	7.53
1800	56.08	335.56	76.75	-188.82	-248.45	7.21
1900	56.28	338.60	82.37	-189.37	-251.75	6.92
2000	56.45	341.49	88.00	-189.91	-255.01	6.66
2100	56.61	344.25	93.65	-190.50	-258.32	6.42
2200	56.74	346.89	99.32	-191.04	-261.58	6.21
2300	56.86	349.41	105.00	-191.63	-264.89	6.02
2400	56.96	351.83	110.70	-192.17	-268.19	5.84
2500	57.05	354.16	116.39	-192.76	-271.50	5.67
2600	57.14	356.40	122.11	-193.30	-274.76	5.52
2700	57.21	358.56	127.82	-193.89	-278.07	5.38
2800	57.28	360.64	133.54	-194.43	-281.33	5.25
2900	57.34	362.65	139.28	-195.02	-284.60	5.13
3000	57.39	364.59	145.01	-195.56	-287.82	5.01

$CH_2FO\bullet$

ΔH_f°(0 K) = -186.73 kJ mol^{-1}
ΔH_f°(298.15 K) = -194.40 kJ mol^{-1}
S°(298.15 K) = 257.00 J K^{-1} mol^{-1}

Moments of Inertia (10^{-47} kg m^2)

15.36	75.54	85.58

Vibrational Frequencies (cm^{-1})

527.3	911.9	1047.1	1108.4	1198.1
1412.9	1439.9	2885.3	2937.7	

Bond Distances (10^{-10} m)		**Bond Angles** (°)		**Dihedral Angles** (°)	
C1-O1	1.345				
C1-F1	1.354	O1-C1-F1	112.61		
C1-H1	1.084	O1-C1-H1	108.34	F1-C1-H1	119.89
C1-H2	1.084	O1-C1-H2	108.34	F1-C1-H2	-119.89

Enthalpy Reference Temperature = T_r = 298.15 K
Standard State Pressure = p_o = 1 atmosphere

	¦- J K^{-1} mol^{-1} -¦		¦-------- kJ mol^{-1} ---------¦			
T/K	**C_p°**	**S°**	**H°-$H^\circ(T_r)$**	**ΔH_f°**	**ΔG_f°**	**Log K_f**
150	34.80	230.58	-5.78	-190.54	-180.83	62.98
200	37.20	240.89	-3.98	-191.88	-177.44	46.34
250	40.56	249.53	-2.05	-193.22	-173.68	36.29
300	44.61	257.28	0.08	-194.43	-169.70	29.54
350	48.97	264.48	2.42	-195.56	-165.48	24.70
400	53.32	271.31	4.98	-196.56	-161.17	21.04
450	57.45	277.83	7.75	-197.48	-156.69	18.19
500	61.27	284.08	10.72	-198.24	-152.13	15.89
600	67.93	295.86	17.19	-199.49	-142.84	12.43
700	73.42	306.76	24.27	-200.41	-133.30	9.95
800	77.98	316.87	31.84	-201.04	-123.68	8.08
900	81.79	326.28	39.84	-201.46	-113.97	6.62
1000	85.00	335.07	48.18	-201.67	-104.22	5.44
1100	87.71	343.30	56.82	-201.75	-94.43	4.48
1200	90.03	351.03	65.71	-201.71	-84.60	3.68
1300	92.00	358.32	74.81	-201.59	-74.77	3.00
1400	93.70	365.20	84.10	-201.42	-64.98	2.42
1500	95.16	371.71	93.55	-201.12	-55.19	1.92
1600	96.42	377.90	103.13	-200.79	-45.40	1.48
1700	97.52	383.78	112.83	-200.46	-35.65	1.10
1800	98.48	389.38	122.62	-200.04	-25.94	0.75
1900	99.32	394.73	132.52	-199.62	-16.28	0.45
2000	100.06	399.84	142.49	-199.16	-6.69	0.17
2100	100.71	404.74	152.52	-198.66	2.89	-0.07
2200	101.29	409.44	162.63	-198.15	12.38	-0.29
2300	101.81	413.95	172.78	-197.61	21.84	-0.50
2400	102.27	418.30	182.99	-197.07	31.25	-0.68
2500	102.69	422.48	193.23	-196.52	40.63	-0.85
2600	103.06	426.51	203.52	-195.98	49.96	-1.00
2700	103.40	430.41	213.85	-195.39	59.25	-1.15
2800	103.70	434.18	224.20	-194.81	68.49	-1.28
2900	103.98	437.82	234.58	-194.18	77.74	-1.40
3000	104.23	441.35	245.00	-193.59	86.94	-1.51

$CHF_2O\bullet$

ΔH_f°(0 K) = -398.90 kJ mol^{-1}
ΔH_f°(298.15 K) = -405.62 kJ mol^{-1}
S°(298.15 K) = 274.61 J K^{-1} mol^{-1}

Moments of Inertia (10^{-47} kg m^2)
76.21 78.48 141.68

Vibrational Frequencies (cm^{-1})
443.3 499.4 644.7 1014.8 1147.3
1154.8 1355.1 1390.9 2961.3

Bond Distances (10^{-10} m)		**Bond Angles** (°)		**Dihedral Angles** (°)	
C1-O1	1.346				
C1-H1	1.080	O1-C1-H1	106.89		
C1-F1	1.327	O1-C1-F1	111.12	H1-C1-F1	120.39
C1-F2	1.327	O1-C1-F2	111.12	H1-C1-F2	-120.39

Enthalpy Reference Temperature = T_r = 298.15 K
Standard State Pressure = p_o = 1 atmosphere

	- J K^{-1} mol^{-1} -		---------- kJ mol^{-1} ----------			
T/K	**C_p°**	**S°**	**H°-$H^\circ(T_r)$**	**ΔH_f°**	**ΔG_f°**	**Log K_f**
150	37.81	244.21	-6.68	-402.58	-389.53	135.65
200	42.61	255.73	-4.67	-403.76	-385.01	100.56
250	47.71	265.79	-2.42	-404.76	-380.24	79.45
300	52.85	274.94	0.10	-405.64	-375.30	65.34
350	57.84	283.47	2.87	-406.39	-370.20	55.25
400	62.51	291.50	5.88	-407.06	-365.01	47.66
450	66.77	299.11	9.11	-407.56	-359.74	41.76
500	70.58	306.35	12.55	-407.98	-354.43	37.02
600	76.96	319.80	19.94	-408.57	-343.67	29.92
700	81.95	332.06	27.89	-408.90	-332.84	24.84
800	85.89	343.27	36.29	-409.03	-322.00	21.02
900	89.04	353.57	45.04	-408.99	-311.08	18.05
1000	91.61	363.09	54.08	-408.86	-300.20	15.68
1100	93.72	371.92	63.35	-408.61	-289.28	13.74
1200	95.47	380.16	72.81	-408.32	-278.40	12.12
1300	96.93	387.86	82.43	-407.98	-267.52	10.75
1400	98.17	395.09	92.19	-407.61	-256.65	9.58
1500	99.22	401.90	102.06	-407.19	-245.81	8.56
1600	100.13	408.33	112.03	-406.73	-235.02	7.67
1700	100.90	414.43	122.08	-406.22	-224.26	6.89
1800	101.57	420.21	132.21	-405.72	-213.55	6.20
1900	102.16	425.72	142.39	-405.22	-202.88	5.58
2000	102.68	430.97	152.64	-404.68	-192.30	5.02
2100	103.12	435.99	162.93	-404.13	-181.71	4.52
2200	103.52	440.80	173.26	-403.55	-171.21	4.07
2300	103.88	445.41	183.63	-403.00	-160.75	3.65
2400	104.19	449.84	194.04	-402.42	-150.37	3.27
2500	104.47	454.10	204.47	-401.83	-140.04	2.93
2600	104.73	458.20	214.93	-401.20	-129.70	2.61
2700	104.96	462.16	225.41	-400.62	-119.45	2.31
2800	105.16	465.98	235.92	-399.99	-109.20	2.04
2900	105.35	469.67	246.45	-399.36	-98.99	1.78
3000	105.52	473.25	256.99	-398.74	-88.78	1.55

$CF_3O\bullet$

ΔH_f^o(0 K) = -623.37 kJ mol^{-1}
ΔH_f^o(298.15 K) = -628.33 kJ mol^{-1}
S^o(298.15 K) = 292.57 J K^{-1} mol^{-1}

Moments of Inertia (10^{-47} kg m^2)
136.13 139.58 144.70

Vibrational Frequencies (cm^{-1})
224.6 410.9 572.2 583.2 607.1
883.4 1274.8 1277.7 1309.3

Bond Distances (10^{-10} m)		**Bond Angles** (°)		**Dihedral Angles** (°)	
C1-O1	1.353				
C1-F1	1.308	O1-C1-F1	111.34		
C1-F2	1.308	O1-C1-F2	111.33	F1-C1-F2	120.51
C1-F3	1.307	O1-C1-F3	106.73	F1-C1-F3	-119.74

Enthalpy Reference Temperature = T_r = 298.15 K
Standard State Pressure = p_o = 1 atmosphere

	J K^{-1} mol^{-1}		kJ mol^{-1}			
T/K	C_p^o	S^o	$H^o-H^o(T_r)$	ΔH_f^o	ΔG_f^o	Log K_f
150	44.59	255.71	-8.12	-626.68	-609.94	212.39
200	51.68	269.51	-5.71	-627.43	-604.25	157.81
250	58.40	281.78	-2.96	-627.98	-598.44	125.03
300	64.49	292.97	0.12	-628.35	-592.50	103.16
350	69.89	303.33	3.48	-628.56	-586.55	87.53
400	74.63	312.98	7.10	-628.69	-580.53	75.81
450	78.76	322.01	10.93	-628.69	-574.55	66.69
500	82.30	330.49	14.96	-628.65	-568.56	59.39
600	87.95	346.03	23.49	-628.35	-556.60	48.45
700	92.10	359.91	32.51	-627.89	-544.67	40.64
800	95.17	372.42	41.87	-627.35	-532.83	34.79
900	97.49	383.77	51.51	-626.76	-521.03	30.24
1000	99.25	394.14	61.35	-626.18	-509.32	26.60
1100	100.63	403.66	71.35	-625.51	-497.60	23.63
1200	101.72	412.47	81.47	-624.88	-485.93	21.15
1300	102.59	420.65	91.69	-624.25	-474.30	19.06
1400	103.29	428.28	101.98	-623.58	-462.75	17.26
1500	103.88	435.42	112.34	-622.96	-451.20	15.71
1600	104.36	442.14	122.75	-622.29	-439.74	14.35
1700	104.77	448.48	133.21	-621.66	-428.32	13.16
1800	105.11	454.48	143.71	-620.99	-416.94	12.10
1900	105.41	460.17	154.23	-620.36	-405.60	11.15
2000	105.66	465.59	164.79	-619.73	-394.34	10.30
2100	105.88	470.75	175.36	-619.06	-383.13	9.53
2200	106.07	475.67	185.96	-618.40	-372.00	8.83
2300	106.24	480.39	196.58	-617.77	-360.91	8.20
2400	106.38	484.92	207.21	-617.10	-349.87	7.61
2500	106.52	489.26	217.85	-616.43	-338.90	7.08
2600	106.63	493.44	228.51	-615.80	-327.94	6.59
2700	106.73	497.47	239.18	-615.13	-317.06	6.13
2800	106.83	501.36	249.86	-614.46	-306.19	5.71
2900	106.91	505.11	260.54	-613.79	-295.35	5.32
3000	106.99	508.73	271.24	-613.12	-284.51	4.95

•CF_2OH

ΔH_f°(0 K) = -451.87 kJ mol^{-1}
ΔH_f°(298.15 K) = -456.47 kJ mol^{-1}
S°(298.15 K) = 298.07 J K^{-1} mol^{-1}

Moments of Inertia (10^{-47} kg m^2)
76.29 78.01 146.52

Vibrational Frequencies (cm^{-1})
30.9 500.4 514.0 623.0 987.3
1215.0 1267.2 1301.6 3570.6

Bond Distances (10^{-10} m)		**Bond Angles** (°)		**Dihedral Angles** (°)	
C1-O1	1.324				
C1-F1	1.318	O1-C1-F1	114.03		
C1-F2	1.317	O1-C1-F2	114.35	F1-C1-F2	126.17
O1-H1	0.954	C1-O1-H1	111.32	F2-O1-H1	68.56

Enthalpy Reference Temperature = T_r = 298.15 K
Standard State Pressure = p_o = 1 atmosphere

	|- J K^{-1} mol^{-1} -|		|-------- kJ mol^{-1} ---------|			
T/K	**C_p°**	**S°**	**H°-$H^\circ(T_r)$**	**ΔH_f°**	**ΔG_f°**	**Log K_f**
150	45.43	262.55	-7.78	-454.55	-444.26	154.69
200	50.13	276.25	-5.40	-455.30	-440.70	115.10
250	55.09	287.97	-2.77	-455.97	-437.02	91.30
300	59.94	298.44	0.11	-456.47	-433.17	75.42
350	64.49	308.03	3.22	-456.89	-429.28	64.06
400	68.64	316.92	6.55	-457.23	-425.35	55.54
450	72.34	325.22	10.08	-457.44	-421.37	48.91
500	75.59	333.01	13.78	-457.60	-417.35	43.60
600	80.90	347.28	21.61	-457.73	-409.32	35.63
700	84.95	360.08	29.92	-457.73	-401.29	29.94
800	88.11	371.63	38.58	-457.56	-393.25	25.67
900	90.63	382.16	47.52	-457.35	-385.18	22.36
1000	92.70	391.82	56.69	-457.10	-377.15	19.70
1100	94.43	400.74	66.05	-456.77	-369.11	17.53
1200	95.90	409.02	75.57	-456.43	-361.12	15.72
1300	97.15	416.75	85.22	-456.06	-353.13	14.19
1400	98.23	423.99	94.99	-455.64	-345.14	12.88
1500	99.17	430.80	104.86	-455.22	-337.23	11.74
1600	99.99	437.22	114.82	-454.76	-329.32	10.75
1700	100.71	443.31	124.85	-454.30	-321.46	9.88
1800	101.34	449.08	134.96	-453.84	-313.63	9.10
1900	101.90	454.58	145.12	-453.34	-305.85	8.41
2000	102.40	459.82	155.34	-452.83	-298.11	7.79
2100	102.84	464.83	165.60	-452.29	-290.45	7.22
2200	103.24	469.62	175.90	-451.79	-282.84	6.71
2300	103.59	474.21	186.25	-451.24	-275.27	6.25
2400	103.91	478.63	196.62	-450.66	-267.73	5.83
2500	104.20	482.88	207.03	-450.11	-260.29	5.44
2600	104.46	486.97	217.46	-449.53	-252.84	5.08
2700	104.69	490.92	227.92	-448.94	-245.43	4.75
2800	104.91	494.73	238.40	-448.36	-238.07	4.44
2900	105.10	498.41	248.90	-447.77	-230.75	4.16
3000	105.28	501.98	259.42	-447.14	-223.43	3.89

CH_2FOH hocf trans

ΔH_f°(0 K) = -400.07 kJ mol^{-1}
ΔH_f°(298.15 K) = -412.09 kJ mol^{-1}
S°(298.15 K) = 252.25 J K^{-1} mol^{-1}

Moments of Inertia (10^{-47} kg m^2)

17.26	77.89	89.86

Vibrational Frequencies (cm^{-1})

-115.0	507.5	1024.4	1125.5	1150.2
1237.7	1250.2	1482.3	1536.4	2875.1
2917.0	3671.3			

Bond Distances (10^{-10} m)		**Bond Angles** (°)		**Dihedral Angles** (°)	
C1-O1	1.377				
C1-F1	1.344	O1-C1-F1	106.83		
C1-H1	1.084	O1-C1-H1	111.76	F1-C1-H1	117.94
C1-H2	1.084	O1-C1-H2	111.76	F1-C1-H2	-117.94
O1-H3	0.947	C1-O1-H3	110.14	F1-O1-H3	180.00

Enthalpy Reference Temperature = T_r = 298.15 K
Standard State Pressure = p_o = 1 atmosphere

	- J K^{-1} mol^{-1} -		---------- kJ mol^{-1} ----------			
T/K	**C_p°**	**S°**	**H°-$H^\circ(T_r)$**	**ΔH_f°**	**ΔG_f°**	**Log K_f**
150	34.89	225.93	-5.75	-406.06	-387.40	134.90
200	37.10	236.25	-3.96	-408.11	-380.91	99.48
250	40.23	244.84	-2.03	-410.16	-373.88	78.11
300	44.23	252.52	0.08	-412.17	-366.43	63.80
350	48.78	259.68	2.41	-414.05	-358.69	53.53
400	53.50	266.50	4.96	-415.76	-350.70	45.80
450	58.14	273.07	7.75	-417.35	-342.50	39.75
500	62.53	279.43	10.77	-418.82	-334.13	34.90
600	70.37	291.54	17.43	-421.33	-316.98	27.59
700	77.01	302.90	24.81	-423.38	-299.45	22.34
800	82.63	313.56	32.80	-425.09	-281.58	18.39
900	87.43	323.58	41.30	-426.43	-263.55	15.30
1000	91.55	333.01	50.26	-427.56	-245.39	12.82
1100	95.11	341.90	59.60	-428.44	-227.07	10.78
1200	98.20	350.32	69.27	-429.15	-208.66	9.08
1300	100.88	358.28	79.22	-429.70	-190.20	7.64
1400	103.22	365.85	89.43	-430.16	-171.67	6.41
1500	105.26	373.04	99.86	-430.45	-153.13	5.33
1600	107.05	379.89	110.47	-430.70	-134.60	4.39
1700	108.62	386.43	121.26	-430.87	-116.06	3.57
1800	110.01	392.68	132.19	-430.95	-97.53	2.83
1900	111.24	398.66	143.26	-430.99	-78.99	2.17
2000	112.33	404.40	154.44	-430.95	-60.50	1.58
2100	113.30	409.90	165.72	-430.91	-42.01	1.04
2200	114.16	415.19	177.09	-430.78	-23.56	0.56
2300	114.94	420.28	188.55	-430.66	-5.15	0.12
2400	115.64	425.19	200.08	-430.53	13.22	-0.29
2500	116.26	429.92	211.67	-430.32	31.55	-0.66
2600	116.83	434.50	223.33	-430.12	49.87	-1.00
2700	117.34	438.91	235.04	-429.86	68.16	-1.32
2800	117.81	443.19	246.80	-429.61	86.44	-1.61
2900	118.24	447.33	258.60	-429.36	104.73	-1.89
3000	118.62	451.34	270.44	-429.07	123.01	-2.14

CH_2FOH hocf cis

ΔH_f°(0 K) = -408.78 kJ mol^{-1}
ΔH_f°(298.15 K) = -420.73 kJ mol^{-1}
S°(298.15 K) = 252.71 J K^{-1} mol^{-1}

Moments of Inertia (10^{-47} kg m^2)
18.72 76.24 89.66

Vibrational Frequencies (cm^{-1})
-375.3 490.1 997.9 1120.0 1150.6
1239.3 1257.0 1460.0 1542.4 2913.8
2963.3 3672.2

Bond Distances (10^{-10} m)		**Bond Angles** (°)		**Dihedral Angles** (°)	
C1-O1	1.376				
C1-F1	1.360	O1-C1-F1	109.55		
C1-H1	1.081	O1-C1-H1	110.31	F1-C1-H1	118.65
C1-H2	1.081	O1-C1-H2	110.31	F1-C1-H2	-118.65
O1-H3	0.948	C1-O1-H3	108.83	F1-O1-H3	0.00

Enthalpy Reference Temperature = T_r = 298.15 K
Standard State Pressure = p_o = 1 atmosphere

	- J K^{-1} mol^{-1} -		---------- kJ mol^{-1} ----------			
T/K	**C_p°**	**S°**	**H°-$H^\circ(T_r)$**	**ΔH_f°**	**ΔG_f°**	**Log K_f**
150	35.07	226.22	-5.79	-414.72	-396.14	137.94
200	37.34	236.61	-3.98	-416.81	-389.66	101.76
250	40.51	245.26	-2.04	-418.82	-382.63	79.94
300	44.53	252.99	0.08	-420.78	-375.22	65.33
350	49.08	260.19	2.42	-422.67	-367.52	54.85
400	53.80	267.05	4.99	-424.38	-359.53	46.95
450	58.41	273.66	7.80	-425.97	-351.37	40.78
500	62.77	280.04	10.83	-427.40	-343.00	35.83
600	70.55	292.19	17.51	-429.91	-325.93	28.37
700	77.12	303.57	24.90	-431.96	-308.44	23.02
800	82.68	314.25	32.90	-433.63	-290.70	18.98
900	87.43	324.27	41.41	-435.01	-272.71	15.83
1000	91.52	333.69	50.36	-436.10	-254.60	13.30
1100	95.06	342.59	59.69	-436.98	-236.35	11.22
1200	98.12	350.99	69.36	-437.73	-218.03	9.49
1300	100.80	358.95	79.31	-438.27	-199.62	8.02
1400	103.13	366.51	89.50	-438.73	-181.21	6.76
1500	105.17	373.70	99.92	-439.07	-162.72	5.67
1600	106.96	380.54	110.53	-439.28	-144.22	4.71
1700	108.53	387.08	121.31	-439.45	-125.77	3.86
1800	109.92	393.32	132.23	-439.57	-107.28	3.11
1900	111.15	399.30	143.29	-439.61	-88.83	2.44
2000	112.24	405.03	154.46	-439.57	-70.37	1.84
2100	113.22	410.53	165.73	-439.53	-51.97	1.29
2200	114.09	415.81	177.10	-439.45	-33.60	0.80
2300	114.87	420.91	188.54	-439.32	-15.23	0.35
2400	115.57	425.81	200.07	-439.15	3.10	-0.07
2500	116.20	430.54	211.66	-438.99	21.34	-0.45
2600	116.77	435.11	223.30	-438.78	39.62	-0.80
2700	117.29	439.53	235.01	-438.57	57.86	-1.12
2800	117.76	443.80	246.76	-438.32	76.07	-1.42
2900	118.19	447.94	258.56	-438.06	94.27	-1.70
3000	118.58	451.95	270.40	-437.77	112.47	-1.96

CH_2FOH hocf gauche

ΔH_f°(0 K) = -419.24 kJ mol^{-1}
ΔH_f°(298.15 K) = -430.32 kJ mol^{-1}
S°(298.15 K) = 257.60 J K^{-1} mol^{-1}

Moments of Inertia (10^{-47} kg m^2)

18.02	78.78	89.64

Vibrational Frequencies (cm^{-1})

351.4	528.7	1019.3	1068.8	1132.5
1244.4	1362.7	1446.2	1522.1	2903.0
2990.6	3657.1			

Bond Distances (10^{-10} m)		**Bond Angles** (°)		**Dihedral Angles** (°)	
C1-O1	1.364				
C1-F1	1.361	O1-C1-F1	110.75		
C1-H1	1.077	O1-C1-H1	107.47	F1-C1-H1	118.27
C1-H2	1.083	O1-C1-H2	112.40	F1-C1-H2	-119.38
O1-H3	0.948	C1-O1-H3	109.90	F1-O1-H3	63.74

Enthalpy Reference Temperature = T_r = 298.15 K
Standard State Pressure = p_o = 1 atmosphere

	- J K^{-1} mol^{-1} -		kJ mol^{-1}			
T/K	C_p°	S°	H°-$H^\circ(T_r)$	ΔH_f°	ΔG_f°	Log K_f
150	38.24	227.38	-6.56	-425.09	-406.68	141.61
200	42.16	239.00	-4.55	-426.94	-400.28	104.54
250	46.56	248.97	-2.34	-428.73	-393.46	82.20
300	51.52	257.92	0.10	-430.37	-386.27	67.26
350	56.76	266.25	2.79	-431.87	-378.86	56.54
400	61.97	274.16	5.74	-433.21	-371.20	48.47
450	66.89	281.72	8.95	-434.38	-363.42	42.18
500	71.41	288.98	12.39	-435.43	-355.51	37.14
600	79.18	302.68	19.92	-437.06	-339.41	29.55
700	85.49	315.34	28.17	-438.27	-323.00	24.10
800	90.69	327.08	36.99	-439.11	-306.48	20.01
900	95.05	338.01	46.31	-439.70	-289.78	16.82
1000	98.76	348.21	56.03	-440.03	-273.05	14.26
1100	101.96	357.77	66.10	-440.16	-256.23	12.17
1200	104.73	366.75	76.47	-440.20	-239.41	10.42
1300	107.13	375.23	87.10	-440.07	-222.59	8.94
1400	109.24	383.24	97.96	-439.86	-205.73	7.68
1500	111.08	390.84	109.01	-439.57	-188.95	6.58
1600	112.69	398.06	120.23	-439.19	-172.13	5.62
1700	114.12	404.93	131.60	-438.73	-155.39	4.77
1800	115.38	411.49	143.11	-438.27	-138.70	4.02
1900	116.49	417.83	154.73	-437.73	-122.17	3.36
2000	117.48	423.99	166.46	-437.19	-105.86	2.76
2100	118.37	429.89	178.28	-436.56	-89.66	2.23
2200	119.16	435.56	190.18	-435.93	-73.51	1.75
2300	119.87	441.01	202.15	-435.30	-57.45	1.31
2400	120.51	446.27	214.20	-434.63	-41.51	0.90
2500	121.08	451.34	226.30	-433.92	-25.56	0.53
2600	121.60	456.23	238.45	-433.21	-9.75	0.20
2700	122.07	460.96	250.66	-432.50	6.02	-0.12
2800	122.50	465.53	262.90	-431.75	21.76	-0.41
2900	122.89	469.96	275.19	-430.99	37.45	-0.67
3000	123.25	474.26	287.51	-430.24	53.09	-0.92

CHF_2OH hcoh trans

ΔH_f°(0 K) = -674.25 kJ mol^{-1}
ΔH_f°(298.15 K) = -684.31 kJ mol^{-1}
S°(298.15 K) = 275.29 J K^{-1} mol^{-1}

Moments of Inertia (10^{-47} kg m^2)

80.43	81.32	144.72

Vibrational Frequencies (cm^{-1})

300.8	498.6	532.3	640.5	1025.3
1118.6	1192.0	1309.9	1384.2	1437.7
3040.2	3630.2			

Bond Distances (10^{-10} m)		**Bond Angles** ($^\circ$)		**Dihedral Angles** ($^\circ$)	
C1-O1	1.340				
O1-H1	0.951	C1-O1-H1	109.83		
C1-H2	1.073	O1-C1-H2	109.50	H1-C1-H2	180.00
C1-F1	1.337	O1-C1-F1	110.98	H2-C1-F1	121.21
C1-F2	1.337	O1-C1-F2	110.98	H2-C1-F2	-121.21

Enthalpy Reference Temperature = T_r = 298.15 K
Standard State Pressure = p_o = 1 atmosphere

	- J K^{-1} mol^{-1} -		-------- kJ mol^{-1} ---------			
T/K	**C_p°**	**S°**	**H°-$H^\circ(T_r)$**	**ΔH_f°**	**ΔG_f°**	**Log K_f**
150	41.48	240.87	-7.52	-679.98	-658.19	229.18
200	47.87	253.81	-5.29	-681.62	-650.70	169.94
250	54.35	265.22	-2.75	-683.08	-642.83	134.31
300	60.68	275.67	0.11	-684.34	-634.71	110.50
350	66.65	285.45	3.28	-685.42	-626.34	93.47
400	72.12	294.67	6.74	-686.34	-617.89	80.68
450	77.00	303.43	10.46	-687.14	-609.27	70.72
500	81.30	311.74	14.42	-687.72	-600.61	62.74
600	88.39	327.18	22.93	-688.69	-583.08	50.76
700	93.90	341.21	32.08	-689.27	-565.43	42.19
800	98.30	354.03	41.73	-689.61	-547.69	35.76
900	101.92	365.81	51.78	-689.73	-529.86	30.75
1000	104.95	376.70	62.17	-689.73	-512.00	26.74
1100	107.53	386.82	72.83	-689.61	-494.13	23.46
1200	109.75	396.27	83.73	-689.40	-476.26	20.73
1300	111.67	405.13	94.84	-689.10	-458.44	18.42
1400	113.34	413.47	106.12	-688.73	-440.58	16.44
1500	114.80	421.53	117.56	-688.31	-423.09	14.73
1600	116.08	429.17	129.14	-687.85	-405.64	13.24
1700	117.20	436.43	140.83	-687.35	-388.28	11.93
1800	118.20	443.35	152.62	-686.80	-370.95	10.76
1900	119.08	449.94	164.51	-686.22	-353.76	9.72
2000	119.86	456.24	176.49	-685.59	-336.64	8.79
2100	120.56	462.28	188.53	-684.96	-319.57	7.95
2200	121.19	468.07	200.64	-684.34	-302.63	7.18
2300	121.75	473.63	212.80	-683.62	-285.73	6.49
2400	122.25	478.98	225.02	-682.95	-268.91	5.85
2500	122.70	484.12	237.28	-682.24	-252.17	5.27
2600	123.11	489.09	249.59	-681.53	-235.52	4.73
2700	123.49	493.88	261.93	-680.78	-218.91	4.23
2800	123.83	498.52	274.31	-680.03	-202.34	3.77
2900	124.14	503.00	286.73	-679.27	-185.81	3.35
3000	124.42	507.35	299.16	-678.48	-169.33	2.95

CHF_2OH hcoh gauche

ΔH_f°(0 K) = -662.24 kJ mol^{-1}
ΔH_f°(298.15 K) = -671.82 kJ mol^{-1}
S°(298.15 K) = 279.18 J K^{-1} mol^{-1}

Moments of Inertia (10^{-47} kg m^2)
79.20 81.24 146.47

Vibrational Frequencies (cm^{-1})
199.0 485.7 489.9 679.7 1066.7
1096.2 1199.5 1264.6 1403.9 1457.5
2971.2 3666.2

Bond Distances (10^{-10} m)		**Bond Angles** (°)		**Dihedral Angles** (°)	
C1-O1	1.348				
O1-H1	0.949	C1-O1-H1	110.08		
C1-H2	1.079	O1-C1-H2	113.85	H1-C1-H2	68.50
C1-F1	1.321	O1-C1-F1	107.51	H2-C1-F1	121.02
C1-F2	1.339	O1-C1-F2	110.36	H2-C1-F2	-121.31

Enthalpy Reference Temperature = T_r = 298.15 K
Standard State Pressure = p_o = 1 atmosphere

	¦- J K^{-1} mol^{-1} -¦		¦-------- kJ mol^{-1} ---------¦			
T/K	**C_p°**	**S°**	**H°-$H^\circ(T_r)$**	**ΔH_f°**	**ΔG_f°**	**Log K_f**
150	44.53	244.12	-7.75	-667.72	-646.39	225.08
200	49.88	257.57	-5.40	-669.23	-639.06	166.90
250	54.93	269.15	-2.77	-670.61	-631.37	131.91
300	59.97	279.55	0.11	-671.87	-623.37	108.53
350	64.99	289.12	3.26	-672.95	-615.17	91.81
400	69.82	298.09	6.65	-673.96	-606.85	79.24
450	74.35	306.57	10.28	-674.80	-598.40	69.46
500	78.49	314.60	14.13	-675.55	-589.86	61.62
600	85.61	329.55	22.40	-676.72	-572.58	49.84
700	91.37	343.62	31.30	-677.56	-555.38	41.44
800	96.08	356.56	40.72	-678.10	-538.23	35.14
900	99.99	368.51	50.56	-678.48	-521.03	30.24
1000	103.27	379.59	60.76	-678.64	-503.84	26.32
1100	106.08	389.92	71.25	-678.73	-486.64	23.11
1200	108.48	399.58	82.00	-678.64	-469.49	20.44
1300	110.56	408.65	92.98	-678.48	-452.37	18.18
1400	112.36	417.20	104.14	-678.23	-435.30	16.24
1500	113.93	425.27	115.47	-677.93	-418.27	14.57
1600	115.30	432.92	126.95	-677.56	-401.33	13.10
1700	116.51	440.19	138.55	-677.14	-384.43	11.81
1800	117.57	447.10	150.27	-676.68	-367.61	10.67
1900	118.51	453.70	162.08	-676.18	-350.83	9.64
2000	119.35	460.01	173.98	-675.63	-334.18	8.73
2100	120.09	466.05	185.97	-675.05	-317.57	7.90
2200	120.75	471.83	198.02	-674.46	-301.04	7.15
2300	121.35	477.39	210.13	-673.83	-284.55	6.46
2400	121.88	482.75	222.30	-673.16	-268.19	5.84
2500	122.37	487.90	234.52	-672.49	-251.88	5.26
2600	122.80	492.86	246.78	-671.82	-235.64	4.73
2700	123.20	497.66	259.09	-671.11	-219.45	4.25
2800	123.55	502.29	271.43	-670.40	-203.30	3.79
2900	123.88	506.78	283.80	-669.69	-187.19	3.37
3000	124.18	511.12	296.21	-668.94	-171.13	2.98

CF_3OH

ΔH_f°(0 K) = -910.77 kJ mol^{-1}
ΔH_f°(298.15 K) = -919.44 kJ mol^{-1}
S°(298.15 K) = 290.10 J K^{-1} mol^{-1}

Moments of Inertia (10^{-47} kg m^2)
143.10 144.11 145.53

Vibrational Frequencies (cm^{-1})
233.3 427.8 440.7 583.1 607.5
617.1 888.9 1123.5 1234.9 1323.7
1414.0 3654.0

Bond Distances (10^{-10} m)		**Bond Angles** (°)		**Dihedral Angles** (°)	
C1-O1	1.331				
C1-F1	1.320	O1-C1-F1	111.91		
C1-F2	1.320	O1-C1-F2	111.91	F1-C1-F2	119.76
C1-F3	1.304	O1-C1-F3	108.83	F1-C1-F3	-120.12
O1-H1	0.950	C1-O1-H1	110.26	F1-O1-H1	-59.80

Enthalpy Reference Temperature = T_r = 298.15 K
Standard State Pressure = p_o = 1 atmosphere

	|- J K^{-1} mol^{-1} -|		|-------- kJ mol^{-1} ---------|			
T/K	C_p°	S°	H°-$H^\circ(T_r)$	ΔH_f°	ΔG_f°	Log K_f
150	46.20	250.71	-8.70	-916.21	-890.48	310.08
200	54.91	265.20	-6.17	-917.55	-881.69	230.27
250	63.14	278.35	-3.22	-918.64	-872.62	182.32
300	70.58	290.53	0.13	-919.48	-863.37	150.32
350	77.21	301.92	3.83	-920.10	-854.00	127.45
400	83.05	312.62	7.84	-920.52	-844.54	110.28
450	88.13	322.70	12.12	-920.81	-835.04	96.93
500	92.53	332.22	16.64	-921.02	-825.55	86.24
600	99.61	349.75	26.26	-921.07	-806.47	70.20
700	104.93	365.52	36.51	-920.86	-787.39	58.75
800	109.01	379.81	47.21	-920.44	-768.35	50.17
900	112.22	392.84	58.27	-919.89	-749.35	43.49
1000	114.81	404.81	69.63	-919.27	-730.40	38.15
1100	116.95	415.85	81.22	-918.56	-711.49	33.78
1200	118.74	426.11	93.01	-917.76	-692.66	30.15
1300	120.26	435.68	104.96	-916.88	-673.88	27.07
1400	121.55	444.63	117.06	-916.00	-655.13	24.44
1500	122.67	453.06	129.27	-915.08	-636.47	22.16
1600	123.65	461.01	141.59	-914.12	-617.85	20.17
1700	124.49	468.53	153.99	-913.16	-599.36	18.41
1800	125.24	475.67	166.48	-912.11	-580.91	16.86
1900	125.89	482.46	179.04	-911.11	-562.50	15.46
2000	126.47	488.93	191.66	-910.02	-544.21	14.21
2100	126.98	495.11	204.33	-908.97	-526.01	13.08
2200	127.44	501.03	217.05	-907.84	-507.85	12.06
2300	127.85	506.70	229.81	-906.76	-489.82	11.12
2400	128.22	512.16	242.62	-905.63	-471.83	10.27
2500	128.56	517.40	255.46	-904.50	-453.92	9.48
2600	128.86	522.44	268.33	-903.33	-436.06	8.76
2700	129.13	527.31	281.23	-902.20	-418.27	8.09
2800	129.38	532.01	294.16	-901.02	-400.53	7.47
2900	129.60	536.56	307.11	-899.81	-382.84	6.90
3000	129.81	540.95	320.08	-898.64	-365.18	6.36

$CF_3OO\bullet$

$\Delta H_f^\circ(0\ K)$ = -620.53 kJ mol^{-1}
$\Delta H_f^\circ(298.15\ K)$ = -627.46 kJ mol^{-1}
$S^\circ(298.15\ K)$ = 314.37 J K^{-1} mol^{-1}

Moments of Inertia (10^{-47} kg m^2)
144.76 249.01 251.97

Vibrational Frequencies (cm^{-1})
122.1 278.9 420.0 442.3 571.0
593.0 686.4 878.3 1124.2 1251.0
1287.7 1340.3

Bond Distances (10^{-10} m)		**Bond Angles** (°)		**Dihedral Angles** (°)	
C1-O1	1.372				
O1-O2	1.314	C1-O1-O2	110.50		
C1-F1	1.300	O1-C1-F1	106.06	O2-C1-F1	180.00
C1-F2	1.304	O1-C1-F2	111.13	O2-C1-F2	60.61
C1-F3	1.304	O1-C1-F3	111.13	O2-C1-F3	-60.61

Enthalpy Reference Temperature = T_r = 298.15 K
Standard State Pressure = p_o = 1 atmosphere

	¦- J K^{-1} mol^{-1} -¦		¦-------- kJ mol^{-1} ---------¦			
T/K	C_p°	S°	$H^\circ-H^\circ(T_r)$	ΔH_f°	ΔG_f°	Log K_f
150	53.17	269.64	-9.87	-625.42	-596.93	207.86
200	62.72	286.11	-6.98	-626.39	-587.27	153.37
250	71.63	301.09	-3.63	-627.06	-577.43	120.64
300	79.61	314.87	0.15	-627.47	-567.52	98.81
350	86.58	327.67	4.30	-627.64	-557.52	83.20
400	92.55	339.62	8.77	-627.64	-547.56	71.50
450	97.59	350.82	13.52	-627.47	-537.56	62.40
500	101.82	361.32	18.51	-627.22	-527.60	55.12
600	108.32	380.49	29.04	-626.47	-507.77	44.20
700	112.89	397.54	40.12	-625.55	-488.06	36.42
800	116.17	412.84	51.60	-624.50	-468.48	30.59
900	118.57	426.67	63.35	-623.46	-449.03	26.06
1000	120.37	439.26	75.32	-622.41	-429.65	22.44
1100	121.75	450.80	87.45	-621.37	-410.37	19.49
1200	122.83	461.44	99.70	-620.32	-391.12	17.03
1300	123.68	471.30	112.03	-619.32	-372.00	14.95
1400	124.37	480.49	124.45	-618.31	-352.92	13.17
1500	124.93	489.16	136.93	-617.31	-334.05	11.63
1600	125.39	497.43	149.46	-616.35	-315.43	10.30
1700	125.78	505.23	162.03	-615.38	-296.90	9.12
1800	126.10	512.61	174.64	-614.42	-278.49	8.08
1900	126.38	519.62	187.27	-613.50	-260.20	7.15
2000	126.62	526.28	199.93	-612.54	-241.96	6.32
2100	126.83	532.63	212.61	-611.62	-223.84	5.57
2200	127.01	538.69	225.31	-610.70	-205.85	4.89
2300	127.16	544.50	238.03	-609.78	-187.90	4.27
2400	127.30	550.07	250.76	-608.86	-170.08	3.70
2500	127.42	555.42	263.50	-607.89	-152.34	3.18
2600	127.53	560.56	276.26	-606.97	-134.64	2.70
2700	127.62	565.51	289.02	-606.09	-117.03	2.26
2800	127.71	570.30	301.79	-605.17	-99.45	1.86
2900	127.79	574.91	314.57	-604.25	-81.96	1.48
3000	127.86	579.37	327.36	-603.33	-64.48	1.12

CF_3OOH

ΔH_f°(0 K) = -797.30 kJ mol^{-1}
ΔH_f°(298.15 K) = -807.48 kJ mol^{-1}
S°(298.15 K) = 314.50 J K^{-1} mol^{-1}

Moments of Inertia (10^{-47} kg m^2)
146.17 260.61 262.43

Vibrational Frequencies (cm^{-1})
138.6 256.6 289.0 429.1 437.1
571.9 604.2 673.8 879.1 1067.5
1262.5 1293.6 1318.6 1438.0 3629.8

Bond Distances (10^{-10} m)		**Bond Angles** (°)		**Dihedral Angles** (°)	
C1-O1	1.351				
O1-O2	1.388	C1-O1-O2	108.42		
C1-F1	1.305	O1-C1-F1	106.36	O2-C1-F1	179.75
C1-F2	1.306	O1-C1-F2	112.36	O2-C1-F2	60.07
C1-F3	1.314	O1-C1-F3	111.48	O2-C1-F3	-61.40
O2-H1	0.952	O1-O2-H1	102.23	C1-O2-H1	104.50

Enthalpy Reference Temperature = T_r = 298.15 K
Standard State Pressure = p_o = 1 atmosphere

	- J K^{-1} mol^{-1} -		---------- kJ mol^{-1} ----------			
T/K	**C_p°**	**S°**	**H°-$H^\circ(T_r)$**	**ΔH_f°**	**ΔG_f°**	**Log K_f**
150	57.60	265.92	-10.77	-804.16	-766.89	267.04
200	68.35	283.91	-7.62	-805.63	-754.25	196.98
250	78.04	300.13	-3.96	-806.72	-741.24	154.87
300	86.75	315.03	0.16	-807.51	-728.06	126.76
350	94.56	328.95	4.69	-808.01	-714.79	106.67
400	101.50	342.05	9.59	-808.31	-701.49	91.60
450	107.57	354.36	14.81	-808.43	-688.18	79.88
500	112.81	365.97	20.32	-808.39	-674.84	70.50
600	121.14	387.31	32.02	-807.89	-648.19	56.43
700	127.21	406.46	44.45	-807.09	-621.66	46.39
800	131.70	423.75	57.40	-806.05	-595.26	38.86
900	135.08	439.46	70.75	-804.88	-568.94	33.02
1000	137.70	453.83	84.40	-803.62	-542.79	28.35
1100	139.79	467.06	98.29	-802.32	-516.68	24.53
1200	141.48	479.29	112.36	-800.98	-490.70	21.36
1300	142.88	490.67	126.59	-799.60	-464.84	18.68
1400	144.05	501.31	140.95	-798.22	-439.07	16.38
1500	145.05	511.28	155.42	-796.80	-413.38	14.39
1600	145.90	520.67	169.98	-795.42	-387.77	12.66
1700	146.64	529.54	184.62	-794.00	-362.29	11.13
1800	147.28	537.93	199.33	-792.53	-336.90	9.78
1900	147.85	545.91	214.10	-791.11	-311.62	8.57
2000	148.34	553.51	228.92	-789.69	-286.44	7.48
2100	148.78	560.76	243.78	-788.22	-261.33	6.50
2200	149.17	567.69	258.69	-786.76	-236.35	5.61
2300	149.51	574.33	273.63	-785.29	-211.46	4.80
2400	149.82	580.81	288.61	-783.83	-186.94	4.07
2500	150.10	587.06	303.62	-782.37	-162.55	3.40
2600	150.36	593.07	318.65	-780.90	-138.24	2.78
2700	150.58	598.86	333.70	-779.40	-114.01	2.21
2800	150.79	604.46	348.78	-777.93	-89.87	1.68
2900	150.98	609.87	363.88	-776.42	-65.81	1.19
3000	151.15	615.10	378.99	-774.96	-41.80	0.73

CH_3-CH_2F

ΔH_f°(0 K) = -256.98 kJ mol^{-1}
ΔH_f°(298.15 K) = -272.35 kJ mol^{-1}
S°(298.15 K) = 265.04 J K^{-1} mol^{-1}

Moments of Inertia (10^{-47} kg m^2)

22.84	88.06	100.54

Vibrational Frequencies (cm^{-1})

243.8	392.5	783.4	866.8	1043.2
1106.9	1168.9	1269.4	1381.2	1417.4
1452.5	1468.9	1502.8	2868.8	2895.9
2924.5	2929.2	2947.8		

Bond Distances (10^{-10} m)		**Bond Angles** (°)		**Dihedral Angles** (°)	
C1-C2	1.512				
C2-H1	1.084	C1-C2-H1	110.47		
C2-H2	1.084	C1-C2-H2	110.48	H1-C2-H2	119.95
C2-H3	1.086	C1-C2-H3	110.34	H1-C2-H3	239.98
C1-H4	1.083	C2-C1-H4	111.55	H1-C1-H4	59.17
C1-H5	1.083	C2-C1-H5	111.56	H1-C1-H5	180.93
C1-F1	1.373	C2-C1-F1	109.54	H1-C1-F1	300.06

Enthalpy Reference Temperature = T_r = 298.15 K
Standard State Pressure = p_o = 1 atmosphere

	¦- J K^{-1} mol^{-1} -¦		¦-------- kJ mol^{-1} ---------¦			
T/K	**C_p°**	**S°**	**H°-$H^\circ(T_r)$**	**ΔH_f°**	**ΔG_f°**	**Log K_f**
150	42.22	231.14	-7.39	-264.85	-244.05	84.98
200	47.14	244.05	-5.17	-267.44	-236.77	61.83
250	52.92	255.19	-2.69	-269.99	-228.86	47.81
300	59.58	265.41	0.11	-272.42	-220.45	38.38
350	66.68	275.10	3.25	-274.72	-211.67	31.59
400	73.79	284.45	6.75	-276.77	-202.55	26.45
450	80.60	293.52	10.61	-278.65	-193.22	22.43
500	86.99	302.33	14.79	-280.33	-183.68	19.19
600	98.41	319.20	24.09	-283.13	-164.10	14.29
700	108.16	335.10	34.44	-285.27	-144.10	10.75
800	116.55	350.09	45.71	-286.86	-123.76	8.08
900	123.78	364.24	57.77	-287.98	-103.26	5.99
1000	130.03	377.61	70.50	-288.70	-82.59	4.31
1100	135.44	390.25	83.81	-289.11	-61.80	2.93
1200	140.12	402.24	97.62	-289.24	-40.96	1.78
1300	144.18	413.62	111.87	-289.16	-20.13	0.81
1400	147.70	424.43	126.49	-288.86	0.71	-0.03
1500	150.75	434.83	141.44	-288.44	21.38	-0.74
1600	153.42	444.84	156.68	-287.90	41.84	-1.37
1700	155.75	454.40	172.16	-287.23	62.22	-1.91
1800	157.80	463.55	187.87	-286.52	82.51	-2.39
1900	159.59	472.30	203.76	-285.68	102.68	-2.82
2000	161.19	480.70	219.81	-284.80	122.72	-3.20
2100	162.60	488.77	236.02	-283.88	142.63	-3.55
2200	163.85	496.53	252.36	-282.92	162.42	-3.86
2300	164.98	504.00	268.82	-281.92	182.09	-4.14
2400	165.98	511.19	285.38	-280.83	201.67	-4.39
2500	166.88	518.13	302.04	-279.74	221.08	-4.62
2600	167.69	524.84	318.78	-278.65	240.41	-4.83
2700	168.43	531.32	335.60	-277.52	259.66	-5.02
2800	169.09	537.60	352.49	-276.35	278.86	-5.20
2900	169.70	543.67	369.44	-275.18	297.98	-5.37
3000	170.25	549.56	386.45	-273.97	317.06	-5.52

CH_3-CH_2Cl

ΔH_f°(0 K) = -98.58 kJ mol^{-1}
ΔH_f°(298.15 K) = -113.66 kJ mol^{-1}
S°(298.15 K) = 276.16 J K^{-1} mol^{-1}

Moments of Inertia (10^{-47} kg m^2)

26.35	153.85	169.86

Vibrational Frequencies (cm^{-1})

248.4	319.4	641.6	761.9	944.9
1055.8	1062.6	1247.5	1305.9	1398.2
1455.6	1463.7	1468.7	2869.1	2925.6
2938.8	2945.4	2990.0		

Bond Distances (10^{-10} m)		**Bond Angles** (°)		**Dihedral Angles** (°)	
C1-C2	1.517				
C2-H1	1.083	C1-C2-H1	111.05		
C2-H2	1.083	C1-C2-H2	111.05	H1-C2-H2	120.85
C2-H3	1.086	C1-C2-H3	109.22	H1-C2-H3	240.43
C1-H4	1.079	C2-C1-H4	111.79	H1-C1-H4	58.34
C1-H5	1.079	C2-C1-H5	111.80	H1-C1-H5	180.81
C1-Cl1	1.799	C2-C1-Cl1	111.49	H1-C1-Cl1	299.58

Enthalpy Reference Temperature = T_r = 298.15 K
Standard State Pressure = p_o = 1 atmosphere

	|- J K^{-1} mol^{-1} -|		|-------- kJ mol^{-1} ---------|			
T/K	**C_p°**	**S°**	**H°-$H^\circ(T_r)$**	**ΔH_f°**	**ΔG_f°**	**Log K_f**
150	43.87	240.51	-7.80	-106.40	-85.65	29.82
200	49.58	253.94	-5.48	-108.95	-78.37	20.47
250	56.04	265.72	-2.85	-111.42	-70.50	14.73
300	63.15	276.55	0.12	-113.76	-62.13	10.82
350	70.51	286.83	3.44	-115.90	-53.43	7.97
400	77.71	296.70	7.14	-117.86	-44.43	5.80
450	84.49	306.23	11.18	-119.58	-35.19	4.09
500	90.76	315.45	15.56	-121.13	-25.77	2.69
600	101.79	332.98	25.20	-123.68	-6.53	0.57
700	111.11	349.37	35.87	-125.56	13.14	-0.98
800	119.06	364.72	47.40	-126.94	33.10	-2.16
900	125.92	379.14	59.68	-127.86	53.22	-3.09
1000	131.85	392.72	72.60	-128.45	73.47	-3.84
1100	137.00	405.53	86.08	-128.70	93.81	-4.45
1200	141.46	417.64	100.04	-128.74	114.18	-4.97
1300	145.33	429.12	114.41	-128.53	134.60	-5.41
1400	148.70	440.01	129.14	-128.16	154.98	-5.78
1500	151.63	450.37	144.19	-127.65	175.35	-6.11
1600	154.19	460.24	159.51	-127.07	195.64	-6.39
1700	156.44	469.79	175.06	-126.36	215.69	-6.63
1800	158.41	478.96	190.83	-125.56	235.52	-6.83
1900	160.15	487.74	206.78	-124.68	255.27	-7.02
2000	161.69	496.16	222.89	-123.76	274.89	-7.18
2100	163.05	504.24	239.15	-122.80	294.39	-7.32
2200	164.26	512.01	255.53	-121.80	313.76	-7.45
2300	165.35	519.49	272.03	-120.75	333.00	-7.56
2400	166.32	526.69	288.63	-119.66	352.13	-7.66
2500	167.20	533.65	305.32	-118.53	371.12	-7.75
2600	167.99	540.36	322.09	-117.40	390.03	-7.84
2700	168.70	546.85	338.94	-116.23	408.82	-7.91
2800	169.35	553.13	355.86	-115.06	427.56	-7.98
2900	169.93	559.21	372.83	-113.85	446.27	-8.04
3000	170.47	565.11	389.87	-112.63	464.93	-8.09

$CH_2F\text{-}CH_2\bullet$

ΔH_f°(0 K) = -46.02 kJ mol^{-1}
ΔH_f°(298.15 K) = -56.22 kJ mol^{-1}
S°(298.15 K) = 275.18 J K^{-1} mol^{-1}

Moments of Inertia (10^{-47} kg m^2)

20.06	82.42	96.41

Vibrational Frequencies (cm^{-1})

158.7	382.9	439.8	831.2	956.3
1060.3	1100.4	1227.7	1388.3	1426.0
1486.1	2855.7	2906.9	2973.9	3070.7

Bond Distances (10^{-10} m)		**Bond Angles** (°)		**Dihedral Angles** (°)	
C1-C2	1.489				
C1-F1	1.371	C2-C1-F1	110.04		
C1-H1	1.084	C2-C1-H1	111.36	F1-C1-H1	240.16
C2-H2	1.074	C1-C2-H2	119.68	F1-C2-H2	163.95
C2-H3	1.074	C1-C2-H3	119.22	F1-C2-H3	-32.85
C1-H4	1.087	C2-C1-H4	111.93	F1-C1-H4	119.10

Enthalpy Reference Temperature = T_r = 298.15 K
Standard State Pressure = p_o = 1 atmosphere

	|- J K^{-1} mol^{-1} -|		|-------- kJ mol^{-1} ---------|			
T/K	**C_p°**	**S°**	**H°-$H^\circ(T_r)$**	**ΔH_f°**	**ΔG_f°**	**Log K_f**
150	45.71	238.96	-7.95	-51.42	-40.04	13.94
200	50.91	252.83	-5.53	-53.09	-36.02	9.41
250	56.40	264.77	-2.85	-54.73	-31.59	6.60
300	62.27	275.57	0.11	-56.27	-26.86	4.68
350	68.26	285.62	3.38	-57.70	-21.88	3.27
400	74.12	295.11	6.94	-58.99	-16.74	2.19
450	79.64	304.17	10.79	-60.17	-11.42	1.33
500	84.77	312.83	14.90	-61.17	-6.02	0.63
600	93.85	329.11	23.84	-62.84	5.10	-0.45
700	101.57	344.17	33.62	-64.14	16.53	-1.23
800	108.19	358.18	44.12	-65.02	28.12	-1.83
900	113.90	371.26	55.23	-65.61	39.83	-2.31
1000	118.85	383.52	66.87	-65.94	51.63	-2.70
1100	123.14	395.05	78.98	-66.02	63.47	-3.01
1200	126.86	405.93	91.48	-65.94	75.35	-3.28
1300	130.09	416.22	104.33	-65.73	87.28	-3.51
1400	132.90	425.96	117.49	-65.35	99.16	-3.70
1500	135.35	435.22	130.90	-64.89	111.00	-3.87
1600	137.49	444.02	144.54	-64.35	122.84	-4.01
1700	139.36	452.42	158.39	-63.72	134.60	-4.14
1800	141.00	460.43	172.41	-63.05	146.27	-4.24
1900	142.45	468.09	186.59	-62.30	157.90	-4.34
2000	143.73	475.43	200.89	-61.55	169.41	-4.42
2100	144.87	482.47	215.33	-60.71	180.83	-4.50
2200	145.88	489.24	229.86	-59.83	192.17	-4.56
2300	146.79	495.74	244.50	-58.95	203.43	-4.62
2400	147.60	502.00	259.22	-58.03	214.56	-4.67
2500	148.33	508.05	274.02	-57.11	225.60	-4.71
2600	148.99	513.88	288.88	-56.15	236.61	-4.75
2700	149.58	519.51	303.81	-55.15	247.53	-4.79
2800	150.12	524.96	318.80	-54.18	258.36	-4.82
2900	150.61	530.24	333.84	-53.14	269.20	-4.85
3000	151.06	535.35	348.92	-52.13	280.04	-4.88

CH_2=CHF

ΔH_f°(0 K) = -131.00 kJ mol^{-1}
ΔH_f°(298.15 K) = -139.21 kJ mol^{-1}
S°(298.15 K) = 252.27 J K^{-1} mol^{-1}

Moments of Inertia (10^{-47} kg m^2)
12.50 77.57 90.08

Vibrational Frequencies (cm^{-1})
467.3 714.3 915.5 922.0 976.7
1148.6 1300.9 1393.4 1690.0 3003.1
3060.3 3086.1

Bond Distances (10^{-10} m)		**Bond Angles** (°)		**Dihedral Angles** (°)
C1-C2	1.309			
C1-F1	1.329	C2-C1-F1	122.38	
C1-H1	1.072	C2-C1-H1	125.70	
C2-H2	1.073	C1-C2-H2	119.75	
C2-H3	1.074	C1-C2-H3	121.50	

Enthalpy Reference Temperature = T_r = 298.15 K
Standard State Pressure = p_o = 1 atmosphere

	- J K^{-1} mol^{-1} -		-------- kJ mol^{-1} ---------			
T/K	**C_p°**	**S°**	**H°-$H^\circ(T_r)$**	**ΔH_f°**	**ΔG_f°**	**Log K_f**
150	35.88	223.78	-6.26	-134.89	-129.45	45.08
200	39.66	234.58	-4.38	-136.36	-127.49	33.29
250	44.65	243.95	-2.28	-137.86	-125.10	26.14
300	50.26	252.58	0.09	-139.24	-122.47	21.32
350	55.98	260.76	2.75	-140.54	-119.62	17.85
400	61.47	268.60	5.69	-141.75	-116.61	15.22
450	66.57	276.14	8.89	-142.80	-113.43	13.17
500	71.23	283.39	12.34	-143.76	-110.16	11.51
600	79.31	297.12	19.88	-145.44	-103.34	9.00
700	86.01	309.87	28.15	-146.73	-96.27	7.18
800	91.65	321.73	37.05	-147.78	-88.99	5.81
900	96.47	332.81	46.45	-148.57	-81.55	4.73
1000	100.60	343.19	56.32	-149.20	-74.01	3.87
1100	104.17	352.95	66.56	-149.66	-66.36	3.15
1200	107.26	362.15	77.13	-150.00	-58.66	2.55
1300	109.93	370.84	88.00	-150.21	-50.88	2.05
1400	112.25	379.08	99.11	-150.33	-43.14	1.61
1500	114.27	386.89	110.44	-150.37	-35.31	1.23
1600	116.04	394.33	121.96	-150.37	-27.57	0.90
1700	117.58	401.41	133.64	-150.33	-19.79	0.61
1800	118.94	408.17	145.47	-150.21	-12.09	0.35
1900	120.14	414.63	157.42	-150.04	-4.39	0.12
2000	121.20	420.82	169.49	-149.83	3.18	-0.08
2100	122.14	426.76	181.66	-149.62	10.75	-0.27
2200	122.98	432.46	193.91	-149.37	18.24	-0.43
2300	123.73	437.95	206.25	-149.08	25.65	-0.58
2400	124.41	443.23	218.66	-148.74	32.97	-0.72
2500	125.01	448.32	231.13	-148.45	40.25	-0.84
2600	125.56	453.23	243.66	-148.07	47.49	-0.95
2700	126.05	457.98	256.24	-147.74	54.68	-1.06
2800	126.50	462.57	268.87	-147.36	61.84	-1.15
2900	126.90	467.02	281.54	-146.94	68.99	-1.24
3000	127.28	471.33	294.25	-146.52	76.19	-1.33

$CH_2=CF_2$

ΔH_f°(0 K) = -332.84 kJ mol^{-1}
ΔH_f°(298.15 K) = -340.11 kJ mol^{-1}
S°(298.15 K) = 270.73 J K^{-1} mol^{-1}

Moments of Inertia (10^{-47} kg m^2)
74.36 78.66 153.02

Vibrational Frequencies (cm^{-1})
423.0 528.3 629.6 712.8 864.8
918.6 951.6 1332.4 1386.2 1747.8
3026.7 3113.8

Bond Distances (10^{-10} m)		**Bond Angles** (°)		**Dihedral Angles** (°)
C1-C2	1.305			
C1-F1	1.303	C2-C1-F1	125.19	
C1-F2	1.303	C2-C1-F2	125.27	
C2-H1	1.070	C1-C2-H1	119.93	
C2-H2	1.071	C1-C2-H2	119.82	

Enthalpy Reference Temperature = T_r = 298.15 K
Standard State Pressure = p_o = 1 atmosphere

	- J K^{-1} mol^{-1} -		---------- kJ mol^{-1} ----------			
T/K	C_p°	S°	H°-$H^\circ(T_r)$	ΔH_f°	ΔG_f°	Log K_f
150	38.53	238.25	-7.18	-336.64	-327.98	114.21
200	44.95	250.18	-5.10	-337.94	-324.93	84.86
250	52.09	260.98	-2.67	-339.11	-321.58	67.19
300	59.09	271.10	0.11	-340.16	-318.03	55.37
350	65.58	280.70	3.23	-341.04	-314.30	46.91
400	71.40	289.85	6.66	-341.83	-310.49	40.54
450	76.58	298.57	10.36	-342.50	-306.56	35.58
500	81.17	306.88	14.31	-343.09	-302.59	31.61
600	88.83	322.38	22.82	-344.01	-294.47	25.64
700	94.94	336.55	32.02	-344.68	-286.23	21.36
800	99.93	349.56	41.77	-345.18	-277.82	18.14
900	104.06	361.58	51.97	-345.51	-269.37	15.63
1000	107.54	372.73	62.56	-345.72	-260.83	13.62
1100	110.49	383.12	73.47	-345.85	-252.21	11.98
1200	113.00	392.84	84.64	-345.89	-243.59	10.60
1300	115.15	401.97	96.05	-345.85	-234.93	9.44
1400	117.00	410.58	107.66	-345.77	-226.27	8.44
1500	118.60	418.71	119.44	-345.64	-217.61	7.58
1600	119.99	426.40	131.38	-345.47	-208.99	6.82
1700	121.20	433.72	143.44	-345.26	-200.37	6.16
1800	122.26	440.68	155.61	-345.01	-191.84	5.57
1900	123.19	447.31	167.88	-344.76	-183.30	5.04
2000	124.01	453.65	180.25	-344.47	-174.89	4.57
2100	124.74	459.72	192.69	-344.13	-166.48	4.14
2200	125.38	465.54	205.19	-343.80	-158.20	3.76
2300	125.96	471.12	217.76	-343.46	-149.95	3.41
2400	126.48	476.49	230.38	-343.09	-141.80	3.09
2500	126.94	481.67	243.05	-342.71	-133.72	2.79
2600	127.36	486.65	255.77	-342.33	-125.65	2.52
2700	127.73	491.47	268.52	-341.92	-117.65	2.28
2800	128.08	496.12	281.31	-341.50	-109.70	2.05
2900	128.39	500.62	294.14	-341.08	-101.75	1.83
3000	128.67	504.98	306.99	-340.62	-93.76	1.63

CHF=CHF fccf cis

ΔH_f°(0 K) = -294.43 kJ mol^{-1}
ΔH_f°(298.15 K) = -301.29 kJ mol^{-1}
S°(298.15 K) = 274.29 J K^{-1} mol^{-1}

Moments of Inertia (10^{-47} kg m^2)
38.51 139.95 178.47

Vibrational Frequencies (cm^{-1})
225.8 491.8 747.9 803.9 905.7
1004.3 1110.8 1254.7 1380.3 1759.7
3070.6 3094.3

Bond Distances (10^{-10} m)		**Bond Angles** (°)		**Dihedral Angles** (°)	
C1-C2	1.307				
C1-F1	1.324	C2-C1-F1	122.58		
C1-H1	1.070	C2-C1-H1	123.07		
C2-H2	1.070	C1-C2-H2	123.07		
C2-F2	1.324	C1-C2-F2	122.58	F1-C2-F2	0.00

Enthalpy Reference Temperature = T_r = 298.15 K
Standard State Pressure = p_o = 1 atmosphere

	¦- J K^{-1} mol^{-1} -¦		¦-------- kJ mol^{-1} ---------¦			
T/K	**C_p°**	**S°**	**H°-$H^\circ(T_r)$**	**ΔH_f°**	**ΔG_f°**	**Log K_f**
150	41.39	241.12	-7.29	-297.94	-289.70	100.88
200	46.30	253.68	-5.10	-299.11	-286.81	74.91
250	52.07	264.62	-2.65	-300.29	-283.63	59.26
300	58.19	274.65	0.11	-301.33	-280.29	48.80
350	64.22	284.08	3.17	-302.29	-276.73	41.30
400	69.88	293.03	6.52	-303.13	-273.09	35.66
450	75.04	301.56	10.15	-303.88	-269.32	31.26
500	79.67	309.71	14.02	-304.55	-265.47	27.73
600	87.53	324.96	22.39	-305.60	-257.65	22.43
700	93.84	338.94	31.47	-306.39	-249.62	18.63
800	99.00	351.82	41.12	-306.98	-241.46	15.77
900	103.28	363.74	51.24	-307.40	-233.22	13.53
1000	106.87	374.81	61.76	-307.69	-224.89	11.75
1100	109.91	385.14	72.60	-307.90	-216.48	10.28
1200	112.49	394.81	83.72	-307.98	-208.07	9.06
1300	114.70	403.91	95.09	-307.98	-199.62	8.02
1400	116.60	412.48	106.65	-307.94	-191.13	7.13
1500	118.25	420.58	118.39	-307.86	-182.67	6.36
1600	119.67	428.26	130.29	-307.73	-174.22	5.69
1700	120.91	435.55	142.33	-307.52	-165.81	5.09
1800	122.00	442.50	154.47	-307.31	-157.40	4.57
1900	122.96	449.12	166.72	-307.11	-149.12	4.10
2000	123.80	455.45	179.06	-306.81	-140.83	3.68
2100	124.54	461.51	191.48	-306.52	-132.63	3.30
2200	125.20	467.32	203.97	-306.23	-124.52	2.96
2300	125.79	472.90	216.51	-305.89	-116.48	2.64
2400	126.32	478.26	229.12	-305.56	-108.49	2.36
2500	126.80	483.43	241.78	-305.18	-100.54	2.10
2600	127.22	488.41	254.48	-304.80	-92.68	1.86
2700	127.61	493.22	267.22	-304.39	-84.85	1.64
2800	127.96	497.87	280.00	-303.97	-77.07	1.44
2900	128.28	502.36	292.81	-303.55	-69.29	1.25
3000	128.57	506.72	305.65	-303.13	-61.50	1.07

CHF=CHF fccf trans

ΔH_f°**(0 K)** = -295.64 kJ mol^{-1}
ΔH_f°**(298.15 K)** = -302.24 kJ mol^{-1}
S°**(298.15 K)** = 273.56 J K^{-1} mol^{-1}

Moments of Inertia (10^{-47} kg m^2)
14.20 204.16 218.35

Vibrational Frequencies (cm^{-1})

308.1	337.6	538.5	846.3	928.0
1128.5	1144.3	1269.3	1269.3	1747.6
3062.2	3071.4			

Bond Distances (10^{-10} m)		**Bond Angles** (°)		**Dihedral Angles** (°)	
C1-C2	1.306				
C1-F1	1.329	C2-C1-F1	120.24		
C1-H1	1.070	C2-C1-H1	125.28		
C2-H2	1.070	C1-C2-H2	125.28		
C2-F2	1.329	C1-C2-F2	120.25	F1-C2-F2	180.00

Enthalpy Reference Temperature = T_r = 298.15 K
Standard State Pressure = p_o = 1 atmosphere

	J K^{-1} mol^{-1}		kJ mol^{-1}			
T/K	C_p°	S°	$H^\circ-H^\circ(T_r)$	ΔH_f°	ΔG_f°	**Log K_f**
150	42.76	239.06	-7.58	-299.16	-290.66	101.21
200	48.41	252.14	-5.30	-300.29	-287.65	75.13
250	54.12	263.55	-2.74	-301.33	-284.43	59.42
300	59.93	273.93	0.11	-302.29	-281.00	48.92
350	65.63	283.60	3.25	-303.17	-277.44	41.40
400	71.01	292.72	6.67	-303.93	-273.76	35.75
450	75.96	301.37	10.34	-304.64	-269.99	31.34
500	80.45	309.61	14.25	-305.26	-266.14	27.80
600	88.10	324.98	22.70	-306.23	-258.28	22.49
700	94.30	339.04	31.83	-306.98	-250.29	18.68
800	99.39	351.98	41.52	-307.52	-242.13	15.81
900	103.61	363.93	51.68	-307.94	-233.93	13.58
1000	107.16	375.04	62.22	-308.19	-225.60	11.78
1100	110.16	385.40	73.09	-308.36	-217.23	10.32
1200	112.72	395.10	84.24	-308.40	-208.82	9.09
1300	114.91	404.21	95.62	-308.40	-200.41	8.05
1400	116.79	412.79	107.21	-308.36	-191.96	7.16
1500	118.42	420.91	118.97	-308.24	-183.51	6.39
1600	119.83	428.60	130.88	-308.07	-175.10	5.72
1700	121.06	435.90	142.93	-307.90	-166.73	5.12
1800	122.13	442.85	155.09	-307.65	-158.36	4.60
1900	123.08	449.48	167.35	-307.40	-150.08	4.13
2000	123.91	455.81	179.70	-307.15	-141.88	3.71
2100	124.65	461.88	192.13	-306.81	-133.72	3.33
2200	125.30	467.69	204.63	-306.52	-125.65	2.98
2300	125.88	473.27	217.19	-306.19	-117.61	2.67
2400	126.41	478.64	229.80	-305.81	-109.66	2.39
2500	126.88	483.81	242.47	-305.43	-101.80	2.13
2600	127.30	488.80	255.18	-305.06	-93.97	1.89
2700	127.68	493.61	267.93	-304.64	-86.15	1.67
2800	128.02	498.26	280.71	-304.22	-78.41	1.46
2900	128.34	502.76	293.53	-303.80	-70.67	1.27
3000	128.62	507.11	306.38	-303.38	-62.93	1.10

$CHF=CF_2$

ΔH_f°(0 K) = -480.24 kJ mol^{-1}
ΔH_f°(298.15 K) = -485.56 kJ mol^{-1}
S°(298.15 K) = 292.39 J K^{-1} mol^{-1}

Moments of Inertia (10^{-47} kg m^2)
76.88 212.39 289.27

Vibrational Frequencies (cm^{-1})
223.0 306.8 468.9 585.8 605.0
815.9 921.9 1144.8 1265.0 1368.2
1824.4 3105.2

Bond Distances (10^{-10} m)		**Bond Angles** (°)		**Dihedral Angles** (°)
C1-C2	1.304			
C1-F1	1.298	C2-C1-F1	125.42	
C1-F2	1.303	C2-C1-F2	122.87	
C2-H1	1.068	C1-C2-H1	123.39	
C2-F3	1.327	C1-C2-F3	120.55	

Enthalpy Reference Temperature = T_r = 298.15 K
Standard State Pressure = p_o = 1 atmosphere

	- J K^{-1} mol^{-1} -		-------- kJ mol^{-1} ---------			
T/K	**C_p°**	**S°**	**H°-$H^\circ(T_r)$**	**ΔH_f°**	**ΔG_f°**	**Log K_f**
150	47.30	253.10	-8.66	-483.50	-471.66	164.24
200	55.00	267.77	-6.10	-484.34	-467.60	122.12
250	62.34	280.84	-3.16	-485.01	-463.42	96.82
300	69.13	292.82	0.13	-485.60	-459.07	79.93
350	75.30	303.94	3.74	-486.06	-454.68	67.85
400	80.82	314.36	7.65	-486.43	-450.20	58.79
450	85.72	324.17	11.81	-486.72	-445.72	51.73
500	90.05	333.44	16.21	-486.98	-441.16	46.09
600	97.23	350.51	25.59	-487.27	-432.04	37.61
700	102.85	365.94	35.60	-487.44	-422.88	31.55
800	107.31	379.98	46.12	-487.48	-413.67	27.01
900	110.90	392.83	57.04	-487.44	-404.38	23.47
1000	113.83	404.67	68.27	-487.31	-395.10	20.64
1100	116.24	415.63	79.78	-487.14	-385.81	18.32
1200	118.26	425.84	91.51	-486.93	-376.48	16.39
1300	119.95	435.37	103.42	-486.72	-367.15	14.75
1400	121.39	444.32	115.50	-486.43	-357.82	13.35
1500	122.61	452.73	127.70	-486.18	-348.53	12.14
1600	123.66	460.68	140.01	-485.85	-339.24	11.07
1700	124.56	468.21	152.42	-485.55	-330.03	10.14
1800	125.35	475.35	164.92	-485.22	-320.83	9.31
1900	126.03	482.15	177.49	-484.84	-311.71	8.57
2000	126.63	488.62	190.12	-484.51	-302.67	7.90
2100	127.16	494.82	202.81	-484.13	-293.67	7.30
2200	127.63	500.75	215.55	-483.71	-284.76	6.76
2300	128.05	506.43	228.34	-483.34	-275.93	6.27
2400	128.42	511.88	241.16	-482.92	-267.15	5.81
2500	128.75	517.13	254.02	-482.50	-258.45	5.40
2600	129.05	522.19	266.91	-482.08	-249.83	5.02
2700	129.32	527.07	279.83	-481.62	-241.21	4.67
2800	129.56	531.77	292.77	-481.16	-232.67	4.34
2900	129.78	536.32	305.74	-480.70	-224.10	4.04
3000	129.98	540.73	318.73	-480.24	-215.52	3.75

$CF_2=CF_2$

ΔH_f°(0 K) = -650.28 kJ mol^{-1}
ΔH_f°(298.15 K) = -653.67 kJ mol^{-1}
S°(298.15 K) = 311.22 J K^{-1} mol^{-1}

Moments of Inertia (10^{-47} kg m^2)
148.83 252.80 401.64

Vibrational Frequencies (cm^{-1})
198.9 199.9 382.0 431.3 530.1
540.3 563.3 777.2 1163.6 1341.2
1355.2 1915.3

Bond Distances (10^{-10} m)		**Bond Angles** (°)		**Dihedral Angles** (°)
C1-C2	1.300			
C1-F1	1.301	C2-C1-F1	123.44	
C1-F2	1.302	C2-C1-F2	123.45	
C2-F3	1.301	C1-C2-F3	123.45	
C2-F4	1.301	C1-C2-F4	123.43	

Enthalpy Reference Temperature = T_r = 298.15 K
Standard State Pressure = p_o = 1 atmosphere

	¦- J K^{-1} mol^{-1} -¦		¦-------- kJ mol^{-1} ---------¦			
T/K	**C_p°**	**S°**	**H°-$H^\circ(T_r)$**	**ΔH_f°**	**ΔG_f°**	**Log K_f**
150	54.99	265.02	-10.18	-653.08	-637.64	222.03
200	64.99	282.25	-7.17	-653.46	-632.41	165.17
250	73.43	297.68	-3.70	-653.62	-627.18	131.04
300	80.51	311.72	0.15	-653.67	-621.95	108.28
350	86.53	324.59	4.33	-653.62	-616.72	92.03
400	91.74	336.49	8.79	-653.54	-611.49	79.85
450	96.26	347.56	13.49	-653.42	-606.30	70.37
500	100.21	357.92	18.41	-653.25	-601.12	62.79
600	106.65	376.78	28.76	-652.83	-590.78	51.43
700	111.57	393.61	39.69	-652.37	-580.53	43.32
800	115.36	408.77	51.04	-651.87	-570.28	37.23
900	118.29	422.53	62.73	-651.41	-560.07	32.50
1000	120.60	435.12	74.68	-650.90	-549.90	28.72
1100	122.43	446.70	86.83	-650.40	-539.74	25.63
1200	123.90	457.42	99.15	-649.90	-529.57	23.05
1300	125.10	467.39	111.60	-649.44	-519.44	20.87
1400	126.08	476.70	124.16	-648.98	-509.32	19.00
1500	126.90	485.42	136.81	-648.52	-499.23	17.38
1600	127.58	493.63	149.54	-648.06	-489.19	15.97
1700	128.16	501.39	162.33	-647.60	-479.19	14.72
1800	128.65	508.73	175.17	-647.14	-469.24	13.62
1900	129.08	515.69	188.05	-646.68	-459.36	12.63
2000	129.44	522.32	200.98	-646.22	-449.57	11.74
2100	129.76	528.65	213.94	-645.76	-439.86	10.94
2200	130.04	534.69	226.93	-645.30	-430.20	10.21
2300	130.28	540.48	239.95	-644.84	-420.66	9.55
2400	130.50	546.02	252.99	-644.38	-411.16	8.95
2500	130.69	551.36	266.05	-643.88	-401.71	8.39
2600	130.86	556.48	279.13	-643.42	-392.38	7.88
2700	131.01	561.43	292.22	-642.91	-383.05	7.41
2800	131.15	566.20	305.33	-642.41	-373.76	6.97
2900	131.28	570.80	318.45	-641.91	-364.47	6.56
3000	131.39	575.25	331.58	-641.41	-355.18	6.18

CHF=CH• fcch trans

ΔH_f°**(0 K)** = 126.86 kJ mol^{-1}
ΔH_f°**(298.15 K)** = 123.11 kJ mol^{-1}
S°(298.15 K) = 257.01 J K^{-1} mol^{-1}

Moments of Inertia (10^{-47} kg m^2)
9.65 75.95 85.60

Vibrational Frequencies (cm^{-1})
481.1 643.7 756.2 809.8 1080.2
1246.5 1474.5 3017.9 3103.5

Bond Distances (10^{-10} m)		**Bond Angles** (°)		**Dihedral Angles** (°)	
C1-C2	1.322				
C1-H1	1.074	C2-C1-H1	125.44		
C1-F1	1.330	C2-C1-F1	121.98	H1-C1-F1	180.00
C2-H2	1.068	C1-C2-H2	132.85	F1-C2-H2	180.00

Enthalpy Reference Temperature = T_r = 298.15 K
Standard State Pressure = p_o = 1 atmosphere

	¦- J K^{-1} mol^{-1} -¦		¦-------- kJ mol^{-1} ---------¦			
T/K	**C_p°**	**S°**	**H°-$H^\circ(T_r)$**	**ΔH_f°**	**ΔG_f°**	**Log K_f**
150	36.24	227.94	-6.38	125.19	121.71	-42.38
200	40.54	238.94	-4.47	124.43	120.62	-31.51
250	45.61	248.53	-2.31	123.72	119.70	-25.01
300	50.76	257.32	0.09	123.09	118.95	-20.71
350	55.60	265.52	2.75	122.51	118.24	-17.64
400	59.99	273.23	5.64	122.01	117.61	-15.36
450	63.89	280.52	8.74	121.55	117.03	-13.58
500	67.35	287.42	12.02	121.17	116.52	-12.17
600	73.15	300.20	19.05	120.46	115.60	-10.06
700	77.83	311.78	26.59	119.87	114.81	-8.57
800	81.73	322.41	34.56	119.37	114.14	-7.45
900	85.05	332.24	42.89	118.95	113.51	-6.59
1000	87.91	341.36	51.51	118.62	112.97	-5.90
1100	90.38	349.86	60.41	118.28	112.47	-5.34
1200	92.51	357.82	69.53	118.03	112.05	-4.88
1300	94.36	365.29	78.86	117.78	111.67	-4.49
1400	95.94	372.34	88.35	117.61	111.34	-4.15
1500	97.30	379.00	97.99	117.44	111.00	-3.87
1600	98.46	385.31	107.75	117.28	110.67	-3.61
1700	99.45	391.31	117.63	117.15	110.33	-3.39
1800	100.29	397.01	127.61	117.07	109.96	-3.19
1900	101.00	402.45	137.66	116.94	109.58	-3.01
2000	101.60	407.64	147.78	116.86	109.12	-2.85
2100	102.11	412.61	157.96	116.78	108.66	-2.70
2200	102.53	417.36	168.19	116.69	108.11	-2.57
2300	102.89	421.92	178.46	116.61	107.57	-2.44
2400	103.20	426.30	188.77	116.48	106.94	-2.33
2500	103.45	430.52	199.10	116.40	106.27	-2.22
2600	103.66	434.58	209.46	116.32	105.56	-2.12
2700	103.84	438.49	219.85	116.23	104.85	-2.03
2800	103.99	442.27	230.25	116.11	104.10	-1.94
2900	104.11	445.92	240.67	115.98	103.39	-1.86
3000	104.22	449.45	251.10	115.90	102.72	-1.79

CHF=CH• fcch cis

ΔH_f°**(0 K)** = 127.78 kJ mol^{-1}
ΔH_f°**(298.15 K)** = 124.11 kJ mol^{-1}
S°**(298.15 K)** = 257.95 J K^{-1} mol^{-1}

Moments of Inertia (10^{-47} kg m^2)
12.29 71.42 83.71

Vibrational Frequencies (cm^{-1})
437.4 629.4 825.3 853.1 1053.2
1252.8 1452.6 3062.1 3100.3

Bond Distances (10^{-10} m)		**Bond Angles** (°)		**Dihedral Angles** (°)	
C1-C2	1.321				
C1-H1	1.071	C2-C1-H1	125.39		
C1-F1	1.336	C2-C1-F1	121.96	H1-C1-F1	180.00
C2-H2	1.068	C1-C2-H2	135.69	F1-C2-H2	0.00

Enthalpy Reference Temperature = T_r = 298.15 K
Standard State Pressure = p_o = 1 atmosphere

	|- J K^{-1} mol^{-1} -|		|-------- kJ mol^{-1} ---------|			
T/K	**C_p°**	**S°**	**H°-$H^\circ(T_r)$**	**ΔH_f°**	**ΔG_f°**	**Log K_f**
150	36.63	228.77	-6.40	126.15	122.55	-42.67
200	40.76	239.86	-4.47	125.44	121.42	-31.71
250	45.62	249.49	-2.31	124.73	120.50	-25.17
300	50.62	258.26	0.09	124.10	119.62	-20.83
350	55.39	266.43	2.74	123.51	118.91	-17.74
400	59.76	274.12	5.62	122.97	118.24	-15.44
450	63.66	281.39	8.71	122.51	117.61	-13.65
500	67.13	288.27	11.97	122.13	117.03	-12.23
600	72.94	301.02	18.98	121.38	116.02	-10.10
700	77.62	312.58	26.51	120.79	115.19	-8.59
800	81.51	323.16	34.46	120.29	114.43	-7.47
900	84.82	332.95	42.76	119.83	113.72	-6.60
1000	87.66	342.05	51.38	119.45	113.14	-5.91
1100	90.14	350.53	60.25	119.12	112.55	-5.35
1200	92.28	358.46	69.35	118.83	112.09	-4.88
1300	94.14	365.92	78.65	118.57	111.63	-4.49
1400	95.76	372.96	88.12	118.37	111.21	-4.15
1500	97.15	379.61	97.74	118.20	110.83	-3.86
1600	98.35	385.92	107.50	118.03	110.46	-3.61
1700	99.39	391.90	117.36	117.91	110.04	-3.38
1800	100.27	397.61	127.32	117.78	109.62	-3.18
1900	101.02	403.04	137.37	117.65	109.16	-3.00
2000	101.67	408.24	147.49	117.57	108.66	-2.84
2100	102.22	413.20	157.68	117.49	108.11	-2.69
2200	102.68	417.97	167.91	117.40	107.53	-2.55
2300	103.07	422.54	178.19	117.32	106.86	-2.43
2400	103.40	426.93	188.51	117.24	106.19	-2.31
2500	103.68	431.15	198.87	117.15	105.44	-2.20
2600	103.91	435.22	209.25	117.07	104.68	-2.10
2700	104.11	439.14	219.66	117.03	103.89	-2.01
2800	104.27	442.93	230.08	116.94	103.09	-1.92
2900	104.41	446.59	240.52	116.86	102.30	-1.84
3000	104.52	450.12	250.98	116.73	101.55	-1.77

CH_2=CF•

ΔH_f°(0 K) = 112.80 kJ mol^{-1}
ΔH_f°(298.15 K) = 109.10 kJ mol^{-1}
S°(298.15 K) = 256.78 J K^{-1} mol^{-1}

Moments of Inertia (10^{-47} kg m^2)
7.56 81.01 88.57

Vibrational Frequencies (cm^{-1})
427.0 613.9 796.9 905.2 1092.7
1366.6 1536.6 2975.1 3076.3

Bond Distances (10^{-10} m)		**Bond Angles** (°)		**Dihedral Angles** (°)
C1-C2	1.324			
C1-H1	1.076	C2-C1-H1	120.95	
C1-H2	1.072	C2-C1-H2	119.84	
C2-F1	1.306	C1-C2-F1	128.27	

Enthalpy Reference Temperature = T_r = 298.15 K
Standard State Pressure = p_o = 1 atmosphere

	- J K^{-1} mol^{-1} -		-------- kJ mol^{-1} ---------			
T/K	**C_p°**	**S°**	**H°-$H^\circ(T_r)$**	**ΔH_f°**	**ΔG_f°**	**Log K_f**
150	36.77	227.59	-6.39	111.13	107.74	-37.51
200	40.85	238.73	-4.46	110.42	106.65	-27.86
250	45.51	248.35	-2.30	109.75	105.77	-22.10
300	50.25	257.09	0.09	109.08	104.98	-18.28
350	54.78	265.18	2.72	108.45	104.31	-15.56
400	58.97	272.78	5.56	107.91	103.68	-13.54
450	62.75	279.94	8.61	107.40	103.14	-11.97
500	66.15	286.73	11.83	106.94	102.68	-10.72
600	71.94	299.30	18.74	106.15	101.80	-8.86
700	76.67	310.73	26.17	105.44	101.13	-7.55
800	80.62	321.20	34.03	104.85	100.54	-6.57
900	83.96	330.86	42.26	104.31	100.12	-5.81
1000	86.84	339.82	50.80	103.85	99.75	-5.21
1100	89.32	348.18	59.60	103.47	99.50	-4.72
1200	91.47	356.01	68.63	103.09	99.33	-4.32
1300	93.35	363.36	77.87	102.80	99.20	-3.99
1400	94.99	370.29	87.27	102.51	99.12	-3.70
1500	96.42	376.84	96.83	102.26	99.08	-3.45
1600	97.70	383.08	106.53	102.05	98.99	-3.23
1700	98.82	389.04	116.34	101.88	98.87	-3.04
1800	99.81	394.72	126.26	101.71	98.74	-2.87
1900	100.69	400.14	136.28	101.55	98.58	-2.71
2000	101.47	405.33	146.37	101.42	98.32	-2.57
2100	102.17	410.29	156.54	101.34	98.07	-2.44
2200	102.79	415.06	166.77	101.25	97.78	-2.32
2300	103.34	419.64	177.07	101.17	97.40	-2.21
2400	103.82	424.05	187.41	101.13	96.99	-2.11
2500	104.25	428.30	197.81	101.09	96.52	-2.02
2600	104.63	432.39	208.24	101.09	96.02	-1.93
2700	104.96	436.35	218.71	101.04	95.48	-1.85
2800	105.25	440.17	229.20	101.04	94.93	-1.77
2900	105.50	443.86	239.73	101.04	94.39	-1.70
3000	105.73	447.44	250.29	101.04	93.89	-1.63

CHF=CF• fccf cis

ΔH_f°**(0 K)** = -38.79 kJ mol^{-1}
ΔH_f°**(298.15 K)** = -41.10 kJ mol^{-1}
S°**(298.15 K)** = 281.12 J K^{-1} mol^{-1}

Moments of Inertia (10^{-47} kg m^2)
32.42 146.49 178.91

Vibrational Frequencies (cm^{-1})
204.1 401.4 718.9 727.9 945.6
1120.4 1325.5 1579.2 3097.9

Bond Distances (10^{-10} m)		**Bond Angles** (°)		**Dihedral Angles** (°)	
C1-C2	1.324				
C1-H1	1.068	C2-C1-H1	123.49		
C1-F1	1.330	C2-C1-F1	121.44	H1-C1-F1	180.00
C2-F2	1.300	C1-C2-F2	128.59	F1-C2-F2	0.00

Enthalpy Reference Temperature = T_r = 298.15 K
Standard State Pressure = p_o = 1 atmosphere

	¦- J K^{-1} mol^{-1} -¦		¦-------- kJ mol^{-1} ---------¦			
T/K	C_p°	S°	H°-$H^\circ(T_r)$	ΔH_f°	ΔG_f°	**Log K_f**
150	42.88	247.25	-7.41	-40.00	-40.96	14.27
200	47.64	260.26	-5.15	-40.42	-41.25	10.77
250	52.62	271.44	-2.65	-40.79	-41.46	8.66
300	57.55	281.47	0.10	-41.13	-41.63	7.25
350	62.21	290.70	3.10	-41.42	-41.71	6.23
400	66.48	299.29	6.32	-41.67	-41.80	5.46
450	70.31	307.34	9.74	-41.88	-41.88	4.86
500	73.71	314.92	13.34	-42.09	-41.88	4.38
600	79.37	328.86	21.00	-42.38	-41.88	3.65
700	83.81	341.42	29.17	-42.63	-41.80	3.12
800	87.35	352.83	37.73	-42.89	-41.67	2.72
900	90.22	363.27	46.61	-43.05	-41.42	2.40
1000	92.58	372.88	55.75	-43.22	-41.17	2.15
1100	94.55	381.77	65.11	-43.39	-40.84	1.94
1200	96.21	390.05	74.64	-43.56	-40.42	1.76
1300	97.62	397.77	84.33	-43.72	-40.00	1.61
1400	98.83	405.02	94.15	-43.89	-39.54	1.48
1500	99.87	411.85	104.09	-44.02	-39.08	1.36
1600	100.78	418.30	114.11	-44.14	-38.58	1.26
1700	101.57	424.40	124.23	-44.27	-38.07	1.17
1800	102.27	430.19	134.42	-44.39	-37.61	1.09
1900	102.90	435.70	144.67	-44.52	-37.20	1.02
2000	103.46	440.96	154.98	-44.64	-36.78	0.96
2100	103.96	445.98	165.35	-44.73	-36.40	0.91
2200	104.42	450.79	175.76	-44.81	-36.07	0.86
2300	104.83	455.42	186.21	-44.85	-35.86	0.81
2400	105.20	459.89	196.71	-44.94	-35.69	0.78
2500	105.54	464.19	207.24	-44.98	-35.61	0.74
2600	105.85	468.34	217.80	-45.02	-35.56	0.71
2700	106.14	472.34	228.40	-45.02	-35.52	0.69
2800	106.39	476.20	239.02	-45.02	-35.52	0.66
2900	106.63	479.94	249.66	-45.02	-35.48	0.64
3000	106.84	483.56	260.32	-45.02	-35.44	0.62

CHF=CF• fccf trans

ΔH_f°(0 K) = -40.46 kJ mol^{-1}
ΔH_f°(298.15 K) = -42.52 kJ mol^{-1}
S°(298.15 K) = 279.28 J K^{-1} mol^{-1}

Moments of Inertia (10^{-47} kg m^2)
10.31 207.95 218.26

Vibrational Frequencies (cm^{-1})
295.9 297.9 518.3 684.6 1049.1
1163.1 1259.9 1568.4 3051.6

Bond Distances (10^{-10} m)		**Bond Angles** (°)		**Dihedral Angles** (°)	
C1-C2	1.327				
C1-H1	1.072	C2-C1-H1	124.86		
C1-F1	1.327	C2-C1-F1	120.07	H1-C1-F1	180.00
C2-F2	1.304	C1-C2-F2	125.81	F1-C2-F2	180.00

Enthalpy Reference Temperature = T_r = 298.15 K
Standard State Pressure = p_o = 1 atmosphere

	¦- J K^{-1} mol^{-1} -¦		¦-------- kJ mol^{-1} ---------¦			
T/K	**C_p°**	**S°**	**H°-$H^\circ(T_r)$**	**ΔH_f°**	**ΔG_f°**	**Log K_f**
150	44.03	244.16	-7.69	-41.71	-42.22	14.69
200	49.58	257.62	-5.35	-42.01	-42.34	11.06
250	54.62	269.25	-2.74	-42.30	-42.43	8.87
300	59.32	279.65	0.11	-42.51	-42.51	7.40
350	63.69	289.14	3.18	-42.76	-42.51	6.35
400	67.70	297.93	6.47	-42.93	-42.55	5.55
450	71.32	306.12	9.95	-43.10	-42.51	4.94
500	74.55	313.81	13.60	-43.26	-42.51	4.44
600	79.97	327.91	21.33	-43.47	-42.38	3.69
700	84.26	340.57	29.55	-43.68	-42.26	3.15
800	87.68	352.05	38.15	-43.85	-42.01	2.74
900	90.46	362.54	47.07	-44.02	-41.76	2.42
1000	92.75	372.19	56.23	-44.18	-41.42	2.16
1100	94.65	381.12	65.60	-44.35	-41.05	1.95
1200	96.25	389.42	75.14	-44.48	-40.63	1.77
1300	97.60	397.17	84.84	-44.64	-40.12	1.61
1400	98.75	404.44	94.65	-44.77	-39.66	1.48
1500	99.73	411.28	104.58	-44.94	-39.12	1.36
1600	100.58	417.74	114.60	-45.10	-38.62	1.26
1700	101.32	423.86	124.69	-45.23	-38.12	1.17
1800	101.96	429.66	134.85	-45.40	-37.66	1.09
1900	102.53	435.18	145.08	-45.52	-37.20	1.02
2000	103.02	440.45	155.35	-45.69	-36.82	0.96
2100	103.46	445.47	165.67	-45.81	-36.44	0.91
2200	103.85	450.29	176.04	-45.94	-36.11	0.86
2300	104.20	454.91	186.44	-46.07	-35.86	0.81
2400	104.51	459.34	196.87	-46.19	-35.65	0.78
2500	104.79	463.60	207.34	-46.28	-35.44	0.74
2600	105.04	467.71	217.83	-46.40	-35.31	0.71
2700	105.27	471.67	228.34	-46.48	-35.19	0.68
2800	105.48	475.49	238.88	-46.61	-35.06	0.65
2900	105.67	479.19	249.43	-46.69	-34.94	0.63
3000	105.85	482.77	260.01	-46.78	-34.81	0.61

CF_2=CH•

ΔH_f°(0 K) = -64.94 kJ mol^{-1}
ΔH_f°(298.15 K) = -67.66 kJ mol^{-1}
S°(298.15 K) = 276.92 J K^{-1} mol^{-1}

Moments of Inertia (10^{-47} kg m^2)
70.89 76.08 146.97

Vibrational Frequencies (cm^{-1})
416.4 519.1 528.2 624.3 818.7
903.8 1278.3 1585.6 3128.7

Bond Distances (10^{-10} m)		**Bond Angles** (°)		**Dihedral Angles** (°)	
C1-C2	1.311				
C1-F1	1.309	C2-C1-F1	125.05		
C1-F2	1.304	C2-C1-F2	124.78	F1-C1-F2	180.00
C2-H1	1.066	C1-C2-H1	133.92	F1-C2-H1	0.00

Enthalpy Reference Temperature = T_r = 298.15 K
Standard State Pressure = p_o = 1 atmosphere

	¦- J K^{-1} mol^{-1} -¦		¦-------- kJ mol^{-1} ---------¦			
T/K	**C_p°**	**S°**	**H°-$H^\circ(T_r)$**	**ΔH_f°**	**ΔG_f°**	**Log K_f**
150	39.61	243.63	-7.33	-66.48	-66.90	23.30
200	46.39	255.96	-5.19	-66.99	-66.99	17.49
250	53.12	267.05	-2.70	-67.40	-66.99	13.99
300	59.19	277.29	0.11	-67.66	-66.90	11.65
350	64.48	286.81	3.20	-67.86	-66.82	9.97
400	69.04	295.70	6.54	-67.99	-66.73	8.71
450	72.97	304.04	10.08	-68.12	-66.57	7.73
500	76.37	311.91	13.82	-68.16	-66.48	6.94
600	81.94	326.39	21.72	-68.24	-66.23	5.77
700	86.26	339.37	30.12	-68.24	-65.98	4.92
800	89.70	351.13	38.90	-68.24	-65.69	4.29
900	92.46	361.84	47.99	-68.24	-65.35	3.79
1000	94.70	371.70	57.32	-68.24	-64.98	3.39
1100	96.50	380.80	66.86	-68.20	-64.56	3.07
1200	97.96	389.25	76.56	-68.20	-64.10	2.79
1300	99.14	397.13	86.41	-68.20	-63.64	2.56
1400	100.08	404.50	96.36	-68.24	-63.18	2.36
1500	100.84	411.43	106.40	-68.24	-62.68	2.18
1600	101.46	417.94	116.52	-68.32	-62.17	2.03
1700	101.95	424.11	126.70	-68.37	-61.67	1.90
1800	102.35	429.94	136.92	-68.45	-61.21	1.78
1900	102.68	435.47	147.18	-68.58	-60.79	1.67
2000	102.94	440.75	157.48	-68.70	-60.42	1.58
2100	103.15	445.77	167.80	-68.83	-60.08	1.49
2200	103.32	450.57	178.15	-68.95	-59.75	1.42
2300	103.46	455.16	188.51	-69.12	-59.50	1.35
2400	103.58	459.57	198.88	-69.33	-59.29	1.29
2500	103.67	463.79	209.27	-69.50	-59.12	1.24
2600	103.75	467.86	219.66	-69.71	-58.99	1.19
2700	103.81	471.77	230.07	-69.91	-58.87	1.14
2800	103.86	475.55	240.48	-70.12	-58.79	1.10
2900	103.91	479.19	250.89	-70.37	-58.62	1.06
3000	103.94	482.71	261.31	-70.58	-58.45	1.02

CF_2=CF•

ΔH_f°(0 K) = -215.73 kJ mol^{-1}
ΔH_f°(298.15 K) = -216.36 kJ mol^{-1}
S°(298.15 K) = 300.48 J K^{-1} mol^{-1}

Moments of Inertia (10^{-47} kg m^2)
72.80 217.89 290.68

Vibrational Frequencies (cm^{-1})
204.0 279.2 414.0 459.3 588.3
864.4 1203.3 1318.0 1663.5

Bond Distances (10^{-10} m)		**Bond Angles** (°)		**Dihedral Angles** (°)	
C1-C2	1.319				
C1-F1	1.304	C2-C1-F1	124.76		
C1-F2	1.303	C2-C1-F2	122.90	F1-C1-F2	180.00
C2-F3	1.302	C1-C2-F3	126.52	F1-C2-F3	0.00

Enthalpy Reference Temperature = T_r = 298.15 K
Standard State Pressure = p_o = 1 atmosphere

	- J K^{-1} mol^{-1} -		-------- kJ mol^{-1} ---------			
T/K	C_p°	S°	H°-$H^\circ(T_r)$	ΔH_f°	ΔG_f°	Log K_f
150	49.70	260.20	-8.84	-216.65	-214.14	74.56
200	57.00	275.54	-6.17	-216.61	-213.30	55.71
250	63.09	288.94	-3.16	-216.52	-212.55	44.40
300	68.28	300.90	0.13	-216.35	-211.79	36.88
350	72.81	311.77	3.66	-216.19	-211.12	31.50
400	76.81	321.75	7.40	-215.98	-210.46	27.48
450	80.32	330.99	11.33	-215.81	-209.79	24.35
500	83.41	339.60	15.42	-215.60	-209.16	21.85
600	88.47	355.24	24.02	-215.27	-207.99	18.10
700	92.33	369.15	33.07	-214.93	-206.82	15.43
800	95.29	381.64	42.45	-214.64	-205.64	13.43
900	97.58	392.97	52.09	-214.39	-204.47	11.87
1000	99.37	403.30	61.94	-214.18	-203.30	10.62
1100	100.81	412.80	71.95	-214.01	-202.05	9.59
1200	101.98	421.58	82.09	-213.89	-200.83	8.74
1300	102.95	429.73	92.33	-213.76	-199.53	8.02
1400	103.76	437.35	102.66	-213.68	-198.24	7.40
1500	104.45	444.47	113.06	-213.64	-196.94	6.86
1600	105.04	451.18	123.53	-213.59	-195.64	6.39
1700	105.55	457.57	134.06	-213.55	-194.47	5.97
1800	106.00	463.61	144.63	-213.51	-193.30	5.61
1900	106.39	469.36	155.24	-213.47	-192.17	5.28
2000	106.74	474.82	165.89	-213.43	-191.13	4.99
2100	107.04	480.03	176.57	-213.43	-190.12	4.73
2200	107.29	485.02	187.28	-213.38	-189.16	4.49
2300	107.52	489.80	198.02	-213.34	-188.28	4.28
2400	107.72	494.38	208.77	-213.26	-187.44	4.08
2500	107.88	498.77	219.55	-213.22	-186.65	3.90
2600	108.02	503.01	230.34	-213.17	-185.90	3.73
2700	108.13	507.09	241.14	-213.13	-185.18	3.58
2800	108.22	511.02	251.95	-213.05	-184.47	3.44
2900	108.30	514.82	262.78	-213.01	-183.76	3.31
3000	108.35	518.49	273.60	-212.92	-183.05	3.19

C_2HF

ΔH_f°(0 K) = 117.86 kJ mol^{-1}
ΔH_f°(298.15 K) = 117.80 kJ mol^{-1}
S°(298.15 K) = 227.71 J K^{-1} mol^{-1}

Moments of Inertia (10^{-47} kg m^2)
84.53 84.53

Vibrational Frequencies (cm^{-1})
441.6 441.6 685.4 685.4 1042.9
2262.5 3293.0

Bond Distances (10^{-10} m)		**Bond Angles** (°)		**Dihedral Angles** (°)
C1-C2	1.177			
C1-H1	1.055	C2-C1-H1	180.00	
C2-F1	1.269	C1-C2-F1	180.00	

Enthalpy Reference Temperature = T_r = 298.15 K
Standard State Pressure = p_o = 1 atmosphere

	|- J K^{-1} mol^{-1} -|		|-------- kJ mol^{-1} ---------|			
T/K	**C_p°**	**S°**	**H°-$H^\circ(T_r)$**	**ΔH_f°**	**ΔG_f°**	**Log K_f**
150	34.59	199.26	-6.26	117.82	110.42	-38.45
200	39.94	209.94	-4.40	117.78	107.95	-28.19
250	45.02	219.41	-2.27	117.78	105.44	-22.03
300	49.38	228.02	0.09	117.82	102.93	-17.92
350	52.98	235.91	2.65	117.86	100.37	-14.98
400	55.94	243.18	5.38	117.91	97.82	-12.77
450	58.42	249.92	8.24	117.95	95.27	-11.06
500	60.51	256.18	11.21	117.99	92.72	-9.68
600	63.94	267.53	17.44	117.95	87.57	-7.62
700	66.70	277.60	23.98	117.82	82.47	-6.15
800	69.03	286.67	30.77	117.61	77.45	-5.06
900	71.04	294.91	37.78	117.32	72.47	-4.21
1000	72.78	302.49	44.97	117.03	67.57	-3.53
1100	74.30	309.50	52.33	116.69	62.72	-2.98
1200	75.64	316.03	59.82	116.32	57.95	-2.52
1300	76.81	322.13	67.45	115.90	53.26	-2.14
1400	77.83	327.86	75.18	115.52	48.58	-1.81
1500	78.72	333.26	83.01	115.10	43.93	-1.53
1600	79.51	338.36	90.92	114.68	39.33	-1.28
1700	80.20	343.21	98.91	114.31	34.69	-1.07
1800	80.81	347.81	106.96	113.89	30.08	-0.87
1900	81.35	352.19	115.06	113.47	25.44	-0.70
2000	81.83	356.38	123.23	113.09	20.75	-0.54
2100	82.26	360.38	131.43	112.68	16.07	-0.40
2200	82.65	364.22	139.68	112.30	11.30	-0.27
2300	82.99	367.90	147.96	111.92	6.53	-0.15
2400	83.30	371.43	156.27	111.55	1.72	-0.04
2500	83.58	374.84	164.62	111.17	-3.14	0.07
2600	83.83	378.12	172.99	110.79	-8.03	0.16
2700	84.05	381.29	181.38	110.42	-12.89	0.25
2800	84.26	384.35	189.80	110.08	-17.78	0.33
2900	84.45	387.31	198.23	109.75	-22.68	0.41
3000	84.62	390.18	206.69	109.41	-27.49	0.48

C_2F_2

ΔH_f°(0 K) = 29.96 kJ mol^{-1}
ΔH_f°(298.15 K) = 31.82 kJ mol^{-1}
S°(298.15 K) = 245.88 J K^{-1} mol^{-1}

Moments of Inertia (10^{-47} kg m^2)
231.40 231.40

Vibrational Frequencies (cm^{-1})
291.1 291.1 407.1 407.1 771.4
1321.2 2502.4

Bond Distances (10^{-10} m)		**Bond Angles** (°)		**Dihedral Angles** (°)
C1-C2	1.166			
C1-F1	1.275	C2-C1-F1	180.00	
C2-F2	1.275	C1-C2-F2	180.00	

Enthalpy Reference Temperature = T_r = 298.15 K
Standard State Pressure = p_o = 1 atmosphere

	¦- J K^{-1} mol^{-1} -¦		¦-------- kJ mol^{-1} ---------¦			
T/K	**C_p°**	**S°**	**H°-$H^\circ(T_r)$**	**ΔH_f°**	**ΔG_f°**	**Log K_f**
150	43.72	210.49	-7.76	30.42	26.69	-9.30
200	50.36	224.02	-5.40	30.84	25.40	-6.63
250	55.28	235.81	-2.75	31.34	23.93	-5.00
300	59.05	246.24	0.11	31.84	22.38	-3.89
350	62.05	255.58	3.14	32.30	20.71	-3.09
400	64.51	264.03	6.31	32.72	18.95	-2.48
450	66.59	271.75	9.59	33.10	17.20	-1.99
500	68.37	278.86	12.96	33.39	15.36	-1.60
600	71.31	291.60	19.95	33.85	11.63	-1.01
700	73.66	302.78	27.20	34.14	7.87	-0.59
800	75.58	312.74	34.67	34.31	4.10	-0.27
900	77.16	321.74	42.30	34.35	0.33	-0.02
1000	78.48	329.93	50.09	34.31	-3.35	0.18
1100	79.58	337.47	57.99	34.18	-7.03	0.33
1200	80.51	344.44	66.00	34.02	-10.63	0.46
1300	81.30	350.91	74.09	33.81	-14.23	0.57
1400	81.96	356.96	82.26	33.56	-17.78	0.66
1500	82.53	362.64	90.48	33.26	-21.30	0.74
1600	83.01	367.97	98.76	32.97	-24.81	0.81
1700	83.43	373.02	107.08	32.64	-28.37	0.87
1800	83.80	377.80	115.44	32.34	-31.88	0.93
1900	84.12	382.34	123.84	32.01	-35.44	0.97
2000	84.39	386.66	132.26	31.67	-39.04	1.02
2100	84.63	390.79	140.72	31.34	-42.63	1.06
2200	84.85	394.73	149.19	31.00	-46.32	1.10
2300	85.04	398.51	157.69	30.67	-50.04	1.14
2400	85.21	402.13	166.20	30.33	-53.76	1.17
2500	85.36	405.61	174.73	30.00	-57.53	1.20
2600	85.50	408.96	183.27	29.66	-61.34	1.23
2700	85.62	412.19	191.83	29.33	-65.19	1.26
2800	85.73	415.30	200.39	29.00	-68.99	1.29
2900	85.83	418.32	208.97	28.70	-72.80	1.31
3000	85.93	421.23	217.56	28.37	-76.57	1.33

•C_2F

ΔH_f°(0 K) = 448.94 kJ mol^{-1}
ΔH_f°(298.15 K) = 453.86 kJ mol^{-1}
S°(298.15 K) = 218.02 J K^{-1} mol^{-1}

Moments of Inertia (10^{-47} kg m^2)
75.82 75.82

Vibrational Frequencies (cm^{-1})
217.8 1003.0 2071.7

Bond Distances (10^{-10} m)		**Bond Angles** (°)		**Dihedral Angles** (°)
C1-C2	1.196			
C1-F1	1.272	C2-C1-F1	179.35	

Enthalpy Reference Temperature = T_r = 298.15 K
Standard State Pressure = p_o = 1 atmosphere

	¦- J K^{-1} mol^{-1} -¦		¦-------- kJ mol^{-1} ---------¦			
T/K	**C_p°**	**S°**	**H°-$H^\circ(T_r)$**	**ΔH_f°**	**ΔG_f°**	**Log K_f**
150	39.16	190.07	-6.05	451.91	437.65	-152.39
200	40.38	201.51	-4.07	452.71	432.75	-113.01
250	41.44	210.64	-2.02	453.38	427.60	-89.34
300	42.49	218.28	0.08	453.88	422.37	-73.54
350	43.53	224.91	2.23	454.26	417.06	-62.24
400	44.53	230.79	4.43	454.51	411.66	-53.75
450	45.49	236.09	6.68	454.68	406.27	-47.15
500	46.40	240.93	8.98	454.76	400.83	-41.87
600	48.08	249.54	13.70	454.68	389.99	-33.95
700	49.53	257.06	18.59	454.34	379.15	-28.29
800	50.77	263.76	23.61	453.80	368.48	-24.06
900	51.81	269.80	28.74	453.13	357.86	-20.77
1000	52.68	275.31	33.96	452.33	347.40	-18.15
1100	53.40	280.36	39.27	451.45	337.02	-16.00
1200	54.00	285.04	44.63	450.45	326.81	-14.22
1300	54.50	289.38	50.06	449.40	316.69	-12.72
1400	54.93	293.43	55.53	448.32	306.65	-11.44
1500	55.29	297.24	61.04	447.14	296.69	-10.33
1600	55.60	300.81	66.59	445.97	286.81	-9.36
1700	55.86	304.19	72.16	444.76	276.98	-8.51
1800	56.08	307.39	77.76	443.55	267.19	-7.75
1900	56.28	310.43	83.38	442.29	257.40	-7.08
2000	56.45	313.32	89.01	440.99	247.65	-6.47
2100	56.60	316.08	94.67	439.74	237.94	-5.92
2200	56.73	318.72	100.34	438.44	228.20	-5.42
2300	56.85	321.24	106.01	437.14	218.49	-4.96
2400	56.95	323.66	111.70	435.85	208.74	-4.54
2500	57.04	325.99	117.40	434.55	199.03	-4.16
2600	57.13	328.23	123.11	433.25	189.33	-3.80
2700	57.20	330.39	128.83	431.96	179.66	-3.48
2800	57.27	332.46	134.55	430.62	170.00	-3.17
2900	57.33	334.48	140.28	429.32	160.41	-2.89
3000	57.38	336.42	146.02	428.02	150.88	-2.63

CHF=C=O

ΔH_f°(0 K) = -144.68 kJ mol^{-1}
ΔH_f°(298.15 K) = -147.19 kJ mol^{-1}
S°(298.15 K) = 270.51 J K^{-1} mol^{-1}

Moments of Inertia (10^{-47} kg m^2)
14.45 180.24 194.69

Vibrational Frequencies (cm^{-1})
252.4 479.7 615.2 681.3 1027.8
1207.3 1425.2 2107.9 3073.7

Bond Distances (10^{-10} m)		**Bond Angles** (°)		**Dihedral Angles** (°)
C1-C2	1.308			
C1-F1	1.339	C2-C1-F1	120.10	
C1-H1	1.067	C2-C1-H1	122.43	
C2-O1	1.147	C1-C2-O1	180.00	

Enthalpy Reference Temperature = T_r = 298.15 K
Standard State Pressure = p_o = 1 atmosphere

	- J K^{-1} mol^{-1} -		---------- kJ mol^{-1} ----------			
T/K	C_p°	S°	H°-$H^\circ(T_r)$	ΔH_f°	ΔG_f°	Log K_f
150	41.64	237.24	-7.30	-146.06	-145.35	50.61
200	46.89	249.94	-5.09	-146.48	-145.06	37.88
250	52.00	260.95	-2.62	-146.86	-144.68	30.23
300	56.74	270.86	0.10	-147.19	-144.26	25.12
350	61.06	279.93	3.05	-147.49	-143.80	21.46
400	64.95	288.34	6.20	-147.74	-143.30	18.71
450	68.45	296.20	9.54	-147.99	-142.76	16.57
500	71.58	303.58	13.04	-148.20	-142.21	14.86
600	76.94	317.12	20.48	-148.53	-141.08	12.28
700	81.30	329.32	28.40	-148.87	-139.83	10.43
800	84.89	340.41	36.71	-149.20	-138.53	9.04
900	87.88	350.59	45.35	-149.49	-137.15	7.96
1000	90.40	359.99	54.27	-149.75	-135.69	7.09
1100	92.51	368.70	63.42	-150.04	-134.18	6.37
1200	94.30	376.83	72.76	-150.29	-132.59	5.77
1300	95.83	384.44	82.27	-150.54	-130.96	5.26
1400	97.13	391.59	91.92	-150.79	-129.33	4.83
1500	98.25	398.33	101.69	-151.04	-127.65	4.45
1600	99.22	404.71	111.57	-151.25	-125.98	4.11
1700	100.06	410.75	121.53	-151.50	-124.31	3.82
1800	100.79	416.49	131.57	-151.71	-122.67	3.56
1900	101.44	421.96	141.69	-151.92	-121.04	3.33
2000	102.00	427.17	151.86	-152.13	-119.45	3.12
2100	102.50	432.16	162.08	-152.34	-117.95	2.93
2200	102.94	436.94	172.36	-152.51	-116.44	2.76
2300	103.33	441.52	182.67	-152.72	-114.98	2.61
2400	103.68	445.93	193.02	-152.88	-113.60	2.47
2500	104.00	450.17	203.41	-153.05	-112.21	2.34
2600	104.28	454.25	213.82	-153.18	-110.92	2.23
2700	104.54	458.19	224.26	-153.34	-109.62	2.12
2800	104.77	462.00	234.73	-153.47	-108.32	2.02
2900	104.98	465.68	245.22	-153.64	-107.03	1.93
3000	105.17	469.24	255.72	-153.76	-105.69	1.84

CF_2=C=O

ΔH_f°(0 K) = -289.91 kJ mol^{-1}
ΔH_f°(298.15 K) = -290.43 kJ mol^{-1}
S°(298.15 K) = 288.81 J K^{-1} mol^{-1}

Moments of Inertia (10^{-47} kg m^2)
76.39 209.01 285.39

Vibrational Frequencies (cm^{-1})
206.6 273.3 378.2 442.2 672.8
793.3 1314.7 1450.3 2208.3

Bond Distances (10^{-10} m)		**Bond Angles** (°)		**Dihedral Angles** (°)
C1-C2	1.300			
C1-F1	1.312	C2-C1-F1	122.97	
C1-F2	1.312	C2-C1-F2	122.97	
C2-O1	1.151	C1-C2-O1	180.00	

Enthalpy Reference Temperature = T_r = 298.15 K
Standard State Pressure = p_o = 1 atmosphere

	|- J K^{-1} mol^{-1} -|		|-------- kJ mol^{-1} ---------|			
T/K	**C_p°**	**S°**	**H°-$H^\circ(T_r)$**	**ΔH_f°**	**ΔG_f°**	**Log K_f**
150	50.22	248.43	-8.86	-290.79	-286.35	99.71
200	57.28	263.88	-6.16	-290.75	-284.89	74.40
250	63.05	277.30	-3.15	-290.62	-283.47	59.22
300	67.84	289.23	0.13	-290.41	-282.09	49.12
350	71.94	300.01	3.62	-290.20	-280.79	41.90
400	75.49	309.85	7.31	-290.03	-279.49	36.50
450	78.62	318.93	11.16	-289.83	-278.24	32.29
500	81.39	327.36	15.17	-289.66	-276.98	28.94
600	86.04	342.62	23.55	-289.32	-274.55	23.90
700	89.73	356.17	32.34	-289.07	-272.17	20.31
800	92.67	368.36	41.47	-288.91	-269.74	17.61
900	95.03	379.41	50.86	-288.78	-267.36	15.52
1000	96.93	389.52	60.46	-288.70	-264.89	13.84
1100	98.47	398.84	70.23	-288.65	-262.42	12.46
1200	99.73	407.46	80.14	-288.65	-259.91	11.31
1300	100.77	415.48	90.17	-288.70	-257.40	10.34
1400	101.64	422.99	100.29	-288.74	-254.85	9.51
1500	102.37	430.02	110.49	-288.82	-252.30	8.79
1600	102.98	436.65	120.76	-288.91	-249.78	8.15
1700	103.51	442.91	131.08	-289.03	-247.23	7.60
1800	103.96	448.84	141.46	-289.11	-244.72	7.10
1900	104.35	454.47	151.88	-289.24	-242.25	6.66
2000	104.69	459.83	162.33	-289.37	-239.83	6.26
2100	104.98	464.95	172.81	-289.49	-237.44	5.91
2200	105.24	469.84	183.32	-289.62	-235.10	5.58
2300	105.47	474.52	193.86	-289.74	-232.84	5.29
2400	105.67	479.01	204.42	-289.87	-230.62	5.02
2500	105.85	483.33	214.99	-289.99	-228.40	4.77
2600	106.01	487.49	225.58	-290.12	-226.27	4.55
2700	106.16	491.49	236.20	-290.20	-224.14	4.34
2800	106.29	495.35	246.82	-290.33	-222.00	4.14
2900	106.40	499.08	257.45	-290.45	-219.87	3.96
3000	106.51	502.70	268.10	-290.54	-217.69	3.79

•CF=C=O

ΔH_f°(0 K) = 66.65 kJ mol^{-1}
ΔH_f°(298.15 K) = 69.03 kJ mol^{-1}
S°(298.15 K) = 276.17 J K^{-1} mol^{-1}

Moments of Inertia (10^{-47} kg m^2)
5.47 195.70 201.18

Vibrational Frequencies (cm^{-1})
250.8 279.2 496.8 764.5 1332.9
1712.2

Bond Distances (10^{-10} m)		**Bond Angles** (°)		**Dihedral Angles** (°)	
C1-C2	1.398				
C1-F1	1.296	C2-C1-F1	125.03		
C2-O1	1.163	X1-C2-O1	128.40	C1-C2-O1	180.00

Enthalpy Reference Temperature = T_r = 298.15 K
Standard State Pressure = p_o = 1 atmosphere

	|- J K^{-1} mol^{-1} -|		|-------- kJ mol^{-1} ---------|			
T/K	**C_p°**	**S°**	**H°-$H^\circ(T_r)$**	**ΔH_f°**	**ΔG_f°**	**Log K_f**
150	45.16	241.23	-7.63	67.70	59.54	-20.74
200	49.89	254.90	-5.25	68.16	56.74	-14.82
250	53.68	266.45	-2.66	68.62	53.81	-11.24
300	56.84	276.52	0.10	69.04	50.75	-8.84
350	59.56	285.50	3.02	69.45	47.66	-7.11
400	61.96	293.61	6.05	69.83	44.43	-5.80
450	64.10	301.03	9.21	70.12	41.21	-4.78
500	66.02	307.89	12.46	70.42	37.95	-3.96
600	69.23	320.22	19.23	70.84	31.34	-2.73
700	71.75	331.09	26.28	71.09	24.69	-1.84
800	73.72	340.80	33.56	71.21	18.03	-1.18
900	75.27	349.58	41.02	71.17	11.42	-0.66
1000	76.49	357.58	48.61	71.04	4.90	-0.25
1100	77.46	364.91	56.30	70.84	-1.63	0.08
1200	78.24	371.69	64.09	70.54	-8.08	0.35
1300	78.89	377.98	71.95	70.17	-14.52	0.58
1400	79.41	383.84	79.86	69.75	-20.88	0.78
1500	79.85	389.34	87.83	69.29	-27.20	0.95
1600	80.22	394.50	95.83	68.78	-33.51	1.09
1700	80.53	399.38	103.87	68.24	-39.79	1.22
1800	80.79	403.99	111.93	67.66	-46.11	1.34
1900	81.02	408.36	120.03	67.07	-52.38	1.44
2000	81.22	412.52	128.14	66.44	-58.70	1.53
2100	81.39	416.49	136.27	65.81	-65.06	1.62
2200	81.53	420.28	144.41	65.19	-71.42	1.70
2300	81.67	423.91	152.58	64.56	-77.82	1.77
2400	81.78	427.38	160.75	63.89	-84.22	1.83
2500	81.89	430.72	168.93	63.26	-90.67	1.89
2600	81.98	433.94	177.13	62.59	-97.11	1.95
2700	82.06	437.03	185.33	61.92	-103.60	2.00
2800	82.14	440.02	193.54	61.30	-110.04	2.05
2900	82.20	442.90	201.75	60.63	-116.44	2.10
3000	82.26	445.69	209.98	59.96	-122.80	2.14

CH_2F-CHO fcco trans

ΔH_f°(0 K) = -319.20 kJ mol^{-1}
ΔH_f°(298.15 K) = -328.72 kJ mol^{-1}
S°(298.15 K) = 286.63 J K^{-1} mol^{-1}

Moments of Inertia (10^{-47} kg m^2)
20.71 190.45 205.95

Vibrational Frequencies (cm^{-1})

84.2	315.4	514.9	721.1	1019.8
1078.4	1105.5	1222.5	1328.4	1391.8
1461.2	1821.7	2857.6	2910.4	2959.4

Bond Distances (10^{-10} m)		**Bond Angles** (°)		**Dihedral Angles** (°)	
C1-C2	1.511				
C2-O1	1.186	C1-C2-O1	122.12		
C2-H1	1.093	O1-C2-H1	122.54	C1-C2-H1	180.00
C1-F1	1.364	C2-C1-F1	109.29	O1-C1-F1	180.00
C1-H2	1.082	C2-C1-H2	109.91	F1-C1-H2	119.87
C1-H3	1.082	C2-C1-H3	109.91	F1-C1-H3	-119.87

Enthalpy Reference Temperature = T_r = 298.15 K
Standard State Pressure = p_o = 1 atmosphere

	- J K^{-1} mol^{-1} -		-------- kJ mol^{-1} ---------			
T/K	**C_p°**	**S°**	**H°-$H^\circ(T_r)$**	**ΔH_f°**	**ΔG_f°**	**Log K_f**
150	48.26	248.84	-8.27	-324.22	-308.74	107.51
200	53.38	263.40	-5.74	-325.81	-303.38	79.23
250	58.64	275.86	-2.95	-327.31	-297.65	62.19
300	64.14	287.03	0.12	-328.78	-291.62	50.77
350	69.75	297.33	3.46	-330.12	-285.39	42.59
400	75.28	307.00	7.10	-331.33	-278.95	36.42
450	80.60	316.17	11.00	-332.46	-272.34	31.61
500	85.60	324.92	15.17	-333.46	-265.64	27.75
600	94.55	341.33	24.20	-335.14	-251.96	21.94
700	102.19	356.50	34.07	-336.44	-238.03	17.76
800	108.68	370.58	44.64	-337.44	-223.89	14.62
900	114.22	383.75	55.81	-338.15	-209.66	12.17
1000	118.94	396.35	67.48	-338.65	-195.56	10.21
1100	122.98	408.18	79.60	-338.95	-181.46	8.62
1200	126.43	419.32	92.09	-339.11	-167.36	7.28
1300	129.40	429.84	104.89	-339.11	-153.26	6.16
1400	131.95	439.79	117.97	-339.03	-139.20	5.19
1500	134.16	449.22	131.29	-338.90	-125.14	4.36
1600	136.07	458.18	144.80	-338.65	-111.17	3.63
1700	137.73	466.70	158.50	-338.36	-97.28	2.99
1800	139.18	474.83	172.36	-338.03	-83.43	2.42
1900	140.46	482.60	186.35	-337.65	-69.71	1.92
2000	141.59	490.03	200.46	-337.23	-56.02	1.46
2100	142.58	497.16	214.67	-336.77	-42.47	1.06
2200	143.46	503.99	228.98	-336.31	-29.04	0.69
2300	144.25	510.56	243.37	-335.77	-15.65	0.36
2400	144.95	516.88	257.83	-335.26	-2.38	0.05
2500	145.58	522.97	272.36	-334.68	10.79	-0.23
2600	146.15	528.85	286.95	-334.13	23.85	-0.48
2700	146.67	534.53	301.60	-333.55	36.90	-0.71
2800	147.13	540.02	316.29	-332.92	49.87	-0.93
2900	147.55	545.33	331.03	-332.34	62.80	-1.13
3000	147.93	550.47	345.80	-331.67	75.77	-1.32

CH_2F-CHO fcco gauche

ΔH_f°(0 K) = -312.67 kJ mol^{-1}
ΔH_f°(298.15 K) = -322.75 kJ mol^{-1}
S°(298.15 K) = 281.30 J K^{-1} mol^{-1}

Moments of Inertia (10^{-47} kg m^2)
41.73 135.31 171.87

Vibrational Frequencies (cm^{-1})
164.6 251.0 722.4 726.2 845.9
1111.1 1124.2 1239.4 1380.4 1405.7
1464.4 1835.0 2815.4 2881.6 2918.0

Bond Distances (10^{-10} m)		**Bond Angles** (°)		**Dihedral Angles** (°)	
C1-C2	1.507				
C2-O1	1.183	C1-C2-O1	124.47		
C2-H1	1.096	O1-C2-H1	121.76	C1-C2-H1	180.03
C1-F1	1.351	C2-C1-F1	111.18	O1-C1-F1	0.10
C1-H2	1.085	C2-C1-H2	109.23	F1-C1-H2	120.95
C1-H3	1.085	C2-C1-H3	109.21	F1-C1-H3	-120.96

Enthalpy Reference Temperature = T_r = 298.15 K
Standard State Pressure = p_o = 1 atmosphere

	- J K^{-1} mol^{-1} -		---------- kJ mol^{-1} ----------			
T/K	**C_p°**	**S°**	**H°-$H^\circ(T_r)$**	**ΔH_f°**	**ΔG_f°**	**Log K_f**
150	46.37	245.13	-7.96	-317.94	-301.92	105.13
200	50.97	259.05	-5.53	-319.62	-296.35	77.39
250	56.38	270.93	-2.85	-321.25	-290.37	60.66
300	62.45	281.68	0.12	-322.80	-284.05	49.46
350	68.80	291.71	3.39	-324.22	-277.52	41.41
400	75.10	301.24	6.99	-325.47	-270.79	35.36
450	81.15	310.35	10.89	-326.60	-263.88	30.63
500	86.83	319.18	15.08	-327.57	-256.90	26.84
600	96.93	335.93	24.27	-329.11	-242.71	21.13
700	105.41	351.53	34.39	-330.16	-228.28	17.03
800	112.46	366.07	45.28	-330.83	-213.68	13.95
900	118.31	379.67	56.82	-331.16	-198.99	11.55
1000	123.16	392.39	68.90	-331.25	-184.22	9.62
1100	127.19	404.32	81.42	-331.16	-169.41	8.05
1200	130.55	415.53	94.31	-330.91	-154.60	6.73
1300	133.37	426.10	107.51	-330.54	-139.79	5.62
1400	135.73	436.07	120.98	-330.08	-125.02	4.66
1500	137.74	445.50	134.66	-329.53	-110.25	3.84
1600	139.44	454.45	148.53	-328.99	-95.52	3.12
1700	140.90	462.95	162.56	-328.36	-80.88	2.48
1800	142.16	471.04	176.72	-327.69	-66.27	1.92
1900	143.26	478.75	191.00	-327.02	-51.76	1.42
2000	144.20	486.13	205.38	-326.35	-37.32	0.97
2100	145.03	493.18	219.86	-325.60	-22.97	0.57
2200	145.76	499.95	234.41	-324.89	-8.74	0.21
2300	146.41	506.44	249.03	-324.18	5.44	-0.12
2400	146.98	512.68	263.71	-323.42	19.54	-0.42
2500	147.49	518.69	278.44	-322.67	33.51	-0.70
2600	147.95	524.49	293.22	-321.88	47.45	-0.95
2700	148.35	530.08	308.05	-321.12	61.34	-1.19
2800	148.72	535.48	322.91	-320.33	75.14	-1.40
2900	149.06	540.70	337.81	-319.57	88.99	-1.60
3000	149.36	545.76	352.74	-318.78	102.80	-1.79

CHF_2-CHO hcco cis

ΔH_f°(0 K) = -530.70 kJ mol^{-1}
ΔH_f°(298.15 K) = -538.95 kJ mol^{-1}
S°(298.15 K) = 304.75 J K^{-1} mol^{-1}

Moments of Inertia (10^{-47} kg m^2)
87.24 211.96 272.48

Vibrational Frequencies (cm^{-1})

76.3	315.5	368.5	416.3	592.2
977.7	1081.8	1127.5	1131.2	1312.2
1368.9	1395.3	1841.3	2875.1	3003.1

Bond Distances (10^{-10} m)		**Bond Angles** (°)		**Dihedral Angles** (°)	
C1-C2	1.516				
C2-O1	1.183	C1-C2-O1	122.03		
C2-H1	1.091	O1-C2-H1	123.13	C1-C2-H1	180.00
C1-H2	1.077	C2-C1-H2	112.55	O1-C1-H2	0.00
C1-F1	1.339	C2-C1-F1	108.25	H2-C1-F1	121.72
C1-F2	1.339	C2-C1-F2	108.25	H2-C1-F2	-121.72

Enthalpy Reference Temperature = T_r = 298.15 K
Standard State Pressure = p_o = 1 atmosphere

	¦- J K^{-1} mol^{-1} -¦		¦-------- kJ mol^{-1} ---------¦			
T/K	**C_p°**	**S°**	**H°-$H^\circ(T_r)$**	**ΔH_f°**	**ΔG_f°**	**Log K_f**
150	53.07	261.96	-9.38	-535.51	-516.60	179.89
200	60.40	278.25	-6.55	-536.81	-510.11	133.22
250	67.02	292.44	-3.37	-537.94	-503.38	105.17
300	73.30	305.21	0.13	-538.98	-496.39	86.43
350	79.34	316.95	3.95	-539.90	-489.28	73.02
400	85.08	327.93	8.07	-540.74	-482.04	62.94
450	90.42	338.26	12.46	-541.45	-474.67	55.10
500	95.34	348.04	17.11	-542.08	-467.27	48.81
600	103.90	366.20	27.10	-543.08	-452.25	39.37
700	110.95	382.76	37.87	-543.79	-437.06	32.61
800	116.78	397.97	49.28	-544.21	-421.79	27.54
900	121.62	412.01	61.22	-544.51	-406.43	23.59
1000	125.66	425.19	73.60	-544.59	-391.12	20.43
1100	129.06	437.62	86.36	-544.59	-376.02	17.85
1200	131.94	449.25	99.42	-544.46	-360.87	15.71
1300	134.38	460.18	112.75	-544.30	-345.81	13.89
1400	136.47	470.47	126.31	-544.00	-330.75	12.34
1500	138.26	480.20	140.05	-543.71	-315.77	11.00
1600	139.80	489.41	153.96	-543.33	-300.83	9.82
1700	141.14	498.14	168.02	-542.92	-285.98	8.79
1800	142.30	506.46	182.20	-542.50	-271.21	7.87
1900	143.32	514.39	196.48	-542.00	-256.56	7.05
2000	144.21	521.95	210.87	-541.54	-241.96	6.32
2100	145.00	529.20	225.33	-540.99	-227.48	5.66
2200	145.70	536.14	239.87	-540.45	-213.13	5.06
2300	146.32	542.80	254.48	-539.90	-198.82	4.52
2400	146.88	549.21	269.14	-539.32	-184.68	4.02
2500	147.38	555.38	283.86	-538.73	-170.58	3.56
2600	147.82	561.32	298.62	-538.15	-156.57	3.15
2700	148.23	567.06	313.43	-537.52	-142.63	2.76
2800	148.59	572.60	328.27	-536.89	-128.74	2.40
2900	148.93	577.96	343.15	-536.22	-114.89	2.07
3000	149.23	583.15	358.06	-535.59	-101.09	1.76

CHF_2-CHO hcco trans

ΔH_f°(0 K) = -514.55 kJ mol^{-1}
ΔH_f°(298.15 K) = -525.02 kJ mol^{-1}
S°(298.15 K) = 287.06 J K^{-1} mol^{-1}

Moments of Inertia (10^{-47} kg m^2)
99.38 183.42 232.28

Vibrational Frequencies (cm^{-1})

-109.3	266.0	308.3	496.2	782.7
871.4	960.5	1151.3	1157.2	1379.3
1385.4	1413.6	1842.9	2853.1	2964.4

Bond Distances (10^{-10} m)		**Bond Angles** (°)		**Dihedral Angles** (°)	
C1-C2	1.529				
C2-O1	1.181	C1-C2-O1	121.33		
C2-H1	1.092	O1-C2-H1	122.22	C1-C2-H1	180.00
C1-H2	1.079	C2-C1-H2	112.87	O1-C1-H2	180.00
C1-F1	1.335	C2-C1-F1	108.92	H2-C1-F1	120.90
C1-F2	1.335	C2-C1-F2	108.92	H2-C1-F2	-120.90

Enthalpy Reference Temperature = T_r = 298.15 K
Standard State Pressure = p_o = 1 atmosphere

	- J K^{-1} mol^{-1} -		---------- kJ mol^{-1} ----------			
T/K	**C_p°**	**S°**	**H°-$H^\circ(T_r)$**	**ΔH_f°**	**ΔG_f°**	**Log K_f**
150	44.57	250.93	-7.95	-520.15	-499.57	173.96
200	50.58	264.57	-5.57	-521.87	-492.46	128.62
250	56.80	276.52	-2.88	-523.54	-484.97	101.32
300	63.27	287.44	0.12	-525.09	-477.14	83.08
350	69.76	297.69	3.44	-526.51	-469.11	70.01
400	76.02	307.42	7.09	-527.81	-460.87	60.18
450	81.89	316.71	11.04	-528.94	-452.50	52.52
500	87.28	325.62	15.27	-529.99	-443.96	46.38
600	96.66	342.39	24.48	-531.79	-426.64	37.14
700	104.34	357.89	34.54	-533.17	-409.07	30.52
800	110.65	372.25	45.30	-534.30	-391.25	25.55
900	115.86	385.59	56.64	-535.13	-373.30	21.66
1000	120.19	398.03	68.45	-535.84	-355.22	18.55
1100	123.82	409.66	80.65	-536.35	-337.02	16.00
1200	126.87	420.57	93.19	-536.77	-318.78	13.87
1300	129.45	430.83	106.01	-537.10	-300.45	12.07
1400	131.64	440.50	119.07	-537.31	-282.09	10.52
1500	133.52	449.65	132.33	-537.48	-263.72	9.18
1600	135.14	458.32	145.77	-537.60	-245.39	8.01
1700	136.54	466.56	159.35	-537.64	-227.02	6.98
1800	137.75	474.40	173.07	-537.69	-208.70	6.06
1900	138.81	481.88	186.90	-537.69	-190.46	5.24
2000	139.74	489.02	200.82	-537.64	-172.21	4.50
2100	140.56	495.86	214.84	-537.56	-154.05	3.83
2200	141.29	502.41	228.93	-537.48	-135.94	3.23
2300	141.93	508.71	243.09	-537.35	-117.86	2.68
2400	142.51	514.76	257.32	-537.23	-99.87	2.17
2500	143.02	520.59	271.59	-537.06	-81.96	1.71
2600	143.49	526.21	285.92	-536.89	-64.06	1.29
2700	143.90	531.63	300.29	-536.72	-46.19	0.89
2800	144.28	536.87	314.70	-536.51	-28.37	0.53
2900	144.62	541.94	329.14	-536.31	-10.54	0.19
3000	144.93	546.85	343.62	-536.10	7.32	-0.13

CF_3-CHO fcco cis

ΔH_f°(0 K) = -767.26 kJ mol^{-1}
ΔH_f°(298.15 K) = -774.30 kJ mol^{-1}
S°(298.15 K) = 318.28 J K^{-1} mol^{-1}

Moments of Inertia (10^{-47} kg m^2)
148.91 273.72 278.81

Vibrational Frequencies (cm^{-1})

73.1	251.9	309.1	423.1	514.7
515.0	688.4	834.9	981.5	1225.3
1226.0	1329.8	1382.7	1857.1	2893.7

Bond Distances (10^{-10} m)		**Bond Angles** (°)		**Dihedral Angles** (°)	
C1-C2	1.524				
C2-O1	1.178	C1-C2-O1	122.16		
C2-H1	1.089	O1-C2-H1	123.85	C1-C2-H1	180.00
C1-F1	1.306	C2-C1-F1	112.37	O1-C1-F1	0.00
C1-F2	1.321	C2-C1-F2	109.29	F1-C1-F2	121.11
C1-F3	1.321	C2-C1-F3	109.29	F1-C1-F3	-121.11

Enthalpy Reference Temperature = T_r = 298.15 K
Standard State Pressure = p_o = 1 atmosphere

	|- J K^{-1} mol^{-1} -|		|-------- kJ mol^{-1} ---------|			
T/K	**C_p°**	**S°**	**H°-$H^\circ(T_r)$**	**ΔH_f°**	**ΔG_f°**	**Log K_f**
150	57.57	271.58	-10.32	-771.74	-748.85	260.76
200	65.83	289.25	-7.22	-772.78	-741.07	193.54
250	73.49	304.75	-3.72	-773.62	-733.08	153.16
300	80.68	318.78	0.15	-774.33	-724.92	126.21
350	87.39	331.72	4.37	-774.92	-716.68	106.95
400	93.55	343.80	8.91	-775.42	-708.35	92.50
450	99.14	355.41	13.74	-775.80	-700.11	81.26
500	104.15	366.44	18.84	-776.09	-691.87	72.27
600	112.60	386.82	29.71	-776.42	-675.38	58.80
700	119.27	405.25	41.33	-776.59	-658.94	49.17
800	124.59	422.03	53.55	-776.55	-642.54	41.95
900	128.85	437.41	66.24	-776.38	-626.14	36.34
1000	132.31	451.58	79.31	-776.13	-609.82	31.85
1100	135.14	464.70	92.70	-775.80	-593.50	28.18
1200	137.48	476.91	106.34	-775.42	-577.22	25.12
1300	139.43	488.31	120.19	-774.96	-560.99	22.54
1400	141.07	499.00	134.22	-774.54	-544.84	20.33
1500	142.45	509.07	148.41	-774.04	-528.73	18.41
1600	143.63	518.56	162.72	-773.54	-512.71	16.74
1700	144.65	527.54	177.13	-772.99	-496.77	15.26
1800	145.52	536.07	191.65	-772.45	-480.91	13.95
1900	146.28	544.18	206.24	-771.91	-465.14	12.79
2000	146.94	551.91	220.91	-771.32	-449.45	11.74
2100	147.52	559.29	235.63	-770.73	-433.92	10.79
2200	148.04	566.36	250.41	-770.11	-418.44	9.93
2300	148.49	573.13	265.24	-769.48	-403.09	9.15
2400	148.89	579.63	280.11	-768.85	-387.81	8.44
2500	149.26	585.89	295.02	-768.22	-372.67	7.79
2600	149.58	591.91	309.96	-767.60	-357.61	7.18
2700	149.87	597.72	324.94	-766.93	-342.59	6.63
2800	150.13	603.32	339.94	-766.26	-327.61	6.11
2900	150.37	608.74	354.97	-765.59	-312.71	5.63
3000	150.58	613.98	370.02	-764.92	-297.78	5.18

CH_2F-CO• fcco trans

ΔH_f°(0 K) = -166.94 kJ mol^{-1}
ΔH_f°(298.15 K) = -172.61 kJ mol^{-1}
S°(298.15 K) = 286.12 J K^{-1} mol^{-1}

Moments of Inertia (10^{-47} kg m^2)
16.81 192.13 203.68

Vibrational Frequencies (cm^{-1})
137.9 312.2 496.2 841.8 895.3
1100.8 1215.2 1346.3 1450.6 1924.3
2907.3 2963.7

Bond Distances (10^{-10} m)		**Bond Angles** (°)		**Dihedral Angles** (°)	
C1-C2	1.518				
C2-O1	1.163	C1-C2-O1	126.50		
C1-F1	1.354	C2-C1-F1	110.32	O1-C1-F1	180.00
C1-H1	1.082	C2-C1-H1	108.76	F1-C1-H1	120.13
C1-H2	1.082	C2-C1-H2	108.76	F1-C1-H2	-120.13

Enthalpy Reference Temperature = T_r = 298.15 K
Standard State Pressure = p_o = 1 atmosphere

	¦- J K^{-1} mol^{-1} -¦		¦-------- kJ mol^{-1} ---------¦			
T/K	**C_p°**	**S°**	**H°-$H^\circ(T_r)$**	**ΔH_f°**	**ΔG_f°**	**Log K_f**
150	46.86	249.59	-8.03	-170.04	-162.92	56.73
200	51.81	263.63	-5.57	-170.96	-160.41	41.89
250	56.95	275.65	-2.86	-171.84	-157.69	32.95
300	62.26	286.50	0.11	-172.63	-154.85	26.96
350	67.50	296.49	3.35	-173.34	-151.88	22.67
400	72.46	305.83	6.84	-174.01	-148.82	19.44
450	77.02	314.63	10.57	-174.56	-145.73	16.91
500	81.14	322.95	14.52	-175.06	-142.55	14.89
600	88.15	338.39	23.00	-175.85	-136.02	11.84
700	93.82	352.41	32.10	-176.44	-129.37	9.65
800	98.47	365.25	41.74	-176.90	-122.59	8.00
900	102.33	377.07	51.79	-177.28	-115.73	6.72
1000	105.57	388.02	62.21	-177.53	-108.83	5.68
1100	108.32	398.22	72.92	-177.74	-101.80	4.83
1200	110.65	407.74	83.89	-177.90	-94.77	4.12
1300	112.64	416.68	95.07	-177.99	-87.70	3.52
1400	114.34	425.09	106.43	-178.07	-80.58	3.01
1500	115.81	433.03	117.96	-178.15	-73.47	2.56
1600	117.09	440.54	129.62	-178.20	-66.36	2.17
1700	118.20	447.68	141.40	-178.20	-59.29	1.82
1800	119.16	454.55	153.28	-178.20	-52.38	1.52
1900	120.01	461.18	165.25	-178.20	-45.69	1.26
2000	120.76	467.51	177.30	-178.20	-39.08	1.02
2100	121.42	473.57	189.42	-178.15	-32.55	0.81
2200	122.01	479.39	201.60	-178.11	-26.07	0.62
2300	122.53	484.97	213.84	-178.07	-19.71	0.45
2400	122.99	490.34	226.12	-178.03	-13.39	0.29
2500	123.41	495.51	238.45	-177.95	-7.15	0.15
2600	123.79	500.49	250.82	-177.86	-1.00	0.02
2700	124.13	505.31	263.22	-177.78	5.15	-0.10
2800	124.44	509.96	275.66	-177.69	11.21	-0.21
2900	124.72	514.46	288.13	-177.61	17.28	-0.31
3000	124.97	518.81	300.62	-177.53	23.39	-0.41

CH_2F-CO• fcco gauche

ΔH_f°(0 K) = -164.01 kJ mol^{-1}
ΔH_f°(298.15 K) = -169.85 kJ mol^{-1}
S°(298.15 K) = 285.88 J K^{-1} mol^{-1}

Moments of Inertia (10^{-47} kg m^2)
36.25 139.26 170.32

Vibrational Frequencies (cm^{-1})
180.3 228.0 671.5 809.3 894.7
1081.2 1240.7 1370.1 1453.3 1943.7
2914.0 2961.7

Bond Distances (10^{-10} m)		**Bond Angles** (°)		**Dihedral Angles** (°)	
C1-C2	1.513				
C2-O1	1.160	C1-C2-O1	129.10		
C1-F1	1.356	C2-C1-F1	111.84	O1-C1-F1	0.00
C1-H1	1.082	C2-C1-H1	108.40	F1-C1-H1	120.87
C1-H2	1.082	C2-C1-H2	108.38	F1-C1-H2	-120.84

Enthalpy Reference Temperature = T_r = 298.15 K
Standard State Pressure = p_o = 1 atmosphere

	¦- J K^{-1} mol^{-1} -¦		¦-------- kJ mol^{-1} ---------¦			
T/K	**C_p°**	**S°**	**H°-$H^\circ(T_r)$**	**ΔH_f°**	**ΔG_f°**	**Log K_f**
150	46.47	250.10	-7.86	-167.11	-160.08	55.74
200	50.74	264.00	-5.44	-168.07	-157.61	41.16
250	55.51	275.76	-2.79	-168.99	-154.89	32.36
300	60.67	286.26	0.11	-169.87	-152.05	26.47
350	65.92	295.92	3.27	-170.67	-149.03	22.24
400	71.02	304.98	6.69	-171.42	-145.90	19.05
450	75.82	313.63	10.36	-172.05	-142.72	16.57
500	80.26	321.85	14.25	-172.59	-139.49	14.57
600	88.01	337.19	22.66	-173.43	-132.88	11.57
700	94.35	351.25	31.78	-174.01	-126.11	9.41
800	99.51	364.19	41.47	-174.43	-119.29	7.79
900	103.71	376.15	51.63	-174.68	-112.34	6.52
1000	107.16	387.26	62.18	-174.81	-105.31	5.50
1100	110.00	397.61	73.04	-174.85	-98.28	4.67
1200	112.35	407.29	84.17	-174.85	-91.17	3.97
1300	114.32	416.36	95.51	-174.81	-84.06	3.38
1400	115.98	424.89	107.04	-174.72	-76.94	2.87
1500	117.38	432.94	118.72	-174.64	-69.83	2.43
1600	118.58	440.55	130.53	-174.51	-62.72	2.05
1700	119.61	447.78	142.45	-174.39	-55.65	1.71
1800	120.49	454.64	154.47	-174.26	-48.62	1.41
1900	121.26	461.17	166.57	-174.14	-41.63	1.14
2000	121.93	467.41	178.74	-173.97	-34.69	0.91
2100	122.52	473.37	190.98	-173.85	-27.78	0.69
2200	123.04	479.08	203.27	-173.68	-21.00	0.50
2300	123.50	484.56	215.61	-173.55	-14.23	0.32
2400	123.90	489.83	227.99	-173.38	-7.53	0.16
2500	124.27	494.89	240.42	-173.22	-0.92	0.02
2600	124.60	499.77	252.87	-173.09	5.69	-0.11
2700	124.89	504.48	265.35	-172.92	12.26	-0.24
2800	125.16	509.03	277.87	-172.76	18.79	-0.35
2900	125.39	513.51	290.41	-172.59	25.06	-0.45
3000	125.61	517.87	302.97	-172.42	31.30	-0.55

CHF_2-CO• hcco cis

ΔH_f°(0 K) = -372.92 kJ mol^{-1}
ΔH_f°(298.15 K) = -377.35 kJ mol^{-1}
S°(298.15 K) = 310.33 J K^{-1} mol^{-1}

Moments of Inertia (10^{-47} kg m^2)
82.99 209.20 274.09

Vibrational Frequencies (cm^{-1})
53.8 366.7 407.3 410.6 590.0
946.7 1133.6 1150.5 1319.5 1366.4
1940.6 2976.4

Bond Distances (10^{-10} m)		**Bond Angles** (°)		**Dihedral Angles** (°)	
C1-C2	1.539				
C2-O1	1.158	C1-C2-O1	126.14		
C1-H1	1.078	C2-C1-H1	112.14	O1-C1-H1	0.00
C1-F1	1.330	C2-C1-F1	108.00	H1-C1-F1	121.17
C1-F2	1.330	C2-C1-F2	108.00	H1-C1-F2	-121.17

Enthalpy Reference Temperature = T_r = 298.15 K
Standard State Pressure = p_o = 1 atmosphere

	¦- J K^{-1} mol^{-1} -¦		¦-------- kJ mol^{-1} ---------¦			
T/K	**C_p°**	**S°**	**H°-$H^\circ(T_r)$**	**ΔH_f°**	**ΔG_f°**	**Log K_f**
150	50.83	270.46	-8.79	-375.47	-366.10	127.47
200	56.46	285.83	-6.09	-376.14	-362.84	94.76
250	61.86	299.01	-3.11	-376.77	-359.45	75.10
300	67.12	310.75	0.13	-377.35	-355.97	61.98
350	72.19	321.71	3.62	-377.90	-352.50	52.60
400	76.96	332.08	7.36	-378.36	-349.03	45.58
450	81.38	341.80	11.33	-378.78	-345.56	40.11
500	85.41	350.95	15.51	-379.15	-342.04	35.73
600	92.32	367.82	24.42	-379.78	-335.01	29.16
700	97.91	383.07	33.95	-380.24	-327.94	24.47
800	102.42	396.97	43.99	-380.62	-320.87	20.95
900	106.11	409.72	54.43	-380.91	-313.76	18.21
1000	109.14	421.48	65.20	-381.12	-306.65	16.02
1100	111.64	432.39	76.25	-381.33	-299.49	14.22
1200	113.73	442.55	87.52	-381.50	-292.34	12.72
1300	115.48	452.04	98.99	-381.62	-285.18	11.46
1400	116.97	460.96	110.62	-381.71	-278.07	10.37
1500	118.23	469.36	122.38	-381.79	-270.96	9.43
1600	119.32	477.29	134.26	-381.87	-263.88	8.61
1700	120.25	484.80	146.24	-381.96	-256.86	7.89
1800	121.06	491.93	158.31	-382.00	-249.87	7.25
1900	121.76	498.72	170.45	-382.00	-242.92	6.68
2000	122.38	505.19	182.66	-382.04	-236.06	6.17
2100	122.92	511.37	194.93	-382.04	-229.28	5.70
2200	123.40	517.29	207.25	-382.04	-222.59	5.28
2300	123.83	522.97	219.61	-382.04	-215.98	4.90
2400	124.20	528.43	232.01	-382.04	-209.41	4.56
2500	124.54	533.67	244.45	-382.00	-202.92	4.24
2600	124.85	538.72	256.92	-381.96	-196.48	3.95
2700	125.12	543.60	269.42	-381.92	-190.12	3.68
2800	125.37	548.30	281.95	-381.87	-183.76	3.43
2900	125.59	552.85	294.50	-381.79	-177.40	3.20
3000	125.80	557.25	307.06	-381.75	-171.04	2.98

CF_3-CO• fcco cis

ΔH_f°(0 K) = -606.51 kJ mol^{-1}
ΔH_f°(298.15 K) = -609.88 kJ mol^{-1}
S°(298.15 K) = 323.59 J K^{-1} mol^{-1}

Moments of Inertia (10^{-47} kg m^2)
144.25 275.19 275.38

Vibrational Frequencies (cm^{-1})
58.1 234.3 388.6 411.9 523.5
531.4 667.3 795.4 1203.3 1240.3
1269.0 1959.9

Bond Distances (10^{-10} m)		**Bond Angles** (°)		**Dihedral Angles** (°)	
C1-C2	1.541				
C2-O1	1.155	C1-C2-O1	126.31		
C1-F1	1.310	C2-C1-F1	112.19	O1-C1-F1	0.00
C1-F2	1.313	C2-C1-F2	108.91	F1-C1-F2	120.64
C1-F3	1.313	C2-C1-F3	108.91	F1-C1-F3	-120.64

Enthalpy Reference Temperature = T_r = 298.15 K
Standard State Pressure = p_o = 1 atmosphere

	- J K^{-1} mol^{-1} -		---------- kJ mol^{-1} ----------			
T/K	C_p°	S°	H°-$H^\circ(T_r)$	ΔH_f°	ΔG_f°	Log K_f
150	53.57	277.64	-9.77	-608.94	-595.22	207.26
200	62.06	294.65	-6.86	-609.40	-590.61	154.25
250	69.84	310.08	-3.54	-609.69	-586.09	122.45
300	76.67	324.08	0.14	-609.86	-581.58	101.26
350	82.65	336.94	4.14	-609.99	-577.10	86.12
400	87.87	348.83	8.41	-609.99	-572.66	74.78
450	92.42	359.91	12.93	-609.94	-568.23	65.96
500	96.37	370.28	17.66	-609.90	-563.84	58.90
600	102.82	389.17	27.64	-609.69	-555.13	48.33
700	107.71	406.03	38.19	-609.44	-546.56	40.78
800	111.45	421.21	49.16	-609.19	-538.02	35.13
900	114.35	434.99	60.46	-608.94	-529.53	30.73
1000	116.63	447.60	72.02	-608.69	-521.08	27.22
1100	118.43	459.19	83.78	-608.52	-512.67	24.34
1200	119.88	469.92	95.70	-608.31	-504.26	21.95
1300	121.06	479.90	107.75	-608.14	-495.89	19.92
1400	122.03	489.21	119.91	-608.02	-487.56	18.19
1500	122.83	497.94	132.15	-607.89	-479.28	16.69
1600	123.50	506.16	144.47	-607.81	-470.99	15.38
1700	124.08	513.92	156.85	-607.68	-462.79	14.22
1800	124.56	521.26	169.28	-607.60	-454.68	13.19
1900	124.98	528.23	181.77	-607.52	-446.60	12.28
2000	125.34	534.86	194.28	-607.43	-438.61	11.45
2100	125.65	541.19	206.83	-607.35	-430.70	10.71
2200	125.93	547.23	219.41	-607.27	-422.84	10.04
2300	126.16	553.02	232.02	-607.18	-415.09	9.43
2400	126.38	558.57	244.65	-607.06	-407.40	8.87
2500	126.57	563.90	257.29	-606.97	-399.78	8.35
2600	126.73	569.03	269.96	-606.89	-392.25	7.88
2700	126.89	573.97	282.64	-606.81	-384.76	7.44
2800	127.02	578.74	295.34	-606.68	-377.27	7.04
2900	127.14	583.35	308.05	-606.60	-369.82	6.66
3000	127.26	587.80	320.77	-606.47	-362.33	6.31

CF_3-CO• fcco trans

ΔH_f°(0 K) = -606.43 kJ mol^{-1}
ΔH_f°(298.15 K) = -611.24 kJ mol^{-1}
S°(298.15 K) = 306.16 J K^{-1} mol^{-1}

Moments of Inertia (10^{-47} kg m^2)
142.55 273.76 275.81

Vibrational Frequencies (cm^{-1})
-78.5 225.9 320.7 417.8 518.9
527.3 664.5 792.6 1199.3 1240.1
1270.4 1953.8

Bond Distances (10^{-10} m)		**Bond Angles** (°)		**Dihedral Angles** (°)	
C1-C2	1.546				
C2-O1	1.155	C1-C2-O1	124.97		
C1-F1	1.311	C2-C1-F1	110.39	O1-C1-F1	180.00
C1-F2	1.312	C2-C1-F2	109.83	F1-C1-F2	119.86
C1-F3	1.312	C2-C1-F3	109.83	F1-C1-F3	-119.86

Enthalpy Reference Temperature = T_r = 298.15 K
Standard State Pressure = p_o = 1 atmosphere

	¦- J K^{-1} mol^{-1} -¦		¦-------- kJ mol^{-1} ---------¦			
T/K	**C_p°**	**S°**	**H°-$H^\circ(T_r)$**	**ΔH_f°**	**ΔG_f°**	**Log K_f**
150	49.12	264.78	-9.13	-609.65	-594.00	206.84
200	58.05	280.15	-6.44	-610.36	-588.69	153.74
250	65.93	293.97	-3.34	-610.86	-583.25	121.86
300	72.78	306.61	0.13	-611.24	-577.73	100.59
350	78.74	318.29	3.92	-611.53	-572.16	85.39
400	83.94	329.15	8.00	-611.78	-566.56	73.98
450	88.46	339.31	12.31	-611.95	-560.95	65.11
500	92.40	348.83	16.83	-612.08	-555.34	58.01
600	98.80	366.27	26.41	-612.29	-544.00	47.36
700	103.67	381.89	36.54	-612.45	-532.67	39.75
800	107.39	395.98	47.10	-612.62	-521.24	34.03
900	110.28	408.81	57.99	-612.79	-509.82	29.59
1000	112.54	420.55	69.14	-612.96	-498.27	26.03
1100	114.34	431.36	80.48	-613.17	-486.72	23.11
1200	115.78	441.37	91.99	-613.42	-475.09	20.68
1300	116.95	450.69	103.63	-613.67	-463.42	18.62
1400	117.91	459.39	115.37	-613.92	-451.70	16.85
1500	118.71	467.55	127.21	-614.21	-439.99	15.32
1600	119.38	475.24	139.11	-614.50	-428.27	13.98
1700	119.95	482.49	151.08	-614.84	-416.52	12.80
1800	120.43	489.36	163.10	-615.13	-404.80	11.75
1900	120.84	495.88	175.16	-615.47	-393.13	10.81
2000	121.20	502.09	187.27	-615.80	-381.46	9.96
2100	121.51	508.01	199.40	-616.14	-369.82	9.20
2200	121.78	513.67	211.57	-616.47	-358.23	8.51
2300	122.02	519.09	223.76	-616.81	-346.69	7.87
2400	122.24	524.29	235.97	-617.10	-335.18	7.29
2500	122.42	529.28	248.20	-617.43	-323.72	6.76
2600	122.59	534.09	260.45	-617.77	-312.25	6.27
2700	122.74	538.72	272.72	-618.06	-300.83	5.82
2800	122.88	543.18	285.00	-618.40	-289.41	5.40
2900	123.00	547.50	297.30	-618.69	-277.98	5.01
3000	123.11	551.67	309.60	-619.02	-266.48	4.64

Appendix B. Fluorinated Hydrocarbon Reaction Rate Constants

REACTION	A	b	E	note/reference	H
H_2/O_2 System: Combination, Decomposition					
H + H +M = H2 + M H2/0/ H2O/0/ CO2/0/	1.00E18	-1.00	0.	!MBA139	
H + H +H2 = 2H2	9.20E16	-0.60	0.	!MBA140	
H + H +H2O = H2 + H2O	6.00E19	-1.25	0.	!MBA141	
H + H +CO2 = H2 + CO2	5.49E20	-2.00	0.	!MBA142	
O + O +M = O2 + M	1.89E13	0.00	-1788.	!MBA145	86TSA/HAM
H + OH +M = H2O + M H2O/5/	1.60E22	-2.00	0.	!MBA143	
H + O +M = OH + M H2O/5/	6.20E16	-0.60	0.	!MBA144	
H_2/O_2 System: Atom Transfers					
O + OH = O2 + H	4.00E14	-0.50	0.	!MBA132	81HOW/SMI
O + H2 = OH + H	5.06E04	2.67	6290.	!MBA133	88SUT/MIC
2OH = O + H2O	6.00E08	1.30	0.	!MBA138	
H2 + O2 = 2OH	1.70E13	0.00	47780.	!MBA130	71JAC/HOU
OH + H2 = H2O + H	1.17E09	1.30	3626.	!MBA131	79COH/WES
H_2/O_2 System: Peroxyl and Peroxide					
H + O2 + M = HO2 + M H2O/18.6/ CO2/4.2/ H2/2.9/ CO/2.1/ N2/1.3/	3.61E17	-0.72	0.	!MBA134	
H + HO2 = H2 + O2	1.25E13	0.00	0.	!MBA146	
O + HO2 = O2 + OH	1.40E13	0.00	1073.	!MBA137	
OH + HO2 = H2O + O2	7.50E12	0.00	0.	!MBA135	
H2O2 + M = 2OH + M	1.30E17	0.00	45500.	!MBA148	
H + HO2 = 2OH	1.40E14	0.00	1073.	!MBA136	
2HO2 = H2O2 + O2	2.00E12	0.00	0.	!MBA147	
REACTION	A	b	E	note/reference	H
C_1 Hydrocarbons: Methane					
CH4 + H = CH3 + H2	2.20E04	3.00	8750.	!MBA004	73CLA/DOV
CH4 + O = CH3 + OH	1.02E09	1.50	8604.	!MBA005	86SUT/MIC
CH4 + OH = CH3 + H2O	1.60E06	2.10	2460.	!MBA005	83BAU/CRA
CH4 + O2 = CH3 + HO2	7.90E13	0.00	56000.	!MBA003	72SKI/LIF
CH4 + HO2 = CH3 + H2O2	1.80E11	0.00	18700.	!MBA006	72SKI/LIF
C_1 Hydrocarbons: Methyl					
CH3 + H (+M) = CH4 (+M) LOW/8.00E26 -3.0 0./ SRI/0.45 797. 979./ H2/2.0/ CO/2.0/ CO2/3.0/ H2O/5.0/	6.00E16	-1.00	0.	!MBA002 !(89STE/SMI2)	84WAR
CH3 + H = CH2 + H2	9.00E13	0.00	15100.	!MBA013	
CH3 + O = CH2O + H	8.00E13	0.00	0.	!MBA009	
CH3 + OH = CH2 + H2O	7.50E06	2.00	5000.	!MBA012	
CH3 + OH = CH3OH	2.24E40	-8.20	11673.	!87DEA/WES	
CH3 + OH = CH2OH + H	2.64E19	-1.80	8068.	!87DEA/WES	
CH3 + OH = CH3O + H	5.74E12	-0.23	13931.	!87DEA/WES	
CH3 + OH = CH2SING + H2O	8.90E19	-1.80	8067.	!87DEA/WES	
CH3 + O2 = CH3O + O	2.05E18	-1.57	29229.	!MBA008	86TSA/HAM
CH3 + HO2 = CH3O + OH	2.00E13	0.00	0.	!MBA007	86TSA/HAM
CH3 + CH3(+M) = C2H6 (+M) LOW/3.18E41 -7.0 2762./ TROE/0.6041 6927. 132./ H2/2.0/ CO/2.0/ CO2/3.0/ H2O/5.0/	9.03E16	-1.20	654.	!MBA001 !(88WAG/WAR)	88WAG/WAR

C_1 Hydrocarbons: Methylene (triplet)					
CH2+OH = CH2O+H	2.50E13	0.00	0.	!MBA026	
CH2+O = CO+2H	5.00E13	0.00	0.	!MBA043	
CH2+CO2 = CH2O+CO	1.10E11	0.00	1000.	!MBA042	
CH2+O = CO+H2	3.00E13	0.00	0.	!MBA044	
CH2+O2 = CO2+2H	1.60E12	0.00	1000.	!MBA045	
CH2+O2 = CH2O+O	5.00E13	0.00	9000.	!MBA046	
CH2+O2 = CO2+H2	6.90E11	0.00	500.	!MBA047	
CH2+O2 = CO+H2O	1.90E10	0.00	-1000.	!MBA048	
CH2+O2 = CO+OH+H	8.60E10	0.00	-500.	!MBA049	
CH2+O2 = HCO+OH	4.30E10	0.00	-500.	!MBA050	
CH2+CH3 = C2H4+H	3.00E13	0.00	0.	!MBA072	
2CH2 = C2H2+H2	4.00E13	0.00	0.	!MBA114	
C_1 Hydrocarbons: Methylene (singlet)					
CH2SING+M = CH2+M	1.00E13	0.00	0.	!MBA106	
H/0.0/					
CH2SING+H = CH2+H	2.00E14	0.00	0.	!MBA111	
CH2SING+O2 = CO+OH+H	3.00E13	0.00	0.	!MBA109	
CH2SING+H2 = CH3+H	7.00E13	0.00	0.	!MBA110	
CH2SING+CH4 = 2CH3	4.00E13	0.00	0.	!MBA107	
CH2SING+C2H6 = CH3+C2H5	1.20E14	0.00	0.	!MBA108	
C_1 Hydrocarbons: Methylidyne					
CH2+H = CH+H2	1.00E18	-1.56	0.	!MBA024	
CH2+OH = CH+H2O	1.13E07	2.00	3000.	!MBA025	
CH+O2 = HCO+O	3.30E13	0.00	0.	!MBA027	82BER/FLE
CH+O = CO+H	5.70E13	0.00	0.	!MBA028	83MES/FIL
CH+OH = HCO+H	3.00E13	0.00	0.	!MBA029	
CH+CO2 = HCO+CO	3.40E12	0.00	690.	!MBA030	82BER/FLE
CH+H2O = CH2O+H	1.17E15	-0.75	0.	!MBA032	
CH+CH2O = CH2CO+H	9.46E13	0.00	-515.	!MBA033	88ZAB/FLE
CH+CH2 = C2H2+H	4.00E13	0.00	0.	!MBA035	
CH+CH3 = C2H3+H	3.00E13	0.00	0.	!MBA036	
CH+CH4 = C2H4+H	6.00E13	0.00	0.	!MBA037	80BUT/FLE
C2H3+CH = CH2+C2H2	5.00E13	0.00	0.	!MBA086	
HCCO+CH = C2H2+CO	5.00E13	0.00	0.	!MBA104	

REACTION	A	b	E	note/reference	H
Oxidized C_1 Hydrocarbons: Methanol					
CH3OH + H = CH3O + H2	8.00E12	0.00	6095.	!90NOR	
CH3OH + OH = CH3O + H2O	1.50E13	0.00	5960.	!75BOW	
CH3OH + CH3 = CH3O + CH4	1.45E+1	3.10	6935.	!90NOR	
+16					
CH3OH + O2 = CH2OH+ HO2	2.05E13	0.00	44717.	!90NOR	
CH3OH + H = CH2OH+ H2	3.20E13	0.00	6095.	!90NOR	
CH3OH + O = CH2OH+ OH	3.88E05	2.50	3080.	!90NOR	
CH3OH + OH = CH2OH+ H2O	1.50E13	0.00	5960.	!75BOW	
CH3OH + HO2 = CH2OH+ H2O2	3.98E13	0.00	19400.	!90NOR	
CH3OH + CH3 = CH2OH+ CH4	3.19E01	3.17	7172.	!90NOR	
Oxidized C_1 Hydrocarbons: Methoxy, Hydroxymethyl					
CH3O+M = CH2O+H+M	1.00E14	0.00	25000.	!MBA014	
CH3O+O2 = CH2O+HO2	6.30E10	0.00	2600.	!MBA022	
CH3O+H = CH2O+H2	2.00E13	0.00	0.	!MBA016	
CH3O+O = CH2O+OH	1.00E13	0.00	0.	!MBA020	
CH3O+OH = CH2O+H2O	1.00E13	0.00	0.	!MBA018	
CH2OH+M = CH2O+H+M	1.00E14	0.00	25000.	!MBA015	
CH2OH+O2 = CH2O+HO2	1.48E13	0.00	1500.	!MBA023	
CH2OH+H = CH2O+H2	2.00E13	0.00	0.	!MBA017	
CH2OH+O = CH2O+OH	1.00E13	0.00	0.	!MBA021	
CH2OH+OH = CH2O+H2O	1.00E13	0.00	0.	!MBA019	

Oxidized C_1 Hydrocarbons: Formaldehyde					
CH2O+M = HCO+H+M	3.31E16	0.00	81000.	!MBA053	80DEA/JOH
CH2O+H = HCO+H2	2.19E08	1.77	3000.	!MBA052	86TSA/HAM
CH2O+O = HCO+OH	1.80E13	0.00	3080.	!MBA054	80KLE/SOK
CH2O+OH = HCO+H2O	3.43E09	1.18	-447.	!MBA051	86TSA/HAM
Oxidized C_1 Hydrocarbons: Formyl					
HCO + M = CO + H + M	2.50E14	0.00	16802.	!MBA056	84WAR
CO/1.9/ H2/1.9/ CH4/2.8/ CO2/3.0/ H2O/5.0/					
HCO + H = CO + H2	1.19E13	0.25	0.	!MBA057	
HCO + O = CO + OH	3.00E13	0.00	0.	!MBA058	84WAR
HCO + O = CO2 + H	3.00E13	0.00	0.	!MBA059	84WAR
HCO + OH = CO + H2O	1.00E14	0.00	0.	!MBA055	84TEM/WAG
HCO + O2 = CO + HO2	3.30E13	-0.40	0.	!MBA060	81VEY/LES
Oxidized C_1 Hydrocarbons: Carbon Monoxide					
CO + O+M = CO2 + M	6.17E14	0.00	3000.	!MBA061	86TSA/HAM
CO + OH = CO2 + H	1.51E07	1.30	-758.	!MBA062	
CO + O2 = CO2 + O	1.60E13	0.00	41000.	!MBA063	71BRA/BEL
CO + HO2 = CO2 + OH	5.80E13	0.00	22934.	!MBA064	77ATR/BAL
REACTION	A	b	E	note/reference	H
C_2 Hydrocarbons: Ethane					
C2H6 + H = C2H5 + H2	5.40E02	3.50	5210.	!MBA066	73CAL/DOV
C2H6 + O = C2H5 + OH	3.00E07	2.00	5115.	!MBA067	84WAR
C2H6 + OH = C2H5 + H2O	8.70E09	1.05	1810.	!MBA068	83TUL/RAV
C2H6 + CH3 = C2H5 + CH4	5.50E-1	4.00	8300.	!MBA065	73CLA/DOV
C_2 Hydrocarbons: Ethyl					
C2H5+H = CH3+CH3	1.00E14	0.00	0.	!MBA074	
C2H5 + O = CH2O + CH3	1.60E13	0.	0.	!86TSA/HAM	
C2H5+O2 = C2H4+HO2	2.56E19	-2.77	1977.	!90BOZ/DEA	
C_2 Hydrocarbons: Ethylene					
C2H4+M = C2H2+H2+M	1.50E15	0.00	55800.	!MBA128	83KIE/KAP
C2H4+M = C2H3+H+M	1.40E16	0.00	82360.	!MBA129	
C2H4+H(+M) = C2H5(+M)	8.40E08	1.5	990.	!86TSA/HAM	
LOW/6.37E27 -2.8 -54./				!MBA073	
H2/2.0/ CO/2.0/ CO2/3.0/ H2O/5.0/				!MBA073	
C2H4+H = C2H3+H2	1.10E14	0.00	8500.	!MBA069	73PEE/MAH
C2H4+O = CH3+HCO	1.60E09	1.20	746.	!MBA070	84WAR
C2H4+OH = C2H3+H2O	4.50E06	2.00	2850.	!fit	ref
C_2 Hydrocarbons: Vinyl					
C2H3+H = C2H2+H2	1.20E13	0.00	0.	!92BAU/COB	
C2H3+OH = C2H2+H2O	5.00E12	0.00	0.	!MBA083	
C2H3+CH2 = C2H2+CH3	3.00E13	0.00	0.	!MBA084	
C2H3+O2 = CH2O+HCO	1.05E38	-8.22	7030.	!92WES a/s	
C2H3+O2 = CH2O+HCO	4.48E26	-4.55	5480.	!92WES direct	
C2H3+O = CH2CO+H	3.00E13	0.00	0.	!MBA081	84WAR
C_2 Hydrocarbons: Acetylene					
C2H2+H(+M) = C2H3(+M)	5.54E12	0.00	2410.	!MBA079	76PAY/STI
LOW/2.67E27 -3.5 2410./					
H2/2.0/ CO/2.0/ CO2/3.0/ H2O/5.0/					
C2H2+OH = HCCOH+H	5.04E05	2.30	13500.	!MBA088	
C2H2+OH = CH2CO+H	2.18E-4	4.50	-1000.	!MBA089	
C2H2+OH = CH3+CO	4.83E-4	4.00	-2000.	!MBA090	
C2H2+O = CH2+CO	1.02E07	2.00	1900.	!MBA076	
C2H2+O = HCCO+H	1.02E07	2.00	1900.	!MBA077	
C2H2+O2 = HCCO+OH	2.00E08	1.50	30100.	!MBA126	

Oxidized C_2 Hydrocarbons: Ketene, HCCOH							
HCCOH+H	=	CH2CO+H	1.00E13	0.00	0.	!MBA091	
CH2CO+H	=	CH3+CO	1.13E13	0.00	3428.	!MBA094	
CH2CO+H	=	HCCO+H2	5.00E13	0.00	8000.	!MBA095	
CH2CO+O	=	CO2+CH2	1.75E12	0.00	1350.	!MBA093	
CH2CO+O	=	HCCO+OH	1.00E13	0.00	8000.	!MBA096	
CH2CO+OH	=	HCCO+H2O	7.50E12	0.00	2000.	!MBA097	
CH2CO(+M)	=	CH2+CO(+M)	3.00E14	0.00	70980.	!MBA098	
LOW/3.60E15 0.0 59270./							
Oxidized C_2 Hydrocarbons: Ketyl							
HCCO+H	=	CH2SING+CO	1.00E14	0.00	0.	!MBA101	
HCCO+O	=	H+2CO	1.00E14	0.00	0.	!MBA102	
HCCO+O2	=	2CO+OH	1.60E12	0.00	854.	!MBA103	
2HCCO	=	C2H2+2CO	1.00E13	0.00	0.	!MBA105	
HCCO+CH2	=	C2H3+CO	3.00E13	0.00	0.	!MBA115	

REACTION					A	b	E	note/reference		H
H/F/O Chemistry										
HF	+ M	= H	+ F		3.12E13	0.00	99320.	!	81BAU/DUX	+134
H2	+ F	= H	+ HF		2.56E12	0.50	650.	!fit	89STE/BRU	-31
OH	+ F	= O	+ HF		2.00E13	0.00	0.	!ref	H+HNO3	-33
HO2	+ F	= O2	+ HF		2.89E12	0.50	0.	!fit	83WAL/WAG	-86
H2O	+ F	= OH	+ HF		1.30E09	1.50	0.	!fit	83WAL/WAG	-16
H2O2	+ F	= HO2	+ HF		1.73E12	0.50	0.	!fit	83WAL/WAG	-48
Fluoromethanes: Thermal Decomposition										
CH2SING	+ HF	= CH3F			1.91E23	-3.62	1780.	!fit	73SCH/WAG	-88
CHF	+ H2	= CH3F			2.25E17	-2.85	13000.	!RRKM	BAC	
CH2F	+ H	= CH3F			3.03E21	-3.38	3460.	!RRKM	BAC	-97
CHF	+ HF	= CH2F2			3.64E24	-4.26	4060.	!RRKM	BAC	-71
CF2	+ H2	= CH2F2			1.70E06	-0.71	40900.	!RRKM	BAC	
CHF2	+ H	= CH2F2			2.75E06	-0.32	7690.	!RRKM	BAC	-102
CHF3	+ M	= CF2	+ HF		2.39E30	-4.00	69050.	!fit	91HID/NAK	+61
CF3	+ F	= CF4			3.60E15	-1.00	0.	!fit	86PLU/RYA	-130
Fluoromethanes: Activated Decomposition										
CH2F	+ H	= CH2SING	+ HF		8.19E15	-0.63	505.	!RRKM	BAC	-8
CH2F	+ H	= CHF	+ H2		5.21E08	1.16	1000.	!RRKM	BAC	
CH2SING	+ HF	= CHF	+ H2		2.08E07	1.27	8330.	!RRKM	BAC	-14
CHF2	+ H	= CHF	+ HF		1.49E14	-0.11	101.	!RRKM	BAC	
CHF2	+ H	= CF2	+ H2		5.50E03	2.42	-420.	!RRKM	BAC	
CHF	+ HF	= CF2	+ H2		5.77E06	1.35	17900.	!RRKM	BAC	
CF3	+ H	= CF2	+ HF		5.50E13	0.00	0.	!RRKM	89TSA/MCF	-46

REACTION				A	b	E	note/reference	H
Fluoromethanes: H Atom Abstraction by H, O, F, OH, HO2								
CH3F	+ H	= CH2F	+ H2	2.70E03	3.00	5300.	!fit 75WES/DEH	-6
CH2F2	+ H	= CHF2	+ H2	1.65E03	3.00	5600.	!fit 72RIN/DAV	-6
CHF3	+ H	= CF3	+ H2	1.70E04	3.00	8500.	!fit 78ART/BEL	
CH3F	+ O	= CH2F	+ OH	6.50E07	1.50	7000.	!fit 67PAR/AZA	
CH2F2	+ O	= CHF2	+ OH	2.25E07	1.50	6100.	!fit 68PAR/NAL	
CHF3	+ O	= CF3	+ OH	1.00E08	1.50	9250.	!fit 78JOU/LEB	
CH4	+ F	= CH3	+ HF	5.90E12	0.50	450.	!fit 71WAG/WAR	-31
CH3F	+ F	= CH2F	+ HF	1.35E14	0.00	1200.	!fit	-37
CH2F2	+ F	= CHF2	+ HF	9.00E13	0.00	1850.	!fit	-35
CHF3	+ F	= CF3	+ HF	4.50E13	0.00	3700.	!fit	-27
CH3F	+ OH	= CH2F	+ H2O	2.60E08	1.50	2940.	! 91COH/WES	-20
CH2F2	+ OH	= CHF2	+ H2O	2.80E07	1.70	2540.	! 91COH/WES	-10
CHF3	+ OH	= CF3	+ H2O	5.77E06	1.80	4292.	! 87COH/BEN	-10
CH2F	+ H2O2	= CH3F	+ HO2	1.20E10	0.00	-600.	!ref	-11
CHF2	+ H2O2	= CH2F2	+ HO2	1.20E10	0.00	-600.	!ref	-12
CF3	+ H2O2	= CHF3	+ HO2	1.20E10	0.00	-600.	!ref	-21
Fluoromethanes: H Atom Abstraction by CH3, C2H3, C2H5								
CH3F	+ CH3	= CH2F	+ CH4	1.50E11	0.00	11400.	!65PRI/BRY	- 6
CH2F2	+ CH3	= CHF2	+ CH4	8.70E10	0.00	10200.	!65PRI/BRY chk	- 2
CF3	+ CH4	= CHF3	+ CH3	8.34E11	0.00	10920.	!78ART/BEL	- 4
CH3F	+ C2H3	= CH2F	+ C2H4	1.50E11	0.00	10300.	!ref E*0.90	- 8
CH2F2	+ C2H3	= CHF2	+ C2H4	9.00E10	0.00	9200.	!ref E*0.90	- 6
CF3	+ C2H4	= CHF3	+ C2H3	8.00E11	0.00	12000.	!ref E*1.1	- 2
CH3F	+ C2H5	= CH2F	+ C2H6	1.50E11	0.00	16300.	!ref E*1.43	0
CH2F2	+ C2H5	= CHF2	+ C2H6	9.00E10	0.00	14600.	!ref E*1.43	+ 2
CF3	+ C2H6	= CHF3	+ C2H5	7.59E11	0.00	7980.	!78ART/BEL	-10
Fluoromethanes: H Atom Abstraction by Fluoromethyls								
CH3F	+ CF3	= CH2F	+ CHF3	1.35E12	0.00	11200.	!67GIL/QUI	-10
CH2F2	+ CH2F	= CHF2	+ CH3F	9.00E10	0.00	14000.	!ref CH3 E*1.4	+ 1
CH2F2	+ CF3	= CHF2	+ CHF3	7.20E11	0.00	11200.	!67GIL/QUI	- 8
Fluoromethanes: F Atom Abstraction								
CH3F	+ H	= CH3	+ HF	2.75E14	0.00	31400.	!BAC	-28
CH2F2	+ H	= CH2F	+ HF	5.50E13	0.00	34100.	!BAC	-16
CHF3	+ H	= CHF2	+ HF	8.00E13	0.00	40300.	!BAC	-4
CF4	+ H	= CF3	+ HF	1.10E15	0.00	44600.	! 71KOC/MOI	-4

Fluoromethyls: H Atom Abstraction from CH2O, CH3OH, HCO									
CH2O	+ CH2F = HCO	+ CH3F	5.54E03	2.81	8300.	!ref	E*1.4	- 9	
CH2O	+ CHF2 = HCO	+ CH2F2	5.54E03	2.81	7800.	!ref	E*1.3	-10	
CH2O	+ CF3 = HCO	+ CHF3	5.54E03	2.81	4600.	!ref	E*.79	-19	
CH3OH	+ CH2F = CH3O	+ CH3F	1.44E01	3.10	9800.	!ref	E*1.4	+ 5	
CH3OH	+ CHF2 = CH3O	+ CH2F2	1.44E01	3.10	9000.	!ref	E*1.3	+ 4	
CH3OH	+ CF3 = CH3O	+ CHF3	1.44E01	3.10	5500.	!ref	E*.79	- 4	
CH3OH	+ CH2F = CH2OH	+ CH3F	3.20E01	3.20	10000.	!ref	E*1.4	- 3	
CH3OH	+ CHF2 = CH2OH	+ CH2F2	3.20E01	3.20	9300.	!ref	E*1.3	- 5	
CH3OH	+ CF3 = CH2OH	+ CHF3	3.20E01	3.20	5700.	!ref	E*.79	-13	
HCO	+ CH2F = CO	+ CH3F	0.90E14	0.00	0.	!ref			
HCO	+ CHF2 = CO	+ CH2F2	0.90E14	0.00	0.	!ref			
HCO	+ CF3 = CO	+ CHF3	0.90E14	0.00	0.	!ref		-91	
HCO	+ CH2F = CH2CO	+ HF	2.70E13	0.00	0.	!est			
HCO	+ CHF2 = CHFCO	+ HF	2.70E13	0.00	0.	!est			
HCO	+ CF3 = CF2CO	+ HF	2.70E13	0.00	0.	!est			
REACTION			A	b	E	note/reference			H
Fluoromethyls: Oxidation									
CH2F	+ O2 =>CHF:O	+ O +H	2.26E09	1.14	19500.	!ref	cf3 +dH		
CHF2	+ O2 =>CF2:O	+ O +H	2.26E09	1.14	20500.	!ref	cf3 +dH		
CF3	+ O2 = CF3O	+ O	2.26E09	1.14	21500.	!RRKM			
CF3O	+ M = CF2:O	+ F	9.03E26	-3.42	21700.	!RRKM			
CH2F	+ O = CHF:O	+ H	5.70E13	0.00	0.	!ref	ch3 cf3	-90	
CHF2	+ O = CF2:O	+ H	3.70E13	0.00	0.	!ref	ch3 cf3	-103	
CF3	+ O = CF2:O	+ F	1.90E13	0.00	0.	!	89TSA/BEL	-80	
CH2F	+ OH = CH2O	+ HF	2.50E13	0.00	0.	!ref	ch3	-95	
CHF2	+ OH = CHF:O	+ HF	2.50E13	0.00	0.	!ref	ch3	-105	
CF3	+ OH = CF2:O	+ HF	2.00E13	0.00	0.	!ref	ch3	-114	
CH2F	+ HO2 = CH3F	+ O2	3.00E12	0.00	0.	!ref	ch3	-48	
CHF2	+ HO2 = CH2F2	+ O2	3.00E12	0.00	0.	!ref	ch3	-50	
CF3	+ HO2 = CHF3	+ O2	2.00E12	0.00	0.	!ref	ch3		
CH2F	+ HO2 =>CHF:O	+ OH+ H	1.50E13	0.00	0.	!ref			
CHF2	+ HO2 =>CF2:O	+ OH+ H	1.50E13	0.00	0.	!ref			
CF3	+ HO2 = CF3O	+ OH	1.00E13	0.00	0.	!ref			
CF3O	+ M = CF2:O	+ F	9.03E26	-3.42	21700.	!wt k19			
CF3O	+ H = CF2:O	+ HF	1.00E14	0.00	0.	!nistk19			
CH3	+ F = CH2SING	+ HF	1.62E16	-0.88	-981.	!ref		-17	
CH2F	+ F = CHF	+ HF	5.00E13	0.00	0.	!ref		-46	
CHF2	+ F = CF2	+ HF	3.00E13	0.00	0.	!ref		-68	
CH3	+ F = CH2F	+ H	1.36E12	-0.39	-265.	!ref		- 9	
REACTION			A	b	E	note/reference			H

Fluoromethylenes: Oxidation								
CHF	+ O2	= CHF:O	+ O	2.00E13	0.00	16500.	!ref	cf2 E-10 -60
CF2	+ O2	= CF2:O	+ O	2.00E13	0.00	26500.	!	77KEA/MAT -50
CHF	+ O	= CO	+ HF	9.00E13	0.00	0.	!	90TSA/MCF-181
CF2	+ O	= CF:O	+ F	5.00E13	0.00	0.	!ref	chf -169
CHF	+ OH	= HCO	+ HF	5.00E12	0.00	0.	!ref	cf2 -94
CF2	+ OH	= CF:O	+ HF	5.00E12	0.00	0.	!ref	cf2 -71
CHF	+ OH	= CHF:O	+ H	5.00E12	0.00	0.	!ref	cf2 -77
CF2	+ OH	= CF2:O	+ H	5.00E12	0.00	0.	!fit	78BIO/LAZ -68
Fluoromethylenes: Destruction								
CHF	+ H2O	= CH2F	+ OH	5.00E12	0.00	29000.	!est	Hrxn +29
CF2	+ H2O	= CHF2	+ OH	5.00E12	0.00	51000.	!est	Hrxn +51
CHF	+ H	= CH	+ HF	2.00E14	0.00	0.	!	89TSA/MCF
CF2	+ H	= CF	+ HF	2.00E14	0.00	0.	!	89TSA/MCF
CF4	+CH2SING	= CHF:CF2	+ HF	4.00E13	0.00	5000.	!ref	ch4
CH4	+ CHF	= C2H4	+ HF	4.00E13	0.00	29000.	!BAC	
CH4	+ CF2	= CH2:CHF	+ HF	4.00E13	0.00	80000.	!BAC	
CHF	+ H2O	= CH2F	+ OH	5.00E12	0.00	29000.	!est dH	+29
CF2	+ H2O	= CHF2	+ OH	5.00E12	0.00	51000.	!est dh	+51
CH2O	+ CHF	= HCO	+ CH2F	1.00E13	0.00	29000.	!ref CH4	
CH2O	+ CHF	= CH2CO	+ HF	1.00E13	0.00	29000.	!ref CH4	
CH2O	+ CF2	= HCO	+ CHF2	1.00E13	0.00	80000.	!ref CH4	+22
CH2O	+ CF2	= CHFCO	+ HF	1.00E13	0.00	80000.	!ref CH4	
HCO	+ CHF	= CO	+ CH2F	2.00E13	0.00	29000.	!ref CH4	
HCO	+ CF2	= CO	+ CHF2	2.00E13	0.00	80000.	!ref CH4	
Fluoromethylenes: Insertion into Fluoromethanes								
CH3F	+CH2SING	= C2H4	+ HF	4.00E13	0.00	0.	!ref	
CH2F2	+CH2SING	= CH2:CHF	+ HF	4.00E13	0.00	0.	!ref	
CHF3	+CH2SING	= CH2:CF2	+ HF	4.00E13	0.00	0.	!ref	
CF4	+CH2SING	= CHF:CF2	+ HF	4.00E13	0.00	5000.	!ref	
CH4	+ CHF	= C2H4	+ HF	4.00E13	0.00	29000.	!BAC	
CH3F	+ CHF	= CH2:CHF	+ HF	4.00E13	0.00	29000.	!ref CH4	
CH2F2	+ CHF	= CH2:CF2	+ HF	2.00E13	0.00	29000.	!ref CH4	
CH2F2	+ CHF	= CHF:CHF-Z	+HF	1.00E13	0.00	29000.	!ref CH4	
CH2F2	+ CHF	= CHF:CHF-E	+HF	1.00E13	0.00	29000.	!ref CH4	
CHF3	+ CHF	= CHF:CF2	+ HF	4.00E13	0.00	29000.	!ref CH4	
CF4	+ CHF	= CF2:CF2	+ HF	4.00E13	0.00	29000.	!ref CH4	
CH4	+ CF2	= CH2:CHF	+ HF	4.00E13	0.00	80000.	!BAC	
CH3F	+ CF2	= CH2:CF2	+ HF	2.00E13	0.00	80000.	!ref CH4	
CH3F	+ CF2	= CHF:CHF-Z	+HF	1.00E13	0.00	80000.	!ref CH4	
CH3F	+ CF2	= CHF:CHF-E	+HF	1.00E13	0.00	80000.	!ref CH4	
CH2F2	+ CF2	= CHF:CF2	+ HF	4.00E13	0.00	80000.	!ref CH4	
CHF3	+ CF2	= CF2:CF2	+ HF	4.00E13	0.00	80000.	!ref CH4	
CF4	+ CF2	= CF3-CF3		4.00E13	0.00	80000.	!ref CH4	

Fluoromethylenes: Insertion into Fluoromethyls								
CH2F	+ CH2	= CH2:CHF	+ H	4.00E13	0.00	0.	!ref CH3	
CH2F	+ CH2	= C2H4	+ F	4.00E13	0.00	0.	!ref CH3	
CHF2	+ CH2	= CH2:CF2	+ H	4.00E13	0.00	0.	!ref CH3	
CHF2	+ CH2	= CH2:CHF	+ F	4.00E13	0.00	0.	!ref CH3	
CF3	+ CH2	= CH2:CF2	+ F	4.00E13	0.00	0.	!ref CH3	
CH2F	+ CH2SING	= CH2:CHF	+ H	4.00E12	0.00	0.	!ref CH3	
CH2F	+ CH2SING	= C2H4	+ F	2.00E12	0.00	0.	!ref CH3	
CHF2	+ CH2SING	= CH2:CF2	+ H	2.00E12	0.00	0.	!ref CH3	
CHF2	+ CH2SING	= CH2:CHF	+ F	4.00E12	0.00	0.	!ref CH3	
CF3	+ CH2SING	= CH2:CF2	+ F	6.00E12	0.00	0.	!ref CH3	
CH3	+ CHF	= CH2:CHF	+ H	1.00E12	0.00	2000.	!est	-46
CH2F	+ CHF	= CHF:CHF-Z	+ H	1.00E12	0.00	2000.	!est	-46
CH2F	+ CHF	= CHF:CHF-E	+ H	1.00E12	0.00	2000.	!est	-46
CH2F	+ CHF	= CH2:CHF	+ F	1.00E12	0.00	2000.	!est	-37
CHF2	+ CHF	= CHF:CF2	+ H	1.00E12	0.00	2000.	!est	-42
CHF2	+ CHF	= CHF:CHF-Z	+ F	1.00E12	0.00	2000.	!est	-27
CHF2	+ CHF	= CHF:CHF-E	+ F	1.00E12	0.00	2000.	!est	-27
CF3	+ CHF	= CHF:CF2	+ F	1.00E12	0.00	5000.	!est	-20
CH3	+ CF2	= CH2:CF2	+ H	1.10E11	0.00	5200.	!ref	-21
CH2F	+ CF2	= CHF:CF2	+ H	1.10E11	0.00	5200.	!ref	-20
CH2F	+ CF2	= CH2:CF2	+ F	1.10E11	0.00	5200.	!ref	-12
CHF2	+ CF2	= CF2:CF2	+ H	1.10E11	0.00	5200.	!ref	- 6
CHF2	+ CF2	= CHF:CF2	+ F	1.10E11	0.00	5200.	!ref	- 1
Fluoromethylidyne: Oxidation								
CF	+ O2	= CF:O	+ O	3.00E13	0.00	0.	!ref ch	
CF	+ H2O	=>CHF:O	+ H	3.00E13	0.00	0.	!ref ch	
CF	+ O	=>CO + F		7.00E12	0.00	0.	!fit	
CF	+ OH	=>CO	+ HF	3.00E13	0.00	0.	!est	
CF	+ HO2	=>CF:O	+ OH	1.00E13	0.00	0.	!est	
Fluoromethylidyne: Destruction								
CH	+ HF	= CF	+ H2	3.00E13	0.00	0.	!ref ch	-17
CF	+ CH3	=>CH2:CF	+ H	3.00E13	0.00	0.	!est	
CF	+ C2H5	=>CH2:CF	+ CH3	3.00E13	0.00	0.	!est	
CF	+ C2H3	=>C2HF	+ CH2	3.00E13	0.00	0.	!est	
CF	+ CH2	=>C2HF	+ H	3.00E13	0.00	0.	!est	
CF	+ CH2SING	=>C2HF	+ H	3.00E12	0.00	0.	!est	
CF	+ CH4	=>CH2:CHF	+ H	1.00E13	0.00	0.	!est	
CF	+ C2H4	=>C2H2	+ CH2F	1.00E13	0.00	0.	!est	
CF	+ CH2O	=>CHF	+ HCO	1.00E13	0.00	8000.	!est	+ 7
CF	+ HCO	=>CHF	+ CO	1.00E13	0.00	0.	!est	
CF	+ F	= CF2		6.00E13	0.00	0.	!fit	

Carbonyl Fluorides: CHF=O, CF2=O							
CHF:O + M	= CO + HF	2.48E25	-3.00	43000.	!fit	85SAI/KUR	
CF2:O + H2O	=>CO2 +2HF	3.92E00	3.08	27600.	!BAC		
CF2:O + H	= CF:O + HF	2.91E13	-0.03	32910.	!QRRK	BAC Oadd	
CF2:O + H	= CF:O + HF	1.02E02	2.89	32980.	!QRRK	BAC Cadd	
CHF:O + H	= HCO + HF	2.91E13	-0.03	32910.	!ref	cf2o Oadd	
CHF:O + H	= HCO + HF	1.02E02	2.89	32980.	!ref	cf2o Cadd	
CHF:O + H	= CF:O + H2	1.10E08	1.77	3000.	!ref/2		- 4
CHF:O + O	= CF:O + OH	9.00E12	0.00	3080.	!ref	ch2o	-2
CHF:O + OH	= CF:O + H2O	1.72E09	1.18	-447.	!ref	ch2o	-18
CF:O + H2O2	= CHF:O + HO2	1.00E11	0.00	3900.	!ref	E*0.56	-13
CHF:O + CH3	= CF:O + CH4	2.00E12	0.00	9000.	!ref	uplim	- 5
CHF:O + CH2F	= CF:O + CH3F	2.00E12	0.00	9000.	!ref	uplim	+ 1
CHF:O + CHF2	= CF:O + CH2F2	2.00E12	0.00	9000.	!ref		0
CHF:O + CF3	= CF:O + CHF3	2.00E12	0.00	9000.	!ref		- 8
CHF:O + C2H3	= CF:O + C2H4	2.00E12	0.00	5000.	!ref	E*0.9	
CHF:O + C2H5	= CF:O + C2H6	2.00E12	0.00	13000.	!ref	E*1.43	
Carbonyl Fluorides: CF=O							
CF:O + M	= CO + F	1.89E18	-0.865	39000.	!RRKM		+32
CF:O + H	= CO + HF	1.20E14	0.00	0.	!ref	hco	
CF:O + O	= CO2 + F	3.00E13	0.00	0.	!ref	hco	
CF:O + OH	= CO2 + HF	3.00E13	0.00	0.	!ref	hco	
CF:O + HO2	=>CO2 + F+OH	3.00E13	0.00	0.	!ref		
CF:O + CH3	= CO + CH3F	1.00E13	0.00	0.	!est		
CF:O + CH3	= CH2CO + HF	2.70E13	0.00	0.	!est		
CF:O + F	= CF2:O	1.00E12	0.00	0.	!wtsang1		-131
CF:O + O2	=>CO2 + F + O	2.00E13	0.00	24000.	!nist k20		+24
CF:O + CH2F	= CO + CH2F2	1.00E13	0.00	0.	!est, k19		
CF:O + CHF2	= CO + CHF3	1.00E13	0.00	0.	!est, k19		
CF:O + CF3	= CO + CF4	1.00E13	0.00	0.	!est, k19		
CF:O + CH2F	= CHFCO + HF	2.70E13	0.00	0.	!est, k19		
CF:O + CHF2	= CF2CO + HF	2.70E13	0.00	0.	!est, k19		
CF:O + CF:O	= CO + CF2:O	2.23E13	0.00	318.	!92MAR/SZE2		
Fluoroethanes: Thermal Decomposition							
CH3-CH2F	= C2H4 + HF	2.00E13	0.00	58800.	!	70CAD/DAY	+11
CH3-CHF2	= CH2:CHF + HF	7.94E13	0.00	61900.	!	70TSC/QUI	+22
CH3-CF3	= CH2:CF2 + HF	1.00E14	0.00	69000.	!	71TSC/QUI	
CH2F-CH2F	= CH2:CHF + HF	2.50E13	0.00	61800.	!	71KER/TIM	+ 5
CH2F-CHF2	= CHF:CHF-Z+ HF	1.20E14	0.00	69600.	!	74SEK/TSC	
CH2F-CHF2	= CHF:CHF-E+ HF	3.00E13	0.00	65800.	!	74SEK/TSC	
CH2F-CHF2	= CH2:CF2 + HF	1.00E13	0.00	65800.	!	74SEK/TSC	+ 8
CH2F-CF3	= CHF:CF2 + HF	2.50E13	0.00	63200.	!	72MIL/TSC	+37
CHF2-CHF2	= CHF:CF2 + HF	2.00E13	0.00	70000.	!	71MIL/HAR	+32
CHF2-CF3	= CF2:CF2 + HF	4.00E13	0.00	72000.	!	71TSC/MIL	+41

Fluoroethanes: Activated Decomposition, Ethyl + H (HF elimination)					
CH2F-CH2 + H	= C2H4 + HF	1.44E20	-2.12	1730.	!RRKM
CH3-CHF + H	= C2H4 + HF	2.27E20	-2.21	1950.	!RRKM
CH2F-CHF + H	= CH2:CHF + HF	2.06E23	-3.23	2280.	!RRKM
CHF2-CH2 + H	= CH2:CHF + HF	5.24E16	-0.933	880.	!RRKM
CH3-CF2 + H	= CH2:CHF + HF	2.09E16	-0.854	848.	!RRKM
CHF2-CHF + H	= CHF:CHF-Z+ HF	1.86E20	-2.29	1750.	!RRKM
CHF2-CHF + H	= CHF:CHF-E+ HF	1.07E19	-1.84	1520.	!RRKM
CHF2-CHF + H	= CH2:CF2 + HF	9.95E19	-2.34	1780.	!RRKM
CH2F-CF2 + H	= CHF:CHF-Z+ HF	6.32E19	-2.21	1630.	!RRKM
CH2F-CF2 + H	= CHF:CHF-E+ HF	3.95E18	-1.77	1390.	!RRKM
CH2F-CF2 + H	= CH2:CF2 + HF	3.36E19	-2.26	1660.	!RRKM
CF3-CH2 + H	= CH2:CF2 + HF	1.12E21	-2.27	2240.	!RRKM
CHF2-CF2 + H	= CHF:CF2 + HF	1.81E22	-2.92	3070.	!RRKM
CF3-CF2 + H	= CF2:CF2 + HF	1.41E21	-2.40	3630.	!RRKM
Fluoroethanes: Activated Decomposition, Ethyl + H (methyl formation)					
CH2F-CH2 + H	= CH3 + CH2F	3.80E11	0.635	633.	!RRKM
CH3-CHF + H	= CH3 + CH2F	3.47E10	0.90	1370.	!RRKM
CH2F-CHF + H	= CH2F + CH2F	1.79E14	-0.105	1320.	!RRKM
CHF2-CH2 + H	= CH3 + CHF2	2.02E06	2.16	451.	!RRKM
CH3-CF2 + H	= CH3 + CHF2	1.62E05	2.50	1370.	!RRKM
CHF2-CHF + H	= CH2F + CHF2	6.36E12	0.318	1460.	!RRKM
CH2F-CF2 + H	= CH2F + CHF2	3.64E12	0.329	1180.	!RRKM
CF3-CH2 + H	= CH3 + CF3	2.48E11	0.816	2870.	!RRKM
CHF2-CF2 + H	= CHF2 + CHF2	3.25E15	-0.524	3000.	!RRKM
CF3-CF2 + H	= CHF2 + CF3	4.37E16	-0.746	4360.	!RRKM
Fluoroethanes: Activated Decomposition, Ethyl + H (stabilization)					
CH2F-CH2 + H	= CH3-CH2F	1.19E35	-8.51	8140.	!RRKM
CH3-CHF + H	= CH3-CH2F	9.57E38	-9.24	7360.	!RRKM
CH2F-CHF + H	= CH2F-CH2F	1.56E45	-10.80	8070.	!RRKM
CHF2-CH2 + H	= CH3-CHF2	2.96E37	-9.05	7160.	!RRKM
CH3-CF2 + H	= CH3-CHF2	3.11E40	-9.59	7190.	!RRKM
CHF2-CHF + H	= CH2F-CHF2	1.20E44	-10.60	7520.	!RRKM
CH2F-CF2 + H	= CH2F-CHF2	2.74E43	-10.50	7670.	!RRKM
CF3-CH2 + H	= CH3-CF3	7.27E42	-9.86	7360.	!RRKM
CHF2-CF2 + H	= CHF2-CHF2	3.77E46	-10.80	8980.	!RRKM
CF3-CF2 + H	= CHF2-CF3	1.12E47	-10.80	4100.	!RRKM
Fluoroethanes: Activated Decomposition, Ethyl + H (H atom elimination)					
CH2F-CH2 + H	= CH3-CHF + H	1.87E01	3.10	137.	!RRKM
CHF2-CH2 + H	= CHF2-CH2 + H	1.59E-3	4.35	157.	!RRKM
CH2F-CF2 + H	= CHF2-CHF + H	0.64E00	3.53	1830.	!RRKM
Fluoroethanes: Activated Decomposition, Methyl + Methyl (HF elimination)					
CH3 + CH2F	= C2H4 + HF	2.35E19	-1.86	1870.	!RRKM
CH2F + CH2F	= CH2:CHF + HF	7.56E21	-2.79	2590.	!RRKM
CH3 + CHF2	= CH2:CHF + HF	1.90E15	-0.586	634.	!RRKM
CH2F + CHF2	= CHF:CHF-Z+ HF	3.88E20	-2.35	2888.	!RRKM
CH2F + CHF2	= CHF:CHF-E+ HF	1.09E19	-1.83	2670.	!RRKM
CH2F + CHF2	= CH2:CF2 + HF	2.23E20	-2.41	2910.	!RRKM
CH3 + CF3	= CH2:CF2 + HF	5.53E19	-1.94	2440.	!RRKM
CHF2 + CHF2	= CHF:CF2 + HF	2.20E19	-1.95	4100.	!RRKM
CHF2 + CF3	= CF2:CF2 + HF	7.00E16	-1.17	4330.	!RRKM

Fluoroethanes: Activated Decomposition, Methyl + Methyl (stablization)							
CH3	+ CH2F = CH3-CH2F		1.57E31	-6.27	4440.	!RRKM	
CH2F	+ CH2F = CH2F-CH2F		2.37E24	-3.79	2290.	!RRKM	
CH3	+ CHF2 = CH3-CHF2		1.93E35	-7.69	5760.	!RRKM	
CH2F	+ CHF2 = CH2F-CHF2		9.61E38	-8.36	6940.	!RRKM	
CH3	+ CF3 = CH3-CF3		1.78E33	-6.64	5020.	!RRKM	
CHF2	+ CHF2 = CHF2-CHF2		2.26E24	-3.50	3360.	!RRKM	
CHF2	+ CF3 = CHF2-CF3		2.61E26	-4.16	4100.	!RRKM	
CF3	+ CF3 = CF3-CF3		1.63E36	-7.26	7050.	!RRKM	
Fluoroethanes: H Atom Abstraction by H, O, OH							
CH3-CH2F	+ H = CH2F-CH2 + H2		5.50E08	1.60	9100.	!ref 10AE+8	+2
CH3-CH2F	+ O = CH2F-CH2 + OH		2.90E08	1.60	6100.	!ref 5AE+5	+3
CH3-CH2F	+ OH = CH2F-CH2 + H2O		5.50E07	1.60	1093.	!ref	-13
CH3-CH2F	+ H = CH3-CHF + H2		3.30E08	1.60	9100.	!ref 10AE+8	
CH3-CH2F	+ O = CH3-CHF + OH		1.60E08	1.60	6100.	!ref 5AE+5	
CH3-CH2F	+ OH = CH3-CHF + H2O		3.30E07	1.60	1093.	!ref	
CH3-CHF2	+ H = CHF2-CH2 + H2		1.50E08	1.60	9600.	!ref 10A E+8	
CH3-CHF2	+ O = CHF2-CH2 + OH		7.50E08	1.60	6600.	!ref A*5 E+5	
CH3-CHF2	+ OH = CHF2-CH2 + H2O		1.54E07	1.60	1132.	!ref	
CH3-CHF2	+ H = CH3-CF2 + H2		0.44E08	1.60	9300.	!ref A*10 E+8	
CH3-CHF2	+ O = CH3-CF2 + OH		2.20E07	1.60	6300.	!ref A*5 E+5	
CH3-CHF2	+ OH = CH3-CF2 + H2O		0.44E07	1.60	1332.	!ref	
CH3-CF3	+ H = CF3-CH2 + H2		4.00E10	1.10	12700.	!ref A*10E+8	+ 3
CH3-CF3	+ O = CF3-CH2 + OH		2.00E10	1.10	9700.	!ref A*5E+5	+ 4
CH3-CF3	+ OH = CF3-CH2 + H2O		4.08E09	1.10	4670.	!87COH/BEN	-12
CH2F-CH2F	+ H = CH2F-CHF + H2		6.00E08	1.70	9600.	!ref A*10 E+8	-11
CH2F-CH2F	+ O = CH2F-CHF + OH		3.00E08	1.70	6600.	!ref A*5 E+5	-10
CH2F-CH2F	+ OH = CH2F-CHF + H2O		6.16E07	1.70	1610.	!87COH/BEN	-26
CH2F-CHF2	+ H = CHF2-CHF + H2		2.00E08	1.70	9800.	!ref A*10 E+8	
CH2F-CHF2	+ O = CHF2-CHF + OH		1.00E08	1.70	6800.	!ref A*5 E+5	
CH2F-CHF2	+ OH = CHF2-CHF + H2O		2.05E07	1.70	1800.	!ref	
CH2F-CHF2	+ H = CH2F-CF2 + H2		1.00E08	1.70	11000.	!ref A*10 E+8	
CH2F-CHF2	+ O = CH2F-CF2 + OH		5.00E07	1.70	8000.	!ref A*5 E+5	
CH2F-CHF2	+ OH = CH2F-CF2 + H2O		1.06E07	1.70	3000.	!ref	
CH2F-CF3	+ H = CF3-CHF + H2		2.00E08	1.70	10500.	!ref A*10 E+8	- 2
CH2F-CF3	+ O = CF3-CHF + OH		1.00E08	1.70	7500.	!ref A*5 E+5	- 1
CH2F-CF3	+ OH = CF3-CHF + H2O		2.10E07	1.70	2524.	!87COH/BEN	-17
CHF2-CHF2	+ H = CHF2-CF2 + H2		1.60E07	1.70	10600.	!ref A*10 E+8	
CHF2-CHF2	+ O = CHF2-CF2 + OH		8.00E07	1.70	7600.	!ref A*5 E+5	
CHF2-CHF2	+ OH = CHF2-CF2 + H2O		1.60E07	1.70	2643.	!87COH/BEN	
CHF2-CF3	+ H = CF3-CF2 + H2		1.40E07	1.60	10200.	!ref A*10 E+8	+ 0
CHF2-CF3	+ O = CF3-CF2 + OH		7.00E07	1.60	7200.	!ref A*5 E+5	+ 1
CHF2-CF3	+ OH = CF3-CF2 + H2O		1.40E07	1.60	2246.	!87COH/BEN	-15
!*** NOTE F ATOM ABSTRACTION ***							
CF3-CF3	+ H = CF3-CF2 + HF		1.00E15	0.00	30000.	!ref CF4	

Fluoroethanes: H Atom Abstraction by F						
C2H6 + F = C2H5 + HF	8.00E12	0.00	300.	!60FET/KNO2	-36	
CH3-CH2F + F = CH2F-CH2 + HF	9.00E13	0.00	800.	!ref		
CH3-CHF2 + F = CHF2-CH2 + HF	1.00E14	0.00	800.	!ref		
CH3-CF3 + F = CF3-CH2 + HF	1.00E14	0.00	4000.	!ref		
CH3-CH2F + F = CH3-CHF + HF	6.00E13	0.00	200.	!ref		
CH2F-CH2F + F = CH2F-CHF + HF	1.30E14	0.00	800.	!ref		
CH2F-CHF2 + F = CHF2-CHF + HF	1.30E14	0.00	800.	!ref		
CH2F-CF3 + F = CF3-CHF + HF	6.00E13	0.00	1200.	!ref		
CH3-CHF2 + F = CH3-CF2 + HF	3.00E13	0.00	800.	!ref		
CH2F-CHF2 + F = CH2F-CF2 + HF	3.00E13	0.00	1200.	!ref		
CHF2-CHF2 + F = CHF2-CF2 + HF	6.00E13	0.00	1200.	!ref		
CHF2-CF3 + F = CF3-CF2 + HF	4.00E13	0.00	1400.	!ref	-33	
Fluoroethanes: Association with HO2						
CH3-CHF + H2O2 = CH3-CH2F + HO2	9.00E09	0.00	1000.	!ref		
CH3-CF2 + H2O2 = CH3-CHF2 + HO2	9.00E09	0.00	1000.	!ref		
CH2F-CH2 + H2O2 = CH3-CH2F + HO2	9.00E09	0.00	1000.	!ref		
CH2F-CHF + H2O2 = CH2F-CH2F+ HO2	9.00E09	0.00	1000.	!ref		
CH2F-CF2 + H2O2 = CH2F-CHF2+ HO2	9.00E09	0.00	1000.	!ref		
CHF2-CH2 + H2O2 = CH3-CHF2 + HO2	9.00E09	0.00	1000.	!ref		
CHF2-CHF + H2O2 = CH2F-CHF2+ HO2	9.00E09	0.00	1000.	!ref		
CHF2-CF2 + H2O2 = CHF2-CHF2+ HO2	9.00E09	0.00	1000.	!ref		
CF3-CH2 + H2O2 = CH3-CF3 + HO2	9.00E09	0.00	1000.	!ref		
CF3-CHF + H2O2 = CH2F-CF3 + HO2	9.00E09	0.00	1000.	!ref		
CF3-CF2 + H2O2 = CHF2-CF3 + HO2	9.00E09	0.00	1000.	!ref		

Fluoroethanes: H Atom Abstraction by CH3, C2H5, C2H3							
CH3-CH2F + CH3 = CH2F-CH2 + CH4	2.00E11	0.00	13400.	!ref		+ 1
CH3-CH2F + C2H5 = CH2F-CH2 + C2H6	2.00E11	0.00	16000.	!ref CH3 +3		+ 6
CH3-CH2F + C2H3 = CH2F-CH2 + C2H4	2.00E11	0.00	10000.	!ref CH3 -3		+ 4
CH3-CH2F + CH3 = CH3-CHF + CH4	1.50E11	0.00	10000.	!ref		
CH3-CH2F + C2H5 = CH3-CHF + C2H6	1.50E11	0.00	13000.	!ref CH3 +3		
CH3-CH2F + C2H3 = CH3-CHF + C2H4	1.50E11	0.00	7000.	!ref CH3 -3		
CH3-CHF2 + CH3 = CHF2-CH2 + CH4	2.00E11	0.00	12000.	!ref		
CH3-CHF2 + C2H5 = CHF2-CH2 + C2H6	2.00E11	0.00	15000.	!ref CH3 +3		
CH3-CHF2 + C2H3 = CHF2-CH2 + C2H4	2.00E11	0.00	9000.	!ref CH3 -3		
CH3-CHF2 + CH3 = CH3-CF2 + CH4	8.00E10	0.00	10000.	!ref		
CH3-CHF2 + C2H3 = CH3-CF2 + C2H4	8.00E10	0.00	7000.	!ref CH3 -3		
CH3-CHF2 + C2H5 = CH3-CF2 + C2H6	8.00E10	0.00	13000.	!ref CH3 +3		
CH3-CF3 + CH3 = CF3-CH2 + CH4	2.00E11	0.00	12000.	!ref		+ 2
CH3-CF3 + C2H3 = CF3-CH2 + C2H4	2.00E11	0.00	9000.	!ref CH3 -3		+ 5
CH3-CF3 + C2H5 = CF3-CH2 + C2H6	2.00E11	0.00	15000.	!ref CH3 +3		+ 7
CH2F-CH2F + CH3 = CH2F-CHF + CH4	3.00E11	0.00	10400.	!ref		-12
CH2F-CH2F + C2H3 = CH2F-CHF + C2H4	3.00E11	0.00	7000.	!ref CH3 -3		- 9
CH2F-CH2F + C2H5 = CH2F-CHF + C2H6	3.00E11	0.00	13000.	!ref CH3 +3		- 7
CH2F-CHF2 + CH3 = CHF2-CHF + CH4	2.00E11	0.00	10000.	!ref		
CH2F-CHF2 + C2H3 = CHF2-CHF + C2H4	2.00E11	0.00	7000.	!ref CH3 -3		
CH2F-CHF2 + C2H5 = CHF2-CHF + C2H6	2.00E11	0.00	13000.	!ref CH3 +3		
CH2F-CHF2 + CH3 = CH2F-CF2 + CH4	1.00E11	0.00	9600.	!ref		
CH2F-CHF2 + C2H3 = CH2F-CF2 + C2H4	1.00E11	0.00	7000.	!ref CH3 -3		
CH2F-CHF2 + C2H5 = CH2F-CF2 + C2H6	1.00E11	0.00	13000.	!ref CH3 +3		
CH2F-CF3 + CH3 = CF3-CHF + CH4	2.00E11	0.00	10000.	!ref		- 3
CH2F-CF3 + C2H3 = CF3-CHF + C2H4	2.00E11	0.00	7000.	!ref CH3 -3		+ 0
CH2F-CF3 + C2H5 = CF3-CHF + C2H6	2.00E11	0.00	13000.	!ref CH3 +3		+ 2
CHF2-CHF2 + CH3 = CHF2-CF2 + CH4	3.00E11	0.00	10000.	!ref		
CHF2-CHF2 + C2H3 = CHF2-CF2 + C2H4	3.00E11	0.00	7000.	!ref CH3 -3		
CHF2-CHF2 + C2H5 = CHF2-CF2 + C2H6	3.00E11	0.00	13000.	!ref CH3 +3		
CHF2-CF3 + CH3 = CF3-CF2 + CH4	5.70E10	0.00	9500.	!64PRI/THO		- 1
CHF2-CF3 + C2H3 = CF3-CF2 + C2H4	6.00E10	0.00	7000.	!ref CH3 -3		+ 2
CHF2-CF3 + C2H5 = CF3-CF2 + C2H6	6.00E10	0.00	13000.	!ref CH3 +3		+ 4

Fluoroethanes: H Atom Abstraction by Fluoromethyls						
CH3-CH2F + CH2F = CH2F-CH2 + CH3F	2.00E11	0.00	13000.	!ref CH3		+ 6
CH3-CH2F + CH2F = CH3-CHF + CH3F	1.50E11	0.00	10000.	!ref CH3		
CH3-CHF2 + CH2F = CHF2-CH2 + CH3F	2.00E11	0.00	12000.	!ref CH3		
CH3-CHF2 + CH2F = CH3-CF2 + CH3F	8.00E10	0.00	10000.	!ref CH3		
CH3-CF3 + CH2F = CF3-CH2 + CH3F	2.00E11	0.00	12000.	!ref CH3		+ 7
CH2F-CH2F + CH2F = CH2F-CHF + CH3F	3.00E11	0.00	10000.	!ref CH3		- 7
CH2F-CHF2 + CH2F = CHF2-CHF + CH3F	2.00E11	0.00	10000.	!ref CH3		
CH2F-CHF2 + CH2F = CH2F-CF2 + CH3F	1.00E11	0.00	10000.	!ref CH3		
CH2F-CF3 + CH2F = CF3-CHF + CH3F	2.00E11	0.00	10000.	!ref CH3		+ 2
CHF2-CHF2 + CH2F = CHF2-CF2 + CH3F	3.00E11	0.00	11000.	!ref CH3		+10
CHF2-CF3 + CH2F = CF3-CF2 + CH3F	2.00E11	0.00	10000.	!ref CH3		+ 4
CH3-CH2F + CHF2 = CH2F-CH2 + CH2F2	2.00E11	0.00	13000.	!ref CH3		
CH3-CH2F + CHF2 = CH3-CHF + CH2F2	1.50E11	0.00	10000.	!ref CH3		
CH3-CHF2 + CHF2 = CHF2-CH2 + CH2F2	2.00E11	0.00	12000.	!ref CH3		
CH3-CHF2 + CHF2 = CH3-CF2 + CH2F2	8.00E10	0.00	10000.	!ref CH3		
CH3-CF3 + CHF2 = CF3-CH2 + CH2F2	2.00E11	0.00	12000.	!ref CH3		
CH2F-CH2F + CHF2 = CH2F-CHF + CH2F2	3.00E11	0.00	10000.	!ref CH3		
CH2F-CHF2 + CHF2 = CHF2-CHF + CH2F2	2.00E11	0.00	10000.	!ref CH3		
CH2F-CHF2 + CHF2 = CH2F-CF2 + CH2F2	1.00E11	0.00	10000.	!ref CH3		
CH2F-CF3 + CHF2 = CF3-CHF + CH2F2	2.00E11	0.00	10000.	!ref CH3		
CHF2-CHF2 + CHF2 = CHF2-CF2 + CH2F2	3.00E11	0.00	10000.	!ref CH3		
CHF2-CF3 + CHF2 = CF3-CF2 + CH2F2	2.00E11	0.00	10000.	!ref CH3		
CH3-CH2F + CF3 = CH2F-CH2 + CHF3	9.50E11	0.00	8200.	!71QUI/WHI		
CH3-CH2F + CF3 = CH3-CHF + CHF3	9.50E11	0.00	8200.	!71QUI/WHI		
CH3-CHF2 + CF3 = CHF2-CH2 + CHF3	3.10E10	0.00	7100.	!66OKS/PRA		
CH3-CHF2 + CF3 = CH3-CF2 + CHF3	3.10E10	0.00	7100.	!66OKS/PRA		
CH3-CF3 + CF3 = CF3-CH2 + CHF3	1.45E12	0.00	13500.	!67GIL/QUI		
CH2F-CH2F + CF3 = CH2F-CHF + CHF3	5.00E11	0.00	7600.	!ref		
CH2F-CHF2 + CF3 = CHF2-CHF + CHF3	3.00E11	0.00	7200.	!ref		
CH2F-CHF2 + CF3 = CH2F-CF2 + CHF3	2.00E11	0.00	8000.	!ref		
CH2F-CF3 + CF3 = CF3-CHF + CHF3	3.00E11	0.00	6400.	!ref		
CHF2-CHF2 + CF3 = CHF2-CF2 + CHF3	5.70E11	0.00	11900.	!67GIL/QUI		
CHF2-CF3 + CF3 = CF3-CF2 + CHF3	1.40E11	0.00	10100.	!67GIL/QUI		
Fluoroethanes: H Atom Abstraction by HCO						
CH3-CHF + CH2O = CH3-CH2F + HCO	5.50E03	2.80	5900.	!ref		
CH3-CF2 + CH2O = CH3-CHF2 + HCO	5.50E03	2.80	5900.	!ref		
CH2F-CH2 + CH2O = CH3-CH2F + HCO	5.50E03	2.80	5900.	!ref		
CH2F-CHF + CH2O = CH2F-CH2F+ HCO	5.50E03	2.80	5900.	!ref		
CH2F-CF2 + CH2O = CH2F-CHF2+ HCO	5.50E03	2.80	5900.	!ref		
CHF2-CH2 + CH2O = CH3-CHF2 + HCO	5.50E03	2.80	5900.	!ref		
CHF2-CHF + CH2O = CH2F-CHF2+ HCO	5.50E03	2.80	5900.	!ref		
CHF2-CF2 + CH2O = CHF2-CHF2+ HCO	5.50E03	2.80	5900.	!ref		
CF3-CH2 + CH2O = CH3-CF3 + HCO	5.50E03	2.80	5900.	!ref		
CF3-CHF + CH2O = CH2F-CF3 + HCO	5.50E03	2.80	5900.	!ref		
CF3-CF2 + CH2O = CHF2-CF3 + HCO	5.50E03	2.80	5900.	!ref		

Fluoroethyls: Association with O2						
CH3-CHF	+ O2	= CH2:CHF + HO2	2.56E19	-2.77	1977.	!ref
CH3-CF2	+ O2	= CH2:CF2 + HO2	2.56E19	-2.77	1977.	!ref
CH2F-CH2	+ O2	= CH2:CHF + HO2	2.56E19	-2.77	1977.	!ref
CH2F-CHF	+ O2	= CHF:CHF-E +HO2	1.28E19	-2.77	1977.	!ref
CH2F-CHF	+ O2	= CHF:CHF-Z +HO2	1.28E19	-2.77	1977.	!ref
CH2F-CF2	+ O2	= CHF:CF2 + HO2	2.56E19	-2.77	1977.	!ref
CHF2-CH2	+ O2	= CH2:CF2 + HO2	2.56E19	-2.77	1977.	!ref
CHF2-CHF	+ O2	= CHF:CF2 + HO2	2.56E19	-2.77	1977.	!ref
CHF2-CF2	+ O2	= CF2:CF2 + HO2	2.56E19	-2.77	1977.	!ref
CF3-CH2	+ O2	=>CF3 + CH2O + O	1.30E13	0.00	44000.	!ref CF3+dH
CF3-CHF	+ O2	=>CF3 + CHF:O+ O	1.30E13	0.00	23000.	!ref CF3
CF3-CF2	+ O2	=>CF3 + CF2:O+ O	1.30E13	0.00	23000.	!ref CF3
Fluoroethyls: Association with O						
CH2F-CH2	+ O	= CH2O + CH2F	6.60E13	0.00	0.	!ref
CHF2-CH2	+ O	= CH2O + CHF2	6.60E13	0.00	0.	!ref
CF3-CH2	+ O	= CH2O + CF3	6.60E13	0.00	0.	!ref
CH3-CHF	+ O	= CHF:O + CH3	4.40E13	0.00	0.	!ref
CH2F-CHF	+ O	= CHF:O + CH2F	4.40E13	0.00	0.	!ref
CHF2-CHF	+ O	= CHF:O + CHF2	4.40E13	0.00	0.	!ref
CF3-CHF	+ O	= CHF:O + CF3	4.40E13	0.00	0.	!ref
CH3-CF2	+ O	= CF2:O + CH3	2.20E13	0.00	0.	!ref
CH2F-CF2	+ O	= CF2:O + CH2F	2.20E13	0.00	0.	!ref
CHF2-CF2	+ O	= CF2:O + CHF2	2.20E13	0.00	0.	!ref
CF3-CF2	+ O	= CF2:O + CF3	2.20E13	0.00	0.	!ref

Fluoroethyls: Association with HO2						
CH3-CHF	+ HO2	=>CH3+CHF:O+OH	3.00E13	0.00	0.	!ref
CH3-CF2	+ HO2	=>CH3+CF2:O+OH	3.00E13	0.00	0.	!ref
CH2F-CH2	+ HO2	=>CH2F+CH2O+ OH	3.00E13	0.	0.	!ref
CH2F-CHF	+ HO2	=>CH2F+CHF:O+OH	3.00E13	0.	0.	!ref
CH2F-CF2	+ HO2	=>CH2F+CF2:O+OH	3.00E13	0.	0.	!ref
CHF2-CH2	+ HO2	=>CHF2+CH2O+ OH	3.00E13	0.	0.	!ref
CHF2-CHF	+ HO2	=>CHF2+CHF:O+OH	3.00E13	0.	0.	!ref
CHF2-CF2	+ HO2	=>CHF2+CF2:O+OH	3.00E13	0.	0.	!ref
CF3-CH2	+ HO2	=>CF3 +CH2O+ OH	3.00E13	0.	0.	!ref
CF3-CHF	+ HO2	=>CF3 +CHF:O+OH	3.00E13	0.	0.	!ref
CF3-CF2	+ HO2	=>CF3 +CF2:O+OH	3.00E13	0.	0.	!ref
CH3-CHF	+ HO2	= CH2:CHF + H2O2	3.00E11	0.	0.	!ref
CH3-CF2	+ HO2	= CH2:CF2 + H2O2	3.00E11	0.	0.	!ref
CH2F-CH2	+ HO2	= CH2:CHF + H2O2	2.00E11	0.	0.	!ref
CH2F-CHF	+ HO2	= CHF:CHF-Z+ H2O2	2.00E11	0.	0.	!ref
CH2F-CHF	+ HO2	= CHF:CHF-E+ H2O2	2.00E11	0.	0.	!ref
CH2F-CF2	+ HO2	= CHF:CF2 + H2O2	2.00E11	0.	0.	!ref
CHF2-CH2	+ HO2	= CH2:CF2 + H2O2	1.00E11	0.	0.	!ref
CHF2-CHF	+ HO2	= CHF:CF2 + H2O2	1.00E11	0.	0.	!ref
CHF2-CF2	+ HO2	= CF2:CF2 + H2O2	1.00E11	0.	0.	!ref
CH3-CHF	+ HO2	= CH3-CH2F + O2	3.00E11	0.	0.	!ref
CH3-CF2	+ HO2	= CH3-CHF2 + O2	3.00E11	0.	0.	!ref
CH2F-CH2	+ HO2	= CH3-CH2F + O2	3.00E11	0.	0.	!ref
CH2F-CHF	+ HO2	= CH2F-CH2F+ O2	3.00E11	0.	0.	!ref
CH2F-CF2	+ HO2	= CH2F-CHF2+ O2	3.00E11	0.	0.	!ref
CHF2-CH2	+ HO2	= CH3-CHF2 + O2	3.00E11	0.	0.	!ref
CHF2-CHF	+ HO2	= CH2F-CHF2+ O2	3.00E11	0.	0.	!ref
CHF2-CF2	+ HO2	= CHF2-CHF2+ O2	3.00E11	0.	0.	!ref
CF3-CH2	+ HO2	= CH3-CF3 + O2	3.00E11	0.	0.	!ref
CF3-CHF	+ HO2	= CH2F-CF3 + O2	3.00E11	0.	0.	!ref
CF3-CF2	+ HO2	= CHF2-CF3 + O2	3.00E11	0.	0.	!ref
Fluoroethylenes: Activated Decomposition, Methylene comb'n (HF elimination)						
CH2SING	+ CHF	= C2H2 + HF	17.02E19	-2.12	2380.	!ref
CH2SING	+ CF2	= C2HF + HF	17.02E19	-2.12	2380.	!ref
CHF	+ CHF	= C2HF + HF	17.02E19	-2.12	2380.	!ref
CHF	+ CF2	= C2F2 + HF	8.51E19	-2.12	2380.	!RRKM
Fluoroethylenes: Activated Decomposition, Methylene comb'n (stabilization)						
CH2SING	+ CHF	= CH2:CHF	3.10E24	-3.80	2830.	!ref
CH2SING	+ CF2	= CH2:CF2	3.10E24	-3.80	2830.	!ref
CHF	+ CHF	= CHF:CHF-Z	1.55E24	-3.80	2830.	!ref
CHF	+ CHF	= CHF:CHF-E	1.55E24	-3.80	2830.	!ref
CHF	+ CF2	= CHF:CF2	3.10E24	-3.80	2830.	!RRKM
Fluoroethylenes: Activated Decomposition, Methylene comb'n (H atom elim'n)						
CH2SING	+ CHF	= CH2:CF + H	1.64E07	1.56	5740.	!ref
CH2SING	+ CHF	= CHF:CH-Z + H	1.64E07	1.56	5740.	!ref
CH2SING	+ CHF	= CHF:CH-E + H	1.64E07	1.56	5740.	!ref
CH2SING	+ CF2	= CF2:CH + H	3.28E07	1.56	5740.	!ref
CHF	+ CHF	= CHF:CF-Z + H	1.64E07	1.56	5740.	!ref
CHF	+ CHF	= CHF:CF-E + H	1.64E07	1.56	5740.	!ref
CHF	+ CF2	= CF2:CF + H	1.64E07	1.56	5740.	!RRKM

```
Fluoroethylenes: Activated Decomposition, Vinyl + H (HF elimination)
CH2:CF    + H    = C2H2       + HF   5.98E20  -2.31    1940.  !ref
CHF:CH-Z  + H    = C2H2       + HF   5.98E20  -2.31    1940.  !ref
CHF:CH-E  + H    = C2H2       + HF   5.98E20  -2.31    1940.  !ref
CF2:CH    + H    = C2HF       + HF   5.98E20  -2.31    1940.  !ref
CHF:CF-Z  + H    = C2HF       + HF   5.98E20  -2.31    1940.  !ref
CHF:CF-E  + H    = C2HF       + HF   5.98E20  -2.31    1940.  !ref
CF2:CF    + H    = C2F2       + HF   5.98E20  -2.31    1940.  !RRKM
Fluoroethylenes: Activated Decomposition, Vinyl + H (stabilization)
CH2:CF    + H    = CH2:CHF           2.40E34  -7.11    5040.  !ref
CHF:CH-Z  + H    = CH2:CHF           2.40E34  -7.11    5040.  !ref
CHF:CH-E  + H    = CH2:CHF           2.40E34  -7.11    5040.  !ref
CF2:CH    + H    = CH2:CF2           2.40E34  -7.11    5040.  !ref
CHF:CF-Z  + H    = CHF:CHF-Z         2.40E34  -7.11    5040.  !ref
CHF:CF-E  + H    = CHF:CHF-E         2.40E34  -7.11    5040.  !ref
CF2:CF    + H    = CHF:CF2           2.40E34  -7.11    5040.  !RRKM
Fluoromethylene Combination
CHF       + CF2 = CF2:CF    + H   1.64E07   1.56    5740.  !ref
CF2:CF2   + M   = CF2 + CF2 + M   7.80E15   0.50   55690.  !      65TSC
Fluoroethylenes: Thermal Decompositions
CH2:CHF         = C2H2    + HF     1.00E14   0.00   70800.  !70TSC
CH2:CF2         = C2HF    + HF     2.50E14   0.00   86000.  !70TSC
CHF:CHF-Z       = C2HF    + HF     2.50E14   0.00   78000.  !ref +dH          37
CHF:CHF-E       = C2HF    + HF     2.50E14   0.00   79000.  !ref +dH          38

CF2:CF2   + M   = CF2 + CF2 + M    7.80E15   0.50   55690.  !65TSC

CHF:CHF-Z       = CHF:CHF-E      2.63E13  0.00    60700.  !74JEF

CH2:CF2   + CF3   = CF2:CH   + CHF3  7.24E10  0.00   4000.  !72KER/PAR      + 7
C2H4      + F2    = CH2F-CH2 + F     1.38E14  0.00  13600.  !88RAF
C2H4      + F2    = CH2:CHF  + HF    1.90E13  0.00  11040.  !88RAF
C2H4      + F     = C2H3     + HF    1.00E14  0.00   2000.  !ref              -34
Fluoroethylenes: H Atom Addition (stabilization)
CH2:CHF  + H(+M)= CH2F-CH2  (+M) 4.20E08   1.50     990.  !ref
CH2:CHF  + H(+M)= CH3-CHF   (+M) 4.20E08   1.50     990.  !ref
CH2:CF2  + H(+M)= CHF2-CH2  (+M) 4.20E08   1.50     990.  !ref
CH2:CF2  + H(+M)= CH3-CF2   (+M) 4.20E08   1.50     990.  !ref
     LOW/3.19E27   -2.8     -54./                        !ref
     H2/2.0/ CO/2.0/ CO2/3.0/ H2O/5.0/                   !ref
CHF:CHF-Z+ H(+M)= CH2F-CHF  (+M) 8.40E08   1.50     990.  !ref
CHF:CHF-E+ H(+M)= CH2F-CHF  (+M) 8.40E08   1.50     990.  !ref
     LOW/6.37E27   -2.8     -54./                        !ref
     H2/2.0/ CO/2.0/ CO2/3.0/ H2O/5.0/                   !ref
CHF:CF2  + H(+M)= CHF2-CHF  (+M) 4.20E08   1.50     990.  !ref
CHF:CF2  + H(+M)= CH2F-CF2  (+M) 4.20E08   1.50     990.  !ref
     LOW/3.19E27   -2.8     -54./                        !ref
     H2/2.0/ CO/2.0/ CO2/3.0/ H2O/5.0/                   !ref
CF2:CF2  + H(+M)= CHF2-CF2  (+M) 8.40E08   1.50     990.  !ref
     LOW/6.37E27   -2.8     -54./                        !ref
     H2/2.0/ CO/2.0/ CO2/3.0/ H2O/5.0/                   !ref
Fluoroethylenes: H Atom Addition (F atom displacement)
C2H4      + F   = CH2:CHF  + H     2.00E13  0.00      0.  !ref
CH2:CHF   + F   = CH2:CF2  + H     2.00E12  0.00      0.  !ref
CH2:CHF   + F   = CHF:CHF-Z+ H     5.00E12  0.00      0.  !ref
CH2:CHF   + F   = CHF:CHF-E+ H     5.00E12  0.00      0.  !ref
CHF:CHF-Z + F   = CHF:CF2  + H     4.00E12  0.00      0.  !ref
CHF:CHF-E + F   = CHF:CF2  + H     4.00E12  0.00      0.  !ref
CHF:CF2   + F   = CF2:CF2  + H     2.00E12  0.00      0.  !ref
```

Fluoroethylenes: H Atom Abstraction by H						
CH2:CHF + H	= CHF:CH-Z + H2	0.33E06	2.53	12241.	!ref	
CH2:CHF + H	= CHF:CH-E + H2	0.33E06	2.53	12241.	!ref	
CH2:CHF + H	= CH2:CF + H2	0.33E06	2.53	12241.	!ref	
CH2:CF2 + H	= CF2:CH + H2	0.67E06	2.53	12241.	!ref	
CHF:CHF-Z + H	= CHF:CF-Z + H2	0.33E06	2.53	12241.	!ref	
CHF:CHF-E + H	= CHF:CF-E + H2	0.33E06	2.53	12241.	!ref	
CHF:CF2 + H	= CF2:CF + H2	0.33E06	2.53	12241.	!ref	
Fluoroethylenes: Oxidation by O						
CH2:CHF + O	= CH2F + HCO	5.30E09	1.00	1310.	!fit	87CVE
CHF:CHF-Z + O	= CH2F + CF:O	7.00E09	1.00	1590.	!fit	87CVE
CHF:CHF-E + O	= CH2F + CF:O	8.00E09	1.00	1320.	!fit	87CVE
CH2:CF2 + O	= CHF2 + HCO	4.30E09	1.00	1490.	!fit	87CVE
CHF:CF2 + O	= CHF2 + CF:O	6.00E09	1.00	1150.	!fit	87CVE
CF2:CF2 + O	= CF2 + CF2:O	1.90E09	1.00	0.	!fit	87CVE
CH2:CHF + O	= CH3 + CF:O	5.30E09	1.00	2300.	!ref+1	74SLA/GUT
Fluoroethylenes: H Atom Abstraction by OH						
CH2:CHF + OH	= CHF:CH-Z+ H2O	2.00E06	2.00	2850.	!ref	-6
CH2:CHF + OH	= CHF:CH-E+ H2O	2.00E06	2.00	2850.	!ref	-6
CH2:CHF + OH	= CH2:CF + H2O	1.00E06	2.00	2850.	!ref	-10
CHF:CHF-Z + OH	= CHF:CF-Z+ H2O	2.00E06	2.00	2850.	!ref	- 5
CHF:CHF-E + OH	= CHF:CF-E+ H2O	2.00E06	2.00	2850.	!ref	- 5
CH2:CF2 + OH	= CF2:CH + H2O	2.00E06	2.00	2850.	!ref	
CHF:CF2 + OH	= CF2:CF + H2O	1.00E06	2.00	2850.	!ref	+ 1
Fluorovinyls: Oxidation by O2						
CH2:CF + O2	= CH2O + CF:O	4.48E26	-4.55	5480.	!ref	direct
CHF:CH-Z + O2	= CHF:O + HCO	4.48E26	-4.55	5480.	!ref	direct
CHF:CH-E + O2	= CHF:O + HCO	4.48E26	-4.55	5480.	!ref	direct
CHF:CF-E + O2	= CHF:O + CF:O	4.48E26	-4.55	5480.	!ref	direct
CHF:CF-Z + O2	= CHF:O + CF:O	4.48E26	-4.55	5480.	!ref	direct
CF2:CH + O2	= CF2:O + HCO	4.48E26	-4.55	5480.	!ref	direct
CF2:CF + O2	= CF2:O + CF:O	4.48E26	-4.55	5480.	!ref	direct
CH2:CF + O2	= CH2O + CF:O	1.05E38	-8.22	7030.	!ref	a/s
CHF:CH-Z + O2	= CHF:O + HCO	1.05E38	-8.22	7030.	!ref	a/s
CHF:CH-E + O2	= CHF:O + HCO	1.05E38	-8.22	7030.	!ref	a/s
CHF:CF-E + O2	= CHF:O + CF:O	1.05E38	-8.22	7030.	!ref	a/s
CHF:CF-Z + O2	= CHF:O + CF:O	1.05E38	-8.22	7030.	!ref	a/s
CF2:CH + O2	= CF2:O + HCO	1.05E38	-8.22	7030.	!ref	a/s
CF2:CF + O2	= CF2:O + CF:O	1.05E38	-8.22	7030.	!ref	a/s
Fluorovinyls: Oxidation by O						
CH2:CF + O	= CH2CO + F	3.00E13	0.00	0.	!ref	
CHF:CF-E + O	= CHFCO + F	3.00E13	0.00	0.	!ref	
CHF:CF-Z + O	= CHFCO + F	3.00E13	0.00	0.	!ref	
CF2:CF + O	= CF2CO + F	3.00E13	0.00	0.	!ref	
CHF:CH-E + O	= CHFCO + H	3.00E13	0.00	0.	!ref	
CHF:CH-Z + O	= CHFCO + H	3.00E13	0.00	0.	!ref	
CF2:CH + O	= CF2CO + H	3.00E13	0.00	0.	!ref	

```
Fluorovinyls: Oxidation by OH
CH2:CF     + OH    = CH2CO + HF     3.00E13    0.00        0.   !ref
CHF:CH-E   + OH    = CH2CO + HF     3.00E13    0.00        0.   !ref
CHF:CH-Z   + OH    = CH2CO + HF     3.00E13    0.00        0.   !ref
CHF:CF-E   + OH    = CHFCO + HF     2.00E13    0.00        0.   !ref
CHF:CF-Z   + OH    = CHFCO + HF     2.00E13    0.00        0.   !ref
CF2:CF     + OH    = CF2CO + HF     1.00E13    0.00        0.   !ref

CH2:CF     + OH    = CH3    + CF:O  3.00E13    0.00        0.   !ref
CHF:CH-E   + OH    = CH2F   + HCO   3.00E13    0.00        0.   !ref
CHF:CH-Z   + OH    = CH2F   + HCO   3.00E13    0.00        0.   !ref
CHF:CF-E   + OH    = CH2F   + CF:O  4.00E13    0.00        0.   !ref
CHF:CF-Z   + OH    = CH2F   + CF:O  4.00E13    0.00        0.   !ref
CF2:CF     + OH    = CHF2   + CF:O  5.00E13    0.00        0.   !ref
Fluoroethynes: H Atom Addition/Stabilization
C2HF       +H (+M)= CH2:CF    (+M)     2.80E12  0.00      2410.  !ref
C2HF       +H (+M)= CHF:CH-Z  (+M)     1.40E12  0.00      2410.  !ref
C2HF       +H (+M)= CHF:CH-E  (+M)     1.40E12  0.00      2410.  !ref
     LOW/0.67E27   -3.5     2410./
     H2/2./ CO/2./ CO2/3./ H2O/5./
C2F2       +H (+M)= CHF:CF-Z  (+M)     2.80E12  0.00      2410.  !ref
C2F2       +H (+M)= CHF:CF-E  (+M)     2.80E12  0.00      2410.  !ref
     LOW/1.33E27   -3.5     2410./
     H2/2./ CO/2./ CO2/3./ H2O/5./
Fluoroethynes: Oxidation
C2HF  + O      = FCCO-E  + H       1.00E07    2.00   1900.  !ref*2 MB A077
C2F2  + O      = FCCO-E  + F       1.00E07    2.00   1900.  !ref*2 MB A077

C2HF  + OH     = CHFCO   + H       2.18E-4    4.50  -1000.  !ref MB A089
C2HF  + OH     = CH2F    + CO      2.50E-4    4.00  -2000.  !ref/2 MB A090
C2HF  + OH     = HCCO    + HF      2.50E-4    4.00  -2000.  !ref/2 MB A090
C2F2  + OH     = CF2CO   + H       2.18E-4    4.50  -1000.  !ref MB A089
C2F2  + OH     = FCCO-E  + HF      2.50E-4    4.00  -2000.  !ref MB A090
Fluoroketenes, Fluoroketyl
CHFCO      + H    = CH2F   + CO   1.13E13    0.00   3428.  !ref MB A094
CF2CO      + H    = CHF2   + CO   1.13E13    0.00   3428.  !ref MB A094
CHFCO      + H    = FCCO-E + H2   5.00E13    0.00   8000.  !ref MB A095

CHFCO      + O    = CHF:O  + CO   1.00E13    0.00   8000.  !est
CF2CO      + O    = CF2:O  + CO   1.00E13    0.00   8000.  !est

CHFCO      + OH   = FCCO-E + H2O  7.50E12    0.00   2000.  !ref MB A097

HCCO       + F    = CHF    + CO   3.00E13    0.00      0.  !ref MB A101
FCCO-E     + F    = CF2    + CO   3.00E13    0.00      0.  !ref MB A101
FCCO-E     + H    = CHF    + CO   1.00E14    0.00      0.  !ref MB A101
FCCO-E     + O    = CF:O   + CO   1.00E14    0.00      0.  !ref MB A102
```

F Atom Reactions							
CH3OH + F	= CH3O + HF	2.62E09	1.44	-205.	!91GLA/KOS	
CH3OH + F	= CH2OH + HF	4.62E07	1.97	-300.	!91GLA/KOS	
CH2O + F	= HCO + HF	6.00E13	0.00	2000.	!ref	-45
CHF:O + F	= CF:O + HF	2.65E13	0.00	1800.	!90FRA/ZHA	-35
CH3O + F	= CH2O + HF	3.00E13	0.00	0.	!est	-114
HCO + F	= CO + HF	1.00E13	0.00	0.	!est	-120
C2H3 + F	= C2H2 + HF	2.00E13	0.00	0.	!ref	
CH2:CF + F	= C2HF + HF	2.00E13	0.00	0.	!ref	
CHF:CH-Z + F	= C2HF + HF	2.00E13	0.00	0.	!ref	
CHF:CH-E + F	= C2HF + HF	2.00E13	0.00	0.	!ref	
CHF:CF-Z + F	= C2F2 + HF	2.00E13	0.00	0.	!ref	
CHF:CF-E + F	= C2F2 + HF	2.00E13	0.00	0.	!ref	
CF2:CH + F	= C2F2 + HF	2.00E13	0.00	0.	!ref	
CHF:CF-Z + F	= CHF + CF2	1.00E13	0.00	0.	!ref	
CHF:CF-E + F	= CHF + CF2	1.00E13	0.00	0.	!ref	
CF2:CF + F	= CF2 + CF2	2.00E13	0.00	0.	!ref	
CF2:CF2 + F	= CF3 + CF2	3.00E13	0.00	0.	!ref	-18

NOTATION

$k = AT^b e^{-E/RT}$

A: prefactor (s^{-1}, *etc.*)
b: temperature dependence (dimensionless)
E: activation energy (J/mol/4.18)
H: heat of reaction (kJ/mol/4.18)

REFERENCES

65PRI/BRY Pritchard *et al.*, 1965
65TSC Tschuikow-Roux, 1965
67PAR/AZA Parsamyan *et al.*, 1970
68PAR/NAL Parsamyan and Nalbanddyan, 1968
70CAD/DAY Cadman *et al.*, 1970
70TSC/QUI Tschuikow-Roux and Quiring, 1970
71KER/TIM Kerr and Timlin, 1971
71KOC/MOI Kochubei and Moin, 1971
71MIL/HAR Millward *et al.*, 1971
71TSC/MIL Tschuikow-Roux *et al.*, 1971a
71TSC/QUI Tschuikow-Roux *et al.*, 1971b
71WAG/WAR Wagner *et al.*, 1971
72KER/PAR Kerr and Parsonage, 1972
72MIL/TSC Millward and Tschuikow-Roux, 1972
72RID/DAV Ridley *et al.*, 1972
73SCH/WAG Schug and Wagner, 1973
74SEK/TSC Sekhar and Tschuikow-Roux, 1974
74SLA/GUT Slagle *et al.*, 1974
75WES/DEH Westenberg and deHaas, 1975
76PAY/STI Payne and Stief, 1976
77KEA/MAT Keating and Matula, 1977
78ART/BEL Arthur and Bell, 1978
78BIO/LAZ Biordi *et al.*, 1978
78JOU/LEB Jourdain *et al.*, 1978
79SCH/WAG Schug *et al.*, 1979

REFERENCES (continued)
81BAU/DUX Baulch *et al.*, 1981
83WAL/WAG Walther and Wagner, 1983
84RYA/PLU Ryan and Plumb, 1984
84WAR Warnatz, 1984
85SAI/KUR Saito *et al.*, 1985
86PLU/RYA Plumb and Ryan, 1986a, 1986b
86TSA/HAM Tsang and Hampson, 1986
87COH/BEN Cohen and Benson, 1987a, 1987b
87CVE Cvetanovic, 1987
87DEA/WES Dean and Westmoreland, 1987
89STE/BRU Stevens *et al.*, 1989
89TSA/BEL Tsai *et al.*, 1989
89TSA/MCF Tsai and McFadden, 1989
90BOZ/DEA Bozzelli and Dean, 1990
90TSA/MCF Tsai and McFadden, 1990a, 1990b
91COH/WES Cohen and Westberg, 1991
91HID/NAK Hidaka *et al.*, 1991
92BAU/COB Baulch *et al.*, 1992
92MAR/SZE Maricq and Szente, 1992

RRKM this work, RRKM calculations
QRRK this work, QRRK calculations
BAC this work, BAC-MP4 & RRKM calculations
ref this work, by analogy to hydrocarbon reaction

6. AGENT STABILITY UNDER STORAGE AND DISCHARGE RESIDUE

Richard D. Peacock, Thomas G. Cleary, and Richard H. Harris Jr.
Building and Fire Research Laboratory

6.1 Agent Stability Under Storage

Halon 1301 is known to be stable in metal containers for many years. Any by-products do not affect its fire suppression effectiveness or result in an unacceptable residue. For candidate replacement chemicals, comparable data are needed, reflecting the storage conditions of elevated temperature and pressure. Significant losses in fire suppression effectiveness and increases in toxicity are possible if the extinguishing agent degrades during storage. Thus, stability during the multi-year storage environment is an important concern.

The storage environment fosters conditions which may have an adverse effect on the stability of halon replacements. Stored chemicals may engage in oxidation-reduction reactions, hydrolysis, and other corrosive interactions with metal cylinders. They are also subject to unimolecular decomposition and attack by reactive impurities in the agent. Water and oxygen, for example, will sorb to surfaces of cylinders and transfer lines and can never be completely excluded. These sources of instability, along with the possibility of catalytic interactions with the cylinder walls, can promote the evolution of undesirable products and a concomitant loss of fire suppression effectiveness. Toxicity and corrosiveness are particularly important concerns with respect to halogenated compounds, due to the tendency to liberate hydrogen halide in the process of degradation.

NIST Technical Note 1278 (Gann *et al.*, 1990) details a screening test for the stability of chemicals, with the purity of the chemical determined by infrared spectral analysis. This test involves storing the candidate in a carbon-steel cylinder for two days at a temperature of 170 °C (338 °F). The infrared spectra of the original and "aged" samples are compared. Although appropriate for a screening procedure, promising candidate agents need a more rigorous examination.

In this project, samples of each of the 12 candidate agents were evaluated in pressurized cylinders. It was presumed that $NaHCO_3$ is stable under the likely storage temperatures and pressures. In order to allow for potential interactions analogous to actual storage conditions, a measured amount of metal (with separate tests for each candidate cylinder metal) was introduced into the containers prior to the experiments. The vessel and its contents were stored in an oven at elevated temperature for 28 days. After cooling to ambient conditions, an infrared spectrum of the aged sample was compared to a spectrum of the original sample. Degradation of the sample would be indicated by a systematic decrease in the absorbance of peaks attributable to the agent and/or the appearance of new peaks in the IR spectrum of the aged agent.

6.1.1 Selection of Experimental Technique. The most reliable way to assess storage stability is to determine the shelf life of each chemical by monitoring its degradation in the actual storage environment. Existing ASTM test methods for assessing the storage stability of aircraft cleaning compounds are available (ASTM, 1987a and 1987b). After storage at specified conditions for 12 months, samples are inspected for signs of corrosion and sediment formation, and their performance is tested

against contract specifications. For evaluation of potential halon replacements, such long term storage is only practical for evaluating a near-final selection of agents. For the current project, an alternative approach must be taken.

The temperature dependence of potential reactions can be dramatic. For example, the rate of a chemical reaction with an activation energy of 126 kJ/mole, which is reasonable for catalytic degradation, increases by almost a factor of 10^9 over the temperature range from 25 to 225 °C. The ASTM test method for distillate fuels uses this phenomenon to accelerate aging in samples stored from 4 to 24 weeks at 43 °C. The elevated temperatures used in these test accelerate aging and make it possible to complete long-term stability assessments in a time frame of weeks rather than years.

The strategy of using temperature to study stability is also the basis of differential thermal analysis (DTA). This technique is frequently used to study phase transitions and assess thermal stability in liquids and solids (Wendlandt, 1964) In DTA, thermocouples are used to monitor the temperature difference between the sample and an inert reference material as a function of increasing temperature. A thermal event is signaled by a peak in the trace of voltage versus temperature and is indicative of a reaction in the sample. DTA is useful for measuring transition temperatures and for determining the signs of observed enthalpy changes. An ASTM standard test method for assessing thermal stability using DTA (E 537-86) is performed by observing the temperature changes which result from heating the sample from room temperature to about 500 °C. In performing this test, the investigator makes note of all enthalpy changes, the temperatures at which these transitions occur, whether they are exothermic or endothermic, and the effects of changing the atmosphere in the test cell. The criteria for thermal stability is the absence of a reaction.

Neither DTA (or the related differential scanning calorimetry) are appropriate for the current study. These techniques are typically applied to detect chemical reactions and phase transitions in solids. They would be difficult, if not impossible, to apply to potential halon replacements, which are, almost exclusively, gases and volatile liquids. More importantly, they measure thermal, as opposed to storage stability. The presence of reactive impurities or heterogenous catalysis in the storage environment cannot be determined by studying pure samples of the agent alone.

Actual storage at elevated temperatures for some period of time is thus desirable. Degradation can be monitored via conventional analytical techniques, such as gas chromatography (GC) (Grob, 1977) or infrared spectroscopy (IR) (Willis, *et al.*, 1987).

A GC consists of a heated injection port connected to a column which is coated with an adsorbent material called the stationary phase. Mixtures are transported through the column by an inert gas. The components are separated on the basis of the amount of time they require to traverse the length of the column. Retention times in the column increase with the affinity of the component to the stationary phase. A detector is positioned so that it can respond to the individual components as they are sequentially eluted from the column. Ideally, the chromatogram, which is a plot of detector response versus retention time, consists of a series of well-resolved peaks, each of which corresponds to a pure compound. In practice, however, co-elution of components is an important concern which must be addressed by temperature programming and careful selection of the stationary phase. Accurate measurements of the concentrations of identified mixture components are frequently made using a GC equipped by an ionization detection or electron capture detector. To make definitive compound identifications, the GC is often paired with a mass spectrometer.

Chemical analysis by IR spectroscopy is based on the assumption that the IR spectrum of a compound is sufficiently unique to identify it. An IR spectrum is obtained by measuring the ratio of the intensity of IR radiation which passes through the sample, I, to the intensity of the incident radiation, I_o, as a function of frequency. Concentrations of individual components are quantified by applications of Beer's law

$$C_i = \left[\frac{A_i(\nu)}{A_r(\nu)}\right] C_r, \qquad A(\nu) = -\log\frac{I(\nu)}{I_o(\nu)}, \tag{1}$$

where the subscript r indicates known values obtained from a reference sample. IR spectroscopy is extremely versatile in the sense that almost all compounds, with the notable exception of single atomic and homonuclear diatomics, are IR active. In principle, IR analysis makes it possible to monitor the degradation of each candidate and identify the corresponding products from a simple before and after comparison of the spectra. In practice, IR analysis can suffer from overlapping peaks in a spectrum similar to problems with gas chromatography. In addition, quantitative determination of degradation products require either pre-existing spectra for comparison (libraries of spectra for common materials are commercially available) or available reference samples.

GC is much more sensitive than IR. The major disadvantage is the considerable effort and expense involved in column preparation and selection. This situation is exacerbated by the need to use different columns to resolve a wide variety of alternative chemicals from their degradation products. In addition, since it was expected that the additional sensitivity afforded by GC would not be needed in most cases (most of the compounds were expected to be stable), the speed, cost, and acceptable resolution of IR spectroscopy made this approach the best alternative for the screening tests conducted. For longer-term studies, to be performed once the list of acceptable chemicals has been reduced to a few alternatives, IR studies can be supplemented with GC analysis as appropriate.

Since the agents may interact with metal storage cylinders during long term storage, it is important to evaluate the agents in the presence of a variety of metals which may be encountered during typical use. Table 1 shows the metals selected for the current study. Although the primary interest is in storage cylinder materials, additional materials which may come in contact with the agents for extended periods of time were included. Ideally, containers constructed of each material would be used for agent storage during the study. However, cost and availability of containers made from the eight metals necessitated the use of metal coupons inside an inert container. In this approach, an amount of metal with surface area roughly equal to the storage cylinder was introduced into teflon-lined stainless steel cylinders prior to agent filling. With new metal samples for each experiment, this also eliminated potential longer-term degradation of the metals over multiple experiments.

6.1.2 Experimental. A total of thirteen agents were screened for their long-term storage stability (twelve candidate replacement agents and halon 1301). Each agent was exposed to fixed amounts of eight different metals at elevated temperature and pressure. Testing conditions dictated that the exposure temperature be fixed at 149 °C, and that the room temperature fill pressure be 4.13 MPa (600 psia). In order to assure that the storage cylinder pressure not exceed the pressure rating on the cylinder or valve when exposed to the elevated temperature, a conservatively low amount of agent was placed in each cylinder. The cylinders were filled with agent up to a maximum pressure of the saturation vapor pressure of the agent at room temperature (in the case of the gaseous agent, up to a fixed pressure). Nitrogen was then added to achieve the final pressure. Since small amounts of additional liquid would vaporize at the elevated temperature only a single phase would exist anyway, though a significant pressure increase would be observed. The effect of the system pressure on degradation was not explored, but is thought to be small.

Eight different metals were chosen to be exposed to the agents for the screening. The metals were introduced into the cylinders as coupons 10.2 cm long, 0.8 cm wide, and 0.2 cm thick. The number of coupons was fixed at 30 for each cylinder because that amount is approximately the

Table 1. Metals used in Agent Stability Study

Metal	Major Constituents	Typical Use
Nitronic-40 (21-6-9 Stainless)	Cr Mn Ni Fe	Pressure vessel
304 Stainless	Cr Ni Fe	Pressure vessel, pressure vessel fitting, gage fitting, and diagnostic devices
AM 355 Stainless	Cr Mo Ni Fe	Outlet closure
4130 Alloy Steel	Cr Mn Si Fe	Pressure vessel
13-8 Mo Alloy Steel	Al Cr Mo Ni Fe	
Inconel 625	Cr Fe Mo Ni	Bourdon tube
6061-T6 Aluminum Alloy	Al Si Fe Mg	Compression gasket, fill fitting
CDA 172 Cu-Be Alloy	Cu Be	Bourdon tube, outlet closure

surface area of the interior of the cylinder. Overlapping of the coupons in the cylinder effectively decreased the exposed surface area, but this decrease, though not calculated, should be similar for all tests.

6.1.2.1 Test Preparation. The storage cylinders were constructed of stainless steel, lined with polytetrafluoroethylene (PTFE), and had a 1000 ml capacity. All new cylinders were assembled with high temperature/high pressure stainless steel valves and end plugs, then heated to 149 °C (300 °F) for at least 48 hours with the valves completely open. For re-used cylinders, the heating time was cut to 24 hours.

The metal coupons were immersed in dichloromethane solvent and stirred around to remove any oil residue and markings on the surfaces. The coupons were removed from the solvent, stripped with clean paper towels, and dried at room temperature. Care was taken to handle the cleaned coupons with gloved hands only. Thirty pieces of each metal were weighed and placed into their respective cylinders. The end plugs threads were wrapped with PTFE tape and tightened. The cylinder valves were opened and the cylinders were heated for at least 12 hours at 149 °C. After the cylinders were removed from the ovens, the valves were closed.

6.1.2.2 Filling Procedure. When the cylinders were cool enough to be handled with gloves, they were evacuated to an absolute pressure of less than 20 Pa (0.15 torr). Each evacuated cylinder was weighed. The agents were added and the cylinder was pressurized to the final pressure with nitrogen. The detailed filling procedure is given below.

The filling procedure was designed to insure low levels of contaminant (including room air) and a reasonably accurate measurement of the amounts of material introduced into the cylinder. Highly accurate measurement of amounts of agent and/or nitrogen are not required in this screening method

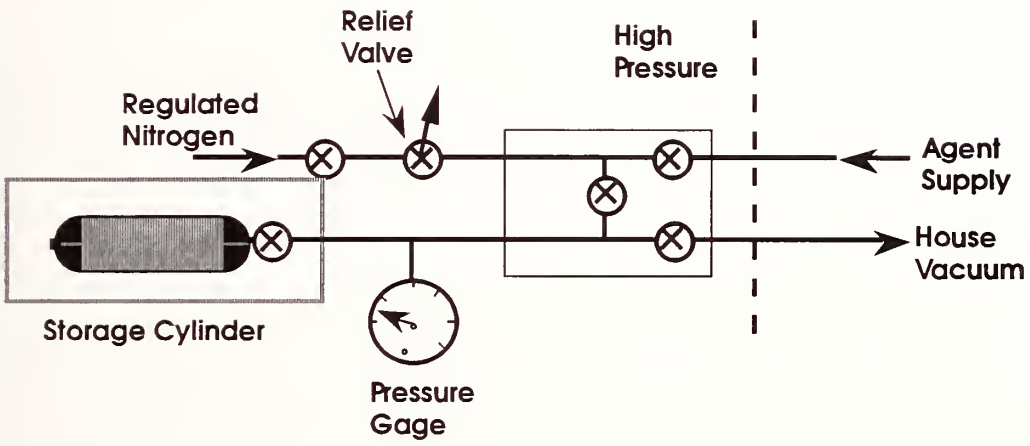

Figure 1. Experimental apparatus for agent filling study.

since it is the change in spectra that was desired. Figure 1 is a schematic of the filling apparatus. It consisted of a three valve manifold, an absolute pressure gage, and filling lines, all constructed from stainless steel and capable of handling high pressures. The lines to the agent tank and the house vacuum were not high pressure rated and were isolated by valves. The following steps outline the filing procedure.

1. The evacuated cylinder was attached to the filling apparatus.

2. The apparatus was evacuated with the house vacuum which was capable of pulling a vacuum down to 34 kPa. Then the valve to the house vacuum was closed.

3. The apparatus was pressurized with nitrogen in excess of 1.4 MPa. The pressure was released through the relief valve.

4. The apparatus was then evacuated again with the house vacuum. Steps 2-4 purge the filling apparatus. After purging the amount of room air in the apparatus was less than 1% of the original amount. The volume of the filling apparatus is much less than a storage cylinder, so the percentage of air in any filled cylinder was very small (on the order of 0.01%).

5. The agent inlet valve was opened slowly and the pressure in the apparatus checked (the agent inlet line is pre-charged with agent). At this point if the agent cylinder included a regulator, the delivery pressure could be adjusted. The valve to the cylinder is slowly opened and agent flowed in. Both the inlet valve and the cylinder valve must be opened slowly to avoid the possibility of drawing liquid agent into the apparatus. The system was allowed to equilibrate for one to two minutes, the pressure recorded, and the agent inlet valve closed.

   Here we note that the delivery pressure of the agent was, in most cases, the saturation vapor pressure at room temperature of that particular agent. One agent (FC-116) was available as a high pressure gas, and two other agents (HFC-125 and the azeotrope of HFC-32 and HFC-125) had saturation vapor pressures somewhat higher than the other agents, therefore the delivery pressure for these agents was specified to yield a mass of agent delivered to the cylinder close to the mass delivered for most of the other agents.

6. Nitrogen was added to increase the total pressure to nominally 4.20 MPa. This pressure was slightly higher than the prescribed target pressure of 4.13 MPa, but because a small amount of the agent/N_2 mixture was removed from the cylinder for the initial FTIR analysis, a slight decrease in the initial (cold) storage pressure was observed. The total pressure was recorded and the valve to the storage cylinder closed.

7. The pressure was bled from the apparatus and the cylinder disconnected and weighed. At this point, a new cylinder can be connected and filled starting with Step 1 above.

6.1.2.3 Conduct of the Tests. Each cylinder was connected to the inlet of the gas cell on the FTIR system. A vacuum of less than 20 Pa was drawn on the gas cell and inlet line up to the cylinder valve. A needle valve was placed in line between the cylinder valve and the gas cell to accurately control the flow of the agent into the gas cell. The agent/N_2 was introduced into the gas cell to an absolute pressure of 1330 $\pm$ 10 Pa (9.95 $\pm$ .05 torr). Three spectra were taken for each sample. The cylinders were then re-weighed.

The filled cylinders were placed in the ovens at 149 °C and the time and date were recorded. Periodically, the cylinders were removed and weighed while still hot, then placed back in the oven to check for leakage. It was observed that the valves had to be re-tightened (while hot) after being in the ovens for a day or two. In very few cases was leakage significant, though it appeared that the valves used in this study degraded after some re-use leading to some leaking. In any long term study the valves should be capped to prevent leakage. After 28 days the cylinders were removed from the ovens and allowed to cool before the spectra were taken.

The final spectra were obtained in the same manner as the initial spectra. Comparisons between the initial and final spectra were made.

6.1.2.4 Exposed metals. The agent/N_2 mixture was released from each cylinder in an exhaust hood. The end plugs were removed and the metal coupons shaken from the cylinders. The metals were examined visually for changes, wrapped in aluminum foil and retained for reference. The cylinders were then ready for reuse.

6.1.3 Results. Table 2 lists the metal mass, agent pressure, calculated agent mass, and initial agent/N_2 pressure and mass before and after storage. In this table, the agent mass was calculated from the agent density at the recorded pressure and ambient temperature (along with the fixed 1000 ml volume of the cylinders). The error in this calculated value is the combination of the uncertainty in the agent pressure reading which is estimated to be $\pm$ 0.01 MPa ($\pm$ 2 psia), deviations of the agent temperature from ambient temperature (at least two minutes were allowed for the system to equilibrate) and the error associated with the equation of state. Here, generalized compressibility charts were used (Balzhiser *et al.*, 1972). The combined uncertainties in the calculated values were not estimated. Uncertainty in the recorded masses depends on the weighing apparatus (agent/N_2 masses were obtained by subtracting the initial mass of the evacuated cylinder with metals in place). Neglecting the cases where obvious leaking occurred, the masses of the agent/N_2 were within $\pm$ 5% for any given agent with the exception of FC-31-10. Inspection of the calculated agent masses, and measured agent/N_2 masses for the FC-31-10 indicates that some liquid agent was probably drawn into the cylinder during filling (approximately 40 extra grams of agent). It is remarkable that the filling procedure still yielded final agent/N_2 masses within $\pm$ 10%. The extra liquid vaporized at the elevated temperature.

6.1.3.1 FTIR Spectra. The spectra taken before and after the storage period were examined to identify changes in the gas phase. Any new peaks observed in the spectra taken after storage would indicate that some degradation of the agent had occurred during the storage time. In addition a decrease in the area under specific peaks of the final spectra would indicate degradation. Equation 1 would yield quantitative concentrations.

Figures 2-4 show the initial and final overlaid IR spectra for three of the agents. In some of the spectra, baseline perturbations can be seen. However, these perturbations generally occur above 2500 cm^{-1} outside the area of interest for fluorinated compounds and are likely due to detector sensitivity fall off or gas cell window contamination.

For all thirteen agents examined, no new peaks were observed in any of the spectra. Peaks of new compounds could be masked by the peaks formed by the original compound, so examination of the peak heights or areas under the peaks would provide further validation of whether or not the agents were stable.

During the course of the storage experiments, the FTIR system experienced a catastrophic failure of the computer. The FTIR was updated with new computer hardware, but several electronic files were lost which included the initial and final spectra for the agents HCFC-22, HCFC-124, HFC-125,

Table 2. Agent and Metal Amounts in Storage Cylinders for Stability Under Storage Tests

Agent: HCFC-22

Metal	Metal Mass (±0.01 g)	Agent		Agent/N_2		
		Pressure (± 0.02 MPa)	Mass (g)	Pressure (± 0.02 MPa)	Mass Before Storage (± 0.1 g)	Mass After Storage (± 0.1 g)
304 stainless steel	272.07	0.97	40	4.13	75.6	74.8
Nitronic-40 (21-6-9)	325.45	0.97	40	4.13	72.8	73.0
Inconel 625	320.29	0.97	40	4.13	75.4	75.2
6061-T6 aluminum	96.55	0.97	40	4.13	76.8	75.5
4130 alloy steel	304.45	0.95	39	4.17	76.5	75.0
AM 350 stainless	285.68	0.94	39	4.13	--[a]	77.1
Cu/Be C82500	311.20	0.96	39	4.17	77.8	76.6
13-8 Mo stainless	280.13	0.95	39	4.13	74.6	73.5

Agent: HCFC-124

Metal	Metal Mass (± 0.01 g)	Agent		Agent/N_2		
		Pressure (± 0.02 MPa)	Mass (g)	Pressure (± 0.02 MPa)	Mass Before Storage (± 0.1 g)	Mass After Storage (± 0.1 g)
304 stainless steel	272.61	0.31	19	4.13	--	--
Nitronic-40 (21-6-9)	323.56	0.31	19	4.20	63.1	63.1
Inconel 625	319.78	0.33	20	4.15	62.9	63.3
6061-T6 aluminum	96.95	0.31	19	4.13	64.8	63.8
4130 alloy steel	303.52	0.33	20	4.13	63.5	63.6
AM 350 stainless	283.72	0.33	20	4.17	62.8	51.3
Cu/Be C82500	311.48	0.33	20	4.17	65.3	63.2
13-8 Mo stainless	285.73	0.31	19	4.17	64.2	64.6

[a] -- data not available

Table 2. (continued) Agent and Metal Amounts in Storage Cylinders for Stability Under Storage Tests

Agent: HFC-125

Metal	Metal Mass (± 0.01 g)	Agent		Agent/N_2		
		Pressure (± 0.02 MPa)	Mass (g)	Pressure (± 0.02 MPa)	Mass Before Storage (± 0.1 g)	Mass After Storage (± 0.1 g)
304 stainless steel	273.08	0.69	38	4.20	72.1	72.7
Nitronic-40 (21-6-9)	323.72	0.69	38	4.20	74.4	74.2
Inconel 625	320.11	0.69	38	4.20	74.1	74.4
6061-T6 aluminum	96.87	0.69	38	4.20	76.5	76.7
4130 alloy steel	303.57	0.69	38	4.20	73.4	73.6
AM 350 stainless	286.23	0.69	38	4.20	76.0	45.5
Cu/Be C82500	311.06	0.72	39	4.20	76.9	77.2
13-8 Mo stainless	283.45	0.69	38	4.20	72.6	73.2

Agent: HFC-32/HFC-125

Metal	Metal Mass (± 0.01 g)	Agent		Agent/N_2		
		Pressure (± 0.02 MPa)	Mass (g)	Pressure (± 0.02 MPa)	Mass Before Storage (± 0.1 g)	Mass After Storage (± 0.1 g)
304 stainless steel	273.49	0.69	24	4.20	55.2	55.4
Nitronic-40 (21-6-9)	323.03	0.69	24	4.20	55.2	55.7
Inconel 625	320.34	0.69	24	4.20	53.9	54.7
6061-T6 aluminum	96.72	0.69	24	4.20	55.2	55.4
4130 alloy steel	303.44	0.69	24	4.20	55.7	56.1
AM 350 stainless	286.22	0.69	24	4.20	55.6	55.7
Cu/Be C82500	311.02	0.69	24	4.20	58.1	58.3
13-8 Mo stainless	284.32	0.69	24	4.20	55.2	56.0

Table 2 (continued). Agent and Metal Amounts in Storage Cylinders for Stability Under Storage Tests

Agent: HFC-134a

Metal	Metal Mass (± 0.01 g)	Agent		Agent/N_2		
		Pressure (± 0.02 MPa)	Mass (g)	Pressure (± 0.02 MPa)	Mass Before Storage (± 0.1 g)	Mass After Storage (± 0.01 g)
304 stainless steel	273.60	0.59	27	4.20	66.8	66.6
Nitronic-40 (21-6-9)	324.52	0.59	27	4.20	62.3	60.1
Inconel 625	319.85	0.59	27	4.20	64.2	63.6
6061-T6 aluminum	96.83	0.59	27	4.41	68.3	67.9
4130 alloy steel	303.77	0.59	27	4.20	64.1	63.9
AM 350 stainless	284.73	0.59	27	4.20	66.7	66.9
Cu/Be C82500	311.65	0.59	27	4.20	62.2	61.6
13-8 Mo stainless	285.24	0.59	27	4.20	64.2	64.3

Agent: FC-218

Metal	Metal Mass (± 0.01 g)	Agent		Agent/N_2		
		Pressure (± 0.02 MPa)	Mass (g)	Pressure (± 0.02 MPa)	Mass Before Storage (± 0.1 g)	Mass After Storage (± 0.1 g)
304 stainless steel	274.10	0.81	80.1	4.24	107.7	107.3
Nitronic-40 (21-6-9)	324.78	0.79	78.7	4.24	104.7	104.2
Inconel 625	317.72	0.79	78.7	4.24	107.1	107.1
6061-T6 aluminum	97.01	0.79	78.7	4,24	107.2	107.2
4130 alloy steel	303.34	0.79	78.7	4.24	101.1	102.1
AM 350 stainless	284.92	0.79	78.7	4.24	101.9	105.9
Cu/Be C82500	311.66	0.79	78.7	4.24	103.7	103.6
13-8 Mo stainless	282.99	0.76	75.3	4.28	--	83.4

Table 2 (continued). Agent and Metal Amounts in Storage Cylinders for Stability Under Storage Tests

Agent: HFC-227

Metal	Metal Mass (± 0.01 g)	Agent		Agent/N_2		
		Pressure (± 0.02 MPa)	Mass (g)	Pressure (± 0.02 MPa)	Mass Before Storage (± 0.1 g)	Mass After Storage (± 0.1 g)
304 stainless steel	272.8	0.40	31	4.26	72.8	73.0
Nitronic-40 (21-6-9)	323.29	0.40	31	4.20	71.6	71.5
Inconel 625	318.02	0.41	32	4.20	69.6	70.3
6061-T6 aluminum	97.02	0.41	32	4.20	69.7	69.7
4130 alloy steel	303.18	0.40	31	4.20	66.4	66.5
AM 350 stainless	285.37	0.40	31	4.20	70.0	69.9
Cu/Be C82500	310.51	0.41	32	4.24	70.2	70.0
13-8 Mo stainless	282.26	0.40	31	4.24	68.5	68.5

Agent: FC-31-10

Metal	Metal Mass (± 0.01)	Agent		Agent/N_2		
		Pressure (± 0.02 MPa)	Mass (g)	Pressure (± 0.02 MPa)	Mass Before Storage (± 0.1 g)	Mass After Storage (± 0.1 g)
304 stainless steel	273.79	0.23	24	4.20	97.7	97.8
Nitronic-40 (21-6-9)	325.27	0.21	22	4.20	103.4	103.3
Inconel 625	320.01	0.21	22	4.20	111.9	112.4
6061-T6 aluminum	97.03	0.21	22	4.20	117.1	100.4
4130 alloy steel	302.73	0.21	22	4.20	113.6	111.9
AM 350 stainless	287.56	0.21	22	4.20	106.4	106.4
Cu/Be C82500	311.62	0.21	22	4.20	110.9	110.9
13-8 Mo stainless	284.99	0.21	22	4.20	110.8	110.3

Table 2. (continued) Agent and Metal Amounts in Storage Cylinders for Stability Under Storage Tests

Agent: FC-116

Metal	Metal Mass (± 0.01 g)	Agent		Agent/N_2		
		Pressure (± 0.0 2 MPa)	Mass (g)	Pressure (± 0.02 MPa)	Mass Before Storage (± 0.1 g)	Mass After Storage (± 0.1 g)
634 stainless steel	273.23	0.55	32.4	4.20	66.4	66.0
Nitronic-40 (21-6-9)	324.53	0.55	32.4	4.20	68.7	68.6
Inconel 625	320.85	0.56	33.2	4.20	71.2	71.4
6061-T6 aluminum	97.01	0.56	33.2	4.20	71.8	71.6
4130 alloy steel	304.05	0.56	33.2	4.27	72.2	71.8
AM 350 stainless	286.24	0.56	32.8	4.20	72.7	72.6
Cu/Be C82500	311.97	0.57	33.6	4.22	47.5	47.2
13-8 Mo stainless	281.79	0.57	33.6	4.21	70.8	70.6

Agent: FC-318

Metal	Metal Mass (± 0.01 g)	Agent		Agent/N_2		
		Pressure (± 0.02 MPa)	Mass (g)	Pressure (± 0.02 MPa)	Mass Before Storage (± 0.1 g)	Mass After Storage (± 0.1 g)
304 stainless steel	272.47	0.26	23.4	4.20	66.3	66.3
Nitronic-40 (21-6-9)	324.44	0.26	23.4	4.20	65.6	65.4
Inconel 625	319.30	0.25	22.7	4.20	66.5	66.3
6061-T6 aluminum	69.55	0.25	22.7	4.22	67.0	66.9
4130 alloy steel	303.38	0.26	23.4	4.20	60.5	60.6
AM 350 stainless	284.62	0.25	22.7	4.20	64.5	64.5
Cu/Be C82500	313.05	0.26	23.4	4.20	64.2	63.9
13-8 Mo stainless	281.84	0.25	22.7	4.22	65.6	65.4

Table 2 (continued). Agent and Metal Amounts in Storage Cylinders for Stability Under Storage Tests

Agent: HFC-236

Metal	Metal Mass (± 0.01 g)	Agent		Agent/N_2		
		Pressure (± 0.02 MPa)	Mass (g)	Pressure (± 0.02 MPa)	Mass Before Storage (± 0.1 g)	Mass After Storage (± 0.1 g)
304 stainless steel	274.32	0.26	18	4.20	57.1	57.1
Nitronic-40 (21-6-9)	325.85	0.25	17	4.20	58.0	58.0
Inconel 625	320.19	0.26	18	4.21	58.2	58.3
6061-T6 aluminum	97.18	0.25	17	4.20	57.8	57.8
4130 alloy steel	302.58	0.25	17	4.22	57.0	57.2
AM 350 stainless	283.61	0.25	17	4.22	58.4	58.7
Cu/Be C82500	311.32	0.24	16	4.20	57.6	57.8
13-8 Mo stainless	283.96	0.24	16	4.21	56.6	56.6

Agent: halon 1301

Metal	Metal Mass (± 0.01 g)	Agent		Agent/N_2		
		Pressure (± 0.02 MPa)	Mass (g)	Pressure (± 0.02 MPa)	Mass Before Storage (± 0.1 g)	Mass After Storage (± 0.1 g)
304 stainless steel	272.72	1.46	113	4.22	128.3	--
Nitronic-40 (21-6-9)	324.55	1.46	113	4.24	142.6	142.7
Inconel 625	318.41	1.45	112	4.27	143.3	143.6
6061-T6 aluminum	97.73	1.41	109	4.24	141.0	141.2
4130 alloy steel	301.56	1.36	102	4.13	141.3	141.3
AM 350 stainless	284.83	1.34	101	4.19	136.6	136.8
Cu/Be C82500	323.26	1.32	99	4.15	137.1	137.4
13-8 Mo stainless	289.68	1.32	99	4.19	134.3	134.5

Table 2 (continued). Agent and Metal Amounts in Storage Cylinders for Stability Under Storage Tests

Agent: CF_3I

Metal	Metal Mass (± 0.01 g)	Agent		Agent/N_2		
		Pressure (± 0.02 MPa)	Mass (g)	Pressure (± 0.02 MPa)	Mass Before Storage (± 0.1 g)	Mass After Storage (± 0.1 g)
304 stainless steel	271.69	0.34	30	4.20	71.5	71.2
Nitronic-40 (21-6-9)	324.22	0.34	30	4.20	70.4	70.4
Inconel 625	318.68	0.34	30	4.20	66.5	66.5
6061-T6 aluminum	98.99	0.34	30	4.20	69.3	67.0
4130 alloy steel	300.22	0.34	30	4.20	71.7	71.8
AM 350 stainless	286.06	0.34	30	4.20	71.3	52.4
Cu Be C82500	323.63	0.34	30	4.20	73.8	72.9
13-8 Mo stainless	297.59	0.34	30	4.20	71.2	71.6

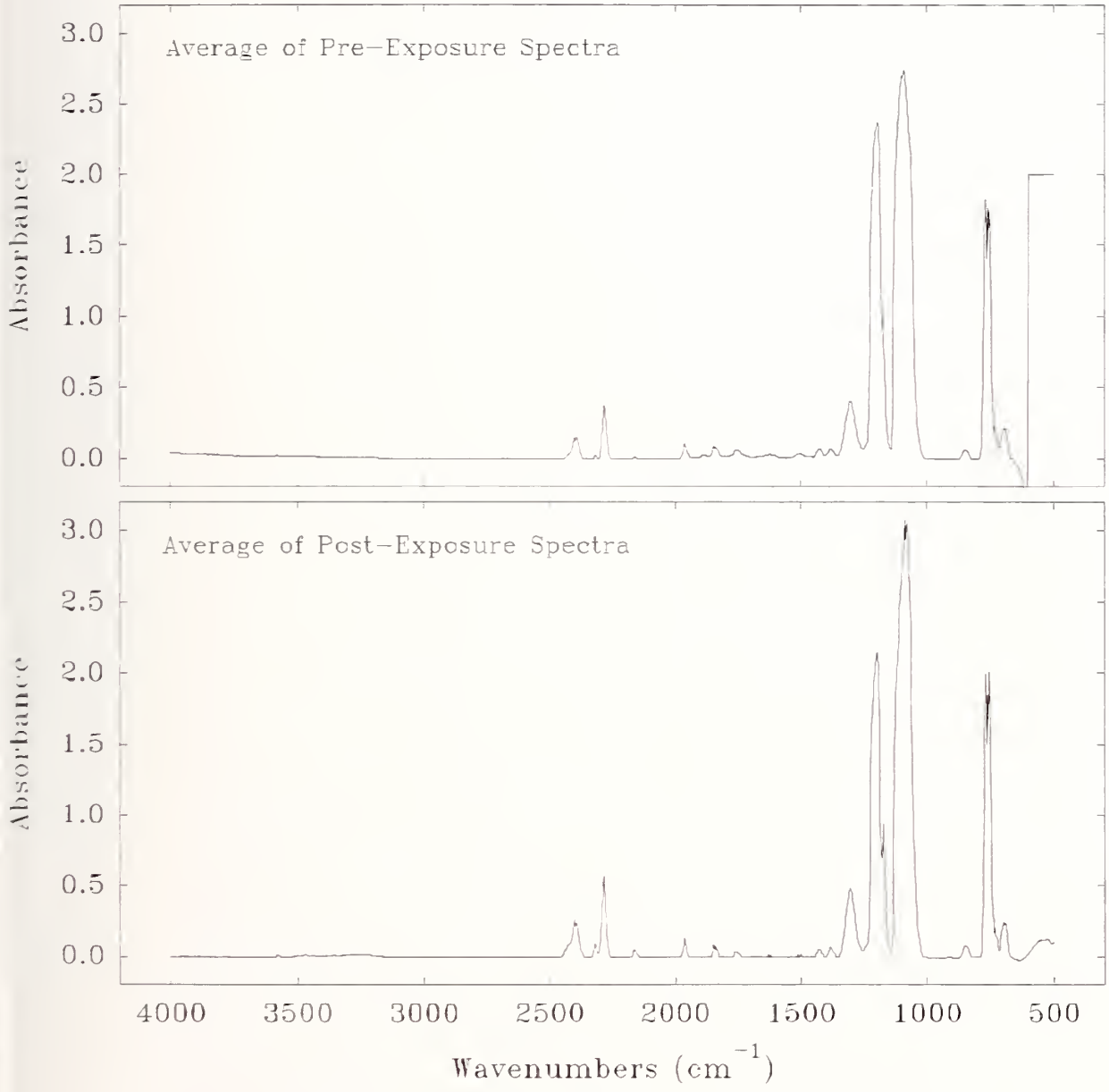

Figure 2. Pre- and post-storage spectra for halon 1301.

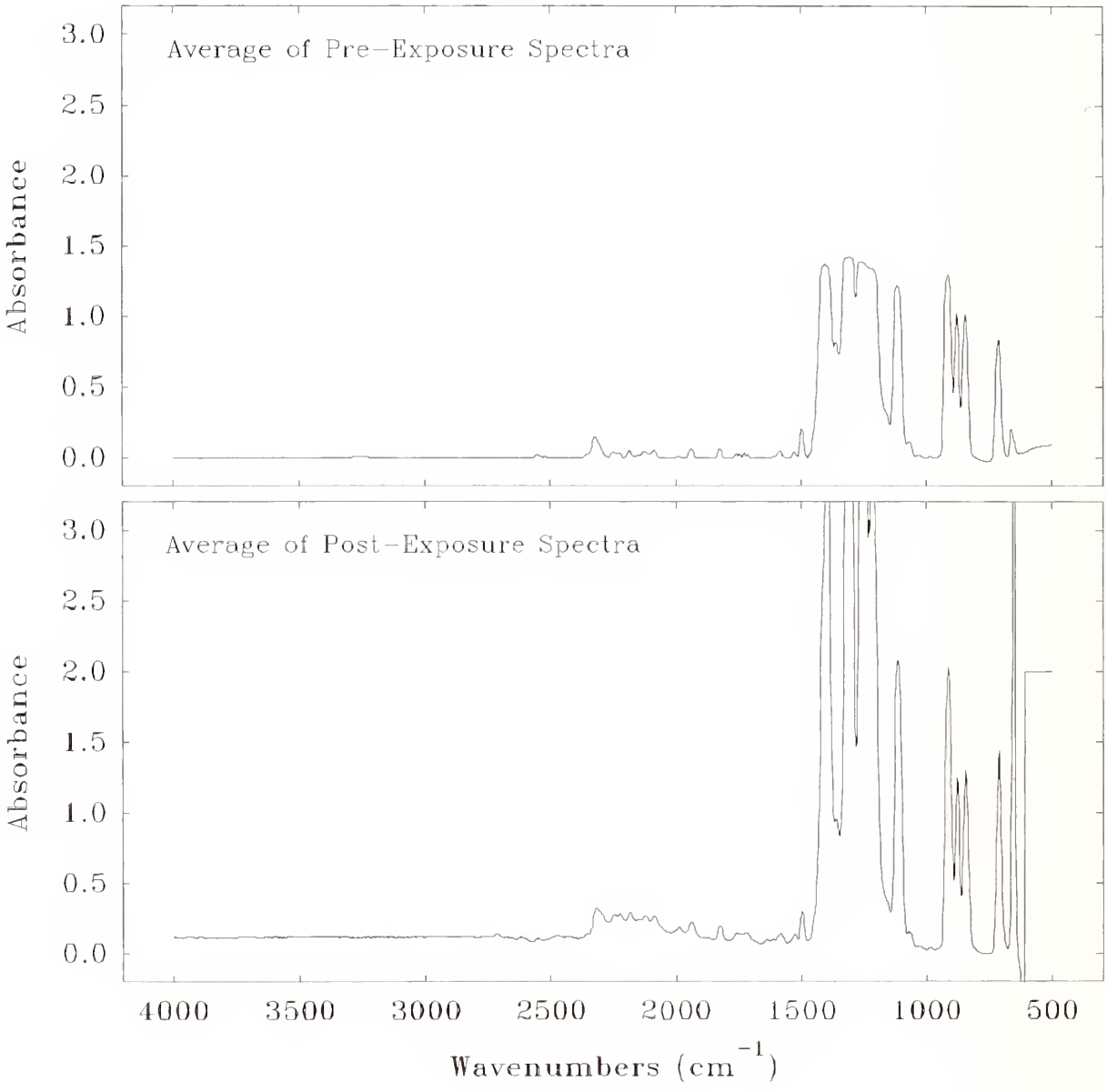

Figure 3. Pre- and post-storage spectra for HFC-236.

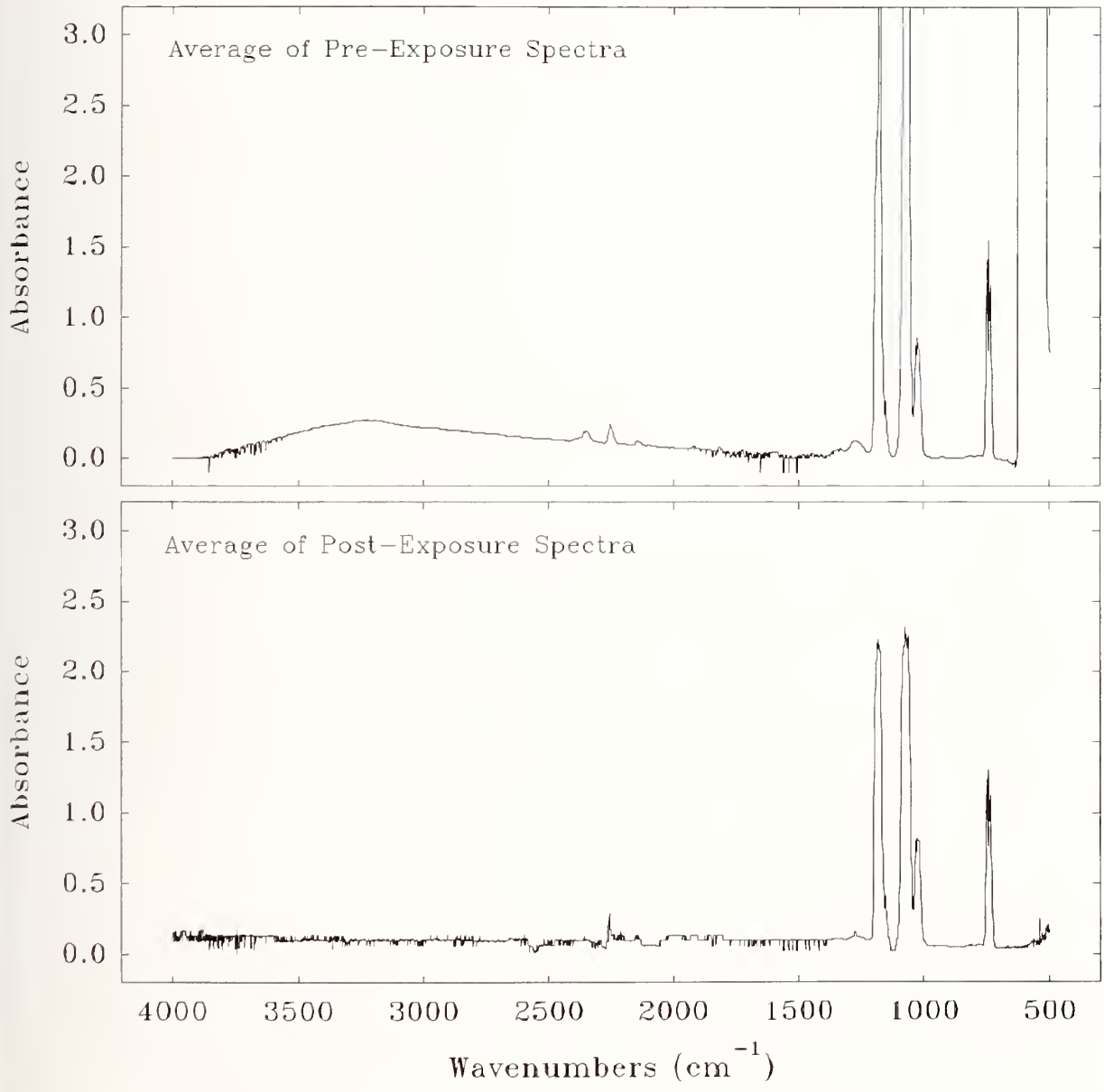

Figure 4. Pre- and Post-storage spectra for CF_3I.

and HFC-32/HFC-125. Therefore no peak areas are available for those agents. Judgment for these agents were based on inspection of the hard-copy plots of the spectra.

Selected peaks in the spectra before and after the 28 day storage were integrated for the remaining agents. Table 3 lists the initial and final integrated areas of selected peaks for halon 1301, HFC-236, and CF_3I. The integrated peaks were selected on the basis of the following criteria to ensure possible absorbance linearity:

- an absorbance of < 1
- acceptable baseline resolution
- wave number greater than 700 cm^{-1}

For halon 1301, there was a tendency for the peak areas to increase, whereas for CF_3I there was a tendency for the peak areas to decrease. The experiments are very repeatable within a short time span (as indicated by the small uncertainties for each agent-metal combination). Over longer time periods, alignment of the FTIR becomes critical and the comparison of initial and final spectra can be expected to have a larger uncertainty. Thus, the key indicator of degradation should be taken as the formation of new compounds evidenced in the spectra. No new compounds were identified in any of the spectra for any of the agents. For CF_3I, an initial spectra and two final spectra were available (one taken after eight days of storage and one after the full 28 day exposure). The peak areas systematically decreased over the four week exposure, but the change may be within the experimental measurement error. Since no new compounds were observed in the CF_3I spectra, the possible degradation of CF_3I deserves further examination and will be included in the forthcoming longer term studies.

6.1.3.2 Examination of Metals. The metals were removed from the cylinders, examined, and then wrapped in aluminum foil for later reference. Changes in the appearance of the metals are given in Table 4. When the metals from the CF_3I cylinders were removed, a dark solid was apparent on the coupons, then disappeared within seconds. The solid may have been I_2 which then sublimed to gaseous I_2. For the other metals, visual changes may be due to the prolonged heating of the metal or by interaction with the agent. For the former, effects would be observed for all of the agents (for example, the Cu/Be C82500 coupons). Interaction with the agents is far more common, with some metals affected by only a few agents and others effected by nearly all of the agents. HCFC-22 and CF_3I affected most of the metals, while for others, only the Cu/Be C82500 coupons were affected.

6.2 Agent Residue Study

The objective of this phase of the project was to determine if the agents as received contained measurable contamination that might have an effect on the results of our experiments. An attempt was made to determine high volatile residue contaminants as well as low volatile residue contaminants. If a residue was discovered some effort was made to determine the source of the contamination.

6.2.1 Experimental Method. The apparatus used for determining residue is shown in Figure 5. The cylinders as received were fitted with hardware that allowed them to be connected to the copper cooling coil with a commercially available flexible hose commonly used in the refrigerant industry. Graduated tubes of *ca.* 2 ml capacity (the bottoms of larger graduated centrifuge tubes) were used to

Table 3. Initial and Final Integrated Areas of Selected Peaks in the IR Spectra of Halon 1301

Metal	Band (cm^{-1})	Integrated Area		c_f/c_i
		Initial	Final	
304 stainless steel	1351.85-1259.28	15.45±0.01	17.49±0.01	1.13
Nitronic 40 (21-6-9)	"	15.56±0.02	18.32±0.02	1.18
Inconel 625	"	15.72±0.02	18.55±0.04	1.18
6061-T6 aluminum	"	15.90±0.02	19.80±0.66	1.25
4130 alloy steel	"	15.32±0.04	18.46±0.04	1.20
AM 350 stainless	"	15.14±0.03	18.44±0.04	1.22
Cu/Be C82500	"	15.24±0.03	18.61±0.03	1.22
13-8 Mo stainless	"	14.98±0.05	17.51±0.11	1.17
304 stainless steel	1984.39-1928.46	1.88±0.01	2.08±0.02	1.11
Nitronic 40 (21-6-9)	"	1.90±0.01	2.16±0.02	1.14
Inconel 625	"	1.95±0.01	2.21±0.01	1.13
6061-T6 aluminum	"	1.95±0.02	2.35±0.07	1.21
4130 alloy steel	"	1.88±0.02	2.18±0.01	1.16
AM 350 stainless	"	1.87±0.01	2.18±0.01	1.17
Cu/Be C82500	"	1.89±0.01	2.23±0.02	1.18
13-8 Mo stainless	"	1.85±0.02	2.11-0.01	1.14
304 stainless steel	2302.58-2250.52	7.90±0.03	8.20±0.08	1.04
Nitronic 40 (21-6-9)	"	7.92±0.10	8.63±0.10	1.09
Inconel 625	"	8.10±0.05	8.80±0.02	1.09
6061-T6 aluminum	"	8.10±0.03	9.30±0.25	1.15
4130 alloy steel	"	7.78±0.01	8.64±0.03	1.11
AM 350 stainless	"	7.77±0.04	8.74±0.06	1.12
Cu/Be C82500	"	7.82±0.01	8.88±0.12	1.14
13-8 Mo stainless	"	7.65±0.04	8.41±0.05	1.10

Table 3, (continued). Initial and Final Integrated Areas of Selected Peaks in the IR Spectra of CF_3I.

Metal	Band (cm^{-1})	Integrated Area		c_f/c_i
		Initial	Final	
Blank	1312.32±1225.54	3.55±0.02	3.30±0.01	0.93
304 stainless steel	"	3.77±0.02	3.60±0.03	0.95
Nitronic 40 (21-6-9)	"	3.55±0.03	3.47±0.05	0.98
Inconel 625	"	3.63±0.01	3.26±0.01	0.90
6061-T6 aluminum	"	3.68±0.01	3.56±0.01	0.97
4130 alloy steel	"	3.70±0.02	3.46±0.03	0.94
AM 350 stainless	"	3.27±0.02[a]	3.35±0.04	1.02
Cu/Be C82500	"	3.69±0.01	3.69±0.04	1.00
13-8 Mo stainless	"	3.48+0.03	3.39+0.02	0.97
Blank	762.70-717.38	27.02±0.12	22.63±0.04	0.84
304 stainless steel	"	29.03±0.08	24.38±0.13	0.84
Nitronic 40 (21-6-9)	"	27.18±0.23	23.75±0.04	0.87
Inconel 625	"	27.58±0.03	22.54±0.04	0.82
6061-T6 aluminum	"	28.21±0.13	24.07±0.05	0.85
4130 alloy steel	"	27.99±0.12	23.47±0.03	0.84
AM 350 stainless	"	24.69±0.12[a]	22.95±0.10	0.93
Cu/Be C82500	"	27.64±0.27	24.66±0.01	0.89
13-8 Mo stainless	"	26.13±0.27	22.99±0.02	0.88

[a] - Outliers

Table 3, (continued). Initial and Final Integrated Areas for Selected Peaks in the IR Spectra of HFC-236

Metal	Band (cm^{-1})	Integrated Area		c_f/c_i
		Initial	Final	
304 stainless steel	1508.06-1473.34	3.71[a]	4.29±0.09	1.16
Nitronic 40 (21-6-9)	"	3.68±0.23	4.65[a]	1.26
Inconel 625	"	3.78±0.24	4.77[a]	1.26
6061-T6 aluminum	"	3.66±0.14	3.37±0.01	0.92
4130 alloy steel	"	3.78±0.33	3.15±0.01	0.83
AM 350 stainless	"	3.65±0.14	3.27±0.01	0.90
Cu/Be C82500	"	3.62±0.10	3.28±0.01	0.91
13-8 Mo stainless	"	3.70±0.26	3.28±0.01	0.89
304 stainless steel	1843.61-1799.25	2.16[a]	2.30±0.04	1.06
Nitronic 40 (21-6-9)	"	2.09±0.14	2.42[a]	1.16
Inconel 625	"	2.11±0.15	2.45[a]	1.16
6061-T6 aluminum	"	2.03±0.08	1.93±0.01	0.95
4130 alloy steel	"	2.09±0.20	1.82±0.06	0.87
AM 350 stainless	"	2.00±0.09	1.82±0.01	0.91
Cu/Be C82500	"	1.97±0.06	1.84±0.01	0.93
13-8 Mo stainless	"	2.02±0.15	1.83±0.03	0.91

[a] - Only two usable spectra

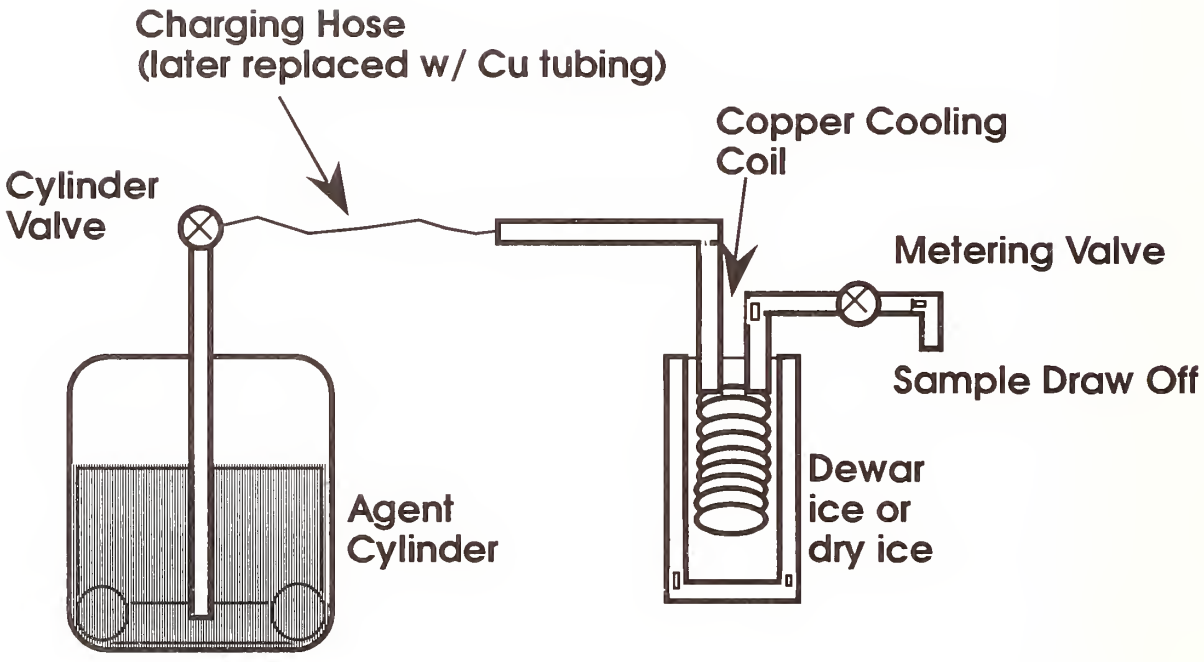

Figure 5. Apparatus for determining agent residue.

collect 1 ml of liquid agent. All tubes were dried at 105 °C for one hour, kept in a desiccator, then weighed with an analytical balance with 0.1 mg accuracy before filling. Three tubes were used to collect each agent. After the 1 ml samples were collected, the tubes were kept in an ice or dry ice

Table 4. Visible Changes in Metals After 28 Day Exposure at 149°C (300°F)

Agent	304 stainless steel	Nitronic-40 (21-6-9)	Inconel 625	6061-T6 aluminum	4130 alloy steel	AM 350 stainless	Cu/Be C82500	13-8 Mo stainless
HCFC-22	✓[a]	✓	✓	✓	✓		✓	✓
HCFC-124							✓	
HFC-125							✓	
HFC-32/HFC-125							✓	
HFC-134a					✓		✓	
FC-218		✓		✓	✓		✓	
HFC-227					✓		✓	
FC-31-10		✓		✓	✓		✓	✓
FC-116					✓		✓	
FC-318	✓				✓		✓	
HFC-236							✓	
halon 1301							✓	
CF_3I	✓	✓	--[b]	✓	✓	✓	--	✓

a - ✓ indicates visible change in metal appearance after exposure
b - data not available

bath (depending on the boiling point of the agent) to allow controlled evaporation. When all of the agent had evaporated, the tubes were then placed in a desiccator for at least one hour and weighed on the previously described balance.

Agents with a boiling point greater than -26 °C were processed with the cooling coil immersed in ice and the tubes evaporated in ice. Those agents with a boiling point less than -39 °C required dry ice and acetone in the dewar holding the cooling coil and controlled evaporation of the tubes in a tray containing dry ice. All agents with the exception of FC-116, which is a gas at room temperature, were removed from the cylinders as a liquid and collected in the graduated tubes as a liquid. The FC-116 condensed in the cooling coil and was collected as a liquid.

An effort was made to determine the presence of highly volatile residues when the graduated tubes were at low temperature after filling and during the controlled evaporation. The formation of frost prevented any clear observation of the presence of residue.

If measurable residue was present in the graduated tubes after the agents had boiled away and a weighing at ambient was done, the tubes were then heated to 150 °C for one hour, cooled to ambient in a desiccator, and reweighed.

6.1.2 Results of residue analyses. Initially, the residue analysis was performed on several of the agents contained in 1000 ml cylinders. These agents were prepared in small laboratory quantities and no measurable residues were detected. A representative of the manufacturer of these agents indicated that no low volatile residues should be present because they are distilled prior to filling and are of high purity.

As production and pilot quantities were received, the residue analysis was performed. Initially, the HCFC-22 and HCFC-124 samples were found to have as much as 1.3 and 0.3%, respectively, of a yellow, oily residue. The residue was still visible when the tubes were heated to 150 °C, however, the amount was reduced to 0.9 and less than 0.1%, respectively. The manufacturer of these agents was contacted with a lot number from the HCFC-22. One of their research chemists contacted the plant where this agent had been filled and found that the 13.6 kg non-returnable cylinders do contain a small amount of oil to protect the inner walls. Since many of the applications of HCFC-22 require the addition of oil to the agent, no effort was made to remove the oil. In later discussions with another representative of the manufacturer, this statement was said to be incorrect.

If left in the high pressure flexible filling lines commonly used by the refrigeration industry (and used to connect the cylinders to the cooling coil in our experiments), interaction between HCFC-22 and HCFC-124 and the black, rubber lining resulted in a yellow, oily residue. If the connection from the cylinder to the cooling coil was made with a metal tube such as copper, no significant residue was collected. This dissolution or extraction phenomenon was only seen with HCFC-22 and HCFC-124, which also contain chlorine.

Table 5 summarizes the results of the low volatile residue analyses for all agents, except FC-318 and CF_3I. There was some uncertainty in the weighing of the tubes after they were conditioned to ambient temperature in the desiccator and weighed. In some cases, the weight after collection was actually slightly less than the initial weight. In the table, a report of a trace amount indicates that the tubes showed less than 1 mg of residue. Only the HFC-134a and HFC-236 contained low volatile residues greater than 1 mg and the weight increase was consistent for the three tubes.

6.3 Conclusions

- No new compounds, observable above the background, were evident after 28 day, 150 °C exposure of any of the candidate agents.

- A possible decrease in integrated areas for selected spectral peaks was observed only for CF_3I. This observation may be within the experimental error, and was without accompanying formation of new compounds. An observation of a dark solid on metal coupons post-exposure for this agent may have been I_2 which could result from either degradation or impurity in the original agent. Longer term study is warranted for this agent.

Table 5. Low Volatile Residue Results

Agent	Weight % Residue
HCFC-22	Trace
HCFC-124	Trace
HFC-134a	<0.1
HFC-125	Trace
HFC-32/HFC-125	Trace
HFC-227	Trace
FC-31-10	Trace
HFC-236	0.2
FC-116	Trace
FC-218	Trace
FC-318	Not Measured
CF_3I	Not Measured

- All agents except HFC-134a and HFC-236 appeared to be relatively free of low volatile residues. The small amounts detected for the two agents appeared to be oily and might have come from the container walls.

- For the chemicals studied, stability in long-term storage and agent residue should not be major deciding factors in determining selection of appropriate agents for further study. As noted above, CF_3I could be an exception.

6.4 References

Standard Test Method for Preparing Aircraft Cleaning Compounds, Liquid Type, Water Based for Storage Stability Testing, ASTM F-1104, Annual Book of ASTM Standard, Volume 15.03, American Society for Testing and Materials, 1987.

Standard Test Method for Preparing Aircraft Cleaning Compounds, Liquid Type, Solvent Based for Storage Stability Testing, ASTM F-1105, Annual Book of ASTM Standard, Volume 15.03, American Society for Testing and Materials, 1987.

Gann, R.G., Barnes, J.D., Davis, S., Harris, J.S., Harris, R.H., Jr., Herron, J.T., Levin, B.C., Mopsik, F.I., Notarianni, K.A., Nyden, M.R., Paabo, M., and Ricker, R. E., *Preliminary Screening Procedures and Criteria for Replacements for Halons 1211 and 1301,* Natl. Inst. Stand. Technol., Technical Note 1278, 1990.

Grob, R.L. (Ed.), *Modern Practice of Gas Chromatography,* John Wiley & Sons, New York, 1977.

Wendlandt, W.W., *Thermal Methods of Analysis,* John Wiley & Sons, New York, 1964.

Willis, H.A., Van der Maas, J.H., and Miller, R.G.J. (Eds.), *Laboratory Methods in Vibrational Spectroscopy,* John Wiley & Sons, New York, 1987.

7. CORROSION OF METALS

Richard E. Ricker, Mark R. Stoudt, James F. Dante, James L. Fink,
Carlos R. Beauchamp and Thomas P. Moffat
Materials Science and Engineering Laboratory

7.1 Introduction

Since a fire suppressant which is corrosive to either the materials used for storage and distribution of the agent or to aircraft materials after deployment would be undesirable, experiments were conducted to assess the relative corrosivity of the potential fire suppressants to different metallic alloys used on aircraft. These experiments were designed to evaluate the propensity of the different agents to cause failure by any of the possible corrosion failure modes during service or after deployment. In addition to these experiments, experiments were conducted to develop an electrochemical technique that would rapidly, and less expensively, evaluate the corrosivity of an agent and the influence of changes in composition, temperature and contaminant levels on the corrosivity of an agent.

Corrosion is usually defined as degradation of the properties of a material as a result of chemical reaction with the environment. Corrosion can be classified into different categories based on the material, environment, or the morphology of the corrosion damage. Based on the morphology of the damage, corrosion can be classified into eight different modes of attack:

1. General Corrosion - General corrosion is the result of chemical or electrochemical reactions which proceed over the entire exposed surface at about the same rate. General corrosion results in the metal becoming thinner and usually alters the appearance of the surface. General corrosion could result in failure through lowering the mechanical strength of components or by reducing wall thickness until leaking results.

2. Pitting Corrosion - Pitting corrosion is corrosion at a high rate in a small spot on the surface of a material. It commonly occurs at flaws in coatings applied to prevent corrosion of the underlying metal, but pitting corrosion also occurs in metals that resist corrosion through the formation of a native oxide, hydroxide or salt film ("passive" metals or alloys). To prevent corrosion, these films must be continuous and they must be able to reform rapidly by reaction between the material and the environment when the film cracks, ruptures or becomes damaged through any mechanical or chemical process. Apparently, halide ions either stimulate the breakdown of these films or inhibit their reformation (repassivation) as pitting is commonly observed in environments that contain ions of these elements. The time required to initiate pitting depends on temperature and the composition of the environment typically increasing in a logarithmic fashion as the halide ion concentration (activity) decreases. Once initiated, the corrosion rate at the bottom of a pit can be several orders of magnitude greater than that outside the pit and pitting could cause perforation of storage bottles, etc. or it could initiate cracks that propagate to failure by other mechanisms.

3. Crevice Corrosion - When a material is exposed to an environment, there are usually occluded regions, such as crevices, where the environment in this region does not freely mix with the bulk environment. The chemistry of the environment in these occluded regions can differ significantly from that of the bulk environment and this difference can result in corrosive attack. Crevice corrosion is frequently observed in passivated metals and alloys when they are exposed to environments that contain halide ions (especially chloride). Similar to pitting corrosion, a long incubation period may be required to initiate this attack, but once initiated, this attack can occur at rates that are orders of magnitude greater than rates outside the crevice. Crevice corrosion could result in failure through leaking of joints, mechanical failure of joints, freezing of joints, or it could lead to the initiation of cracks that propagate to failure through other mechanisms.

4. Intergranular Corrosion - Virtually all engineering alloys are fabricated by solidifying a melt composed of a mixture of elements. During this solidification process, crystals nucleate and grow together; forming the solid. As a result of this process, the chemical composition and the properties of the region between the crystals can differ significantly from those inside the crystals or grains. Alloy manufacturers have a variety of techniques that they employ to homogenize alloys and reduce this difference, but complete elimination of this difference is virtually impossible. As a result, certain alloy environment combinations can result in rapid corrosion of the region between the crystals. This is referred to as intergranular corrosion. When intergranular corrosion occurs, the surface of the material can appear unattacked, but the mechanical strength of the alloy can deteriorate slowly or rapidly until the materials break under any applied load or until individual grains begin to fall out and the material falls apart.

5. Environmentally Induced Fracture - When a material is exposed to a chemically reactive environment, the application of a mechanical stress to this material can result in the formation and propagation of a crack at stresses well below those required for cracking by purely mechanical processes in the absence of the corrosive environment. Exposure to aqueous solutions, organic solvents, liquid metals, solid metals, and gases have been found to cause failure in this manner. Depending on the environment and the type of loading, this type of failure has many different names such as stress corrosion cracking (SCC), chloride stress cracking, hydrogen embrittlement, liquid metal embrittlement, solid metal embrittlement, sulfide stress cracking, and corrosion fatigue, but they all consist of crack propagation induced by exposure to an environment. The environments that cause this type of failure are not always very aggressive and this mechanism of failure could cause sudden loss of agent or prevent the proper operation of valves.

6. Dealloying - Because different elements have different chemical activities, one element in an alloy may be selectively removed from the surface. This selective leaching of an alloying element can result in the surface becoming dealloyed and in some cases this dealloyed layer is not limited to the surface and it grows into the solid causing a serious loss of mechanical strength. In addition to lowering the strength of any component, dealloyed layers are porous and dealloying could cause loss of agent from a storage container.

7. Galvanic Corrosion - Because different elements have different chemical activities, different alloys with different chemical compositions will have different chemical and

electrochemical properties in the same environment. Joining of dissimilar metals in a manner such that an electrical circuit is completed through the joint and the environment will result in increasing the rate of corrosion of the more active metal and reducing the rate of corrosion of the more noble metal. The extent of the change depends on a variety of factors including the ratio of the areas of each alloy exposed to the environment, the potential difference between the alloys, the electrical resistivity of the joint, and the conductivity of the environment. In the case of metals and alloys exposed to fire suppressants, the conductivity of these suppressants is usually extremely low (unless they become contaminated with impurities) and this should minimize the damage that galvanic coupling of dissimilar alloys can cause.

8. Erosion Corrosion - Mixing or stirring of a solution can accelerate the rate of corrosion either by simply increasing the rate of transport to the surface or by mechanically damaging or removing surface films that may protect the underlying metal from attack. An increase in the rate of corrosion as a result of relative motion of the environment is termed "erosion corrosion." In general, the relative motion of the agents in the storage and distribution systems will be quite low; except during deployment, where erosion corrosion may occur in the nozzles.

Of these eight corrosion failure modes, six are of potential concern for the storage, distribution, and post deployment corrosivity of fire suppressant agents on aircraft: general corrosion, pitting corrosion, crevice corrosion, intergranular corrosion, environmental induced fracture and dealloying. Erosion corrosion may be a concern for nozzles but, the duration of the flow through the nozzle is very short and damage by this mechanisms should be noted in the fire suppressant efficiency tests if it occurs. Galvanic coupling may influence corrosion damage accumulation, but due to the relatively low conductivity of these agents, galvanic effects should be at a minimum. As a result, experiments were designed to evaluate the propensity of the different agents to cause failure by these six corrosion failure modes.

On board aircraft, metallic materials will be exposed to fire suppressant agents during storage (storage containers, valves etc.), deployment (distribution tubes, nozzles, etc.) and post-deployment (structural and engine components exposed to residuals and combustion products) but, the exposures during deployment are very short and should not be of concern. Of greatest concern for the safe operation of aircraft is the possibility that the fire suppressant might cause attack of the storage container resulting in loss of agent or preventing the proper operation of the release valve. These storage containers hold the agent for up to five years at high pressures ($\approx$5.8 MPa) and temperatures as high as 150 °C. Very little is known about the corrosion of metals in these environments and there is virtually no information in the literature on the corrosivity of most of these agents to the metals used for aircraft storage containers. As a result, corrosion experiments that emulate the suppressant storage conditions were determined to be a necessary part of the evaluation of new fire suppressant agents.

A second concern for the safe operation of aircraft, is the potential for significant corrosion damage to the structural metals of the aircraft and aircraft components by residual suppressant or by suppressant combustion products. Of particular concern would be the formation of halide acids or salts as a result of the combustion of the agent during fire suppression. For suppressants that are not a gas at normal temperatures and pressures, residual suppressant left on the surface of metals after suppressant deployment could result in corrosion damage before the agent is cleaned off the surface (30 days maximum exposure). As a result of this concern, experiments were designed to evaluate the potential for corrosion damage to metals by suppressant residual and combustion products.

7.2 Experimental

There were two main objectives of this initial phase of the study: 1) to rank the corrosivity of the alternative fire suppressants with respect to storage vessel materials and 2) to rank the corrosion resistance of the storage vessel materials when exposed to alternative fire suppressants. This allows the elimination of the most corrosive fire suppressants and the least corrosion resistant storage vessel material. To achieve these objectives, experiments were designed to evaluate the propensity of the different agents to cause failure by the possible corrosion failure modes during service or post-deployment. In addition to these experiments, experiments were also conducted to develop an electrochemical technique that would rapidly, and less expensively, evaluate the corrosivity of an agent and the influence of changes in composition, temperature and contaminant levels on the corrosivity of an agent.

7.2.1 Aircraft Storage System Corrosion. Experiments were designed and conducted to evaluate the corrosivity of the different potential fire suppressants during normal service in aircraft storage containers. Since no electrochemical techniques have been developed for the rapid evaluation of the corrosivity of low conductivity media such as fire suppressants, these experiments had to consist of exposures that emulate the conditions under which corrosion is expected to occur followed by careful examination and evaluation of the resulting corrosion damage. To evaluate the potential for failure of the aircraft storage containers by the six potential corrosion failure modes during normal service, three different types of exposures tests were conducted to evaluate the potential for failure of the aircraft storage containers by the six possible corrosion failure modes expected during normal service. Exposure tests were conducted to determine the changes in mass during the exposures which would, in turn, assess the rate of formation of corrosion scales or the rate of removal of metallic species by corrosion. Also, visual and optical microscope examination of these samples after exposure allowed for the evaluation of the occurrence of pitting, intergranular corrosion and dealloying. Using the mass change and the exposure time data, the average mass change was estimated allowing for a comparison between the agents. The weld/crevice coupon exposures were conducted to allow for the evaluation of localized corrosion failure modes such as crevice corrosion, weld zone attack, and intergranular attack in the heat affected zone. The environmental induced fracture resistance of the alloys in the agents was evaluated by conducting exposure tests on cylindrical samples of the alloys that are loaded in tension by slowly increasing the strain on the sample until failure occurs by either normal mechanical means or by an environmentally assisted or induced means (the slow strain rate tensile test). By comparing the strain or load required to cause failure in an inert environment to that required to cause failure in the agents, the propensity of each agent to cause environmentally induced fracture in each alloy can be evaluated.

7.2.1.1 Materials. The following materials were chosen for this study: 304 stainless steel, 13-8 Mo stainless steel, AM 355 stainless steel, stainless steel alloy 21-6-9 (Nitronic 40), 4130 alloy steel, Inconel alloy 625, CDA-172 copper/beryllium alloy and 6061-T6 aluminum alloy. (The compositions of these alloys are given in Table 1.) These alloys were selected for these experiments based on discussions with the Air Force on the materials typically used for aircraft storage containers and distribution system components.

7.2.1.2 Mass Change (Smooth Coupon) Exposure Experiments. The samples used for the mass change experiments were flat smooth surface coupons of the geometry shown in Figure 1(a).

Table 1. Composition of the alloys in weight percent

Element	Nit 40	Al 6061	In 625	304 SS	CDA 172	13-8 Steel	AM 355	AISI 4130
Ni	7.1	- -	61.39	8.26	0.06	8.4	4.23	0.08
Cr	19.75	0.04	21.71	18.11	0.01	12.65	15.28	0.98
Mn	9.4	0.15	0.08	1.41	- -	0.02	0.8	0.51
Mg	- -	1	- -	- -	- -	- -	- -	- -
Si	0.5	0.4	0.09	0.49	0.08	0.04	0.16	0.23
Mo	- -	- -	8.82	0.17	- -	2.18	2.6	0.16
Nb	- -	- -	3.41	- -	- -	- -	- -	- -
N	0.29	- -	- -	0.03	- -	0	0.12	- -
C	0.02	- -	0.02	0.06	- -	0.03	0.12	0.32
Be	- -	- -	- -	- -	1.9	- -	- -	- -
Co	- -	- -	- -	0.11	0.2	- -	- -	- -
Zn	- -	0.25	- -	- -	- -	- -	- -	- -
Cu	- -	0.15	- -	- -	97.9	- -	- -	- -
Fe	bal	0.7	3.97	bal	0.06	bal	bal	bal
Al	- -	bal	0.23	- -	0.04	1.11	- -	0.04
g/cm^3[a]	7.83	2.70	8.44	7.94	8.23	7.76	7.91	7.85
kg/m^3	7,830	2,700	8,440	7,940	8,230	7,760	7,910	7,850

[a]Nominal Density

After machining, the surfaces were glass bead blasted to remove any remaining surface oxides or scale and to provide a consistent smooth surface finish (120 grit nominal). Additional preparation prior to the start of these tests consisted of cleaning and three initial weight measurements for each individual sample. Each sample was ultrasonically cleaned, first in acetone and then in alcohol, dried with warm air and immediately weighed. Three separate weighings were taken at approximately 30 second intervals and averaged. This average value was then referred to as the initial weight of the coupon. The balance used for these weight measurements was self calibrating on start-up to maintain an accuracy to within $\pm 10 \times 10^{-6}$ g with a reproducibility of no less than $\pm 1.51 \times 10^{-8}$ g. Representative photographs of the surface of each alloy were also taken prior to the start of testing.

At the start of each exposure test, three coupons of each of the eight alloys were mounted on a polytetraflouroethylene (PTFE) rod with PTFE spacers between the samples as shown in Figure 2. This was done 1) to separate and 2) to isolate the samples electrically; thus eliminating galvanic coupling effects. Three samples of each alloy type were tested and PTFE shields were placed between the different alloys sets to protect the samples from contact with any corrosion products that may form. The samples were next placed in a custom designed PTFE liner and charged into a two

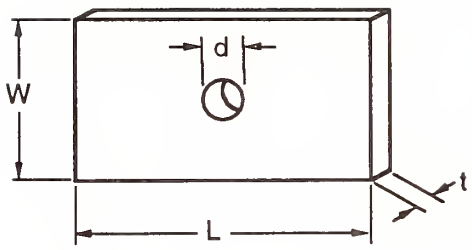

W= 25.4 mm (1.0 in)
L= 50.8 mm (2.0 in)
t= 1.6 mm (0.0625 in)
d= 6.7 mm (0.265 in)

(a) General corrosion coupon design (ASTM G-01).

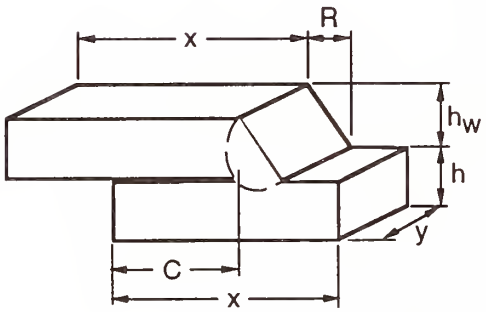

x = 50.8 mm (2.0 in)
y = 50.8 mm (2.0 in)
R = 4.75 mm (0.1875 in)
C = 31.75 mm (1.25 in)
h = 3.2 mm (0.125 in)
h_W = 3.2 mm (0.125 in)

(b) Weld/crevice corrosion coupon design.

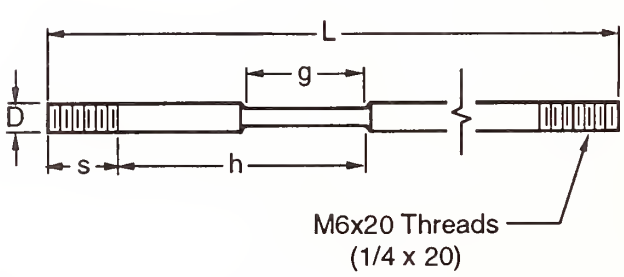

D = 19 mm (0.25 in)
L = 178 mm (7 in)
g = 25.4 mm (1 in)
h = 57 mm (2.25 in)
s = 19 mm (0.75 in)

(c) Slow strain rate tensile sample design (ASTM E-8, G-49).

Figure 1. Design of samples used in immersion and slow strain rate tensile tests.

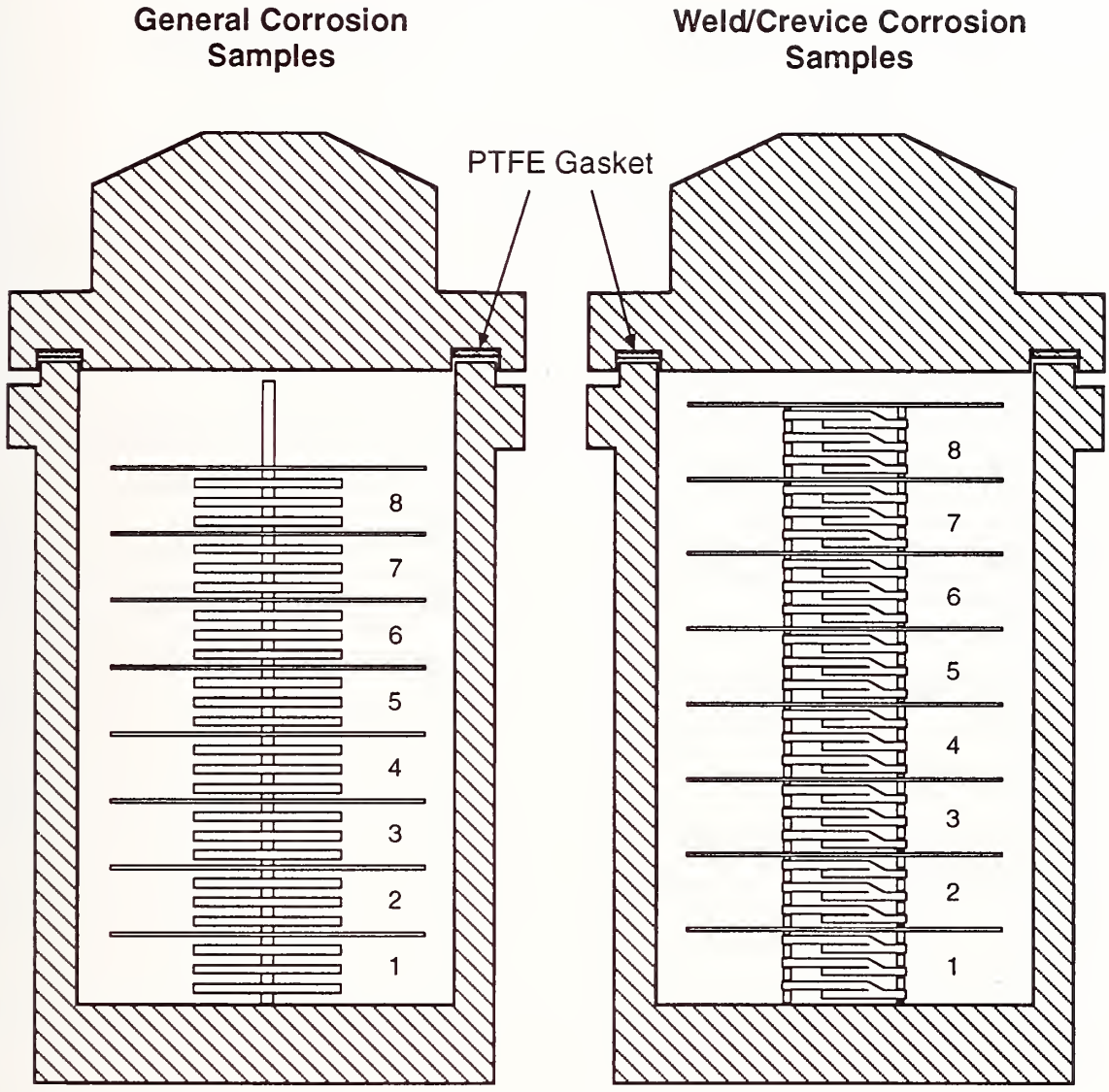

Figure 2. Immersion testing chamber used for general corrosion coupon tests and weld/crevice corrosion coupon tests.

liter pressure vessel for testing. The vessel was then attached to a mechanical vacuum pump and evacuated for a minimum of 30 minutes.

The mass of agent required to produce a pressure of approximately 5.86 MPa at 150 °C was determined by using the mass balance shown in Equation 1:

$$M_T = \rho_1 V_1 + \rho_g V_g \quad (1)$$

where M_T is the total mass of the system, ρ_l is the density of the liquid agent at 20 °C, V_l is the volume of the liquid agent at 20 °C, ρ_g is the density of the vapor phase at 20 °C, and V_g is the volume of the vapor at 20 °C. A computer program based on Equation 1, the available thermodynamic data, and the ideal gas law was developed to calculate the required mass. To facilitate charging of the agents, the test vessels were chilled in a bath of either ice and water, or dry ice and alcohol, depending on the temperature necessary to maintain the liquid phase. The vessels were then placed on a balance that allowed weighing of the entire vessel and determination of the mass of the agent added continuously during filling. Upon completion of the charging step, the vessels were placed in proportionally controlled, calrod-type heaters that kept the temperature constant at 150 ± 1 °C for the 25 day exposure period.

At the conclusion of the testing period, the heaters were turned off and the vessels were allowed to cool naturally to ambient temperature. After the agent was released, the coupons were extracted and immediately re-weighed using the same procedure that was used for the initial weight measurements. The average of those three measurements was then referred to as the final weight of the coupon. Representative photographs of the surfaces were again taken and compared to those of the initial condition.

7.2.1.3 Localized Corrosion (Weld/Crevice Coupon) Exposure Experiments. The samples used for these experiments were designed to provide specific information about changes in the nature of the corrosion in a crevice and in a weld heat affected zone. The geometry of these is shown in Figure 1(b). The testing procedure used for these experiments was identical to the procedure used for the smooth coupon mass change experiments except that the samples were not weighed before and after the exposures.

At the conclusion of the 25 day test period, the samples were removed from the test chambers and the samples were split along the fusion boundary using a water cooled slitting saw. The internal surfaces of the crevice were then analyzed by eye and in an optical microscope. The resulting appearance within the crevice region of the three samples for each agent/alloy combination was then given a numerical rating based on the appearance of the corrosion damage within the crevice region. In addition, the relative performance of each alloy in a given agent was determined by placing all of the samples tested in that agent on a table and making direct (optical) comparisons. Then, the relative corrosivity of the different agents for a given alloy was determined by placing all of the samples of that type of alloy on a table and making direct (optical) comparisons between the damage that resulted in each agent.

7.2.1.4 Environmental Induced Fracture (Slow Strain Rate Tensile Tests). The stress corrosion cracking susceptibilities of the eight alloys in the replacement candidates were evaluated using the slow strain rate (SSR) tensile test technique. This technique was selected because it generates mechanical properties data that reveals any interactions that may have occurred between that alloy and the testing environment within a relatively short time frame.

All of the samples used for these experiments were machined with the tensile axis parallel to the rolling direction of the plate stock (Figure 1(c)) and tested in the "as received" condition. The sample preparation consisted of measurement followed by degreasing in acetone and alcohol. The vessels used for these experiments, Figure 3, were 250 ml volume autoclaves with a similar design to those used for the exposure testing, except that these vessels were modified so that load could be applied to the tensile specimen *in situ* under constantly maintained environmental conditions (5.86 MPa at 150±1 °C). The test vessels were evacuated and charged with agent in the same manner as the exposure test vessels, but due to the number of mechanical tests required per agent, and the reduced capacity of the test vessels, the appropriate mass was based solely on the ideal gas law. This approach was selected over the mass balance because it produced a slightly lower final pressure and the number of moles of the agent was held constant for each test; regardless of the agent used.

The mechanical tests were conducted using a computer controlled slow strain rate testing system which operated at a constant crosshead speed of 0.0254 μm/sec. The computer was configured to sample and record the applied load, the crosshead displacement and the elapsed time at 90 second intervals. After failure, the agent was released, the vessels were allowed to cool to ambient temperature, and the samples were removed from the vessel and stored in a desiccator until analyzed.

The fracture surfaces were cut from the broken SSR samples for analysis. The influence of the agents on the ductility of the alloys was determined from reduction in area (RA) measurements performed on the fracture surfaces with a optical measuring microscope with a $\pm$ 0.5x10^{-6} m resolution. Scanning electron microscopy was performed on selected samples to allow evaluation of the mechanism of crack propagation based on the fracture morphology. The results of these experiments were used to formulate a ranking of the potential for failure by stress corrosion cracking for each of the alloys in a replacement candidate.

7.2.2 Post Deployment Experiments. When a fire suppressant is applied to a fire, the metals in the aircraft engine nacelle or dry bays may become covered with deposits of the fire suppressant or fire suppressant combustion products. As a result, an evaluation of the relative corrosivity of the expected combustion product layers was included in this investigation.

7.2.2.1 Materials and Sample Preparation. The alloys used for these experiments were the same as those used for the aircraft storage and distribution system experiments. These alloys were used because samples were readily available and because this matrix included representative alloys of the different types that might be exposed to fire suppressant combustion products. The samples used were identical to those given in Figure 1(a) except that these samples did not contain the hole in the center. As before, the samples were glass bead blasted to the equivalent of a 120 grit finish. The samples were cleaned in acetone in an ultrasonic cleaner and then treated with acid solutions in an ultrasonic cleaner to remove existing corrosion products and surface films. The acid solutions were rinsed off of the metal surfaces using distilled water. Following is a list of the acid mixtures used for surface cleaning or pretreatment:

- **6061-T6**. The surface was treated by exposing it to concentrated HNO_3 for three minute intervals until the mass loss for this exposure time became constant.

- **CDA-172**. The surface was treated by exposing it to 250 ml of a solution made by adding 25 ml of H_2SO_4 to double distilled water for three minute intervals until the mass loss for this exposure became constant.

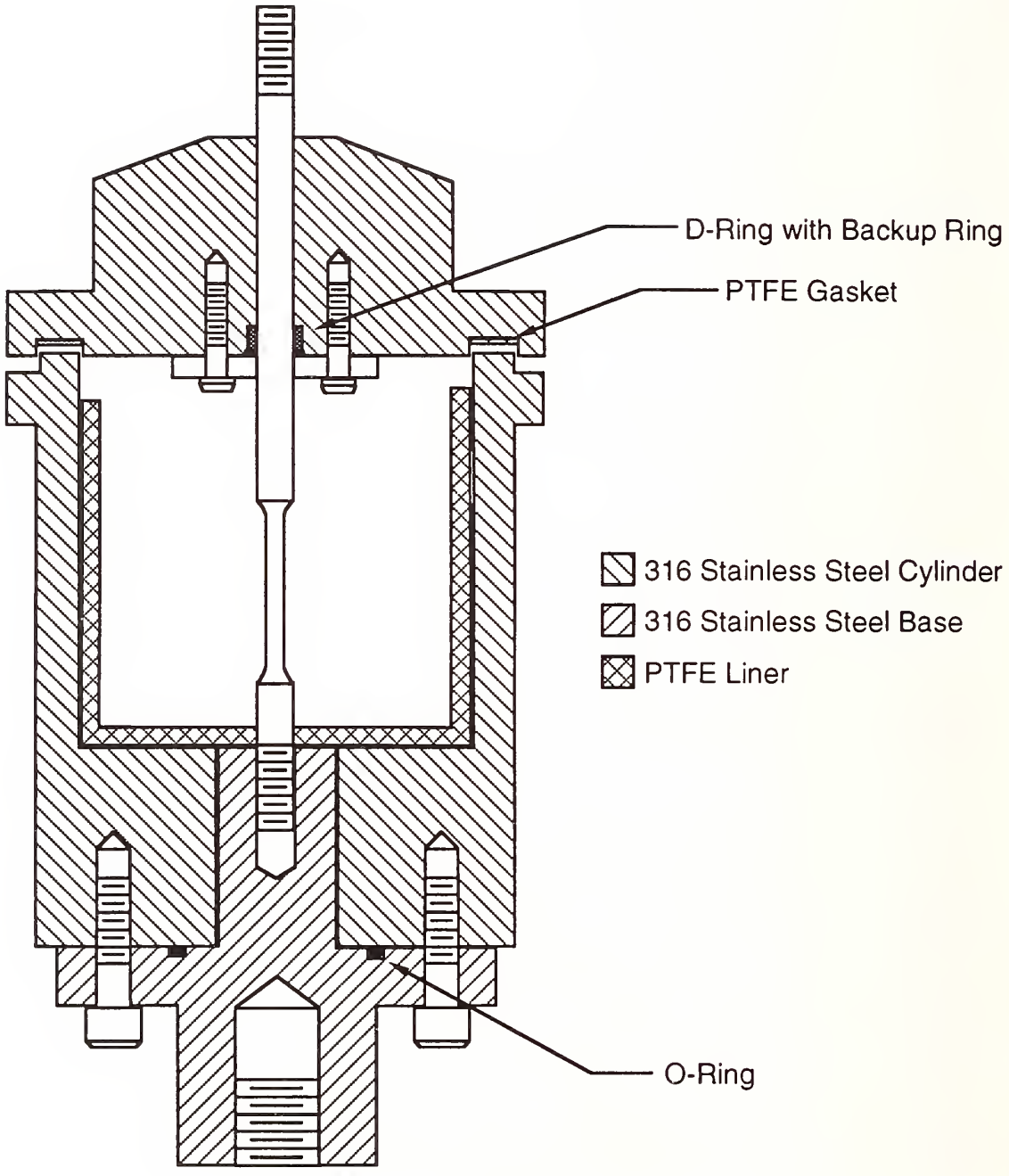

Figure 3. Slow strain rate tensile test chamber.

- **IN 625**. The surface was treated by exposing it to 250 ml of a solution made by adding 37.5 ml of HCl to double distilled water for three minute intervals until the mass loss for this exposure became constant.

- **AISI 4130, AM 355 and 13-8 Mo Steel**. A solution was prepared by adding 80 ml of a 35 weight % solution of 2 butyne 1,4 diol to 60 ml of HCl and then adding double distilled water to make one liter of solution. The AM355 and 13-8 Mo surfaces were exposed to this mixture for three minute intervals until the mass loss for this exposure became constant. The 4130 surface was exposed to this mixture for one minute intervals until the mass loss for this exposure became constant. The 4130 steel became tarnished by the water rinse used to clean the surface.

- **Nitronic 40 and 304 Stainless Steel**. One liter of solution was prepared by adding 100 ml of HNO_3 to 20 ml to double distilled water. The samples were exposed to this mixture for five minute intervals until the mass loss for this exposure became constant.

7.2.2.2 Combustion Product Surface Layer Emulation. The fire suppressant candidates can be classified into two categories: those that contain fluorine and/or other halides and those that contain sodium bicarbonate. Fire suppressants that contain halides, of which fluorine is usually the worst, will produce halide ions during combustion that will deposit on metallic surfaces and form halide acids when they react with water. Sodium bicarbonate ($NaHCO_3$) will decompose on heating to form sodium carbonate (Na_2CO_3), and on combustion to form sodium hydroxide (NaOH). As a result, there are essentially three different combustion product surface films of interest: (1) fluoride ions, (2) $NaHCO_3/Na_2CO_3$ and (3) NaOH.

To produce a surface film rich in fluoride ions, the surface of the samples were first sprayed with ASTM artificial seawater then sprinkled with sodium fluoride (NaF) powder while the surface was still wet. While the films produced by combustion will be much more complex than this simple analog, this surface film should contain the most critical corrosive species that can be expected following deployment: water, chloride and fluoride. The ASTM seawater step was included to simulate the conditions in a marine atmosphere, which should be the worst case situation, as well as to provide water for reaction with the sodium fluoride. To simulate the sodium bicarbonate and sodium carbonate ($NaHCO_3/Na_2CO_3$) surface film, the samples were sprayed with ASTM artificial seawater and sprinkled with a 50/50 mixture of sodium bicarbonate/sodium carbonate. The 50/50 mixture was created by heating 100 g of sodium bicarbonate + 1.5 weight % SiO_2 overnight at 150 °C to form sodium carbonate and then mixing this with another 100 g of sodium bicarbonate + 1.5 weight % SiO_2. To simulate the NaOH rich surface film that may result from the deposition of $NaHCO_3$ combustion products, the samples were sprayed with ASTM artificial seawater and then sprayed with a 0.1 M solution of NaOH. The samples were placed into their exposure chambers immediately following these surface treatments.

7.2.2.3 Exposure Environment. After deployment of a fire suppressant, a layer of combustion products may remain on the exposed surfaces for up to one month before the surfaces are cleaned to remove the surface film. During this time, the environment which will cause corrosion will be the ambient air environment and the hydration of the surface film that may result from absorption of water from the ambient environment (corrosion in condensate droplets as a result of thermal cycling was not included in this study). As a result, the exposures were conducted in three different glass desiccators each with the a different fixed relative humidity (RH). To keep the relative humidity constant, the desiccant in each of the desiccators was replaced with a saturated salt solution which has

a different equilibrium water vapor partial pressure or relative humidity. For a low relative humidity exposure, a saturated solution of potassium acetate ($KC_2H_3O_2$) was included in the desiccator for which the equilibrium relative humidity is 20%. For a moderate relative humidity environment, a saturated sodium dichromate dihydrate ($Na_2Cr_2O_7 \cdot 2H_2O$) solution was used in the desiccator for which the equilibrium relative humidity is 52%. And for a high relative humidity, a saturated solution of sodium sulfate decahydrate ($Na_2SO_4 \cdot 10H_2O$) for which the equilibrium relative humidity is 93% was used.

7.2.2.4 Testing Procedure. The samples of the different alloys were exposed under nine different conditions: three different pretreatments and three different humidities. The samples were weighed between the cleaning and the surface pre-treatment steps. After the application of the ASTM artificial seawater, the samples were weighed again in order to determine the mass present on the surface. Then, after the NaF, 50/50 $NaHCO_3$/Na2CO3 mixture, or the NaOH was applied, the samples were weighed again. Then, the specimens were exposed for 30 days with one of each alloy and pretreatment in each humidity. Following the exposure, the coupons were weighed, then rinsed in double distilled water, dried and reweighed. Finally, the corrosion product films were chemically removed by using the same cleaning procedure used during the sample preparation and the samples were weighed again to determine the total mass loss due to corrosion.

7.2.3 Development of an Electrochemical Measurement Technique. Electrochemical techniques can be used to measure the interfacial properties directly associated with the rate of corrosion. These measurements allow for a relatively fast determination of the corrosion resistance of a metal or alloy in solution as compared to the time required for acquisition of similar data from exposure tests in the same environment. The development of such a technique would provide a more thorough assessment of the corrosion rates of the storage vessel materials in the alternative fire suppressants.

Figure 4 is a schematic representation of the most simple equivalent electrical circuit that can be used to describe the processes that occur in an electrochemical cell. In this figure, R_s represents the resistance between the sample and the measurement point that arises due to the resistivity of the electrolyte, C_{dl} is the capacitance of the sample electrode solution interface and R_{ct} is the charge transfer resistance that arises from the kinetics of the electrochemical reactions occurring at the electrode surface (*e.g.*, corrosion). If R_s is high, as in the case of the extremely high resistivity associated with fire suppressants, significant error or artifacts in the measured interfacial properties can be expected. Therefore, a technique must be developed to either 1) reduce the solution resistivity (without compromising the relative order of corrosivity of the agents) or 2) allow for the correction of the solution resistivity and eliminate the observed artifacts. Experimentally, the best approach for obtaining useful data is done by applying a low amplitude sine wave to the sample and measuring the cell impedance as the frequency of the sine wave is varied. By examining Figure 4, it can be seen that for a low frequency sine wave the impedance of this circuit becomes $R_s + R_{ct}$, while for a high frequency signal the impedance of the circuit becomes just R_s. This technique is known as ac impedance or electrochemical impedance spectroscopy (EIS).

For EIS, one normally uses a potentiostat and three electrode cell, Figure 5. The sample, a reference electrode and a counter electrode make up the three electrodes in this system. This allows for the measurement of the potential of the sample with respect to a reference electrode with a fixed and well known potential on the hydrogen electrode (thermodynamic) scale while applying current with a counter electrode whose potential can vary with current without creating measurement errors. However, as the resistivity of the media increases, problems arise due to the appearance of artifacts which result in considerable measurement errors. Investigators have shown that a two electrode system is more suited for EIS measurements in high resistivity media than a three electrode system

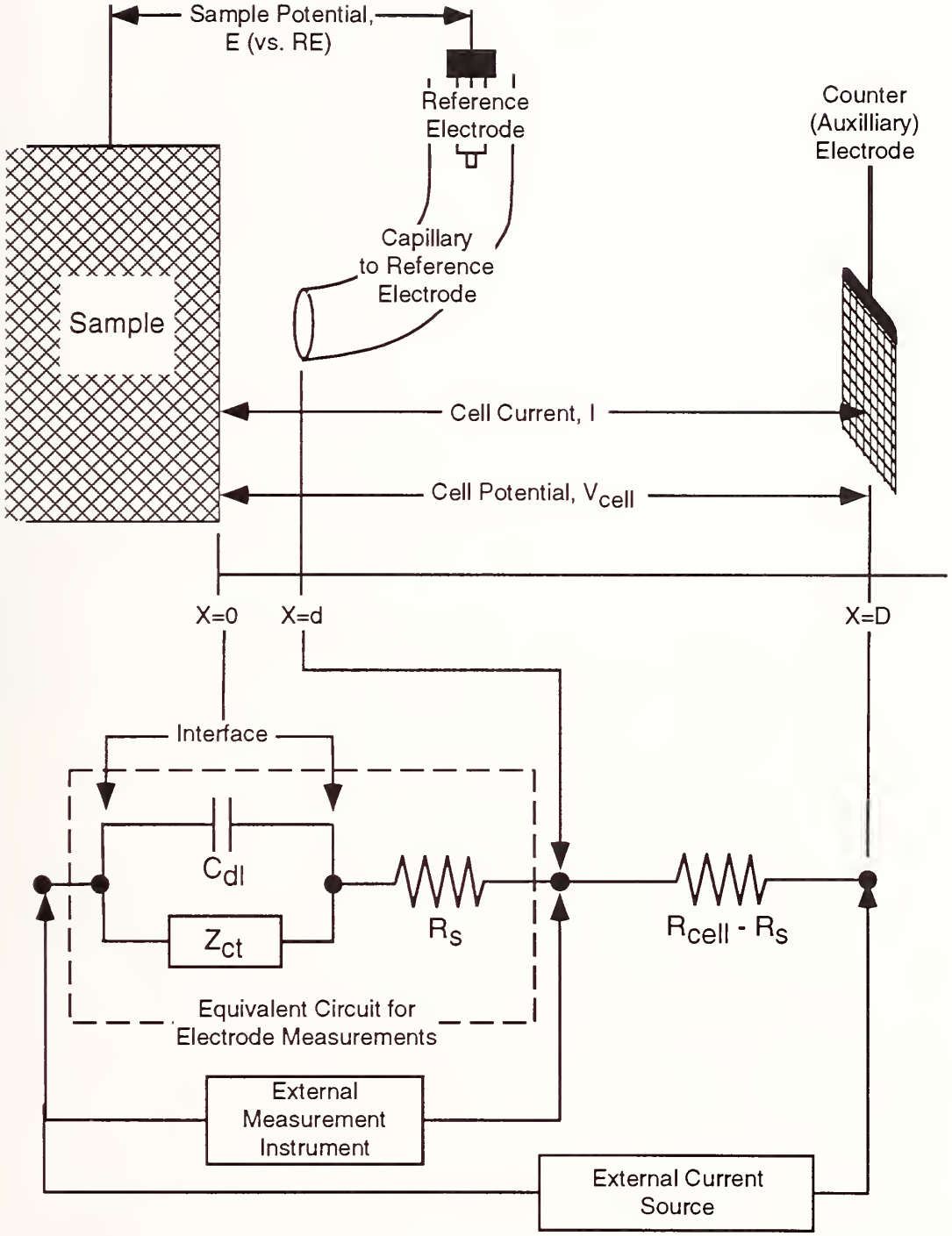

Figure 4. Simple equivalent circuit for an electrochemical interface.

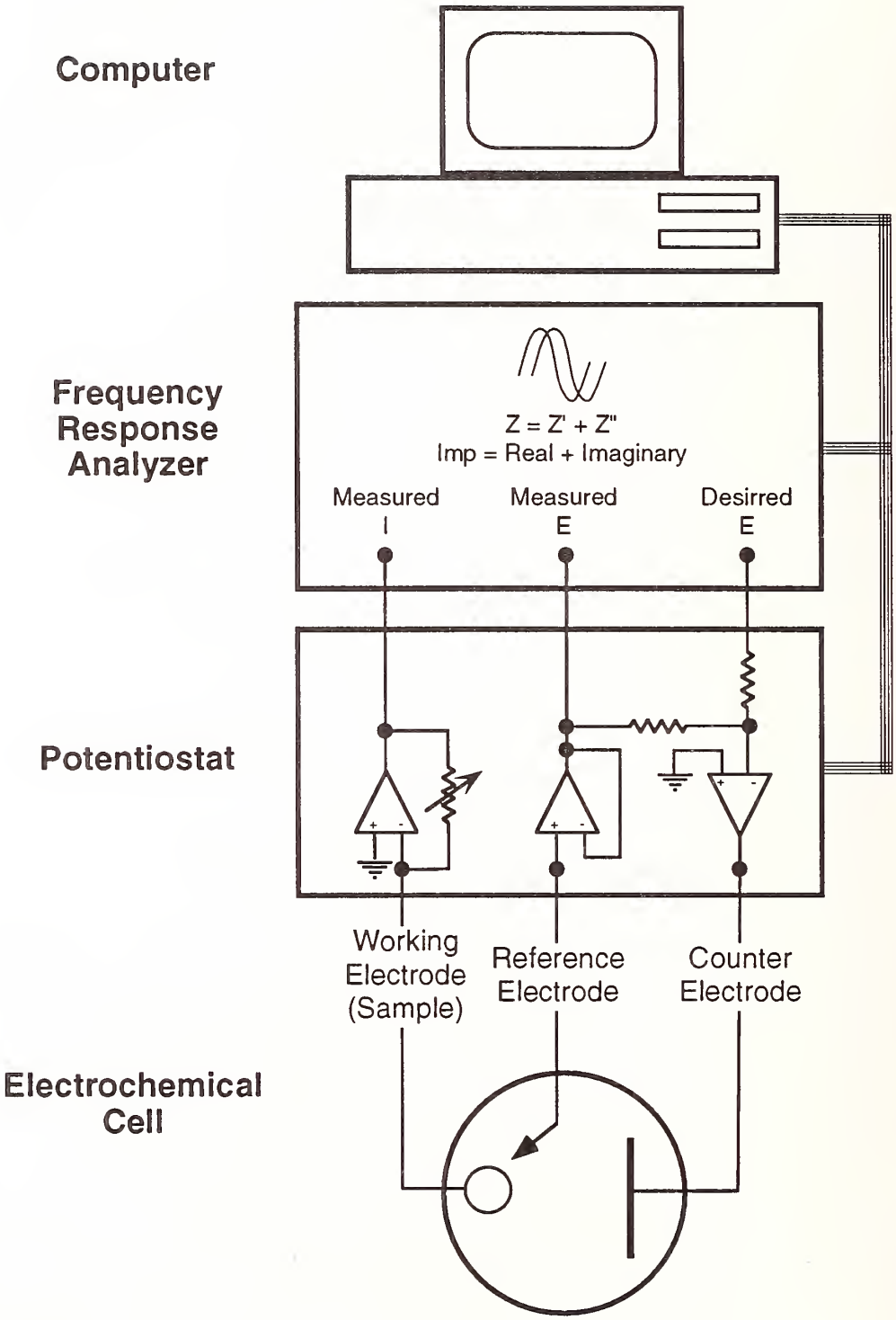

Figure 5. Simple diagram of a three electrode cell used for electrode impedance measurements.

(Halsal, 1992, and DeSouza, 1986). As a result, a two electrode cell capable of placing two relatively large area samples in close proximity and conducting EIS measurements at different temperatures and pressures was designed and fabricated. This cell design is shown schematically in Figure 6 and consists essentially of a autoclave similar to that used for the exposure tests modified by the addition of electrical feed troughs in the head along with a micrometer for adjusting the distance between the samples. Inside the chamber, two identical disk samples are held in place by PTFE holders one of which is moved by the micrometer. To evaluate the functionality of this chamber, measurements were made on samples in an environment similar to that used by the previous investigators (Halsal, 1992, and DeSouza, 1986).

7.2.3.1 Materials. Disk shaped samples 38 mm in diameter and 12.7 mm thick were machined out of 304 stainless steel and polished to a 0.05 μm finish. Before placing the samples into the cell, they were rinsed with reagent anhydrous ethyl alcohol. Anhydrous ethyl alcohol with approximately 0.005 % water and a conductivity on the order of 10^{-6} ohms^{-1} cm^{-1} was used initially for the testing environment because this is similar to the environment used by the previous investigators. It should be remembered that the conductivity of the halon alternatives is orders of magnitude lower than this value. However, results of tests performed in ethyl alcohol should reveal the effectiveness of the cell in measuring electrochemical parameters in low conductivity media. The addition of nonaggressive charge carriers to the fire suppressants may increase their conductivity up to or above this level.

7.2.3.2 Procedure. After the cell was assembled, ethyl alcohol was introduced. The initial separation distance of the electrodes was measured. The impedance of this cell at different frequencies from 65,000 Hz to 0.1 Hz was determine with a 10 mV amplitude signal. From this data, the solution resistance was determined. The separation of the electrodes was increased by 1 mm and another scan was taken. This procedure was repeated until the electrodes were 4 mm from there original position. The electrodes were then reset to their original position and the entire procedure was repeated.

7.3 Results

7.3.1 Aircraft Storage and Distribution System Corrosion.

7.3.1.1 Mass Change (Smooth Sample) Exposure Experiments. The mean mass changes observed for three samples of each of the alloys on exposure to each of the agents for 25 days at 150 °C are given in Table 2, the standard deviation determined for these measurements are given in Table 3 and the original measurements are given in Appendix A. On examination of these tables, it can be seen that all of the mass changes are relatively small and most are mass increases (positive values in Table 2). The mass change rate was estimated from these mass change measurements from the relationship

$$R = \frac{\Delta M}{At} \tag{2}$$

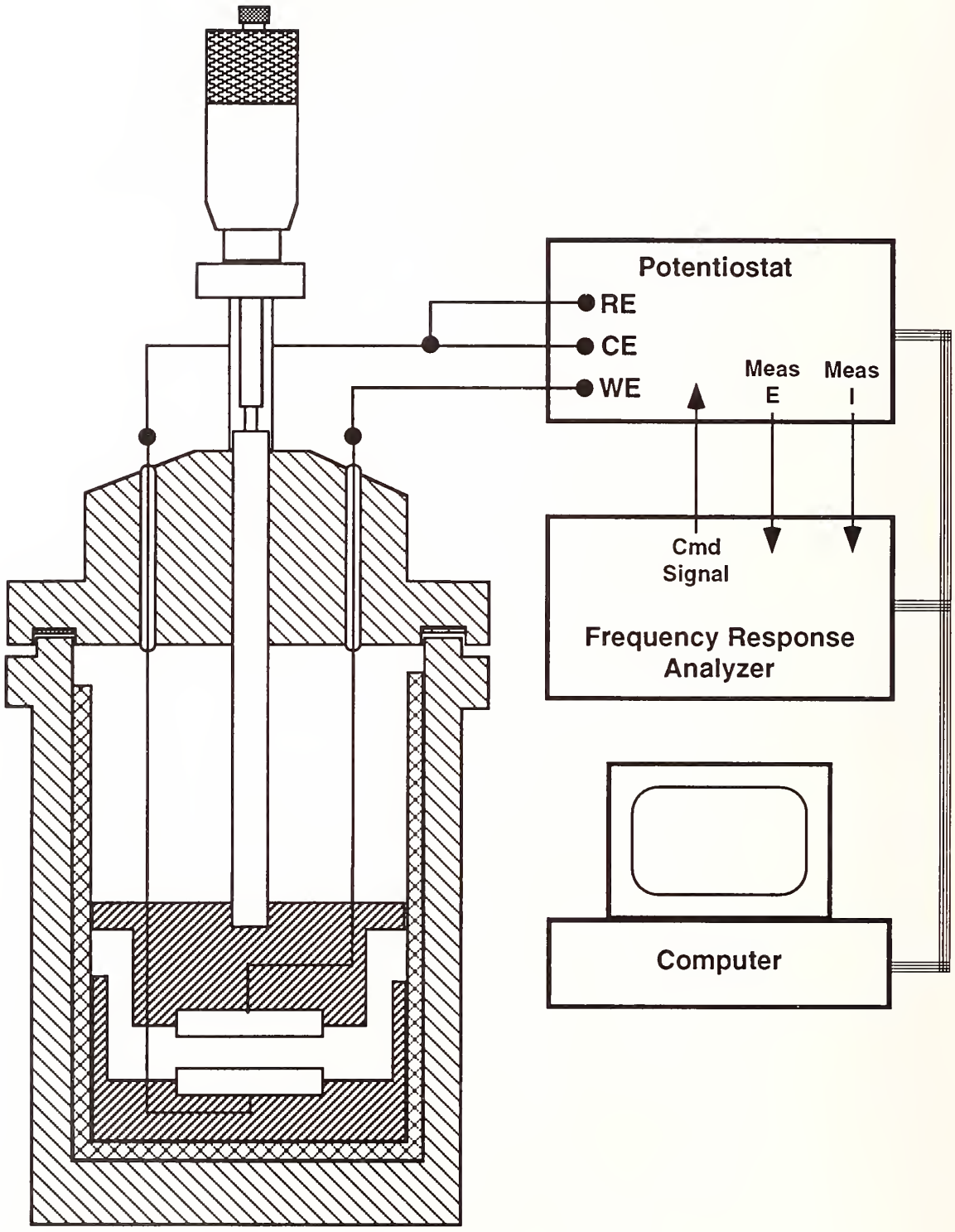

Figure 6. Electrochemical cell for two electrode impedance measurements in low conductivity electrolytes at elevated temperatures and pressures.

Table 2. Mean Mass Change for the three samples of Each Alloy tested in Each Agent After 25 Day Immersion at 150 °C [mg]

Environment	Nit 40	Al 6061	In 625	304 SS	CDA 172	13-8 Steel	AM 355	AISI 4130	Agent Avg.	Std. Dev.
HCFC-22	0.176	0.458	-0.329	0.168	3.064	-0.033	-0.087	2.847	0.783	1.362
HCFC-124	0.092	0.219	-0.267	-0.037	1.474	-0.086	-0.206	0.319	0.189	0.557
FC-31-10	0.247	0.533	-0.037	0.583	2.663	0.357	0.219	1.102	0.708	0.858
HFC-227	0.009	0.128	-0.056	0.141	1.973	0.069	0.007	0.297	0.321	0.676
HFC-125	-0.011	0.199	0.031	0.136	0.890	0.151	0.029	0.673	0.262	0.333
FC-116	0.006	0.240	0.026	0.147	1.509	0.210	0.139	0.403	0.335	0.491
HFC-134a	0.013	0.131	-0.103	0.069	0.229	0.088	-0.014	0.262	0.084	0.122
HFC-236	0.024	2.479	-0.063	0.078	0.866	0.107	0.007	0.343	0.480	0.861
FC-C318	0.008	1.183	0.018	0.199	0.431	0.169	0.006	0.310	0.290	0.392
FC-218	0.153	0.373	0.051	0.090	0.768	0.279	0.150	0.381	0.281	0.232
HFC-32/125	0.300	0.587	0.146	0.241	2.263	0.492	0.311	0.227	1.960	3.851
NaHCO3	0.396	1.038	0.079	0.262	2.182	0.800	0.259	0.890	0.738	0.677
Alloy Avg.	0.118	0.631	-0.042	0.173	1.526	0.217	0.068	1.597		
Std. Dev.	0.137	0.675	0.138	0.152	0.911	0.243	0.150	3.152		

Positive Values = Scaling
Negative Values = Mass Loss

where ΔM is the mass change, A is the total exposed area of the sample and t is the exposure time in days and are given in Table 4. This relationship estimates the average mass change rate over the exposure period and assumes that the mass change rate was essentially constant over the entire exposure period.

The magnitudes of these mass changes (Table 4) are small but, they are, for the most part, larger than that required to be statistically significant for the measurement equipment and measurement techniques employed. Since each sample was weighed three times before and after each exposure, the standard deviation for the mass measurement process can be estimated and it was found to be less than 1.4×10^{-5} g. If one conducts a t-test for the significance of the change in mass based on this estimated standard deviation, one will find t values that indicate significant mass change at the 99% confidence level in all but 20 of the 96 agent/alloy combinations. However, when the mass change measurements over the three samples of each alloy tested in each agent are averaged, a larger standard deviation is determined because this standard deviation includes scatter from the natural corrosion processes and sample handling during preparation and removal from the exposure chamber in addition to the normal measurement scatter. In Table 5, a minimum and maximum mass change rate at the 90% confidence level is given for each alloy/agent combination. The values in this table were determined from the standard deviation estimated from the three samples of each alloy tested in each agent and estimated standard deviations for the surface area and exposure time using standard

Table 3. Standard Deviation of mass change measurements for the three samples of each alloy tested in each environment (mg)

Environment	Nit 40	Al 6061	In 625	304 SS	CDA 172	13-8 Steel	AM 355	AISI 4130	Agent Avg.
HCFC-22	0.079	0.113	0.088	0.057	0.331	0.043	0.050	1.280	0.255
HCFC-124	0.045	0.091	0.048	0.040	0.294	0.072	0.103	0.099	0.099
FC-31-10	0.040	0.079	0.028	0.035	0.107	0.070	0.046	0.173	0.072
HFC-227	0.034	0.043	0.018	0.025	0.159	0.063	0.020	0.047	0.051
HFC-125	0.121	0.117	0.044	0.013	0.018	0.014	0.007	0.091	0.053
FC-116	0.124	0.087	0.025	0.033	0.157	0.012	0.063	0.013	0.064
HFC-134a	0.021	0.025	0.024	0.002	0.039	0.061	0.048	0.091	0.039
HFC-236	0.024	1.895	0.030	0.030	0.028	0.015	0.090	0.043	0.269
FC-C318	0.040	0.602	0.065	0.054	0.072	0.014	0.109	0.035	0.124
FC-218	0.083	0.048	0.011	0.050	0.032	0.021	0.044	0.080	0.046
HFC-32/125	0.033	0.324	0.022	0.037	0.217	0.140	0.035	0.122	0.116
NaHCO3	0.297	0.501	0.022	0.047	0.235	0.263	0.042	0.168	0.197
Alloy Avg.	0.078	0.327	0.035	0.035	0.141	0.066	0.055	0.187	

error propagation techniques (Bevington, 1969). Many of these ranges include zero which indicates that we cannot conclude at this level of confidence that the corrosion rate is a value other than zero. On the other hand, scale formation and spalling off of this scale will increase measurement scatter which could result in an estimated mass change rate range that includes zero. As a result, each agent/alloy combination was given a numerical rating based on the absolute value of the maximum or minimum indicated mass change rate in Table 4 rather than on the mean mass change rate. Table 6 gives the absolute mass change rate range for each numerical rating and the equivalent penetration rate for each alloy for mass loss at the maximum rate for the range, while Table 7 gives the score for each agent/alloy combination. Because on cannot determine the amount of metal reacting for mass increases without information on the chemical composition of the scale, mass increases and decreases were given the same weighting for this analysis. It is believed that this rating basis will result in conservative scores for each agent/alloy combination especially since scale formation usually results in a corrosion rate that decreases with time as the scale inhibits mass transport.

Visual examination confirmed the presence of surface films on many of the samples. These films were very thin and could be detected by a color change in the samples. For these exposures, the films may be the result of reaction with residual gasses, decomposition products or the agents themselves. The formation of salt films when metal are exposed to organic solvents has been observed by other investigators. Mass increases are not uncommon during immersion testing and usually descalling techniques are employed to removed these scales for the determination of the remaining metal. Considerable research has been conducted into the development of techniques for the removal of the scales which form in aqueous solutions without attacking the underlying metal. Even with this

Table 4. Mean Mass Change Rate for Each Alloy in Each Agent for 25 Day Immersion at 150 °C [mg/(square meter•day)

Environment	Nit 40	Al 6061	In 625	304 SS	CDA 172	13-8 Steel	AM 355	AISI 4130	Agent Avg.	Std. Dev.
HCFC-22	2.512	6.550	-4.706	2.401	43.847	-0.477	-1.240	40.731	11.202	19.481
HCFC-124	1.320	3.132	-3.816	-0.525	21.097	-1.224	-2.941	4.563	2.701	7.965
FC-31-10	3.529	7.631	-0.525	8.346	38.108	5.103	3.132	15.771	10.137	12.278
HFC-227	0.127	1.828	-0.795	2.019	28.235	0.986	0.095	4.245	4.593	9.677
HFC-125	-0.159	2.846	0.445	1.940	12.734	2.162	0.413	9.634	3.752	4.770
FC-116	0.079	3.434	0.366	2.099	21.589	3.005	1.987	5.771	4.791	7.021
HFC-134a	0.191	1.876	-1.479	0.986	3.275	1.256	-0.207	3.752	1.206	1.752
HFC-236	0.350	35.468	-0.906	1.113	12.385	1.526	0.095	4.912	6.868	12.321
FC-C318	0.111	16.931	0.254	2.846	6.168	2.416	0.079	4.436	4.155	5.610
FC-218	2.194	5.342	0.731	1.288	10.986	3.990	2.146	5.453	4.016	3.326
HFC-32/125	4.292	8.394	2.083	3.450	32.384	7.043	4.451	3.243	28.040	55.097
NaHCO3	5.660	14.849	1.129	3.752	31.224	11.447	3.704	12.734	10.562	9.690
Alloy Avg.	1.684	9.023	-0.601	2.476	21.836	3.103	0.976	22.852		
Std. Dev.	1.953	9.652	1.973	2.181	13.039	3.480	2.151	45.098		

Positive Values = Scaling
Negative Values = Mass Loss

research, these techniques usually remove some unreacted metal or leave scales of their own which induce an error in this mass measurement. Normally, this mass error is small and insignificant compared to the mass of the scale being removed but, the films on the samples in this study are very thin and the composition could be very different from that formed in aqueous solutions. As a result, descalling was not attempted as a means of estimating the thickness of the scales.

Evaluation of the relative performance of the alloy/agent combinations was hampered by the comparison of mass loss and mass gain measurements. Typically, mass loss measurements are evaluated by assuming that all of the lost mass was the result of corrosion and that no corrosion products were left on the surface to create errors in this determination. Then, the quantity of metal reacting and rate of the reactions can be calculated directly from the mass loss. Similarly, mass gain measurements can be evaluated if the reaction and the reaction products are known and it is assumed that none of the scale spalls off and is lost to the environment. However, when these are not known, evaluation contains greater uncertainties, but it is clear that the relative magnitude of mass change is still related to the reaction rate between the metallic species and the environment.

7.3.1.2 Localized Corrosion (Crevice/Weld Coupon) Exposure Experiments. The weld/crevice coupons were cut open and the corrosion damage in the crevice region was examined. Based on these examinations, the results of these experiments were evaluated in three different ways. First, the type of damage observed for each alloy/environment combinations was categorized into one of five different categories based on the appearance of the overlap region: (1) no visible evidence of attack, (2) light discoloration of surface, (3) moderate discoloration with slight attack visible, (4) substantial discoloration and some attack visible, and (5) attack throughout the overlap region.

Table 5. Maximum and minimum estimated mass change rate at 90% confidence level based on the three measurements for each alloy/agent combination and standard statistical error estimation techniques (mg((m^2•day))

Environment	Nit 40	Al 6061	In 625	304 SS	CDA 172	13-8 Steel	AM 355	AISI 4130
HCFC-22	4.418	9.290	-2.587	3.770	51.856	0.570	-0.037	71.660
	0.606	3.810	-6.825	1.031	35.837	-1.524	-2.443	9.801
HCFC-124	2.416	5.325	-2.654	0.452	28.206	0.511	-0.444	6.955
	0.223	0.939	-4.977	-1.501	13.987	-2.959	-5.438	2.171
FC-31-10	4.506	9.530	0.163	9.199	40.691	6.795	4.231	19.957
	2.553	5.732	-1.213	7.494	35.524	3.412	2.033	11.584
HFC-227	0.942	2.867	-0.351	2.613	32.087	2.506	0.585	5.387
	-0.687	0.790	-1.238	1.425	24.383	-0.535	-0.394	3.103
HFC-125	2.758	5.661	1.518	2.265	13.162	2.497	0.581	11.824
	-3.076	0.030	-0.627	1.614	12.306	1.827	0.246	7.445
FC-116	3.068	5.532	0.959	2.892	25.389	3.295	3.499	6.094
	-2.909	1.335	-0.228	1.305	17.790	2.714	0.476	5.448
HFC-134a	0.694	2.480	-0.898	1.032	4.219	2.724	0.944	5.945
	-0.312	1.271	-2.059	0.939	2.331	-0.212	-1.358	1.559
HFC-236	0.932	81.249	-0.190	1.835	13.070	1.877	2.276	5.960
	-0.233	-10.312	-1.622	0.391	11.699	1.175	-2.085	3.865
FC-C318	1.072	31.476	1.835	4.155	7.900	2.752	2.709	5.288
	-0.849	2.387	-1.326	1.536	4.437	2.081	-2.550	3.583
FC-218	4.188	6.503	0.990	2.490	11.752	4.508	3.202	7.375
	0.200	4.180	0.472	0.085	10.219	3.473	1.090	3.531
HFC-32/125	5.098	16.217	2.619	4.348	37.627	10.416	5.305	6.183
	3.487	0.571	1.546	2.552	27.141	3.670	3.598	0.303
NaHCO3	12.843	26.941	1.653	4.880	36.903	17.800	4.711	16.800
	-1.524	2.757	0.605	2.623	25.544	5.094	2.697	8.669

Table 8 gives the results of this analysis, and the only alloy to show category five attack was the 4130 steel which received a five rating in HCFC-22 and HCFC-124. This table also gives the average rating for each agent and ranking of the agents based on this average rating. The lowest rated agents on this basis were HCFC-22 (agent average=3.143), sodium bicarbonate (agent average=3.125), and

Table 6. Mass Change Rate Values Used in Rating Alloy/Agent Behavior in Mass Change Measurements and equivalent penetration rate based on alloy nominal density

Score	Mass Chg Rate mg/(m^2•d)		Equivalent Penetration Rate for Upper Boundary μm/year							
	Lower Bound	Upper Bound	Nit 40	Al 6061	In 625	304 SS	CDA 172	13-8 Steel	AM 355	AISI 4130
1	0	0.1487	0.0069	0.0201	0.0064	0.0068	0.0066	0.0070	0.0069	0.0069
2	0.1487	0.923	0.0431	0.1249	0.0399	0.0425	0.0410	0.0434	0.0426	0.0429
3	0.923	5.00	0.2332	0.6764	0.2164	0.2300	0.2219	0.2353	0.2309	0.2326
4	5.00	25.00	1.166	3.382	1.082	1.150	1.109	1.177	1.154	1.163
5	25.00	125	5.831	16.909	5.409	5.750	5.547	5.883	5.772	5.816
6	125	600	27.99	81.16	25.96	27.60	26.63	28.24	27.70	27.92
7	600	3,000	139.9	405.8	129.8	138.0	133.1	141.2	138.5	139.6
8	3,000	15,000	699.7	2029.1	649.1	690.0	665.7	706.0	692.6	697.9
9	15,000	75,000	3498	10146	3246	3450	3328	3530	3463	3490
10	75,000	∞	∞	∞	∞	∞	∞	∞	∞	∞

(Rating is based on absolute value of mass change rate and penetration rate is only valid for mass loss.)

HFC-227 (agent average=2.750). The best rated agents by this technique were HFC-236 (agent average=1.750), FC-31-10 (agent average=1.875), and HFC-134a (agent average=2.0). However, one should keep in mind that agent averages can be adversely influenced by a single rating, when in service, that specific alloy/agent combination could be avoided and the agent would serve satisfactorily. On this basis, only five of the twelve agents did not have an alloy where no evidence of attack was observed (a one rating) and all of the agents had at least three alloys where only slight discoloration was observed (a two rating). As a result, the crevice/weld immersion experiments show that while there is a clear difference in the corrosivity of the agents, it should be possible to find container alloys for each of the candidates.

While a visual rating of the appearance is a fair estimate of the relative corrosivity of each agent, there are numerous cases where several alloy/agent combinations received the same rating and there is no indication of which agent was more or less corrosive for a specific alloy. As a result, all of the weld/crevice samples of each alloy were compared to each other and the agents were ranked based on the appearance of the corrosion damage in the crevice region for each alloy. Each agent was given a score between one and twelve for each alloy where one showed less evidence of corrosion damage than two and so forth. This analysis allows the identification of the least corrosive agent for each alloy and the results are given in Table 9. The data in this table indicates the same general trend as Table 8 with the low ranking agents in Table 8 receiving most of the lower rankings; but since there is no relationship between the scores from one agent to another (*e.g.*, an eight for one agent/alloy combination may have less attack than a much lower rating for another combination), this table should

Table 7. Mass Loss Rate Evaluation of Agents and Alloys based on 25 Day Immersion at 150 °C

Environment	Nit 40	Al 6061	In 625	304 SS	CDA 172	13-8 Steel	AM 355	AISI 4130	Agent Avg.	Std. Dev.	Agent Rank
HCFC-22	3	4	3	3	5	2	3	5	3.50	1.07	9
HCFC-124	3	3	3	2	4	3	3	3	3.00	0.53	7
FC-31-10	3	4	2	4	5	4	3	4	3.63	0.92	11
HFC-227	1	3	2	3	5	3	1	3	2.63	1.30	1
HFC-125	2	3	2	3	4	3	2	4	2.88	0.83	4
FC-116	1	3	2	3	4	3	3	4	2.88	0.99	4
HFC-134a	2	3	3	3	3	3	2	3	2.75	0.46	3
HFC-236	2	5	2	3	4	3	1	3	2.88	1.25	4
FC-C318	1	4	2	3	4	3	1	3	2.63	1.19	1
FC-218	3	4	2	3	4	3	3	4	3.25	0.71	8
HFC-32/125	3	4	3	3	5	4	3	3	3.50	0.76	9
NaHCO3	4	4	3	3	5	4	3	4	3.75	0.71	12
Alloy Avg.	2.33	3.67	2.42	3.00	4.33	3.17	2.33	3.58			
Std. Dev.	0.98	0.65	0.51	0.43	0.65	0.58	0.89	0.67			
Alloy Rank	1	7	3	4	8	5	1	6			

Score	Freq.	
1	6	No evidence of attack ($t<0.741$, 50% CI).
2	14	Some inconclusive evidence of attack (0.741(50% CI) $< t <$ 4.6 (99% CI)).
3	47	Conclusive evidence of attack ($t>4.6$, 99% CI).
4	22	Corrosion of little concern, (less than ≈ 1 μm/year, 3μm for Al alloy).
5	7	Corrosion may be a concern
6	0	Corrosion rate should be considered in design
7	0	Corrosion about 1 to 5 mils per year
8	0	Rapid Corrosion
9	0	Very rapid corrosion
10	0	Extremely rapid corrosion

only be used for identifying the relative corrosivity of each agent to a specific alloy. However, it is worthy of note that sodium bicarbonate ($NaHCO_3$) received a twelve rating for half of the alloys and a ten or higher rating for six of the eight alloys.

Perhaps a more valuable comparison would be a comparison of the performance of the alloy in a given agent, Table 10. As with Table 9, this ranking was developed by a side by side comparison of the crevice/weld region of the samples only this time the different alloys tested in the same agent were compared. This ranking allows for identification of the alloy which is more resistant to attack in the crevice and weld heat affected zone by each agent. Again, a low rating in one alloy/environment combination may be considerably better than a higher rating in another combination

Table 8. Weld/Crevice Coupon Visual Classification of Attack After 25 Day Immersion at 150 °C

Environment	Nit 40	Al 6061	In 625	304 SS	CDA 172	13-8 Steel	AM 355	AISI 4130	Agent Avg.	Std. Dev.	Agent Rank
HCFC-22	2	2	2	3	4	3	3	5	3.14	1.07	12
HCFC-124	2	2	1	2	3	3	3	5	2.63	1.19	8
FC-31-10	1	1	2	2	2	2	2	3	1.88	0.64	2
HFC-227	2	2	2	3	3	3	3	4	2.75	0.71	10
HFC-125	2	2	2	2	3	2	3	2	2.25	0.46	5
FC-116	2	2	1	2	2	3	2	3	2.13	0.64	4
HFC-134a	1	1	1	2	2	3	4	2	2.00	1.07	3
HFC-236	2	2	1	1	2	2	2	2	1.75	0.46	1
FC-C318	2	3	2	2	2	2	2	4	2.38	0.74	6
FC-218	3	4	2	2	2	2	2	4	2.63	0.92	8
HFC-32/125	3	2	1	2	2	2	3	4	2.38	0.92	6
NaHCO3	2	3	2	2	4	4	4	4	3.13	0.99	11
Alloy Avg.	2.00	2.17	1.58	2.08	2.58	2.58	2.75	3.50	2.42		
Std. Dev.	0.60	0.83	0.51	0.51	0.79	0.67	0.75	1.09	0.45		
Alloy Rank	2	4	1	3	5	5	7	8	0.45		

Classification Criteria
1=No visible staining
2=Light Staining in overlap region
3=Moderate staining with slight attack visible in overlap region.
4=Substantial staining with moderate attack in overlap region.
5=Heavy attack throughout overlap region.

so comparisons between environments should not be done with this data, but this tabulates the results of a direct visual comparison of the different alloy's performance in each agent.

7.3.1.3 Environmental Induced Fracture Experiments (Slow Strain Rate Tensile Tests). Slow strain rate tensile tests result in three parameters that can be used as an indicator of environmental induced fracture. First, the ultimate tensile strength (UTS) is a measure of the fracture strength of the sample and it is determined from the maximum load observed during the tensile test according to the relationship:

$$UTS = \frac{P_{max}}{A_o} \tag{3}$$

where P_{max} is the maximum load supported by the sample during the test and A_0 is the initial cross-sectional area of the gage section of the sample. Environmental interactions that lower the strength of the sample either by corrosion, cracking or other interaction will result in a change in this parameter. Environments can also interact with deformation occurring at surfaces and at crack tips in the sample to limit ductility and cause cracking. So, a second indicator of environmental induced fracture is total strain to cause failure (ϵ_f) which is determined from the relationship

$$\epsilon_f = \frac{\ell_f - \ell_o}{\ell_o} \tag{4}$$

Table 9. Weld/Crevice Coupon Visual Ranking of Agents for Each Alloy After 25 Day Immersion at 150 °C

Environment	Nit 40	Al 6061	In 625	304 SS	CDA 172	13-8 Steel	AM 355	AISI 4130	Agent Avg.	Std. Dev.
HCFC-22	4	4	7	12	11	9	9	11	8.38	3.11
HCFC-124	3	3	3	8	10	7	8	12	6.75	3.45
FC-31-10	1	1	6	4	1	2	3	5	2.88	1.96
HFC-227	8	7	8	11	9	8	5	7	7.88	1.73
HFC-125	5	5	9	7	8	5	10	4	6.63	2.20
FC-116	7	6	4	9	4	11	4	2	5.88	3.00
HFC-134a	2	2	2	10	7	10	11	1	5.63	4.31
HFC-236	6	9	5	1	2	6	6	3	4.75	2.60
FC-C318	9	11	10	3	6	3	1	9	6.50	3.78
FC-218	11	12	11	2	5	1	2	8	6.50	4.57
HFC-32/125	12	8	1	5	3	4	7	10	6.25	3.69
NaHCO3	10	10	12	6	12	12	12	6	10.00	2.62

1 = Best Performance

where l_f is the total change in sample length during the experiment and l_o is the initial gage length. This value includes the elastic and plastic strains required to cause failure. Another means for measuring the ductility of the sample is the reduction in area (RA) which is a third means for indicating environmentally induced fracture. The RA is determined by measuring the area of the fracture surface after the test is completed and the relationship

$$RA = \frac{A_f - A_o}{A_o} \tag{5}$$

where A_f is the cross sectional area of the fracture surface and A_o is the initial gage section cross sectional area. This measurement includes only the plastic deformation required to cause failure and for some alloys is a better measure of environmental interactions than the strain to failure. Typically, these parameters are analyzed by forming a ratio of the value observed in the environment to observed in a reference environment (usually an inert environment). Another approach to analysis is to estimate the statistical significance of the difference between the mean determined for the parameter in the inert reference environment and the mean determined for the agent. The significance of this difference is determined by dividing the difference in the means by the standard deviation estimated for that parameter for that specific alloy and temperature in this type of test.

Table 10. Weld/Crevice Coupon Visual Ranking of Alloys for Each Agent After 25 Day Immersion at 150 °C

Environment	Nit 40	Al 6061	In 625	304 SS	CDA 172	13-8 Steel	AM 355	AISI 4130
HCFC-22	1	2	3	4	7	5	6	8
HCFC-124	3	2	1	4	7	5	6	8
FC-31-10	2	1	3	4	5	6	7	8
HFC-227	3	1	2	4	6	7	5	8
HFC-125	3	4	2	1	7	5	8	6
FC-116	2	3	1	4	6	8	5	7
HFC-134a	2	3	1	4	6	7	8	5
HFC-236	4	3	1	2	5	7	6	8
FC-C318	2	7	3	1	6	5	4	8
FC-218	4	7	2	1	6	3	5	8
HFC-32/125	6	3	1	2	4	5	7	8
NaHCO3	2	4	3	1	8	5	6	7
Alloy Avg.	2.83	3.33	1.92	2.67	6.08	5.67	6.08	7.42
Std. Dev.	1.34	1.97	0.90	1.44	1.08	1.37	1.24	1.00

1 = Best Performance

Tables 11 and 12 gives the average UTS determined for each alloy in air at room temperature, argon at 150 °C, and each agent at 150 °C. The ratio of the average UTS in each agent to the average UTS in Ar at the same temperature is given in Table 13. In this table, it can be seen that for 87 of the 96 agent alloy combinations the UTS ratio is $1.00 \pm .05$. For the nine outside this range, two have a higher average UTS in the agent than in Ar. Of the seven with a lower average UTS in the agent, only two is more than 10% below the value determined in Ar: 304 and 4130 steel in FC-C318. Table 14 gives the results of an estimate of the significance of the differences. A significant decrease in the average UTS may be an indication of cracking, but it could also be due to corrosion reactions reducing effective cross-section or a flaw in the sample. An increase in the average UTS is unusual and this indicates that sample/environment interactions are inhibiting deformation and fracture, but it could also indicate a interference between the corrosion products being generated on the sample and the seal of the autoclave through which the sample must slide. The most important point is that no agent caused significant changes in all alloys indicating that materials for the containment and reliable distribution of any of these candidates can be identified.

The ductility results for the SSR tests are given in Tables 15-20. Table 15 gives the average strain to failure for each alloy/environment combination, laboratory air at room temperature and Ar at 150 °C. Table 16 gives the ratio of the average strain to failure for each alloy in each environment to that observed in the same alloy in Ar at the same temperature and Table 17 gives the statistical

Table 11. Average Ultimate Tensile Strength in Each Agent at 150 °C as Compared to Ar at 150 °C and Air at 25 °C (MPa)

Environment	Nit 40	Al 6061	In 625	304 SS	CDA 172	13-8 Steel	AM 355	AISI 4130
Air, 25 °C	727	341	957	773	763	1117	1005	673
Ar, 150 °C	610	240	927	667	874	1136	969	647
HCFC-22	602	232	892	674	855	1155	938	624
HCFC-124	624	235	937	648	860	1027	945	665
FC-31-10	619	235	910	649	841	1176	935	673
HFC-227	610	235	911	667	865	1156	928	650
HFC-125	611	235	924	650	847	1154	917	669
FC-116	599	221	880	638	830	1163	922	629
HFC-134a	618	225	932	653	851	1144	929	688
HFC-236	612	245	930	633	861	1168	935	648
FC-C318	597	289	924	550	851	1182	950	558
FC-218	624	235	944	681	842	1170	928	663
HFC-32/125	624	225	886	622	843	1138	919	631
NaHCO3	623	252	947	643	852	1217	953	674
Alloy Avg.	614	239	918	642	850	1154	933	648
Std. Dev*.	16	16	22	37	22	44	15	35

Alloy Avg. Average of the means determine for each of the agents.
Std. Dev.* The "Alloy Standard Deviation" was estimated from the Ar at 150 °C tests

analysis of the significance of this difference. In Table 16, it can be seen that measured strain to failure increased for most of the alloy/environment combinations indicating the deformation was easier in these environments than in Ar. Environmentally induced cracking, or stress corrosion cracking (SCC), is usually indicated by a reduction in ductility. Of the 96 alloy environment combinations, the strains to failure of three of the alloy/environment combinations were more than 10% less than that observed in Ar: Nit 40 in HCFC-124 (0.87), Nit 40 in FC-31-10 (0.88), and Nit 40 in HFC-236 (0.88). However, these strain to failure measurements are based on load frame displacement measurements taken by a transducer outside of the autoclave during the experiment. As a result, the reduction in area measurements which are based on measurement of the fracture surface are in an optical microscope after the experiment are a more reliable indication of changes in ductility. Table 18 presents this data for each alloy in laboratory air at 25 °C, Ar gas at 150 °C and each agent at 150 °C. Table 19 gives the ratio of the average reduction in area measured for each alloy/agent combination to Ar at 150 °C and the statistical significance of this difference is given in Table 20. In Table 19, it can be seen that the reduction in area is reduced by more than 5% in 11 of

Table 12. Average Ultimate Tensile Strength in Each Agent at 150 °C as Compared to Ar at 150 °C and Air at 25 °C (ksi)

Environment	Nit 40	Al 6061	In 625	304 SS	CDA 172	13-8 Steel	AM 355	AISI 4130
Air, 25°C	105.4	49.4	138.8	112.1	110.7	162.0	145.7	97.6
Ar, 150°C	88.5	34.8	134.4	96.7	126.7	164.7	140.5	93.8
HCFC-22	87.3	33.6	129.4	97.7	123.9	167.5	136.0	90.4
HCFC-124	90.5	34.1	135.9	93.9	124.8	149.0	137.1	96.4
FC-31-10	89.7	34.1	131.9	94.2	122.0	170.6	135.7	97.7
HFC-227	88.5	34.0	132.2	96.7	125.4	167.6	134.6	94.3
HFC-125	88.6	34.1	134.0	94.3	122.9	167.4	133.0	97.0
FC-116	86.9	32.1	127.6	92.5	120.3	168.6	133.7	91.2
HFC-134a	89.7	32.6	135.2	94.7	123.4	165.9	134.7	99.8
HFC-236	88.8	35.5	134.9	91.8	124.8	169.5	135.6	94.0
FC-C318	86.6	41.9	134.1	79.8	123.4	171.4	137.8	80.9
FC-218	90.5	34.1	136.9	98.8	122.1	169.6	134.5	96.1
HFC-32/125	90.5	32.6	128.4	90.2	122.2	165.0	133.2	91.5
NaHCO3	90.3	36.5	137.4	93.3	123.6	176.5	138.1	97.8
Alloy Avg.	89.0	34.6	133.2	93.2	123.2	167.4	135.3	93.9
Std. Dev.*	2.3	2.3	3.2	5.3	3.2	6.4	2.2	5.1

Alloy Avg. = Average of the means determine for each of the agents.
Std. Dev.* = The "Alloy Standard Deviation" was estimated from the Ar at 150°C tests

the 96 alloy/agent combinations and is reduced by more than 10% in only four alloy/agent combinations: Al 6061 in HCFC-124 (0.85), Al 6061 in $NaHCO_3$ (0.83), SS 304 in $NaHCO_3$ (0.83), and AISI 4130 in $NaHCO_3$ (0.87). Since three of these five are with the same agent, $NaHCO_3$, this agent may have problems with this failure mode.

To summarize the results of the SSR tensile tests, Table 21 was assembled by taking the highest (worst) score received by each agent/alloy combination in Tables 14, 17, and 20 (UTS, strain to failure and RA) and assigning a number to each agent/alloy combination. Since the agent/alloy scores given in these tables are the absolute value of the difference between the mean for the alloy in the agent and Ar divided by the standard deviation for this alloy and parameter at 150 °C, this rating is a measure of the significance of any postulated environmental influence on the deformation and fracture of the agent/alloy combinations. If the maximum deviation was less than one standard deviation, the agent/alloy combination was assigned a value of one, if it was greater than one standard deviation, but less than two, it was assigned a two and so on. In Table 21, it can be seen that 65 of the 96 agent/alloy combinations received a one or two rating. Every agent had at least one alloy with a one rating and only two agents had only one alloy with a rating of one.

Table 13. Average Ultimate Tensile Strength Ratios [(Mean for Envir.)/(Mean for Hot Ar)]

Environment	Nit 40	Al 6061	In 625	304 SS	CDA	13-8 Steel	AM355 SS	AISI 4130	Agent Avg.
HCFC-22	0.99	0.97	0.96	1.01	0.98	1.02	0.97	0.96	0.96
HCFC-124	1.02	0.98	1.01	0.97	0.98	0.90	0.98	1.03	0.98
FC-31-10	1.01	0.98	0.98	0.97	0.96	1.04	0.97	1.04	0.99
HFC-227	1.00	0.98	0.98	1.00	0.99	1.02	0.96	1.00	0.98
HFC-125	1.00	0.98	1.00	0.97	0.97	1.02	0.95	1.03	0.98
FC-116	0.98	0.92	0.95	0.96	0.95	1.02	0.95	0.97	0.98
HFC-134a	1.00	0.94	1.01	0.98	0.97	1.01	0.96	1.06	0.98
HFC-236	1.00	1.02	1.00	0.95	0.99	1.03	0.97	1.00	0.99
FC-C318	0.98	1.20	1.00	0.83	0.97	1.04	0.98	0.86	0.96
FC-218	1.02	0.98	1.02	1.02	0.96	1.03	0.96	1.02	0.99
HFC-32/125	1.02	0.94	0.96	0.93	0.96	1.00	0.95	0.97	0.99
NaHCO3	1.02	1.05	1.02	0.96	0.98	1.07	0.98	1.04	1.01
Alloy Avg.	1.00	1.00	0.98	0.97	0.97	1.01	0.96	0.98	

On the negative side, no alloy received only one's and two's in all of the agents and no agent received only one's and two's for all of the alloys. The best performance by an alloy was demonstrated by the 304 stainless steel alloy which received a one in all except for three of the environments. The best performing agents were HFC-236 and HFC-125 with FC-31-10 coming in third. However, each of these agents received a three or a four rating on at least one alloy. Since the alloys have different chemical compositions, surface films and corrosion susceptibilities, this is not surprising, but it indicates the importance of conducting experiments of this type.

7.3.1.4 Summary of Aircraft Storage and Distribution System Corrosion Experiments. To combine the performance of the different agent/alloy performances on the three different types of tests that comprise this part of the investigation, each agent/alloy combination was given a rating between one and ten based on its performance in that particular test. Table 22 reviews the results for each agent/alloy combination in the three types of experiments that comprise this part of this investigation: Mass Change Exposure Experiments (Exp.), Localized Corrosion Exposure Experiments (Crevice) and Environmental Induced Fracture (SSR). To allow for ready comparison between these results, a similar rating scheme was adopted for each of the three different types of tests used in this part of this study. Basically, this scheme assigned a numerical score between one and ten to each agent/alloy combination investigated in that particular test. Whenever possible, a numerical rule was used for the rating scheme with the magnitude of the standard deviation used to distinguish between one, two, and three while order of magnitude steps were used from six to 10. The interpretation of the meaning of the numerical ratings is given at the bottom of Table 22. Basically, a one indicates no discernable evidence of attack, a five indicates attack that may be a problem, and a ten indicates extremely rapid

Table 14. Score for the Average Ultimate Tensile Strength|[(Mean for Envir.)-(Mean for Hot Ar)]/(Alloy Std. Dev.)|

Environment	Nit 40	Al 6061	In 625	304 SS	CDA 172	13-8 Steel	AM355 SS	AISI 4130	Agent Avg.
HCFC-22	0.49	0.53	1.57	0.18	0.88	0.43	2.06	0.67	0.85
HCFC-124	0.89	0.30	0.47	0.52	0.61	2.45	1.55	0.50	0.91
FC-31-10	0.55	0.34	0.79	0.48	1.49	0.91	2.20	0.76	0.92
HFC-227	0.00	0.35	0.70	0.00	0.41	0.45	2.70	0.09	0.59
HFC-125	0.04	0.31	0.13	0.46	1.20	0.41	3.41	0.62	0.82
FC-116	0.68	1.22	2.13	0.79	2.01	0.60	3.11	0.51	1.38
HFC-134a	0.52	0.97	0.23	0.38	1.03	0.17	2.64	1.17	0.89
HFC-236	0.14	0.29	0.13	0.93	0.59	0.73	2.23	0.02	0.63
FC-C318	0.80	3.14	0.12	3.19	1.04	1.04	1.24	2.55	1.64
FC-218	0.89	0.33	0.76	0.39	1.46	0.76	2.73	0.45	0.97
HFC-32/125	0.87	1.00	1.87	1.23	1.42	0.05	3.33	0.46	1.28
NaHCO3	0.79	0.74	0.92	0.65	0.99	1.83	1.07	0.78	0.97
Alloy Avg.	0.56	0.79	0.82	0.77	1.09	0.82	2.36	0.71	

attack. A rating above four indicates more than just superficial corrosion and a better understanding of the attack responsible for this score should be developed before putting these combinations in service.

From Table 22, it can be seen that some agent/alloy combinations that did well in one test did poorly in another. For example, AISI 4130 steel performed well in the SSR tests in all of the agents, but did poorly in most of the other tests. On the other hand, some of the alloys which apparently retain passivity in the agents, had some indications of problems in the SSR tests such as 304 stainless steel in FC-C318. The results of these tests can be combined into a single overall rating number for each agent/alloy combination by either averaging the results of the tests, Table 23, or by taking the worst rating achieved for the three tests as the overall rating, Table 24. Since a good rating on two of the tests could bring an unacceptable rating on one of the tests into the acceptable range for the overall rating based on averaging, it was decided that an overall rating which is the worst rating received on the three different tests was the best way to evaluate the overall performance of an agent/alloy combination, Table 24. By examining this table, it can be seen that by this rating scheme the best rated agents are HFC-134a with HFC-227, HFC-125 and HFC-236 not far behind. None of the agents received an agent average rating for the eight alloys higher than five, but $NaHCO_3$ was over four. Also, all of the agents had at least two alloys with a three or lower rating. That is, none of the agents were so corrosive that an alloy could not be identified for aircraft storage and distribution systems, but clearly some agents were less aggressive than others and some agent/alloy combinations may be undesirable. The origin of the differences in the corrosivity of the agents could be due to reactions between the metals and the agents or it could be due to different contamination or

Table 15. Average Strain to Failure in Each Agent at 150 °C (Except lab air which was at room temperature) (%)

Environment	Nit 40	Al 6061	In 625	304 SS	CDA 172	13-8 Steel	AM355 SS	AISI 4130
Lab Air	49.9	13.0	44.4	30.3	13.0	5.9	10.7	8.3
Hot Ar	41.5	7.9	41.0	13.6	10.1	6.2	9.2	7.9
HCFC-22	37.8	8.9	37.7	12.5	12.4	7.5	9.8	8.9
HCFC-124	36.0	10.5	43.7	14.1	12.4	7.9	9.1	8.2
FC-31-10	36.7	10.1	37.2	12.4	12.9	6.5	7.8	8.0
HFC-227	37.8	10.7	42.6	13.6	11.7	6.9	9.6	7.7
HFC-125	40.4	9.8	43.4	15.1	11.6	6.7	9.8	8.1
FC-116	40.5	9.6	46.5	17.1	12.2	6.9	9.1	8.8
HFC-134a	37.7	9.4	46.5	12.7	10.1	7.7	9.2	7.8
HFC-236	36.3	9.7	41.5	16.9	9.7	7.0	9.7	8.2
FC-C318	41.7	8.5	43.1	36.0	12.8	8.1	9.1	9.6
FC-218	41.0	9.1	45.0	15.0	11.7	6.6	9.0	9.5
HFC-32/125	39.4	9.2	46.2	17.4	11.6	7.2	9.6	8.5
NaHCO3	42.5	7.5	46.0	17.4	11.6	10.5	9.5	7.5
CF3I	40.6	8.6	47.8	21.3	11.0	7.4	8.0	6.8
Alloy Avg.	39.3	9.3	43.4	16.8	11.6	7.4	9.2	8.3
Std. Dev.*	3.0	1.2	2.6	5.5	1.6	0.9	0.6	0.7

Alloy Avg. Average of the means determine for each of the agents.
Std. Dev.* The "Alloy Standard Deviation" was estimated from the Ar at 150 °C tests

residual levels in the agents. If the corrosivity is due to contaminants and residuals, then changes in processing or storage that alters these levels would also alter the corrosivity of the agents. Additional testing will be required to determine the cause of the observed corrosion behaviors and the role of contaminants and residuals in determining the corrosivity.

7.3.2 Post-Deployment Corrosion.

7.3.2.1 Literature Review of Corrosion of Metals in Halide Ions. All of the fire suppressants investigated in this study except for $NaHCO_3$, contain fluoride and produce fluoride ions and HF during combustion. Since other halogens are also incorporated in these, and other potential fire suppressants, other halogen acids will be produced by combustion of these suppressants. Therefore, the post-deployment corrosion damage to aircraft materials will depend on the corrosivity of surface films containing these species on the metals of the aircraft frame, engine components, etc.

Table 16. Average Strain to Failure Ratio in Each Agent at 150 °C [(Agent)/(Hot Ar)]

Environment	Nit 40	Al 6061	In 625	304 SS	CDA 172	13-8 Steel	AM355 SS	AISI 4130	Agent Avg.
HCFC-22	0.91	1.12	0.92	0.92	1.23	1.20	1.06	1.13	1.01
HCFC-124	0.87	1.32	1.06	1.04	1.23	1.28	0.99	1.03	1.10
FC-31-10	0.88	1.27	0.91	0.91	1.28	1.05	0.85	1.01	0.96
HFC-227	0.91	1.34	1.04	1.00	1.17	1.11	1.05	0.97	1.13
HFC-125	0.97	1.24	1.06	1.11	1.16	1.08	1.06	1.02	1.14
FC-116	0.98	1.21	1.13	1.26	1.21	1.11	0.99	1.12	1.06
HFC-134a	0.91	1.19	1.13	0.93	1.00	1.24	1.00	0.99	1.09
HFC-236	0.88	1.23	1.01	1.25	0.97	1.13	1.05	1.03	1.13
FC-C318	1.00	1.07	1.05	2.65	1.27	1.30	0.99	1.22	1.13
FC-218	0.99	1.14	1.10	1.11	1.17	1.06	0.97	1.20	1.14
HFC-32/125	0.95	1.16	1.13	1.28	1.15	1.16	1.04	1.08	1.11
NaHCO3	1.03	0.94	1.12	1.29	1.15	1.70	1.03	0.95	1.21
Alloy Avg.	0.94	1.19	1.05	1.23	1.17	1.20	1.01	1.06	

Most engineering alloys that exhibit good corrosion resistance do so due to the formation of a "passivating" surface film. Aluminum alloys and stainless steels are excellent examples of alloys based on active elements that behave in a relatively noble manner due to the formation of continuous protective corrosion product films. These films are usually oxides, hydroxides or oxide-hydroxide mixtures. These surface films may be crystalline and they may be precipitated out of the solution adjacent to the metals surface, but it is generally believed that the more rapidly grown, amorphous films are more protective than precipitated crystalline films. No matter what the nature of the surface film, it is generally found that halogen ions in the environment and on these films tend to destabilize the protective passivating films. Presumably, this is because the soluble metal-halide salt is thermodynamically preferred over the relatively insoluble metal-oxide or hydroxide compounds in the passive film at the passive film to environment interface. This is a very simplified view which ignores many kinetic issues in passive film growth and breakdown, but many of the essential details in the relationship between halogen ions and passivity breakdown can be understood based on this simple model: (1) increasing halide ion activity reduces passive film stability, (2) the more aggressive halide is the more electronegative ($F^- > Cl^- > Br^- > I^- > At^-$), (3) pH influences stability, (4) electrode potential influences stability and (5) metal-halide salt solubility should exhibit an influence.

Aluminum alloys are the most common metallic alloy type used in airframe construction and the most susceptible to pitting by halide ions of the metals of concern so this review will focus on the effect of halide ions on the corrosion behavior of these alloys. Aluminum is a relatively active element and aluminum alloys corrode as rapidly as mass transport to the surface will allow if the passive film becomes unprotective for any reason. As a result, aluminum alloys are not used in environments where passivity is not maintained (*e.g.*, $pH < 4$ or $pH > 10$). However, pitting, crevice

Table 17. Score for the Average Strain to Failure ¦[(Mean for Envir.)-(Mean for Hot Ar)]/(Alloy Std. Dev.)¦

Environment	Nit 40	Al 6061	In 625	304.00 SS	CDA 172	13-8 Steel	AM355 SS	AISI 4130	Agent Avg.
HCFC-22	1.22	0.78	1.29	0.20	1.44	1.47	0.97	1.51	1.11
HCFC-124	1.80	2.10	1.02	0.10	1.46	2.04	0.17	0.42	1.14
FC-31-10	1.57	1.79	1.47	0.22	1.76	0.34	2.26	0.10	1.19
HFC-227	1.21	2.26	0.61	0.01	1.03	0.81	0.69	0.31	0.87
HFC-125	0.36	1.55	0.90	0.28	0.97	0.60	0.97	0.23	0.73
FC-116	0.32	1.35	2.10	0.64	1.32	0.81	0.18	1.39	1.01
HFC-134a	1.23	1.22	2.11	0.16	0.02	1.78	0.00	0.14	0.83
HFC-236	1.69	1.49	0.18	0.61	0.21	0.96	0.79	0.41	0.79
FC-C318	0.07	0.49	0.78	4.11	1.68	2.19	0.19	2.61	1.51
FC-218	0.17	0.95	1.51	0.27	1.03	0.44	0.44	2.45	0.91
HFC-32/125	0.66	1.06	1.98	0.69	0.95	1.15	0.59	0.90	1.00
NaHCO3	0.35	0.40	1.90	0.71	0.94	5.09	0.48	0.66	1.32
Alloy Avg.	0.89	1.29	1.32	0.67	1.07	1.47	0.64	0.93	

corrosion or stress corrosion cracking may result in environments where aluminum is normally passive if halide ion concentrations exceed critical values.

As discussed above, when aluminum is exposed to solutions containing different types of halide ions, passive film breakdown and pitting should vary with the electronegativity of the halide ion. Chloride, bromide and iodide follow this trend, but fluoride was found to be less aggressive to aluminum alloys than chloride and bromide (Davies and Prigmore 1984). Since aluminum salts formed with fluoride are less soluble than other aluminum halide salts, several investigators have postulated that this difference is due to the formation of different types of salt films (Zotikov, Bakhmutova *et al.* 1974; Davies and Prigmore 1984). In general, aluminum alloys have excellent atmospheric corrosion resistance and, in most atmospheres, the corrosion rate of aluminum decreases with time as the passive film become thicker (Fink and Boyd 1970; Bailey, Porter *et al.* 1976). However, cyclic wetting and drying and the presence of aggressive species in the atmosphere can accelerate attack by damaging the passivating film. Marine and coastal environments with their high humidity and particulates rich in chloride ions can be particularly aggressive. Also, gases such as sulfur dioxide (SO_2) chlorine (Cl_2) and hydrogen chloride gas have been found to be aggressive for aluminum alloys (Bailey, 1976; Scully, 1990(a)).

7.3.2.2 Post-deployment Corrosion Test Results. The results of the post-deployment corrosion tests are shown in Figures 7 through 14 for Alloy 6061-T6, AISI 4130, 13-8 Mo steel, AM 355, 304 stainless steel, Nitronic 40, Inconel 625, and CDA 172 (Cu-Be) respectively. The data in these figures are for 30 days of exposure at three different humidities (20, 52 and 93% RH) following

Table 18. Average Reduction in Area in Each Agent at 150 °C (Except lab air which was at room temperature) (%)

Environment	Nit 40	Al 6061	In 625	304 SS	CDA 172	13-8 Steel	AM355 SS	AISI 4130
Lab Air	78.1	50.9	73.7	76.7	66.3	69.4	48.6	52.1
Hot Ar	79.2	42.3	69.5	67.8	27.5	60.0	48.6	50.8
HCFC-22	79.3	40.2	65.7	67.9	38.7	61.5	49.3	50.4
HCFC-124	79.6	35.8	65.7	71.7	36.6	56.2	48.3	48.7
FC-31-10	80.2	40.0	64.2	70.2	37.8	60.5	51.4	47.6
HFC-227	79.5	39.1	68.9	69.8	43.3	61.1	48.7	48.2
HFC-125	80.4	39.4	67.3	68.7	40.0	61.9	48.6	49.2
FC-116	79.6	41.1	69.6	71.9	40.5	62.5	48.5	49.2
HFC-134a	80.3	39.0	69.9	69.0	31.1	59.6	50.4	49.6
HFC-236	79.1	40.7	65.7	72.6	32.9	60.1	48.6	49.1
FC-C318	79.5	40.9	70.3	68.6	36.3	61.1	47.5	49.5
FC-218	86.2	42.2	69.3	70.8	31.4	59.5	47.2	47.5
HFC-32/125	79.5	40.9	67.0	72.5	37.9	62.3	48.5	50.1
NaHCO3	80.1	35.2	68.4	56.3	33.8	58.1	51.5	44.3
Alloy Avg.	80.2	39.8	67.8	69.1	36.0	60.3	49.1	48.8
Std. Dev.*	2.3	2.3	3.2	5.3	3.2	6.4	2.2	5.1

Alloy Avg. Average of the means determine for each of the agents.
Std. Dev.* The "Alloy Standard Deviation" was estimated from the Ar at 150°C tests

three different surface pretreatments: (1) artificial seawater plus NaF, (2) artificial seawater plus $NaHCO_3/Na_2CO_3$ and (3) artificial seawater plus NaOH. The mass changes (after washing with distilled water) for this exposure period are plotted in these figures as a function of the relative humidity of the exposure environment. In these figures, it can be seen that for most of the alloys and pretreatments, no particular surface pretreatment was consistently worse than the others, that there is no clear trend in the magnitude of the mass change with relative humidity, and that, except for three alloys, the mass changes were almost always small mass losses.

A mass loss indicates the formation of corrosion products that were removed by washing in distilled water prior to weighing of the samples. These products may be either ions in thin electrolyte layers on the surface or solid corrosion products that are dissolved or physically removed by the washing process. In either case, these measurements indicate corrosion of the underlying alloy. However, for all of these alloys the mass changes were <2 mg for these exposures which corresponds to a corrosion rate of <0.024 grams per meter squared per day (0.24 MDD) which is a relatively low corrosion rate. The three exceptions were: aluminum alloy 6061-T6, AISI 4130 steel, and the Cu-Be alloy CDA-172. These alloys exhibited mass increases of a much larger magnitude

Table 19. Average Reduction in Area Ratio in Each Agent at 150 °C [(Agent)/(Hot Ar)]

Environment	Nit 40	Al 6061	In 625	304 SS	CDA 172	13-8 Steel	AM355 SS	AISI 4130	Agent Avg.
HCFC-22	1.00	0.95	0.95	1.00	1.41	1.03	1.00	0.99	1.04
HCFC-124	1.01	0.85	0.95	1.06	1.33	0.94	0.98	0.96	1.01
FC-31-10	1.02	0.95	0.92	1.03	1.37	1.02	1.05	0.94	1.04
HFC-227	1.00	0.92	0.99	1.03	1.58	1.03	0.99	0.95	1.06
HFC-125	1.01	0.93	0.97	1.01	1.45	1.04	0.99	0.97	1.05
FC-116	1.01	0.97	1.00	1.06	1.48	1.05	0.99	0.97	1.06
HFC-134a	1.01	0.92	1.01	1.02	1.13	0.99	1.04	0.98	1.01
HFC-236	1.00	0.96	0.95	1.07	1.20	1.01	0.99	0.97	1.02
FC-C318	1.00	0.97	1.01	1.01	1.32	1.02	0.97	0.98	1.04
FC-218	1.09	1.00	1.00	1.04	1.14	1.00	0.96	0.94	1.02
HFC-32/125	1.00	0.97	0.97	1.07	1.38	1.04	0.99	0.99	1.05
NaHCO3	1.01	0.83	0.99	0.83	1.23	0.97	1.05	0.87	0.97
Alloy Avg.	1.02	0.94	1.00	1.00	1.23	1.05	0.99	1.01	

than the small mass losses of the other five alloys and required the use of a much larger scale for plotting the results for these alloys. For aluminum alloy 6061 (Figure 7), the mass changes ranged from a small mass loss of about 2 mg at 20% RH for the NaOH pretreatment to a mass increase of about 15 mg at 93% RH for the carbonate/bicarbonate pretreatment. The NaF pretreatment showed mass increases between 2 and 6 mg for these exposures. Apparently, adding NaF to the surface electrolyte film was not as detrimental to this alloy as the carbonate/bicarbonate treatment. Since the films were prepared by first spraying with artificial seawater, all of the surface films contained chloride ions which are typically found to be more detrimental than fluoride ions to aluminum alloys. While the NaOH pretreatment resulted in only small mass changes, it should be noted that this pretreatment resulted in the formation of small pits on the surface for the low humidity exposure (20% RH). For the AISI 4130 steel alloy (Figure 8), the carbonate/bicarbonate and the NaOH surface pretreatments resulted in mass changes between -1 mg and 2 mg. However, the NaF pretreatment resulted in the growth of an insoluble corrosion product film as indicated by a mass increase of over 17 mg. Apparently, unlike the aluminum alloy, adding NaF to the thin electrolyte film on the surface of this alloy resulted in significant changes in the corrosivity of this film. For the Cu-Be alloy (Figure 14), the mass changes for the high humidity exposure (93% RH) were so large that a much larger scale had to be used for plotting the results than used for any other alloy. For the carbonate/bicarbonate pretreatment, the mass increased more than 100 mg for the 30 day exposure at 93% RH. This was almost an order of magnitude greater than that observed for aluminum alloy 6061 and 4130 steel and almost two orders of magnitude greater than the magnitude of the mass losses observed in the other five alloys. For the NaF pretreatment, the mass increased more than 21 mg for the 93% RH exposure (the second largest mass change observed). Clearly, in the high humidity

Table 20. Score for the Average Reduction in Area for Each Agent at 150 °C [(Mean for Envir.)-(Mean for Hot Ar)]/(Alloy Std. Dev.)

Environment	Nit 40	Al 6061	In 625	304 SS	CDA 172	13-8 Steel	AM355 SS	AISI 4130	Agent Avg.
HCFC-22	0.01	0.93	1.16	0.02	3.53	0.29	0.06	0.06	0.76
HCFC-124	0.18	2.87	1.17	0.72	2.88	0.53	0.37	0.40	1.14
FC-31-10	0.63	1.02	1.63	0.44	3.22	0.14	1.04	0.62	1.09
HFC-227	0.13	1.44	0.16	0.37	4.98	0.24	0.21	0.51	1.00
HFC-125	0.50	1.30	0.67	0.16	3.91	0.35	0.23	0.32	0.93
FC-116	0.18	0.52	0.05	0.77	4.10	0.45	0.31	0.32	0.84
HFC-134a	0.45	1.46	0.13	0.22	1.14	0.01	0.58	0.23	0.53
HFC-236	0.07	0.70	1.16	0.91	1.70	0.07	0.24	0.32	0.65
FC-C318	0.11	0.63	0.26	0.15	2.76	0.23	0.75	0.24	0.64
FC-218	2.99	0.03	0.04	0.56	1.24	0.01	0.87	0.64	0.80
HFC-32/125	0.11	0.60	0.75	0.88	3.26	0.42	0.27	0.13	0.80
NaHCO3	0.37	3.16	0.32	2.17	1.97	0.24	1.07	1.26	1.32
Alloy Avg.	0.48	1.22	0.62	0.61	2.89	0.25	0.50	0.42	

environment water vapor was absorbed onto the surface to form insoluble corrosion products at a much higher rate than at the lower humidities. Also, it appears that the addition of NaOH to the thin surface electrolyte film resulted in altering the surface films in a manner that prevented this process.

A mass increase indicates the formation of insoluble corrosion products. These corrosion products could be a protective surface film or it could be a non-protective scale. For a continuous protective film, the corrosion rate will decrease as the film grows thicker and, at least theoretically, the corrosion rate for this situation will exponentially approach zero. However, films can become non-protecting if they crack or spall as they grow allowing the environment access to bare metal through the fissures in the surface film. A non-protective scale could form as the metal corrodes to form ions in a thin electrolyte film on the surface which migrate through the electrolyte film to nucleate and grow precipitates. These precipitates grow to form relatively loose aggregate layers which do not prevent wetting of the metal by the electrolyte film nor do they prevent atmospheric gases from interacting with the thin electrolyte film, thereby allowing corrosion to continue.

The results for the aluminum alloy were a little surprising in that research has found that the hydroxide ion is the most detrimental ion with respect to the corrosion of aluminum alloys (Foley and Trazaskoma 1977). This is a direct result of the amphoteric nature of the passivating films that form on aluminum alloys and the formation of the aluminate ion (AlO_2^-). Typically, if the passive film is removed for any reason, aluminum alloys will corrode as rapidly as mass transport can provide reactants to the surface. In aqueous solutions, the passive film is stable in a pH range between 4 and 9.5. If for any reason the pH goes below or above these values the corrosion rate increases very rapidly. Apparently, adding NaOH to the artificial seawater sprayed on the surface did not increase

Table 21. Slow Strain Rate Tensile Tests at 150°C Rating for Each Alloy/Agent Combination

Environment	Nit 40	Al 6061	In 625	304 SS	CDA 172	13-8 Steel	AM355 SS	AISI 4130	Agent Avg.	Std. Dev.	Agent Rank
HCFC-22	2	1	2	1	4	2	3	2	2.13	0.99	5
HCFC-124	2	3	2	1	3	3	2	1	2.13	0.83	5
FC-31-10	2	2	2	1	4	1	3	1	2.00	1.07	3
HFC-227	2	3	1	1	5	1	3	1	2.13	1.46	5
HFC-125	1	2	1	1	4	1	4	1	1.88	1.36	2
FC-116	1	2	3	1	5	1	4	2	2.38	1.51	10
HFC-134a	2	2	3	1	2	2	3	2	2.13	0.64	5
HFC-236	2	2	2	1	2	1	3	1	1.75	0.71	1
FC-C318	1	4	1	5	3	3	2	3	2.75	1.39	11
FC-218	3	1	2	1	2	1	3	3	2.00	0.93	3
HFC-32/125	1	2	2	2	4	2	4	1	2.25	1.16	9
NaHCO3	1	4	2	3	2	6	2	2	2.75	1.58	10
Alloy Avg.	1.67	2.33	1.92	1.58	3.33	2.00	3.00	1.67			
Std. Dev.	0.65	0.98	0.67	1.24	1.15	1.48	0.74	0.78			
Alloy Rank	2	6	4	1	8	5	7	2			

Rating	Freq	Interpretation
1	31	No evidence of environment influence on deformation and fracture in this test.
2	34	Slight indication of possible environmental influence
3	18	Some evidence
4	9	Strong evidence
5	3	Nature of interaction should be evaluated.
6	1	Nature of interaction should be evaluated.
7	0	Nature of interaction should be evaluated.
8	0	Nature of interaction should be evaluated.
9	0	Nature of interaction should be evaluated.
10	0	Nature of interaction should be evaluated.

the pH of the surface electrolyte enough to destabilize the passive film. Also, it appears that increasing the humidity promoted mixing of this electrolyte film keeping the pH below critical levels and preventing the small pits which were observed at lower humidities. However, the quantity of NaOH produced by the application of a fire suppressant may exceed that applied in this experiment and pitting under droplets or particles similar to that observed in these experiments, or much worse, could occur. As a result, even though the samples treated with NaOH did not exhibit significant attack we believe that it is very risky to use a fire suppressant that produces NaOH during combustion around aluminum alloys.

The other two alloys which showed mass increases, AISI 4130 and CDA-172, are not used as commonly on aircraft as aluminum alloys. Both of these alloys showed a significant increase in the

Table 22. Summary Table of Mass Change Exposure Test Results, Crevice Corrosion Visual Examination Results and Slow Strain Rate Tensile Test Results

Environment	Expt.	Nit 40	Al 6061	In 625	304 SS	CDA 172	13-8 Steel	AM355 SS	AISI 4130	Agent Avg.
HCFC-22	Exp.	3	4	3	3	5	2	3	5	3.50
	Crevice	2	2	2	3	4	3	3	5	3.14
	SSR	2	1	2	1	4	2	3	2	2.13
HCFC-124	Exp.	3	3	3	2	4	3	3	3	3.00
	Crevice	2	2	1	2	3	3	3	5	2.63
	SSR	2	3	2	1	3	3	2	1	2.13
FC-31-10	Exp.	3	4	2	4	5	4	3	4	3.63
	Crevice	1	1	2	2	2	2	2	3	1.88
	SSR	2	2	2	1	4	1	3	1	2.00
HFC-227	Exp.	1	3	2	3	5	3	1	3	2.63
	Crevice	2	2	2	3	3	3	3	4	2.75
	SSR	2	3	1	1	5	1	3	1	2.13
HFC-125	Exp.	2	3	2	3	4	3	2	4	2.88
	Crevice	2	2	2	2	3	2	3	2	2.25
	SSR	1	2	1	1	4	1	4	1	1.88
FC-116	Exp.	1	3	2	3	4	3	3	4	2.88
	Crevice	2	2	1	2	2	3	2	3	2.13
	SSR	1	2	3	1	5	1	4	2	2.38
HFC-134a	Exp.	2	3	3	3	3	3	2	3	2.75
	Crevice	1	1	1	2	2	3	4	2	2.00
	SSR	2	2	3	1	2	2	3	2	2.13
HFC-236	Exp.	2	5	2	3	4	3	1	3	2.88
	Crevice	2	2	1	1	2	2	2	2	1.75
	SSR	2	2	2	1	2	1	3	1	1.75
FC-C318	Exp.	1	4	2	3	4	3	1	3	2.63
	Crevice	2	3	2	2	2	2	2	4	2.38
	SSR	1	4	1	5	3	3	2	3	2.75
FC-218	Exp.	3	4	2	3	4	3	3	4	3.25
	Crevice	3	4	2	2	2	2	2	4	2.63
	SSR	3	1	2	1	2	1	3	3	2.00
HFC 32/125	Exp.	3	4	3	3	5	4	3	3	3.50
	Crevice	3	2	1	2	2	2	3	4	2.38
	SSR	1	2	2	2	4	2	4	1	2.25
NaHCO3	Exp.	4	4	3	3	5	4	3	4	3.75
	Crevice	2	3	2	2	4	4	4	4	3.13
	SSR	1	4	2	3	2	6	2	2	2.75
Alloy Avg.	Exp.	2.33	3.67	2.42	3.00	4.33	3.17	2.33	3.58	
	Crevice	2.00	2.17	1.58	2.08	2.58	2.58	2.75	3.50	
	SSR	1.67	2.33	1.92	1.58	3.33	2.00	3.00	1.67	

Rating	Freq	Interpretation
1	47	No evidence of environmental attack
2	100	Some evidence of attack.
3	86	Evidence of superficial attack.
4	42	Superficial attack (more study may be required)
5	12	Attack could be a problem.
6	1	Attack needs to be considered.
7	0	Attack can be managed.
8	0	Rapid attack.
9	0	Very rapid attack.
10	0	Extremely rapid attack.

Table 23. Average Rating for Mass Change Exposure Tests, Crevice Visual Examination, and Slow Strain Rate Tensile Test

Environment	Nit 40	Al 6061	In 625	304 SS	CDA 172	13-8 Steel	AM355 SS	AISI 4130	Agent Avg.	Std. Dev.	Agent Rank
HCFC-22	2.33	2.33	2.33	2.33	4.33	2.33	3.00	4.00	2.88	0.83	11
HCFC-124	2.33	2.67	2.00	1.67	3.33	3.00	2.67	3.00	2.58	0.56	8
FC-31-10	2.33	2.33	2.00	2.33	3.67	2.33	2.67	2.67	2.50	0.53	5
HFC-227	1.67	2.67	1.67	2.33	4.33	2.33	2.33	2.67	2.50	0.84	5
HFC-125	1.67	2.33	1.67	2.00	3.67	2.00	3.00	2.33	2.33	0.69	3
FC-116	1.33	2.33	2.00	2.00	3.67	2.33	3.00	3.00	2.46	0.73	4
HFC-134a	1.67	2.00	2.33	2.00	2.33	2.67	3.00	2.33	2.29	0.42	2
HFC-236	2.00	3.00	1.67	1.67	2.67	2.00	2.00	2.00	2.13	0.47	1
FC-C318	1.33	3.67	1.67	3.33	3.00	2.67	1.67	3.33	2.58	0.90	7
FC-218	3.00	3.00	2.00	2.00	2.67	2.00	2.67	3.67	2.63	0.60	9
HFC-32/125	2.33	2.67	2.00	2.33	3.67	2.67	3.33	2.67	2.71	0.55	10
NaHCO3	2.33	3.67	2.33	2.67	3.67	4.67	3.00	3.33	3.21	0.80	12
Alloy Avg.	2.00	2.72	1.97	2.22	3.42	2.58	2.69	2.92			
Std. Dev.	0.49	0.53	0.26	0.46	0.64	0.73	0.48	0.59			
Alloy Rank	2	6	1	3	8	4	5	7			

atmospheric corrosion rate as a result of a pretreatment with NaF. As a result, cleaning the surfaces of these alloys after exposure to fire suppressant combustion products is a very good practice and substitution of another alloy which is not attack to this extent should be considered in locations where this type of exposure is expected.

7.3.3 Results of Electrochemical Measurements. The objective of these experiments was 1) to determine whether or not electrochemical measurements could be made in low conductivity electrolytes at elevated temperatures and pressures and 2) to define the lower conductivity limit for these types of measurements. As a result, a special cell was designed and constructed for this type of measurement, Figure 6. Then, experiments were conducted in an electrolyte with conductivities near and below that used by previous investigators (Halsal, 1992, deSouza, 1987). Figure 15 shows a typical impedance scan from 1 mHz to 65 kHz for 304 stainless steel in a low conductivity electrolyte (ethyl alcohol). This figure includes a Bode amplitude and phase angle plot (Figure 15(a)) and a Nyquist plot (Figure 15(b)). The resistance of the solution between the two parallel faces on the two identical samples can be determined from the Nyquist plot as the high frequency real axis (Z') intercept. By repeating these measurements at different electrode separations, a plot of the solution resistance as a function of electrode separation can be developed, Figure 16. The line in this figure is a linear regression fit through all of the resistance values determined at each separation setting. A

Table 24. Maximum (Worst) Rating for Mass Change Exposure Tests, Crevice Visual Examination, and Slow Strain Rate Tensile Test

Environment	Nit 40	Al 6061	In 625	304 SS	CDA 172	13-8 Steel	AM 355	AISI 4130	Agent Avg.	Std. Dev.	Agent Rank
HCFC-22	3	4	3	3	5	3	3	5	3.63	0.92	9
HCFC-124	3	3	3	2	4	3	3	5	3.25	0.89	5
FC-31-10	3	4	2	4	5	4	3	4	3.63	0.92	9
HFC-227	2	3	2	3	5	3	3	4	3.13	0.99	2
HFC-125	2	3	2	3	4	3	4	4	3.13	0.83	2
FC-116	2	3	3	3	5	3	4	4	3.38	0.92	8
HFC-134a	2	3	3	3	3	3	4	3	3.00	0.53	1
HFC-236	2	5	2	3	4	3	3	3	3.13	0.99	2
FC-C318	2	4	2	5	4	3	2	4	3.25	1.16	5
FC-218	3	4	2	3	4	3	3	4	3.25	0.71	5
HFC-32/125	3	4	3	3	5	4	4	4	3.75	0.71	11
NaHCO3	4	4	3	3	5	6	4	4	4.13	0.99	12
Alloy Avg.	2.58	3.67	2.50	3.17	4.42	3.42	3.33	4.00			
Std. Dev.	0.67	0.65	0.52	0.72	0.67	0.90	0.65	0.60			
Alloy Rank	2	6	1	3	8	5	4	7			

correlation coefficient of 0.978, indicating a good fit, was determined for this line. As seen from the figure, the data follow a linear relationship between the electrode separation and the resistance. Since

$$R = \rho\ (d/A), \tag{6}$$

where R is resistance, ρ is resistivity, d is the electrode separation and A is the electrode surface area. If the cell is constructed properly, the instrumentation is stable, and the experimental technique is applied properly, then one should get a linear relationship between the resistance of the electrolyte and the electrode separation as shown in this figure. However, the corrosion rate must be determined by subtracting the solution resistance, R_s, the high frequency real axis intercept in a Nyquist plot, from the cell resistance ($R_s + R_{ct}$) which is the low frequency real axis intercept in the Nyquist plot. By examining Figure 16, it can be seen the line in the Nyquist plot has not started approaching the real axis even for the lowest frequency (0.001 Hz). Since the corrosion rate is inversely proportional to the charge transfer resistance, very low frequencies will be required for these measurements even with estimating the real axis intercept from the curvature of the Nyquist plot. In addition, one can calculate the resistivity of the ethyl alcohol electrolyte from the experimental results. It is equal to

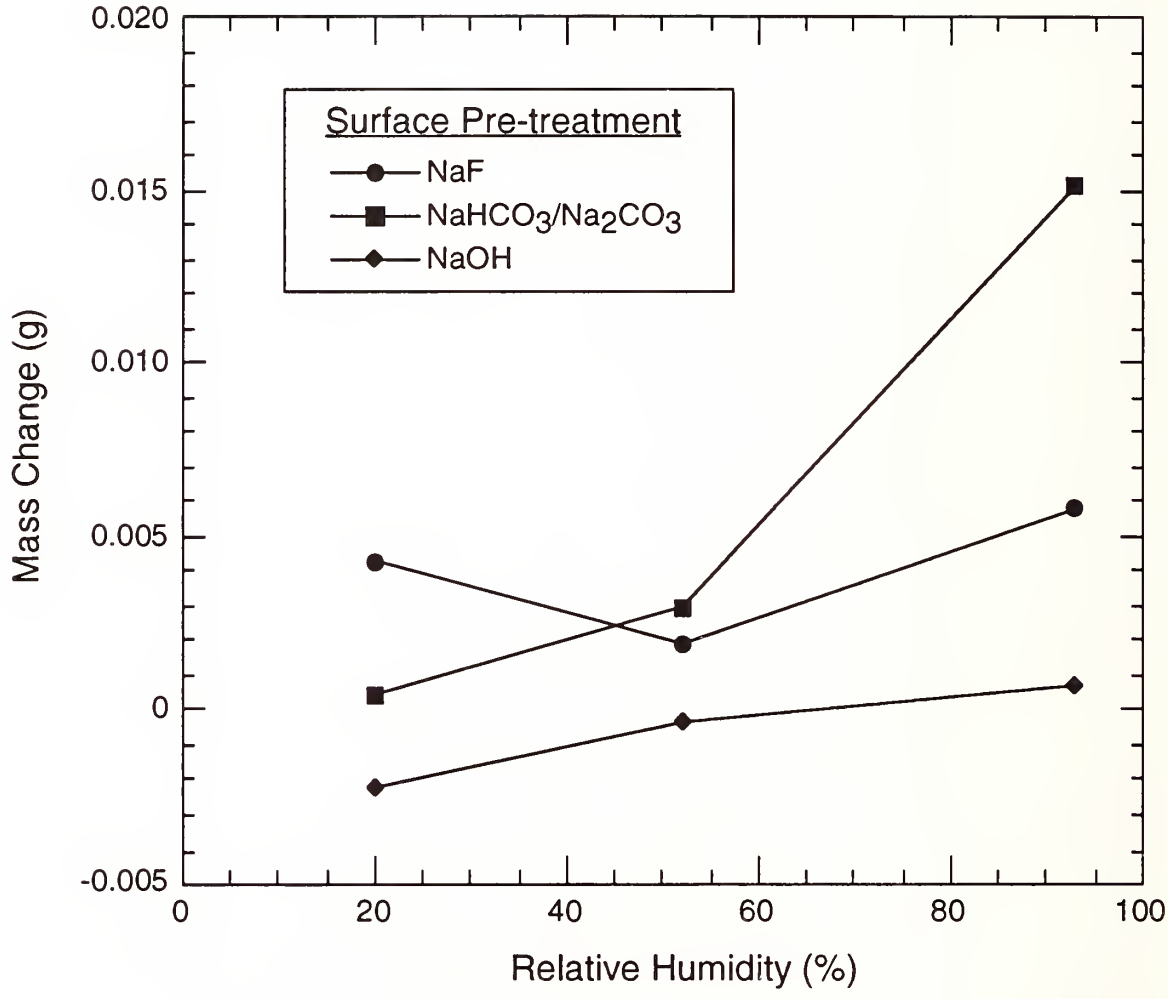

Figure 7. Mass change during atmospheric exposures at different relative humidities for aluminum alloy 6061-T6 after surface pretreatment with artificial seawater and either NaF, $NaHCO_3/Na_2CO_3$, or NaOH.

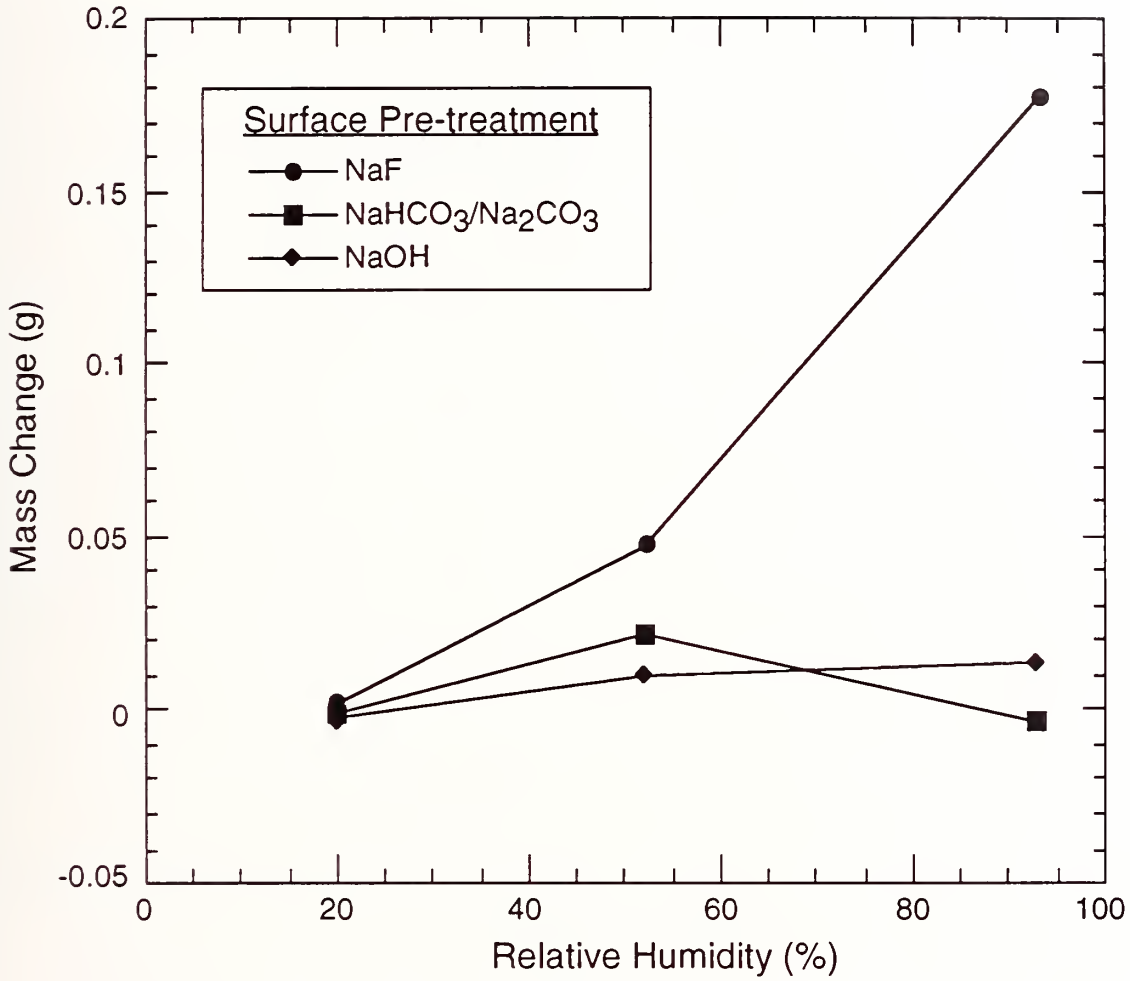

Figure 8. Mass change during atmospheric exposures at different relative humidities for AISI 4130 steel after surface pretreatment with artificial seawater and either NaF, $NaHCO_3/Na_2CO_3$, or NaOH.

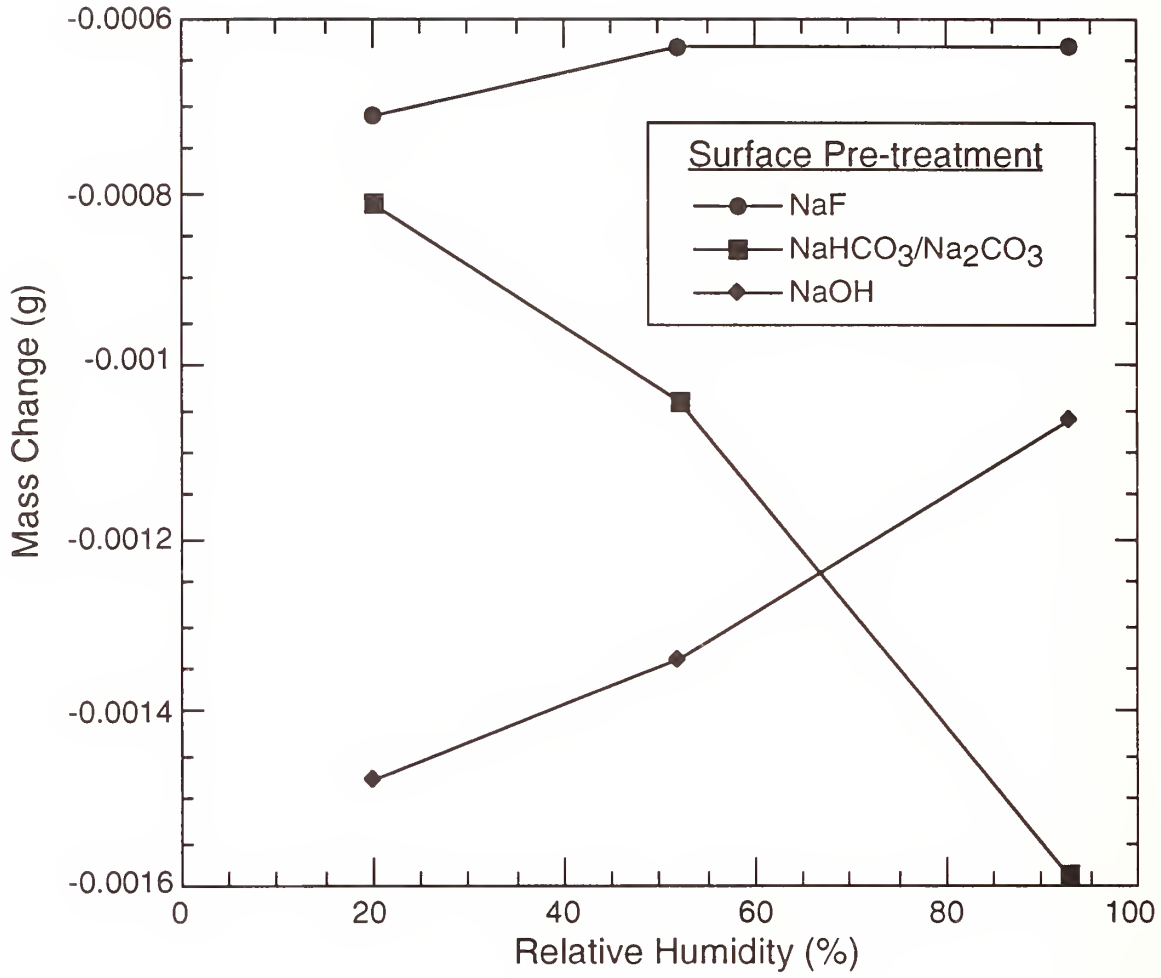

Figure 9. Mass change during atmospheric exposures at different relative humidities for 13-8 Mo steel after surface pretreatment with artificial seawater and either NaF, $NaHCO_3/Na_2CO_3$, or NaOH.

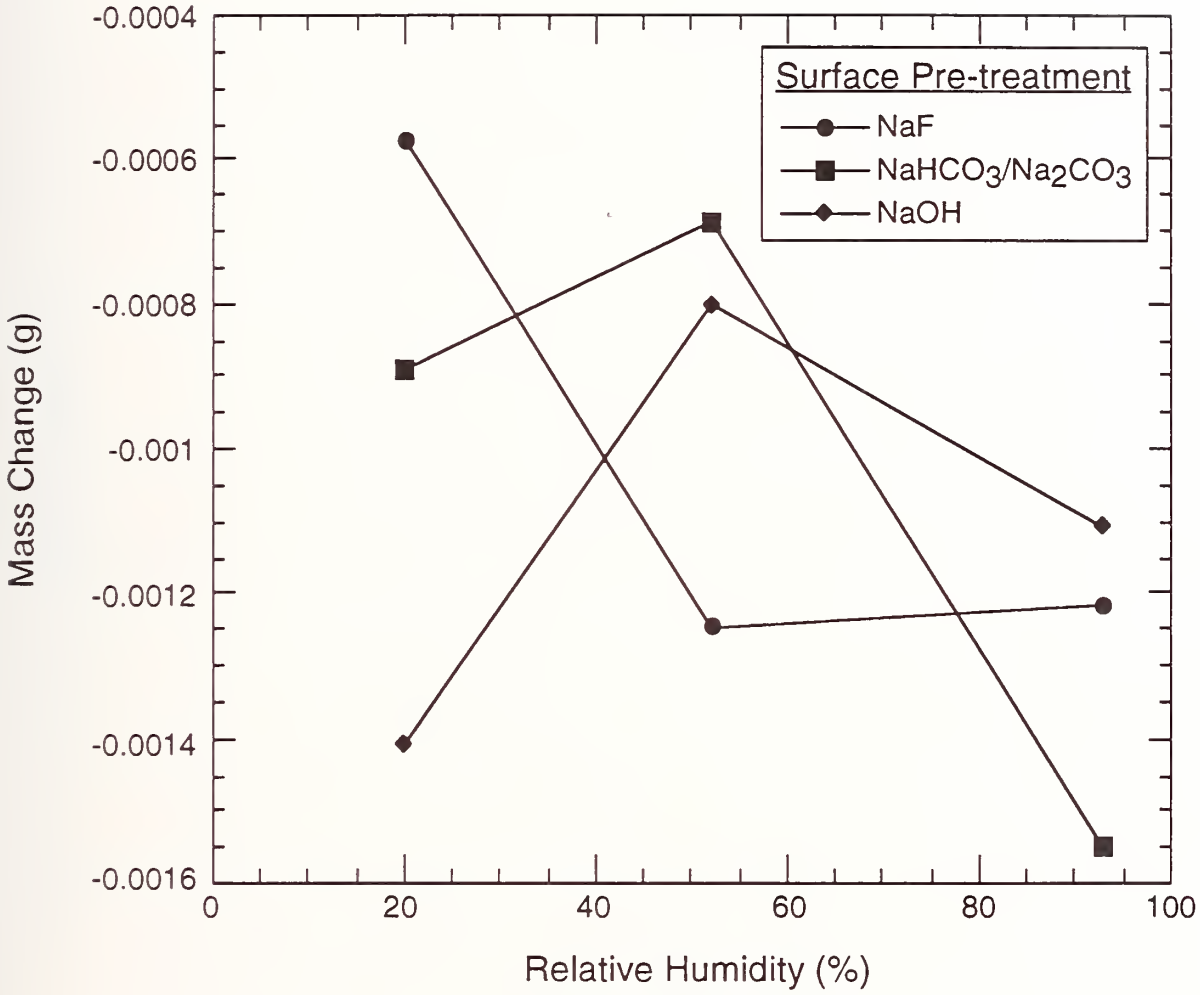

Figure 10. Mass change during atmospheric exposures at different relative humidities for AM 355 alloy after surface pretreatment with artificial seawater and either NaF, $NaHCO_3/Na_2CO_3$, or NaOH.

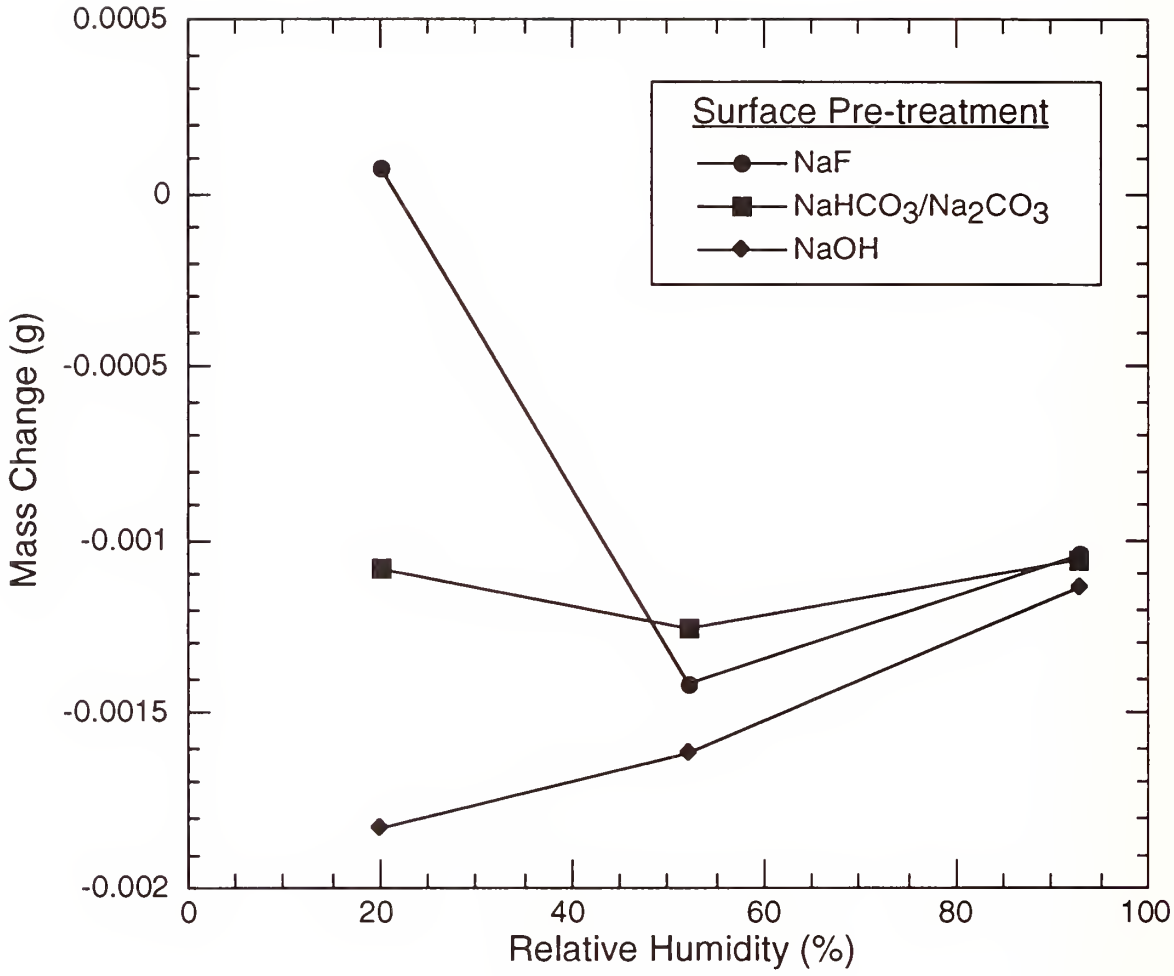

Figure 11. Mass change during atmospheric exposures at different relative humidities for 304 stainless steel after surface pretreatment with artificial seawater and either NaF, $NaHCO_3/Na_2CO_3$, or NaOH.

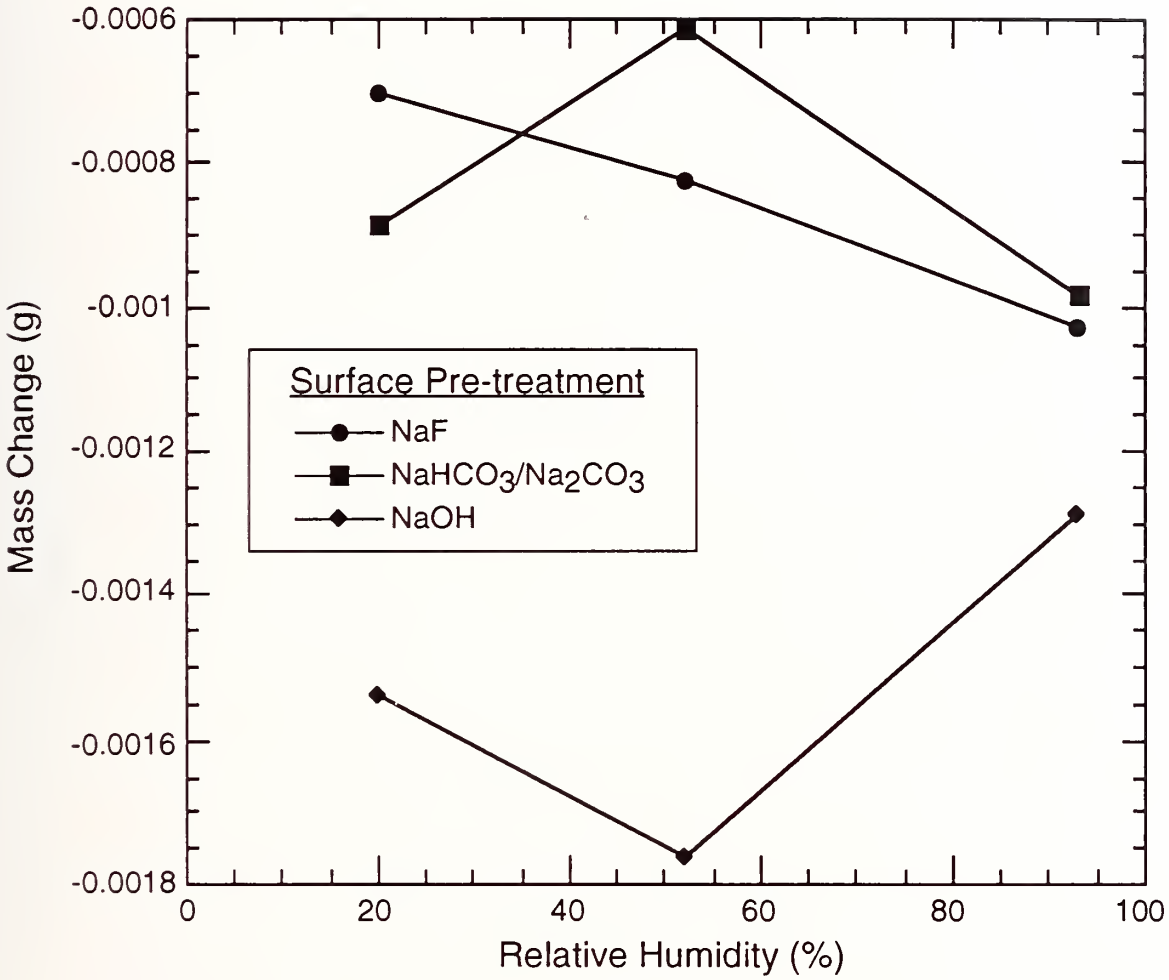

Figure 12. Mass change during atmospheric exposures at different relative humidities for Nitronic 40 alloy after surface pretreatment with artificial seawater and either NaF, $NaHCO_3/Na_2CO_3$, or NaOH.

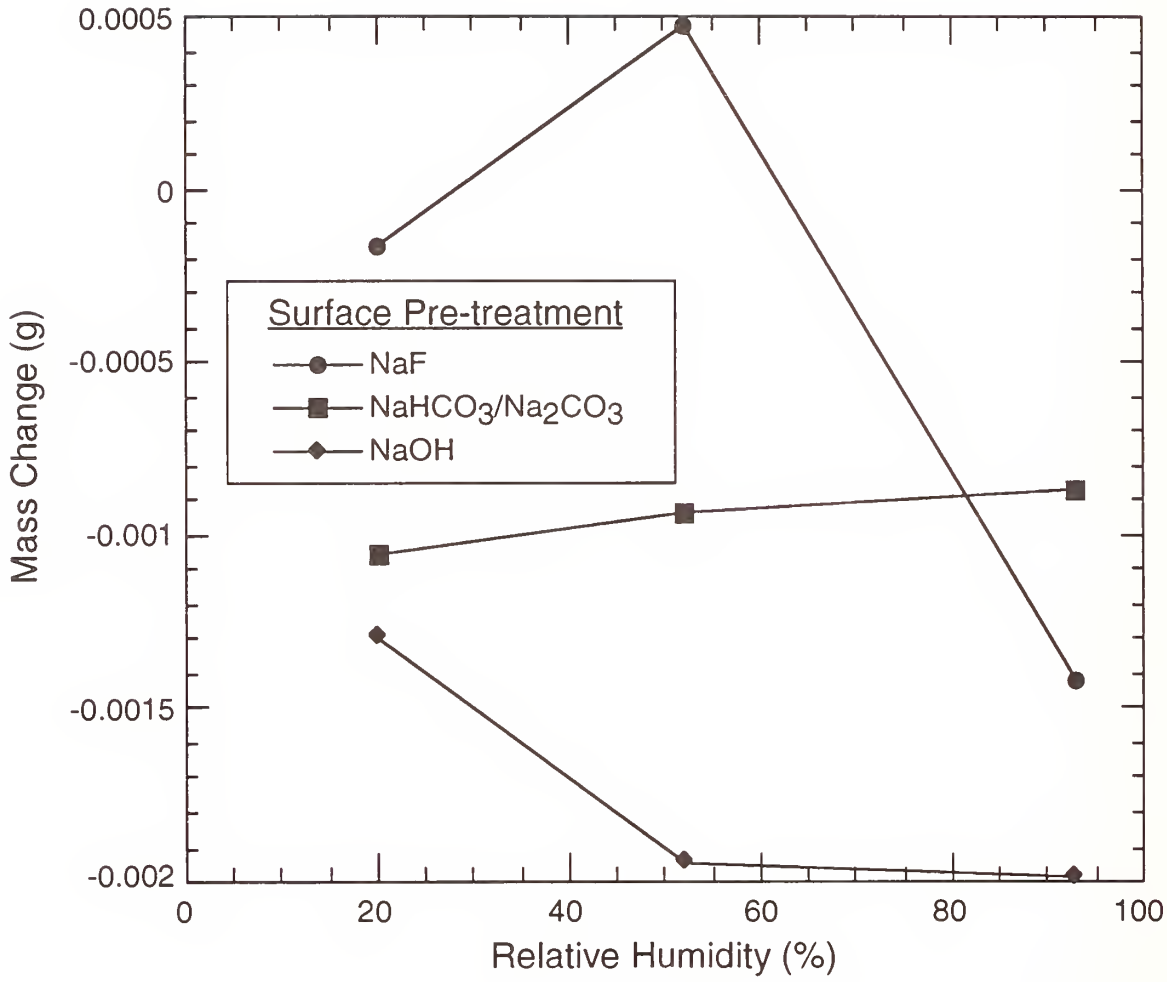

Figure 13. Mass change during atmospheric exposures at different relative humidities for Inconel 625 after surface pretreatment with artificial seawater and either NaF, $NaHCO_3/Na_2CO_3$, or NaOH.

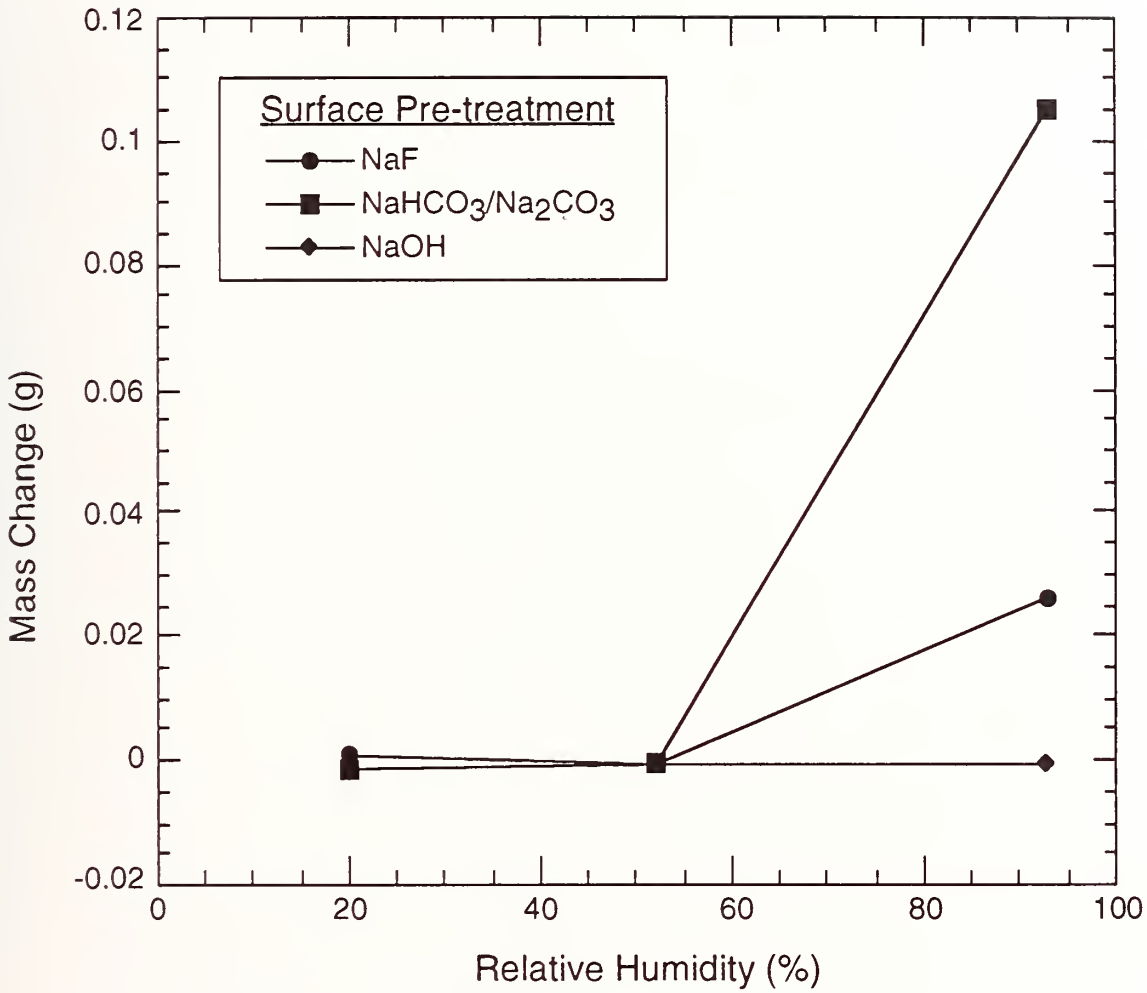

Figure 14. Mass change during atmospheric exposures at different relative humidities for the CDA 172 alloy after surface pretreatment with artificial.

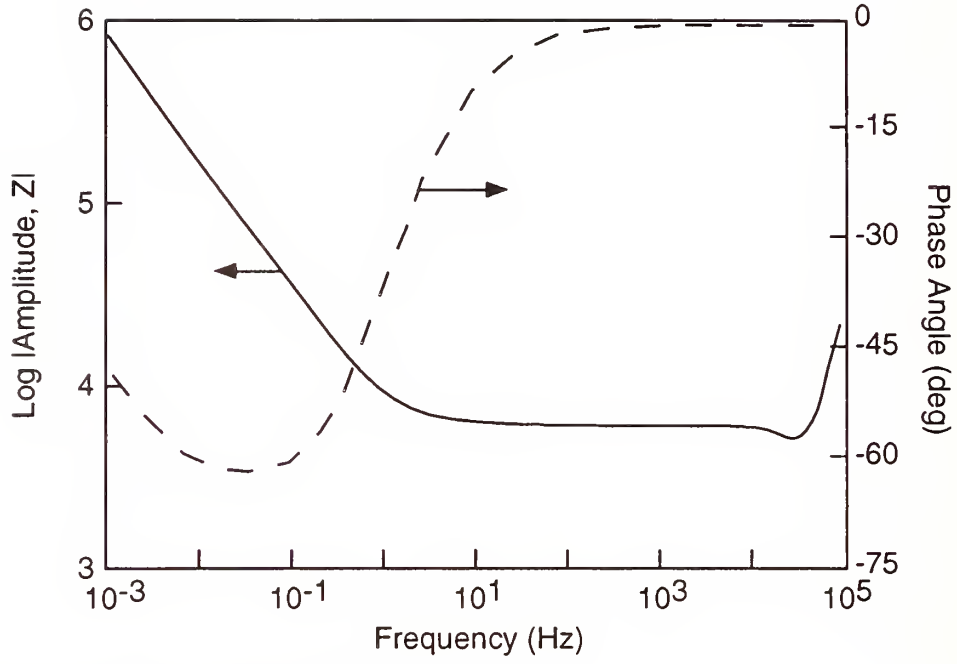

(a) Bode Amplitude and Phase Angle Plot

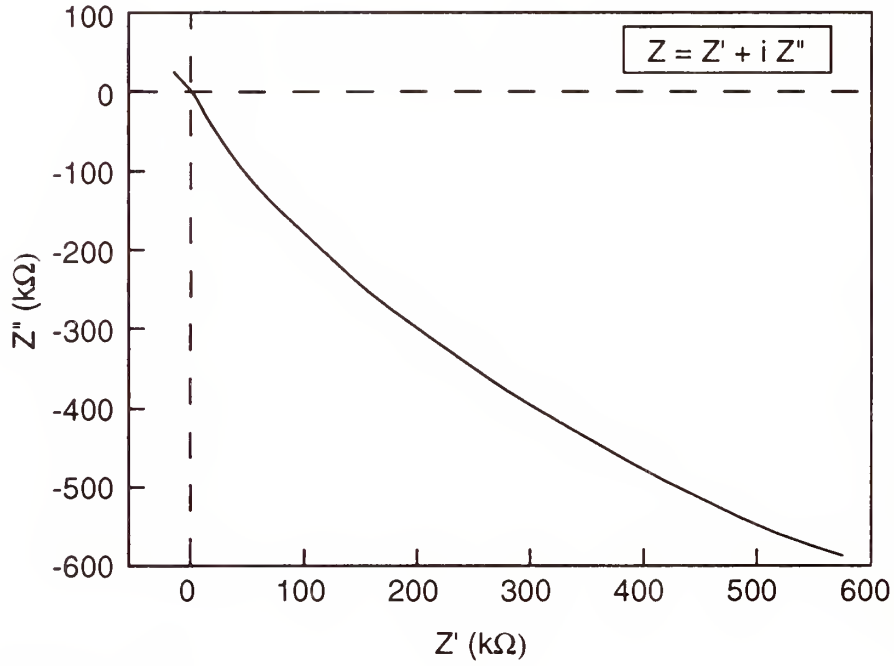

(b) Nyquist Plot

Figure 15. Bode and Nyquist plots of the impedance of 304 stainless steel in high purity ethanol.

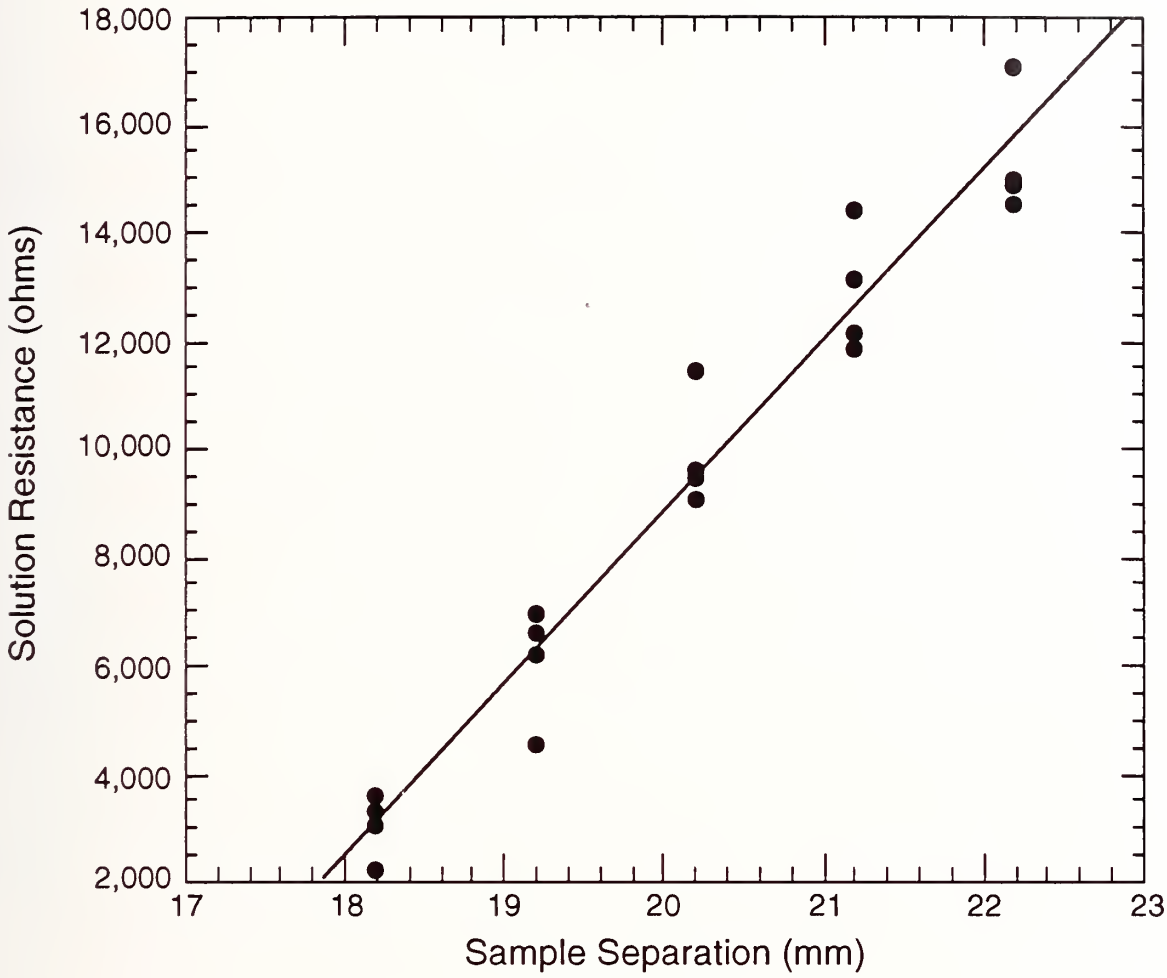

Figure 16. Solution resistance determined from two electrode impedance measurements for different electrode separations.

the slope of the curve in Figure 16 times the electrode area. Since A = 1,140 mm^2 and the slope in Figure 16 is 31,820 ohm/mm, the resistivity of the electrolyte is 3.63 x 10^7 ohm·m. This resistivity is still several orders of magnitude lower than the fire suppressants. Lowering the resistivity of the electrolyte will also make the required testing frequency range lower. As a result, other techniques for making these measurements are being explored.

7.4 Conclusions

The primary objective of this investigation was to determine if there were any of the candidates that should be eliminated from consideration because they were unacceptably corrosive to metals. This study did not identify any agent for which it would not be possible to identify a suitable alloy for the fabrication of aircraft storage and distributions systems. However, while no serious concerns were observed for all of the alloys in any of the agents, several agents consistently performed poorer than the others or yielded results that indicate further testing is warranted before they should be placed into service. Similarly, the post-deployment corrosion test results did not indicate any serious problems with any of the agents. However, the use of an agent which produces deposits of mixtures of bicarbonate, carbonate and sodium hydroxide may cause corrosion problems especially with aluminum alloys. A review of the literature on the corrosion of aluminum alloys indicates the hydroxide ion is very aggressive to these metals and very high corrosion rates can result if the pH of a surface film becomes too high. As a result, sodium bicarbonate is not considered a desirable candidate from a corrosion prevention point of view.

The secondary objective was to identify alloys that were suitable for use in each of the agents. Nitronic 40, AM 355, and 304 stainless steel consistently performed better than the other alloys in the agents, but examination of the behavior in the specific agent should be consulted before making decisions. For example, the slow strain rate tensile tests on 304 stainless steel indicated that there may be a potential environmentally induced cracking problem with this material in FC-C318, but additional testing would be required before this can be concluded.

The third objective was to develop a rapid electrochemical technique for the assessment of the corrosivity of fire suppressant agents. The technique examined enables the measurement of corrosion rates in media of much lower electrical conductivity, higher temperatures and pressures than normally examined, but very low testing frequencies and long testing times will be required for these low corrosion rate and very low conductivities. As a result, other techniques for making these measurements are being explored.

7.5 References

ASTM, Standard Guide for Applying Statistics to Analysis of Corrosion Data, *Annual Book of ASTM Standards Section 3, Metals Test Methods and Analytical Procedures*, Phil., PA, ASTM, 1993.

ASTM, Standard Practice for Laboratory Immersion Corrosion Testing of Metals, *Annual Book of ASTM Standards Section 3, Metals Test Methods and Analytical Procedures*, Phil., PA, 1993.

Bailey, J. C., Porter, F. C., and Pearson, A. W., Aluminum and Aluminum Alloys, *Corrosion*. Chapter 4.1, 4:3-4:33, Newnes - Butterworths, 1976.

Baumert, B. A., *A Study of the Corrosion Behavior of Aluminum Alloys*, Univ. of Notre Dame, Notre Dame, IN, 1986.

Bevington, P. R., *Data Reduction and Error Analysis for the Physical Sciences*, McGraw-Hill, New York, 1969.

Boyer, H. E., and Gall, T. L., *Metals Handbook— Desk Edition*, Metals Park, OH, ASM International, 1985.

Brett, C. M. A., "On the Electrochemical Behaviour of Aluminium in Acidic Chloride Solution," *Corrosion Science* 33, No. 2, 203-210, 1992.

Cabot, P. L., Centellas, F. A., Garrido, J. A., Perez, E., and Vidal, H., "Electrochemical Study of Aluminum Corrosion in Acid Chloride Solutions," *Electrochim. Acta* 36, 1, 179-187, 1991.

Davies, D. E., and Prigmore, R. M., "The Effect of Sodium Fluoride on the Localized Corrosion of Aluminum in Distilled Water and 50% Ethanediol Solution," *International Congress on Metallic Corrosion*, Toronto, Canada, National Research Council of Canads, 1984.

deSouza, J. P., Mattos, O. R., Sather, L., and Takenouti, H.,"Impedance Measurements of Corroding Mild Steel in an Automotive Fuel Ethanol With and Without Inhibitor in a Two and Three Electrode Cell." *Corro. Sci.* 27, 1351-1364, 1987.

Fink, F. W., and Boyd, W. K., *The Corrosion of Metals in Marine Environments*, Columbus, Bayer and Company Inc., Columbus, OH, 1970.

Flarsheim, W. M., Tsou, Y. M., Trachtenberg, I., Johnston, K. P., and Bard, A. J., "Electrochemistry in Near-Critical and Supercritical Fluids, 3, Studies of Br-, I-, and Hydroquionone in Aqueous Solutions", *J. Phys. Chem.*, 90, 3857-3862, 1986.

Foley, R. T., and Trazaskoma, P. P., "The Chemical Nature of the Anion Dependency of the Corrosion of Aluminum Alloy 7075-T6," *Corro.*, 33, 12, 435, 1977.

Halsall, R., *Corrosion of Metals in Ethanol and Methanol Containing Fuels*, General Motors, Warren, MI, 1992.

McDonald, A. C., Fan, F.-R. F., and Bard, A. J., "Electrochemistry in Near-Critical and Supercritical Fluids, Water, Experimental Techniques and the Copper (II) System," *J. Phys. Chem.* 90, 2, 196-202, 1986.

Mendenhall, W., and Sincich, T., *Statistics for Engineering and the Sciences*, San Francisco, Dellen Publ. Co., 1992.

Pourbaix, M., *Atlas of Electrochemical Equilibria in Aqueous Solutions. Houston, TX, National Association of Corrosion Engineers*, 1974.

Ricker, R. E., and Duquette, D. J., *Potentiodynamic Polarization Studies of an Al-Mg-Li Alloy*, Aluminum Lithium Alloys II, Warrendale, PA, The Metallurgy Society of AIME, 581-596, 1984.

Romans, H. B., and H. L. C., Jr., "Atmospheric Stress Corrosion Testing of Aluminum Alloys," *Metal Corrosion in the Atmosphere*, Boston, MA, ASTM, 1967.

Scully, J. R., Frankenthal, R. P., Hanson, K. J., Siconolfi, D. J., and Sinclair, J. D., "Localized Corrosion of Sputtered Aluminum and Al-0.5% Cu Alloy Thin Films in Aqueous HF Solution: 1 Corrosion Phenomena," *J. Electrochem. Soc.*, 137, 5, 1365-1372, 1990a.

Scully, J. R., Frankenthal, R. P., Hanson, K. J., Siconolfi, D. J., and Sinclair, J. D., "Localized Corrosion of Sputtered Aluminum and Al-0.5% Cu Aloy Thin Films in Aqueous HF Solution: II. Inhibition by CO_2," *J. Electrochem. Soc.*, 137, 1373-1377, 1990b.

Scully, J. R., Peebles, A. D., Romig, A. D., Frear, D. R., and Hills, C. R., "Metallurgical Factors Influencing the Corrosion of Aluminum, Al-Cu, and Al-Si Alloy Thin Films in Dilute Hydrofluoric Solution," *Metallurgical Transactions A* 23A, 2641-2655, September 1992.

Smith, W. F., *Structure and Properties of Engineering Alloys*, McGraw-Hill Book Company, New York, 1981.

Stoudt, M. R., Vasudévan, A. K., and Ricker, R. E., "Examination of the Influence of Lithium on the Repassivation Rate of Aluminum Alloys," *Corrosion Testing of Aluminum Alloys*, San Francisco, CA, ASTM, Phila., PA., 1990.

Walpole, R. E., and Myers, R. H., *Probability and Statistics of Engineers and Scientists*, The Macmillan Co., New York, 1972.

Wheeler, K. R., A. B. J. Jr., and May, R. P., "Aluminum Alloy Performance in Industrial Air-Cooled Applications," *Atmospheric Corrosion of Metals*, Denver, CO, ASTM, 1980A.

Zotikov, V. S., Bakhmutova, G. B., Bocharova, N. A., and Semenyuk, E. Y., "Corrosion of Al and its Alloys in Hydrofluoric Acid," *Prot. Met.*, 10, 2, 154-156, 1974.

Appendix A. Corrosion Rate Exposure Test Results

Alloy	Sample No.	Test Envir.	Average Initial Wt., grams	Average grams	Δ Wt.	Average Wt. Loss	Standard Deviation
NIT40	01	HCFC-22	14.12380	14.12393	0.00013		
NIT40	02	HCFC-22	14.31539	14.31552	0.00013	-0.00018	0.00008
NIT40	03	HCFC-22	13.78000	13.78027	0.00027		
NIT40	04	HCFC-124	14.30209	14.30217	0.00008		
NIT40	05	HCFC-124	14.11364	14.11370	0.00006	-0.00009	0.00005
NIT40	06	HCFC-124	14.14462	14.14476	0.00014		
NIT40	07	FC-31-10	14.01056	14.01079	0.00022		
NIT40	08	FC-31-10	14.07978	14.08000	0.00022	-0.00025	0.00004
NIT40	09	FC-31-10	14.03391	14.03421	0.00029		
NIT40	10	HFC-227	14.26208	14.26211	0.00003		
NIT40	11	HFC-227	14.21813	14.21816	0.00003	-0.00001	0.00003
NIT40	12	HFC-227	14.15156	14.15153	-0.00003		
NIT40	13	HFC-125	14.29082	14.29093	0.00012		
NIT40	14	HFC-125	14.21129	14.21117	-0.00012	0.00001	0.00012
NIT40	15	HFC-125	13.91204	13.91201	-0.00003		
NIT40	16	FC-116	14.09377	14.09379	0.00002		
NIT40	17	FC-116	13.88219	13.88232	0.00012	-0.00001	0.00012
NIT40	18	FC-116	14.06229	14.06216	-0.00012		
NIT40	19	HFC-134a	13.94796	13.94795	-0.00001		
NIT40	20	HFC-134a	14.24534	14.24537	0.00003	-0.00001	0.00002
NIT40	21	HFC-134a	14.21014	14.21016	0.00002		
NIT40	22	HFC-236	14.12528	14.12532	0.00004		
NIT40	23	HFC-236	14.11809	14.11812	0.00004	-0.00002	0.00002
NIT40	24	HFC-236	14.26927	14.26926	0.00000		
NIT40	25	FC-C318	14.35759	14.35764	0.00005		
NIT40	26	FC-C318	14.33708	14.33707	-0.00001	-0.00001	0.00004
NIT40	27	FC-C318	14.18774	14.18772	-0.00002		
NIT40	28	FC-218	14.30586	14.30608	0.00022		
NIT40	29	FC-218	13.95517	13.95535	0.00018	-0.00015	0.00008
NIT40	30	FC-218	14.27204	14.27210	0.00006		
NIT40	1a	HFC-32/125	14.85542	14.85569	0.00027		
NIT40	2a	HFC-32/125	14.79800	14.79830	0.00030	-0.00030	0.00003
NIT40	3a	HFC-32/125	14.79587	14.79621	0.00033		
NIT40	4a	NaHCO3	14.82673	14.82690	0.00017		
NIT40	5a	NaHCO3	14.79937	14.79965	0.00028	-0.00040	0.00030
NIT40	6a	NaHCO3	14.80710	14.80783	0.00073		
6061-T6	01	HCFC-22	5.15897	5.15956	0.00059		
6061-T6	02	HCFC-22	5.14160	5.14202	0.00041	-0.00046	0.00011
6061-T6	03	HCFC-22	5.16151	5.16188	0.00037		
6061-T6	04	HCFC-124	5.15992	5.16021	0.00029		

Alloy	Sample No.	Test Envir.	Average Initial Wt., grams	Average grams	Δ Wt.	Average Wt. Loss	Standard Deviation
NIT40	01	HCFC-22	14.12380	14.12393	0.00013		
6061-T6	05	HCFC-124	5.15997	5.16009	0.00012	-0.00022	0.00009
6061-T6	06	HCFC-124	5.16249	5.16274	0.00025		
6061-T6	07	FC-31-10	5.15805	5.15867	0.00062		
6061-T6	08	FC-31-10	5.15762	5.15808	0.00047	-0.00053	0.00008
6061-T6	09	FC-31-10	5.15774	5.15825	0.00051		
6061-T6	10	HFC-227	5.14240	5.14254	0.00014		
6061-T6	11	HFC-227	5.15458	5.15475	0.00016	-0.00013	0.00004
6061-T6	12	HFC-227	5.16393	5.16401	0.00008		
6061-T6	13	HFC-125	5.14067	5.14096	0.00029		
6061-T6	14	HFC-125	5.14888	5.14912	0.00024	-0.00020	0.00012
6061-T6	15	HFC-125	5.16261	5.16267	0.00007		
6061-T6	16	FC-116	5.14425	5.14459	0.00034		
6061-T6	17	FC-116	5.16136	5.16155	0.00018	-0.00024	0.00009
6061-T6	18	FC-116	5.15905	5.15924	0.00020		
6061-T6	19	HFC-134a	5.15888	5.15901	0.00013		
6061-T6	20	HFC-134a	5.15054	5.15069	0.00016	-0.00013	0.00003
6061-T6	21	HFC-134a	5.13945	5.13955	0.00011		
6061-T6	22	HFC-236	5.15121	5.15562	0.00442		
6061-T6	23	HFC-236	5.14617	5.14856	0.00239	-0.00248	0.00189
6061-T6	24	HFC-236	5.15225	5.15288	0.00063		
6061-T6	25	FC-C318	5.15709	5.15884	0.00174		
6061-T6	26	FC-C318	5.15927	5.16053	0.00126	-0.00118	0.00060
6061-T6	27	FC-C318	5.14241	5.14295	0.00055		
6061-T6	01a	FC-218	5.10076	5.10108	0.00032		
6061-T6	02a	FC-218	5.11183	5.11221	0.00039	-0.00037	0.00005
6061-T6	03a	FC-218	5.11843	5.11884	0.00041		
6061-T6	10a	HFC-32/125	5.11563	5.11658	0.00095		
6061-T6	11a	HFC-32/125	5.11169	5.11215	0.00047	-0.00059	0.00032
6061-T6	12a	HFC-32/125	5.11423	5.11457	0.00034		
6061-T6	13a	NaHCO3	5.10236	5.10328	0.00092		
6061-T6	14a	NaHCO3	5.11181	5.11242	0.00061	-0.00104	0.00050
6061-T6	15a	NaHCO3	5.11315	5.11474	0.00159		
I625	01	HCFC-22	16.71024	16.70993	-0.00031		
I625	02	HCFC-22	16.73534	16.73509	-0.00025	0.00033	0.00009
I625	03	HCFC-22	16.74050	16.74008	-0.00042		
I625	04	HCFC-124	16.72578	16.72552	-0.00025		
I625	05	HCFC-124	16.71996	16.71964	-0.00032	0.00027	0.00005
I625	06	HCFC-124	16.78778	16.78755	-0.00023		
I625	07	FC-31-10	16.73050	16.73044	-0.00007		
I625	08	FC-31-10	16.71615	16.71614	-0.00001	0.00004	0.00003

Alloy	Sample No.	Test Envir.	Average Initial Wt., grams	Average grams	∆ Wt.	Average Wt. Loss	Standard Deviation
NIT40	01	HCFC-22	14.12380	14.12393	0.00013		
I625	09	FC-31-10	16.43237	16.43234	-0.00003		
I625	10	HFC-227	16.73460	16.73455	-0.00005		
I625	11	HFC-227	16.73019	16.73015	-0.00004	0.00006	0.00002
I625	12	HFC-227	16.78825	16.78818	-0.00008		
I625	13	HFC-125	16.72097	16.72095	-0.00002		
I625	14	HFC-125	16.70044	16.70050	0.00006	-0.00003	0.00004
I625	15	HFC-125	16.72375	16.72380	0.00005		
I625	16	FC-116	16.79899	16.79900	0.00002		
I625	17	FC-116	16.76286	16.76287	0.00001	-0.00003	0.00002
I625	18	FC-116	16.80056	16.80061	0.00005		
I625	19	HFC-134a	16.72989	16.72981	-0.00008		
I625	20	HFC-134a	16.40575	16.40562	-0.00013	0.00010	0.00002
I625	21	HFC-134a	16.72400	16.72390	-0.00010		
I625	22	HFC-236	16.38116	16.38111	-0.00005		
I625	23	HFC-236	16.71103	16.71099	-0.00004	0.00006	0.00003
I625	24	HFC-236	16.73446	16.73437	-0.00010		
I625	25	FC-C318	16.79867	16.79876	0.00009		
I625	26	FC-C318	16.68154	16.68152	-0.00002	-0.00002	0.00007
I625	27	FC-C318	16.73452	16.73450	-0.00002		
I625	01a	FC-218	17.04525	17.04529	0.00004		
I625	02a	FC-218	17.04924	17.04931	0.00006	-0.00005	0.00001
I625	03a	FC-218	17.03955	17.03959	0.00005		
I625	10a	HFC-32/125	17.04597	17.04613	0.00016		
I625	11a	HFC-32/125	17.02094	17.02106	0.00012	-0.00015	0.00002
I625	12a	HFC-32/125	17.03789	17.03805	0.00016		
I625	13a	NaHCO3	17.00623	17.00631	0.00008		
I625	14a	NaHCO3	16.98212	16.98218	0.00006	-0.00008	0.00002
I625	15a	NaHCO3	17.00205	17.00215	0.00010		
304	01	HCFC-22	14.50690	14.50701	0.00011		
304	02	HCFC-22	14.54831	14.54854	0.00022	-0.00017	0.00006
304	03	HCFC-22	14.54721	14.54738	0.00017		
304	04	HCFC-124	14.55392	14.55389	-0.00003		
304	05	HCFC-124	14.52197	14.52197	0.00000	0.00004	0.00004
304	06	HCFC-124	14.55766	14.55758	-0.00008		
304	07	FC-31-10	14.57636	14.57693	0.00057		
304	08	FC-31-10	14.59461	14.59524	0.00062	-0.00058	0.00004
304	09	FC-31-10	14.53066	14.53122	0.00056		
304	10	HFC-227	14.50282	14.50297	0.00015		
304	11	HFC-227	14.48668	14.48684	0.00016	-0.00014	0.00002
304	12	HFC-227	14.49441	14.49453	0.00011		

Alloy	Sample No.	Test Envir.	Average Initial Wt., grams	Average grams	Δ Wt.	Average Wt. Loss	Standard Deviation
NIT40	01	HCFC-22	14.12380	14.12393	0.00013		
304	13	HFC-125	14.53445	14.53459	0.00014		
304	14	HFC-125	14.58747	14.58759	0.00012	-0.00014	0.00001
304	15	HFC-125	14.51819	14.51834	0.00014		
304	16	FC-116	14.60180	14.60199	0.00018		
304	17	FC-116	14.58646	14.58660	0.00014	-0.00015	0.00003
304	18	FC-116	14.56847	14.56859	0.00012		
304	19	HFC-134a	14.54856	14.54863	0.00007		
304	20	HFC-134a	14.57147	14.57154	0.00007	-0.00007	0.00000
304	21	HFC-134a	14.51002	14.51008	0.00007		
304	22	HFC-236	14.50289	14.50299	0.00009		
304	23	HFC-236	14.56563	14.56573	0.00010	-0.00008	0.00003
304	24	HFC-236	14.49324	14.49329	0.00004		
304	25	FC-C318	14.55940	14.55956	0.00016		
304	26	FC-C318	14.48874	14.48892	0.00018	-0.00020	0.00005
304	27	FC-C318	14.52980	14.53006	0.00026		
304	01a	FC-218	14.70650	14.70657	0.00007		
304	02a	FC-218	14.59916	14.59922	0.00005	-0.00009	0.00005
304	03a	FC-218	14.67582	14.67597	0.00015		
304	10a	HFC-32/125	14.62390	14.62411	0.00021		
304	11a	HFC-32/125	14.72853	14.72875	0.00023	-0.00024	0.00004
304	12a	HFC-32/125	14.66874	14.66902	0.00028		
304	13a	NaHCO3	14.66832	14.66853	0.00021		
304	14a	NaHCO3	14.71106	14.71136	0.00030	-0.00026	0.00005
304	15a	NaHCO3	14.57512	14.57540	0.00028		
172	01	HCFC-22	16.08959	16.09228	0.00269		
172	02	HCFC-22	16.60931	16.61261	0.00331	-0.00306	0.00033
172	03	HCFC-22	16.35164	16.35484	0.00320		
172	04	HCFC-124	16.37510	16.37691	0.00181		
172	05	HCFC-124	16.38782	16.38919	0.00137	-0.00147	0.00029
172	06	HCFC-124	16.31289	16.31414	0.00125		
172	07	FC-31-10	16.47673	16.47927	0.00254		
172	08	FC-31-10	16.47398	16.47671	0.00273	-0.00266	0.00011
172	09	FC-31-10	16.15224	16.15496	0.00272		
172	10	HFC-227	16.42018	16.42233	0.00215		
172	11	HFC-227	16.20014	16.20199	0.00185	-0.00197	0.00016
172	12	HFC-227	16.52838	16.53030	0.00192		
172	13	HFC-125	16.57400	16.57489	0.00088		
172	14	HFC-125	16.60772	16.60860	0.00088	-0.00089	0.00002
172	15	HFC-125	16.48618	16.48709	0.00091		
172	16	FC-116	16.53656	16.53792	0.00136		

Alloy	Sample No.	Test Envir.	Average Initial Wt., grams	Average grams	Δ Wt.	Average Wt. Loss	Standard Deviation
NIT40	01	HCFC-22	14.12380	14.12393	0.00013		
172	17	FC-116	16.41082	16.41249	0.00167	-0.00151	0.00016
172	18	FC-116	16.52522	16.52671	0.00149		
172	19	HFC-134a	16.18493	16.18514	0.00021		
172	20	HFC-134a	16.48381	16.48401	0.00020	-0.00023	0.00004
172	21	HFC-134a	16.37599	16.37626	0.00027		
172	22	HFC-236	16.52102	16.52189	0.00087		
172	23	HFC-236	16.49087	16.49177	0.00089	-0.00087	0.00003
172	24	HFC-236	16.82507	16.82590	0.00084		
172	25	FC-C318	16.27482	16.27525	0.00043		
172	26	FC-C318	16.47234	16.47284	0.00050	-0.00043	0.00007
172	27	FC-C318	16.52698	16.52734	0.00036		
172	01a	FC-218	16.65123	16.65199	0.00077		
172	02a	FC-218	16.61390	16.61470	0.00080	-0.00077	0.00003
172	03a	FC-218	16.71205	16.71278	0.00074		
172	10a	HFC-32/125	16.64347	16.64594	0.00247		
172	11a	HFC-32/125	16.67785	16.67989	0.00204	-0.00226	0.00022
172	12a	HFC-32/125	16.56278	16.56506	0.00228		
172	13a	NaHCO3	16.69064	16.69282	0.00218		
172	14a	NaHCO3	16.69839	16.70081	0.00242	-0.00218	0.00024
172	15a	NaHCO3	16.60099	16.60294	0.00195		
13-8	01	HCFC-22	15.04714	15.04715	0.00001		
13-8	02	HCFC-22	15.16177	15.16169	-0.00008	0.00003	0.00004
13-8	03	HCFC-22	15.07196	15.07193	-0.00003		
13-8	04	HCFC-124	15.41550	15.41533	-0.00017		
13-8	05	HCFC-124	15.21775	15.21769	-0.00006	0.00009	0.00007
13-8	06	HCFC-124	15.01510	15.01507	-0.00003		
13-8	07	FC-31-10	15.37818	15.37857	0.00039		
13-8	08	FC-31-10	15.26949	15.26977	0.00028	-0.00036	0.00007
13-8	09	FC-31-10	15.15930	15.15971	0.00041		
13-9	10	HFC-227	15.19980	15.19988	0.00008		
13-8	11	HFC-227	15.14515	15.14527	0.00012	-0.00007	0.00006
13-8	12	HFC-227	15.36752	15.36752	0.00000		
13-8	13	HFC-125	15.32942	15.32956	0.00014		
13-8	14	HFC-125	15.26229	15.26243	0.00015	-0.00015	0.00001
13-8	15	HFC-125	15.13633	15.13649	0.00017		
13-8	16	FC-116	15.05156	15.05179	0.00022		
13-8	17	FC-116	14.98056	14.98077	0.00021	-0.00021	0.00001
13-8	18	FC-116	15.21466	15.21486	0.00020		
13-8	19	HFC-134a	15.42397	15.42412	0.00015		
13-8	20	HFC-134a	15.22669	15.22673	0.00003	-0.00009	0.00006

Alloy	Sample No.	Test Envir.	Average Initial Wt., grams	Average grams	Δ Wt.	Average Wt. Loss	Standard Deviation
NIT40	01	HCFC-22	14.12380	14.12393	0.00013		
13-8	21	HFC-134a	15.15183	15.15190	0.00008		
13-8	22	HFC-236	15.12782	15.12793	0.00012		
13-8	23	HFC-236	15.01663	15.01672	0.00009	-0.00011	0.00001
13-8	24	HFC-236	15.34009	15.34021	0.00011		
13-8	25	FC-C318	15.09380	15.09395	0.00015		
13-8	26	FC-C318	15.37339	15.37357	0.00018	-0.00017	0.00001
13-8	27	FC-C318	15.44205	15.44223	0.00017		
13-8	01a	FC-218	15.29468	15.29494	0.00026		
13-8	02a	FC-218	15.10975	15.11002	0.00027	-0.00028	0.00002
13-8	03a	FC-218	15.23719	15.23749	0.00030		
13-9	10a	HFC-32/125	15.11540	15.11581	0.00042		
13-8	11a	HFC-32/125	15.34063	15.34103	0.00041	-0.00049	0.00014
13-8	12a	HFC-32/125	15.03324	15.03389	0.00065		
13-8	13a	NaHCO3	14.85465	14.85575	0.00110		
13-8	14a	NaHCO3	15.10975	15.11041	0.00066	-0.00080	0.00026
13-8	15a	NaHCO3	15.08130	15.08194	0.00064		
355	01	HCFC-22	15.29150	15.29145	-0.00005		
355	02	HCFC-22	15.00926	15.00912	-0.00014	0.00009	0.00005
355	03	HCFC-22	15.32792	15.32785	-0.00007		
355	04	HCFC-124	15.01662	15.01629	-0.00032		
355	05	HCFC-124	15.42594	15.42581	-0.00013	0.00021	0.00010
355	06	HCFC-124	14.92252	14.92236	-0.00016		
355	07	FC-31-10	14.98140	14.98163	0.00023		
355	08	FC-31-10	15.39432	15.39458	0.00026	-0.00022	0.00005
355	09	FC-31-10	15.36341	15.36358	0.00017		
355	10	HFC-227	15.51429	15.51431	0.00002		
355	11	HFC-227	15.39858	15.39860	0.00002	-0.00001	0.00002
355	12	HFC-227	14.84048	14.84047	-0.00002		
355	13	HFC-125	14.97517	14.97520	0.00003		
355	14	HFC-125	14.75849	14.75853	0.00004	-0.00003	0.00001
355	15	HFC-125	15.34143	15.34145	0.00002		
355	16	FC-116	15.23439	15.23460	0.00021		
355	17	FC-116	14.88056	14.88069	0.00013	-0.00014	0.00006
355	18	FC-116	14.87070	14.87078	0.00008		
355	19	HFC-134a	14.89687	14.89690	0.00003		
355	20	HFC-134a	15.51394	15.51393	0.00000	0.00001	0.00005
355	21	HFC-134a	14.97787	14.97780	-0.00007		
355	22	HFC-236	15.26546	15.26536	-0.00010		
355	23	HFC-236	14.88965	14.88972	0.00007	-0.00001	0.00009
355	24	HFC-236	15.50902	15.50906	0.00005		

Alloy	Sample No.	Test Envir.	Average Initial Wt., grams	Average grams	Δ Wt.	Average Wt. Loss	Standard Deviation
NIT40	01	HCFC-22	14.12380	14.12393	0.00013		
355	25	FC-C318	14.74122	14.74128	0.00006		
355	26	FC-C318	15.22578	15.22585	0.00007	-0.00001	0.00011
355	27 *	FC-C318	14.74538	14.74526	-0.00012		
355	01a	FC-218	15.33161	15.33171	0.00010		
355	02a	FC-218	15.71182	15.71198	0.00016	-0.00015	0.00004
355	03a	FC-218	15.27753	15.27772	0.00019		
355	10a	HFC-32/125	15.39200	15.39234	0.00034		
355	11a	HFC-32/125	15.44073	15.44101	0.00027	-0.00031	0.00004
355	12a	HFC-32/125	15.36869	15.36901	0.00032		
355	13a	NaHCO3	15.52390	15.52416	0.00026		
355	14a	NaHCO3	15.52734	15.52756	0.00022	-0.00026	0.00004
355	15a	NaHCO3	15.46160	15.46190	0.00030		
4130	01	HCFC-22	15.65953	15.66151	0.00198		
4130	02	HCFC-22	15.60112	15.60544	0.00432	-0.00285	0.00128
4130	03	HCFC-22	15.62642	15.62867	0.00225		
4130	04	HCFC-124	15.64049	15.64073	0.00024		
4130	05	HCFC-124	15.67752	15.67795	0.00043	-0.00032	0.00010
4130	06	HCFC-124	15.63756	15.63785	0.00029		
4130	07	FC-31-10	15.66338	15.66454	0.00116		
4130	08	FC-31-10	15.68480	15.68603	0.00124	-0.00110	0.00017
4130	09	FC-31-10	15.71161	15.71252	0.00091		
4130	10	HFC-227	15.66745	15.66773	0.00028		
4130	11	HFC-227	15.69433	15.69459	0.00026	-0.00030	0.00005
4130	12	HFC-227	15.69102	15.69137	0.00035		
4130	13	HFC-125	15.67280	15.67345	0.00065		
4130	14	HFC-125	15.69388	15.69465	0.00077	-0.00067	0.00009
4130	15	HFC-125	15.61443	15.61503	0.00060		
4130	16	FC-116	15.67118	15.67160	0.00042		
4130	17	FC-116	15.65998	15.66037	0.00039	-0.00040	0.00001
4130	18	FC-116	15.63905	15.63945	0.00040		
4130	19	HFC-134a	15.65736	15.65765	0.00029		
4130	20	HFC-134a	15.67523	15.67539	0.00016	-0.00026	0.00009
4130	21	HFC-134a	15.68774	15.68808	0.00033		
4130	22	HFC-236	15.64327	15.64356	0.00029		
4130	23	HFC-236	15.70320	15.70357	0.00037	-0.00034	0.00004
4130	24	HFC-236	15.72882	15.72919	0.00037		
4130	25	FC-C318	15.67104	15.67137	0.00034		
4130	26	FC-C318	15.69345	15.69372	0.00027	-0.00031	0.00004
4130	27	FC-C318	15.67568	15.67600	0.00032		
4130	01a	FC-218	15.63867	15.63896	0.00029		

Alloy	Sample No.	Test Envir.	Average Initial Wt., grams	Average grams	Δ Wt.	Average Wt. Loss	Standard Deviation
NIT40	01	HCFC-22	14.12380	14.12393	0.00013		
4130	02a	FC-218	15.66631	15.66673	0.00042	-0.00038	0.00008
4130	03a	FC-218	15.57494	15.57537	0.00044		
4130	10a	HFC-32/125	15.68322	15.68357	0.00035		
4130	11a	HFC-32/125	15.72594	15.72617	0.00023	-0.01134	0.01914
4130	12a	HFC-32/125	15.65444	15.68788	0.03344		
4130	13a	NaHCO3	15.67555	15.67662	0.00107		
4130	14a	NaHCO3	15.63064	15.63150	0.00086	-0.00089	0.00017
4130	15a	NaHCO3	15.69020	15.69093	0.00074		

8. ELASTOMER SEAL COMPATIBILITY

Gregory B. McKenna, William K. Waldron Jr. and Ferenc Horkay
Materials Science and Engineering Laboratory

8.1 Introduction

Excessive swelling or deterioration of the elastomer seal (o-ring and its lubricant) in the fire suppressant storage container could lead to leakage of the agent leaving the system unready to respond in case of fire. Short term exposure experiments have been conducted and data have been generated on the proclivity of the eleven fluid agents to alter the properties of various elastomers and greases. The compatibilities of the fire suppressant agents with commonly used elastomers and greases have been characterized using two types of measurements.

The first type was based on solution thermodynamics and characterizes swelling due to sorption of the agent into the elastomer or grease. The degree of swelling was determined by measuring the solvent (agent) weight fraction w_1 in the polymer (elastomer or grease)/solvent (agent) system at various temperatures and vapor pressures. Using these weight fractions and the Flory-Huggins theory (Flory, 1942; Huggins, 1943), a single polymer-solvent interaction parameter χ was calculated for each polymer/agent system at various temperatures. The χ values were used to characterize the compatibility of the solvents (agents) with the polymers (elastomers and greases). Small χ values correspond to good solubility or, for present purposes, bad compatibility. Above $\chi = 0.5$, the solubility of polymers gradually decreases with increasing χ. A rating system was defined based on the values of χ parameters obtained from swelling measurements at 35 °C. Good compatibility ($\chi > 1.2$, $w_1 < 0.22$) implies that an elastomer or lubricant is acceptable for use in the fire suppressant system. Bad compatibility ($\chi < 0.9$, $w_1 > 0.38$) corresponds to excessive swelling. For values of $0.9 < \chi < 1.2$, the agent was considered to have fair compatibility with the elastomer or grease and represents a marginally acceptable system.

The second type, durability measurements, produced data on residual mechanical (rheological) properties of the elastomers (greases) after exposure to the fluids at elevated temperature and pressure (150 °C, 5.86 MPa). Compatibility ratings were based on the results of compression set and tensile test measurements of the elastomers and viscosity measurements of the greases. These tests provide direct information on the physical and chemical damage to the samples at extreme conditions. While the following procedures were used to define the fire suppressant agent/elastomer or lubricant compatibilities, it is important to note that the long term exposure response of these materials cannot be extracted from the tests as performed. A major conclusion from the results of the durability testing is that the 150 °C condition is too severe, *i.e.*, property changes for the most-part were extreme. Further testing at lower temperatures will be required to provide better estimates of elastomer and lubricant durabilities in the final down-selected candidate fluids.

In compression set measurements, good compatibility was defined as a condition when the compression set (percent of original deflection retained after release from compression) was less than 90% after a 2 week exposure. Elastomers have bad compatibility if the compression set exceeded 90% after 4 weeks. If the compression set was less that 90% after 2 weeks but exceeded 90% after a 4 week exposure, the agent was considered to have fair compatibility with the elastomer and represents a marginally acceptable system. If a specimen was split or broken, the agent was considered to have bad compatibility with the elastomer.

In the tensile test measurements, good compatibility was defined as a condition when the decrease in ultimate elongation (percent increase of inner circumference at rupture) was less than 65% after a 4 week exposure. Elastomers have bad compatibility if the decrease in ultimate elongation exceeded 65% after a 2 week exposure. If the decrease in ultimate elongation was less than 65% after 2 weeks but exceeded 65% after 4 weeks, the agent was considered to have fair compatibility with the elastomer and represents a marginally acceptable system.

The viscosity of the greases, when measurable, did not show systematic variation with exposure time, indicating that no significant chemical degradation occurred. It was found, however, that mobile substances or fractions were extracted by some of the candidate fire suppressant fluids which resulted in the greases becoming powder-like, *i.e.*, their viscosities were not measurable. Therefore, the ratings for the lubricant compatibility were based on the following criteria: Good compatibility was defined as a condition when the grease did not become powder-like after a 6 week exposure. Lubricants have bad compatibility if the grease became powder-like after a 4 week exposure. If the grease's viscosity was measurable after 4 weeks, but became powder-like after 6 weeks, the lubricant was considered to have fair compatibility with the agent.

The following describes the section organization: Section 8.2 describes the characterization of the agents in terms of thermodynamic swelling measurements. After briefly describing the theoretical basis of the thermodynamic investigations (Section 8.2.1), the vapor sorption experiments are described (Section (8.2.2) and the results of swelling measurements are presented (Section 8.2.3). Section 8.3 describes the characterization of the agents in terms of the durability measurements. After describing the high temperature exposure method (Section 8.3.1) and each durability measurement technique, the results of mechanical property measurements (compression set, tensile test, and viscosity) performed on the elastomers and greases are described (Sections 8.3.2 and 8.3.3). In Section 8.4, the results of the durability measurements in combination with the thermodynamic (swelling) investigations are used to characterize the compatibility of fire suppressants with elastomer seals.

8.2 Thermodynamic Compatibility

8.2.1 Theoretical Considerations. Swelling is a powerful method for characterizing the affinity of a polymer (elastomer or grease) to a solvent (fire suppressant agent). The driving force for swelling is the change in the free energy of mixing. The Flory-Huggins lattice theory of polymer solutions (Flory, 1942; Huggins, 1943) describes the free energy of mixing under subcritical conditions and characterizes the affinity of the polymer to the solvent by a single polymer-solvent interaction parameter χ. Existing network theories allow the evaluation of the relevant thermodynamic parameters from equilibrium swelling measurements when the polymer is crosslinked (James and Guth, 1943; Flory and Rehner, 1943; Flory and Erman, 1982). Proposed improvements of the theories lead to more complicated expressions containing more adjustable parameters. The corresponding states theory of polymers (Flory *et al.*, 1964a and 1964b.; Flory, 1965) provides a more general framework to analyze the thermodynamic properties of polymer systems both under subcritical and supercritical conditions.

In swelling measurements, the solvent activity is varied to swell the polymer by different amounts. In vapor sorption experiments, first conducted by Gee *et al.* (1965), the solvent uptake of the polymer is controlled by varying the partial pressure (activity) of the swelling agent in the equilibrium phase. Similar experiments have been performed by Brotzman and Eichinger (1982 and 1983) and McKenna and Crissmann (1993). The same thermodynamic information can also be

obtained using other methods to vary the solvent activity around a swollen network (Boyer, 1945; Pennings and Prins, 1961; Horkay and Zrinyi, 1982; McKenna *et al.*, 1989; Horkay *et al.*, 1989; McKenna *et al.*, 1990). However, vapor sorption experiments were used to measure the degree of swelling because of their straightforward interpretation and many polymer/solvent systems can be analyzed simultaneously.

8.2.1.1 Flory-Huggins Theory. The thermodynamics of mixing is governed by the change in free energy

$$\Delta G_m = \Delta H_m - T\Delta S_m \,, \tag{1}$$

where ΔG_m is the change in Gibbs free energy, T is the absolute temperature, ΔH_m is the heat of mixing, and ΔS_m is the entropy of mixing. A negative value of ΔG_m indicates that the mixing process occurs spontaneously. The term $T\Delta S_m$ is always positive because the entropy increases upon mixing.

The thermodynamic properties of polymer solutions both in the semi-dilute and concentrated regimes can be described in a straightforward way using the Flory-Huggins lattice theory (Flory, 1953). This theory calculates the entropy of mixing from the possible arrangements of component molecules (*i.e.*, solvent molecules and monomeric units of the polymer) with respect to each other, *i.e.*, ΔS_m is given by

$$\Delta S_m = k\,(N_1 \ln v_1 + N_2 \ln v_2) \,, \tag{2}$$

where N_1 and N_2 are the number of molecules of the solvent and polymer, respectively, v_1 and v_2 are the corresponding volume fractions and k is the Boltzmann factor. The Flory-Huggins theory calculates the heat of mixing by introducing the dimensionless interaction parameter

$$\chi = \frac{\Delta H_m}{(kTN_1 v_2)} \tag{3}$$

which when combined with Equation 2 leads to the total free energy of mixing

$$\Delta G_m = kT\,(N_1 \ln v_1 + N_2 \ln v_2 + \chi N_1 v_2) \,. \tag{4}$$

The value of χ depends on the thermodynamic quality of the solvent: in good solvent conditions $\chi < 0.5$ and in "theta" conditions $\chi = 0.5$. For poor solvents $\chi > 0.5$.

In general, χ depends on the polymer volume fraction (Flory, 1970), *i.e.*,

$$\chi = \chi_0 + \chi_1 v_2 + \cdots \,. \tag{5}$$

The chemical potential of the solvent μ_1 can be obtained by differentiating the Gibbs free energy of mixing with respect to the number of solvent moles and

$$\mu_1 - \mu_1^o = \Delta\mu_1 = RT\,[\ln(1 - v_2) + (1 - 1/P)v_2 + \chi v_2^2] \,, \tag{6}$$

where $\mu_1{}^o$ is the chemical potential of the pure solvent and P is the degree of polymerization. $\Delta\mu_1$ is related to measurable macroscopic quantities, such as the vapor pressure of the solvent p and the osmotic pressure of the solution Π. From general thermodynamic considerations,

$$\Delta\mu_1 = RT \ln(p/p^o) = -\Pi V_1 , \tag{7}$$

where p^o is the saturation pressure of the solvent at temperature T, V_1 is the partial molar volume of the solvent and R is the gas constant.

Combining Equations 6 and 7 yields

$$\ln(p/p^o) = \ln(1 - v_2) + (1-1/P)v_2 + \chi v_2^2 , \tag{8}$$

which can be fit to experimental data using adjustable parameters χ_0, χ_1, ... from Equation 5. Thus, chemical potentials obtained from vapor pressure or osmotic pressure measurements yield empirical values of χ. These values allow the estimation of the solubility of polymers. Small χ values ($\chi <$ 0.5) correspond to good solubility. In good solvents, crosslinked polymers exhibit a large amount of swelling which can lead to seal failure in elastomeric o-ring based joints. High χ values ($\chi > 0.5$) are characteristic of polymer/solvent systems with limited miscibility. Crosslinked polymers swell only a small amount in thermodynamically poor solvents.

The simple Flory-Huggins theory discussed above is based on a series of arbitrary assumptions (*e.g.*, lattice sites are the same size for polymer segments and solvent molecules, uniform distribution of the polymer segments in the lattice). The χ parameter is, by definition (see Equation 3), governed by the interaction energy. In reality, χ is a measure of Gibbs free energy, *i.e.*, it also contains an entropy contribution. Because of several assumptions involved in the Flory-Huggins theory, χ can only be considered an empirical fitting parameter, without precisely defined physical significance, which accurately describes the thermodynamics of the system in question.

Although the Flory-Huggins theory is formulated in terms of volume fractions (v_1 and v_2), the theory can also be expressed in terms of weight fractions (w_1 and w_2). This substitution is arbitrary, but the functional form of Equation 8 remains the same

$$\ln(p/p^o) = \ln(1 - w_2) + w_2 + \chi_0 w_2^2 + \chi_1 w_2^3, \tag{9}$$

where $\chi = \chi_0 + \chi_1 w_2$ has been substituted and the term (1 - 1 / P) has become unity since P is large for polymeric materials and infinite in crosslinked networks. Strictly speaking the use of the volume fraction in the Flory-Huggins theory is also a simplification because the surface area fraction is the relevant quantity in deriving the enthalpy of mixing on a lattice. In this case the χ values differ from those calculated from the equilibrium volume fractions (v_1 and v_2). Throughout the present report weight fractions are used instead of volume fractions because they are directly measured quantities.

8.2.1.2 Flory's Equation-of-State Theory. The principle of the corresponding state theories rests on the assumption that the intermolecular potentials for the polymer and solvent have equivalent forms when expressed as functions of the distance between molecular (or segment) centers. If the thermodynamic properties are known for one reference fluid, those for any corresponding fluids are determined by two scale factors: one for the separation distance of molecular centers and the other for the magnitude of intermolecular potential. These factors are embodied in a characteristic temperature T^* and a characteristic pressure p^*. In the case of polymers the third important parameter is the number of intermolecular degrees of freedom.

Flory formulated the partition function of liquids by combining a rudimentary factor for hard spheres with an intermolecular energy of the van der Waals form (Flory *et al.*, 1964a; Flory *et al.*, 1964b; Flory 1965). The reduced equation of state of a pure liquid is

$$\frac{\pi \upsilon}{\tau} = \frac{\upsilon^{1/3}}{\upsilon^{1/3}-1} - \frac{1}{\upsilon \tau} , \tag{10}$$

where $\upsilon = v / v^*$, $\tau = T / T^*$, $\pi = p / p^*$ are the reduced variables and v^* is the characteristic (hard core) volume. A pure component is completely characterized by the three parameters v^*, T^*, and p^*. The values of these parameters can be evaluated from *pvT* (pressure-volume-temperature) data by nonlinear regression fit to the theoretical equation of state (Equation 10). These parameters are tabulated in the literature for many small molecules as well as for several polymers (Shih and Flory, 1972).

The application of the equation-of-state theory for a two component mixture requires the knowledge of the parameters of the pure components as well as their interactions in the mixture defined by an interaction enthalpy parameter X_{12} and interaction entropy parameter Q_{12}. The chemical potential of mixing is given by

$$\begin{aligned} \frac{\Delta \mu_1}{RT} &= \ln(1 - \varphi) + (1 - 1/P)\varphi \\ &+ \frac{p_1^* v_1^*}{RT}\left[3T_1 \ln\left(\frac{\upsilon_1^{1/3} - 1}{\upsilon^{1/3} - 1}\right) + \frac{1}{\upsilon_1} - \frac{1}{\upsilon} + p_1(\upsilon - \upsilon_1)\right] \\ &+ \frac{v_1^* X_{12} \theta_2^2}{RT\upsilon} - \frac{v_1^* Q_{12} \theta_2^2}{R} , \end{aligned} \tag{11}$$

where φ is the segment fraction and θ_2 is the site fraction of the polymer.

For the mixture the reduction parameters can be calculated from

$$p^* = p_1^*(1 - \varphi) + p_2^* \varphi - (1 - \varphi)\theta_2 X_{12} \tag{12}$$

and

$$T^* = p^* / ((1 - \varphi) p_1^* / T_1^* + \varphi p_2^* / T_2^*) . \tag{13}$$

Knowing p^* and T^*, υ can be obtained from Equation 10. The only remaining unknown parameters are X_{12} and Q_{12}. Since the interaction terms usually have very little effect, X_{12} and Q_{12} are usually treated as free variables (adjustable parameters).

Equation 11 allows the calculation of the chemical potential both below and above the critical temperature of the solvent and therefore can be used to describe the solubility of a supercritical gas in a polymer. (The simple Flory-Huggins lattice theory discussed in the previous section cannot be used above the critical temperature of the fluid because the saturated pressure of the vapor p^o is not defined under supercritical conditions.)

In Section 8.2.3 some examples are shown which use Flory's equation-of-state theory to describe the experimental results both below and above T_c. This analysis has not been performed for all of the

polymer/solvent systems because the solvent uptake was relatively small above T_c at the pressures tested.

8.2.2 Swelling Measurements

8.2.2.1 Experimental Setup. The degrees of swelling of three greases and six sets of crosslinked and uncrosslinked elastomers were determined by measuring the displacement of each quartz spring using a cathetometer as in the experimental arrangement illustrated in Figure 1. The elastomer's or grease's mass uptake of the agent (solvent) was calculated from the relative displacement of the springs. The cathetometer had a vernier scale permitting readings to 0.01 mm but measurements were recorded to the nearest 0.05 mm because of difficulties in viewing the spring and pan assemblies.

Six pressure vessels were designed and built for this purpose. The pressure vessels were made of type 304 stainless steel and designed for a maximum working pressure of 5.86 MPa with two view ports 180° apart for viewing and backlighting purposes. The view ports were made with 10.2 cm diameter and 25.4 mm thick circular plates of tempered Corning Glass Pyrex (trademark for borosilicate) glass. The cylindrical vessel had 2.25 liters of inner volume (17.8 cm height by 12.7 cm diameter) and was large enough to admit a 7.6 cm square by 15.2 cm high stainless steel spring stand with sixteen fused quartz spring and pan assemblies. The quartz springs had a coil diameter of 6.4 mm and either 1 mg/mm or 1.25 mg/mm sensitivity (spring rate). The quartz pans were slightly curved with diameters of 7-9 mm and weighed 10-25 mg when empty.

Each vessel was placed in a 41 cm diameter by 30 cm high cylindrical Pyrex jar and completely immersed in Dow Corning silicone bath oil, clear 200 type, with a viscosity of 0.05 Pa · s. For insulation, a 10 mm thick aluminum lid was placed over the jar and 76 mm thick fiberglass sheet was wrapped around the circumference of the Pyrex jar. Two rectangular holes were made so that the view ports were visible. The bath was heated using a 1000 W Vycor (Corning Incorporated trademark) immersion heater and stirred to maintain temperature uniformity using a 37 W Cole-Parmer Stir-Pak mixer with a 51 mm diameter propeller. The temperature was monitored using a Fluke thermometer with a type K thermocouple and 0.1 °C resolution.

A pressure charging and recovery system was designed and built to allow the admission of the agent into the previously evacuated vessel and the recovery of the agent after each measurement. The system was also capable of overpressurizing the vessels with nitrogen but this capability was not employed. The pressure was monitored using a Druck DPI 602 digital pressure indicator and PDCR 910 transducer with an absolute pressure range of 0-6.21 MPa, combined nonlinearity, hysteresis and repeatability of $\pm$ 0.1% using the best straight line method (BSL).

8.2.2.2 Experimental Materials. The elastomers and lubricants used in this study are shown in Tables 1 and 2, respectively. Both crosslinked and uncrosslinked elastomers were studied. The 85% butadiene-15% acrylonitrile crosslinked copolymer was prepared by first dissolving approximately 2 g of polymer in 50 ml of benzene. Next, one part dicumyl peroxide per hundred parts butadiene rubber (1 phr) was added and dissolved. The benzene was allowed to evaporate and the specimen was placed in an oven at 150 °C for a period of 2 hours in order to crosslink the peroxide containing specimen. The 55% butadiene-45% acrylonitrile copolymer was crosslinked in a similar manner using pyridine as the solvent. The silicone, fluorosilicone, and neoprene polymers were supplied crosslinked and uncrosslinked by the vendor. The fluorocarbon polymers were cured at NIST for 1 hour at 150 °C and post-cured at 240 °C for 24 hours.

8.2.2.3 Experimental Methods. Samples of the three greases, six crosslinked and six uncrosslinked polymers weighing 25-50 mg were placed on 15 quartz pans. A glass bead with an

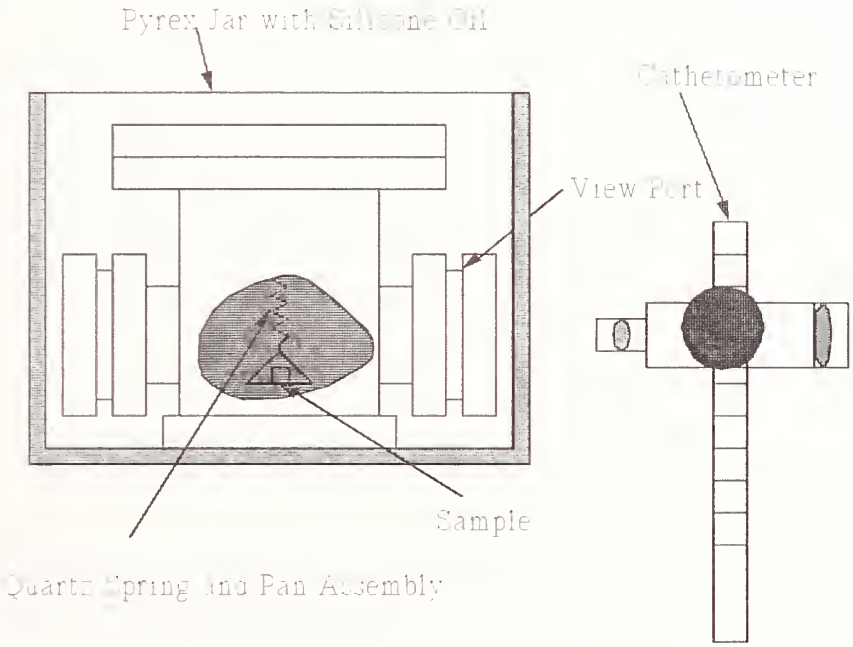

Figure 1. Schematic of the experimental apparatus for isopiestic swelling measurements.

Table 1. Elastomers used in swelling experiments

Elastomer	Vendor	Designation
Silicone	Colonial Rubber	Si
55% Butadiene-45% Acrylonitrile	Goodyear	N206
Fluorosilicone	Colonial Rubber	FSi
Viton E-60 Fluorocarbon	Du Pont	FKM
Neoprene	Colonial Rubber	CR
85% Butadiene-15% Acrylonitrile	Goodyear	N926

Table 2. Lubricants used in swelling experiments

Lubricant	Vendor	Designation
Krytox 240AC Fluorinated Grease	Du Pont	240AC
Braycote 600 Perfluoropolyether Grease, Low Volatility	Castrol	600
Braycote 807 Aircraft Grease MIL-G-27617, Type IV	Castrol	807

approximate mass of 50 mg and volume of 0.02 cm^3 was placed on a sixteenth pan to correct for buoyancy effects. The 16 pans were suspended from quartz springs which were hung on the spring stand and placed in the pressure vessel described above and shown in Figure 1. After aligning the spring stand so that all 16 springs were visible through the view port, the lid of the vessel was bolted in place and the vessel was completely immersed in silicone bath oil. The aluminum lid was placed over the Pyrex jar and the mixer, heater and thermoregulator were adjusted to maintain the maximum test temperature. After evacuation and temperature equilibrium was achieved, the displacements of the calibrated springs were measured using a cathetometer. Next, the pressure was increased to the maximum pressure considered.

Following a swelling equilibration time, which was determined independently and checked, the displacements of the springs were measured again for each sample. The vapor pressure was then decreased to the next lower value, allowed to equilibrate and then measurements were taken. The process was repeated for the remaining pressures considered. The thermoregulator was then reset for the next lower temperature and the system was allowed to equilibrate overnight. After measurements were obtained for all temperatures considered, the vessel was evacuated and the spring displacements were checked for reversibility.

This method of increasing the temperature and pressure to the maximum value considered and then reducing the pressure in increments (instead of increasing the pressure incrementally from a vacuum) was used in order to minimize the disruption of the system which occurs when pumping at

high pressures. The undesired saturation condition and associated liquid condensation, which could ruin the measurements, was also more easily avoided.

In this work, swelling measurements at four vapor pressures were taken for each temperature and were usually done in the morning after equilibration overnight and in the late afternoon after equilibration during the working hours. Measurements were taken at 35, 70, 105, and 150 °C. In addition, FC-116 (hexafluoroethane) was also tested at 5 °C (p^o=2.133 MPa) because this fluid has a low critical temperature (T_c = 19.7 °C) and little swelling was observed at temperatures above T_c. The maximum pressure considered was 5.86 MPa. For test temperatures above the critical temperature of the agent, vapor pressures were chosen to cover the range from the maximum pressure (5.86 MPa) to the saturation pressure of the highest test temperature for which saturation occurs. For temperatures below T_c, vapor pressures were chosen to cover the range from saturation for the test temperature to the saturation pressure of the next lower temperature considered. Saturation pressures for each temperature were determined using thermodynamic properties software (Gallagher *et al.*, 1991; Allied Signal, Inc., 1989) or vendor supplied data (E.I. du Pont de Nemours, Inc., 1968 and 1993; Robin, 1992; Wilson *et al.*, 1992) and are shown in Table 3.

Table 3. Saturation data for agents

Trade name	Formula	Chemical name	p^o @ 35°C	p^o @ 70 °C	p^o @ 105°C	T_c (°C)	p_c (MPa)
HFC-236fa	$CF_3CH_2CF_3$	hexafluoropropane	0.381	1.07	2.11	130.6	3.18
HFC-32/125	CH_2F_2/CHF_2CF_3	azeotrope	2.16	4.74	--[a]	73.2	5.06
HFC-227ea	C_3HF_7	heptafluoropropane	0.615	1.49	--	101.7	2.91
HCFC-22	CHF_2Cl	chlorodifluoromethane	1.35	3.00	--	96.0	4.99
HFC-134a	CH_2FCF_3	tetrafluoroethane	0.887	2.12	--	101.1	4.07
FC-116	C_2F_6	hexafluoroethane	--	--	--	19.7	3.03
HCFC-124	$CHFClCF_3$	chlorotetrafluoroethane	0.516	1.26	2.63	118.9	4.60
HFC-125	CHF_2CF_3	pentafluoroethane	1.78	--	--	66.3	3.62
FC-218	C_3F_8	octafluoropropane	1.15	2.41	--	71.9	2.68
FC-31-10	C_4F_{10}	decafluorobutane	0.364	0.921	1.97	113.2	2.30
FC-318	cyclo-C_4F_8	octafluorocyclobutane	0.428	1.08	2.25	115.2	2.78

[a]not defined

8.2.3 Results and Discussion. In Figures 2-4 typical plots of solvent weight fraction w_1 *vs.* vapor pressure p are shown for different elastomer/agent systems. The solvent uptake of the polymers strongly increases with the vapor pressure. The vertical arrows in the figures show the saturation vapor pressures of the solvent p^o_T at different temperatures. In Figure 4 it is demonstrated that the swelling degree of silicone in decafluorobutane (FC-31-10) significantly decreases with increasing

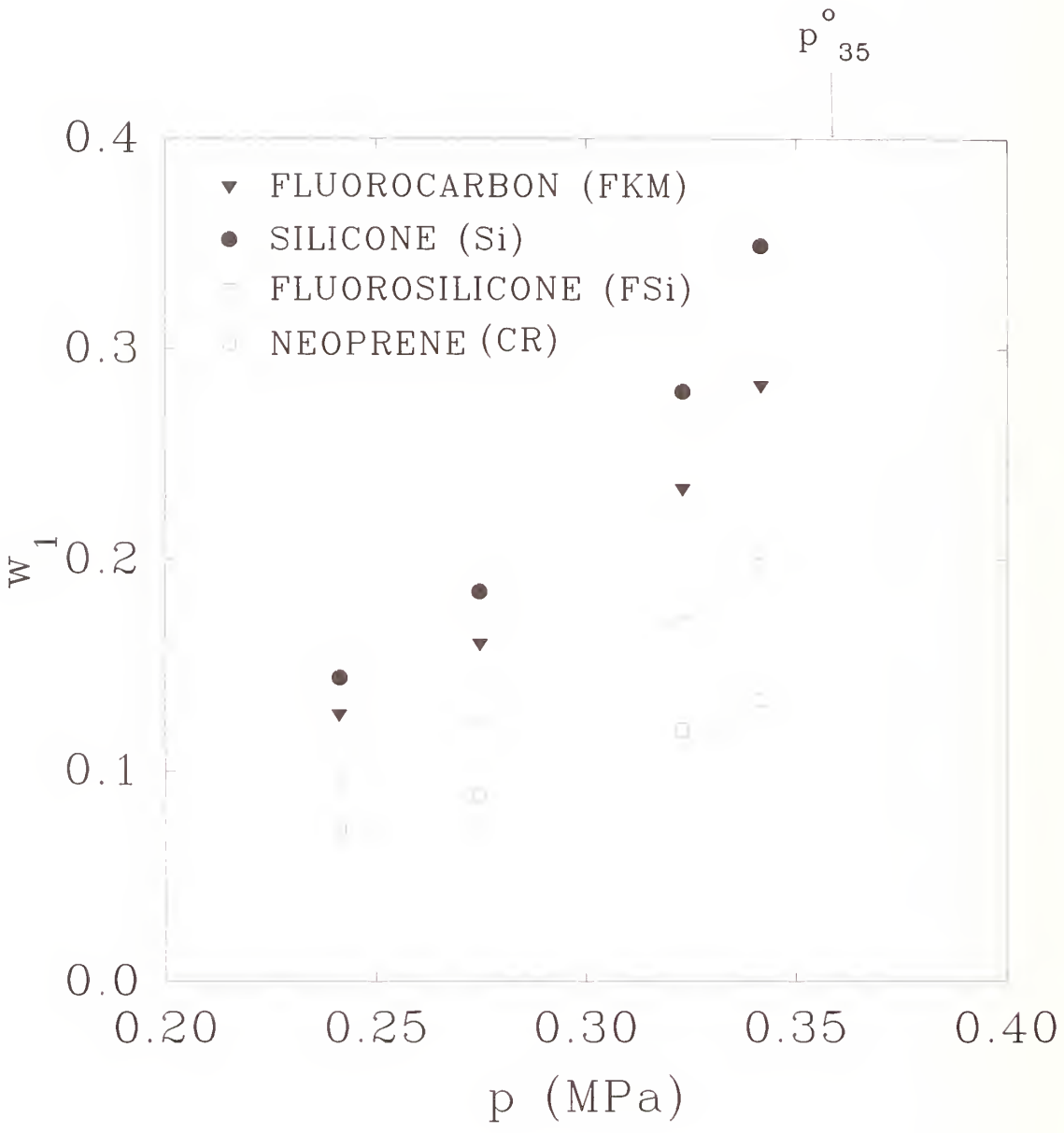

Figure 2. Weight fraction w_1 of FC-31-10 as a function of pressure for various polymers at 35 °C. The arrow shows the saturation vapor pressure p^o = 0.36 MPa of the agent.

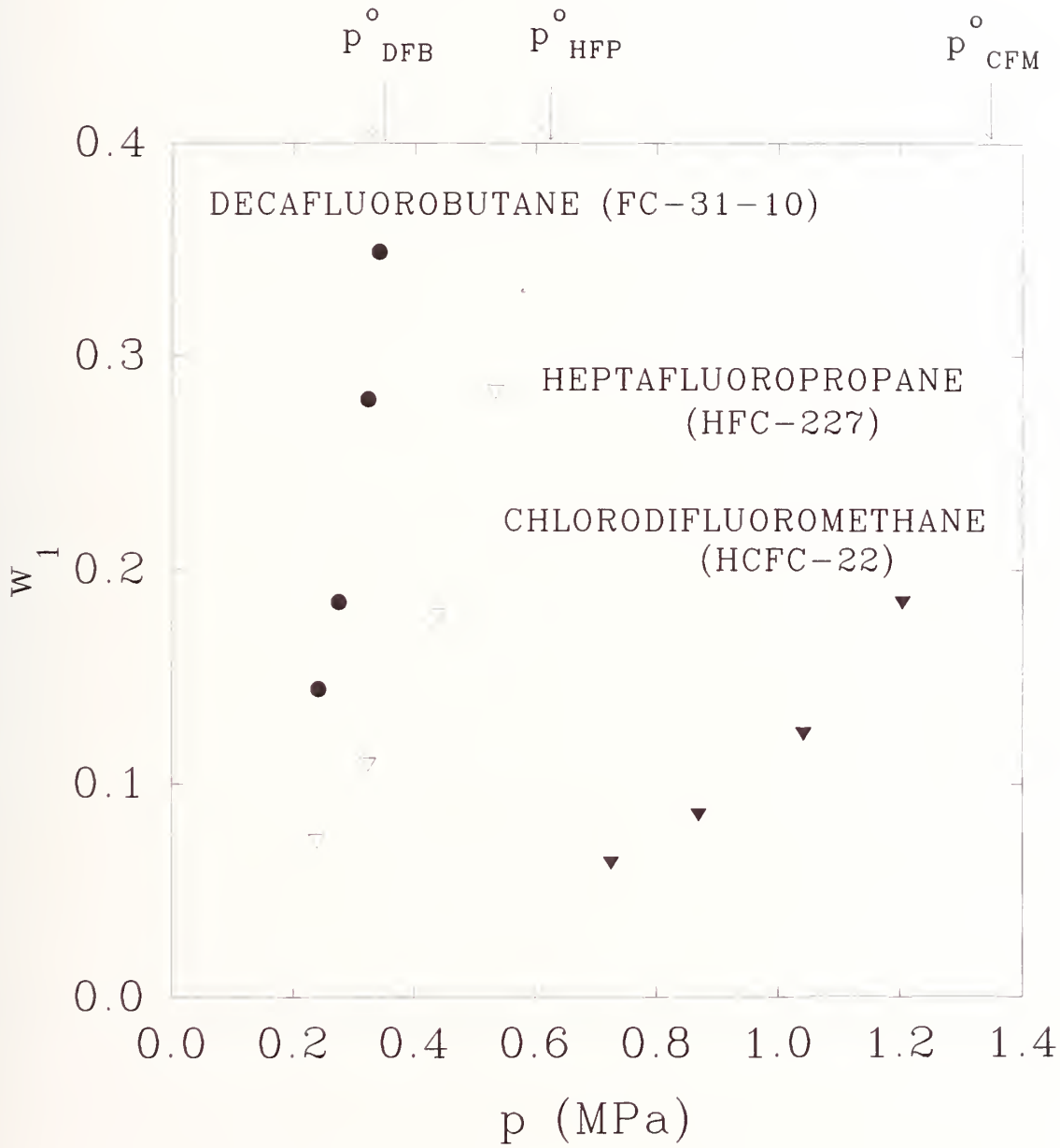

Figure 3. Swelling of uncrosslinked silicone in various agents as a function of pressure at 35 °C. The arrows show the saturation vapor pressures of the respective agents.

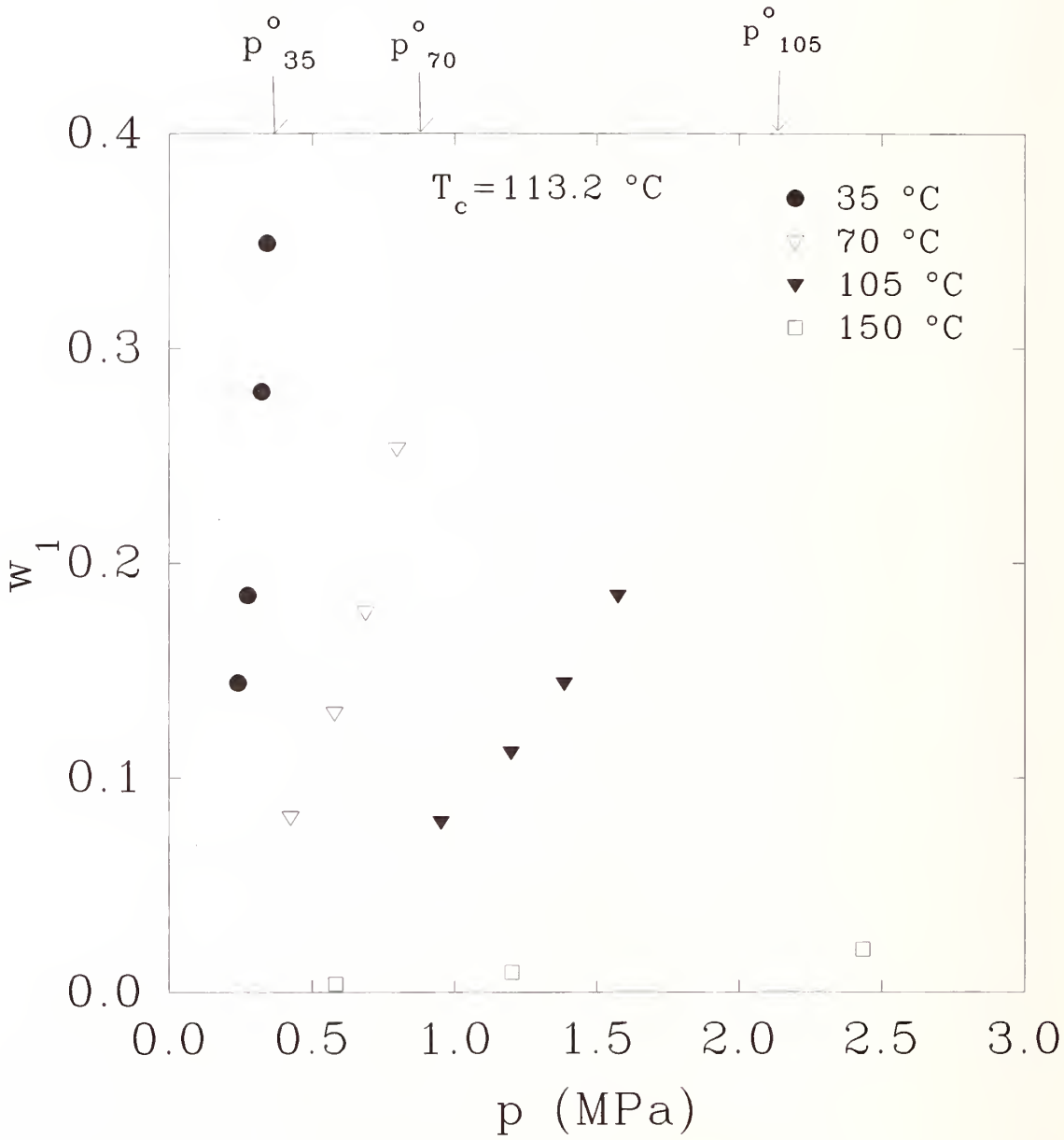

Figure 4. Weight fraction w_1 of FC-31-10 as a function of vapor pressure in uncrosslinked silicone at various temperatures. The arrows show the saturation vapor pressures at the respective temperatures.

temperature. At 150 °C, *i.e.*, above the critical temperature of decafluorobutane (T_c = 113.2 °C), the fluid uptake was approximately one order of magnitude smaller than at 105 °C.

In Figures 5-6, the same experimental data shown in Figures 2-4 are shown according to the Flory-Huggins representation. The continuous curves were calculated using least squares fits of Equation 9 to the data points. The experimental values of ln (p / p^o) *vs.* w_2 were satisfactorily described using a temperature and concentration dependent interaction parameter. The values of the Flory-Huggins interaction parameters ($\chi = \chi_0 + \chi_1$) calculated from solubility data at different temperatures are given in Tables 4 and 5 for all the polymer/solvent systems investigated. The χ values are measures of the solubilities (compatibilities) of the subcritical agents in various polymers. (Small χ values correspond to good solubility or, for present purposes, bad compatibility. Above χ = 0.5, solubility of the polymers gradually decreases with increasing χ.)

In Figure 7 the swelling of crosslinked and uncrosslinked silicone are compared. The difference between the swelling behavior of the two samples is apparent: the crosslinked polymer exhibits considerably lower affinity to the solvent than the uncrosslinked one. The values of the interaction parameters calculated from solubility data at 35 °C for the crosslinked and uncrosslinked polymers are χ = 0.99 and χ = 1.04, respectively. Strictly speaking Equation 9 can only be applied for the uncrosslinked polymer. The appropriate expression for the crosslinked polymer contains an additional term arising from the change in Gibbs free energy due to the elastic deformation of the network on swelling. For lightly crosslinked networks at high polymer concentration ($w_2 > 0.7$), the contribution of the elastic term is negligible in comparison to the mixing term.

Above the critical temperature of the fluid the swelling behavior of the polymers can be analyzed on the basis of Equation 11 (Flory's equation-of-state theory). In Figure 8, the fits of Equation 11 to the swelling data for the silicone/decafluorobutane system at four temperatures between 35 °C and 150 °C are shown. Values of the equation-of-state parameters used in these calculations were obtained from the literature (Shih and Flory, 1972; Wilson *et al.*, 1992). The fit of Equation 9 (Flory-Huggins theory) to the data are also shown in Figure 8 for the three temperatures below the critical temperature T_c = 113.2 °C of FC-31-10 (decafluorobutane). Both theories yield reasonable fits to the experimental data below the critical temperature of the solvent. In addition, Flory's equation-of-state theory yields a reasonable fit to the experimental data above T_c.

In order to rank the agents in terms of their compatibility with the sealing materials, a rating system was defined for the data at 35 °C. This temperature was chosen for several reasons. First, as shown in Figure 4, swelling is greatest at 35 °C and decreases with increasing temperature. Second, it is near the initial storage temperature of 25 °C and third, it is below the critical temperature for every agent considered except FC-116 (hexafluoroethane). FC-116 was rated based on its swelling data at 5 °C because it has a critical temperature of 19.7 °C. A good, bad, or fair rating is given for each agent/crosslinked elastomer and agent/lubricant system in Table 6. Bad compatibility was defined as a condition of excessive swelling and corresponding to $\chi < 0.9$, where χ is the Flory-Huggins polymer-solvent interaction parameter. Good compatibility implies that the elastomer or lubricant is acceptable for use in the fire suppressant system and corresponds to $\chi > 1.2$. For values of χ between 0.9 and 1.2, the agent was considered to have fair compatibility with the elastomer or grease and represents a marginally acceptable system. Under saturation conditions, χ values of 0.9 and 1.2 represent agent weight fractions of 0.38 and 0.22, respectively.

The χ values shown in Tables 4 and 5 were calculated using the curve fitter in the scientific graphing software SigmaPlot for DOS (Jandel, 1992). The curve fitter uses the Marquardt-Levenberg algorithm (Press *et al.*, 1986) to find the parameters which minimize the variance s^2 (ln p / p^o), *i.e.*, the squared differences between the observed and predicted values of the dependent variable. The standard error or experimental standard deviation of the χ parameter, s (χ), and the coefficient of variation, CV = s (χ) / χ x 100, were also calculated for each χ value. Thus, the standard

Table 4. Flory-Huggins interaction parameters χ for the subcritical temperatures studied for each agent/lubricant system considered

Agent (T °C)	Krytox 240AC	Braycote 600	Braycote 807
236fa (35)	1.54	1.60	1.72
236fa (70)	1.53	1.61	1.75
236fa (105)	1.65	1.73	1.88
32/125 (35)	1.98[b]	1.63	1.86[b]
32/125 (70)	2.08	1.66	1.96
227ea (35)	1.14[a]	0.93	0.93[b]
227ea (70)	1.23	0.97	1.02
22 (35)	1.08	1.30	1.20
22 (70)	1.10	1.31	1.23
134a (35)	1.64	1.21	1.76
134a (70)	1.68	1.24	1.65
116 (5)	1.08	1.13	1.05
124 (35)	1.31[b]	1.37[b]	1.31
124 (70)	1.28	1.37	1.30
124 (105)	1.30	1.39	1.33
125 (35)	1.18	1.37	1.35
218 (35)	1.83[b]	1.45	1.76
218 (70)	1.86	1.47	1.79
31-10 (35)	0.93	0.73	0.82
31-10 (70)	0.95	0.75	0.83
31-10 (105)	1.01	0.80	0.88
318 (35)	1.03	1.00	1.00
318 (70)	1.04	1.03	1.01
318 (105)	1.10	1.10	1.10

[a] $12.5 < CV < 20\%$ and $0.64 < \chi < 1.5$ (35 °C)
[b] $CV > 20\%$ (35 °C)

uncertainty of the parameter χ is $u(\chi) = s(\chi)$ and the percentage of relative standard uncertainty is $u(\chi) / \chi \times 100 = CV$. The expanded uncertainty is $U = k\,u(\chi)$, where $k = 2$, and the percentage of relative expanded uncertainty is $U / \chi \times 100 = k\,CV$.

Unless otherwise indicated in Tables 4, 5, and 6, the coefficient of variation was less than 12.5% for the χ parameters at 35 °C which gives a percentage of relative expanded uncertainty of 25%.

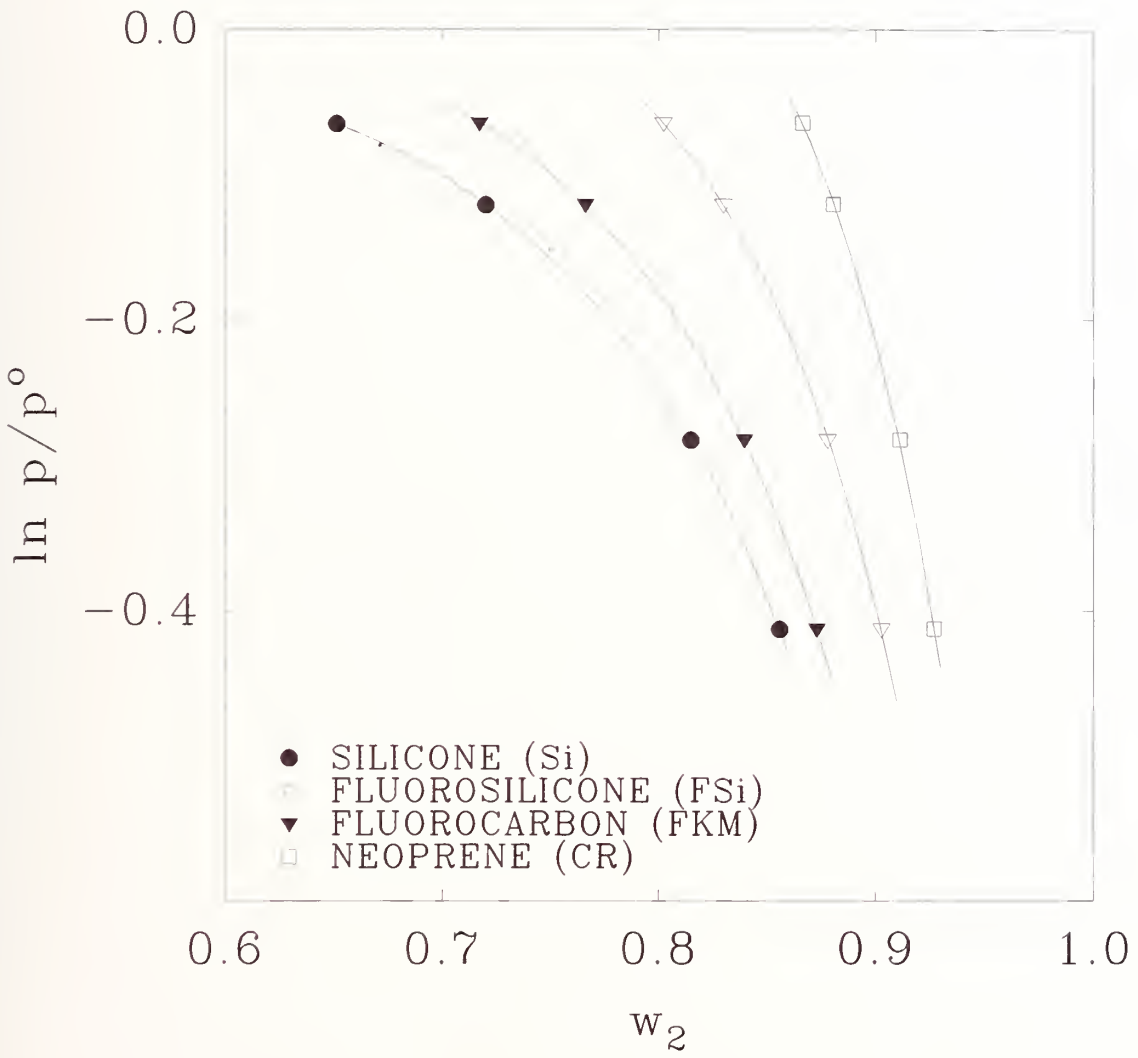

Figure 5. Solvent activity in various polymers in FC-31-10 as a function of polymer weight fraction w_2 at 35 °C. The continuous curves show the least squares fits according to Equation 9.

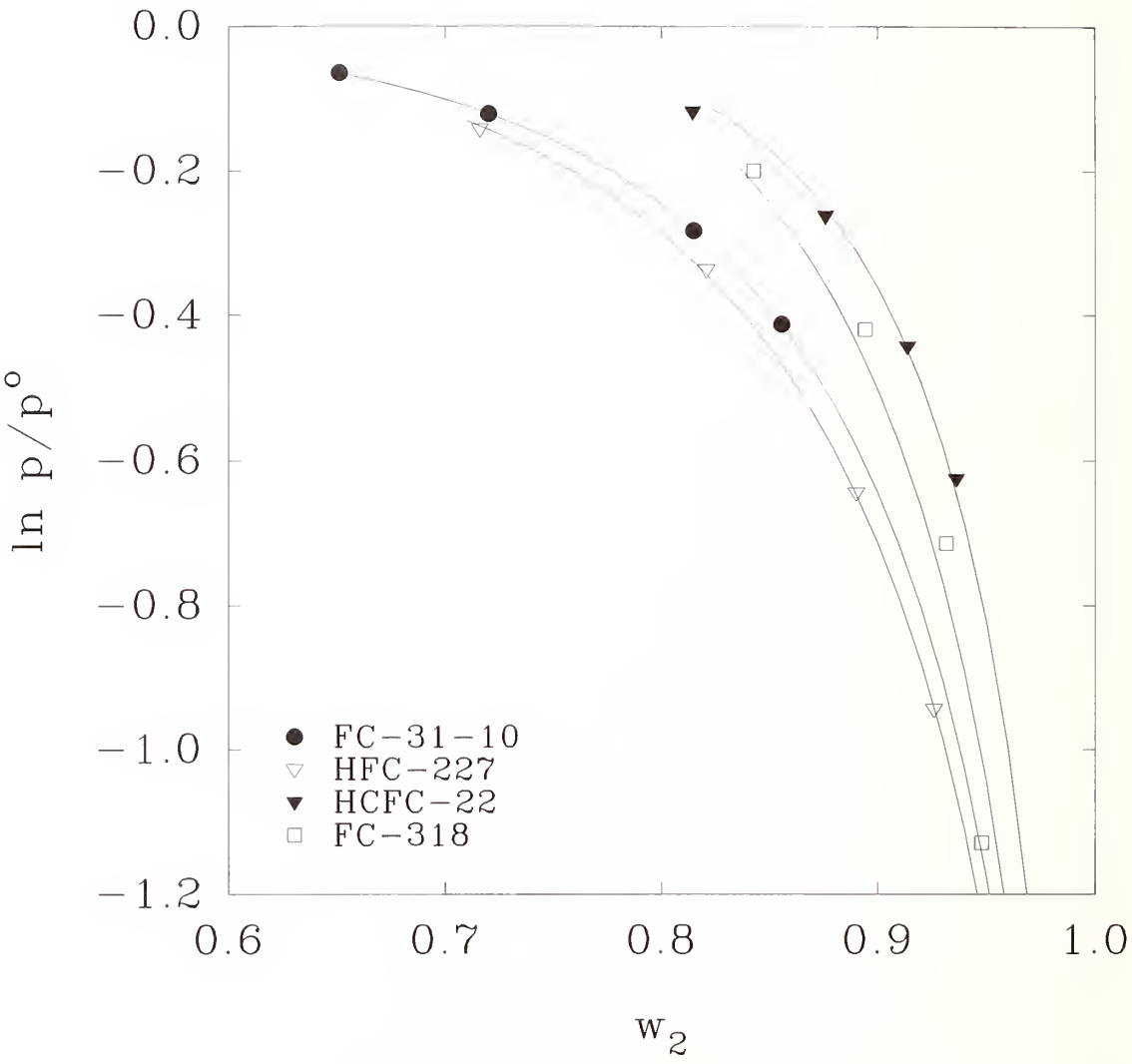

Figure 6. Solvent activity in uncrosslinked silicone as a function of the polymer weight fraction w_2 at 35 °C in various agents. The continuous curves show the fits according to Equation 9.

Table 5. Flory-Huggins interaction parameters χ for subcritical temperatures studied for each agent/elastomer system considered

Agent (T °C)	u[c] Si	x[d] Si	u N206	x N206	u FSi	x FSi	u FKM	x FKM	u CR	x CR	u N926	x N926
236fa (35)	1.09	1.10	1.02	1.05	0.66	0.68	0.76	0.77	0.81	0.84	0.60	0.64
236fa (70)	1.08	1.12	1.03	1.07	0.68	0.71	0.77	0.79	0.83	0.85	0.61	0.65
236fa (105)	1.12	1.15	1.19	1.20	0.76	0.79	0.81	0.83	0.90	0.92	0.84	0.86
32/125 (35)	1.03	1.06	1.48	1.52[b]	1.24[b]	1.28	1.14[b]	1.19	1.12	1.16	1.37	1.41[b]
32/125 (70)	1.08	1.13	1.51	1.56	1.27	1.34	1.18	1.23	1.16	1.15	1.41	1.47
227ea (35)	0.89	0.93[a]	1.34[b]	1.40[b]	0.97	1.04[a]	1.01	1.07[b]	1.25[b]	1.33[a]	0.80	0.84
227ea (70)	0.94	0.96	1.48	1.50	1.10	1.13	1.09	1.13	1.31	1.38	0.85	0.87
22 (35)	0.98	1.00	0.72	0.75	1.02	1.05	0.97	1.02	1.20[b]	1.26	0.76	0.81
22 (70)	0.99	1.00	0.74	0.75	1.05	1.07	0.99	1.06	1.26	1.28	0.78	0.82
134a (35)	1.16	1.20	1.35	1.36	1.00	1.02	1.25	1.30	1.96	2.00[b]	1.42	1.44
134a (70)	1.19	1.22	1.37	1.38	1.02	1.06	1.28	1.31	2.03	2.04	1.44	1.46
116 (5)	1.41[a]	1.47[a]	1.94[b]	1.92[b]	1.35[b]	1.42	1.33[a]	1.40	1.60	1.68[b]	2.11[b]	2.27[b]
124 (35)	0.88[b]	0.91[b]	0.88[b]	0.92[b]	0.93[b]	0.95[b]	0.96[b]	0.97[b]	0.97[b]	0.98[b]	0.91[b]	0.94[b]
124 (70)	0.85	0.88	0.86	0.89	0.90	0.93	0.95	0.96	0.96	0.98	0.89	0.92
124 (105)	0.86	0.91	0.91	0.94	0.93	0.95	0.97	0.97	0.98	1.01	0.92	0.96
125 (35)	1.29	1.30	1.69[b]	1.72	1.33	1.35	1.18	1.21	4.10[b]	1.99	1.23	1.28
218 (35)	1.55	1.62	1.77[b]	1.84	1.56[b]	1.64	1.65	1.65	1.63	1.68	1.56[b]	1.71
218 (70)	1.64	1.69	2.04	1.99	1.67	1.74	1.66	1.67	1.75	1.77	1.69	1.74
31-10 (35)	0.99	1.03	1.18	1.24	1.32	1.39	1.09	1.15	1.55	1.59	1.10	1.13
31-10 (70)	1.01	1.06	1.20	1.25	1.35	1.44	1.13	1.19	1.58	1.66	1.13	1.15
31-10 (105)	1.09	1.09	1.30	1.31	1.40	1.45	1.18	1.25	1.60	1.64	1.19	1.23
318 (35)	1.04[b]	1.27	1.41	1.46	1.27	1.32[a]	1.32	1.34	1.32[b]	1.35	1.10	1.14
318 (70)	1.26	1.29	1.46	1.47	1.27	1.33	1.33	1.36	1.32	1.38	1.10	1.16
318 (105)	1.29	1.37	1.52	1.56	1.33	1.37	1.41	1.44	1.34	1.39	1.19	1.23

[a] $12.5 < CV < 20\%$ and $0.64 < \chi < 1.5$ (35 °C)
[b] $CV > 20\%$ (35 °C)
[c] uncrosslinked polymer
[d] crosslinked polymer

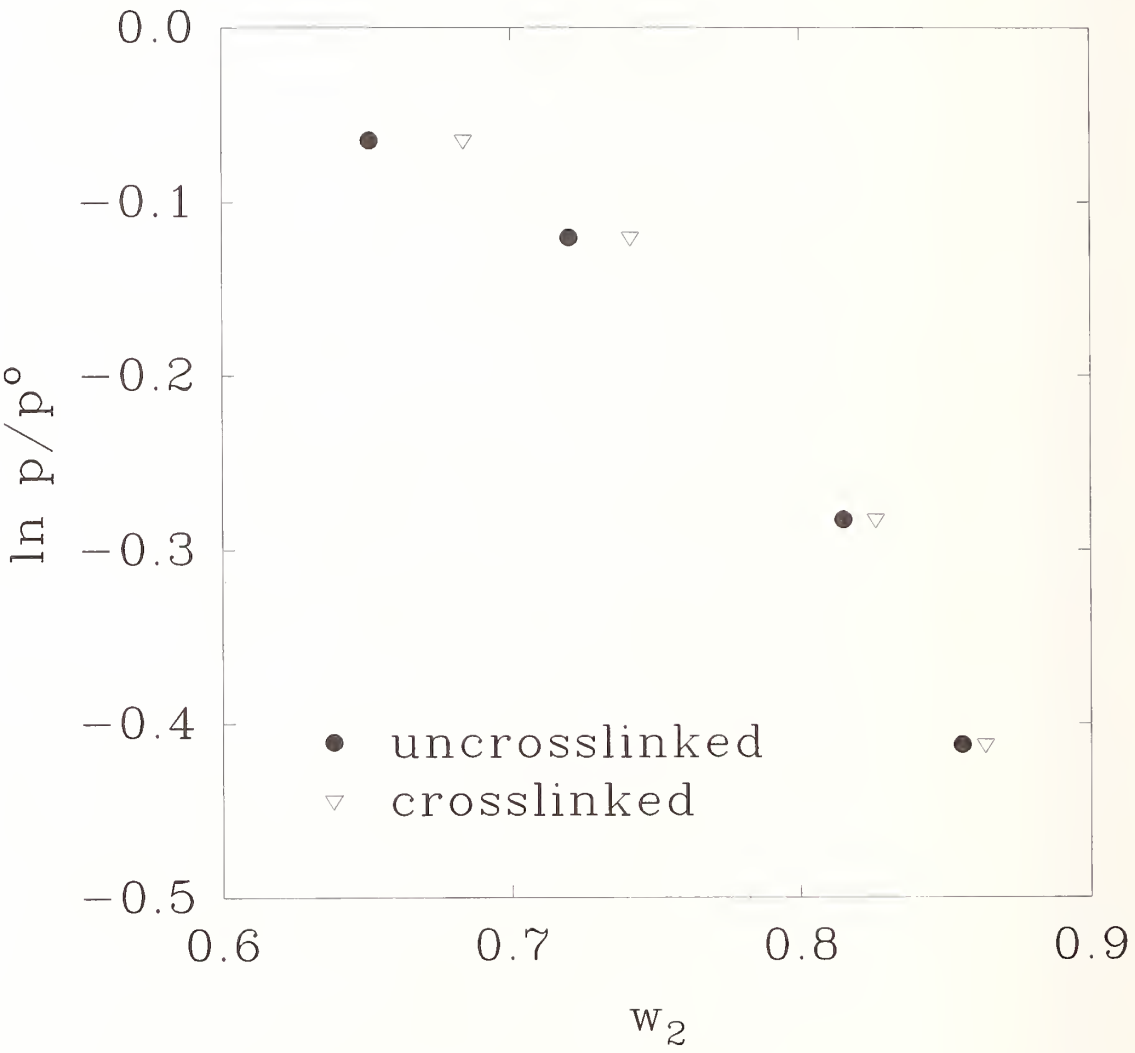

Figure 7. Comparison between the swelling of crosslinked and uncrosslinked silicone in FC-31-10 at 35 °C.

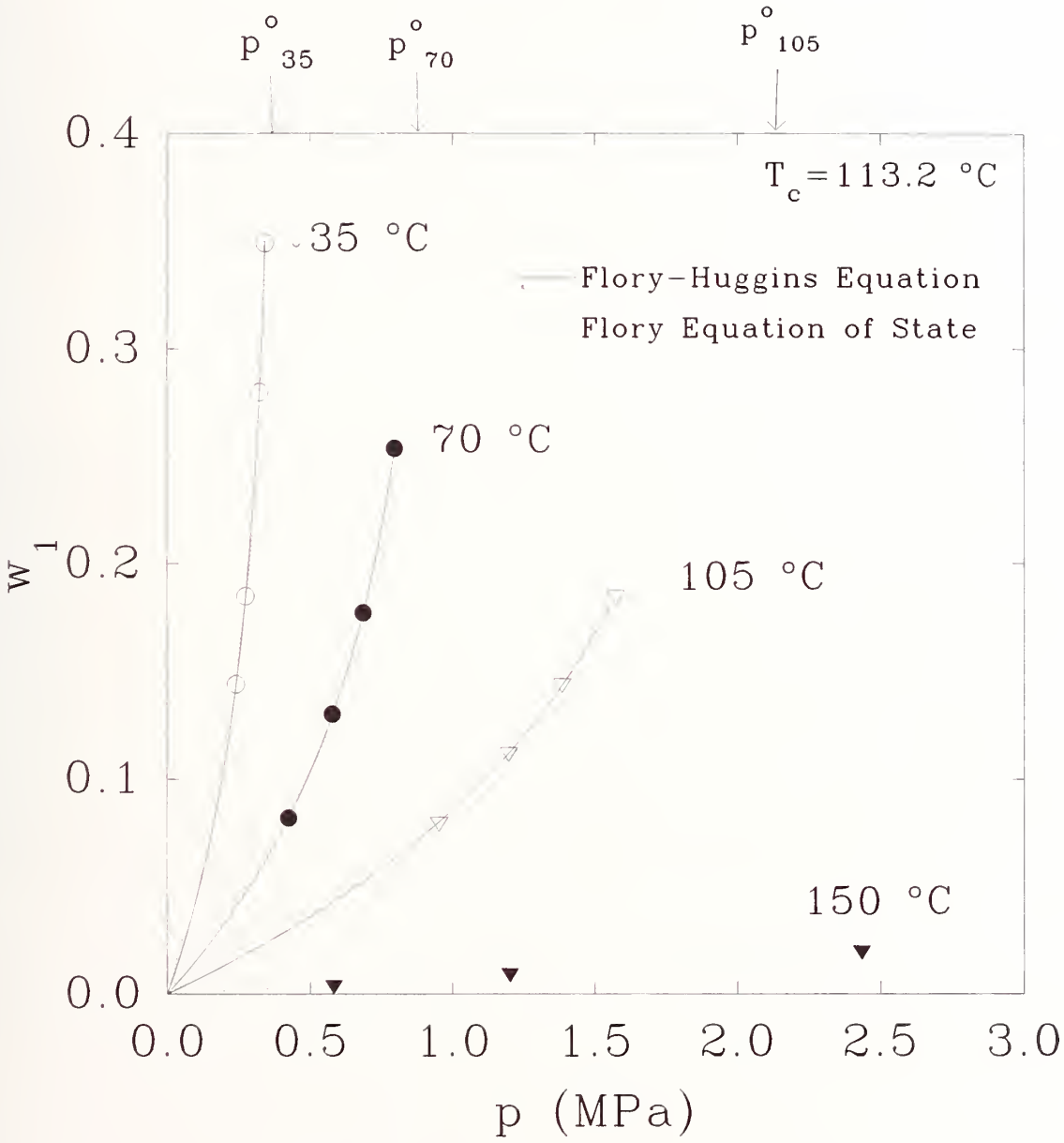

Figure 8. Comparison between measured and calculated values of the weight fraction w_1 of FC-31-10 in silicone.

Hence, for an estimated χ value of 1.2, the measurand (true value of χ) is 1.2 $\pm$ 0.3. This level of confidence suggests that an agent which was assigned a good rating with a χ value slightly greater than 1.2 may actually fall into the fair range ($0.9 < \chi < 1.2$) but a bad rating ($\chi < 0.9$) is statistically unlikely. A similar argument can be made for an agent with a bad rating and an estimated χ value slightly less than 0.9.

The agent/polymer systems for which $0.64 < \chi < 1.5$ and $12.5 < CV < 20\%$ at 35 °C are shown in Tables 4 and 5 with superscripts. If $\chi = 1.5$ and $CV = 20\%$, the value of the measurand is 1.5 $\pm$ 0.6 and the agent may fall into the fair range but a bad rating ($\chi < 0.9$) is statistically unlikely. Similarly, if $\chi = 0.64$ and $CV = 20\%$, the value of the measurand is 0.64 $\pm$ 0.26 and the agent may fall into the fair range but a good rating ($\chi > 1.2$) is statistically unlikely.

Estimated values of χ for which $CV > 20\%$ are also shown with superscripts in Tables 4 and 5. In some instances, the uncertainty represented by large coefficients of variation may be attributed to the small degree of swelling ($w_2 \approx 1.0$) in poor solvents. Using the idealization that the mixing contribution to the chemical potential is zero gives the expression

$$\chi = -\frac{\ln(1 - w_2) + w_2}{w_2^2}, \tag{14}$$

where the slope of χ goes to infinity as $w_2 \rightarrow 1.0$. Hence, small errors in w_2 due to uncertainty in the cathetometer readings ($\pm$ 0.05 mm) produce large differences in the estimate of χ as $w_2 \rightarrow 1.0$ because $-\ln(1 - w_2) \rightarrow \infty$.

8.3 Durability

8.3.1 High Temperature Exposure Methods. As an independent method of characterizing the compatibility of fire suppressant agents, mechanical property measurements of the elastomers and greases were obtained after short term exposures to the agents at extreme conditions of 150 °C and 5.86 MPa. For this purpose, two separate pressure vessels without view ports were designed and built. These pressure vessels were also made of stainless steel and designed for a maximum working pressure of 5.86 MPa. The cylindrical vessel had 10 liters of inner volume (25 cm height by 23 cm diameter) and was large enough to fit an 18 cm diameter compression set fixture, (20) samples for each of the six elastomers, and a 2 ml vial for each of the three greases.

After placing the test samples in the vessel, it was placed in a Fisher Scientific Isotemp forced air lab oven with an inside capacity of 51 x 61 x 51 cm, temperature range of 30 to 200 °C with 1 °C resolution, $\pm$ 3 °C accuracy and $\pm$ 3 °C uniformity. After evacuating the vessel, the charging and recovery system described previously was used to pump a predetermined mass of agent into the chamber at room temperature (24 $\pm$ 1 °C). The value of mass necessary to obtain 5.86 MPa at 150 °C was determined using thermodynamic properties software (Gallagher *et al.*, 1991; Allied Signal, Inc., 1989) or vendor supplied data (E.I. du Pont de Nemours, Inc., 1968 and 1993; Robin, 1992; Wilson *et al.*, 1992).

The oven was turned on, set to 150 °C, and monitored using a Fluke thermometer with a type K thermocouple and 0.1 °C resolution. The pressure was monitored using a Druck DPI 602 digital pressure indicator and PDCR 910 transducer with an absolute pressure range of 0-6.21 MPa, combined nonlinearity, hysteresis and repeatability of $\pm$ 0.1% using the best straight line method (BSL). After attaining thermal equilibrium, the pressure was reduced until the desired pressure of

Table 6. Compatibility of lubricants and crosslinked elastomers based on swelling measurements in various fluorocarbon agents at 35 °C

Agent	240AC	600	807	Si	N206	FSi	FKM	CR	N926
HFC-236fa	good[a]	good	good	fair[b]	fair	bad[c]	bad	bad	bad
HFC-32/125	good[f]	good	good[f]	fair	good[f]	good	good	good	good[f]
HFC-227ea	fair[e]	fair	fair[f]	fair[e]	good[f]	fair[e]	fair[f]	good[e]	bad
HCFC-22	fair	good	fair	fair	bad	fair	fair	good	bad
HFC-134a	good	fair	good	fair	good	fair	good	good[f]	good
FC-116[d]	fair	fair	fair	good[e]	good[f]	good	good	good[f]	good[f]
HCFC-124	good[f]	good[f]	good	bad[f]	fair[f]	fair[f]	fair[f]	fair[f]	fair[f]
HFC-125	fair	good	good	good	good	good	fair	good	good
FC-218	good[f]	good	good	good	good	good	good	good	good
FC-31-10	fair	bad	bad	fair	fair	good	fair	good	fair
FC-318	fair	fair	fair	good	good	good[e]	good	good	fair

[a] $\chi > 1.2$
[b] $0.9 \leq \chi \leq 1.2$
[c] $\chi < 0.9$
[d] measured at 5 °C
[e] $12.5 < CV < 20\%$ and $0.64 < \chi < 1.5$
[f] $CV > 20\%$

5.86 MPa was achieved. The pressurized vessel was then left undisturbed until the exposure time was completed. Short term exposure times of one, 2, 4, and 6 weeks were considered for the initial screening of the agents. After the completion of each exposure, the oven was turned off and the agent was recovered into an evacuated storage cylinder immersed in a water bath.

To maintain the project time schedule, two of the small pressure vessels used for swelling measurements were used as containers for additional high temperature exposures. The procedure described above was followed except a silicone oil bath setup similar to that used for the swelling measurements was employed for heating. However, in order to expedite the sample placement and removal process, the pressure vessels were only partially (approximately half) immersed in the silicone oil. This allowed for the removal of the vessel's top without waiting for the silicone oil to cool and eliminated subsequent pumping of oil to access the samples. The compression set fixtures and lubricant samples were placed near the bottom of the vessel, below the level of the silicone oil. The tensile test samples were placed on top of the compression set fixtures. Some were above and some were below the level of the silicone oil.

A set of tests was conducted in which two thermocouples were placed inside a small pressure vessel filled with air at ambient pressure (high pressure agent could not be used because of leaks due to the presence of the thermocouples). One was placed near the bottom and the other near the top of the vessel. A third thermocouple was immersed in the silicone oil bath which was heated to 150 °C.

These tests show that temperature within the pressure vessel may have varied from 140 to 149 °C when the temperature of the silicone oil was 150 °C. During the actual experiments, this variation was probably less due to the larger heat conduction (relative to air) of the supercritical fluids at 5.86 MPa.

This setup was used for high temperature exposures of FC-116 (hexafluoroethane), FC-218 (octafluoropropane), FC-31-10 (decafluorobutane), and FC-318 (octafluorocyclobutane). As will be shown in the following sections, high temperature exposures to these agents were severe for most of the elastomers and lubricants. Consequently, the results show that exposures throughout the entire temperature range of 140-150 °C are severe.

8.3.2 Elastomers

8.3.2.1 Experimental Materials. The o-rings used in this study were Parker No. 2-214 with a nominal cross section diameter of 3.2 mm (1/8 in.), actual cross section diameter of 3.53 ± 0.10 mm, and a mean outside diameter of 3.2 cm. The Parker compounds considered are listed in Table 7.

Table 7. Elastomers used in durability experiments

Elastomer	Vendor	Designation
Silicone	Parker	S604-70[a]
Nitrile (standard industrial)	Parker	N674-70
Fluorosilicone	Parker	L1120-70
Fluorocarbon	Parker	V1164-75
Neoprene	Parker	C1185-70
Nitrile (low temperature industrial)	Parker	N103-70

[a]The number following the dash in the designation (compound number) represents the Shore hardness of the elastomer.

8.3.2.2 Compression Set Measurements. Compression set tests were conducted per standard test methods (ASTM, 1989 and 1990b). Measurements were taken after the one, 2, 4, and 6 week exposure times. For this purpose, eight compression set fixtures were designed and built. Each fixture consisted of two 18 cm diameter and 12.7 mm thick plates, seven spacers 19 mm in diameter and 2.65 ± 0.01 mm thick, and seven sets of 10 mm bolts, nuts, and washers. The plates were made of stainless steel 304, ground to a maximum roughness of 250 nm, chrome plated and polished. The spacers were also made of stainless steel 304 and their thickness was specified to be 75% of the actual mean value of the o-rings (0.75 x 3.53 mm).

Specimens were prepared by cutting 52 mm sections from sample o-rings. The original thickness of each specimen was measured using a hand micrometer with a 6 mm diameter hemispherical tip.

Measurements were taken at four marked locations equally distributed around the circumference in both the radial and axial direction. The average reading was used for subsequent calculations. Two specimens of each compound were placed into a fixture and closed by tightening the bolts in a criss-cross manner so that the plates were drawn together uniformly. The compression set fixtures were placed in a vessel at the beginning of each high temperature exposure. After the pressure vessel was removed from the oven, the compression set fixture was removed from the vessel and the specimens were placed on a poor conducting surface (wood table) and allowed to cool at room temperature for 30 minutes. After the rest period, the thickness measurements were made as described above at the same marked locations. The same specimens were used for all exposures (one, 2, 4, and 6 weeks) to a given agent.

The compression set C_B was calculated using the average thickness readings before and after the exposure and is expressed as a percentage of the original deflection as follows:

$$C_B = \frac{t_o - t_i}{t_o - t_n} \times 100 , \tag{15}$$

where t_o and t_i are the original and final thickness, respectively. $t_n = 2.65$ mm is the thickness of the spacers used in the compression set fixtures. This calculation was made for both specimens of each compound after each exposure. The average of these two values was reported as the compression set C_B.

Table 8 shows the experimental values of compression set for each of the compounds after exposures of one, 2, 4, and 6 weeks at 5.86 MPa and 150 °C in each fluorocarbon agent. In some instances, the specimen was split or broken after a given exposure time. For these cases, the compression set measurements were still taken but the value is superscripted in Table 8.

In Table 9, compatibility ratings of the agents based on compression set measurements of each elastomer are shown. Bad compatibility was defined as a condition when the compression set exceeded 90% after a 2 week exposure. Elastomers have good compatibility if the compression set was less that 90% after 4 weeks. If the compression set was less than 90% after 2 weeks but exceeded 90% after a 4 week exposure, the agent was considered to have fair compatibility with the elastomer and represents a marginally acceptable system. If a specimen was split or broken, the agent was considered to have bad compatibility with the elastomer.

As specified in Option 1 of the standards for compression set (ASTM, 1989 and 1990b), the value of compression set for each elastomer/agent system reported in Table 8 is the average of the compression set calculated from measurements of two samples. The experimental standard deviation $s\ (C_B)$ and the standard uncertainty of the mean $u\ (C_B) = s\ (C_B) / \sqrt{n}$, where $n = 2$ is the number of samples, were also calculated. The coefficient of variation is $CV = u\ (C_B) / C_B$ x 100, the expanded uncertainty is $U = k\ u\ (C_B)$, where k = 2, and the percentage of relative expanded uncertainty is $k\ CV$. The maximum value of CV was 10%. Hence, for an estimated compression set of 90%, the measurand (true value) is 90 ± 18%. This level of confidence suggests that an elastomer with an estimated compression set value of approximately 90% after 4 weeks may fall into the good or fair category. However, in order for an elastomer assigned a good rating to actually have bad compatibility, the estimate for compression set based on a separate set of data after 2 weeks must also exceed 90% which is unlikely because compression set decreases monotonically with decreasing exposure time. Similar arguments can be made for elastomers with estimated compression set values of approximately 90% after 2 weeks.

8.3.2.3 Tensile Testing. Tensile tests were conducted per standard test methods (ASTM, 1990a and 1990b). For each agent, twenty sample o-rings of each compound were tied together with wire

Table 8. Compression set measurements after 1, 2, 4, and 6 week exposures at 5.86 MPa and 150 °C in various fluorocarbon agents

Compound (weeks)	236fa	32/ 125	227ea	22	134a	116	124	125	218	31-10	318
S604-70 (1)	27	34	25	16	35	30	11	33	41	41	31
S604-70 (2)	38	36	34	28	37	41	26	36	48	50	35
S604-70 (4)	52	48	48	66	47	53	35	50	50	61	45
S604-70 (6)	56	69	57	109[a]	59	61	59[a]	58	52	62	51
N674-70 (1)	81	79	77	76	84	59	98	70	77	78	61
N674-70 (2)	92	92	84	96[a]	87	78	103	84	88	89	82
N674-70 (4)	96	93	93	110[a]	98	90	104	91	92	98	94
N674-70 (6)	98	99[a]	97	113[a]	102	96	104	96	95	98	97
L1120-70 (1)	53	66	51	48	60	64	30	65	68	82	60
L1120-70 (2)	65	78	56	62	54	73	51	65	74	87	65
L1120-70 (4)	88	87	72	86	72	83	69	80	76	91	77
L1120-70 (6)	94	104[a]	83	99	78	88	89	90[a]	79	91	87
V1164-75 (1)	31	41	21	46	36	19	14	35	25	25	62
V1164-75 (2)	47[a]	63	33[a]	100[a]	40[a]	31	30	46[a]	39	39	80
V1164-75 (4)	67[a]	82[a]	60[a]	100[a]	55[a]	55	59[a]	72[a]	56	64	92
V1164-75 (6)	94[a]	99[a]	77[a]	100[a]	94[a]	70[a]	91[a]	90[a]	58[a]	66[a]	95
C1185-70 (1)	69	67	66	68	72	54	96	68	67	71	49
C1185-70 (2)	76	76	75	77	79	68	100	70	79	78	70
C1185-70 (4)	84	78	81	95	86	79	105	80	83	89	79
C1185-70 (6)	86	81	84	100	94	84	107	98	82	90	84
N103-70 (1)	79	81	79	79	82	70	88	73	78	82	62
N103-70 (2)	87	91	87	89	85	82	91	83	87	91	80
N103-70 (4)	93	95	91	110	96	92	94	92	90	97	89
N103-70 (6)	95	98	94	113	99	95	98	83	95	97	93

[a]specimen was split or broken

Table 9. Compatibility of elastomers based on compression set measurements after exposures at 5.86 MPa and 150 °C in various fluorocarbon agents

Agent	S604-70	N674-70	L1120-70	V1164-75	C1185-70	N103-70
HFC-236fa	good[a]	bad[c]	good	good	bad	bad
HFC-32/125	good	bad	fair[c]	bad	fair	bad
HFC-227ea	good	bad	good	good	fair	bad
HCFC-22	good	fair	good	good	fair	fair
HFC-134a	good	bad	good	good	fair	bad
FC-116	good	fair	good	fair	good	bad
HCFC-124	good	bad	good	good	bad	bad
HFC-125	good	bad	good	bad	good	bad
FC-218	good	fair	good	fair	good	bad
FC-31-10	good	bad	good	fair	fair	bad
FC-318	good	fair	good	good	good	fair

[a]compression set is less than 90% after four weeks
[b]compression set is less than 90% after two weeks but exceeds 90% after four weeks
[c]compression set exceeds 90% after two weeks

and stored in a pressure vessel. Ultimate elongation, tensile stress, and modulus measurements were taken after one, 2, 4, and 6 week exposure times. A type TT-B Instron tensile testing instrument was used for this purpose. Grips for testing o-rings were designed and built from low carbon steel. The grips consisted of ball-bearing spools 8.9 mm in diameter and were capable of being brought within 19 mm center-to-center distance at closest approach. Stresses were minimized by lubricating the contact surfaces of the spools with Super-Lube o-ring lubricant.

After the exposure was completed, the pressure vessel was removed as described in the previous section and five samples of each compound were removed, placed in sealed plastic bags and labeled with the agent, compound, exposure time and date. All tensile tests were conducted within a 2 week period near the end of the short term exposures in August 1993. Each specimen's thickness W was measured at four points equally distributed around the circumference in the radial and axial direction using a dial indicator with a contact force of 0.2 N. The average reading was used for calculation. The internal diameter of each specimen was measured using a stepped cone with diametric intervals of 0.50 mm.

The grips were brought together and the o-ring specimen was installed with minimal stretching. The crosshead and recorder were set to a speed of 500 ± 50 mm/min. A load cell with full scale load ranges of 2, 5, 10, 20, and 50 kg was used. Chart paper with a grid of 2.54 x 2.54 mm was used to plot load *vs.* jaw travel. The charts were labeled with the initial jaw position starting point, load range, agent, compound, sample number, temperature, date, average thickness and inside

diameter. The force F was recorded at rupture and at an elongation of 100% (if the ultimate elongation exceeded 100%).

The tensile strength *T.S.* is the tensile stress at rupture and is calculated as

$$T.S. = \frac{F}{A} , \tag{16}$$

where F is the breaking force and A is twice the cross-sectional area calculated from the thickness W as

$$A = \frac{\pi W^2}{2} . \tag{17}$$

The ultimate elongation *U.E.* is expressed as a percentage of the original inside circumference as follows:

$$U.E. = [\frac{2D + G - C}{C}] \times 100 , \tag{18}$$

where D is the distance between centers of the spool grips at the time of rupture, G is the circumference of one spool (π x spool diameter), and C is the inside circumference (π x inside diameter) of the specimen. Assuming neo-Hookean behavior (Mooney, 1940; Treloar, 1948; Atkin and Fox, 1980), the modulus C_1 is expressed as

$$C_1 = \frac{F}{2A(\lambda^2 - 1/\lambda)} , \tag{19}$$

where F is the tensile force and λ is the stretch ratio in the direction of extension. The center-to-center distance of the spool grips D for a prescribed stretch ratio λ is calculated as

$$D = \frac{1}{2}[\lambda C - G] . \tag{20}$$

The median of three specimens was taken as the characteristic value. Table 10 shows the percent decrease in ultimate elongation for each of the compounds after one, 2, 4, and 6 week exposures at 5.86 MPa and 150 °C in each fluorocarbon agent. In some instances, the o-ring could not be installed without breaking the specimen because of embrittlement due to the high temperature exposure. For these cases, the specimen was considered to have a 100% decrease in ultimate elongation.

In Table 11, ratings for the compatibility of elastomers are shown based on tensile testing after exposures at 5.86 MPa and 150 °C in various fluorocarbon agents. Bad compatibility was defined as a condition when the decrease in ultimate elongation exceeded 65% after a 2 week exposure. Elastomers have good compatibility if the decrease was less that 65% after 4 weeks. If the decrease in ultimate elongate was less that 65% after 2 weeks but exceeded 65% after a 4 week exposure, the agent was considered to have fair compatibility with the elastomer and represents a marginally acceptable system.

Table 10. Percent decrease in ultimate elongation measurements after 1, 2, 4, and 6 week exposures at 5.86 MPa and 150 °C in various fluorocarbon agents

Compound (weeks)	236fa	32 /125	227ea	22	134a	116	124	125	218	31-10	318
S604-70 (1)	-7.1	-8.4	7.52	5.75	1.77	23	12.8	8.41	-1.3	7.08	3.1
S604-70 (2)	-1.3	8.85	10.6	8.85	22.1	8.85	11.5	7.08	6.19	3.1	12.8
S604-70 (4)	18.1	13.7	-1.8	8.85	-13	10.6	-9.7	5.31	9.29	12.8	3.1
S604-70 (6)	-3.1	14.6	-6.2	100	-2.7	18.6	0	10.6	4.42	15	13.3
N674-70 (1)	50.3	57.1	32.9	40.3	43.4	36.6	92	48.9	37.7	46.9	23.4
N674-70 (2)	83.9	87.3	80.7	52.9	90.7	64.9	98.2	74.6	59.1	76	52.6
N674-70 (4)	100	98	100	100	98	84.5	100	95.1	73.7	87.9	73.2
N674-70 (6)	100	98.7	99.8	100	100	93	100	98.7	81.6	95.8	83.5
L1120-70 (1)	-0.6	29.3	17.8	48.9	42.5	17.8	-13	8.62	47.9	25.3	2.87
L1120-70 (2)	5.17	37.4	6.9	29.9	25.3	49.7	-4.6	22.4	31	45.2	29.3
L1120-70 (4)	42.5	80.1	41.4	41.4	60.1	64.2	39.7	56.3	43.2	53.4	52.6
L1120-70 (6)	78.8	100	41.4	62.3	71.3	46.8	46	75.1	43.2	61.3	60.1
V1164-75 (1)	38.1	54.8	53.9	44.2	50	42.2	34.5	59.8	50.9	47.9	58.6
V1164-75 (2)	55.6	68.3	41.2	55.1	43.1	60.6	28.6	69.6	52.8	51.7	41.1
V1164-75 (4)	64.5	76.1	62.5	52.8	61.7	73.2	48.9	70.3	72.2	68.3	47
V1164-75 (6)	76.8	92.5	68.3	65.7	72.9	77.4	46	87.7	76.2	80	66
C1185-70 (1)	36.7	37.9	36.7	26.2	27.7	31.3	78.4	23.8	25	27.7	12.9
C1185-70 (2)	65.8	62.6	63.9	38.7	63.9	27.3	88.6	41	41.4	46.9	36.3
C1185-70 (4)	85.6	78.9	85.2	100	95.5	55.1	97.4	63.9	48.8	69.6	48.8
C1185-70 (6)	97.4	86.6	95.9	100	100	69.5	98.5	88	58.6	77.7	57.4
N103-70 (1)	45.2	48	29.4	13.1	36.1	41.3	95.2	60.8	50.8	39.3	9.13
N103-70 (2)	83.6	88.5	79.9	34.5	94.4	73.7	100	79	72.9	78.5	45.2
N103-70 (4)	100	99.1	99.6	100	100	90	100	94.4	83.5	90.4	72.5
N103-70 (6)	100	100	100	100	100	95	100	100	89	96.4	82.7

Since the standards for tensile testing (ASTM, 1990a and 1990b) specify the characteristic value as the median of three specimens, an expression of uncertainty is not easily determined without additional analysis and/or testing. However, arguments similar to those in Section 8.3.2.2 on compression set can be made. That is, an elastomer with an estimated percent decrease in ultimate elongation of approximately 65% after 4 weeks may fall into the good or fair category but bad

Table 11. Compatibility of elastomers based on tensile testing after exposures at 5.86 MPa and 150 °C in various fluorocarbon agents

Agent	S604-70	N674-70	L1120-70	V1164-75	C1185-70	N103-70
HFC-236fa	good[a]	bad[c]	good	bad	good	fair[b]
HFC-32/125	good	bad	bad	bad	good	bad
HFC-227ea	good	fair	good	bad	good	fair
HCFC-22	bad	bad	good	bad	fair	fair
HFC-134a	good	fair	good	bad	good	fair
FC-116	good	fair	good	bad	good	fair
HCFC-124	bad	bad	good	bad	bad	bad
HFC-125	good	fair	bad	bad	good	fair
FC-218	good	fair	good	bad	good	fair
FC-31-10	good	fair	fair	bad	good	bad
FC-318	good	fair	good	good	good	good

[a]decrease in ultimate elongation is less than 65% after 4 weeks
[b]decrease in ultimate elongation is less than 65% after 2 weeks but exceeds 65 % after 4 weeks
[c]decrease in ultimate elongation exceeds 65% after 2 weeks

compatibility is unlikely. Similar arguments can be made for elastomers with an estimated percent decrease in ultimate elongation of approximately 65% after 2 weeks.

8.3.3 Lubricants. The same types of lubricants used in the swelling experiments (listed in Table 2), *i.e.,* Krytox 240AC, Braycote 600 and 807, were subjected to high temperature exposures and then tested for changes in viscosity.

8.3.3.1 Viscosity Measurements. The original rheological properties of each grease were characterized using the Rheometrics Mechanical Spectrometer Model 800. Approximately 10 mg of grease was evenly placed in a cone and plate fixture with a diameter of 25 mm, cone angle of 0.02 radians, and gap of 0.023 mm. The instrument was used to perform steady shear testing of the sample. During the test, the instrument subjects the sample to a rotational shear at a given shear rate $\dot{\gamma}$ and measures the resulting torque. The instrument analyzes the sample's rotational response and calculates the shear stress τ and steady shear viscosity η.

An open 2 ml vial was filled with approximately 100 mg of grease and placed in the pressure vessel. After each exposure approximately 25 mg of grease was removed and stored in a closed 2 ml vial and labeled with the agent, lubricant name, exposure time, and date. All rheology tests were conducted near the end of the short term exposures. Each grease was subjected to rate sweep measurements. The rate sweep test was used to determine the response of the sample to a range of steady shear rates at room temperature (24 $\pm$ 1 °C). The test was performed with strain rates of $\dot{\gamma}$ = 0.010, 0.016, 0.025, 0.040, 0.063, and 0.100 s^{-1} which correspond to six points in a logarithmic

decade. Figure 9 shows typical results for Krytox 240AC after high temperature exposures to HFC-125 (pentafluoroethane). Note the absence of systematic time dependence of viscosity at 150 °C. The viscosity of the grease increases after 1 week exposure to HFC-125, but then decreases after the remaining exposures. This suggests that the differences are due to experimental uncertainty and no significant chemical degradation occurs. However, in some instances, viscosity measurements were not possible because mobile substances were extracted and the greases became powder-like.

Table 12 lists the number of weeks after which the grease's viscosity was still measurable, *i.e.*, had not become powder-like. Table 13 shows the ratings for the compatibility of lubricants based on the viscosity measurements after exposures at 5.86 MPa and 150 °C in various fluorocarbon agents. Bad compatibility was defined as a condition when the grease became powder-like after a 4 week exposure. Lubricants have good compatibility if the grease did not become powder-like after 6 weeks. If the grease became powder-like after 6 weeks, the lubricant was considered to have fair compatibility with the agent.

Due to the nature of the criteria regarding the powder-like nature of the lubricants, an expression of uncertainty is not readily determined without additional testing. However, arguments similar to those in Section 8.3.2.2 on compression set can be made. That is, a lubricant whose viscosity was still measurable after 6 weeks may fall into the fair category but bad compatibility is unlikely. Similar arguments can be made for lubricants which were powder-like after 4 weeks.

8.4 Summary and Conclusion

In order to investigate the potential for deterioration of the o-ring and its lubricant in the fire suppressant storage system, short term exposure experiments have been conducted and data have been generated on the changes in the properties of various elastomers and greases after exposure to the eleven fluid agents. Isopiestic measurements and durability testing proved to be sensitive methods for characterizing the compatibility of elastomers and lubricants with fluorocarbon agents. However, exposures between 140 and 150 °C were found to be severe for most of the elastomers and lubricants. Additional testing at lower temperatures and for longer times is required to better simulate the in-service conditions.

In Table 14, the compatibility of elastomers and lubricants are shown based on the durability ratings in Tables 9, 11, and 13 (G = good, F = fair, B = bad). If the ratings for compression set and tensile testing were different, the worse compatibility is listed. In parentheses, the ratings based on the swelling compatibility only (Table 6) are listed if different than the durability ratings. The swelling ratings for crosslinked 55% butadiene-45% acrylonitrile (N206) and 85% butadiene-15% acrylonitrile (N926) are listed with the standard industrial nitrile (N674-70) and low temperature industrial (N103-70) compounds, respectively. These ratings are summarized below for the 11 agents. If the ratings for durability and swelling compatibility were different, the worse compatibility is reported.

HFC-236

Lubricants Krytox 240AC, Braycote 600 and 807 have good compatibility and silicone is a fairly compatible elastomer. The nitrile, fluorosilicone, fluorocarbon, and neoprene elastomers are incompatible.

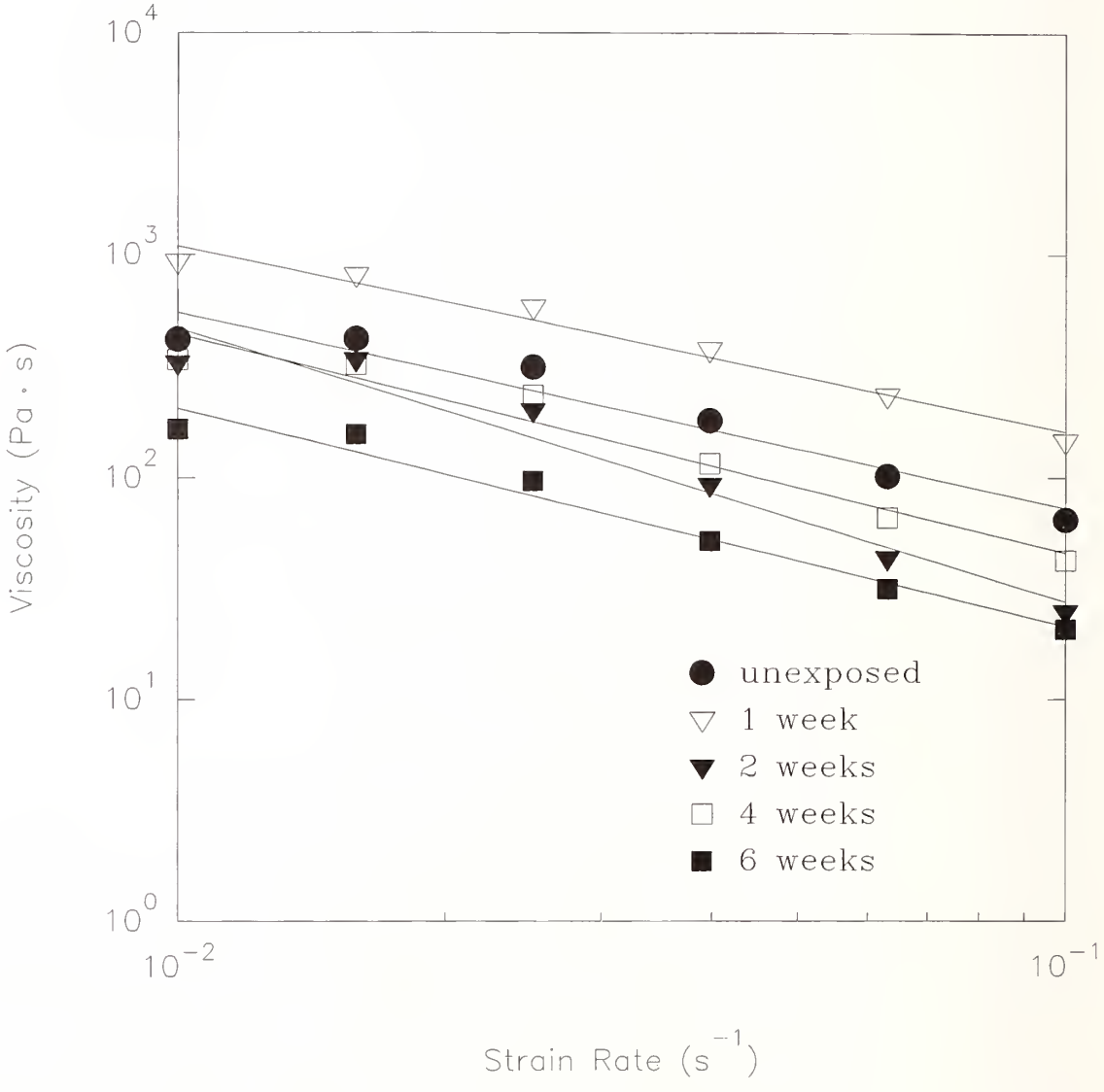

Figure 9. Viscosity measurements of the lubricant Krytox 240AC after various exposure times in HFC-125 (pentafluoroethane) at 150 °C.

Table 12. Number of weeks of exposure at 5.86 MPa and 150 °C in various fluorocarbon agents after which viscosity measurements were still possible, *i.e.*, the grease was not powder-like

Grease	236fa	32 /125	227ea	22	134a	116	124	125	218	31-10	318
Krytox 240AC	6 wks	6 wks	2 wks	2 wks	0 wks	4 wks	6 wks	6 wks	0 wks	0 wks	0 wks
Braycote 600	6 wks	6 wks	6 wks	2 wks	1 wk	6 wks	6 wks	6 wks	2 wks	0 wks	0 wks
Braycote 807	6 wks	6 wks	6 wks	4 wks	0 wks	6 wks	6 wks	6 wks	1 wk	0 wks	0 wks

HFC-32/125

Lubricants Krytox 240AC, Braycote 600 and 807 have good compatibility and silicone and neoprene are fairly compatible elastomers. The nitrile, fluorosilicone, and fluorocarbon elastomers are incompatible.

HFC-227

Braycote 600 and 807 are fairly compatible lubricants and silicone, fluorosilicone, and neoprene are fairly compatible elastomers. Krytox 240AC lubricant and nitrile, fluorosilicone, and fluorocarbon elastomers are incompatible.

HCFC-22

Braycote 807 is a fairly compatible lubricant and fluorosilicone is a fairly compatible elastomer. Krytox 240AC and Braycote 600 lubricants and silicone, nitrile, neoprene, and fluorocarbon elastomers are incompatible.

HFC-134a

Silicone, fluorosilicone, and neoprene are fairly compatible elastomers. Krytox 240AC, Braycote 600 and 807 lubricants and nitrile and fluorocarbon elastomers are incompatible.

FC-116

Krytox 240AC, Braycote 600 and 807 are fairly compatible lubricants. Elastomers silicone, fluorosilicone, and neoprene have good compatibility and nitrile (N674-70) is fairly compatible. Fluorocarbon and nitrile (N103-70) elastomers are incompatible.

HCFC-124

Lubricants Krytox 240AC, Braycote 600 and 807 have good compatibility and fluorosilicone is a fairly compatible elastomer. Silicone, nitrile, and fluorocarbon elastomers are incompatible.

HFC-125

Lubricants Braycote 600 and 807 have good compatibility and Krytox 240AC is a fairly good lubricant. Elastomers silicone and neoprene have good compatibility. Fluorosilicone, nitrile, and fluorocarbon elastomers are incompatible.

Table 13. Compatibility of lubricants based on viscosity measurements after exposures at 5.86 MPa and 150°C in various fluorocarbon agents

Agent	Krytox 240AC	Braycote 600	Braycote 807
HFC-236fa	good[a]	good	good
HFC-32/125	good	good	good
HFC-227ea	bad[c]	good	good
HCFC-22	bad	bad	fair[b]
HFC-134a	bad	bad	bad
FC-116	fair	good	good
HCFC-124	good	good	good
HFC-125	good	good	good
FC-218	bad	bad	bad
FC-31-10	bad	bad	bad
FC-318	bad	bad	bad

[a]grease was not powder-like after 6 weeks
[b]grease was not powder-like after 4 weeks but was powder-like after 4 weeks
[c]grease became powder-like after 4 weeks

FC-218

Elastomers silicone, fluorosilicone, and neoprene have good compatibility and nitrile (N674-70) is fairly compatible. Krytox 240AC, Braycote 600 and 807 lubricants and fluorocarbon and nitrile (N103-70) elastomers are incompatible.

FC-31-10

Silicone, fluorosilicone, and neoprene are fairly compatible elastomers. Krytox 240AC, Braycote 600 and 807 lubricants and nitrile and fluorocarbon elastomers are incompatible.

FC-318

Elastomers silicone, fluorosilicone, fluorocarbon, and neoprene have good compatibility and the nitrile elastomers are fairly compatible. Krytox 240AC, Braycote 600 and 807 lubricants are incompatible.

Table 14. Compatibility of elastomers and lubricants based on the durability ratings in Tables 10, 12, and 14 (G = good, F = fair, B = bad)

Agent	240AC	600	807	S604-70	N674-70 (N206)	L1120-70	V1164-75	C1185-70	N103-70 (N926)
HFC-236fa	G[a]	G	G	G (F)[b]	B (F)	G (B)	B	B	B
HFC-32/125	G	G	G	G (F)	B (G)	B (G)	B (G)	F (G)	B (G)
HFC-227ea	B (F)	G (F)	G (F)	G (F)	B (G)	G (F)	B (F)	F (G)	B
HCFC-22	B (F)	B (G)	F	B (F)	B	G (F)	B (F)	B (G)	F (B)
HFC-134a	B (G)	B (F)	B (G)	G (F)	B (G)	G (F)	B (G)	F (G)	B (G)
FC-116	F	G (F)	G (F)	G	F (G)	G	B (G)	G	B (G)
HCFC-124	G	G	G	B	B (F)	G (F)	B (F)	B (F)	B (F)
HFC-125	G (F)	G	G	G	B (G)	B (G)	B (F)	G	B (G)
FC-218	B (G)	B (G)	B (G)	G	F (G)	G	B (G)	G	B (G)
FC-31-10	B (F)	B	B	G (F)	B (F)	F (G)	B (F)	F (G)	B (F)
FC-318	B (F)	B (F)	B (F)	G	F (G)	G	G	G	F

[a]If the ratings for compression set and tensile testing were different, the worse compatibility is listed
[b]If different, the rating for swelling compatibility (Table 7) is listed in parentheses

8.5 References

Allied Signal, Inc., *Thermodynamic Properties of Refrigerants (Genie)*, SML Services, Inc. (1989).

ASTM, Designation D 395-89, "Standard Test Methods for Rubber Property - Compression Set," *Annual Book of ASTM Standards*, **09.01**, 24 (1989).

ASTM, Designation D 412-87, "Standard Test Methods for Rubber Properties in Tensions," *Annual Book of ASTM Standards*, **09.02**, 100 (1990a).

ASTM, Designation D 1414-90, "Standard Test Methods for Rubber O-Rings," *Annual Book of ASTM Standards*, **09.02**, 181 (1990b).

Atkin, R.J. and Fox, N., *An Introduction to the Theory of Elasticity*, Longman, New York (1980).

Boyer, R.F., "Deswelling of Gels by High Polymer Solutions," *J.Chem.Phys.*, **13**, 363 (1945).

Brotzman, R.W. and Eichinger, B.E., "Volume Dependence of the Elastic Equation of State. 3. Bulk-Cured Poly(dimethylsiloxane)," *Macromolecules* **15**, 531 (1982).

Brotzman, R.W. and Eichinger, B.E., "Swelling of Model Poly(dimethylsiloxane) Networks," *Macromolecules*, **16**, 1131 (1983).

E.I. du Pont de Nemours and Co., Inc., *Thermodynamic Properties of "Freon" 116 Refrigeran* (1968).

E.I. du Pont de Nemours and Co., Inc., *Thermodynamic Properties of HFC-236fa Refrigerant*, (1993).

Flory, P.J., "Thermodynamics of High Polymer Solutions," *J. Chem. Phys.*, **10**, 51 (1942).

Flory, P.J., *Principles of Polymer Chemistry*, Cornell University Press, Ithaca, New York (1953).

Flory, P.J., "Statistical Thermodynamics of Liquid Mixtures," *J. Am. Chem. Soc.*, **87**, 1833 (1965).

Flory, P.J., "Thermodynamics of Polymer Solutions," *Disc. Faraday. Soc.*, **49**, 7 (1970).

Flory, P.J. and Erman, B., "Theory of Elasticity of Polymer Networks 3.,"*Macromolecules* **15**, 800 (1982).

Flory, P.J., Orwoll, R.A., and Vrij, A., "Statistical Thermodynamics of Chain Molecule Liquids. I. An Equation of State for Normal Paraffin Hydrocarbons," *J. Am. Chem. Soc.*, **86**, 3507 (1964a).

Flory, P.J., Orwoll, R.A., and Vrij, A., "Statistical Thermodynamics of Chain Molecule Liquids. II. Liquid Mixtures of Normal Paraffin Hydrocarbons," *J. Am. Chem. Soc.*, **86**, 3515 (1964b).

Flory, P.J. and Rehner, J., Jr., "Statistical Mechanics of Cross-Linked Polymer Networks," *J.Chem.Phys.*, **11**, 521 (1943).

Gallagher J., McLinden, M., Huber, M., and Ely, J., *NIST Standard Reference Database 23: Thermodynamic Properties of Refrigerants and Refrigerant Mixtures Database (REFPROP), Version 3.0*, U.S. Department of Commerce, Washington, DC (1991).

Gee, G., Herbert, J.B.M. and Roberts, R.C., "The Vapor Pressure of a Swollen Cross-Linked Elastomer," *Polymer* **6**, 51 (1965).

Horkay, F. and Zrinyi, M., "Studies on Mechanical and Swelling Behavior of Polymer Networks on the Basis of the Scaling Concept. 4. Extension of the Scaling Approach to Gels Swollen to Equilibrium in a Diluent of Arbitrary Activity," *Macromolecules* **15**, 1306 (1982).

Horkay, F., Hecht, A.-M. and Geissler, E., "The Effects of Cross-Linking on the Equation of State of a Polymer Solution," *J. Chem. Phys.*, **91**, 2706 (1989).

Huggins, M.L., "Some Properties of Solutions of Long-Chain Compounds," *J. Phys. Chem.*, **46**, 151 (1942).

James, H.M. and Guth, E., "Theory of Elastic Properties of Rubber," *J. Chem. Phys.*, **11**,455 (1943).

Jandel Scientific, *SigmaPlot Scientific Graphing Software, Version 5.0*, (1992).

McKenna, G.B. and Crissmann, J.M., "Thermodynamics of Crosslinked Polymer Networks: The Anomalous Peak in Swelling Activity Measurements," *Macromolecules 1992*, ed by J. Kahovec, VSP, Utrecht, The Netherlands, pp. 67-81 (1993).

McKenna, G.B., Flynn, K.M. and Chen, Y., "Experiments on the Elasticity of Dry and Swollen Networks: Implications for the Frenkel-Flory-Rehner Hypothesis," *Macromolecules* **22**, 4507 (1989).

McKenna, G.B., Flynn, K.M. and Chen, Y., "Swelling in Crosslinked Natural Rubber: Experimental Evidence of the Crosslink Density Dependence of χ," *Polymer* **31**,1937 (1990).

Mooney, M., "A Theory of Large Elastic Deformation," *J. Appl. Phys.*, **11**, 582 (1940).

Pennings, A.J. and Prins, W., J. "A Versatile Osmometer for Polymer Gels and Solutions with Applications to Cellulosic Gels," *Polym. Sci.*, **49**, 507 (1961).

Press, W.H., Flannery, B.P., Teukolsky, S.A., and Vetterling, W.T., "Numerical Recipes," Cambridge University Press (1986).

Robin, M.L., *Thermodynamic and Transport Properties of FM-200*, Great Lakes Corporation (1992)

Shih, H., Flory, P.J., "Equation-of-State Parameters for Poly(dimethylsiloxane)," *Macromolecules*, **5**, 758 (1972).

Treloar, L.R.G., "Stresses and Birefringence in Rubber Subjected to General Homogeneous Strain," *Proc. Phys. Soc.*, **60**, 135 (1948).

Wilson, L.C., Wilding, W.V., and Wilson, G.M., *Thermo-Physical Properties of Perfluorobutane*, Wiltech Research Company (1992).

9. HUMAN EXPOSURE AND ENVIRONMENTAL IMPACT

Emil Braun, Richard D. Peacock, Glenn P. Forney, George W. Mulholland, and Barbara C. Levin
Building and Fire Research Laboratory

9.1 Potential Human Exposure

Although these agents are typically employed in unoccupied sections of an aircraft, the possibility of human exposure still exists during handling, storage, and transport. Thus, it is important to know if the accidental release of the 12 agents in areas of typical occupancy would result in differing threats to life safety. At least two topics are important in assessing the impact of a potential release of an agent: 1) how does the agent distribute in an occupied space upon an accidental release, and 2) how does this release affect personnel who may be exposed? For the former, a series of tests was conducted to study the release of four of the twelve agents in a sealed compartment to measure the airborne concentration of agent that results from complete venting of containers of typical size into spaces of typical volume. These tests were augmented with field modeling to extend the range of the test results to other compartment geometries. For the latter, published toxicological results for chronic or acute exposure are summarized. It is important to note that in these tests, no humans were exposed.

9.1.1 Full-Scale Tests. In order to evaluate the effects of an agent release in a closed compartment on potential human occupants, a series of experiments were conducted under full-scale geometries to determine

- agent distribution within the compartment, and
- temperature distribution within the compartment

for near (within the jet plume) and far field conditions over a short period of time, *i.e.*, acute exposure conditions. The test duration was 30 minutes. Temperature and gas concentrations at various levels within the compartment were measured during this "exposure" period. All agent release tests were conducted with the cylinder oriented such that the agent liquid was at the bottom of the cylinder and release occurred from the top. Cylinders were filled with a measured amount of agent and pressurized to a nominal 4,200 kPa with nitrogen gas. Since resources (i.e., time, funding, and agent availability) were limited for this phase of the project, tests were conducted on a subset of agents that spanned a broad range (greater than a factor of 3) of molecular weights and vapor pressures. While furnishing detailed data on the release process for a specific subset of agents, it was the also the intent of these experiments to provide data that could be used to verify the computational modeling of the release process. Therefore, in addition to halon 1301, only four agents were selected for evaluation. These agents are listed in Table 1 along with the amounts and initial pressurization states. Halon 1301 was used as a reference agent to determine if the observed conditions were significantly different than those currently experienced through accidental releases of halon 1301.

9.1.2 Instrumentation. A compartment, measuring 2.45 m by 3.66 m by 2.45 m high, was constructed and instrumented as shown in Figure 1. Because of an extended doorway entrance the

Table 1. Agents tested in the full-scale geometry

Compound	Formula	Molecular Weight	Vapor Press. @ 25 °C (MPa)	Test Mass (g)
FC-116	C_2F_6	138	--[a]	465
Halon 1301	CF_3Br	149	1.61	420
				391
HCFC-22	CHF_2Cl	87	1.05	189
				297
HFC-227	C_3HF_7	170	0.47	108
HFC-32/HFC-125	CH_2F_2/C_2HF_5	67	1.67	227

[a]above critical pressure

total volume of the compartment was 22.7 m^3. A 1 liter stainless steel flask identical to those used in the stability tests was filled with test agent at approximately 4,200 kPa. The flask was attached to a support stand located in the center of the compartment. The support stand consisted of a swagelock mating nut, pneumatic actuator and valve, and a 10 mm ID tube that extended to a release point 0.9 m from the floor (Figure 2). Each experiment involved installing the charged agent cylinder into the support frame, sealing the compartment, and actuating the pneumatic valve to release agent into the compartment. The agent cylinder was left open through the duration of the test, 30 minutes. Thermocouple data were collected every ten seconds and evacuated flasks were filled in a specified pattern (Table 2) to ensure that if stratification or settling occurred it could be detected.

Three types of measurements were made during the release of each agent. Thermocouple measurements were made to determine the thermal effects of a rapid release of agent. Gas concentrations were measured using evacuated flasks as well as FTIR measurements to determine agent distribution in the compartment.

9.1.2.1 Temperature. Thermocouples were located on two vertical strings. One string of thermocouples was located in a corner of the compartment, 0.6 m from each adjoining wall. A second string of thermocouples was located 0.5 m north of the release point. Each thermocouple string consisted of eight thermocouples spaced 0.3 m apart starting at the ceiling. Thermocouples were also located 0.3, 0.6, and 0.9 m above the release point as well as one thermocouple 0.15 m above and 0.08 m north and another thermocouple 0.3 m above and 0.15 m north of the release point. Thermocouple data was collected every 10 seconds.

9.1.2.2 Gas Concentration. Using evacuated flasks, gas were sampled at three locations in the compartment. One sampling probe was placed 1.23 m above the release point (0.31 m from the ceiling). The other two sampling probes were located 0.46 m from the south wall. For tests involving agents FC-116, halon 1301, and HCFC-22 the two probes were located 0.92 m and 1.98 m, respectively, from the ceiling. For agents halon 1301, HCFC-22, HFC-227, and HFC-32/HFC-125 the lower probe was placed 44.5 mm from the floor (approximately 2.41 m from the ceiling). This was done to determine if agent settling was occurring. Each sampling probe was connected to a four

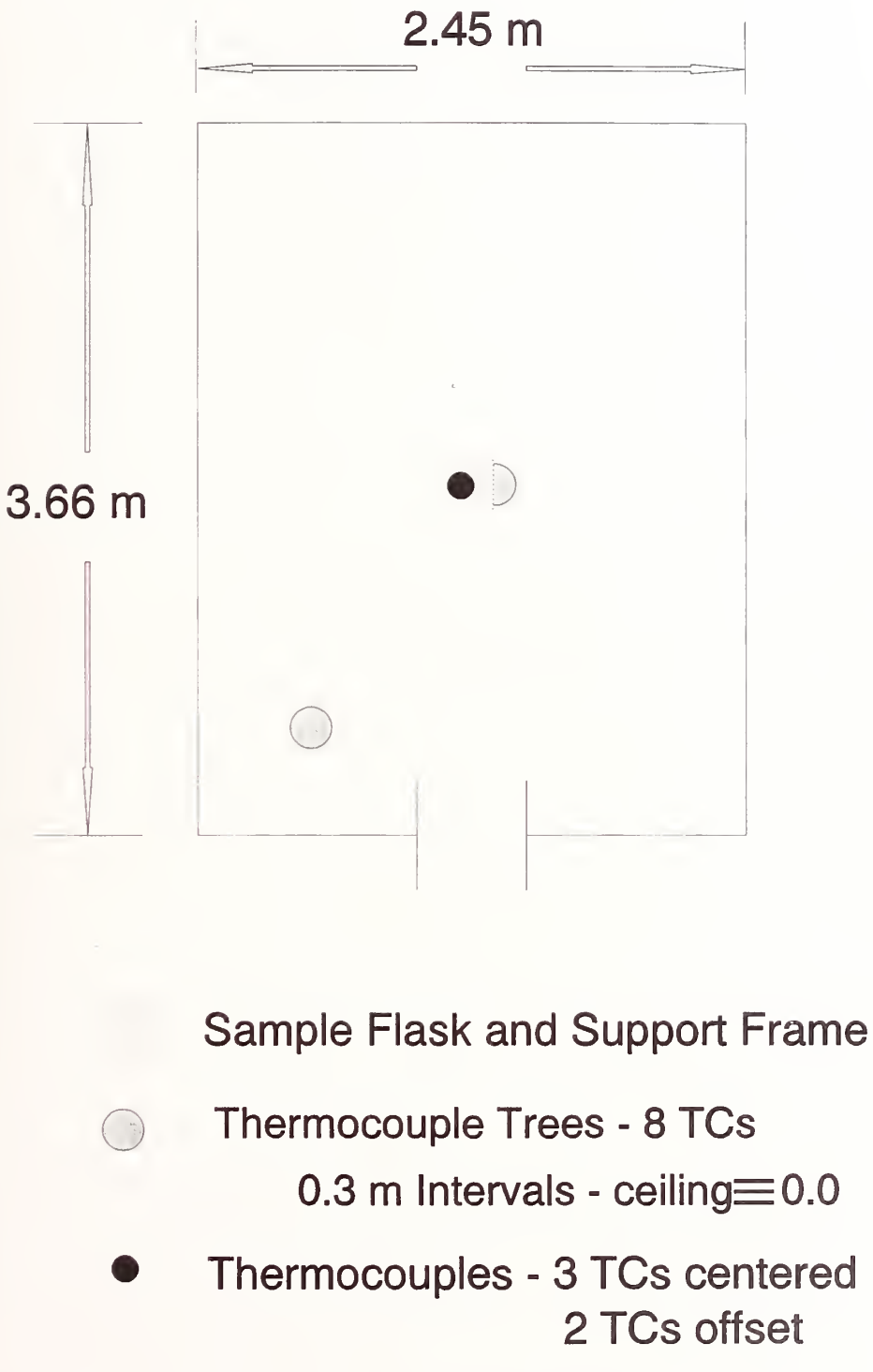

Figure 1. Floor plan and instrument layout for halon 1301 replacement release tests.

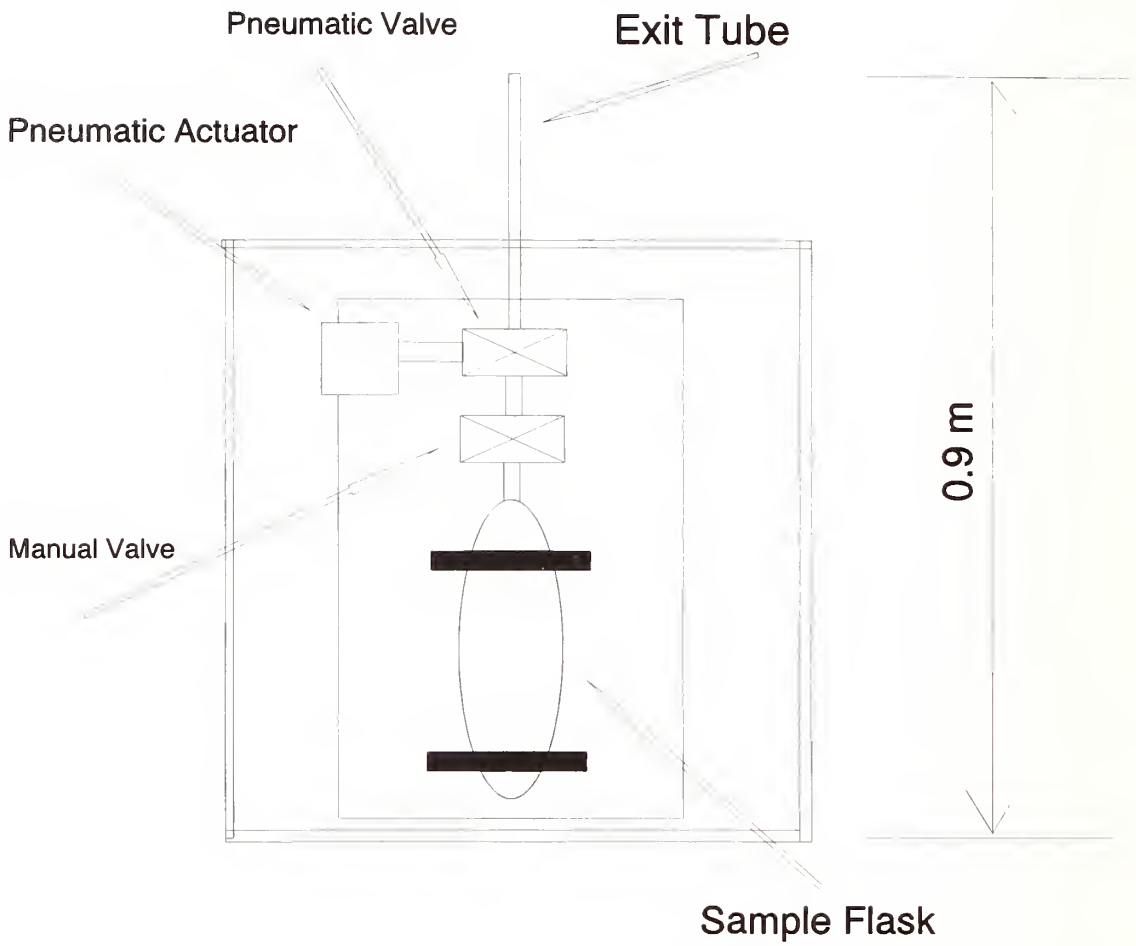

Figure 2. Schematic of agent sample flask, support frame, manual valve, pneumatic valve, and exit tube in relationship to the floor of the compartment.

flask manifold. Room atmosphere was drawn through the manifold by a vacuum pump operating at 2.5 l/m. In order to reduce atmospheric mixing in the compartment, gas samples drawn through each manifold were returned to the compartment at the same level from which they were taken at approximately the same location. Prior to a test, 12 flasks, 125 ml each, were evacuated. Four flasks were connected to each manifold. The vacuum pump for each manifold operated continuously, except during the time it took to fill a flask. The content of each flask was analyzed by a Hewlett Packard HP5730A gas chromatograph equipped with a flame ionization detector (FID). A column packed with 60/80 Carbopack B/ 5% Fluorcol was used to separate the agent from the background atmosphere. For the two component agent (HFC-32/HFC-125), peaks were detected representing each component. The carrier gas was nitrogen flowing at 30 ml/min. Each injection represented 500 μl of gas drawn from a flask. An approximate calibration was determined for each agent by injecting 500 μl samples drawn from a flask containing a known amount of agent dispersed in a know volume of air. Measurement errors associated with this calibration procedure consist of the error in measuring the volume of the calibration flask, the weight of the calibration flask before and after the addition of the agent, and the volume of gas drawn from the flask for injection into the GC carrier gas. A balance with a reading resolution of 0.1 mg was used to determine the mass of agent added to the flask. The balance was also used to determine the volume of the flask by measuring the mass of water needed to completely fill the flask. An error of 0.1 mg in the mass of agent in 125 ml flask represents a variation of approximately 0.8 mg/l in agent concentration or, for agent concentration range of 5 to 21 mg/l, represents a variation of about 4 to 15%. Errors associated with the GC system are a combination of syringe volume variation and GC system variation. These errors can be approximated by computing the variation in integrator area calculations. This error was found to vary from 1 to 4%. Combining these errors results in a final error approximation ranging from 5 to 19%.

Relative gas concentrations were also monitored in-situ with a Fourier Transform InfraRed (FTIR) spectrometer. The FTIR was relocated for each test depending on the intent of the measurement. For tests of FC-116, halon 1301 (test 1301-1), and HCFC-22 (test 22-1), the FTIR was located such that the sampling beam was approximately 1.2 m from the ceiling aimed diagonally across the compartment. For tests of HFC-32/HFC-125 and HCFC-22 (test 22-2), the FTIR was located 0.45 m from the ceiling with the beam parallel to and 0.52 m from the north wall. For the retest of halon 1301 (test 1301-2), the FTIR was placed along the north wall 0.05 m from the floor. While the FTIR provided better time resolution of agent concentration than the evacuated flasks, spatial resolution was provided by the data obtained from the use of evacuated flasks to sample the enclosure atmosphere as specified above. It was hoped that comparable trends would be observed by both measurement techniques.

9.1.3 Experimental Results

9.1.3.1 Temperature. The data from the thermocouple string located in the corner of the compartment displayed only small deviations from ambient conditions, less than 1 °C. These far field temperature measurements indicate that the rapid release of any of the agents at the loading concentrations used in these experiments produced little deviation from ambient conditions. Near field measurements below the point of release also showed deviations of less than 1 °C from ambient conditions for all tested agents. Data from these locations will not be shown or discussed further. Figures 3 to 9 show the temperature data for each test at the following three general sets of locations:

Table 2. Description of evacuated flask location, sampling sequence and timing

Sequence Number	Location Distance from Ceiling (m)		Designation	Sample Time (s)
1	0.31[a]		I.1	30
2	0.31[a]		I.2	90
3	0.91[b]		II.1	120
4	1.98[b,c]	2.41[b,d]	III.1	180
5	0.31[a]		I.3	300
6	0.91[b]		II.2	420
7	1.98[b,c]	2.41[b,d]	III.2	480
8	0.91[b]		II.3	600
9	1.98[b,c]	2.41[b,d]	III.3	720
10	0.31[a]		I.4	1320
11	1.98[b,c]	2.41[b,d]	III,4	1500
12	0.91[b]		II.4	1680

[a] Centered over exit tube
[b] 0.46 m from South Wall and 1.43 m from East Wall
[c] Height for agent release test: halon 1301, FC-116, HCFC-22
[d] Height for agent release test: halon 1301, HCFC-22, HFC-227, HFC-32/HFC-125

1. directly above the exit tube,
2. for a thermocouple 0.15 m above and 0.08 m north and another thermocouple 0.3 m above and 0.15 m north of the release point, and
3. for the upper four thermocouples 0.5 m north of the release point.

To provide the most visually clear set of data for each test, we have used different temperature ranges in the graphs. Care must therefore be exercised when comparing results between agents.

Figure 10 schematically shows the relationship between the thermocouples in the vicinity of the exit tube, including all of the thermocouples displayed in Figures 3 to 9. For all tests, the largest deviations from ambient occurred directly above the exit tube with the minimum temperature recorded by the thermocouple closest to the exit tube. Based on the thermocouple data in Figures 3 to 9, the release pattern can clearly be discerned. In every "A" graph of Figures 3 to 9, the change in minimum temperature decreases as the distance from the exit tube increases. In the "C" graphs, the deviation increases as the height above the exit tube level increases. Furthermore, the data from the two off-axis thermocouples displayed in the graphs labeled "B" show no significant response to the

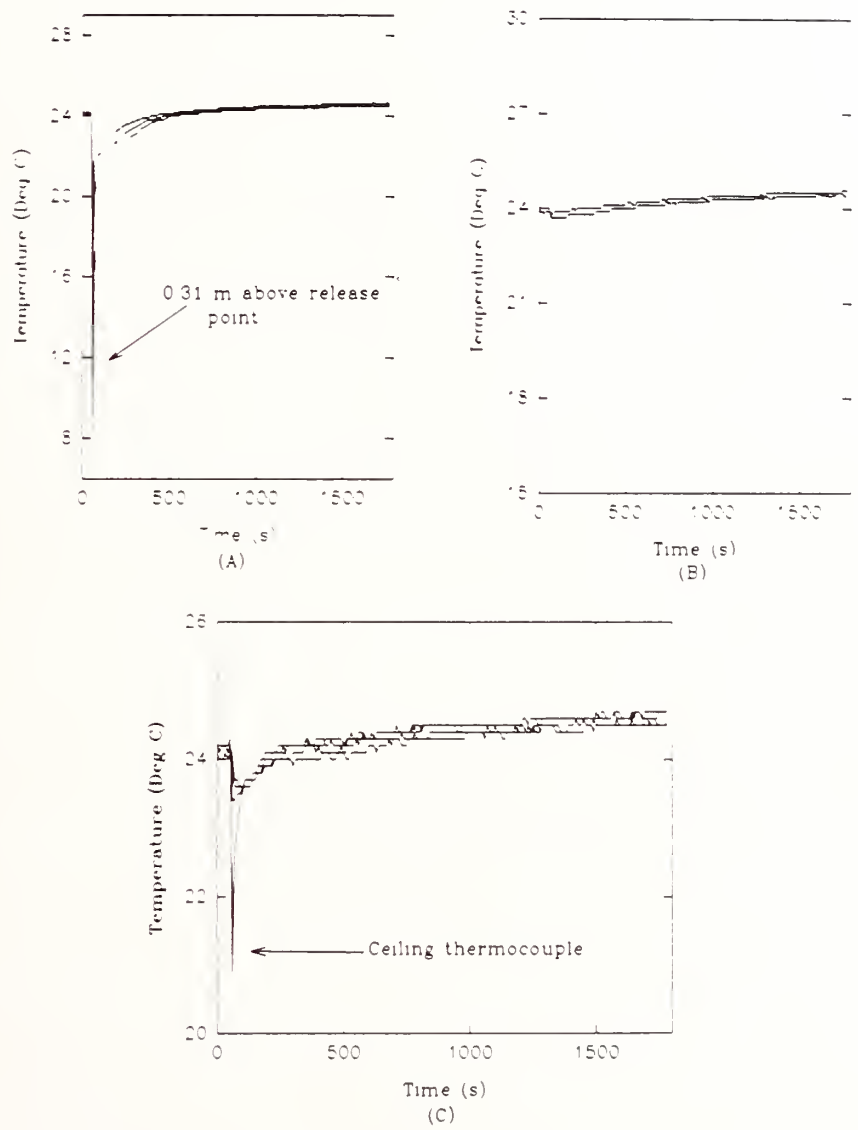

Figure 3. Temperature data FC-116: A-at 0.3, 0.6, and 0.9 m above tube; B-one 0.15 m above, 0.08 m offset and one 0.3 m above, 0.15 m offset; C-four 0.5 m offset, 0.0, 0.31, 0.62, and 0.93 m from ceiling.

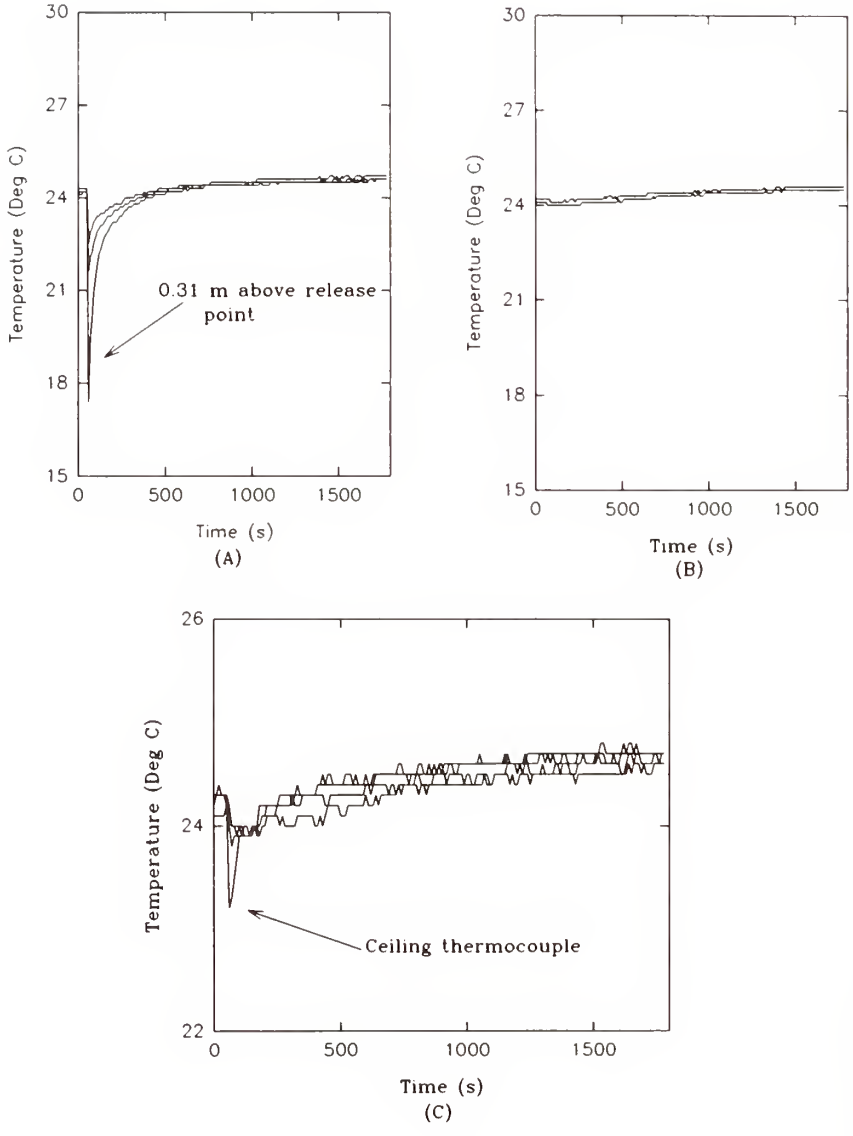

Figure 4. Temperature data Halon 1301, test 1: A-at 0.3, 0.6, and 0.9 m above tube; B-one 0.15 m above, 0.08 m offset and one 0.3 m above, 0.15 m offset; C-four 0.5 m offset, 0.0, 0.31, 0.62, and 0.93 m from ceiling.

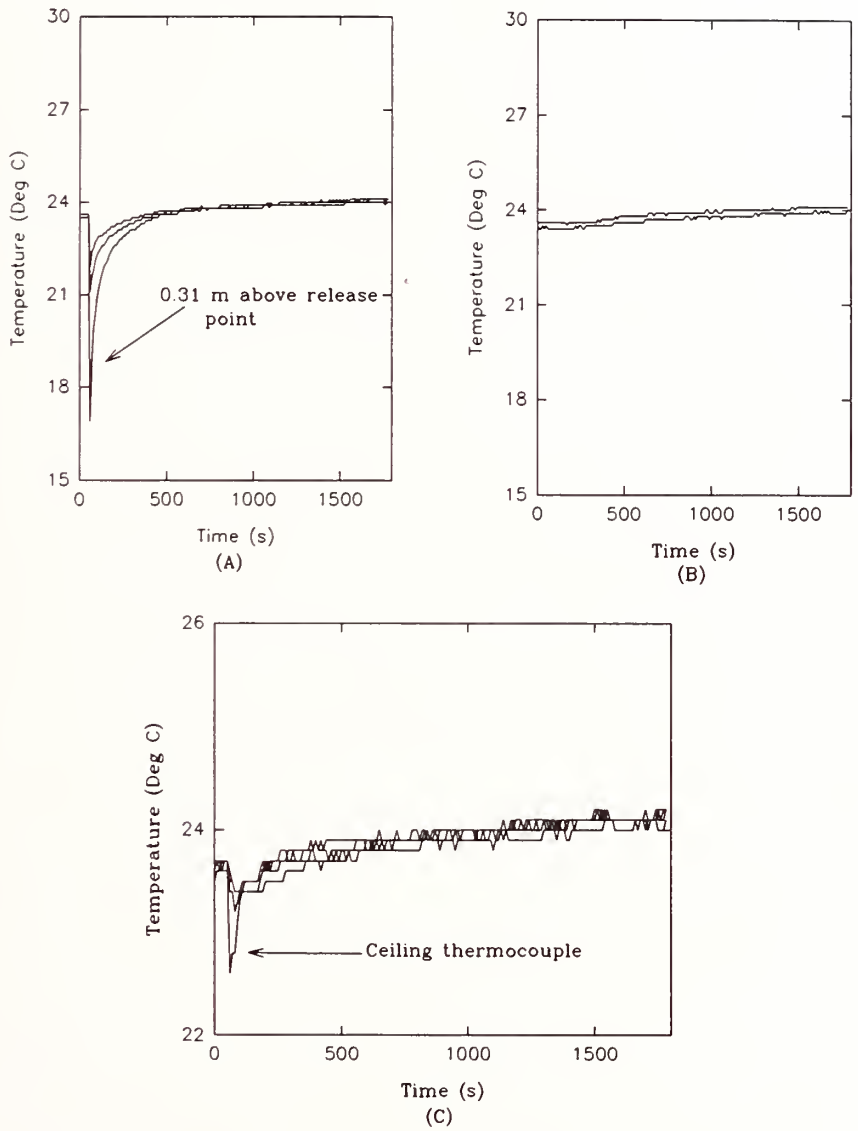

Figure 5. Temperature data Halon 1301, test 2: A-at 0.3, 0.6, and 0.9 m above tube; B-one 0.15 m above, 0.08 m offset and one 0.3 m above, 0.15 m offset; C-four 0.5 m offset, 0.0, 0.31, 0.62, and 0.93 m from ceiling.

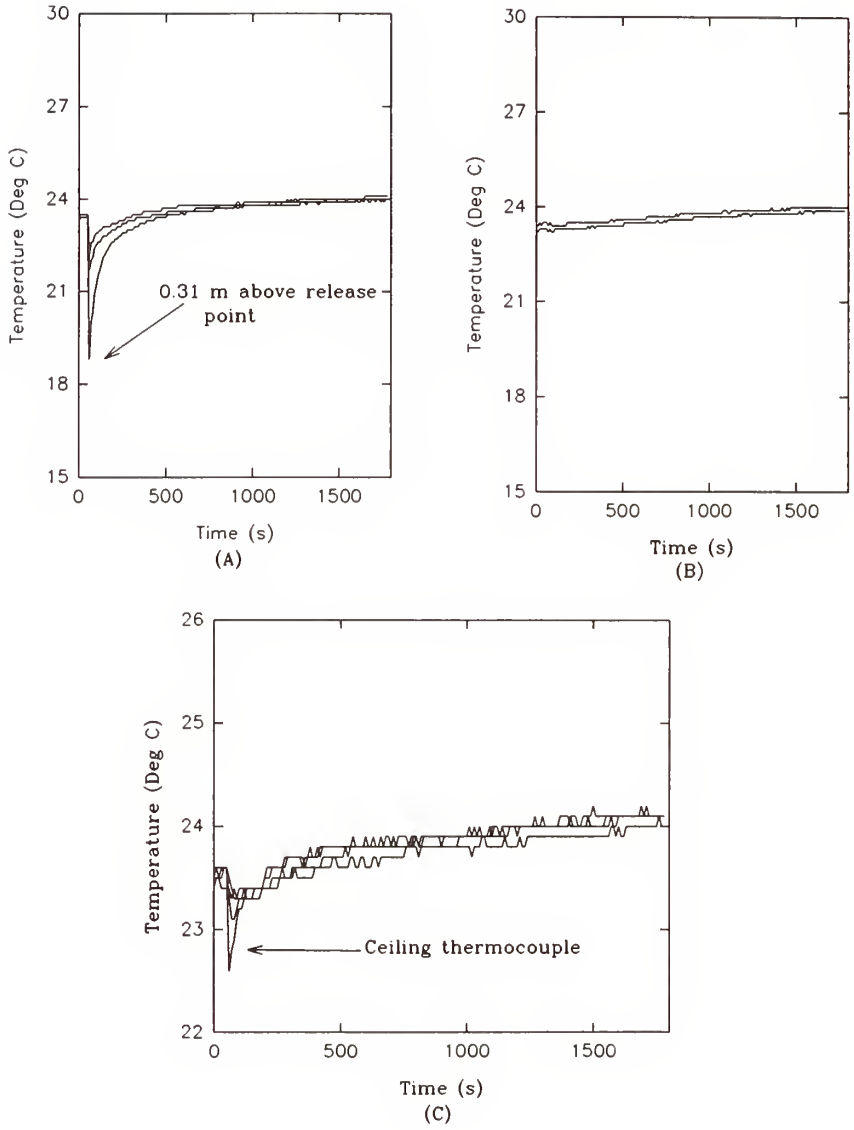

Figure 6. Temperature data HCFC-22, test 1: A-at 0.3, 0.6, and 0.9 m above tube; B-one 0.15 m above, 0.08 m offset and one 0.3 m above, 0.15 m offset; C-four 0.5 m offset, 0.0, 0.31, 0.62, and 0.93 m from ceiling.

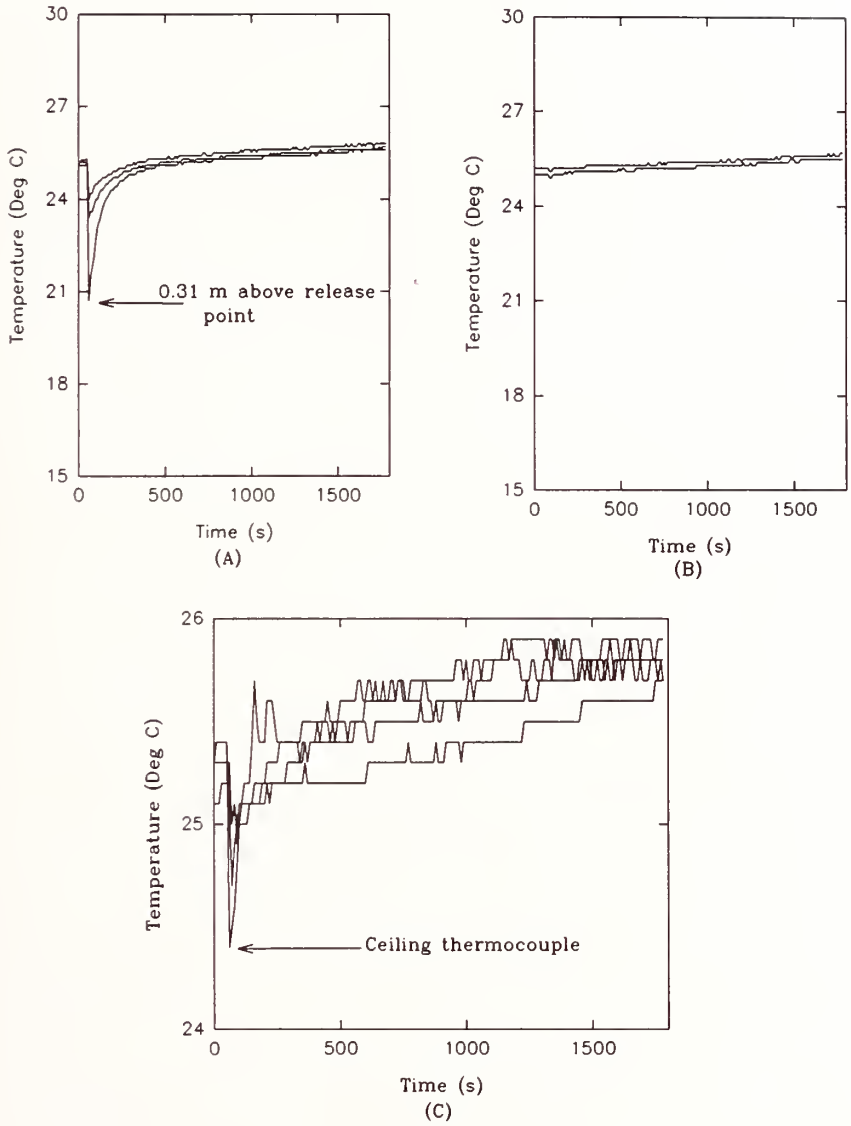

Figure 7. Temperature data HCFC-22, test 2: A-at 0.3, 0.6, and 0.9 m above tube; B-one 0.15 m above, 0.08 m offset and one 0.3 m above, 0.15 m offset; C-four 0.5 m offset, 0.0, 0.31, 0.62, and 0.93 m from ceiling.

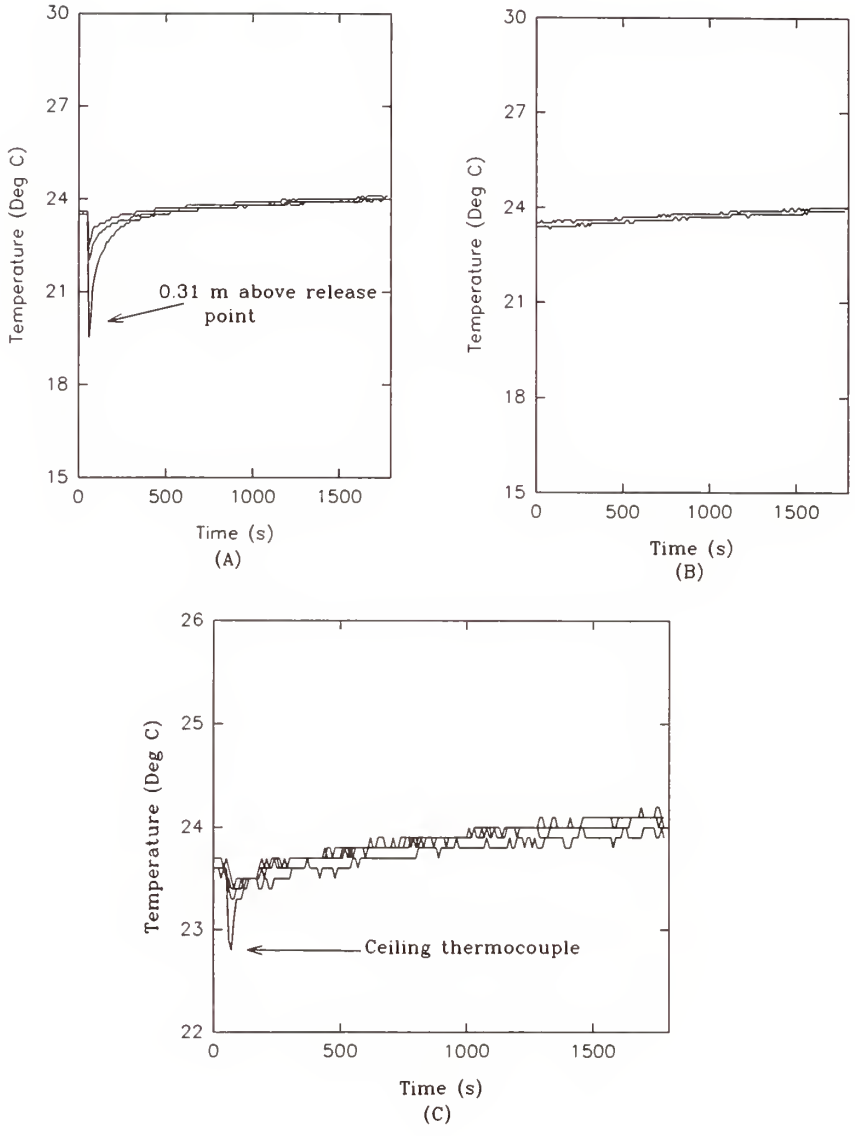

Figure 8. Temperature data HFC-227: A-at 0.3, 0.6, and 0.9 m above tube; B-one 0.15 m above, 0.08 m offset and one 0.3 m above, 0.15 m offset; C-four 0.5 m offset, 0.0, 0.31, 0.62, and 0.93 m from ceiling.

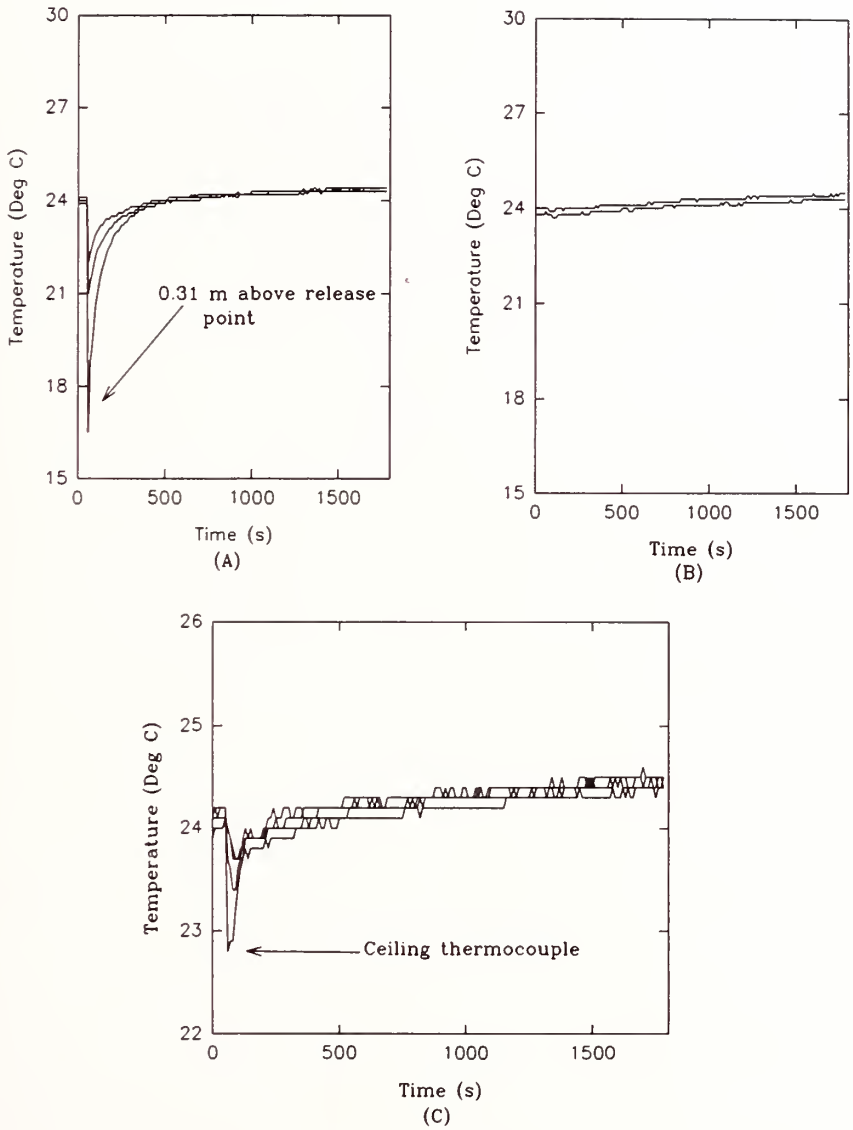

Figure 9. Temperature data HFC-32/125: A-at 0.3, 0.6, and 0.9 m above tube; B-one 0.15 m above, 0.08 m offset and one 0.3 m above, 0.15 m offset; C-four 0.5 m offset, 0.0, 0.31, 0.62, and 0.93 m from ceiling.

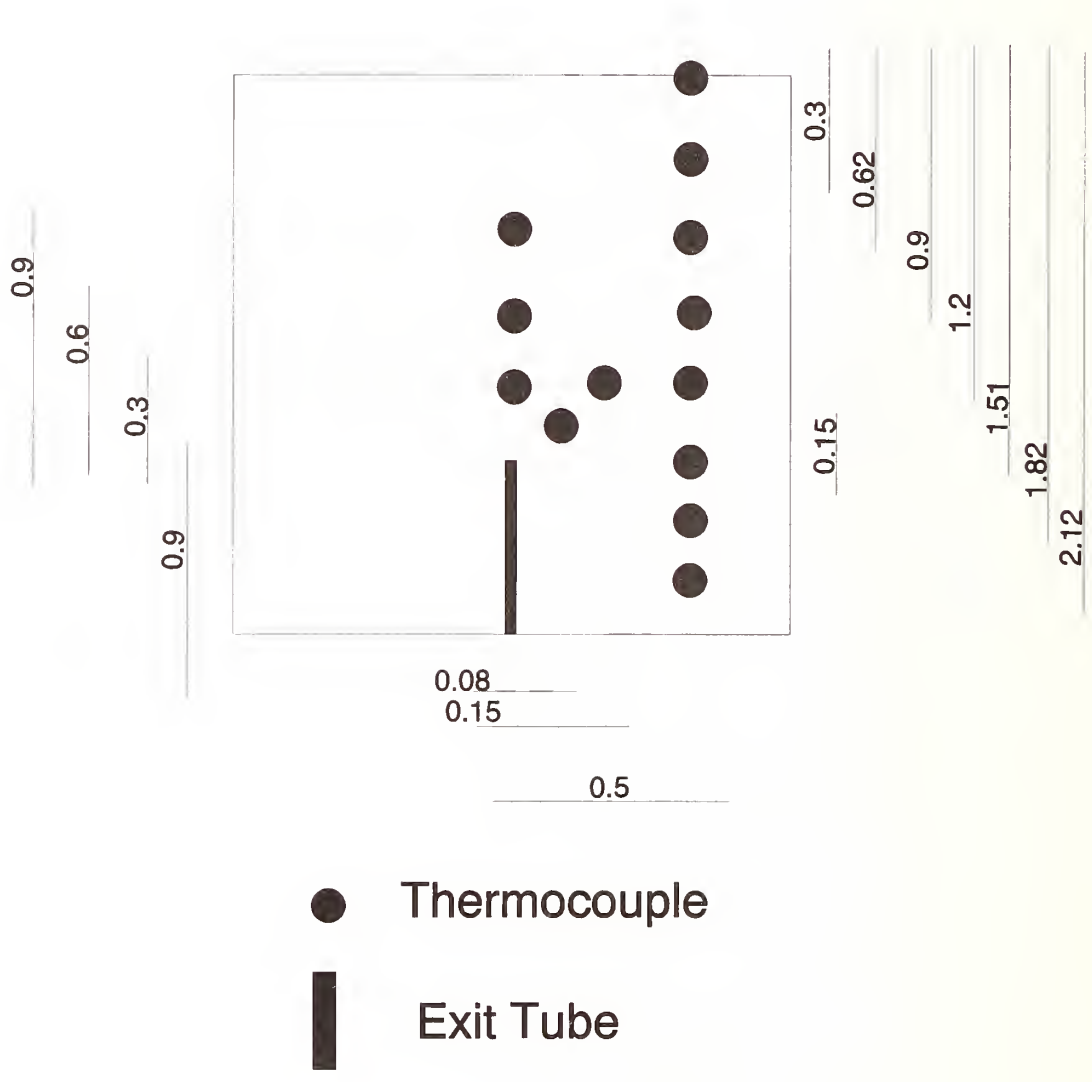

Figure 10. Schematic drawing showing the relationship of the near field thermocouples to the exit tube in the north-south vertical plane of the agent sample flask.

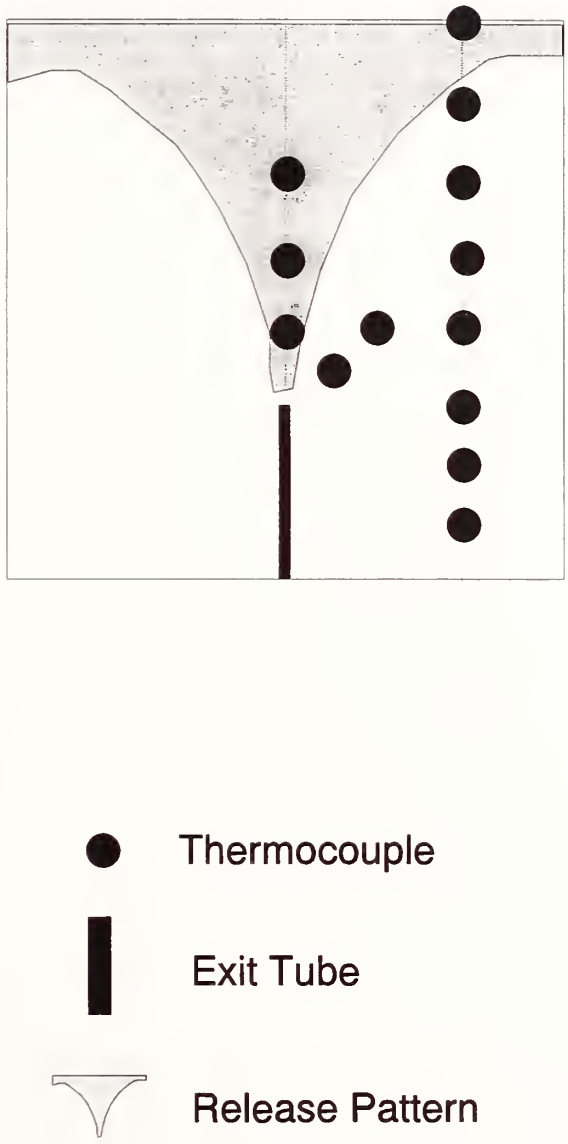

Figure 11. Theoretical representation of agent plume in relationship to the thermocouples located in the north-south vertical plane of the agent sample flask.

Table 3. Summary of the extent of temperature depression of two thermocouple locations

Compound		Thermocouple @ 0.31 m above exit tube		Thermocouple @ ceiling 0.5 m north of exit tube	
		Maximum Depression (°C)	Time to Recover to 90% of Ambient (s)	Maximum Depression (°C)	Time to Recover to 90% of Ambient (s)
FC-116		15.8	170	3.3	130
Halon 1301	1	6.8	140	1.1	390
	2	6.6	180	1.1	130
HCFC-22	1	4.6	190	1.0	170
	2	4.4	135	1.0	185
HFC-227		4.0	180	0.8	80
HFC-32/HFC-125		7.4	185	1.4	90

sudden release of agent. This suggests that the release plume is very narrow and quickly reached the compartment ceiling. The plume spreads rapidly along the ceiling and expands down towards the floor of the compartment. This is shown idealized in Figure 11. Based on the thermocouple data, this process occurs rapidly.

Table 3 summarizes the magnitude of the maximum depression from ambient temperature for the thermocouple located 0.3 m above the exit tube and the time to return to within 90% of ambient conditions. The same data are also tabulated for the ceiling thermocouple of the 0.5 m north thermocouple string. Maximum depression directly above the exit tube ranged from 15.8 °C for agent FC-116 to 4.0 °C for agent HFC-227. The maximum depression of the ceiling thermocouple was 3.3 °C for FC-116 to 0.8 °C for HFC-227. The 90% recovery time to near ambient conditions, with one exception, ranges from 80 s to 190 s. The recovery time data displays a classically exponential increase in temperature consistent with the natural convective heating of an object.

9.1.3.2 Concentration. In-situ FTIR and atmospheric samples captured in evacuated flasks represented the two methods employed in this study to determine agent concentration in the compartment. The FTIR apparatus is a line-of-sight measurement of the gas concentration of the released agents. The evacuated flasks are point measurements made at specific time intervals and, because three distinct sampling probes were employed, specific locations as previously described.

Figures 12 to 18 show the measured gas concentrations as a function of time for the three probe locations. Also noted on each figure (dashed line) is the average agent concentration in the compartment assuming (a) complete release of the agent from the cylinder, (b) even distribution within the compartment, and (c) no losses from the compartment.

While an effort was made to ensure that the compartment was completely sealed, the rapid decay in the early data (first half of the test period) indicates that significant leakage may have occurred.

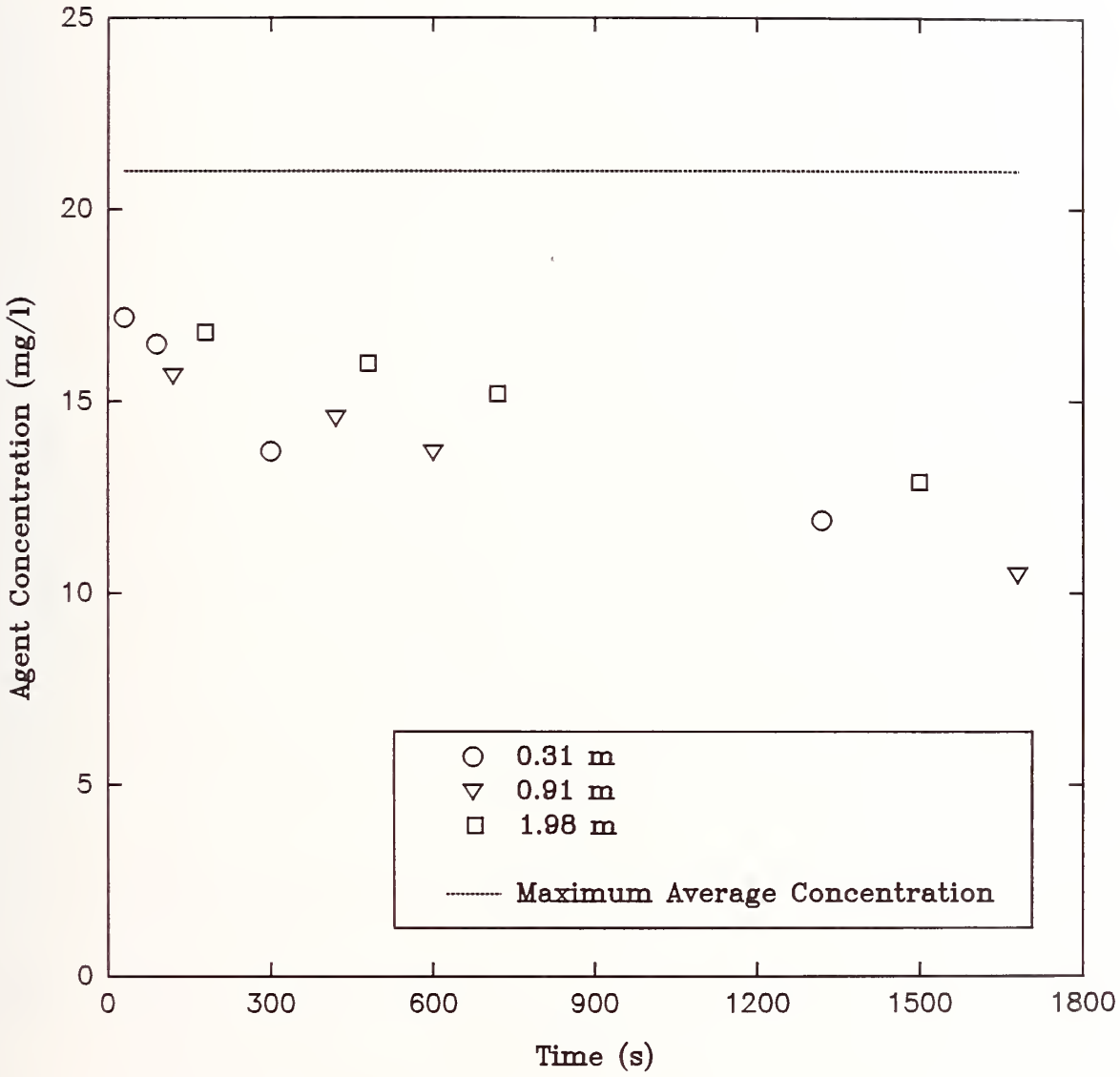

Figure 12. Agent concentration for agent FC-116 as a function of position and time with the maximum average concentration of agent shown (----) assuming uniform distribution within the compartment.

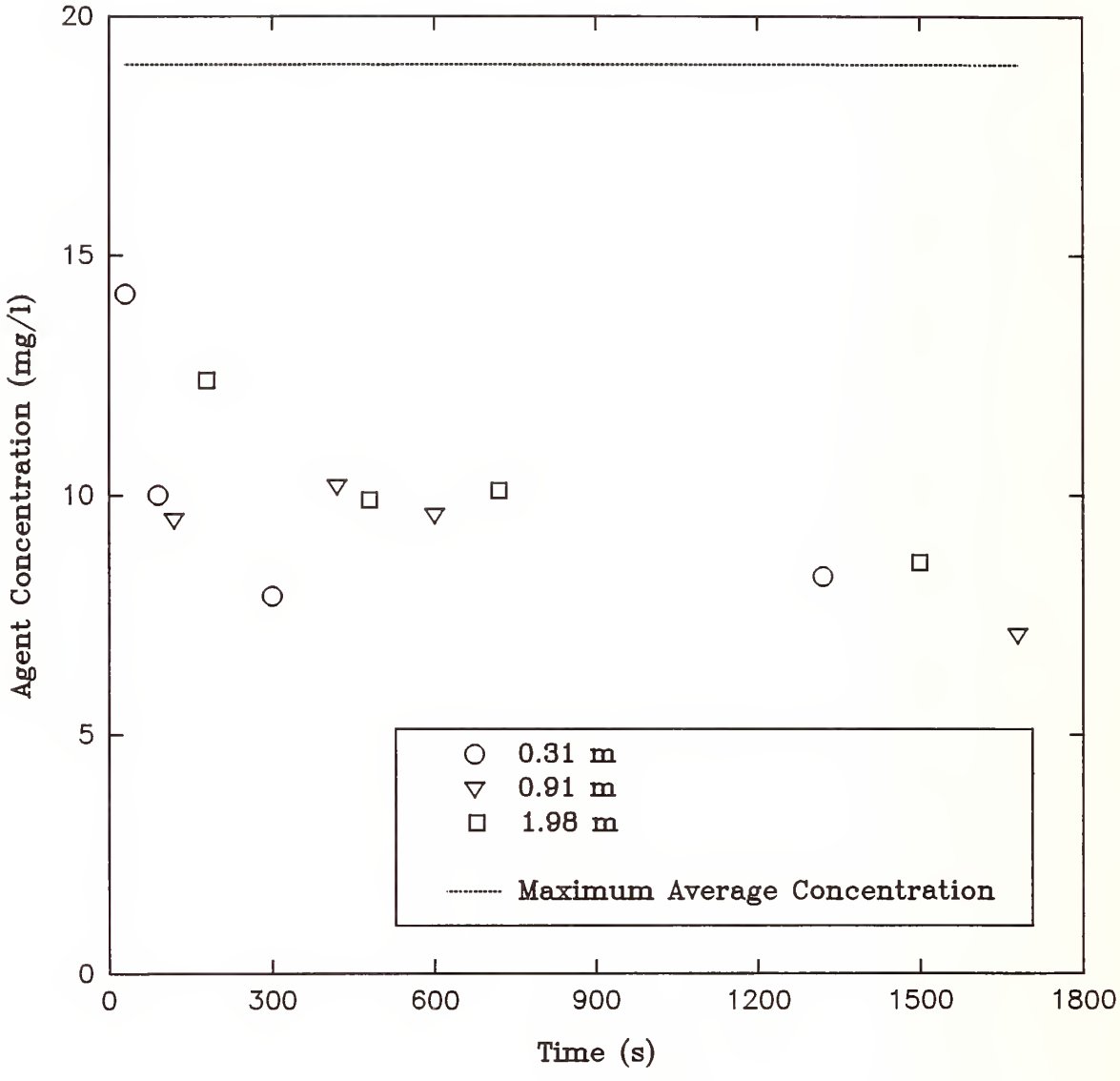

Figure 13. Agent concentration for halon 1301 test 1 as function of position and time with the maximum average concentration of agent shown (----) assuming uniform distribution within the compartment.

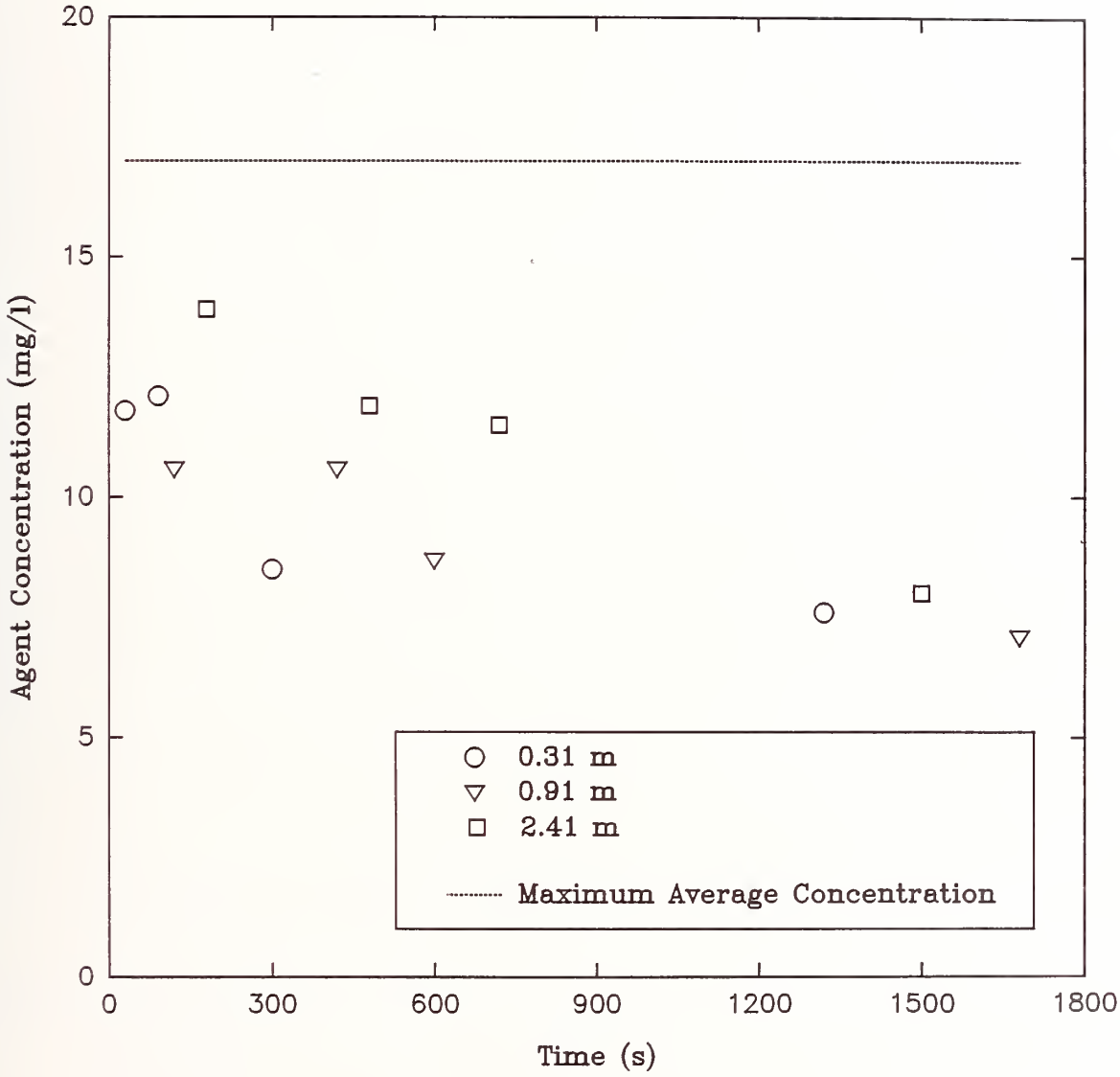

Figure 14. Agent concentration for halon 1301 test 2 as a function of position and time with the maximum average concentration of agent shown (----) assuming uniform distribution within the compartment.

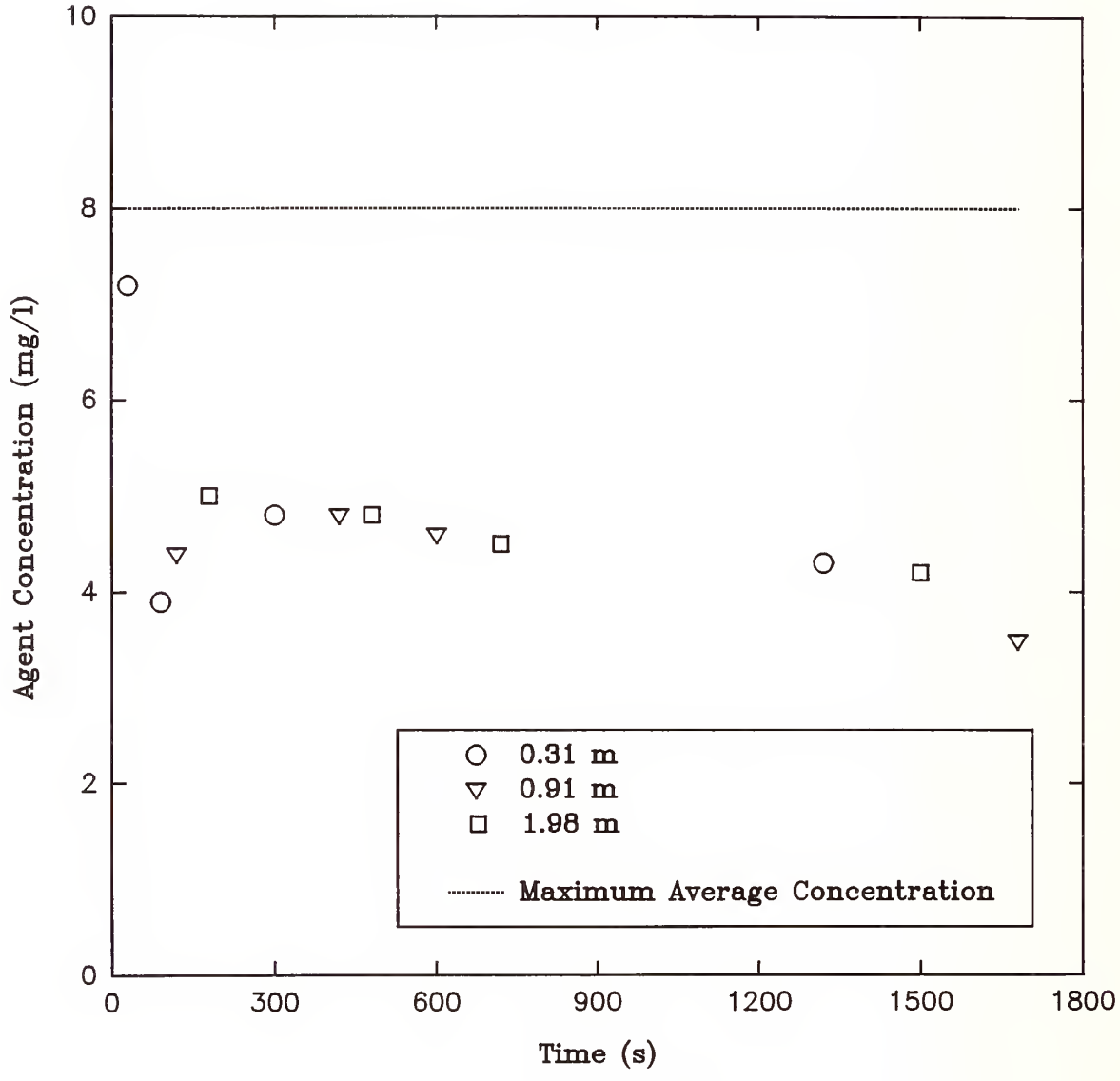

Figure 15. Agent concentration for HCFC-22 test 1 as a function of position and time with the maximum average concentration of agent shown (----) assuming uniform distribution within the compartment.

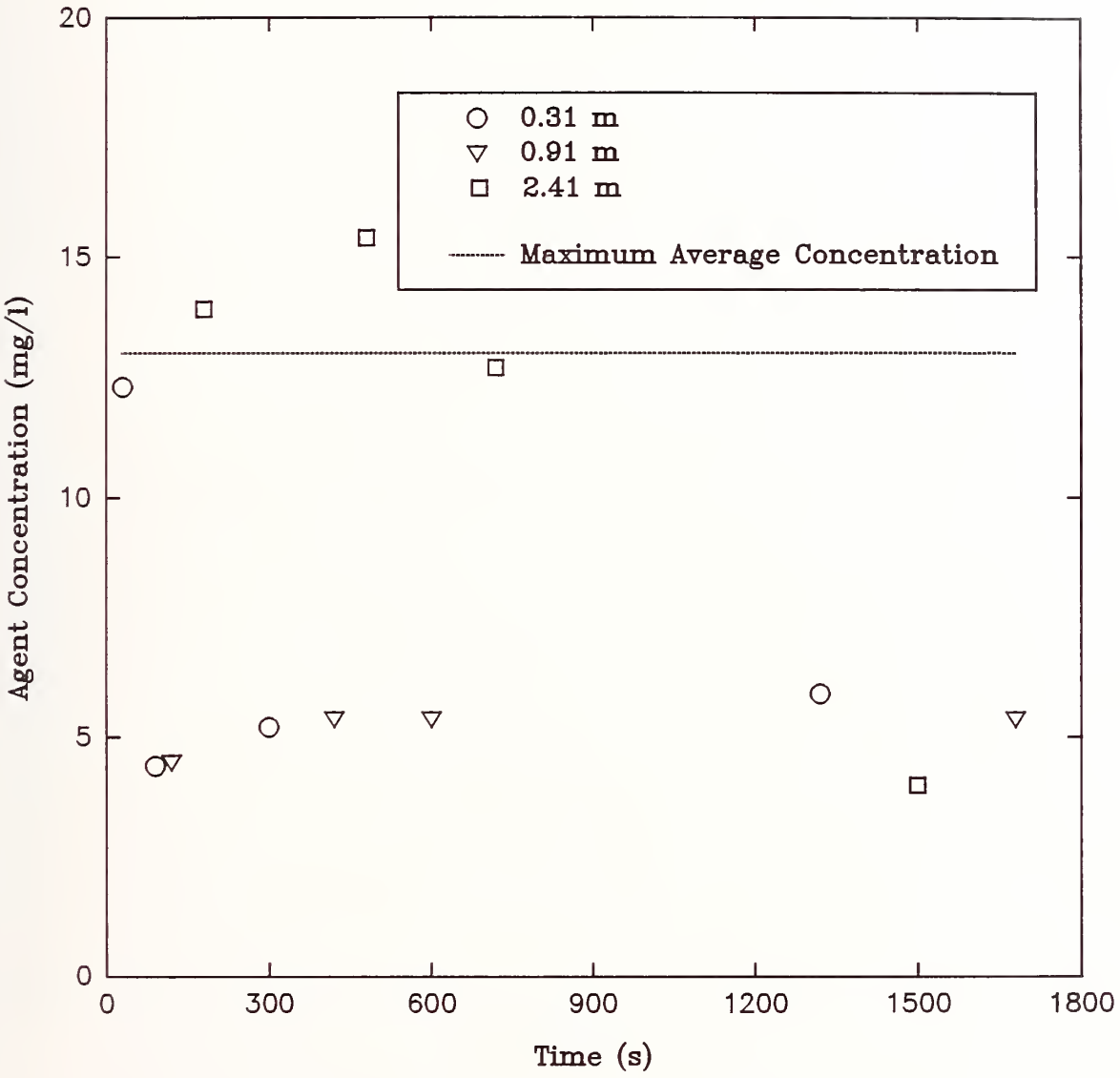

Figure 16. Agent concentration for HCFC-22 test 2 as a function of position and time with the maximum average concentration of agent shown (----) assuming uniform distribution within the compartment.

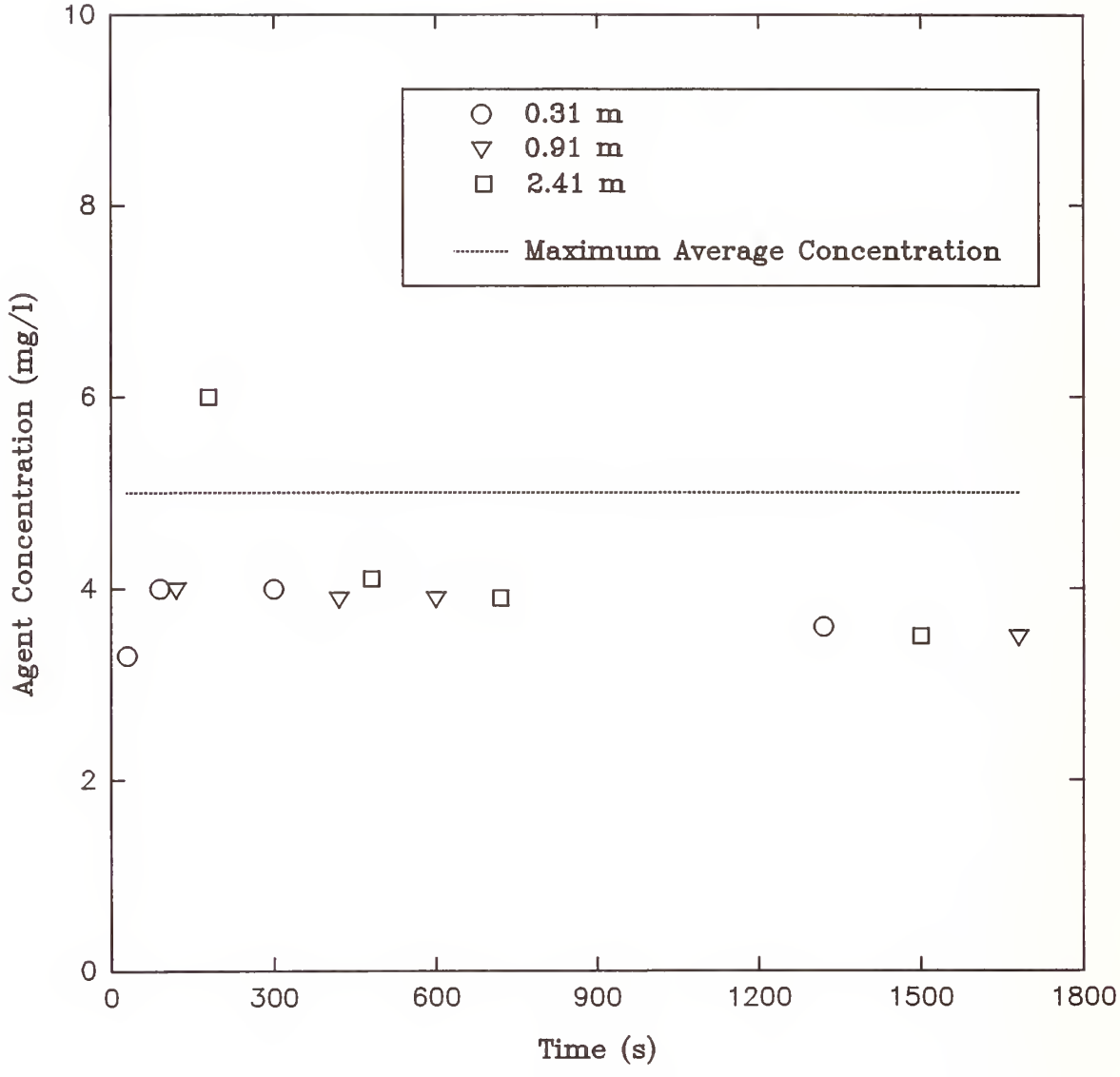

Figure 17. Agent concentration for agent HFC-227 as a function of position and time with the maximum average concentration of agent shown (----) assuming uniform distribution within the compartment.

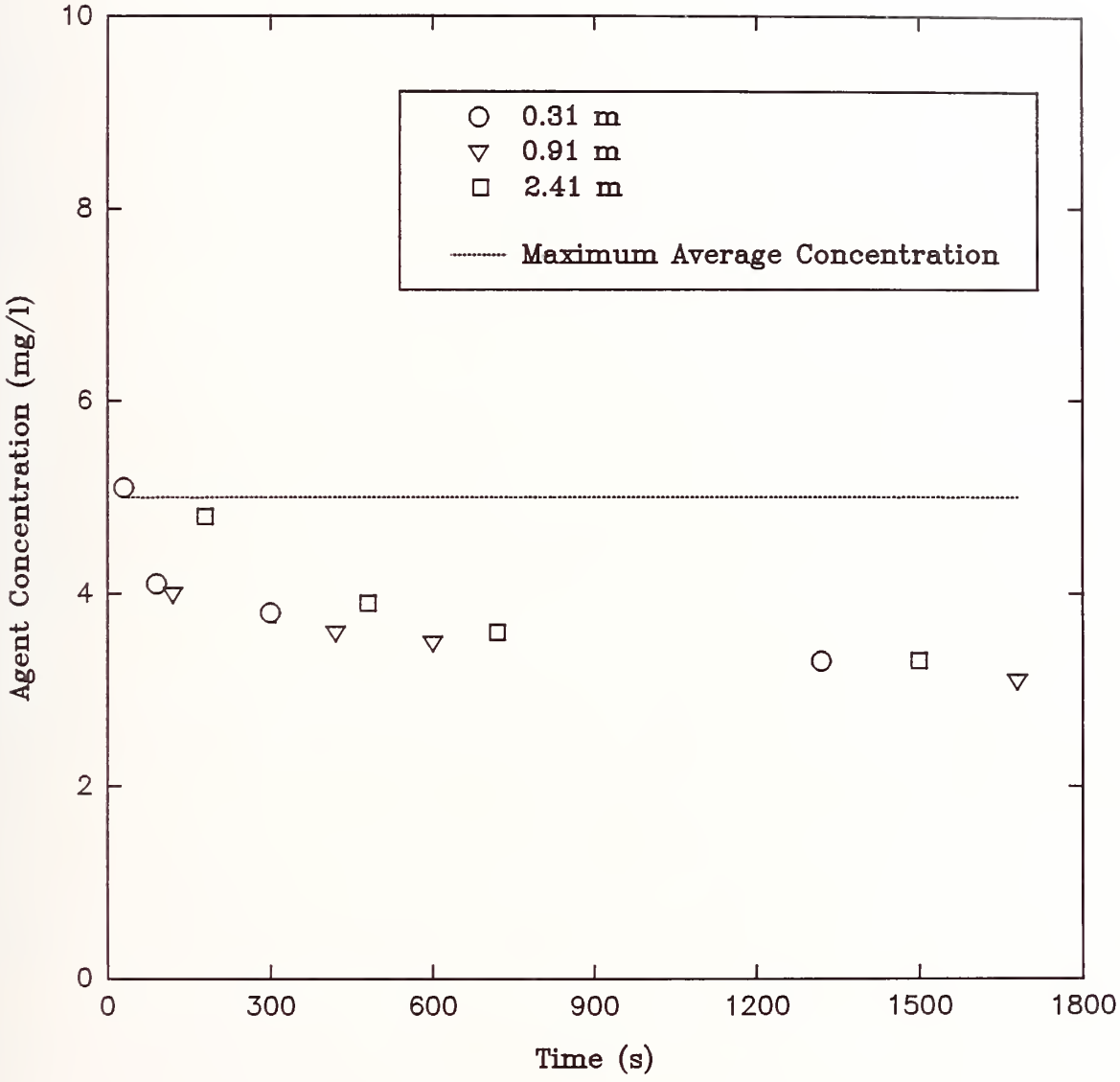

Figure 18. Agent concentration for agent HFC-32/125 as a function of position and time with the maximum average concentration of agent shown (----) assuming uniform distribution within the compartment.

However, once the turbulent action of the initial agent release had dissipated, further leakage would only affect the final compartment concentration and not the ultimate distribution of agent within the compartment.

Table 4 summarizes the average agent concentration for each release test, based on the average of the last sampling time period for the three locations (this represents a time period of 6 minutes) as well as the theoretical average concentration. The coefficient of variation, computed as the ratio of the standard deviation to the sample mean, for all tests was 3 to 19%. This was within the measurement variation of the GC analysis procedure. The data also shows that the final measured average agent concentration was always less than the theoretical average value. This could be due to (a) not all of the agent being released into the compartment (*i.e.*, residual agent remaining in cylinder after the discharge) or (b) leakage of agent from the compartment.

In general, the data show that the initial concentration in the compartment was below the expected average agent concentration assuming complete release of agent and that the concentration at a given level within the compartment decreased as a function of time. All the data indicate that an average steady-state concentration was reached within the 30 minute test period. Table 5 compares the final average agent concentration within the compartment with the 300 s agent concentration 0.31 m from the ceiling. The data show that the 300 s data was never more than 20.0% from the final compartment average agent concentration. In 4 out of 7 cases the 300 s data was less than 15% above the final average concentration. Within measurement errors, the data appear to indicate that a uniform agent distribution was developed within a short period of time (approximately 300 s).

In the 30 min duration of the experiments, it is not likely that significant amounts of agent would be left in the cylinders. Leakage from the compartment is likely, especially during the initial, high velocity release of the agent. The tests, however, indicate that computing the theoretical average concentration would represent a conservative estimate of occupant exposure conditions shortly after an accidental release of agent.

A comparison of the data for agent HCFC-22, Figures 15 and 16, shows how quickly agent concentrations can change at various levels in the test compartment. While the data for the two release tests show a dramatic difference for the first 600 s after agent release, the final measured average agent concentration did not significantly differ. This was probably due to a combination of convective mixing, diffusion, and compartment leakage.

Tests on halon 1301 (Figures 13 and 14) were also repeated to determine the effects of probe location on the measured agent concentrations. For the data in Figure 13, the lower probe was 1.98 m from the ceiling. For Figure 14, the lower probe was located 2.41 m from the ceiling (nearly at the floor). Unlike HCFC-22 agent release tests, which showed a short term stratification of agent, the halon 1301 tests showed no such stratification. There was no significant difference between the data at all levels between these two tests.

To further determine the time response of agent mixing and, therefore, concentration within the compartment, an open path FTIR was installed to measure the compartment atmospheric concentration of each agent at a specified level within the compartment. The results from the FTIR represent line-of-sight average values and are reported in Figures 19 to 22 as the integrated area of absorption peaks in the spectral data for each agent. These data present a finer time resolution on agent concentration than the evacuated flask data previously presented. Data for agent release tests involving halon 1301 and the second HCFC-22 test were lost because of instrumentation failures associated with the FTIR. However, the data presented does indicate that a significant amount of mixing occurs very rapidly after release of the agent. In all cases, an initial peak was detected, the magnitude of the peak

Table 4. Final agent concentration for 30 minute release test

Compound		Theoretical Average (mg/l)	Measured Average[a] (mg/l)	Final Instantaneous Value Specific Locations		
				Sample I,4 (mg/l)	Sample II,4 (mg/l)	Sample III,4 (mg/l)
FC-116		21.0	11.8 ± 1.2[c]	11.9	10.5	12.9
Halon 1301	1	19.0	8.0 ± 0.8	8.3	7.1	8.6
	2	17.0	7.6 ± 0.5	7.6	7.1	8.0
HCFC-22	1	8.0	4.0 ± 0.4	4.3	3.5	4.2
	2	13.0	5.1 ± 1.0	5.9	5.4	4.0
HFC-227		5.0	3.5 ± 0.1	3.6	3.5	3.5
HFC-32/HFC-125[b]		5.0	3.2 ± 0.1	3.3	3.1	3.3

[a] Average of last sampling flask at each location.
[b] Weighted average values listed for mixture.
[c] Standard deviation of three samples

Table 5. Comparison of final average agent concentration within the compartment to agent concentration at sample probe located 0.31 m from ceiling at 300 s

Compound		Final Average Concentration (mg/l)	Probe 0.31 m at 300 s (mg/l)	Difference (%)
FC-116		11.8	13.7	16.1
Halon 1301	1	8.0	7.9	-1.3
	2	7.6	8.5	11.8
HCFC-22	1	4.0	4.8	20.0
	2	5.1	5.2	2.0
HFC-227		3.5	4.0	14.3
HFC-32/HFC-125		3.2	3.8	18.7

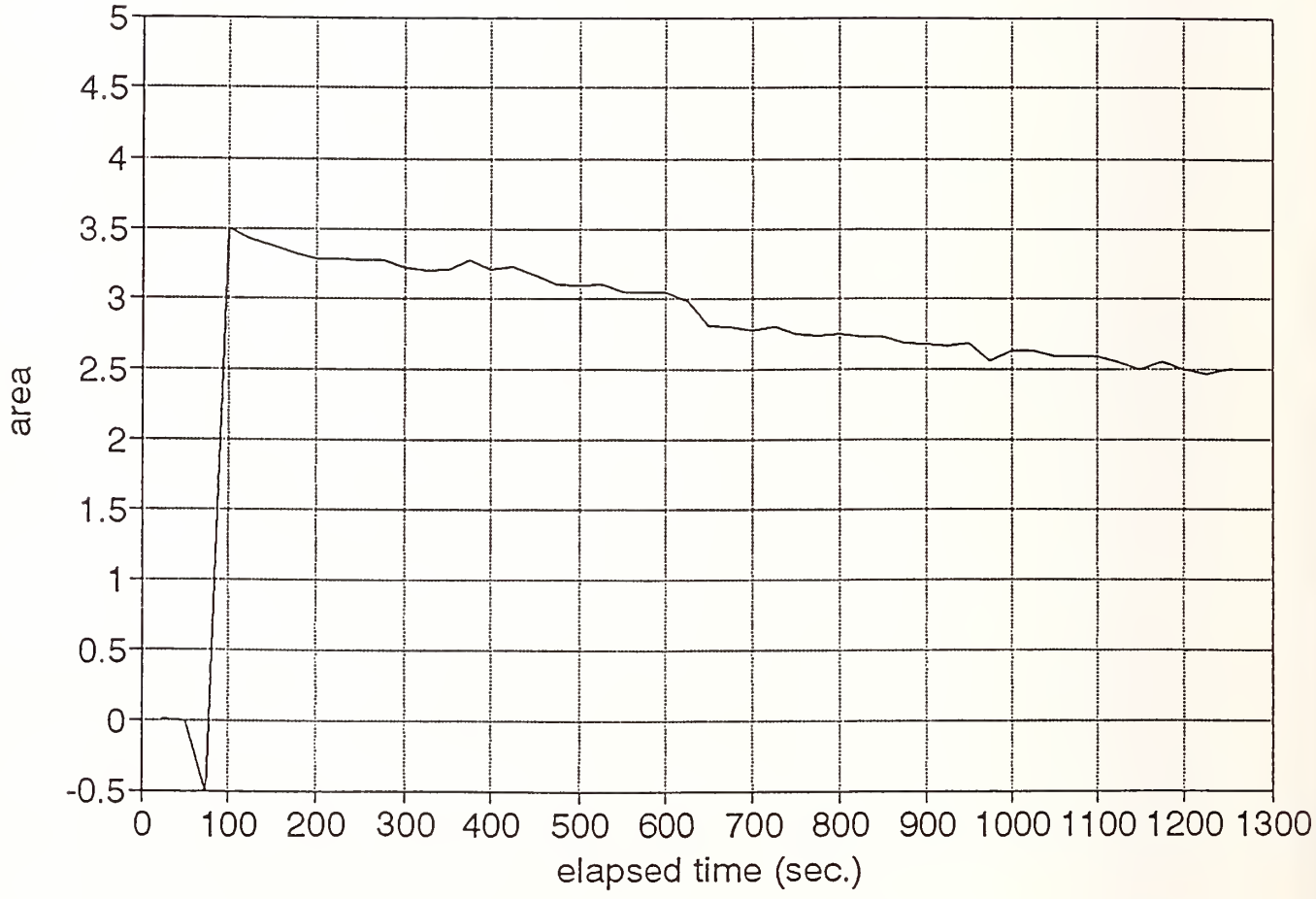

Figure 19. Time dependent agent concentration for agent FC-116 as measured by an open path FTIR located 0.3 m above and slightly off center of the exit tube with measurement beam diagonally across compartment.

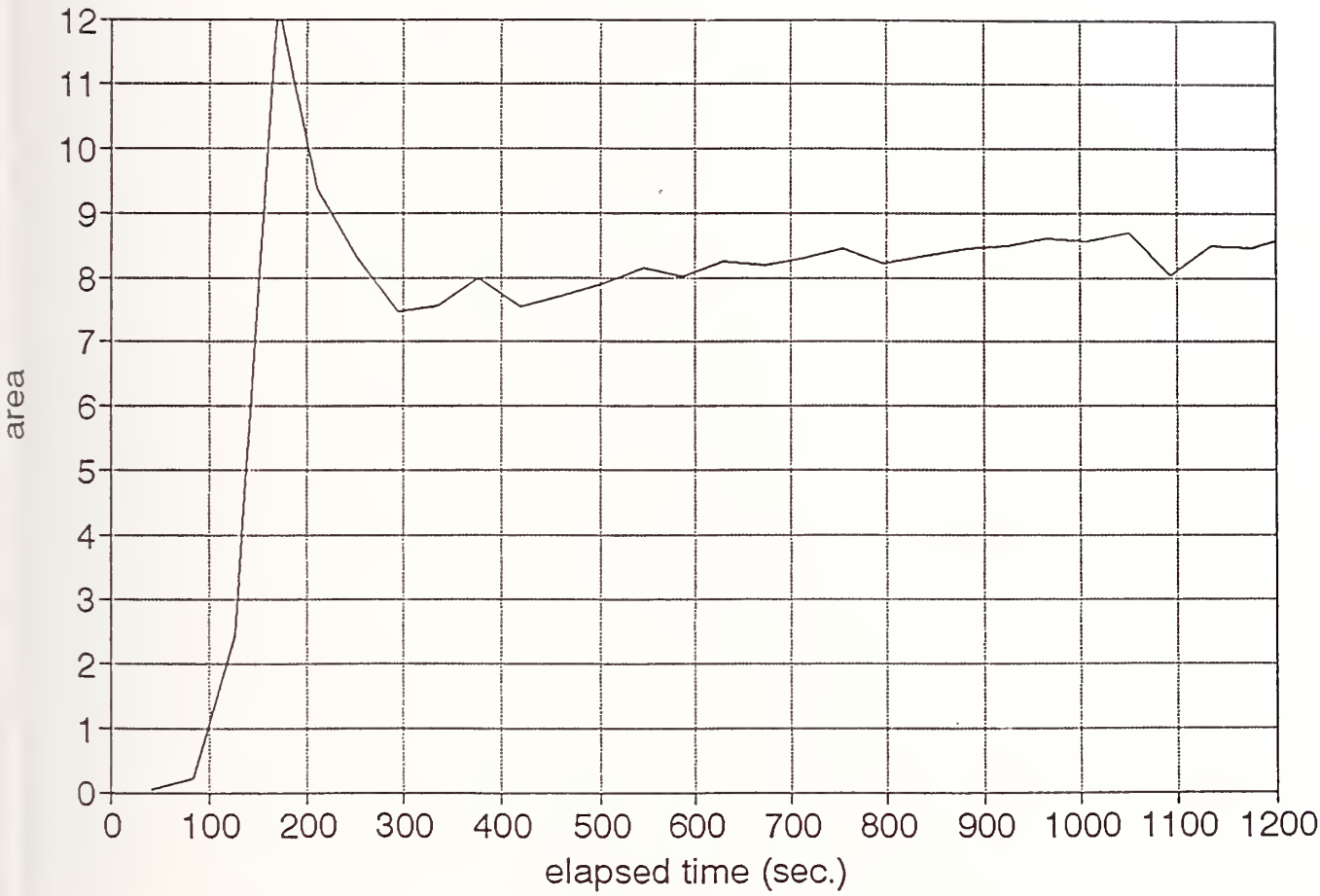

Figure 20. Time dependent agent concentration for agent HCFC-22 as measured by an open path FTIR located 0.3 m above and slightly off center of the exit tube with measurement beam diagonally across compartment.

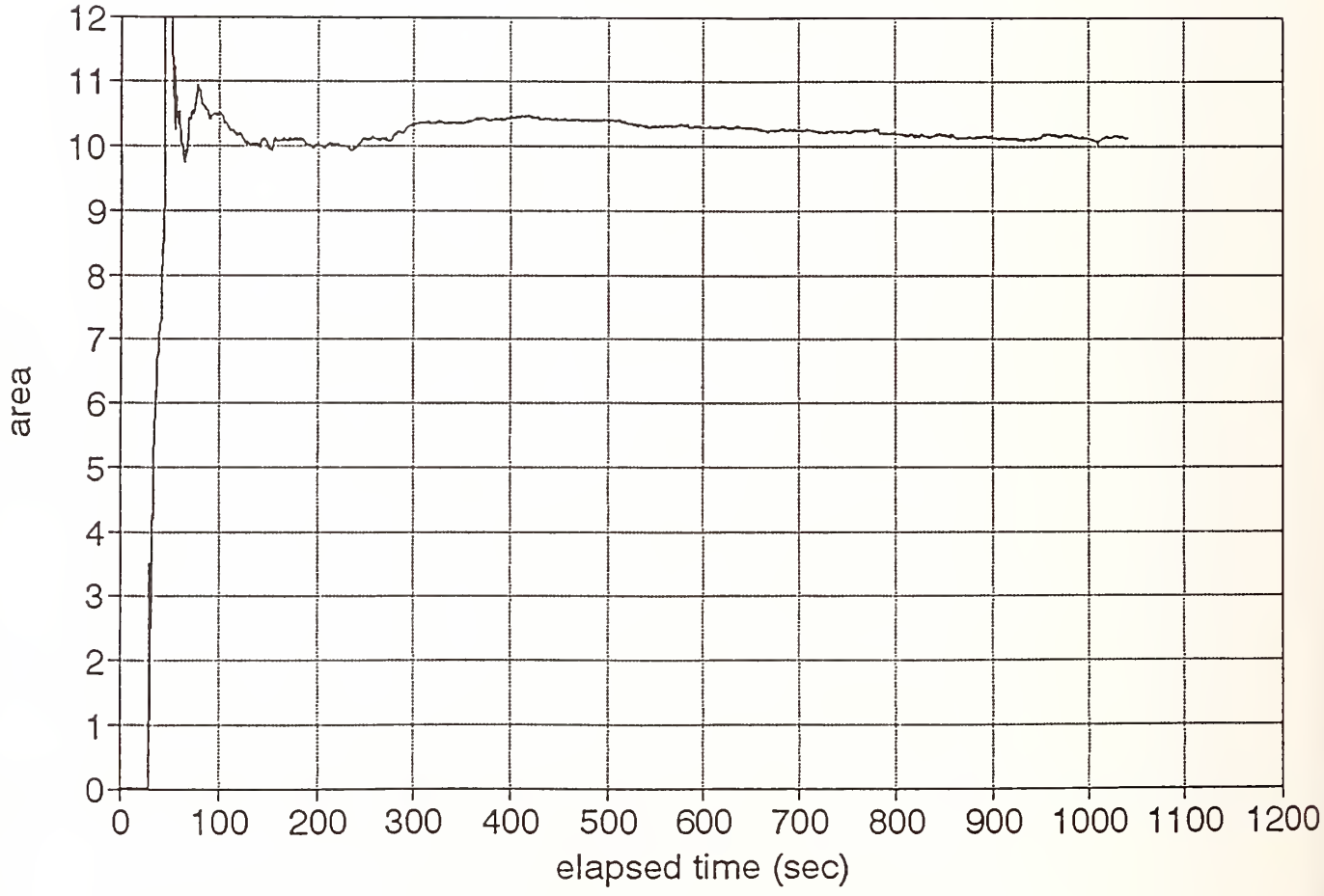

Figure 21. Time dependent agent concentration for agent HCFC-227 as measured by an open path FTIR located 0.3 m above and slightly off center of the exit tube with measurement beam diagonally across compartment.

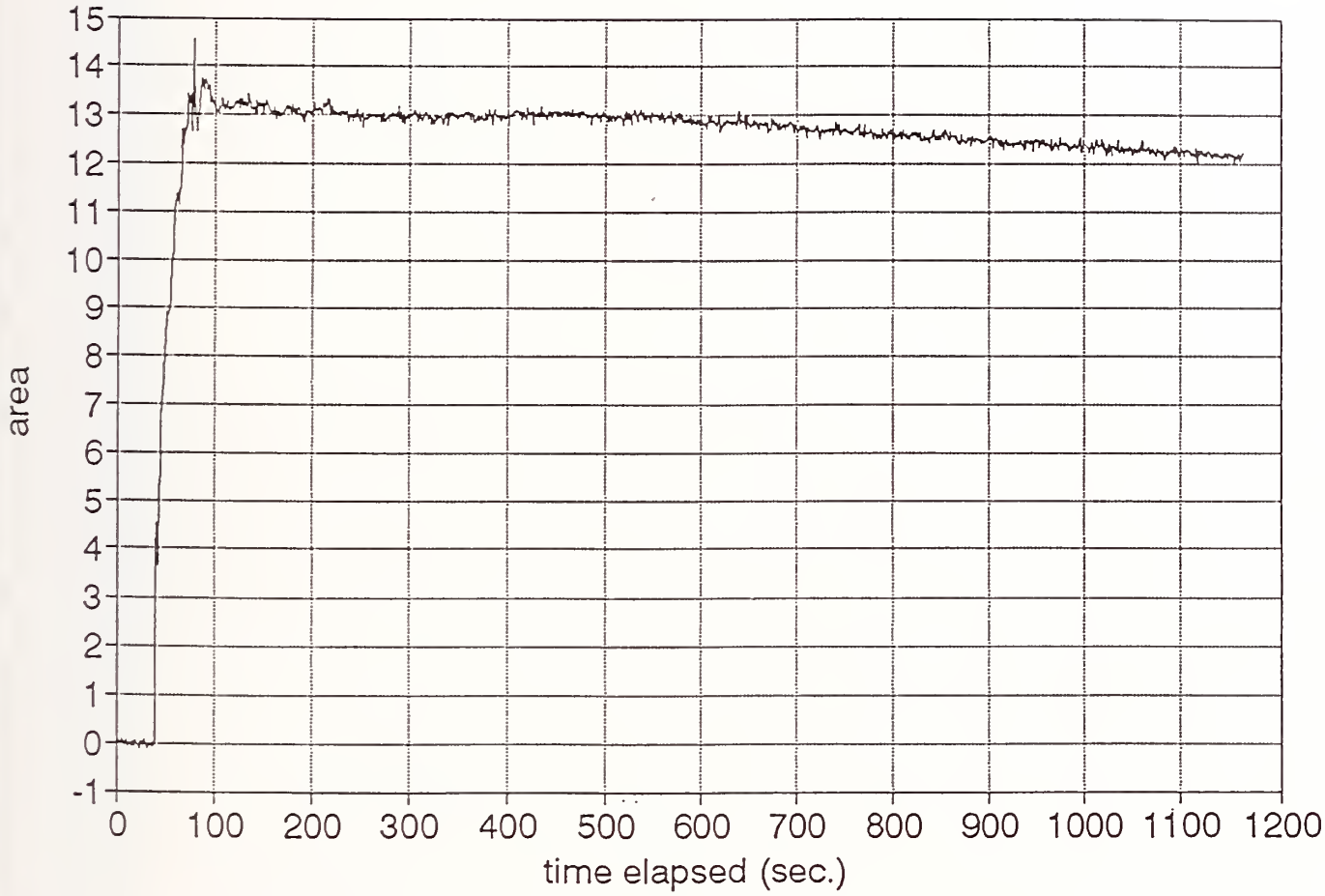

Figure 22. Time dependent agent concentration for agent FC-32/FC-125 as measured by an open path FTIR located 0.3 m above and slightly off center of the exit tube with measurement beam diagonally across compartment.

depending upon the actual position of the FTIR sampling beam relative to the release point, that quickly dissipated, within 60 s. The data for agents HCFC-22, Figure 20, and HCFC-227, Figure 21, show a relatively steady agent concentration after the dissipation of the initial peak. Figure 19, agent FC-116, shows a small initial peak, which may be due to a combination of scan average and short duration of the initial release for this agent, followed by a steady but small decline in agent concentration. These measurements were made with the FTIR beam located approximately 0.3 m above the release point traversing the diagonal of the compartment slightly off center of the exit tube. For agent HFC-32/HFC-125, Figure 22, the FTIR was placed such that the sampling beam traveled along the north wall approximately 0.35 m from the ceiling/wall junction. The data also show a steady but small decline in agent concentration after an initially small peak that lasted less than 60 seconds. Qualitatively, the FTIR data is in agreement with the evacuated flask data previously presented. At the location of the FTIR line-of-sight measurement, immediately after agent release, the agent concentration began to decay to a relatively steady state concentration. Since the FTIR instrument was not calibrated for agent concentration, only relative concentration numbers are reported. Therefore, the FTIR data is not directly comparable to the evacuated flask data. Nevertheless, the relative decay rates calculated from the data in figures 19 and 22, 8.5×10^{-4} and 1.0×10^{-3}, respectively, are within an order of magnitude of those determined by the evacuated flask measurements.

9.1.4 Modeling Results. In an effort to generalize the results of the full scale agent release tests discussed in the previous section, various modeling techniques ranging from an analysis of agent diffusion characteristics to performing 3-D fluid flow calculations using Harwell-Flow3d (CFD 1990) were employed to model the dispersal behavior of halon alternatives escaping from a pressurized storage container into a closed compartment. Techniques for determining diffusion coefficients are available in the literature (Bennett and Myers, 1974). These techniques were used to describe agent diffusion characteristics as a function of temperature and molecular weight. The modeling technique used to simulate agent dispersion in a compartment is to divide the enclosure into a collection of small rectangular boxes or control volumes. Harwell-Flow3d is a member of a class of computer models known as field models that perform this operation. The conditions in each control volume are initially ambient. Agent is then released in several control volumes over time. The resulting flow or exchange of mass, momentum and energy between control volumes is determined so that these three quantities are conserved. The momentum conservation equations are equivalent to Newton's second law of motion and are referred to as the Navier-Stokes equations. The energy conservation equation is equivalent to the first law of thermodynamics. These fluid flow equations are expressed mathematically as a set of simultaneous, non-linear partial differential equations. After being discretized, the resulting finite volume equations are solved iteratively using a variant of Newton's method for computing coupled non-linear algebraic equations. Details of the fluid flow are realized by performing these calculations for each control volume throughout the compartment.

Two main factors affect the dispersion of an agent release within a compartment, **convection** caused by high gas velocities at the exit hole of the pressurized bottle and **molecular diffusion**. These velocities were predicted by Harwell-Flow3d to decrease to a negligible size soon after the bottle had finished evacuating. Figures 23 and 24 show shaded velocity contours in a vertical plane of the bottle evacuation at the end of the bottle evacuation and 65 seconds later. Note how the velocity contours in Figure 24 are small compared to the ones in Figure 23. This was also observed experimentally. Therefore, the significant dispersion occurs during the initial agent release, with diffusion controlling further dispersion.

Bennett and Myers (1974) outline a procedure for determining the diffusion coefficient for a binary mixture (air and the halon alternative in this case) given the temperature, and molecular

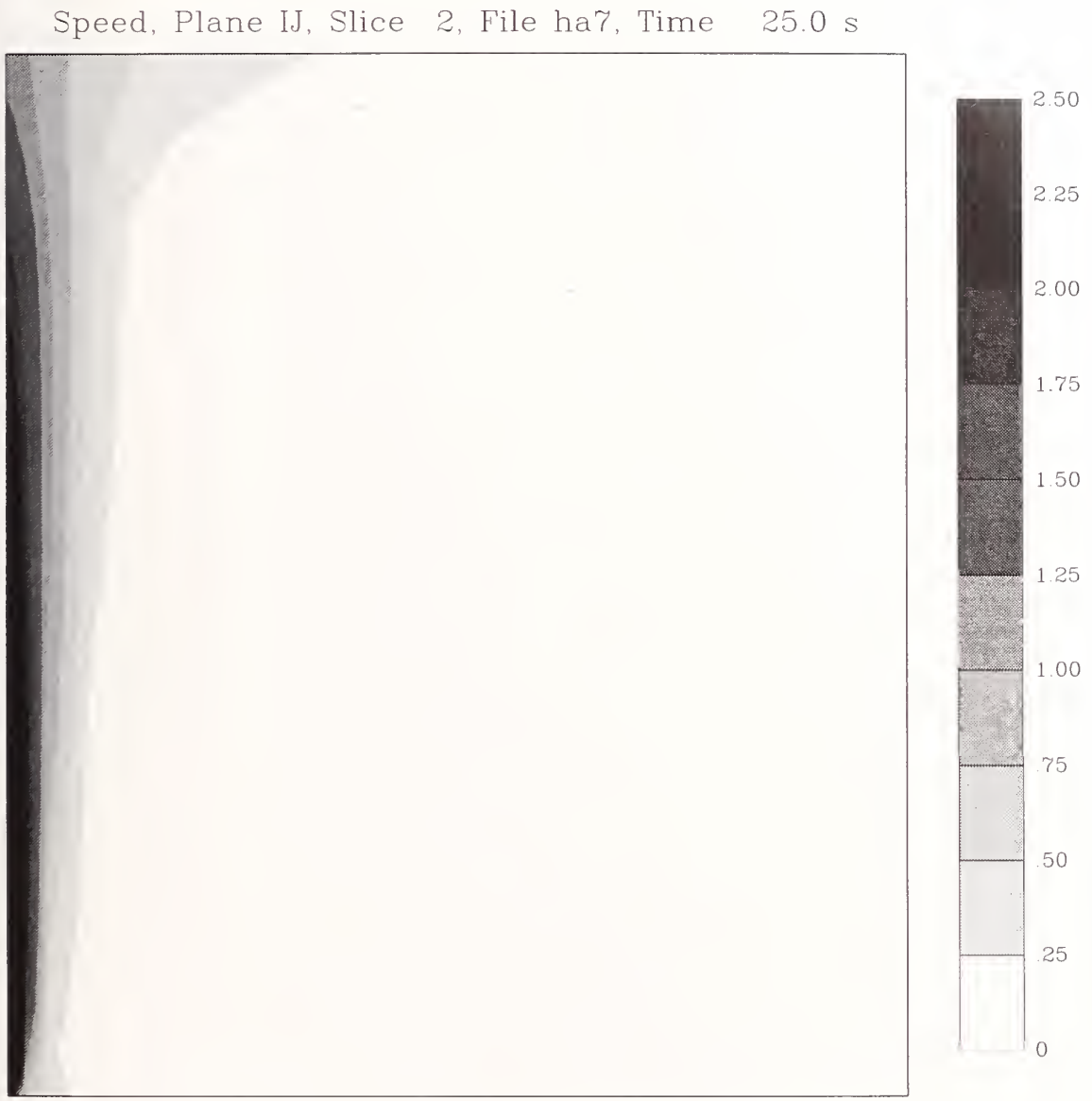

Figure 23. Velocity magnitude shaded contours 25 seconds after discharge has begun in an ASTM standard room.

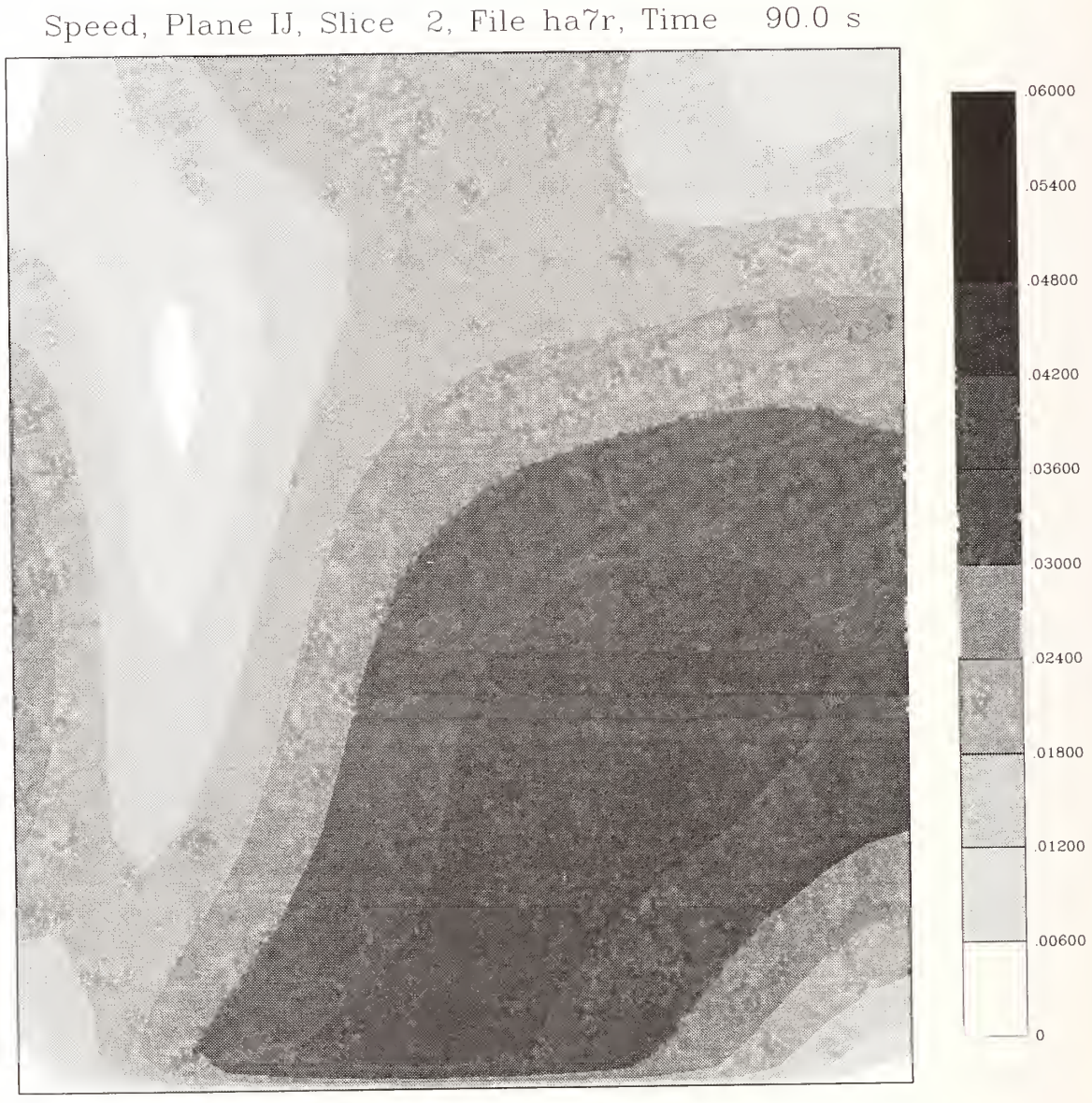

Figure 24. Velocity magnitude shaded contours 90 seconds after discharge has begun in an ASTM standard room.

weights of the two gasses. Incorpera and De Witt (1990) list diffusion coefficients for various gases in air ranging from 0.62×10^{-5} m^2/s for naphthalene, $C_{10}H_{10}$, (molecular weight of 132) to 0.16×10^{-4} m^2/s for CO_2 (molecular weight of 46). Since the molecular weights of halon alternatives range from 50 to 240 it is expected that the diffusivity of a halon alternative would be close to this range of 0.62×10^{-5} m^2/s to 0.16×10^{-4} m^2/s. A value of 7.2×10^{-5} was used in the field modeling studies in this report. The distance x that a gas diffuses (assuming the gas is free to diffuse in three dimensions) in $t=600$ seconds for diffusion coefficient within this range can be estimated using the formula $\Delta x = \sqrt{6D\Delta t}$ to be from 0.15 m to 0.24 m. This is a fraction of the room dimensions. Thus, for a quiescent compartment, steady conditions should be reached quickly, with slow changes thereafter. This is consistent with experimentally observed results.

Two scenarios were modeled using Harwell-Flow3d. Both scenarios involved a storage bottle vented upwards in the center of a compartment with dimensions 2.4 m x 3.4 m x 2.4 m. The compartment in both scenarios contained a small leak. In the first scenario, the room was free of obstructions. In the second scenario, the compartment contained two solid baffles in order to partially block the initial flow from the pressurized bottle. Figures 25 and 26 illustrate the results of the simulation after the initial release from the bottle. For the compartment without blockages, the dispersion is relatively uniform throughout. This is consistent with the results from the experimental observations. For the room with blockages, the initial flow is restricted resulting in a more concentrated region contained within the space between the storage bottle and the first baffle. This shows that, for storage areas with exposed structural members along the ceiling or for high bay rack storage areas, vertical obstructions can result in much higher agent concentrations than would normally be anticipated based the total compartment volume. Care must therefore be exercised in the placement and storage of large quantities of any agent.

9.1.5 Exposure Limits. The preceding sections indicate that dispersion of these chemicals throughout an unobstructed volume is relatively rapid. Should an accidental discharge occur, the threat to any trapped people would be determined by the toxicity of the fluid. Table 6 presents recommended chronic and acute limits, as available, for the 12 agents. These provide working guidelines (rather than definitive exposure limits) for safe exposures. For many of the agents, little data is available. For each agent, the CAS number provides unique identification of the chemical and much of the material safety data sheet (MSDS) information is summarized in Table 6. In addition, information on human exposure to the agents is included, to the extent such information is available. This information falls in basically four categories: acute exposure (effects of short-term, usually high-level exposure to the chemical), chronic exposure (long-term low-level exposure to the chemical), contact exposure (effects of exposure to the skin or eyes), and carcinogenicity.

For exposure during an accidental release, acute exposure effects are most important. These effects are most often reported by an LC_{50} value. This is the level which caused 50% of the test animals in a given experiment to die during and/or after the stated exposure. In all cases where the toxicity information is known, the levels which cause lethal effects are high (greater than 24 %). However, information for most of the agents is not known. Thus, more information will be required for those agents chosen for further study to place the results in appropriate context.

Chronic exposure data are typically used to determine maximum allowable exposure for workers exposed to chemicals over long periods of time. These limits are established by the Occupational Safety and Health Administration (OSHA), American Conference of Governmental Industrial Hygienists (ACGIH), or National Institute of Occupational Safety and Health (NIOSH). Chronic exposure limits are typically reported by time-weighted averages of maximum allowable concentrations over an 8 hour workday or 40 hour work week.

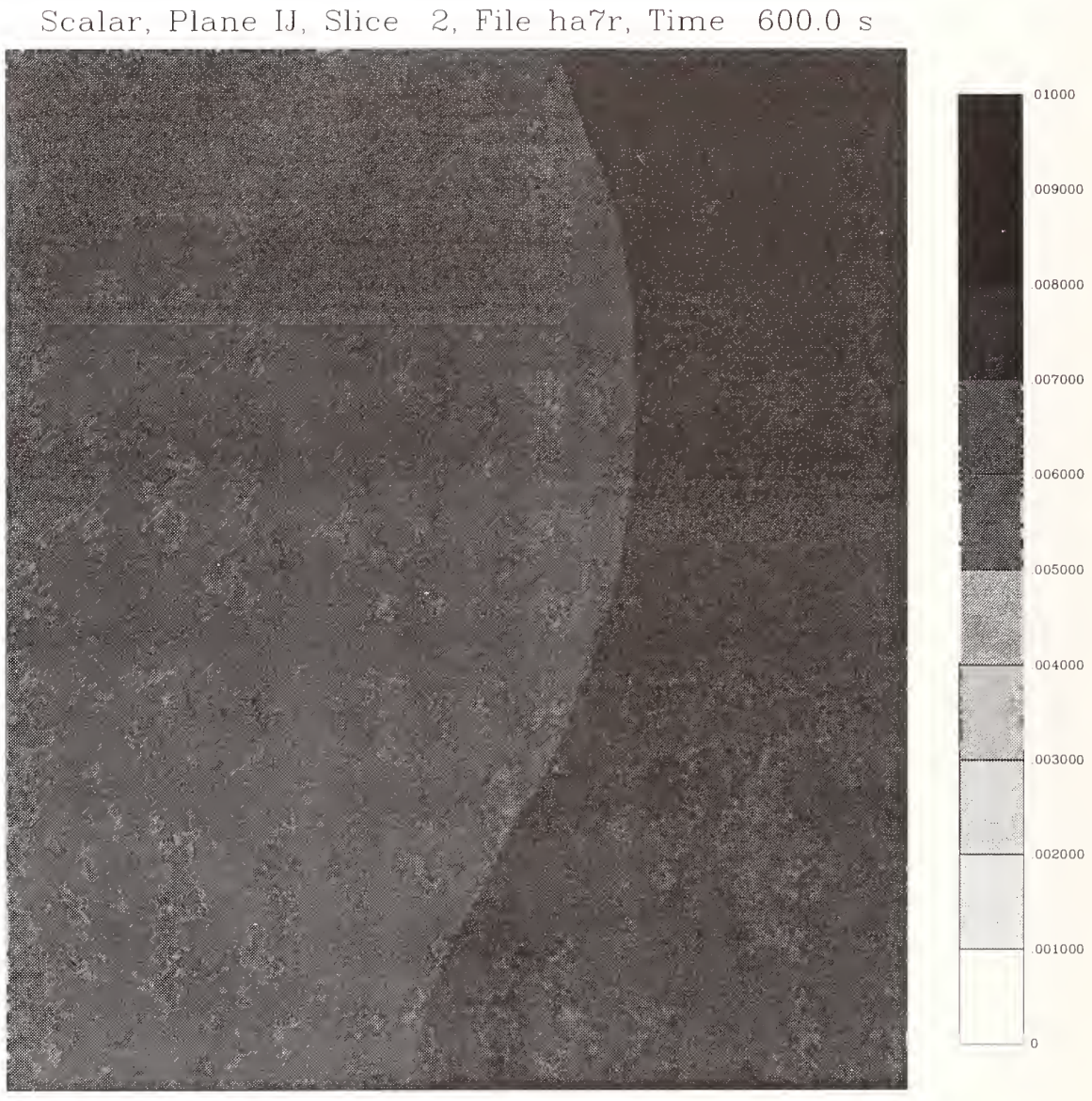

Figure 25. Mass fraction shaded contours 600 seconds after discharge has begun (570 seconds after pressurized bottle has finished evacuating) in an ASTM standard room.

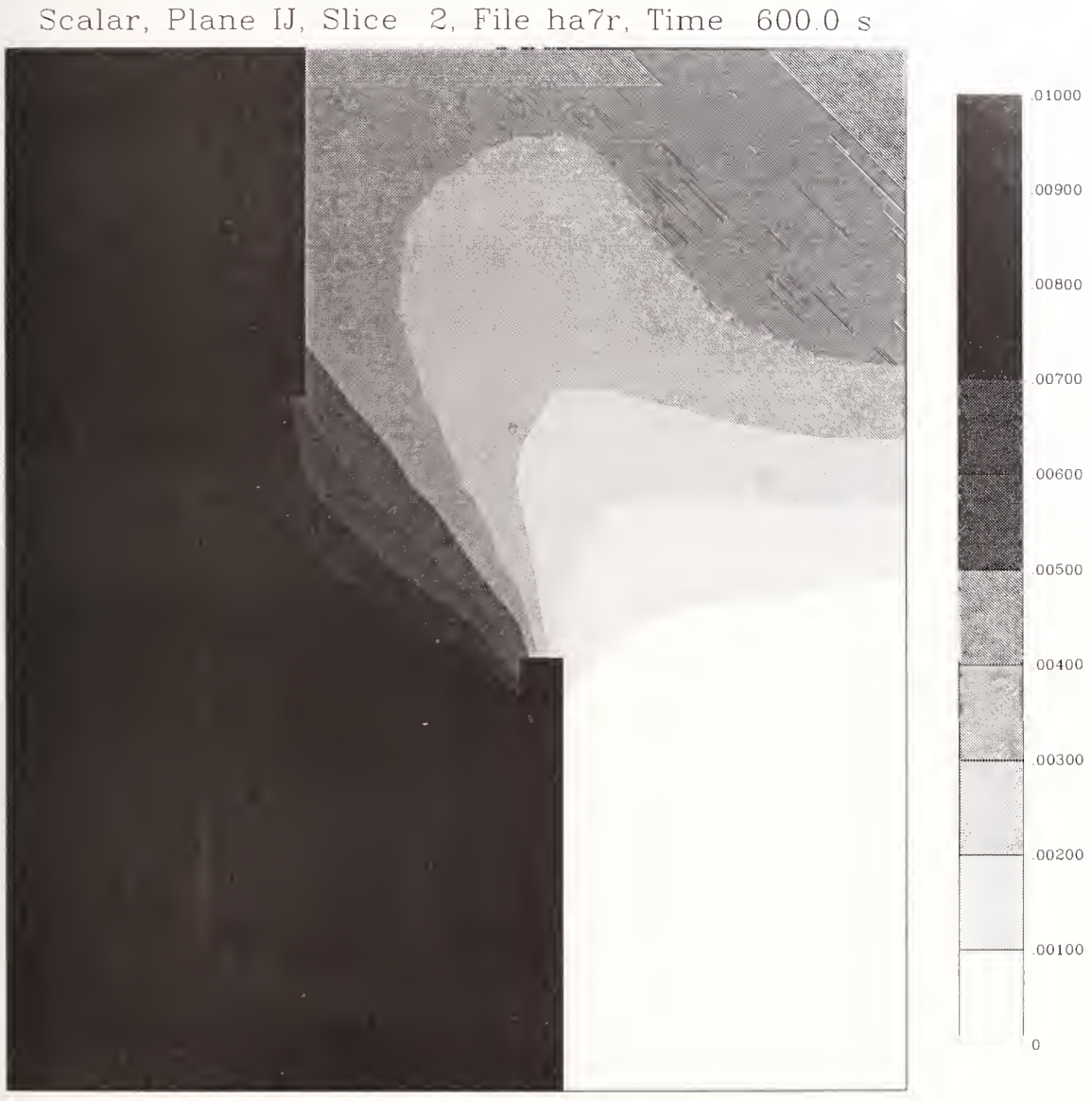

Figure 26. Mass fraction shaded contours 600 seconds after discharge has begun (570 seconds after pressurized bottle has finished evacuating) in an ASTM standard room containing baffles that restrict flow.

Table 6. Available Toxicity Information for Candidate Replacement Agents

Agent HFC-32

CAS #	MSDS	Exposure	Toxicity Information
75-10-5	yes 9/91	Acute	No limits established by OSHA[a], ACGIH[b], or NIOSH[c]. Freons in high concentration may cause pulmonary irritation, narcosis, dizziness, incoordination, confusion, nausea, vomiting, tremors, and rarely, coma. When oxygen deficiency has been corrected, these effects appear to reverse.
		Chronic	No limits established by OSHA[a], ACGIH[b], or NIOSH[c].
		Contact	Skin: No adverse effects reported. Due to rapid evaporation, frostbite with redness, tingling, pain and numbness may occur. Skin may become hard and white and develop blisters.
			Eyes: No adverse effects reported. Due to rapid evaporation, frostbite with redness, pain and blurred vision may occur.
		Carcinogenicity	No data available

a OSHA = Occupational Safety and Health Administration
b ACGIH = American Conference of Governmental Industrial Hygienists.
c NIOSH = National Institute of Occupational Safety and Health

Agent HFC-32/HFC-125

CAS #	MSDS	Exposure	Toxicity Information
75-10-5 354-33-6	yes 9/91 4/89		See above for HFC-32 See below for HFC-125

Agent HFC-227

CAS #	MSDS	Exposure	Toxicity Information
431-89-0	yes 9/90	Acute	No limits established by OSHA, ACGIH, or NIOSH. The toxicological properties of this material have not been determined. Preliminary testing indicates the acute inhalation LC_{50} in rats is greater than 241,000 ppm, 4 hour LC_{50} is greater than 800,000. Stimulants such as epinephrine may induce ventricular fibrillation.
		Chronic	No limits established by OSHA, ACGIH, or NIOSH.
		Contact	Skin: No data available
			Eyes: No data available
		Carcinogenicity	No data available

Table 6. (continued) Available Toxicity Information for Candidate Replacement Agents

Agent HCFC-22

CAS #	MSDS	Exposure	Toxicity Information
75-45-6	yes 10/91	Acute	Relatively non-toxic by inhalation.. Rat LC_{50}: 350,000 ppm (15 min), Mouse LC_{50}: 280,000 ppm (30 min), Dog LC_{50}: 700,000 ppm. Central nervous system depressant, simple asphyxiant. Stimulants such as epinephrine may induce ventricular fibrillation.
		Chronic	1000 ppm (3540 mg/m^3) = OSHA TWA[d], ACGIH TWA, and NIOSH recommended TWA. 1250 ppm (4375 mg/m^3) NIOSH recommended STEL[e]. 500 ppm (1770 mg/m^3) DFG MAK[f] TWA. 1000 ppm (3540 mg/m^3) DFG MAK 60 min peak, momentary value, 3 times/shift.
		Contact	Skin: No adverse effects reported due to the gas. The liquid may cause frostbite; skin could turn red, tingle, and may become hard and white and develop blisters. Pain and numbness may develop.
			Eyes: No adverse effects have been reported from the gas. Due to rapid evaporation, the liquid may cause frostbite with redness, pain and blurred vision.
		Carcinogenicity	No information for humans. Male rats had increased incidences of fibrosarcomas and zymbal-gland tumors. Not found in females.

[d] TWA Time Weighted Average: Time-weighted average concentration for a normal 8 hour workday or 40 hour work week.

[e] STEL Short Term Exposure Limit: 15 min time weighted average exposure which should not be exceeded at any time during a work day even if the 8 hour time weighted average is within established threshold limit value. Exposures at the STEL should not be longer than 15 min and should not be repeated more than 4 times per day with at least 60 min between successive exposures at the STEL.

[f] DFG MAK Maximum concentration values in the work place from the Federal Republic of Germany.

Table 6. (continued) Available Toxicity Information for Candidate Replacement Agents

Agent HFC-134a

CAS #	MSDS	Exposure	Toxicity Information
811-97-2	yes 11/91	Acute	Presently available data are indicative of a low order of toxicity. Nonflammable gas with low water solubility and low chemical reactivity.. LC_{50}(4 hr), rat, >500,000 ppm. Acute symptoms are indicative of central nervous system depression with anesthetic effects induced at sub-lethal levels. The cardiac sensitizing potential is very low (threshold - 75,000 ppm in dogs).
		Chronic	rats, 6 h/day, 5 days/week, 90 days, NOEL = 50,000 ppm.
		Contact	Skin No data available
			Eyes No data available
		Carcinogenicity	rats, one year study, oral doses of 300 mg/kg body weight (in corn oil). After 125 weeks, no carcinogenic potential found.

a NOEL No Observable Effect Level.

Agent FC-116

CAS #	MSDS	Exposure	Toxicity Information
76-16-4	yes 5/92	Acute	No limiting data available. Simple asphyxiant, Inhalation of high concentrations may cause disorientation and narcosis.
		Chronic	No limits established by OSHA, ACGIH, or NIOSH.
		Contact	Skin No adverse effects reported. due to rapid evaporation, liquid may cause frostbite with redness, tingling and pain or numbness. Severe exposures: skin can become hard and white and develop blisters.
			Eyes No adverse effects reported. Due to rapid evaporation, liquid may cause frostbite with redness, pain and blurred vision.
		Carcinogenicity	No data available

Table 6. (continued) Available Toxicity Information for Candidate Replacement Agents

Agent HCFC-124

CAS #	MSDS	Exposure	Toxicity Information
2837-89-0	yes 7/91	Acute	Very low acute toxicity. Moderate cardiac sensitizer for dogs exposed to 25,000 ppm plus given epinephrine. In a two week subchronic inhalation study, 100,000 ppm caused mild anesthesia in rats, but recovery occurred in 15 min. Guinea pigs exposed for 30 min, one hour, and two hours at concentration ranging from 9000 to 207,000 ppm had no deaths. Anesthetic effects occurred at concentrations greater than 47,000 ppm, but the guinea pigs recovered following the exposure. High concentrations may cause heart irregularities, unconsciousness or death. Vapors decrease oxygen availability. Frostbite could occur from liquid exposure. The effects in animals from a single exposure by inhalation include central nervous system effects, anesthesia and decreased blood pressure. Repeated exposures increased liver weights, and caused anesthetic effects, irregular respiration, poor coordination, and nonspecific effects such as decreased body weight. However, histopathological evaluation showed no irreversible effects.
		Chronic	No limits established by OSHA, ACGIH, or NIOSH.
		Contact	Skin No data available
			Eyes No data available
		Carcinogenicity	An impurity in FC-124, FC-133a, has been shown to be a potential carcinogen in one published study.

Agent HFC-125

CAS #	MSDS	Exposure	Toxicity Information
354-33-6	yes 4/89	Acute	Not determined. Exposure may be harmful and could cause frostbite. Vapors can cause headache, nausea, giddiness, unconsciousness.
		Chronic	No limits established by OSHA, ACGIH, or NIOSH.
		Contact	Skin No data available
			Eyes No data available
		Carcinogenicity	No data available

Table 6. (continued) Available Toxicity Information for Candidate Replacement Agents

Agent FC-218

CAS #	MSDS	Exposure	Toxicity Information
76-19-7	yes 10/91	Acute	No limits established by OSHA, ACGIH, or NIOSH. Asphyxia may occur with symptoms such as headache, dizziness, incoordination, dyspnea on mild exertion, sweating, malaise, tremors, convulsive movements, irregular breathing and death.
		Chronic	No limits established by OSHA, ACGIH, or NIOSH.
		Contact	Skin No data available
			Eyes No data available
		Carcinogenicity	No data available

Agent FC-31-10

CAS #	MSDS	Exposure	Toxicity Information
355-25-9	yes 7/92	Acute	The toxicity of this material has not been determined. May be harmful if inhaled, ingested or by skin absorption.
		Chronic	No limits established by OSHA, ACGIH, or NIOSH.
		Contact	Skin No data available
			Eyes No data available
		Carcinogenicity	No data available

Agent FC-318

CAS #	MSDS	Exposure	Toxicity Information
115-25-3	yes 6/92	Acute	No limits established by OSHA, ACGIH, or NIOSH. Simple asphyxiant. Stimulants such as epinephrine may induce ventricular fibrillation.
		Chronic	No limits established by OSHA, ACGIH, or NIOSH.
		Contact	Skin No adverse effects reported. The liquid could cause frostbite accompanied by redness, tingling, pain or numbness. The skin may harden and turn white and develop blisters.
			Eyes No adverse effects from gas. The liquid could cause frostbite accompanied by redness, pain and blurred vision.
		Carcinogenicity	No data available

Table 6. (continued) Available Toxicity Information for Candidate Replacement Agents

Agent CF_3I

CAS #	MSDS	Exposure	Toxicity Information
2314-97-8	yes 8/90	Acute	The toxicity of this material has not been determined. May have adverse effects if inhaled, ingested or absorbed by the skin.
		Chronic	No limits established by OSHA, ACGIH, or NIOSH.
		Contact	Skin Exposed skin may show signs of frostbite.
			Eyes No data available
		Carcinogenicity	No data available

Table 6 will be updated over the next two years as new information becomes available. A final version will appear in the September, 1995 final report.

9.2 Environmental Requirements for Candidate Replacements for Halon 1301

In addition to being effective in extinguishing fires, a replacement for halon 1301 must not cause greater damage to human health and the environment. Environmental issues include ozone depletion, global warming, water and air pollution. Health and safety effects include acute toxicity from an accidental release (some presented in Section 9.1, above), long term carcinogenic effects from repeated exposures, and fires resulting from the flammability of the chemical.

The U.S. Environmental Protection Agency has established the Significant New Alternative Policy Program (SNAP) under Section 612 of the Clean Air Act to evaluate alternative substances to ozone-depleting chemicals. The program includes a wide range of applications including fire and explosion protection agents, which is the application of interest for this report. The SNAP Program requires a manufacturer to provide specific information in order for EPA to determine the suitability of the agent as a replacement for halon 1301. The information includes not only the environmental/safety parameters but also information pertaining to the amount of substance that would be released and the practicality of using the replacement chemical in terms of availability, cost, and amount required relative to halon 1301. In addition the relevant physical properties of the replacement compound must be included.

Here we consider each of the candidate replacements chemicals relative to the SNAP protocol. We also consider halon 1301 as a reference point and N_2 as a neutral chemical. This review focuses on major issues that might affect the application of a specific chemical rather than on a detailed analysis for each chemical. Information on each of 14 chemicals is contained in a database entitled "Environmental/Health Information on Candidate Replacements for halon 1301" and is also included in hard copy form as Appendix A. The data base is available by request from the editors of this report. The key findings are included in Section 9.2.2 below. Some of the candidate chemicals have already gone through a preliminary screening by EPA, and this information is identified as well.

In the paragraphs below, each of the pertinent elements of the SNAP protocol is described. The remainder of the section discusses the major implications of the tabulated information.

9.2.1 SNAP Protocol. The information required under the SNAP Protocol (Federal Register, 1993) regarding the environmental and health impact of each chemical is described below. The protocol also requires detailed confidential business information and process-specific information, which is not discussed here. Information about each entry is provided below.

1. **Name and Description of Substitute.** The chemical formula and the standard nomenclature for refrigerants are given.

2. **Physical and Chemical Information**. This includes molecular weight, normal boiling point, vapor pressure, and water solubility. This information is pertinent both to the performance of the replacement chemical and to its dispersion in the environment.

3. **Application**. How will the substance be used? In this case the application is for engine nacelle and the dry bay protection. The engine nacelle is the region enclosing the engine. The fire suppression agent would be directed into the nacelle and not into the engine itself. Dry bays are compartments adjacent to fuel cells and can be located in either wing or fuselage areas. They may contain electronic, hydraulic or mechanical equipment. In both of these applications it is important that the agent extinguish the fire rapidly.

4. **Ozone Depletion Potential (ODP)**. Stratospheric ozone is critical to blocking ultraviolet (UV) radiation from the sun. An increase in the UV solar radiation will have deleterious effects including increased incidence of skin cancer. The ODP value is a dimensionless number with a value of 1 corresponding to the ODP of CFC-11, CHF_2Cl. The ideal value is zero. The values listed in Appendix A are obtained from The Scientific Assessment of Stratospheric Ozone (Pyle *et al.*, 1991).

5. **Atmospheric Lifetime**. The global warming potential (GWP) of a chemical is determined by its absorption of thermal radiation from the earth and by its tropospheric lifetime relative to the value for carbon dioxide (IPCC, 1990). For the compounds selected here, the atmospheric lifetime provides a good estimate of the GWP. An ideal candidate would have a lifetime of a year or less; whereas, a molecule lasting for 1,000 years would be considered a problem.

6. **Flammability**. The substance should not be flammable at ambient oxygen concentration at atmospheric pressure and temperature. This would create special needs in terms of the storage and use of the chemical. Of course, one would not expect a fire suppressant agent to be flammable.

7. **Toxicity data**. The toxicity data include acute exposure leading to death, the chronic effects of a long term, low level exposure, cardiac sensitization such as an increase in the pulse or irregular heartbeats, and the tendency to cause cancer or to have a mutagenic effect. Instead of determining the absolute health impact of a chemical, it is often easier to compare its impact with that of halon 1301.

8. **Release**. The expected amount of chemical released per event. The amount released for an engine or dry bay fire is on the order of a fraction of a kg for halon 1301.

9. **Replacement Ratio**. This ratio is based on the volume of an agent (as a saturated liquid @ 25 °C) relative to the volume of halon 1301 necessary to suppress various flame arrangements. Our value corresponds to the average of spray burner and detonation tube tests discussed in Section 4. This is thought to be the most appropriate number for dry bays. A different estimate for the replacement ratio is obtained for engine nacelles and the resulting values (see Section 4) are as much as 50% greater than the dry bay values.

10. **Availability.** The issue is whether the chemical is currently (as of September 30, 1993) available in the amount required for replacing halon 1301.

11. **Cost**. The cost is a variable, which fluctuates with the market. The tabulated values are our best estimates as of September 30, 1993 based on the purchase of 909 kg (2000 lbs) of the agent.

12. **Required Technological Changes**. This refers to changes in the method for dispensing the agent relative to halon 1301.

9.2.2 Discussion of Key Results in Database. A summary of the key issues for each agent is included in Table 7, with details in Appendix A. Important aspects of the information in the database are discussed in the sections below.

9.2.2.1 Physical/Chemical Information. The database includes information for 16 different compounds. It is helpful to divide the compounds into various classes. Two chemicals stand out from the others: N_2 and $NaHCO_3$. Nitrogen was chosen to provide test data for a gas with no expected chemical effect on a fire and no environmental impact since the earth's atmosphere is 80% nitrogen. The $NaHCO_3$ dry powder releases CO_2 when heated.

The other compounds involve carbon bonded to halogens (fluorine, chlorine, bromine, and iodine), to hydrogen, and/or to other carbon atoms. The bond dissociation energy (BDE) decreases monotonically with increasing atomic weight of the halogen for the carbon halogen bonds in CF_3X from a value of 546 kJ per mole for C-F (McMillan *et al.*, 1982), to 331 for C-Cl, to 301 for C-Br, to 223 for C-I. The last three BDE's were computed by the method described in Section 6.1.3.1.5 (Nyden, 1993). The C-H BDE in CF_3H is 447 kJ/mole (McMillan *et al.*, 1982) and the C-Cl BDE in CHF_2Cl is about 330 kJ/mole. It is convenient to classify fire extinguishing agents with regard to the bond most easily broken. We have the following classes in order from weakest to strongest:

C-I bond (CF_3I)
C-Br bond (CF_3Br)
C-Cl bond (HCFC-22, HCFC-124)
C-H bond (HFC-32, HFC-125, HFC-32/HFC-125, HFC-227ea, HFC-236fa, HFC-134a)
C-F bond (FC-116, FC-218, FC-3110, FC-318)

As discussed below, the smaller BDE correlates with a shorter atmospheric lifetime; for example, the estimated lifetime of CF_3I is about 2 weeks compared to an estimated 10,000 years for FC-116 (Wuebbles, 1993).

Another qualitative trend is the decreasing vapor pressure and increasing boiling point with increasing molecular weight. For example the normal boiling point is -78 °C for FC-116 (C_2F_6) compared to -2 °C for FC-3110 (C_4F_{10}). The vaporization characteristics are important for the two phase dispersal as the fluid leaves the nozzle.

Table 7. Summary of Issues Regarding Candidate Chemicals

Agent	Comments
halon 1301	Not acceptable because of high ozone depletion potential
CF_3I	ODP not known; toxicity and corrosivity not known
sodium bicarbonate	Corrosive to aluminum; technology for rapidly dispersing the powder must be developed
perfluorinated compounds, (FC-116, FC-218, FC-318, FC-3110)	long atmospheric lifetime; high price for FC-318
HCFC-22, HCFC-124	Both on SNAP short list; however, finite ozone depletion potential and cardiac sensitivity
HFC-32	Not acceptable because of flammability
HFC-125, HFC-227	Both on SNAP short list; slight cardiac sensitivity
HFC-32/HFC-125	High HF production from flame; cardiac sensitivity
HFC-134a	On SNAP short list; high HF production from flame, cardiac sensitivity
HFC-236fa	Possible cardiac sensitivity; more difficult to disperse because of high boiling point

Because of their high vapor pressures, these chemicals are not expected to persist as a liquid pool or dissolved in water. The water solubility for most of the compounds is small. The most soluble is HCFC-22 (CHF_2Cl) with a water solubility of 3.3 kg/m^3 followed by CF_3Br with a value of 0.3 kg/m^3. The available data indicate that the other compounds are less soluble. Even the moderate solubility of HCFC-22 is not a water pollution issue for a release in an engine nacelle or dry bay.

9.2.2.2 Ozone Depletion Potential. As can be seen in the results tabulated in Appendix A, the ozone depletion potential of most of the compounds is zero. The exceptions are CF_3Br, which is being proscribed because of its high ozone depletion potential of 16; CF_3I, which is currently being evaluated, and the two chlorine containing molecules, HCFC-22 and HCFC-124, with ozone depletion potentials of 0.055 and 0.022, respectively. These values are considered small enough relative to what they replace that both of these chemicals are on the short list of proposed acceptable alternatives under SNAP Program.

9.2.2.3 Atmospheric Lifetime. As discussed above, the tropospheric lifetime is used as a surrogate for the global warming potential. Based on the heuristic bond energy analysis given above, one would expect CF_3I to have the shortest atmospheric lifetime since it has the smallest bond energy. This expectation is in qualitative agreement with the statement in Section 5 that the absorption spectra of CF_3I is shifted to the red relative to the other CF_3X's. Work in progress also indicates a very short lifetime of about 2 weeks (Wuebbles, 1993). Since $NaHCO_3$ releases CO_2 when heated, its

impact on the environment is determined by the CO_2 life-cycle and is not considered to be an issue. Chlorine containing molecules are next in increasing atmospheric lifetimes followed by the hydrogen containing molecules. The lifetime of the perfluorinated compounds is the longest, with Wuebbles (1993) estimating 50,000 years for CF_4. Because the five candidate perfluorinated compounds considered here have C-C bonds, which are weaker than the C-F bond, the lifetime is expected to be less than 50,000 years but may still be on the order of tens of thousands of years. This long lifetime is a serious issue with regard to their suitability as candidate replacement chemicals.

9.2.2.4 Flammability. The chemical HFC-32 (CH_2F_2) is flammable at an ambient oxygen concentration. In a mixture with HFC-125, HFC-32 is not flammable. While the compounds are not flammable, one should note that the increased number of C-C and C-H bonds will increase the heat release of these molecules in a flame environment.

9.2.2.5 Replacement Ratio. In all cases except $NaHCO_3$ more material will be required than for the currently used suppression agent CF_3Br; however, in the worst case only about twice as much is required. While this is a narrow range, it could still be important because of the weight and volume limitations on an aircraft. The replacement ratio computed here is on a volumetric basis. The corresponding mass ratio, that is the mass of an agent relative to the mass of halon 1301 necessary to suppress various flame arrangements, can be determined from the tabulated results and the densities given in Sections 2 and 4 of this report.

9.2.2.6 SNAP Alternative. There are five compounds from the above list that are on EPA's short list as proposed acceptable alternatives under the SNAP Program for total flooding of unoccupied areas. These are HFC-125 (C_2HF_5), HFC-227ea (C_3HF_7), HCFC-22 (CHF_2Cl), HFC-134a ($C_2H_2F_4$), and HCFC-124 (C_2HF_4Cl). Many of the other chemicals in the database we are considering are similar to these. The exceptions are the perfluorinated compounds which have a significantly longer atmospheric lifetime than any of the other chemicals.

9.2.2.7 Required Technological Changes. For each agent there will likely be some changes required relative to the current halon 1301 technology in terms of size of container, material for container, valve type, lubricant, etc. However, for one of these, $NaHCO_3$, a completely different dispersal system must be developed, since the $NaHCO_3$ is in the form of a powder. To be effective, the powder must be distributed essentially as fast as a gas.

9.2.2.8 Availability. The issue of availability is a critical one in the case of iodotrifluoromethane, CF_3I, which, as of this writing, is made in amounts of a few kg per batch. One company (DuBoisson, 1993) uses the so-called Hunsdiecker reaction (Banks, 1971). This involves the careful pyrolysis of an anhydrous mixture of silver trifluoroacetate and iodine:

$$CF_3CO_2Ag + I_2 \rightarrow CF_3I(>90\%) + CO_2 + AgI \qquad (1)$$

The reaction is initiated by gently heating the reagents to about 100 °C. Once initiated the reaction is exothermic and the dissipation of the heat is one of the difficulties in scaling up this process above a few kilogram batch. Another difficulty is the recovery of the AgI from the vessel for reprocessing. The current technology involves collecting the CF_3I in cooled tubes connected to the reactor vessel and breaking the reactor vessel each time to recover the AgI.

Another company (Newhouse, 1993) has just begun manufacturing CF_3I using a 200 *l* reactor with a batch product of about 25 kg. They claim that there is not a major impediment to scaling up the operation. However, until this is demonstrated the availability of CF_3I will remain an issue.

9.2.2.9 Combustion Products. One of the major unwanted products of combustion is HF. Based on cup burner experiments, Appendix A shows that there is more than a factor of 10 variation in the amount of HF released per gram fuel consumed with the two poorest performers, HFC-32/HCF-125 and HFC134a. The HF production of the other compounds is a factor of two or more less than these compounds. For the CF_3I there will also be the issue of the production of HI and I_2.

9.2.2.10 Price. There is a tremendous range in the price from as low as $3.50 per kg for HCFC-22 to $210 per kg for FC-318 and $330 per kg for CF_3I. A major factor in the high price is the limited production of some of the compounds. The cost is likely to drop significantly with greater production.

9.2.2.11 Toxicity. These chemicals are intended for use in areas external to the inhabited areas of the airplane. Therefore, people will not be exposed to the suppressant during fire suppression. However, there is a chance of accidental exposure during the installation and maintenance of the system. In such a case, safety considerations following rapid release of the two-phase flow include:

- low temperatures arising from the flow expansion, and
- asphyxiation from release into a confined space.

Chronic effects from repeated low level exposures should also be considered.

Our toxicity data are abstracted from the Air Force literature survey (Jepson, 1993). The perfluorinated chemicals, which are apparently unreacted in the body, appear to be the least toxic of the candidate chemicals and compare favorably with halon 1301 in acute testing. On the other hand, the most toxic appear to be the chlorine-containing chemicals (HCFC-22 and HCFC-124) because of their elevated levels of cardiac sensitization relative to the other chemicals. There is also a growing popular concern about the toxicity of any chlorine-containing chemical. It is noteworthy that, even so, these chemicals are on the short list for proposed alternatives under the SNAP Program. The chemical HFC-134a, $C_2H_2F_4$, has about the same cardiac sensitization as halon 1301 and has been shown to undergo a metabolism similar to anesthetic agent halothane. This is of some concern since repeated low level exposures of personnel to the anesthetic agent halothane can produce viral-like hepatitis. The perfluorinated halocarbons do not produce the viral-like behavior because they are biologically inert. Toxicity data for CF_3I are just beginning to be generated at this time.

Little is known about the mutagenic/carcinogenic potential of the agents for humans. FC-318, FC-218, and HCFC-22 have all demonstrated some mutagenic activity in an *in vitro* system. Only HCFC-22 has been tested in a mammalian system; based on the results it is classified as Group 3 (the agent is not classifiable as to its carcinogenicity in humans).

9.3 Conclusions

- Experimental measurement, hand calculations, and 3-D fluid flow modeling of an accidental release of a halon alternative show that a reasonably uniform concentration of agent is obtained in a compartment shortly after release of the agent. Thus, simple ideal gas calculations of agent concentrations should suffice for estimating agent concentration following an accidental release.

- For compartments which include baffles to the gas flow, the diffusion controlled flow after agent release may confine the released agent within the baffles near the release point of the agent.

- As of this report, only five candidate agents have been designated as acceptable alternative chemicals to halon 1301. These are: HCFC-124, HCFC-22, HFC-134A, HFC-227, and HFC-125.

9.4 References

Banks, R.E., *Fluorocarbons and their Derivatives,* Elsevier Publishing Co., Inc., New York, 1971.

Barrow, G.M., *Physical Chemistry,* McGraw-Hill, Inc., New York, 1961.

Bennett, C.O. and Myers, J.E., *Momentum, Heat, and Mass Transfer,* McGraw-Hill, Inc., New York, second edition, 1974.

CFD Department, AEA Industrial Technology, Harwell Laboratory, Oxfordshire, United Kingdom. *HARWELL-FLOW3D Release 2.3: User Manual*, 1990.

DuBoisson, R., PCR, Gainesville, Florida, personal communication, 1993.

Federal Register, Volume 58, 90, pp. 28102-28104, May 12, 1993.

Incorpera, F.P. and De Witt, D. P., *Fundamentals of Heat and Mass Transfer,* John Wiley and Sons, New York, third edition, 1990.

Intergovernmental Panel on Climate Change (IPCC): Climate Change; The IPCC Scientific Assessment, Cambridge University Press, Cambridge, UK, 1990.

Jepson, G.W., Memorandum for Capt. Jepson, WL/FIVS (Mr. Bennett), May 21, 1993.

McMillan, D.F., and Golden, D.M., "Hydrocarbon Bond Dissociation Energies," *Annual Review of Physical Chemistry* **33** ,493 (1982)

Newhouse, S., Pacific Scientific, Duarte, CA, personal communication, 1993.

Nyden, M., National Institute of Standards and Technology, personal communications,1993.

Pyle, J.A., Solomon, S., Wuebbles, D., and Zvenigorodsky, S., "Ozone Depletion and Chlorine Loading Potentials," in World Meteorological Organization, Global Ozone Research Monitoring Project - Report No. 25, *Scientific Assessment of Ozone Depletion: 1991*, 1991.

Wuebbles, D.J., Lawrence Livermore National Laboratory, personal communication, 1993.

Appendix A. Halon Replacement Properties

HALON Replacement Chemical Properties Table

Date Recorded:	09/29/93
Formula: CF3Br	Designation: Halon 1301
Molecular Weight:	148.9 kg/kmole
Normal Boiling:	215 K
Vapor Pressure:	1610 kPa @ 298 K
Water Solubility:	0.3000 kg/m3 @ 101 kPa
Ozone Depletion Potential:	16
Atmospheric Life Time (yrs):	110
Flammability:	NO
Replacement Ratio:	1.0 based on HALON 1301
SNAP Alternative:	-
Application:	ENGINE NACELLE/DRY BAY
Availability:	UNLIKELY AFTER 1995
Price:	$61.60 per kg @ 13 kg
Required Technological Changes:	NONE
Environmental--Release:	ABOUT 4 KG PER INCIDENT
Combustion Products:	0.08 G HF/G C3H8 BURNED
Toxicity---------Acute:	
Cardiac:	
Carcinogenic:	
Mutagenic:	
Pyrolysis:	

HALON Replacement Chemical Properties Table

Date Recorded: 10/01/93

Formula: CF3I Designation: Iodotrifluoromethane

Molecular Weight: 196.0 kg/kmole

Normal Boiling: 251 K

Vapor Pressure:

Water Solubility:

Ozone Depletion Potential:

Atmospheric Life Time (yrs): 0.04

Flammability:

Replacement Ratio: 1.2 based on HALON 1301

SNAP Alternative:

Application: ENGINE NACELLE/DRY BAY

Availability: CURRENT CAPACITY ABOUT 25 KG PER BATCH

Price: $330.00 per kg @ 25 kg

Required Technological Changes:

Environmental--Release: ABOUT 4 KG PER INCIDENT

Combustion Products:

Toxicity---------Acute:

Cardiac:

Carcinogenic:

Mutagenic:

Pyrolysis:

HALON Replacement Chemical Properties Table

Date Recorded: 10/01/93

Formula: NaHCO3 Designation: Sodium Bicarbonate

Molecular Weight: 84.0 kg/kmole

Normal Boiling:

Vapor Pressure:

Water Solubility: 69.000 kg/m3 @ 101 kPa

Ozone Depletion Potential: 0.0

Atmospheric Life Time (yrs):

Flammability: NO

Replacement Ratio: 0.8 based on HALON 1301

SNAP Alternative:

Application: ENGINE NACELLE/DRY BAY

Availability: YES

Price: $2.00 per kg @ 1000 kg

Required Technological Changes: MAJOR CHANGES REQUIRED TO RAPIDLY DISPERSE A POWDER

Environmental--Release: ABOUT 4 KG PER INCIDENT

Combustion Products: NaOH

Toxicity---------Acute: NOT A CONCERN

Cardiac: NOT A CONCERN

Carcinogenic: NOT A CONCERN

Mutagenic: NOT A CONCERN

Pyrolysis: NOT A CONCERN

HALON Replacement Chemical Properties Table

Date Recorded: 10/01/93

Formula: C2F6 Designation: FC-116

Molecular Weight:	138.0 kg/kmole
Normal Boiling:	195 K
Vapor Pressure:	3070 kPa @ 293 K
Water Solubility:	
Ozone Depletion Potential:	0.0
Atmospheric Life Time (yrs):	10000
Flammability:	NO
Replacement Ratio:	3.2 based on HALON 1301
SNAP Alternative:	
Application:	ENGINE NACELLE/DRY BAY
Availability:	
Price:	$37.30 per kg @ 450 kg
Required Technological Changes:	
Environmental--Release:	ABOUT 4 KG PER INCIDENT
Combustion Products:	0.7 G HF/G C3H8 BURNED
Toxicity---------Acute:	RAT, 1 hr @ 800,000 ppm - initial hyperactivity followed by hypoactivity, hyperemia, and closed eyes.
Cardiac:	dog, up to 600,000 ppm - no sensitization
Carcinogenic:	
Mutagenic:	not mutagenic in exposed E. coli.
Pyrolysis:	rat, exposure of pyrolysis products from acetone fire resulted in dyspnea, salivation, lacrimation, and gasping. Substantial weight loss.

HALON Replacement Chemical Properties Table

Date Recorded: 10/01/93
Formula: C3F8 Designation: FC-218
Molecular Weight: 188.0 kg/kmole
Normal Boiling: 236 K
Vapor Pressure: 880 kPa @ 298 K
Water Solubility:
Ozone Depletion Potential: 0.0
Atmospheric Life Time (yrs): 10000
Flammability: NO
Replacement Ratio: 1.6 based on HALON 1301
SNAP Alternative:
Application: ENGINE NACELLE/DRY BAY
Availability:
Price: $39.60 per kg @ 654 kg
Required Technological Changes:

Environmental--Release: ABOUT 4 KG PER INCIDENT
Combustion Products: 1.1 G HF/G C3H8 BURNED
Toxicity---------Acute: rat, 1 hr @ 800,000 ppm - initial hyperactivity followed by hypoactivity, hyperemia, and closed eyes.
Cardiac:
Carcinogenic:
Mutagenic: Biochemical mutants were produced in E. coli.
Pyrolysis:

```
            HALON Replacement Chemical Properties Table
Date Recorded: 10/01/93
Formula: C4F10                Designation: FC-31-10
      Molecular Weight: 238.0 kg/kmole
        Normal Boiling: 271 K
        Vapor Pressure:    265 kPa @   298 K
      Water Solubility:
      Ozone Depletion
              Potential: 0.0
     Atmospheric Life
             Time (yrs): 10000
          Flammability: NO
     Replacement Ratio: 1.7 based on HALON 1301
      SNAP Alternative:
           Application: ENGINE NACELLE/DRY BAY
          Availability:
                 Price: $33.00 per kg @ 600 kg
Required Technological
               Changes:

Environmental--Release: ABOUT 4 KG PER INCIDENT
   Combustion Products: 1.2 KG HF/G C3H8 BURNED
Toxicity---------Acute: rat, 16 hrs @ 800,000 ppm no effect
               Cardiac: dog, no cardiac sensitization noted at up to
                        400,000 ppm
          Carcinogenic:
             Mutagenic:
             Pyrolysis:
```

HALON Replacement Chemical Properties Table

Date Recorded: 10/01/93
Formula: CYCLO C4F8 Designation: FC-318
Molecular Weight: 200.0 kg/kmole
Normal Boiling: 266 K
Vapor Pressure: 310 kPa @ 298 K
Water Solubility:
Ozone Depletion Potential: 0.0
Atmospheric Life Time (yrs): 10000
Flammability: NO
Replacement Ratio: 1.7 based on HALON 1301
SNAP Alternative:
Application: ENGINE NACELLE/DRY BAY
Availability: LIMITED PRODUCTION
Price: $209.00 per kg @ 45 LBS
Required Technological Changes:

Environmental--Release: ABOUT 4 KG PER INCIDENT
Combustion Products:
Toxicity---------Acute: rat, 4 hr @ 800,000 ppm, no deaths, signs of irritation
Cardiac: mouse, up to 400,000 ppm alone - no arrhythmias; 200,000 ppm + epinephrine - arrhythmias
Carcinogenic:
Mutagenic: 5/1300 visible mutation (0.38%) compared to 0.008% spontaneous control rate; sex-linked recessive lethal mutation was not significant.
Pyrolysis:

HALON Replacement Chemical Properties Table

Date Recorded: 10/01/93
Formula: CH2F2 Designation: HFC-32
Molecular Weight: 52.0 kg/kmole
Normal Boiling: 221 K
Vapor Pressure:
Water Solubility:
Ozone Depletion Potential: 0.0
Atmospheric Life Time (yrs): 7
Flammability: YES
Replacement Ratio:
SNAP Alternative:
Application: ENGINE NACELLE/DRY BAY
Availability:
Price:
Required Technological Changes:

Environmental--Release: ABOUT 4 KG PER INCIDENT
Combustion Products:
Toxicity---------Acute: rat, 4 hr @ 111,000 to 760,000 ppm - signs of lethargy, loss of mobility, spasms and gnawing of cage during exposure. No abnormal signs 30 min to 14 days after exposure.
Cardiac: 1/12 dogs sensitized @ 250,000 ppm; same dog was normal after 200,000 ppm.
Carcinogenic:
Mutagenic: Ames assay - negative
Pyrolysis: no information

```
            HALON Replacement Chemical Properties Table
Date Recorded: 10/01/93
Formula: CH2F2/C2HF5          Designation: HFC-32/HFC-125
      Molecular Weight:  kg/kmole
        Normal Boiling: 220 K
        Vapor Pressure:   1670 kPa @   298 K
      Water Solubility:
      Ozone Depletion
             Potential: 0.0
     Atmospheric Life
            Time (yrs):
          Flammability: NO
     Replacement Ratio: 2.5 based on HALON 1301
      SNAP Alternative:
           Application: ENGINE NACELLE/DRY BAY
          Availability:
                 Price: $33.00 per kg @ 680 kg
Required Technological
               Changes:

Environmental--Release: ABOUT 4 KG PER INCIDENT
   Combustion Products: 6.2 G HF/G C3H8 BURNED
Toxicity---------Acute:
               Cardiac:
          Carcinogenic:
             Mutagenic:
             Pyrolysis:
```

```
             HALON Replacement Chemical Properties Table
Date Recorded: 10/01/93
Formula: C2HF5                  Designation: HFC-125
      Molecular Weight: 120.0 kg/kmole
        Normal Boiling: 224 K
        Vapor Pressure:   1380 kPa @   298 K
       Water Solubility:
       Ozone Depletion
              Potential: 0.0
     Atmospheric Life
             Time (yrs): 40.5
           Flammability: NO
     Replacement Ratio: 1.8 based on HALON 1301
      SNAP Alternative:  +
            Application: ENGINE NACELLE/DRY BAY
           Availability:
                  Price: $31.46 per kg @ 490 kg
Required Technological
                Changes:

Environmental--Release: ABOUT 4 KG PER INCIDENT
   Combustion Products: 2.1 KG HF/G C3H8 BURNED
Toxicity---------Acute:
                Cardiac:
           Carcinogenic:
              Mutagenic: Ames assay - negative, human lymphocyte - negative,
                          CHO cell assay - negative
              Pyrolysis:
```

HALON Replacement Chemical Properties Table

Date Recorded:	10/01/93
Formula: C3HF7	Designation: HFC-227
Molecular Weight:	170.0 kg/kmole
Normal Boiling:	257 K
Vapor Pressure:	
Water Solubility:	
Ozone Depletion Potential:	0.0
Atmospheric Life Time (yrs):	13
Flammability:	NO
Replacement Ratio:	1.6 based on HALON 1301
SNAP Alternative:	+
Application:	ENGINE NACELLE/DRY BAY
Availability:	
Price:	$49.50 per kg @ 654 kg
Required Technological Changes:	
Environmental--Release:	ABOUT 4 KG PER INCIDENT
Combustion Products:	1.7 G HF/G C3H8 BURNED
Toxicity---------Acute:	rats, 4 hrs @25,000 or 53,000 ppm - no deaths, irreg. breathing, slight lacrimation, red ears, no post exposure effects.
Cardiac:	
Carcinogenic:	
Mutagenic:	
Pyrolysis:	

```
             HALON Replacement Chemical Properties Table
Date Recorded: 10/01/93
Formula: C3H2F6                Designation: HFC-236FA
      Molecular Weight: 152.0 kg/kmole
        Normal Boiling: 272 K
        Vapor Pressure:    270 kPa @   298 K
      Water Solubility:
      Ozone Depletion
              Potential: 0.0
     Atmospheric Life
            Time (yrs):
          Flammability: NO
     Replacement Ratio: 1.6 based on HALON 1301
      SNAP Alternative:
           Application: ENGINE NACELLE/DRY BAY
          Availability:
                 Price:
Required Technological
               Changes:

Environmental--Release: ABOUT 4 KG PER INCIDENT
   Combustion Products: 1.9 G HF/G C3H8 BURNED
Toxicity---------Acute:
               Cardiac:
          Carcinogenic:
             Mutagenic:
             Pyrolysis:
```

HALON Replacement Chemical Properties Table

Date Recorded:	10/01/93
Formula: C2H2F4	Designation: HFC-134A
Molecular Weight:	102.0 kg/kmole
Normal Boiling:	247 K
Vapor Pressure:	670 kPa @ 298 K
Water Solubility:	
Ozone Depletion Potential:	0.0
Atmospheric Life Time (yrs):	15.6
Flammability:	NO
Replacement Ratio:	1.9 based on HALON 1301
SNAP Alternative:	+
Application:	ENGINE NACELLE/DRY BAY
Availability:	
Price:	$11.55 per kg @ 680 kg
Required Technological Changes:	
Environmental--Release:	ABOUT 4 KG PER INCIDENT
Combustion Products:	3.9 G HF/G C3H8 BURNED
Toxicity---------Acute:	rat, 4 hr LC50 > 500,000 ppm
Cardiac:	Threshold level - 75,000 ppm
Carcinogenic:	
Mutagenic:	Ames assay - negative, clastogenicity - negative; rat cytogenetics up to 50,000 ppm negative, mouse dominant lethal up to 50,000 ppm - negative.
Pyrolysis:	

HALON Replacement Chemical Properties Table

Date Recorded:	10/01/93
Formula: CHF2CL	Designation: HCFC-22
Molecular Weight:	87.0 kg/kmole
Normal Boiling:	232 K
Vapor Pressure:	1050 kPa @ 298 K
Water Solubility:	3.3000 kg/m3 @ 101 kPa
Ozone Depletion Potential:	0.055
Atmospheric Life Time (yrs):	15.8
Flammability:	NO
Replacement Ratio:	2.2 based on HALON 1301
SNAP Alternative:	+
Application:	ENGINE NACELLE/DRY BAY
Availability:	
Price:	$3.50 per kg @ 680 kg
Required Technological Changes:	
Environmental--Release:	ABOUT 4 KG PER INCIDENT
Combustion Products:	1.3 G HF/G C3H8 BURNED
Toxicity---------Acute:	rats, guinea pigs; 2 hr exposure - 75,00 - 100,000 ppm -excitation and/or ataxia; 200,000 ppm - CNS depression; 300,000 - 400,000 ppm - death.
Cardiac:	dogs and monkeys; 50,000 - 100,000 ppm caused early respiratory depression, bronchoconstriction, tachycardia, myocardial depression and hypotension.
Carcinogenic:	Inadequate evidence of carcinogenicity in humans; some evidence of tumors in male mice exposed for a long period of time.
Mutagenic:	Ames assay, BHK21 cell transformation - positive results; no induction of unscheduled DNA synthesis in human heteroploid EUE cells treated with a 20 mM soln. generated at 500 ml/min (1:1 air) in presence or absence of S10.
Pyrolysis:	Combustion products highly toxic

HALON Replacement Chemical Properties Table

Date Recorded: 10/01/93
Formula: C2HF4Cl Designation: HCFC124
Molecular Weight: 137.0 kg/kmole
Normal Boiling: 260 K
Vapor Pressure: 380 kPa @ 298 K
Water Solubility:
Ozone Depletion Potential: 0.022
Atmospheric Life Time (yrs): 6.9
Flammability: NO
Replacement Ratio: 1.6 based on HALON 1301
SNAP Alternative: +
Application: ENGINE NACELLE/DRY BAY
Availability:
Price: $17.05 per kg @ 790 kg
Required Technological Changes:

Environmental--Release: ABOUT 4 KG PER INCIDENT
Combustion Products: 0.6 G HF/G C3H8 BURNED
Toxicity---------Acute: Approx. lethal conc. - 230,000- 255,000 ppm.
Cardiac: dog; threshold - 26,155 ppm.
Carcinogenic:
Mutagenic: Ames assay - negative; human lymphocyte assay - negative; CHO cell assay - negative; Micronucleus assay - negative.
Pyrolysis:

```
            HALON Replacement Chemical Properties Table
Date Recorded: 10/01/93
Formula: N2                    Designation: NITROGEN
      Molecular Weight:  28.0 kg/kmole
        Normal Boiling: 77 K
        Vapor Pressure:
      Water Solubility:
      Ozone Depletion
              Potential:
     Atmospheric Life
             Time (yrs):
          Flammability:
     Replacement Ratio:
      SNAP Alternative:
           Application: ENGINE NACELLE/DRY BAY
          Availability:
                 Price: $2.00 per kg @ 450 kg
Required Technological
               Changes:

Environmental--Release: ABOUT 4 KG PER INCIDENT
   Combustion Products:
Toxicity---------Acute:
               Cardiac:
          Carcinogenic:
             Mutagenic:
             Pyrolysis:
```

10. SUMMARY AND RECOMMENDATIONS

William L. Grosshandler, Richard G. Gann and William M. Pitts
Building and Fire Research Laboratory

The main objective of this research program was to provide guidance to the sponsors on which materials to evaluate in the full-scale fire suppression test plan at Wright-Patterson AFB. Specifically, the recommendations were to include the following:

1. the best two agents from the core list of twelve FCs, HFCs and HCFCs provided by the Air Force when NIST began the project in 1992,

2. the best practical alternative from among materials not on the list of twelve, and

3. whether or not sodium bicarbonate powder was a viable option.

New metrics have been developed along the way which can be used to rate other fire fighting compounds for a variety of applications.

The methodology for combining the results of literally hundreds of tests for the purpose of defining an overall performance rating of the chemicals is described in this section. A justification for each agent recommended using the methodology and the ranking of all of the agents evaluated by these methods are included. The report ends with a summary of the continuing investigation into the formation of by-products during the suppression process and long-term materials compatibility for the agents selected by the sponsors for full-scale testing. A list of recommendations for further research is provided.

10.1 Rationale for Selection

The agents have been rated using the criteria given below. The desirable magnitude of each variable is given in parentheses.

- saturation liquid density at 25 °C (high)
- temperature at which storage vessel reaches liquid-filled condition (high)
- boiling point at 101 kPa (low)
- discharge rate from vessel (high)
- dispersion and mixing with air (high)
- distance required for agent vaporization during sudden discharge (short)
- concentration required to extinguish laminar flame in opposed-flow diffusion (OFDF) burner for two air temperatures, multiple fuels, and variable strain rates (low)
- concentration required to suppress cup burner flame for multiple fuels (low)
- concentration required to extinguish turbulent spray flame for two temperatures and fuels, and variable injection rates (low)
- concentration required to suppress a high-speed turbulent flame in detonation tube for two equivalence ratios (low)

- agent residue (low)
- corrosion of metals by neat agent for multiple materials (low)
- swelling of polymers by neat agent for multiple materials (low)
- durability of elastomers and greases by neat agent for multiple materials (high)
- decomposition during storage (low)
- concentration of corrosive byproducts during suppression (low)
- ozone depletion potential (low)
- atmospheric lifetime (short)
- relative potential human exposure (low)
- availability (high)
- price of chemical (low)

Many of the above criteria did not lead to differentiation among the alternative agents to a statistically significant degree. The discriminating factors could be lumped into four categories: agent dispersion and evaporation characteristics, required storage volume, environmental factors, and operational issues.

10.1.1 Dispersion and Evaporation. The rate of agent discharge from the storage vessel was discussed in Section 3.4 for different initial conditions. The average volume flow rate, V_d', of the liquid agent from a 2/3-filled vessel initially at room temperature and 4.1 MPa is summarized here in Table 1. All of the alternative agents leave the vessel at about the same volume flow rate, 10.5 $\pm$ 0.6 *l*/s, which is significantly faster than the discharge rate of halon 1301. Once leaving the bottle, more of an agent is required aboard an aircraft if it disperses and evaporates slowly to ensure that a fire anywhere within the protected space can be extinguished. Measurements taken during a discharge under conditions similar to a large open bay were discussed in Section 3.5. From those measurements, the dispersion, mixing and evaporation behaviors of the alternative agents were evaluated. The rankings from that study are also listed in Table 1.

Unlike the dry bay discharge which is limited to the heat contained in the stored liquid for vaporization of the agent, more opportunity is available for evaporating the liquid droplets in engine nacelle applications. Heat transferred from the piping system and air can provide the additional energy for the vaporization process as long as the surrounding temperature is sufficiently above the agent boiling point. The minimum temperature required to ensure that enough agent is in a fully gaseous state, T_{min}, can be estimated from an energy balance on the protected volume assuming the mass fraction of agent, Y_i, is the amount required to suppress a JP-8 cup burner flame. It can be shown that

$$T_{\min} = T_b + \frac{Y_i \Delta H_{vap}(T_b)}{(1-Y_i) C_{p,air} + Y_i C_{p,i}} \tag{1}$$

where the specific heats are for the liquid agent, $C_{p,i}$, and air, $C_{p,air}$, and ΔH_{vap} is the enthalpy of vaporization at the boiling point, T_b. Values of T_{min} are listed in Table 1 for each of the agents. HFC-134a, FC-318, FC-31-10, HCFC-124 and HFC-236fa require temperatures greater than 25 °C to vaporize fully, making them suspect for low temperature operation. The FC-116 is stored above its critical point, but if one were interested primarily in low temperature operation, its T_{min} value equal to -43 °C would make FC-116 a strong candidate. FC-218, HFC-125 and CF_3I are the only other compounds with T_{min} less than 0 °C.

Table 1. Agent discharge, dispersion and evaporation parameters

Agent	Sect. 3.5 Rank	T_{min}, °C	V'_d, l/s
CF_3Br	n.r.	-42	7.6
FC-116	n.r.	-43	a
FC-218	1	-7	10.8
HFC-125	1	-6	9.8
HFC-32/HFC-125	3	+20	10.0
HCFC-22	4	+21	10.2
HFC-134a	5	+29	10.7
HFC-227ea	6	+19	11.1
HCFC-124	7	+28	10.9
FC-318	8	+28	10.8
FC-31-10	9	+29	10.3
HFC-236fa	10	+37	10.8
CF_3I	n.r.	-1	a

a data not taken n.r. not ranked

The Jakob number, Ja, was defined in Section 3 as the amount of heat available from cooling the liquid agent from ambient temperature to its normal boiling point, divided by the agent's heat of vaporization. A high value for Ja and a low value for T_{min} are both desirable attributes which often, but not always, go hand-in-hand. For example, the Jakob numbers for FC-218 and CF_3Br are 0.59 and 0.51, respectively, while T_{min} for CF_3Br is 35 °C less than the minimum temperature for FC-218. The implication is that the perfluorocarbon will flash more completely from a storage vessel at room temperature than halon 1301 in a dry bay application, but FC-218 will vaporize less efficiently in the engine nacelle at lower operating temperatures.

10.1.2 Storage Volume. The required storage volume is estimated from the measured suppression concentration and the density of the agent within the storage vessel at ambient temperature. The fuel type and temperature of the air were found to be of secondary importance in the measurements of the relative mass of the agents. While the absolute amount of agent necessary to quench the flames varied with the apparatus, the strain rate, the rate of injection, and the equivalence ratio, a single parameter called the volume factor, VF, is useful in comparing the relative suppression performance of the various agents. VF is a measure of the liquid agent volume in the storage vessel normalized by the liquid volume of halon 1301 required to suppress a flame under identical conditions; *i.e.*,

$$VF \equiv \left(\frac{\rho_{1301}}{\rho_i}\right)\left(\frac{Y_i}{Y_{1301}}\right)\left(\frac{1-Y_{1301}}{1-Y_i}\right) \quad (2)$$

The saturation liquid densities at 25 °C, ρ_i, were taken from Section 2 of this report. Table 2 lists the values of VF for each apparatus. The OFDF values were found from the ambient temperature experiments with JP-8, taken at a strain rate of 100 s^{-1}. The cup burner values were measured with heptane as the fuel. For the spray burner, the VF was calculated from the mass of agent injected in the ambient temperature JP-8 experiments. The performance in the detonation tube was based upon the average of the mass of agent required to reduce the pressure ratio by one half and to 10% of the maximum increase, with data restricted to the lean experiments. The uncertainty in the values of VF is estimated to be ± 10%.

Independent of the apparatus, the volume factors for FC-116 and the HFC-32/125 mixture are the highest (*i.e.,* the poorest performers). The best performer in the table is sodium bicarbonate. (Note that the flame suppression number, FSN, is used to rate the powder rather than VF. The direct comparison is valid as long as the powder density is close to the density of liquid halon.) Iodotrifluoromethane is the most effective of the gaseous agents in suppressing the cup and spray burner flames, and HCFC-124 is the best of the core alternatives. FC-218 stands out as the best agent in suppressing the high-speed deflagration. Except for the high value of VF for HCFC-22 in the deflagration tube, there is little basis upon which to say that any one of the remaining agents is better than another in suppressing the flames using this metric.

10.1.3 Environmental Factors. Primary environmental concerns include acute toxicity, ozone depletion potential, and atmospheric lifetime of the alternative agents. None of the core chemicals have been identified as presenting an acute toxicity hazard, so that consideration of application to normally unoccupied spaces like the engine nacelle and dry bay does not lead to any discrimination among them. Toxicity data on CF_3I is incomplete, but preliminary studies (as of this writing) have not uncovered any major health hazards which would prevent its application to unoccupied spaces.

All but two of the core agents have an ODP of zero. The two chlorinated compounds, HCFC-22 and HCFC-124, have an ODP less than one tenth of the present EPA limit. Iodides are not currently regulated, but preliminary estimates indicate that the ODP for CF_3I released in the lower troposphere is small because it easily photodissociates. Any of the chemical released directly into the stratosphere, however, would react efficiently with the local concentration of ozone. The general ranking (from best to worst) based upon ODP is as follows:

$$\mathbf{FCs = HFCs \equiv 0 < CF_3I < HCFCs << CF_3Br} \quad \text{(ODP)}$$

Short atmospheric lifetime is considered a positive attribute in an alternative agent, but as of this writing it is not mandated by governmental regulations nor international agreements. The estimated tropospheric lifetime varies by over four orders-of-magnitude, with CF_3I having the shortest (weeks) and the perfluorocarbons having the longest (1000s of years). Among the remaining compounds, the HCFCs have a shorter lifetime than the HFCs, which are less long-lasting than CF_3Br (estimated lifetime is 66 years). The following ranking applies, from best to worst:

$$\mathbf{CF_3I << HCFCs < HFCs << FCs} \quad \text{(atmospheric lifetime)}$$

Because sodium bicarbonate is a powder, atmospheric chemistry is a non-issue. The powder is also considered to be non-toxic.

Table 2. Volume factors for flame suppression in different apparatus

Agent	OFDF	Cup Burner	Spray Burner	Deflag. Tube
$NaHCO_3$	0.23[b]	0.45[b]	0.85[b]	a
CF_3I	a	0.9	0.8	1.4
HCFC-124	2.5	2.2	1.8	1.5
HCFC-22	3.0	2.8	1.8	2.5
HFC-236fa	3.1	2.3	1.8	1.4
HFC-227	3.2	2.4	1.8	1.4
FC-218	3.6	2.8	2.1	1.2
FC-31-10	3.9	2.6	2.1	1.4
HFC-134a	4.0	2.8	2.0	1.8
HFC-125	4.1	2.8	2.0	1.7
FC-318	4.1	2.6	2.0	1.4
HFC-32/125	5.3	3.5	2.5	2.5
FC-116	7.1	6.0	4.0	2.5

[a] data not taken [b] FSN for powder

10.1.4 Operational Issues. Factors which involve maintenance or logistics can be evaluated separately from fire suppression performance and environmental impact. These include agent residue, stability under storage, accidental discharge under storage, corrosion from combustion byproducts, compatibility of the agent with metals and seals, and availability of the chemical. Table 3 compares the agents on operational issues. A rating of "B" in the table implies the compound has no significant shortcomings nor advantages over the other agents in that particular performance criteria. A "C" indicates a weakness or below average performance, but not necessarily a fatal flaw. An "A" rating means above average performance or a particular operational advantage demonstrated by the compound.

None of the core agents left an undesirable residue when discharged, none segregated in space to a significant degree during a simulated leak, and little decomposition was observed during one-month, high temperature storage. All produced a considerable amount of undesirable HF during suppression. There was some variation in the interaction of the core compounds with metals and polymers, but storage material combinations do exist which are compatible with most of the agents. Industrial sources exist for the core agents, so that neither lack of availability nor price of the agent were issues of major concern.

Iodotrifluoromethane from the initial batch received was observed to be slightly more aggressive than the core agents in attacking some metals and polymers, but the limited amount of short-term testing which was completed did not uncover insurmountable materials compatibility issues. Iodine

Table 3. Rating of agents on various operational issues: A, above average performance or particular advantage; B, average performance or neutral; C, below average, or particular disadvantage.

Agent	Availability	Cost	Stability in Storage	Metals Compatibility	Polymers Compatibility	Combustion Byproducts	Residue
FC-116	B	B	A	A	A	B	A
FC-218	B	B	A	B	B	B	A
FC-318	B	B	A	C	A	B	A
FC-31-10	B	B	A	C	B	B	A
HFC-125	B	B	*	A	A	B	A
HFC-32/125	A	B	B	B	A	C	A
HFC-134a	A	B	A	A	B	C	A
HFC-227ea	B	B	A	A	A	B	A
HFC-236fa	B	B	*	B	A	B	A
HCFC-22	A	A	A	C	B	B	A
HCFC-124	B	B	A	B	A	A	A
CF_3I	C	C	B/C	*	*	*	#
$NaHCO_3$	A	A	B	C	*	C	C

* insufficient data for rating

highly acidic impurity present in some samples

was observed as a decomposition product when the CF_3I was subjected to the high temperature storage test. No other significant decomposition products were identified. (However, noticeable acidic residue was present in batches of CF_3I received later from a second supplier.) U.S. production of CF_3I, as of September 30, 1993, was of the order of 50 kg/yr, and bulk quantities sufficient for full-scale testing were unavailable. The renewed interest generated in iodofluorocarbons could cause industrial production to increase substantially. However, as of this report, bulk production of sufficiently pure chemical has not been demonstrated.

All of the $NaHCO_3$ which is not carried away from a fire remains as an undesirable residue. Instability of the carbonate under high temperature storage was not fully explored, but some metal corrosion was evident. A major product of combustion from the powder is NaOH, which interacts aggressively with aluminum.

10.2 Ranking of Agents

10.2.1 Agents Recommended *Against* Full-Scale Engine Nacelle and Dry Bay Testing. Cup burner tests with HFC-32 confirmed previous reports that the compound is flammable. The decision was made, in consultation with the sponsors, to replace HFC-32 with HFC-236fa in the test matrix.

During the course of the evaluation, seven chemicals were identified which either performed unimpressively or were deficient in other ways. Considering the available alternatives, we do not recommend these for full-scale testing. These chemicals are listed below with the major reasons for our non-recommendation:

Agent	Major Deficiencies
FC-116	highest volume factor in all flame configurations; critical temperature below 20 °C leading to uncertainty in design of storage vessel and speed of discharge
HFC-32/HFC-125	high volume factor in all flame configurations; highest over-pressures in detonation tube; high acid gas levels in combustion products
HFC-236fa	highest vaporization temperature; lowest Jakob number
FC-318	high vaporization temperature; low Jakob number; below average metals compatibility; long atmospheric lifetime
FC-31-10	high vaporization temperature; low Jakob number; below average metals compatibility; long atmospheric lifetime
HCFC-22	highest ODP; poorest compatibility with metals
HFC-134a	overall mediocre performance; higher levels of HF in combustion products

10.2.1 Ranking of Remaining Agents. The performance of all the candidates regarding environmental and operational issues was judged to be sufficient enough that those criteria, alone, were inadequate to disqualify any of the remaining agents. The relative weighting of the suppression and dispersion criteria depended upon the application; *i.e.*, full-scale engine nacelle or dry bay testing.

10.2.1.1 For Full-scale Simulated Engine Nacelle Testing. The release of the agent into the engine nacelle is crew-initiated, and the agent is normally distributed to different engines or regions of a single nacelle via piping manifolds. The fire is relatively slowly growing, and conditions which favor the transition to a detonation are unlikely to be present. The highest premium is placed upon fire suppression efficiency (low VF) for the three atmospheric pressure test flames. The time for dispersion is relatively long, so that heat is transferred from the air to the spray to assist vaporization. Thus, T_{min} is more appropriate than Ja as a measure of dispersion effectiveness. Table 4 summarizes these parameters and the recommended action for each agent regarding full-scale engine nacelle

Table 4. Ranking of agents for full-scale engine nacelle test matrix

Agent	Average VF	T_{min}	Environmental Factors	Operational Issues	Recommendation
HCFC-124	2.2	+ 28 °C	-	+	test
HFC-125	3.0	- 6 °C	+	+	test
FC-218	2.8	- 7 °C	-	+	1st back-up
HFC-227ea	2.5	+ 19 °C	+	+	2nd back-up
$NaHCO_3$	0.5	powder	+	-	partial test matrix
CF_3I	0.8	- 1 °C	0	-	partial test matrix

testing. A "+" indicates overall positive attributes in that category and a "-" indicates that there is at least one serious concern in applying the agent.

The volume factor for the HCFC-124 is the lowest of all the core agents evaluated. Full-scale testing at low temperatures is required to ascertain if a T_{min} of + 28 °C might hamper the agent's effectiveness. The negative environmental factor is the non-zero ODP of the chlorine-containing compound. Nonetheless, HCFC-124 is recommended for full-scale testing, especially to see if the low volume factor is validated.

HFC-125 and FC-218 have similar values for T_{min} and only slightly different values for VF. The HFC-125 is a more conservative choice for full-scale testing because the FC-218 has a much longer atmospheric lifetime. HFC-227ea is a logical back-up because it has the second best volume factor.

Sodium bicarbonate has a volume factor half the size of halon 1301, and less than 1/4 the best of the core agents. There are three concerns with using sodium bicarbonate:

1. powders do not disperse as effectively as gases; hence, the performance of $NaHCO_3$ is likely to be lower in an engine nacelle than is indicated by the bench-scale tests;

2. NaOH, a by-product of the suppression process, reacts strongly with aluminum, which leads to the corrosion of exposed aluminum surfaces; and

3. high temperature storage leads to a deterioration of the flow properties of the powder.

Full-scale engine nacelle tests could determine if the first concern is warranted. In connection with the second concern, it should be ascertained whether the nacelle exhaust would put decomposition products in contact with aluminum. If so, aluminum test coupons strategically placed in the engine nacelle test fixture could be used to assess the significance of corrosion. The third problem

requires additional research to determine the best solution, but it is unlikely, by itself, to be a cause for rejecting sodium bicarbonate.

Iodotrifluoromethane also has a volume factor less than halon 1301. It leaves little residue (if it is pure) and appears to have a short tropospheric lifetime. Only a limited full-scale test matrix is recommended because:

1. greatly increased production levels are required to meet the full-scale test program and fleet needs;

2. toxicity, stability and corrosion test results are incomplete, and

3. detailed atmospheric chemistry and the implications of stratospheric release need to be further investigated.

10.2.1.2 For Full-scale Simulated Dry Bay Testing. Different criteria apply to the performance of an agent in dry bay fire suppression. Here, time is of the essence. Agent release is initiated automatically within milliseconds of a sensed threat. Following ignition, the heat release can create increases in pressure if expansion is restricted, leading to flame acceleration, the generation of turbulence due to high speed flow over obstructions, and the possibility of a strong shock wave. Effectiveness in damping the pressure build-up in the detonation/deflagration tube, averaged with the results in the spray burner, was used to determine an appropriate volume factor for the dry bay. Because the discharge occurs so quickly, there is no time for heat transfer from the surrounding air to vaporize the liquid agent; hence, the rankings on dispersion from Section 3.5 apply. The environmental factors and operational issues are identical to the engine nacelle application, but differences in the amount of agent released in a year and the cleanup procedure following a false discharge affect the way this information is factored into the recommendations. Table 5 gives the ranking of the remaining agents for full-scale simulated dry bay fire testing.

FC-218 and HFC-125 are recommended for testing because they have the highest Jakob numbers. None of the core agents has a volume factor below FC-218. The negative associated with long atmospheric life is of less concern for dry bay applications because the total annual release is much lower than in engine nacelle applications. HFC-125 had a slightly higher VF than FC-218, and produced high over-pressures in the detonation/deflagration tube at concentrations below the suppression level. Testing is recommended, but should similar over-pressures be observed in the simulated dry bay, then HFC-227 is the recommended back-up. The VF for HCFC-124 is the same as for FC-218, but the HCFC is difficult to vaporize. Considering that it has a non-zero ODP, FC-218 remains the better choice.

The CF_3I has a VF only 10% greater than halon 1301, but a very low Jakob number. A unique pressure/concentration behavior was observed with this agent in the detonation/deflagration tube which needs further investigation. If sufficient supplies of CF_3I can be arranged, full-scale testing in the simulated dry bay is recommended, especially at low temperatures. The ongoing toxicity, stability, corrosion and atmospheric chemistry studies should be closely monitored. When one compares VF in the engine nacelle and dry bay applications, the difference in performance between CF_3I and the best core agent is much greater in the engine nacelle application. Adding in the low Ja number makes CF_3I somewhat less attractive for the dry bay application.

The recommendation against sodium bicarbonate in the dry bay program is based upon the much higher premium placed on dispersion to counter the fire threat. A destructive fire can develop in tens of milliseconds, requiring that the fire suppressing agent be distributed throughout the volume in an equivalent time. The gasified agents can easily penetrate a reasonable amount of clutter in the dry

Table 5. Ranking of agents for full-scale dry bay test matrix

Agent	Average VF	Sect 3.5 Rank	Environmental Factors	Operational Issues	Recommendation
FC-218	1.6	1	-	+	test
HFC-125	1.8	1	+	+	test
HFC-227ea	1.6	6	+	+	1st back-up
HCFC-124	1.6	7	-	+	do not test
CF_3I	1.1	not ranked	0	-	partial test matrix
$NaHCO_3$	incomplete data	powder	+	-	do not test

bay, but powders can impact and stick on surfaces and do not follow the carrier gas streamlines, greatly reducing the mass of material which actually is delivered to the fire zone. Clean-up could be more difficult in the dry bay, and since exposed aluminum surfaces are likely to be plentiful, they would be susceptible to NaOH corrosion.

A summary of the recommendations for all of the core agents, CF_3I and $NaHCO_3$ is given in Table 6. The inter-governmental technology transition team will weight the NIST recommendations with other practical concerns to arrive at the final set of chemicals for full-scale testing.

10.3 Ongoing Studies

The original research program begun in 1992 contained several projects which were to continue beyond September 30, 1993. These tasks were designed to enhance the selection and use of the optimal suppressant(s). Intermediate data will be available late in 1994 to assist the sponsors in evaluating the three candidate suppressants for each application. Knowledge developed during the continuation period will guide optimal use of agents selected for deployment.

10.3.1 By-Product Formation.

10.3.1.1 Instability Under Storage. In the one-month exposures, HFC-125, FC-218 and HCFC-227 showed no decomposition at 150 °C in the presence of any of the eight metals. By contrast, CF_3I did show some iodine formation and metals discoloration at 150 °C. During the next two years, the four selected chemicals will be exposed for about 18 months at three temperatures (22, 125, and 150 °C) to three metals: Nitronic-40 (21-6-9 stainless steel), 304 austenitic stainless steel, and titanium 15-3-3-3.

Table 6. Summary of recommended actions by agent

Agent	Recommended Actions	Cautions
HFC-125	Perform full-scale test matrix in nacelle. Screen for high pressures in dry bay, and complete matrix if pressure is not a problem.	Over-pressures may occur in dry bay tests.
HCFC-124	Perform full test matrix in engine nacelle simulator.	Note high T_{min} and non-zero ODP. Care needed when choosing elastomers to reduce chance of swelling.
FC-218	Perform full test matrix in dry bay simulator. Use as a back-up for engine nacelle.	Long atmospheric lifetime, properties of greases affected at high temps.
HFC-227ea	Consider it as a back-up to HFC-125 in engine nacelle and dry bay test program.	Relatively high T_{min} may limit dispersion
$NaHCO_3$	Test in engine nacelle simulator. Truncate test matrix if mass concentrations consistently exceed HFC-125.	Complications associated with powders (particle dispersion, corrosive by-products of combustion, high temperature storage) need to be off-set by superior full-scale fire suppression effectiveness to warrant fleet adoption.
CF_3I	Perform reduced test matrix in engine nacelle simulator to verify superior performance. Perform tests in dry bay consistent with availability of chemical.	Supply for testing limited; pilot scale production capability for 1995 not proven; toxicity, atmospheric chemistry, stability, and materials compatibility not fully documented
HFC-134a	Not recommended for full-scale testing.	Mediocre performance compared to alternative HFCs, higher HF levels
FC-116	Not recommended for full-scale testing.	Critical temperature below ambient limits storage
HFC-236fa	Not recommended for full-scale testing.	High T_{min} limits dispersion
HCFC-22	Not recommended for full-scale testing.	Incompatible with many materials, non-zero ODP
FC-31-10	Not recommended for full-scale testing.	High T_{min}, some materials incompatibility
FC-318	Not recommended for full-scale testing.	High T_{min}, materials issues
HFC-32/125	Not recommended for full-scale testing.	High over-pressure, high VF
HFC-32	Not recommended for full-scale testing.	Flammable

These were selected in conjunction with the sponsors and the manufacturers of suppression storage containers and systems. Samples will be analyzed for decomposition every 1 to 2 months using FTIR, with stretched intervals if no decomposition is observed.

CF_3I will be exposed to the same three metals, with and without the presence of metallic copper, a suggested inhibitor of the agent's decomposition, and perhaps at a fourth temperature. We expect that FTIR analyses will need to be supplemented by gas chromatography, mass spectroscopy or a combination of the two.

Should there be any decomposition of any of the chemicals in the presence of any of the metals, approximate first-order decomposition rate constants will be determined. These results will enable

evaluation of the viability of storing this chemical for extended periods. Alternatively, the results can be used to determine how often cylinders will need to be refilled. The work will be completed by September, 1995.

10.3.1.2 Combustion By-Products. The objective of this project is to develop an understanding of acid gas formation in hydrocarbon flames suppressed by three halon 1301 replacements, HFC-125, HFC-227 and HFC-218. This will provide the basis for a predictive capability for the amount of acid gas formed during the suppression of dry bay and engine nacelle fires, allowing the rank ordering of the three agents with respect to by-product production for these situations. CF_3I will be tested to verify that the amounts of HF formed are comparable to that formed with CF_3Br.

The general approach is to obtain global information on the final products in simple burners which permit operation over a range of conditions imitating those of dry bay and engine nacelle fires. This will allow examination of the effects of fuel and inhibitor structure and concentration. Fluid dynamic effects will be examined through a comparison of diffusion and premixed flames under laminar and turbulent conditions. Since the characteristic time for chemistry is on the order of one millisecond, and fluid dynamic times are usually longer, the chemistry important in HF formation can be studied under steady-state configurations more amenable to species sampling and variation of the individual operating parameters over a range of conditions which simulate those estimated for the dry bay and engine nacelle fires. The results from the steady-state measurements will then be used to predict the HF formed in flames suppressed under transient conditions. To test these predictions, experiments will be conducted where the agent is added rapidly to a flame so that the flame extinguishes, and the HF formed will be measured. These results will be compared to the predictions based on the steady-state measurements.

A second component will develop correlations, based on experimental results and global properties, of acid gas formation in inhibited flames based on inhibitor chemical formula and concentration, fuel type and consumption rate and flame type. The extent of the correlations will depend upon the importance of the chemical kinetic rates of inhibitor and inhibitor fragment decomposition. Measuring the concentration of acid gases formed in the flames described above and comparing these with the estimated concentrations from a simple global model will help elucidate the degree of kinetic control in the acid gas formation process.

Third, we will develop understanding of the chemical mechanism of acid gas formation in hydrocarbon flames to provide a fundamental basis for a true predictive capability. This entails (a) detailed numerical calculations of flame structure using a chemical kinetic code and (b) validation of the mechanism through comparison of model predictions and experimental measurements of temperature and species concentrations in the flame. The latter will be obtained in a laboratory flame using micro-probe gas sampling with mass spectrometry.

10.3.2 Metals Corrosion. The recent data show that a selection of metals are compatible with the down-selected chemicals over a one-month period. Additional testing will be conducted to enable judgments concerning relative performance of the chemicals over their storage lives in the suppression system.

Samples of the three metals will be exposed to the four chemicals plus halon 1301 at both ambient temperature and 150 °C at 5.4 MPa. Periodic (initially monthly) examination will provide a time history of the advancing of any corrosive effects. Slow strain rate tensile tests will be performed at ambient conditions and 150 °C and 5.4 MPa to provide information relating to liquid phase interactions.

Electrochemical experiments of the three metals and four chemicals will be conducted to:

- improve the quality of corrosion ratings by helping to resolve the scientific uncertainties inherent in short-term exposure tests;

- enable assessment of the effects of variations in the exposure conditions that could cause rapid runaway corrosion that would otherwise be missed by the exposure test matrix due to the time limitations; and

- enable assessment of the potential for galvanic attack and local breakdown of protective films to a level not possible with exposure tests.

It is also important to assess the potential for damage from the combustion by-products of the suppressants. Thirty-day surface exposures of key metals (identified by the sponsors) will be conducted in aqueous solutions of HF. Up to three concentrations will be used, depending upon the magnitude of the predicted difference in acid production for the four chemicals. The studies will be conducted at ambient temperature and pressure.

10.3.3 Compatibility with Seals and Elastomers. The recent research showed some differentiation among the chemicals in their interactions with the selected elastomers and greases, and these were factored into the down-selection process. It was also observed that the 150 °C exposures resulted in degradation of many of the seal materials by some of the chemicals. Subsequent information from the Air Force indicated that all-metal storage is used for exposures above about 70 °C.

In the continuing research, mechanical property measurements and additional short-term exposures will be performed at 50, 75, and 100 °C for the four agents and seven elastomers, the original six plus an ethylene-propylene-diene terpolymer (EPDM). These will enable a valid activation energy analysis over the full temperature range of interest. Compression set measurements and tensile testing (ultimate elongation, tensile strength, and modulus at 100% elongation) will be conducted after exposure times of 1, 2, and 4 weeks. The analysis of these measurements using an activated process model will provide reliable estimates of the elastomer resistance to the fluid exposure in service conditions.

Since CF_3I was not included in the initial experimental plan, swelling measurements will be conducted at 35, 70, 105, and 150 °C for all elastomers (crosslinked/uncrosslinked sets of fluorocarbon, standard and low temperature nitrile, silicone, fluorosilicone, and neoprene) and greases (Braycote 600, Krytox 240AC, Braycote 807) at four different vapor pressures. Swelling measurements on a crosslinked/uncrosslinked set of EPDM rubber will also be performed.

Following completion of the above studies, samples of seven elastomers will be exposed for about 18 months to the four fluids at 75 °C. Tensile testing and compression set measurements will be made after 8, 16, 32, 48 and 78 weeks.

10.4 Complementary Research Underway

There are additional projects now beginning at NIST that will provide knowledge important to the implementation of an agent selection decision. The objectives are summarized in this section.

10.4.1 Discharge Optimization. The research documented above shows that the effectiveness of a fire-fighting agent can depend as much on how the material is delivered to the fire zone as it does on its molecular composition. A particular chemical which leads to flame extinction in a laboratory

burner at very low concentrations may, in fact, be a poorer choice than one which exhibits no chemical activity if the inert material can be transported to the critical portions of an actual fire in a much more efficient manner. This project will develop the understanding needed to ensure that the agents chosen by the inter-governmental technology transition team for full-scale testing are delivered to the fire in an efficient manner so that an unbiased evaluation of system effectiveness can be made. The generic scientific data will also aid fire suppression system suppliers and airframe manufacturers in their efforts to design protective systems for existing and future aircraft. To accomplish this, NIST will:

- determine the practical limits to the design of system hardware which constrain what can be done;

- expand temperature-pressure data on the recommended fluids, pure and in mixtures with nitrogen, to enable the development of correlations for total pressure as a function of fill density and temperature for pressures up to 40 MPa;

- for dry bay applications, determine how the initial conditions in the storage bottle and the design of the release mechanism and exit orifice can be modified to enhance the discharge rate of the recommended fluid agents directly into an unconfined space; and

- for engine nacelle applications, determine the performance of the recommended fluid agents flowing through various piping geometries and components in transient operation.

10.4.2 Alternative Agent Concentration Monitors. It is essential to know that the fire suppression system will deliver an appropriate concentration of suppressant to the regions where a fire might occur. This requires a probe capable of extremely fast (milliseconds) measurements at many points. Our research has indicated that the initial flows may be either liquid or two-phase and that the mixing patterns are extremely complex.

The objective of this effort is to evaluate possible methods for real-time measurements of concentrations of alternative fire fighting agents for dry bay and nacelle fire applications. No analytical measurement techniques have yet been applied to such a complex problem. It will therefore be necessary to extend current measurement techniques or to develop completely new approaches. If one or more feasible approaches are identified early in the investigation, a demonstration system will be developed for characterization under actual test situations. This will be accomplished as follows:

- search the concentration measurement literature to identify measurement techniques for the required concentration measurements and two-phase flow characterization and recommend approaches for further research;

- test and evaluate an infrared sensing instrument recently developed by a company under contract to the Air Force for measuring alternative agent concentrations; and

- conduct theoretical and experimental feasibility evaluation of aspirated hot-film probes, recommending whether to pursue further development of this measurement technique.

10.4.3 Engine Nacelle Simulations. There are a number of different aircraft and operating conditions for which a new suppressant for nacelle fires is needed. Because testing cannot be performed

for all possible aircraft and conditions, knowledge is needed which will provide guidance in the extension of the Wright Patterson AFB full-scale data to untested systems and conditions.

Extinguishment occurs when a critical amount of agent is transported to the flame, where it is entrained into the primary reaction zone. The extinction process is affected by a number of parameters, including the velocity of the air flow, the type and quantity of fuel, the system temperature, agent properties and concentration, and the flow field geometry (*e.g.*, the location of obstacles in the flow field). Re-ignition is also dependent on these system parameters and should be considered independently from the extinction phenomena.

The objective of this research is to produce organized guidance for adjusting the needed concentration of candidate fire suppressants over a range of engine nacelle fire conditions. This will include

- review of the range of parameters which characterize the temperature and flow field in various engine nacelle types in an effort to understand better the possible fire scenarios and to develop an appropriate test program;

- use of the coaxial spray burner described earlier to measure (in a well-controlled and reduced-scale environment) the effects of air flow, air temperature, fuel flow, pre-burn time, system pressure, agent type (CF_3I, HFC-125, and HFC-227ea), rate of application, and the flow field geometry (*e.g.*, effect of an obstacle in the flow field) on the amount of chemical needed to suppress a fuel-spray fire;

- measurement of the impact of increased agent temperature on flame stability;

- computational modeling and optimizing the agent concentration as a function of location, rate, and orientation of agent injection, including possible multiple-location injection and differences in nacelle geometry, with wind tunnel validation; and

- compilation of the knowledge and data gained through the study into tools to assist suppression system designers, including information regarding concentration/duration requirements as a function of fire zone conditions.

The engine nacelle simulations will complement and provide guidance to the ongoing full-scale effort at Wright-Patterson.

10.5 Recommendations for Further Research

A significant amount of resources, effort, and science have gone into selecting the best candidates for full-scale evaluation, and it is expected that the additional testing at Wright-Patterson AFB will be successful in identifying one or two chemicals which will be suitable for replacing halon 1301 for in-flight suppression of engine nacelle and dry bay fires. It is equally likely that some inconsistencies will be revealed in scaling up one hundred-fold from the laboratory apparatus to the actual test articles.

More understanding is required of the fundamental principles controlling the suppression of a turbulent flame, the dispersion of a vaporizing spray in an enclosure, the chemistry of halogenated species in the flame and in the atmosphere, and modeling the interaction of all these phenomena to

increase the generality of the laboratory results and suggest improvements in the full-scale test protocol. Specifically, pursuit of the following topics is recommended:

- Inhibition mechanisms by both halocarbons and non-halogenated entities, including chemical kinetics measurements, studies of flame chemistry and dynamics, and computer modeling of chemically perturbed combustion.

- Innovative suppression, such as by non-intrusive flame perturbations or species chemically generated *in situ*.

- Atmospheric chemistry of flame extinguishants other than chlorinated and brominated species, including laboratory measurements of the rate processes and computer modeling of the atmospheric impacts.

- Turbulent two-phase flow, both experimental characterization and numerical modeling of the dynamics.

- Standardized suppression test methods at both small and medium scale, including the appropriate instrumentation.

True understanding of a phenomenon requires a sustained effort, and the flexibility to allow research to explore multiple paths. In the environment of continuously changing regulations and evolving technologies, the understanding which would be generated by the above research is essential so that optimal agents and suppression strategies can be developed in a rational and efficient manner.